

Criteria 3

Research, Innovations and Extension

Key Indicator 3.3

Research Publication and Awards

3.3.1 Number of research papers published per teacher in the Journals notified on UGC website during the last five years



Rajarshi Shahu
College of Pharmacy

Journey Towards Academic Excellence

3.3.1 Number of research papers published per teacher in the Journals notified on UGC website during the last five years

2021-2022

Sr. No.	Title of paper	Name of the author/s	Department of the teacher	Name of journal	Impact Factor	Page No. with Link
1	A recurrent rare intronic variant in CAPN3 alters mRNA splicing and causes autosomal recessive limb-girdle muscular dystrophy-1 in three Pakistani pedigrees	Kamal Khan, Sarmad Mehmood, Chunyu Liu, Maimoona Siddiqui, Arsalan Ahmad, Belqees Yawar Faiz, Barry A Chioza, Emma L Baple, Muhammad I Ullah, Zaineb Akram, Humayoon S Satti, Raees Khan, Gaurav V Harlalka , et al.	Pharmacology	Am J Med Genet A . 2022 Feb;188(2):498-508. (Doi: 10.1002/ajmg.a.62545.)	2.578	<u>01</u>
2	Evidence that the Ser192Tyr/Arg402Gln in cis Tyrosinase gene haplotype is a disease-causing allele in oculocutaneous albinism type 1B (OCA1B)	Siying Lin, Aida Sanchez-Bretaña, Joseph S. Leslie, Katie B. Williams, Helena Lee, N. Simon Thomas, Jonathan Callaway, James Deline, J. Arjuna Ratnayaka, Diana Baralle, Melanie A. Schmitt, Chelsea S. Norman, Sheri Hammond, Gaurav V. Harlalka , Sarah Ennis, et al.	Pharmacology	npj Genomic Medicine (2022) 7:2	6.09	<u>12</u>
3	Role of L-lysine in Ethanol Induced Behavioral Changes in Mice	Sumit Rathod, Vinay Bhalerao, Mangesh Deokar , Shirish Jain	Pharmacology	International Journal of Toxicological and Pharmacological Research 2022; 12(1);36-42	0	<u>23</u>
4	Role of L-lysine in Ethanol Induced Behavioral Changes in Mice	Sumit Rathod, Vinay Bhalerao, Mangesh Deokar , Shirish Jain	Pharmacology	International Journal of Toxicological and Pharmacological Research 2022; 12(1);36-42	0	<u>30</u>

Sr. No.	Title of paper	Name of the author/s	Department of the teacher	Name of journal	Impact Factor	Page No. with Link
5	Calcium Ion-Sodium Alginate-Piperine Based Microspheres: Evidence of Enhanced Encapsulation Efficiency, Bio-adhesion, Controlled Delivery and Oral Bioavailability of Isoniazid	Darshan R Telange, Ravindra R Pandharinath, Anil M Pethe, Shirish P Jain	Pharmaceutics	AAPS PharmSciTech (Accepted)	4.026	37
6	Biallelic variants in TRAPPC10 cause a microcephalic TRAPPopathy disorder in humans and mice	Lettie E. Rawlins, Hashem Almousa, Shazia Khan, Stephan C. Collins, Miroslav P. Milev, Joseph Leslie, Djenann Saint-Dic, Valeed Khan, Ana Maria Hincapie, Jacob O. Day, Lucy McGavin, Christine Rowley, Gaurav V. Harlalka , Valerie E. Vancollie, et al.	Pharmacology	PLoS Genet 18(3): e1010114	6.02	55
7	Explorations of novel pyridine-pyrimidine hybrid phosphonate derivatives as aurora kinase inhibitors	Shailee V. Tiwari, Aniket P. Sarkate, Deepak K. Lokwani , Dattatraya N. Pansare, Surendra G. Gattani, Sameer S. Sheaikh, Shirish P. Jain, Shashikant V. Bhandari	Pharmaceutical Chemistry	Bioorg. Med. Chem. Lett. 67 (2022) 128747	2.94	76
8	Explorations of novel pyridine-pyrimidine hybrid phosphonate derivatives as aurora kinase inhibitors	Shailee V. Tiwari, Aniket P. Sarkate, Deepak K. Lokwani, Dattatraya N. Pansare, Surendra G. Gattani, Sameer S. Sheaikh, Shirish P. Jain , Shashikant V. Bhandari	Pharmaceutical Chemistry	Bioorg. Med. Chem. Lett. 67 (2022) 128747	2.94	83
9	Analytical Standardization and Profiling of Ayush-64: An Ayurvedic Tablet Formulation	Sarang J. Deshpande, Prakash N. Kendre and Abhishek R. Patle	Pharmaceutics	Indian Drugs , 2022, 59, 02, 36-42	0.17	90

Sr. No.	Title of paper	Name of the author/s	Department of the teacher	Name of journal	Impact Factor	Page No. with Link
10	Molecular Dynamic Simulations based Discovery and Development of Thiazolidin-4-one derivatives as EGFR inhibitors targeting resistance in Non-Small Cell Lung Cancer (NSCLC)	Kshipra S. Karnik, Aniket P. Sarkate, Deepak K. Lokwani , Shailee V. Tiwari, Rajaram Azad, , Pravin S. Wakte	Pharmaceutical Chemistry	Journal of Biomolecular Structure and Dynamics (Available online)	5.325	<u>99</u>
11	Effect of Hydrophilic Polymer on the Design Expert Assisted Oro-dispersible Strip (ODS)of Isosorbide Mononitrate	Prakash N. Kendre , Akash R. Aher, Somnath K. Vibhute, Ajinkya K. Pote, Subhash V. Deshmane and Shirish P. Jain	Pharmaceutics	Indian Drugs (Accepted)	0.17	<u>115</u>
12	Effect of Hydrophilic Polymer on the Design Expert Assisted Oro-dispersible Strip (ODS)of Isosorbide Mononitrate	Prakash N. Kendre , Akash R. Aher, Somnath K. Vibhute, Ajinkya K. Pote, Subhash V. Deshmane and Shirish P. Jain	Pharmaceutics	Indian Drugs (Accepted)	0.17	<u>120</u>
13	Effect of Hydrophilic Polymer on the Design Expert Assisted Oro-dispersible Strip (ODS)of Isosorbide Mononitrate	Prakash N. Kendre, Akash R. Aher, Somnath K. Vibhute, Ajinkya K. Pote, Subhash V. Deshmane and Shirish P. Jain	Pharmaceutics	Indian Drugs (Accepted)	0.17	<u>125</u>
14	Effect of Hydrophilic Polymer on the Design Expert Assisted Oro-dispersible Strip (ODS)of Isosorbide Mononitrate	Prakash N. Kendre, Akash R. Aher, Somnath K. Vibhute, Ajinkya K. Pote, Subhash V. Deshmane and Shirish P. Jain	Pharmaceutics	Indian Drugs (Accepted)	0.17	<u>130</u>
15	Phytochemicals: A Novel Approach for the Management of Coronavirus Disease 2019	R. S. Shivatare, R. Musale, N. K. Bhutale, S. M. Kewatkar , H. L. Tare , Vibhavari Chatur , A. N. Khatawakar And D. S. Suryavanshi	Pharmaceognosy	Indian Journal of Pharmaceutical Science 2022, 84(03), 519-531	0.97	<u>135</u>

Sr. No.	Title of paper	Name of the author/s	Department of the teacher	Name of journal	Impact Factor	Page No. with Link
16	Mutations in MINAR2 encoding membrane integral NOTCH2 associated receptor 2 cause deafness in humans and mice.	Guney Bademci , María Lachgar-Ruiz , Mangesh Narayan Deokar , Mohammad faraz Zafeer , Clemer Abad , Muzeyyen Yildirim Baylan , Neil J Ingham , Jing Chen , Claire J Sineni , Nirmal Vadgama , Ioannis Karakikes , Shengru Guo , Duygu Duman , Nitu Singh , Gaurav Harlalka, Shirish P Jain, Barry A Chioza , Katherina Walz , Karen P Steel , Jamal Nasir , Mustafa Tekin	Pharmacology	PNAS (Accepted)	12.779	<u>148</u>
17	Mutations in MINAR2 encoding membrane integral NOTCH2 associated receptor 2 cause deafness in humans and mice.	Guney Bademci , María Lachgar-Ruiz , Mangesh Narayan Deokar , Mohammad faraz Zafeer , Clemer Abad , Muzeyyen Yildirim Baylan , Neil J Ingham , Jing Chen , Claire J Sineni , Nirmal Vadgama , Ioannis Karakikes , Shengru Guo , Duygu Duman , Nitu Singh , Gaurav Harlalka , Shirish P Jain, Barry A Chioza , Katherina Walz , Karen P Steel , Jamal Nasir , Mustafa Tekin	Pharmacology	PNAS (Accepted)	12.779	<u>159</u>



Sr. No.	Title of paper	Name of the author/s	Department of the teacher	Name of journal	Impact Factor	Page No. with Link
18	Mutations in MINAR2 encoding membrane integral NOTCH2 associated receptor 2 cause deafness in humans and mice.	Guney Bademci , Maria Lachgar-Ruiz , Mangesh Narayan Deokar , Mohammad faraz Zafeer , Clemer Abad , Muzeyyen Yildirim Baylan , Neil J Ingham , Jing Chen , Claire J Sineni , Nirmal Vadgama , Ioannis Karakikes , Shengru Guo , Duygu Duman , Nitu Singh , Gaurav Harlalka, Shirish P Jain , Barry A Chioza , Katherina Walz , Karen P Steel , Jamal Nasir , Mustafa Tekin	Pharmacology	PNAS (Accepted)	12.779	170
19	Polymeric nanoparticles: Prospective on the synthesis, characterization and applications in nose-to-brain drug delivery	Prakash N. Kendre , Dhiraj R. Kayande, Shirish P. Jain, Tejaswini G. Malge, Namrata N. Zadpe and Bhupendra G. Prajapati	Pharmaceutics	Current Nanoscience (Accepted)	1.513	181
20	Polymeric nanoparticles: Prospective on the synthesis, characterization and applications in nose-to-brain drug delivery	Prakash N. Kendre, Dhiraj R. Kayande , Shirish P. Jain, Tejaswini G. Malge, Namrata N. Zadpe and Bhupendra G. Prajapati	Pharmaceutics	Current Nanoscience (Accepted)	1.513	195
21	Polymeric nanoparticles: Prospective on the synthesis, characterization and applications in nose-to-brain drug delivery	Prakash N. Kendre, Dhiraj R. Kayande, Shirish P. Jain , Tejaswini G. Malge, Namrata N. Zadpe and Bhupendra G. Prajapati	Pharmaceutics	Current Nanoscience (Accepted)	1.513	209
22	Design, synthesis, and pharmacological evaluation of [1, 3] dioxolo-chromeno[2,3-b]pyridines as anti-seizure agents	Visarapu Malathi, Nissi Sharon, Pannala Padmaja, Deepak Lokwani , Saurabh Khadse, Prashant Chaudhari, Atul A. Shirkhedkar, Pedavenkatagari Narayana Reddy & Vinod G. Ugale	Pharmaceutical Chemistry	Molecular Diversity (Accepted)	3.364	223

Sr. No.	Title of paper	Name of the author/s	Department of the teacher	Name of journal	Impact Factor	Page No. with Link
23	Potential Herbal Anti-Cancer Drug Formulations Using Modern Drug Delivery Methods	Chirag Goda, Ashish Kandalkar, Manish Bhise, Vinod Kumar Tiwari, Sanjay Vasu, Sunny Pahuja, Sandip Hurdade, Balaji Thakare and Satish Shelke	Pharmaceutical Chemistry	Asian Journal of Organic & Medicinal Chemistry, 2022, 7, 552-562	0	242
24	A Study on Medicinal Plants and Its Hepatoprotective Activity	Dr. Ajay Sharma, Dr. Shailesh M. Kewatkar , Mr. Dipak Vikram Bhusari, Dr. Manmeet Singh, Dr. Gaurav Jain, Mr. Salaj Khare, Miss. Vidhi Jain	Pharmacognosy	Jundishapur Journal of Microbiology, 2022, 15, 154-163	0.747	253
25	Design, synthesis, and biological evaluation of novel quinoline derivatives as small molecule mutant EGFR inhibitors targeting resistance in NSCLC: In vitro screening and ADME predictions	Ramakant A. Kardile, Aniket P. Sarkate, Deepak K. Lokwani , Shailee V. Tiwari, Rajaram Azad, Shankar R. Thopate	Pharmaceutical Chemistry	European Journal of Medicinal Chemistry 245 (2023) 114889	7.088	263
26	Formulation Development and Evaluation of Herbal Nanoparticles containing Ointment of Leaves extract of <i>Rhynchosia rothii</i>	Sharad D. Tayade , Narendra Silawat, Neetesh Jain	Pharmaceutics	Journal of Pharmaceutical Negative Results, 2022, 13, 724-738	0	281
27	RP-HPLC Method Development and Validation of Pharmaceutical Tablet Dosage Form Containing Ambrisentan	Rupali M. Petkar, Subhash V. Deshmane , Snehal S. Deshmane and Shirish P. Jain	Pharmaceutics	INDIAN DRUGS 59 (09) SEPTEMBER 2022, 94-97	0.17	296
28	RP-HPLC Method Development and Validation of Pharmaceutical Tablet Dosage Form Containing Ambrisentan	Rupali M. Petkar, Subhash V. Deshmane, Snehal S. Deshmane and Shirish P. Jain	Pharmaceutics	INDIAN DRUGS 59 (09) SEPTEMBER 2022, 94-97	0.17	300

Sr. No.	Title of paper	Name of the author/s	Department of the teacher	Name of journal	Impact Factor	Page No. with Link
29	RP-HPLC Method Development and Validation of Pharmaceutical Tablet Dosage Form Containing Ambrisentan	Rupali M. Petkar, Subhash V. Deshmane, Snehal S. Deshmane and Shirish P. Jain	Pharmaceutics	INDIAN DRUGS 59 (09) SEPTEMBER 2022, 94-97	0.17	304
30	To Enhance The Solubility of Ivermectin With Physical Mixing Method For The Preparation Of Orodispersible Tablets	Vaishali Adsare, Lokhande Rahul Prakash, Pallavi Gholap, Sangameshwar Baburao Kanthale , Shubham Choudante	Pharmaceutics	Journal of Pharmaceutical Negative Results, 2022, 13, 964-971	0	308
31	Molecular Docking Studies and Application of 6-(1-Arylmethanamino)-2-Phenyl-4H-Chromen-4-Ones as Potent Antibacterial Agents	Nitin M. Thorat, Vinnayak S. Khodade, Ajit P. Ingale, Deepak K. Lokwani , Aniket P. Sarkate & Shankar R. Thopate	Pharmaceutical Chemistry	Polycyclic Aromatic Compounds (available Online)	2.195	316
32	Drug-Repurposing Of Some COX-2 Inhibitors As Potential Glucokinase Activators For The Treatment Of T2DM	Badrud Duza Mohammad, Ramsha Aslam, Shyamlila B. Bavage, Vijay Putta, Nandkishor Dinkarrao Gawhale, Shailejkumar D Bonde, Rihana Begum Patnool, Vikram Nirmal Sancheti	Pharmaceutics	Journal of Pharmaceutical Negative Results, 2022, 13, 9, 4550	0	331
33	Preparation And Release Characteristic For Eudragit Coated Chitosan Microsphere For 5-Fluorouracil	Mr. Dipak V. Bhusari, Dr. Shailesh M. Kewatkar , Amol Nanduji Jaybhaye, Dr. Koshish B. Gabhane, Girijesh Kumar Pandey, Dr Manmeet S.Saluja, Dr. Shirish P.Jain, Mrs Neelam M Patel	Pharmacognosy	NeuroQuantology, 2022, 20, (19), 3157-3170	0	339

Sr. No.	Title of paper	Name of the author/s	Department of the teacher	Name of journal	Impact Factor	Page No. with Link
34	Preparation And Release Characteristic For Eudragit Coated Chitosan Microsphere For 5-Fluorouracil	Mr. Dipak V. Bhusari, Dr. Shailesh M. Kewatkar, Amol Nanduji Jaybhaye, Dr. Koshish B. Gabhane, Girijesh Kumar Pandey, Dr Manmeet S. Saluja, Dr. Shirish P.Jain , Mrs Neelam M Patel	Pharmacognosy	NeuroQuantology, 2022, 20, (19), 3157-3170	0	353
35	Formulation And Comparison Between Two Methods For 5-Fluorouracil-Loaded Chitosan Microspheres	Mr. Dipak V. Bhusari, Dr. Shailesh M. Kewatkar , Amol Nanduji Jaybhaye, Puja G. Vyawahare, Yogita Mahesh Vispute, Dr. Manmeet S. Saluja, Dr. Shirish P. Jain, Mrs. Neelam M Patel	Pharmacognosy	NeuroQuantology, 2022, 20, (19), 3171-3181	0	367
36	Formulation And Comparison Between Two Methods For 5-Fluorouracil-Loaded Chitosan Microspheres	Mr. Dipak V. Bhusari, Dr. Shailesh M. Kewatkar, Amol Nanduji Jaybhaye, Puja G. Vyawahare, Yogita Mahesh Vispute, Dr. Manmeet S. Saluja, Dr. Shirish P.Jain , Mrs. Neelam M Patel	Pharmacognosy	NeuroQuantology, 2022, 20, (19), 3171-3181	0	378

A recurrent rare intronic variant in *CAPN3* alters mRNA splicing and causes autosomal recessive limb-girdle muscular dystrophy-1 in three Pakistani pedigrees

Kamal Khan^{1,2,3,4} | Sarmad Mehmood⁵ | Chunyu Liu⁶ | Maimoona Siddiqui⁷ | Arsalan Ahmad⁷ | Belqees Yawar Faiz⁷ | Barry A. Chioza⁸  | Emma A. Baple⁸ | Muhammad I. Ullah⁹ | Zaineb Akram¹⁰ | Humayoon S. Satti¹¹ | Raees Khan¹¹ | Gaurav V. Harlalka^{8,12} | Muhammad Jameel³ | Talia Akram^{3,4} | Shahid M. Baig^{3,4,13,14} | Andrew H. Crosby⁸ | Muhammad J. Hassan^{5,11} | Feng Zhang⁶ | Erica E. Davis^{1,2,15,16}  | Tahir N. Khan^{1,11}

¹Center for Human Disease Modeling, Duke University Medical Center, Durham, North Carolina, USA

²Stanley Manne Children's Research Institute, Ann & Robert H. Lurie Children's Hospital of Chicago, Chicago, Illinois, USA

³Human Molecular Genetics Laboratory, Health Biotechnology Division, National Institute for Biotechnology and Genetic Engineering College (NIBGE-C), Faisalabad, Pakistan

⁴Pakistan Institute of Engineering and Applied Sciences (PIEAS), Islamabad, Pakistan

⁵Atta-ur-Rahman School of Applied Biosciences, National University of Sciences and Technology, Islamabad, Pakistan

⁶Obstetrics and Gynecology Hospital, NHC Key Laboratory of Reproduction Regulation (Shanghai Institute for Biomedical and Pharmaceutical Technologies), Institute of Reproduction and Development, Fudan University, Shanghai, China

⁷Division of Neurology, Shifa International Hospital, Shifa Tameer e Millat University, Islamabad, Pakistan

⁸RILD Wellcome Wolfson Centre - Level 4, Royal Devon and Exeter NHS Foundation Trust, University of Exeter Medical School, Exeter, UK

⁹Department of Clinical Laboratory Sciences, College of Applied Medical Sciences, Jouf University, Sakaka, Saudi Arabia

¹⁰Stem Cell Research Laboratory, AFBMTC, CMH Medical Complex, Rawalpindi, Pakistan

¹¹Department of Biological Sciences, National University of Medical Sciences, Rawalpindi, Pakistan

¹²Department of Pharmacology, Rajarshi Shahu College of Pharmacy, Malvihi, Buldana, Maharashtra, India

¹³Pakistan Science Foundation, Islamabad, Pakistan

¹⁴Department of Biological and Biomedical Sciences, Aga Khan University, Karachi, Pakistan

¹⁵Department of Pediatrics, Feinberg School of Medicine, Northwestern University, Chicago, Illinois, USA

¹⁶Department of Cell and Developmental Biology, Feinberg School of Medicine, Northwestern University, Chicago, Illinois, USA

Correspondence

Erica E. Davis, Stanley Manne Children's Research Institute, Ann & Robert H. Lurie Children's Hospital of Chicago, Chicago, IL, USA.
Email: eridavis@luriechildrens.org

Tahir N. Khan, Department of Biological Sciences, National University of Medical Sciences, Rawalpindi, Pakistan.
Email: tahir.khan@numspak.edu.pk

Funding information

Higher Education Commission, Pakistan, Grant/Award Number: 20-12107/NRPU; National

Abstract

Autosomal recessive limb-girdle muscular dystrophy-1 (LGMDR1) is an autosomal recessive disorder characterized by progressive weakness of the proximal limb and girdle muscles. Biallelic mutations in *CAPN3* are reported frequently to cause LGMDR1. Here, we describe 11 individuals from three unrelated consanguineous families that present with typical features of LGMDR1 that include proximal muscle wasting, weakness of the upper and lower limbs, and elevated serum creatine kinase. Whole-exome sequencing identified a rare homozygous *CAPN3* variant near the exon 2 splice donor

Institute of Advance Studies and Research,
Grant/Award Number: NIASR/NUMS

[Correction added on 15 November 2021,
after first online publication: The middle name
initial for Dr. Gaurav G. Harlalka has been
updated. A new affiliation (12) has been added
for Dr. Haralka and other affiliations have
been renumbered to follow the journal style.]

site that segregates with disease in all three families. mRNA splicing studies showed partial retention of intronic sequence and subsequent introduction of a premature stop codon (NM_000070.3: c.379 + 3A>G; p.Asp128Glyfs*15). Furthermore, we observe reduced *CAPN3* expression in primary dermal fibroblasts derived from an affected individual, suggesting instability and/or nonsense-mediated decay of mutation-bearing mRNA. Genome-wide homozygosity mapping and single-nucleotide polymorphism analysis identified a shared haplotype and supports a possible founder effect for the *CAPN3* variant. Together, our data extend the mutational spectrum of LGMDR1 and have implications for improved diagnostics for individuals of Pakistani origin.

KEYWORDS

calpainopathy, founder effect, intronic retention, LGMDR1, splice site variant

1 | INTRODUCTION

Limb-girdle muscular dystrophy (LGMD) collectively describes a group of muscular dystrophies that are distinct from the common X-linked Duchenne and Becker dystrophinopathies. Affected individuals with LGMD present typically with muscle weakness and atrophy restricted to the skeletal muscles of the limb, with the proximal musculature more severely affected than the distal. Abnormal serum creatine kinase (CK) levels are frequently associated with LGMD disease course, specifically, an increase in CK from early infancy and a further decrease with disease progression, as muscles become increasingly atrophic (Urtasun et al., 1998). More than 30 autosomal dominant and recessive forms of inherited LGMD have been identified (Nallamilli et al., 2018). Calpainopathy is a recessive form of LGMD often referred to as LGMDR1 (MIM: 253600) and is a condition associated with biallelic mutations in the locus encoding calpain-3 (*CAPN3*; MIM: 114240). Heterozygous changes in *CAPN3* have also been shown to cause autosomal dominant limb-girdle muscular dystrophy-4 (LGMD4; MIM: 618129) (Gonzalez-Mera et al., 2021; Lasa-Elgarresta et al., 2019; Vissing et al., 2016). Previous work has suggested roles for Calpain-3 in remodeling and assembly of contractile proteins in the sarcomere (Cohen et al., 2006; Kramerova, Kudryashova, Tidball, & Spencer, 2004; Sorimachi et al., 1995), and it is predicted to be involved in the regulation of Ca^{2+} efflux from the sarcoplasmic reticulum, membrane repair, and muscle regeneration (Hauerslev et al., 2012; Huang et al., 2008; Ojima et al., 2011). LGMDR1 was the first LGMD diagnosed at the molecular level (Richard et al., 1995), and since the initial discovery, >500 pathogenic *CAPN3* variants have been reported, making it the most common form of LGMD subtype worldwide (Human Gene Mutation Database) (Guglieri, Straub, Bushby, & Lochmüller, 2008; Norwood et al., 2009; Zatz & Starling, 2005).

Autosomal recessive forms of LGMD are clinically heterogeneous and present overlapping clinical features, making it challenging to distinguish affected individuals with LGMDR1 from other autosomal recessive forms of LGMD. Multiple features are considered for differential diagnosis including, age of disease onset, symmetrical muscle atrophy and weakness, scapular winging and no cardiac muscle

involvement; these symptoms are typically not present in this combination in other autosomal recessive forms of LGMD (Quick et al., 2015; Sarkozy et al., 2012; Sveen, Thune, Kober, & Vissing, 2008). However, a more precise diagnosis is based on the identification of the underlying genetic cause. Here, we deployed clinical investigation and whole-exome sequencing (WES) in three unrelated consanguineous Pakistani families comprised of a total of 11 affected individuals and identified a recurrent *CAPN3* intronic variant near a splice donor site that segregated with disease (GenBank ID: NM_000070.3: c.379 + 3A > G, p.Asp128Glyfs*15). Furthermore, homozygosity mapping and single-nucleotide polymorphism (SNP) analysis identified a shared homozygous stretch on chromosome 15 (2.7 Mb) in all affected individuals, raising the possibility of a founder effect within this region of Pakistan.

2 | MATERIALS AND METHODS

2.1 | Editorial policies and ethical considerations

Studies and procedures related to clinical examination, human sample collection, WES, and molecular analysis were approved by Institutional Reviews Boards and Ethical committees of the National Institute for Biotechnology and Genetic Engineering, Faisalabad, Pakistan; Duke University Medical Center, NC, USA; and Ann & Robert H. Lurie Children's Hospital of Chicago, IL, USA (family 1); National University of Medical Sciences, Rawalpindi, Pakistan (family 2), and the National University of Science and Technology, Islamabad, Pakistan (family 3). Signed informed consent was obtained from all participants or their legal representatives for study procedures and publication of clinical and genetic findings.

2.2 | Human research participants

This study includes unrelated consanguineous families originating from three different districts of the Khyber Pakhtunkhwa province of

Pakistan. All three families identify their ethnicity as Pashtun. Subsequent to informed consent, we obtained peripheral blood samples from affected individuals and their healthy family members by standard venipuncture. We extracted DNA using a phenol-chloroform extraction method or commercial kits: QIAamp DNA Maxi Kit (Qiagen) and ReliaPrep Blood gDNA Miniprep System (Promega).

2.3 | WES and data analysis

Family 1 (NMD2): We performed WES in a quartet paradigm on genomic DNA obtained from healthy parents (1-I-1 and 1-I-2) and two affected individuals (1-II-1 and 1-II-2) using the NimbleGen EzExome library and Illumina sequencing platforms. Sequencing reads were processed initially with TrimGalore (http://www.bioinformatics.babraham.ac.uk/projects/trim_galore/) to remove any Illumina adapter sequences or low-quality base calls from the 3' ends of reads. Reads were then aligned to the hg19 version of the human genome with the Burrows-Wheeler Aligner (BWA) (Li, 2013). Alignment processing and variant calls were performed using the Genome Analysis Toolkit (GATK) (DePristo et al., 2011; McKenna et al., 2010), following the Broad Institute's Best Practices workflow (Van der Auwera et al., 2013). Variants were then annotated with the Variant Effect Predictor toolkit to identify the potential functional impact of each variant according to the GRCh37r75 version of the human transcriptome. We used the XHMM (Fromer & Purcell, 2014) algorithm to identify copy number variants (CNVs).

Family 2 (NM10): We performed WES on genomic DNA obtained from an affected individual (2-II-6). Genomic DNA was target enriched by the Agilent SureSelect^{XT} Human All Exon Kit. Next-generation sequencing was conducted with the Illumina HiSeq X-TEN platform at Cloud Health Genomics. Reads were aligned to the human genome reference assembly (UCSC Genome Browser hg19) with BWA. Picard software was employed to remove PCR duplicates and evaluate the quality of variants to attain effective reads, quality bases, average coverage depth, and 90×–120× coverage. Single-nucleotide variants and indels were called and analyzed with GATK using an in-house variant filtration pipeline. We then used ANNOVAR for functional annotation with OMIM, GeneOntology, KEGG Pathway, SIFT, PolyPhen-2, and MutationTaster.

Family 3 (NEU43): We performed SNP microarray genotyping using the Illumina Human CytoSNP-12v2.0 and 2.1 arrays on DNA samples obtained from all three affected individuals (3-II-2, 3-II-4, and 3-II-5). To identify causative variants, WES was performed on DNA from a single affected individual (3-II-2). Sequence reads were aligned to the human genome reference sequence (hg 38) for screening the base pair changes using the CLC sequence viewer and Chromas Lite software. The haplotypes identified by homozygosity mapping were considered preferentially while screening for causal mutations.

In all three families, variants identified by WES were assessed and filtered for rare variants with a minor allele frequency (MAF) of <0.01 in ethnicity-matched populations in control databases (including the

Genome Aggregation Database; gnomAD, the Exome Aggregation Consortium, and the 1000 Genomes Project). Nonsynonymous, exonic, or splice variants, conforming to a recessive pattern of disease inheritance in each family were prioritized as candidates. We performed bidirectional Sanger sequencing with BigDye terminator v3.1 cycle sequencing chemistry to confirm candidate variants and segregation in all available family members.

2.4 | Homozygosity mapping and IBD analysis

To identify homozygous regions genome-wide in family 1 and family 3, we used HomozygosityMapper (Seelow, Schuelke, Hildebrandt, & Nurnberg, 2009). For family 1, we generated a jointly called variant call format (vcf) file using WES data from two affected siblings (1-II-1 and 1-II-2) and unaffected parents (1-I-1 and 1-I-2). We used default parameters to identify homozygous regions. To detect identity by descent (IBD) segments in family 1 and family 3, we used TRUFFLE software (Dimitromanolakis, Paterson, & Sun, 2019). We generated a combined vcf file containing exome-wide filtered variants for family 1 and family 3 and IBD1/IBD2 segments were estimated using default parameters.

2.5 | CAPN3 mRNA splicing analysis and expression studies

We obtained primary dermal fibroblasts from an affected individual (1-II-7) in family 1 and an ethnically matched control individual and cultured cells in DMEM (Sigma Aldrich), 10% fetal bovine serum and 1% penicillin-streptomycin. We extracted total RNA from growth-synchronized cells at ~75% confluency with the RNeasy Mini Kit (Qiagen) and generated cDNA with the Quantitect Reverse Transcription Kit (Qiagen). Using this cDNA as template, we PCR-amplified and performed Sanger sequencing by using primers in upstream and downstream exons flanking the CAPN3 variant. We compared CAPN3 expression of an affected individual (1-II-7) to a matched control by performing quantitative PCR using Power SYBR Green PCR Master Mix (Applied Biosystems).

3 | RESULTS

3.1 | Clinical assessment of three families with LGMD

For each of the three families, the healthy parents reported that initially their affected children showed difficulty in walking and difficulty in standing up from a sitting position. As described by their parents, the age of onset of toe walking in affected individuals of family 1 and family 2 is 8 years ± 1 year while in family 3 toe walking was observed between 9 and 16 years of age in affected individuals. These symptoms became progressively severe as evidenced by affected

individuals becoming wheelchair-bound (family 1: II-1; family 3: II-2 at the time of this report) and then bedbound (family 2: II-1, II-2 at the time of this report) with progression of age. Upon examination of affected individuals by a neurologist, we noted proximal muscle wasting and scapular winging for all 11 affected individuals [Figure 1 (a–d)]. We measured serum CK concentration for six available affected individuals, and levels were found to be markedly elevated by comparison to reference ranges in five individuals. One bedbound severely affected individual in family 2 (II-1) has a normal CK value. This finding is not unusual; previous reports have shown that due to disease progression, muscles become increasingly atrophic and CK concentration can decrease over time (Urtasun et al., 1998). Electromyogram studies of four selected affected individuals (family 1: II-1 and II-7; family 3: II-2 and II-4) were indicative of myopathy while nerve conduction velocity studies demonstrated no abnormal findings. Magnetic resonance imaging of the thigh of an affected individual (family 2: II-7) showed marked atrophy of all visualized muscles. This includes muscles of the anterior, medial, and posterior compartments and gluteal and adductor compartments [Figure 1(e–g)]. Among all muscles visualized, the adductor magnus is the most atrophic. Muscles of the quadriceps compartment, which include rectus femoris, vastus medialis, vastus intermedius, and vastus lateralis are all atrophied. The muscle bulk is lost and replaced by fat signal. Some of the affected muscles also show subtle edema. Although disease symptoms and the inheritance pattern are consistent with an autosomal recessive form of muscular dystrophy [Table 1; Figure 2(a–c)], the precise molecular diagnosis of disease subtype could not be achieved with the available

clinical data. Therefore, we used WES as an assistive tool to identify the underlying molecular cause.

3.2 | Genomic studies identify a recessive recurrent pathogenic variant in CAPN3

Family 1: To identify the genetic cause of LGMD, we performed WES in a quartet paradigm that included affected siblings (1-II-1 and 1-II-2) and both parents (1-I-1 and 1-I-2). We obtained a mean target coverage of 125–142× with a mean of 94% of bases covered >20× for both affected siblings and parents (Supplementary Table 1). Based on the consanguinity of the family and apparent autosomal recessive inheritance pattern of disease, we first used HomozygosityMapper to search for shared homozygous genomic regions between the two affected siblings. Using WES data, we jointly recalled variants to identify changes that are shared exclusively between affected individuals. We identified seven homozygous genomic regions with more than 80% of maximal homozygosity score which resided on chromosomes 1, 6, 7, 14, 15, 17, and 19 [Supplementary Figure 1(a)]. Among these, a homozygous region on chromosome 15 was the largest segment shared between affected siblings and comprised four blocks encompassing 38.8 Mb (chr15:40,235,575–79,058,317; build 37), contains 735 homozygous markers, and includes 261 protein-encoding genes [Figure 3(a), Supplementary Figure 1(a)].

We independently filtered rare variants that were homozygous and compound heterozygous in affected individuals using a MAF <1%

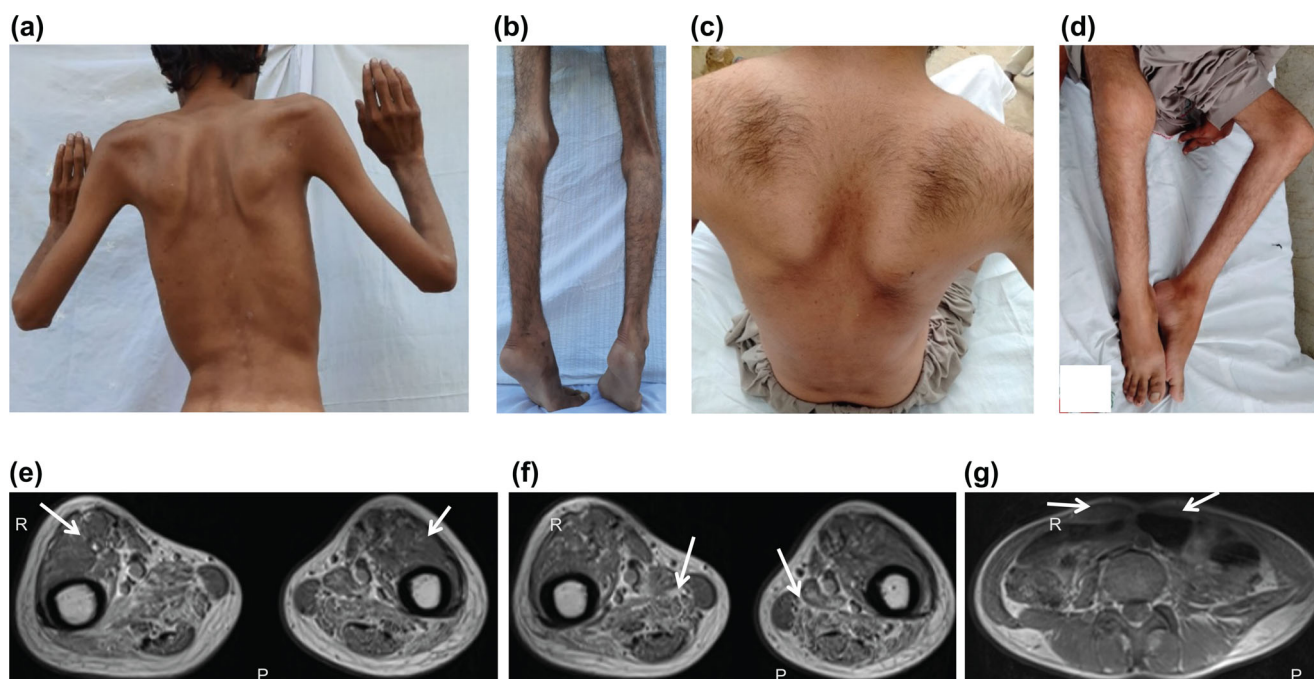


FIGURE 1 Clinical features of affected individuals homozygous for the CAPN3 c.379 + 3A>G variant. (a, b) Images of upper body (back) with scapular winging (a), and legs (b) of individual II-7 from family 2. (c, d) Images of upper body (back) in a sitting position showing scapular winging (c), and legs (d) of individual II-1 from family 1. (e–g) Thigh MRI images of individual II-7 from family 2. Atrophy of anterior compartment muscles with relative sparing of vastus lateralis are marked by arrows

TABLE 1 Clinical features of affected individuals in three families with CAPN3 c.379 + 3A>G

Family	Family 1 (NMD2)				Family 2 (NM10)				Family 3 (NEU43)			
	1-II-1	1-II-2	1-II-7	2-II-1	2-II-2	2-II-5	2-II-6	2-II-7	3-II-2	3-II-4	3-II-5	
CAPN3 c.379 + 3A>G	M/M	M/M	M/M	M/M	M/M	M/M	M/M	M/M	M/M	M/M	M/M	
Sex	Male	Female	Female	Male	Female	Female	Female	Male	Female	Male	Male	
Current age (years)	22	21	19	28	25	13	11	7	22	19	11	
Disease onset (years)	8	8	8	7	9	8	7	7	16	14	9	
Serum CK (U/L)	609	nd	944	225	nd	nd	nd	1,321	15,000	3,246	nd	
Normal range*												
Males:												
39–308 U/L												
Females:												
26–192 U/L												
EMG	Myopathic	nd	Myopathic	nd	nd	nd	nd	nd	Myopathic	Myopathic	nd	
Childhood milestones	Normal	Normal	Normal	Normal	Normal	Normal	Normal	Normal	Normal	Normal	Normal	
Scapular winging	Present	Present	Present	Present	Present	Present	Present	Present	Present	Present	Present	
Ambulation status	Wheelchair bound	Toe-walking	Toe-walking	Nonambulant, bedbound	Nonambulant, bedbound	Toe-walking	Toe-walking	Toe-walking	Wheelchair bound	Toe-walking	Toe-walking	

Note: M/M, homozygous for CAPN3 c.379 + 3A>G; CK, creatine kinase; EMG, electromyogram; nd, not determined. *<https://www.mayocliniclabs.com/test-catalog/Clinical+and+Interpretive/8336>.

and prioritized variants that were shared between affected siblings. None of the compound heterozygous changes fulfilled our filtration criteria. However, we identified homozygous changes in six genes, five of which were localized to chromosome 15 (*DNAJC17*: c.671T>A, p.V224D; *CAPN3*: c.379 + 3A>G; *DUOXA2*: c.118C>T, p.L40F; *LARP6*: c.1079A>G, p.K360R; and *CSPG4*: c.2566C>T, p.R856W) and one to chromosome 19 (*LSM14A*: c.307T>C, p.S103P). No rare, homozygous CNVs were found to be shared in both WES-analyzed affected individuals in family 1. Based on the functional relevance, population frequencies, and presence/absence of homozygous changes in the general population, we prioritized the intronic variant in *CAPN3* as a plausible candidate and processed it for further validation, while we considered the other five changes to be less likely contributors to the LGMD phenotype (Supplementary Table 2). Bidirectional Sanger sequencing of the *CAPN3* exon 2 splice donor site in 16 family members, including the quartet that underwent WES, showed that the variant segregated with disease (Figure 2[a and d]; Supplementary Figure 2).

Family 2: To identify the genetic cause of disease in family 2, we performed WES using a genomic DNA sample from a single affected individual (2-II-6) and obtained a mean target coverage of 116× with 89% of bases covered at >20× read depth (Supplementary Table 1). Filtration and prioritization of WES data using MAF <1% and a recessive mode of inheritance resulted in the identification of 10 homozygous variants including *CAPN3* c.379 + 3A>G as a candidate disease-causing change (Supplementary Table 2). Sanger sequencing confirmed segregation of the *CAPN3* c.379 + 3A>G variant in homozygosity in five affected siblings which were inherited from their heterozygous asymptomatic parental carriers. The asymptomatic siblings of affected individuals were either heterozygous or wild type for the *CAPN3* change [Figure 2(b)].

Family 3: To uncover the underlying genetic cause of disease in family 3, we conducted whole-genome SNP genotyping using microarray data generated on DNA samples obtained from the three affected individuals (3-II-2, 3-II-4, and 3-II-5). Analysis of rare recessive deleterious CNVs did not identify any consistent findings across all the three affected individuals, thus excluding the possibility of a large chromosomal aberration as the genetic cause of disease. All three affected individuals harbored a 22.3 Mb homozygous region demarcated by markers rs16971558 and rs999047 on chromosome 15 (chr15:41,166,421-43,396,718 [hg38]). Next, we performed WES on an affected individual (3-II-2). We obtained 98% of target sequence coverage with 94% of sequence covered >20× with a mean read depth of 148× (Supplementary Table 1). Homozygosity mapping using WES data identified six homozygous regions on chromosomes 5, 7, 9, 10, 15, and 21 with >80% of maximal homozygosity score [Supplementary Figure 1(b)]. Consistent with the microarray data, the homozygous region on chromosome 15 was the largest segment comprised of three blocks encompassing 41 Mb (chr15:42,144,979–83,230,904; build 37), containing 1,415 homozygous markers, and including 260 protein-encoding genes [Figure 3(b), Supplementary Figure 1(b)]. We then focused on rare homozygous variants located within the homozygous loci revealed by SNP array and identified two

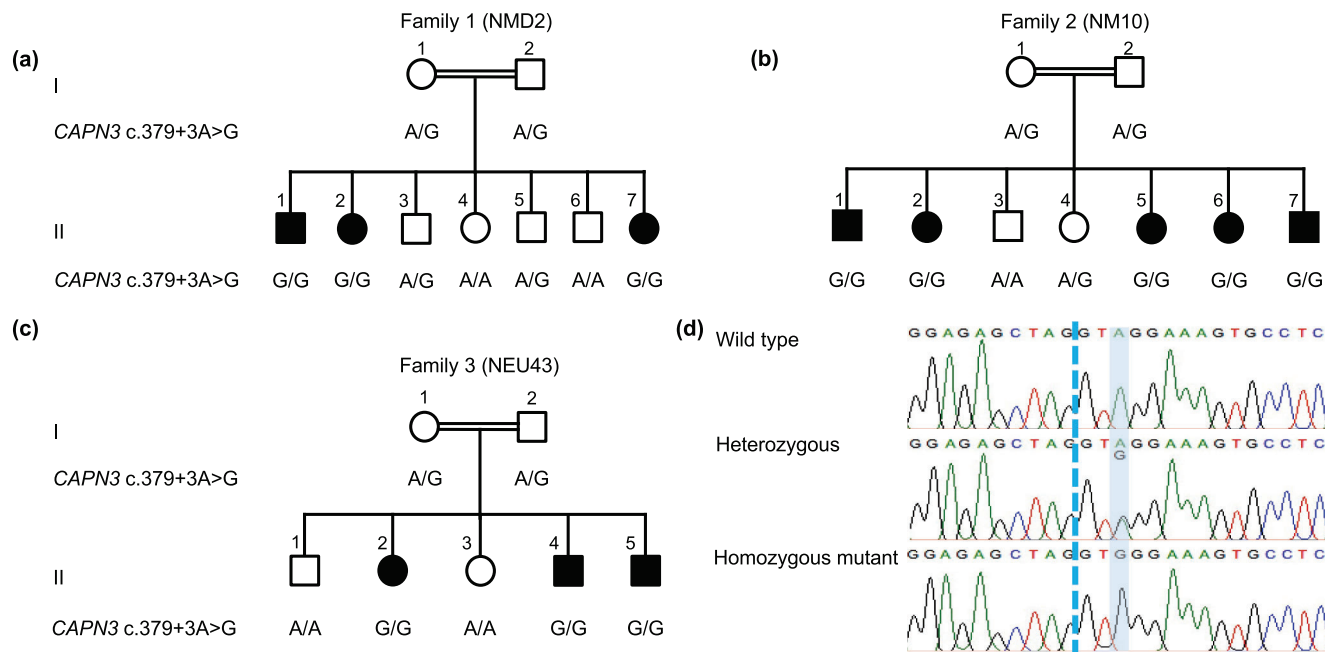


FIGURE 2 A recurrent intronic variant in *CAPN3* is associated with LGMDR1 in three unrelated consanguineous families. (a–c) Pedigrees of three Pakistani families with LGMDR1 symptoms that segregate as an autosomal recessive trait. Filled circles or squares indicate affected females and males, respectively. Double lines indicate consanguinity. The *CAPN3* genotype at position c.379 + 3 (NM_000070.3) is indicated for each individual as A/A (wild type), A/G (heterozygous), and G/G (homozygous variant). (d) Representative chromatograms showing the *CAPN3* exon 2 and intron 2 boundary (left and right, respectively; separated by a blue dotted line) from a healthy wild type (top), heterozygous (middle) and homozygous variant individual (bottom). Position of the *CAPN3* c.379 + 3A>G variant is shaded with a light blue box

variants; *NUP205*: c.3071-4G>A and *CAPN3* c.379 + 3A>G (Supplementary Table 2).

Cross-family comparison of filtered variants identified by WES revealed that all three families share a recurrent A>G nucleotide substitution in the intron near the splice donor site of *CAPN3* exon 2 (c.379 + 3A>G; chr15:42384555A>G [hg 38], chr15:42676753A>G [hg19]). We considered the *CAPN3* variant as a likely disease-causing candidate based on its presence in unrelated patients in our cohort and the previous association of *CAPN3* with LGMD2 (Richard et al., 1995). Crucially, the variant segregated with disease in all three pedigrees (Figure 2[a–c]; Supplementary Figure 2; Supplementary Figure 3). There are two heterozygous individuals reported in gnomAD (v2.1.1 accessed January 2021) who carry the *CAPN3*; c.379 + 3A>G variant (global MAF 0.000007957), one in each of South Asian (MAF 0.00003266) and European non-Finnish (MAF 0.000008796) populations (Supplementary Table 2).

3.3 | The *CAPN3* variant induces aberrant mRNA splicing and transcript depletion

Due to its proximity to the exon 2 splice donor site, we wondered whether *CAPN3* c.379 + 3A>G could induce mRNA splicing defects. To investigate this possibility, we cultured primary dermal fibroblasts from an affected individual carrying the homozygous *CAPN3* variant (family 1: II-7) and an ethnically matched control. We isolated total

RNA, performed reverse transcriptase-mediated cDNA synthesis, and PCR-amplified the target region using primers spanning the exon 2-exon 3 junction. Migration on an agarose gel revealed a larger PCR fragment in the affected individual compared to the matched control [Figure 4(a)]. Sanger sequencing of the RT-PCR products showed that the mutation-bearing transcript retained 54 bp of intron 2 (r.[379 + 1_379 + 54ins; 379 + 3a>g]), which results in 14 additional amino acids causing a frameshift and subsequent introduction of premature stop codon (p.Asp128Glyfs*15; Figure 4[b, c]). We then quantified the *CAPN3* mRNA obtained from the patient and control dermal fibroblasts using qRT-PCR and found a significant reduction ($p < 0.0006$) of *CAPN3* expression in individual 1-II-7 compared to the control [Figure 4(d)].

4 | DISCUSSION

Previous studies have shown that pathogenic variants in *CAPN3* cause LGMDR1, also referred to as calpainopathy (Richard et al., 1995; Richard et al., 1997). Here, we identified a recurrent intronic variant near the splice donor site of *CAPN3* exon 2. This DNA change is predicted to result in premature protein truncation and is present in three unrelated Pakistani families with 11 affected individuals who exhibit clinical features of LGMDR1. All affected individuals show overlapping clinical features including proximal muscle wasting, weakness of the upper and lower limbs, abnormal electromyogram findings,

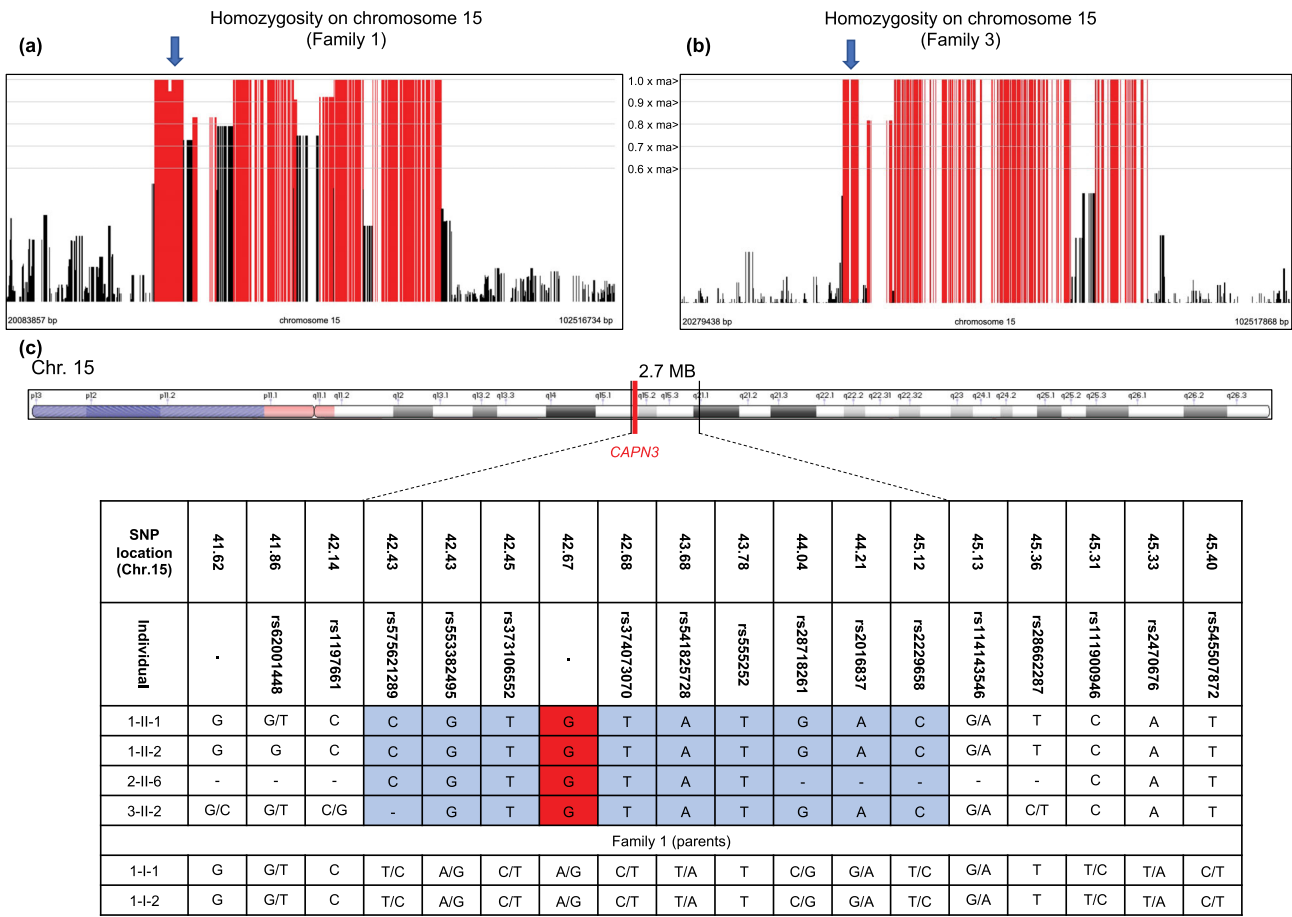


FIGURE 3 Haplotype and SNP analysis flanking the *CAPN3* c.379 + 3A>G variant. (a) Homozygosity map of chromosome 15 in family 1. A jointly called vcf file was used in HomozygosityMapper to search for homozygous SNPs shared exclusively between patients (1-II-1 and 1-II-2) compared to healthy parents (1-I-1 and 1-I-2). Four homozygous genomic stretches on chromosome 15, comprised of 38.8 Mb (chr15:40235575–79058317; build 37), contain 735 homozygous markers and include 261 protein-encoding genes. Position of the *CAPN3* variant is indicated with a blue arrow. Genome-wide homozygosity map of family 1 is shown in Supplementary Figure 1(a). (b) Homozygosity map of chromosome 15 in family 3. Homozygous regions on chromosome 15 were identified using the vcf file of an affected individual (3-II-2). Three homozygous genomic stretches were identified on chromosome 15, comprised of 41 Mb (chr15:42144979–83230904; build 37), contain 1415 homozygous markers, and include 260 protein-encoding genes. Genome-wide homozygosity map of family 3 is shown in Supplementary Figure 1 (b). (c) Top: ideogram of chromosome 15 generated by Genome Data Viewer showing the position of the shared haplotype and *CAPN3* variant (red vertical line). Bottom: analysis of SNP genotypes extracted from WES data from three unrelated families identified a minimal haplotype of 2.7 Mb, shared exclusively among affected individuals with *CAPN3* ablation. The shared haplotype is highlighted in blue. The *CAPN3* variant resides in the shared region and is highlighted in red. Single nucleotides indicate homozygous genotype; “-” indicates no data for that position

and elevated serum CK levels. Importantly multiple additional candidate variants identified by WES were localized to the shared haplotype on chromosome 15 but were subsequently excluded due to their nonassociation with the muscular dystrophy spectrum of genetic disorders.

A combination of *in silico* and RT-PCR analyses has determined that many intronic and splice site variants of *CAPN3* are likely to be pathogenic (Salem et al., 2012). It is challenging to precisely predict the functional impact of a variant located proximal to an mRNA splice site. Hence, to characterize the functional impact of *CAPN3* c.379 + 3A>G variant, we monitored mRNA splicing and quantity in patient versus control cDNA derived from primary fibroblasts. We observed partial retention of intron 2 and mutant mRNA depletion, consistent with a likely premature protein truncation rendering significantly

shorter *CAPN3* and/or nonsense-mediated decay (NMD). These data support the notion that the underlying cause of disease in our patients is due to loss-of-function of *CAPN3*. Skeletal muscle is the most severely affected tissue in LGMDR1 (Krahn et al., 2006; Richard et al., 1995; Straub, Murphy, Udd., & LGMD Workshop Study Group, 2018; Vissing et al., 2016), and notably, different tissues may have different NMD profiles for premature stop codon containing genes (Bao, Tang, Yuan, Porse, & Yan, 2015; Han et al., 2018; Muhlemann, 2016; Shum et al., 2016; Zetoune et al., 2008). Muscle biopsy from affected individuals was unavailable; therefore, we cannot predict the level of NMD in skeletal muscle, a more relevant tissue.

We note with interest that all three families share the same disease-causing *CAPN3* variant. This recurrence could be due to either

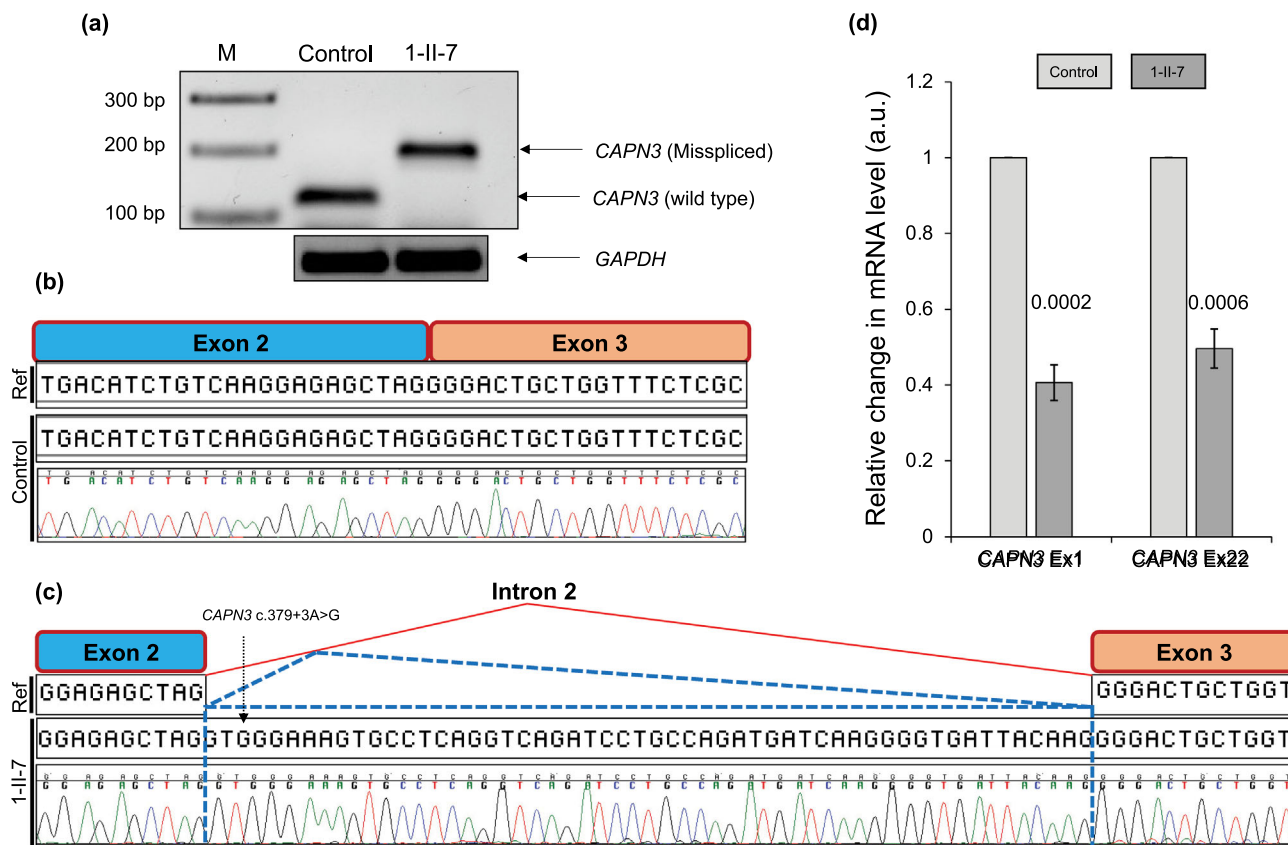


FIGURE 4 *CAPN3* c.379 + 3A > G induces aberrant mRNA splicing and subsequent mRNA reduction in affected individuals compared to controls. (a) Agarose gel images of RT-PCR products from individual 1-II-7 (family 1) show a PCR fragment flanking the *CAPN3* exon 2-intron 2 splice junction that is larger than the fragment observed in a matched control. (b) Top: Partial sequence of *CAPN3* exon 2 and exon 3 (NM_000070.3) of control mRNA obtained from a healthy control individual aligned against the reference sequence. Exons 2 and 3 are shown with blue and orange rectangles, respectively. Bottom: chromatogram spanning the exon 2 and exon 3 boundary. (c) Top: reference schematic and partial sequence of *CAPN3* exons 2 and 3. Bottom: chromatogram of *CAPN3* cDNA from individual 1-II-7 (family 1) showing retention of 54 bp of intron 2 sequence (blue dotted rectangle). Position of c.379 + 3A > G is indicated with a black dotted arrow. (d) Quantitative RT-PCR was performed on total RNA derived from primary skin fibroblasts obtained from a matched control and an affected individual (1-II-7; family 1). Relative expression of *CAPN3* mRNA is significantly reduced in individual 1-II-7 compared to the matched control. Experiments were performed in three independent replicates, each with technical triplicates, and normalized to *GAPDH*. Two different primer sets were used to show similar results. Error bars represent the SEM. *p*-values were calculated with a two-tailed (unpaired, nonparametric) *t*-test

a mutational hotspot or a founder effect. The latter possibility is supported by the observation that all three families originate from the same ethnic background and geographic region of Pakistan. Furthermore, the mutant allele does not reside in a repetitive region which might be indicative of a mutational hotspot. We excluded the possibility of close relatedness among families by evaluating IBD segments genome-wide with TRUFFLE (Dimitromanolakis et al., 2019) (Supplementary Table 3). However, we identified a large IBD2 segment on chromosome 15 that spans the *CAPN3* mutation. It is shared exclusively between affected individuals, thus further supporting our hypothesis of a shared disease haplotype and a possible founder effect at this locus. These data were corroborated with HomozygosityMapper, which identified a homozygous region on chromosome 15 in families 1 and 3 (Figure 3[a, b]; Supplementary Figure 1). Moreover, SNP analysis of WES data identified a minimal homozygous region exclusively shared among affected individuals of

all three families [2.7 Mb; Figure 3(c)]. Importantly, the minimal region did not carry heterozygous SNPs in any affected individual [Figure 3(c)]. However, we cannot exclude the possibility of a mutational hotspot effect based on the presence of the *CAPN3* variant in a European individual in gnomAD. Haplotype analysis of this European carrier would provide more conclusive insights.

A genotype-phenotype correlation has been described previously for individuals harboring pathogenic variants in *CAPN3*, in which dominantly inherited changes associated with LGMDD4 are more likely to cause milder and delayed onset clinical manifestations compared to recessive variants (Lasa-Elgarresta et al., 2019). In some instances, the age of onset and the severity of clinical manifestations vary between siblings even in the presence of identical causal variants (Schessl et al., 2008), suggesting environmental factors or secondary sites elsewhere in the genome that might influence disease. The affected individuals in the series reported here show features typical of LGMDR1

with a relatively consistent rate of disease progression within siblings of each family. However, we observed a modest delay in age of disease onset in family 3 (9–16 years) compared to the other two families (7–9 years). Inspection of CAPN3 protein level in skeletal muscle from each affected individual would provide further insights to correlate the disease progression with the underlying molecular cause.

In sum, we identified a recurrent intronic variant in CAPN3 that impairs mRNA splicing in three Pakistani families with LGMD. Our data suggest that LGMDR1 is under-identified in clinical practice, specifically in populations of Pashtun origin, and CAPN3 c.379 + 3A>G should preferentially be screened in families of this ethnic group with a suspected autosomal recessive form of calpainopathy. This recommendation is supported by the previously reported high incidences of pathogenic variations in CAPN3 with many founder mutations globally (Balci et al., 2006; Canki-Klain et al., 2004; Chae et al., 2001; Fanin, Nascimbeni, Fulizio, & Angelini, 2005; Khadilkar, Chaudhari, Dastur, Gaitonde, & Yadav, 2016; Pogoda et al., 2000). There is a significant clinical overlap in muscular dystrophies and like other clinically and genetically heterogeneous disorders, WES is highly effective toward identifying the molecular cause of disease.

ACKNOWLEDGMENTS

We are grateful to the willing members of these three families who participated in the research. We thank Nicholas Katsanis for his thoughtful discussions. K.K. was funded by an International Research Support Initiative Program fellowship from the Higher Education Commission of Pakistan. E.E.D. is the Ann Marie and Francis Klocke, MD Research Scholar. T.N.K. was supported by grants from the Higher Education Commission of Pakistan (20-12107/NRPU) and the National Institute of Advanced Studies and Research (NIASR/NUMS).

CONFLICT OF INTEREST

The authors declare no conflict of interest.

AUTHOR CONTRIBUTIONS

Kamal Khan: Conceptualization, formal analysis, investigation and clinical assessment, writing original manuscript draft, review and editing of the manuscript. **Sarmad Mehmood:** Investigation and clinical assessment, writing original manuscript draft. **Chunyu Liu:** Investigation and clinical assessment and writing original manuscript draft. **Maimoona Siddiqui:** Investigation and clinical assessment. **Arsalan Ahmad:** Investigation and clinical assessment. **Belqees Yawar Faiz:** Investigation and clinical assessment. **Barry A. Chioza:** Investigation and clinical assessment. **Emma A. Baple:** Investigation and clinical assessment. **Muhammad I. Ullah:** Investigation and clinical assessment. **Zaineb Akram:** Investigation and clinical assessment. **Humayoon S. Satti:** Investigation and clinical assessment. **Raees Khan:** Investigation and clinical assessment. **Gaurav V. Harlalka:** Investigation and clinical assessment. **Muhammad Jameel:** Investigation and clinical assessment. **Talia Akram:** Investigation and clinical assessment. **Shahid M. Baig:** Review and editing of the manuscript (with input and approval from all authors). **Andrew H. Crosby:** Investigation and clinical assessment and Review and editing of the manuscript (with input

and approval from all authors). **Muhammad J. Hassan:** Investigation and clinical assessment. **Feng Zhang:** Investigation and clinical assessment. **Erica E. Davis:** Conceptualization, formal analysis, and review and editing of the manuscript (with input and approval from all authors). **Tahir N. Khan:** Conceptualization, review and editing of the manuscript (with input and approval from all authors), and funding acquisition

WEB RESOURCES

1000 Genomes Project, <https://www.internationalgenome.org/>
 Combined Annotation Dependent Depletion (CADD), <https://cadd.gs.washington.edu/>
 CLC sequence viewer, <https://www.qiagenbioinformatics.com/products/clc-sequence-viewer/>
 Chromas Lite, <http://technelysium.com.au/wp/chromas/>
 Ensembl, <https://ensembl.org>
 Exome Aggregation Consortium (ExAC), <http://exac.broadinstitute.org/>
 GenBank, <http://www.ncbi.nlm.nih.gov/genbank/>
 Gene Ontology, <http://geneontology.org/>
 Genome Aggregation Database (gnomAD), <http://gnomad.broadinstitute.org/>
 Genome Data Viewer, <https://www.ncbi.nlm.nih.gov/genome/gdv/>
 HomozygosityMapper, <http://www.homozygositymapper.org/>
 Human Gene Mutation Database (HGMD), <http://www.hgmd.cf.ac.uk/>
 Kyoto Encyclopedia of Genes and Genomes (KEGG), <https://www.genome.jp/kegg/>
 Mutation Taster, <http://www.mutationtaster.org/>
 Online Mendelian Inheritance in Man (OMIM), <http://www.omim.org>
 PolyPhen-2, <http://genetics.bwh.harvard.edu/pph2/>
 Sorting Intolerant From Tolerant (SIFT), <https://sift.bii.a-star.edu.sg/>

DATA AVAILABILITY STATEMENT

Consent restrictions preclude deposition of whole exome sequencing data. However, specific information (e.g., specific variants, but not full data sets) can be obtained upon request from the corresponding authors.

ORCID

Barry A. Chioza  <https://orcid.org/0000-0002-3546-1726>

Erica E. Davis  <https://orcid.org/0000-0002-2412-8397>

REFERENCES

- Balci, B., Aurino, S., Haliloglu, G., Talim, B., Erdem, S., Akcören, Z., Tan, E., Caglar, E., Richard, I., Nigro, V., Topaloglu, H., & Dincer, P. (2006). Calpain-3 mutations in Turkey. *European Journal of Pediatrics*, 165(5), 293–298. <https://doi.org/10.1007/s00431-005-0046-3>
- Bao, J., Tang, C., Yuan, S., Porse, B. T., & Yan, W. (2015). UPF2, a nonsense-mediated mRNA decay factor, is required for prepubertal Sertoli cell development and male fertility by ensuring fidelity of the transcriptome. *Development*, 142(2), 352–362. <https://doi.org/10.1242/dev.115642>
- Canki-Klain, N., Milic, A., Kovac, B., Trlaja, A., Grgicevic, D., Zurak, N., Fardeau, M., Leturcq, F., Kaplan, J. C., Urtizberea, J. A., Politano, L., Piluso, G., & Feingold, J. (2004). Prevalence of the 550delA mutation

- in calpainopathy (LGMD 2A) in Croatia. *American Journal of Medical Genetics, Part A*, 125A(2), 152–156. <https://doi.org/10.1002/ajmg.a.20408>
- Chae, J., Minami, N., Jin, Y., Nakagawa, M., Murayama, K., Igarashi, F., & Nonaka, I. (2001). Calpain 3 gene mutations: Genetic and clinicopathologic findings in limb-girdle muscular dystrophy. *Neuromuscular Disorders*, 11(6–7), 547–555. [https://doi.org/10.1016/s0960-8966\(01\)00197-3](https://doi.org/10.1016/s0960-8966(01)00197-3)
- Cohen, N., Kudryashova, E., Kramerova, I., Anderson, L. V., Beckmann, J. S., Bushby, K., & Spencer, M. J. (2006). Identification of putative in vivo substrates of calpain 3 by comparative proteomics of overexpressing transgenic and nontransgenic mice. *Proteomics*, 6(22), 6075–6084. <https://doi.org/10.1002/pmic.200600199>
- DePristo, M. A., Banks, E., Poplin, R., Garimella, K. V., Maguire, J. R., Hartl, C., Philippakis, A. A., del Angel, G., Rivas, M. A., Hanna, M., McKenna, A., Fennell, T. J., Kernysky, A. M., Sivachenko, A. Y., Cibulskis, K., Gabriel, S. B., Altshuler, D., & Daly, M. J. (2011). A framework for variation discovery and genotyping using next-generation DNA sequencing data. *Nature Genetics*, 43(5), 491–498.
- Dimitromanolakis, A., Paterson, A. D., & Sun, L. (2019). Fast and accurate shared segment detection and relatedness estimation in un-phased genetic data via TRUFFLE. *American Journal of Human Genetics*, 105(1), 78–88. <https://doi.org/10.1016/j.ajhg.2019.05.007>
- Fanin, M., Nascimbeni, A. C., Fulizio, L., & Angelini, C. (2005). The frequency of limb girdle muscular dystrophy 2A in northeastern Italy. *Neuromuscular Disorders*, 15(3), 218–224. <https://doi.org/10.1016/j.nmd.2004.11.003>
- Fromer, M., & Purcell, S. M. (2014). Using XHMM software to detect copy number variation in whole-exome sequencing data. *Current Protocols in Human Genetics*, 81(1), 7.23.1–7.23.21.
- González-Mera, L., Ravenscroft, G., Cabrera-Serrano, M., Ermolova, N., Domínguez-González, C., Arteché-López, A., Soltanzadeh, P., Evesson, F., Navas, C., Mavillard, F., Clayton, J., Rodrigo, P., Servián-Morilla, E., Cooper, S. T., Waddell, L., Reardon, K., Corbett, A., Hernandez-Lain, A., Sanchez, A., ... Olivé, M. (2021). Heterozygous CAPN3 missense variants causing autosomal-dominant calpainopathy in seven unrelated families. *Neuropathology and Applied Neurobiology*, 47(2), 283–296. <https://doi.org/10.1111/nan.12663>
- Guglieri, M., Straub, V., Bushby, K., & Lochmüller, H. (2008). Limb-girdle muscular dystrophies. *Current Opinion in Neurology*, 21(5), 576–584.
- Han, X., Wei, Y., Wang, H., Wang, F., Ju, Z., & Li, T. (2018). Nonsense-mediated mRNA decay: A 'nonsense' pathway makes sense in stem cell biology. *Nucleic Acids Research*, 46(3), 1038–1051. <https://doi.org/10.1093/nar/gkx1272>
- Hauerslev, S., Sveen, M.-L., Duno, M., Angelini, C., Vissing, J., & Krag, T. O. (2012). Calpain 3 is important for muscle regeneration: Evidence from patients with limb girdle muscular dystrophies. *BMC Musculoskeletal Disorders*, 13(1), 43.
- Huang, Y., de Morrée, A., van Remoortere, A., Bushby, K., Frants, R. R., Dunnen, J. T., & van der Maarel, S. M. (2008). Calpain 3 is a modulator of the dysferlin protein complex in skeletal muscle. *Human Molecular Genetics*, 17(12), 1855–1866.
- Khadilkar, S. V., Chaudhari, C. R., Dastur, R. S., Gaitonde, P. S., & Yadav, J. G. (2016). Limb-girdle muscular dystrophy in the Agarwals: Utility of founder mutations in CAPN3 gene. *Annals of Indian Academy of Neurology*, 19(1), 108–111. <https://doi.org/10.4103/0972-2327.175435>
- Krahn, M., Lopez de Munain, A., Streichenberger, N., Bernard, R., Pécheux, C., Testard, H., Pena-Segura, J. L., Yoldi, E., Cabello, A., Romero, N. B., Poza, J. J., Bouillot-Eimer, S., Ferrer, X., Goicoechea, M., Garcia-Bragado, F., Leturcq, F., Urtizberea, J. A., & Levy, N. (2006). CAPN3 mutations in patients with idiopathic eosinophilic myositis. *Annals of Neurology*, 59(6), 905–911. <https://doi.org/10.1002/ana.20833>
- Kramerova, I., Kudryashova, E., Tidball, J. G., & Spencer, M. J. (2004). Null mutation of calpain 3 (p94) in mice causes abnormal sarcomere formation in vivo and in vitro. *Human Molecular Genetics*, 13(13), 1373–1388. <https://doi.org/10.1093/hmg/ddh153>
- Lasa-Elgarresta, J., Mosqueira-Martin, L., Naldaiz-Gastesi, N., Saenz, A., Lopez de Munain, A., & Vallejo-Illarramendi, A. (2019). Calcium mechanisms in limb-girdle muscular dystrophy with CAPN3 mutations. *International Journal of Molecular Sciences*, 20(18), 4548. <https://doi.org/10.3390/ijms20184548>
- Li, H. (2013). Aligning sequence reads, clone sequences and assembly contigs with BWA-MEM. *arXiv preprint arXiv:1303.3997*.
- McKenna, A., Hanna, M., Banks, E., Sivachenko, A., Cibulskis, K., Kernysky, A., Garimella, K., Altshuler, A., Gabriel, S., Daly, M., & DePristo, M. A. (2010). The genome analysis toolkit: A MapReduce framework for analyzing next-generation DNA sequencing data. *Genome Research*, 20(9), 1297–1303.
- Muhlemann, O. (2016). Spermatogenesis studies reveal a distinct nonsense-mediated mRNA decay (NMD) mechanism for mRNAs with long 3'UTRs. *PLoS Genetics*, 12(5), e1005979. <https://doi.org/10.1371/journal.pgen.1005979>
- Nallamilli, B. R. R., Chakravorty, S., Kesari, A., Tanner, A., Ankala, A., Schneider, T., da Silva, C., Beadling, R., Alexander, J. J., Askree, S. H., Whitt, Z., Bean, L., Collins, C., Khadilkar, S., Gaitonde, P., Dastur, R., Wicklund, M., Mozaffar, T., Harms, M., ... Hegde, M. (2018). Genetic landscape and novel disease mechanisms from a large LGMD cohort of 4656 patients. *Annals of Clinical Translational Neurology*, 5(12), 1574–1587. <https://doi.org/10.1002/actn3.649>
- Norwood, F. L., Harling, C., Chinnery, P. F., Eagle, M., Bushby, K., & Straub, V. (2009). Prevalence of genetic muscle disease in northern England: In-depth analysis of a muscle clinic population. *Brain*, 132(Pt 11), 3175–3186. <https://doi.org/10.1093/brain/awp236>
- Ojima, K., Ono, Y., Ottenheijm, C., Hata, S., Suzuki, H., Granzier, H., & Sorimachi, H. (2011). Non-proteolytic functions of calpain-3 in sarco-plasmic reticulum in skeletal muscles. *Journal of Molecular Biology*, 407(3), 439–449. <https://doi.org/10.1016/j.jmb.2011.01.057>
- Pogoda, T. V., Krakhmaleva, I. N., Lipatova, N. A., Shakhovskaya, N. I., Shishkin, S. S., & Limborska, S. A. (2000). High incidence of 550delA mutation of CAPN3 in LGMD2 patients from Russia. *Human Mutation*, 15(3), 295. [https://doi.org/10.1002/\(SICI\)1098-1004\(200003\)15:3<295::AID-HUMU15>3.0.CO;2-8](https://doi.org/10.1002/(SICI)1098-1004(200003)15:3<295::AID-HUMU15>3.0.CO;2-8)
- Quick, S., Schaefer, J., Waessnig, N., Schultheiss, T., Reuner, U., Schoen, S., Reichmann, H., Strasser, R., & Speiser, U. (2015). Evaluation of heart involvement in calpainopathy (LGMD2A) using cardiovascular magnetic resonance. *Muscle & Nerve*, 52(4), 661–663.
- Richard, I., Brenguier, L., Dinçer, P., Roudaut, C., Bady, B., Burgunder, J. M., Chemaly, R., Garcia, C. A., Halaby, G., Jackson, C. E., Kurnit, D. M., Lefranc, G., Legum, C., Loiselet, J., Merlini, L., Nivelon-Chevallier, A., Ollagnon-Roman, E., Restagno, G., Topaloglu, H., & Beckmann, J. S. (1997). Multiple independent molecular etiology for limb-girdle muscular dystrophy type 2A patients from various geographical origins. *American Journal of Human Genetics*, 60(5), 1128–1138.
- Richard, I., Broux, O., Allamand, V., Fougerousse, F., Chianniikulchai, N., Bourg, N., Brenguier, L., Devaud, C., Pasturaud, P., Roudaut, C., Hillaire, D., Passos-Bueno, M. R., Zatz, M., Tischfield, J. A., Fardeau, M., Jackson, C. E., Cohen, D., & Beckmann, J. S. (1995). Mutations in the proteolytic enzyme calpain 3 cause limb-girdle muscular dystrophy type 2A. *Cell*, 81(1), 27–40.
- Salem, I. H., Hsairi, I., Mezghani, N., Kenoun, H., Triki, C., & Fakhfakh, F. (2012). CAPN3 mRNA processing alteration caused by splicing mutation associated with novel genomic rearrangement of Alu elements. *Journal of Human Genetics*, 57(2), 92–100. <https://doi.org/10.1038/jhg.2011.129>
- Sarkozy, A., Deschauer, M., Carlier, R. Y., Schrank, B., Seeger, J., Walter, M. C., Schoser, B., Reilich, P., Leturcq, F., Radunovic, A., Behin, A., Laforet, P., Eymard, B., Schreiber, H., Hicks, D., Vaidya, S. S., Gläser, D., Carlier, P. G., Bushby, K., ... Straub, V. (2012). Muscle MR

- findings in limb girdle muscular dystrophy type 2L. *Neuromuscular Disorders*, 22(Suppl 2), S122–S129. <https://doi.org/10.1016/j.nmd.2012.05.012>
- Schessl, J., Walter, M. C., Schreiber, G., Schara, U., Müller, C. R., Lochmüller, H., Bönnemann, C. G., Korinthenberg, R., & Kirschner, J. (2008). Phenotypic variability in siblings with calpainopathy (LGMD2A). *Acta Myologica*, 27, 54–58.
- Seelow, D., Schuelke, M., Hildebrandt, F., & Nürnberg, P. (2009). HomozygosityMapper—an interactive approach to homozygosity mapping. *Nucleic Acids Res*, 37, W593–W599. <https://doi.org/10.1093/nar/gkp369>
- Shum, E. Y., Jones, S. H., Shao, A., Dumdie, J., Krause, M. D., Chan, W. K., Lou, C. H., Espinoza, J. L., Song, H. W., Phan, M. H., Ramaiah, M., Huang, L., McCarrey, J. R., Peterson, K. J., de Rooij, D. G., Cook-Andersen, H., & Wilkinson, M. F. (2016). The antagonistic gene paralogs *Upf3a* and *Upf3b* govern nonsense-mediated RNA decay. *Cell*, 165(2), 382–395. <https://doi.org/10.1016/j.cell.2016.02.046>
- Sorimachi, H., Kinbara, K., Kimura, S., Takahashi, M., Ishiura, S., Sasagawa, N., Sorimachi, N., Shimada, H., Tagawa, K., & Maruyama, K. (1995). Muscle-specific calpain, p94, responsible for limb girdle muscular dystrophy type 2A, associates with connectin through IS2, a p94-specific sequence. *Journal of Biological Chemistry*, 270(52), 31158–31162.
- Straub, V., Murphy, A., Udd, B., & LGMD Workshop Study Group. (2018). 229th ENMC international workshop: Limb girdle muscular dystrophies—nomenclature and reformed classification Naarden, The Netherlands, 17–19 march 2017. *Neuromuscular Disorders*, 28(8), 702–710. <https://doi.org/10.1016/j.nmd.2018.05.007>
- Sveen, M. L., Thune, J. J., Kober, L., & Vissing, J. (2008). Cardiac involvement in patients with limb-girdle muscular dystrophy type 2 and Becker muscular dystrophy. *Archives of Neurology*, 65(9), 1196–1201. <https://doi.org/10.1001/archneur.65.9.1196>
- Urtasun, M., Sáenz, A., Roudaut, C., Poza, J. J., Urtizberea, J. A., Cobo, A. M., Richard, I., García Bragado, F., Leturcq, F., Kaplan, J. C., Martí Massó, J. F., Beckmann, J. S., & Lopez de Munain, A. (1998). Limb-girdle muscular dystrophy in Guipuzcoa (Basque Country, Spain). *Brain*, 121(Pt 9), 1735–1747. <https://doi.org/10.1093/brain/121.9.1735>
- Van der Auwera, G. A., Carneiro, M. O., Hartl, C., Poplin, R., Del Angel, G., Levy-Moonshine, A., Jordan, T., Shakir, K., Roazen, D., Thibault, J., Banks, E., Garimella, K. V., Altshuler, D., Gabriel, S., & DePristo, M. A. (2013). From FastQ data to high-confidence variant calls: The genome analysis toolkit best practices pipeline. *Current Protocols in Bioinformatics*, 43(1), 11.10.11–11.10.33.
- Vissing, J., Barresi, R., Witting, N., Van Ghelue, M., Gammelgaard, L., Bindoff, L. A., Straub, V., Lochmüller, H., Hudson, J., Wahl, C. M., Arnardottir, S., Dahlbom, K., Jonsrud, C., & Duno, M. (2016). A heterozygous 21-bp deletion in *CAPN3* causes dominantly inherited limb girdle muscular dystrophy. *Brain*, 139(Pt 8), 2154–2163. <https://doi.org/10.1093/brain/aww133>
- Zatz, M., & Starling, A. (2005). Calpains and disease. *The New England Journal of Medicine*, 352(23), 2413–2423. <https://doi.org/10.1056/NEJMra043361>
- Zetoune, A. B., Fontaniere, S., Magnin, D., Anczukow, O., Buisson, M., Zhang, C. X., & Mazoyer, S. (2008). Comparison of nonsense-mediated mRNA decay efficiency in various murine tissues. *BMC Genetics*, 9, 83. <https://doi.org/10.1186/1471-2156-9-83>

SUPPORTING INFORMATION

Additional supporting information may be found in the online version of the article at the publisher's website.

How to cite this article: Khan, K., Mehmood, S., Liu, C., Siddiqui, M., Ahmad, A., Faiz, B. Y., Chioza, B. A., Baple, E. A., Ullah, M. I., Akram, Z., Satti, H. S., Khan, R., Harlalka, G. V., Jameel, M., Akram, T., Baig, S. M., Crosby, A. H., Hassan, M. J., Zhang, F., ... Khan, T. N. (2022). A recurrent rare intronic variant in *CAPN3* alters mRNA splicing and causes autosomal recessive limb-girdle muscular dystrophy-1 in three Pakistani pedigrees. *American Journal of Medical Genetics Part A*, 188A: 498–508. <https://doi.org/10.1002/ajmg.a.62545>

ARTICLE OPEN



Evidence that the Ser192Tyr/Arg402Gln in *cis* Tyrosinase gene haplotype is a disease-causing allele in oculocutaneous albinism type 1B (OCA1B)

Siyang Lin¹, Aida Sanchez-Bretaño², Joseph S. Leslie¹, Katie B. Williams³, Helena Lee^{2,4}, N. Simon Thomas^{5,6}, Jonathan Callaway^{5,6}, James Deline³, J. Arjuna Ratnayaka², Diana Baralle⁷, Melanie A. Schmitt⁸, Chelsea S. Norman^{2,9}, Sheri Hammond³, Gaurav V. Harlalka^{1,10}, Sarah Ennis¹¹, Harold E. Cross¹², Olivia Wenger^{13,14}, Andrew H. Crosby^{1,15}✉, Emma L. Baple^{1,15}✉ and Jay E. Self^{1,2,4}✉

Oculocutaneous albinism type 1 (OCA1) is caused by pathogenic variants in the *TYR* (tyrosinase) gene which encodes the critical and rate-limiting enzyme in melanin synthesis. It is the most common OCA subtype found in Caucasians, accounting for ~50% of cases worldwide. The apparent 'missing heritability' in OCA is well described, with ~25–30% of clinically diagnosed individuals lacking two clearly pathogenic variants. Here we undertook empowered genetic studies in an extensive multigenerational Amish family, alongside a review of previously published literature, a retrospective analysis of in-house datasets, and tyrosinase activity studies. Together this provides irrefutable evidence of the pathogenicity of two common *TYR* variants, p.(Ser192Tyr) and p.(Arg402Gln) when inherited in *cis* alongside a pathogenic *TYR* variant in *trans*. We also show that homozygosity for the p.(Ser192Tyr)/p.(Arg402Gln) *TYR* haplotype results in a very mild, but fully penetrant, albinism phenotype. Together these data underscore the importance of including the *TYR* p.(Ser192Tyr)/p.(Arg402Gln) in *cis* haplotype as a pathogenic allele causative of OCA, which would likely increase molecular diagnoses in this missing heritability albinism cohort by 25–50%.

npj Genomic Medicine (2022)7:2; <https://doi.org/10.1038/s41525-021-00275-9>

INTRODUCTION

Oculocutaneous albinism (OCA) refers to a group of genetically and clinically heterogeneous disorders characterised by abnormal melanin synthesis, resulting in decreased or absent pigmentation of eyes, skin and hair.

Ocular features are present in individuals with OCA and are characteristic of the disease. These include photophobia, nystagmus, foveal hypoplasia, iris transillumination and abnormal decussation of nerve fibres at the optic chiasm resulting in crossed asymmetry on visual evoked potential testing¹. These ocular features may, however, be variable with no single defining characteristic found to be present in every individual with OCA². The cutaneous phenotype may also vary, ranging from total absence to near-normal levels of pigmentation, and can be difficult to evaluate, particularly in individuals with a lightly pigmented ethnic background^{3,4}. As such, OCA can be difficult to distinguish clinically from several other ocular disorders with overlapping phenotypical features, such as *GPR143*-associated X-linked ocular albinism, where the hypopigmentation is limited to the eye¹, *FRMD7*-associated X-linked idiopathic congenital nystagmus⁵, *SLC38A8*-associated foveal hypoplasia (also known as FHONDA; foveal hypoplasia, optic nerve decussation defects and

anterior segment dysgenesis)⁶, and dominant *PAX6*-related ocular developmental disorders⁷.

OCA1, associated with *TYR* gene variants, is the most common OCA subtype found in Caucasians accounting for ~50% of cases worldwide^{8,9}. *TYR* encodes the enzyme tyrosinase, which is the critical and rate-limiting enzyme in the biosynthesis of melanin in follicular and epidermal melanocytes in hair and skin, as well as in uveal melanocytes in the iris, ciliary body and choroid, and retinal pigment epithelium cells in the eye¹⁰. Disease-associated variants in the *TYR* gene cause complete or partial OCA1 depending on their impact on the residual activity of the encoded mutant tyrosinase enzyme¹¹. *TYR* gene variants that result in a severe reduction or complete abolition of enzyme activity are associated with OCA1A, characterised by an almost complete absence of hair, skin and eye pigmentation^{10,11}. Hypomorphic *TYR* variants in which mutant tyrosinase possess residual catalytic activity are associated with OCA1B, where affected individuals present with a milder phenotype with reduced levels of pigmentation^{10,11}.

The apparent missing heritability in OCA is well described, with ~25–30% of clinically affected individuals lacking two clearly pathogenic sequence alterations within the same OCA gene; this proportion is higher in individuals with a partial OCA phenotype^{11,12}. Several hypotheses have been proposed to explain this

¹RILD Wellcome Wolfson Centre, Royal Devon & Exeter NHS Foundation Trust, Barrack Road, Exeter, UK. ²Clinical and Experimental Sciences, Faculty of Medicine, University of Southampton, Southampton, UK. ³Center for Special Children, Vernon Memorial Healthcare, La Farge, WI, USA. ⁴Southampton Eye Unit, University Hospital Southampton NHS Foundation Trust, Southampton, UK. ⁵Faculty of Medicine, University of Southampton, Southampton, UK. ⁶Wessex Regional Genetics Laboratory, Salisbury District Hospital, Salisbury, UK. ⁷Human Development and Health, Faculty of Medicine, University of Southampton, Southampton, UK. ⁸University of Wisconsin School of Medicine and Public Health, Department of Ophthalmology & Visual Sciences, Madison, WI, USA. ⁹The Rosalind Franklin Institute, Rutherford Appleton Laboratories, Harwell Science and Innovation Campus, Didcot, UK. ¹⁰Rajarshi Shahu College of Pharmacy, Malvihiir, Buldana, India. ¹¹Department of Human Genetics and Genomic Medicine, University of Southampton, Southampton, UK. ¹²Department of Ophthalmology, University of Arizona College of Medicine, Tucson, AZ, USA. ¹³New Leaf Clinic, PO Box 33616014 East Chestnut Street, Mount Eaton, OH 44691, USA. ¹⁴Department of Pediatrics, Akron Children's Hospital, 214 West Bowery Street, Akron, OH 44308, USA. ¹⁵Peninsula Clinical Genetics Service, Royal Devon & Exeter Hospital (Heavitree), Gladstone Road, Exeter, UK. ✉email: a.h.crosby@exeter.ac.uk; E.Baple@exeter.ac.uk; jes3@soton.ac.uk

missing heritability, including variants in the promoter or other regulatory elements, as well as epistatic or synergistic interactions between known genes^{11,13}. Two *TYR* sequence variants [NM_000372.4:c.575 C > A; **p.(Ser192Tyr)** or S192Y and c.1205 G > A; **p.(Arg402Gln)** or R402Q], previously described as non-pathogenic polymorphisms due to their frequency in the general population (25 and 18% respectively), have been found to be enriched in cohorts of OCA patients with only one identified *TYR* pathogenic variant^{8,11,14–22}, leading to suggestions that these variants may in fact account for some of this missing heritability^{8,9,14,15,18,23–27}, although this has, however, been disputed by others^{17,19,28}. We and others have hypothesised that these variants may be pathogenic only when present in *cis* and inherited in bi-allelic fashion with a second deleterious *TYR* variant for tyrosinase activity to be sufficiently reduced to a level that will cause an OCA phenotype^{13,27,29}. However, due to the high frequency of the p.(Ser192Tyr) and p.(Arg402Gln) variants in the general population, and the often small family sizes common to modern European populations, in many cases it has not always been possible to obtain informative allele segregation to phase gene variants and prove inheritance of a *cis* p.(Ser192Tyr)/p.(Arg402Gln) haplotype in *trans* with the pathogenic *TYR* alteration in all affected individuals^{27,30}. This remaining uncertainty in clinical interpretation of this haplotype limits its routine reporting in diagnostic testing. This has important diagnostic implications; designating the *TYR* p.(Ser192Tyr)/p.(Arg402Gln) haplotype as pathogenic could substantially increase the diagnostic yield by ~25–50% in albinism patient cohorts with missing heritability¹³. This also further supports the hypothesis that the prevalence of OCA1, commonly quoted as ~1 in 40,000¹⁰, likely represents a substantial underestimation, particularly amongst Caucasian populations with fair pigmentation³¹. In this study, we present extensive genetic data stemming from our investigation of a large multigenerational extended Amish family, alongside functional studies, a review of genotyped UK based albinism cohorts and a review of existing literature to provide strong evidence to support pathogenicity of the *TYR* p.(Ser192Tyr)/(Arg402Gln) in *cis* haplotype and its contribution to OCA1B in European populations.

RESULTS

Clinical findings in an extended Amish family

We initially investigated a large multigenerational extended Old Order Amish family of Ohio ancestry residing in Wisconsin (USA) with 9 affected individuals all exhibiting nystagmus and variable levels of hair and skin hypopigmentation (Fig. 1; family 4). On the basis of a detailed medical history, assessment of skin and hair pigmentation, and ophthalmic investigations in selected affected individuals, a diagnosis of likely mild OCA was made in all affected individuals. We subsequently recruited two additional Amish families with a total of four affected individuals with a similar clinical phenotype (Fig. 1; families 2 and 3). In addition, a further Amish family with a single affected individual with OCA was recruited to the study (Fig. 1; family 1). This individual displayed clinical features consistent with a complete OCA phenotype, including pale skin and white/blonde hair and eyelashes, nystagmus, iris transillumination defects and foveal hypoplasia. Affected individuals were not noted to bruise or bleed easily, although specific haematological investigations were not performed. Clinical findings for all affected individuals are summarised in Table 1.

Genetic findings in Amish families (families 1–4)

Exome sequencing was initially performed in two affected individuals in family 4 (individuals IX:9 and IX:22) for targeted evaluation using the “Albinism or congenital nystagmus v1.0” PanelApp virtual gene panel (41 genes). Subsequently, variants

predicted to have a functional consequence (including copy number variants) located genome-wide were identified and filtered according to allele frequency (gnomAD minor allele frequency (MAF) of <0.01). This identified only a single plausible candidate disease variant in both individuals, a heterozygous *TYR* missense variant (GRCh38) chr11:g.89178708 T > G; NM_000372.4:c.755 T > G; p.(Met252Arg) or M252R. The p.Met252 amino acid residue is located in the catalytic domain of the tyrosinase protein and is conserved across a variety of vertebrate species (Fig. 1b). This variant was absent in gnomAD and Genome Project population databases, although it was present in an Amish control exome dataset (allele frequency 0.0023) in heterozygous form only. In silico analysis of the p.(Met252Arg) variant using SIFT, PolyPhen-2 and PROVEAN predicted the variant to be deleterious, possibly damaging and deleterious. This variant has been reported in the compound heterozygous form [with a previously reported p.(Arg217Trp) variant] in a single individual with OCA²² and is considered to be likely pathogenic. Exome sequencing did not identify any additional candidate single nucleotide or structural disease variants in any OCA-associated genes.

To explore this apparent missing heritability, targeted dideoxy sequencing of all coding regions and intron-exon junctions of the *TYR* gene was performed in these two individuals. This confirmed the presence of the p.(Met252Arg) variant and also identified a further two *TYR* missense variants (GRCh38) chr11:g.89178528 C > A; NM_000372.4:c.575 C > A; p.(Ser192Tyr) (S192Y) and (GRCh38) chr11:g.89284793 G > A; NM_000372.4:c.1205 G > A; p.(Arg402Gln) (R402Q) in the same two individuals, excluded from the exome sequencing analysis based on individual population frequencies of 0.25 and 0.18, respectively. Segregation of all three *TYR* variants in all Amish families (families 1–4) is shown in Fig. 1, which demonstrates that the p.(Ser192Tyr)/p.(Arg402Gln) variants were linked in *cis* and inherited in a compound heterozygous fashion with p.(Met252Arg) (which itself occurs in *cis* with p.(Arg402Gln)) in all affected individuals except for a single affected individual with OCA, found to be homozygous for p.(Met252Arg) through targeted dideoxy sequencing. Individuals compound heterozygous for *TYR* p.(Met252Arg) and p.(Ser192Tyr)/p.(Arg402Gln) alleles displayed clinical features suggestive of partial albinism with variable skin and hair depigmentation, while the individual homozygous for the *TYR* p.(Met252Arg) variant displayed features of classical OCA including nystagmus, iris transillumination defects, a depigmented fundus and foveal hypoplasia (Table 1). Notably, individuals carrying the *TYR* p.(Met252Arg) variant on one allele and only the p.(Arg402Gln) or the p.(Ser192Tyr) variant on the other allele were apparently unaffected with no clinical features of OCA (individuals VIII:9, IX:2, IX:21, X:6, X:8, IX:1 and IX:4; Fig. 1a).

Additive temperature-sensitive effects of p.(Ser192Tyr) (S192Y) and p.(Arg402Gln) (R402Q) variants on *TYR* enzymatic activity

The *TYR* p.(Arg402Gln) variant alone has previously been proposed to contribute to OCA when inherited in *trans* with a pathogenic *TYR* variant^{9,14–16,22,23,25,26,32}. Our pedigree analysis, however, appears to dispute this, with five individuals compound heterozygous for the pathogenic *TYR* p.(Met252Arg) variant as well as the p.(Arg402Gln) variant and yet showing no clinical features of OCA (individuals VIII:9, IX:2, IX:21, X:6 and X:8; Fig. 1a). At the same time, 13 individuals who were compound heterozygous for *TYR* p.(Met252Arg) and p.(Ser192Tyr)/p.(Arg402Gln) alleles all displayed clinical features of partial albinism, suggesting an additive impact of the p.(Ser192Tyr) and p.(Arg402Gln) variants on tyrosinase function. To investigate this further, we designed functional experiments to study and quantify the effects of the p.(Ser192Tyr) and p.(Arg402Gln) variants both independently and in combination compared to wild-type tyrosinase enzyme.

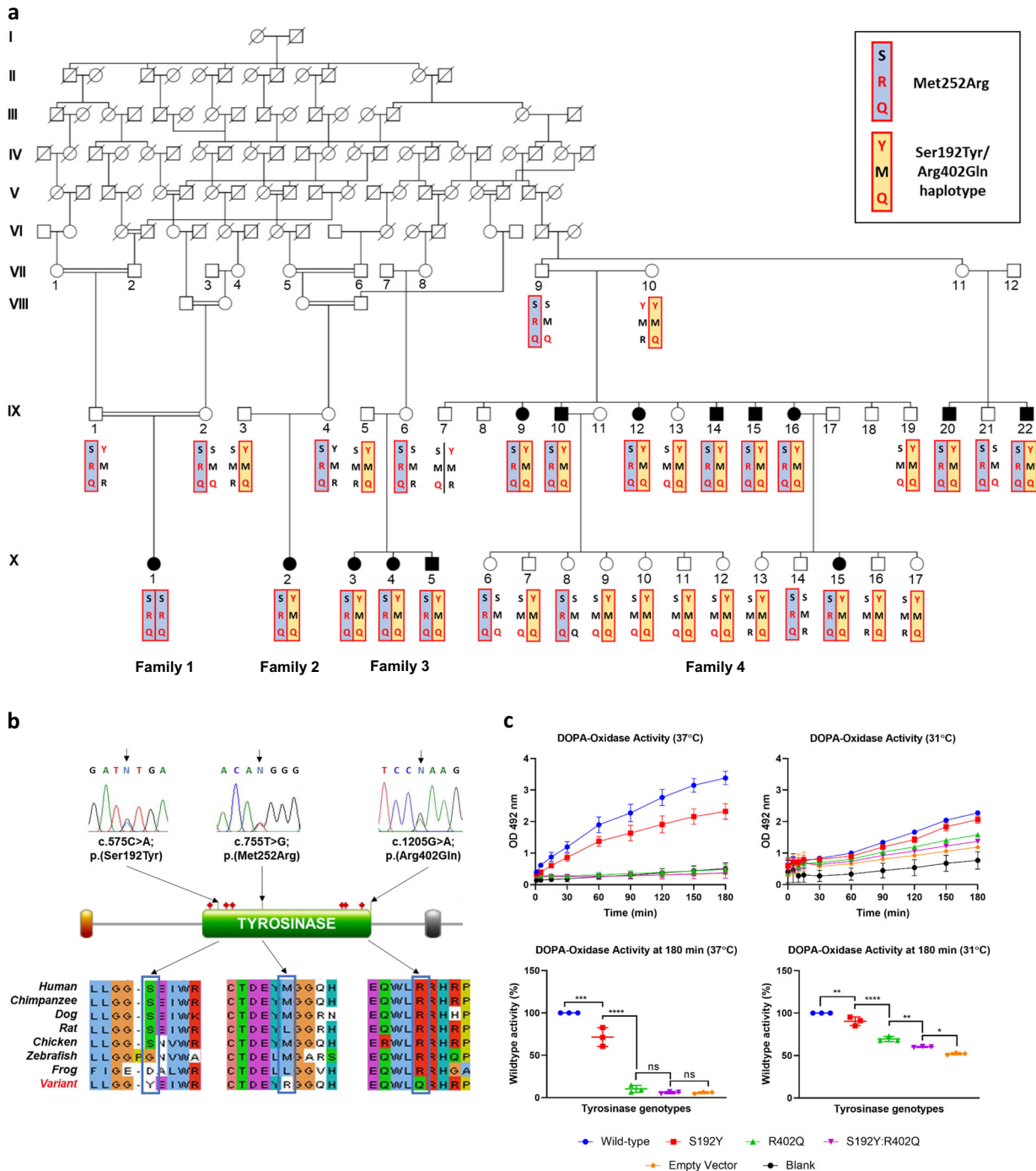


Table 1. Summary of clinical features observed in affected individuals in families 1–4 with OCA.

Family (ID)	Nystagmus	Hair colour	Eye colour	Other ocular features	Other systemic features
1 (X:1)	+	Blonde	Blue	Iris transillumination defects, depigmented fundus, foveal hypoplasia, alternating esotropia, optic disc hypoplasia	–
2 (X:2)	+	NA	NA	Blunted foveal reflex, depigmented fundus. ERG limited and awaiting a repeat	NA
3 (X:3)	+	Blonde	Blue	Iris transillumination defects blunted foveal reflex	–
3 (X:4)	+	Dark blonde	Blue	transillumination defects, foveal hypoplasia, strabismus	–
3 (X:5)	NA	Strawberry blonde	NA	Blunted foveal reflex	–
4 (IX:9)	+	Blonde	Blue	Pale fundi, iris transillumination defects, foveal hypoplasia, myopia, strabismus. Nyctalopia, photosensitivity and peripheral VF loss with normal ERG	–
4 (IX:10)	+	Pigmented	Blue	–	Mild learning difficulties
4 (IX:12)	+	Light brown	NA	–	–
4 (IX:14)	+	Dark brown	Blue	Pale fundi	–
4 (IX:15)	+	Pigmented	Blue	–	–
4 (IX:16)	+	NA	NA	NA	NA
4 (IX:20)	+	Blonde	Blue	–	–
4 (IX:22)	+	White/ blonde	Blue	–	–
4 (X:15)	+	Brown	Brown	Myopia	Neonatal intraventricular haemorrhage

The (+) and (–) symbols indicate the presence or absence of a feature in an affected subject, respectively. ERG electroretinogram, NA information not available.

Figure 1c shows the DOPA-oxidase activity for all tyrosinase mutants analysed from 0 min to 180 min at 31 °C and 37 °C. At 37 °C, a slight decrease in DOPA-oxidase activity of the p.(Ser192Tyr) mutants was observed, and an almost total loss of DOPA-oxidase activity in the p.(Arg402Gln) mutants and p.(Ser192Tyr)/p.(Arg402Gln) double mutants. At 31 °C, the loss of tyrosinase activity caused by all of the TYR-mutants was reduced but still significant when compared to wildtype. For all the TYR mutant cell lines, the p.(Ser192Tyr)/p.(Arg402Gln) double mutants showed the most reduced tyrosinase activity, followed by p.(Arg402Gln) mutant, with the p.(Ser192Tyr) mutant least affected. There was a statistically significant difference between all three mutant groups, indicative of a cumulative effect of both p.(Ser192Tyr) and p.(Arg402Gln) mutations on tyrosinase activity.

Enrichment of the TYR p.(Ser192Tyr)/p.(Arg402Gln) haplotype in OCA and control cohorts

Interrogation of a clinical cohort of 161 affected individuals with nystagmus and/or albinism (Southampton cohort) (including individuals previously reported by Norman et al. and O’Gorman et al.^{13,27}) identified 71 individuals with two pathogenic or likely pathogenic variants (molecularly diagnosed including *TYR*, *OCA2*, *GPR143* and *PAX6* genes), 51 individuals carrying only a single likely disease-associated *TYR* variant with no candidate pathogenic variants identified in other OCA genes (missing heritability), and 39 individuals with no disease-associated *TYR* variants. All patients were sequenced using either the “Albinism or congenital nystagmus v1.0” PanelApp gene panel (41 genes) (<https://panelapp.genomicsengland.co.uk/panels/>) or a broader research panel as previously described^{13,27}. Copy number analysis was not performed. Of these, 2 of the 71 individuals in the molecularly diagnosed group and 49 of the 51 individuals in the missing heritability group were found to have a genotype consistent with the presence of the *TYR* p.(Ser192Tyr)/p.(Arg402Gln) haplotype (i.e. individuals who were homozygous or heterozygous for both these variants) (Table 2); this information was unavailable for the 39 molecularly undiagnosed individuals in this clinical cohort. A

review of seven published OCA cohorts with missing heritability (i.e. individuals in whom only a single pathogenic *TYR* variant has been identified), together with our study cohort, found that approximately half of all affected individuals (50.7%) had a genotype consistent with the *TYR* p.(Ser192Tyr)/p.(Arg402Gln) haplotype (Table 2). This is markedly enriched compared to molecularly diagnosed OCA cohorts (2.0%), as well as a control cohort of Amish individuals with no OCA diagnoses (16.9%; Pearson’s Chi-squared test, $p < 2.2e-16$). These findings strongly suggest that the *TYR* p.(Ser192Tyr)/p.(Arg402Gln) haplotype contributes to the OCA phenotype.

Prevalence of TYR p.(Ser192Tyr)/p.(Arg402Gln) haplotype in OCA cohorts with missing heritability

Forty-nine affected individuals in our (Southampton and Salisbury) study cohorts were identified as carrying only a single pathogenic or likely pathogenic *TYR* variant as well as harbouring homozygous or heterozygous *TYR* p.(Ser192Tyr) and p.(Arg402Gln) variants; of these, familial segregation was performed in 41 individuals and their parents to assess the phase of the variants. In 23 individuals, this confirmed that the *TYR* p.(Ser192Tyr) and p.(Arg402Gln) variants were inherited in *cis*, and this haplotype was in *trans* to the previously identified pathogenic or likely pathogenic *TYR* variant (Table 3). For the remaining 18 cases, definitive segregation was not possible. Notably, no case was identified in which segregation showed that p.(Ser192Tyr) and p.(Arg402Gln) were not in *trans* with the pathogenic or likely pathogenic variant.

In five of the seven published OCA cohorts with missing heritability reviewed (Table 2), it was possible to determine the *cis/trans* phase of the *TYR* p.(Ser192Tyr) and p.(Arg402Gln) variants in a proportion of individuals reported^{17,20,22,30,31} (Table 3); in the remaining individuals this was not possible due to familial samples being unavailable for segregation analysis, or uninformative segregation results (owing to the high allele frequency of the p.(Ser192Tyr) and p.(Arg402Gln) *TYR* variants in the general population). For the remaining two studies of OCA cohorts with

Table 2. Prevalence of both TYR p.(Ser192Tyr)/S192Y and p.(Arg402Gln)/R402Q variants in OCA cohorts.

OCA cohorts with missing heritability (individuals with only 1 TYR pathogenic or likely pathogenic variant identified)		Molecularly diagnosed OCA1 cohorts (individuals with 2 TYR pathogenic or likely pathogenic variant identified)									
This study ^a	Hutton & Spritz ⁸	Hutton & Spritz ¹⁵	Oetting ¹⁷	Ghodsinejad Kalahroudi ²⁰	Lasseaux ²²	Gronskov ³¹	Campbell ³⁰	Hutton & Spritz ¹⁵	Oetting ¹⁷	Ghodsinejad Kalahroudi ²⁰	Gronskov ³¹
Phenotype	Nystagmus and/or mild OCA albinism	ARO/ mild OCA	OCA	OCA1	OCA1	Nystagmus and/or absence of fovea	Albinism (OCA, AROA or OA)	OCA	OCA1	OCA1	Albinism (OCA, AROA or OA)
Country (ethnicity)	England (Caucasian)	USA, Canada, Northern Europe (non-Hispanic/Latino Caucasians)	USA, Canada, Northern Europe (non-Hispanic/Latino Caucasians)	NA (Iranian)	France	Scandinavia (Scandinavian)	Scandinavia (Scandinavian)	USA, Canada, Northern Europe (non-Hispanic/Latino Caucasians)	NA (Iranian)	(Iranian)	Scandinavia (Scandinavian)
No of the individuals in the cohort	51	20	13	3	6	158	29	71	9	19	2
No of individuals hom or het for both TYR S192Y & R402Q	49	1	3	2	0	64	21	2	0	0	0
Proportion of study cohort where S192Y/R402Q haplotype is possible	49/51 (96.1%)	1/20 (5%)	3/13 (23.1%)	2/3 (66.7%)	0/6 (0%)	64/158 (40.5%)	21/29 (72.4%)	2/71 (2.8%)	0/9 (0%)	0/19 (0%)	0/2 (0%)
Combined proportion where S192Y/R402Q haplotype is possible											2/101 (2.0%)
<p>ARO/A autosomal recessive ocular albinism, AXD in-house Amish exome database, het heterozygous, hom homozygous, OCA oculocutaneous albinism, OA ocular albinism, no number.</p> <p>^aThis cohort includes individuals previously reported in Norman et al. and O'Gorman et al.</p>											

missing heritability, the *cis/trans* phase of the *TYR* p.(Ser192Tyr) and p.(Arg402Gln) variants could not be determined from the reported genotypes^{8,15}. There were 41 OCA individuals with missing heritability from these five studies in whom the p.(Ser192Tyr)/p.(Arg402Gln) haplotype was possible, and where the *cis/trans* phase of the *TYR* p.(Ser192Tyr) and p.(Arg402Gln) variants could also be determined. In accordance with the findings from our local research cohorts, together with this additional informative cohort derived from five published studies, the *TYR* p.(Ser192Tyr)/p.(Arg402Gln) haplotype segregated in *trans* with the pathogenic *TYR* variant in all 64 cases (amounting to 25.5% of total missing heritability cases) (Table 3). Taken together with the findings in Table 2, this suggests that the p.(Ser192Tyr)/p.(Arg402Gln) haplotype completes the molecular diagnosis in ~25–50% of OCA individuals with missing heritability.

DISCUSSION

The pathogenicity of *TYR* p.(Ser192Tyr) and p.(Arg402Gln) variants and their contribution to the OCA phenotype, either in isolation or when linked in *cis*, has been heavily debated in many studies^{8,9,14,15,17–19,23–28}. As such, these *TYR* variants are variably reported by clinical testing laboratories and potentially excluded, even when shown to be in *cis*. Here our genomic and functional data, initiated by our search for the cause of OCA in a number of Amish families, provide irrefutably strong evidence that the *TYR* p.(Ser192Tyr) and p.(Arg402Gln) variants are pathogenic when in *cis*. The increased frequency of the *TYR* p.(Met252Arg) variant in the Amish community, likely due to founder effects and endogamy, together with the large family sizes typical within the community, permitted empowered cosegregation studies able to determine the haplotype, phasing and inheritance of the common p.(Ser192Tyr) and p.(Arg402Gln) *TYR* variants together with the p.(Met252Arg) variant in a large number of related individuals.

Both Jagirdar et al. and our group have previously proposed that both *TYR* p.(Ser192Tyr) and p.(Arg402Gln) variants, acting in *cis*, may have an additive effect producing a greater reduction in enzyme activity compared to each variant individually^{27,29}. Both p.(Ser192Tyr) and p.(Arg402Gln) variants are common in Caucasian populations with allele frequencies of 36% and 27%, respectively (gnomAD v2.1.1), and would thus normally be considered benign. Indeed, our study demonstrates that inheritance of either variant individually in compound heterozygous form with the deleterious p.(Met252Arg) variant is insufficient to result in an OCA phenotype (individuals VIII:9, IX:1, IX:2, IX:4, X:6 and X:8; Fig. 1a). The p.(Ser192Tyr) and p.(Arg402Gln) variants are believed to have arisen independently on different ancestral haplotypes³³, and their combined presence in *cis* on a recombinant haplotype is relatively rare, predicted to be between 1.1% to 1.9% in European populations^{27,29,31}. Our studies here, alongside other previous studies^{8,13,17,22,27,30,31}, provide strong support to show that the *TYR* p.(Ser192Tyr)/p.(Arg402Gln) the haplotype is enriched in Caucasian OCA cohorts with missing heritability (Table 2), and contributes to an OCA1B diagnosis when inherited in *trans* with a second deleterious *TYR* variant, particularly in individuals with lower pigmentation backgrounds, who may be more susceptible to the damaging effects of hypomorphic variants^{16,34}. However, given the number of apparently unaffected individuals homozygous for the p.(Ser192Tyr)/p.(Arg402Gln) haplotype reported in the literature (Supplementary Table 1)^{29–31}, the penetrance of the p.(Ser192Tyr)/p.(Arg402Gln) haplotype might appear to be incomplete, confounding the argument that it is a pathogenic allele. The apparently reduced penetrance of the *TYR* p.(Ser192Tyr)/p.(Arg402Gln) haplotype may relate to the modifying effects of sequence variants in genes encoding other melanosomal proteins^{35–39}, although other genetic and molecular studies would be required to confirm this. However, we propose that individuals homozygous for the hypomorphic *TYR* p.(Ser192Tyr)/p.

(Arg402Gln) allele may have instead a consistent but mild phenotype, which is easily missed by incomplete phenotyping. In support of this, our studies identified five individuals with a clinical diagnosis of ‘possible hypomorphic’ OCA who were homozygous for *TYR* p.(Ser192Tyr)/p.(Arg402Gln), with no other known or likely *TYR* or other OCA gene-associated variants identified (Supplementary Table 1). All were noted to have foveal hypoplasia on OCT investigation but most had very mild, if any, other OCA features. Additionally, an apparently unaffected relative in our study was also identified as homozygous for *TYR* p.(Ser192Tyr)/p.(Arg402Gln). Despite the absence of nystagmus or any other pigmentary phenotype in this unaffected individual and visual acuities of 0.1 and 0.08 LogMAR (right and left eye respectively), the further detailed clinical investigation identified very mild iris transillumination and significant foveal hypoplasia (Supplementary Fig. 1). A review of the literature identified a further seven affected individuals in two studies with detailed clinical phenotyping available^{30,31} (Supplementary Table 1). Foveal hypoplasia, as well as iris transillumination, was documented in all thirteen individuals homozygous for both *TYR* p.(Ser192Tyr) and p.(Arg402Gln) (Supplementary Table 1). It, therefore, seems possible that individuals homozygous for the hypomorphic p.(Ser192Tyr)/p.(Arg402Gln) *TYR* allele have such a mild phenotype that they can easily go unidentified and unreported due to minimal effects on visual function or clear features of albinism; further phenotypic studies in large genomic population cohorts may be able to further clarify this potential association.

The *TYR* p.(Arg402Gln) variant is located near the copper-containing catalytic binding site CuB, and functional studies have shown that this amino acid alteration results in an enzyme with decreased thermal stability, disrupted copper-binding and reduced catalytic activity, thought to be mediated by decreased protein stability resulting in increased retention of the mutant tyrosinase protein as an unprocessed and misfolded glycoform in the endoplasmic reticulum (ER)^{29,40–46}. The *TYR* p.(Ser192Tyr) variant is located within the copper-containing catalytic binding site CuA, and has been shown to reduce tyrosinase enzymatic activity and melanocyte pigment production independent of the p.(Arg402Gln) variant^{29,47,48}. Genome-wide association studies have identified associations with skin, hair and eye pigmentation for both p.(Ser192Tyr) and p.(Arg402Gln) variants^{49–53}, suggesting these *TYR* variants have a role in normal pigmentation variation, and that the double-variant p.(Ser192Tyr)/p.(Arg402Gln) haplotype appears to show an additive effect on these pigmentation phenotypes compared to each variant individually²⁹. It is difficult however from the literature review alone to quantify the functional effects of the p.(Ser192Tyr) and p.(Arg402Gln) *TYR* variants both independently and in combination, compared to wild-type tyrosinase enzyme. This issue arises from the historical use of the human *TYR* expression construct pcTYR containing the p.(Ser192Tyr) variant to study the effects of “wildtype” tyrosinase activity^{42,54}. Computational approaches to *TYR* functional activity, based on protein flexibility and dynamic properties, suggest that the p.(Ser192Tyr) and p.(Arg402Gln) variants both result in a *TYR* protein that is less stable and has reduced enzyme activity compared to a wild-type molecule; the combined effect of having both changes together in a single *TYR* molecule, however, has not been previously investigated⁵⁵. Our study now shows for the first time a thermosensitive additive decrease in enzymatic function of the double-variant p.(Ser192Tyr)/p.(Arg402Gln) *TYR* protein compared to each variant acting individually (Fig. 1c), lending further support to the pathogenicity of the p.(Ser192Tyr)/p.(Arg402Gln) haplotype. Homology modelling of tyrosinase protein structure does not appear to show a direct interaction between the 192 and 402 amino acid residues³¹, and therefore this additional reduction in enzyme function in the double-mutant protein may instead be mediated by a combination of increased ER retention of the misfolded mutant protein [caused by p.(Arg402Gln) reducing

protein stability] and reduced enzyme activity of any released mutant protein [possibly resulting from steric hindrance effects of p.(Ser192Tyr) affecting the CuA binding site]⁴⁷, as proposed by Gronskov et al.³¹.

Subcellular localisation studies have determined that disease-associated *TYR* variants commonly result in near-absolute and irreversible ER retention of the mutant protein. The p.(Arg402Gln) variant, however, results in a thermosensitive tyrosinase protein that is retained in the ER at higher temperatures but is able to partially exit the ER at lower, more permissive temperatures^{40,44,46}. Homozygosity for the p.(Ser192Tyr)/p.(Arg402Gln) haplotype may therefore still permit sufficient quantities of mutant tyrosinase to reach the inner surface of the melanosomal membrane, where the mutant protein is still able to participate in protein–protein interactions with other melanosomal proteins involved in melanogenesis, such as TYRP1 and TYRP2^{56,57}, resulting in a less severe functional impact and a milder pigmentary phenotype that may not always be clinically significant. This thermosensitivity of the double-variant mutant TYR protein also provides a compelling explanation for our discovery of a consistent foveal hypoplasia phenotype in individuals who are homozygous for both p.(Ser192Tyr)/p.(Arg402Gln) *TYR* variants, as higher temperatures within the developing eye may result in a larger impact of these variants on tyrosinase function¹⁴, while lower temperatures at the skin and extremities instead result in greater preservation of mutant protein function and a milder and more variable pigmentary phenotype.

Together, our studies define the genotype, biochemical and phenotype correlation of the p.(Met252Arg) and p.(Ser192Tyr)/p.(Arg402Gln) *TYR* variants and collectively demonstrate that the *in cis* p.(Ser192Tyr)/p.(Arg402Gln) allele is pathogenic. As such, the *TYR* p.(Ser192Tyr)/p.(Arg402Gln) haplotype should be included as a pathogenic allele in future and retrospective genetic diagnoses of OCA, supporting the idea for a review of all previously undiagnosed OCA cases where these variants have been excluded. Reporting of the p.(Ser192Tyr)/p.(Arg402Gln) genotype in individuals in whom only a single deleterious *TYR* variant has been identified could permit a 25–50% uplift in confirmatory molecular diagnoses (when the phase has been determined) in this diagnostically challenging patient group (Tables 2, 3). Additionally, for patients with an albinism phenotype but no apparent variants in albinism genes, consideration of these variants when identified *in cis* as a pathogenic allele in its own right may also help provide clinical direction. For example, in individuals heterozygous for this allele, alternative diagnoses such as syndromic albinism might be considered less likely as they would be considered ‘at least a carrier of a pathogenic OCA1B allele’, and genomic data may be re-examined in a targeted fashion to search for further non-coding splice or structural variants in the *TYR* gene. In individuals with a very mild albinism phenotype or isolated foveal hypoplasia, identification of this pathogenic allele in homozygous form may provide the molecular diagnosis, ending their diagnostic odyssey. It will be crucially important to accurately determine the phase of these common variants, and due to the high frequencies of these variants alone in the population which can limit informative phase studies in relatives, consideration should perhaps be given to the use of amplicon-based long-read sequencing technologies that allow haplotype phasing in the genomic workup of such patients⁵⁸. Achieving an accurate molecular diagnosis will bring about important benefits in affected individuals and their families, allowing accurate prognostic information and family counselling to be provided, avoiding the need for further invasive investigations to confirm the clinical diagnosis or rule out syndromic forms of the disease or masquerading conditions, and has important therapeutic implications, given the emerging therapies currently under development and in clinical trials for OCA^{59,60}.

METHODS

Ethics statement

This study was approved by the institutional review board of all participating institutions (University of Arizona IRB—1000000050, Akron Children’s Hospital IRB—project number 986876–3, South Central—Hampshire A Research Ethics Committee—IRAS:174564), and all participating individuals were recruited with written informed consent.

Patient ascertainment and clinical phenotyping

Affected individuals and unaffected family members from four Ohio and Wisconsin Amish families with a common Ohio ancestry were recruited to this study (Fig. 1). Medical history was taken in all recruited family members, as well as detailed phenotyping of skin and hair pigmentation, particularly in the context of familial pigmentary background. A diagnosis of nystagmus was established in all affected individuals, and further ophthalmic investigations including electroretinography and optical coherence tomography (OCT) were performed in selected individuals. Blood/buccal samples were obtained with informed consent.

Molecular genetic analysis

Participating individuals had either peripheral venous blood samples taken in EDTA containing vacutainer tubes or buccal cell collection using the ORACollect® for paediatrics kit (DNA Genotek). Genomic DNA extraction was performed using either the ReliaPrep™ kit (Blood gDNA Miniprep System, Promega) for venous blood samples or the Xtreme DNA kit (Isohelix) for buccal samples, according to the manufacturer’s protocol. Exome sequencing (whole-exome sequencing, Exeter laboratory for individual IX:9 and Illumina TruSight™ One clinical exome sequencing panel, Southampton laboratory for individual IX:22) was performed as previously described^{27,61}. The whole-exome sequencing sample was prepared using Agilent Sureselect Whole Exome v6 targeting, while the TruSight™ One panel provides targeted sequencing for 4813 genes associated with clinical phenotypes and captures most of the coding regions of genes responsible for OCA subtypes 1–4 & 6 (*TYR*, *OCA2*, *TYRP1*, *SLC45A2* and *SLC24A5*, respectively), the ocular albinism gene (*GPR143*), all syndromic albinism genes and *PAX6*. Next-generation sequencing analysis (NextSeq500: Illumina) involved: read alignment (BWA-MEM (v0.7.12), mate-pairs fixed and duplicates removed (Picard v1.129), InDel realignment/base quality recalibration (GATK v3.4–46), single-nucleotide variant (SNV)/InDel detection (GATK HaplotypeCaller), annotation (Alamut v1.4.4), and read depth (GATK DepthOfCoverage). Additional filtering was performed using virtual gene panel analysis of exome data using the “Albinism or congenital nystagmus v1.0” PanelApp gene panel (41 genes) (<https://panelapp.genomicsengland.co.uk/panels/>), with variants prioritised by call quality, frequency in control datasets (Genome Aggregation Database; gnomAD v2.1.1 and 1000 Genomes Project) and predicted functional consequence^{13,27}. Primers were designed with Primer3 web software to cover all five coding exons and associated intron–exon junctions in *TYR*. As the 3′ region encompassing coding exons 4 and 5 of *TYR* shares high homology with a pseudogene, *TYRL*⁶², locus-specific amplification primers were designed for *TYR* exons 4 and 5 to prevent co-amplification of *TYR* and *TYRL* and subsequent misinterpretation of results. Dideoxy sequencing products were sequenced by Source BioScience Lifesciences (<https://www.sourcebioscience.com/>). Primer sequences and polymerase chain reaction conditions are listed in supplementary Table 3. The *TYR* c.755 T > G; p.(Met252Arg) variant and c.[575 C > A;1205 G > A]; p.[Ser192Tyr;Arg402Gln] variants-*in-cis* haplotype were submitted to ClinVar (www.ncbi.nlm.nih.gov/clinvar, accession numbers SCV001984755 and SCV001984756).

Establishment of Tyr mutant cell lines

The plasmid vector p3XFLAG-CMV-14 containing *TYR* cDNA was purchased from Addgene (Massachusetts, USA) and was initially deposited by Ruth Halaban⁶³. Upon arrival, sequencing revealed the p.(Ser192Tyr) (c.C575A) common population variant to be present. Site-directed mutagenesis was used to create the wild-type sequence (c.575 C, p.192Ser) as well as the p.(Arg402Gln) variant. The primers used for each variant inserted through site-directed mutagenesis are listed in Supplementary Table 2. Site-directed mutagenesis was carried out using the non-strand displacing activity of Pfu DNA polymerase to incorporate and extend the mutagenic primers. The reaction mixture contained Phusion Pfu Polymerase and its buffer, forward and reverse primers (0.5 μM), dNTPs (200 μM) and the

cDNA template. PCRs were performed in a total volume of 50 µl. Touch-down PCR conditions were set at 98 °C for 30 sec followed by 30 cycles of 98 °C for 10 sec, 45–72 °C for 10–30 sec and 72 °C for 15–30 sec, and a final extension step of 72 °C for 5–10 min. The PCR product was treated with DpnI to digest the methylated parental DNA.

Purified mutated tyrosinase PCR products were employed to transform NEB® 5-alpha Competent E. coli (High Efficiency; New England Biolabs, UK) via heat shock method. Briefly, 50 µl of thawed cells were kept on ice and combined with ~100 ng of plasmid DNA and incubated for 30 min. The cell-DNA mixture was heat-shocked at 42 °C for 30 sec and then placed on ice for 5 min. Cells were given S.O.C medium and incubated for an hour in a shaking incubator before being plated on ampicillin selection (100 µg/ml) LB agar plates. After overnight incubation at 37 °C, single ampicillin-resistant colonies were picked and grown in LB broth for approximately 16 h, at which point the cells were pelleted by centrifugation and the DNA extracted. When the stocks were diminished, competent cells were produced through treatment with CaCl₂ and subsequently transformed using the heat shock method described above.

Cell culture conditions

Human Embryonic Kidney 293 Freestyle (HEK293F) cells (Invitrogen, California, USA) were cultured in Freestyle culture medium (Invitrogen, California, USA) at 37 °C in a shaking incubator at 125 rpm with 8% CO₂. When cells reached a density of 1 × 10⁶ cells/ml, they were transfected with 30 µg of plasmids containing the p.(Arg402Gln) or p.(Ser192Tyr) mutations or co-transfected with both plasmids. The lipid-based reagent, 293fectin (60 µl) (ThermoFisher, UK), was diluted in Opti-MEM (ThermoFisher, UK) and incubated at room temperature for 5 mins. DNA and 293fectin were combined, gently mixed and incubated at room temperature for 30 mins before adding to cells. Then, cells were incubated in 6 wells plates for 72 h at 31 °C or 37 °C to reach 90% confluency, and the enzymatic activity assays were performed.

Enzymatic activity assays

The DOPA-oxidase activity was assessed in the different mutants. First, transfected cells from the different mutant clones were treated with L-DOPA, and the DOPA-oxidase activity was measured as the accumulation of the downstream product, dopachrome, following the manufacturer's protocol. Briefly, cells cultured in six-well plates were lysed in NP40 Cell Lysis Buffer (ThermoFisher, UK) containing 1 mM phenylmethylsulfonyl fluoride (PMSF) (in DMSO with a final concentration of 1%) and 1X protease and phosphatase inhibitor (Halt™ Phosphatase Inhibitor Cocktail, Thermo Fisher Scientific, UK), and protein concentration was measured by BCA assay (Thermo Scientific™ Pierce™ BCA Protein Assay Kit). Samples were then diluted into 4 µg/µl, and 50 µl or 30 µl sample aliquots were used for the DOPA assays. After adding the volume of the samples to 96-well plates, 150 µl of a phosphate buffer with L-DOPA 1 mM was added to the wells. Enzymatic activity was recorded as the absorbance of dopachrome at 492 nm from the start of L-dopa treatment (0 min) and at 30 min intervals thereafter for a total of 180 min at both 31 °C and 37 °C. Assays were routinely performed in triplicate and the results are presented as the means of the independent assays ± standard error.

Statistics

Results of enzymatic activity at 180 min were normalised to wild-type, with the values for wild-type taken to be 100% of the expected enzymatic activity. One-way ANOVA was performed followed by a Sidak's post-hoc test. A probability level of at least $p < 0.05$ was considered statistically significant ($*p < 0.05$, $**p < 0.01$, $***p < 0.001$, $****p < 0.0001$).

Evaluating the prevalence of TYR p.(Ser192Tyr)/p.(Arg402Gln) haplotype in OCA and control cohorts

A clinical cohort of affected individuals with nystagmus and/or albinism was retrospectively ascertained through the Southampton (161 individuals) and Salisbury (131 individuals) research databases. All individuals had been referred from a regional paediatric nystagmus clinic. Next-generation sequencing (Illumina TruSight One clinical exome sequencing panel), alignment and filtering were performed as previously described^{13,27}. The genomic data were interrogated to ascertain the frequency of the TYR p.(Ser192Tyr)/p.(Arg402Gln) haplotype in this cohort. A literature review was also performed to evaluate the reported prevalence of the TYR p.(Ser192Tyr)/p.(Arg402Gln) haplotype in additional published

OCA cohorts. This was compared against an in-house exome database of Amish individuals unaffected by OCA. Statistical analysis was performed using an established software package (R Core Team 2015; R Foundation for Statistical Computing, Vienna, Austria)⁶⁴.

Reporting summary

Further information on research design is available in the Nature Research Reporting Summary linked to this article.

DATA AVAILABILITY

The genetic variants investigated are deposited in ClinVar (accession codes SCV001984755 and SCV001984756). While the in-house Amish exome database is not publicly accessible due to the informed consent restrictions, de-identified information may be accessible and requested from corresponding authors A.H.C. (a.h.crosby@exeter.ac.uk) and E.L.B. (E.Baple@exeter.ac.uk).

Received: 2 July 2021; Accepted: 19 November 2021;

Published online: 13 January 2022

REFERENCES

- McKay, B. S. Pigmentation and vision: is GPR143 in control? *J. Neurosci. Res.* **97**, 77–87 (2019).
- Kruijt, C. C. et al. The phenotypic spectrum of albinism. *Ophthalmology* **125**, 1953–1960 (2018).
- Sjöström, A., Kraemer, M., Ohlsson, J. & Villarreal, G. Subnormal visual acuity syndromes (SVAS): albinism in Swedish 12–13-year-old children. *Doc. Ophthalmol.* **103**, 35–46 (2001).
- Sjöström, A. et al. Subnormal visual acuity (svas) and albinism in mexican 12–13-year-old children. *Doc. Ophthalmol.* **108**, 9–15 (2004).
- Thomas, M. G., Maconachie, G., Hisaund, M. & Gottlob, I. FRMD7-related infantile nystagmus. *GeneReviews*. <https://www.ncbi.nlm.nih.gov/books/NBK3822/> (2009).
- Poulter, J. A. et al. Recessive mutations in SLC38A8 cause foveal hypoplasia and optic nerve misrouting without albinism. *Am. J. Hum. Genet.* **93**, 1143–1150 (2013).
- Lima Cunha, D., Arno, G., Corton, M. & Moosajee, M. The spectrum of PAX6 mutations and genotype-phenotype correlations in the eye. *Genes (Basel)* <https://doi.org/10.3390/genes10121050> (2019).
- Hutton, S. M. & Spritz, R. A. Comprehensive analysis of oculocutaneous albinism among non-Hispanic caucasians shows that OCA1 is the most prevalent OCA type. *J. Invest. Dermatol.* **128**, 2442–2450 (2008a).
- Rooryck, C. et al. Molecular diagnosis of oculocutaneous albinism: new mutations in the OCA1-4 genes and practical aspects. *Pigment Cell Melanoma Res.* **21**, 583–587 (2008).
- Grønskov, K., Ek, J. & Brøndum-Nielsen, K. Oculocutaneous albinism. *Orphanet J. Rare Dis.* **2**, 1–8 (2007).
- Simeonov, D. R. et al. DNA variations in oculocutaneous albinism: an updated mutation list and current outstanding issues in molecular diagnostics. *Hum. Mutat.* **34**, 827–835 (2013).
- King, R. A. et al. Tyrosinase gene mutations in oculocutaneous albinism 1 (OCA1): definition of the phenotype. *Hum. Genet.* **113**, 502–513 (2003).
- O'Gorman, L. et al. A small gene sequencing panel realises a high diagnostic rate in patients with congenital nystagmus following basic phenotyping. *Sci. Rep.* **9**, 13229 (2019).
- Fukai, K. et al. Autosomal recessive ocular albinism associated with a functionally significant tyrosinase gene polymorphism. *Nat. Genet.* **9**, 92–95 (1995).
- Hutton, S. M. & Spritz, R. A. A comprehensive genetic study of autosomal recessive ocular albinism in Caucasian patients. *Invest. Ophthalmol. Vis. Sci.* **49**, 868–872 (2008b).
- Chiang, P. W., Spector, E. & Tsai, A. C. Oculocutaneous albinism spectrum. *Am. J. Med. Genet. A* **149A**, 1590–1591 (2009).
- Oetting, W. S. et al. The R402Q tyrosinase variant does not cause autosomal recessive ocular albinism. *Am. J. Med. Genet. A* **149A**, 466–469 (2009).
- Gargiulo, A. et al. Molecular and clinical characterization of albinism in a large cohort of Italian patients. *Invest. Ophthalmol. Vis. Sci.* **52**, 1281–1289 (2011).
- Preising, M. N., Forster, H., Gonser, M. & Lorenz, B. Screening of TYR, OCA2, GPR143, and MC1R in patients with congenital nystagmus, macular hypoplasia, and fundus hypopigmentation indicating albinism. *Mol. Vis.* **17**, 939–948 (2011).
- Ghodsinejad Kalahroudi, V. et al. Two novel tyrosinase (TYR) gene mutations with pathogenic impact on oculocutaneous albinism type 1 (OCA1). *PLoS ONE* **9**, e106656 (2014).

21. Mauri, L. et al. Clinical evaluation and molecular screening of a large consecutive series of albino patients. *J. Hum. Genet.* **62**, 277–290 (2017).
22. Lasseaux, E. et al. Molecular characterization of a series of 990 index patients with albinism. *Pigment Cell Melanoma Res.* **31**, 466–474 (2018).
23. Chiang, P.-W., Drautz, J. M., Tsai, A. C.-H., Spector, E. & Clericuzio, C. L. A new hypothesis of OCA1B. *Am. J. Med. Genet. Part A* **146**, 2968–2970 (2008).
24. Kausar, T., Bhatti, M. A., Ali, M., Shaikh, R. S. & Ahmed, Z. M. OCA5, a novel locus for non-syndromic oculocutaneous albinism, maps to chromosome 4q24. *Clin. Genet.* **84**, 91–93 (2013).
25. Kubal, A., Dagnelie, G. & Goldberg, M. Ocular albinism with absent foveal pits but without nystagmus, photophobia, or severely reduced vision. *J. AAPOS* **13**, 610–612 (2009).
26. Thomas, M. G., Maconachie, G. D., Sheth, V., McLean, R. J. & Gottlob, I. Development and clinical utility of a novel diagnostic nystagmus gene panel using targeted next-generation sequencing. *Eur. J. Hum. Genet.* **25**, 725–734 (2017).
27. Norman, C. S. et al. Identification of a functionally significant tri-allelic genotype in the Tyrosinase gene (TYR) causing hypomorphic oculocutaneous albinism (OCA1B). *Sci. Rep.* **7**, 4415 (2017).
28. Gronskov, K. et al. Birth prevalence and mutation spectrum in danish patients with autosomal recessive albinism. *Invest. Ophthalmol. Vis. Sci.* **50**, 1058–1064 (2009).
29. Jagirdar, K. et al. Molecular analysis of common polymorphisms within the human Tyrosinase locus and genetic association with pigmentation traits. *Pigment Cell Melanoma Res.* **27**, 552–564 (2014).
30. Campbell, P. et al. Clinical and genetic variability in children with partial albinism. *Sci. Rep.* **9**, 16576 (2019).
31. Gronskov, K. et al. A pathogenic haplotype, common in Europeans, causes autosomal recessive albinism and uncovers missing heritability in OCA1. *Sci. Rep.* **9**, 645 (2019).
32. Marti, A. et al. Lessons of a day hospital: comprehensive assessment of patients with albinism in a European setting. *Pigment Cell Melanoma Res.* **31**, 318–329 (2018).
33. Hudjashov, G., Villems, R. & Kivisild, T. Global patterns of diversity and selection in human tyrosinase gene. *PLoS ONE* **8**, e74307 (2013).
34. Mondal, M., Sengupta, M. & Ray, K. Functional assessment of tyrosinase variants identified in individuals with albinism is essential for unequivocal determination of genotype-to-phenotype correlation. *Br. J. Dermatol.* **175**, 1232–1242 (2016).
35. King, R. A. et al. MC1R mutations modify the classic phenotype of oculocutaneous albinism type 2 (OCA2). *Am. J. Hum. Genet.* **73**, 638–645 (2003).
36. Manga, P. et al. Rufous oculocutaneous albinism in southern African Blacks is caused by mutations in the TYRP1 gene. *Am. J. Hum. Genet.* **61**, 1095–1101 (1997).
37. Chiang, P. W., Fulton, A. B., Spector, E. & Hisama, F. M. Synergistic interaction of the OCA2 and OCA3 genes in a family. *Am. J. Med. Genet. A* **146A**, 2427–2430 (2008).
38. Sajid, Z. et al. Genetic causes of oculocutaneous albinism in Pakistani population. *Genes (Basel)* <https://doi.org/10.3390/genes12040492> (2021).
39. Wei, A. H., Yang, X. M., Lian, S. & Li, W. Genetic analyses of Chinese patients with digenic oculocutaneous albinism. *Chin. Med. J. (Engl.)* **126**, 226–230 (2013).
40. Berson, J. F., Frank, D. W., Calvo, P. A., Bieler, B. M. & Marks, M. S. A common temperature-sensitive allelic form of human tyrosinase is retained in the endoplasmic reticulum at the nonpermissive temperature. *J. Biol. Chem.* **275**, 12281–12289 (2000).
41. Spritz, R. A., Ho, L., Furumura, M. & Hearing, V. J. Jr. Mutational analysis of copper binding by human tyrosinase. *J. Invest. Dermatol.* **109**, 207–212 (1997).
42. Tripathi, R. K., Giebel, L. B., Strunk, K. M. & Spritz, R. A. A polymorphism of the human tyrosinase gene is associated with temperature-sensitive enzymatic activity. *Gene Expr.* **1**, 103–110 (1991).
43. Tripathi, R. K., Hearing, V. J., Urabe, K., Aroca, P. & Spritz, R. A. Mutational mapping of the catalytic activities of human tyrosinase. *J. Biol. Chem.* **267**, 23707–23712 (1992).
44. Halaban, R. et al. Endoplasmic reticulum retention is a common defect associated with tyrosinase-negative albinism. *Proc. Natl Acad. Sci. USA* **97**, 5889–5894 (2000).
45. Dolinska, M. B. et al. Oculocutaneous albinism type 1: link between mutations, tyrosinase conformational stability, and enzymatic activity. *Pigment Cell Melanoma Res.* **30**, 41–52 (2017).
46. Toyofuku, K., Wada, I., Spritz, R. A. & Hearing, V. J. The molecular basis of oculocutaneous albinism type 1 (OCA1): sorting failure and degradation of mutant tyrosinases results in a lack of pigmentation. *Biochem. J.* **355**, 259–269 (2001).
47. Chaki, M. et al. Molecular and functional studies of tyrosinase variants among Indian oculocutaneous albinism type 1 patients. *J. Invest. Dermatol.* **131**, 260–262 (2011).
48. Wei, A. H., Zang, D. J., Zhang, Z., Yang, X. M. & Li, W. Prenatal genotyping of four common oculocutaneous albinism genes in 51 Chinese families. *J. Genet. Genomics* **42**, 279–286 (2015).
49. Sulem, P. et al. Two newly identified genetic determinants of pigmentation in Europeans. *Nat. Genet.* **40**, 835–837 (2008).
50. Nan, H., Kraft, P., Hunter, D. J. & Han, J. Genetic variants in pigmentation genes, pigmentary phenotypes, and risk of skin cancer in Caucasians. *Int. J. Cancer* **125**, 909–917 (2009).
51. Sulem, P. et al. Genetic determinants of hair, eye and skin pigmentation in Europeans. *Nat. Genet.* **39**, 1443–1452 (2007).
52. Stokowski, R. P. et al. A genome-wide association study of skin pigmentation in a South Asian population. *Am. J. Hum. Genet.* **81**, 1119–1132 (2007).
53. Hu, H. H. et al. Assessment of tyrosinase variants and skin cancer risk in a large cohort of French subjects. *J. Dermatol. Sci.* **64**, 127–133 (2011).
54. Bouchard, B., Fuller, B. B., Vijayaradhhi, S. & Houghton, A. N. Induction of pigmentation in mouse fibroblasts by expression of human tyrosinase cDNA. *J. Exp. Med.* **169**, 2029–2042 (1989).
55. K, B. & Purohit, R. Mutational analysis of TYR gene and its structural consequences in OCA1A. *Gene* **513**, 184–195 (2013).
56. Kobayashi, T. & Hearing, V. J. Direct interaction of tyrosinase with Tyrp1 to form heterodimeric complexes in vivo. *J. Cell Sci.* **120**, 4261–4268 (2007).
57. Orlow, S. J. et al. High-molecular-weight forms of tyrosinase and the tyrosinase-related proteins: evidence for a melanogenic complex. *J. Invest. Dermatol.* **103**, 196–201 (1994).
58. van Dijk, E. L., Jaszczyszyn, Y., Naquin, D. & Thernes, C. The third revolution in sequencing technology. *Trends Genet.* **34**, 666–681 (2018).
59. Adams, D. R. et al. One-year pilot study on the effects of nitisinone on melanin in patients with OCA-1B. *JCI Insight* <https://doi.org/10.1172/jci.insight.124387> (2019).
60. Lee, H., Scott, J., Griffiths, H., Self, J. E. & Lotery, A. Oral levodopa rescues retinal morphology and visual function in a murine model of human albinism. *Pigment Cell Melanoma Res.* **32**, 657–671 (2019).
61. Rawlins, L. E. et al. An Amish founder variant consolidates disruption of CEP55 as a cause of hydranencephaly and renal dysplasia. *Eur. J. Hum. Genet.* **27**, 657–662 (2019).
62. Chaki, M., Mukhopadhyay, A. & Ray, K. Determination of variants in the 3'-region of the tyrosinase gene requires locus specific amplification. *Hum. Mutat.* **26**, 53–58 (2005).
63. Halaban, R., Cheng, E. & Hebert, D. N. Coexpression of wild-type tyrosinase enhances maturation of temperature-sensitive tyrosinase mutants. *J. Invest. Dermatol.* **119**, 481–488 (2002).
64. R Core Team. *R: A language and environment for statistical computing.* (Vienna, Austria, 2013). <https://www.r-project.org/>.

ACKNOWLEDGEMENTS

We would like to thank family members for their involvement in this study, and to acknowledge Dr. Caroline Wright for her assistance with this work and helpful comments on the manuscript. The work was supported by University of Exeter Vice Chancellor Scholarship (S.L.), the Gift of Sight Appeal (J.E.S., H.L., J.A.R., A.S.B., C.S.N.), MRC (Proximity to Discovery and Confidence in Concept grants MC_PC_18047, MC_PC_15054, MC_PC_15047 to University of Exeter, E.L.B. and A.H.C., G1001931 to E.L.B. and G1002279 to A.H.C.).

AUTHOR CONTRIBUTIONS

Clinical data collection, collation and analysis: S.L., J.D., K.B.W., M.A.S., A.V.D., H.E.C., S. H., O.W., E.L.B., A.H.C., J.E.S. Genetic and functional studies and data analysis: S.L., A.S. B., J.S.L., J.A.R., C.S.N., G.V.H., E.L.B., A.H.C., J.E.S. Manuscript writing and revision: S.L., A. S.B., H.L., N.S.T., J.C., D.B., S.E., E.L.B., A.H.C., J.E.S. Design and conception of studies, supervision and coordination: H.L., N.S.T., J.C., D.B., S.E., E.L.B., A.H.C., J.E.S. All authors have read and approve of the final manuscript.

COMPETING INTERESTS

The authors declare no competing interests.

ADDITIONAL INFORMATION

Supplementary information The online version contains supplementary material available at <https://doi.org/10.1038/s41525-021-00275-9>.

Correspondence and requests for materials should be addressed to Andrew H. Crosby, Emma L. Baple or Jay E. Self.

Reprints and permission information is available at <http://www.nature.com/reprints>

Publisher's note Springer Nature remains neutral with regard to jurisdictional claims in published maps and institutional affiliations.



Open Access This article is licensed under a Creative Commons Attribution 4.0 International License, which permits use, sharing, adaptation, distribution and reproduction in any medium or format, as long as you give appropriate credit to the original author(s) and the source, provide a link to the Creative Commons license, and indicate if changes were made. The images or other third party material in this article are included in the article's Creative Commons license, unless indicated otherwise in a credit line to the material. If material is not included in the article's Creative Commons license and your intended use is not permitted by statutory regulation or exceeds the permitted use, you will need to obtain permission directly from the copyright holder. To view a copy of this license, visit <http://creativecommons.org/licenses/by/4.0/>.

© The Author(s) 2022

Role of L-lysine in Ethanol Induced Behavioral Changes in Mice

Sumit Rathod¹, Vinay Bhalerao², Mangesh Deokar², Shirish Jain²

¹Department of Pharmacology, SVKM's Institute of Pharmacy, Dhule, (M.S.), India

²Department of Pharmacology, Rajarshi Shahu College of Pharmacy, Buldana, (M.S.), India

Received: 01-11-2021 / Revised: 28-11-2021 / Accepted: 22-12-2021

Corresponding author: Mr. Sumit S. Rathod

Conflict of interest: Nil

Abstract

Lysine, (S)-2,6,-diaminohexanoic acid, is a basic amino acid. Following ingestion, L-lysine is absorbed by the active transport process from the lumen of the small intestine into the enterocytes. L-lysine is a 5-HT₄ antagonist that can increase and decrease ethanol intake when they are given intraperitoneal administration. 5-HT₄ antagonist can block the rewarding and motivation effect as indicated by attenuation of sensitization to the locomotor stimulant effect of ethanol, decreased ethanol-induced conditioned place preference, and reduced ethanol drinking. Young healthy mice (21–30 g) were group-housed (five per cage) in opaque polypropylene cages. Animals were naive to drug treatment and experimentation at the beginning of all studies. Each experimental group was comprised of five mice. Testing was carried out in counterbalanced order concerning the treatment conditions in the noise-free room. Locomotor activity and conditioned place preference was assessed followed by acute and chronic exposure of ethanol to animals. The results revealed that acute as well as administration of L-lysine (20 and 40 mg/kg, i.p.) pre-treatment, 30 min before the test significantly reduced place preference in ethanol control-treated groups. In locomotor activity L-lysine (20 and 40 mg/kg, i.p.) pre-treatment, 30 min before the test significantly reduced locomotor count in ethanol control-treated groups in both acute and chronic groups. In conclusion, Results indicated that L-lysine exhibited an inhibitory influence against ethanol-induced behavioral changes in mice.

Keywords: L-lysine; 5-HT₄ antagonist, Ethanol dependence; Locomotor Activity; Conditioned Place Preference.

This is an Open Access article that uses a funding model which does not charge readers or their institutions for access and distributed under the terms of the Creative Commons Attribution License (<http://creativecommons.org/licenses/by/4.0>) and the Budapest Open Access Initiative (<http://www.budapestopenaccessinitiative.org/read>), which permit unrestricted use, distribution, and reproduction in any medium, provided original work is properly credited.

Introduction:

Ethanol is one of the most widely abused addictive drugs and has hazardous health consequences resulting from its chronic use[2]. Ethanol produces a striking array of behavioral effects in humans that are dependent on the dose of ethanol administered[3]. When used in low to

moderate quantities, it relieves anxiety and fosters a feeling of well-being and euphoria. Alcohol abuse is a pattern of drinking that results in harm to one's health, interpersonal relationships, or ability to work[9]. Alcohol abuse can result in brain damage which causes impairments in executive functioning

such as impairments to working memory, visuospatial skills, and can cause an abnormal personality as well as affective disorders to develop[11]. Several neurotransmitter systems like glutamate, noradrenaline, dopamine, serotonin, opiates, gamma-aminobutyric acid (GABA), and certain plasma membrane ion channels like voltage-sensitive calcium channels have been implicated in the effects of ethanol[4,15].

Serotonin is produced in and released from neurons that originate within discrete regions, or in the nuclei[12]. The neurotransmitter serotonin has long been a target of interest for potential pharmacotherapies for alcoholism because of the well-established link between serotonin depletion, impulsivity, and alcohol drinking behavior in mice and humans[6].

Lysine, (S)-2,6, -diaminohexanoic acid, is a basic amino acid. Following ingestion, L-lysine is absorbed by the active transport process from the lumen of the small intestine into the enterocytes[13]. The 5-HT₄ antagonist increased and decreased ethanol intake when they are given intraperitoneal administration. 5-HT₄ antagonist can block the rewarding and motivation effect as indicated by attenuation of sensitization to the locomotors stimulant effect of ethanol, decreased ethanol-induced conditioned placed preference, and reduced ethanol drinking. Functional and binding studies have shown that the 5-HT₄ receptor, is the G-protein coupled receptor which positively coupled to adenylate cyclase and increases the cAMP production or by generating IP₃ /DAG as second messengers. 5-HT receptor subtype 5-HT₄ receptor may involve in the control of voluntary ethanol intake in mice. The high densities of this receptor in the nucleus accumbens and other regions suggest the influence of ethanol intake with its reinforcing properties. The present study is carried out to evaluate the efficacy of serotonin 4 receptor antagonist on ethanol-

induced motivational and rewarding effect in mice[1].

Animals

Experimental Animals (Swiss Albino) Mice will be procured from Animal House of Rajarshi Shahu College of Pharmacy Buldana, Dist.-Buldana, and will be used in this study. The animal care and handling will be done according to the guidelines set by the CPCSEA. Young healthy mice (21–30 g) were group-housed (five per cage) in opaque polypropylene cages (28×21×14 cm) and maintained at the local conditions (23±2 °C and 40±2 % humidity) under 12:12 h light/dark cycle, with free access to rodent chow and tap water. The animal studies were approved by the Institutional Animal Ethics Committee (IAEC), constituted for control and supervision of experimental animals by the Ministry of Environment and Forests, Government of India, New Delhi, India. Animals were naive to drug treatment and experimentation at the beginning of all studies. Each experimental group was comprised of five mice. Testing was carried out in counterbalanced order concerning the treatment conditions in the noise-free room.

Drugs and solutions

L-LYSINE [Base] Monohydrate [C₆H₁₄N₂O₂H₂O] M.W.164.21 (Research-lab Fine Chem Industries Mumbai), ethanol (Changshu Yangyuan Chemical, China) used in the present study were dissolved in 0.9% saline. Drug solutions were prepared fresh, and doses of L-lysine are expressed in terms of its free base. The doses of l-lysine were selected based on previous reports[5].

Role of l-lysine in alcohol addiction

The 5-HT₄ antagonist increased and decreased ethanol intake when they are given intraperitoneal administration. 5-HT₄ antagonist can block the rewarding and motivation effect as indicated by attenuation of sensitization to the locomotors stimulant

effect of ethanol, decreased ethanol-induced conditioned place preference, and reduced ethanol drinking. Functional and binding studies have shown that the 5-HT₄ receptor, is the G-protein coupled receptor which positively coupled to adenylate cyclase and increases the cAMP production or by generating IP₃ /DAG as second messengers. 5-HT receptor subtype 5-HT₄ receptor may involve in the control of voluntary ethanol intake in mice. The high densities of this receptor in the nucleus accumbens and other regions suggest the influence of ethanol intake with its reinforcing properties[8].

Methods

Locomotor Activity

Locomotor activity was assessed in an actophotometer (VJ Instruments, Amaravati, India), having a diameter of 40 cm, equipped with three infrared beam cells pair (pair: one emitter and one receiver), 20 cm apart from each other and located on the walls of the circular arena and were connected to the digital counter. Locomotor activity was expressed in terms of the total number of counts of beams interruptions in 30 min.[7].

Conditioned place preferences

CPP experiments were conducted in a three-chambered place conditioning apparatus connected to a digital recorder and housed in a light- and sound-attenuated chamber. Two

(6.6"×5") conditioning chambers, one white with a rough floor and the other black with a smooth floor, were connected by a smaller (2.85"×5") central access chamber with gray walls and a smooth polyvinyl chloride floor. In addition, each chamber was equipped with a house light, with the luminance (40 lx) adjusted such that the environmental (visual and tactile) cues should not produce a significant baseline preference for a specific chamber. All chambers were separated by manually operated guillotine doors. The individual chamber activity was determined by photo beam breaks recorded by a digital recorder. The CPP test was carried out using Swiss mice as per the method described by Font et al. (2008) with slight modifications. This experiment involved three phases such as habituation (one session), conditioning (eight sessions), and testing (one session)[3].

Administration of Drug

L-lysine was administered intraperitoneally

Statistical analysis

The data from the present investigations were analyzed by parametric tests[15], using either one-way ANOVA followed by Tukey's test or two-way repeat measure ANOVA followed by the Bonferroni test for multiple comparisons. All values are expressed as the mean \pm SEM of 6–7mice per group. A value of p 0.05 was considered statistically significant in all the cases.

Result

Table 1A: Acute effect of L- Lysine on the ethanol-induced conditioned place preference

Groups	Conditioned Place Preference in (sec)
Vehicle + saline	10.33 \pm 51.10
L- Lysine (10mg/kg i.p.) + Saline	39.00 \pm 24.12
L- Lysine (20mg/kg i.p.) + Saline	29.67 \pm 32.91
L- Lysine (40mg/kg i.p.) + Saline	15.50 \pm 32.41
Vehicle + Ethanol	383.0 \pm 26.3 [#]

L- Lysine (10mg/kg i.p.) + Ethanol	363.2±43.16
L- Lysine (20mg/kg i.p.) + Ethanol	108.8±50.69*
L- Lysine (40mg/kg i.p.) +Ethanol	88.67±40.83**

Each value represents the Mean ± S.E.M. (n=6) using one-way ANOVA following Tukey's multiple comparison test &P < 0.001 as compared to control, *P<0.05 and **P < 0.01 as compared to ethanol.

Table 1B: Chronic effect of L- Lysine on the ethanol-induced conditioned place preference.

Groups	Conditioned Place Preference in (sec)
Vehicle + Saline	36.50±62.69
L- Lysine (10mg/kg i.p.) + Saline	32.50±72.05
L- Lysine (20mg/kg i.p.) + Saline	47.33±58.08
L- Lysine (40mg/kg i.p.) + Saline	52.00±45.17
Vehicle + Ethanol	587.0±46.25#
L- Lysine (10mg/kg i.p.) + Ethanol	328.7±56.45*
L- Lysine (20mg/kg i.p.) + Ethanol	286.7±29.68**
L- Lysine (40mg/kg i.p.) +Ethanol	105.2±13.79***

Each value represents the Mean ± S.E.M. (n=6) using one-way ANOVA following Tukey's multiple comparison test #P < 0.001 as compared to control, *P<0.05, **P < 0.01 and ***P < 0.001 as compared to ethanol.

Table 2A: Effect of L- Lysine on the expression sensitization to the locomotor stimulant effect of ethanol.

Groups	Number of locomotor counts (in 30 min)
Saline(ch) + Vehicle(a) + Saline(a)	228.3±55.77
Saline(ch) + Vehicle(a)+ Ethanol(a)	496.5±31.81@
Ethanol(ch)+Vehicle(a)+Ethanol(a)	1163±58.08#
Ethanol(ch)+ L- Lysine (10mg/kg)(a) + Ethanol(a)	988.2±42.61
Ethanol(ch)+ L- Lysine (20mg/kg)(a) + Ethanol(a)	849.5±57.39*
Ethanol(ch)+ L- Lysine (40mg/kg)(a) + Ethanol(a)	819.8±62.82**

Each bar represents the mean ± S.E.M. of n=6 mice per group. @P < 0.05 vs. [saline (ch) + vehicle (a) + saline (a)]; #P < 0.001 vs. [saline (ch) + vehicle (a) + ethanol (a)], *P < 0.05, **P < 0.01 vs. [ethanol (ch) + vehicle (a) + ethanol (a)] treated group (One-way ANOVA followed by Tukey's multiple comparison test). (a): acute; (ch): chronic.

Table 2B: Effect of L- Lysine on the development of sensitization to locomotor stimulant effect of ethanol.

Groups	Number of locomotor counts (in 30min)
Saline(ch) + Saline(ch) + saline(a)	203.5±17.03
Saline(ch) + Saline(ch)+ Ethanol(a)	333.3±17.85
Saline(ch)+Ethanol(ch)+Ethanol(a)	825.3±46.37\$
L- Lysine (10mg/kg)(ch)+ Ethanol(ch)+Ethanol(a)	702.2±37.85*
L- Lysine (20mg/kg)(ch)+ Ethanol(ch)+Ethanol(a)	613.9±31.08#
L- Lysine (40mg/kg)(ch)+ Ethanol(ch)+Ethanol(a)	519.1±40.10@

Each bar represents the mean \pm S.E.M. of n=6 mice per group. \$P < 0.001 vs. [saline (ch) + saline (ch) + ethanol(a)]; *P<0.05 [saline (ch)+ ethanol(a) +ethanol (a), #P < 0.01, @P < 0.001 vs. [Saline (ch) + ethanol (ch) + ethanol (a)] treated group (One-way ANOVA followed by Tukey's multiple comparison test). (a): acute; (ch): chronic.

Conditioned Place Preference

Acute effect of L- Lysine on the ethanol-induced conditioned place preference.

L-lysine (20 and 40 mg/kg, i.p.) pretreatment, 30 min before the test significantly reduced place preference in ethanol control-treated groups. Values are mean \pm SEM of six observations per group. * $p < 0.001$ vs. respective vehicle treatment in ethanol diet withdrawn group (one-way ANOVA followed by Tukey's posthoc test). [$F(5,30) 294.33, p < 0.0001$], whereas a lower dose (10 mg/kg, i.p.) did not influence reduced place preference ($p > 0.05$).

Chronic effect of L- Lysine on the ethanol-induced conditioned place preference.

Chronic treatment with L-lysine (20 and 40 mg/kg, i.p.), during ethanol conditioning sessions, significantly reduced place preference in ethanol control-treated groups. Values are mean \pm SEM of six observations per group. * $p < 0.001$ vs. respective vehicle treatment in ethanol diet withdrawn group (one-way ANOVA followed by Tukey's posthoc test). [$F(5,30) 482, p < 0.0001$],

whereas a lower dose (10 mg/kg, i.p.) shows less influence on place preference ($p > 0.05$).

Locomotor Activity:

Effect of L- Lysine on the expression sensitization to the locomotor stimulant effect of ethanol.

L-lysine (20 and 40 mg/kg, i.p.) pretreatment, 30 min before the test significantly reduced locomotor count in ethanol control-treated groups. Values are mean \pm SEM of six observations per group. * $p < 0.001$ vs. respective vehicle treatment in ethanol diet withdrawn group (one-way ANOVA followed by Tukey's posthoc test). [$F(5,30) 243.20, p < 0.0001$], whereas a lower dose (10 mg/kg, i.p.) did not significantly lower the locomotor count ($p > 0.05$).

Effect of L- Lysine on the expression sensitization to the locomotor stimulant effect of ethanol.

Chronic treatment with L-lysine (20 and 40 mg/kg, i.p.) pretreatment, 30 min before the test significantly reduced locomotor count in ethanol control-treated groups. Values are mean \pm SEM of six observations per group. * $p < 0.001$ vs. respective vehicle treatment in

ethanol diet withdrawn group (one-way ANOVA followed by Tukey's posthoc test). [$F(5,30) 305.90, p < 0.0001$], whereas a lower dose (10 mg/kg, i.p.) shows less significant decreases in the locomotor count ($p > 0.05$)

Discussion

Ethanol acts on many cellular targets of several neuromodulators within many neural networks in the brain. There is evidence that suggests that 5-HT₄ is an important target for ethanol in the brain. Ethanol actions at 5-HT₄-R contribute to the behavioral changes in animals and humans. 5-HT₄ receptor-mediated neurotransmission is involved in the development of behavioral sensitization produced by the drug of abuse. It has been shown that the locomotor stimulatory and stereotype-inducing effects of these drugs can be attenuated by both competitive and uncompetitive 5-HT₄ receptor antagonists. 5-HT₄-R antagonist treatment has the potential to interfere with neuroadaptive changes in the brain that contribute to the maintenance of addictive behavior. It has been found that chronic consumption of ethanol is responsible for the upregulation of the 5-HT₄ receptor and 5-HT₄-R appears to adapt to the inhibitory effects of alcohol by increasing their excitatory activity through glutamate. Therefore, the drugs which can antagonize the 5-HT₄-R are useful in the reduction of ethanol dependence and tolerance by suppression of the hyper glutaminergic state. L-lysine is a non-selective 5-HT₄-R antagonist found to inhibit the acquisition of morphine self-administration in rats.

It has been reported that 5-HT₄ receptors are involved in the modulation of acetylcholine release. 5-HT₄ agonist such as cisapride is all able to increase Ach release from electrically or nicotine stimulated gastrointestinal tract since they also show an affinity for other subtypes of 5HT receptor as well as for dopaminergic and muscarinic ones[10]. The

simultaneous administration of L-lysine and zinc reduced the lead and ethanol-induced biochemical alterations. Literature also suggests that lysine affects 5-HT₄ receptor not only in the guts but also in the brain[16]. The mechanism by which L-lysine inhibited the rewarding effects of ethanol is not known. Recently Evidence was obtained suggesting that 6 g/day of adjunctive L-lysine treatment is a sufficient dose for increasing blood L-lysine levels above the nutritional, naturally occurring levels, without inducing adverse side-effects. In addition, there was a significant decrease in the positive PANSS scores and WCST over the whole study period[17].

We observed that the acute effect of L-Lysine (20 and 40 mg/kg, i.p.) pretreatment, 30 min before the test significantly reduced place preference in ethanol control-treated groups. When chronic treatment was carried out with L-lysine (20 and 40 mg/kg, i.p.), during ethanol conditioning sessions significantly reduced place preference in ethanol control-treated groups. Further, the locomotor activity was observed where, acute treatment with L-lysine (20 and 40 mg/kg, i.p.) pretreatment, 30 min before the test significantly reduced locomotor count in ethanol control-treated groups. When chronic treatment was carried out with Chronic treatment with L-lysine (20 and 40 mg/kg, i.p.) pretreatment, 30 min before the test significantly reduced locomotor count in ethanol control-treated groups.

Acknowledgment

The authors would like to thank **Shri Dhurpatrao Sawale**, President, Rajarshi Shahu College of Pharmacy, Buldana, for his positive motivation under the head of Excellence in Research and Academics.

References

1. Tabakoff B, Hoffman PL. Alcohol addiction: an enigma among us. *Neurology*,1996; 16:909–12.
2. Koob, G.F. & Le Moal, M. Drug addiction, dysregulation of reward, and all stasis. *Neuropsychopharmacol.*,2001;24:97-12.
3. Pravinkumar Bhutada, Yogita Mundhada, Kuldeep Bansod, Sumit Rathod, Rahul Hiware, Pankaj Dixit, Sudhir Umathe, Dharmendra Mundhada. Inhibitory effect of berberine on the motivational effects of ethanol in mice. *Progress in Neuro-Psychopharmacology & Biological Psychiatry*, 2010:1472-1479.
4. Chastain G. Alcohol, neurotransmitter systems, and behavior. *J Gen Psychol*, 2006;**133**: 329– 335.
5. Smriga and Torii. L-lysine act as a partial serotonin receptor 4 antagonist and inhibits serotonin-mediated intestinal pathologies and anxiety in rats. *PNAS*, 2003;100(26), 15370-1537.
6. Risinger F., Malott D., Riley A., Cunningham C. Effect of Ro 15-4513 on ethanol-induced conditioned place preference. *Pharmacology Biochemistry and Behavior*.1992; 43:97-102.
7. Stevenson R., Besheer J., Hodge C. Comparison of ethanol locomotor sensitization in adolescent and adult mice. *Psychopharmacology*,2008:361-370.
8. Smriga and Torii. L-lysine act as a partial serotonin receptor 4 antagonist and inhibits serotonin-mediated intestinal pathologies and anxiety in rats. *PNAS*,2003;100(26):15370-1537.
9. Mayo MF, Beecher LH, Fischer TL. Management of alcohol withdrawal delirium an evidence-based practice guideline,2005;164:1405–12.
10. Ghelardini C, Romanelli N, Dei S, Scapecchi S, et al. Role of 5-HT4 receptor subtype in central antinociception. *Pharmacological Res.*1992;26(1):326-328.
11. Fitzpatrick LE, Jackson M, Crowe SF. "The relationship between alcoholic cerebellar degeneration and cognitive and emotional functioning". *Neurosci Biobehav Rev.* 2008;32 (3): 466–85.
12. Linkola J, Fyhrquist F, Nieminen MM, Weber TH, Tontti K. Renin-aldosterone axis in ethanol intoxication and hangover. *Eur J Clin Invest.* 1976;6(2):191-194.
13. Hendler, S.S., Rorvik, D. Lysine. In: *PDR for Nutritional Supplements*. Medical, 2001.
14. Economics TM Thomson Healthcare, Montvale, NJ,270-271.
15. Umathe S, Bhutada P, Dixit P, et al. Increased marble-burying behavior in ethanol-withdrawal state: modulation by gonadotropin-releasing hormone agonist. *Eur J Pharmacol.* 2008; 587: 175-180.
16. Chichovska, A., A. Anguelov: Study on the influence of L-lysine and zinc administration during exposure to lead and ethanol in rats. *Vet. Arhiv*, 2006;76:65-73.
17. Wass Caroline, Klamer Daniel, Katsarogiannis Evangelos, Pålsson Erik, Svensson Lennart, Fejgin Kim, Bogren Inga-Britt, et al. "L-lysine as adjunctive treatment in patients with schizophrenia: a single-blinded, randomized, cross-over pilot study." *BMC medicine*, 2011;9:40.

Role of L-lysine in Ethanol Induced Behavioral Changes in Mice

Sumit Rathod¹, Vinay Bhalerao², Mangesh Deokar², Shirish Jain²

¹Department of Pharmacology, SVKM's Institute of Pharmacy, Dhule, (M.S.), India

²Department of Pharmacology, Rajarshi Shahu College of Pharmacy, Buldana, (M.S.), India

Received: 01-11-2021 / Revised: 28-11-2021 / Accepted: 22-12-2021

Corresponding author: Mr. Sumit S. Rathod

Conflict of interest: Nil

Abstract

Lysine, (S)-2,6,-diaminohexanoic acid, is a basic amino acid. Following ingestion, L-lysine is absorbed by the active transport process from the lumen of the small intestine into the enterocytes. L-lysine is a 5-HT₄ antagonist that can increase and decrease ethanol intake when they are given intraperitoneal administration. 5-HT₄ antagonist can block the rewarding and motivation effect as indicated by attenuation of sensitization to the locomotor stimulant effect of ethanol, decreased ethanol-induced conditioned place preference, and reduced ethanol drinking. Young healthy mice (21–30 g) were group-housed (five per cage) in opaque polypropylene cages. Animals were naive to drug treatment and experimentation at the beginning of all studies. Each experimental group was comprised of five mice. Testing was carried out in counterbalanced order concerning the treatment conditions in the noise-free room. Locomotor activity and conditioned place preference was assessed followed by acute and chronic exposure of ethanol to animals. The results revealed that acute as well as administration of L-lysine (20 and 40 mg/kg, i.p.) pre-treatment, 30 min before the test significantly reduced place preference in ethanol control-treated groups. In locomotor activity L-lysine (20 and 40 mg/kg, i.p.) pre-treatment, 30 min before the test significantly reduced locomotor count in ethanol control-treated groups in both acute and chronic groups. In conclusion, Results indicated that L-lysine exhibited an inhibitory influence against ethanol-induced behavioral changes in mice.

Keywords: L-lysine; 5-HT₄ antagonist, Ethanol dependence; Locomotor Activity; Conditioned Place Preference.

This is an Open Access article that uses a funding model which does not charge readers or their institutions for access and distributed under the terms of the Creative Commons Attribution License (<http://creativecommons.org/licenses/by/4.0>) and the Budapest Open Access Initiative (<http://www.budapestopenaccessinitiative.org/read>), which permit unrestricted use, distribution, and reproduction in any medium, provided original work is properly credited.

Introduction:

Ethanol is one of the most widely abused addictive drugs and has hazardous health consequences resulting from its chronic use[2]. Ethanol produces a striking array of behavioral effects in humans that are dependent on the dose of ethanol administered[3]. When used in low to

moderate quantities, it relieves anxiety and fosters a feeling of well-being and euphoria. Alcohol abuse is a pattern of drinking that results in harm to one's health, interpersonal relationships, or ability to work[9]. Alcohol abuse can result in brain damage which causes impairments in executive functioning

such as impairments to working memory, visuospatial skills, and can cause an abnormal personality as well as affective disorders to develop[11]. Several neurotransmitter systems like glutamate, noradrenaline, dopamine, serotonin, opiates, gamma-aminobutyric acid (GABA), and certain plasma membrane ion channels like voltage-sensitive calcium channels have been implicated in the effects of ethanol[4,15].

Serotonin is produced in and released from neurons that originate within discrete regions, or in the nuclei[12]. The neurotransmitter serotonin has long been a target of interest for potential pharmacotherapies for alcoholism because of the well-established link between serotonin depletion, impulsivity, and alcohol drinking behavior in mice and humans[6].

Lysine, (S)-2,6, -diaminohexanoic acid, is a basic amino acid. Following ingestion, L-lysine is absorbed by the active transport process from the lumen of the small intestine into the enterocytes[13]. The 5-HT₄ antagonist increased and decreased ethanol intake when they are given intraperitoneal administration. 5-HT₄ antagonist can block the rewarding and motivation effect as indicated by attenuation of sensitization to the locomotors stimulant effect of ethanol, decreased ethanol-induced conditioned placed preference, and reduced ethanol drinking. Functional and binding studies have shown that the 5-HT₄ receptor, is the G-protein coupled receptor which positively coupled to adenylate cyclase and increases the cAMP production or by generating IP₃ /DAG as second messengers. 5-HT receptor subtype 5-HT₄ receptor may involve in the control of voluntary ethanol intake in mice. The high densities of this receptor in the nucleus accumbens and other regions suggest the influence of ethanol intake with its reinforcing properties. The present study is carried out to evaluate the efficacy of serotonin 4 receptor antagonist on ethanol-

induced motivational and rewarding effect in mice[1].

Animals

Experimental Animals (Swiss Albino) Mice will be procured from Animal House of Rajarshi Shahu College of Pharmacy Buldana, Dist.-Buldana, and will be used in this study. The animal care and handling will be done according to the guidelines set by the CPCSEA. Young healthy mice (21–30 g) were group-housed (five per cage) in opaque polypropylene cages (28×21×14 cm) and maintained at the local conditions (23±2 °C and 40±2 % humidity) under 12:12 h light/dark cycle, with free access to rodent chow and tap water. The animal studies were approved by the Institutional Animal Ethics Committee (IAEC), constituted for control and supervision of experimental animals by the Ministry of Environment and Forests, Government of India, New Delhi, India. Animals were naive to drug treatment and experimentation at the beginning of all studies. Each experimental group was comprised of five mice. Testing was carried out in counterbalanced order concerning the treatment conditions in the noise-free room.

Drugs and solutions

L-LYSINE [Base] Monohydrate [C₆H₁₄N₂O₂H₂O] M.W.164.21 (Research-lab Fine Chem Industries Mumbai), ethanol (Changshu Yangyuan Chemical, China) used in the present study were dissolved in 0.9% saline. Drug solutions were prepared fresh, and doses of L-lysine are expressed in terms of its free base. The doses of l-lysine were selected based on previous reports[5].

Role of l-lysine in alcohol addiction

The 5-HT₄ antagonist increased and decreased ethanol intake when they are given intraperitoneal administration. 5-HT₄ antagonist can block the rewarding and motivation effect as indicated by attenuation of sensitization to the locomotors stimulant

effect of ethanol, decreased ethanol-induced conditioned place preference, and reduced ethanol drinking. Functional and binding studies have shown that the 5-HT₄ receptor, is the G-protein coupled receptor which positively coupled to adenylate cyclase and increases the cAMP production or by generating IP₃ /DAG as second messengers. 5-HT receptor subtype 5-HT₄ receptor may involve in the control of voluntary ethanol intake in mice. The high densities of this receptor in the nucleus accumbens and other regions suggest the influence of ethanol intake with its reinforcing properties[8].

Methods

Locomotor Activity

Locomotor activity was assessed in an actophotometer (VJ Instruments, Amaravati, India), having a diameter of 40 cm, equipped with three infrared beam cells pair (pair: one emitter and one receiver), 20 cm apart from each other and located on the walls of the circular arena and were connected to the digital counter. Locomotor activity was expressed in terms of the total number of counts of beams interruptions in 30 min.[7].

Conditioned place preferences

CPP experiments were conducted in a three-chambered place conditioning apparatus connected to a digital recorder and housed in a light- and sound-attenuated chamber. Two

(6.6"×5") conditioning chambers, one white with a rough floor and the other black with a smooth floor, were connected by a smaller (2.85"×5") central access chamber with gray walls and a smooth polyvinyl chloride floor. In addition, each chamber was equipped with a house light, with the luminance (40 lx) adjusted such that the environmental (visual and tactile) cues should not produce a significant baseline preference for a specific chamber. All chambers were separated by manually operated guillotine doors. The individual chamber activity was determined by photo beam breaks recorded by a digital recorder. The CPP test was carried out using Swiss mice as per the method described by Font et al. (2008) with slight modifications. This experiment involved three phases such as habituation (one session), conditioning (eight sessions), and testing (one session)[3].

Administration of Drug

L-lysine was administered intraperitoneally

Statistical analysis

The data from the present investigations were analyzed by parametric tests[15], using either one-way ANOVA followed by Tukey's test or two-way repeat measure ANOVA followed by the Bonferroni test for multiple comparisons. All values are expressed as the mean \pm SEM of 6–7mice per group. A value of p 0.05 was considered statistically significant in all the cases.

Result

Table 1A: Acute effect of L- Lysine on the ethanol-induced conditioned place preference

Groups	Conditioned Place Preference in (sec)
Vehicle + saline	10.33 \pm 51.10
L- Lysine (10mg/kg i.p.) + Saline	39.00 \pm 24.12
L- Lysine (20mg/kg i.p.) + Saline	29.67 \pm 32.91
L- Lysine (40mg/kg i.p.) + Saline	15.50 \pm 32.41
Vehicle + Ethanol	383.0 \pm 26.3 [#]

L- Lysine (10mg/kg i.p.) + Ethanol	363.2±43.16
L- Lysine (20mg/kg i.p.) + Ethanol	108.8±50.69*
L- Lysine (40mg/kg i.p.) +Ethanol	88.67±40.83**

Each value represents the Mean ± S.E.M. (n=6) using one-way ANOVA following Tukey's multiple comparison test &P < 0.001 as compared to control, *P<0.05 and **P < 0.01 as compared to ethanol.

Table 1B: Chronic effect of L- Lysine on the ethanol-induced conditioned place preference.

Groups	Conditioned Place Preference in (sec)
Vehicle + Saline	36.50±62.69
L- Lysine (10mg/kg i.p.) + Saline	32.50±72.05
L- Lysine (20mg/kg i.p.) + Saline	47.33±58.08
L- Lysine (40mg/kg i.p.) + Saline	52.00±45.17
Vehicle + Ethanol	587.0±46.25#
L- Lysine (10mg/kg i.p.) + Ethanol	328.7±56.45*
L- Lysine (20mg/kg i.p.) + Ethanol	286.7±29.68**
L- Lysine (40mg/kg i.p.) +Ethanol	105.2±13.79***

Each value represents the Mean ± S.E.M. (n=6) using one-way ANOVA following Tukey's multiple comparison test #P < 0.001 as compared to control, *P<0.05, **P < 0.01 and ***P < 0.001 as compared to ethanol.

Table 2A: Effect of L- Lysine on the expression sensitization to the locomotor stimulant effect of ethanol.

Groups	Number of locomotor counts (in 30 min)
Saline(ch) + Vehicle(a) + Saline(a)	228.3±55.77
Saline(ch) + Vehicle(a)+ Ethanol(a)	496.5±31.81@
Ethanol(ch)+Vehicle(a)+Ethanol(a)	1163±58.08#
Ethanol(ch)+ L- Lysine (10mg/kg)(a) + Ethanol(a)	988.2±42.61
Ethanol(ch)+ L- Lysine (20mg/kg)(a) + Ethanol(a)	849.5±57.39*
Ethanol(ch)+ L- Lysine (40mg/kg)(a) + Ethanol(a)	819.8±62.82**

Each bar represents the mean ± S.E.M. of n=6 mice per group. @P < 0.05 vs. [saline (ch) + vehicle (a) + saline (a)]; #P < 0.001 vs. [saline (ch) + vehicle (a) + ethanol (a)], *P < 0.05, **P < 0.01 vs. [ethanol (ch) + vehicle (a) + ethanol (a)] treated group (One-way ANOVA followed by Tukey's multiple comparison test). (a): acute; (ch): chronic.

Table 2B: Effect of L- Lysine on the development of sensitization to locomotor stimulant effect of ethanol.

Groups	Number of locomotor counts (in 30min)
Saline(ch) + Saline(ch) + saline(a)	203.5±17.03
Saline(ch) + Saline(ch)+ Ethanol(a)	333.3±17.85
Saline(ch)+Ethanol(ch)+Ethanol(a)	825.3±46.37\$
L- Lysine (10mg/kg)(ch)+ Ethanol(ch)+Ethanol(a)	702.2±37.85*
L- Lysine (20mg/kg)(ch)+ Ethanol(ch)+Ethanol(a)	613.9±31.08#
L- Lysine (40mg/kg)(ch)+ Ethanol(ch)+Ethanol(a)	519.1±40.10@

Each bar represents the mean ± S.E.M. of n=6 mice per group. \$P < 0.001 vs. [saline (ch) + saline (ch) + ethanol(a)]; *P<0.05 [saline (ch)+ ethanol(a) +ethanol (a), #P < 0.01, @P < 0.001 vs. [Saline (ch) + ethanol (ch) + ethanol (a)] treated group (One-way ANOVA followed by Tukey's multiple comparison test). (a): acute; (ch): chronic.

Conditioned Place Preference

Acute effect of L- Lysine on the ethanol-induced conditioned place preference.

L-lysine (20 and 40 mg/kg, i.p.) pretreatment, 30 min before the test significantly reduced place preference in ethanol control-treated groups. Values are mean ± SEM of six observations per group. * $p < 0.001$ vs. respective vehicle treatment in ethanol diet withdrawn group (one-way ANOVA followed by Tukey's posthoc test). [$F(5,30) 294.33, p < 0.0001$], whereas a lower dose (10 mg/kg, i.p.) did not influence reduced place preference ($p > 0.05$).

Chronic effect of L- Lysine on the ethanol-induced conditioned place preference.

Chronic treatment with L-lysine (20 and 40 mg/kg, i.p.), during ethanol conditioning sessions, significantly reduced place preference in ethanol control-treated groups. Values are mean ± SEM of six observations per group. * $p < 0.001$ vs. respective vehicle treatment in ethanol diet withdrawn group (one-way ANOVA followed by Tukey's posthoc test). [$F(5,30) 482, p < 0.0001$],

whereas a lower dose (10 mg/kg, i.p.) shows less influence on place preference ($p > 0.05$).

Locomotor Activity:

Effect of L- Lysine on the expression sensitization to the locomotor stimulant effect of ethanol.

L-lysine (20 and 40 mg/kg, i.p.) pretreatment, 30 min before the test significantly reduced locomotor count in ethanol control-treated groups. Values are mean ± SEM of six observations per group. * $p < 0.001$ vs. respective vehicle treatment in ethanol diet withdrawn group (one-way ANOVA followed by Tukey's posthoc test). [$F(5,30) 243.20, p < 0.0001$], whereas a lower dose (10 mg/kg, i.p.) did not significantly lower the locomotor count ($p > 0.05$).

Effect of L- Lysine on the expression sensitization to the locomotor stimulant effect of ethanol.

Chronic treatment with L-lysine (20 and 40 mg/kg, i.p.) pretreatment, 30 min before the test significantly reduced locomotor count in ethanol control-treated groups. Values are mean ± SEM of six observations per group. * $p < 0.001$ vs. respective vehicle treatment in

ethanol diet withdrawn group (one-way ANOVA followed by Tukey's posthoc test). [$F(5,30) 305.90, p < 0.0001$], whereas a lower dose (10 mg/kg, i.p.) shows less significant decreases in the locomotor count ($p > 0.05$)

Discussion

Ethanol acts on many cellular targets of several neuromodulators within many neural networks in the brain. There is evidence that suggests that 5-HT₄ is an important target for ethanol in the brain. Ethanol actions at 5-HT₄-R contribute to the behavioral changes in animals and humans. 5-HT₄ receptor-mediated neurotransmission is involved in the development of behavioral sensitization produced by the drug of abuse. It has been shown that the locomotor stimulatory and stereotype-inducing effects of these drugs can be attenuated by both competitive and uncompetitive 5-HT₄ receptor antagonists. 5-HT₄-R antagonist treatment has the potential to interfere with neuroadaptive changes in the brain that contribute to the maintenance of addictive behavior. It has been found that chronic consumption of ethanol is responsible for the upregulation of the 5-HT₄ receptor and 5-HT₄-R appears to adapt to the inhibitory effects of alcohol by increasing their excitatory activity through glutamate. Therefore, the drugs which can antagonize the 5-HT₄-R are useful in the reduction of ethanol dependence and tolerance by suppression of the hyper glutaminergic state. L-lysine is a non-selective 5-HT₄-R antagonist found to inhibit the acquisition of morphine self-administration in rats.

It has been reported that 5-HT₄ receptors are involved in the modulation of acetylcholine release. 5-HT₄ agonist such as cisapride is all able to increase Ach release from electrically or nicotine stimulated gastrointestinal tract since they also show an affinity for other subtypes of 5HT receptor as well as for dopaminergic and muscarinic ones[10]. The

simultaneous administration of L-lysine and zinc reduced the lead and ethanol-induced biochemical alterations. Literature also suggests that lysine affects 5-HT₄ receptor not only in the guts but also in the brain[16]. The mechanism by which L-lysine inhibited the rewarding effects of ethanol is not known. Recently Evidence was obtained suggesting that 6 g/day of adjunctive L-lysine treatment is a sufficient dose for increasing blood L-lysine levels above the nutritional, naturally occurring levels, without inducing adverse side-effects. In addition, there was a significant decrease in the positive PANSS scores and WCST over the whole study period[17].

We observed that the acute effect of L-Lysine (20 and 40 mg/kg, i.p.) pretreatment, 30 min before the test significantly reduced place preference in ethanol control-treated groups. When chronic treatment was carried out with L-lysine (20 and 40 mg/kg, i.p.), during ethanol conditioning sessions significantly reduced place preference in ethanol control-treated groups. Further, the locomotor activity was observed where, acute treatment with L-lysine (20 and 40 mg/kg, i.p.) pretreatment, 30 min before the test significantly reduced locomotor count in ethanol control-treated groups. When chronic treatment was carried out with Chronic treatment with L-lysine (20 and 40 mg/kg, i.p.) pretreatment, 30 min before the test significantly reduced locomotor count in ethanol control-treated groups.

Acknowledgment

The authors would like to thank **Shri Dhurpatrao Sawale**, President, Rajarshi Shahu College of Pharmacy, Buldana, for his positive motivation under the head of Excellence in Research and Academics.

References

1. Tabakoff B, Hoffman PL. Alcohol addiction: an enigma among us. *Neurology*,1996; 16:909–12.
2. Koob, G.F. & Le Moal, M. Drug addiction, dysregulation of reward, and all stasis. *Neuropsychopharmacol.*,2001;24:97-12.
3. Pravinkumar Bhutada, Yogita Mundhada, Kuldeep Bansod, Sumit Rathod, Rahul Hiware, Pankaj Dixit, Sudhir Umathe, Dharmendra Mundhada. Inhibitory effect of berberine on the motivational effects of ethanol in mice. *Progress in Neuro-Psychopharmacology & Biological Psychiatry*, 2010:1472-1479.
4. Chastain G. Alcohol, neurotransmitter systems, and behavior. *J Gen Psychol*, 2006;**133**: 329– 335.
5. Smriga and Torii. L-lysine act as a partial serotonin receptor 4 antagonist and inhibits serotonin-mediated intestinal pathologies and anxiety in rats. *PNAS*, 2003;100(26), 15370-1537.
6. Risinger F., Malott D., Riley A., Cunningham C. Effect of Ro 15-4513 on ethanol-induced conditioned place preference. *Pharmacology Biochemistry and Behavior*.1992; 43:97-102.
7. Stevenson R., Besheer J., Hodge C. Comparison of ethanol locomotor sensitization in adolescent and adult mice. *Psychopharmacology*,2008:361-370.
8. Smriga and Torii. L-lysine act as a partial serotonin receptor 4 antagonist and inhibits serotonin-mediated intestinal pathologies and anxiety in rats. *PNAS*,2003;100(26):15370-1537.
9. Mayo MF, Beecher LH, Fischer TL. Management of alcohol withdrawal delirium an evidence-based practice guideline,2005;164:1405–12.
10. Ghelardini C, Romanelli N, Dei S, Scapecchi S, et al. Role of 5-HT4 receptor subtype in central antinociception. *Pharmacological Res.*1992;26(1):326-328.
11. Fitzpatrick LE, Jackson M, Crowe SF. "The relationship between alcoholic cerebellar degeneration and cognitive and emotional functioning". *Neurosci Biobehav Rev.* 2008;32 (3): 466–85.
12. Linkola J, Fyhrquist F, Nieminen MM, Weber TH, Tontti K. Renin-aldosterone axis in ethanol intoxication and hangover. *Eur J Clin Invest.* 1976;6(2):191-194.
13. Hendler, S.S., Rorvik, D. Lysine. In: *PDR for Nutritional Supplements*. Medical, 2001.
14. Economics TM Thomson Healthcare, Montvale, NJ,270-271.
15. Umathe S, Bhutada P, Dixit P, et al. Increased marble-burying behavior in ethanol-withdrawal state: modulation by gonadotropin-releasing hormone agonist. *Eur J Pharmacol.* 2008; 587: 175-180.
16. Chichovska, A., A. Anguelov: Study on the influence of L-lysine and zinc administration during exposure to lead and ethanol in rats. *Vet. Arhiv*, 2006;76:65-73.
17. Wass Caroline, Klamer Daniel, Katsarogiannis Evangelos, Pålsson Erik, Svensson Lennart, Fejgin Kim, Bogren Inga-Britt, et al. "L-lysine as adjunctive treatment in patients with schizophrenia: a single-blinded, randomized, cross-over pilot study." *BMC medicine*, 2011;9:40.



Research Article

Calcium Ion-Sodium Alginate-Piperine-Based Microspheres: Evidence of Enhanced Encapsulation Efficiency, Bio-Adhesion, Controlled Delivery, and Oral Bioavailability of Isoniazid

Darshan R. Telange,^{1,3} Ravindra R. Pandharinath,² Anil M. Pethe,³
Shirish P. Jain,¹ and Prashant L. Pingale^{4,5}

Received 16 October 2021; accepted 9 February 2022; published online 25 March 2022

Abstract. Isoniazid (INH) is a first-line chemotherapeutic drug employed in the management of tuberculosis. However, its extensive first-pass metabolism, short-life life, and low oral bioavailability confined its medical application. Therefore, the calcium ion-alginate-piperine microspheres (INH-CaSP Ms) was prepared to enhance encapsulation efficiency, controlled delivery, and oral bioavailability of INH. The INH-CaSP Ms was developed using a modified emulsification method and optimized via Box-Behnken design (BBD). Optimized INH-CaSP Ms were characterized for encapsulation efficiency, differential scanning calorimetry (DSC), Fourier-transform infrared spectroscopy (FT-IR), bio-adhesion, *in vitro* dissolution, *ex vivo* permeation, and oral bioavailability studies. Characterization studies confirmed the formation of microspheres. The INH-CaSP Ms showed spherical microspheres with enhanced encapsulation efficiency ($\sim 93.03 \pm 1.54\%$ w/w). The optimized INH-CaSP Ms exhibited higher bio-adhesion around ($\sim 81.41 \pm 1.31\%$). The INH-CaSP Ms enhanced the dissolution rate of INH ($\sim 57\%$) compared to pure INH ($\sim 57\%$) and INH-SA Ms ($\sim 81\%$) in simulated gastric fluid (SGF, pH 1.2) and simulated intestinal fluid (SIF, pH 7.4). The same formulations improved the permeation rate of INH ($\sim 90\%$) compared to pure INH ($\sim 55\%$) and INH-SA Ms ($\sim 80\%$). The oral bioavailability results indicated that INH-CaSP Ms appreciably improved the oral bioavailability of INH via increasing the C_{max} , T_{max} , $t_{1/2}$, and AUC parameters compared to pure INH. The study demonstrates that the development of INH-CaSP Ms via cross-linked coordinate bond interaction between divalent cation calcium ion-alginate complex and anion piperine bio-enhancer is an effective approach for enhancing the encapsulation efficiency, bio-adhesion, controlled release, and oral bioavailability of INH.

KEY WORDS: Isoniazid; Sodium alginate; Piperine; Microspheres; Oral bioavailability.

INTRODUCTION

The oral route is the most desirable route for drug administration because of easy drug administration, non-invasive approach, convenience, high patient compliance, and feasibility for solid dosage formulations. Moreover, the prominent surface area ($300\text{--}400\text{ m}^2$) of the oral route

provides an excellent attachment to the drug and promotes its absorption via enterocytes (1). Despite these positive benefits, the oral route displays multiple drawbacks such as drug stability and solubility issues in the GI tract, variable and poor absorption, extensive first-pass metabolism, and high P-gp efflux. This mechanism produces low oral bioavailability of many active pharmaceutical ingredients (APIs) (2). Various formulations have been introduced for enhancing the oral bioavailability of the drug. The nanoformulations are considered the best choice due to nanometer in size and demonstrated a significant improvement in oral bioavailability via localized and targeted drug delivery in the GI tract. It achieved the oral targeted delivery via enhancing drug residence duration, increased release, and assisting interaction with cells in the GI tract (2). This interaction can facilitate permeation absorption, thereby enhancing the oral bioavailability of the drug (3).

¹ Rajarshi Shahu College of Pharmacy, MaharashtraBuldhana, India.

² School of Pharmacy and Technology Management, SVKM's NMIMS (Deemed to be University), Shirpur, Maharashtra, India.

³ Datta Meghe College of Pharmacy, Datta Meghe Institute of Medical Sciences (Deemed to be University), Sawangi (Meghe), Wardha, Maharashtra, India.

⁴ GES's Sir Dr. M. S. Gosavi College of Pharmaceutical Education and Research, Nashik, Maharashtra, India.

⁵ To whom correspondence should be addressed. (e-mail: prashant.pingale@gmail.com)

Previous reports have shown that nanoformulations appreciably improved the bioavailability of several drugs via localized and targeted delivery to the stomach, small intestine, intestinal lymphatic system, and colon (4–10). Conversely, while preparing and administering the following, it displays various shortcomings such as low encapsulation efficiency, uncontrolled release profile, and poor drug absorption. These drawbacks provide variable absorption and thus, reduce the oral bioavailability of drugs (11–13). Novel formulation strategy involving forming a cross-linked coordinate bonding interaction between positive charge divalent calcium ion-alginate complex and negative charge piperine bio-enhancer improves encapsulation efficiency, controlled release, and drug absorption (14).

Compared to reported literature, calcium ion-alginate microspheres formulations are preferred due to ease of preparation, high muco-adhesivity, and biocompatibility toward biological membranes (12). It forms through ionotropic gelation between cationic divalent calcium ion and guluronic acid unit of anionic sodium alginate polymer (15). Despite these benefits, positive divalent calcium ion-alginate complex also establishes a strong interaction with negative charge bio-enhancer and cross-linking agents. Earlier reports have shown that calcium-alginate nanoparticles formed interaction with negative charge cross-linking agent tannic acid and produced calcium-alginate-tannic acid nanoparticles with improved biopharmaceutical profile of diltiazem hydrochloride (14). In the present study, positive calcium ion-alginate complex build-up association and interaction with the negative carbonyl group of piperine bio-enhancer leading to produce alginate microspheres (CaSP Ms) via cross-linked coordinate bond interaction. This mechanism enhances further interaction with hydrophilic drugs. It increases its holding within the alginate microspheres to a great extent, resulting in enhancement of stability, encapsulation efficiency, and controlled release pattern of the drug. Moreover, the positive calcium ion-alginate complex increases interaction with negative charge phospholipids bilayer. Subsequently, it enhances its bio-adhesion, retention, miscibility, and then permeation across the biological membrane (16), while piperine bio-enhancer high permeability coefficient and apolar nature induced modification in membrane lipids dynamics, enzyme kinetics, reduce the lipids steric restrictions to proteins, and increase the microvilli length and absorptive surface area of the small intestine via increasing synthesis of cytoskeleton protein facilitates the permeation of hydrophilic drug (17–19). The cross-linked coordinate bond interaction within the alginate microspheres increases hydration, swelling, protects the alginate matrices, and prevents its degradation, resulting in controlled drug release. Besides this, a coordinate bond containing piperine may inhibit the P-gp efflux function and improve the oral bioavailability of the drug. The generation of a high shearing rate during emulsification may cause the formation of small globules and subsequently produce calcium ion-alginate-piperine microspheres through cross-linked coordinate bond interaction.

Isoniazid is a first-line chemotherapeutic API employed in the management of tuberculosis (20). It exhibits the anti-tubercular action by inhibiting nicotinamide adenine dinucleotide (NADH) specific enoyl-acyl carrier protein reductase and β -ketoacyl ACP synthase enzyme involved in the fatty

acid synthesis (21, 22). It has high aqueous solubility, around ~ 14% at 25°C, and increased permeability; therefore, it is categorized as biopharmaceutical classification system (BCS) class I (20). However, following oral administration, isoniazid revealed a short half-life ~ (1 to 4 h) (23) and low oral bioavailability around ~ (58%) in guinea pig at a dose of 12 mg/kg (24, 25), attributes to its poor permeability, extensive metabolism, and high P-gp efflux transportation. Thus, INH was selected as a potential drug candidate to recover its permeability and oral bioavailability. Several formulation schemes, including microparticles (26, 27), liposome formulations (28), and polymeric microspheres (29), have been explored to a large extent; however, after critical analysis, they demonstrated limited success in the formulations mentioned above due to their non-effectiveness in formulation strategy. Thus, an earlier failure formulation strategy guides us to develop a calcium ion-alginate-piperine cross-linked coordinate bond interaction microsphere to enhance encapsulation efficiency, controlled release, permeability, and oral bioavailability of INH.

This research aimed to develop and evaluate calcium ion-alginate-piperine cross-linked coordinate bond microspheres to enhance encapsulation efficiency, controlled release, permeability, and oral bioavailability of isoniazid. Microspheres were prepared using a modified emulsification method and optimized using BBD. Optimized microspheres were physico-chemically and functionally analyzed for particle size and zeta potential, scanning electron microscopy, thermal and Fourier-transforms infrared spectroscopy, dissolution, *ex vivo* permeation, and oral bioavailability studies.

MATERIALS AND METHODS

Materials

INH (> 90% purity) was obtained as a gift sample from Alkem Laboratories Ltd. Mumbai, India. Sodium alginate was purchased from HiMedia Laboratories Pvt. Ltd., Mumbai, India. Calcium chloride, Chloroform, dimethylformamide, ethanol, light liquid paraffin, methanol, and span 80 were purchased from Loba Chemicals Pvt. Ltd., Mumbai, India. Disodium hydrogen phosphate, sodium dihydrogen phosphate, and sodium hydroxide were purchased from Sigma Chemicals, Sigma-Aldrich Corporation, St. Louis, MO. All the procured chemicals were of analytical grade and used in this work.

Preparation of INH-CaSP Ms

The INH-CaSP Ms was prepared using a modified emulsification method with many changes (30). This formulation was prepared using INH, piperine, sodium alginate, light liquid paraffin, and calcium chloride. Briefly, the INH (~ 75 mg) and piperine bio-enhancer (~ 5, 10, or 15 mg) were accurately weighed and transferred into 10 mL of freshly prepared sodium alginate solution (~ 4, 5, or 6% w/v). This dispersion was then added into light liquid paraffin (containing 2% v/v span 80) in the ratio (1:7) and stirred using a mechanical stirrer (Model: RQ-126/D, Remi Group Laboratories Instruments, Mumbai, India) at a speed of 1800 rpm for a time period of (~ 30, 45, or 60 min) to get

complete emulsification. To this W/O emulsion, 5 mL of calcium chloride solution (~ 5, 7.5, or 10% w/v, prepared in a mixture of methanol and isopropyl alcohol ratio of 1:1, 2:3, 2:8, and 3:7 respectively) at a rate of 2 mL/min was added to compete cross-linking between the components. The obtained microspheres via calcium-polymer-piperine cross-linked coordinate bond mechanism were kept in calcium chloride solution in dark overnight and filtered using vacuum. The filtered INH-CaSP Ms was washed using isopropyl alcohol thrice and dried at room temperature (25°C). The dried INH-CaSP Ms was placed in nitrogen (N₂) purged amber-colored glass vials and stored in desiccators till further characterization. Similarly, the blank microspheres, i.e., CaSP Ms (free of INH), were also prepared following the same method described above.

BBD Optimization

In this work, the quality by design (QbD)-based design of experiments (DOE), i.e., Box-Behnken design (BBD), was employed to study the influence of critical material attributes (CMAs) and critical process attributes (CPAs) on the performance of isoniazid microspheres. According to previously reported data, we have selected four independent variables, namely sodium alginate concentration (% w/v, X₁), bio-enhancer concentration (mg, X₂), calcium chloride concentration (% w/v, X₃), and time required for cross-linking (min, X₄) respectively. The encapsulation efficiency and *in vitro* release were selected as dependent variables. The four independent variables were investigated at three levels and coded as - 1 (low), 0 (middle), and (+ 1) higher, respectively. The real and coded values of independent and dependent variables are depicted in Table I. The investigation of variables by the BBD generated possible experimental trials, statistical models, and polynomial equations, which were used further to optimize INH-CaSP Ms.

Table I. Coded Levels and Real Values for Each Independent Variable

Variables	Coded levels		
	- 1	0	+ 1
Independent	Real values		
Sodium alginate concentration (X ₁ , % w/v)	4	5	6
Bio-enhancer concentration (X ₂ , mg)	5	10	15
Cross-linking agent concentration (X ₃ , % w/v)	5	7.5	10
Cross-linking time (X ₄ , min)	15	30	45
Dependent			
Encapsulation efficiency (% w/w)			
<i>In vitro</i> dissolution (%)			

$$\begin{aligned}
 Y = & b_0 + b_1X_1 + b_2X_2 + b_3X_3 \\
 & + b_4X_4 + b_{11}X_1^2 + b_{22}X_2^2 \\
 & + b_{33}X_3^2 + b_{44}X_4^2 \\
 & + b_{12}X_1X_2 + b_{13}X_1X_3 + b_{23}X_2X_3 \\
 & + b_{24}X_1X_4 + b_{34}X_2X_4 + b_{45}X_3X_4
 \end{aligned} \quad (1)$$

In the above equation, the Y terms represent the encapsulation efficiency (% w/w), b₀ represents the coefficient of independent variables of X. The four variables of X₁, X₂, X₃, and X₄ represent the main effects of the study. The interaction terms signify the additive effect of all selected variables on the encapsulation efficiency. The polynomial expression of X₁², X₂², X₃², and X₄² demonstrates the non-linearity response of the dependent variables. The possible experimental trials and the estimated value of encapsulation efficiency and *in vitro* dissolution are shown in Table II.

Determination of Encapsulation Efficiency

A method previously described by Rastogi *et al.* was employed to estimate the encapsulation efficiency of INH within optimized INH-CaSP Ms (30). Briefly, the optimized INH-CaSP Ms formulations (~ 10 mg) were weighed and dissolved in 10 mL of freshly prepared isotonic phosphate buffer (pH 6.8). This solution was filtered using a Millipore filter (0.22 μm), diluted suitably, and analyzed for absorbance at a maximum wavelength (λ_{max} ~ 263 nm) on a UV-Visible spectrophotometer (Model: V-630, JASCO International Co., Ltd., Tokyo, Japan) against the blank. The encapsulation efficiency of INH within INH-CaSP Ms was calculated using the below-mentioned equations.

$$\begin{aligned}
 & \text{Encapsulation efficiency (\%)} \\
 & = \frac{\text{Total amount of INH-Free INH}}{\text{Total amount of INH}} \times 100
 \end{aligned} \quad (2)$$

Physico-Chemical Characterization of INH-CaSP Ms

Particle Size and Zeta Potential Analysis

The procedure earlier reported by our group was followed for the determination of particle size and zeta potential of optimized INH-CaSP Ms using photon cross-correlation spectroscopy (PCCS) equipped with dynamic light scattering (DLS) methodology (31, 32). Briefly, ~ 10 mg of optimized INH-CaSP Ms was weighed and dispersed in 10 mL of deionized water. The resulting dispersion was then analyzed for particle size within the sensitivity range of 1 nm to 10 μm using a particle size analyzer (Model: Nanophox Sympatec, GmbH, Clausthal-Zellerfeld, Germany). After this analysis, the prepared dispersion was also employed for its zeta potential analysis using nano particle analyzer (Model:

Table II. BBD Experimental Trial Formulations with Calculated Encapsulation Efficiency (% w/w) and *In Vitro* Dissolution Values (%) (Mean \pm SD)

Experimental trials	X_1	X_2	X_3	X_4	Encapsulation efficiency (% w/w)*	<i>In vitro</i> dissolution (%)*
1	+ 1	0	0	- 1	56.12 \pm 1.20	50.21 \pm 0.63
2	0	+ 1	0	0	60.03 \pm 1.36	54.02 \pm 0.89
3	0	0	- 1	+ 1	69.33 \pm 0.95	62.18 \pm 1.52
4	- 1	- 1	0	0	51.17 \pm 0.78	45.06 \pm 1.65
5	+ 1	0	0	0	58.28 \pm 2.10	64.09 \pm 0.55
6	- 1	- 1	0	0	53.30 \pm 1.41	42.28 \pm 0.11
7	- 1	0	+ 1	0	47.07 \pm 2.08	49.57 \pm 0.80
8	- 1	0	0	+ 1	62.11 \pm 1.88	67.39 \pm 1.44
9	0	- 1	+ 1	0	63.32 \pm 0.61	59.19 \pm 1.91
10	0	0	- 1	- 1	50.09 \pm 1.57	41.29 \pm 1.53
11	0	- 1	0	+ 1	82.40 \pm 1.72	92.60 \pm 1.24
12	0	- 1	0	- 1	71.02 \pm 1.12	69.20 \pm 0.10
13	- 1	0	0	- 1	45.29 \pm 0.88	47.56 \pm 0.78
14	0	0	+ 1	+ 1	67.52 \pm 2.78	72.46 \pm 1.96
15	+ 1	+ 1	0	0	78.50 \pm 1.65	80.74 \pm 0.18
16	0	+ 1	0	+ 1	84.05 \pm 1.47	82.10 \pm 0.82
17	0	- 1	- 1	0	80.63 \pm 0.38	76.52 \pm 0.11
18	-	0	0	+ 1	55.46 \pm 0.56	56.71 \pm 2.12
19	- 1	0	- 1	0	48.74 \pm 0.22	53.16 \pm 2.67
20	+ 1	0	- 1	0	86.37 \pm 0.08	85.62 \pm 1.85
21	0	0	+ 1	- 1	44.67 \pm 1.68	51.25 \pm 1.56
22	0	+ 1	0	- 1	55.71 \pm 1.50	56.4 \pm 0.66
23	0	+ 1	- 1	0	88.03 \pm 2.75	87.1 \pm 0.39
24	+ 1	0	0	0	75.6 \pm 0.28	75.37 \pm 0.96
25–29	0	0	0	0	93.75 \pm 0.98	90.88 \pm 1.69

BBD Box Behnken design, X_1 sodium alginate concentration (% w/v), X_2 bio-enhancer concentration (mg), X_3 cross-linking agent concentration (% w/v), X_4 cross-linking time (min)
 *All the values are mean \pm Std. Dev.; (n = 3)

NanoPlusTM-2, Particulate System, Norcross, GA, USA) within the sensitivity range - 200 to + 200 mV. The entire analysis was conducted at room temperature.

SEM

The scanning electron microscope (Model: Supra[®]55, Carl Zeiss NTS Ltd., Germany) was utilized to study the surface characterization of INH, sodium alginate, and optimized formulations, respectively. Briefly, ~ 50 mg of each sample was applied as a thin film on double-faced carbon tape and transferred into SEM analyzing area. Next, the applied film was coated using gold (400 $^\circ$) for 10 s with the help of a sputter coater and analyzed at an accelerating voltage of 10 kV. The analyzed samples were recorded, converted into scanned images, and interpreted using attached software (Smart[®]SEM V05.06). The detailed SEM analysis was carried out as per the procedure reported earlier (33).

DSC

The samples of INH, sodium alginate, and physical mixture (PM) of INH and sodium alginate and optimized INH-CaSP Ms were analyzed to investigate their thermal pattern using differential scanning calorimeter (Model: DSC-1821e, Mettler Toledo AG, Analytical, Schwerzenbach, Switzerland). These samples were analyzed using the same DSC procedure reported by our group earlier (34). Briefly, ~ 2 mg of each piece was

accurately weighed, sealed in an aluminum pan, and subjected to heating between the temperature ranges of 0 to 400 $^\circ$ C at a heating rate of 10 $^\circ$ C/min under a constant flow of nitrogen gas (50 mL/min). Following heating, the developed DSC pattern for each sample was read and interpreted by software (Universal Analysis 2000, V4.5A, build 4.5.0.5) supplied with the instrument.

FT-IR

The samples of INH, sodium alginate, PM, and optimized INH-CaSP Ms were tested using an FT-IR spectrophotometer (Model: FTIR-8300, Shimadzu, Kyoto, Japan). Briefly, ~ 2 mg of each sample and potassium bromide (KBr, IR grade) were mixed, triturated, and compressed into thin circular discs using Mini Hand Press Machine (Model: MHP-1, P/N-200-66747-91, Shimadzu, Kyoto, Japan). Circular transparent discs were scanned between the wavenumber region of 4000 to 400 /cm⁻¹ at an average scan of 45. The scanning resolution for the entire analysis was set at 4 cm⁻¹. The instrument-generated spectrum for each sample was recorded, compared, and read using software (IRSolution, FT-IR Control Software, Version 1.10) supplied with the instrument. The detailed procedure for the FT-IR analysis was reported earlier and followed in this analysis (Telange *et al.* (35), Telange *et al.* (36)).

Bio-Adhesion Study

The bio-adhesion potential of optimized INH-CaSP Ms formulations to the small intestine was performed using a procedure reported earlier in the literature (37). On the experiment day, the fresh albino rat small intestine (~ 2 cm) was excised and kept in a freshly prepared kerb's solution. Briefly, ~ 50 mg of INH-CaSP Ms was accurately weighed, loaded into small intestine tissue, and then stored at humidity temperature control chamber under the controlled conditions of relative humidity (RH, ~ 75 %) and temperature (~ 25 ± 2°C) for 20 min. Next, the hydrated INH-CaSP Ms formulations were thoroughly washed using isotonic phosphate buffer (pH 6.8) solution, collected washing, and dried at 70°C using the hot-air oven. The dried microspheres were collected and weighed. The percentage of bio-adhesion was calculated using the below-described equation.

$$\% \text{Bio-adhesion} = \frac{\text{Weight of adhered INH-CaSP Ms}}{\text{Weight of applied INH-CaSP Ms}} \times 100 \quad (3)$$

In Vitro Dissolution Studies

The comparative *in vitro* dissolution pattern of pure INH, PM, or optimized INH-CaSP Ms formulations was evaluated using the method reported previously (38, 39). The dissolution studies were carried out in simulated gastric fluid (SGF, pH 1.2) and simulated intestinal fluid (SIF, pH 7.4) media. Briefly, INH (~ 10 mg), INH-SA Ms (~ 10 mg of INH), or optimized formulations (~ 10 mg of INH) were weighed, loaded into empty capsule shells, and then placed into the basket assembly. The basket containing samples was transferred into 500 mL of freshly prepared dissolution media. The dissolution flask contents were stirred at 50 rpm and maintained at 37 ± 0.5°C for the entire study. At the fixed intervals, 2 mL of solution was pipette out and replaced with an equal quantity of fresh dissolution media. The removed samples were suitably diluted and analyzed for absorbance using UV-Visible spectrophotometer (Model: V-630, JASCO International Co., Ltd., Tokyo, Japan) at the maximum wavelength (λ_{max} ~ 263 nm). The recorded absorbance values were calculated and reported in percentage cumulative INH release.

Ex Vivo Permeation Studies

The comparative permeation pattern of pure INH, PM, or optimized INH-CaSP Ms formulations across the intestine tissue was performed using the intestinal everted sac method described earlier in the literature (40). Briefly, the freshly excised intestine tissue was everted using a glass rod and rinsed with the saline solution. The everted tissue was cut and secured to the tip of 1 mL disposable syringe barrel. The freshly prepared modified Kerb's ringer phosphate bicarbonate solution (pH 7.4) as serosal fluid was then filled into the sac. The filled sac was suspended into the flask containing 50 mL of pure INH suspension (~ 2 mg/mL), INH-SA Ms (~ 2 mg/mL of INH), or optimized INH-CaSP Ms formulations (~ 2 mg/mL of INH)

prepared in modified Kerb's ringer phosphate bicarbonate solution. The flask contents were stirred at 50 rpm using a magnetic stirrer and aerated continuously utilizing a 95% O₂ and 5% CO₂ mixture. The media temperature was maintained at 37 ± 0.5°C throughout the study. A small aliquot was removed, diluted approximately, and analyzed for isoniazid absorbance at the maximum wavelength (λ_{max} ~ 263 nm) using UV-Visible spectrophotometer (Model: V-630, JASCO International Co., Ltd., Tokyo, Japan). At each time interval, the recorded absorbance values were calculated and expressed in terms of cumulate INH permeated.

Oral Bioavailability Studies

Bioanalytical Method Development

In this method, INH (~ 10 mg) was accurately weighed and mixed with 10 mL of HPLC grade water, forming a stock solution with a 100 µg/mL concentration. This solution was stored at 4°C till further analysis by HPLC. After this, the stock solution was diluted and spiked with a sufficient quantity of blank plasma to get the final solution in the concentration range of 250–25,000 ng/mL. The blank plasma solution was prepared into three different concentrations of quality control samples, such as low (~ 250 ng/mL), medium (~ 500 ng/mL), and higher (~ 1000 ng/mL) respectively, and stored at – 20°C till further analysis by HPLC.

The quantitative determination of INH in rat plasma samples was performed as per the method described earlier in the literature (41). Briefly, the HPLC apparatus (Model: e-2695 Water Alliance, Water Corporation, MA, USA) with the following specifications of PDA detector, auto-injector, column oven, line degasser, and sample heater-cooler was used to determine the isoniazid in plasma samples. The stationary phase consisted of RP-18 (specifications of 4.6 mm × 150 cm, 5 µ particle size) was employed to perform the separations of the analyte. The mobile phase was composed of phosphate buffer (0.1 M, pH 5 adjusted using orthophosphoric acid) and methanol run at the combination of 50:50 for the first minute and after that, 90:10 throughout the analysis. While analysis, the flow rate was set at 0.9 mL/min. The 20 µL solution was injected and analyzed for the isoniazid content at the maximum wavelength (~ 263 nm). The data acquisition and peak integration were interpreted using HPLC attached software (Empower 2® software).

Extraction of INH and Preparation of Samples

The extraction of INH from rat plasma samples was performed using the liquid-liquid extraction method described earlier (41). Briefly, the group I and II animals (containing six animals in each group) were received pure INH (~ 30 mg of INH) or optimized INH-CaSP Ms formulations (~ 30 mg of INH), respectively. The animals were anesthetized, withdrawn their blood samples from retro-orbital plexus, and transferred into a heparinized Eppendorf® Safe-Lock microcentrifuge tube (1.5 mL). The blood samples were centrifuged at 800 g× for 15 min, collected the plasma, and then stored at – 20°C for further analysis by developed HPLC method.

Validation of the Extraction and Quantification Method

According to the established International Conference on Harmonization (ICH) guidelines, the developed HPLC method was validated. The validation parameters such as interday accuracy and precision were analyzed on six replicates of quality control samples on the same day. Likewise, the intraday accuracy and precision were analyzed on the six replicates quality control samples following three days. The extraction of isoniazid from plasma samples and standard solutions were performed and compared concerning extraction recoveries. The quality samples were also analyzed for long-term (14 days) and short-term (24 h) stability studies.

Study of Pharmacokinetic Parameters

The effect of orally administered INH or optimized INH-CaSP Ms formulations on the pharmacokinetic parameters of group I and II animals were studied and compared. The C_{max} and T_{max} parameters were analyzed using the plasma concentration-time profile curve. The area under the curve from zero to time of final samples (AUC_{0-t}) and from zero to infinity ($AUC_{0-\infty}$), half-life ($t_{1/2}$), and clearance (CL/F) was analyzed and interpreted using WinNonlin® software (Version 4.1, Certara USA Inc., Princeton, NJ, USA).

RESULTS AND DISCUSSION

Preparation of INH-CaSP Ms

In the present study, the INH-CaSP Ms was prepared using a modified emulsification method. In this method, the optimum sodium alginate and light liquid paraffin ratio are vital because both provide compatibility, resulting in a homogenous emulsion. Earlier reports have also suggested that sodium alginate and light liquid paraffin in an optimum ratio (1:10) produced the stable emulsion (30). The same concept was also employed in the current study and found that the ratio (1:10) produced the highly viscous solution. A higher concentration of sodium alginate increased the polymer density resulting in failure of the emulsion. This problem was solved by exploring the various ratios of these ingredients, including (1:9), (1:8), (1:7), (1:6), and (1:5), respectively. The ratio (1:9) and (1:8) produced the same highly viscous solution as observed in the ratio (1:10), while the ratio (1:5) and (1:6) produced the emulsion; however, after a few minutes, it showed the phase separation indicating the lower concentration of sodium alginate might create the phase separation. It was also suggested that insufficient sodium alginate concentration could show its unavailability for interaction with light liquid paraffin caused phase separation of the emulsion. Compared to all, the ratio (1:7) demonstrated the best suitability for emulsion and microspheres preparations due to multiple advantages such as providing high dispersibility to INH in an aqueous polymer solution and setting up possible interaction between sodium alginate and light liquid paraffin resulting in the formation of a

homogenous stable emulsion. Therefore, the ratio (1:7) was chosen as an optimum ratio for developing emulsion and INH-CaSP Ms.

Additionally, the preparation of cross-linking agent (calcium chloride solution) also plays an essential role in the formation of INH-CaSP Ms. It is believed that the prepared calcium chloride solution in a suitable mixture of solvents can favor the formation of spherical microspheres. In this study, the calcium chloride solution was prepared in a mixture of methanol and isopropyl alcohol ratios such as 1:1, 2:3, 2:8, and 3:7, respectively. The ratio 1:1, 2:8, and 3:7 exhibits low dispersibility to the calcium chloride leading to failure of cross-linking between the polymer and calcium chloride. In contrast to this, the ratio of 2:3 produced promising results. This ratio provides high dispersibility to the calcium chloride, resulting in a successful cross-linking between the polymer and calcium chloride. Moreover, while adding this solution to the prepared emulsion, the methanol could offer immediate gel formation with high entrapment of INH. In contrast, the isopropyl alcohol could provide rapid gel hardening to prevent INH leakage from a gel into the aqueous solution. Therefore, the mixture of methanol and isopropyl alcohol in a ratio (2:3) was chosen as an optimal solvent system for the dissolution of calcium chloride and successful preparation of INH-CaSP Ms (30). Moreover, the developed positive charge calcium ion-alginate complex also interacted with the negative carbonyl group of piperine bio-enhancer formed cross-linked coordinate bond interaction between them, resulting in INH-CaSP Ms.

BBD Optimization

The BBD offers an excellent optimization to the final formulation due to its robust coefficient estimate near the center of the design space and more efficiency. It also provides an economical choice to central composite design (CCD) to fit the quadratic model that requires three levels for each variable. The QbD-based BBD analyzed the impact of selected independent variables on the dependent variables, and their results are shown in Table II. As shown in the table, the BBD displayed 29 numbers of experimental trials. Each trial was based on a combination of four independent variables, which exhibited a significant variation in the encapsulation efficiency and *in vitro* release. Both the variables showed their values in the range of ~ 44.67 to 95.51% w/w and ~ 41.29 to 91.30%, respectively. Some trials were found common among all trial formulations, but their effect on the value of encapsulation efficiency and *in vitro* release was found slightly different. Following the interpretation of table values, the BBD also analyzed the entire data and presented it in terms of fit summary statistics Table III, analysis of variance (ANOVA) Tables IV and V, model summary, diagnostics, contour, and 3D surface response plot, respectively. In ANOVA, the obtained polynomial equations, coefficient of magnitude, and associated sign (i.e., + or -) were used further to optimize independent variables.

Table III. Fit Statistics of Encapsulation Efficiency and *In Vitro* Dissolution

Fit statistics	Std. Dev.	Mean	C.V %	R ²	AdjustedR ²	PredictedR ²	Adeq precision
Encapsulation efficiency	6.67	69.09	9.65	0.9240	0.8479	0.6548	12.0563
<i>In vitro</i> dissolution	11.00	68.16	16.14	0.8004	0.8256	0.6310	6.6909

C.V coefficient of variation

Encapsulation efficiency (Y_1)

$$\begin{aligned}
 &= 93.76 + 9.66X_1 - 0.7317X_2 - 6.86X_3 \\
 &+ 8.16X_4 - 21.08X_1^2 - 5.36X_2^2 - 15.32X_3^2 - 17.86X_4^2 \\
 &+ 1.26X_1X_2 - 6.61X_1X_3 - 2.67X_2X_3 - 1.04X_1X_4 \\
 &+ 4.24X_2X_4 + 0.9025X_3X_4
 \end{aligned} \quad (4)$$

In vitro dissolution (Y_2) = 90.93

$$\begin{aligned}
 &+ 10.76X_1 - 0.8117X_2 - 4.61X_3 + 9.79X_4 - 19.17X_1^2 - 6.31X_2^2 - 14.33X_3^2 - 15.22X_4^2 \\
 &+ 0.6475X_1X_2 - 4.49X_1X_3 - 3.94X_2X_3 + 2.01X_1X_4 + 0.5750X_2X_4 + 0.08X_3X_4
 \end{aligned} \quad (5)$$

The above polynomial equation for encapsulation efficiency and *in vitro* release shows the combination of positive and negative terms of magnitude coefficient. The coefficients of encapsulation efficiency (b1, b3, b4, b11, b33, and b44) and *in vitro* release (b1, b4, b11, b33, and b44) were found significant, whereas the remaining coefficients were found as non-significant. The obtained *F* value and *P* value for encapsulation efficiency and *in vitro* release around (~ 12.15 and < 0.0001) and (~ 4.01 and < 0.05) indicates that the quadratic model is significant and the best fit for this experiment. The fit statistics between the adjusted and predicted correlation coefficient value was < 0.2 suggests the suitability of the quadratic model. Moreover, the obtained good precision value around ~ 12.0563 and ~ 6.6909 (> 4),

implying that the quadratic model is desirable for encapsulation efficiency and *in vitro* release and, therefore, can be employed to navigate the design space. The press value appeared around ~ 3561.69, and ~ 9723.20 suggests the model's suitability for trial formulations. Additionally, the associated positive and negative signs of the coefficient of magnitude significantly impacted the value of encapsulation efficiency and *in vitro* release. The positive sign showed that

as the concentration of X_1 and X_4 increases, the encapsulation efficiency and *in vitro* release increases. The negative sign displayed that as the concentration of X_2 and X_3 increases, the encapsulation efficiency and *in vitro* release decreases. It indicates a direct correlation between the positive character of the coefficient of magnitude and dependent variables. At the same time, there is an inverse correlation between the negative sign of the coefficient of magnitude and dependent variables. The effect of X_1 , X_2 , X_3 , and X_4 on the encapsulation efficiency and *in vitro* release is presented in (Fig. 1 a and b), respectively. The figure showed that as the concentration of independent variables increases specifically to the middle level, the encapsulation efficiency and release rate

Table IV. Summary of ANOVA Used for Data Analysis of Encapsulation Efficiency

Source	Sum of squares	df	Mean square	Fvalue	Pvalue	Remark
ANOVA: Encapsulation efficiency (Quadratic model)						
Model	7560.99	14	540.07	12.15	0.0001	Significant
A–Sodium alginate concentration	1120.37	1	1120.37	25.21	0.0002	
B–Bio-enhancer concentration	6.42	1	6.42	0.1445	0.7095	
C–Cross-linking agent concentration	564.44	1	564.44	12.70	0.0031	
D–Cross-linking time	799.84	1	799.84	18.00	0.0008	
AB	6.33	1	6.33	0.1423	0.7116	
AC	174.50	1	174.50	3.93	0.0675	
AD	4.37	1	4.37	0.0983	0.7585	
BC	28.57	1	28.57	0.6428	0.4361	
BD	71.91	1	71.91	1.62	0.2241	
CD	3.26	1	3.26	0.0733	0.7905	
A²	2881.60	1	2881.60	64.83	< 0.0001	
B²	186.24	1	186.24	4.19	0.0599	
C²	1522.08	1	1522.08	34.25	< 0.0001	
D²	2068.40	1	2068.40	46.54	< 0.0001	
Residual	622.23	14	44.45			
Cor Total	8183.22	28				

df degree of freedom

Table V. Summary of ANOVA Used for Data Analysis of *In Vitro* Dissolution

Source	Sum of squares	df	Mean square	Fvalue	Pvalue	Remark
ANOVA:In vitrodissolution (Quadratic model)						
Model	6793.43	14	485.25	4.01	0.0069	Significant
A–Sodium alginate concentration	1388.47	1	1388.47	11.48	0.0044	
B–Bio-enhancer concentration	7.91	1	7.91	0.0653	0.8020	
C–Cross-linking agent concentration	254.75	1	254.75	2.11	0.1688	
D–Cross-linking time	1151.11	1	1151.11	9.51	0.0081	
AB	1.68	1	1.68	0.0139	0.9079	
AC	80.46	1	80.46	0.6651	0.4284	
AD	16.12	1	16.12	0.1332	0.7205	
BC	62.02	1	62.02	0.5126	0.4858	
BD	1.32	1	1.32	0.0109	0.9182	
CD	0.0256	1	0.0256	0.0002	0.9886	
A²	2382.86	1	2382.86	19.70	0.0006	
B²	258.60	1	258.60	2.14	0.1658	
C²	1332.05	1	1332.05	11.01	0.0051	
D²	1502.16	1	1502.16	12.42	0.0034	
Residual	1693.70	14	120.98			
Cor total	8487.14	28				

df degree of freedom

increases simultaneously, and after that, it goes on decreases as the concentration decreases, suggesting that the middle-level concentration of X_1 , X_2 , X_3 , and X_4 is a significant part and hence, could be used for the final optimization of INH-CaSP Ms formulations.

Based on figure interpretation and middle-level concentrations, the optimization of independent variables was processed using numerical and graphical optimization techniques. Before optimization, the constraints in the form of goal were applied for X_1 (~ 4 to 6% w/v), X_2 (~ 5 to 15 mg), X_3 (~ 5 to 15% w/v), X_4 (~ 15 to 45% w/v), encapsulation efficiency (~ 80.63 to 95.51% w/v), and *in vitro* release (~ 90.36 to 93.2%) respectively. Following analysis, the BBD showed one possible solution with a desirability value close to 1 for INH-CaSP Ms indicates the suitability of applied constraints for numerical optimization. Their results are shown in (Fig. 1c). The graphical technique with the same constraints for encapsulation efficiency and *in vitro* release also displayed the same possible solution in the design space overlay plot (Fig. 1d). The combined results of desirability and design space overlay plot provided the optimal values for X_1 (~ 5.04% w/v), X_2 (~ 8.43 mg), X_3 (~ 7.57% w/v), and X_4 (~ 31.56 min), respectively, which could be utilized further for the preparation of stable INH-CaSP Ms formulations. Following optimization, the post-analysis results in the form of point prediction also suggest the suitability and validity of BBD for preparation and optimization of INH-CaSP Ms. The post-analysis data are presented in Table VI.

Validation of the Model

The validation of the quadratic model was carried out by forming an extra INH-CaSP Ms formulation using optimal values X_1 , X_2 , X_3 , and X_4 , respectively. Following this, the obtained results of trial formulation were compared with model-predicted values. The comparative analysis showed

that both the models are in close agreement with each other. Their bias (%) difference calculated using the below-described equation was found to be less than 3% suggesting the validity and robustness of BBD. Moreover, the obtained correlation coefficient value around ~ 0.9240 and ~ 0.8004 during analysis indicates BBD is the best-fit response surface design for optimizing INH-CaSP Ms formulations.

$$\text{Bias (\%)} = \frac{\text{Predicted value} - \text{observed value}}{\text{Predicted value}} \times 100 \quad (6)$$

Physico-Chemical Characterization of INH-CaSP Ms

Estimation of Encapsulation Efficiency

According to optimization results, the INH-CaSP Ms demonstrated higher encapsulation efficiency around ~ 93.03 ± 1.54% w/w compared to earlier published reports signifies the suitability of modified emulsification methodology toward enhancement of encapsulation efficiency of INH within INH-CaSP Ms. It was suggested that the mixture of solvents, i.e., methanol and IPA in ratio 2:3 (in which calcium chloride solution was prepared) and piperine might contribute to the significant enhancement of encapsulation efficiency of INH. These results could be explained by the fact that methanol could combine with the internal phase of aqueous sodium alginate solution, forming a strong association with each other, resulting in the formation of immediate gel, whereas IPA solvent could combine with the external phase the emulsion caused a rapid hardening of the gel. This combined mechanism facilitates the encapsulation of INH within sodium alginate polymer and prevents its escape in the surrounding solution (42). Moreover, the piperine bio-enhancer in aqueous sodium alginate solution may set up interaction with INH, leading to increased holding and

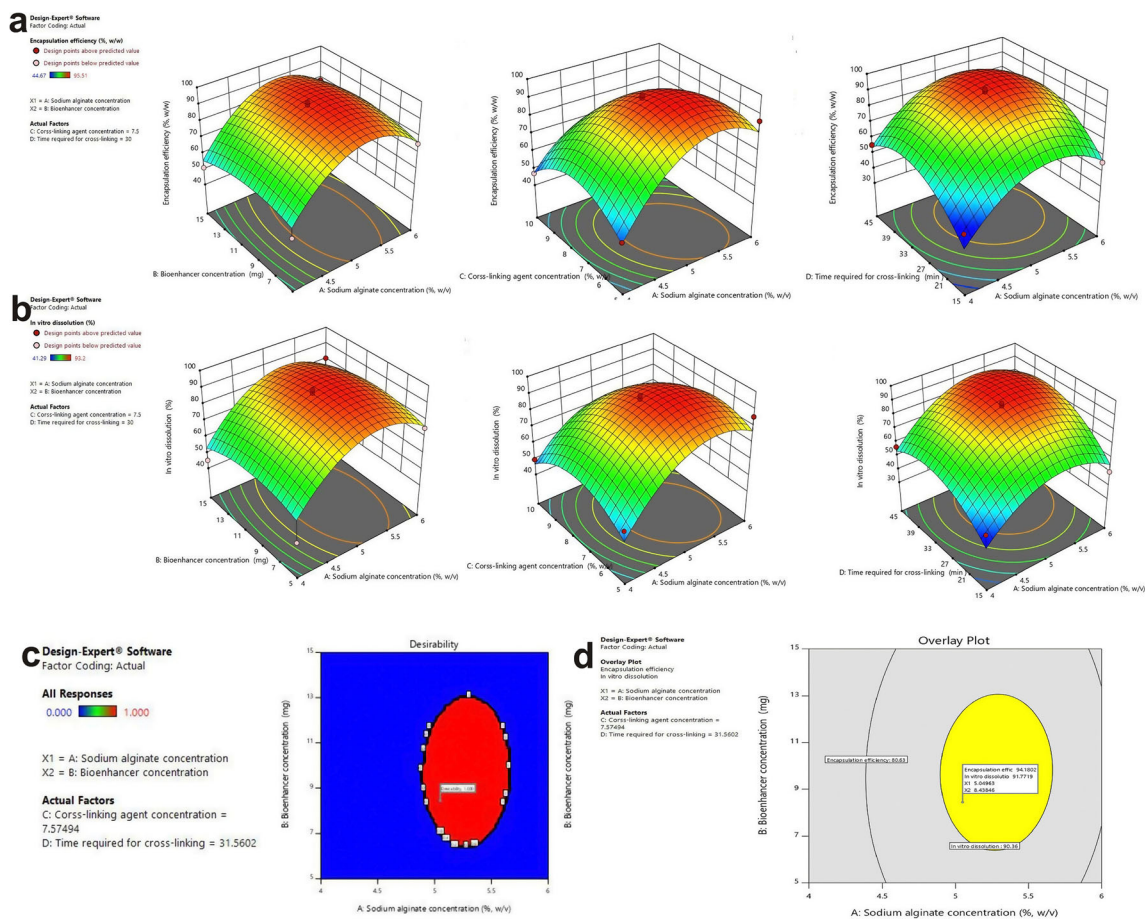


Fig. 1. 3D response plot shows the effect of sodium alginate concentration (X_1 , % w/v), bio-enhancer concentration (X_2 , mg), calcium chloride concentration (X_3 , %, w/v), and cross-linking time (X_4 , min) on **a** encapsulation efficiency, **b** *in vitro* dissolution, **c** desirability plot, and **d** design space plot

interaction within the gel, resulting in enhanced INH encapsulation within the microspheres. It was also suggested that the negative carbonyl group of piperine might interact, associate, and form a strong additional cross-linking coordinate bond with positive calcium ions within the alginate microspheres. This phenomenon could increase the stability of the microspheres and thereby enhance the encapsulation efficiency and the controlled release pattern of INH. The lipophilic property of piperine could repel water molecules via growing strong coordinate bonds with calcium ions, resulting in enhanced INH encapsulation efficiency within the alginate microspheres (43). The results conclude that calcium chloride, its preparation solvent, and bio-enhancer provide the basis for interaction and thus increase the INH encapsulation efficiency and controlled release profile.

Particle Size and Zeta Potential Analysis

The particle size analysis provides information about its distribution within prepared formulations. This information can be used to understand the influence of particle size on the stability, release behavior, and bioavailability of the formulations. The results of particle size and zeta potential analysis of optimized INH-CaSP Ms are discussed below. The optimized INH-CaSP Ms revealed an average particle size and low polydispersity index (PDI) around $\sim 117.34 \pm 1.28 \mu\text{m}$ and 0.29 ± 0.05 , respectively. It indicates the narrow distribution of isoniazid within an optimized INH-CaSP Ms. Findings are in close agreement with earlier published reports which suggests that alginate microspheres prepared using emulsification and

Table VI. Post Analysis Confirmation at Two-Tailed 95% Confidence Level

Response	Predicted mean	Predicted median	Std. Dev.	n	SE Pred	95 % PI low	95 % PI high
Encapsulation efficiency	93.75	93.75	6.66	1	7.3030	78.0925	109.419
<i>In vitro</i> dissolution	90.93	90.93	10.99	1	12.0488	65.0918	116.776

ionic gelation method produces a particle size around $\sim 84.47 \pm 20.78 \mu\text{m}$ and $65.88 \pm 5.20 \mu\text{m}$ and provides the suitability of the delivery system to the oral route (44, 45). The larger particle size of the formulations could plausibly be attributed to a higher concentration of alginate polymer may cause to enhance the viscosity of the solution, resulting in the formation of large particle size during emulsification (45). It was also suggested that a higher concentration of calcium chloride as a cross-linking agent and cross-linking time could increase the interaction between the polymer's calcium ion and guluronic acid. This interaction may increase the viscosity of the solution resulted in large particle size of INH-CaSP Ms (44).

Moreover, it was also noted that piperine bio-enhancer increases the interfacial tension between two phases, reduces the shearing rate in emulsion, and increases the particle size of INH-CaSP Ms (46). Zeta potential (ζ) of optimized INH-CaSP Ms formulations observed around $\sim -31.13 \pm 0.32 \text{ mV}$ ascribed to a negative carboxylic acid group of sodium alginate. This value was kept higher than the potential zeta range of $\pm 30 \text{ mV}$. A higher value, either positive or negative, indicates the physical stability of the formulations. This value was appeared due to the reduction of positive calcium ions from the surface of swelled alginate microspheres (47). The results conclude that larger particle size, zeta potential, and lower PDI value are suitable for better physical stability of INH-CaSP Ms formulations.

SEM

SEM analysis provides information about the formulation components' sample morphology, homogeneity, and microstructure. The SEM photographs of INH, sodium alginate, and optimized INH-CaSP Ms formulations are depicted in (Fig. 2 a, b, and c), respectively. The surface morphology of INH (Fig. 2a) exhibited small and large needle-shaped crystals with well-defined edges. The surface of the particles appeared as a smooth surface and was found consistent with earlier reports (48). The SEM of sodium alginate is presented in (Fig. 2b). As can be seen, it displays large aggregate particles with a heterogeneous surface. Results are well justified with the reports published by Salisu *et al.* (49). The optimized INH-CaSP Ms formulation SEM image is shown in (Fig. 2c). The figure shows that the formulations revealed spherical shape particles indicating positive interaction between sodium alginate, piperine, and calcium chloride. It was suggested that a high shearing rate of emulsification could generate spherical globules of polymer followed by interaction with calcium chloride solution resulted in the formation and hardening of globules as spherical microspheres. Moreover, the proper dispersion of calcium chloride within the internal and external phases of the emulsion may also contribute to forming spherical microspheres.

DSC

DSC is an advanced analytical technique widely employed to investigate the physical interaction between drugs and excipients. (Fig. 3a–d) exhibits the DSC thermograms of pure INH, PM, placebo microspheres, and optimized INH-CaSP Ms formulations, respectively. The DSC of pure INH (Fig. 3a)

shows the sharp and high-intensity endothermic peak around $\sim 175^\circ\text{C}$ indicating the crystalline nature of isoniazid (29). Figure 3b shows the DSC thermograms of PM. The figure shows that peaks correspond to sodium alginate and pure INH. Compared to the original peak, the peak position and intensity of INH in PM were shifted to a lower temperature, indicating that positive interaction between sodium alginate and INH could shift the peak position and intensity of INH. It is also suggested that PM at a higher temperature may absorb the heat and transform into partial in situ mixture powder, exhibiting low peak intensity. Moreover, the two small miniature peaks of sodium alginate also appeared in PM. The first and second peaks appeared in between the range of $\sim 80\text{--}90^\circ\text{C}$ and $\sim 200\text{--}225^\circ\text{C}$, respectively. The first peak could be due to the evaporation of hydrated water molecules, while the second was likely due to the oxidative degradation of sodium alginate at a higher temperature. The findings are consistent with those of literature published earlier (43). The DSC thermograms of the placebo microspheres (Fig. 3c) exhibited a broad and diffused endothermic peak in between the range of $\sim 80\text{--}120^\circ\text{C}$, indicating the presence of sodium alginate in the microspheres. The DSC thermograms of optimized INH-CaSP Ms (Fig. 3d) showed the low-intensity peak around $\sim 180^\circ\text{C}$ compared to the original INH peak, suggesting that the O-H group of sodium alginate interacted with the N-H group of INH through hydrogen bonding and van der Waals forces. These forces facilitated the dispersion and lowering of drug crystallinity within polymer matrix resulting in development of microspheres with low intensity characteristics of INH. It is worth to point out that carbonyl group of piperine could establish interaction with polar group of INH and sodium alginate, thereby optimized INH-CaSP Ms could show shifted peak. Furthermore, the dilution factor may also find the reason for low-intensity peak of INH in formulations. According to findings, it can be concluded that functional group interaction between INH, polymer and piperine confirms the formation of drug loaded microspheres.

FT-IR

FT-IR instruments analyze, interpret, and provide essential information concerning functional group interaction among the API and excipients. The FT-IR spectrum of pure INH, optimized INH-CaSP Ms, and placebo microspheres are shown in (Fig. 4 a, b, and c), respectively. FT-IR spectra of pure INH (Fig. 4a) exhibits a series of absorption peaks around ~ 3302.82 (due to N-H stretching), 3111.35 (due to secondary amide group), 3013.57 (due to C-H stretching), 1664.65 (for N-H bending), 1636.10 (for C=O bending), 1554.61 (due to aromatic compound). Moreover, it also showed few peaks around ~ 1410.09 (due to C=C stretching), ~ 1332.69 (due to strong C-N stretching aromatic amine), 1138.62 (due to $-\text{NH}_2$ stretching), and $\sim 995.19/\text{cm}^{-1}$ (due to C=C bending) respectively (29). The FT-IR spectrum of the placebo microspheres is shown in (Fig. 4c). The figure shows absorption peaks around ~ 3410.12 (O-H stretching) and ~ 2940.11 (C-H stretching). In contrast, the remaining peaks correspond to polymer disappeared completely, suggesting that sodium alginate polymer interaction with calcium chloride solution could cause

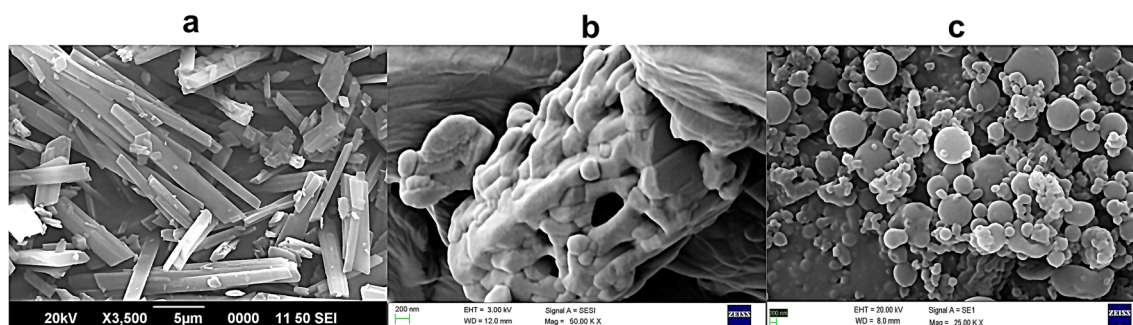


Fig. 2. SEM images of **a** pure INH, **b** sodium alginate, and **c** optimized INH-CaSP Ms

shifting and disappearance of the polymer peak and thus produced placebo microspheres. Figure 4b revealed a significant change in the absorption peaks of optimized INH-CaSP Ms. It exhibits broad peaks at low absorption frequencies around ~ 3215.22 and $3115.35/\text{cm}^{-1}$ compared to the original INH peak at ~ 3302.82 and $3111.5/\text{cm}^{-1}$, respectively. Furthermore, the formulation demonstrated a

complete disappearance of prominent N-H bending and C=O absorption peak at $\sim 1664.65/\text{cm}^{-1}$ and $\sim 1636.10/\text{cm}^{-1}$. Results suggested that polar functional groups of sodium alginate and piperine could establish weak intermolecular forces (hydrogen bonding and van der Waals forces) with N-H and C=O groups of INH resulted in broadening, shifting, and disappearance of INH peaks

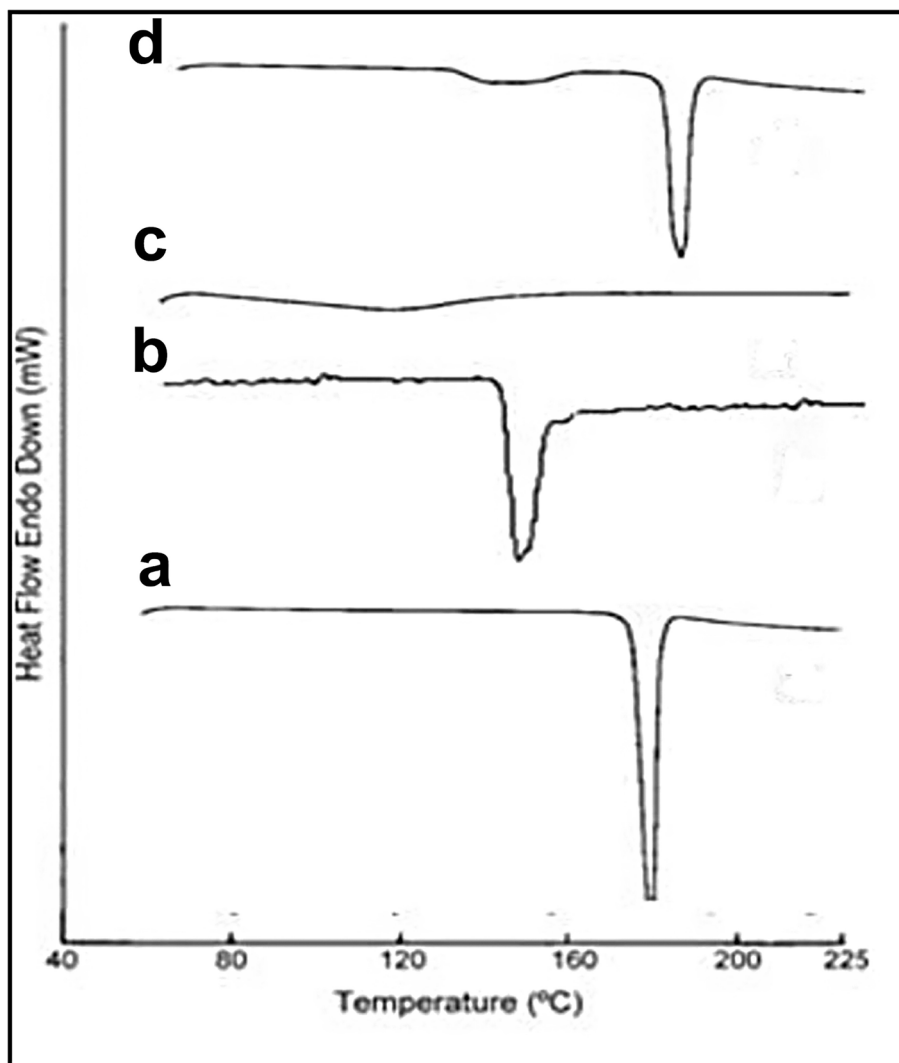


Fig. 3. DSC thermograms of **a** pure INH, **b** the PM of sodium alginate and INH, **c** placebo microspheres, and **d** optimized INH-CaSP Ms

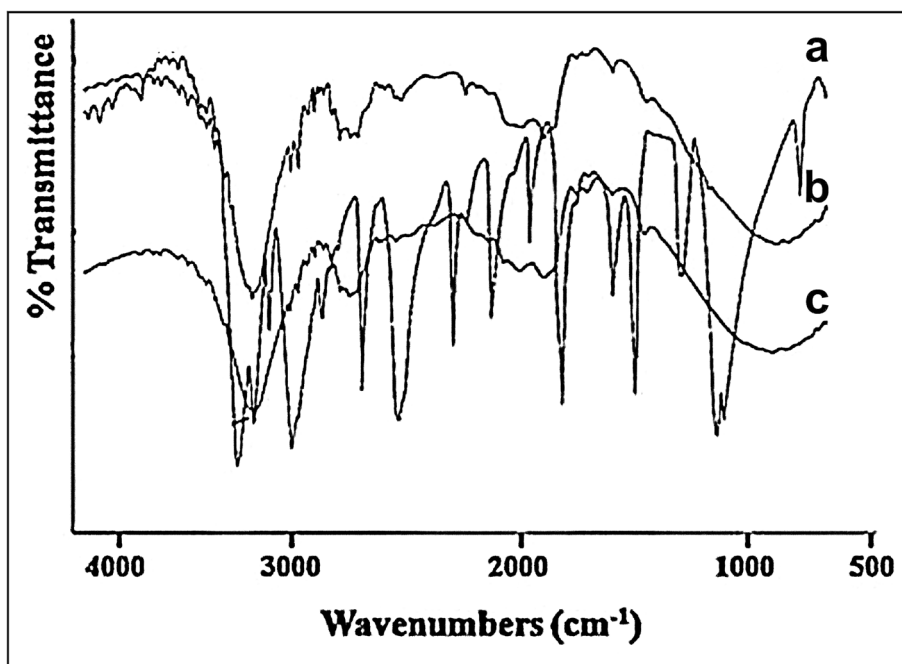


Fig. 4. FT-IR spectra of **a** pure INH, **b** optimized INH-CaSP Ms, and **c** placebo microspheres

in optimized INH-CaSP Ms formulations. The FT-IR findings suggest hydrogen bonding and van der Waals forces between the INH, polymer, and piperine bio-enhancer favor microspheres development via shifting absorption frequencies.

Bio-Adhesion Study

The optimized INH-CaSP Ms formulations exhibited higher bio-adhesion around $\sim 81.41 \pm 1.31\%$ compared to earlier reports, indicating piperine, sodium alginate, and calcium chloride improve the bio-adhesion of INH microspheres to the small intestine. It suggests that the positive charge of calcium ion of microspheres builds alliance with the negative charge of phospholipids bilayer of the small intestine could enhance its adhesion and retention, thereby increasing the bio-adhesion of INH to the small intestine. It is worth mentioning that sodium alginate polymer itself acts as a bioadhesive polymer. Its bio-adhesivity could be explained on the basis that swelled and wetted sodium alginate polymer containing carboxyl and hydroxyl groups increased association and, thereby, interaction with functional groups of the biological membrane through physical entanglement and chemical forces. This interaction forms a cross-linked network with the membrane, resulting in bio-adhesion and interpenetration of INH (16). It was also indicated that a developed strong cross-linked coordinate bond interaction between the negative charge of piperine and positive charge of calcium ion might increase its adhesion and retention to the small intestine resulting in higher bio-adhesion.

In Vitro Dissolution Studies

Figure 5 depicts the comparative release behavior of pure INH from suspension, PM, and optimized INH-CaSP Ms formulations, respectively. As seen in the figure, the pure INH at the end of 5 h showed only $\sim 27\%$ of drug dissolution.

Afterward, its dissolution was increased and reached around $\sim 57\%$ at the end of 12 h study indicating high solubility of INH. INH-SA Ms displayed around $\sim 36\%$ of INH dissolution at the end of the 5 h dissolution period. After 5 h, the INH dissolution appeared and reached around $\sim 81\%$, indicating that sodium alginate and calcium chloride improve the solubility and dissolution performance of INH. Obtained results suggest that polar functional groups of sodium alginate could associate and interact with polar functional groups of INH, which induced its physico-chemical modification enhancing INH dissolution. Also, suggesting that established cross-linking between positive calcium ion and negative guluronic acid of sodium alginate could produce polymer gel sustaining INH dissolution. In contrast to pure drug and INH-SA Ms, the optimized INH-CaSP Ms formulations displayed higher drug dissolution.

At early 5 h, the optimized formulations showed around $\sim 50\%$ of INH dissolution represents burst release attributed to the highly aqueous solubility of the drug (50). The burst effect could also be caused by substituting calcium ion with proton, resulting in the generation of protonated alginic acid polymer with enhanced susceptibility to water attack and, therefore, shows the rapid release of INH (12, 13). By the end of dissolution, the same formulation exhibited around $\sim 94\%$ of drug dissolution, indicating sustained INH release. The optimized INH-CaSP Ms significantly improved the INH dissolution at time points of $\sim 4, 5, 6, 7, 8, 11,$ and 12 h, respectively, compared to pure INH and INH-SA Ms. The level of significance was $\sim p < 0.05$ and 0.01 . Enhanced INH dissolution could be attributed to sodium alginate polymer, piperine bio-enhancer, calcium chloride, INH-sodium alginate polymer ratio, and cross-linking time. Sodium alginate is a hydrophilic, natural polysaccharide, and anionic polymer that demonstrates excellent biocompatibility, biodegradability, and bio-adhesivity to a large extent in drug delivery systems (51). In contact with dissolution media, sodium

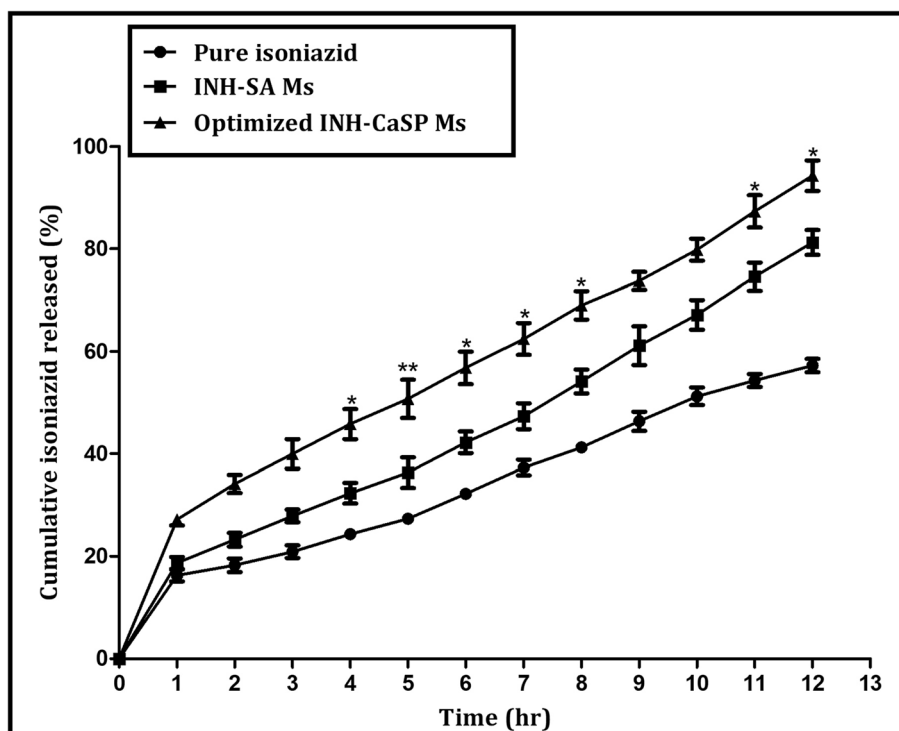


Fig. 5. The *in vitro* dissolution profiles of pure INH, the PM of INH and sodium alginate, and the optimized INH-CaSP Ms

alginate-based microspheres exhibit hydration, swelling, and formation of gel diffusion layer surrounding the microspheres. This gel layer could offer water entry into the internal core of the microspheres induced obstruction in the outward movement of drug produced sustained release of INH. Moreover, the polymer in contact with alkaline media exhibits slow erosion, sustaining INH release (52). The utilized drug-polymer ratio in INH-CaSP Ms formulations could enhance the sodium alginate concentration produced rigid and compact polymer matrix followed by increase in diffusion path length resulted in sustained release of INH (50). Beside this, an additional cross-linked coordinate bond interaction between negative charge of carbonyl group of piperine bio-enhancer and positive charge of calcium ion, i.e., Calcium ion-alginate-piperine within alginate matrices could increase hydration, swelling, and subsequently protect the alginate matrices and prevent its degradation resulted in sustained release of INH. The obtained optimal value of calcium chloride around ~ 7.98% using BBD offered an efficient cross-linking with sodium alginate via guluronic acid residues. This positive association caused the development of rigid polymer gel, and thus, INH could release a sustained manner from INH-CaSP Ms (44, 53). The lower concentration was not from the microspheres due to insufficient calcium ion concentration, whereas higher calcium chloride concentration could lower the encapsulation efficiency and release profile. It could be due to rapid gelling followed by expelling the water phase from the gel matrix. As is reported previously, the cross-linking time greater than 5 min or equal to 20 min shows complete gelling of sodium alginate (30, 44). Our study reported the cross-linking time around ~ 32.49 min compared to reported time. The reported time facilitated the penetration of calcium chloride solution to the outer calcium

ion-alginate-piperine residue and thus, induced efficient cross-linking coordinate bond interaction with the inner portion of the sodium alginate matrix.

The cumulative release values of optimized INH-CaSP Ms formulations were introduced into first order, zero order, Higuchi and Korsmeyer-Peppas model, and analyzed accordingly (54). The analyzed data reported the correlation coefficient values around ~ 0.9786, ~ 0.9412, and ~ 0.9561, respectively. Higher values indicate that optimized INH-CaSP Ms followed the Higuchi as the best-fit kinetic model. Additionally, the analyzed data also displayed the release exponent (n) value less than 0.5, indicating that diffusion is the mechanism through which the INH is released from the microspheres, suggesting that INH follows a two-step dissolution mechanism, first, INH dissociates from piperine bio-enhancer; secondly, the dissociated INH could diffuse from the rigid gel diffusion layer of the alginate microspheres; and then enter into dissolution media.

Ex Vivo Permeation Studies

The permeability is a principal indicator of the biopharmaceutical process that exclusively measures the amount of dissolved API traveling from the intestinal portion to the systemic blood circulation (55). The permeation pattern of pure INH forms suspension, INH-SA Ms, and optimized INH-CaSP Ms formulations are illustrated in (Fig. 6). At the end of the permeation period, the INH suspension revealed only ~ 55% of drug permeation, indicating low permeability of INH. The INH-SA Ms enhanced permeation efficiency of INH compared to suspension. At the end of 12 h, the INH-SA Ms demonstrated around ~ 80% of drug permeation, indicating that hydrophilic

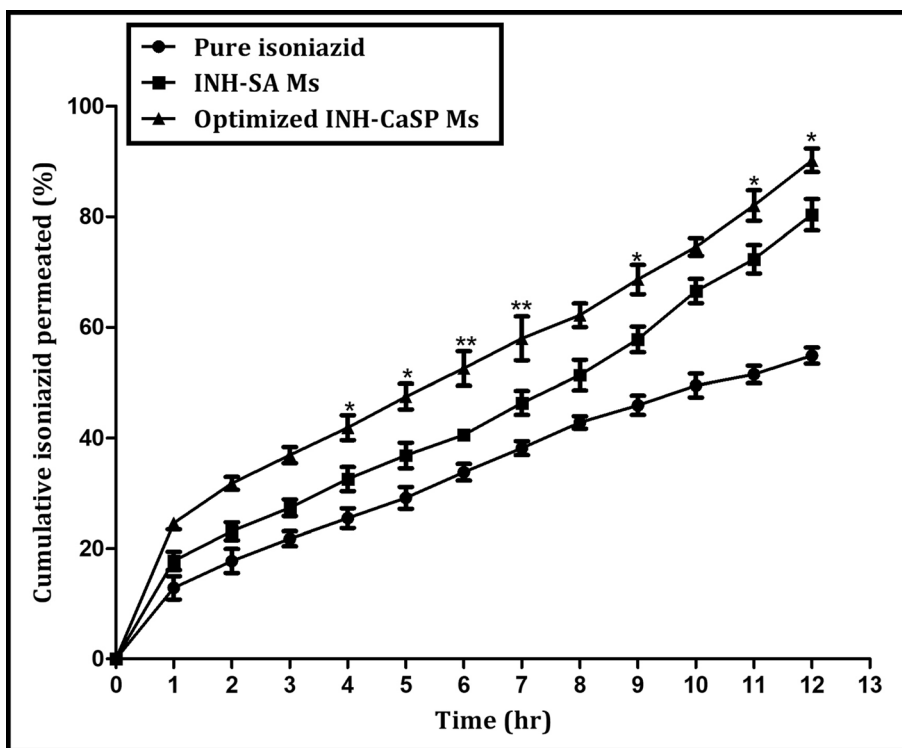


Fig. 6. The *ex vivo* permeation profiles of pure INH, the PM of INH and sodium alginate, and the optimized INH-CaSP Ms

sodium alginate polymer interacted with biological membrane. This phenomenon could be explained because developed association and subsequent interaction between biocompatible sodium alginate polymer and biological membrane may increase their miscibility within the membrane, thereby enhancing INH

permeation. The optimized INH-CaSP Ms showed higher permeation than suspension and INH-SA Ms. Optimized formulation exhibits around ~ 90% of drug permeation. Formulation significantly enhanced the INH permeation at time points of ~ 4, 5, 6, 7, 9, 11, and 12 h, respectively, and their level significance was

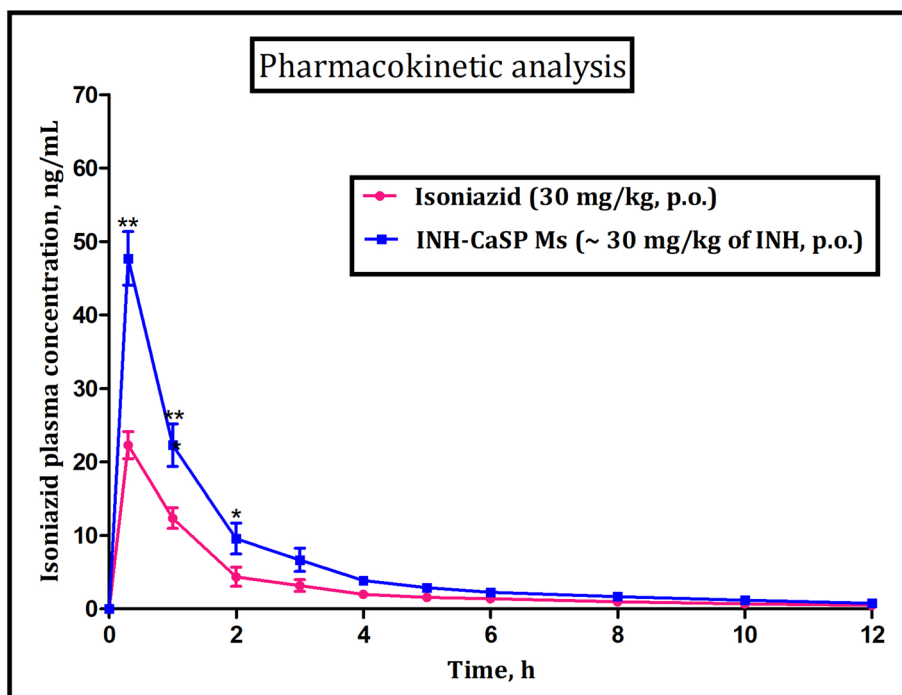


Fig. 7. Mean plasma concentration–time profile curve following oral administration of INH (~ 30 mg/kg, p.o.), and optimized INH-CaSP Ms (~ 30 mg/kg, p.o.)

Table VII. Results of Pharmacokinetic Parameters Obtained in Group of Animals Administered Oral Administration of INH (~ 30 mg/kg, p.o.) and INH-CaSP Ms (~ 30 mg/kg, p.o.)

Pharmacokinetic parameters	Formulations	
	INH	INH-CaSP Ms
C_{max} (ng/mL)	22.3 ± 2.54	47.8 ± 1.37
T_{max} (h)	0.30 ± 0.05	0.33 ± 0.08
$t_{1/2el}$ (h)	1.16 ± 0.71	2.21 ± 1.42
AUC_{0-t} (ng h mL ⁻¹)	41.12 ± 1.29	66.47 ± 2.87
$AUC_{0-∞}$ (ng h mL ⁻¹)	45.07 ± 1.67	70.54 ± 1.24
CL/F (L h ⁻¹ Kg ⁻¹)	1.43 ± 0.57	0.90 ± 0.10
V/F (L Kg ⁻¹)	2.28 ± 1.49	2.75 ± 1.88

INH isoniazid, INH-CaSP Ms isoniazid-encapsulated calcium ion-sodium alginate-piperine microspheres

*All the values are mean ± SEM; (n = 3)

~ $p < 0.05$ and 0.01 Results indicating that sodium alginate and piperine enhanced the permeability of INH across the biological membrane. This phenomenon could be caused by carboxyl and hydroxyl groups of sodium alginate. It forms strong interaction with biological membrane polar functional groups via physical and chemical forces. These forces develop a cross-linked network with a membrane that could provide powerful bio-adhesion, retention, miscibility, and subsequently, permeation of INH into the biological membrane. Findings are consistent with earlier published reports (16). Likewise, the cross-linking agent calcium chloride was also found to enhance the permeability of API. The interaction between positive calcium ion of INH-CaSP Ms and negative phospholipids bilayer of the membrane could facilitate and improve its adhesion, retention, miscibility, and INH permeation.

Supporting this, the piperine bio-enhancer also substantially influenced the permeation efficiency of many herbals and APIs. Earlier studies have shown that piperine improved the oral bioavailability of numerous drugs via increasing their absorption and permeation into intestinal epithelium (56–59). In the current study, the developed interaction between calcium ion-alginate-piperine and INH guides us to believe that piperine physico-chemical and biological properties could also assist in enhancing the permeation of INH from optimized formulations. According to this, piperine high permeability coefficient and apolar characteristics might increase its partitioning in the hydrophobic core of the lipids. This observable fact could modify membrane lipids dynamics resulting in significant INH permeation (18, 60). It is also observed that piperine enhances the permeation of INH via enhancing the leucine aminopeptidase (LAP) and glycyl-glycine dipeptidase (GGDP) enzyme activity. This result could be described because piperine shifted the kinetic values (i.e., V_{max} and K_m) of LAP and GGDP enzyme induced modification of enzyme and increased protein turnover number facilitating the INH permeation. It was also suggested that the piperine alliance with the γ -GT enzyme could modify its enzyme kinetics and increase the INH permeation (17). Moreover, the piperine association with the surrounding lipids and hydrophobic part of protein may reduce the stearic lipid restrictions to proteins, modify the enzyme conformations, and thus enhance the INH permeation. It was also suggested that piperine on long-time interaction with

intestinal epithelium could increase the synthesis of cytoskeleton protein (which is mainly responsible for maintaining the shape, stability, and motility of microvilli), microvilli length and absorptive surface area of small intestine enhanced the INH permeation (19). Furthermore, it may be observed that piperine may also decrease the transepithelial electrical resistance caused by an opening of pore size between the cells. Therefore, INH permeation could increase across the intestine (61). The above findings suggest that apart from polymer and cross-linking calcium ions, the piperine bio-enhancer physico-chemical properties could also assist in enhancing the permeability efficiency of INH.

Oral Bioavailability Study

HPLC Method Validation

HPLC analysis demonstrated an excellent linearity and correlation coefficient ($r^2 = 0.991$) per the linearity range. Following an investigation, the limit of detection (LOD) and limit of quantification (LOQ) values were ~ 150 ng/mL and 200 ng/mL, respectively. The intra-day and inter-day precision values were observed as less than 5%. The remaining validation parameters, such as extraction recovery of isoniazid from samples, showed values in between the range of ~ 88–94%, respectively. Finally, stability studies demonstrated no sign of drug degradation suggests better stability.

Pharmacokinetic Analysis

Figure 7 shows the plasma concentration-time profile curve of INH and optimized INH-CaSP Ms formulations, respectively. As seen in the figure, the optimized INH-CaSP Ms elevated the C_{max} , T_{max} , and $t_{1/2}$ value around ~ (47.8 ng/mL, 0.33 min, and 2.21 h) compared to pure INH lower value around ~ (22.3 ng/mL, 0.30 min, and 1.16 h) indicating sustained release characteristics of INH-CaSP Ms. It suggests that the sodium alginate hydration, swelling, and gel diffusion layer formation surrounding the microspheres inhibited the outward transportation of INH caused its sustained release. Thus, the pharmacokinetic value could increase significantly. The additional pharmacokinetic parameters were analyzed via WinNonlin® software (Version 4.1, Certara USA Inc., Princeton, NJ, USA), and their values are shown in Table VII. According to the table, the INH-CaSP Ms showed a lower clearance value around ~ (0.90 min) than a higher value ~ (1.43 min), indicating more retention of formulations in the plasma. This fact attributes to the sustained release property of INH-CaSP Ms formulations.

Additionally, the higher AUC_{0-t} and $AUC_{0-∞}$ values appeared for INH-CaSP Ms around ~ (66.47 and 70.54 ng h mL⁻¹) than pure INH lower value around ~ (41.12 and 45.07 ng h mL⁻¹), indicating INH-CaSP Ms improved the oral bioavailability of INH. It attributed to calcium ion-alginate-piperine bio-enhancer cross-linked coordinate bond interaction phenomenon respectively. It was suggested that building up interaction between polymer and biological membrane through physico-chemical forces could provide strong bio-adhesion and increase INH miscibility and permeation across the membrane. Moreover, the generated cross-linked coordinate bond interaction of calcium ion-alginate-piperine within alginate

matrices could also contribute to the sustained release and enhanced bioavailability of INH. The piperine properties, including modification in membrane lipid dynamics, stimulation of LAP and GGDP enzyme activity, reduce lipid stearic limitation to the proteins and increase in microvilli length and the absorptive surface area of the small intestine via an increase in the synthesis of cytoskeleton protein, could promote the permeability and bioavailability of INH. Earlier studies have shown that N-acetyltransferase 2, CYP3A4, and CYP2E1 enzymes played a crucial role in the INH metabolism. The metabolism resulted in reduced bioavailability and induced hepatotoxicity (62). Moreover, it has been suggested that the piperine inhibits the CYP3A4 and CYP2E1 enzymes that participate in the biotransformation of INH (63, 64). In this study, calcium ion-alginate-piperine cross-linked coordinate bond may alter the kinetic of these enzymes induced modification and increase in protein number of enzymes, leading to reduced metabolism and increased bioavailability of INH. It was also suggested that piperine could interact with the P-gp efflux pump overexpressed in membrane cells caused inhibition of its function. It enhances the intracellular concentration of INH within the biological membrane and improves its oral bioavailability (65). Results conclude that piperine association with calcium ion-alginate complex via cross-linked coordinate bond interaction within alginate microspheres inhibits enzyme activity and P-gp efflux pump functions and subsequently enhances INH oral bioavailability.

CONCLUSIONS

This research work showed a successful formation of INH-CaSP Ms formulations using the modified emulsification method via a cross-linked coordinate bond interaction mechanism. Results of encapsulation efficiency suggested that INH-CaSP Ms significantly enhanced the encapsulation of INH compared to earlier reported literature. Particle size, zeta potential, and SEM analysis indicated that INH-CaSP Ms produced a spherical particle with better physical stability. Thermal and FT-IR studies suggested forming INH-CaSP Ms via the contribution of hydrogen bonding and van der Waals forces between formulation components. Bio-adhesion study suggested that optimized microspheres enhanced the bio-adhesion to the small intestine via ionic interaction phenomenon. Dissolution and permeation studies revealed that optimized INH-CaSP Ms formulations improved the INH-controlled release and permeation pattern compared to pure INH and PM. Pharmacokinetic results suggested significantly improving C_{max} , T_{max} , and AUC parameters of optimized INH-CaSP Ms formulations compared to pure INH. These findings indicate that developed calcium ion-sodium alginate-piperine cross-linked coordinate bond interaction within sodium alginate microspheres could be a promising strategy for enhancing encapsulation efficiency, bio-adhesion potential, controlled release, and pharmacokinetic parameters of INH and other hydrophilic APIs.

ACKNOWLEDGEMENTS

The corresponding author thanks Dr. Ravindra RP, Ph.D. supervisor of School of Pharmacy and Technology Management, SVKM's NMIMS, Shirpur, for providing all the essential facilities to complete this project.

AUTHOR CONTRIBUTIONS

Darshan R Telange: analysis, interpretation of data for the work, drafting of the work, editing. Ravindra R Pandharinath: conceptualization, supervision, visualization, interpretation of the data for the work. Anil M Pethe: design of the work, writing of the original draft, investigation. Shirish P Jain: Analysis, validation, data curation. Prashant L Pingale: design of the work, analysis, interpretation of data for the work, final approval of the version to be published.

FUNDING

The conducted research did not receive any funding from the university and government agencies.

DECLARATIONS

Conflict of Interest The authors declare no conflict of interest.

Ethical Approval The ethics committee is "Institute of Animal Ethical Committee" protocol number "RSCOP/IAEC/2019 - 20 dated August 17 , 2020.

REFERENCES

1. Homayun B, Lin X, Choi HJ. Challenges and recent progress in oral drug delivery systems for biopharmaceuticals. *Pharmaceutics*. 2019;11.
2. Date AA, Justin Hanes LME. Nanoparticles for oral delivery: design, evaluation and state-of-the-art. *J Control Release*. 2016;240:504–26.
3. Taghipour YD, Hajialyani M, Naseri R, Hesari M, Mohammadi P, Stefanucci A, et al. Nanoformulations of natural products for management of metabolic syndrome. *Int J Nanomedicine*. 2019;14:5303–21.
4. Adeola O, Adebisi BRC. No TitleModification of drug delivery to improve antibiotic targeting to the stomach. *Ther Deliv*. 2015;6:741–62.
5. Hüscher J, Dutagaci B, Glaubitz C, Geppert T, Schneider G, Harms M, Müller-Goymann CC, Fink L, Schmidt MU, Setzer C, Zirkel J, Rebmann H, Schubert-Zsilavecz M, Abdel-Tawab M. Structural properties of so-called NSAID-phospholipid-complexes. *Eur J Pharm Sci*. 2011;44:103–16.
6. Wilcox MD, Van Rooij LK, Chater PI, Pereira De Sousa I, Pearson JP. The effect of nanoparticle permeation on the bulk rheological properties of mucus from the small intestine. *Eur J Pharm Biopharm* [Internet] Elsevier BV; 2015;96:484–487. Available from: <https://doi.org/10.1016/j.ejpb.2015.02.029>
7. Fievez V, Plapied L, des Rieux A, Pourcelle V, Freichels H, Wascotte V, et al. Targeting nanoparticles to M cells with non-peptidic ligands for oral vaccination. *Eur J Pharm Biopharm*

- [Internet]. Elsevier B.V.; 2009;73:16–24. Available from: <https://doi.org/10.1016/j.ejpb.2009.04.009>
8. Trevasakis NL, Charman WN, Porter CJH. Lipid-based delivery systems and intestinal lymphatic drug transport: A mechanistic update. *Adv Drug Deliv Rev.* 2008;60:702–16.
 9. Zhang L, Sang Y, Feng J, Li Z, Zhao A. Polysaccharide-based micro/nanocarriers for oral colon-targeted drug delivery. *J Drug Target.* 2016;24:579–89.
 10. Canevari M, Castagliuolo I, Brun P, Cardin M, Schiavon M, Pasut G, Veronese FM. Poly(ethylene glycol)-mesalazine conjugate for colon specific delivery. *Int J Pharm.* 2009;368:171–7.
 11. Boonthekul T, Kong HJ, Mooney DJ. Controlling alginate gel degradation utilizing partial oxidation and bimodal molecular weight distribution. *Biomaterials.* 2005;26:2455–65.
 12. Lee KY, Mooney DJ. Alginate: properties and biomedical applications. *Prog Polym Sci* [Internet]. Elsevier Ltd; 2012;37:106–26. Available from: <https://doi.org/10.1016/j.progpolymsci.2011.06.003>
 13. Tone Ostberg EML, a CG. Calcium alginate matrices for oral multiple unit administration: IV. Release characteristics in different media. *Int J Pharm.* 1994;112:241–8.
 14. Abulateefeh SR, Taha MO. Enhanced drug encapsulation and extended release profiles of calcium–alginate nanoparticles by using tannic acid as a bridging cross-linking agent. *J Microencapsul.* 2015;32:96–105.
 15. Grant GT, Morris ER, Rees DA, Smith PJC, Thom D. Biological interactions between polysaccharides and divalent cations: The egg-box model. *FEBS Lett.* 1973;32:195–8.
 16. Kumar K, Dhawan N, Sharma H, Vaidya S, Vaidya B. Bioadhesive polymers: novel tool for drug delivery. *Artif Cells, Nanomedicine Biotechnol.* 2014;42:274–83.
 17. Johri RK, Thusu N, Khajuria A, Zutshi U. Piperine-mediated changes in the permeability of rat intestinal epithelial cells. *Biochem Pharmacol.* 1992;43:1401–7.
 18. Khajuria A, Zutshi U, Bedi KL. Permeability characteristics of piperine on oral absorption—an active alkaloid from peppers and a bioavailability enhancer. *Indian J Exp Biol.* 1998;36:46–50.
 19. Mark S, Moosekar. Organization, chemistry, and assembly of the cytoskeletal apparatus of the intestinal brush border. *Annu Rev Cell Biol.* 1985;1:209–41.
 20. Santoveña-Estévez A, Suárez-González J, Cáceres-Pérez AR, Ruiz-Noda Z, Machado-Rodríguez S, Echezarreta M, Soriano M, Fariña JB. Stability study of isoniazid and rifampicin oral solutions using hydroxypropyl- β -cyclodextrin to treat tuberculosis in paediatrics. *Pharmaceutics.* 2020;12:1–13.
 21. Vilchêze C, Wang F, Arai M, Hazbón MH, Colangeli R, Kremer L, Weisbrod TR, Alland D, Sacchetti JC, Jacobs WR Jr. Transfer of a point mutation in *Mycobacterium tuberculosis* inhA resolves the target of isoniazid. *Nat Med.* 2006;12:1027–9.
 22. Mdululi K, Slayden RA, Zhu YQ, Ramaswamy S, Pan X, Mead D, *et al.* Inhibition of a *Mycobacterium tuberculosis* β -Ketoacyl ACP synthase by isoniazid. *Science (80-).* 1998;280:1607–10.
 23. Mariappan TT, Singh S. Regional gastrointestinal permeability of rifampicin and isoniazid (alone and their combination) in the rat. *Int J Tuberc Lung Dis.* 2003;7:797–803.
 24. Pandey R, Sharma A, Zahoor A, Sharma S, Khuller GK, Prasad B. Poly (DL-lactide-co-glycolide) nanoparticle-based inhalable sustained drug delivery system for experimental tuberculosis. *J Antimicrob Chemother.* 2003;52:981–6.
 25. Pandey R, Sharma S, Khuller GK. Liposome-based antitubercular drug therapy in a guinea pig model of tuberculosis [1]. *Int J Antimicrob Agents.* 2004;23:414–5.
 26. Dutt M, Khuller GK. Sustained release of isoniazid from a single injectable dose of poly (DL-lactide-co-glycolide) micro-particles as a therapeutic approach towards tuberculosis. *Int J Antimicrob Agents.* 2001;17:115–22.
 27. Zhou H, Zhang Y, Biggs DL, Manning MC, Randolph TW, Christians U, Hybertson BM, Ng KY. Microparticle-based lung delivery of INH decreases INH metabolism and targets alveolar macrophages. *J Control Release.* 2005;107:288–99.
 28. Labana S, Pandey R, Sharma S, Khuller GK. Chemotherapeutic activity against murine tuberculosis of once weekly administered drugs (isoniazid and rifampicin) encapsulated in liposomes. *Int J Antimicrob Agents.* 2002;20:301–4.
 29. Pandey G, Yadav SK, Mishra B. Preparation and characterization of isoniazid and lamivudine co-loaded polymeric microspheres. *Artif Cells, Nanomedicine Biotechnol.* 2016;44:1867–77.
 30. Rastogi R, Sultana Y, Aqil M, Ali A, Kumar S, Chuttani K, *et al.* Alginate microspheres of isoniazid for oral sustained drug delivery. *Int J Pharm.* 2007;334:71–7.
 31. Telange DR, Patil AT, Pethe AM, Fegade H, Anand S, Dave VS. Formulation and characterization of an apigenin-phospholipid phytosome (APLC) for improved solubility, in vivo bioavailability, and antioxidant potential. *Eur J Pharm Sci.* Elsevier B.V.; 2017;108:36–49.
 32. Telange DR, Nirgulkar SB, Umekar MJ, Patil AT, Pethe AM, Bali NR. Enhanced transdermal permeation and anti-inflammatory potential of phospholipids complex-loaded matrix film of umbelliferone: Formulation development, physico-chemical and functional characterization. *Eur J Pharm Sci.* Elsevier B.V.; 2019;131:23–38.
 33. Telange DR, Jain SP, Pethe AM, Kharkar PS, Rarokar NR. Use of combined nanocarrier system based on chitosan nanoparticles and phospholipids complex for improved delivery of ferulic acid. *Int J Biol Macromol* [Internet]. Elsevier B.V.; 2021;171:288–307. Available from: <https://doi.org/10.1016/j.ijbiomac.2020.12.211>
 34. Telange DR, Jain SP, Pethe AM, Kharkar PS. Egg white protein carrier-assisted development of solid dispersion for improved aqueous solubility and permeability of poorly water soluble hydrochlorothiazide. *AAPS PharmSciTech AAPS PharmSciTech.* 2021;22:1–15.
 35. Telange DR, Ukey SA, Hemke AT, Umekar MJ, Pethe AM, Kharkar PS. LIPOID SPC-3-based coprecipitates for the enhancement of aqueous solubility and permeability of Ranolazine. *J Pharm Innov. Journal of Pharmaceutical Innovation;* 2020
 36. Telange DR, Sohail NK, Hemke AT, Kharkar PS, Pethe AM. Phospholipid complex-loaded self-assembled phytosomal soft nanoparticles: evidence of enhanced solubility, dissolution rate, ex vivo permeability, oral bioavailability, and antioxidant potential of mangiferin. *Drug Deliv Transl Res.* 2021;11:1056–83.
 37. Rao KVR, Buri P. A novel in situ method to test polymers and coated microparticles for bioadhesion. *Int J Pharm.* 1989;52:265–70.
 38. Dinarvand R, Rahmani E, Farbod E. Gelatin microspheres for the controlled release of all-trans-retinoic acid topical formulation and drug delivery evaluation. *Iran J Pharm Res.* 2010;2:47–50.
 39. Phutane P, Shidhaye S, Lotlikar V, Ghule A, Sutar S, Kadam V. In vitro evaluation of novel sustained release microspheres of glipizide prepared by the emulsion solvent diffusion-evaporation method. *J Young Pharm.* 2010;2:35–41.
 40. Bagre AP, Jain K, Jain NK. Alginate coated chitosan core shell nanoparticles for oral delivery of enoxaparin: in vitro and in vivo assessment. *Int J Pharm.* 2013;456:31–40.
 41. Bhandari R. A sensitive HPLC method for determination of isoniazid in rat plasma, brain, liver and kidney. *J Chromatogr Sep Tech.* 2012;03.
 42. Lemoine D, Wauters F, S. Bouchend’homme VP. Preparation and characterization of alginate microspheres containing a model antigen. *Int J Pharm.* 1998;176:9–19.
 43. Samer R. Abulateefeh1 and Mutasem O. Taha. Enhanced drug encapsulation and extended release profiles of calcium–alginate nanoparticles by using tannic acid as a bridging cross-linking agent. *J Microencapsul.* 2014;2–11.
 44. Rajinikanth PS, Sankar C, Mishra B. Sodium alginate microspheres of metoprolol tartrate for intranasal systemic delivery: Development and evaluation. *Drug Deliv J Deliv Target Ther Agents.* 2003;10:21–8.
 45. Uyen NTT, Hamid ZAA, Nurazreena A. Fabrication and characterization of alginate microspheres. *Mater Today Proc* [Internet]. Elsevier Ltd.; 2019;17:792–7. Available from: <https://doi.org/10.1016/j.matpr.2019.06.364>
 46. Khatri S, Awasthi R. Piperine containing floating microspheres: an approach for drug targeting to the upper gastrointestinal tract. *Drug Deliv Transl Res.* 2016;6:299–307.
 47. Chun KH, Kwon IC, Kim YH, La SB, Sohn YT, Jeong SY. Preparation of sodium alginate microspheres containing hydrophilic β -lactam antibiotics. *Arch Pharm Res.* 1996;19:106–11.

48. Sibum I, Hagedoorn P, Frijlink HW, Grasmeyer F. Characterization and formulation of isoniazid for high-dose dry powder inhalation. *Pharmaceutics*. 2019;11.
49. Salisu A, Sanagi MM, Abu Naim A, Abd Karim KJ, Wan Ibrahim WA, Abdulganiyu U. Alginate graft polyacrylonitrile beads for the removal of lead from aqueous solutions. *Polym Bull. Springer. Berlin Heidelberg*. 2016;73:519–37.
50. Mandal S, Senthil Kumar S, Krishnamoorthy B, Basu SK. Development and evaluation of calcium alginate beads prepared by sequential and simultaneous methods. *Brazilian J Pharm Sci*. 2010;46:785–93.
51. Rajaonarivony M, Vauthier C, Couarraze G, Puisieux F, Couvreur P. Development of a new drug carrier made from alginate. *J Pharm Sci*. 1993;82:912–7.
52. Chong-Kook K (Seoul NU), Eun-Jin L (Seoul NU). The controlled release of blue dextran from alginate beads. *Int J Pharm*. 1992;79:11–9.
53. EL-Kamel AH, O.M.N. AL-Gohary EAH. Alginate diltiazem hydrochloride beads: optimization of formulation factors, in vitro and in vivo availability. *J Microencapsul* 2003;20, 799, 810.
54. Costa P, Manuel J. Lobô S. Modeling and comparison of dissolution profiles [Internet]. *Eur J Pharm Sci*. 2001; Available from: www.elsevier.nl/locate/ejps.
55. Cárdenas PA, Kratz JM, Hernández A, Costa GM, Ospina LF, Baena Y, Simões CMO, Jimenez-Kairuz Á, Aragon M. In vitro intestinal permeability studies, pharmacokinetics and tissue distribution of 6-methylcoumarin after oral and intraperitoneal administration in Wistar rats. *Brazilian J Pharm Sci*. 2017;53.
56. Johnson JJ, Nihal M, Siddiqui IA, Scarlett CO, Bailey HH, Mukhtar H, Ahmad N. Enhancing the bioavailability of resveratrol by combining it with piperine. *Mol Nutr Food Res*. 2011;55:1169–76.
57. Jin MJ, Han HK. Effect of piperine, a major component of black pepper, on the intestinal absorption of fexofenadine and its implication on food-drug interaction. *J Food Sci*. 2010;75:H93–6.
58. Shaikh J, Ankola DD, Beniwal V, Singh D, Kumar MNVR. Nanoparticle encapsulation improves oral bioavailability of curcumin by at least 9-fold when compared to curcumin administered with piperine as absorption enhancer. *Eur J Pharm Sci*. 2009;37:223–30.
59. Smita Pattanaik, Debasish Hota, Sudesh Prabhakar PK and, Pandhi P. Effect of Piperine on the steady-state pharmacokinetics of phenytoin in patients with epilepsy. *Phyther Res* 2006;20:683–686
60. Khajuria A, Thusu N, Zutshi U. Piperine modulates permeability characteristics of intestine by inducing alterations in membrane dynamics: influence on brush border membrane fluidity, ultrastructure and enzyme kinetics. *Phytomedicine*. 2002;9:224–31.
61. Singh A, Pawar VK, Jakhmola V, Parabia MH, Awasthi R, Sharma G. In - vivo assessment of enhanced bioavailability of metronidazole with piperine in rabbits. *Res J Pharm, Biol Chem Sci*. 2010;1:273–8.
62. Wang P, Pradhan K, Zhong X bo, Ma X. Isoniazid metabolism and hepatotoxicity. *Acta Pharm Sin B* [Internet]. Elsevier; 2016;6:384–92. Available from: <https://doi.org/10.1016/j.apsb.2016.07.014>
63. DB M, S S, KR M. Role of piperine as an effective bioenhancer in drug absorption. *Pharm Anal Acta* 2018;09:7–10.
64. Ajazuddin, Alexander A, Qureshi A, Kumari L, Vaishnav P, Sharma M, *et al*. Role of herbal bioactives as a potential bioavailability enhancer for Active Pharmaceutical Ingredients. *Fitoterapia* [Internet]. Elsevier B.V.; 2014;97:1–14. Available from: <https://doi.org/10.1016/j.fitote.2014.05.005>
65. Gollapudi S, Reddy M, Gangadharam P, Takashi Tsuruo SG. Mycobacterium tuberculosis induces expression of P-glycoprotein in promonocytic U1 cells chronically infected with HIV type 1. *Biochem Biophys Res Commun*. 1994;199:1181–7.

Publisher's Note Springer Nature remains neutral with regard to jurisdictional claims in published maps and institutional affiliations.

RESEARCH ARTICLE

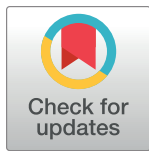
Biallelic variants in *TRAPPC10* cause a microcephalic TRAPPopathy disorder in humans and mice

Lettie E. Rawlins^{1,2}, Hashem Almousa³, Shazia Khan^{1,4}, Stephan C. Collins^{5,6}, Miroslav P. Milev³, Joseph Leslie¹, Djenann Saint-Dic³, Valeed Khan⁷, Ana Maria Hincapie³, Jacob O. Day^{1,8}, Lucy McGavin⁹, Christine Rowley¹⁰, Gaurav V. Harlalka^{1,11}, Valerie E. Vancollie¹⁰, Wasim Ahmad¹², Christopher J. Lelliott¹⁰, Asma Gul⁴, Binnaz Yalcin^{5,6}, Andrew H. Crosby¹, Michael Sacher^{3,13}, Emma L. Baple^{1,2}*

1 RILD Wellcome Wolfson Medical Research Centre, RD&E (Wonford) NHS Foundation Trust, University of Exeter Medical School, Exeter, United Kingdom, **2** Peninsula Clinical Genetics Service, Royal Devon & Exeter Hospital (Heavitree), Exeter, United Kingdom, **3** Department of Biology, Concordia University, Montreal, Quebec, Canada, **4** Department of Biological Sciences, International Islamic University, Islamabad, Pakistan, **5** Institute of Genetics and Molecular and Cellular Biology, Inserm, Illkirch, France, **6** Inserm, University of Bourgogne Franche-Comté, Dijon, France, **7** Department of Molecular Diagnostics, Rehman Medical Institute, Peshawar, Pakistan, **8** Faculty of Health, University of Plymouth, Plymouth, United Kingdom, **9** University Hospitals Plymouth NHS Trust, Plymouth, United Kingdom, **10** Wellcome Sanger Institute, Hinxton, Cambridge, United Kingdom, **11** Department of Pharmacology, Rajarshi Shahu College of Pharmacy, Malvihi, Buldana, India, **12** Department of Biochemistry, Faculty of Biological Sciences, Quaid-i-Azam University, Islamabad, Pakistan, **13** Department of Anatomy and Cell Biology, McGill University, Montreal, Quebec, Canada

* These authors contributed equally to this work.

* E.Baple@exeter.ac.uk



OPEN ACCESS

Citation: Rawlins LE, Almousa H, Khan S, Collins SC, Milev MP, Leslie J, et al. (2022) Biallelic variants in *TRAPPC10* cause a microcephalic TRAPPopathy disorder in humans and mice. *PLoS Genet* 18(3): e1010114. <https://doi.org/10.1371/journal.pgen.1010114>

Editor: Gregory S. Barsh, HudsonAlpha Institute for Biotechnology, UNITED STATES

Received: September 26, 2021

Accepted: February 20, 2022

Published: March 17, 2022

Copyright: © 2022 Rawlins et al. This is an open access article distributed under the terms of the [Creative Commons Attribution License](https://creativecommons.org/licenses/by/4.0/), which permits unrestricted use, distribution, and reproduction in any medium, provided the original author and source are credited.

Data Availability Statement: All relevant data are within the manuscript and its [Supporting Information](#) files.

Funding: The authors are grateful for funding support provided by Wellcome Trust (209083/Z/17/Z to ELB) <https://wellcome.org/grant-funding>, the Newlife Foundation for Disabled Children (AHC, LER and ELB) <https://newlifecharity.co.uk/>, Mitacs Globalink research award (IT14910 to LER) <https://www.mitacs.ca/en/programs/globalink> and Higher Education Commission (HEC), Pakistan (IRSIP I-8/

Abstract

The highly evolutionarily conserved transport protein particle (TRAPP) complexes (TRAPP II and III) perform fundamental roles in subcellular trafficking pathways. Here we identified biallelic variants in *TRAPPC10*, a component of the TRAPP II complex, in individuals with a severe microcephalic neurodevelopmental disorder. Molecular studies revealed a weakened interaction between mutant *TRAPPC10* and its putative adaptor protein *TRAPPC2L*. Studies of patient lymphoblastoid cells revealed an absence of *TRAPPC10* alongside a concomitant absence of *TRAPPC9*, another key TRAPP II complex component associated with a clinically overlapping neurodevelopmental disorder. The *TRAPPC9/10* reduction phenotype was recapitulated in *TRAPPC10*^{-/-} knockout cells, which also displayed a membrane trafficking defect. Notably, both the reduction in *TRAPPC9* levels and the trafficking defect in these cells could be rescued by wild type but not mutant *TRAPPC10* gene constructs. Moreover, studies of *Trappc10*^{-/-} knockout mice revealed neuroanatomical brain defects and microcephaly, paralleling findings seen in the human condition as well as in a *Trappc9*^{-/-} mouse model. Together these studies confirm autosomal recessive *TRAPPC10* variants as a cause of human disease and define TRAPP-mediated pathomolecular outcomes of importance to *TRAPPC9* and *TRAPPC10* mediated neurodevelopmental disorders in humans and mice.

HEC/HRD/2017/6914 to SK) <https://www.hec.gov.pk/english/pages/home.aspx>. Functional studies were supported by the Canadian Institutes of Health Research (to MS) <https://cihr-irsc.gc.ca/e/193.html> and the Natural Sciences and Engineering Research Council of Canada (to MS) https://www.nserc-crsng.gc.ca/index_eng.asp. The mouse neuroanatomical studies were supported by The French National Research Agency (ANR-18-CE12-0009 JGJC to BY) <https://anr.fr/en/anrs-role-in-research/missions/>. This work was also supported by Wellcome Trust grant WT098051 (to BY) <https://wellcome.org/grant-funding>. The funders had no role in study design, data collection and analysis, decision to publish, or preparation of the manuscript.

Competing interests: The authors have declared that no competing interests exist.

Author summary

Microcephalic neurodevelopmental disorders are a group of conditions that are often inherited in families, involving small head size and abnormal brain development and function. This often results in delayed development of an affected child, affecting their movement, language and/or non-verbal communication and learning, as well as seizures and neuropsychiatric problems. A group of proteins called the transport protein particles (TRAPPs) are important for the transport of cargos inside cells. Alterations within a number of the TRAPP proteins have previously been associated with human inherited diseases called the ‘TRAPPopathies’, which involve neurodevelopmental and skeletal abnormalities. Here we show that *TRAPPC10* gene alterations cause a new TRAPPopathy microcephalic neurodevelopmental disorder, and we provide a detailed clinical description of the condition termed ‘*TRAPPC10*-related disorder’. Our studies in mice lacking the *TRAPPC10* gene identified similar features to those of affected humans, including small brain size and skeletal abnormalities. Our molecular studies showed that an affected individual with an alteration in the *TRAPPC10* gene has no functional TRAPPC10 protein in their cells, which in turn causes a reduction in levels of another important TRAPP molecule, TRAPPC9. Cells lacking TRAPPC10 also display abnormalities in cellular transport processes. Together our data confirm alterations in *TRAPPC10* as a cause of a microcephalic neurodevelopmental disorder in both humans and mice.

Introduction

The transport protein particles (TRAPPs) comprise highly evolutionarily conserved multiprotein complexes, originally identified in yeast. Three yeast TRAPP complexes have been described (TRAPP I, II and III) which play important roles in secretory and endocytic subcellular trafficking pathways [1,2]. Humans possess only two complexes (TRAPP II and III), both sharing the same core proteins alongside additional complex-specific components, some not identified in yeast. Previous studies have identified diverse cellular roles for the TRAPP II complex including Golgi, COP (coat protein)-I vesicular, lipid droplet, centrosomal and ciliary functions [3–5]. The TRAPP II complex contains two complex-specific subunits; TRAPPC9 and TRAPPC10 [6]. An additional TRAPP II complex-associated protein has recently been described (TRAPPC14/C7orf43) [7]. However, TRAPPC14 does not appear to be required for TRAPP II complex-associated guanine nucleotide exchange factor activity [8,9] and lack of the molecule does not affect TRAPP II complex assembly or stability [7]. Thus, further studies are required to clarify the role of TRAPPC14 in TRAPP II. TRAPPC9 has been implicated in COP II vesicle trafficking [10] and NF- κ B signalling pathway activation [11], with TRAPPC9 depletion associated with increased lipid droplet formation [4]. TRAPPC14 plays a role in Rabin 8 binding to the TRAPP II complex and its tethering of preciliary vesicles to the mother centriole during ciliogenesis [7]. No detailed studies of TRAPPC10 function have been conducted, although it has been shown to interact with TRAPPC2L and may have roles in guanine nucleotide exchange factor (GEF) activity regulation [12].

Ten of the 15 TRAPP complex proteins have been associated with human inherited diseases, collectively termed “TRAPPopathies” [6]. This includes TRAPPC2, the only subunit associated with skeletal dysplasia (spondyloepiphyseal dysplasia tarda (SEDT); OMIM #313400) [13], and nine other TRAPP subunits (TRAPPC2L, TRAPPC4, TRAPPC6A, TRAPPC6B, TRAPPC9, TRAPPC10, TRAPPC11, TRAPPC12 and TRAPPC14) associated

with neurodevelopmental disorders [12,14–24]. While diverse, the clinical features of these disorders are overlapping and include neurodevelopmental delay, intellectual disability, developmental regression, primary and postnatal-onset microcephaly, epilepsy, hypotonia, craniofacial dysmorphism and structural brain abnormalities including thinning of the corpus callosum and reduced white matter volume (S1 Table).

Of the TRAPP II complex specific subunits, only TRAPPC9 has been robustly associated with human disease, an autosomal recessive neurodevelopmental disorder (OMIM #613192) characterized by postnatal-onset microcephaly with reduced white matter volume and corpus callosum thinning, intellectual disability, dysmorphic features, hypotonia, epilepsy, and raised body mass index [18–20]. TRAPP II plays important roles in Golgi membrane trafficking. “Golgipathy” neurodevelopmental disorders including the TRAPPopathies comprise an expansive group of conditions associated with variants in Rab GTPases, conserved oligomeric Golgi (COG) complex, and coat protein (COP) complex proteins among others [25,26] and are characterized by primary or postnatal-onset microcephaly, intellectual disability, seizures and white matter brain abnormalities.

Here, we present comprehensive genetic, clinical, functional and mouse data to define biallelic *TRAPPC10* gene variants as a cause of a microcephalic neurodevelopmental disorder, providing important insight into the TRAPPopathy family of disorders.

Results

Biallelic *TRAPPC10* variants are associated with a microcephalic neurodevelopmental disorder

Table 1 summarizes the clinical features of affected individuals in this study. Family 1 comprises a large interlinking multi-nuclear Pakistani family, with eight individuals (4.1–18.1 years) affected by a severe microcephalic neurodevelopmental disorder (Fig 1A, Family 1). All but one individual presented with microcephaly (>3 standard deviations (SDS) below mean), and all displayed short stature (-1.78 to -5.09 SDS). All eight were born at full term, prenatal histories were unremarkable, although antenatal ultrasound scans were not performed. The parents did not report that any affected infant’s head was noticeably small (no weight or occipitofrontal circumference (OFC) measurements were recorded). The earliest OFC measurement documented was at 2.5 years (1-IV:4), and at age 4.1 years his microcephaly had not worsened. Affected individuals displayed mild craniofacial dysmorphism (S1A–S1C Fig). Although standardized intelligence quotient (IQ) testing was not possible due to cultural and language barriers, all affected individuals were assessed as severely intellectually impaired (DSM-5 criteria). Developmental trajectories were similar in all, as was the degree of impairment across all developmental domains. Hypotonia in infancy was universal and walking was delayed to between 2.5–4 years. All affected individuals have speech impairment, five have only a few words and three are non-verbal. Behavioural abnormalities including autistic features and aggressive episodes were a consistent feature. A history of seizures from early infancy was reported in four individuals, one has ongoing generalised tonic-clonic seizures (1-IV:2) and the remaining three (1-IV:3, 1-IV:7, 1-IV:13) are seizure free on medication. Neuroimaging was only performed for one case (1-IV:2) due to the remote family location and as sedation/general anaesthesia was deemed necessary. This revealed microcephaly with corpus callosum thinning and no other abnormalities (Fig 1B and 1C). All had normal systemic examination findings and no evidence of gross skeletal disproportion (S1A Fig). It was only possible to obtain skeletal radiographs for a single individual (1-IV:12) aged 9 years, these were unremarkable but unfortunately spinal imaging was incomplete.

Table 1. A comparison of clinical features of affected individuals with biallelic variants in TRAPPC10.

FAMILY	FAMILY 1							FAMILY 2		
	IV:2	IV:3	IV:4	IV:7	IV:8	IV:10	IV:12	IV:13	IV:1	IV:2
Pedigree reference										
Genotype	p.(G1131Vfs*19)/ p.(G1131Vfs*19)	p.(G1131Vfs*19)/ p.(G1131Vfs*19)	p.(G1131Vfs*19)/ p.(G1131Vfs*19)	p.(G1131Vfs*19)/ p.(G1131Vfs*19)	p.(G1131Vfs*19)/ p.(G1131Vfs*19)	p.(G1131Vfs*19)/ p.(G1131Vfs*19)	p.(G1131Vfs*19)/ p.(G1131Vfs*19)	p.(G1131Vfs*19)/ p.(G1131Vfs*19)	p.(P929L)/ p.(P929L)	p.(P929L)/ p.(P929L)
Gender	M	M	M	F	F	F	M	M	M	M
Age at evaluation (years)	18.1	13.8	4.1	14.1	15.6	5.5	9.0	13.7	25	22
GROWTH										
Birth weight kg (SDS)	NK	NK	2.5 (-2.25)	NK	NK	NK	NK	NK	NK	NK
OFC cm (SDS)	55 (-1.32)	50 (-3.49)	47 (-3.59)	46 (-6.64)	49 (-4.56)	43 (-7.46)	43 (-7.05)	47 (-5.28)	50 (-4.24)	53 (-2.49)
Height cm (SDS)	164 (-1.87)	146 (-1.78)	94 (-2.23)	127 (-5.09)	142 (-3.41)	99 (-2.78)	119 (-2.48)	125 (-4.26)	150 (-3.92)	140 (-5.29)
Weight kg (SDS)	52 (-1.96)	40 (-0.99)	18 (0.6)	25 (-4.9)	45 (-1.39)	16 (-1.44)	20 (-2.77)	28 (-3.16)	45 (-3.9)	38 (-4.87)
BMI	19.3	18.7	20.4	15.5	22.3	16.3	14.1	17.9	20	19
DEVELOPMENT										
Intellectual disability	Severe	Severe	Severe	Severe	Severe	Severe	Severe	Severe	Severe	Severe
Global developmental delay	✓	✓	✓	✓	✓	✓	✓	✓	✓	✓
Speech impairment	<10 words	Non-verbal	<10 words	Non-verbal	<10 words	Non-verbal	<10 words	<10 words	✓	✓
Walked (years)	4	4	Standing	3.5	2.5	4	4	3	NK	NK
Hearing	No concerns	Otitis media	No concerns	No concerns	No concerns	No concerns	No concerns	No concerns	No concerns	No concerns
Vision	No concerns	No concerns	No concerns	No concerns	No concerns	No concerns	Strabismus	No concerns	Strabismus	Strabismus
NEUROLOGY										
Childhood hypotonia	✓	✓	✓	✓	✓	✓	✓	✓	NK	NK
Seizures	✓	✓	-	✓	-	-	-	✓	-	-
Gait abnormalities	-	Waddling gait	-	-	-	-	Waddling gait	Waddling gait	NK	NK
Behavioural abnormalities	✓	✓	✓	✓	✓	✓	✓	✓	✓	✓

Abbreviations: M, male; F, female; NK, not known; SDS, standard deviation score; OFC, occipitofrontal circumference; G, glycine; V, valine; fs, frameshift; (✓), indicates presence of a feature in an affected individual; (-), indicates absence of a feature in an affected individual. Height, weight and OFC Z-scores were calculated using a Microsoft Excel add-in to access growth references based on the LMS method^a using UK 1990 reference population^b

^a Pan H, Cole TJ. LMS growth, a Microsoft Excel add-in to access growth references based on the LMS method. Version 2.77, <http://www.healthforalchildren.co.uk/2012>

^b Cole TJ, Freeman JV, Preece MA: British 1990 growth reference centiles for weight, height, body mass index and head circumference fitted by maximum penalized likelihood. Stat Med. 1998, 17 (4):407–4.

<https://doi.org/10.1371/journal.pgen.1010114.t001>

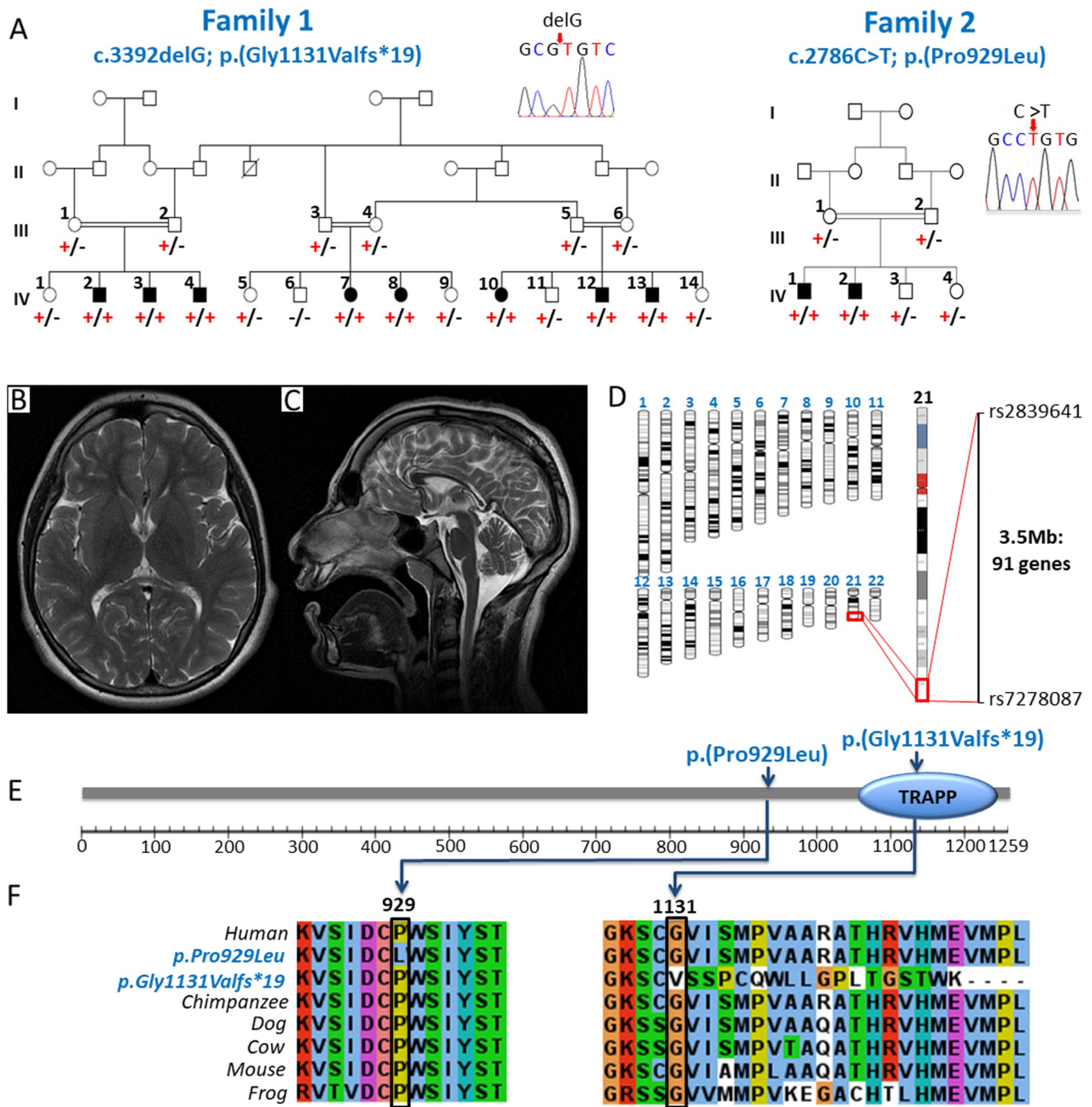


Fig 1. Biallelic TRAPPC10 variants identified in two families with individuals affected by a microcephalic neurodevelopmental disorder. (A) Family 1 Extended pedigree comprising three interlinking families and a total of eight affected individuals all of whom are homozygous for the TRAPPC10 c.3392delG; p.(Gly1131Valfs*19) variant (+), with co-segregation confirmed in other family members (- indicates the wild type allele). **Inset:** Dideoxy sequence chromatogram of an affected individual homozygous for the TRAPPC10 c.3392delG; p.(Gly1131Valfs*19) variant. **Family 2** Previously reported family (MR107) [27] showing co-segregation of the TRAPPC10 c.2786C>T; p.(Pro929Leu) variant (+) in a four generation pedigree (- indicates the wild type allele). **Inset:** Dideoxy sequence chromatogram of an affected individual homozygous for the TRAPPC10 c.2786C>T; p.(Pro929Leu) variant. (B, C) MRI neuroimaging of individual IV:2 from family 1 demonstrates microcephaly and profound thinning of the corpus callosum with no other abnormalities. (D) Genome-wide SNP mapping in seven affected individuals (1-IV:2-4, 1-IV:7-8 and 1-IV:12-13) identified a single (3.5Mb) region of shared homozygosity, containing 91 genes including TRAPPC10. (E) Schematic diagram of the TRAPPC10 protein identifying TRAPPC10 sequence variants and TRAPP domain. (F) Multi-species alignment showing conservation of the molecular region encompassing the p.Gly1131Valfs*19 and p.Pro929Leu variants.

<https://doi.org/10.1371/journal.pgen.1010114.g001>

Assuming homozygosity for a founder variant was responsible, we undertook SNP genotyping (1-IV:2–4, 1-IV:7–8, 1-IV:12–13) in parallel with exome sequencing (1-IV:2) to identify the cause of disease. SNP mapping identified a single notable (>1Mb) homozygous region common to all affected individuals (3.5Mb, rs2839641-rs7278087; chr21:g.43,179,611–46,678,912 [hg38]) as the likely disease locus (Fig 1D). Concomitant exome sequencing data analysis to identify candidate homozygous and compound heterozygous rare (<0.01 frequency) variants predicted to have a functional impact, identified a single candidate variant within this region which could not be excluded. This frameshift variant (chr21:g.44102823del; NM_003274.4:c.3392del; p.(Gly1131Valfs*19)[hg38]; Fig 1A) in the penultimate (22/23) exon of *TRAPPC10* located in the chromosome 21q22.12 region, is present within the C-terminal TRAPP domain (Fig 1E) and is predicted to result in nonsense mediated mRNA decay of the mutant transcript (Fig 1F). The variant was confirmed in the lymphocyte RNA of an affected individual (S2 Fig), is not listed in publicly available genomic databases (including gnomAD v2.1.1/v3.1.1) and co-segregates appropriately (Fig 1A).

This finding enabled us to revisit the genetic data and more comprehensively phenotype two siblings in an unrelated Pakistani family (Fig 1A, Family 2) included in a larger study to identify novel candidate neurodevelopmental disease genes ([27] Family MR107). Both male siblings (2-IV:1, 22 years and 2-IV:2, 25 years), were described to have “severe intellectual disability, aggressive behaviour and poor speech”. A homozygous exon 18 *TRAPPC10* variant (chr21:g.44089849C>T; NM_003274.4:c.2786C>T; p.(Pro929Leu) [hg38]) (Fig 1A) was identified as a potential cause of disease [27]. This variant, which co-segregated appropriately, is absent from gnomAD v2.1.1/v3.1.1. Multiple species alignment confirms stringent conservation of Pro929 across vertebrates (Fig 1F). Additional clinical features noted and not previously reported, included microcephaly/borderline microcephaly (-2.49 SDS, -4.2 SDS), short stature (-3.86, -5.29 SDS) and mild dysmorphism, all consistent with Family 1.

TRAPPC10 variants exhibit reduced interaction with TRAPPC2L, destabilize the TRAPP II complex and result in an anterograde trafficking defect

We next sought to determine the molecular consequences of each *TRAPPC10* genetic variant. As we previously determined that TRAPPC10 interacts with TRAPPC2L in the TRAPP II complex [12], we used yeast two-hybrid assays to investigate how TRAPPC10 alteration affects TRAPPC2L interactions. When TRAPPC10 was in the bait (pGBKT7) or prey (pGADT7) vector, TRAPPC2L interaction was observed (Fig 2A and 2B). However, both p.Gly1131Valfs*19 and p.Pro929Leu variants showed reduced TRAPPC2L interaction (Fig 2A and 2B), though the proteins were expressed in the yeast cells (not shown). This was confirmed quantitatively by measuring β -galactosidase activity (Fig 2C), one of the yeast two-hybrid system markers. Given this, we generated a patient lymphoblastoid cell line (LCL) (1-IV:2; *TRAPPC10* p.(Gly1131Valfs*19)) to investigate TRAPP complex outcomes. We examined core TRAPP protein (TRAPPC2, TRAPPC2L, TRAPPC3) levels, as well as TRAPP III-specific (TRAPPC8, TRAPPC12), and TRAPP II-specific (TRAPPC10, TRAPPC9) levels. TRAPPC2L, TRAPPC2 and TRAPPC3 levels were slightly reduced in the p.(Gly1131Valfs*19) lysate compared to control (Fig 2D). As expected we did not detect TRAPPC10 as the commercially available TRAPPC10 antibody is directed to the molecular region downstream (C-terminal) to the p.(Gly1131Valfs*19) alteration. Intriguingly we also noted an absence of full length TRAPPC9, although in contrast, TRAPP III-specific proteins levels were not affected. We then fractionated p.(Gly1131Valfs*19) and control LCL lysates on a size exclusion column. While TRAPPC10 and TRAPPC9 fractionated as expected in controls, they were absent from p.

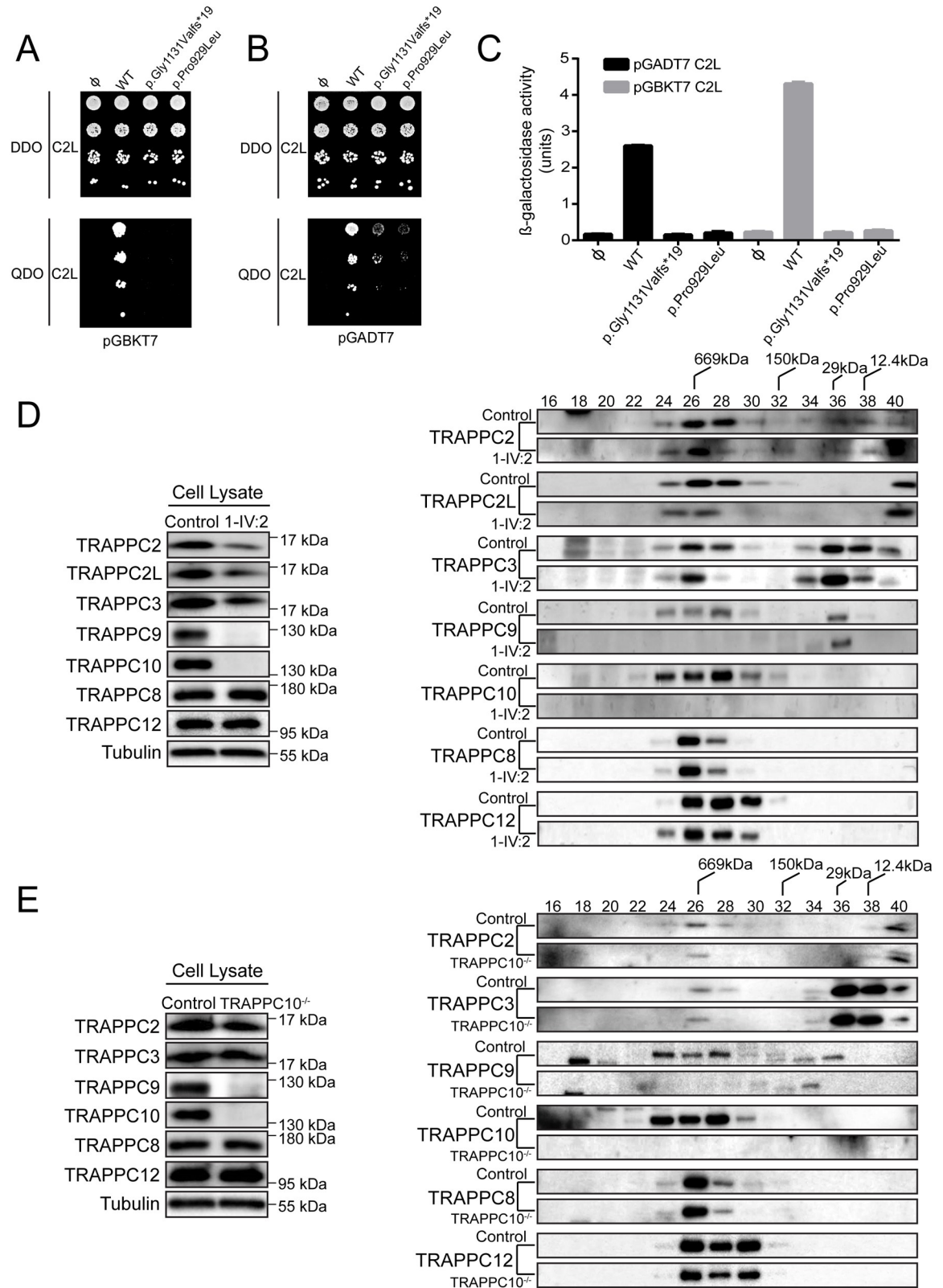


Fig 2. TRAPP II complex integrity is affected by TRAPPC10 variants and in TRAPPC10^{-/-} cells. Yeast cells transformed with pGBKT7 or pGADT7 expressing either wild type TRAPPC10, the p.Gly1131Valfs*19 variant or the p.Pro929Leu variant (A), or pGADT7 or pGADT7

expressing either wild type TRAPPC10, the p.Gly1131Valfs*19 variant or the p.Pro929Leu variant (B) were mated with yeast expressing either pGBKT7-TRAPPC2L (A) or pGADT7-TRAPPC2L (B). Serial dilutions of the diploid cells were grown on SC medium lacking leucine and tryptophan (DDO) or SC medium lacking leucine, tryptophan, histidine and adenine (QDO). (C) Diploid cells from (A) and (B) were quantitatively tested for β -galactosidase activity. Units of activity were calculated according to the following formula: $(OD_{420} \times 1000)/(OD_{600} \times \text{time in hours})$. Note that western analysis revealed that all forms of TRAPPC10 and the two variants were expressed in the yeast cells. (D) Lymphoblastoid cells from control or an individual homozygous for the TRAPPC10 p.(Gly1131Valfs*19) variant were lysed and probed for the TRAPP proteins indicated and for tubulin as a representative loading control. The lysates were fractionated on a Superose 6 size exclusion column. Fractions of 0.5ml were collected. Neighbouring fractions were pooled and fractionated by SDS-PAGE and probed for the indicated TRAPP proteins. (E) Wild type HEK293 or TRAPPC10^{-/-} cells were lysed and probed for the TRAPP proteins indicated and for tubulin as a representative loading control. The lysates were fractionated on a Superose 6 size exclusion column. Fractions of 0.5ml were collected. Neighbouring fractions were pooled and fractionated by SDS-PAGE and probed for the indicated TRAPP proteins. The fractionation of molecular size standards are indicated above the top-most panel of the size exclusion portion of (D) and (E).

<https://doi.org/10.1371/journal.pgen.1010114.g002>

(Gly1131Valfs*19) lysate (Fig 2D) indicating an absence of TRAPP II (peak in fraction 28 of control cells). There was no change in core protein (TRAPPC2, TRAPPC2L, TRAPPC3) fractionation consistent with their presence in TRAPP III, although the portion that co-fractionates with TRAPP II was reduced. Similarly, no change in TRAPP III proteins (TRAPPC8, TRAPPC12) fractionation was seen, indicating that this complex was not affected in p.(Gly1131Valfs*19) cells.

We then examined the consequences of TRAPPC10 loss on membrane trafficking. Since we were unable to perform trafficking assays in smaller LCLs, we generated HEK293 TRAPPC10 knockout cell lines using CRISPR/Cas9. Three different TRAPPC10 knockout lines were generated (S3 Fig), two were examined and behaved identically (TRAPPC10^{-/-} KO1/KO7); as such we present data from one line (KO7, hereafter referred to as TRAPPC10^{-/-}). We first examined TRAPP protein levels in TRAPPC10^{-/-} cells. Consistent with observations in LCLs, we noted a slight reduction in core TRAPP proteins, no effect on TRAPP III-specific proteins (TRAPPC8, TRAPPC12), and the absence of TRAPPC9, consistent with size exclusion chromatography results (Fig 2E). We then performed the VSVG-GFP ts045 trafficking assay [28] in TRAPPC10^{-/-} cells. In this assay, the marker protein VSVG-GFP ts045 is retained in the ER at elevated temperature, but synchronously released at 32°C. The fluorescently-tagged marker protein accumulated in the Golgi region in controls, with peak signal at ~25 minutes (Fig 3A, black curve). From that point onward the signal was cleared from the Golgi as the protein travelled to the plasma membrane. In contrast, the arrival into, trafficking through and release from the Golgi of the marker protein in TRAPPC10^{-/-} cells was delayed compared to controls (Fig 3A, green curve). Importantly, the trafficking delay was shown to be TRAPPC10-dependent as cell transfection with wild type (WT) TRAPPC10 resulted in a trafficking defect rescue (Fig 3A, blue curve). Although both p.Gly1131Valfs*19 and p.Pro929Leu variants were able to partially rescue these defects, neither rescued anterograde trafficking to the same extent as WT protein (Fig 3A, red/grey curves). Taken together, these results demonstrate that the TRAPPC10 variants cause partial functional defects, and that the absence of TRAPPC10 results in a concomitant absence of TRAPPC9.

Expression of TRAPPC10 is important for the detection of a cellular pool of TRAPPC9

As no antibody was available to determine whether mutant TRAPPC10 p.(Gly1131Valfs*19) polypeptide may be expressed in affected individuals, we generated WT and both (p.Gly1131Valfs*19, p.Pro929Leu) constructs to investigate protein stability. The constructs were transfected into HEK293 cells and lysates prepared daily for four days. As shown in Fig 3B, WT protein levels on day 4 dropped to ~70% of that on day 1. In contrast, levels of both altered TRAPPC10 proteins (day 4) dropped to 25–50% (day 1), with the drop in the p.

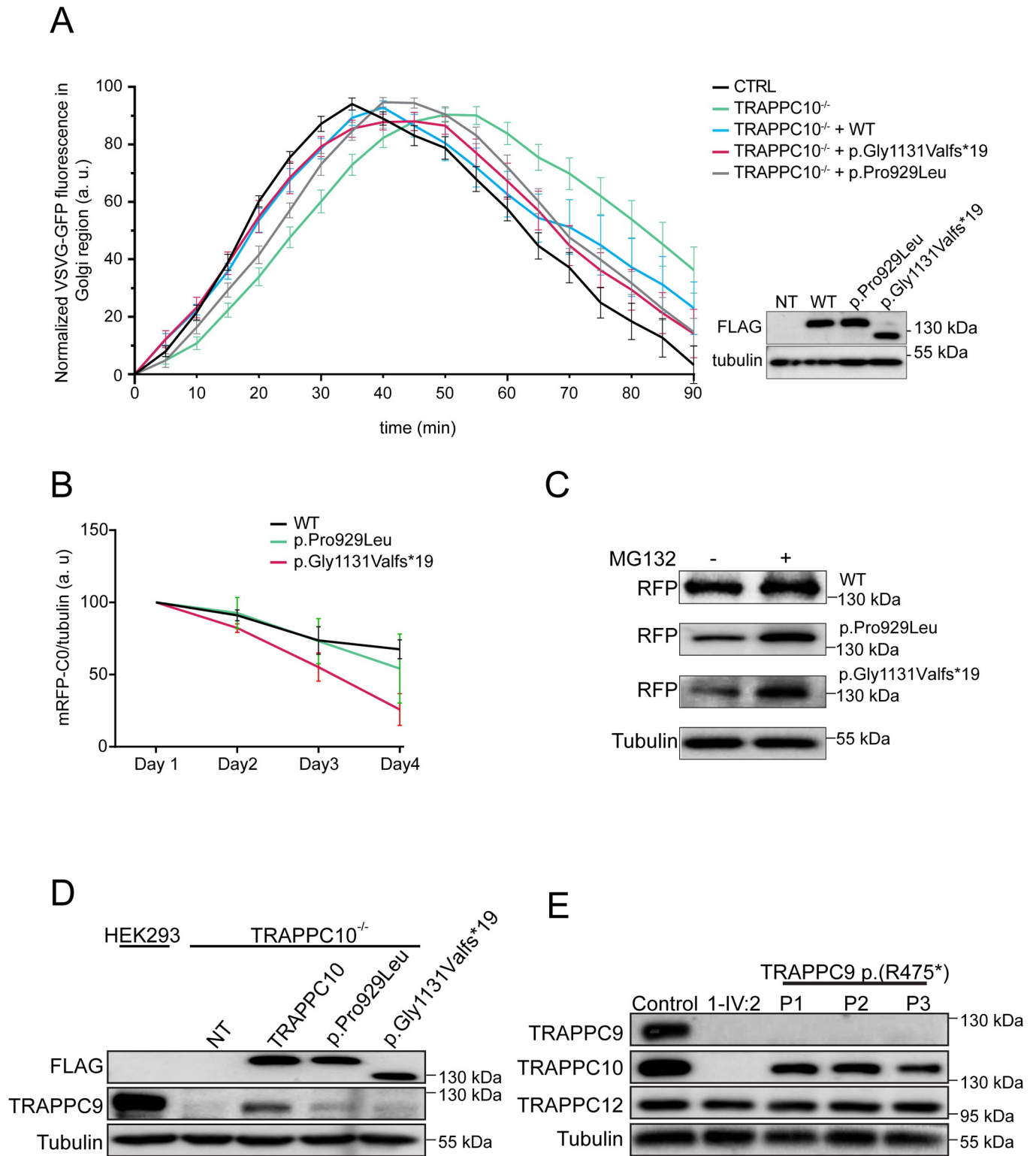


Fig 3. Cells devoid of TRAPPC10 display a membrane trafficking defect and lack detectable levels of TRAPPC9. (A) Wild type HEK293 cells or TRAPPC10^{-/-} cells either not transfected or transfected with FLAG-tagged wild type TRAPPC10 or one of the TRAPPC10 variants indicated were infected with VSVG-GFP ts045

4 hours after transfection. After an overnight incubation at 40°C, the cells were shifted to 32°C and imaged every minute. The fluorescence intensity in the Golgi was quantified and plotted versus time as described in the Materials and Methods section. The inset shows a western blot for the transfected proteins probed with anti-FLAG antibody. Representative images are shown in S7 Fig. (B) RFP-tagged versions of either wild type TRAPPC10, the p.Gly1131Valfs*19 variant or the p.Pro929Leu variant were transfected into HeLa cells and lysates prepared every day for 4 days. The lysates were fractionated by SDS-PAGE and probed with anti-mCherry antibody to reveal the RFP-tagged construct. Though the trends were consistent, statistical significance was seen only at day 4. The half-life for each overexpressed protein was found to be approximately 5.4 days, 4.4 days and 3.1 days for the wild type, p.Gly1131Valfs*19 and p.Pro929Leu variants, respectively. (C) RFP-tagged TRAPPC10 and the p.Gly1131Valfs*19 and p.Pro929Leu variants were transfected into HEK293 cells. The cells were either untreated (-) or treated (+) with 50 μM MG132 for 24 hours on the third day post-transfection. Lysates were then prepared, fractionated by SDS-PAGE and probed with anti-mCherry and tubulin as a loading control. (D) TRAPPC10^{-/-} cells were either untransfected or transfected with FLAG-tagged wild type TRAPPC10, the p.Gly1131Valfs*19 variant or the p.Pro929Leu variant. After 24 hours, lysates were prepared and probed for the FLAG constructs to verify expression, TRAPPC9 and tubulin as a loading control. Parental HEK293 cells were also probed to assess the level of TRAPPC9 in the presence of TRAPPC10. (E) Lysates were prepared from lymphoblastoid cells from either control, an individual homozygous for the TRAPPC10 p.Gly1131Valfs*19 variant or three individuals homozygous for the TRAPPC9 p.(Arg475*) variant and subjected to western analysis to reveal the proteins indicated.

<https://doi.org/10.1371/journal.pgen.1010114.g003>

Gly1131Valfs*19 protein being most dramatic. The decrease in expression of WT and both p.Gly1131Valfs*19 and p.Pro929Leu TRAPPC10 proteins was blocked by inclusion of proteasome inhibitor MG132 (Fig 3C). These results suggest that the two mutant proteins are subject to enhanced degradation compared to WT protein.

The absence of TRAPPC9 in TRAPPC10 p.(Gly1131Valfs*19) LCLs prompted us to closely examine the inter-relationship between TRAPPC9 and TRAPPC10. We first investigated whether TRAPPC10 expression in TRAPPC10^{-/-} cells would restore TRAPPC9 levels. Upon transfection of WT TRAPPC10 into TRAPPC10^{-/-} cells, the appearance of TRAPPC9 was noted, although not to parental HEK293 cell levels (Fig 3D). Overexpression of the p.Pro929Leu variant, and to a much lesser degree p.Gly1131Valfs*19, restored some TRAPPC9 protein although again not to the same extent as WT TRAPPC10.

We next investigated whether a reciprocal absence of TRAPPC10 occurred in cells devoid of TRAPPC9. We probed LCL lysates from three individuals with the p.(Arg475*) TRAPPC9 variant [19]. As expected TRAPPC9 was not detected in these cells (Fig 3E), nor was it detected in TRAPPC10 p.(Gly1131Valfs*19) cells (as shown above). Importantly, while TRAPPC10 levels were significantly reduced in p.(Arg475*) TRAPPC9 lysates, the protein was nevertheless present. Collectively, these results suggest that the detection of a cellular pool of TRAPPC9 is strongly dependent upon the expression of full length TRAPPC10.

***Trappc10*^{-/-} mice have similar neurodevelopmental deficits to patients with biallelic TRAPPC10 variants**

We then evaluated tissue sections and datasets from a *Trappc10*^{tm1b(EUCOMM)Wtsi} mouse model, with a focus on the phenotypical components of the human disorder in particular neuroanatomical findings. At weaning age, mouse survival was evaluated from successfully genotyped mice originating from multiple litters derived from a heterozygous-by-heterozygous breeding scheme. We obtained the expected number of WT, heterozygous and homozygous mice. Male and female mice were weighed the same day each week from 4 until 16 weeks of age (S4 Fig).

Using a recently developed robust approach to assess 63 brain parameters across 23 brain regions [29], we analyzed neuroanatomical defects in adult *Trappc10*^{-/-} mice blinded for genotype. To minimize environmental and genetic variation, male mice aged 16 weeks were used. In the homozygous mutant mice, many neuroanatomical parameters were reduced in size when compared to WTs (Fig 4A and 4B). The total brain area parameter was significantly reduced (14%, $P = 0.0003$), concomitantly with smaller white matter structure size including the genu of the corpus callosum (-25%, $P = 0.026$), hippocampal commissure (-38%, $P = 0.013$), hippocampal fimbria (-17%, $P = 0.0049$), anterior commissure (-28%, $P = 3.8E10^{-8}$)

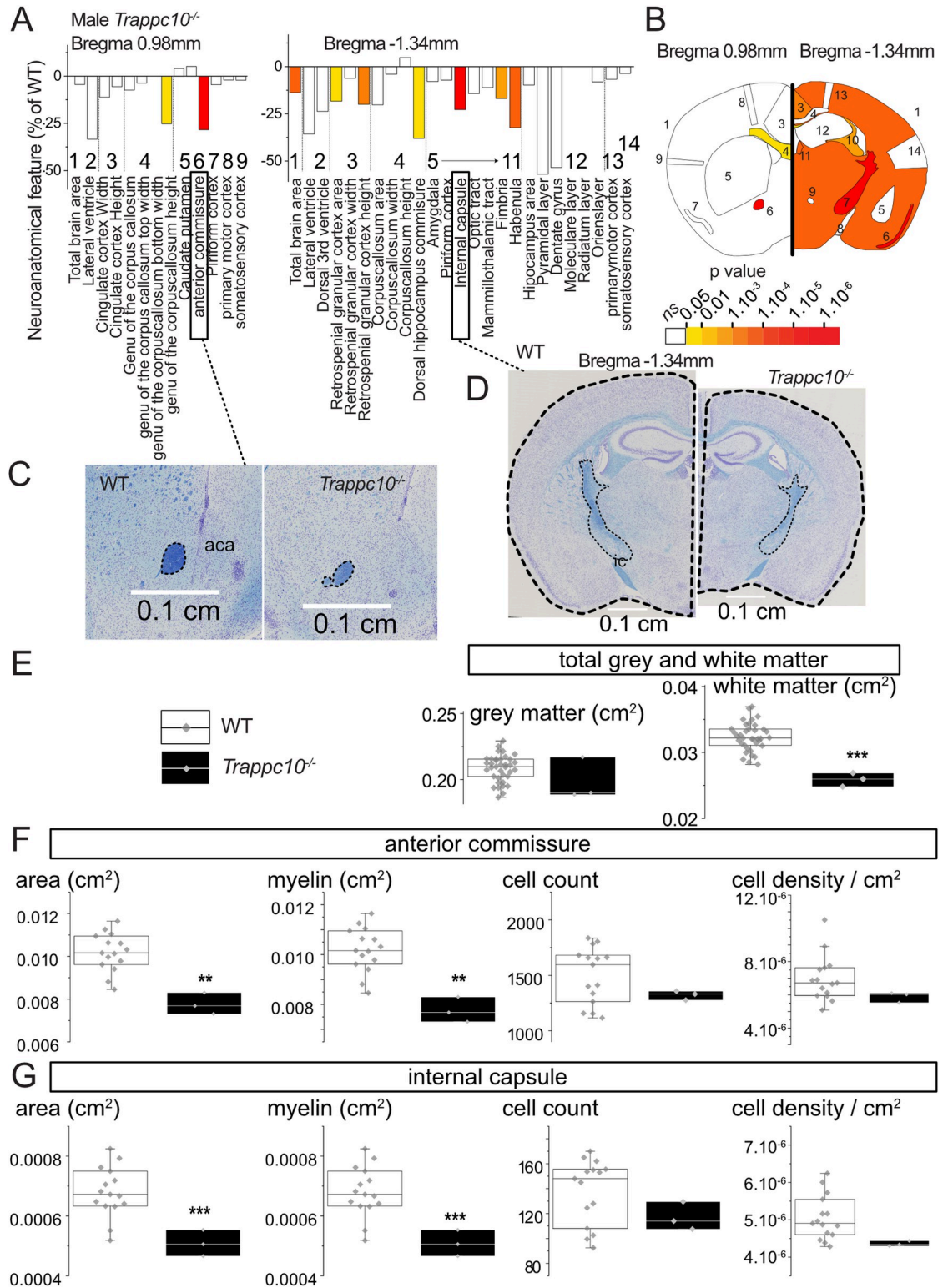


Fig 4. Mouse studies implicate TRAPPC10 in the formation of white matter structures. (A) Histograms for three homozygous *Trappc10*^{-/-} mice showing variation (decreased-minus scale or increased-positive scale) in areas and lengths expressed as percentage of 498 WT mice together with a color map indicating the significance level (white indicates not significant). The list of measurements and corresponding numbers are shown below the histograms. (B) Schematic representation of a section at Bregma +0.98 mm and Bregma -1.34 mm. Colored regions indicate the presence of at least one significant parameter within the brain region at the 0.05

level. (C-D) Nissl-stained sagittal brain sections from *Trappc10^{tm1b/tm1b}* mice, showing the anterior commissure (C) and the total brain area and internal capsule size reduction in mutants (D). The corresponding scale is shown in each panel. (E) Box plots of combined grey and white matter structures expressed in cm² using a set of 37 local WTs (same genetic background, housing conditions, age, sex, experimental and necropsy dates) compared to three *Trappc10^{tm1b/tm1b}* mice. (F-G) Box plots with raw data points detailing the cellular and myelination characterisation of the anterior commissure (F) and internal capsule (G) using a set of 15 local WTs. Statistical analyses were performed with GraphPad Prism 8.0.2, using two-tailed Student's *t*-tests of equal variances. **p*<0.05 ***p*<0.01 ****p*<0.001.

<https://doi.org/10.1371/journal.pgen.1010114.g004>

and the internal capsule (-23%, $P = 1.1E10^{-6}$) (Fig 4C and 4D). When combining neuroanatomical parameters from either grey or white matter structures, only white matter structures were reduced in size (-20%, $P = 8E10^{-6}$) (Fig 4E). Interestingly, the size reductions of the anterior commissure and internal capsule were correlated with loss of myelination whilst oligodendrocyte cell population count and density were unaffected (Fig 4F and 4G). Together these findings suggest that both mouse and human microcephaly stems from defects in white matter structures and myelin biogenesis.

Given the short stature exhibited by patients with TRAPPC10-related disorder we also evaluated *Trappc10^{-/-}* mice growth parameters (S1 Text). While long bone length was marginally reduced in both sexes, it only reached significance for female *Humerus* (S4A Fig), although body length overall was unaffected (S4B Fig). While weight was unaffected in *Trappc10^{-/-}* males, female *Trappc10^{-/-}* mice were overweight, showing a rapid weight increase commencing week 10 (S4C Fig). We investigated the cause of the female obesity phenotype and noted a highly significant fat mass increase ($P = 9E-08$; S4D Fig), alongside a blood cholesterol increase ($P = 4E-05$) and high-density lipoprotein levels ($P = 0.003$) (S4E Fig).

We finally sought to further characterize the phenotypical relationship between *Trappc10^{-/-}* mice, and a previously published *Trappc9^{-/-}* mouse model [30]. Due to the unavailability of live *Trappc9^{-/-}* animals, these evaluations were limited to assessments undertaken on historical brain tissue sections. Overall, the impact of TRAPPC10 loss on brain anatomy was more severe than TRAPPC9 loss (S5 Fig). While there were some overlaps between affected brain regions (e.g. corpus callosum reduced size), some neuroanatomical phenotypes were specific to *Trappc10^{-/-}* including reduced size of the anterior commissure.

Discussion

Here, we define biallelic TRAPPC10 variants as a cause of a neurodevelopmental TRAPPopathy disorder, with core clinical features including microcephaly, severe global developmental delay and intellectual disability, short stature and pervasive behavioural abnormalities (Table 1). Additional variable features include hypotonia, gait abnormalities and seizures. The overlapping phenotypical nature of the TRAPPopathies suggests a common pathomolecular basis of disease involving disruption of TRAPP II/III complex functions. The clinical features of TRAPPC10-related disorder also show extensive overlap with many other Golgipathy disorders [25,26] indicative of a common disease mechanism relating to disrupted Golgi trafficking processes. We observed notable phenotypic overlap with *Trappc10^{-/-}* mice which display microcephaly, reduced size of white matter brain structures with hypomyelination and skeletal involvement. Brain abnormalities in mice appear to be more severe than those in humans, in which neuroimaging identified profound thinning of the corpus callosum but no other white matter abnormalities or hypomyelination. However as neuroimaging was only available on a single affected individual who appears to display the least severe phenotype of those assessed, it is possible that more extensive abnormalities may be present in other affected individuals who display a greater degree of microcephaly.

Our genetic studies in combination with our functional investigations on both *TRAPPC10*^{-/-} and patient-derived cells indicate that TRAPPC10 loss of function likely underlies the clinical phenotype. Previous subcellular trafficking studies of TRAPPC10 depleted COS-7 [3] and HEK293 [4] cells determined that TRAPPC10 mediates early Golgi (although not endoplasmic reticulum) trafficking, revealing disrupted Golgi architecture and vesicular accumulation indicative of an anterograde trafficking defect. Our cell model membrane trafficking assays are in complete alignment with such a TRAPPC10 molecular role, defining delayed Golgi trafficking associated with gene KO which importantly could be rescued, though not completely, by WT, and to a lesser extent by mutant TRAPPC10. These findings may in part be explained by differing outcomes of the *TRAPPC10* variants, including the possibility that the protein C-terminus plays a specific though as yet unknown post-Golgi secretory pathway role. Interestingly, in previous studies the yeast homologue of TRAPPC10 (Trs130) was rendered conditionally lethal by short truncations in the C-terminal portion of the protein, indicative of a critical functional role of this region [1]. The observed trafficking defects herein may be explained by the loss of GEF activity of TRAPP II towards Rab1 [3], Rab11 [9] and/or Rab18 [4], which alongside other Rab GTPases are key regulators of cellular trafficking by recruiting specific effector proteins to membranes, including lipid droplet homeostasis. Rab18 has specifically been implicated in secretory pathway regulation [31], and *RAB18* variants are associated with a neurodevelopmental disorder phenotypically overlapping *TRAPPC10*-related disorder. Although the specific molecular role of TRAPPC10 in neurological development and function remains unclear, it is tempting to speculate that the predominantly neurological phenotype seen in individuals affected by *TRAPPC10*-related disorder may be due to the relatively high rates of membrane trafficking shown to be required in the brain for processes such as synapse remodeling [32,33].

An important outcome of our findings was that absence of TRAPPC10 is also associated with a concomitant absence of TRAPPC9. Additionally, although other TRAPP III and core specific components were detected, levels of core TRAPPC2L were reduced suggesting an absence of TRAPP II complex, with no effect on TRAPP III complex. These findings indicate that TRAPPC10 is crucial to TRAPP II complex stability and function. Consistent with our findings, careful examination of the data in Li et al (2017) [4], though not commented on, reveals a decrease in the levels of TRAPPC9 protein in *TRAPPC10*^{-/-} HEK293 cells (see Fig 6D in Ref 4). However, our studies showed TRAPPC10 was still detectable in LCLs lacking TRAPPC9 p.(Arg475*), suggesting that TRAPPC9 may only incorporate into TRAPP II in the presence of TRAPPC10, while the reciprocal is not true. Our overexpression studies of mutant TRAPPC10 provide further insight into this, and in particular identify the expression of full length TRAPPC10 to be of importance for the detection of TRAPPC9 within the TRAPP II complex. Collectively, our results suggest that the absence of the TRAPPC10 C-terminus results in TRAPPC10 protein degradation, and consequent loss of TRAPPC9 (through protein degradation or some other mechanism), leading to the absence of TRAPP II.

The concomitant loss of TRAPPC9 associated with pathogenic *TRAPPC10* variants is reflected in the close phenotypical parity of human *TRAPPC9*- (OMIM 613192) and *TRAPPC10*-related conditions (S1 Table) and with both knockout mouse models. Individuals with *TRAPPC9*-related disorder have postnatal-onset microcephaly [34,35]. While the families reported here did not have any recorded birth OFC measurements, there were no reports of affected children having noticeably small head size at birth suggesting microcephaly associated with *TRAPPC10*-related disorder may be postnatal. Head growth trajectory was only available for one child, with two measurements available (2.5 and 4.1 years), that indicate microcephaly is present from early childhood and is not progressive. However it remains unclear whether the brain growth was initially normal and then slowed, or whether microcephaly was present

from/before birth. Identification of further affected families will help clarify the nature of the microcephaly in *TRAPPC10*-related disorder, as with *TRAPPC9*-related disorder where this was also unclear initially [19].

Biallelic *TRAPPC10* loss of function appears to have a more severe phenotypic impact in mice and humans, compared with biallelic *TRAPPC9* loss. In human *TRAPPC10*-related disorder, microcephaly appears to be a relatively consistent feature, (8/10 individuals), as compared to ~60% of *TRAPPC9* patients [20,36]. Similarly in mouse models, while the age of onset and progression of microcephaly is unclear, *Trappc10*^{-/-} mice display more extensive brain size reduction and loss of white matter structures than *Trappc9*^{-/-} mice. These findings may be explained by the concomitant loss of *TRAPPC9* observed with *TRAPPC10* absence, possibly acting as a double knockout. Obesity is reported in ~50% of individuals with *TRAPPC9*-related disorder and is the only clinical feature not currently observed in individuals with *TRAPPC10*-related disorder. It is important to note that these differences are based on a relatively small sample size, a limitation of this study. Nevertheless, the *Trappc10*^{-/-} mice share similar phenotypic outcomes compared to individuals with biallelic *TRAPPC10* variants.

Neuroanatomical studies of *Trappc9*^{-/-} mice showed overlapping features with *Trappc10*^{-/-} mice including reduced brain size predominantly of white matter structures (S5 Fig) [37], although findings of enlarged striatal size were not identified in *Trappc10*^{-/-} mice. *TRAPPC9* plays a role in the NF- κ B signalling pathway through its interaction with NF- κ B inducing kinase (NIK) and the beta subunit of IKK, which both regulate the NF- κ B pathway [11,38]. Given the associated loss of *TRAPPC9* observed with both the *TRAPPC10* variants and *TRAPPC10*^{-/-} cells, it is plausible that *TRAPPC10* loss of function may also impact NF- κ B signalling pathways through disruption of *TRAPPC9*, although the involvement of *TRAPPC9* in this pathway in brain has been recently questioned [37]. Taken together, we define the genetic, clinical and molecular basis of a novel microcephalic neurodevelopmental disorder associated with biallelic *TRAPPC10* variants in both humans and mice. Our data provides a molecular rationale for the phenotypic overlap between *TRAPPC10*- and *TRAPPC9*-related TRAPPopathy disorders, both involving disruption of TRAPP II-mediated post-Golgi trafficking processes.

Material and methods

Ethics statement

This study was carried out in accordance with institutional ethics review board-approved research protocols from the Institutional Review Board, International Islamic University (IIU), Islamabad, Pakistan. All individuals (or their families) whose data is included in this study provided written informed consent and where applicable specific written consent for publication of photographs.

Genetic studies

Genomic DNA was extracted from blood/buccal samples using the ReliaPrep kit (Blood gDNA Miniprep System, Promega) and RNA was extracted using the PAXgene blood miRNA kit and converted to cDNA via reverse transcriptase PCR. Single nucleotide polymorphism (SNP) genotyping was performed using Illumina HumanCytoSNP-12 v2.1 beadchip array, as previously described [39]. WES analysis was performed (NextSeq500; Illumina, San Diego, CA, USA) and involved Agilent Sureselect Whole Exome v6 (Agilent Technologies, Santa Clara, CA) targeting, read alignment (BWA-MEM v0.7.17), mate-pairs fixed and duplicates removed (Picard v2.15), InDel realignment and base quality recalibration (GATK v3.7.0), single nucleotide variant and InDel detection (GATK HaplotypeCaller), variant annotation

(Alamut batch v1.10 and SnpEff (http://snpeff.sourceforge.net/SnpEff_manual.html)) and read depth assessment (GATK DepthOfCoverage). Copy number variants (CNVs) were detected using SavvyCNV [40]. Variants with <5 reads and/or an allele frequency >0.01 in public genome databases including the Genome Aggregation Database (gnomAD v2.1.1 and v3.1) and the 1000 Genomes Project were excluded. Homozygous and compound heterozygous variants that were exonic and non-synonymous, synonymous with predicted splicing impact or intronic at ± 6 nucleotides from splice site were evaluated and cross referenced against the SNP data. Dideoxy sequencing validation of *TRAPPC10* variants was undertaken using standard techniques.

Molecular studies

Construction of *TRAPPC10*^{-/-} cell lines. Guide RNA (gRNA) design and cloning (CRISPR plasmid pSPCas9(BB)-2A-Puro (PX459) V2.0, Addgene #62988) was performed as described previously [41], with primers: 5'-CACCGCATCTTCGGAGCCCGGCCAT-3' and 5'-AAACATGGCCGGGCTCCGAAGATGC-3'. HEK293 cells were transfected (70% confluency) using JetPRIME with 500ng DNA expressing the gRNA. Following selection (puromycin) and colony expansion, genomic DNA was extracted. The *TRAPPC10* gene region of interest was amplified using oligonucleotide pair: 5'-AGCGTAGTTATGATTTGGGGT-3 and 5'-GCCAAGGAATGAAGGGACAA-3. The resulting PCR product (~540bp, agarose gel electrophoresis) was sequenced. Knockout verification was performed by western analysis (S3 Fig).

Membrane trafficking assay. Cells were infected with virus expressing VSVG-GFP-tsO45 (one hour, 37°C). In rescue experiments, cells were transfected with either FLAG-TRAPPC10, FLAG-TRAPPC10 p.Gly1131Valfs*19 or FLAG-TRAPPC10 p.Pro929Leu constructs, then infected with VSVG-GFP tsO45 (one hour, 37°C). Cells were maintained at 40°C overnight. Cycloheximide was added (final concentration, 10µg/ml), prior to shifting cells to 32°C. Time-lapse microscopy started three minutes after temperature shift to allow time to select fluorescent cells (Nikon inverted confocal microscope) as previously described [22]. Movies used for quantitative fluorescence analysis were not subjected to processing. Integrated fluorescence intensity at the Golgi region (defined by the region of perinuclear intensity seen 20–40 minutes after temperature shift) and from whole cell was measured using ImageJ (measurements obtained every 5 minutes). The ratio between fluorescent intensities within the Golgi region and whole cell was generated for each time point. The kinetics of VSVG-GFP-tsO45 trafficking represent change in that ratio over time (0 to 90 min).

Cell lysis and size exclusion chromatography. Cells were grown in either DMEM (for HEK293) or RPMI 1640 (for lymphoblastoid cells) medium containing 10% fetal bovine serum (FBS). Cells were lysed in a solution containing 50mM Tris pH 7.2, 150 mM NaCl, 0.5 mM EDTA, 1 mM DTT, 1% Triton X-100 and protease inhibitor cocktail (EDTA-free; Roche). A total of 2–5 mg of protein was fractionated on a Superose 6 Increase 10/300 GL column at a flow rate of 0.4 ml/min. Fractions of 0.5 ml were collected in wash buffer (50 mM Tris pH 7.2, 150 mM NaCl, 0.5 mM EDTA, 1 mM DTT, 0.1% Triton X-100) and probed with the indicated antibodies.

Yeast two hybrid assay. Open reading frames (ORFs) encoding TRAPP proteins were cloned (pGADT7 and pGBKT7 vectors; Clontech). Plasmids were transformed into yeast cells (AH109, Y187). Diploids containing the respective TRAPP ORFs were produced by mating and selecting on synthetic complete medium (SC) lacking leucine and tryptophan. Interactions were assessed on SC medium lacking leucine, tryptophan, histidine and adenine. Serial cell dilutions were spotted onto solid medium. Quantification of interaction was assessed using a β -galactosidase assay employing ONPG and normalized to total protein.

Molecular biology techniques and reagents. Standard molecular biological techniques were used to generate FLAG-tagged constructs and the stated *TRAPPC10* variants. Commercially available antibodies used in this study were: anti-TRAPPC2 (rabbit polyclonal, homemade), anti-TRAPPC2L (mouse monoclonal, Santa Cruz sc-377322), anti-TRAPPC3 (rabbit polyclonal, homemade), anti-TRAPPC8 (rabbit polyclonal, Abcam ab122692), anti-TRAPPC9 (rabbit polyclonal, LS Bio LS-C750497), anti-TRAPPC10 (mouse monoclonal, Santa Cruz sc-101259), anti-TRAPPC12 (rabbit polyclonal, homemade), anti-FLAG (mouse monoclonal, Sigma F1804), anti- α -Tubulin (mouse monoclonal, Sigma T6199).

***Trappc10* knockout mouse model**

The mouse model was generated by homologous recombination in embryonic stem cells using the Knockout-first allele method [42], adopting a strategy identifying an exon common to all transcripts (exon 14), upstream of which a LacZ cassette was inserted (S6 Fig). Exon 14 of the *Trappc10* allele, flanked by *loxP* sequences bilaterally, was deleted using a Cre recombinase that recognizes *loxP* sites, producing the *Trappc10*^{tm^b(EUCOMM)Wtsi} knockout allele. Mice were phenotyped by the Mouse Genetics Project (MGP) pipeline at the Wellcome Sanger Institute, UK (S1 Text).

Mouse neuroanatomical studies

The use of mice in the Wellcome Sanger Institute study was carried out in accordance with UK Home Office regulations (license number 80/2076), UK Animals (Scientific Procedures) Act of 1986. Neuroanatomical studies were carried out using three homozygous *Trappc10*^{-/-} and 498 baseline WT mice on a C57BL/6N pure genetic background at 16-weeks of age as previously described [29,43]. We used a recognized statistical model (Gpower) validated for comparison of modest numbers ($n = 3$) of animals to evaluate neuroanatomical defects with an effect size of 10% or more with 80% detection power [43]. Paraffin embedded brain samples were cut at 5 μ m thickness (sliding microtome, Leica RM 2145) to obtain coronal brain region at Bregma +0.98 mm and Bregma -1.34 mm according to the Allen Mouse Brain Atlas [44]. Sections were stained with 0.1% Luxol Fast Blue (Solvent Blue 38; Sigma-Aldrich) and 0.1% Cresyl violet acetate (Sigma-Aldrich) and scanned (Nanozoomer 2.0HT, C9600 series) at 20 \times resolution. Sixty-three brain parameters made up of area and length measurements as well as cell level features, were taken across the two coronal sections (S1 Text). Co-variables, for example sample processing dates and usernames, were collected at every step of the procedure and used to identify data drifts. Using in-house ImageJ plugins, an image analysis pipeline was used to standardize measurements of areas and lengths. Images were quality controlled for the accuracy of sectioning relative to the reference atlas and controlled for asymmetries and histological artefacts. All samples were also systematically assessed for cellular ectopia (misplaced neurons). Data were analyzed using a linear mixed model framework to determine whether a brain region is associated with neuroanatomical defect or not.

Supporting information

S1 Text. Supplementary Material and Methods.
(DOCX)

S1 Table. Clinical features associated with TRAPPopathy disorders. Abbreviations: TRAPP; transport protein particles. XLR; X-linked recessive, AR; autosomal recessive, BMI; body mass index, CK; creatine kinase.
(DOCX)

S1 Fig. Clinical features of individuals with biallelic TRAPPC10 variants. (A) Individual 1-IV:2 (Family 1) with no evidence of skeletal disproportion. (A-C) Show the facial features of two affected individuals from Family 1 displaying mild craniofacial dysmorphism comprising microcephaly, synophrys and upslanting palpebral fissures. (TIFF)

S2 Fig. Chromatogram of TRAPPC10 c.3392del rtPCR product. Confirmation of the outcome of the c.3392del; p.(Gly1131Valfs*19) TRAPPC10 gene variant on the RNA transcript in blood of an affected individual (individual IV:2, Family 1), demonstrating that this frameshift variant results in a premature stop codon 19 codons downstream. (TIFF)

S3 Fig. Characterization of the TRAPPC10^{-/-} cell lines in HEK293 cells. Lysate was prepared from parental HEK293 cells and from 3 clones (KO1, KO3 and KO7) that were treated with sgRNA targeting TRAPPC10. The lysates were fractionated by SDS-PAGE and probed for TRAPPC10. Tubulin was included as a loading control. (TIFF)

S4 Fig. Whole-body phenotype analysis of Trappc10^{-/-} knockout mouse. (A) Bone length for long bones (Femur and Humerus) in both sexes (n = 7 for all groups) (B) Body length for male Trappc10^{-/-} (n = 7) and WT (n = 41) and females Trappc10^{-/-} (n = 7) and WT (n = 27). (C) Body weight curves in grams of male and female Trappc10^{-/-} mice, between 4 and 16 weeks of age. (D) Fat body composition in grams of male and female Trappc10^{-/-} mice at 16 weeks of age. (E) *Left*: List of 27 assessed clinical blood chemistry parameters and association in female Trappc10^{-/-} mice at 16 weeks of age. *Right*: Box plots with raw data points showing results for levels of total cholesterol and high-density lipoprotein (HDL) in millimoles per liter in female Trappc10^{-/-} mice at 16 weeks of age. Statistical analyses were performed with GraphPad Prism 8.0.2, using two-tailed Student's *t*-tests of equal variances. **p*<0.05 ***p*<0.01 ****p*<0.001. Arrows indicate directionality of effect and "ns" indicates not significant (p-value>0.05). (TIFF)

S5 Fig. Neuroanatomical assessment of Trappc9 knockout mouse. (A) Histograms of percentage change relative to Trappc9^{+/+} (set as 0) for each of the measured parameters. (B) Schematic representation of the 22 brain regions quantified at lateral +0.60 mm on sagittal section from Trappc9^{+/+} (n = 4) and Trappc9^{-/-} (n = 4) mice. Colored regions indicate the presence of at least one significant parameter within the brain region at the 0.05 level. White indicates a p-value > 0.05, grey shows not enough data to calculate a p-value. (C) List of assessed brain parameters. (TIFF)

S6 Fig. Allelic construction showing targeting of critical exon 14 in the Trappc10^{tm1b} (EUCOMM)Wtsi mouse. (TIFF)

S7 Fig. Representative images for VSV-G trafficking at 0, 20, 40 and 90 minutes. Wild type HEK293 cells or TRAPPC10^{-/-} cells either not transfected or transfected with FLAG-tagged wild type TRAPPC10 or one of the TRAPPC10 variants indicated were infected with VSVG-GFP ts045 4 hours after transfection. After an overnight incubation at 40°C, the cells were shifted to 32°C and imaged every minute. Representative images at 0, 20, 40 and 90 minutes are shown. (TIFF)

Acknowledgments

First and foremost, the authors would like to thank the patients and their family members for their participation in this study. We thank members of the Sanger Institute Mouse Pipelines teams and the Research Support Facility for the provision and management of the *Trappc10*^{-/-} and *Trappc9*^{-/-} mice. We thank Dorinda Wright for the histological work. We are grateful to Dr. John Vincent (Centre for Addiction & Mental Health, Toronto, Canada) for providing the TRAPPC9 p.(Arg475*) LCLs. We would like to thank Professor Christine Hall for reviewing the skeletal radiographs.

Author Contributions

Conceptualization: Andrew H. Crosby, Michael Sacher, Emma L. Baple.

Data curation: Lettie E. Rawlins, Hashem Almousa, Shazia Khan, Stephan C. Collins.

Formal analysis: Lettie E. Rawlins, Hashem Almousa, Shazia Khan, Stephan C. Collins.

Funding acquisition: Lettie E. Rawlins, Binnaz Yalcin, Andrew H. Crosby, Michael Sacher, Emma L. Baple.

Investigation: Lettie E. Rawlins, Hashem Almousa, Shazia Khan, Stephan C. Collins, Miroslav P. Milev, Joseph Leslie, Djenann Saint-Dic, Valeed Khan, Ana Maria Hincapie, Jacob O. Day, Lucy McGavin, Christine Rowley, Gaurav V. Harlalka, Valerie E. Vancollie, Wasim Ahmad, Christopher J. Lelliott, Asma Gul, Binnaz Yalcin.

Methodology: Miroslav P. Milev, Binnaz Yalcin, Andrew H. Crosby, Michael Sacher, Emma L. Baple.

Project administration: Binnaz Yalcin, Andrew H. Crosby, Michael Sacher, Emma L. Baple.

Supervision: Asma Gul, Binnaz Yalcin, Andrew H. Crosby, Michael Sacher, Emma L. Baple.

Visualization: Lettie E. Rawlins, Hashem Almousa, Shazia Khan, Stephan C. Collins, Andrew H. Crosby, Michael Sacher, Emma L. Baple.

Writing – original draft: Lettie E. Rawlins, Hashem Almousa, Stephan C. Collins, Binnaz Yalcin, Andrew H. Crosby, Michael Sacher, Emma L. Baple.

Writing – review & editing: Lettie E. Rawlins, Hashem Almousa, Stephan C. Collins, Binnaz Yalcin, Andrew H. Crosby, Michael Sacher, Emma L. Baple.

References

1. Sacher M, Barrowman J, Wang W, Horecka J, Zhang Y, Pypaert M, et al. TRAPP I implicated in the specificity of tethering in ER-to-Golgi transport. *Mol Cell*. 2001; 7(2):433–42. [https://doi.org/10.1016/S1097-2765\(01\)00190-3](https://doi.org/10.1016/S1097-2765(01)00190-3) PMID: 11239471.
2. Cai H, Yu S, Menon S, Cai Y, Lazarova D, Fu C, et al. TRAPPI tethers COPII vesicles by binding the coat subunit Sec23. *Nature*. 2007; 445(7130):941–4. Epub 2007/02/07. <https://doi.org/10.1038/nature05527> PMID: 17287728.
3. Yamasaki A, Menon S, Yu S, Barrowman J, Meerloo T, Oorschot V, et al. mTrs130 is a component of a mammalian TRAPP II complex, a Rab1 GEF that binds to COPI-coated vesicles. *Mol Biol Cell*. 2009; 20(19):4205–15. Epub 2009/08/05. <https://doi.org/10.1091/mbc.e09-05-0387> PMID: 19656848; PubMed Central PMCID: PMC2754934.
4. Li C, Luo X, Zhao S, Siu GK, Liang Y, Chan HC, et al. COPI-TRAPP II activates Rab18 and regulates its lipid droplet association. *EMBO J*. 2017; 36(4):441–57. Epub 2016/12/21. <https://doi.org/10.1525/emboj.201694866> PMID: 28003315; PubMed Central PMCID: PMC5694949.
5. Westlake CJ, Baye LM, Nachury MV, Wright KJ, Ervin KE, Phu L, et al. Primary cilia membrane assembly is initiated by Rab11 and transport protein particle II (TRAPP II) complex-dependent trafficking of

- Rabin8 to the centrosome. *Proc Natl Acad Sci U S A*. 2011; 108(7):2759–64. Epub 2011/01/27. <https://doi.org/10.1073/pnas.1018823108> PMID: 21273506; PubMed Central PMCID: PMC3041065.
6. Sacher M, Shahrzad N, Kamel H, Milev MP. TRAPPopathies: An emerging set of disorders linked to variations in the genes encoding transport protein particle (TRAPP)-associated proteins. *Traffic*. 2019; 20(1):5–26. Epub 2018/09/24. <https://doi.org/10.1111/tra.12615> PMID: 30152084.
 7. Cuenca A, Insinna C, Zhao H, John P, Weiss MA, Lu Q, et al. The C7orf43/TRAPPC14 component links the TRAPP complex to Rabin8 for preciliary vesicle tethering at the mother centriole during ciliogenesis. *J Biol Chem*. 2019; 294(42):15418–34. Epub 2019/08/29. <https://doi.org/10.1074/jbc.RA119.008615> PMID: 31467083; PubMed Central PMCID: PMC6802515.
 8. Riedel F, Galindo A, Muschalik N, Munro S. The two TRAPP complexes of metazoans have distinct roles and act on different Rab GTPases. *J Cell Biol*. 2018; 217(2):601–17. Epub 2017/12/22. <https://doi.org/10.1083/jcb.201705068> PMID: 29273580; PubMed Central PMCID: PMC5800803.
 9. Jenkins ML, Harris NJ, Dalwadi U, Fleming KD, Ziemianowicz DS, Rafiei A, et al. The substrate specificity of the human TRAPP complex's Rab-guanine nucleotide exchange factor activity. *Commun Biol*. 2020; 3(1):735. Epub 2020/12/04. <https://doi.org/10.1038/s42003-020-01459-2> PMID: 33277614; PubMed Central PMCID: PMC7719173.
 10. Zong M, Satoh A, Yu MK, Siu KY, Ng WY, Chan HC, et al. TRAPPC9 mediates the interaction between p150 and COPII vesicles at the target membrane. *PLoS One*. 2012; 7(1):e29995. Epub 2012/01/18. <https://doi.org/10.1371/journal.pone.0029995> PMID: 22279557; PubMed Central PMCID: PMC3261171.
 11. Hu WH, Pendergast JS, Mo XM, Brambilla R, Bracchi-Ricard V, Li F, et al. NIBP, a novel NIK and IKK (beta)-binding protein that enhances NF-(kappa)B activation. *J Biol Chem*. 2005; 280(32):29233–41. Epub 2005/06/10. <https://doi.org/10.1074/jbc.M501670200> PMID: 15951441; PubMed Central PMCID: PMC3707486.
 12. Milev MP, Graziano C, Karall D, Kuper WFE, Al-Deri N, Cordelli DM, et al. Bi-allelic mutations in TRAPPC2L result in a neurodevelopmental disorder and have an impact on Rab11 in fibroblasts. *J Med Genet*. 2018; 55(11):753–64. Epub 2018/08/17. <https://doi.org/10.1136/jmedgenet-2018-105441> PMID: 30120216.
 13. Fiedler J, Le Merrer M, Mortier G, Heuertz S, Faivre L, Brenner RE. X-linked spondyloepiphyseal dysplasia tarda: Novel and recurrent mutations in 13 European families. *Hum Mutat*. 2004; 24(1):103. <https://doi.org/10.1002/humu.9254> PMID: 15221797.
 14. Al-Deri N, Okur V, Ahimaz P, Milev M, Valivullah Z, Hagen J, et al. A novel homozygous variant in TRAPPC2L results in a neurodevelopmental disorder and disrupts TRAPP complex function. *J Med Genet*. 2020. Epub 2020/08/25. <https://doi.org/10.1136/jmedgenet-2020-107016> PMID: 32843486.
 15. Van Bergen NJ, Guo Y, Al-Deri N, Lipatova Z, Stanga D, Zhao S, et al. Deficiencies in vesicular transport mediated by TRAPPC4 are associated with severe syndromic intellectual disability. *Brain*. 2020; 143(1):112–30. <https://doi.org/10.1093/brain/awz374> PMID: 31794024; PubMed Central PMCID: PMC6935753.
 16. Mohamoud HS, Ahmed S, Jelani M, Alrayes N, Childs K, Vadgama N, et al. A missense mutation in TRAPPC6A leads to build-up of the protein, in patients with a neurodevelopmental syndrome and dysmorphic features. *Sci Rep*. 2018; 8(1):2053. Epub 2018/02/01. <https://doi.org/10.1038/s41598-018-20658-w> PMID: 29391579; PubMed Central PMCID: PMC5794855.
 17. Marin-Valencia I, Novarino G, Johansen A, Rosti B, Issa MY, Musaev D, et al. A homozygous founder mutation in TRAPPC6B associates with a neurodevelopmental disorder characterised by microcephaly, epilepsy and autistic features. *J Med Genet*. 2018; 55(1):48–54. Epub 2017/06/16. <https://doi.org/10.1136/jmedgenet-2017-104627> PMID: 28626029; PubMed Central PMCID: PMC6056005.
 18. Mortreux J, Busa T, Germain DP, Nadeau G, Puechberty J, Coubes C, et al. The role of CNVs in the etiology of rare autosomal recessive disorders: the example of TRAPPC9-associated intellectual disability. *Eur J Hum Genet*. 2018; 26(1):143–8. Epub 2017/11/29. <https://doi.org/10.1038/s41431-017-0018-x> PMID: 29187737; PubMed Central PMCID: PMC5838970.
 19. Mir A, Kaufman L, Noor A, Motazacker MM, Jamil T, Azam M, et al. Identification of mutations in TRAPPC9, which encodes the NIK- and IKK-beta-binding protein, in nonsyndromic autosomal-recessive mental retardation. *Am J Hum Genet*. 2009; 85(6):909–15. <https://doi.org/10.1016/j.ajhg.2009.11.009> PMID: 20004765; PubMed Central PMCID: PMC2790571.
 20. Abbasi AA, Blasius K, Hu H, Latif Z, Picker-Minh S, Khan MN, et al. Identification of a novel homozygous TRAPPC9 gene mutation causing non-syndromic intellectual disability, speech disorder, and secondary microcephaly. *Am J Med Genet B Neuropsychiatr Genet*. 2017; 174(8):839–45. Epub 2017/10/14. <https://doi.org/10.1002/ajmg.b.32602> PMID: 29031008.
 21. Liang WC, Zhu W, Mitsuhashi S, Noguchi S, Sacher M, Ogawa M, et al. Congenital muscular dystrophy with fatty liver and infantile-onset cataract caused by TRAPPC11 mutations: broadening of the

- phenotype. *Skelet Muscle*. 2015; 5:29. Epub 2015/08/28. <https://doi.org/10.1186/s13395-015-0056-4> PMID: 26322222; PubMed Central PMCID: PMC4551700.
22. Koehler K, Milev MP, Prematilake K, Reschke F, Kutzner S, Jühlen R, et al. A novel *TRAPPC11* mutation in two Turkish families associated with cerebral atrophy, global retardation, scoliosis, achalasia and alacrima. *J Med Genet*. 2017; 54(3):176–85. Epub 2016/10/05. <https://doi.org/10.1136/jmedgenet-2016-104108> PMID: 27707803.
 23. Milev MP, Grout ME, Saint-Dic D, Cheng YH, Glass IA, Hale CJ, et al. Mutations in *TRAPPC12* Manifest in Progressive Childhood Encephalopathy and Golgi Dysfunction. *Am J Hum Genet*. 2017; 101(2):291–9. <https://doi.org/10.1016/j.ajhg.2017.07.006> PMID: 28777934; PubMed Central PMCID: PMC5544387.
 24. Perez Y, Bar-Yaacov R, Kadir R, Wormser O, Shelef I, Birk OS, et al. Mutations in the microtubule-associated protein MAP11 (C7orf43) cause microcephaly in humans and zebrafish. *Brain*. 2019; 142(3):574–85. <https://doi.org/10.1093/brain/awz004> PMID: 30715179; PubMed Central PMCID: PMC6391606.
 25. Passemard S, Perez F, Colin-Lemesre E, Rasika S, Gressens P, El Ghouzi V. Golgi trafficking defects in postnatal microcephaly: The evidence for "Golgiopathies". *Prog Neurobiol*. 2017; 153:46–63. Epub 2017/04/02. <https://doi.org/10.1016/j.pneurobio.2017.03.007> PMID: 28377289.
 26. Rasika S, Passemard S, Verloes A, Gressens P, El Ghouzi V. Golgiopathies in Neurodevelopment: A New View of Old Defects. *Dev Neurosci*. 2018; 40(5–6):396–416. Epub 2019/03/15. <https://doi.org/10.1159/000497035> PMID: 30878996.
 27. Santos-Cortez RLP, Khan V, Khan FS, Mughal ZU, Chakchouk I, Lee K, et al. Novel candidate genes and variants underlying autosomal recessive neurodevelopmental disorders with intellectual disability. *Hum Genet*. 2018; 137(9):735–52. Epub 2018/08/22. <https://doi.org/10.1007/s00439-018-1928-6> PMID: 30167849; PubMed Central PMCID: PMC6201268.
 28. Scales SJ, Pepperkok R, Kreis TE. Visualization of ER-to-Golgi transport in living cells reveals a sequential mode of action for COPII and COPI. *Cell*. 1997; 90(6):1137–48. [https://doi.org/10.1016/s0092-8674\(00\)80379-7](https://doi.org/10.1016/s0092-8674(00)80379-7) PMID: 9323141
 29. Mikhaleva A, Kannan M, Wagner C, Yalcin B. Histomorphological Phenotyping of the Adult Mouse Brain. *Curr Protoc Mouse Biol*. 2016; 6(3):307–32. Epub 2016/09/01. <https://doi.org/10.1002/cpmo.12> PMID: 27584555.
 30. Liang ZS, Cimino I, Yalcin B, Raghupathy N, Vancollie VE, Ibarra-Soria X, et al. *Trappc9* deficiency causes parent-of-origin dependent microcephaly and obesity. *PLoS Genet*. 2020; 16(9):e1008916. Epub 2020/09/02. <https://doi.org/10.1371/journal.pgen.1008916> PMID: 32877400; PubMed Central PMCID: PMC7467316.
 31. Vazquez-Martinez R, Cruz-Garcia D, Duran-Prado M, Peinado JR, Castaño JP, Malagon MM. Rab18 inhibits secretory activity in neuroendocrine cells by interacting with secretory granules. *Traffic*. 2007; 8(7):867–82. Epub 2007/05/04. <https://doi.org/10.1111/j.1600-0854.2007.00570.x> PMID: 17488286.
 32. Winkle CC, Gupton SL. Membrane Trafficking in Neuronal Development: Ins and Outs of Neural Connectivity. *Int Rev Cell Mol Biol*. 2016; 322:247–80. Epub 2016/10/06. <https://doi.org/10.1016/bs.ircmb.2015.10.003> PMID: 26940520; PubMed Central PMCID: PMC4797321.
 33. Ethell IM, Hagihara K, Miura Y, Irie F, Yamaguchi Y. Synbindin, A novel syndecan-2-binding protein in neuronal dendritic spines. *J Cell Biol*. 2000; 151(1):53–68. <https://doi.org/10.1083/jcb.151.1.53> PMID: 11018053; PubMed Central PMCID: PMC2189810.
 34. Mochida GH, Mahajnah M, Hill AD, Basel-Vanagaite L, Gleason D, Hill RS, et al. A truncating mutation of *TRAPPC9* is associated with autosomal-recessive intellectual disability and postnatal microcephaly. *Am J Hum Genet*. 2009; 85(6):897–902. <https://doi.org/10.1016/j.ajhg.2009.10.027> PMID: 20004763; PubMed Central PMCID: PMC2790576.
 35. Hnoonual A, Graidist P, Kritsaneepaiboon S, Limprasert P. Novel Compound Heterozygous Mutations in the *TRAPPC9* Gene in Two Siblings With Autism and Intellectual Disability. *Front Genet*. 2019; 10:61. Epub 2019/02/11. <https://doi.org/10.3389/fgene.2019.00061> PMID: 30853973; PubMed Central PMCID: PMC6396715.
 36. Bodnar B, DeGruttola A, Zhu Y, Lin Y, Zhang Y, Mo X, et al. Emerging role of NIK/IKK2-binding protein (NIBP)/trafficking protein particle complex 9 (*TRAPPC9*) in nervous system diseases. *Transl Res*. 2020; 224:55–70. Epub 2020/05/17. <https://doi.org/10.1016/j.trsl.2020.05.001> PMID: 32434006; PubMed Central PMCID: PMC7442628.
 37. Ke Y, Weng M, Chhetri G, Usman M, Li Y, Yu Q, et al. *Trappc9* deficiency in mice impairs learning and memory by causing imbalance of dopamine D1 and D2 neurons. *Sci Adv*. 2020; 6(47). Epub 2020/11/18. <https://doi.org/10.1126/sciadv.abb7781> PMID: 33208359; PubMed Central PMCID: PMC7673810.

38. Zhang Y, Liu S, Wang H, Yang W, Li F, Yang F, et al. Elevated NBP/TRAPPC9 mediates tumorigenesis of cancer cells through NFκB signaling. *Oncotarget*. 2015; 6(8):6160–78. <https://doi.org/10.18632/oncotarget.3349> PMID: 25704885; PubMed Central PMCID: PMC4467429.
39. Rawlins LE, Jones H, Wenger O, Aye M, Fasham J, Harlalka GV, et al. An Amish founder variant consolidates disruption of CEP55 as a cause of hydranencephaly and renal dysplasia. *Eur J Hum Genet*. 2019; 27(4):657–62. Epub 2019/01/08. <https://doi.org/10.1038/s41431-018-0306-0> PMID: 30622327; PubMed Central PMCID: PMC6420058.
40. Laver et al. SavvyCNV: Genome-wide CNV calling from off-target reads. *PLoS Comput Biol*. 2022 Mar 16; 18(3):e1009940. <https://doi.org/10.1371/journal.pcbi.1009940>
41. Ran FA, Hsu PD, Wright J, Agarwala V, Scott DA, Zhang F. Genome engineering using the CRISPR-Cas9 system. *Nat Protoc*. 2013; 8(11):2281–308. Epub 2013/10/24. <https://doi.org/10.1038/nprot.2013.143> PMID: 24157548; PubMed Central PMCID: PMC3969860.
42. Skarnes WC, Rosen B, West AP, Koutsourakis M, Bushell W, Iyer V, et al. A conditional knockout resource for the genome-wide study of mouse gene function. *Nature*. 2011; 474(7351):337–42. Epub 2011/06/15. <https://doi.org/10.1038/nature10163> PMID: 21677750; PubMed Central PMCID: PMC3572410.
43. Collins SC, Mikhaleva A, Vrcelj K, Vancollie VE, Wagner C, Demeure N, et al. Large-scale neuroanatomical study uncovers 198 gene associations in mouse brain morphogenesis. *Nat Commun*. 2019; 10(1):3465. Epub 2019/08/01. <https://doi.org/10.1038/s41467-019-11431-2> PMID: 31371714; PubMed Central PMCID: PMC6671969.
44. Sunkin SM, Ng L, Lau C, Dolbeare T, Gilbert TL, Thompson CL, et al. Allen Brain Atlas: an integrated spatio-temporal portal for exploring the central nervous system. *Nucleic Acids Res*. 2013; 41(Database issue):D996–D1008. Epub 2012/11/28. <https://doi.org/10.1093/nar/gks1042> PMID: 23193282; PubMed Central PMCID: PMC3531093.



Explorations of novel pyridine-pyrimidine hybrid phosphonate derivatives as aurora kinase inhibitors

Shailee V. Tiwari^{a,*}, Aniket P. Sarkate^b, Deepak K. Lokwani^c, Dattatraya N. Pansare^d, Surendra G. Gattani^e, Sameer S. Sheikh^a, Shirish P. Jain^c, Shashikant V. Bhandari^f

^a Department of Pharmaceutical Chemistry, Durgamata Institute of Pharmacy, Dharmapuri, Parbhani 431401, Maharashtra, India

^b Department of Chemical Technology, Dr. Babasaheb Ambedkar Marathwada University, Aurangabad 431 004, Maharashtra, India

^c Rajarshi Shahu College of Pharmacy, Buldana 443001, Maharashtra, India

^d Department of Chemistry, Deogiri College, Station Road, Aurangabad 431 005, MS, India

^e School of Pharmacy, S.R.T.M. University, Nanded 431006, Maharashtra, India

^f Department of Pharmaceutical Chemistry, AISSMS College of Pharmacy, Near RTO, Kennedy Road, Pune 411001, Maharashtra, India

ARTICLE INFO

Keywords:

Anticancer activity
Synthesis
Pyridine-pyrimidine hybrid phosphonate derivatives
Structure activity relationships
Docking

ABSTRACT

For developing novel therapeutic agents with good anticancer activities, a series of novel pyridine-pyrimidine hybrid phosphonate derivatives 4(a–q) were synthesized by the Kabachnik-Fields method using CAN as catalyst. The compound 4o exhibited the most potent anticancer activity with an IC₅₀ value of 13.62 μM, 17.49 μM, 5.81 μM, 1.59 μM and 2.11 μM against selected cancer cell lines A549, Hep-G2, HeLa, MCF-7, and HL-60, respectively. Compound 4o displayed seven times more selectivity towards Hep-G2 cancer cell lines compared to the human normal hepatocyte cell line LO2 (IC₅₀ value 95.33 μM). Structure-Activity Relationship (SAR) studies were conducted on the variation in the aromatic ring (five-membered heterocyclic ring, six-membered heterocyclic ring) and the variation of substituents on the phenyl ring (electron donating groups, electron withdrawing groups). Furthermore, the mechanism of anticancer activity was clarified by further explorations in bioactivity by using in vitro aurora kinase inhibitory activity and molecular docking studies. The results showed that the compound 4o at IC₅₀ concentration demonstrated distinctive morphological changes such as cell detachment, cell wall deformation, cell shrinkage and reduced number of viable cells in cancer cell lines. Compound 4o induced early apoptosis and late apoptosis of 27.7% and 6.1% respectively.

Cancer is characterized as uncontrolled cell proliferation in the body. It is the second most life-threatening disease, taking approximately 9.6 million lives worldwide each year.¹ Different strategies are in the development stages for the treatment of cancer. Mitotic kinases play an essential role in mitosis, and are often observed to be over-expressed in human solid and many hematologic cancers.² Anti-mitotic agents, which disrupt mitotic spindle assembly, are one of the recent flourishing strategies, which include protein kinase inhibitors such as Aurora kinase. The literature survey highlighted that the over-expression of Aurora kinase leads to tumorigenesis via multiple mechanisms.¹ After being enlightened with this knowledge, a deep study was done on aurora kinase inhibitors.

More and more evidence indicates that the heterocyclic scaffold is a significant tool for finding new active substances with many potential applications. Pyridine and pyrimidine derivatives have received great

interest in recent pharmacological research, being effective in the treatment of various malignancies, such as myeloid leukemia, breast cancer, and idiopathic pulmonary fibrosis. The majority of FDA-approved drugs have a pyridine or pyrimidine core with various substituents.³ Pyridine and pyrimidine derivatives have a variety of biological activities, such as hypoglycemic, anti-inflammatory, anti-virus, anti-cancer activity and so on.³ In recent years, a series of anticancer compounds with a pyridine pyrimidine moiety have been designed and synthesized.³ Pyrimidine derivatives such as VX-680, MLN 8054, and CYC-116 are Aurora Kinase inhibitors. AMG900 has been reported to demonstrate significant inhibitory activity against aurora kinase. AMG900 consists of pyridine pyrimidine framework in its structure. The pyridine pyrimidine framework played a key role in the interaction with Aurora kinase. Thus, developing such small molecules with a pyridine pyrimidine framework that can easily form hydrogen bonds with aurora

* Corresponding author.

E-mail address: shailee2010@gmail.com (S.V. Tiwari).

<https://doi.org/10.1016/j.bmcl.2022.128747>

Received 7 February 2022; Received in revised form 18 April 2022; Accepted 19 April 2022

Available online 26 April 2022

0960-894X/© 2022 Elsevier Ltd. All rights reserved.

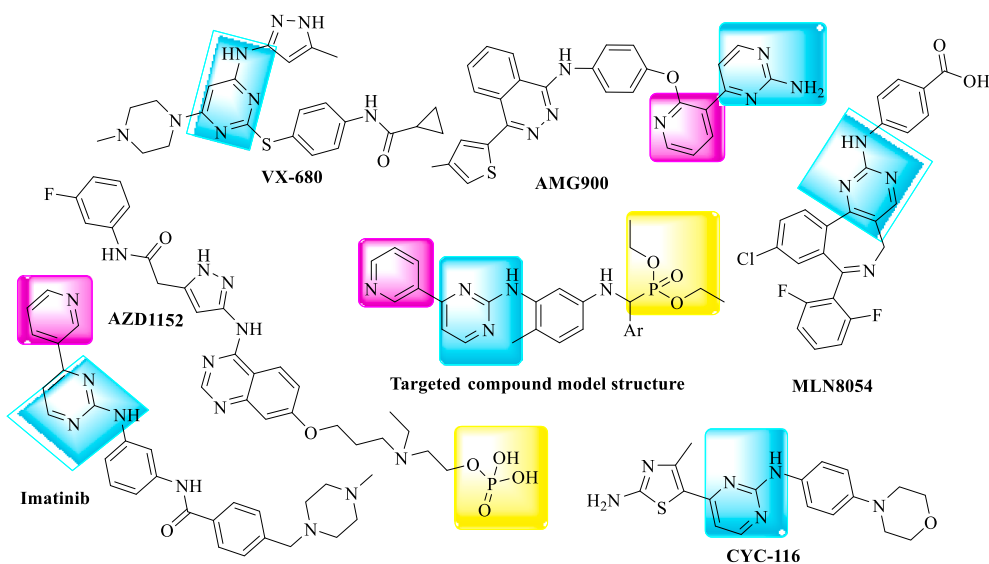
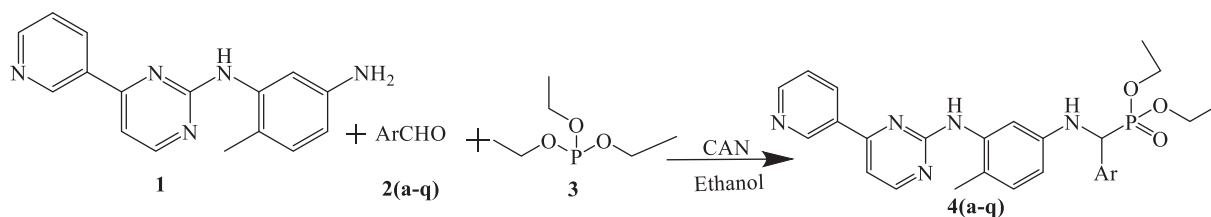


Fig. 1. Designing protocol for target compounds 4(a–q).



Scheme 1. Synthesis of pyridine-pyrimidine hybrid phosphonate derivatives 4(a–q).

Table 1

In vitro anticancer activity results of pyridine-pyrimidine hybrid phosphonate derivatives 4(a–q).

Compound	Ar	IC ₅₀ μM						
		A549	Hep-G2	HeLa	MCF-7	HL-60	LO2	
4a	Phenyl	40.18 ± 0.9	42.06 ± 1.6	32.11 ± 1.2	8.88 ± 1.1	9.02 ± 0.6	ND	
4b	4-Chlorophenyl	24.02 ± 0.4	24.82 ± 1.1	12.01 ± 0.9	6.09 ± 0.4	7.19 ± 1.4	ND	
4c	3,4-Dichlorophenyl	25.02 ± 0.8	24.96 ± 0.4	12.92 ± 1.6	7.07 ± 0.8	8.24 ± 1.1	ND	
4d	4-Fluorophenyl	24.11 ± 0.9	24.88 ± 1.1	12.32 ± 1.4	6.11 ± 0.6	7.23 ± 0.9	ND	
4e	4-Aminophenyl	21.41 ± 1.6	21.46 ± 0.9	10.22 ± 0.4	5.32 ± 0.4	6.39 ± 1.6	ND	
4f	Methylthiazol-5-yl	13.82 ± 1.1	17.99 ± 0.6	6.02 ± 0.8	1.55 ± 0.9	2.32 ± 0.4	74.91 ± 0.9	
4g	Thiophen-3-yl	15.68 ± 1.0	18.76 ± 1.1	7.01 ± 0.9	2.46 ± 1.4	2.99 ± 0.8	ND	
4h	4-Methoxyphenyl	24.32 ± 1.1	24.88 ± 1.6	12.96 ± 1.4	6.42 ± 1.2	7.87 ± 0.6	ND	
4i	Furan-2-yl	15.77 ± 0.8	18.92 ± 0.8	7.16 ± 1.2	3.36 ± 0.6	3.78 ± 1.2	ND	
4j	Pyrazol-5-yl	15.12 ± 0.6	18.60 ± 0.9	6.88 ± 1.2	2.36 ± 1.1	3.01 ± 0.4	83.16 ± 1.1	
4k	Pyridin-4-yl	28.06 ± 0.4	28.46 ± 0.6	18.11 ± 0.4	6.38 ± 0.4	7.22 ± 1.1	ND	
4l	Indol-3-yl	18.21 ± 1.8	19.86 ± 1.2	8.94 ± 1.6	4.66 ± 0.8	4.92 ± 0.4	ND	
4m	Morpholino	29.18 ± 0.9	30.54 ± 0.8	20.32 ± 1.1	6.82 ± 1.2	7.65 ± 0.6	ND	
4n	Piperidin-1-yl	32.62 ± 0.4	34.01 ± 1.6	21.14 ± 0.6	6.86 ± 1.1	8.18 ± 0.4	ND	
4o	Pyrrol-2-yl	13.62 ± 1.6	17.49 ± 1.1	5.81 ± 1.2	1.59 ± 0.4	2.11 ± 0.9	95.33 ± 0.6	
4p	4-Hydroxyphenyl	21.56 ± 0.8	21.59 ± 0.6	10.42 ± 0.8	5.67 ± 0.9	5.98 ± 0.8	ND	
4q	4-Methylphenyl	22.01 ± 1.1	21.88 ± 1.6	10.64 ± 0.4	5.96 ± 1.4	6.75 ± 1.2	ND	
VX-680		15.06 ± 1.8	18.01 ± 1.1	6.24 ± 0.9	1.02 ± 0.4	1.88 ± 0.6	ND	

^aThe IC₅₀ values are the means of at least two experiments; A549: Human lung carcinoma; Hep-G2: Human hepatocellular liver carcinoma cells; HeLa: Human cervical carcinoma epithelial; MCF-7: Human breast cancer cell line; HL-60: human leukemia cell line; LO2: Human normal hepatocyte cell line ND: Not determined.

kinase enzymes is a potential strategy for developing new active chemicals.

The α -aminophosphonates belong to a relevant class of molecules for various pharmacological actions, such as antibiotic,⁴ anticancer agents,^{5,6} herbicide,^{7,8} pesticide,⁹ enzyme inhibitors,^{10–12} peptide mimetic,¹³ antioxidant,¹⁴ antiviral,¹⁵ anti-thrombotic agents,¹⁶ pharmacological agents,¹⁷ anti-HIV agents,¹⁸ anti-inflammatory activities¹⁹ and plant growth regulators.²⁰ AZD1152 is an Aurora Kinase inhibitor

with a phosphonate group in its structure. The structure of AZD1152 gave us an idea of incorporating the phosphonate group into the designed structure for good anticancer activity. The α -amino phosphonates could offer a useful structure for the discovery of new active compounds. To our knowledge, the α -amino phosphonates structure reports good anticancer activity according to literature study.²¹

It was thought of interest to study the combination of pyridine pyrimidine moiety and α - amino phosphonates framework combination

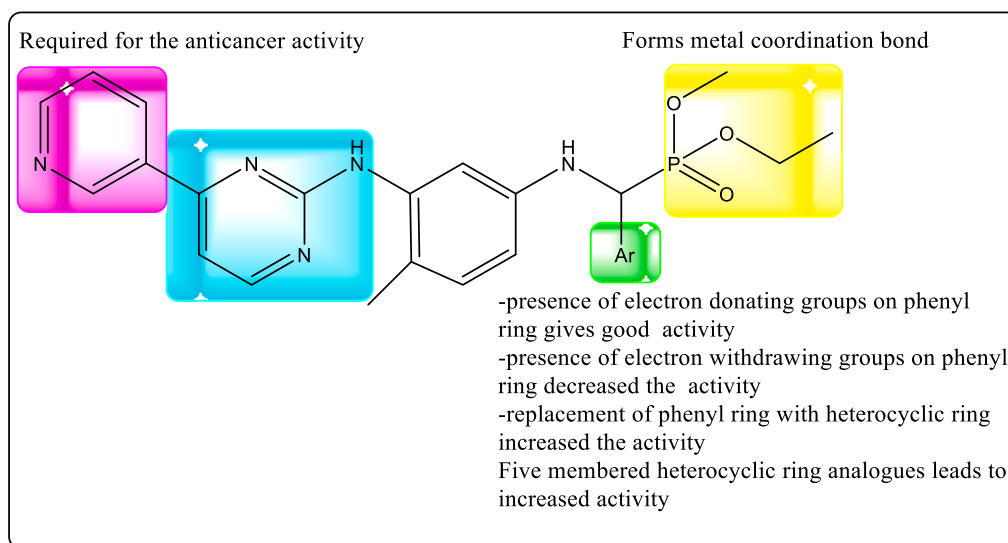


Fig. 2. Structure-activity relationship in pictorial form.

Table 2

Kinase inhibitions of selected compounds (in vitro).

Compound	IC ₅₀ nM ^a	
	Aurora A	Aurora B
4f	33 ± 1.3	15 ± 1.9
4j	15 ± 0.6	12 ± 0.8
4o	42 ± 1.8	22 ± 0.2
VX-680	1.9 ± 0.7	18.6 ± 1.1

^aIC₅₀ values are the means of at least two experiments.

which were probable to reveal an anticancer effect. Hence, after a thorough literature survey on available aurora kinase inhibitors as revealed in Fig. 1, the targeted molecules were designed. A one-pot procedure can minimize chemical waste, save time and simplify the practical aspects.

It's stunning that there's no compound possessing such a molecular skeleton according to the literature to date. In continuation of our recent

work aimed at the synthesis of a variety of heterocyclic systems with exceptional biological importance,²²⁻²⁴ we reported here the synthesis of novel pyridine pyrimidine hybrid phosphonate derivatives 4(a-q) by Kabachnik-Fields method using ceric ammonium nitrate (CAN) as catalyst. Accordingly, seventeen derivatives have been designed and synthesized. Various substituents were introduced to the phenyl ring with the purpose of exploring the influence of substituents on anticancer activity by regulating the electronic and steric effects. Further modifications were performed by introducing various heterocyclic ring systems in place of the phenyl ring.

Novel pyridine pyrimidine hybrid phosphonate derivatives 4(a-q) were synthesized by the Kabachnik-Fields method by reacting 6-methyl-N1-(4-(pyridin-3-yl)pyrimidin-2-yl)benzene-1,3-diamine (1), substituted aldehydes/ heterocyclic aldehydes 2(a-q) and triethylphosphite (3) via a one pot synthetic step in the presence of CAN as a green catalyst.²¹ The green synthesis used to make the title compounds is shown in scheme 1.

All the synthesized novel pyridine-pyrimidine hybrid phosphonate

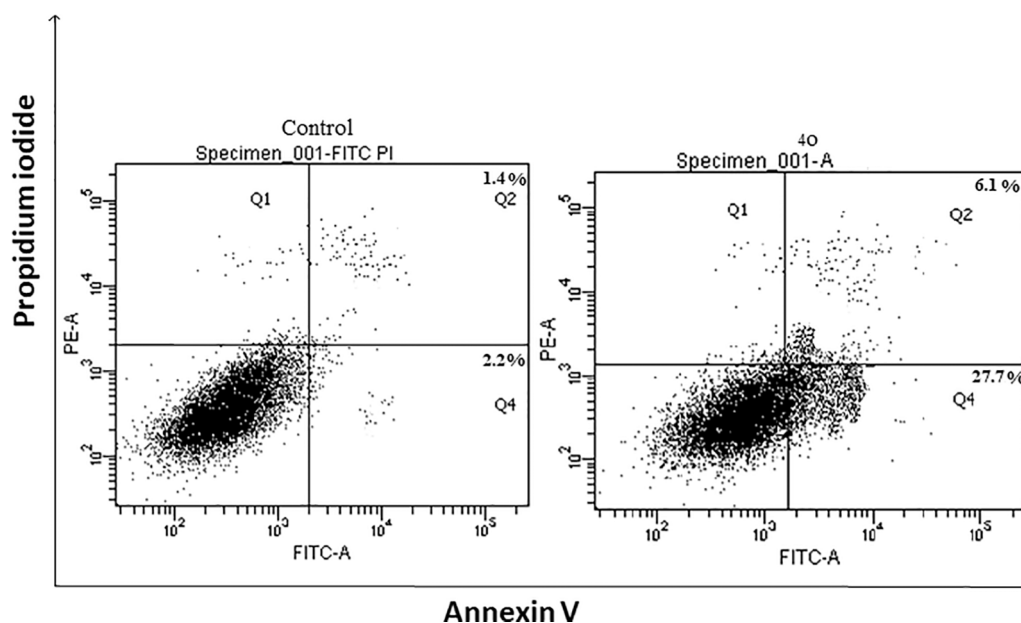


Fig. 3. Apoptosis study by Annexin V/FITC assay of compound 4o.

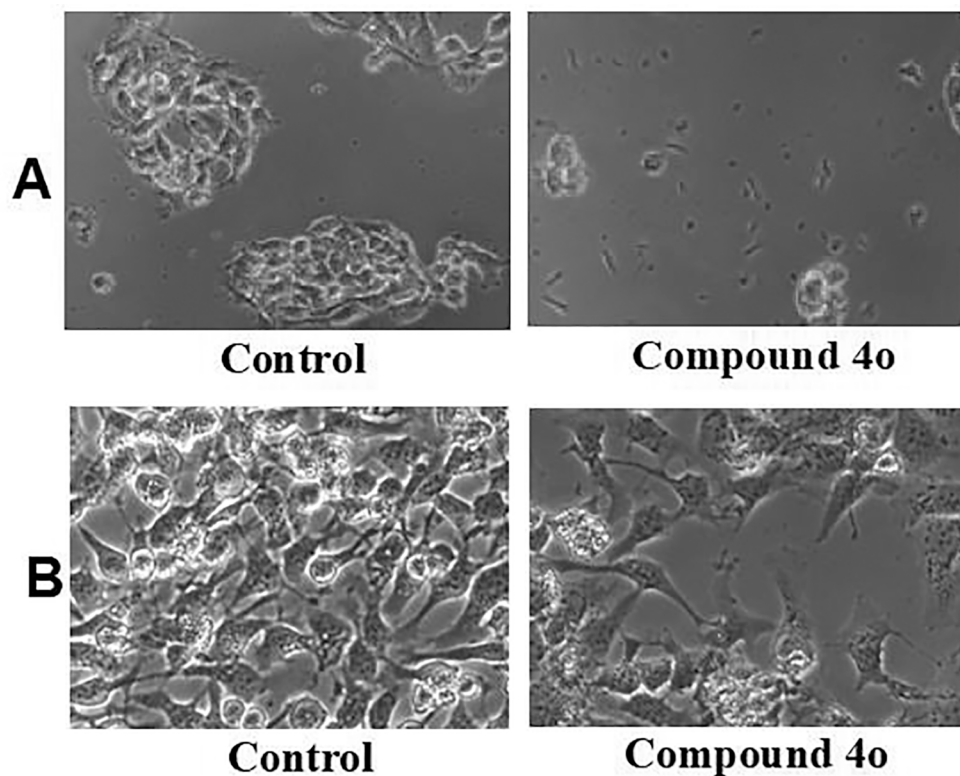


Fig. 4. A. Morphological Changes in Hep-G2 cell line; B. Morphological Changes in HeLa cell line.

derivatives 4(a–q) were allowed to go under evaluation to check their ability to kill cancer cell lines. The cancer cell lines selected for the evaluation are human lung carcinoma A549 cells, human hepatocellular liver carcinoma Hep-G2 cells, human cervical carcinoma epithelial HeLa cells, human breast cancer cell line MCF-7, and human leukemia cell line HL-60 using the MTT assay²⁵. The normal cell line selected was the human normal hepatocyte cell line LO2. The VX-680, an aurora kinase inhibitor, was used as a standard drug for the *in vitro* anticancer evaluation.

As exemplified in Table 1, the majority of the synthesized novel pyridine pyrimidine hybrid phosphonate derivatives 4(a–q) demonstrated moderate-to-excellent potency against five selected cancer cell lines in the μM range, indicating that the combination of pyridine pyrimidine hybrid moiety and α -aminophosphonate framework have good anticancer activity.

The synthesized compound 4o was found to be most potent compared to the other synthesized sixteen derivatives. The compound 4o showed an IC_{50} value of 13.62 μM , 17.49 μM , 5.81 μM , 1.59 μM and 2.11 μM against A549, Hep-G2, HeLa, MCF-7 and HL-60 cancer cell lines respectively. The compound 4j also showed good anticancer activity against selected cancer cell lines. The active compounds 4f, 4j and 4o were also tested on the normal human normal hepatocyte cell line LO2 to check their selectivity towards cancer cell lines. The compound 4o revealed seven times more selectivity towards Hep-G2 cancer cell line compared to human normal hepatocyte cell line LO2 (IC_{50} value 95.33 μM). The compounds 4f and 4j also displayed 5.5 times more selectivity towards Hep-G2 cells when compared with the human normal hepatocyte cell line LO2.

Our primary aim was to explore the anticancer activity of compounds with different substituents on the phenyl ring in order to understand the structure–activity relationship. Later, we replaced the phenyl ring with different heterocyclic ring systems, which included five-membered and six-membered heterocyclic rings. The synthesized compound 4p with an “OH” group on the phenyl ring revealed 21.56 μM , 21.59 μM , 10.42 μM , 5.67 μM and 5.98 μM *in vitro* anticancer

activity against A549, Hep-G2, HeLa MCF-7, and HL-60, respectively. The synthesized compound 4b with a “Cl” group on the phenyl ring revealed 24.02 μM , 24.82 μM , 12.01 μM , 6.09 μM and 7.19 μM *in vitro* anticancer activity against A549, Hep-G2, HeLa, MCF-7 and HL-60 respectively. We can state that the introduction of electron-donating groups (EDGs) on phenyl ring exhibited a positive effect on the anti cancer activity on the selected cancer cell lines, such as compounds 4e, 4p, and 4q. By contrast, electron-withdrawing groups (EWGs) exhibited a negative effect in compound such as 4b, 4c, 4d, and 4h.

Generally, five-membered ring system analogs (4f, 4g, 4i, 4j and 4o) were more active than corresponding six-membered analogs (4k, 4m, and 4n). It was also observed that the compound 4l with the indole ring as a substituent gave good anticancer activity when compared with six-membered analogs (4k, 4m, and 4n). Fig 2 enlightens the structure–activity relationship in pictorial form.

The synthesized compounds 4f, 4j, and 4o, which had shown good anticancer activity as per the MTT assay data, were further tested to predict their mechanism of action. They were evaluated to check their ability to inhibit aurora kinase. The standard drug used during this evaluation is VX-680. The inhibition activity against Aurora enzymes was performed by the Kinase-Glo luminescent kinase assay *in vitro*.²⁶ The results obtained after evaluation are represented in Table 2. Compound 4o was found to be a potent aurora kinases inhibitor with an IC_{50} value of 42 nM and 22 nM against Aurora kinase A and Aurora kinase B, respectively. The results of the Aurora kinase inhibitory activities suggest that the synthesized compounds exert their antitumor activity by inhibiting the aurora kinase enzyme.

Apoptosis, autophagy and necrosis are the major types of cell death. Apoptosis, or programmed cell death, is a normal physiologic process for removal of unwanted cells. The synthesized compound 4o was selected to test whether it has the ability to induce apoptosis in cancer cell lines. The ability of synthesized compound 4o to induce apoptosis was determined using an Annexin V (conjugated to FITC) apoptosis detection kit.²⁷ From Fig.3, it is clear that the compound 4o have induced early apoptosis and late apoptosis of 27.7% and 6.1% respectively **079**

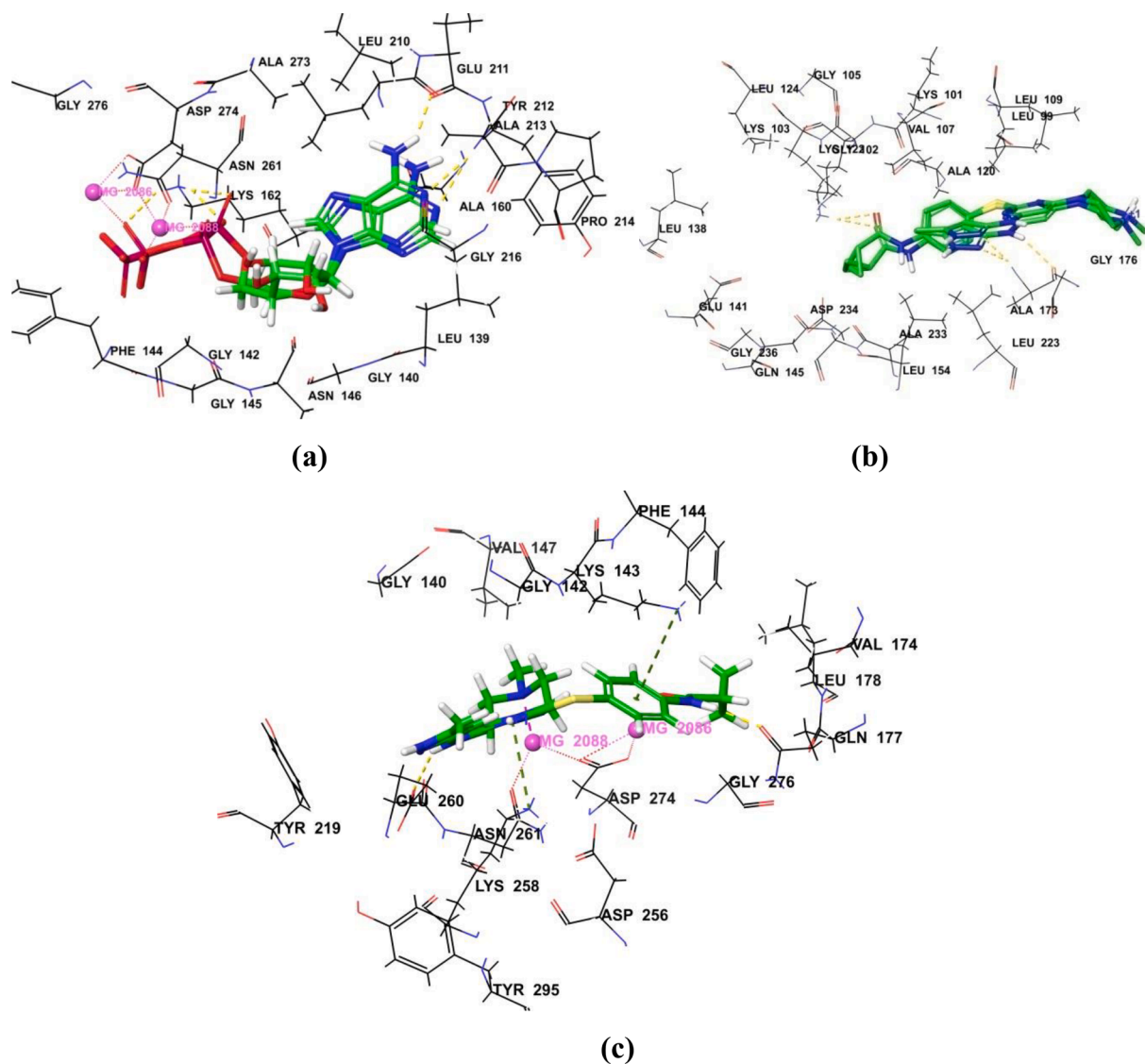


Fig. 5. (a) Superimposition of docked pose of compound **ADP** over its crystal structure (enzyme bound conformer) in the active site of enzyme **Aurora kinase A**, (b) Superimposition of docked pose of compound **VX-680** over its crystal structure (enzyme bound conformer) in the active site of **Aurora kinase B**. (c) Docked pose of **VX-680** in active site of enzyme **Aurora kinase A**. Yellow colored dotted line indicate H-bond interaction, purple colored dotted line indicates metal coordination and Green colored dotted line indicates pi-pi stacking. (For interpretation of the references to colour in this figure legend, the reader is referred to the web version of this article.)

comparison with control with early apoptosis of 2.2% and late apoptosis of 1.4%.

Cell morphology was experiential at the IC_{50} concentration of the synthesized compounds **4(a-q)** and photographs were taken under a Nikon Eclipse Ti-S Inverted Research Microscope and the images were processed using the NIS-Elements software. The images of the in vitro anticancer activity of the active compounds **4o** on the Hep-G2 and HeLa cancer cell lines are shown in **Figures 4A and 4B** respectively. At the IC_{50} concentration of the potent compound **4o**, the distinct morphological changes such as cell detachment, cell wall deformation, cell shrinkage, and a reduction in the number of viable cells were seen in Hep-G2 cancer cells, as shown in **(Fig. 4 A)**. From **Figure 4B**, it can be concluded that in HeLa cancer cell lines, at the IC_{50} concentration of the most active compound **4o**, there have been distinct morphological changes such as cellular detachment, cell wall deformation, cell shrinkage, and a decreased number of viable cells as compared to control cells.

The docking studies were performed on Aurora kinase A (PDB ID: 1MQ4) and Aurora kinase B (PDB ID: 4B8M) respectively using Smina molecular docking software.²⁸ Smina is the fork of AutoDock Vina and is

customized to better support scoring function development and high-performance energy minimization. The docking methodology was validated by redocking the inbound ligands **ADP** and **VX-680**, placed in the active site of Aurora kinase A and Aurora kinase B enzymes, respectively.^{29,30} The RMSD value was then calculated by superimposing the docked pose of the bound ligand over its crystal form conformer (**Fig 5**). The RMSD value was found to be 1.25 Å and 0.725 Å for Aurora kinase A and Aurora kinase B respectively.

The docked poses of synthesized compounds were compared with that of the standard molecule **VX-680**. The docking score of synthesized compounds was found to be in the range of -8.86 to -4.34 for Aurora kinase A and -6.08 to -4.09 for Aurora kinase B (**Table S1**). Among all the docked compounds, the compounds **4o** and **4j** were found to have the highest binding affinity for both enzymes.

All synthesized molecules were found to interact with the enzymes via hydrogen bond interactions with various amino acid residues. The main amino acid residues of Aurora A kinase which were involved in the hydrogen bonding with synthesized compounds are Lys 141, Lys 143, Lys 162, Ala 213, and Glu 260 (**Fig. 6**). Similarly, the key Aurora **080**

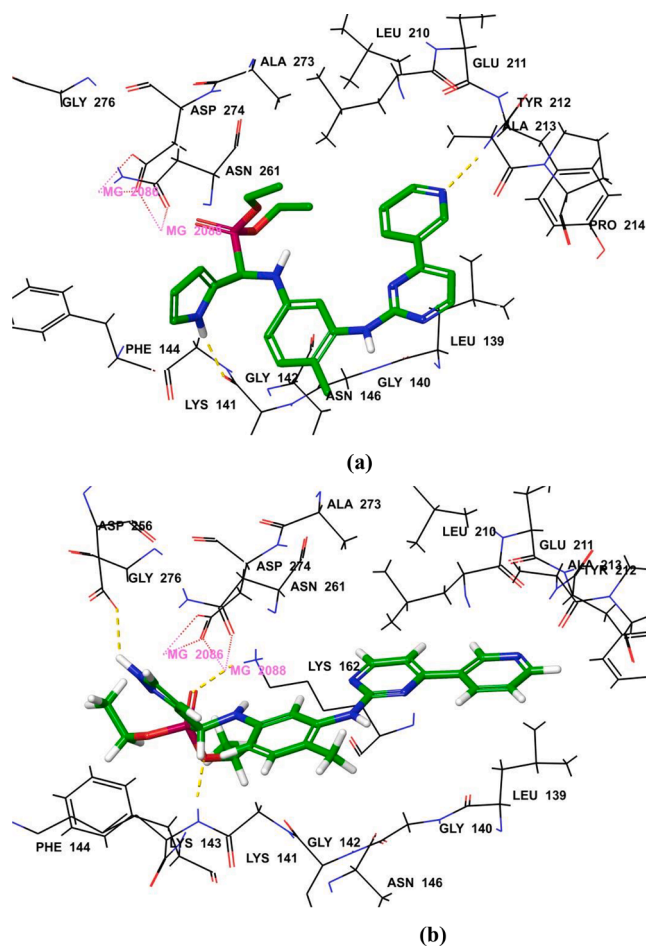


Fig. 6. Docked pose of compounds (a) **4o** and (b) **4j** in the active site of enzyme **Aurora kinase A**. Yellow colored dotted line indicate H-bond interaction and purple colored dotted line indicates metal coordination. (For interpretation of the references to colour in this figure legend, the reader is referred to the web version of this article.)

kinase amino acid residues involved in hydrogen bonding are Glu 171, Lys 122, Ala 173, and Asp 234 (Fig. 7). However, the synthesized compounds in the active site of Aurora A kinase also formed metal coordinate bonds with Mg^{2+} ions which support the stability of ligand-enzyme complex.

In conclusion, the novel series of pyridine pyrimidine hybrid phosphonatederivatives **4(a-q)** were synthesized by the Kabachnik-Fields method using CAN as green catalyst. The synthesized novel derivatives were allowed to undergo in vitro anticancer activity testing. The structure-activity relationship (SAR) was discussed, and the results confirmed that the most promising compounds **4o** and **4f** showed the most potent anticancer activity against selected cancer cell lines. The compound **4j** has also shown good anticancer activity. Taken together, the data of in vitro anticancer activity, in vitro enzyme assay and molecular docking study, compound **4o** is a potential anticancer agent by targeting Aurora kinase.

Declaration of Competing Interest

The authors declare that they have no known competing financial interests or personal relationships that could have appeared to influence the work reported in this paper.

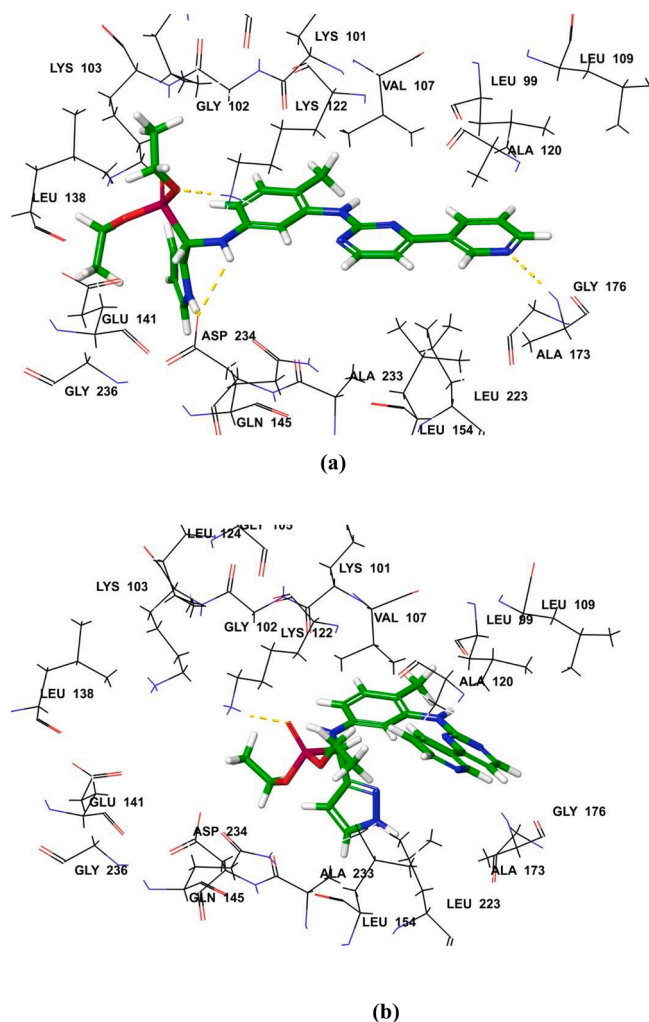


Fig. 7. Docked pose of compounds (a) **4o** and (b) **4j** in the active site of enzyme **Aurora kinase B**. Yellow colored dotted line indicate H-bond interaction and purple colored dotted line indicates metal coordination. (For interpretation of the references to colour in this figure legend, the reader is referred to the web version of this article.)

Acknowledgement

Author S.V. T. is thankful to Swami Ramanand Teerth Marathwada University, Nanded-431606, Maharashtra, India for the minor research project (APDS/Uni.MRP/Sci. & Tech.-Micro./2019-20/2827).

Appendix A. Supplementary data

Supplementary data to this article can be found online at <https://doi.org/10.1016/j.bmcl.2022.128747>.

References

- Bray F, Ferlay J, Soerjomataram I, Siegel RL, Torre LA, Jemal A. Global cancer statistics 2018: GLOBOCAN estimates of incidence and mortality worldwide for 36 cancers in 185 countries. *CA Cancer J Clin.* 2018;68:394–424.
- Li JJ, Li SA. Mitotic kinases: the key to duplication, segregation, and cytokinesis errors, chromosomal instability, and oncogenesis. *Pharmacol Ther.* 2006;111: 974–984.
- (a) ChiacchioAM ID, Romeo R, Giofrè VS, Legnani L. Pyridine and pyrimidine derivatives as privileged scaffolds in biologically active agents. *Curr Med Chem.* 2019; 26:7166–7195.(b) Dofe VS, Sarkate AP, Shaikh ZM, Jadhav CK, Nipte AS, Gill CH. Ultrasound assisted synthesis of novel pyrazole and pyrimidine derivatives as antimicrobial agents. *J Heterocycl Chem.* 2018;55:756–762.

- 4 Atherton FR, Hassall CH, Lambert RW. Synthesis and structure-activity relationships of antibacterial phosphonopeptides incorporating (1-aminoethyl)phosphonic acid and (aminomethyl)phosphonic acid. *J Med Chem.* 1986;29:29–40.
- 5 Lajczak B, Kafarski P, Sztajer H, Mastalerz P. Antibacterial activity of phosphono dipeptides related to alafosfalin. *J Med Chem.* 1986;29:2212–2217.
- 6 Kafarski P, Lejezak B. Aminophosphonic acids of potential medical importance. *Curr Med Chem Anti-Cancer Agents.* 2001;1:301–312.
- 7 Yong SL, Da QJ, Eun JK, et al. Asiatic acid, a triterpene, induces apoptosis through intracellular Ca^{2+} release and enhanced expression of p53 in HepG2 human hepatoma cells. *Canc Lett.* 2002;186:83–91.
- 8 Maier L. Organic Phosphorus compounds 91.1 synthesis and properties of 1-amino-2-arylethylphosphonic and-phosphinic acids as well as -phosphine oxides. *Phos Sul Sil Relat Elem.* 1990;53:43–67.
- 9 Che JY, Xu YZ X, Tang LY, Gu C, Shi DQ. Synthesis and herbicidal activity evaluation of novel α -amino phosphonate derivatives containing a uracil moiety. *Bioorg Med Chem Lett.* 2016;26:1310–1313.
- 10 Occhipinti A, Berlicki L, Giberti S, Dziedzic G, Kafarski P, Forlani G. Effectiveness and mode of action of phosphonate inhibitors of plant glutamine synthetase. *Pest Manage Sci.* 2010;66:51–58.
- 11 Srinivasulu D, Reddy MVB, Rajasekar D, Balaji M, Nagaraju C. Design, synthesis and antimicrobial activity of α -aminophosphonates of quinoline and their molecular docking studies against DNA Gyrase A. *Lett Drug Des Dis.* 2013;10:967–976.
- 12 Grzywa R, Sienczyk M. Phosphonic esters and their application of protease control. *Curr Pharm Des.* 2013;19:1154–1178.
- 13 Allen MC, Fuhrer W, Tuck B, Wade R, Wood JM. Renin inhibitors. Synthesis of transition-state analog inhibitors containing phosphorus acid derivatives at the scissile bond. *J Med Chem.* 1989;32:1652–1661.
- 14 Kafarski P, Lejczak B. Biological activity of aminophosphonic acids. *Phos Sul Sil Relat Elem.* 1991;63:193–215.
- 15 (a) Rao AJ, Rao PV, Rao VK, Mohan C, Raju CN, Reddy CS. Microwave Assisted One-pot Synthesis of Novel α -Aminophosphonates and their Biological Activity. *Bull Kor Chem Soc.* 2010;31:1863–1868. (b) Jadhav SA, Shioorkar MG, Chavan OS, Sarkate AP, Shinde DB. Rapid and efficient one pot microwave assisted synthesis of 2-phenylimidazo[1,2-a]pyridines and 2-phenylimidazo[1,2-a]quinoline in Water-PEG-400. *Syn Comm.* 2017;47:285–290. (c) Dofe VS, Sarkate AP, Shaikh ZM, Gill CH. Ultrasound mediated synthesis of novel 1,2,3-triazole based pyrazole and pyrimidine derivatives as antimicrobial agents. *J Het Chem.* 2017;54:3195–3201. (d) Bhosle MR, Khillare LD, Mali JR, Sarkate AP, Lokwani DK, Tiwari SV. DIPEAc promoted one-pot synthesis of dihydropyrido[2,3-d:6,5-d']dipyrimidinetetraone and pyrimido[4,5 d] pyrimidine derivatives as potent tyrosinase inhibitors and anticancer agents: in vitro screening, Molecular docking and ADMET predictions. *N J Chem.* 2018;42:18621–18632.
- 16 Xu Y, Yan K, Song B, et al. Synthesis and antiviral bioactivities of α -aminophosphonates containing alkoxyethyl moieties. *Molecules.* 2006;11:666–676.
- 17 Meyer JH, Barlett PA. Macrocyclic inhibitors of penicillopepsin. 1. Design, synthesis, and evaluation of an inhibitor bridged between P1 and P3. *J Am Chem Soc.* 1998;120:4600–4609.
- 18 Aziz N, Saidi MR. Synthesis of tertiary α -amino phosphonate by one-pot three-component coupling mediated by LPDE. *Tetrahedron.* 2003;59:5329–5332.
- 19 (a) Bhattacharya AK, Rana KC, Pannecouque C, De Clercq E. An efficient synthesis of a hydroxyethylamine (HEA) isostere and its α aminophosphonate and phosphoramidate derivatives as potential anti HIV agents. *Chem Med Chem.* 2012;7:1601–1611. (b) Doherty W, Adler N, Knox A, et al. Synthesis and evaluation of 1,2,3-triazole-containing vinyl and allyl sulfones as anti-trypanosomal agents. *Eur J Org Chem.* 2017;1:175–185.
- 20 Sujatha B, Mohan S, Subramanyam C, Rao P. Microwave-assisted synthesis and anti-inflammatory activity evaluation of some novel α -aminophosphonates. *Phos Sul Sil Relat Elem.* 2017;192:1110–1113.
- 21 Tiwari SV, Sharif NS, Gajare RI, et al. New 2-oxoindolin phosphonates as novel agents to treat cancer: a green synthesis and molecular modeling. *Molecules.* 2018;23:1981.
- 22 Chate AV, Tagad PA, Bondle GM, Sarkate AP, Tiwari SV, Azad R. Design, synthesis and biological evaluation of tetrahydroindeno[1,2-b:3,4-b']naphthyridinones as potential anticancer agents and novel aurora kinases inhibitors. *Chemistry Select.* 2021;6:3444.
- 23 (a) Nikalje APG, Tiwari SV, Sangshetti JN, Damale MD. Ultrasound-mediated synthesis, biological evaluation, docking and in vivo acute oral toxicity study of novel indolin-2-one coupled pyrimidine derivatives. *Res Chem Intermed.* 2018;44:3031–3059. (b) Chate AV, Redlawar AA, Bondle GM, Sarkate AP, Tiwari SV, Lokwani DK. A new efficient domino approach for the synthesis of coumarin-pyrazolines as antimicrobial agents targeting bacterial D-alanine-D-alanine ligase. *N J Chem.* 2019;43:9002–9011.
- 24 Nikalje APG, Gawhane PA, Sangshetti JN, Damale MD. Ultrasound promoted green synthesis, docking study of indole spliced thiaziazole, α -amino phosphonates as anticancer agents and anti-tyrosinase agents. *Anti-Cancer Agents in Med Chem (Formerly Current Medicinal Chemistry - Anti-Cancer Agents).* 2018;18:1267–1280.
- 25 (a) Dofe VS, Sarkate AP, Azad R, Charansingh HG. Novel quinoline-based oxadiazole derivatives induce G2/M arrest and apoptosis in human breast cancer MCF-7 cell line. *Res Chem Interme.* 2017;43:7331–7345. (b) Chate AV, Kamdi SP, Bhagat AV, et al. Design, synthesis and SAR study of novel spiro[pyrimido[5,4-b]quinoline-10,5'-pyrrolo[2,3-d]pyrimidine] derivatives as promising anticancer agents. *J Het Chem.* 2018;55:2297–2302.
- 26 Wang W, Feng X, Liu HX, Chen SW, Hui L. Synthesis and biological evaluation of 2,4-disubstituted phthalazinones as Aurora kinase inhibitors. *Bioorg Med Chem.* 2018;26:3217–3226.
- 27 Abdelhaleem EF, Abdelhameid MK, Kassab AB, Kandeel MM. Design and synthesis of thienopyrimidine urea derivatives with potential cytotoxic and pro-apoptotic activity against breast cancer cell line MCF-7. *Eur J Med Chem.* 2018;143:1807–1825.
- 28 Koes DR, Baumgartner MP, Camacho CJ. Lessons learned in empirical scoring with smina from the csar 2011 benchmarking exercise. *J Chem Inform Model.* 2013;53:1893–1904.
- 29 (a) Tiwari SV, Seijas JA, Vazquez-Tato MP, Sarkate AP, Karnik KS, Nikalje APG. Ionic liquid promoted synthesis of novel chromone-pyrimidine coupled derivatives, antimicrobial analysis, enzyme assay. *Docking Study Tox Study Mol.* 2018;23:440. (b) Tiwari SV, Siddiqui S, Seijas JA, et al. Microwave-assisted facile synthesis, anticancer evaluation and docking study of N-(5-(substituted methylene amino)-1,3,4-thiadiazol-2-yl)methyl benzamide derivatives. *Molecules.* 2017;22:995.
- 30 Lokwani D, Azad R, Sarkate AP, Reddanna P, Shinde D. Structure based library design (SBLD) for new 1,4-dihydropyrimidine scaffold as simultaneous COX-1/COX-2 and 5-LOX inhibitors. *Bioorg Med Chem.* 2015;23:4533–4543.



Explorations of novel pyridine-pyrimidine hybrid phosphonate derivatives as aurora kinase inhibitors

Shailee V. Tiwari^{a,*}, Aniket P. Sarkate^b, Deepak K. Lokwani^c, Dattatraya N. Pansare^d, Surendra G. Gattani^e, Sameer S. Sheikh^a, Shirish P. Jain^c, Shashikant V. Bhandari^f

^a Department of Pharmaceutical Chemistry, Durgamata Institute of Pharmacy, Dharmapuri, Parbhani 431401, Maharashtra, India

^b Department of Chemical Technology, Dr. Babasaheb Ambedkar Marathwada University, Aurangabad 431 004, Maharashtra, India

^c Rajarshi Shahu College of Pharmacy, Buldana 443001, Maharashtra, India

^d Department of Chemistry, Deogiri College, Station Road, Aurangabad 431 005, MS, India

^e School of Pharmacy, S.R.T.M. University, Nanded 431006, Maharashtra, India

^f Department of Pharmaceutical Chemistry, AISSMS College of Pharmacy, Near RTO, Kennedy Road, Pune 411001, Maharashtra, India

ARTICLE INFO

Keywords:

Anticancer activity
Synthesis
Pyridine-pyrimidine hybrid phosphonate derivatives
Structure activity relationships
Docking

ABSTRACT

For developing novel therapeutic agents with good anticancer activities, a series of novel pyridine-pyrimidine hybrid phosphonate derivatives 4(a–q) were synthesized by the Kabachnik-Fields method using CAN as catalyst. The compound 4o exhibited the most potent anticancer activity with an IC₅₀ value of 13.62 μM, 17.49 μM, 5.81 μM, 1.59 μM and 2.11 μM against selected cancer cell lines A549, Hep-G2, HeLa, MCF-7, and HL-60, respectively. Compound 4o displayed seven times more selectivity towards Hep-G2 cancer cell lines compared to the human normal hepatocyte cell line LO2 (IC₅₀ value 95.33 μM). Structure-Activity Relationship (SAR) studies were conducted on the variation in the aromatic ring (five-membered heterocyclic ring, six-membered heterocyclic ring) and the variation of substituents on the phenyl ring (electron donating groups, electron withdrawing groups). Furthermore, the mechanism of anticancer activity was clarified by further explorations in bioactivity by using in vitro aurora kinase inhibitory activity and molecular docking studies. The results showed that the compound 4o at IC₅₀ concentration demonstrated distinctive morphological changes such as cell detachment, cell wall deformation, cell shrinkage and reduced number of viable cells in cancer cell lines. Compound 4o induced early apoptosis and late apoptosis of 27.7% and 6.1% respectively.

Cancer is characterized as uncontrolled cell proliferation in the body. It is the second most life-threatening disease, taking approximately 9.6 million lives worldwide each year.¹ Different strategies are in the development stages for the treatment of cancer. Mitotic kinases play an essential role in mitosis, and are often observed to be over-expressed in human solid and many hematologic cancers.² Anti-mitotic agents, which disrupt mitotic spindle assembly, are one of the recent flourishing strategies, which include protein kinase inhibitors such as Aurora kinase. The literature survey highlighted that the over-expression of Aurora kinase leads to tumorigenesis via multiple mechanisms.¹ After being enlightened with this knowledge, a deep study was done on aurora kinase inhibitors.

More and more evidence indicates that the heterocyclic scaffold is a significant tool for finding new active substances with many potential applications. Pyridine and pyrimidine derivatives have received great

interest in recent pharmacological research, being effective in the treatment of various malignancies, such as myeloid leukemia, breast cancer, and idiopathic pulmonary fibrosis. The majority of FDA-approved drugs have a pyridine or pyrimidine core with various substituents.³ Pyridine and pyrimidine derivatives have a variety of biological activities, such as hypoglycemic, anti-inflammatory, anti-virus, anti-cancer activity and so on.³ In recent years, a series of anticancer compounds with a pyridine pyrimidine moiety have been designed and synthesized.³ Pyrimidine derivatives such as VX-680, MLN 8054, and CYC-116 are Aurora Kinase inhibitors. AMG900 has been reported to demonstrate significant inhibitory activity against aurora kinase. AMG900 consists of pyridine pyrimidine framework in its structure. The pyridine pyrimidine framework played a key role in the interaction with Aurora kinase. Thus, developing such small molecules with a pyridine pyrimidine framework that can easily form hydrogen bonds with aurora

* Corresponding author.

E-mail address: shailee2010@gmail.com (S.V. Tiwari).

<https://doi.org/10.1016/j.bmcl.2022.128747>

Received 7 February 2022; Received in revised form 18 April 2022; Accepted 19 April 2022

Available online 26 April 2022

0960-894X/© 2022 Elsevier Ltd. All rights reserved.

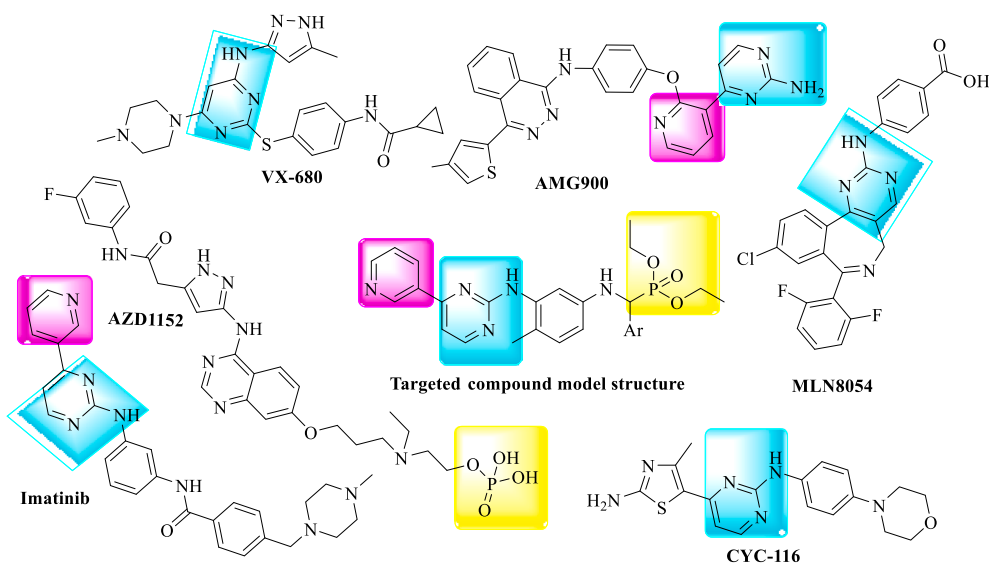
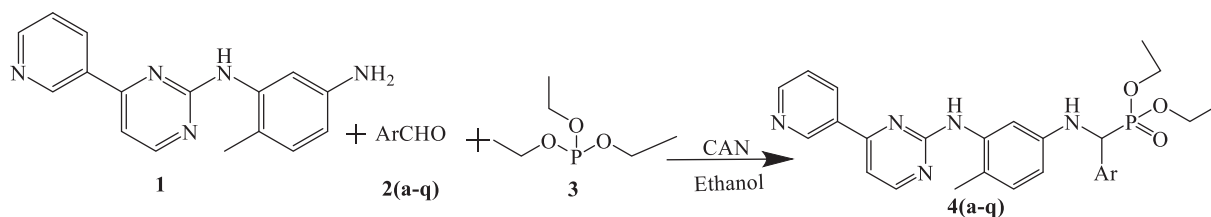


Fig. 1. Designing protocol for target compounds 4(a–q).



Scheme 1. Synthesis of pyridine-pyrimidine hybrid phosphonate derivatives 4(a–q).

Table 1

In vitro anticancer activity results of pyridine-pyrimidine hybrid phosphonate derivatives 4(a–q).

Compound	Ar	IC ₅₀ μM						
		A549	Hep-G2	HeLa	MCF-7	HL-60	LO2	
4a	Phenyl	40.18 ± 0.9	42.06 ± 1.6	32.11 ± 1.2	8.88 ± 1.1	9.02 ± 0.6	ND	
4b	4-Chlorophenyl	24.02 ± 0.4	24.82 ± 1.1	12.01 ± 0.9	6.09 ± 0.4	7.19 ± 1.4	ND	
4c	3,4-Dichlorophenyl	25.02 ± 0.8	24.96 ± 0.4	12.92 ± 1.6	7.07 ± 0.8	8.24 ± 1.1	ND	
4d	4-Fluorophenyl	24.11 ± 0.9	24.88 ± 1.1	12.32 ± 1.4	6.11 ± 0.6	7.23 ± 0.9	ND	
4e	4-Aminophenyl	21.41 ± 1.6	21.46 ± 0.9	10.22 ± 0.4	5.32 ± 0.4	6.39 ± 1.6	ND	
4f	Methylthiazol-5-yl	13.82 ± 1.1	17.99 ± 0.6	6.02 ± 0.8	1.55 ± 0.9	2.32 ± 0.4	74.91 ± 0.9	
4g	Thiophen-3-yl	15.68 ± 1.0	18.76 ± 1.1	7.01 ± 0.9	2.46 ± 1.4	2.99 ± 0.8	ND	
4h	4-Methoxyphenyl	24.32 ± 1.1	24.88 ± 1.6	12.96 ± 1.4	6.42 ± 1.2	7.87 ± 0.6	ND	
4i	Furan-2-yl	15.77 ± 0.8	18.92 ± 0.8	7.16 ± 1.2	3.36 ± 0.6	3.78 ± 1.2	ND	
4j	Pyrazol-5-yl	15.12 ± 0.6	18.60 ± 0.9	6.88 ± 1.2	2.36 ± 1.1	3.01 ± 0.4	83.16 ± 1.1	
4k	Pyridin-4-yl	28.06 ± 0.4	28.46 ± 0.6	18.11 ± 0.4	6.38 ± 0.4	7.22 ± 1.1	ND	
4l	Indol-3-yl	18.21 ± 1.8	19.86 ± 1.2	8.94 ± 1.6	4.66 ± 0.8	4.92 ± 0.4	ND	
4m	Morpholino	29.18 ± 0.9	30.54 ± 0.8	20.32 ± 1.1	6.82 ± 1.2	7.65 ± 0.6	ND	
4n	Piperidin-1-yl	32.62 ± 0.4	34.01 ± 1.6	21.14 ± 0.6	6.86 ± 1.1	8.18 ± 0.4	ND	
4o	Pyrrol-2-yl	13.62 ± 1.6	17.49 ± 1.1	5.81 ± 1.2	1.59 ± 0.4	2.11 ± 0.9	95.33 ± 0.6	
4p	4-Hydroxyphenyl	21.56 ± 0.8	21.59 ± 0.6	10.42 ± 0.8	5.67 ± 0.9	5.98 ± 0.8	ND	
4q	4-Methylphenyl	22.01 ± 1.1	21.88 ± 1.6	10.64 ± 0.4	5.96 ± 1.4	6.75 ± 1.2	ND	
VX-680		15.06 ± 1.8	18.01 ± 1.1	6.24 ± 0.9	1.02 ± 0.4	1.88 ± 0.6	ND	

^aThe IC₅₀ values are the means of at least two experiments; A549: Human lung carcinoma; Hep-G2: Human hepatocellular liver carcinoma cells; HeLa: Human cervical carcinoma epithelial; MCF-7: Human breast cancer cell line; HL-60: human leukemia cell line; LO2: Human normal hepatocyte cell line ND: Not determined.

kinase enzymes is a potential strategy for developing new active chemicals.

The α -aminophosphonates belong to a relevant class of molecules for various pharmacological actions, such as antibiotic,⁴ anticancer agents,^{5,6} herbicide,^{7,8} pesticide,⁹ enzyme inhibitors,^{10–12} peptide mimetic,¹³ antioxidant,¹⁴ antiviral,¹⁵ anti-thrombotic agents,¹⁶ pharmacological agents,¹⁷ anti-HIV agents,¹⁸ anti-inflammatory activities¹⁹ and plant growth regulators.²⁰ AZD1152 is an Aurora Kinase inhibitor

with a phosphonate group in its structure. The structure of AZD1152 gave us an idea of incorporating the phosphonate group into the designed structure for good anticancer activity. The α -amino phosphonates could offer a useful structure for the discovery of new active compounds. To our knowledge, the α -amino phosphonates structure reports good anticancer activity according to literature study.²¹

It was thought of interest to study the combination of pyridine pyrimidine moiety and α - amino phosphonates framework combination

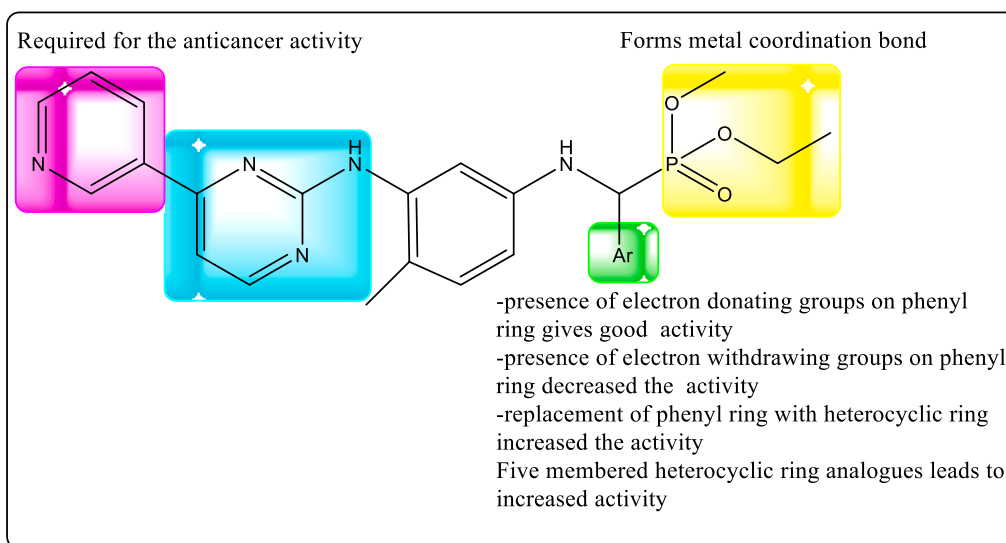


Fig. 2. Structure-activity relationship in pictorial form.

Table 2

Kinase inhibitions of selected compounds (in vitro).

Compound	IC ₅₀ nM ^a	
	Aurora A	Aurora B
4f	33 ± 1.3	15 ± 1.9
4j	15 ± 0.6	12 ± 0.8
4o	42 ± 1.8	22 ± 0.2
VX-680	1.9 ± 0.7	18.6 ± 1.1

^aIC₅₀ values are the means of at least two experiments.

which were probable to reveal an anticancer effect. Hence, after a thorough literature survey on available aurora kinase inhibitors as revealed in Fig. 1, the targeted molecules were designed. A one-pot procedure can minimize chemical waste, save time and simplify the practical aspects.

It's stunning that there's no compound possessing such a molecular skeleton according to the literature to date. In continuation of our recent

work aimed at the synthesis of a variety of heterocyclic systems with exceptional biological importance,²²⁻²⁴ we reported here the synthesis of novel pyridine pyrimidine hybrid phosphonate derivatives 4(a-q) by Kabachnik-Fields method using ceric ammonium nitrate (CAN) as catalyst. Accordingly, seventeen derivatives have been designed and synthesized. Various substituents were introduced to the phenyl ring with the purpose of exploring the influence of substituents on anticancer activity by regulating the electronic and steric effects. Further modifications were performed by introducing various heterocyclic ring systems in place of the phenyl ring.

Novel pyridine pyrimidine hybrid phosphonate derivatives 4(a-q) were synthesized by the Kabachnik-Fields method by reacting 6-methyl-N1-(4-(pyridin-3-yl)pyrimidin-2-yl)benzene-1,3-diamine (1), substituent aldehydes/ heterocyclic aldehydes 2(a-q) and triethylphosphite (3) via a one pot synthetic step in the presence of CAN as a green catalyst.²¹ The green synthesis used to make the title compounds is shown in scheme 1.

All the synthesized novel pyridine-pyrimidine hybrid phosphonate

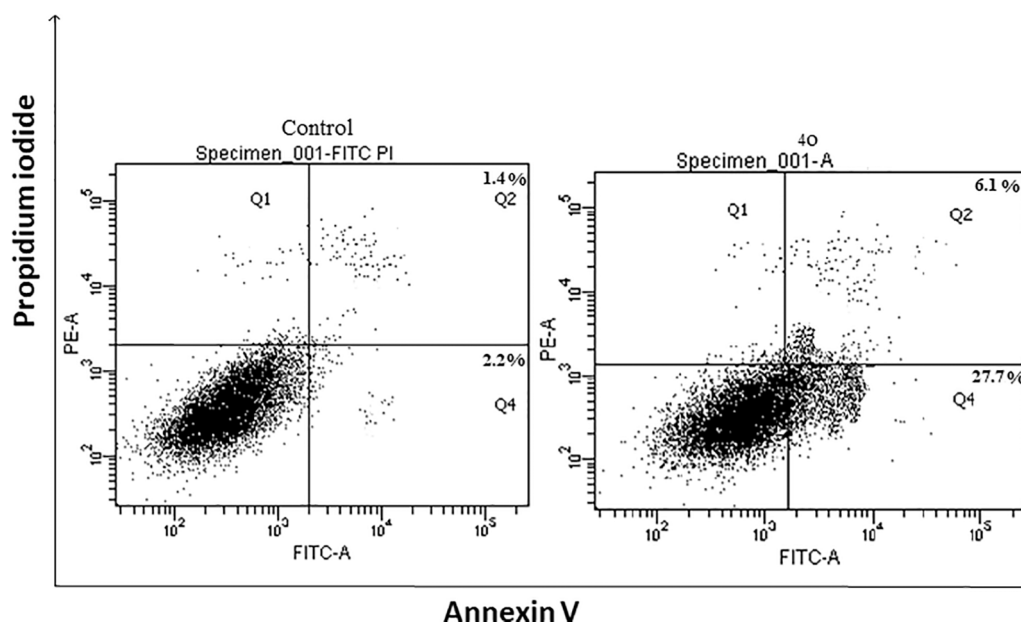


Fig. 3. Apoptosis study by Annexin V/FITC assay of compound 4o.

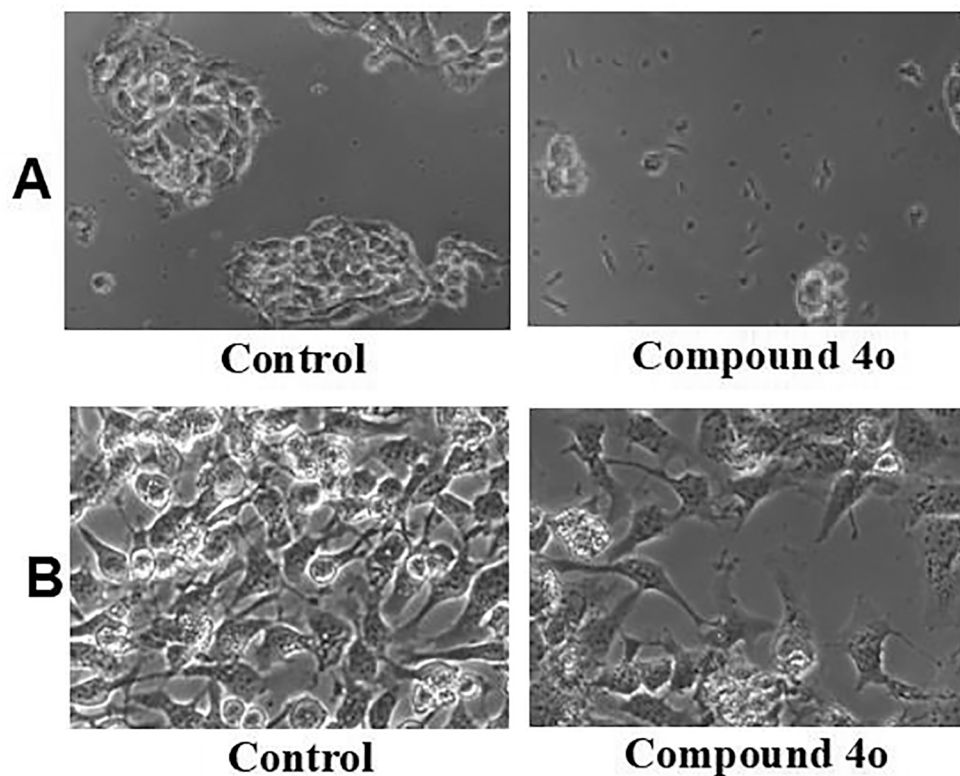


Fig. 4. A. Morphological Changes in Hep-G2 cell line; B. Morphological Changes in HeLa cell line.

derivatives 4(a–q) were allowed to go under evaluation to check their ability to kill cancer cell lines. The cancer cell lines selected for the evaluation are human lung carcinoma A549 cells, human hepatocellular liver carcinoma Hep-G2 cells, human cervical carcinoma epithelial HeLa cells, human breast cancer cell line MCF-7, and human leukemia cell line HL-60 using the MTT assay²⁵. The normal cell line selected was the human normal hepatocyte cell line LO2. The VX-680, an aurora kinase inhibitor, was used as a standard drug for the *in vitro* anticancer evaluation.

As exemplified in Table 1, the majority of the synthesized novel pyridine pyrimidine hybrid phosphonate derivatives 4(a–q) demonstrated moderate-to-excellent potency against five selected cancer cell lines in the μM range, indicating that the combination of pyridine pyrimidine hybrid moiety and α -aminophosphonate framework have good anticancer activity.

The synthesized compound 4o was found to be most potent compared to the other synthesized sixteen derivatives. The compound 4o showed an IC_{50} value of 13.62 μM , 17.49 μM , 5.81 μM , 1.59 μM and 2.11 μM against A549, Hep-G2, HeLa, MCF-7 and HL-60 cancer cell lines respectively. The compound 4j also showed good anticancer activity against selected cancer cell lines. The active compounds 4f, 4j and 4o were also tested on the normal human normal hepatocyte cell line LO2 to check their selectivity towards cancer cell lines. The compound 4o revealed seven times more selectivity towards Hep-G2 cancer cell line compared to human normal hepatocyte cell line LO2 (IC_{50} value 95.33 μM). The compounds 4f and 4j also displayed 5.5 times more selectivity towards Hep-G2 cells when compared with the human normal hepatocyte cell line LO2.

Our primary aim was to explore the anticancer activity of compounds with different substituents on the phenyl ring in order to understand the structure–activity relationship. Later, we replaced the phenyl ring with different heterocyclic ring systems, which included five-membered and six-membered heterocyclic rings. The synthesized compound 4p with an “OH” group on the phenyl ring revealed 21.56 μM , 21.59 μM , 10.42 μM , 5.67 μM and 5.98 μM *in vitro* anticancer

activity against A549, Hep-G2, HeLa MCF-7, and HL-60, respectively. The synthesized compound 4b with a “Cl” group on the phenyl ring revealed 24.02 μM , 24.82 μM , 12.01 μM , 6.09 μM and 7.19 μM *in vitro* anticancer activity against A549, Hep-G2, HeLa, MCF-7 and HL-60 respectively. We can state that the introduction of electron-donating groups (EDGs) on phenyl ring exhibited a positive effect on the anti cancer activity on the selected cancer cell lines, such as compounds 4e, 4p, and 4q. By contrast, electron-withdrawing groups (EWGs) exhibited a negative effect in compound such as 4b, 4c, 4d, and 4h.

Generally, five-membered ring system analogs (4f, 4g, 4i, 4j and 4o) were more active than corresponding six-membered analogs (4k, 4m, and 4n). It was also observed that the compound 4l with the indole ring as a substituent gave good anticancer activity when compared with six-membered analogs (4k, 4m, and 4n). Fig 2 enlightens the structure–activity relationship in pictorial form.

The synthesized compounds 4f, 4j, and 4o, which had shown good anticancer activity as per the MTT assay data, were further tested to predict their mechanism of action. They were evaluated to check their ability to inhibit aurora kinase. The standard drug used during this evaluation is VX-680. The inhibition activity against Aurora enzymes was performed by the Kinase-Glo luminescent kinase assay *in vitro*.²⁶ The results obtained after evaluation are represented in Table 2. Compound 4o was found to be a potent aurora kinases inhibitor with an IC_{50} value of 42 nM and 22 nM against Aurora kinase A and Aurora kinase B, respectively. The results of the Aurora kinase inhibitory activities suggest that the synthesized compounds exert their antitumor activity by inhibiting the aurora kinase enzyme.

Apoptosis, autophagy and necrosis are the major types of cell death. Apoptosis, or programmed cell death, is a normal physiologic process for removal of unwanted cells. The synthesized compound 4o was selected to test whether it has the ability to induce apoptosis in cancer cell lines. The ability of synthesized compound 4o to induce apoptosis was determined using an Annexin V (conjugated to FITC) apoptosis detection kit.²⁷ From Fig.3, it is clear that the compound 4o have induced early apoptosis and late apoptosis of 27.7% and 6.1% respectively **086**

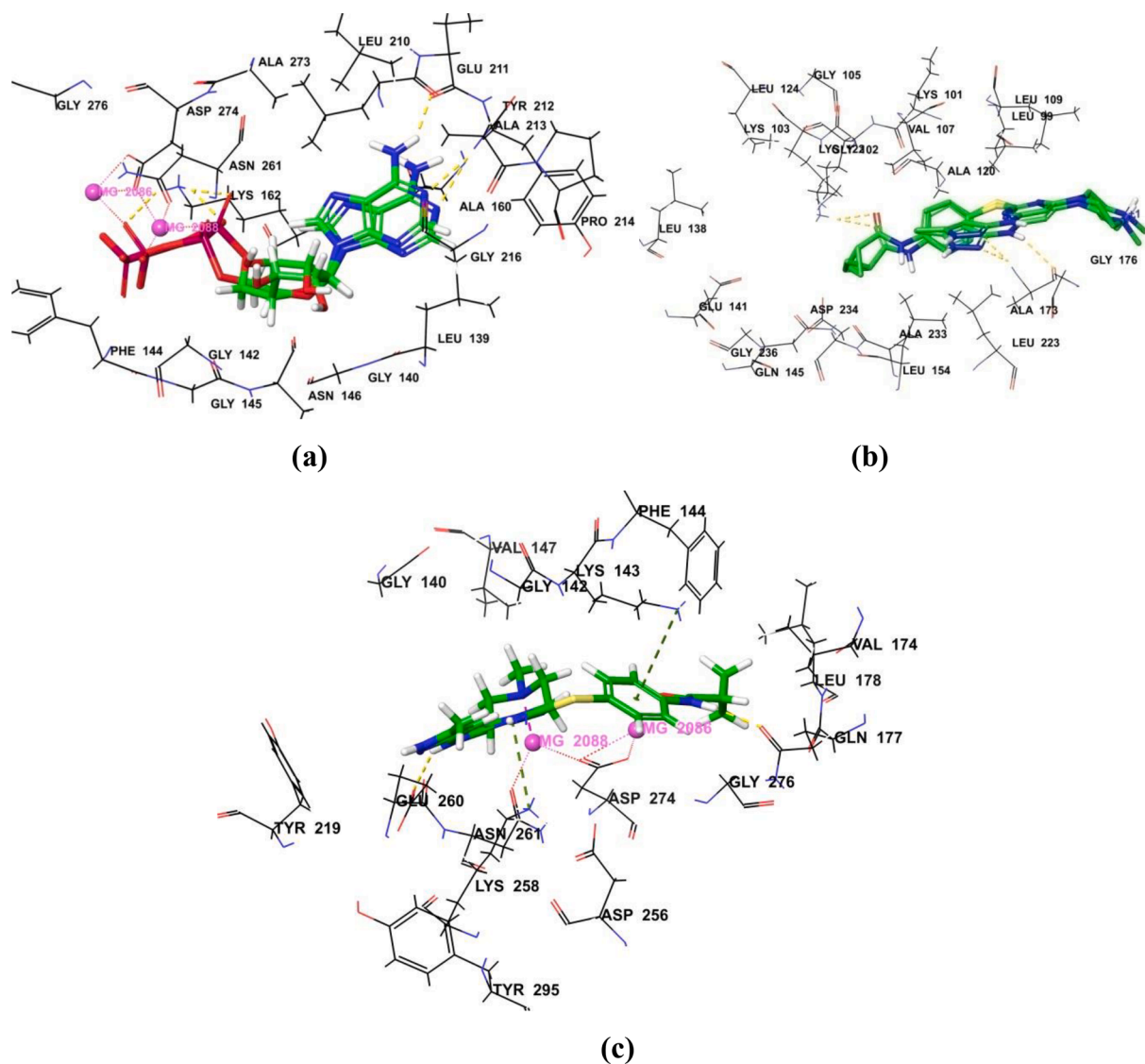


Fig. 5. (a) Superimposition of docked pose of compound **ADP** over its crystal structure (enzyme bound conformer) in the active site of enzyme **Aurora kinase A**, (b) Superimposition of docked pose of compound **VX-680** over its crystal structure (enzyme bound conformer) in the active site of **Aurora kinase B**. (c) Docked pose of **VX-680** in active site of enzyme **Aurora kinase A**. Yellow colored dotted line indicate H-bond interaction, purple colored dotted line indicates metal coordination and Green colored dotted line indicates pi-pi stacking. (For interpretation of the references to colour in this figure legend, the reader is referred to the web version of this article.)

comparison with control with early apoptosis of 2.2% and late apoptosis of 1.4%.

Cell morphology was experiential at the IC_{50} concentration of the synthesized compounds **4(a-q)** and photographs were taken under a Nikon Eclipse Ti-S Inverted Research Microscope and the images were processed using the NIS-Elements software. The images of the in vitro anticancer activity of the active compounds **4o** on the Hep-G2 and HeLa cancer cell lines are shown in **Figures 4A and 4B** respectively. At the IC_{50} concentration of the potent compound **4o**, the distinct morphological changes such as cell detachment, cell wall deformation, cell shrinkage, and a reduction in the number of viable cells were seen in Hep-G2 cancer cells, as shown in **(Fig. 4 A)**. From **Figure 4B**, it can be concluded that in HeLa cancer cell lines, at the IC_{50} concentration of the most active compound **4o**, there have been distinct morphological changes such as cellular detachment, cell wall deformation, cell shrinkage, and a decreased number of viable cells as compared to control cells.

The docking studies were performed on Aurora kinase A (PDB ID: 1MQ4) and Aurora kinase B (PDB ID: 4B8M) respectively using Smina molecular docking software.²⁸ Smina is the fork of AutoDock Vina and is

customized to better support scoring function development and high-performance energy minimization. The docking methodology was validated by redocking the inbound ligands **ADP** and **VX-680**, placed in the active site of Aurora kinase A and Aurora kinase B enzymes, respectively.^{29,30} The RMSD value was then calculated by superimposing the docked pose of the bound ligand over its crystal form conformer (**Fig 5**). The RMSD value was found to be 1.25 Å and 0.725 Å for Aurora kinase A and Aurora kinase B respectively.

The docked poses of synthesized compounds were compared with that of the standard molecule **VX-680**. The docking score of synthesized compounds was found to be in the range of -8.86 to -4.34 for Aurora kinase A and -6.08 to -4.09 for Aurora kinase B (**Table S1**). Among all the docked compounds, the compounds **4o** and **4j** were found to have the highest binding affinity for both enzymes.

All synthesized molecules were found to interact with the enzymes via hydrogen bond interactions with various amino acid residues. The main amino acid residues of Aurora A kinase which were involved in the hydrogen bonding with synthesized compounds are Lys 141, Lys 143, Lys 162, Ala 213, and Glu 260 (**Fig. 6**). Similarly, the key Aurora **087**

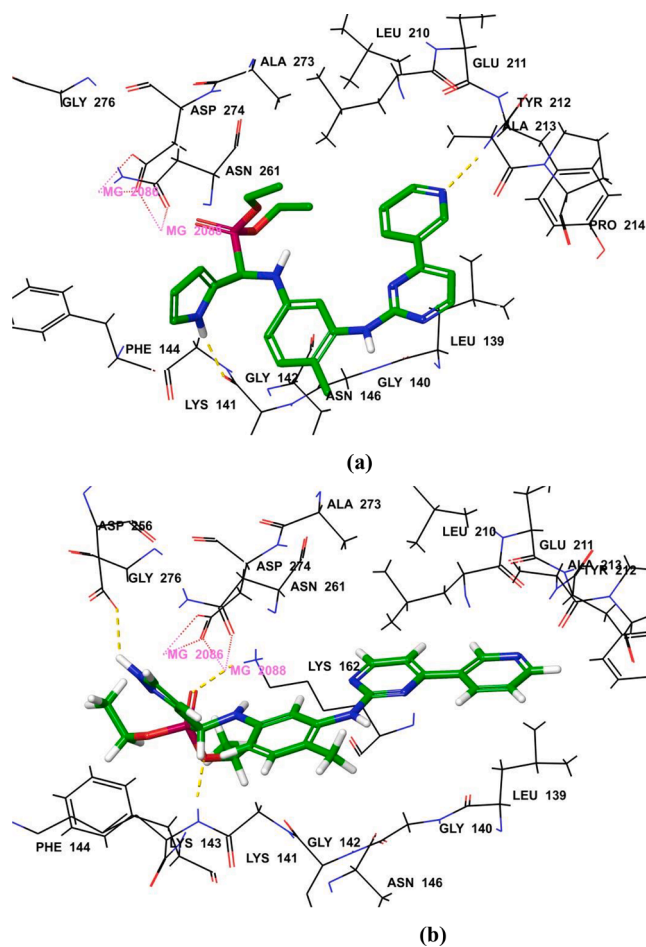


Fig. 6. Docked pose of compounds (a) **4o** and (b) **4j** in the active site of enzyme **Aurora kinase A**. Yellow colored dotted line indicate H-bond interaction and purple colored dotted line indicates metal coordination. (For interpretation of the references to colour in this figure legend, the reader is referred to the web version of this article.)

kinase amino acid residues involved in hydrogen bonding are Glu 171, Lys 122, Ala 173, and Asp 234 (Fig. 7). However, the synthesized compounds in the active site of Aurora A kinase also formed metal coordinate bonds with Mg^{2+} ions which support the stability of ligand-enzyme complex.

In conclusion, the novel series of pyridine pyrimidine hybrid phosphonatederivatives **4(a-q)** were synthesized by the Kabachnik-Fields method using CAN as green catalyst. The synthesized novel derivatives were allowed to undergo in vitro anticancer activity testing. The structure-activity relationship (SAR) was discussed, and the results confirmed that the most promising compounds **4o** and **4f** showed the most potent anticancer activity against selected cancer cell lines. The compound **4j** has also shown good anticancer activity. Taken together, the data of in vitro anticancer activity, in vitro enzyme assay and molecular docking study, compound **4o** is a potential anticancer agent by targeting Aurora kinase.

Declaration of Competing Interest

The authors declare that they have no known competing financial interests or personal relationships that could have appeared to influence the work reported in this paper.

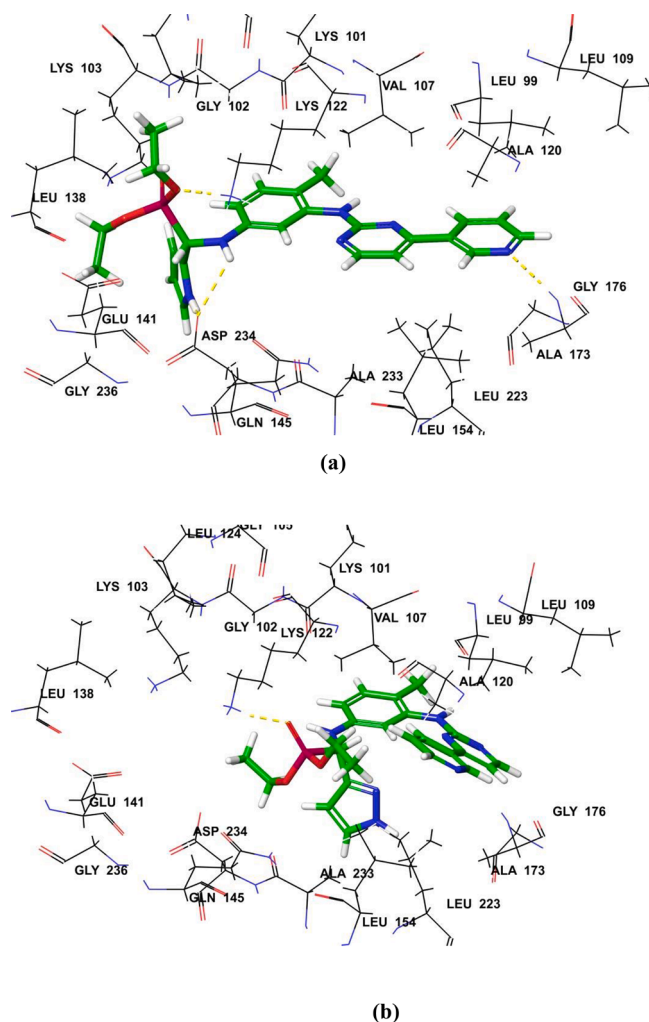


Fig. 7. Docked pose of compounds (a) **4o** and (b) **4j** in the active site of enzyme **Aurora kinase B**. Yellow colored dotted line indicate H-bond interaction and purple colored dotted line indicates metal coordination. (For interpretation of the references to colour in this figure legend, the reader is referred to the web version of this article.)

Acknowledgement

Author S.V. T. is thankful to Swami Ramanand Teerth Marathwada University, Nanded-431606, Maharashtra, India for the minor research project (APDS/Uni.MRP/Sci. & Tech.-Micro./2019-20/2827).

Appendix A. Supplementary data

Supplementary data to this article can be found online at <https://doi.org/10.1016/j.bmcl.2022.128747>.

References

- Bray F, Ferlay J, Soerjomataram I, Siegel RL, Torre LA, Jemal A. Global cancer statistics 2018: GLOBOCAN estimates of incidence and mortality worldwide for 36 cancers in 185 countries. *CA Cancer J Clin.* 2018;68:394–424.
- Li JJ, Li SA. Mitotic kinases: the key to duplication, segregation, and cytokinesis errors, chromosomal instability, and oncogenesis. *Pharmacol Ther.* 2006;111: 974–984.
- (a) ChiacchioAM ID, Romeo R, Giofrè VS, Legnani L. Pyridine and pyrimidine derivatives as privileged scaffolds in biologically active agents. *Curr Med Chem.* 2019; 26:7166–7195.(b) Dofe VS, Sarkate AP, Shaikh ZM, Jadhav CK, Nipte AS, Gill CH. Ultrasound assisted synthesis of novel pyrazole and pyrimidine derivatives as antimicrobial agents. *J Heterocycl Chem.* 2018;55:756–762.

- 4 Atherton FR, Hassall CH, Lambert RW. Synthesis and structure-activity relationships of antibacterial phosphonopeptides incorporating (1-aminoethyl)phosphonic acid and (aminomethyl)phosphonic acid. *J Med Chem.* 1986;29:29–40.
- 5 Lajczak B, Kafarski P, Sztajer H, Mastalerz P. Antibacterial activity of phosphono dipeptides related to alafosfalin. *J Med Chem.* 1986;29:2212–2217.
- 6 Kafarski P, Lejezak B. Aminophosphonic acids of potential medical importance. *Curr Med Chem Anti-Cancer Agents.* 2001;1:301–312.
- 7 Yong SL, Da QJ, Eun JK, et al. Asiatic acid, a triterpene, induces apoptosis through intracellular Ca^{2+} release and enhanced expression of p53 in HepG2 human hepatoma cells. *Canc Lett.* 2002;186:83–91.
- 8 Maier L. Organic Phosphorus compounds 91.1 synthesis and properties of 1-amino-2-arylethylphosphonic and-phosphinic acids as well as -phosphine oxides. *Phos Sul Sil Relat Elem.* 1990;53:43–67.
- 9 Che JY, Xu YZ X, Tang LY, Gu C, Shi DQ. Synthesis and herbicidal activity evaluation of novel α -amino phosphonate derivatives containing a uracil moiety. *Bioorg Med Chem Lett.* 2016;26:1310–1313.
- 10 Occhipinti A, Berlicki L, Giberti S, Dziedzic G, Kafarski P, Forlani G. Effectiveness and mode of action of phosphonate inhibitors of plant glutamine synthetase. *Pest Manage Sci.* 2010;66:51–58.
- 11 Srinivasulu D, Reddy MVB, Rajasekar D, Balaji M, Nagaraju C. Design, synthesis and antimicrobial activity of α -aminophosphonates of quinoline and their molecular docking studies against DNA Gyrase A. *Lett Drug Des Dis.* 2013;10:967–976.
- 12 Grzywa R, Sienczyk M. Phosphonic esters and their application of protease control. *Curr Pharm Des.* 2013;19:1154–1178.
- 13 Allen MC, Fuhrer W, Tuck B, Wade R, Wood JM. Renin inhibitors. Synthesis of transition-state analog inhibitors containing phosphorus acid derivatives at the scissile bond. *J Med Chem.* 1989;32:1652–1661.
- 14 Kafarski P, Lejczak B. Biological activity of aminophosphonic acids. *Phos Sul Sil Relat Elem.* 1991;63:193–215.
- 15 (a) Rao AJ, Rao PV, Rao VK, Mohan C, Raju CN, Reddy CS. Microwave Assisted One-pot Synthesis of Novel α -Aminophosphonates and their Biological Activity. *Bull Kor Chem Soc.* 2010;31:1863–1868. (b) Jadhav SA, Shioorkar MG, Chavan OS, Sarkate AP, Shinde DB. Rapid and efficient one pot microwave assisted synthesis of 2-phenylimidazo[1,2-a]pyridines and 2-phenylimidazo[1,2-a]quinoline in Water-PEG-400. *Syn Comm.* 2017;47:285–290. (c) Dofe VS, Sarkate AP, Shaikh ZM, Gill CH. Ultrasound mediated synthesis of novel 1,2,3-triazole based pyrazole and pyrimidine derivatives as antimicrobial agents. *J Het Chem.* 2017;54:3195–3201. (d) Bhosle MR, Khillare LD, Mali JR, Sarkate AP, Lokwani DK, Tiwari SV. DIPEAc promoted one-pot synthesis of dihydropyrido[2,3-d:6,5-d']dipyrimidinetetraone and pyrimido[4,5 d] pyrimidine derivatives as potent tyrosinase inhibitors and anticancer agents: in vitro screening, Molecular docking and ADMET predictions. *N J Chem.* 2018;42:18621–18632.
- 16 Xu Y, Yan K, Song B, et al. Synthesis and antiviral bioactivities of α -aminophosphonates containing alkoxyethyl moieties. *Molecules.* 2006;11:666–676.
- 17 Meyer JH, Barlett PA. Macrocyclic inhibitors of penicillopepsin. 1. Design, synthesis, and evaluation of an inhibitor bridged between P1 and P3. *J Am Chem Soc.* 1998;120:4600–4609.
- 18 Aziz N, Saidi MR. Synthesis of tertiary α -amino phosphonate by one-pot three-component coupling mediated by LPDE. *Tetrahedron.* 2003;59:5329–5332.
- 19 (a) Bhattacharya AK, Rana KC, Pannecouque C, De Clercq E. An efficient synthesis of a hydroxyethylamine (HEA) isostere and its α aminophosphonate and phosphoramidate derivatives as potential anti HIV agents. *Chem Med Chem.* 2012;7:1601–1611. (b) Doherty W, Adler N, Knox A, et al. Synthesis and evaluation of 1,2,3-triazole-containing vinyl and allyl sulfones as anti-trypanosomal agents. *Eur J Org Chem.* 2017;1:175–185.
- 20 Sujatha B, Mohan S, Subramanyam C, Rao P. Microwave-assisted synthesis and anti-inflammatory activity evaluation of some novel α -aminophosphonates. *Phos Sul Sil Relat Elem.* 2017;192:1110–1113.
- 21 Tiwari SV, Sharif NS, Gajare RI, et al. New 2-oxoindolin phosphonates as novel agents to treat cancer: a green synthesis and molecular modeling. *Molecules.* 2018;23:1981.
- 22 Chate AV, Tagad PA, Bondle GM, Sarkate AP, Tiwari SV, Azad R. Design, synthesis and biological evaluation of tetrahydrodibenzo[b, g][1,8]naphthyridinones as potential anticancer agents and novel aurora kinases inhibitors. *Chemistry Select.* 2021;6:3444.
- 23 (a) Nikalje APG, Tiwari SV, Sangshetti JN, Damale MD. Ultrasound-mediated synthesis, biological evaluation, docking and in vivo acute oral toxicity study of novel indolin-2-one coupled pyrimidine derivatives. *Res Chem Intermed.* 2018;44:3031–3059. (b) Chate AV, Redlawar AA, Bondle GM, Sarkate AP, Tiwari SV, Lokwani DK. A new efficient domino approach for the synthesis of coumarin-pyrazolines as antimicrobial agents targeting bacterial D-alanine-D-alanine ligase. *N J Chem.* 2019;43:9002–9011.
- 24 Nikalje APG, Gawhane PA, Sangshetti JN, Damale MD. Ultrasound promoted green synthesis, docking study of indole spliced thiadiazole, α -amino phosphonates as anticancer agents and anti-tyrosinase agents. *Anti-Cancer Agents in Med Chem (Formerly Current Medicinal Chemistry - Anti-Cancer Agents).* 2018;18:1267–1280.
- 25 (a) Dofe VS, Sarkate AP, Azad R, Charansingh HG. Novel quinoline-based oxadiazole derivatives induce G2/M arrest and apoptosis in human breast cancer MCF-7 cell line. *Res Chem Interme.* 2017;43:7331–7345. (b) Chate AV, Kamdi SP, Bhagat AV, et al. Design, synthesis and SAR study of novel spiro[pyrimido[5,4-b]quinoline-10,5'-pyrrolo[2,3-d]pyrimidine] derivatives as promising anticancer agents. *J Het Chem.* 2018;55:2297–2302.
- 26 Wang W, Feng X, Liu HX, Chen SW, Hui L. Synthesis and biological evaluation of 2,4-disubstituted phthalazinones as Aurora kinase inhibitors. *Bioorg Med Chem.* 2018;26:3217–3226.
- 27 Abdelhaleem EF, Abdelhameid MK, Kassab AB, Kandeel MM. Design and synthesis of thienopyrimidine urea derivatives with potential cytotoxic and pro-apoptotic activity against breast cancer cell line MCF-7. *Eur J Med Chem.* 2018;143:1807–1825.
- 28 Koes DR, Baumgartner MP, Camacho CJ. Lessons learned in empirical scoring with smina from the csar 2011 benchmarking exercise. *J Chem Inform Model.* 2013;53:1893–1904.
- 29 (a) Tiwari SV, Seijas JA, Vazquez-Tato MP, Sarkate AP, Karnik KS, Nikalje APG. Ionic liquid promoted synthesis of novel chromone-pyrimidine coupled derivatives, antimicrobial analysis, enzyme assay. *Docking Study Tox Study Mol.* 2018;23:440. (b) Tiwari SV, Siddiqui S, Seijas JA, et al. Microwave-assisted facile synthesis, anticancer evaluation and docking study of N-(5-(substituted methylene amino)-1,3,4-thiadiazol-2-yl)methyl benzamide derivatives. *Molecules.* 2017;22:995.
- 30 Lokwani D, Azad R, Sarkate AP, Reddanna P, Shinde D. Structure based library design (SBLD) for new 1,4-dihydropyrimidine scaffold as simultaneous COX-1/COX-2 and 5-LOX inhibitors. *Bioorg Med Chem.* 2015;23:4533–4543.



Monthly Publication
Price per Copy Rs. 75/-
LICENSED TO POST WITHOUT PREPAYMENT
LICENCE NO. MR/Tech/WPP-338/West/2021-23
RNI REGN. NO. 11547/1963
REGN.NO.MCW/98/2021-23
ISSN 0019-462X

INDIAN DRUGS

Vol. 59 Issue No. 02 (Pages: 76) FEBRUARY 2022

SCIENTIFIC & RESEARCH PUBLICATION FROM
INDIAN DRUG MANUFACTURERS' ASSOCIATION

Pharmaceutical Chemistry

Pharmacognosy,
Natural Products &
Phytochemistry

Biotechnology

Pharmaceutics

Pharmaceutical Analysis

Pharmacology

ATTENTION ALL AUTHORS!

INDIAN DRUGS *journal is online.*

ALL SUBMISSIONS OF REVIEW ARTICLES,
ORIGINAL RESEARCH PAPERS, SHORT COMMUNICATIONS ETC FOR
INDIAN DRUGS WILL ONLY BE ACCEPTED VIA OUR ONLINE PORTAL

www.indiandrugsonline.org

The online process will speed up the review and publication process.

Authors can submit their article for peer scrutiny by registering and creating an account.

The account can be used to submit any number of original papers for publication in

'**INDIAN DRUGS**' Journal.

*In case of any difficulty in registering, please contact by
email: publications@idmaindia.com or call: 022-24944624 / 24974308.*



090



C O N T E N T S

Editorial..... 5

REVIEW ARTICLE

- **Lead Phytomolecules for Hepatoprotective Drug Development**
Krishn K. Agrawal and Yogesh Murti 7

ORIGINAL RESEARCH ARTICLES

- **Design, Synthesis and Evaluation of Novel Azetidinonyl/Formazonyl/Thiazolidinonylphenothiazines as Potential Anti-Inflammatory Agents**
Archana, Sakshi Chaudhary and Nancy 27
- **Analytical Standardization and Profiling of Ayush-64: An Ayurvedic Tablet Formulation**
Sarang J. Deshpande, Prakash N. Kendre and Abhishek R. Patle 36
- **Evaluation of Radical Scavenging Activity and Proliferative Activity of Herbal Decoction on Cultured Cardiac Cells**
Mangalagowri A. and Priya S. 43
- **Analytical Method Development and Validation of a Novel HPTLC (METHOD) for the Simultaneous Estimation of Berberine, Gallic Acid, Quercetin and Piperine in a Polyherbal Formulation**
Shivani A. Vaidya, Rishikesh R. Kshirsagar, Kirti S. Laddha and Vandana N. Jain 47
- **Simultaneous Estimation of Impurities in Melatonin by RP-HPLC Method Coupled with Diode Array Detection**
Shubhangi Sutar, Veerendra C. Yeligar, Prafulla B. Choudhari and Sachinkumar Patil 52
- **Microbiological and AntibioGram Study of Bacterial Pathogens Associated with Bovine Mastitis in and Around Meerut**
Harshit Verma, Amit Kumar, Prabhat Kumar, Surendra Upadhyay, Anamika Bhardia and Jitender Singh..... 58

SHORT COMMUNICATIONS

- **Stability Indicating RP-HPLC Method Development and Validation of Meropenem and Vaborbactam In Pharmaceutical Dosage form**
Prasanthi T., Lakshmana Rao A. and Mohana Rao B. 64
- **Microsphere and Tablet in Capsule System: A Novel Chronotherapeutic System of Diclofenac Sodium for Site and Time Specific Delivery**
Lalita Palariya, Sweta Bawari and Archana N. Sah 68

Recent Publications From Indian Patent Office Journal With PCT/WIPO Number 71



INDIAN DRUG MANUFACTURERS' ASSOCIATION

102-B, 'A-Wing', Poonam Chambers, Dr. A.B. Road, Worli, Mumbai - 400 018, India

Tel : 022-2494 4624 / 2497 4308 Fax: 022-2495 0723

E-mail: publications@idmaindia.com, Website: www.idma-assn.org / www.indiandrugsonline.org

(C) Copyright: No part of this publication may be reproduced by any means without prior written permission of the publisher.

- Annual Subscription (India) - For members: ₹ 1000/-. For bonafide students: ₹ 1000/-. For Govt Research/Educational Institutions: ₹2000/-
For non-members: ₹ 4000/-. Price per copy: ₹ 75/- only. (Foreign US\$ 25) Annual Subscription (Foreign): US\$ 400.
- All payments to be made in favour of **Indian Drug Manufacturers' Association, Payable at Mumbai.**

ABSTRACTED BY:

Scopus, EMBASE, International Pharmaceuticals Abstracts, Genamics JournalSeek, EBSCO, CiteFactor, OCLC Worldcat, Scimago, Journal Guide, TDNet, Science Library Index, DRJI, CCC (Infotrieve), Index Copernicus, Electronic Journals Library, Sherpa/Romeo, ResearchBib, Indian Citation Index, i-Journals, i-Focus, ResearchGate, Russian Science Index, PharmaPendium, Cabells, Scilit, Dimensions, COSMOS (Germany), MIAR (Universitat de Barcelona).

Listed in Journals approved by UGC for CAS & Appointment of University Teachers

ANALYTICAL STANDARDIZATION AND PROFILING OF AYUSH-64: AN AYURVEDIC TABLET FORMULATION

Sarang J. Deshpande^a, Prakash N. Kendre^{b*} and Abhishek R. Patle^c

(Received 16 October 2020) (Accepted 15 June 2021)

ABSTRACT

Success of any healthcare product is based on its performance, which is further dependent upon the quality of the product. Quality of the polyherbal ayurvedic formulation is assured by developing proper analytical standards with the help of the guidelines provided by CCRAS (Central Council for Research in Ayurvedic Sciences), which will also ensure its authentication. Ayush-64 is a polyherbal formulation and its analytical standards were developed for various parameters like organoleptic properties, physical-chemical and chromatographic profiling etc. These standards were developed by studying and analyzing three batches of self-manufactured Ayush-64 tablets with the help of good manufacturing practices (GMP). These parameters were found to be sufficient to standardize and authenticate the quality of the formulation, which can be used further as a reference standard for quality control and quality assurance of the final product.

Keywords: Ayush-64 tablets, CCRAS, Standardization, Polyherbal formulation

INTRODUCTION

Ayush-64 is an antimalarial tablet invented and patented by CCRAS. It's a polyherbal tablet, widely used in treatment of malaria and allied fevers. In the past 80-100 years chemically synthetic products have been researched and manufactured in a very widespread revolutionary manner and still most of the population in the world relies on traditional health care practitioners for their day to day primary healthcare. Most of the populations of Indian and African sub-continent are using the traditional healthcare measures to meet their health requirements¹.

Commercialization of ayurvedic pharmacies in the past era with pharmaceutical practices of Ayurved drugs according to ancient methods created a need of quality and standardization². Standardization ensures quality and therapeutic effect of a product. Ayurvedic/herbal product cannot be considered as suitable or valid for medicinal use unless it proves the reproducibility of batch-to-batch manufacturing³. The present study reports on evaluating the analytical standards of polyherbal Ayush-64 tablets based on organoleptic properties, physico-chemical characterization and chromatographic

profiling. Standardization of such ayurvedic products can be carried out using GMP (Good Manufacturing Practices) and GLP (Good Laboratory Practices) guidelines⁴⁻⁶. The present study was successfully conducted at Unijules Life Sciences Ltd. Nagpur (MS), India, a WHO-GMP approved Ayurvedic Pharmaceutical Company. All the chemicals used in the experimentation were of analytical grade and procured from Merck Specialties Pvt. Ltd. Mumbai (India).

MATERIALS AND METHODS

Ayush-64 tablet formulation was developed as per the composition (Table I) and procedure described by CCRAS (Central Council for Research in Ayurvedic Sciences). All the required ingredients were procured from authentic sources in Nagpur region. The quality and authenticity of all the ingredients was ensured as per the analytical specifications of API (Ayurvedic Pharmacopoeia of India) at quality control laboratory of Unijules Life Sciences⁷. A separate *kashay* (decoction) of all the three items was made and *ghanasatva* (concentrated extract) was obtained. Formulation of Ayush-64 tablet was prepared by accurately weighing all the ingredients. One part each of ghanasatva was mixed with two parts of powder of *Caesalpinia bonducella* (Latakaranj). Finally, tablets were prepared by wet granulation method, each

^a Department of Ayurveda, Vijyashree Ayurved College and Hospital, JDA Scheme No.41/65, Vijay Nagar, Behind MPSEB Substation, Basha Jabalpur - 482 002, Madhya Pradesh, India

^b Department of Pharmaceutics, Rajarshi Shahu College of Pharmacy, Buldana – 443 001, Maharashtra, India

^c Quality Control Dept, Unijules Life Sciences Ltd., MIDC Industrial Area, Kalmeshwar, Nagpur – 441 501, Maharashtra, India

*For Correspondence: E-mail: drsarangdeshpande@gmail.com

<https://doi.org/10.53879/id.59.02.12757>

weighing 500 mg along with all necessary excipients using 10 mm round shape punches⁸. The exact composition of Ayush-64 is given in following Table I.

Table I: Composition of Ayush-64 ayurvedic tablet formulation

Sr. No.	Name of key ingredient	Quantity
1.	<i>Swertia Chirayata</i> (Chirayata) ghan	1 part
2.	<i>Alstonia scolaris</i> (Saptaparni) ghan	1 part
3.	<i>Picrorrhiza kurroa</i> (Kutki) ghan	1 part
4.	<i>Caesalpinia crista</i> (Latakaranj) powder	2 parts

*Note: All the batches contain compatible excipients in appropriate quantities

The procedure was repeated and three batches of tablets (S-1, S-2 and S-3) were formulated. The prepared tablets were analyzed and compared for organoleptic, physio-chemical and chromatographic characteristics.

Organoleptic properties of all the three batches were analyzed on the basis of procedures described by Siddique *et al.*⁹. All the physical-chemical parameters were analyzed as per the procedures described in Ayurvedic Pharmacopeia of India.

Total ash content of all the three batches was determined by incinerating 2 g of accurately weighed sample in a previously ignited and tarred silica crucible at a temperature not exceeding 450 °C. The samples were heated until free from carbon particles and then cooled to room temperature and kept in a desiccator till further study. The ash was then weighed and percentage ash content was determined using following equation (1):

$$\% \text{ Ash Content} = \frac{\text{Weight of ash}}{\text{Weight of original sample}} \times 100 \quad (1)$$

Obtained ash was boiled with 25 mL of dilute hydrochloric acid for 5 min and insoluble matter was collected on dust and particle free filter paper. The ash was then washed with hot water and ignited to constant

weight. This acid insoluble ash percentage was calculated with reference to the air-dried drug.

Alcohol soluble extractive was determined by macerating 5 g of air dried coarsely powdered drug with 100 mL alcohol of specified strength in a closed flask with frequent shaking during first 6 h. The flask was then allowed to stand for eighteen hours and mixture was then filtered rapidly preventing loss of solvent. About 25 mL of filtrate was evaporated to dryness in a tared flat-bottomed petri dish at 105 °C to constant its weight. Finally, the percentage of alcohol-soluble extractive was calculated with reference to the air-dried drug. The same process was repeated using water by replacing the alcohol and extractive value was determined for all three samples¹⁰.

Evaluation of powdered drug

The powdered drug materials were evaluated for physical properties like bulk density, tapped density, Hausner's ratio and flow properties etc.

Bulk and tapped density were determined by using bulk density apparatus. Accurately weighed (100 g) powdered material was poured in previously calibrated measuring cylinder and reading mark was noted. This measuring cylinder was then tapped on the intact surface of rubber at the distance of 2.5 cm for 100 times and final reading mark on the cylinder was noted and finally, the bulk density and tapped density was calculated using following equations (2 & 3):

$$\text{Bulk Density} = \frac{\text{Bulk Volume}}{\text{Mass of Powdered Drug}} \quad (2)$$

$$\text{Tapped Density} = \frac{\text{Tapped Volume}}{\text{Mass of Powdered Drug}} \quad (3)$$

Based on the results of bulk density and tapped density, Hausner's ratio was determined using another equation (5):

$$\text{Hausner's ratio} = \frac{\text{Tapped Density}}{\text{Bulk Density}} \quad (4)$$

Table II: Bulk density, tapped density, Hausner's ratio and Carr's index values of Ayush-64 tablet formulations

Sr. No.	Test Parameter	Sample (S-1)	Sample (S-2)	Sample (S-3)	Average
1.	Bulk density	0.6698 g cc ⁻¹	0.6721 g cc ⁻¹	0.6742 g cc ⁻¹	0.6720 g cc ⁻¹
2.	Tap density	0.8373 g cc ⁻¹	0.8456 g cc ⁻¹	0.8498 g cc ⁻¹	0.8442 g cc ⁻¹
3.	Carr's index	0.20 %	0.21 %	0.21 %	0.20 %
4.	Hausner's ratio	1.25	1.2581	1.2604	1.2561

Table III: Physical-chemical properties of Ayush-64 tablet formulation

Sr. No.	Test parameter	Sample (S-1)	Sample (S-2)	Sample (S-3)	Average
1.	Color	Dark-blackish brown color	Dark-blackish brown color	Dark-blackish brown color	Dark-blackish brown color
2.	Odor	Characteristic odor	Characteristic odor	Characteristic odor	Characteristic odor
3.	Taste	Bitter taste	Bitter taste	Bitter taste	Bitter taste
4.	Shape of tablet	Circular. Flat uncoated tablet	Circular. Flat uncoated tablet	Circular. Flat uncoated tablet	Circular. Flat uncoated tablet
5.	Diameter (mm)	10.18	10.20	10.29	10.22
6.	Thickness (mm)	4.20	4.22	4.21	4.21
7.	Hardness (Kg cm ⁻²)	2.5	2.5	3.0	2.66
8.	Friability (%)	0.12	0.21	0.15	0.16
9.	Weight variation (%)	0.50	0.4	0.44	0.446
10.	Disintegration time (minute)	9	12	10	10.33
11.	Loss on drying (%)	2.37	2.34	2.36	2.35
12.	Water soluble extractives (%)	39.02	-38.42	38.10	38.51
13.	Alcohol soluble extractives (%)	27.14	28.10	28.44	27.89
14.	Total Ash (%)	5.03	5.63	5.23	5.29
15.	Acid insoluble ash (%)	2.84	2.74	2.79	2.79
16.	pH	4.59	4.66	4.39	4.54

Table IV: Standard physical-chemical parameters of Ayush-64 tablet formulation

Sr. No.	Parameter	Standard value
1.	Color	Dark-blackish brown color
2.	Odor	Characteristic odor
3.	Taste	Bitter taste
4.	Shape of tablet	Circular. Flat uncoated tablet
5.	Diameter (mm)	10 to 10.25
6.	Thickness (mm)	4 to 4.5
7.	Hardness (Kg cm ⁻²)	2 to 4
8.	Friability (%)	NMT 1
9.	Weight variation (%)	NMT 1
10.	Disintegration time (min)	NMT 15
11.	Loss on drying (%)	NMT 3
12.	Water soluble extractives (%)	NLT 34
13.	Alcohol soluble extractives (%)	NLT 25
14.	Total Ash (%)	NMT 6
15.	Acid insoluble Ash (%)	NMT 3
16.	pH	4 to 5

Obtained results were compared with standard values of Hausner's ratio as given in the pharmacopeia (Hausner's ratio <1.25 suggest good flow of material whereas ratio between 1.25 to 1.50 suggest moderate flow and >1.50 suggests poor flow powdered material).

Based on the observed values, the flow properties were improved by adding suitable lubricant at an appropriate amount.

Evaluation of Ayush-64 tablets

All the three batches of tablets were evaluated for physical parameters like, thickness, hardness, friability, disintegration and weight variation as per the Pharmacopeial standards.

Thickness of all the tablet formulations was measured using digital Vernier caliper and hardness (Strength of the tablets measure as Kg cm⁻²) was measured using Monsanto hardness tester.

Friability is an important physical parameter of the tablet formulation which ensures its intactness and strength to during handling and transport. It was checked using friability test apparatus (Roche Friability Test Apparatus) by accurately weighing 20 tablets and adding in to the drum which was further rotated at 25 rpm for 4 minutes.

Table V: R_f Values of all the three formulated batches of tablets

At 256 nm					
Sr. No.	Description	Blank	R_f value of Sample-1	R_f value of Sample-2	R_f value of Sample-3
1.	Dark grey color	--	0.04	0.04	0.04
2.	Dark grey color	--	0.06	0.06	0.06
3.	Dark grey color	--	0.16	0.17	0.16
4.	Dark grey color	--	0.25	0.25	0.25
5.	Dark grey color	--	0.30	0.30	0.30
6.	Dark grey color	--	0.37	0.38	0.38
7.	Dark grey color	--	0.42	0.42	0.42
8.	Dark grey color	--	0.44	0.44	0.44
9.	Dark grey color	--	0.49	0.49	0.49
10.	Dark grey color	--	0.54	0.53	0.53
11.	Dark grey color	--	0.57	0.57	0.57
12.	Dark grey color	--	0.61	0.60	0.60
13.	Dark grey color	--	0.78	0.78	0.78
At 360 nm					
1.	Bright sky blue	--	0.05	0.04	0.05
2.	Bright sky blue	--	0.07	0.07	0.07
3.	Bright sky blue	--	0.17	0.18	0.17
4.	Bright sky blue	--	0.22	0.22	0.22
5.	Bright sky blue	--	0.28	0.28	0.28
6.	Bright sky blue	--	0.33	0.34	0.34
7.	Bright sky blue	--	0.40	0.40	0.40
8.	Bright sky blue	--	0.45	0.45	0.45
9.	Bright sky blue	--	0.47	0.47	0.47
10.	Bright sky blue	--	0.57	0.58	0.58
11.	Bright sky blue	--	0.59	0.59	0.59
12.	Bright sky blue	--	0.80	0.79	0.79
13.	Red color	--	0.95	0.95	0.95
In Day Light					
1.	Light violet color	--	0.05	0.05	0.05

2.	Light violet color	--	0.06	0.06	0.06
3.	Light violet color	--	0.15	0.16	0.15
4.	Light violet color	--	0.19	0.19	0.19
5.	Light violet color	--	0.24	0.24	0.24
6.	Light violet color	--	0.29	0.30	0.31
7.	Light violet color	--	0.39	0.39	0.39
8.	Light violet color	--	0.43	0.43	0.43
9.	Light violet color	--	0.48	0.48	0.48
10.	Light violet color	--	0.55	0.56	0.56
11.	Light violet color	--	0.59	0.59	0.59
12.	Light violet color	--	0.77	0.76	0.76
13.	Light violet color	--	0.95	0.95	0.95

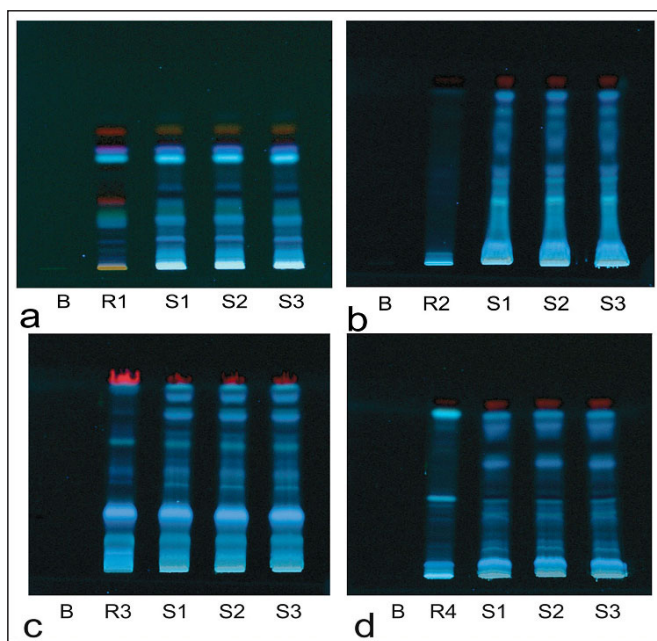


Fig. 1: TLC fingerprint profile of ingredients of Ayush-64 tablet formulation

- (a) *Swertia chirayata* (B: Blank, R1: Chirayata; S1: Sample 1, S2: Sample 2, S3: Sample 3),
 (b) *Alstonia scholaris* (B: blank, R2: Saptaparni; S1: Sample 1, S2: Sample 2, S3: Sample 3),
 (c) *Picrorrhiza kurroa* (B: Blank, R3: Kutki; S1: Sample 1, S2: Sample 2, S3: Sample 3),
 (d) *Casealpanea bonducella* (B: Blank, R4: Latakaranj, S1: Sample 1, S2: Sample 2, S3: Sample 3)

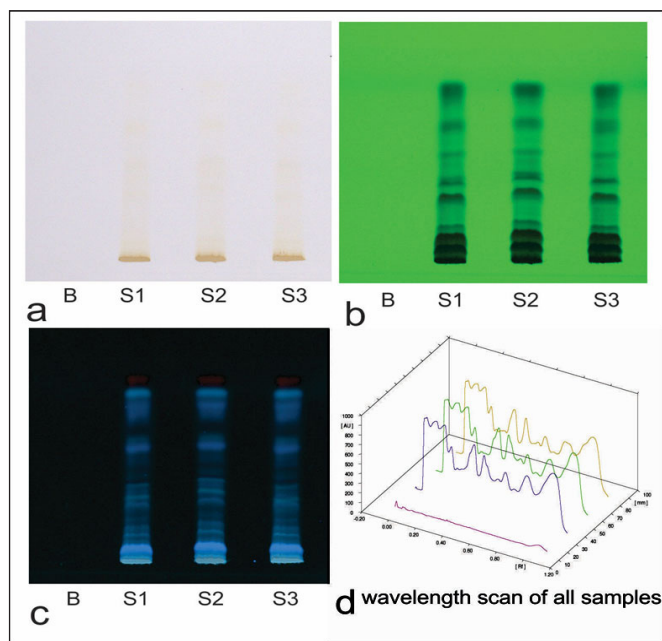


Fig. 2: TLC fingerprint profile of Ayush-64 tablet formulation

- (a) Day light (B: Blank, S1: Sample 1, S2: Sample 2, S3: Sample 3);
 (b) 254nm (B: Blank, S1: Sample 1, S2: Sample 2, S3: Sample 3),
 (c) 366nm (B: Blank, S1: Sample 1, S2: Sample 2, S3: Sample 3),
 (d) Wavelength scanning of all samples

Tablets were then observed for breakage (if any) and powder was removed and remaining tablets were re-weighed. Finally, percentage friability was determined using following equation (5):

$$\% \text{ Friability} = \frac{W1 - W2}{W1} \times 100 \quad (5)$$

where W1 is the initial weight of 20 tablets and W2 is the weight of tablets after friability. The friability (loss due to breakage) should not be more than 1 %.

Weight variation study is also very important parameter which will decides the potency (drug strength) of the tablet formulation. In this study, 20 tablets were weighed individually and in group of 20 and finally compared with average weight of the tablets. The percentage weight variation should not be more than 5 % (for 500 mg tablet).

Disintegration test was conducted to check the time required to disintegrate the tablets in the distilled water. In this method, 6 tablets were added to the beaker consisting of 6 separate tubes. These 6 tablets in the tubes were dipped in to another large beaker containing 1000 mL distilled water at $37 \text{ }^\circ\text{C} \pm 2.0 \text{ }^\circ\text{C}$ and moved up and down in at a distance of 2.5 cm, after 28 to 30 such a stroke, the tablets were observed for disintegration in to small particles in the large beaker^{11,12}.

Another important parameter of standardization is its analytical profiling. Chromatographic profile was determined using HPTLC (High Performance Thin-Layered Chromatography) method¹³⁻¹⁵. Methanolic extracts of individual herbal materials of the formulation and all the three tablet formulations (S-1, S-2 and S-3) were obtained separately by extracting 2 g of each sample with 25 mL of methanol and which were then placed on a water bath for 25 minutes for removal of excess of methanol to get concentrate form of extract. Chromatogram was performed by spotting standard of each herb and extract of tablet samples S-1, S-2 and S-3 on same silica gel aluminum plate (60F-254) of 10 cm x 10 cm with thickness of 250 mm using CAMAG Hamilton syringe and Linomat IV sample applicator. Thus, five samples on each plate (blank demineralized water, raw standard and three samples) and one plate along with blank and all the three samples with 8 mm band length were spotted. All the TLC plates were developed using suitable mobile phase and then dried with the help of air-drier. Densitometric scanning was done for all plates in CAMAG TLC scanner III in the absorbance and reflectance mode.

RESULTS

All the values were found to be in compliance with the Pharmacopeial standards. The results of powdered drug material are presented in the Table II.

All the three tablet formulations (S-1, S-2 and S-3) were tested for organoleptic and physical chemical properties of materials and results are highlighted in Table III.

All the three samples of tablet formulation were found to be shiny and dark blackish-brown in appearance with characteristic bitter odor and taste. Bulk density and tap density of the formulation before punching was found in the range of 0.650 to 0.675 and 0.835 to 0.850, respectively, with the average of 0.6720 and 0.8442, respectively. Average Hausner's ratio was found to be 1.25, which indicates good flow of the material during tablet compression.

All the tablets were examined for diameter and average diameter was found to be 10.22 mm whereas average thickness was found to be 4.21 mm. Hardness of all the tablet formulation was found to be in the range of 2.5-3.0 Kg cm⁻². In friability study all the prepared tablets were checked for breakage and average friability was found to be below 1 %. Weight variation for all tablet formulation batches S-1, S-2 and S-3 was found to be 0.5 %, 0.4 % and 0.44 %, respectively, whereas disintegration time of 9 minutes, 12 minutes and 10 minutes was found for all the batches of S-1, S-2 and S-3, respectively. All the results of physical parameters are highlighted in Table III.

All other physical-chemical parameters i.e., loss on drying, water soluble extractives, alcohol soluble extractive, ash value, acid insoluble ash value, pH were noted and observed value and average value are presented in Table III.

In analysis study, Fig. 1 (a) to (d) represents the TLC profile of all the samples in comparison with reference standard of chirayata, saptaparni, kutki and latakaranj, respectively, and bands of reference standards were visible in bands of all the samples, which confirmed the presence of those particular ingredients in all sample batches. In another study of HPTLC profiling, Fig. 2 (b) to (d) represents the HPTLC fingerprinting profile of all the three batches visualized in daylight at 254 nm and 366 nm and their densitogram, which confirms that all the three sample batches were identical with no impurity and consistency with no batch-to-batch variation being observed.

The standard physical-chemical parameters of Ayush-64 are summarized in Table IV. Fingerprinting profile of the ingredients and of Ayush-64 tablets are shown in Figs. 1 and 2 respectively, The Rf values of all the three batches are presented in Table V.

DISCUSSION

An important step in ensuring the quality of any ayurvedic product in terms of its identification, purity and strength is carried out by determining its analytical profiling and HPTLC fingerprinting. This study helps in maintaining its standard, quality and efficacy in a very precise manner to fulfill the requirements of regulatory authority. The present study has focused on the physical, chemical and analytical profiling of ayurvedic Ayush-64 tablet formulation. In this study, all the three batches of tablet formulation have shown the almost identical observations of all the evaluation parameters without much significant differences.

CONCLUSION

Ayush-64 is well known ayurvedic tablet formulation for its antimalarial activity approved by CCRAS in 1980. Rights for manufacturing of this tablet formulation is given to some ayurvedic pharmaceutical industries and they are supplying it to various government organizations for malarial eradication program. From this study, it is concluded that all the Ayush-64 tablet formulations show identical results for physical as well as analytical parameters, indicating its standardization as per the guidelines of the CCRAS. These standards will definitely help industries to set and check their in-house analytical standards during manufacturing to keep batch-to-batch similarities consistently.

ACKNOWLEDGEMENTS

Authors are very thankful to WHO-GMP Certified Ayurvedic Pharmaceutical unit, Unijules Life Sciences Ltd. Nagpur for providing their manufacturing and quality control lab facilities to carry conduct this study. Also, we are thankful to Regional research Institute of Mother and

Child-Care Nagpur for providing necessary technical support.

REFERENCES

1. Benzie IFF, Wachtel-Galor S, Editor, Boca Raton (FL): CRC Press; Taylor & Francis, 2011.
2. Anonymous.: The Ayurvedic Formulary of India, New Delhi, Govt. of India, Ministry of Health and Family Welfare; 1976.
3. Zafar R., Panwar R. and Sagar Bhanu P.S.: Herbal drug standardization: **The Indian Pharmacist**. 2005, 4(3), 21-25.
4. Indian Herbal Pharmacopeia, Indian Drug Manufacturers' Association (IDMA), Mumbai, 2002, 16.
5. British Herbal Pharmacopeia, British Herbal Medicine Association. 1996, 17.
6. Quality Control Methods for Medicinal Plant Materials. WHO, Geneva, 1996.
7. Anonymous.: The Ayurvedic Formulary of India, New Delhi, Govt. of India, Ministry of Health and Family Welfare; 1965.
8. Anonymous.: Central Council for Research in Ayurveda and Siddha, New Delhi, Govt. of India, Ministry of Health and Family Welfare; 1987.
9. Siddiqui A. and Hakim M.A.: Format for the Pharmacopeial Analytical Standards of Compound Formulation, Workshop on Standardization of Unani Drugs (Appendix), New Delhi; Central Council for Research in Unani Medicine; 1995, pp25.
10. Mukherjee P.K.: Quality Control of Herbal Drugs. Mumbai: Business Horizons Pharmaceutical Publisher; 2002, pp192.
11. Lachman L., Liberman H.A. and Kanig J.L.: Theory and Practice of Industrial Pharmacy, Mumbai; Varghese Publishing House. 1987.
12. Aulton M.E.: Pharmaceutics, The Science of Dosage Form Design. New Delhi: Churchill Livingstone; 2002, pp 205.
13. Anonymous.: Quality Standards of Indian Medicinal Plants. Vol. 1. New Delhi: Indian Council of Medical Research; 2003, pp 10.
14. Sante. Organization Mondiale De La., Quality control methods for medicinal plant materials, World Health Organization, 559, Rev. 1, Original English, 1992, pp159.
15. Chothani D.L., Patel M.B. and Mishra S.H.: HPTLC Fingerprint Profile and Isolation of Marker Compound of *Ruellia tuberosa*, Chromatogr. Res. Intt. 2012, 1-6; doi: 10.1155/2012/100103



Molecular dynamic simulations based discovery and development of thiazolidin-4-one derivatives as EGFR inhibitors targeting resistance in non-small cell lung cancer (NSCLC)

Kshipra S. Karnik, Aniket P. Sarkate, Deepak K. Lokwani, Shailee V. Tiwari, Rajaram Azad & Pravin S. Wakte

To cite this article: Kshipra S. Karnik, Aniket P. Sarkate, Deepak K. Lokwani, Shailee V. Tiwari, Rajaram Azad & Pravin S. Wakte (2022): Molecular dynamic simulations based discovery and development of thiazolidin-4-one derivatives as EGFR inhibitors targeting resistance in non-small cell lung cancer (NSCLC), Journal of Biomolecular Structure and Dynamics, DOI: [10.1080/07391102.2022.2071339](https://doi.org/10.1080/07391102.2022.2071339)

To link to this article: <https://doi.org/10.1080/07391102.2022.2071339>



Published online: 09 May 2022.



Submit your article to this journal [↗](#)



Article views: 73





View related articles [↗](#)



View Crossmark data [↗](#)



Molecular dynamic simulations based discovery and development of thiazolidin-4-one derivatives as EGFR inhibitors targeting resistance in non-small cell lung cancer (NSCLC)

Kshipra S. Karnik^a, Aniket P. Sarkate^a, Deepak K. Lokwani^b , Shailee V. Tiwari^c, Rajaram Azad^d and Pravin S. Wakte^a 

^aDepartment of Chemical Technology, Dr. Babasaheb Ambedkar, Marathwada University, Aurangabad, Maharashtra, India; ^bDepartment of Pharmaceutical Chemistry, Rajarshi Shahu College of Pharmacy, Buldhana, Maharashtra, India; ^cDepartment of Pharmaceutical Chemistry, Durgamata Institute of Pharmacy, Parbhani, Maharashtra, India; ^dDepartment of Animal Biology, University of Hyderabad, Hyderabad, India

Communicated by Ramaswamy H. Sarma

ABSTRACT

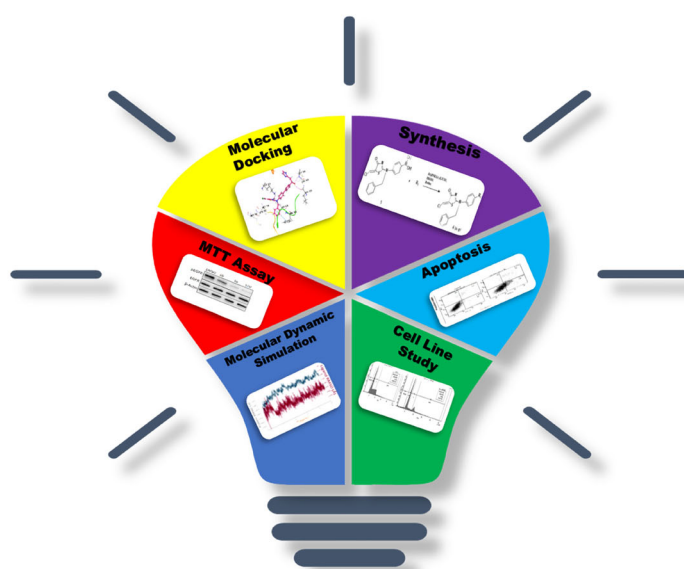
Targeting kinases with oncogenic driver mutations in malignancies with allosteric kinase inhibitors is a promising new treatment technique. EGFR inhibitors targeting the L858R/T790M/C797S mutation bearing thiazolidine-4-one scaffold were discovered, optimized, synthesized, and biologically evaluated. According to *in silico* and *in vitro* studies, compounds **6a** and **6b** resulted to be highly potent with IC₅₀ values of 120 nM and 134 nM and good selectivity. Compound **6a** displayed significant antioxidant activity, with a DPPH radical scavenging value of 92.15%. The potency of compounds was also compared with ADMET and molecular dynamics simulations study. A comparative simulation of model protein and protein-ligand complex in presence and absence of compound **6a** has been carried out.

ARTICLE HISTORY

Received 13 November 2021
Accepted 25 April 2022

KEYWORDS

EGFR; allosteric; thiazolidine-4-one; ADMET; molecular docking; molecular dynamic simulations



Abbreviations: Cys797 to Ser797 (C797S): Cysteine to Serine; T790M: Threonine 790 Methionine; EGFR: Epidermal Growth Factor Receptor; PDB: Protein Data Bank; ADMET: Absorption, Distribution, Metabolism, Excretion and Toxicity; MDS: Molecular Dynamic Simulations; Mol MW: Molecular Weight; NSCLC: Non-Small Cell Lung Cancer; MTT: 3-(4,5-dimethylthiazol-2-yl)-2,5-diphenyl tetrazolium bromide

1. Introduction

The epidermal growth factor receptor (EGFR) is a key enzyme in the ErbB family of receptor tyrosine kinases, which comprises ErbB2 (HER-2 or Neu), ErbB3 (HER-3), and ErbB4 (HER-4) (Voldborg et al., 1997; Kolibaba & Druker, 1997). Overexpression of EGFR can cause complications, most notably in lung cancer, breast cancer, and glioblastoma (Dacic et al., 2006). When epidermal growth factor pathways are activated, cancer proliferation, metastatic potential, and neo-angiogenesis are initiated (Ogiso et al., 2002). Overexpression of EGFR activates numerous downstream signalling pathways, resulting in more aggressive development and invasiveness (Baselga & Arteaga, 2005). Activating mutations in the EGFR gene had a significant impact on non-small cell lung cancer therapy techniques (NSCLC). A recent discovery of novel EGFR inhibitors had a crucial role in overcoming such mutations (Santhi et al., 2016).

Missense mutations have undoubtedly occurred in EGFR enzymes. Such alterations have a significant influence on medications by causing resistance (Sharma et al., 2007). Researchers have had to find new medications to avoid and inhibit resistance due to changes in the protein's activity.

The nucleotide alterations that occur in EGFR mutations are classified. The first mutation was discovered as an exon19 deletion (Abdellatif et al., 2017). Resistance was found in drugs like erlotinib and gefitinib, which were widely used to treat lung cancer (Liao et al., 2015). Mutation gave rise to new targets and compounds, which were given names in the form of generations. First-generation medicines were those that inhibited the target enzyme. Using the same quinazoline scaffold, second-generation medicines were created by altering the R-groups that were already present.

Afatinib and neratinib are two drugs that have shown to block continuing mutations (Westover et al., 2008). Everything was well until a novel missense mutation in the wild-type EGFR enzyme was discovered, resulting in the replacement of a specific AUG gene with the UAU gene (Sequist, 2007). As a result of this the amino acid threonine was changed to methionine at position 790. The binding property functions of this novel T790M mutation were also altered, as evidenced by toxicity (Politi et al., 2015). A new class of medicines emerged with a shift in structure from quinazoline to pyrimidine ring to overcome mutations and reported toxicity (Tan et al., 2018). Rociletinib and AZD9291, which were recently developed as third-generation compounds, demonstrated better efficacy against mutations such as exon 19 deletion and T790M mutant (Russo et al., 2017). Despite their effectiveness, the molecules had a number of downsides, including the formation of novel resistance in the form of a genetic code alteration that resulted in the C797S mutation (Minari et al., 2016). Proteins showed functional and structural alterations as a result of the C797S mutation.

The allosteric binding site of the EGFR enzyme was named after these modifications, which created a novel binding site with high pocket affinities. A novel binding site was discovered to be effective in both overcoming resistance and inhibiting the protein. EAI001 and EAI045 have demonstrated their ability to inhibit the EGFR enzyme by attaching to the

allosteric site (Wang et al., 2017). In heterocyclic compounds, nitrogen is the primary moiety in a wide range of synthetic medications, bioactive natural products, pharmaceuticals, and agrochemicals (Antypenko et al., 2016).

Nitrogen-containing heterocyclic molecules have been significant in improving medication potency. The activity of an active nitrogen atom is increased through a variety of interactions (Yulya et al., 2020). Thiazolidin-4-one nucleus containing molecules act as Acetylcholinesterase inhibitors (Neves et al., 2020), anticancer (Türe et al., 2021), antihyperglycemic and antidyslipidemic agents (Raza et al., 2013), antimicrobial (Rani et al., 2020) as well as *Mycobacterium tuberculosis* DNA gyrase inhibitors (Salve et al., 2021).

Due to the high prediction of effective compounds and proper screening of molecules, computational strategies for creating new compounds are now routinely used. Scaffold hopping methodology is currently the most extensively utilised computational strategy in drug design and discovery. It relates to the study of molecules with the same action but distinct fundamental structures (Li et al., 2011).

Taking our previous work (Chate et al., 2018; Dofe et al., 2017, 2018; Pansare & Shinde, 2015; Shelke et al., 2019a, 2019b) a step further by changing the reactants and reaction methodologies keeping the basic skeleton similar, a detailed synthetic scheme was designed and to understand the binding pocket and forecast potency, novel compounds were submitted to molecular docking and ADMET experiments. Compounds were next tested in vitro on mutant cell lines, and the most powerful molecule was exposed to molecular dynamics simulations.

2. Experimental

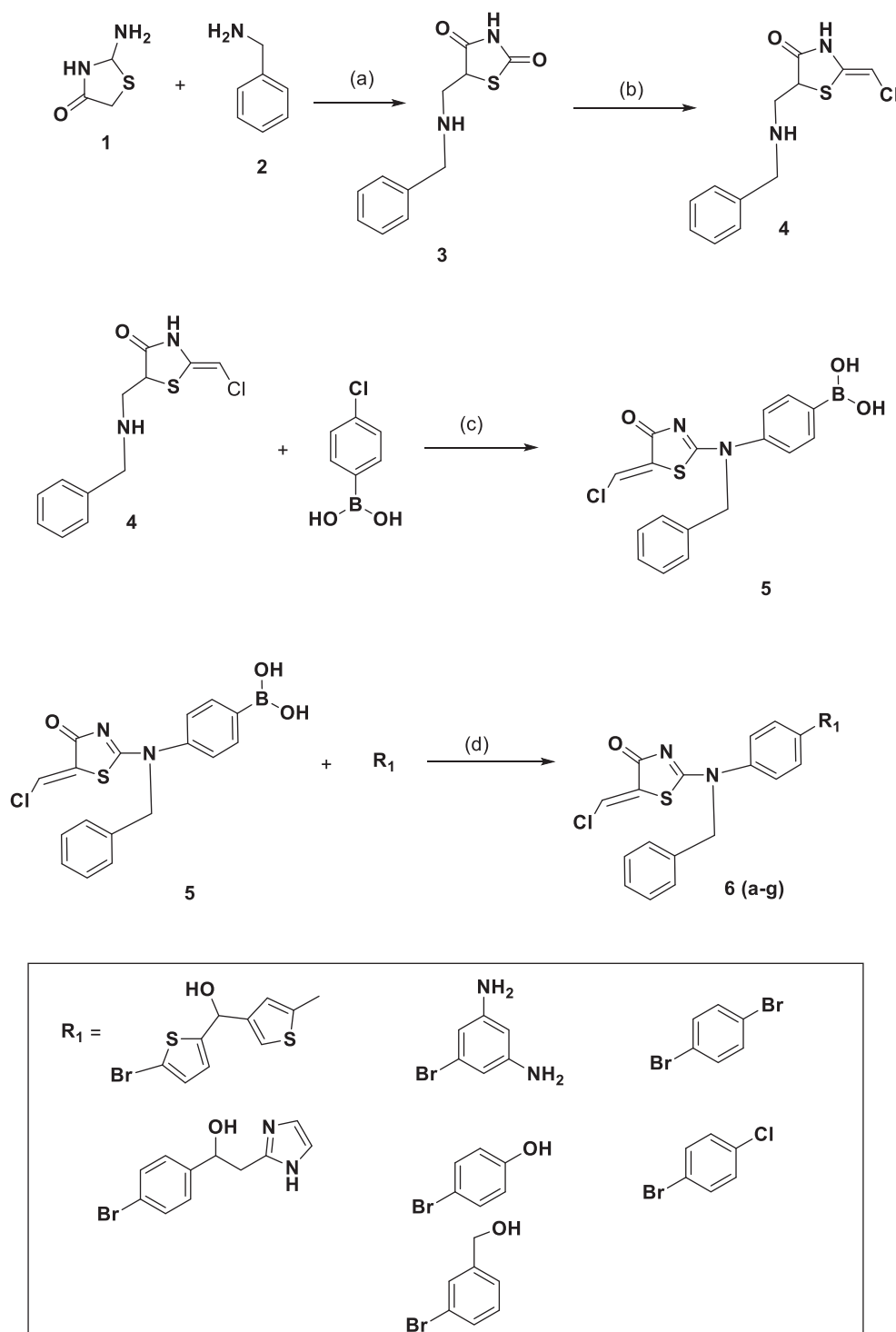
2.1. Chemistry

A detailed synthetic protocol of compounds **6(a-g)** is shown in [Scheme 1](#) below. The complete multi-step reaction resulted high yields in each step. Synthesized compounds with their yields are shown ([Table 1](#)).

As described in [Scheme 1](#), at first 2-aminothiazolidin-4-one (**1**) was reacted with benzylamine (**2**) in presence of sodium formate and acetic acid to yield compound (**3**). The compound (**3**) was reacted with chloroform in presence of palladium acetate under basic condition to yield compound (**4**). The compound (**4**) was converted to compound (**5**) by subjecting to react with 4-chlorophenyl boronic acid. In the last step, via a Suzuki coupling reaction, compound (**5**) was reacted with different substituted bromo compounds to obtain final derivatives **6(a-g)**.

2.2. General procedures

Chemicals were purchased from commercial sources, viz. TCI and Avra Labs, and used without further purification. Progress of the reaction was monitored by thin-layer chromatography (TLC) on pre-coated silica gel F254 aluminium sheets (Merck), and visualization was done by UV light. ¹H NMR (500 MHz) and ¹³C NMR (125 MHz) spectra were recorded on Bruker AVANCE II NMR spectrometer in



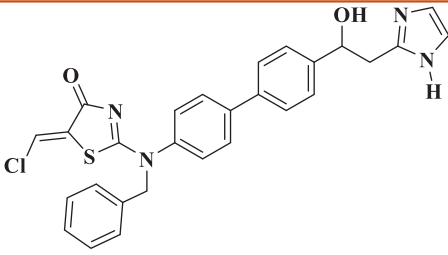
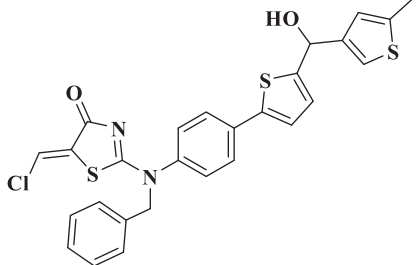
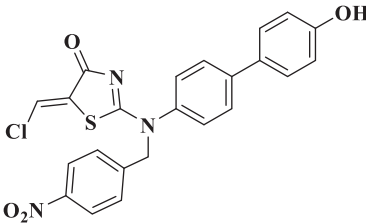
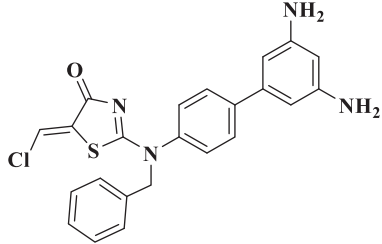
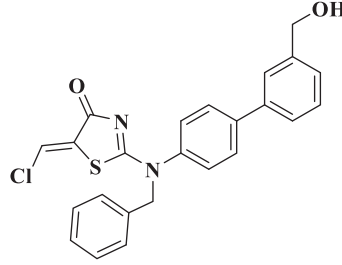
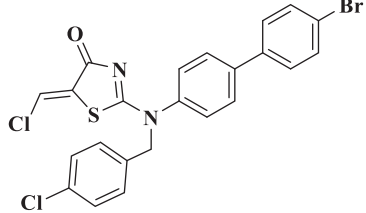
Scheme 1. Synthesis of compounds 6(a–g). Reagents and conditions: (a) Sodium formate, acetic acid, reflux; (b) chloroform, palladium acetate, TEA, toluene, reflux; (c) TEA, DCM, RT; (d) Pd(PPh₃)₄, K₂CO₃, DMSO, reflux.

Dimethylsulfoxide-d₆ solution. Tetramethyl silane was used as an internal standard. Chemical shift values are given in ppm relative to TMS as an internal reference and coupling constants (*J*) in Hertz. The splitting pattern abbreviations are assigned as singlet (s), doublet (d), triplet (t), broad singlet (brs), double doublet (dd), and multiplet (m). High-resolution mass were recorded on a XEVO G2-XS QTOF instrument. Elemental analysis was performed on Perkin-Elmer EAL-240 elemental analyzer.

2.3. Synthesis of 5-((benzylamino)methyl)thiazolidine-2,4-dione (3)

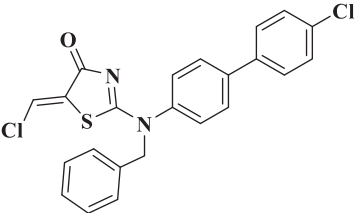
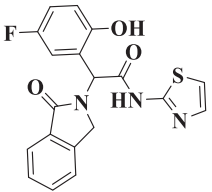
In a 50 mL round bottom flask, 5 g of 2-aminothiazolidin-4-one with 5 mL of benzylamine was added in presence of sodium formate and acetic acid and was refluxed for 24 h. The reaction was monitored by TLC. After completion of the reaction, the reaction mixture was allowed to stand at room temperature. Further cold water or ice was added to the reaction mixture which yielded precipitate, signalling the

Table 1. Structures, docking scores and isolated yields of synthesized compounds **6(a-g)**.

Compound	Structure	Docking scores T790M/C797S mutated (5D41)	Yield ^a (%)
6a		-10.72	90%
6b		-9.61	88%
6c		-7.51	84%
6d		-8.92	89%
6e		-9.49	85%
6f		-7.94	82%
6g		-8.55	91%

(continued)

Table 1. Continued.

Compound	Structure	Docking scores T790M/C797S mutated (5D41)	Yield ^a (%)
			
EAI045		-10.46	-

^aIsolated yield.

formation of the solid product. The product was obtained by vacuum filtration. The obtained solid was then dried and further recrystallized using rectified spirit.

2.4. Synthesis of (Z)-5-((benzylamino)methyl)-2-(chloromethylene)thiazolidine-4-one (4)

The compound (3) was reacted with chloroform in presence of palladium acetate, triethylamine with toluene as a solvent and was refluxed for 12 h. The reaction was monitored by TLC. After completion of the reaction, the mixture was set to cool at room temperature. The solvent was diluted with 20 ml ethyl acetate and washed with 10 ml water. The organic layer was extracted and treated with anhydrous Na₂SO₄ to remove water. The solvent was evaporated using a rotary vacuum evaporator to obtain the required intermediate.

2.5. Synthesis of (Z)-4-(benzyl(5-(chloromethylene)-4-oxo-4,5-dihydrothiazol-2-yl)amino)phenyl)boronic acid (5)

The compound (4) was reacted with 4-chlorophenyl boronic acid in presence of triethylamine, DCM as a solvent and was stirred at room temperature for 24 h. The reaction was monitored by TLC. After completion of the reaction, the reaction mixture was diluted with 10 mL DCM and 10 mL water. The organic layer was extracted and treated with anhydrous Na₂SO₄ to remove water. The solvent was evaporated using a rotary vacuum evaporator to obtain the required intermediate.

2.6. Synthesis of substituted thiazolidine-4-one derivatives 6(a-g)

A Suzuki coupling reaction was performed of compound (5) with different bromo derivatives in presence of

Tetrakis(triphenyl)phosphopalladium (5 mol %) as a catalyst, potassium carbonate was used as a base and DMSO as a solvent. The reaction was refluxed for 24 h. The reaction was monitored by TLC. After completion of reaction, product was isolated with layers of water-ethyl acetate. The organic layer was extracted and treated with anhydrous Na₂SO₄ to remove water. The solvent was evaporated in rotary vacuum evaporator. The obtained products were purified by column chromatography using 20% EA:nH mobile phase and were sent for HRMS, ¹H and ¹³C NMR analysis.

2.6.1. (Z)-2-(benzyl(4'-(1-hydroxy-2-(1H-imidazol-2-yl)ethyl)-[1,1'-biphenyl]-4-yl)amino)-5-(chloromethylene)thiazol-4(5H)-one (6a)

Yellow solid; mp: 183–186 °C. ¹H NMR (500 MHz, Chloroform-*d*) δ 7.63–7.57 (m, 2H), 7.53–7.47 (m, 2H), 7.40–7.33 (m, 2H), 7.33–7.25 (m, 7H), 7.23 (s, 1H), 7.05 (dd, *J* = 5.3, 2.9 Hz, 1H), 6.99 (d, *J* = 2.9 Hz, 1H), 5.19–5.11 (m, 1H), 5.02 (s, 1H), 5.02 (d, *J* = 1.8 Hz, 0H), 4.03 (d, *J* = 5.9 Hz, 1H), 3.02 (dd, *J* = 16.0, 7.0 Hz, 1H), 2.94 (dd, *J* = 16.0, 7.0 Hz, 1H), ¹³C NMR (125 MHz, DMSO) δ 179.20, 170.90, 146.71, 144.88, 143.70, 139.01, 135.71, 131.34, 128.70, 122.30, 119.08, 117.11, 72.72, 50.66, 38.06; HRMS: *m/z* calcd: 515.03, found [M + H]⁺:515.9; Anal. Calcd. for C₂₈H₂₃ClN₄O₂S (515.03): C, 65.30; H, 4.50; N, 10.88. Found: C, 65.49; H, 4.59; N, 11.02.

2.6.2. (Z)-2-(benzyl(4-(5-(hydroxy(5-methylthiophen-3-yl)methyl)thiophen-2-yl)phenyl)amino)-5-(chloromethylene)thiazol-4(5H)-one (6b)

Yellow-orange solid; mp: 182–184 °C. ¹H NMR (500 MHz, Chloroform-*d*) δ 7.42–7.36 (m, 2H), 7.33–7.28 (m, 1H), 7.30 (s, 1H), 7.31–7.24 (m, 6H), 7.23 (s, 1H), 7.17 (d, *J* = 6.6 Hz, 1H), 6.72–6.68 (m, 1H), 6.46 (d, *J* = 1.6 Hz, 1H), 5.70–5.65 (m, 1H), 5.02 (s, 1H), 4.00 (d, *J* = 4.2 Hz, 1H), ¹³C NMR (125 MHz, DMSO) δ 179.20, 170.90, 148.70, 143.84, 142.23, 141.91, 135.71, 130.01, 128.70, 127.68, 127.06, 125.78, 125.47, 121.06, 104

118.20, 117.11, 73.70, 50.66, 15.86; HRMS: m/z calcd: 537.1, found $[M + H]^+$:537.0; Anal. Calcd. for $C_{27}H_{21}ClN_2O_2S_3$ (537.11): C, 60.38; H, 3.94; N, 5.22. Found: C, 60.57; H, 4.03; N, 5.36.

2.6.3. (Z)-5-(chloromethylene)-2-((4'-hydroxy-[1,1'-biphenyl]-4-yl)(4-nitrobenzyl)amino)thiazol-4(5H)-one (6c)

Yellow solid; mp: 210–215 °C. 1H NMR (500 MHz, Chloroform-*d*) δ 8.16–8.10 (m, 1H), 7.57 (dt, $J=8.6, 1.1$ Hz, 1H), 7.52–7.47 (m, 1H), 7.47–7.41 (m, 1H), 7.33–7.28 (m, 1H), 6.93–6.85 (m, 1H), 5.07 (t, $J=1.0$ Hz, 1H), ^{13}C NMR (125 MHz, DMSO) δ 179.20, 170.86, 158.32, 147.51, 143.70, 140.05, 131.52, 129.36, 128.24, 127.31, 123.84, 119.08, 117.11, 115.98, 50.44; HRMS: m/z calcd: 465.9, found $[M + H]^+$:466.0; Anal. Calcd. for $C_{23}H_{16}ClN_3O_4S$ (465.91): C, 59.29; H, 3.46; N, 9.02. Found: C, 58.89; H, 3.06; N, 8.88.

2.6.4. (Z)-2-(benzyl(3',5'-diamino-[1,1'-biphenyl]-4-yl)amino)-5-(chloromethylene)thiazol-4(5H)-one (6d)

Orange solid; mp: 159–160 °C. 1H NMR (500 MHz, Chloroform-*d*) δ 7.50–7.44 (m, 1H), 7.33–7.21 (m, 4H), 6.24 (d, $J=2.0$ Hz, 1H), 5.85 (t, $J=2.2$ Hz, 0H), 5.01 (d, $J=13.6$ Hz, 2H), ^{13}C NMR (125 MHz, DMSO) δ 179.20, 170.90, 148.81, 143.82, 135.71, 132.30, 128.70, 127.78, 119.04, 117.11, 105.82, 102.16, 50.66; HRMS: m/z calcd: 434.9, found $[M + H]^+$:435.1; Anal. Calcd. for $C_{23}H_{19}ClN_4OS$ (434.94): C, 63.51; H, 4.40; N, 12.88. Found: C, 63.91; H, 4.80; N, 13.28.

2.6.5. (Z)-2-(benzyl(3'-(hydroxymethyl)-[1,1'-biphenyl]-4-yl)amino)-5-(chloromethylene)thiazol-4(5H)-one (6e)

Yellow solid; mp: 165–169 °C. 1H NMR (500 MHz, Chloroform-*d*) δ 7.67 (tt, $J=2.2, 1.1$ Hz, 1H), 7.52–7.46 (m, 3H), 7.45 (t, $J=7.7$ Hz, 1H), 7.37 (ddd, $J=7.3, 2.3, 1.2$ Hz, 1H), 7.33–7.23 (m, 8H), 5.02 (s, 2H), 4.76 (dt, $J=5.8, 1.1$ Hz, 2H), 2.24 (d, $J=11.3$ Hz, 1H), ^{13}C NMR (125 MHz, DMSO) δ 179.20, 170.90, 143.83, 141.56, 140.57, 135.71, 134.54, 128.70, 127.68, 126.20, 119.03, 117.11, 64.67, 50.66; HRMS: m/z calcd: 434.9, found $[M + H]^+$:435.0; Anal. Calcd. for $C_{23}H_{19}ClN_2O_2S$ (434.94): C, 66.28; H, 4.40; N, 6.44. Found: C, 66.09; H, 4.49; N, 6.58.

2.6.6. (Z)-2-((4'-bromo-[1,1'-biphenyl]-4-yl)(4-chlorobenzyl)amino)-5-(chloromethylene)thiazol-4(5H)-one (6f)

Yellow solid; mp: 240–242 °C. 1H NMR (500 MHz, Chloroform-*d*) δ 7.68–7.58 (m, 4H), 7.53–7.47 (m, 2H), 7.39–7.34 (m, 2H), 7.34–7.27 (m, 3H), 7.23 (s, 1H), 5.05 (t, $J=0.9$ Hz, 2H), ^{13}C NMR (125 MHz, DMSO) δ 179.20, 170.90, 143.70, 139.21, 133.47, 132.11, 131.33, 130.09, 128.75, 127.31, 121.57, 119.08, 117.11, 50.57; HRMS: m/z calcd: 518.2, found $[M + H]^+$:518.9; Anal. Calcd. for $C_{23}H_{15}BrCl_2N_2OS$ (518.25): C, 53.30; H, 2.92; N, 5.41. Found: C, 53.49; H, 3.01; N, 5.55.

2.6.7. (Z)-2-(benzyl(4'-chloro-[1,1'-biphenyl]-4-yl)amino)-5-(chloromethylene)thiazol-4(5H)-one (6g)

Yellow solid; mp: 227–230 °C. 1H NMR (500 MHz, Chloroform-*d*) δ 7.54–7.47 (m, 3H), 7.33–7.24 (m, 4H), 7.23 (s, 0H), 5.02 (s,

1H), ^{13}C NMR (125 MHz, DMSO) δ 179.20, 170.90, 143.70, 138.30, 135.71, 133.36, 131.70, 129.07, 128.52, 127.68, 119.08, 117.11, 50.66; HRMS: m/z calcd: 439.3, found $[M + H]^+$: 439.0; Anal. Calcd. for $C_{23}H_{16}Cl_2N_2OS$ (439.35): C, 62.88; H, 3.67; N, 6.38. Found: C, 62.69; H, 3.58; N, 6.24.

2.7. In silico methodology

All computational studies were performed using AutoDock Vina. The molecular docking tool, AutoDock Vina, was used for docking studies of all compounds on the EGFR enzyme. SwissADME tool was used to determine ADMET studies. Molecular dynamic simulations were carried out using GROMACS.

2.7.1. Molecular docking

To investigate the binding pocket, residue interactions and predicted binding affinity of the enumerated compounds, molecular docking protocol was carried out using AutoDock tools. Through Chimera modeller, the protein was fetched from the open source PDB libraries. Explicit hydrogen bonds were added followed by removal of water molecules. Using Gastegier charges, ions were removed and finally the protein was minimized using Amber94 force field. The total number of loops were set to 1000 to ensure maximum minimization of the protein. The minimization was terminated when the energy converged or the root mean square deviation (RMSD) reached a maximum cut-off of 0.30 Å. Ramachandran plot was set to check the total number of disallowed residues. Through AutoDock 4.0 GUI, the minimized PDB was converted to PDBQT file followed by generation of grid. To perform flexible docking, torsions were chosen in the selected residues and saved as flex. PDBQT. The configuration file, which was used to outline the grid area as well as the protein and ligand input, was defined and saved as a text document. All the ligands were prepared using Gastegier charges and saved as PDBQT file. The files saved in the fold were called through command line under vina environment to start the docking process. The results for each input ligand were saved as a text file consisting of docking scores and RMSD values of each ligand conformation which was used for analysis of data. The output file was then converted into Maestro readable extension for image saving (Forli et al., 2016; Karnik et al., 2021; Seeliger & Groot, 2010; Trott & Olson, 2010).

2.7.2. ADMET studies

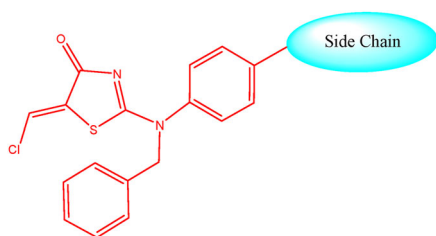
The ADMET results were generated using SwissADME (Karnik et al., 2021; <http://www.swissadme.ch/> (accessed 13 February 2021).

2.7.3. Molecular dynamic simulations

The GROningen MACHine for Chemical Simulations (GROMACS) version 2021.2 was used to run the MD simulations (Abraham et al., 2015; Hess et al., 2008; Van Der Spoel **105** et al., 2005). The GROMOS-96 43A1 force field was used to

Table 2. *In vitro* anticancer activity of the synthesized compounds against cells harbouring a different status of the EGFR.

Compound	IC ₅₀ μM ^a			
	HCC827	NCI-H1975	A549	HT-29
6a	0.0070	0.09	2.16	1.22
6b	0.0092	0.09	2.33	1.28
6c	0.330	3.15	6.99	7.50
6d	0.020	1.18	3.82	1.96
6e	0.022	1.94	4.23	3.66
6f	0.122	2.82	5.08	5.42
6g	0.18	2.06	4.06	2.34
Osimertinib	0.0042	0.04	0.92	1.18



do the energy minimization. The 'pdb2gmx' software was used to create the protein topology. The system was solvated in a cubic box using TIP3P as a water model, then neutralised by introducing counter ions (Mark & Nilsson, 2001). During the MD simulation, periodic boundary conditions were applied. The system's energy was minimised using the steepest descent technique with a limitation of 1000 kJ mol⁻¹nm⁻¹. The system was then equilibrated for 100 ps utilising NVT and NPT ensembles. During the equilibration process, the Berendsen algorithm was employed for the thermostat and barostat (Berendsen et al., 1984). Finally, the system was subjected to a 100 ns production MD, with trajectories created every 2 fs and snapshots stored every 2 picoseconds (PS). *g_rms*, *g_rmsf*, *g_hbond*, and *g_gyrate* were used to assess changes in the architecture of EGFR kinase protein in the presence and absence of compound **6a**.

2.8. In vitro methodology

2.8.1. In vitro enzymatic activity assay

The assay was performed as reported by Kashem et al. (Abdelhaleem et al., 2018; Karnik et al., 2021; Kashem et al., 2007). All of the enzymatic reactions were conducted at 30 °C for 40 minutes. The 50 μL reaction mixture contains 40 mM Tris, pH 7.4, 10 mM MgCl₂, 0.1 mg/mL BSA, 1 mM DTT, 10 μM ATP, 25 ng kinase and the 0.2 mg/mL enzyme-substrate (Poly (Glu, Tyr)). The compounds were diluted in 10% DMSO and 5 μL of the dilution was added to a 50 μL reaction so that the final concentration of DMSO is 1% in all of the reactions. The assay was performed by using the Kinase-Glo Plus luminescence kinase assay kit. It measures kinase activity by quantitating the amount of ATP remaining in the solution following a kinase reaction. The luminescent signal from the assay is correlated with the amount of ATP present and is inversely correlated with the amount of kinase activity. The IC₅₀ values were calculated using nonlinear regression with normalized dose-response fit using GraphPad Prism 5.0 Software.

2.8.2. Western blot assay

HCC827 cells (5 × 10⁵/well) were seeded in 6-well plates overnight. The cell was exposed to 1 μM synthesized analogues for 1 h at 37 °C and then either immediately treated with media containing EGF (20 ng/mL) for 15 min or thoroughly washed with fresh medium 10 times for 5 h before EGF treatment. Whole-cell lysates were prepared and total protein concentrations were determined. Proteins were extracted with lysis buffer (50 mM Tris-HCl, 150 mM NaCl, 1 mM EDTA, 0.1% SDS, 0.5% deoxycholic acid, 0.02% sodium azide, 1% NP-40, 2.0 μg/mL aprotinin, 1 mM phenylmethylsulfonyl fluoride). The lysates were centrifuged at 13,000 rpm for 30 min at 40 °C. Equivalent amounts of proteins were loaded on SDS-PAGE gels for electrophoresis and were subjected to transfer onto PVDF membranes. Appropriate antibodies to EGFR and p-EGFR from Cell signaling Technology (Danvers, MA) and anti-β-actin from Santa Cruz Biotech (Santa Cruz, CA) were used. Proteins were visualized with peroxidase-coupled secondary antibody from Southern Biotech (Birmingham, UK), using an ECL-plus kit from Amersham Biosciences (UK) for detection.

2.8.3. MTT assay

Virtually screened compounds had been screened against HCC827, H1975, A549, and HT-29 cells by standard MTT assay. These cell lines were cultured in 10% fetal bovine serum (FBS). In exact 4 × 10³ cells have been suspended in MEM medium and plated into the 96-well plate in 5% CO₂ for 24 hours. The synthesized compounds were added to the culture medium and cells cultured maintained for 72 hours. Freshly prepared MTT was added to each well and incubated with cells at 37 °C for 4 h. MTT reduction was quantified by measurement of absorbance at 492 nm using a multimode reader (Synergy Mx, BioTek).

2.8.4. DPPH (1,1-diphenyl-2-picrylhydrazyl) assay

The reported DPPH method was applied to assess the scavenging ability of the compounds (Blois, 1958). The compounds were tested in the range of 0–25 μg/mL in methanol. To 2.5 mL of compound in three different concentrations, 1 mL of 0.3 mM DPPH ethanol solution was added. Then 1 mL of methanol was added to the solution and allowed to react for 30 min in the dark at room temperature. The change in the absorbance was read at 518 nm. The blank was comprised of 2.5 mL of test compound and 1 mL methanol, while the mixture of 1 mL DPPH and 2.5 mL of methanol served as negative control. The percentage antioxidant activity was calculated as follows:

$$\% \text{ Inhibition} = \frac{A_A - A_B}{A_B} \times 100$$

where *A_B*: absorption of blank sample, *A_A*: absorption of test samples. The percentage inhibition value was calculated and compared with that of ascorbic acid as a reference. **106**

Table 3. *In vitro* enzymatic inhibitory activity of synthesized compounds against EGFR L858R/T790M/C797S.

Compound	EGFR inhibition IC ₅₀ (nM) ^a
6a	120 ± 0.26
6b	134 ± 0.33
Osimertinib	112 ± 0.44

^aThe data reported are the mean values from three independent experiments.

2.8.5. Apoptosis

Apoptosis was determined by staining the cells with Annexin V-Fluorescein isothiocyanate (FITC) and counterstaining with PI using the Annexin V-FITC/PI apoptosis detection kit (BD Biosciences, San Diego, CA) according to the manufacturer's instructions. Briefly, 4×10^6 cell/T 75 flasks were exposed to compound at its IC₅₀ concentration for 24 and 48 h. The cells then were collected by trypsinization and 0.5×10^6 cells were washed twice with phosphate-buffered saline (PBS) and stained with 5 μ L Annexin V-FITC and 5 μ L PI in 1 \times binding buffer for 15 minutes at room temperature in the dark. Analyses were performed using BD LSR Fortessa) with FACS Diva version 6.2 software (Abdelhaleem et al., 2018; Karnik et al., 2021; Kashem et al., 2007).

3. Result and discussion

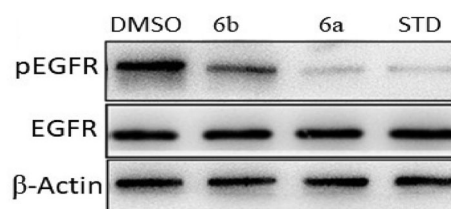
3.1. Biological activity

3.1.1. *In vitro* anticancer activity

The synthesized derivatives were screened for their *in vitro* anticancer activity against the selected cancer cell lines. The cancer cell lines selected were HCC827 cell line, harbouring an EGFR-activating mutation (EGFR Del E746-A750), gefitinib-resistant non-small cell lung cancer NSCLC cell H1975 possessing L858R/T790M mutant EGFR, A549 over-expressing wild-type EGFR (WT-EGFR), and colon cancer cells HT 29, which expressed a non-special gene type, to test their toxic effects. The MTT assay was used to screen the anticancer activity against the selected cancer cell lines. Osimertinib was used as a standard drug. The values of the results are presented in the form of IC₅₀ values as shown (Table 2).

The synthesized thiazole derivatives have shown good to moderate anticancer activity against the selected cell lines. The compounds **6a**, **6b**, and **6d** had shown good activity among the synthesized compounds. The thiazole derivative **6a** was found to be most active derivative among the synthesized derivatives. The IC₅₀ values reported by compound **6a** are 0.007 μ M, 0.09 μ M, 2.16 μ M and 1.22 μ M against HCC827 (EGFR Del E746-A750), NCI-H1975 (EGFR L858R/T790M), A549/ATCC (WT EGFR) and HT-29, respectively.

We introduced side chains of different lengths at the end of ring attached to the end of 'N' group to investigate the effect of side chain length and whether the side chain containing heterocycle can affect the activity of the compounds. From the *in vitro* anticancer activity data, it is clear that the length of the side chain from the ring attached to the 'N' group have an effect on activity. It was observed that when we introduced a phenyl group and an imidazole ring as the side chain it gave compound **6a** with the most promising activity. Similarly, the compound **6b** with two thiophene

**Figure 1.** Inhibition of EGFR autophosphorylation in HCC827 cells by western blot assay. STD: Standard drug Osimertinib.**Table 4.** Radical scavenging activity.

Antioxidant (DPPH radical scavenging activity %)			
Compound	100 μ M	50 μ M	10 μ M
6a	92.15	86.22	34.58
6b	90.82	84.32	33.16
Ascorbic acid	99.66	95.14	52.77

heterocycles with an -OH chain linker gave good activity. When the heterocyclic rings were replaced by substituted phenyl rings on side chain, a decrease in activity was observed.

3.1.2. *In vitro* enzymatic activity assay

The synthesized compounds **6a** and **6b** were screened to study their inhibitory enzymatic activity against EGFR L858R/T790M/C797S *in vitro*. Osimertinib was used as a standard drug. The results are reported (Table 3). The synthesized compound **6a** exhibited potent inhibitory activity against triple mutant EGFR L858R/T790M/C797S with IC₅₀ values of 120 nM, which was also the most potent compound in anti-proliferative activities against cancer cells *in vitro*.

3.1.3. Western blot assay

To put a light on the way the compounds are acting on the mutated cancer cell lines a Western blot assay was carried out for the most active compounds **6a** and **6b**. HCC827 cells were used for the test. (Figure 1) represents the activity results obtained after treating HCC827 cells with the synthesized compounds **6a** and **6b**.

The compounds **6a** and **6b** were selected to inhibit the phosphorylation of EGFR in a no-wash (left) and a wash-out (right) experiment as shown (Figure 1). It is observed that the compounds **6a** and **6b**. inhibited EGFR phosphorylation in the no-wash experiment and also in the washout.

3.1.4. DPPH Radical scavenging activity

Antioxidant agents have a significant role in pharmacy. Free radicals play an important role in cancer, cardiovascular, and auto-immune diseases, as well as aging-related problems, which has led to new perspectives in medicine (Youssif et al., 2018).

The reported DPPH (1,1-diphenyl-2-picrylhydrazyl) method was applied to assess the scavenging ability of the synthesized compounds (Blois, 1958). Ascorbic acid was used as a control. The synthesized compounds **6a** and **6b** were tested at various concentrations such as 10 μ M, 50 μ M and 100 μ M

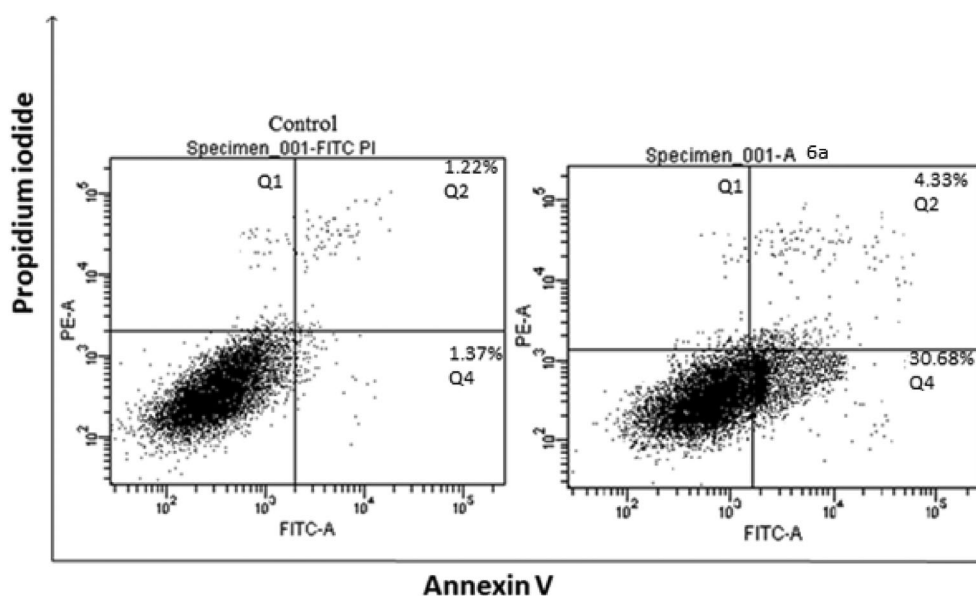


Figure 2. Apoptosis study by Annexin V/FITC assay of compound 6a.

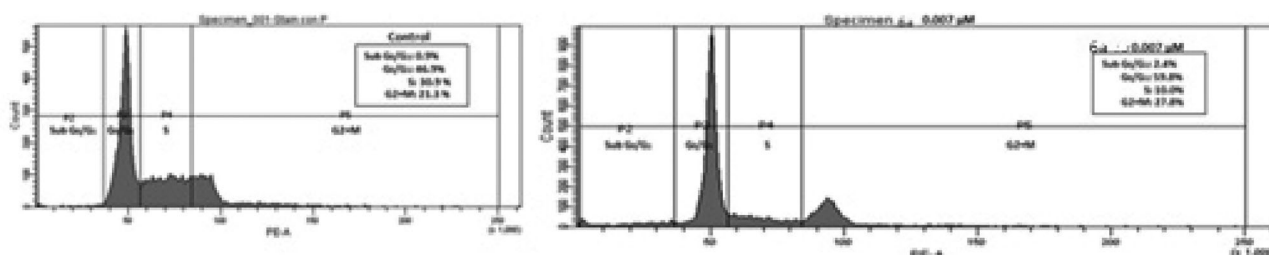


Figure 3. Flow cytometry cell cycle analysis of HCC827 cells treated with synthesized compound 6a and control (with 0.1% DMSO).

as shown (Table 4). The tested compounds, **6a** and **6b** had shown good antioxidant property. At a concentration of 100 μM , **6a** compound demonstrated significant antioxidant activity, with DPPH radical scavenging value 92.15%.

3.1.5. Apoptosis

The three main types of cell death are apoptosis, autophagy, and necrosis. Apoptosis, or programmed cell death, is a natural physiologic mechanism that allows undesirable cells to be removed. The translocation of membrane phosphatidylserine (PS) from the inner side of the plasma membrane to the surface is one of the earliest processes in apoptosis. PS has a high affinity for Annexin V, a Ca^{2+} -dependent phospholipid-binding protein. PS is expressed on the surface of apoptotic cells and fluoresces green when it interacts with the tagged Annexin V in this test. Membrane asymmetry is lost during early apoptosis, and PS translocate from the cytoplasmic side to the exterior leaflet. The counterstain used in this experiment, propidium iodide (PI), can only cross damaged membranes and intercalate into the DNA. As a result, the presence of red fluorescence in the late phases of apoptosis and necrosis is detected using PI.

From the results (Figure 2), it is clear that compound **6a** induced early apoptosis (30.68%) and late apoptosis (4.33%)

in comparison with control (early apoptosis 1.37%, late apoptosis 1.22%).

3.1.6. Cell cycle analysis

To determine whether selected compound induced cell cycle arrest in HCC827 cells, the cell was treated with 0.1% DMSO, compound **6a** (0.007 μM) for 24 h, then stained with PI and cell cycle distributions were analyzed via flow cytometric. After treated with compound **6a** for 24 h, the number of HCC827 cells in the G0/G1 phase was increased significantly as observed (Figure 3). Briefly speaking, selected compounds could induce cell cycle arrests in HCC827 cells.

3.2. In silico studies

3.2.1. Molecular docking with T790M and C797S mutated protein

The molecular docking of the final derivatives was carried out with mutated EGFR enzyme co-crystallized with EAI045 (PDB: 5D41). The newly discovered C797S mutation, combined with the previously known T790M mutation, has altered the protein's binding properties. The C797S mutation reduced the potency of compounds that interact with the ATP binding site. A new binding pocket in the form of an

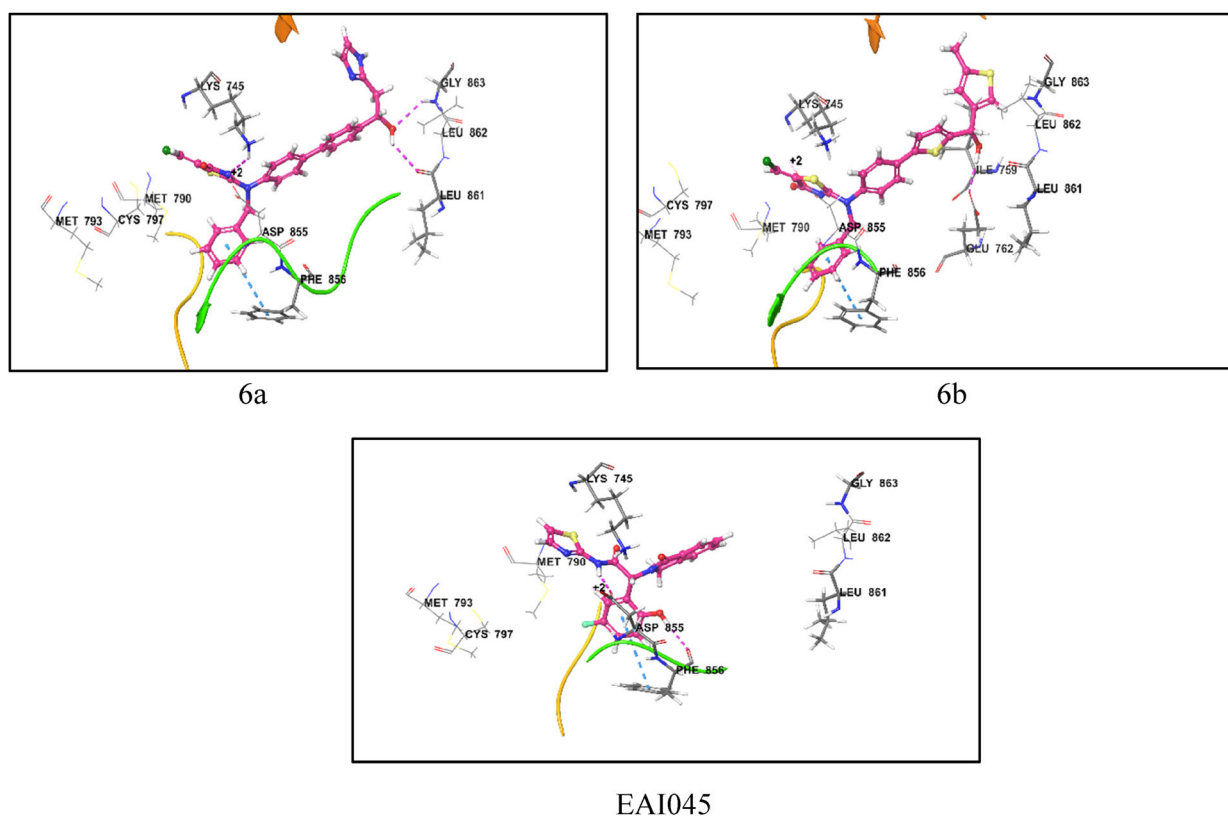


Figure 4. Allosteric binding of designed compounds 6a, 6b and standard EAI045 over C797S and T790M mutated EGFR protein (PDB ID: 5D41). Blue lines in the figures indicate π - π stacking interaction and pink lines indicate hydrogen bonding interaction.

Table 5. *In silico* ADMET results of synthesized compounds 6(a-g).

Compd. no.	Mol. wt.	TPSA ^a	WLOGP ^b	Solubility	GI absorption	BBB permeant ^c	Lipinski	Bioavailability score	PAINS alerts ^d	Brenk alerts
EAI045	383.41	110.77	2.7	Moderately soluble	High	No	0	0.55	0	0
6a	515.03	106.88	5.21	Moderately soluble	High	No	1	0.55	0	0
6b	537.12	134.68	6.73	Moderately soluble	Low	No	1	0.55	0	0
6c	465.91	124.02	5.15	Poorly soluble	Low	No	0	0.17	0	0
6d	434.94	110.01	4.72	Moderately soluble	High	No	0	0.55	0	0
6e	434.94	78.2	4.88	Moderately soluble	High	No	0	0.55	0	0
6f	518.25	57.97	6.95	Poorly soluble	Low	No	1	0.17	0	0
6g	439.36	57.97	6.19	Poorly soluble	High	No	0	0.55	0	0

^aTPSA < 140 Å² good intestinal absorption. TPSA < 70 Å² good brain penetration).

^bLipophilicity WLOGP (acceptable range: for oral and intestinal absorption the idea value is 1.35–1.8, while a drug intended for sub-lingual absorption should have a logP value >5).

^cBBB permeant (Blood Brain Barrier permeant).

^dPan-Assay Interference compounds.

allosteric binding site was searched to address these issues. EAI045 and other allosteric binding pocket interacting structures have demonstrated high potency and market acceptability. The pocket properties of the 'Y' shaped compound were also found to be more dependent on the shape configuration. The docking and simulation study has been carried out on Chain A of EGFR protein (PDB: 5D41). Chain A contains residues starting from 698 to 1014. In this study, allosteric binding site of the protein has been specifically targeted rather than the ATP binding site, to learn more about mutations. The allosteric binding site contains amino acid residues like LYS745, GLY863, LEU861, ASP855 and PHE866 respectively. While, the ATP binding site contains amino acid residues like MET790, MET793 and CYS797, respectively.

Compound **6a** and **6b** showed different hydrogen bonding interactions than EAI045, fitting properly into the binding

pocket with higher docking score. Common interacting residue among all compounds was found to be PHE856 with a π - π stacking interaction. Compound **6a** exhibited binding interactions with amino acid residues LYS745, LEU862 and GLY863. Similarly, compound **6b** with a slight decrease in docking score than EAI045 displayed binding interactions with amino acid residue GLU762. Molecular docking studies revealed that compounds in their conformational states fit easily into the pocket, as shown (Figure 4). Compound binding affinities were also found to be effective. The combined docking scores along with structures is shown (Table 1).

3.2.2. ADMET studies

A number of compounds fail to become useful drugs and enter into the market due to pharmacokinetic issues. We **109** used the SwissADME website (<http://www.swissadme/>)

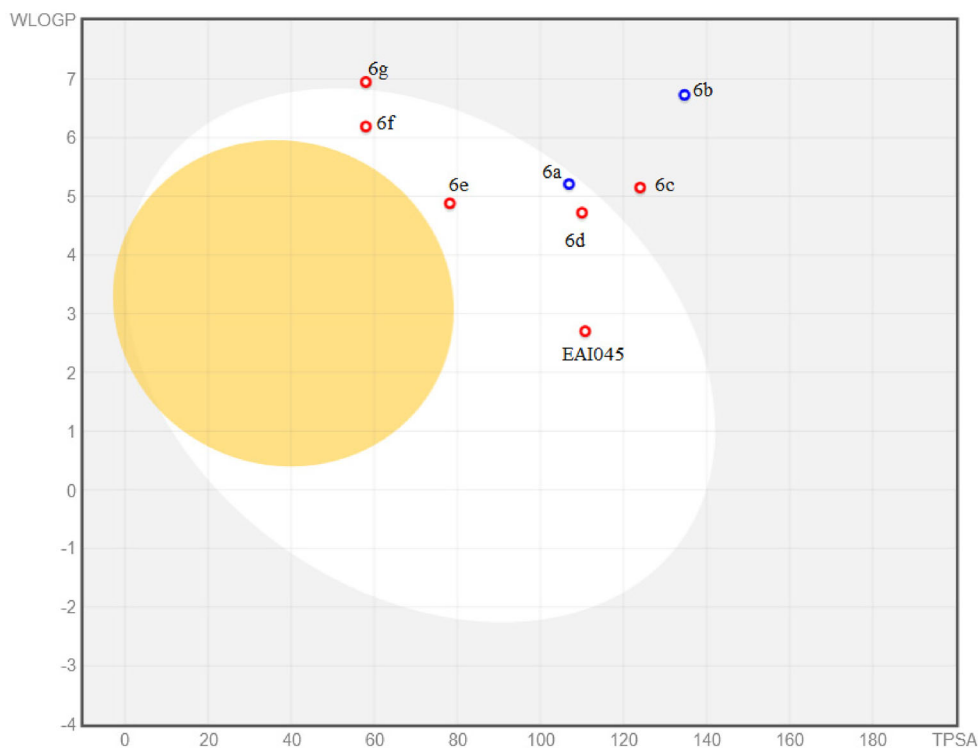


Figure 5. BOILED egg plot of synthesized compounds 6(a–g) versus EAI045.

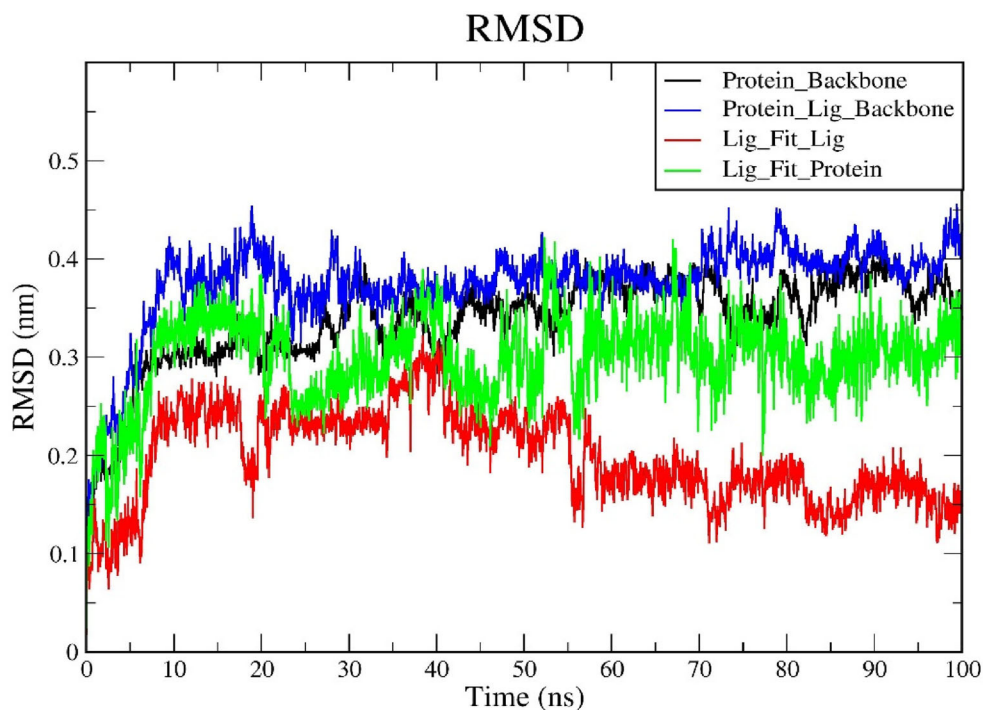


Figure 6. RMSD of mutant EGFR protein in presence and absence of compound 6a.

[index.php](#)) to evaluate the physicochemical and pharmacokinetic properties of the synthesized derivatives with respect to EAI045 (Sivanandan et al., 2019). (Table 5) shows the analysis of the pharmacokinetic parameters needed for ADMET study of compounds **6(a–g)**.

BOILED-Egg method calculates polarity of target compounds expressed in TPSA and lipophilicity expressed in

WLOGP which accurately indicates their GI absorption and BBB permeability. Compounds **6a**, **6d**, **6e** and **6g** showed high GI absorption as compared to EAI045. Also, the final compounds displayed rational polarity (TPSA 57.97–134.68Å²) (Figure 5).

The physicochemical properties of molecular weight **110** (MW), total polar surface area (PSA), and GI absorption were

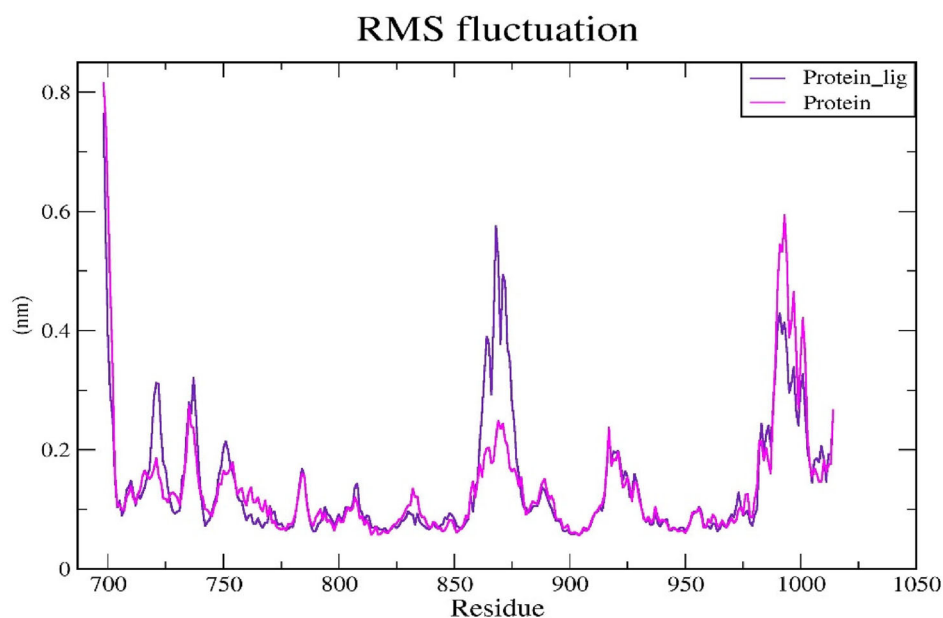


Figure 7. RMS fluctuation plot of EGFR protein in presence and absence of compound 6a.

used to assess the drug-likeness resemblance of compounds. The use of *in silico* ADMET predictions in the drug development process aids in the development of novel molecules that are non-toxic and have good oral human absorption. In humans, compounds that pass Lipinski's rule have good oral absorption (Angelis & Turco, 2011; Lipinski et al., 2012). The partition coefficient ($\log P_{o/w}$) is used to assess drug absorption and distribution within the body. The percent of GI absorption was well observed, indicating that the compounds were found to be well absorbed.

All the target compounds were checked for different pharmacokinetic parameters and were found within an acceptable range as per human consumption, signifying their probable usage as drug-like molecules. Compounds **6a**, **6b** and **6f** violated the Lipinski's rule for their $MW > 500$ g/mol, although it didn't affect much for GI absorption (Bhosle et al., 2018; Lokwani et al., 2015; Tiwari et al., 2018). It was also observed from PAINS and Brenk alerts that there was absence of toxic or unwanted moiety in the compound keeping the biological activity unchanged. Through bioavailability scores, it was indicated that potent compound is available at the site of action. Overall, the compounds showed satisfactory pharmacokinetic parameters range defined for human use along with good docking scores.

3.2.3. Molecular dynamic simulations

The molecular dynamic (MD) simulations were performed on the EGFR protein in presence and absence of compound **6a** to check the protein-ligand interactions. The movements of atoms and molecules were analyzed during this step. We used molecular dynamic simulations to verify and compare the stability of the model protein and protein-ligand complex, which were interpreted using RMSD, RMSF, number of hydrogen bonds and radius of gyration.

The root mean square deviation (RMSD) of the simulated structure over time is a useful and widely used measure for

ensuring the stability of molecular dynamics simulations. Figure 6 reveals that the start of ligand-protein stability began approximately 50 ns, with stability occurring around 60 ns. While the protein alone in absence of ligand was found to be stable throughout the time period. As a result, the ligand remained coupled to the protein throughout the simulation, controlling the system's stability.

The α -carbon's root mean square fluctuation (RMSF) is used to assess mobility and structural flexibility. The RMSF figure (Figure 7) indicate that comparative minor fluctuations were observed in both the systems. The peaks in the RMSF figure represent an amino acid's volatility during the process. Low RMSF values of the discovered protein also imply that the system is in equilibrium.

Furthermore, the gyration radius is a significant indicator of the degree of protein folding. The gyration radius of a protein is fixed during simulation if it is folded correctly. This factor gives important information regarding the spherical distribution of proteins. As a result, the gyration radius may be used to investigate changes in the structure of a protein. During the 100 ps time period, we computed the radius of gyration of EGFR protein in presence and absence of compound **6a**. The stability of the structure was indicated by the radius of gyration, as illustrated in Figure 8.

Hydrogen bonds are one of the most important components of biological systems' molecular interactions. By adding directionality and explicitness to molecular interactions, hydrogen bonds serve as the foundation for molecular recognition and selectivity. The interactions between proteins and ligands were directed by changes in secondary structures, which were governed by hydrogen bonds. Different conformations of a protein might be discovered in real biological situations, according to MD simulations. Each shape of a protein is meant to interact with the ligand in a unique way. As shown in Figure 9, we estimated the number of hydrogen bonds produced over the whole run of MD simulations for chosen complexes. There were ten hydrogen bonds

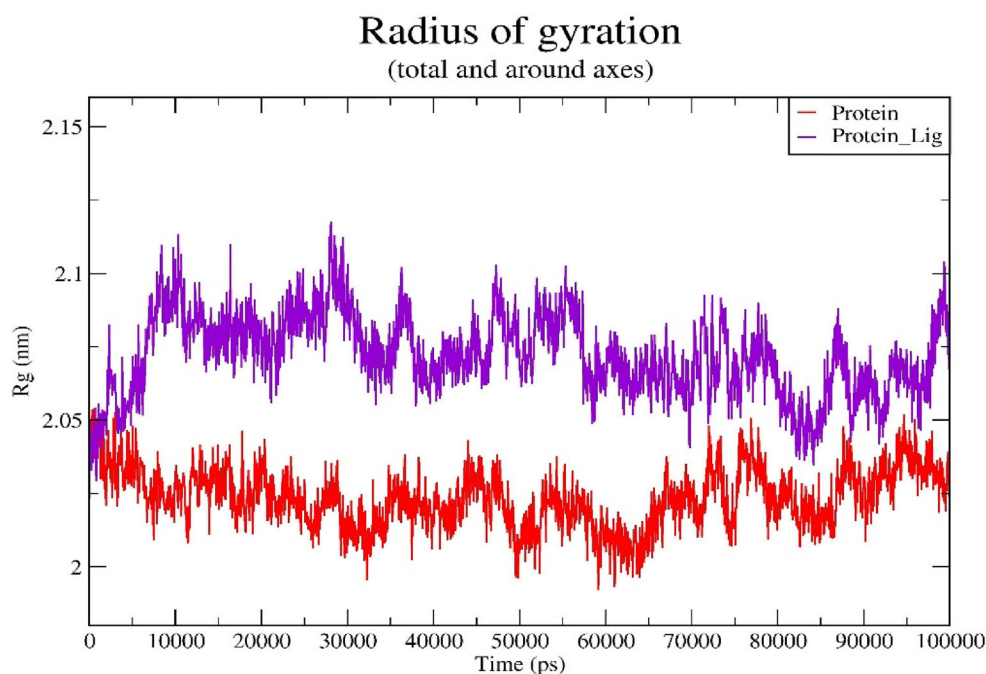


Figure 8. Radius of gyration of EGFR protein and EGFR protein-ligand complex, revealed the stability of structure.

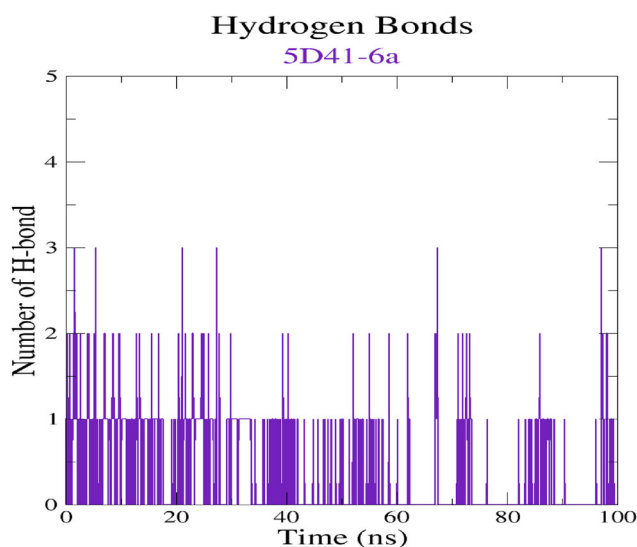


Figure 9. Total number of molecular hydrogen bonds for compound **6a**-5D41 complex over the simulation time.

discovered. Hydrogen bond formation is one of the indicators of a chemical structure's bond strength and long-term stability.

4. Conclusion

Seven novel substituted thiazolidin-4-one derivatives were designed, optimized and synthesized as small molecule L858R/T790M/C797S mutant EGFR inhibitors targeting resistance in Non-Small Cell Lung Cancer (NSCLC). From the synthesized compounds, compounds **6a** and **6b** were observed to be most potent in enzyme-based inhibition. The compounds inhibited the EGFR L858R/T790M/C797S with IC_{50} values of 120 nM and 134 nM, respectively. Further, it was clear that compound **6a** induced early apoptosis (30.68%) and late

apoptosis (4.33%) in comparison with control (early apoptosis 1.37%, late apoptosis 1.22%). It has also shown cell cycle arrest at G0/G1 phase. Compound **6a** displayed significant antioxidant activity, with a DPPH radical scavenging value 92.15%. Compounds in their conformational state fit well into the pocket of the T790M/C797S mutant (PDB ID: 5D41) EGFR enzyme at the allosteric binding site, according to molecular docking studies. Molecular dynamic simulations and an *in silico* ADMET study were used to examine the potency of compound **6a**. The molecular dynamic (MD) simulations were performed on the EGFR protein in presence and absence of compound **6a** to check the protein-ligand interactions and stability of protein-ligand complex.

Acknowledgement

The authors are thankful to The Head, Department of Chemical Technology, Dr. Babasaheb Ambedkar Marathwada University, Aurangabad 431 004 (MS), India, for providing the laboratory facility.

Disclosure statement

The authors report no conflicts of interest in this work.

Funding

The authors K. S. K and P. S. W. are thankful to Indian Council of Medical Research (ICMR) for providing funding in support of Senior Research Fellowship with Ref No: 3/2/2/33/2018/OnlineOncoFship/NCD-III.

ORCID

Deepak K. Lokwani  <http://orcid.org/0000-0003-2858-678X>

Pravin S. Wakte  <http://orcid.org/0000-0002-8118-2963>

Data availability statement

The data that support the findings of this study are available from the corresponding author, P.S.W, upon reasonable request.

PDB codes

PDB ID: 5D41.

References

- Abdellatif, K., Abdelall, E., Abdelgawad, M. A., Amin, D., & Omar, H. A. (2017). Design, synthesis and biological evaluation of new 4-(4-substitutedanilino)quinoline derivatives as anticancer agents. *Medicinal Chemistry Research*, 26(5), 929–939. <https://doi.org/10.1007/s00044-017-1798-9>
- Abdelhaleem, E. F., Abdelhameid, M. K., Kassab, A. B., & Kandeel, M. M. (2018). Design and synthesis of thienopyrimidine urea derivatives with potential cytotoxic and pro-apoptotic activity against breast cancer cell line MCF-7. *European Journal of Medicinal Chemistry*, 143, 1807–1825. <https://doi.org/10.1016/j.ejmech.2017.10.075>
- Abraham, M. J., Murtola, T., Schulz, R., Pall, S., Smith, J. C., Hess, B., & Lindahl, E. (2015). GROMACS: High performance molecular simulations through multi-level parallelism from laptops to supercomputers. *SoftwareX*, 1–2, 19–25. <https://doi.org/10.1016/j.softx.2015.06.001>
- Angelis, I. D., & Turco, L. (2011). Caco- 2 cells as a model for intestinal absorption. *Current Protocols in Toxicology*, 47(1), 20–26. <https://doi.org/10.1002/0471140856.tx2006s47>
- Antypenko, L. M., Kovalenko, S. I., Karpenko, O. V., Katsev, A. M., Novikov, V. P., & Fedyunina, N. S. (2016). 1-R-2- (1,2,4 triazolo 1,5-c quiazoline-2-ylthio) etanon(ol): Synthesis, bioluminescence inhibition, molecular docking studies. *Current Computer-Aided Drug Design*, 12(1), 29–41. <https://doi.org/10.2174/1573409912666160126142236>
- Baselga, J., & Arteaga, C. L. (2005). Critical update and emerging trends in epidermal growth factor receptor targeting in cancer. *Journal of Clinical Oncology*, 23(11), 2445–2459. <https://doi.org/10.1200/JCO.2005.11.890>
- Berendsen, H., Postma, J., van Gunsteren, W. F., DiNola, A., & Haak, J. R. (1984). Molecular dynamics with coupling to an external bath. *The Journal of Chemical Physics*, 81(8), 3684–3690. <https://doi.org/10.1063/1.448118>
- Bhosle, M. R., Khillare, L. D., Mali, J. R., Sarkate, A. P., Lokwani, D. K., & Tiwari, S. V. (2018). DIPEAc promoted one-pot synthesis of dihydropyrido[2,3-d:6,5-d']dipyrimidinetetraone and pyrimido[4,5-d]pyrimidine derivatives as potent tyrosinase inhibitors and anticancer agents: in vitro screening, molecular docking and ADMET predictions. *New Journal of Chemistry*, 42(23), 18621–18632. <https://doi.org/10.1039/C8NJ04622K>
- Blois, M. S. (1958). Antioxidant determinations by the use of a stable free radical. *Nature*, 181(4617), 1199–1200. <https://doi.org/10.1038/1811199a0>
- Chate, A. V., Kamdi, S. P., Bhagat, A. N., Jadhav, C. K., Nipte, A. S., Sarkate, A. P., Tiwari, S. V., & Gill, C. H. (2018). Design, synthesis and SAR study of novel spiro [pyrimido[5,4-b]quinoline-10,50-pyrrolo[2,3-d]pyrimidine] derivatives as promising anticancer agents. *Journal of Heterocyclic Chemistry*, 55(10), 2297–2769. <https://doi.org/10.1002/jhet.3286>
- Dacic, S., Flanagan, M., Cieply, K., Ramalingam, S., Luketich, J., Belani, C., & Yousem, S. A. (2006). Significance of EGFR protein expression and gene amplification in non-small cell lung carcinoma. *American Journal of Clinical Pathology*, 125(6), 860–865. <https://doi.org/10.1309/H5UW6CPCWWC92241>
- Dofe, V. S., Sarkate, A. P., Shaikh, Z. M., & Gill, C. H. (2017). Ultrasound mediated synthesis of novel 1,2,3-triazole-based pyrazole and pyrimidine derivatives as antimicrobial agents. *Journal of Heterocyclic Chemistry*, 54(6), 3195–3201. <https://doi.org/10.1002/jhet.2935>
- Dofe, V. S., Sarkate, A. P., Shaikh, Z. M., Jadhav, C. K., Nipte, A. S., & Gill, C. H. (2018). Ultrasound-assisted synthesis of novel pyrazole and pyrimidine derivatives as antimicrobial agents. *Journal of Heterocyclic Chemistry*, 55(3), 756–763. <https://doi.org/10.1002/jhet.3105>
- Forli, S., Huey, R., Pique, M. E., Sanner, M., Goodsell, D. S., & Olson, A. J. (2016). Computational protein-ligand docking and virtual drug screening with the AutoDock suite. *Nature Protocols*, 11, 905–919. <http://www.swissadme.ch/>
- Hess, B., Kutzner, C., van der Spoel, D., & Lindahl, E. (2008). GROMACS 4: Algorithms for highly efficient, load-balanced, and scalable molecular simulation. *Journal of Chemical Theory and Computation*, 4(3), 435–447. <https://doi.org/10.1021/ct700301q>
- Karnik, K. S., Sarkate, A. P., Tiwari, S. V., Azad, R., Burra, P., & Wakte, P. S. (2021). Computational and synthetic approach with biological evaluation of substituted quinoline derivatives as small molecule L858R/T790M/C797S triple mutant EGFR inhibitors targeting resistance in non-small cell lung cancer (NSCLC). *Bioorganic Chemistry*, 107, 104612–104628. <https://doi.org/10.1016/j.bioorg.2020.104612>
- Karnik, K. S., Sarkate, A. P., Tiwari, S. V., Azad, R., & Wakte, P. S. (2021). Free energy perturbation guided synthesis with biological evaluation of substituted quinoline derivatives as small molecule L858R/T790M/C797S mutant EGFR inhibitors targeting resistance in non-small cell lung cancer (NSCLC). *Bioorganic Chemistry*, 115, 105226–105238. <https://doi.org/10.1016/j.bioorg.2021.105226>
- Kashem, M. A., Nelson, R. M., Yingling, J. D., Pullen, S. S., Prokopowicz, A. S., Jones, J. W., Wolak, J. P., Rogers, G. R., Morelock, M. M., Snow, R. J., Homon, C. A., & Jakes, S. (2007). Three mechanistically distinct kinase assays compared: measurement of intrinsic ATPase activity identified the most comprehensive set of ITK inhibitors. *Journal of Biomolecular Screening*, 12(1), 70–83. <https://doi.org/10.1177/1087057106296047>
- Kolibaba, K. S., & Druker, B. J. (1997). Protein tyrosine kinases and cancer. *Biochimica et Biophysica Acta*, 1333(3), F217–F248. [https://doi.org/10.1016/S0304-419X\(97\)00022-X](https://doi.org/10.1016/S0304-419X(97)00022-X)
- Li, R., Stumpfe, D., Vogt, M., Geppert, H., & Bajorath, J. (2011). Development of a method to consistently quantify the structural distance between scaffolds and to assess scaffold hopping potential. *Journal of Chemical Information and Modeling*, 51(10), 2507–2514. <https://doi.org/10.1021/ci2003945>
- Liao, B. C., Lin, C. C., & Hsin Yang, J. C. (2015). Second and third-generation epidermal growth factor receptor tyrosine kinase inhibitors in advanced nonsmall cell lung cancer. *Current Opinion in Oncology*, 27(2), 94–101. <https://doi.org/10.1097/CCO.0000000000000164>
- Lipinski, C. A., Lombardo, F., Dominy, B. W., & Feeney, P. J. (2012). Experimental and computational approaches to estimate solubility and permeability in drug discovery and development settings. *Advanced Drug Delivery Reviews*, 64, 4–17. <https://doi.org/10.1016/j.addr.2012.09.019>
- Lokwani, D. K., Azad, R., Sarkate, A. P., Reddanna, P., & Shinde, D. B. (2015). Structure based library design (SBLD) for new 1,4-dihydropyrimidine scaffold as simultaneous COX-1/COX-2 and 5-LOX inhibitors. *Bioorganic & Medicinal Chemistry*, 23(15), 4533–4543. <https://doi.org/10.1016/j.bmc.2015.06.008>
- Mark, P., & Nilsson, L. (2001). Structure and dynamics of the TIP3P, SPC, and SPC/E water models at 298K. *The Journal of Physical Chemistry A*, 105(43), 9954–9960. <https://doi.org/10.1021/jp003020w>
- Minari, R., Bordi, P., & Tiseo, M. (2016). Third-generation epidermal growth factor receptor-tyrosine kinase inhibitors in T790M-positive non-small cell lung cancer: Review on emerged mechanisms of resistance. *Translational Lung Cancer Research*, 5(6), 695–708. <https://doi.org/10.21037/tlcr.2016.12.02>
- Neves, A. M., Berwaldt, G. A., Avila, C. T., Goulart, T. B., Moreira, B. C., Ferreira, T. P., Soares, M., Pedra, N. S., Spohr, L., de Souza, A., Spanevello, R. M., & Cunico, W. (2020). Synthesis of thiazolidin-4-ones and thiazinan-4-ones from 1-(2-aminoethyl)pyrrolidine as acetylcholinesterase inhibitors. *Journal of Enzyme Inhibition and Medicinal Chemistry*, 35(1), 31–41. <https://doi.org/10.1080/14756366.2019.1680659>
- Ogiso, H., Ishitani, R., Nureki, O., Fukai, S., Yamanaka, M., Kim, J.-H., Saito, K., Sakamoto, A., Inoue, M., Shirouzu, M., & Yokoyama, S. (2002). Crystal structure of the complex of human epidermal growth factor

- and receptor extracellular domains. *Cell*, 110(6), 775–787. [https://doi.org/10.1016/S0092-8674\(02\)00963-7](https://doi.org/10.1016/S0092-8674(02)00963-7)
- Pansare, D. N., & Shinde, D. B. (2015). A facile synthesis of (Z)-2-((5-(4-fluorobenzylidene)-4-oxo-4,5-dihydrothiazol-2-yl) amino) substituted acid using microwave irradiation and conventional method. *Open Chemistry Journal*, 2(1), 40–46. <https://doi.org/10.2174/1874842201502010040>
- Politi, K., Ayeni, D., & Lynch, T. (2015). The next wave of EGFR tyrosine kinase inhibitors enter the clinic. *Cancer Cell*, 27(6), 751–753. <https://doi.org/10.1016/j.ccell.2015.05.012>
- Rani, N., Salahuddin, S., Mazumder, A., Kumar, R., Sahu, R., Ahsan, M. J., Sarafroz, M., Siddiqui, S. A., & Yar, M. S. (2020). Synthesis, antimicrobial, and molecular docking studies of 1,3-thiazolidin-4-one analogs bearing benzothiazole. *Indian Journal of Heterocyclic Chemistry*, 30, 325–335.
- Raza, S., Srivastava, S. P., Srivastava, D. S., Srivastava, A. K., Haq, W., & Katti, S. B. (2013). Thiazolidin-4-one and thiazinan-4-one derivatives analogous to rosiglitazone as potential antihyperglycemic and antidiabetic agents. *European Journal of Medicinal Chemistry*, 63, 611–620. <https://doi.org/10.1016/j.ejmech.2013.01.054>
- Russo, A., Franchina, T., Ricciardi, G., Smirolto, V., Picciotto, M., Zanghi, M., Rolfo, C., & Adamo, V. (2017). Third generation EGFR TKIs in EGFR-mutated NSCLC: Where are we now and where are we going. *Critical Reviews in Oncology/Hematology*, 117, 38–47. <https://doi.org/10.1016/j.critrevonc.2017.07.003>
- Salve, P. S., Parchure, P., Araujo, L., Kavalapure, R. S., Jalalpure, S. S., Sriram, D., Krishna, V. S., Esthara, M. R., & Alegaon, S. G. (2021). Design and synthesis of new 3-((7-chloroquinolin-4-yl)amino)thiazolidin-4-one analogs as *Mycobacterium tuberculosis* DNA gyrase inhibitors. *Future Journal of Pharmaceutical Sciences*, 7(1), 10. <https://doi.org/10.1186/s43094-020-00162-7>
- Santhi, M. P., Bupesh, G., SenthilKumar, V., Meenakumari, K., Prabhu, K., Sugunthan, S., Manikandan, E., & Saravanan, K. (2016). Anticancer activity and drug likeliness of quinoline through insilico docking against cervical and liver cancer receptors. *Indian Journal of Medical Research and Pharmaceutical Sciences*, 3, 83–93.
- Seeliger, D., & Groot, B. L. (2010). Ligand docking and binding site analysis with PyMOL and Autodock/Vina. *Journal of Computer-Aided Molecular Design*, 24(5), 417–422. <https://doi.org/10.1007/s10822-010-9352-6>
- Sequist, L. V. (2007). Second-generation epidermal growth factor receptor tyrosine kinase inhibitors in non-small cell lung cancer. *The Oncologist*, 12(3), 325–330. <https://doi.org/10.1634/theoncologist.12-3-325>
- Sharma, S. V., Bell, D. W., Settleman, J., & Haber, D. A. (2007). Epidermal growth factor receptor mutations in lung cancer. *Nature Reviews Cancer*, 7(3), 169–181. <https://doi.org/10.1038/nrc2088>
- Shelke, R. N., Pansare, D. N., Sarkate, A. P., Karnik, K. S., Sarkate, A. P., Shinde, D. B., & Thopate, S. R. (2019a). Synthesis of (Z)-5-((substituted benzylidene)-2-((substituted phenyl) amino)thiazol-4(5H)-one analogues with antitubercular activity. *Journal of Taibah University for Science*, 13(1), 678–686. <https://doi.org/10.1080/16583655.2019.1622846>
- Shelke, R. N., Pansare, D. N., Pawar, C. D., Khade, M. C., Jadhav, V. N., Deshmukh, S. U., Sarkate, A. P., Gore, N. S., Pawar, R. P., Shinde, D. B., & Thopate, S. R. (2019b). Synthesis of 2-((5-benzylidene-4-oxo-4,5-dihydrothiazol-2-yl)-substituted amino acids as anticancer and antimicrobial agents. *European Chemical Bulletin*, 8(2), 63–70. <https://doi.org/10.17628/ecb.2019.8.63-70>
- Sivanandan, S., Jain, K., Plakkal, N., Bahl, M., Sahoo, T., Mukherjee, S., Gupta, Y. K., & Agarwal, R. (2019). Issues, challenges, and the way forward in conducting clinical trials among neonates: investigators' perspective. *Journal of Perinatology*, 39(S1), 20–30. <https://doi.org/10.1038/s41372-019-0469-8>
- Tan, C., Kumarakulasinghe, N. B., Huang, Y., Ang, Y., Choo, J. R., Goh, B. C., & Soo, R. A. (2018). Third generation EGFR TKIs: current data and future directions. *Molecular Cancer*, 17(1), 29. <https://doi.org/10.1186/s12943-018-0778-0>
- Tiwari, S. V., Seijas, J. A., Vazquez-Tato, M. P., Sarkate, A. P., Karnik, K. S., & Nikalje, A. (2018). Ionic liquid-promoted synthesis of novel chromone-pyrimidine coupled derivatives, antimicrobial analysis, enzyme assay, docking study and toxicity study. *Molecules*, 23(2), 440–423. <https://doi.org/10.3390/molecules23020440>
- Trott, O., & Olson, A. J. (2010). AutoDock Vina: Improving the speed and accuracy of docking with a new scoring function, efficient optimization and multithreading. *Journal of Computational Chemistry*, 31(2), 455–461.
- Türe, A., Ergül, M., Ergül, M., Altun, A., & Küçükğüzel, I. (2021). Design, synthesis, and anticancer activity of novel 4-thiazolidinone-phenylaminopyrimidine hybrids. *Molecular Diversity*, 25(2), 1025–1050. <https://doi.org/10.1007/s11030-020-10087-1>
- Van Der Spoel, D., Lindahl, E., Hess, B., Groenhof, G., Mark, A. E., & Berendsen, H. (2005). GROMACS: Fast, flexible, and free. *Journal of Computational Chemistry*, 26(16), 1701–1718. <https://doi.org/10.1002/jcc.20291>
- Voldborg, B. R., Damstrup, L., Thomsen, M. S., & Poulsen, H. S. (1997). Epidermal growth factor receptor (EGFR) and EGFR mutations, function and possible role in clinical trial. *Annals of Oncology*, 8(12), 1197–1206. <https://doi.org/10.1023/A:1008209720526>
- Wang, S., Song, Y., & Liu, D. (2017). EAI045: The fourth-generation EGFR inhibitor overcoming T790M and C797S resistance. *Cancer Letters*, 385, 51–54. <https://doi.org/10.1016/j.canlet.2016.11.008>
- Westover, D., Zugazagoitia, J., Cho, B. C., Lovly, C. M., & Paz-Ares, L. (2008). Mechanisms of acquired resistance to first- and second-generation EGFR tyrosine kinase inhibitors. *Clinical Cancer Research*, 29, i10–i19.
- Yousif, B. G. M., Abdelrahman, M. H., Abdelazeem, A. H., Abdelgawad, M. A., Ibrahim, H. M., Salem, O. I. A., Mohamed, M. F. A., Treambleau, L., & Bukhari, S. N. A. (2018). Design, synthesis, mechanistic and histopathological studies of small-molecules of novel indole-2-carboxamides and pyrazino[1,2-a]indol-1(2H)-ones as potential anticancer agents effecting the reactive oxygen species production. *European Journal of Medicinal Chemistry*, 146, 260–273. <https://doi.org/10.1016/j.ejmech.2018.01.042>
- Yulya, M., Oleksii, A., Inna, N., Galina, B., & Sergii, K. (2020). Directed search of anti-inflammatory agents among (3H-quinazoline-4-ylidene) hydrazides of N-protected amino acids and their heterocyclization products. *Anti-Inflammatory & Anti-Allergy Agents in Medicinal Chemistry*, 19, 61–73.

EFFECT OF HYDROPHILIC POLYMER ON DESIGN EXPERT ASSISTED ORO-DISPERSIBLE STRIP (ODS) OF ISOSORBIDE MONONITRATE

ABSTRACT

Oral conventional formulations like tablets, capsules and liquids have many limitations. Due to this and patient incompliance, there is a need to develop new formulations with better efficiency and stability. The aim of the present study was to develop and optimize fast dissolving Oro-dispersible strips (ODS) of isosorbide mononitrate by 3²-full factorial design. HPMC E15 (X₁) concentration and glycerin (X₂) concentration were selected as the independent variables, whereas, *in vitro* disintegration time (Y₁), percent drug release (Y₂) and tensile strength (Y₃) were selected as dependent variables. Fast dissolving Oro-dispersible strips of isosorbide mononitrate were prepared by the solvent casting method. Tensile strength, disintegration time and *in vitro* dissolution of ODS of the strip were found to be within accepted range for optimized formulation. Statistical validity of the polynomials was established by ANOVA using Design-Expert software. The study suggests isosorbide mononitrate fast dissolving Oro-dispersible strip as potential alternative dosage form in management of angina pectoris.

Keywords: Oro-dispersible strips, Full factorial design, Solvent casting method, Isosorbide mononitrate

INTRODUCTION

The origin of Fast Dissolving Drug Delivery Systems (FDDDS) can be traced back to the late 1970's as a potential substitute for other oral dosage forms like tablets, capsules, syrups and other formulations. Their major benefit is for pediatric and geriatric patients suffering from dysphasia problems. The FDDDS possesses the advantages of conventional tablets and liquid formulation^{1,2}. The ease of administration and better patient compliance makes FDDDS a formulation of choice for pediatric, geriatric and mentally challenged persons³.

Delivery of the drug to the site of action successfully is the prime moto of any drug delivery system. The drug delivery system should be safe, effective, convenient and economical with highest patient compliance^{4,5}. In FDDDS, the drug gets disintegrated, dissolved or swallowed and then reaches into the systemic circulation to show desired therapeutic effect^{6,7}.

Oro-dispersible strips (ODS) is one of the convenient novel drug delivery systems for the delivery of the drugs. It is based upon the technology of trans-dermal patch and consists of a very thin oral strip, to be placed on the patient's tongue or any oral mucosal tissue. This film then gets instantly wet by saliva and the strip rapidly hydrates and adheres onto the site of application⁸.

Ease of administration, dosing accuracy, self-medication and patient compliance are the advantages offered by ODS over the other dosage forms⁹. For

ODS administration, there is no need of water and can administered anytime, anywhere. These strips provide better disintegration and dissolution in the oral cavity due to its large surface area¹⁰.

Isosorbide mononitrate is the long-acting metabolite of isosorbide dinitrate utilized as the vasodilator's specialist in the administration of angina pectoris by expanding the vessels. It brings down the circulatory strain and decreases the left ventricular pre-load and after-load, in this manner prompts a decrease of myocardial oxygen necessity. Usual dose of isosorbide mononitrate is 10-60 mg. The limit of absolute oral bioavailability of isosorbide mononitrate is about 90-95% and absorption is about 100%. Oral fast dissolving Oro-dispersible strips of isosorbide mononitrate will be convenient for geriatric patients and adults with swallowing difficulty¹¹.

The present research work involves the formulation and optimization of Oro-dispersible strips of isosorbide mononitrate by applying 3²-factorial designs to understand the effect of formulation variables likes concentration of polymer (HPMC E15) and concentration of plasticizer (glycerin) on *in vitro* evaluation parameter.

METHODS

Isosorbide mononitrate was procured from Piramal Laboratories Ltd. Mumbai, India. HPMC E15 was obtained from Loba Chemie, Mumbai, India. Glycerin, citric acid and mannitol were procured from SD Fine Chem Ltd., Mumbai, India. All the materials used in this study were of analytical grade. Double distilled water was used throughout the study. The drug and all materials

were analyzed for FT-IR and DSC to check compatibility among the selected materials^{12,13}.

Formulation of Oro-dispersible strips (ODS)

The Solvent Casting Method was used to prepare quickly dissolving Oro-dispersible strips of isosorbide mononitrate¹⁴. The polymer HPMC E15 and plasticizer (glycerin) were dissolved in purified water and permitted to swirl for 4 h and held for 1 h to eliminate any trapped air bubbles; this solution was referred to as 'aqueous solution-I'. Drug and other excipients, such as mannitol and saliva stimulating agent (citric acid) were allowed to dissolve in distilled water, referring to as 'Aqueous 'solution-II'. Then 'solution-I' and 'solution-II' were mixed and agitated for 1 h. The resultant mixture was eventually permitted to spill into the glass petri dish and was dried overnight. The dried strips were carefully removed from the petri dish, checked for any imperfections, and cut in squares of 6 cm². For further analyses, samples were placed in airtight containers.

Experimental design

For the optimization of ODS, the 3²-full factorial design was used. All the batches designed as per the 3²-full- factorial are shown in Table I. The mechanical property of ODS was studied using two factors at 3 levels and the identification and performance of nine possible combinations of experimental trials. Independent variables selected for this analysis were concentration of HPMC E15 (X₁) and concentration of glycerin (X₂), whereas *in vitro* disintegration time; (DT), percentage of drug release (% DR) and tensile strength (TS) were selected as dependent variables at three levels low, medium and high. The corresponding factor levels were marked as -1, 0 and +1. In Design-Expert 8.0.7.1 software, the data were subjected to a contour and linear correlation plot to determine the effect of polymers on the dependent variables. A statistical model incorporating interactive and polynomial terms was used to calculate the responses as follows:

$$Y = b_0 + b_1 X_1 + b_2 X_2 + b_{12} X_1 X_2 + b_{11} X_1^2 + b_{22} X_2^2 \quad \dots (1)$$

where Y is the dependent variable, b₀ is the arithmetic mean response of the nine runs and b_i is the estimated coefficient for the corresponding factor X_i, which represent the average result of changing one factor at a time from its low to high value. The term interaction (X₁, X₂) indicates how the response varies as two factors shift at the same time. To investigate the nonlinearity, the polynomial terms (X₁X₁ and X₂ X₂) are included.

Evaluation of Oro-dispersible strips

The assessment parameters for the Oro-dispersible strips of isosorbide mononitrate were weight, surface pH strength, width, product quality, folding endurance, content uniformity, disintegration time and *in vitro* dissolution¹⁵⁻¹⁹.

The percentage moisture loss was calculated as follows²⁰. The experiments were performed in triplicate and recorded mean values are reported.

$$\text{Tensile strength} = \frac{\text{Load at failure}}{\text{Strip thickness} \times \text{Strip width}} \times 100 \quad \dots(2)$$

In vitro dissolution studies

The *in vitro* dissolution studies for strips were performed using USP Type II dissolution apparatus at 37±0.5 °C and 50 rpm speed in 900 mL of phosphate buffer (pH 6.8). 5 mL aliquots were withdrawn at the time interval of every 60 seconds and was replaced with equal volume of fresh dissolution medium and analyzed by spectrophotometer at 221 nm. The cumulative amount of drug release at various time intervals was calculated.

Stability study

Stability study on the optimized formulation of Oro-dispersible strip was carried out as per ICH Q1A (R2) guidelines to determine the effect of temperature and humidity on the stability of the formulation. The optimized formulation was stored in stability chamber at 40±2 °C /75±5% RH and 25 °C/40% RH for duration of 90 days. The sample, were withdrawn at 15, 30, 60- and 90-days intervals; evaluated for physical and chemical parameters²¹.

Data analysis

Statistical validation of the polynomial equation was developed by the Design-Expert, based on ANOVA provision in the software. It produced a total of nine runs (F1-F9) with a triplicate center point. The findings of the resulting experimental response properties were correlated with those of the forecasted values.

Polynomial equations:

$$Y_1 = 28.44 + 8.17X_1 + 0.50X_2 + 2.50X_1X_2 + 4.83X_1^2 + 2.83X_2^2 \quad \dots (3)$$

$$Y_2 = 94.36 - 2.95X_1 + 0.25X_2 \quad \dots (4)$$

Table I: Evaluation of physical parameters of prepared oro-dispersible film

Formulation code	*Drug content (%)	*Thickness (mm)	*Weight variation (mg)	*Surface pH	*Folding endurance	*Percent moisture loss
F1	96.45±0.4	0.26±0.01	54.00±0.52	6.73±0.28	356±1.52	6.10±0.22
F2	97.91±0.2	0.29±0.01	53.89±0.37	6.80±0.33	392±3.89	3.81±0.43
F3	96.76±0.3	0.25±0.01	53.33±0.49	6.83±0.29	248±2.76	6.10±0.15
F4	97.12±0.5	0.33±0.01	55.11±0.41	6.81±0.33	402±4.01	3.78±0.32
F5	97.82±0.5	0.27±0.01	53.69±0.37	6.83±0.29	247±1.52	6.96±0.19
F6	98.17±0.2	0.23±0.01	52.48±0.34	6.97±0.35	216±2.00	5.98±0.29
F7	98.02±0.5	0.24±0.01	53.95±0.52	6.96±0.32	270±3.05	2.80±0.24
F8	96.88±0.3	0.21±0.01	50.00±0.36	7.10±0.26	202±2.08	6.25±0.28
F9	96.50±0.6	0.26±0.01	50.70±0.51	6.90±0.30	215±3.20	3.41±0.35

Evaluation of physical and chemical stability of optimized batch (F6) at 40±2°C/75±5% RH as per ICH Q1A (R2) guidelines of stability study

Time (days)	Physical change		Chemical change	
	Appearance	*Weight variation (mg)	*Percent drug content	*Surface pH
1	No Change	53.69±0.22	97.80±1.25	6.83±0.12
15	(Film appears transparent, uniform and clear)	53.30±0.15	97.45±2.35	6.76±0.25
30		53.18±0.11	96.90±1.44	6.69±0.14
60		53.00±0.32	96.61±2.25	6.66±0.25
90		52.30±0.22	96.55±1.84	6.59±0.55

*All the observations were taken in triplicate as ±SD, (n=3)

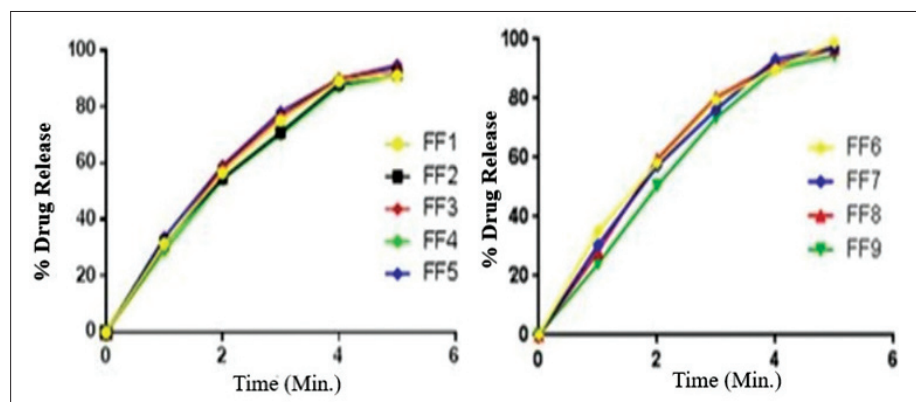


Fig. 1: In vitro drug release profile of fast dissolving strips

parameters are presented in Table I and drug release study of all the batches according to 3²-full factorial design is shown in Fig. 1.

Fitting model to the data

Full factorial statistical experimental design needs 9 runs, as provided by the Response Surface Methodology (RSM). The Y₁, Y₂ and Y₃ ranges are 30.00-47.00 seconds, 91.2-97.8% and 0.18-0.21 N m⁻², respectively. Simultaneously fitted to first order, second order,

$$Y_3 = 0.20 + 5.333X_1 + 9.833X_2 + 2.250 X_1X_2 - 1.000 X_1^2 - 4.500 X_2^2 \dots (5)$$

RESULTS AND DISCUSSION

Optimized Oro-dispersible strips (ODS) were evaluated for parameters like weight of strips, thickness, surface pH, folding endurance, drug content, tensile strength, percent moisture loss, *in vitro* disintegration time and *in vitro* dissolution. All the results of these

linear and quadratic models using Design-Expert for all response observed for 9 formulations were prepared. It is clear that both of the two independent variables, namely polymer concentration (X₁) and plasticizer concentration (X₂), have interactive effects on the three responses Y₁, Y₂ and Y₃, respectively. A positive value reflects an influence that supports optimization, while a negative value implies an inverse factor-response relationship.

Contour plot and response surface analysis

Two-dimensional contour plots for all three responses are for response Y_1 , Y_2 and Y_3 . These plots are known to study the interaction effect (studying the effects of two factors at one time) of the factor on the response properties were drawn. Linear correlation plot showed high R-squared values for all three responses taken between the predicted values and the experimental ones. The R-squared values of Y_1 , Y_2 and Y_3 were found to be in the range of 0.9958-0.9984, 0.9837-0.9877 and 0.9856-0.9946, respectively.

Response 1 (Y_1): Effect on disintegration time

The following polynomial equation prevailed from the model for disintegration time,

$$Y_1 = 28.44 + 8.17X_1 + 0.50X_2 + 2.50X_1X_2 + 4.83X_1^2 + 2.83X_2^2 \quad \dots (6)$$

where Y_1 is disintegration time. All the formulations have shown response of $Y_1 < 60$ s. The model F-value is 0.0002. There is only a 0.02% chance that a "Model F-value" this large could occur due to noise. Values of "Prob $> F$ " less than 0.0500 indicate model terms are significant. In this case X_1 , X_2 , X_1X_2 , X_1^2 , X_2^2 are significant model terms. When the values surpass 0.1, the model terms are insignificant. A positive correlation was found between the concentrations of the two independent variables (X_1 and X_2) and the consequent dependent variable (As amount of polymer and plasticizer is directly proportional to the disintegration time).

Response 2 (Y_2): Effect on drug release

The model proposes the following polynomial equation for drug release,

$$Y_2 = 94.36 - 2.95X_1 + 0.25X_2 \quad \dots (7)$$

where Y_2 is drug release, X_1 is the polymer concentration and X_2 is the concentration of plasticizer.

The model F-value of 241.90 implies the model significant $p < 0.0001$. Thus, this model can be used to explore the design space. The contour diagram shows the impact of different independent variables on the percentage release of drugs (Y_2). The percentage of drug release declines as the quantity of polymer rises, since the drug persists inside the matrix of polymer and vice versa. The pattern of drug release in Oro-dispersible strips (ODS) is often influenced by plasticizer concentration (X_2) and maintains a direct relationship as plasticizer quantity decreases. A positive value for the coefficient (hereinafter referred to as equation) is an indicator of the favorable

effect while a negative value for the coefficient implies an unfavorable effect. Because of noise, there is just a 0.01 percent probability that a model F-value this high will occur. Value of $\text{prob} > F$ less than 0.0500 indicates that the model terms are significant. In this case X_1 are significant model terms and value greater than 0.1000 indicate that the model terms are not significant.

Response 3 (Y_3): Effect on tensile strength

The polynomial equation for tensile strength is as follows:

$$Y_3 = 0.20 + 5.333X_1 + 9.833X_2 + 2.250X_1X_2 - 1.000X_1^2 - 4.500X_2^2 \quad \dots (8)$$

where the tensile force is Y_3 . All the formulations showed the Y_3 response, 0.181-0.210. The model F-value of 110.52 implies that the model is important. Owing to noise, there is only 0.13 percent chance that a model F-value this huge could occur. Values of "Prob F" that are lower than 0.0500 suggest that the model terms are significant. In this case X_1 , X_2 , X_1X_2 , X_1^2 and X_2^2 are significant model terms and response showed a positive response due to increases in impart flexibility to the strip i.e., as the amount of polymer and plasticizer increases the tensile strength also increases. Values greater than 0.1000 indicate that the model terms are not significant.

Optimization model validation

In the Design-Expert software, statistical validity of the polynomials has been developed on the basis of ANOVA provision. The feasibility and grid analysis were subsequently performed to find the composition of optimal formulations. After developing the polynomial equation for the responses Y_1 , Y_2 and Y_3 with the independent variables X_1 and X_2 , the contour plots were constructed using the output files generated by the Design-Experts software, and the formulation was optimized. Optimization was carried out to evaluate the level of the independent variable (X_1 and X_2) which would give a maximum value of F6. The R-squared values were 0.9984, 0.9877 and 0.9946.

Stability studies

No remarkable physical change in appearance and weight variation of Oro-dispersible strips (ODS) was observed in stability studies.

CONCLUSION

The present work is an attempt to develop fast dissolving strip of isosorbide mononitrate using water

soluble polymers. Use of HPMC E15 and glycerin played significant role in design of Oro-dispersible strip. Optimization approach favors in the modification of the disintegration time and release which could be helpful in better utilization of drug. The findings suggest that isosorbide mononitrate fast dissolving Oro-dispersible strip has the potential as an alternative dosage form in treating acute disease like angina pectoris.

ACKNOWLEDGEMENTS

Authors are very thankful to Piramal Laboratories Ltd. Mumbai, India for providing free drug sample. Authors are also thankful to the all the service providers to complete this research work successfully.

REFERENCES

- Patel A.R., Prajapati D.S. and Raval J. A.: Fast dissolving films (FDFs) as a newer venture in fast dissolving dosage forms. *Int. J. Drug Dev. Res.*, 2010, 2(2), 232–246.
- Chaudhary H., Gauri S., Rathee P. and Kumar V.: Development and optimization of fast dissolving oro-dispersible films of granisetron HCl using Box–Behnken statistical design, *Bull. Fac. Pharmacy*, 2013, 51(2), 193–201.
- Dixit R.P. and Puthli S.P.: Oral strip technology: Overview and future potential. *J. Control. Rele.*, 2009, 139(2), 94–107.
- Babu A. and Akhtar M.S.: Overview of formulation and evaluation of fast dissolving tablet: A promising tablet dosage form. *J. Appl. Pharm. Res.*, 2020, 8(3), 1–9.
- Irfan M., Rabel S., Bukhtar Q., Qadir M.I., Jabeen F. and Khan A.: Orally disintegrating films: A modern expansion in drug delivery system. *Saudi Pharm. J.*, 2016, 24(5), 537–546.
- Aher S.S., Saudagar R.B. and Shinde M.S.: Review: fast dissolving tablet. *Int. J. Curr. Pharm. Res.*, 2018, 10(2), 5.
- El-Setouhy D.A. and El-Malak NSA.: Formulation of a Novel Tianeptine Sodium Orodispersible Film. *AAPS Pharm. Sci. Tech.*, 2010, 11(3), 1018–1025.
- Reema P. and Richard G.Z.: Dissolvable film. US 2007/0042023 A1 1–8, 2007.
- Gohel M., Soniwala M., Sharma R. and Parikh R.: Development of taste masked film of valdecoxib for oral use. *Indian J. Pharm. Sci.*, 2007, 69(2), 320.
- Arya A., Chandra A. and Sharma V.: PKF dissolving oral films: A innovative drug delivery system and dosage form. *IJCTR*, 2010, 2(1), 576–583.
- Ravi G., Bose PSC., Ravi V., Sarita D. and Kanna S.: Design, Development and Evaluation of Isosorbide Mononitrate Orally Disintegrating Tablets. *Int. J. Pharma. Res. Health Sci.*, 2020, 8(2) 3147–3150.
- ElMeshad A.N. and El Hagrasy A.S.: Characterization and Optimization of Orodispersible Mosapride Film Formulations. *AAPS Pharm.Sci.Tech.*, [Internet]. 2011, 19, 12(4), 1384–1392.
- Linku A. and Sijimol J.: Formulation and evaluation of fast dissolving oral film of anti-allergic drug. *Asian J. Pharm. Res. Dev.*, 2018, 10, 6(3), 5–16.
- Patel R., Shardul N., Patel J. and Baria A.: Formulation, development & evaluation of oral fast dissolving anti-allergic film of levocetirizine dihydrochloride. *APSR*, 2009, 1(2), 212–217.
- Kunte S. and Tandale P.: Fast dissolving strips: A novel approach for the delivery of verapamil. *J. Pharm. Bioallied Sci.*, [Internet], 2010, 2(4), 325.
- Mishra R. and Amin A.: Formulation and characterization of rapidly dissolving films of cetirizine hydrochloride using pullulan as a film forming agent. *IJPER*, 2011, 45(1), 71–77.
- Shelke P.V., Dumbare A.S., Gadhav M.V., Jadhav S. L., Sonawane A.A. and Gaikwad D.D.: Formulation and evaluation of rapidly disintegrating film of amlodipine besylate. *JDDT*, 2012, 2(2), 72–75.
- Patel R.S. and Poddar S. S.: Development and characterization of mucoadhesive buccal patches of salbutamol sulphate. *CDD*, 2009, (6), 140–144.
- Chavan R., Pande V., Sonawane R. and Zawar L.: Design development and evaluation of thin films of montelukast sodium. *AJPTR*, 2013, 3(4), 386–398.
- ICH Guidelines. Stability testing of new drug substances and products Q1A(R₂) http://www.ich.org/fileadmin/Public_Web_Site/ICH_Products/Guidelines/Quality/Q1A_R2/Step4/Q1A_R2_Guideline.pdf; accessed on 15-April-2020.

^a Department of Pharmaceutics, Rajarshi Shahu College of Pharmacy, Buldana - 443 001, Maharashtra, India

^b Department of Pharmaceutics, Sanjivani College of Pharmaceutical Education and Research, Kopergaon - 423 601, Maharashtra, India

^c Department of Pharmacology, Rajarshi Shahu College of Pharmacy, Buldana - 443 001, Maharashtra, India

*For Correspondence: E-mail: prakashkendre@gmail.com

Prakash N. Kendre^{a*}, Akash R. Aher^b, Somnath K. Vibhute^a, Ajinkya K. Pote^a, Subhash V. Deshmane^a and Shirish P. Jain^c

(Received 25 September 2020) (Accepted 27 October 2021)

<https://doi.org/10.53879/id.59.04.12744>

EFFECT OF HYDROPHILIC POLYMER ON DESIGN EXPERT ASSISTED ORO-DISPERSIBLE STRIP (ODS) OF ISOSORBIDE MONONITRATE

ABSTRACT

Oral conventional formulations like tablets, capsules and liquids have many limitations. Due to this and patient incompliance, there is a need to develop new formulations with better efficiency and stability. The aim of the present study was to develop and optimize fast dissolving Oro-dispersible strips (ODS) of isosorbide mononitrate by 3²-full factorial design. HPMC E15 (X₁) concentration and glycerin (X₂) concentration were selected as the independent variables, whereas, *in vitro* disintegration time (Y₁), percent drug release (Y₂) and tensile strength (Y₃) were selected as dependent variables. Fast dissolving Oro-dispersible strips of isosorbide mononitrate were prepared by the solvent casting method. Tensile strength, disintegration time and *in vitro* dissolution of ODS of the strip were found to be within accepted range for optimized formulation. Statistical validity of the polynomials was established by ANOVA using Design-Expert software. The study suggests isosorbide mononitrate fast dissolving Oro-dispersible strip as potential alternative dosage form in management of angina pectoris.

Keywords: Oro-dispersible strips, Full factorial design, Solvent casting method, Isosorbide mononitrate

INTRODUCTION

The origin of Fast Dissolving Drug Delivery Systems (FDDDS) can be traced back to the late 1970's as a potential substitute for other oral dosage forms like tablets, capsules, syrups and other formulations. Their major benefit is for pediatric and geriatric patients suffering from dysphasia problems. The FDDDS possesses the advantages of conventional tablets and liquid formulation^{1,2}. The ease of administration and better patient compliance makes FDDDS a formulation of choice for pediatric, geriatric and mentally challenged persons³.

Delivery of the drug to the site of action successfully is the prime moto of any drug delivery system. The drug delivery system should be safe, effective, convenient and economical with highest patient compliance^{4,5}. In FDDDS, the drug gets disintegrated, dissolved or swallowed and then reaches into the systemic circulation to show desired therapeutic effect^{6,7}.

Oro-dispersible strips (ODS) is one of the convenient novel drug delivery systems for the delivery of the drugs. It is based upon the technology of trans-dermal patch and consists of a very thin oral strip, to be placed on the patient's tongue or any oral mucosal tissue. This film then gets instantly wet by saliva and the strip rapidly hydrates and adheres onto the site of application⁸.

Ease of administration, dosing accuracy, self-medication and patient compliance are the advantages offered by ODS over the other dosage forms⁹. For

ODS administration, there is no need of water and can administered anytime, anywhere. These strips provide better disintegration and dissolution in the oral cavity due to its large surface area¹⁰.

Isosorbide mononitrate is the long-acting metabolite of isosorbide dinitrate utilized as the vasodilator's specialist in the administration of angina pectoris by expanding the vessels. It brings down the circulatory strain and decreases the left ventricular pre-load and after-load, in this manner prompts a decrease of myocardial oxygen necessity. Usual dose of isosorbide mononitrate is 10-60 mg. The limit of absolute oral bioavailability of isosorbide mononitrate is about 90-95% and absorption is about 100%. Oral fast dissolving Oro-dispersible strips of isosorbide mononitrate will be convenient for geriatric patients and adults with swallowing difficulty¹¹.

The present research work involves the formulation and optimization of Oro-dispersible strips of isosorbide mononitrate by applying 3²-factorial designs to understand the effect of formulation variables likes concentration of polymer (HPMC E15) and concentration of plasticizer (glycerin) on *in vitro* evaluation parameter.

METHODS

Isosorbide mononitrate was procured from Piramal Laboratories Ltd. Mumbai, India. HPMC E15 was obtained from Loba Chemie, Mumbai, India. Glycerin, citric acid and mannitol were procured from SD Fine Chem Ltd., Mumbai, India. All the materials used in this study were of analytical grade. Double distilled water was used throughout the study. The drug and all materials

were analyzed for FT-IR and DSC to check compatibility among the selected materials^{12,13}.

Formulation of Oro-dispersible strips (ODS)

The Solvent Casting Method was used to prepare quickly dissolving Oro-dispersible strips of isosorbide mononitrate¹⁴. The polymer HPMC E15 and plasticizer (glycerin) were dissolved in purified water and permitted to swirl for 4 h and held for 1 h to eliminate any trapped air bubbles; this solution was referred to as 'aqueous solution-I'. Drug and other excipients, such as mannitol and saliva stimulating agent (citric acid) were allowed to dissolve in distilled water, referring to as 'Aqueous 'solution-II'. Then 'solution-I' and 'solution-II' were mixed and agitated for 1 h. The resultant mixture was eventually permitted to spill into the glass petri dish and was dried overnight. The dried strips were carefully removed from the petri dish, checked for any imperfections, and cut in squares of 6 cm². For further analyses, samples were placed in airtight containers.

Experimental design

For the optimization of ODS, the 3²-full factorial design was used. All the batches designed as per the 3²-full- factorial are shown in Table I. The mechanical property of ODS was studied using two factors at 3 levels and the identification and performance of nine possible combinations of experimental trials. Independent variables selected for this analysis were concentration of HPMC E15 (X₁) and concentration of glycerin (X₂), whereas *in vitro* disintegration time; (DT), percentage of drug release (% DR) and tensile strength (TS) were selected as dependent variables at three levels low, medium and high. The corresponding factor levels were marked as -1, 0 and +1. In Design-Expert 8.0.7.1 software, the data were subjected to a contour and linear correlation plot to determine the effect of polymers on the dependent variables. A statistical model incorporating interactive and polynomial terms was used to calculate the responses as follows:

$$Y = b_0 + b_1 X_1 + b_2 X_2 + b_{12} X_1 X_2 + b_{11} X_1^2 + b_{22} X_2^2 \quad \dots (1)$$

where Y is the dependent variable, b₀ is the arithmetic mean response of the nine runs and b_i is the estimated coefficient for the corresponding factor X_i, which represent the average result of changing one factor at a time from its low to high value. The term interaction (X₁, X₂) indicates how the response varies as two factors shift at the same time. To investigate the nonlinearity, the polynomial terms (X₁X₁ and X₂ X₂) are included.

Evaluation of Oro-dispersible strips

The assessment parameters for the Oro-dispersible strips of isosorbide mononitrate were weight, surface pH strength, width, product quality, folding endurance, content uniformity, disintegration time and *in vitro* dissolution¹⁵⁻¹⁹.

The percentage moisture loss was calculated as follows²⁰. The experiments were performed in triplicate and recorded mean values are reported.

$$\text{Tensile strength} = \frac{\text{Load at failure}}{\text{Strip thickness} \times \text{Strip width}} \times 100 \quad \dots(2)$$

In vitro dissolution studies

The *in vitro* dissolution studies for strips were performed using USP Type II dissolution apparatus at 37±0.5 °C and 50 rpm speed in 900 mL of phosphate buffer (pH 6.8). 5 mL aliquots were withdrawn at the time interval of every 60 seconds and was replaced with equal volume of fresh dissolution medium and analyzed by spectrophotometer at 221 nm. The cumulative amount of drug release at various time intervals was calculated.

Stability study

Stability study on the optimized formulation of Oro-dispersible strip was carried out as per ICH Q1A (R2) guidelines to determine the effect of temperature and humidity on the stability of the formulation. The optimized formulation was stored in stability chamber at 40±2 °C /75±5% RH and 25 °C/40% RH for duration of 90 days. The sample, were withdrawn at 15, 30, 60- and 90-days intervals; evaluated for physical and chemical parameters²¹.

Data analysis

Statistical validation of the polynomial equation was developed by the Design-Expert, based on ANOVA provision in the software. It produced a total of nine runs (F1-F9) with a triplicate center point. The findings of the resulting experimental response properties were correlated with those of the forecasted values.

Polynomial equations:

$$Y_1 = 28.44 + 8.17X_1 + 0.50X_2 + 2.50X_1X_2 + 4.83X_1^2 + 2.83X_2^2 \quad \dots (3)$$

$$Y_2 = 94.36 - 2.95X_1 + 0.25X_2 \quad \dots (4)$$

Table I: Evaluation of physical parameters of prepared oro-dispersible film

Formulation code	*Drug content (%)	*Thickness (mm)	*Weight variation (mg)	*Surface pH	*Folding endurance	*Percent moisture loss
F1	96.45±0.4	0.26±0.01	54.00±0.52	6.73±0.28	356±1.52	6.10±0.22
F2	97.91±0.2	0.29±0.01	53.89±0.37	6.80±0.33	392±3.89	3.81±0.43
F3	96.76±0.3	0.25±0.01	53.33±0.49	6.83±0.29	248±2.76	6.10±0.15
F4	97.12±0.5	0.33±0.01	55.11±0.41	6.81±0.33	402±4.01	3.78±0.32
F5	97.82±0.5	0.27±0.01	53.69±0.37	6.83±0.29	247±1.52	6.96±0.19
F6	98.17±0.2	0.23±0.01	52.48±0.34	6.97±0.35	216±2.00	5.98±0.29
F7	98.02±0.5	0.24±0.01	53.95±0.52	6.96±0.32	270±3.05	2.80±0.24
F8	96.88±0.3	0.21±0.01	50.00±0.36	7.10±0.26	202±2.08	6.25±0.28
F9	96.50±0.6	0.26±0.01	50.70±0.51	6.90±0.30	215±3.20	3.41±0.35

Evaluation of physical and chemical stability of optimized batch (F6) at 40±2°C/75±5% RH as per ICH Q1A (R2) guidelines of stability study

Time (days)	Physical change		Chemical change	
	Appearance	*Weight variation (mg)	*Percent drug content	*Surface pH
1	No Change	53.69±0.22	97.80±1.25	6.83±0.12
15	(Film appears transparent, uniform and clear)	53.30±0.15	97.45±2.35	6.76±0.25
30		53.18±0.11	96.90±1.44	6.69±0.14
60		53.00±0.32	96.61±2.25	6.66±0.25
90		52.30±0.22	96.55±1.84	6.59±0.55

*All the observations were taken in triplicate as ±SD, (n=3)

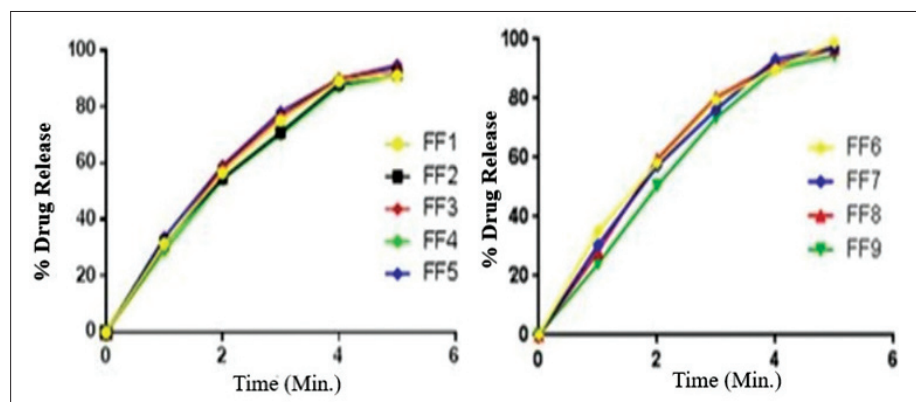


Fig. 1: In vitro drug release profile of fast dissolving strips

parameters are presented in Table I and drug release study of all the batches according to 3²-full factorial design is shown in Fig. 1.

Fitting model to the data

Full factorial statistical experimental design needs 9 runs, as provided by the Response Surface Methodology (RSM). The Y₁, Y₂ and Y₃ ranges are 30.00-47.00 seconds, 91.2-97.8% and 0.18-0.21 N m⁻², respectively. Simultaneously fitted to first order, second order,

$$Y_3 = 0.20 + 5.333X_1 + 9.833X_2 + 2.250 X_1X_2 - 1.000 X_1^2 - 4.500 X_2^2 \dots (5)$$

RESULTS AND DISCUSSION

Optimized Oro-dispersible strips (ODS) were evaluated for parameters like weight of strips, thickness, surface pH, folding endurance, drug content, tensile strength, percent moisture loss, *in vitro* disintegration time and *in vitro* dissolution. All the results of these

linear and quadratic models using Design-Expert for all response observed for 9 formulations were prepared. It is clear that both of the two independent variables, namely polymer concentration (X₁) and plasticizer concentration (X₂), have interactive effects on the three responses Y₁, Y₂ and Y₃, respectively. A positive value reflects an influence that supports optimization, while a negative value implies an inverse factor-response relationship.

Contour plot and response surface analysis

Two-dimensional contour plots for all three responses are for response Y_1 , Y_2 and Y_3 . These plots are known to study the interaction effect (studying the effects of two factors at one time) of the factor on the response properties were drawn. Linear correlation plot showed high R-squared values for all three responses taken between the predicted values and the experimental ones. The R-squared values of Y_1 , Y_2 and Y_3 were found to be in the range of 0.9958-0.9984, 0.9837-0.9877 and 0.9856-0.9946, respectively.

Response 1 (Y1): Effect on disintegration time

The following polynomial equation prevailed from the model for disintegration time,

$$Y_1 = 28.44 + 8.17X_1 + 0.50X_2 + 2.50X_1X_2 + 4.83X_1^2 + 2.83X_2^2 \quad \dots (6)$$

where Y_1 is disintegration time. All the formulations have shown response of $Y_1 < 60$ s. The model F-value is 0.0002. There is only a 0.02% chance that a "Model F-value" this large could occur due to noise. Values of "Prob $> F$ " less than 0.0500 indicate model terms are significant. In this case X_1 , X_2 , X_1X_2 , X_1^2 , X_2^2 are significant model terms. When the values surpass 0.1, the model terms are insignificant. A positive correlation was found between the concentrations of the two independent variables (X_1 and X_2) and the consequent dependent variable (As amount of polymer and plasticizer is directly proportional to the disintegration time).

Response 2 (Y2): Effect on drug release

The model proposes the following polynomial equation for drug release,

$$Y_2 = 94.36 - 2.95X_1 + 0.25X_2 \quad \dots (7)$$

where Y_2 is drug release, X_1 is the polymer concentration and X_2 is the concentration of plasticizer.

The model F-value of 241.90 implies the model significant $p < 0.0001$. Thus, this model can be used to explore the design space. The contour diagram shows the impact of different independent variables on the percentage release of drugs (Y_2). The percentage of drug release declines as the quantity of polymer rises, since the drug persists inside the matrix of polymer and vice versa. The pattern of drug release in Oro-dispersible strips (ODS) is often influenced by plasticizer concentration (X_2) and maintains a direct relationship as plasticizer quantity decreases. A positive value for the coefficient (hereinafter referred to as equation) is an indicator of the favorable

effect while a negative value for the coefficient implies an unfavorable effect. Because of noise, there is just a 0.01 percent probability that a model F-value this high will occur. Value of $\text{prob} > F$ less than 0.0500 indicates that the model terms are significant. In this case X_1 are significant model terms and value greater than 0.1000 indicate that the model terms are not significant.

Response 3 (Y3): Effect on tensile strength

The polynomial equation for tensile strength is as follows:

$$Y_3 = 0.20 + 5.333X_1 + 9.833X_2 + 2.250 X_1X_2 - 1.000 X_1^2 - 4.500 X_2^2 \quad \dots (8)$$

where the tensile force is Y_3 . All the formulations showed the Y_3 response, 0.181-0.210. The model F-value of 110.52 implies that the model is important. Owing to noise, there is only 0.13 percent chance that a model F-value this huge could occur. Values of "Prob F" that are lower than 0.0500 suggest that the model terms are significant. In this case X_1 , X_2 , X_1X_2 , X_1^2 and X_2^2 are significant model terms and response showed a positive response due to increases in impart flexibility to the strip i.e., as the amount of polymer and plasticizer increases the tensile strength also increases. Values greater than 0.1000 indicate that the model terms are not significant.

Optimization model validation

In the Design-Expert software, statistical validity of the polynomials has been developed on the basis of ANOVA provision. The feasibility and grid analysis were subsequently performed to find the composition of optimal formulations. After developing the polynomial equation for the responses Y_1 , Y_2 and Y_3 with the independent variables X_1 and X_2 , the contour plots were constructed using the output files generated by the Design-Experts software, and the formulation was optimized. Optimization was carried out to evaluate the level of the independent variable (X_1 and X_2) which would give a maximum value of F6. The R-squared values were 0.9984, 0.9877 and 0.9946.

Stability studies

No remarkable physical change in appearance and weight variation of Oro-dispersible strips (ODS) was observed in stability studies.

CONCLUSION

The present work is an attempt to develop fast dissolving strip of isosorbide mononitrate using water

soluble polymers. Use of HPMC E15 and glycerin played significant role in design of Oro-dispersible strip. Optimization approach favors in the modification of the disintegration time and release which could be helpful in better utilization of drug. The findings suggest that isosorbide mononitrate fast dissolving Oro-dispersible strip has the potential as an alternative dosage form in treating acute disease like angina pectoris.

ACKNOWLEDGEMENTS

Authors are very thankful to Piramal Laboratories Ltd. Mumbai, India for providing free drug sample. Authors are also thankful to the all the service providers to complete this research work successfully.

REFERENCES

- Patel A.R., Prajapati D.S. and Raval J. A.: Fast dissolving films (FDFs) as a newer venture in fast dissolving dosage forms. *Int. J. Drug Dev. Res.*, 2010, 2(2), 232–246.
- Chaudhary H., Gauri S., Rathee P. and Kumar V.: Development and optimization of fast dissolving oro-dispersible films of granisetron HCl using Box–Behnken statistical design, *Bull. Fac. Pharmacy*, 2013, 51(2), 193–201.
- Dixit R.P. and Puthli S.P.: Oral strip technology: Overview and future potential. *J. Control. Rele.*, 2009, 139(2), 94–107.
- Babu A. and Akhtar M.S.: Overview of formulation and evaluation of fast dissolving tablet: A promising tablet dosage form. *J. Appl. Pharm. Res.*, 2020, 8(3), 1–9.
- Irfan M., Rabel S., Bukhtar Q., Qadir M.I., Jabeen F. and Khan A.: Orally disintegrating films: A modern expansion in drug delivery system. *Saudi Pharm. J.*, 2016, 24(5), 537–546.
- Aher S.S., Saudagar R.B. and Shinde M.S.: Review: fast dissolving tablet. *Int. J. Curr. Pharm. Res.*, 2018, 10(2), 5.
- El-Setouhy D.A. and El-Malak NSA.: Formulation of a Novel Tianeptine Sodium Orodispersible Film. *AAPS Pharm. Sci. Tech.*, 2010, 11(3), 1018–1025.
- Reema P. and Richard G.Z.: Dissolvable film. US 2007/0042023 A1 1–8, 2007.
- Gohel M., Soniwala M., Sharma R. and Parikh R.: Development of taste masked film of valdecoxib for oral use. *Indian J. Pharm. Sci.*, 2007, 69(2), 320.
- Arya A., Chandra A. and Sharma V.: PKF dissolving oral films: A innovative drug delivery system and dosage form. *IJCTR*, 2010, 2(1), 576–583.
- Ravi G., Bose PSC., Ravi V., Sarita D. and Kanna S.: Design, Development and Evaluation of Isosorbide Mononitrate Orally Disintegrating Tablets. *Int. J. Pharma. Res. Health Sci.*, 2020, 8(2) 3147–3150.
- EIMeshad A.N. and El Hagrasy A.S.: Characterization and Optimization of Orodispersible Mosapride Film Formulations. *AAPS Pharm.Sci.Tech.*, [Internet]. 2011, 19, 12(4), 1384–1392.
- Linku A. and Sijimol J.: Formulation and evaluation of fast dissolving oral film of anti-allergic drug. *Asian J. Pharm. Res. Dev.*, 2018, 10, 6(3), 5–16.
- Patel R., Shardul N., Patel J. and Baria A.: Formulation, development & evaluation of oral fast dissolving anti-allergic film of levocetirizine dihydrochloride. *APSR*, 2009, 1(2), 212–217.
- Kunte S. and Tandale P.: Fast dissolving strips: A novel approach for the delivery of verapamil. *J. Pharm. Bioallied Sci.*, [Internet], 2010, 2(4), 325.
- Mishra R. and Amin A.: Formulation and characterization of rapidly dissolving films of cetirizine hydrochloride using pullulan as a film forming agent *IJPER*, 2011, 45(1), 71–77.
- Shelke P.V., Dumbare A.S., Gadhav M.V., Jadhav S. L., Sonawane A.A. and Gaikwad D.D.: Formulation and evaluation of rapidly disintegrating film of amlodipine besylate, *JDDT*, 2012, 2(2), 72–75.
- Patel R.S. and Poddar S. S.: Development and characterization of mucoadhesive buccal patches of salbutamol sulphate, *CDD*, 2009, (6), 140–144.
- Chavan R., Pande V., Sonawane R. and Zawar L.: Design development and evaluation of thin films of montelukast sodium, *AJPTR*, 2013, 3(4), 386–398.
- ICH Guidelines. Stability testing of new drug substances and products Q1A(R₂) http://www.ich.org/fileadmin/Public_Web_Site/ICH_Products/Guidelines/Quality/Q1A_R2/Step4/Q1A_R2_Guideline.pdf; accessed on 15-April-2020.

^a Department of Pharmaceutics, Rajarshi Shahu College of Pharmacy, Buldana - 443 001, Maharashtra, India

^b Department of Pharmaceutics, Sanjivani College of Pharmaceutical Education and Research, Kopergaon - 423 601, Maharashtra, India

^c Department of Pharmacology, Rajarshi Shahu College of Pharmacy, Buldana - 443 001, Maharashtra, India

*For Correspondence: E-mail: prakashkendre@gmail.com

(Received 25 September 2020) (Accepted 27 October 2021)

<https://doi.org/10.53879/id.59.04.12744>

Prakash N. Kendre^{a*}, Akash R. Aher^b, Somnath K. Vibhute^a, Ajinkya K. Pote^a, Subhash V. Deshmane^a and Shirish P. Jain^c

EFFECT OF HYDROPHILIC POLYMER ON DESIGN EXPERT ASSISTED ORO-DISPERSIBLE STRIP (ODS) OF ISOSORBIDE MONONITRATE

ABSTRACT

Oral conventional formulations like tablets, capsules and liquids have many limitations. Due to this and patient incompliance, there is a need to develop new formulations with better efficiency and stability. The aim of the present study was to develop and optimize fast dissolving Oro-dispersible strips (ODS) of isosorbide mononitrate by 3²-full factorial design. HPMC E15 (X₁) concentration and glycerin (X₂) concentration were selected as the independent variables, whereas, *in vitro* disintegration time (Y₁), percent drug release (Y₂) and tensile strength (Y₃) were selected as dependent variables. Fast dissolving Oro-dispersible strips of isosorbide mononitrate were prepared by the solvent casting method. Tensile strength, disintegration time and *in vitro* dissolution of ODS of the strip were found to be within accepted range for optimized formulation. Statistical validity of the polynomials was established by ANOVA using Design-Expert software. The study suggests isosorbide mononitrate fast dissolving Oro-dispersible strip as potential alternative dosage form in management of angina pectoris.

Keywords: Oro-dispersible strips, Full factorial design, Solvent casting method, Isosorbide mononitrate

INTRODUCTION

The origin of Fast Dissolving Drug Delivery Systems (FDDDS) can be traced back to the late 1970's as a potential substitute for other oral dosage forms like tablets, capsules, syrups and other formulations. Their major benefit is for pediatric and geriatric patients suffering from dysphasia problems. The FDDDS possesses the advantages of conventional tablets and liquid formulation^{1,2}. The ease of administration and better patient compliance makes FDDDS a formulation of choice for pediatric, geriatric and mentally challenged persons³.

Delivery of the drug to the site of action successfully is the prime moto of any drug delivery system. The drug delivery system should be safe, effective, convenient and economical with highest patient compliance^{4,5}. In FDDDS, the drug gets disintegrated, dissolved or swallowed and then reaches into the systemic circulation to show desired therapeutic effect^{6,7}.

Oro-dispersible strips (ODS) is one of the convenient novel drug delivery systems for the delivery of the drugs. It is based upon the technology of trans-dermal patch and consists of a very thin oral strip, to be placed on the patient's tongue or any oral mucosal tissue. This film then gets instantly wet by saliva and the strip rapidly hydrates and adheres onto the site of application⁸.

Ease of administration, dosing accuracy, self-medication and patient compliance are the advantages offered by ODS over the other dosage forms⁹. For

ODS administration, there is no need of water and can administered anytime, anywhere. These strips provide better disintegration and dissolution in the oral cavity due to its large surface area¹⁰.

Isosorbide mononitrate is the long-acting metabolite of isosorbide dinitrate utilized as the vasodilator's specialist in the administration of angina pectoris by expanding the vessels. It brings down the circulatory strain and decreases the left ventricular pre-load and after-load, in this manner prompts a decrease of myocardial oxygen necessity. Usual dose of isosorbide mononitrate is 10-60 mg. The limit of absolute oral bioavailability of isosorbide mononitrate is about 90-95% and absorption is about 100%. Oral fast dissolving Oro-dispersible strips of isosorbide mononitrate will be convenient for geriatric patients and adults with swallowing difficulty¹¹.

The present research work involves the formulation and optimization of Oro-dispersible strips of isosorbide mononitrate by applying 3²-factorial designs to understand the effect of formulation variables likes concentration of polymer (HPMC E15) and concentration of plasticizer (glycerin) on *in vitro* evaluation parameter.

METHODS

Isosorbide mononitrate was procured from Piramal Laboratories Ltd. Mumbai, India. HPMC E15 was obtained from Loba Chemie, Mumbai, India. Glycerin, citric acid and mannitol were procured from SD Fine Chem Ltd., Mumbai, India. All the materials used in this study were of analytical grade. Double distilled water was used throughout the study. The drug and all materials

were analyzed for FT-IR and DSC to check compatibility among the selected materials^{12,13}.

Formulation of Oro-dispersible strips (ODS)

The Solvent Casting Method was used to prepare quickly dissolving Oro-dispersible strips of isosorbide mononitrate¹⁴. The polymer HPMC E15 and plasticizer (glycerin) were dissolved in purified water and permitted to swirl for 4 h and held for 1 h to eliminate any trapped air bubbles; this solution was referred to as 'aqueous solution-I'. Drug and other excipients, such as mannitol and saliva stimulating agent (citric acid) were allowed to dissolve in distilled water, referring to as 'Aqueous 'solution-II'. Then 'solution-I' and 'solution-II' were mixed and agitated for 1 h. The resultant mixture was eventually permitted to spill into the glass petri dish and was dried overnight. The dried strips were carefully removed from the petri dish, checked for any imperfections, and cut in squares of 6 cm². For further analyses, samples were placed in airtight containers.

Experimental design

For the optimization of ODS, the 3²-full factorial design was used. All the batches designed as per the 3²-full- factorial are shown in Table I. The mechanical property of ODS was studied using two factors at 3 levels and the identification and performance of nine possible combinations of experimental trials. Independent variables selected for this analysis were concentration of HPMC E15 (X_1) and concentration of glycerin (X_2), whereas *in vitro* disintegration time; (DT), percentage of drug release (% DR) and tensile strength (TS) were selected as dependent variables at three levels low, medium and high. The corresponding factor levels were marked as -1, 0 and +1. In Design-Expert 8.0.7.1 software, the data were subjected to a contour and linear correlation plot to determine the effect of polymers on the dependent variables. A statistical model incorporating interactive and polynomial terms was used to calculate the responses as follows:

$$Y = b_0 + b_1 X_1 + b_2 X_2 + b_{12} X_1 X_2 + b_{11} X_1^2 + b_{22} X_2^2 \quad \dots (1)$$

where Y is the dependent variable, b_0 is the arithmetic mean response of the nine runs and b_i is the estimated coefficient for the corresponding factor X_i , which represent the average result of changing one factor at a time from its low to high value. The term interaction (X_1, X_2) indicates how the response varies as two factors shift at the same time. To investigate the nonlinearity, the polynomial terms ($X_1 X_1$ and $X_2 X_2$) are included.

Evaluation of Oro-dispersible strips

The assessment parameters for the Oro-dispersible strips of isosorbide mononitrate were weight, surface pH strength, width, product quality, folding endurance, content uniformity, disintegration time and *in vitro* dissolution¹⁵⁻¹⁹.

The percentage moisture loss was calculated as follows²⁰. The experiments were performed in triplicate and recorded mean values are reported.

$$\text{Tensile strength} = \frac{\text{Load at failure}}{\text{Strip thickness} \times \text{Strip width}} \times 100 \quad \dots(2)$$

In vitro dissolution studies

The *in vitro* dissolution studies for strips were performed using USP Type II dissolution apparatus at 37±0.5 °C and 50 rpm speed in 900 mL of phosphate buffer (pH 6.8). 5 mL aliquots were withdrawn at the time interval of every 60 seconds and was replaced with equal volume of fresh dissolution medium and analyzed by spectrophotometer at 221 nm. The cumulative amount of drug release at various time intervals was calculated.

Stability study

Stability study on the optimized formulation of Oro-dispersible strip was carried out as per ICH Q1A (R2) guidelines to determine the effect of temperature and humidity on the stability of the formulation. The optimized formulation was stored in stability chamber at 40±2 °C /75±5% RH and 25 °C/40% RH for duration of 90 days. The sample, were withdrawn at 15, 30, 60- and 90-days intervals; evaluated for physical and chemical parameters²¹.

Data analysis

Statistical validation of the polynomial equation was developed by the Design-Expert, based on ANOVA provision in the software. It produced a total of nine runs (F1-F9) with a triplicate center point. The findings of the resulting experimental response properties were correlated with those of the forecasted values.

Polynomial equations:

$$Y_1 = 28.44 + 8.17X_1 + 0.50X_2 + 2.50X_1X_2 + 4.83X_1^2 + 2.83X_2^2 \quad \dots (3)$$

$$Y_2 = 94.36 - 2.95X_1 + 0.25X_2 \quad \dots (4)$$

Table I: Evaluation of physical parameters of prepared oro-dispersible film

Formulation code	*Drug content (%)	*Thickness (mm)	*Weight variation (mg)	*Surface pH	*Folding endurance	*Percent moisture loss
F1	96.45±0.4	0.26±0.01	54.00±0.52	6.73±0.28	356±1.52	6.10±0.22
F2	97.91±0.2	0.29±0.01	53.89±0.37	6.80±0.33	392±3.89	3.81±0.43
F3	96.76±0.3	0.25±0.01	53.33±0.49	6.83±0.29	248±2.76	6.10±0.15
F4	97.12±0.5	0.33±0.01	55.11±0.41	6.81±0.33	402±4.01	3.78±0.32
F5	97.82±0.5	0.27±0.01	53.69±0.37	6.83±0.29	247±1.52	6.96±0.19
F6	98.17±0.2	0.23±0.01	52.48±0.34	6.97±0.35	216±2.00	5.98±0.29
F7	98.02±0.5	0.24±0.01	53.95±0.52	6.96±0.32	270±3.05	2.80±0.24
F8	96.88±0.3	0.21±0.01	50.00±0.36	7.10±0.26	202±2.08	6.25±0.28
F9	96.50±0.6	0.26±0.01	50.70±0.51	6.90±0.30	215±3.20	3.41±0.35

Evaluation of physical and chemical stability of optimized batch (F6) at 40±2°C/75±5% RH as per ICH Q1A (R2) guidelines of stability study

Time (days)	Physical change		Chemical change	
	Appearance	*Weight variation (mg)	*Percent drug content	*Surface pH
1	No Change	53.69±0.22	97.80±1.25	6.83±0.12
15	(Film appears transparent, uniform and clear)	53.30±0.15	97.45±2.35	6.76±0.25
30		53.18±0.11	96.90±1.44	6.69±0.14
60		53.00±0.32	96.61±2.25	6.66±0.25
90		52.30±0.22	96.55±1.84	6.59±0.55

*All the observations were taken in triplicate as ±SD, (n=3)

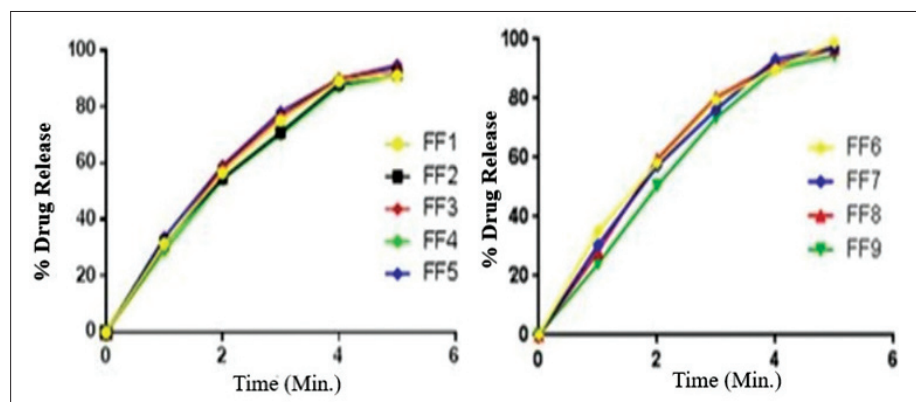


Fig. 1: In vitro drug release profile of fast dissolving strips

parameters are presented in Table I and drug release study of all the batches according to 3²-full factorial design is shown in Fig. 1.

Fitting model to the data

Full factorial statistical experimental design needs 9 runs, as provided by the Response Surface Methodology (RSM). The Y₁, Y₂ and Y₃ ranges are 30.00-47.00 seconds, 91.2-97.8% and 0.18-0.21 N m⁻², respectively. Simultaneously fitted to first order, second order,

$$Y_3 = 0.20 + 5.333X_1 + 9.833X_2 + 2.250 X_1X_2 - 1.000 X_1^2 - 4.500 X_2^2 \dots (5)$$

RESULTS AND DISCUSSION

Optimized Oro-dispersible strips (ODS) were evaluated for parameters like weight of strips, thickness, surface pH, folding endurance, drug content, tensile strength, percent moisture loss, *in vitro* disintegration time and *in vitro* dissolution. All the results of these

linear and quadratic models using Design-Expert for all response observed for 9 formulations were prepared. It is clear that both of the two independent variables, namely polymer concentration (X₁) and plasticizer concentration (X₂), have interactive effects on the three responses Y₁, Y₂ and Y₃, respectively. A positive value reflects an influence that supports optimization, while a negative value implies an inverse factor-response relationship.

Contour plot and response surface analysis

Two-dimensional contour plots for all three responses are for response Y_1 , Y_2 and Y_3 . These plots are known to study the interaction effect (studying the effects of two factors at one time) of the factor on the response properties were drawn. Linear correlation plot showed high R-squared values for all three responses taken between the predicted values and the experimental ones. The R-squared values of Y_1 , Y_2 and Y_3 were found to be in the range of 0.9958-0.9984, 0.9837-0.9877 and 0.9856-0.9946, respectively.

Response 1 (Y1): Effect on disintegration time

The following polynomial equation prevailed from the model for disintegration time,

$$Y_1 = 28.44 + 8.17X_1 + 0.50X_2 + 2.50X_1X_2 + 4.83X_1^2 + 2.83X_2^2 \quad \dots (6)$$

where Y_1 is disintegration time. All the formulations have shown response of $Y_1 < 60$ s. The model F-value is 0.0002. There is only a 0.02% chance that a "Model F-value" this large could occur due to noise. Values of "Prob $> F$ " less than 0.0500 indicate model terms are significant. In this case X_1 , X_2 , X_1X_2 , X_1^2 , X_2^2 are significant model terms. When the values surpass 0.1, the model terms are insignificant. A positive correlation was found between the concentrations of the two independent variables (X_1 and X_2) and the consequent dependent variable (As amount of polymer and plasticizer is directly proportional to the disintegration time).

Response 2 (Y2): Effect on drug release

The model proposes the following polynomial equation for drug release,

$$Y_2 = 94.36 - 2.95X_1 + 0.25X_2 \quad \dots (7)$$

where Y_2 is drug release, X_1 is the polymer concentration and X_2 is the concentration of plasticizer.

The model F-value of 241.90 implies the model significant $p < 0.0001$. Thus, this model can be used to explore the design space. The contour diagram shows the impact of different independent variables on the percentage release of drugs (Y_2). The percentage of drug release declines as the quantity of polymer rises, since the drug persists inside the matrix of polymer and vice versa. The pattern of drug release in Oro-dispersible strips (ODS) is often influenced by plasticizer concentration (X_2) and maintains a direct relationship as plasticizer quantity decreases. A positive value for the coefficient (hereinafter referred to as equation) is an indicator of the favorable

effect while a negative value for the coefficient implies an unfavorable effect. Because of noise, there is just a 0.01 percent probability that a model F-value this high will occur. Value of $\text{prob} > F$ less than 0.0500 indicates that the model terms are significant. In this case X_1 are significant model terms and value greater than 0.1000 indicate that the model terms are not significant.

Response 3 (Y3): Effect on tensile strength

The polynomial equation for tensile strength is as follows:

$$Y_3 = 0.20 + 5.333X_1 + 9.833X_2 + 2.250 X_1X_2 - 1.000 X_1^2 - 4.500 X_2^2 \quad \dots (8)$$

where the tensile force is Y_3 . All the formulations showed the Y_3 response, 0.181-0.210. The model F-value of 110.52 implies that the model is important. Owing to noise, there is only 0.13 percent chance that a model F-value this huge could occur. Values of "Prob F" that are lower than 0.0500 suggest that the model terms are significant. In this case X_1 , X_2 , X_1X_2 , X_1^2 and X_2^2 are significant model terms and response showed a positive response due to increases in impart flexibility to the strip i.e., as the amount of polymer and plasticizer increases the tensile strength also increases. Values greater than 0.1000 indicate that the model terms are not significant.

Optimization model validation

In the Design-Expert software, statistical validity of the polynomials has been developed on the basis of ANOVA provision. The feasibility and grid analysis were subsequently performed to find the composition of optimal formulations. After developing the polynomial equation for the responses Y_1 , Y_2 and Y_3 with the independent variables X_1 and X_2 , the contour plots were constructed using the output files generated by the Design-Experts software, and the formulation was optimized. Optimization was carried out to evaluate the level of the independent variable (X_1 and X_2) which would give a maximum value of F6. The R-squared values were 0.9984, 0.9877 and 0.9946.

Stability studies

No remarkable physical change in appearance and weight variation of Oro-dispersible strips (ODS) was observed in stability studies.

CONCLUSION

The present work is an attempt to develop fast dissolving strip of isosorbide mononitrate using water

soluble polymers. Use of HPMC E15 and glycerin played significant role in design of Oro-dispersible strip. Optimization approach favors in the modification of the disintegration time and release which could be helpful in better utilization of drug. The findings suggest that isosorbide mononitrate fast dissolving Oro-dispersible strip has the potential as an alternative dosage form in treating acute disease like angina pectoris.

ACKNOWLEDGEMENTS

Authors are very thankful to Piramal Laboratories Ltd. Mumbai, India for providing free drug sample. Authors are also thankful to the all the service providers to complete this research work successfully.

REFERENCES

- Patel A.R., Prajapati D.S. and Raval J. A.: Fast dissolving films (FDFs) as a newer venture in fast dissolving dosage forms. *Int. J. Drug Dev. Res.*, 2010, 2(2), 232–246.
- Chaudhary H., Gauri S., Rathee P. and Kumar V.: Development and optimization of fast dissolving oro-dispersible films of granisetron HCl using Box–Behnken statistical design, *Bull. Fac. Pharmacy*, 2013, 51(2), 193–201.
- Dixit R.P. and Puthli S.P.: Oral strip technology: Overview and future potential. *J. Control. Rele.*, 2009, 139(2), 94–107.
- Babu A. and Akhtar M.S.: Overview of formulation and evaluation of fast dissolving tablet: A promising tablet dosage form. *J. Appl. Pharm. Res.*, 2020, 8(3), 1–9.
- Irfan M., Rabel S., Bukhtar Q., Qadir M.I., Jabeen F. and Khan A.: Orally disintegrating films: A modern expansion in drug delivery system. *Saudi Pharm. J.*, 2016, 24(5), 537–546.
- Aher S.S., Saudagar R.B. and Shinde M.S.: Review: fast dissolving tablet. *Int. J. Curr. Pharm. Res.*, 2018, 10(2), 5.
- El-Setouhy D.A. and El-Malak NSA.: Formulation of a Novel Tianeptine Sodium Orodispersible Film. *AAPS Pharm. Sci. Tech.*, 2010, 11(3), 1018–1025.
- Reema P. and Richard G.Z.: Dissolvable film. US 2007/0042023 A1 1–8, 2007.
- Gohel M., Soniwala M., Sharma R. and Parikh R.: Development of taste masked film of valdecoxib for oral use. *Indian J. Pharm. Sci.*, 2007, 69(2), 320.
- Arya A., Chandra A. and Sharma V.: PKF dissolving oral films: A innovative drug delivery system and dosage form. *IJCTR*, 2010, 2(1), 576–583.
- Ravi G., Bose PSC., Ravi V., Sarita D. and Kanna S.: Design, Development and Evaluation of Isosorbide Mononitrate Orally Disintegrating Tablets. *Int. J. Pharma. Res. Health Sci.*, 2020, 8(2) 3147–3150.
- EIMeshad A.N. and El Hagrasy A.S.: Characterization and Optimization of Orodispersible Mosapride Film Formulations. *AAPS Pharm.Sci.Tech.*, [Internet]. 2011, 19, 12(4), 1384–1392.
- Linku A. and Sijimol J.: Formulation and evaluation of fast dissolving oral film of anti-allergic drug. *Asian J. Pharm. Res. Dev.*, 2018, 10, 6(3), 5–16.
- Patel R., Shardul N., Patel J. and Baria A.: Formulation, development & evaluation of oral fast dissolving anti-allergic film of levocetirizine dihydrochloride. *APSR*, 2009, 1(2), 212–217.
- Kunte S. and Tandale P.: Fast dissolving strips: A novel approach for the delivery of verapamil. *J. Pharm. Bioallied Sci.*, [Internet], 2010, 2(4), 325.
- Mishra R. and Amin A.: Formulation and characterization of rapidly dissolving films of cetirizine hydrochloride using pullulan as a film forming agent *IJPER*, 2011, 45(1), 71–77.
- Shelke P.V., Dumbare A.S., Gadhav M.V., Jadhav S. L., Sonawane A.A. and Gaikwad D.D.: Formulation and evaluation of rapidly disintegrating film of amlodipine besylate, *JDDT*, 2012, 2(2), 72–75.
- Patel R.S. and Poddar S. S.: Development and characterization of mucoadhesive buccal patches of salbutamol sulphate, *CDD*, 2009, (6), 140–144.
- Chavan R., Pande V., Sonawane R. and Zawar L.: Design development and evaluation of thin films of montelukast sodium, *AJPTR*, 2013, 3(4), 386–398.
- ICH Guidelines. Stability testing of new drug substances and products Q1A(R₂) http://www.ich.org/fileadmin/Public_Web_Site/ICH_Products/Guidelines/Quality/Q1A_R2/Step4/Q1A_R2_Guideline.pdf; accessed on 15-April-2020.

^a Department of Pharmaceutics, Rajarshi Shahu College of Pharmacy, Buldana - 443 001, Maharashtra, India

^b Department of Pharmaceutics, Sanjivani College of Pharmaceutical Education and Research, Kopergaon - 423 601, Maharashtra, India

^c Department of Pharmacology, Rajarshi Shahu College of Pharmacy, Buldana - 443 001, Maharashtra, India

*For Correspondence: E-mail: prakashkendre@gmail.com

(Received 25 September 2020) (Accepted 27 October 2021)

<https://doi.org/10.53879/id.59.04.12744>

Prakash N. Kendre^{a*}, Akash R. Aher^b, Somnath K. Vibhute^a, Ajinkya K. Pote^a, Subhash V. Deshmane^a and Shirish P. Jain^c

EFFECT OF HYDROPHILIC POLYMER ON DESIGN EXPERT ASSISTED ORO-DISPERSIBLE STRIP (ODS) OF ISOSORBIDE MONONITRATE

ABSTRACT

Oral conventional formulations like tablets, capsules and liquids have many limitations. Due to this and patient incompliance, there is a need to develop new formulations with better efficiency and stability. The aim of the present study was to develop and optimize fast dissolving Oro-dispersible strips (ODS) of isosorbide mononitrate by 3²-full factorial design. HPMC E15 (X₁) concentration and glycerin (X₂) concentration were selected as the independent variables, whereas, *in vitro* disintegration time (Y₁), percent drug release (Y₂) and tensile strength (Y₃) were selected as dependent variables. Fast dissolving Oro-dispersible strips of isosorbide mononitrate were prepared by the solvent casting method. Tensile strength, disintegration time and *in vitro* dissolution of ODS of the strip were found to be within accepted range for optimized formulation. Statistical validity of the polynomials was established by ANOVA using Design-Expert software. The study suggests isosorbide mononitrate fast dissolving Oro-dispersible strip as potential alternative dosage form in management of angina pectoris.

Keywords: Oro-dispersible strips, Full factorial design, Solvent casting method, Isosorbide mononitrate

INTRODUCTION

The origin of Fast Dissolving Drug Delivery Systems (FDDDS) can be traced back to the late 1970's as a potential substitute for other oral dosage forms like tablets, capsules, syrups and other formulations. Their major benefit is for pediatric and geriatric patients suffering from dysphasia problems. The FDDDS possesses the advantages of conventional tablets and liquid formulation^{1,2}. The ease of administration and better patient compliance makes FDDDS a formulation of choice for pediatric, geriatric and mentally challenged persons³.

Delivery of the drug to the site of action successfully is the prime moto of any drug delivery system. The drug delivery system should be safe, effective, convenient and economical with highest patient compliance^{4,5}. In FDDDS, the drug gets disintegrated, dissolved or swallowed and then reaches into the systemic circulation to show desired therapeutic effect^{6,7}.

Oro-dispersible strips (ODS) is one of the convenient novel drug delivery systems for the delivery of the drugs. It is based upon the technology of trans-dermal patch and consists of a very thin oral strip, to be placed on the patient's tongue or any oral mucosal tissue. This film then gets instantly wet by saliva and the strip rapidly hydrates and adheres onto the site of application⁸.

Ease of administration, dosing accuracy, self-medication and patient compliance are the advantages offered by ODS over the other dosage forms⁹. For

ODS administration, there is no need of water and can administered anytime, anywhere. These strips provide better disintegration and dissolution in the oral cavity due to its large surface area¹⁰.

Isosorbide mononitrate is the long-acting metabolite of isosorbide dinitrate utilized as the vasodilator's specialist in the administration of angina pectoris by expanding the vessels. It brings down the circulatory strain and decreases the left ventricular pre-load and after-load, in this manner prompts a decrease of myocardial oxygen necessity. Usual dose of isosorbide mononitrate is 10-60 mg. The limit of absolute oral bioavailability of isosorbide mononitrate is about 90-95% and absorption is about 100%. Oral fast dissolving Oro-dispersible strips of isosorbide mononitrate will be convenient for geriatric patients and adults with swallowing difficulty¹¹.

The present research work involves the formulation and optimization of Oro-dispersible strips of isosorbide mononitrate by applying 3²-factorial designs to understand the effect of formulation variables likes concentration of polymer (HPMC E15) and concentration of plasticizer (glycerin) on *in vitro* evaluation parameter.

METHODS

Isosorbide mononitrate was procured from Piramal Laboratories Ltd. Mumbai, India. HPMC E15 was obtained from Loba Chemie, Mumbai, India. Glycerin, citric acid and mannitol were procured from SD Fine Chem Ltd., Mumbai, India. All the materials used in this study were of analytical grade. Double distilled water was used throughout the study. The drug and all materials

were analyzed for FT-IR and DSC to check compatibility among the selected materials^{12,13}.

Formulation of Oro-dispersible strips (ODS)

The Solvent Casting Method was used to prepare quickly dissolving Oro-dispersible strips of isosorbide mononitrate¹⁴. The polymer HPMC E15 and plasticizer (glycerin) were dissolved in purified water and permitted to swirl for 4 h and held for 1 h to eliminate any trapped air bubbles; this solution was referred to as 'aqueous solution-I'. Drug and other excipients, such as mannitol and saliva stimulating agent (citric acid) were allowed to dissolve in distilled water, referring to as 'Aqueous 'solution-II'. Then 'solution-I' and 'solution-II' were mixed and agitated for 1 h. The resultant mixture was eventually permitted to spill into the glass petri dish and was dried overnight. The dried strips were carefully removed from the petri dish, checked for any imperfections, and cut in squares of 6 cm². For further analyses, samples were placed in airtight containers.

Experimental design

For the optimization of ODS, the 3²-full factorial design was used. All the batches designed as per the 3²-full- factorial are shown in Table I. The mechanical property of ODS was studied using two factors at 3 levels and the identification and performance of nine possible combinations of experimental trials. Independent variables selected for this analysis were concentration of HPMC E15 (X₁) and concentration of glycerin (X₂), whereas *in vitro* disintegration time; (DT), percentage of drug release (% DR) and tensile strength (TS) were selected as dependent variables at three levels low, medium and high. The corresponding factor levels were marked as -1, 0 and +1. In Design-Expert 8.0.7.1 software, the data were subjected to a contour and linear correlation plot to determine the effect of polymers on the dependent variables. A statistical model incorporating interactive and polynomial terms was used to calculate the responses as follows:

$$Y = b_0 + b_1 X_1 + b_2 X_2 + b_{12} X_1 X_2 + b_{11} X_1^2 + b_{22} X_2^2 \quad \dots (1)$$

where Y is the dependent variable, b₀ is the arithmetic mean response of the nine runs and b_i is the estimated coefficient for the corresponding factor X_i, which represent the average result of changing one factor at a time from its low to high value. The term interaction (X₁, X₂) indicates how the response varies as two factors shift at the same time. To investigate the nonlinearity, the polynomial terms (X₁X₁ and X₂ X₂) are included.

Evaluation of Oro-dispersible strips

The assessment parameters for the Oro-dispersible strips of isosorbide mononitrate were weight, surface pH strength, width, product quality, folding endurance, content uniformity, disintegration time and *in vitro* dissolution¹⁵⁻¹⁹.

The percentage moisture loss was calculated as follows²⁰. The experiments were performed in triplicate and recorded mean values are reported.

$$\text{Tensile strength} = \frac{\text{Load at failure}}{\text{Strip thickness} \times \text{Strip width}} \times 100 \quad \dots(2)$$

In vitro dissolution studies

The *in vitro* dissolution studies for strips were performed using USP Type II dissolution apparatus at 37±0.5 °C and 50 rpm speed in 900 mL of phosphate buffer (pH 6.8). 5 mL aliquots were withdrawn at the time interval of every 60 seconds and was replaced with equal volume of fresh dissolution medium and analyzed by spectrophotometer at 221 nm. The cumulative amount of drug release at various time intervals was calculated.

Stability study

Stability study on the optimized formulation of Oro-dispersible strip was carried out as per ICH Q1A (R2) guidelines to determine the effect of temperature and humidity on the stability of the formulation. The optimized formulation was stored in stability chamber at 40±2 °C /75±5% RH and 25 °C/40% RH for duration of 90 days. The sample, were withdrawn at 15, 30, 60- and 90-days intervals; evaluated for physical and chemical parameters²¹.

Data analysis

Statistical validation of the polynomial equation was developed by the Design-Expert, based on ANOVA provision in the software. It produced a total of nine runs (F1-F9) with a triplicate center point. The findings of the resulting experimental response properties were correlated with those of the forecasted values.

Polynomial equations:

$$Y_1 = 28.44 + 8.17X_1 + 0.50X_2 + 2.50X_1X_2 + 4.83X_1^2 + 2.83X_2^2 \quad \dots (3)$$

$$Y_2 = 94.36 - 2.95X_1 + 0.25X_2 \quad \dots (4)$$

Table I: Evaluation of physical parameters of prepared oro-dispersible film

Formulation code	*Drug content (%)	*Thickness (mm)	*Weight variation (mg)	*Surface pH	*Folding endurance	*Percent moisture loss
F1	96.45±0.4	0.26±0.01	54.00±0.52	6.73±0.28	356±1.52	6.10±0.22
F2	97.91±0.2	0.29±0.01	53.89±0.37	6.80±0.33	392±3.89	3.81±0.43
F3	96.76±0.3	0.25±0.01	53.33±0.49	6.83±0.29	248±2.76	6.10±0.15
F4	97.12±0.5	0.33±0.01	55.11±0.41	6.81±0.33	402±4.01	3.78±0.32
F5	97.82±0.5	0.27±0.01	53.69±0.37	6.83±0.29	247±1.52	6.96±0.19
F6	98.17±0.2	0.23±0.01	52.48±0.34	6.97±0.35	216±2.00	5.98±0.29
F7	98.02±0.5	0.24±0.01	53.95±0.52	6.96±0.32	270±3.05	2.80±0.24
F8	96.88±0.3	0.21±0.01	50.00±0.36	7.10±0.26	202±2.08	6.25±0.28
F9	96.50±0.6	0.26±0.01	50.70±0.51	6.90±0.30	215±3.20	3.41±0.35

Evaluation of physical and chemical stability of optimized batch (F6) at 40±2°C/75±5% RH as per ICH Q1A (R2) guidelines of stability study

Time (days)	Physical change		Chemical change	
	Appearance	*Weight variation (mg)	*Percent drug content	*Surface pH
1	No Change	53.69±0.22	97.80±1.25	6.83±0.12
15	(Film appears transparent, uniform and clear)	53.30±0.15	97.45±2.35	6.76±0.25
30		53.18±0.11	96.90±1.44	6.69±0.14
60		53.00±0.32	96.61±2.25	6.66±0.25
90		52.30±0.22	96.55±1.84	6.59±0.55

*All the observations were taken in triplicate as ±SD, (n=3)

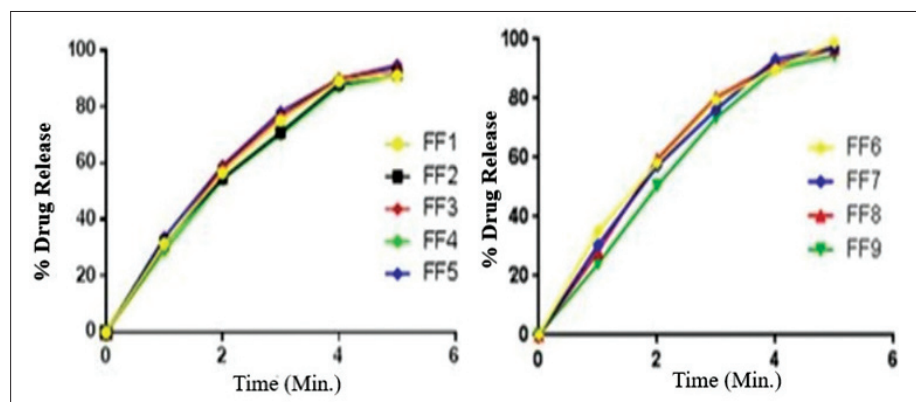


Fig. 1: In vitro drug release profile of fast dissolving strips

parameters are presented in Table I and drug release study of all the batches according to 3²-full factorial design is shown in Fig. 1.

Fitting model to the data

Full factorial statistical experimental design needs 9 runs, as provided by the Response Surface Methodology (RSM). The Y₁, Y₂ and Y₃ ranges are 30.00-47.00 seconds, 91.2-97.8% and 0.18-0.21 N m⁻², respectively. Simultaneously fitted to first order, second order,

$$Y_3 = 0.20 + 5.333X_1 + 9.833X_2 + 2.250 X_1X_2 - 1.000 X_1^2 - 4.500 X_2^2 \quad \dots (5)$$

RESULTS AND DISCUSSION

Optimized Oro-dispersible strips (ODS) were evaluated for parameters like weight of strips, thickness, surface pH, folding endurance, drug content, tensile strength, percent moisture loss, *in vitro* disintegration time and *in vitro* dissolution. All the results of these

linear and quadratic models using Design-Expert for all response observed for 9 formulations were prepared. It is clear that both of the two independent variables, namely polymer concentration (X₁) and plasticizer concentration (X₂), have interactive effects on the three responses Y₁, Y₂ and Y₃, respectively. A positive value reflects an influence that supports optimization, while a negative value implies an inverse factor-response relationship.

Contour plot and response surface analysis

Two-dimensional contour plots for all three responses are for response Y_1 , Y_2 and Y_3 . These plots are known to study the interaction effect (studying the effects of two factors at one time) of the factor on the response properties were drawn. Linear correlation plot showed high R-squared values for all three responses taken between the predicted values and the experimental ones. The R-squared values of Y_1 , Y_2 and Y_3 were found to be in the range of 0.9958-0.9984, 0.9837-0.9877 and 0.9856-0.9946, respectively.

Response 1 (Y1): Effect on disintegration time

The following polynomial equation prevailed from the model for disintegration time,

$$Y_1 = 28.44 + 8.17X_1 + 0.50X_2 + 2.50X_1X_2 + 4.83X_1^2 + 2.83X_2^2 \quad \dots (6)$$

where Y_1 is disintegration time. All the formulations have shown response of $Y_1 < 60$ s. The model F-value is 0.0002. There is only a 0.02% chance that a "Model F-value" this large could occur due to noise. Values of "Prob $> F$ " less than 0.0500 indicate model terms are significant. In this case X_1 , X_2 , X_1X_2 , X_1^2 , X_2^2 are significant model terms. When the values surpass 0.1, the model terms are insignificant. A positive correlation was found between the concentrations of the two independent variables (X_1 and X_2) and the consequent dependent variable (As amount of polymer and plasticizer is directly proportional to the disintegration time).

Response 2 (Y2): Effect on drug release

The model proposes the following polynomial equation for drug release,

$$Y_2 = 94.36 - 2.95X_1 + 0.25X_2 \quad \dots (7)$$

where Y_2 is drug release, X_1 is the polymer concentration and X_2 is the concentration of plasticizer.

The model F-value of 241.90 implies the model significant $p < 0.0001$. Thus, this model can be used to explore the design space. The contour diagram shows the impact of different independent variables on the percentage release of drugs (Y_2). The percentage of drug release declines as the quantity of polymer rises, since the drug persists inside the matrix of polymer and vice versa. The pattern of drug release in Oro-dispersible strips (ODS) is often influenced by plasticizer concentration (X_2) and maintains a direct relationship as plasticizer quantity decreases. A positive value for the coefficient (hereinafter referred to as equation) is an indicator of the favorable

effect while a negative value for the coefficient implies an unfavorable effect. Because of noise, there is just a 0.01 percent probability that a model F-value this high will occur. Value of $\text{prob} > F$ less than 0.0500 indicates that the model terms are significant. In this case X_1 are significant model terms and value greater than 0.1000 indicate that the model terms are not significant.

Response 3 (Y3): Effect on tensile strength

The polynomial equation for tensile strength is as follows:

$$Y_3 = 0.20 + 5.333X_1 + 9.833X_2 + 2.250 X_1X_2 - 1.000 X_1^2 - 4.500 X_2^2 \quad \dots (8)$$

where the tensile force is Y_3 . All the formulations showed the Y_3 response, 0.181-0.210. The model F-value of 110.52 implies that the model is important. Owing to noise, there is only 0.13 percent chance that a model F-value this huge could occur. Values of "Prob F" that are lower than 0.0500 suggest that the model terms are significant. In this case X_1 , X_2 , X_1X_2 , X_1^2 and X_2^2 are significant model terms and response showed a positive response due to increases in impart flexibility to the strip i.e., as the amount of polymer and plasticizer increases the tensile strength also increases. Values greater than 0.1000 indicate that the model terms are not significant.

Optimization model validation

In the Design-Expert software, statistical validity of the polynomials has been developed on the basis of ANOVA provision. The feasibility and grid analysis were subsequently performed to find the composition of optimal formulations. After developing the polynomial equation for the responses Y_1 , Y_2 and Y_3 with the independent variables X_1 and X_2 , the contour plots were constructed using the output files generated by the Design-Experts software, and the formulation was optimized. Optimization was carried out to evaluate the level of the independent variable (X_1 and X_2) which would give a maximum value of F6. The R-squared values were 0.9984, 0.9877 and 0.9946.

Stability studies

No remarkable physical change in appearance and weight variation of Oro-dispersible strips (ODS) was observed in stability studies.

CONCLUSION

The present work is an attempt to develop fast dissolving strip of isosorbide mononitrate using water

soluble polymers. Use of HPMC E15 and glycerin played significant role in design of Oro-dispersible strip. Optimization approach favors in the modification of the disintegration time and release which could be helpful in better utilization of drug. The findings suggest that isosorbide mononitrate fast dissolving Oro-dispersible strip has the potential as an alternative dosage form in treating acute disease like angina pectoris.

ACKNOWLEDGEMENTS

Authors are very thankful to Piramal Laboratories Ltd. Mumbai, India for providing free drug sample. Authors are also thankful to the all the service providers to complete this research work successfully.

REFERENCES

- Patel A.R., Prajapati D.S. and Raval J. A.: Fast dissolving films (FDFs) as a newer venture in fast dissolving dosage forms. *Int. J. Drug Dev. Res.*, 2010, 2(2), 232–246.
- Chaudhary H., Gauri S., Rathee P. and Kumar V.: Development and optimization of fast dissolving oro-dispersible films of granisetron HCl using Box–Behnken statistical design, *Bull. Fac. Pharmacy*, 2013, 51(2), 193–201.
- Dixit R.P. and Puthli S.P.: Oral strip technology: Overview and future potential. *J. Control. Rele.*, 2009, 139(2), 94–107.
- Babu A. and Akhtar M.S.: Overview of formulation and evaluation of fast dissolving tablet: A promising tablet dosage form. *J. Appl. Pharm. Res.*, 2020, 8(3), 1–9.
- Irfan M., Rabel S., Bukhtar Q., Qadir M.I., Jabeen F. and Khan A.: Orally disintegrating films: A modern expansion in drug delivery system. *Saudi Pharm. J.*, 2016, 24(5), 537–546.
- Aher S.S., Saudagar R.B. and Shinde M.S.: Review: fast dissolving tablet. *Int. J. Curr. Pharm. Res.*, 2018, 10(2), 5.
- El-Setouhy D.A. and El-Malak NSA.: Formulation of a Novel Tianeptine Sodium Orodispersible Film. *AAPS Pharm. Sci. Tech.*, 2010, 11(3), 1018–1025.
- Reema P. and Richard G.Z.: Dissolvable film. US 2007/0042023 A1 1–8, 2007.
- Gohel M., Soniwala M., Sharma R. and Parikh R.: Development of taste masked film of valdecoxib for oral use. *Indian J. Pharm. Sci.*, 2007, 69(2), 320.
- Arya A., Chandra A. and Sharma V.: PKF dissolving oral films: A innovative drug delivery system and dosage form. *IJCTR*, 2010, 2(1), 576–583.
- Ravi G., Bose PSC., Ravi V., Sarita D. and Kanna S.: Design, Development and Evaluation of Isosorbide Mononitrate Orally Disintegrating Tablets. *Int. J. Pharma. Res. Health Sci.*, 2020, 8(2) 3147–3150.
- EIMeshad A.N. and El Hagrasy A.S.: Characterization and Optimization of Orodispersible Mosapride Film Formulations. *AAPS Pharm.Sci.Tech.*, [Internet]. 2011, 19, 12(4), 1384–1392.
- Linku A. and Sijimol J.: Formulation and evaluation of fast dissolving oral film of anti-allergic drug. *Asian J. Pharm. Res. Dev.*, 2018, 10, 6(3), 5–16.
- Patel R., Shardul N., Patel J. and Baria A.: Formulation, development & evaluation of oral fast dissolving anti-allergic film of levocetirizine dihydrochloride. *APSR*, 2009, 1(2), 212–217.
- Kunte S. and Tandale P.: Fast dissolving strips: A novel approach for the delivery of verapamil. *J. Pharm. Bioallied Sci.*, [Internet], 2010, 2(4), 325.
- Mishra R. and Amin A.: Formulation and characterization of rapidly dissolving films of cetirizine hydrochloride using pullulan as a film forming agent *IJPER*, 2011, 45(1), 71–77.
- Shelke P.V., Dumbare A.S., Gadhav M.V., Jadhav S. L., Sonawane A.A. and Gaikwad D.D.: Formulation and evaluation of rapidly disintegrating film of amlodipine besylate, *JDDT*, 2012, 2(2), 72–75.
- Patel R.S. and Poddar S. S.: Development and characterization of mucoadhesive buccal patches of salbutamol sulphate, *CDD*, 2009, (6), 140–144.
- Chavan R., Pande V., Sonawane R. and Zawar L.: Design development and evaluation of thin films of montelukast sodium, *AJPTR*, 2013, 3(4), 386–398.
- ICH Guidelines. Stability testing of new drug substances and products Q1A(R₂) http://www.ich.org/fileadmin/Public_Web_Site/ICH_Products/Guidelines/Quality/Q1A_R2/Step4/Q1A_R2_Guideline.pdf; accessed on 15-April-2020.

^a Department of Pharmaceutics, Rajarshi Shahu College of Pharmacy, Buldana - 443 001, Maharashtra, India

^b Department of Pharmaceutics, Sanjivani College of Pharmaceutical Education and Research, Kopergaon - 423 601, Maharashtra, India

^c Department of Pharmacology, Rajarshi Shahu College of Pharmacy, Buldana - 443 001, Maharashtra, India

*For Correspondence: E-mail: prakashkendre@gmail.com

(Received 25 September 2020) (Accepted 27 October 2021)

<https://doi.org/10.53879/id.59.04.12744>

Prakash N. Kendre^{a*}, Akash R. Aher^b, Somnath K. Vibhute^a, Ajinkya K. Pote^a, Subhash V. Deshmane^a and Shirish P. Jain^c

Phytochemicals: A Novel Approach for the Management of Coronavirus Disease 2019

R. S. SHIVATARE*, R. MUSALE, N. K. BHUTALE, S. M. KEWATKAR¹, H. L. TARE², VIBHAVARI CHATUR³, A. N. KHATAWAKAR⁴ AND D. S. SURYAVANSHI⁵

Department of Pharmacy, Jagdishprasad Jhabarwal Tiberval University, Jhunjhunu, Rajasthan 333001, ¹Department of Pharmacognosy, Rajarshi Shahu College of Pharmacy, Buldana, Maharashtra 443001, ²Department of Pharmacy, Sharadchandra Pawar College of Pharmacy, Otur, Maharashtra 412409, ³Department of Pharmaceutics, Rasiklal M. Dhariwal Institute of Pharmaceutical Education and Research, Pune, Maharashtra 411019, ⁴Department of Pharmacy, Anuradha College of Pharmacy, Chikhli, Maharashtra 443201, ⁵Department of Pharmaceutics, Dr. D. Y. Patil College of Pharmacy, Pune, Maharashtra 411044, India

Shivatare *et al.*: Phytochemicals in the Management of Coronavirus Disease 2019

The severe acute respiratory syndrome coronavirus 2, formerly known as 2019 novel coronavirus, the causative pathogen of coronavirus disease 2019 is a major source of disaster in the 21st century. In the second meeting of the Emergency Committee, the World Health Organization declared that coronavirus disease 2019 is a “public-health emergency of international concern” on 30 January, 2020. Coronavirus is transmitted *via* airborne droplets from human to human or human to animal. Through membrane angiotensin-converting enzyme 2 exopeptidase receptor coronavirus enters in human cell. For the treatment of this sudden and lethal disease during coronavirus disease 2019, there are no specific anti-virus drugs or vaccines. Still, the development of these medicines will take months, even years. Currently there is need of supportive care and non-specific treatment to improve the symptoms of coronavirus disease 2019 infected patient. For this specific indication, rapid performance of herbal medicine or phytochemicals can contribute as an alternative measure. Phytochemicals are a powerful group of chemicals that are derived from plants origin hence causing fewer side effects because of less use of additives, preservatives or excipients. Hence, this review will focus on some phytochemicals which may control and prevent severe acute respiratory syndrome coronavirus 2. Further, the existing healing options, drugs accessible, ongoing trials and current diagnostics to treat severe acute respiratory syndrome coronavirus 2 have been discussed. We suggested phytochemicals extracted from herbal plants are potential novel therapeutic approaches, completely targeting severe acute respiratory syndrome coronavirus 2 and its pathways.

Key words: Severe acute respiratory syndrome coronavirus 2, phytochemicals, herbal medicine, coronavirus disease 2019

Coronaviruses (CoVs) classified to the subfamily Orthocoronavirinae in the family Coronaviridae and order Nidovirales. The subfamilies Orthocoronavirinae again contain four genera, namely Alphacoronavirus (α -CoV), Betacoronavirus (β -CoV), Gammacoronavirus (γ -CoV) and Deltacoronavirus (δ -CoV). From that, α and β -CoV genera are known to infect mammals, whilst δ and γ -CoVs are identified to infect birds. Coronavirus Disease 2019 (COVID-19) is not the first severe respiratory infection epidemic originated by the corona virus. In the past few decades, CoVs have caused three outbreak infections, namely, COVID-19, Severe Acute Respiratory Syndrome (SARS) and Middle East Respiratory Syndrome (MERS)^[1,2]. This article gives a bird's eye view about this new virus i.e. COVID-19 and phytochemicals which may be effective in the treatment of COVID-19 as given in fig. 1. In view of the fact that awareness about this new virus is speedily developing,

readers are urged to modernize themselves repeatedly.

HISTORY

Novel Coronavirus (nCoV)-precipitated pneumonia, which was named by the World Health Organization (WHO) on the February 11, 2020 as COVID-19, has swiftly accelerated in epidemic scale since it first appeared during December 2019, inside Wuhan city, China. The international virus classification commission, on the same day, declared that the nCoV was named as Severe Acute Respiratory Syndrome Coronavirus 2 (SARS-CoV-2). Right now, the

This is an open access article distributed under the terms of the Creative Commons Attribution-NonCommercial-ShareAlike 3.0 License, which allows others to remix, tweak, and build upon the work non-commercially, as long as the author is credited and the new creations are licensed under the identical terms

*Address for correspondence

E-mail: rakeshshivatarer@gmail.com

Accepted 02 May 2022
Revised 20 August 2021
Received 01 June 2020
Indian J Pharm Sci 2022;84(3):519-531

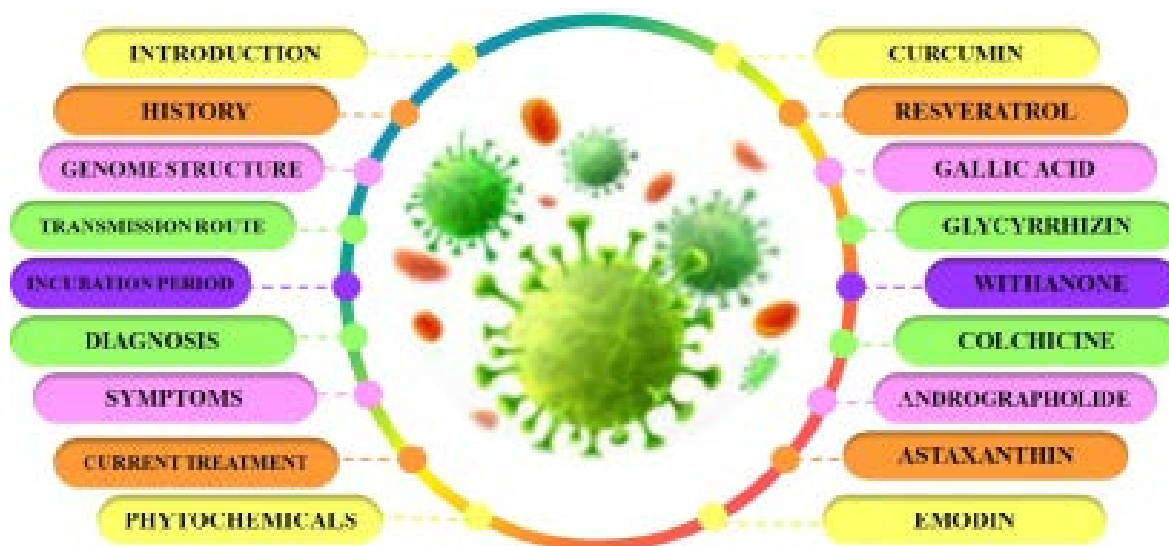


Fig. 1: Information about COVID-19 and phytochemicals used for the treatment of COVID-19

COVID-19 cases have been found in many countries around the world including United States of America (USA), India, Germany, Brazil, France etc.^[3].

Genome structure:

COVID-19 is a sphere-shaped or pleomorphic enclosed particles surrounding single-stranded (positive-sense) Ribonucleic Acid (RNA) linked with a nucleo-protein within a capsid comprised of matrix protein. The envelope bears club-shaped glycoprotein protrusions. A few CoVs also enclose a Hemagglutinin-Esterase (HE) protein. A typical CoV have minimum six Open Reading Frames (ORFs) in its genome. Apart from γ -CoV that takes non-structural protein 1 (nsp1), the primary ORFs (ORF1a/b) constitute about two-thirds of the entire genome length, encoding sixteen nsps (nsp1-16). ORF1a and ORF1b fit in a frame shift among which it creates two polypeptides: Protein phosphatase (pp)1a and pp1ab. These polypeptides are progressed *via* virally encoded 3-Chymotrypsin Like protease (3CLpro) or Main protease (M^{pro}) and one or more papain-like protease into 16nsps. All the structural and accent proteins are translated from the single guide RNAs (sgRNAs) of CoVs^[4]. Four main structural proteins contain Spike (S), Membrane (M), Envelope (E) and Nucleocapsid (N) proteins are encoded by ORFs on the one-third of the genome near the 30-terminus. In addition to these four main structural proteins, different CoVs instruct particular structural and accessory proteins, such as 3a/b protein, HE protein and 4a/b protein. These established proteins are responsible for

numerous vital functions in genome safeguarding and virus reproduction. There are 3 or 4 viral proteins in the coronavirus membrane. The most enough structural protein is the membrane (M) glycoprotein; it extends the membrane belayed 3 times, parting a short Amine (NH_2)-terminal area outdoor the virus and a long Carboxyl ($COOH$) terminus (cytoplasm domain) inner the virion. The spike protein (S) as a kind of membrane glycoprotein constitutes the peplomers. In fact, the primary inducer of neutralizing antibodies is S protein. Between the envelopes proteins there exists a molecular interplay that probably determines the formation and composition of the corona viral membrane. M performs a predominant function in the intracellular formation of virus particles except requiring S. In the existence of tunicamycin, CoV develop and generate spikeless, noninfectious virions that incorporate M but devoid of S^[5].

Symptoms:

The signs and indications of COVID-19 contamination come out later than an incubation length of about 5.2 d. The time from the onset of COVID-19 symptoms to finish ranged from 6 to 41 d with a center of 14 d. This duration is dependent on the age of the affected person and repute of the patient's immune system. It was once shorter among sufferers >70 y old in contrast with those under the age of 70. The most frequent signs and symptoms at onset of COVID-19 illness are fever, cough and fatigue, while other signs consist of sputum production, headache, haemoptysis, diarrhoea,

dyspnoea and lymphopenia. Clinical facets published with the aid of a chest Computed Tomography (CT) scan introduced as pneumonia; however, there were bizarre facets such as RNAemia, acute respiratory distress syndrome, acute cardiac injury and occurrence of ground-glass opacities that led to death. In some cases, the couple of peripheral ground-glass opacities were observed in subpleural regions of each lung that in all likelihood precipitated both systemic and localized immune response that led to extended inflammation. Regrettably, treatment of some instances with Interferon (IFN) inhalation showed no scientific effect and rather appeared to irritate the circumstance by using progressing pulmonary opacities^[6,7].

Transmission route:

Transmission of the virus is primarily *via* inhalation of suspended respiratory secretions, i.e., droplets generated when an infected individual coughs, sneezes or speaks, or through direct contact with an infected patient. There is a possibility that viral RNA may also be transmitted through microparticles of saliva, e.g. in exhaled air or when speaking, although this remains to be confirmed. Viral load in saliva peaks at presentation and remains high for at least the 1st w of symptomatic illness, gradually declining thereafter but remaining detectable for 20 d or more.

The virus can also be transmitted *via* fomites. It remains viable for up to 24 h on cardboard and for up to 72 h on plastic and stainless steel. Infectious droplets and body fluids can also contaminate the human conjunctival epithelium, producing ocular complications that may then progress to respiratory infection. At later stages of infection, viral persistence has been detected in anal swabs, blood and serum, suggesting additional shedding mechanisms and the potential for transmission *via* the oral-fecal or body fluid routes^[4,8].

Incubation period:

The mean incubation period of SARS-CoV-2 is estimated to be 3-7 d (range, 2-14 d), indicating a long transmission period of SARS-CoV-2. It is estimated that SARS-CoV-2 latency is consistent with those of other known human CoVs, including non-SARS human CoVs (mean 3 d, range 2-5 d), SARS-CoV (mean 5 d, range 2-14 d) and MERS-CoV (mean 5.7 d, range 2-14 d). Moreover, it has been reported that asymptomatic COVID-19 patients during their incubation periods can effectively transmit SARS-CoV-2, which is different from SARS-CoV because most SARS-CoV cases are

infected by 'superspreaders' and SARS-CoV cases cannot infect susceptible persons during the incubation period. Taken together, these data fully support the current period of active monitoring recommended by the WHO of 14 d^[9,10].

Diagnosis:

Quick and precise detection of SARS-CoV-2 is important to manage the outbreak of COVID-19. Nucleic acid detection may be a major technique of laboratory designation. Reverse Transcription quantitative Polymerase Chain Reaction (RT-qPCR) may be a molecular biological analysis technology based on nucleic acid sequences. The entire SARS-CoV-2 genome sequences are existing in GenBank. Thus, the nucleic acid of SARS-CoV-2 is often identified by RT-qPCR or through viral gene sequencing of nasopharyngeal and oropharyngeal swabs, sputum, stool or blood samples. However, assortment of these specimen arrange by healthcare workers involve close contact with patients, that poses a possibility of scattering the virus to healthcare workers. Furthermore, gathering of nasopharyngeal or oropharyngeal specimens could cause bleeding, particularly in patients with blood disease. Significantly, To *et al.* establish that SARS-CoV-2 may be effectively detected within the saliva samples of infected patients, signifying that saliva may be a promising non-invasive specimen form for analysis, monitoring and infection control of COVID-19 patients^[11,12].

Further RT-qPCR, Zhang *et al.* explained a protocol by means of Clustered Regularly Interspaced Short Palindromic Repeats (CRISPR)-based Specific High-sensitivity Enzymatic Reporter UNLOCKing (SHERLOCK) method for the finding of SARS-CoV-2. With artificial SARS-CoV-2 virus RNA fragments, the authors established that this technique is able to constantly detect target sequences of SARS-CoV-2 in a range between 20 and 200 attometer (am) (10-100 copies per microlitre of input). This test will be read out by a dipstick in <1 h, without requiring complicated instrumentation. As compared to RT-qPCR, the SHERLOCK technique is more precise and also the detection time is reduced by one-half. Therefore, utilization of the SHERLOCK technique for the finding of SARS-CoV-2 in clinical patient samples is estimated^[13-15].

Current treatment:

The person-to-person communication of COVID-19 contamination led to the segregation of patients that

were administered a range of treatments. Currently, there are no definite antiviral drugs or vaccine to treat COVID-19 infection for potential treatment of humans. The sole alternative accessible is using broad-spectrum antiviral drugs similar to nucleoside analogues and moreover Human Immunodeficiency Virus (HIV)-protease inhibitors that might attenuate the infection until the precise antiviral becomes existing. The treatment that has been so far used proved that 75 patients were administrated existing antiviral drugs. The track of treatment enclosed double on a daily basis oral administration of 75 mg oseltamivir, 500 mg lopinavir, 500 mg ritonavir and therefore the intravenous administration of 0-25 g ganciclovir for 3-14 d. One more information showed that the broad-spectrum antivirals remdesivir and chloroquine are extremely effective within the management of 2019-nCoV infection *in vitro*. These antiviral compounds are utilized in human patients with a security record. Hence, these therapeutic agents are thought to treat COVID-19 infection. Additionally, there are varieties of alternative compounds that are in development. These contain the clinical applicant Molnupiravir (EIDD-2801) that has exposed high therapeutic potential against seasonal and epidemic contagion virus infections and this shows another potential drug to be considered for the management of COVID-19 infection. Beside those lines, until additional precise therapeutics become existing, it is sensible to judge more broad-spectrum antivirals that offer drug treatment alternative for COVID-19 infection which contain neuraminidase inhibitors, peptide (EK1), lopinavir/ritonavir and RNA synthesis inhibitors. It is still obvious, that additional analysis is desperately required to spot novel chemotherapeutic medicines for treating COVID-19 infections. So as to develop pre and post exposure prevention against COVID-19, there is an urgent requirement to set up an animal model to reproduce the severe disease presently ascertained in humans. Several teams of scientists are presently operating and exhausting to build up a non-human primate model to learn COVID-19 infection to determine fast track novel therapeutics and for the testing of possible vaccines in addition to providing a superior understanding of virus-host interactions^[16,17].

Importance of phytochemicals:

Medicines originated from herbals include Ayurveda, Siddha and Unani that are effectively accomplished for treating various diseases. These came into continuation 5000 y ago and these systems are seen and scripted in olden literature. The phytochemicals are created

by plants to shield themselves against environmental hazards like water changes and microorganisms and to relinquish them their specific color, aroma, flavor and texture. Additionally, recent analysis demonstrated that they also need significant effects on human health nonetheless they never thought of essential nutrients. Research facility studies have exposed that these phytochemicals have the capability to stop certain compounds in drink, food and breathe from changing into carcinogens. It will moreover, decrease the swelling that triggers cancer growth. Besides, the phytochemicals reduce the oxidative damage to cells which will cause a variety of diseases and help in hormonal regulation. Researchers predicted that there are about 4000 phytochemicals that have been recognized so far, but only a little fraction of them have been studied strongly. These phytochemicals are frequently found in an extensive range of plants and are mainly present in consumed foods such as vegetables, fruits, green tea, coffee, grains, beans and so on. Phytochemicals are usually unnoticed in research and development of current drugs because their translational potentials are frequently belittled^[18,19]. In spite of the fact that these medicines are ambiguous, there is wide background for their utilization in non-Western medical technology. A single herb may contain numerous phytochemical constituents that work alone or in combination with other compounds to deliver the specified pharmacological impact. The seek for new compounds with antiviral action has regularly been unsuitable due to viral resistance together with viral inactivity and repetitive contamination in immune-compromised patients. Among antiviral therapeutic technique, the bulk of them are non-specific for viruses. The progressions in creating antiviral agents are the major spotlight in medical research. The antiviral impacts of phytochemicals have played a huge part at diverse stages of viral development^[20]. Phytochemicals derived pharmacological formulations stamped a major commitment for viral contaminations. Based on the accessibility of reasonable, proficient and fast bioassay systems, the antiviral compounds have been utilized for quick screening from plant extracts and fractions. Rather than synthetic antiviral drugs, phytochemicals convey fundamental raw materials for significant antiviral drugs. Synthetic drugs have been supplemented by phytochemicals, as life-saving drugs in a variety of viral diseases. Shockingly, the usage of this medicine has been passed down to eras by word of mouth and most of them have been misplaced over time, due to the need of appropriate documentation.

Research on these phytochemicals may offer assistance to advance their utilization in clinical settings to avoid or treat different ailments. Since numerous Indian medicinal plants display anti-inflammatory, antiviral and antioxidant properties, it could be favorable to believe them for the treatment of COVID-19. It is obvious that standard clinical trials ought to be carried out to logically demonstrate its adequacy^[21,22].

PHYTOCHEMICALS IN THE MANAGEMENT OF COVID-19

Curcumin:

In recent times a molecular docking study indicated that curcumin have higher binding capability to the receptors and should restrain the entry of COVID-19 virus. Angiotensin Converting Enzyme 2 (ACE2) is the receptor that connects with SARS-CoV-2 spike glycoprotein which supports the membrane fusion and virus infection happens through endocytosis. Hence, spike glycoprotein could be a potential candidate for drug targeting to restrain the entry of virus, that *in silico* docking studies exposed that curcumin may possibly restrain ACE2 to suppress COVID19 passage to the cell^[23].

Wen *et al.* have examined the impact of curcumin on viral replication by measurement of the amount of spike proteins that show in cultures of Vero E6 cells infected with SARS-CoV. Their result is incontestible that the inhibitory result of curcumin in EC50 values was higher than 10 μ M on SARS-CoV replication^[24].

Khaerunnisa *et al.* inspected the part of many phytochemical compounds like curcumin that will have the potential to repress the COVID-19 disease by molecular docking. Curcumin appeared generally with low binding energies and inhibition constants. They recommended that curcumin may have a latent inhibitory consequence on COVID-19 M^{pro} and might potentially act as a therapeutic agent^[25].

There is growing proof on the repressive actions of curcumin on inflammatory cytokines. Curcumin obstructs the vital signals, directing the expression of different pro-inflammatory cytokines together with Nuclear Factor-Kappa B (NF- κ B) and Mitogen-Activated Protein Kinase (MAPK) pathways. Curcumin have anti-inflammatory and anti-fibrotic impacts by diminishing the expression of vital chemokines and cytokines included in lung infection such as Interferon gamma (IFN- γ), Monocyte Chemoattractant Protein-1 (MCP-1), Interleukin (IL)-6 and IL-10. Curcumin has

an inhibitory impact against the human Respiratory Syncytial Virus (RSV) contamination by avoiding RSV replication, the discharge of Tumour Necrosis Factor alpha (TNF- α) and down regulation of phospho-NF- κ B^[26].

Resveratrol:

Lin *et al.* illustrated conceivable antiviral mechanisms for resveratrol. Resveratrol has been reported to stimulate Extracellular Signal-Regulated Kinase 1/2 (ERK1/2) signaling pathway and support cell proliferation and improve Sirtuin 1 (SIR1) signaling, both of which are connected to cellular survival and Deoxyribonucleic Acid (DNA) restore in response to DNA harm. On the other hand, resveratrol may neutralize the MERS-CoV-induced apoptosis by down-regulating Fibroblast Growth Factor-2 (FGF-2) signaling. In addition, MERS-CoV infection might lead to the generation of inflammatory cytokines while resveratrol could decrease the inflammation *via* interfering with the NF- κ B pathway. In their experiment, the levels of cleaved caspase 3 were decreased by resveratrol later than MERS-CoV infection. These modifications may be consequences of direct inhibition of caspase 3 cleavage by reversion of cell survival and the decrease of virus-induced apoptosis by resveratrol or restraint of an upstream incident that is required for caspase 3 cleavage^[27].

Resveratrol-treatment curbed the TNF- α generation, showing that the anti-retroviral action of resveratrol may be accomplished by lessening the inflammatory response. The IFN- γ level was prominent in the dose of 10 mg/kg/d resveratrol treated cluster as well as 30 mg/kg/d resveratrol-treated set after RV infection. The proportion of Cluster of Differentiation (CD) 4⁺/CD8⁺ in resveratrol-treated sets were the similar as that in mock infected cluster, signifying that resveratrol may maintain the immune function in Rotavirus-infected piglets. It was found that resveratrol might reduce diarrhea stimulated by Rotavirus infection^[28].

Zhao *et al.* examined the antiviral action of resveratrol against Pseudorabies Virus (PRV) and its mechanism of action. The consequences proved that resveratrol potently repressed PRV replication in a dose-dependent manner. The inhibition of virus reproduction in the existence of resveratrol was not credited to straight inactivation or inhibition of viral entrance into the host cells but due to the inhibition of viral reproduction in host cells. Additional studies illustrated that resveratrol may be a strong inhibitor of both NF- κ B activation and NF-

κ B-dependent gene expression through its capacity to restrain Inhibitor of NF- κ B (I κ B) kinase activity, which is the key controller in NF- κ B actuation. Therefore, the inhibitory impact of resveratrol on PRV-induced cell passing and gene expression may be due to its capacity to restrain the degradation of I κ B kinase^[29]. In spite of the fact that there are no information for utilizing resveratrol in peoples infected with SARS-CoV-2, the above results illustrate that this compound might be an adjunctive antiviral agent to believe, particularly based on the information distributed by Linn *et al.* showing activity against MERS-CoV *in vitro*.

Gallic acid:

Gallic acid interfered with different intra-cellular inflammatory pathways that actuate ulcerative colitis. The compound hinders the expression of nuclear transcription variables, such as NF- κ B and Signal Transducer and Activator of Transcription 3 (STAT3), and down-regulates their inflammatory downstream objectives. It too decreases the expression and/or action of pro-inflammatory cytokines and inflammatory proteins, including INF- γ , TNF- α , IL-1 β , IL-17, IL-6, IL-23, IL-21, inducible Nitric Oxide Synthase (iNOS) and Cyclooxygenase (COX)-2, and diminishes the expression and invasion of neutrophils and CD68⁺ macrophages into the colon^[30,31]. Gallic acid is able to quench the flames of inflammation by means of distinctive mechanisms. It diminishes the expression and discharge of pro-inflammatory and inflammatory mediators, such as substance P, bradykinin, COX-2, NF- κ B, IL-4, IL-2, IL-5, TNF- α and IFN- γ . The compound moreover represses the phagocyte or Polymorphonuclear (PMN) mediated inflammatory reactions by scavenging Reactive Oxygen Species (ROS) and diminishing the Myeloperoxidase (MPO) action^[32].

Gallic acid is able to restrain HIV-1 integrase, HIV-1 protease dimerization, HIV-1 transcriptase, Hepatitis C Virus (HCV) replication, HCV attachment and penetration, the Herpes Simplex Virus (HSV)-1, HCV serine protease and HSV-2 attachment and diffusion. It as well causes disturbance in *Haemophilus influenzae* A and B particles^[32,33].

Phenolic compounds through their phenol rings interaction with viral proteins and/or RNA, or *via* its modifiable MAPK signaling in host cell defense, act as antiviral activity against many viruses such as HCV and HIV. Gallic acid polyphenols executed hydrogen bonds with 1 or 2 of the Nucleoside Triphosphate (NTP)

entry channels amino acids in COVID-19 polymerase. Polyphenols binds with NTP of COVID-19 polymerase could influence in the access of the substrate and divalent cations into the central active site cavity, repressing the enzyme activity. It shows promising result that gallic acid displayed high binding resemblance than ribavirin to COVID-19 polymerase and show good drug resemblance and pharmacokinetic properties. Thus, gallic acid may be considered as a potential treatment option for COVID-19^[34].

Glycyrrhizin:

As the host cell receptor is significant for virus access, focusing on ACE2 could be a promising potential approach for avoiding SARS-CoV-2 contamination and more valuably, repressing the virus from diffusing out of the contaminated cell and attaching to and entering new permissive target cells. Glycyrrhizin has newly been shown to have the potential to attach with ACE2. Even though this investigation was performed *in silico* by means of molecular docking and the *in vitro* exhibition of an interaction remains to be confirmed, glycyrrhizin may still be considered as a latent treatment for COVID-19 because it has an antiviral outcome on SARS-CoV^[35].

In addition, glycyrrhizin has been reported to produce endogenous IFN. IFN is suggested in all 7 descriptions of the diagnosis and treatment of pneumonia contaminated by nCoV issued by the National Health Commission of China, maybe because of the current experience of clinical practice on COVID-19 and earlier settlement in management of severe MERS-CoV infection. While IFN is a broad-spectrum antiviral, it would restrain spreading of infection by restraining replication of both DNA and RNA infections at diverse stages of their replicative cycles and by actuating immune cell populations to clear virus infections. For that reason, glycyrrhizin may too play an indirect part in treatment of COVID-19. In the absence of a pathogen-specific antiviral or a targeted vaccine, numerous drugs with antiviral potential have been explored as of late for the treatment of COVID-19. Drug-producing liver injury has become a severe health problem. Glycyrrhizin, with its recognized liver-protection actions, could play a supporting role in COVID-19 treatment^[36].

Since ROS play an essential role in inflammatory reaction, antioxidants can also be efficient for the management of cytokine storm stimulated by infection. Glycyrrhizin may be able to inhibit the accumulation

of intracellular ROS caused by virus contamination. Inhibition of ROS development through glycyrrhizin can also decrease the activation of c-Jun N-terminal Kinase (JNK), NF- κ B, p38 and redox-sensitive signaling procedures that are known to be appropriate for virus reproduction, by this means of suppressing virus reproduction. In expansion, a steady inflammatory or cytokine storm reaction caused by SARS-CoV-2 can result in enactment of coagulation and complement cascades, which may lead to several organs failure. Records appeared that glycyrrhizin could be a specific inhibitor of thrombin. These results indicate that glycyrrhizin has significant therapeutic benefits for COVID-19 through multisite mechanisms^[37,38].

Withanone:

Kumar *et al.* inspected the binding potential of withanone (active withanolides extracted from Ashwagandha) to an extremely conserved protein, M^{pro} of SARS-CoV-2. They established that withanone attach to the substrate-binding pocket of SARS-CoV-2 M^{pro} with adequacy and binding energies corresponding to a previously claimed N3 protease inhibitor. Comparative to N3 inhibitor, withanone were binding with the extremely preserved residues of the proteases of CoVs. The interacting stability of these molecules was further evaluated by means of molecular dynamics replication. The interacting free energies deliberated *via* Molecular Mechanics/Generalized Born Surface Area (MM/GBSA) for N3 inhibitor. Information at this point predicted that these natural compounds may have the potential to repress the efficient activity of SARS-CoV-2 protease (a crucial protein for virus endurance) and therefore may save time and cost required for designing/development and early screening for anti-COVID drugs; may propose few therapeutic value for the management of original deadly coronavirus disease; warrants prioritized advance approval within the research facility and clinical tests^[39].

Balkrishna *et al.* reported that withanone, docked exceptionally well in the binding border of ACE2-Receptor Binding Domain (RBD) complex and were found to shift somewhat towards the interface middle on simulation. Withanone altogether diminished electrostatic component of interacting free energies of ACE2-RBD complex. Two salt bridges were moreover distinguished at the interface; inclusion of withanone destabilized these salt bridges and diminished their occupancies. They hypothesize, such an intrusion of electrostatic interactions between the RBD and ACE2

would obstruct or deteriorate COVID-19 access and its subsequent contamination^[40].

Colchicine:

Colchicine interacts to unpolymerized tubulin heterodimers, producing a constant compound that successfully restrains microtubule dynamics upon interacting to microtubule ends. Besides, colchicine may be a non-selective inhibitor of Nod-Like Receptor Protein 3 (NLRP3) inflammasome. Whereas firstly it has been thought of just as an inhibitor of microtubule polymerization and leucocyte invasion, it is presently assumed that a considerable part of colchicine is recognized to restraint of the NLRP3 inflammasome. Colchicine represses inflammasome on two levels: it restrains P2X Purinoceptor 7 (P2X7) receptor enactment and Apoptosis-associated Speck-like protein containing a Caspase-activation and recruitment domain (ASC) polymerization, in that way hindering interaction among pyrin-like domains^[41]. Moreover, colchicine smoothen the transport of mitochondria and consequent approximation of ASC to NLRP3, showing that microtubules mediated the transfer of mitochondria to produce best sites for enactment of the NLRP3 inflammasome. Colchicine has been appeared to constrain IL-1 β production as a response to diverse NLRP3 inflammasome inducers in a dose-dependent manner. For instance, in the situation of acute coronary syndrome, colchicine was useful in stifling IL-1 β , IL-6 and IL-18, which was credited to inflammasome inhibition^[42,43].

The Greek Study in the Effects of Colchicine in COVID-19 complications prevention (GRECCO-19) will be a planned, open-labeled, randomized, controlled study to evaluate the effects of colchicine in COVID-19 complications anticipation. Patients with research lab established SARS-CoV-2 infection (beneath RT-PCR) and clinical picture that includes temperature more than 37.5° and at least 2 out of the below will be included: Sustained throat; sustained coughing pain; fatigue/tiredness; anosmia and/or ageusia; Partial pressure of oxygen (PaO₂) < 95 mmHg. Patients will be randomized (1:1) in colchicine or control set^[44].

Andrographolide:

Andrographolide is a laboratory diterpenoid derived from *Andrographis paniculata* stem and leaves. Andrographolide hindered IFN- γ , IL-2 and IL-6 expression, diminishing the cellular and humoral adaptive immune reaction in T cells. Andrographolide

diminished the antigen presenting potential of dendritic cells to T cells. The andrographolide administration decreased the serum immunoglobulin, IL-4, IL-13, IL-5 and T helper type 2 (Th2) cytokine, in an ovalbumin-induced asthma rat model. Andrographolide signifying its role in angiogenesis by decreasing migration and invasion, adhesion molecule Intercellular Adhesion Molecule 1 (ICAM-1) and endothelial cell proliferation^[45]. The andrographolide hindered NF- κ B interacting to DNA and hence diminishing pro-inflammatory proteins expression like iNOS and COX-2^[46]. Zhang *et al.* carried out an experiment to conclude the effect of andrographolide on insulinoma tumor growth. Andrographolide restrain the development of insulinoma tumor by focusing the Toll-Like Receptor 4 (TLR4)/NF- κ B signaling pathway^[47]. In neutrophils, the generation of ROS was restrained by andrographolide. Andrographolide directed the generation of components such as IFN- γ , Natural Killer (NK) cells, IL-2 and TNF- α . The andrographolide enhanced the expression of CD markers and generation of TNF- α , as a result increasing the cytotoxic potential of lymphocytes^[48]. Enmozhi *et al.* assessed andrographolide as a potential inhibitor of the M^{pro} of SARS-COV-2 through *in silico* studies such as target analysis, molecular docking, Absorption, Distribution, Metabolism and Excretion (ADME) prediction and toxicity prediction. Andrographolide was docked effectively in the binding position of SARS-CoV-2 M^{pro}. This molecule moreover complies with the Lipinski's rule, which makes it a promising compound to seek after assisting biochemical and cell based assays to investigate its potential for utilization against COVID-19^[49].

Astaxanthin:

Astaxanthin is a xanthophyll carotenoid, which is present in *Haematococcus pluvialis*, *Chlorella zofingiensis*, *Chlorococcum* and *Phaffia rhodozyma*. Astaxanthin essentially constrict pathological elevation, inflammatory cell signaling NF- κ B pathway together with *in vitro* and *in vivo* study and diminish TNF- α in humans, ensuring reduction in numerous pro-inflammatory cytokine level, which might show potential in maintaining lung health and reducing the impact of SARS-CoV-2 infection. Astaxanthin moreover identified to notably decrease other significant mediators of inflammation, including IL-1 β , IL-6, C-Reactive Protein (CRP), COX-2, iNOS, Prostaglandin E2 (PGE2) and Nitric Oxide (NO)^[50]. Miyachi *et al.* studied that treatment with astaxanthin show localization of NF- κ B/p65 and the level of inflammatory cytokines (TNF- α ,

IL-6) tend to decrease and considerable enhancement of cell proliferation *in vitro*. Astaxanthin moreover reported to hinder apoptosis in alveolar epithelial cells. Furthermore, to the restraint of NF- κ B pathway activation, reduction in the M1/M2 macrophage phenotype proportion is significant in diminishing levels of inflammatory cytokines^[51]. These molecules also modulate the generation of Th1 cytokines, such as IFN- γ and IL-2, without causing considerable cytotoxic effects in primary cultured lymphocytes. Astaxanthin applies regulatory activities on the immune system and specifically upgrades the immune response by improving multiplication and development of NK cells, granulocytes, T and B lymphocytes and monocytes^[52].

Immunomodulation by natural bioactive molecules is able to give additional therapeutic support to conventional chemotherapy for a range of diseases together with COVID-19, particularly when discriminating immunosuppression is required for autoimmune disorders. Dietary astaxanthin regulate immune response; protect oxidative damage and inflammation simultaneously in human model. Astaxanthin enhanced both cell-mediated and humoral immune responses. Considerable increase of immune markers including B-cell and T-cell mitogen-induced lymphocyte proliferation, Leukocyte Function-associated Antigen-1 (LFA-1) expression and IFN- γ and IL-6 production were reported^[53]. With the viral disease of respiratory epithelial cells, dendritic cells phagocytose the virus and given antigens to T cells. Effector T cells worked by killing the infected epithelial cells and cytotoxic CD8⁺ T cells create and free pro-inflammatory cytokines which bring cell apoptosis. Both the cell apoptosis and pathogen activate and intensify the host innate immune response. Characteristics of COVID-19 recommend a reduced level of lymphocytes, neutrophils, CD8⁺ T and CD4⁺ T cells in peripheral blood specify disease severity^[50].

Emodin:

Emodin may show its antiviral activity by restraining casein kinase 2, which is broken by many viruses for the phosphorylation of proteins that are crucial for their life cycle^[54]. Emodin also interrupted the lipid bilayer, resulting in the inactivation of enclosed virus^[55]. Ho *et al.* demonstrated that emodin was able to block the SARS-CoV S protein and ACE2 interaction. Preincubation of S protein or S protein-pseudo type retrovirus with emodin also eliminated the SARS-CoV and Vero E6 cell interaction. These conclusion recommended that in

addition to disrupting the viral envelope, emodin might stop SARS-CoV infection by opposing the interacting site of S protein with ACE2^[56]. Promazine is a phenolic compound consisting of three cyclic rings which has been considered to show anti-SARS-CoV effect. Emodin along with promazine inhibited the S protein and ACE2 in a dose-dependent manner. This outcome suggested that the side chains except the anthraquinone skeleton have an immense impact on the S protein and ACE2 binding. These conclusions also point out that promazine shown anti-SARS effect by restraining both the virus access and protein processing^[56,57]. Schwarz *et al.* observed that emodin capable of restraining the 3a ion channel of coronavirus SARS-CoV and Human Coronavirus OC43 (HCoV-OC43) plus virus discharge from HCoV-OC43 with a K_{1/2} value of about 20 μM. They propose that viral ion channels could be an excellent target for the development of antiviral agents^[58].

Some other phytochemicals used in the treatment of COVID-19:

A product of the plant *Artemisia annua*, artemisinin is a class of antimalarial medicines that have been marketed is used in the treatment. Increasing the severity of SARS-CoV-2 infection is associated with the development of pulmonary fibrosis, which is mediated by IL-1. There have been many studies that indicate that oxidative stress is linked with pulmonary illnesses and it is probable that the intake of natural antioxidants is beneficial in the treatment of lung fibrosis. The antioxidant activity of *Artemisia annua* extract is considerable, which is most likely owing to the high phenolic content of the extract. A derivative of *Artemisia annua* is artesunate, has shown promising effect in the treatment of pulmonary fibrosis. It works by blocking pro-fibrotic molecules linked with the disease^[59]. Artemisinin and its derived molecules demonstrated an additional mode of interaction by binding to the Lysine (Lys) 353 and Lys31-binding hotspots of the SARS-CoV-2 spike protein and producing a better Autodock Vina score than hydroxychloroquine. Artemisinin and its derived molecules were found to have a higher Autodock Vina score than hydroxychloroquine. The findings of the research also showed that the complexes produced interfered with the SARS-CoV-2 Spike protein receptor site and stayed stable on the receptor site. Additionally, *Artemisia* has a high concentration of zinc, which has been shown to be beneficial for the immunomodulation impact of the host response as well as an increase in CD4 cell count^[60].

Betulinic acid (Bet) is a naturally occurring product with a pentacyclic triterpene nucleus that exhibits a broad spectrum of biological and pharmacological activities including antiviral, anti-HIV, antibacterial, anti-inflammatory, anthelmintic, anticancer and antimalarial properties. Bet is found in plants and has a pentacyclic triterpene nucleus. Bet (A8) interacts with Glycine 274 (GLY 274), Leucine 287 (LEU 287), Methionine 276 (MET 276) and LEU 286 amino acids and forms two hydrogen bonds with each of these amino acids, which represents the majority of sulfhydryl groups in the amino acid. Despite this, Bet (A3) and Bet (A4) were the most often suggested possible inhibitors of COVID-19's primary protease^[61].

Luteolin substantially increases the amount of CD4⁺ CD25⁺ regulatory T-cells in murine splenic CD4⁺-T cells that have been activated with anti-CD3/anti-CD28 antibodies, as shown in this study. Luteolin also shown immunomodulatory action, reducing the amount of immune cells such as CD19⁺ B, CD4⁺ T, CD3-C-C chemokine receptor type 3⁺ (CCR3⁺) and CD11b⁺ Granulocyte-1 (Gr-1⁺) in the lungs of an inflamed airway mouse model with inflamed airways. Luteolin also has anti-inflammatory properties, since it inhibits the NF-κB pathway, lowers TNF-α, IL-6 and IL-1α levels and substantially decreases MPO activity in the blood. Additionally, luteolin had a protective effect against the Lipopolysaccharide (LPS)-induced Acute Lung Injury (ALI), mice model by inhibiting MAPK pathways, which resulted in the suppression of the NF-κB pathway and the degradation of IκB protein. By inhibiting microsomal PGE synthase 1 and 5-lipoxygenase, caflanone has anti-inflammatory action on the body.

It is widely known that flavonoids are phenolic natural compounds that are used in the treatment of a variety of illnesses, including viral infection, in both traditional and contemporary medicine. CoVs, particularly the current pandemic epidemic caused by the SARS-CoV-2 and identified as COVID-19, have been shown to be susceptible to flavonoids potential inhibitory action against them. All flavonoids were found in *in silico* as possible SARS-CoV-2 inhibitors. Specifically, it has been determined that M^{pro} is needed for the replication of the SARS-CoV^[62]. Further investigation revealed that the M^{pro} of SARS-CoV-2 and SARS-CoV are very similar. A dose-dependent antiviral activity against the HSV-1 and HSV-2 was also shown in cell cultures using quercetin. In cultured cells, it has been shown to suppress a number of different respiratory viruses.

Several rhinovirus, echovirus (type 7, 11, 12 and 19), coxsackievirus (A21 and B1) and poliovirus serotypes are inhibited in their cytopathic effects by this substance (type 1 Sabin). Antiviral action against the Canine distemper virus is shown by the fact that it reduces viral expression while increasing cellular survival. This compound has been investigated in different kinds and models of viral infection because of its potential antiviral actions on polymerases, proteases, reverse transcriptase, decreasing DNA gyrase and binding viral capsid proteins. 3CLpro was shown to be inhibited by this compound, which was discovered as one of the components of *Pichia pastoris*. Phytochemical studies have shown that quercetin-3-O-galactoside binds to SARS-CoV 3CLpro and inhibits its proteolytic activity^[63]. Chrysin has the ability to inhibit the NF- κ B, which regulates the production of genes encoding pro-inflammatory cytokines such as COX-2 and iNOS. Furthermore, it is an agonist of the Peroxisome Proliferator-Activated Receptors (PPAR) receptor, which inhibits the expression of COX-2, MPO and iNOS. The pre-treatment of mice with chrysin before they were exposed to cigarette smoking to induce inflammation of airway epithelial cells alleviated the inflammation by suppressing the release of TNF- α , IL-1 α , IL-8 and MPO expression in the lung tissue, as well as the expression of MPO in the lung tissue. Chrysin also has the additional effect of inhibiting ERK and p38 phosphorylation. The immunomodulatory effect of chrysin on rat peritoneal macrophages was investigated in another study. Chrysin was found to stimulate macrophage lysosomal activity, which was involved in killing and digesting the microbial pathogens, as well as inhibiting the production of NO in this study. A docking research revealed that chrysin may bind poorly to COX-1 enzymes but strongly to COX-2 enzymes, suggesting that it has relative selectivity for COX-2 enzymes and as a result, lowers the likelihood of unwanted Gastrointestinal (GIT) side effects. Similar results were obtained when apigenin was administered prior to the induction of inflammation in human macrophages^[62,63].

Apigenin was shown to significantly decrease IL-6 production as well as the stability of IL-6 messenger RNA (mRNA). HCoV-Netherlands 63 (NL63) replication was shown to be inhibited by tryptanthrin, which was discovered to be the most active component in *Strobilanthes cusia* leaf methanol extract in a cell-type-independent manner. Intriguingly, tryptanthrin has a higher antiviral activity against HCoV-NL63 than indigodole B (5aR-ethyltryptanthrin), which has an additional ethyl moiety at C5a instead of the double

bond in tryptanthrin. This demonstrates that the double bond in the quinazoline ring of the tryptanthrin skeleton is the active contributor to the antiviral tryptanthrin which also changes the antigenic structure of viral spike proteins and reduces the cleavage activity of Proteolipid Protein 2 (PLP2), which is linked with virucidal activity and inhibits the post-entry stage of HCoV-NL63 replication, in addition to other effects. Our particular interest is that the spike protein from HCoV-NL63 has significant sequence and structural similarities with the viruses that cause SARS and COVID-19, indicating that all of these viruses use the ACE2 receptor^[64]. This is consistent with the fact that all of these viruses use the ACE2 receptor. Lycorine is a phenanthridine alkaloid from the Amaryllidaceae family that was discovered in the bulbs of the plant *Lycoris radiata*. Several CoV infections, including the SARS-CoV infection and four additional CoV infections, such as the HCoV-OC43 infection, the MERS-CoV infection, the Mouse Hepatitis Virus strain A59 (MHV-A59) infection, and the HCV-OC43 infection, have been shown to be inhibited by lycorine. Lycorine has been shown to inhibit viral RNA replication as well as viral protein synthesis in the presence of poliovirus, Enterovirus 71 (EV71) and H5N1 avian influenza virus. Recently, it was proposed that lycorine may block Zika virus viral RNA production and bind to the Zika RNA-dependent RNA polymerase (RdRp) protein, thus preventing the virus from spreading. According to the findings, lycorine forms hydrogen bonds with RdRp at the amino acid residues Aspartic acid 623 (Asp623), Asp691 and Serine 759 (Ser759), which is comparable to remdesivir^[65].

CONCLUSION

nCoV (COVID-19) is causing an increasing number of cases of pneumonia and was declared a Public Health Emergency of International concern by the World Health Organization.

According to WHO, major concern among public health throughout the world and many countries have taken precautionary measures against the virus and Government officials in all countries continue to make hard work to diminish person to person contact by facilitating area wise shutdowns of public places plus a variety of steps have been instigated to ensure the security of the public, similar to social distancing and self-quarantine which limits our social interactions.

Although a large number of review articles have been published since the COVID-19 epidemic, the

significance of natural products in the prevention and treatment of SARS-CoV-2 has received little attention. However, there is a body of research describing a variety of naturally occurring chemicals that have strong anti-SARS-CoV and anti-MERS-CoV action. Unquestionably, there is a high degree of sequence similarity between SARS CoV-2 and either SARS-CoV or MERS-CoV. The use of computational methods to repurpose these anti-SARS-CoV or anti-MERS-CoV natural compounds may lead to the identification of candidates for the development of COVID-19 medication that is both safe and cost-effective.

Herbal medicines have gathered thousand-of-year's experiences in the treatment of pandemic and endemic diseases. Providing complementary and alternative treatments are still urgently needed for the management of patients with SARS-CoV-2 infection, experiences in herbal medicine is certainly worth learning. Fighting against existing pandemic also give an opportunity to test the true significance of phytomedicine in treating promising infectious diseases. Numerous phytochemicals have revealed inhibitory activity against HIV proteases which also have immunomodulatory activity and these molecules can be promising drugs for COVID-19. These phytochemicals can be used to ameliorate the symptoms of COVID-19. Though many phytochemicals have been identified, a lot of research has to be carried out for the development of drug specific to SARS-CoV-2. Therefore, it is important to explore the effect of these prescribed phytochemicals on SARS-CoV-2.

Acknowledgements:

The authors recognize the contribution of MPREX healthcare for the financial and infrastructural assistance provided during the present review work.

Conflict of interests:

The authors declared no conflict of interest.

REFERENCES

1. Yang Y, Peng F, Wang R, Guan K, Jiang T, Xu G, *et al.* The deadly coronaviruses: The 2003 SARS pandemic and the 2020 novel coronavirus epidemic in China. *J Autoimmun* 2020;109:102434.
2. Fung TS, Liu DX. Human coronavirus: Host-pathogen interaction. *Annu Rev Microbiol* 2019;73:529-57.
3. Seah I, Agrawal R. Can the coronavirus disease 2019 (COVID-19) affect the eyes? A review of coronaviruses and ocular implications in humans and animals. *Ocul Immunol Inflamm* 2020;28(3):391-5.
4. Li H, Liu SM, Yu XH, Tang SL, Tang CK. Coronavirus disease 2019 (COVID-19): Current status and future perspectives. *Int J Antimicrob Agents* 2020;55(5):105951.
5. Mousavizadeh L, Ghasemi S. Genotype and phenotype of COVID-19: Their roles in pathogenesis. *J Microbiol Immunol Infect* 2021;54(2):159-63.
6. Rothan HA, Byrareddy SN. The epidemiology and pathogenesis of coronavirus disease (COVID-19) outbreak. *J Autoimmun* 2020;109:102433.
7. Zhou P, Yang XL, Wang XG, Hu B, Zhang L, Zhang W, *et al.* A pneumonia outbreak associated with a new coronavirus of probable bat origin. *Nature* 2020;579(7798):270-3.
8. Rothe C, Schunk M, Sothmann P, Bretzel G, Froeschl G, Wallrauch C, *et al.* Transmission of 2019-nCoV infection from an asymptomatic contact in Germany. *N Engl J Med* 2020;382(10):970-1.
9. Liu Y, Gayle AA, Wilder-Smith A, Rocklöv J. The reproductive number of COVID-19 is higher compared to SARS coronavirus. *J Travel Med* 2020;27(2):1-4.
10. Zu ZY, Jiang MD, Xu PP, Chen W, Ni QQ, Lu GM, *et al.* Coronavirus disease 2019 (COVID-19): A perspective from China. *Radiology* 2020;296(2):E15-25.
11. Chu DK, Pan Y, Cheng SM, Hui KP, Krishnan P, Liu Y, *et al.* Molecular diagnosis of a novel coronavirus (2019-nCoV) causing an outbreak of pneumonia. *Clin Chem* 2020;66(4):549-55.
12. To KK, Tsang OT, Yip CC, Chan KH, Wu TC, Chan JM, *et al.* Consistent detection of 2019 novel coronavirus in saliva. *Clin Infect Dis* 2020;71(15):841-3.
13. Zhang F, Abudayyeh OO, Gootenberg JS. A protocol for detection of COVID-19 using CRISPR diagnostics. A protocol for detection of COVID-19 using CRISPR diagnostics; 2020:1-8.
14. Elfiky AA. Anti-HCV, nucleotide inhibitors, repurposing against COVID-19. *Life Sci* 2020;248:117477.
15. Bunte K, Beikler T. Th17 cells and the IL-23/IL-17 axis in the pathogenesis of periodontitis and immune-mediated inflammatory diseases. *Int J Mol Sci* 2019;20(14):3394.
16. Chen N, Zhou M, Dong X, Qu J, Gong F, Han Y, *et al.* Epidemiological and clinical characteristics of 99 cases of 2019 novel coronavirus pneumonia in Wuhan, China: A descriptive study. *Lancet* 2020;395(10223):507-13.
17. Wang M, Cao R, Zhang L, Yang X, Liu J, Xu M, *et al.* Remdesivir and chloroquine effectively inhibit the recently emerged novel coronavirus (2019-nCoV) *in vitro*. *Cell Res* 2020;30(3):269-71.
18. Almadaifer S, Alsibaie N, Alhoumendan G, Alammari G, Kavita MS. Role of phytochemicals in health and nutrition. *BAO J Nutr* 2017;3:28-34.
19. Mukhopadhyay MK, Banerjee P, Nath D. Phytochemicals-biomolecules for prevention and treatment of human diseases-a review. *Int J Sci Eng Res* 2012;3(7):1-32.
20. Naithani R, Huma LC, Holland LE, Shukla D, McCormick DL, Mehta RG, *et al.* Antiviral activity of phytochemicals: A comprehensive review. *Mini Rev Med Chem* 2008;8(11):1106-33.
21. Vellingiri B, Jayaramayya K, Iyer M, Narayanasamy A, Govindasamy V, Giridharan B, *et al.* COVID-19: A promising cure for the global panic. *Sci Total Environ* 2020;725:138277.
22. Akram M, Tahir IM, Shah SM, Mahmood Z, Altaf A, Ahmad K, *et al.* Antiviral potential of medicinal plants against HIV, HSV, influenza, hepatitis and coxsackievirus: A systematic review. *Phytother Res* 2018;32(5):811-22.

23. Utomo RY, Ikawati M, Meiyanto E. Revealing the potency of citrus and galangal constituents to halt SARS-CoV-2 infection. Preprints 2020:1-8.
24. Wen CC, Kuo YH, Jan JT, Liang PH, Wang SY, Liu HG, *et al.* Specific plant terpenoids and lignoids possess potent antiviral activities against severe acute respiratory syndrome coronavirus. *J Med Chem* 2007;50(17):4087-95.
25. Khaerunnisa S, Kurniawan H, Awaluddin R, Suhartati S, Soetjipto S. Potential inhibitor of COVID-19 main protease (M^{pro}) from several medicinal plant compounds by molecular docking study. Preprints 2020:1-14.
26. Obata K, Kojima T, Masaki T, Okabayashi T, Yokota S, Hirakawa S, *et al.* Curcumin prevents replication of respiratory syncytial virus and the epithelial responses to it in human nasal epithelial cells. *PLoS One* 2013;8(9):e70225.
27. Lin SC, Ho CT, Chuo WH, Li S, Wang TT, Lin CC. Effective inhibition of MERS-CoV infection by resveratrol. *BMC Infect Dis* 2017;17(1):1-10.
28. Cui Q, Fu Q, Zhao X, Song X, Yu J, Yang Y, *et al.* Protective effects and immunomodulation on piglets infected with rotavirus following resveratrol supplementation. *PLoS One* 2018;13(2):e0192692.
29. Zhao X, Cui Q, Fu Q, Song X, Jia R, Yang Y, *et al.* Antiviral properties of resveratrol against pseudorabies virus are associated with the inhibition of IκB kinase activation. *Sci Rep* 2017;7(1):1-1.
30. Pandurangan AK, Mohebbi N, Esa NM, Looi CY, Ismail S, Saadatdoust Z. Gallic acid suppresses inflammation in dextran sodium sulfate-induced colitis in mice: Possible mechanisms. *Int Immunopharmacol* 2015;28(2):1034-43.
31. Park JC, Han WD, Park JR, Choi SH, Choi JW. Changes in hepatic drug metabolizing enzymes and lipid peroxidation by methanol extract and major compound of *Orostachys japonicus*. *J Ethnopharmacol* 2005;102(3):313-8.
32. Kahkeshani N, Farzaei F, Fotouhi M, Alavi SS, Bahramsoltani R, Naseri R, *et al.* Pharmacological effects of gallic acid in health and diseases: A mechanistic review. *Iran J Basic Med Sci* 2019;22(3):225.
33. Lee JH, Oh M, Seok JH, Kim S, Lee DB, Bae G, *et al.* Antiviral effects of black raspberry (*Rubus coreanus*) seed and its gallic acid against influenza virus infection. *Viruses* 2016;8(6):157.
34. El Sohaimy S, Abdo N, Shehata MG, Moheyeldin O. Inhibition of COVID-19 RNA-dependent RNA polymerase by natural bioactive compounds: Molecular docking analysis. *Egypt J Chem* 2021;64(4):3-4.
35. Kuhn JH, Li W, Choe H, Farzan M. Angiotensin-converting enzyme 2: A functional receptor for SARS coronavirus. *Cell Mol Life Sci* 2004;61(21):2738-43.
36. Luo P, Liu D, Li J. Pharmacological perspective: Glycyrrhizin may be an efficacious therapeutic agent for COVID-19. *Int J Antimicrob Agents* 2020;55(6):105995.
37. Mauricio I, Francischetti B, Monteiro RQ, Guimarães JA. Identification of glycyrrhizin as a thrombin inhibitor. *Biochem Biophys Res Commun* 1997;235(1):259-63.
38. Mendes-Silva W, Assafim M, Rota B, Monteiro RQ, Guimarães JA, Zingali RB. Antithrombotic effect of glycyrrhizin, a plant-derived thrombin inhibitor. *Thromb Res* 2003;112(1):93-8.
39. Kumar V, Dhanjal JK, Kaul SC, Wadhwa R, Sundar D. Withanone and caffeic acid phenethyl ester are predicted to interact with main protease (M^{pro}) of SARS-CoV-2 and inhibit its activity. *J Biomol Struct Dyn* 2021;39(11):3842-54.
40. Balkrishna A, Pokhrel S, Singh J, Varshney A. Withanone from *Withania somnifera* may inhibit novel coronavirus (COVID-19) entry by disrupting interactions between viral S-protein receptor binding domain and host ACE2 receptor. *Research Square* 2020;1-21.
41. Misawa T, Takahama M, Kozaki T, Lee H, Zou J, Saitoh T, *et al.* Microtubule-driven spatial arrangement of mitochondria promotes activation of the NLRP3 inflammasome. *Nat Immunol* 2013;14(5):454-60.
42. Martínez GJ, Robertson S, Barraclough J, Xia Q, Mallat Z, Bursill C, *et al.* Colchicine acutely suppresses local cardiac production of inflammatory cytokines in patients with an acute coronary syndrome. *J Am Heart Assoc* 2015;4(8):e002128.
43. Robertson S, Martínez GJ, Payet CA, Barraclough JY, Celermajer DS, Bursill C, *et al.* Colchicine therapy in acute coronary syndrome patients acts on caspase-1 to suppress NLRP3 inflammasome monocyte activation. *Clin Sci* 2016;130(14):1237-46.
44. Deftereos SG, Siasos G, Giannopoulos G, Vrachatis DA, Angelidis C, Giotaki SG, *et al.* The Greek study in the effects of colchicine in COVID-19 complications prevention (GRECCO-19 study): Rationale and study design. *Hellenic J Cardiol* 2020;61(1):42-5.
45. Chiou WF, Chen CF, Lin JJ. Mechanisms of suppression of inducible nitric oxide synthase (iNOS) expression in RAW 264.7 cells by andrographolide. *Br J Pharmacol* 2000;129(8):1553-60.
46. Jantan I, Ahmad W, Bukhari SN. Plant-derived immunomodulators: An insight on their preclinical evaluation and clinical trials. *Front Plant Sci* 2015;6:655.
47. Zhang QQ, Ding Y, Lei Y, Qi CL, He XD, Lan T, *et al.* Andrographolide suppress tumor growth by inhibiting TLR4/NF-κB signaling activation in insulinoma. *Int J Biol Sci* 2014;10(4):404.
48. Rajagopal S, Kumar RA, Deevi DS, Satyanarayana C, Rajagopalan R. Andrographolide, a potential cancer therapeutic agent isolated from *Andrographis paniculata*. *J Exp Ther Oncol* 2003;3(3):147-58.
49. Enmochi SK, Raja K, Sebastine I, Joseph J. Andrographolide as a potential inhibitor of SARS-CoV-2 main protease: An *in silico* approach. *J Biomol Struct Dyn* 2021;39(9):3092-8.
50. Talukdar J, Dasgupta S, Nagle V, Bhadra B. COVID-19: Potential of microalgae derived natural astaxanthin as adjunctive supplement in alleviating cytokine storm. *SSRN* 2020:1-17.
51. Miyachi M, Matsuno T, Asano K, Mataga I. Anti-inflammatory effects of astaxanthin in the human gingival keratinocyte line NDUSD-1. *J Clin Biochem Nutr* 2015:14-9.
52. Lin KH, Lin KC, Lu WJ, Thomas PA, Jayakumar T, Sheu JR. Astaxanthin, a carotenoid, stimulates immune responses by enhancing IFN-γ and IL-2 secretion in primary cultured lymphocytes *in vitro* and *ex vivo*. *Int J Mol Sci* 2015;17(1):44.
53. Park JS, Kim HW, Mathison BD, Hayek MG, Massimino S, Reinhart GA, *et al.* Astaxanthin uptake in domestic dogs and cats. *Nutr Metab* 2010;7(1):1-8.
54. Battistutta R, Sarno S, de Moliner E, Papinutto E, Zanotti G, Pinna LA. The replacement of ATP by the competitive inhibitor emodin induces conformational modifications in the catalytic site of protein kinase CK2. *J Biol Chem* 2000;275(38):29618-22.
55. Sydiskis RJ, Owen DG, Lohr JL, Rosler KH, Blomster RN. Inactivation of enveloped viruses by anthraquinones extracted from plants. *Antimicrob Agents Chemother* 1991;35(12):2463-6.

56. Ho TY, Wu SL, Chen JC, Li CC, Hsiang CY. Emodin blocks the SARS coronavirus spike protein and angiotensin-converting enzyme 2 interaction. *Antiviral Res* 2007;74(2):92-101.
57. Alves DS, Pérez-Fons L, Estepa A, Micol V. Membrane-related effects underlying the biological activity of the anthraquinones emodin and barbaloin. *Biochem Pharmacol* 2004;68(3):549-61.
58. Schwarz S, Wang K, Yu W, Sun B, Schwarz W. Emodin inhibits current through SARS-associated coronavirus 3a protein. *Antiviral Res* 2011;90(1):64-9.
59. Haq FU, Roman M, Ahmad K, Rahman SU, Shah SM, Suleman N, *et al.* *Artemisia annua*: Trials are needed for COVID-19. *Phytother Res* 2020;1:1-10.
60. Orege JI, Adeyemi SB, Tihamiyu BB, Akinyemi TO, Ibrahim YA, Orege OB. *Artemisia* and *Artemisia*-based products for COVID-19 management: Current state and future perspective. *Adv Tradit Med* 2021:1-12.
61. Savita S, Mishra S, Jaiswal K. Molecular docking studies of betulinic acid and its structurally modified derivatives as potential inhibitors of COVID-19 main protease protein. *Biochem Cell Arch* 2020;20(2):4503-10.
62. Alzaabi MM, Hamdy R, Ashmawy NS, Hamoda AM, Alkhayat F, Khademi NN, *et al.* Flavonoids are promising safe therapy against COVID-19. *Phytochem Rev* 2022;21(1):291-312.
63. Derosa G, Maffioli P, D'Angelo A, Di Pierro F. A role for quercetin in coronavirus disease 2019 (COVID-19). *Phytother Res* 2021;35(3):1230-6.
64. Tsai YC, Lee CL, Yen HR, Chang YS, Lin YP, Huang SH, *et al.* Antiviral action of tryptanthrin isolated from *Strobilanthes cusia* leaf against human coronavirus NL63. *Biomolecules* 2020;10(3):366.
65. Jin YH, Min JS, Jeon S, Lee J, Kim S, Park T, *et al.* Lycorine, a non-nucleoside RNA dependent RNA polymerase inhibitor, as potential treatment for emerging coronavirus infections. *Phytomedicine* 2021;86:153440.



Mutations in *MINAR2* encoding membrane integral NOTCH2-associated receptor 2 cause deafness in humans and mice

Guney Bademci^a, María Lachgar-Ruiz^{b,c,d}, Mangesh Deokar^{e,f}, Mohammad Faraz Zafeer^g, Clemer Abad^h, Muzeyyen Yildirim Baylan^h, Neil J. Ingham^b, Jing Chen^b, Claire J. Sineni^g, Nirmal Vadgamaⁱ, Ioannis Karakikesⁱ, Shengru Guo^g, Duygu Dumanⁱ, Nitu Singh^f, Gaurav Harlalka^e, Shirish P. Jain^e, Barry A. Chioza^k, Katherina Walz^{a,g}, Karen P. Steel^b, Jamal Nasir^l, and Mustafa Tekin^{a,g,m,1}

Edited by Mary-Claire King, University of Washington, Seattle, WA; received March 8, 2022; accepted May 11, 2022

Discovery of deafness genes and elucidating their functions have substantially contributed to our understanding of hearing physiology and its pathologies. Here we report on DNA variants in *MINAR2*, encoding membrane integral NOTCH2-associated receptor 2, in four families underlying autosomal recessive nonsyndromic deafness. Neurologic evaluation of affected individuals at ages ranging from 4 to 80 y old does not show additional abnormalities. *MINAR2* is a recently annotated gene with limited functional understanding. We detected three *MINAR2* variants, c.144G > A (p.Trp48*), c.412_419delCGGTTTGG (p.Arg138Valfs*10), and c.393G > T, in 13 individuals with congenital- or prelingual-onset severe-to-profound sensorineural hearing loss (HL). The c.393G > T variant is shown to disrupt a splice donor site. We show that *Minar2* is expressed in the mouse inner ear, with the protein localizing mainly in the hair cells, spiral ganglia, the spiral limbus, and the stria vascularis. Mice with loss of function of the *Minar2* protein (*Minar2^{tm1b/tm1b}*) present with rapidly progressive sensorineural HL associated with a reduction in outer hair cell stereocilia in the shortest row and degeneration of hair cells at a later age. We conclude that *MINAR2* is essential for hearing in humans and mice and its disruption leads to sensorineural HL. Progressive HL observed in mice and in some affected individuals and as well as relative preservation of hair cells provides an opportunity to interfere with HL using genetic therapies.

autosomal recessive | deafness | hearing loss | *MINAR2* | NOTCH2

Hearing loss (HL) is one of the most common sensory deficits, affecting ~1 in 500 newborns (1). Genetic factors are implicated in the majority of cases, with more than 80% of the inherited form exhibiting autosomal recessive transmission (2). No additional findings are present in over 70% of the cases, which are then classified as nonsyndromic HL (Hereditary Hearing Loss Homepage, <https://hereditaryhearingloss.org/>) (2, 3). Genetic testing for etiologic evaluation has become a standard of care in people with congenital or childhood-onset sensorineural HL, which is caused by pathologies of the inner ear and auditory nerve (4, 5). Recent studies have shown that screening all recognized HL genes for variants reveals underlying cause in about half of the affected individuals, leaving a significant portion of people with HL with an unknown etiology (6–9). In the era of emerging genetic therapies for HL, finding the etiology of HL in affected individuals has become a critical task. This is especially relevant for progressive HL, as genetic therapies may potentially stop progression while cochlear hair cells are still alive (10–12).

MINAR2 (previously known as uncharacterized protein KIAA1024L and mouse gene *A730017C20Rik*) has recently been identified, and based on its structural similarity to *MINAR1*, named as major intrinsically disordered NOTCH2-associated receptor 2 or membrane integral NOTCH2-associated receptor 2 (13). A mutant mouse model of *Minar2* showed motor deficits similar to those seen in Parkinson disease, with no information about hearing abnormalities (13). A *Minar2* mutant mouse line, *Minar2^{tm1b}*, has also recently been reported to show no auditory brainstem responses at 14 wk old as part of a large HL screen (Mouse Genome Informatics [MGI]: 2442934) (11). Functional aspects of *MINAR2* and consequences of its dysfunction in humans remain unknown.

In this study, to better map the landscape of hereditary HL, we sought DNA variants underlying deafness in 13 affected individuals from four families. We identified three different *MINAR2* variants in the families cosegregating with HL. We further showed that homozygous *Minar2^{tm1b}* mutant mice develop rapidly progressive HL associated with changes in outer hair cell stereocilia. Finally, via in vitro studies we demonstrated that *MINAR2* suppresses NOTCH2, suggesting that notch signaling might play a role in pathogenesis.

Significance

Molecular components of hearing in mammals are not completely delineated. Via a genetic approach conducted in families with sensorineural hearing loss, this study presents *MINAR2* as an indispensable element of hearing in humans. Similarly, disruption of *Minar2* in mice leads to progressive hearing loss associated with alterations in the stereocilia of hair cells, the receptors of hearing, while hair cells remain intact until later in life. We present *MINAR2* as a gene working in the inner ear that is essential for hearing in humans and mice. Degeneration of sensory epithelium is a common consequence of hereditary deafness precluding genetic therapies. The preservation of hair cells in mutant mice at young ages makes *MINAR2* a good candidate for intervention.

The authors declare no competing interest.

This article is a PNAS Direct Submission.

Copyright © 2022 the Author(s). Published by PNAS. This open access article is distributed under Creative Commons Attribution-NonCommercial-NoDerivatives License 4.0 (CC BY-NC-ND).

¹To whom correspondence may be addressed. Email: mtekin@miami.edu.

This article contains supporting information online at <http://www.pnas.org/lookup/suppl/doi:10.1073/pnas.2204084119/-/DCSupplemental>.

Published June 21, 2022.

Results

Nonsyndromic Sensorineural HL Is Diagnosed in 13 Individuals from Four Unrelated Families. A summary of the auditory phenotype is shown in *SI Appendix, Table S1*. Ages ranged from 4 to 80 y old at the last examination. Each affected individual was diagnosed with HL either at birth or during infancy. Families 1 and 2 were of Turkish ancestry (Fig. 1). Parents of family 1 stated that in individuals II:1 and II:2, HL was milder in younger ages and progressed to a severe or profound degree by around age 10. Otoacoustic emissions were absent in these individuals. These siblings received unilateral cochlear implants at ages 12 and 10, respectively, which improved their oral communication. Individual II:3 in family 1 was diagnosed with profound sensorineural HL after failing the newborn hearing screening test. Otoacoustic emissions were absent at diagnosis. He received a unilateral cochlear implant at age 1 and communicates orally. Pure tone audiograms in parents showed normal thresholds (*SI Appendix, Fig. S1*).

Families 3 and 4 were of Indian ancestry. While there is no known consanguinity in any of the marriages in these two pedigrees, they are all from the same small town belonging to the same ethnic background, i.e., Hindu (religion) and Mali (Caste). All affected individuals in family 3 were born deaf and used signs, simple words, or sounds to be able to communicate. Severity of HL appeared to have remained the same in all the affected individuals from the beginning of life. Individuals IV:1 and IV:2 in family 4 were diagnosed with severe to profound sensorineural HL at the age of 3 y via auditory brainstem response (ABR) studies. Parents indicated a progression in the severity of HL. Their mode of communication at that age was predominantly nonverbal.

A high-resolution temporal bone CT scan or MRI was normal in at least one affected member of each family (*SI Appendix, Fig. S1*). None of the affected individuals had additional clinical findings for a syndromic form of deafness. Their neurodevelopmental skills were on target except for speech delay. None of the affected individuals showed impaired balance on tandem walking and Romberg test. Neurological examination was normal except for hearing loss in six affected individuals with ages ranging from 4 to 80 y. No affected individual was noted to have bradykinesia, tremor, or rigidity similar to those seen in Parkinson disease (*SI Appendix, Table S2*).

MINAR2 Variants Cosegregate with Autosomal Recessive Deafness. We performed genome sequencing in four affected individuals in families 1 (14) and 2 (15) and exome sequencing in three affected individuals in families 3 and 4 (Fig. 1*A*, individuals marked with an asterisk and *SI Appendix, Table S3*). Sequencing data in affected individuals were first analyzed for variants [single nucleotide variants (SNVs); insertions and/or deletions (indels); and copy number variants (CNVs) in recognized HL genes retrieved from the Hereditary Hearing Loss Homepage (<https://hereditaryhearingloss.org/>) (3), Online Mendelian Inheritance in Man (OMIM: <https://omim.org/>)], University of Miami Molecular Genetics Laboratory HL gene panel, and a virtual gene panel for HL (v2.176) from PanelApp (<https://www.genomicsengland.co.uk>)]. Minor allele frequency (MAF) thresholds of 0.005 for recessive and 0.001 for dominant variants were used. Population allele frequencies were obtained from the genome aggregation database (gnomAD: <https://gnomad.broadinstitute.org/>) (16) and the single nucleotide polymorphism database (dbSNP: <https://www.ncbi.nlm.nih.gov/projects/SNP/>), as well as from our internal exome/

genome database that includes >7,000 samples from different ethnicities. American College of Medical Genetics (ACMG) and ClinGen HL expert panel guidelines were followed for variant interpretation (17, 18). This analysis did not reveal a plausible variant under any inheritance model.

After excluding variants in previously recognized deafness genes, in family 1 we filtered shared homozygous coding and splice variants (SNVs, indels, and CNVs) in three affected siblings with a MAF of <0.005 in dbSNP, gnomAD highest subethnicity, and our internal control database. This filter reveals only a *MINAR2* (GeneBank: NM_001257308.2) c.412_419delCGGTTTTG (p.Arg138Valfs*10) variant in the family. The variant is located within a 9.4-MB shared homozygous run in three siblings, which is the only homozygous region >1 MB (*SI Appendix, Tables S4 and S5*). This frame-shift variant is predicted to introduce a premature stop codon and lead to early truncation of *MINAR2*.

In the proband of family 2, *MINAR2* is located within the second longest homozygous run at chromosome 5 (chr5):128,253,080 to 141,730,596 (hg19) (*SI Appendix, Table S6*). She is homozygous for the c.144G > A (p.Trp48*) variant in *MINAR2*. This nonsense variant is predicted to cause an early stop codon and result in truncation of *MINAR2*.

In the exome data of two affected individuals from family 3, filtering variants via the same criteria used in family 1 reveals only one variant for which both individuals are homozygous: *MINAR2* c.393G > T (p.Lys131Asn). SNP arrays show that this variant is located within the only shared homozygous run, >1 MB, in all seven affected individuals in family 3. This homozygous run is flanked by markers rs13174854 and rs37767449, which is 2.96 MB on chr5:128,738,407 to 131,705,915 (hg19). In family 4, two affected siblings share a 5.76-MB homozygous run on chr5:126,978,108 to 132,742,450 (hg19), flanked by markers rs11241936 and rs11242152. Exome sequencing showed that the proband in family 4 is homozygous for the same *MINAR2* variant detected in family 3.

None of the detected *MINAR2* variants is listed in dbSNP or gnomAD databases and all variants are predicted to be deleterious (*SI Appendix, Table S7*). Sanger sequencing confirmed all three *MINAR2* variants and showed that each variant cosegregates with autosomal recessive HL in all families (Fig. 1*A*).

MINAR2 c.393G > T (p.Lys131Asn) Leads to Aberrant Splicing. While it is a missense change, the c.393G > T (p.Lys131Asn) variant substitutes the last nucleotide of exon 2, and is predicted to abolish a splice donor site (*SI Appendix, Table S7 and Fig. S2*). Via exon trapping experiments, we show that this variant leads to an addition of 85 intronic nucleotides into exon 2, which alters the amino acid composition of the rest of the protein leading to a premature stop codon (Fig. 1*D* and *SI Appendix, Fig. S2*). The same variant also leads to skipping of exon 2 entirely (Fig. 1*D*).

Minar2^{tm1b} Homozygous Mutant Mice Show Sensorineural HL. To prove causality of disruption of *Minar2* in sensorineural HL, we evaluated hearing in *Minar2* mutant mice. Hearing sensitivity of *Minar2^{tm1b}* mutant mice (*SI Appendix, Fig. S3*) was assessed using two methods: ABR, a measure of neural activity in the auditory nerve and brainstem, and distortion product otoacoustic emission (DPOAE), a measure of outer hair cell electromotility and resulting nonlinearities in the cochlea. Thresholds for both ABRs and DPOAEs were raised in homozygous mutants compared with wild-type littermates from the earliest age studied, postnatal day (P) 14, only 21 d after the usual onset of hearing (Fig. 2). By 4 wk old, the

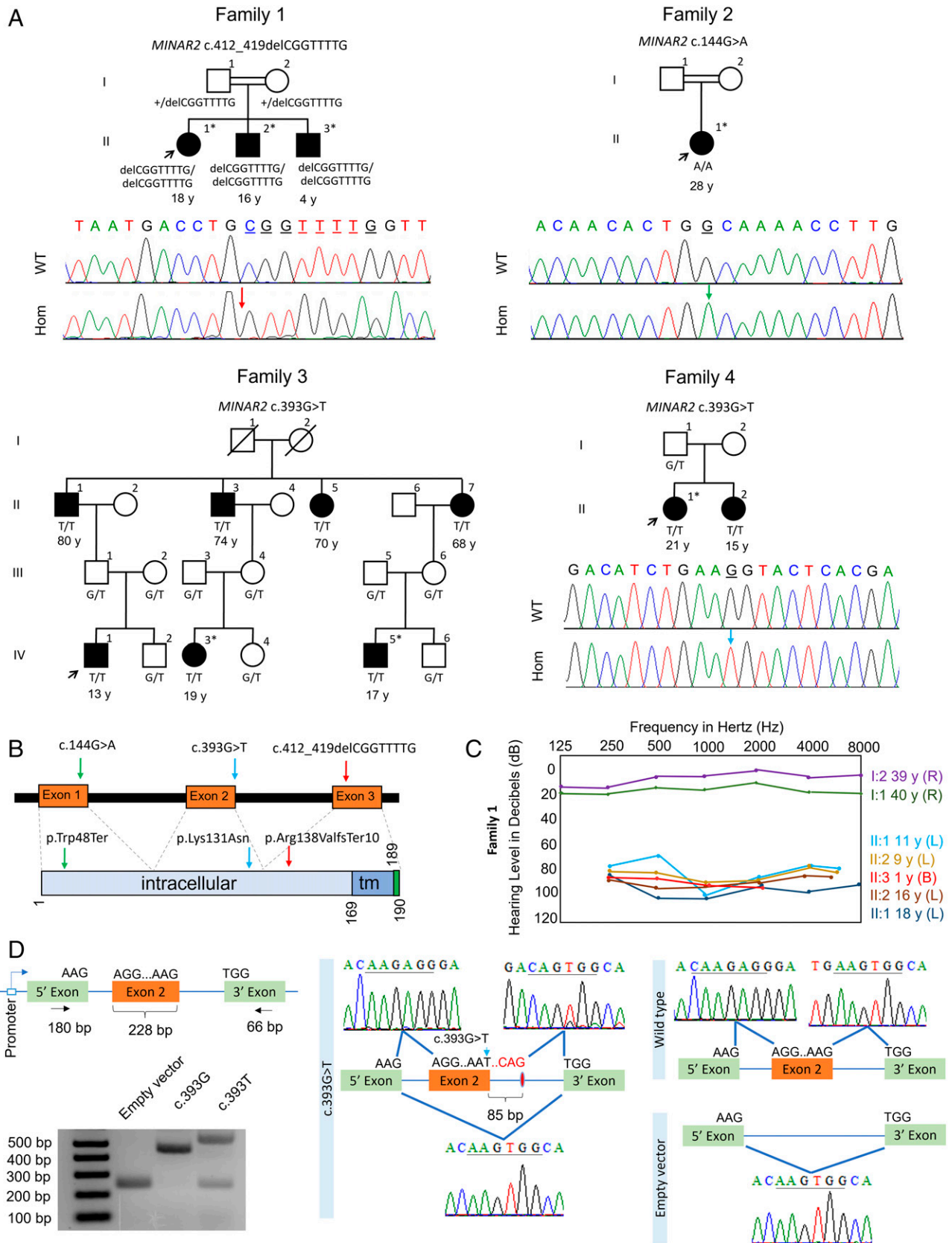


Fig. 1. Families, *MINAR2* variants, and the effects of the c.393G > T variant on splicing. (A) Pedigrees and segregation of the *MINAR2* variants in families. Filled symbols denote affected individuals and double lines indicate first cousin consanguinity. Electropherograms show the identified variant. The wild-type traces are from an unrelated individual. WT, wild type; Hom, homozygous mutant; exome/genome sequencing was performed in individuals marked with an (*) asterisk. (B) Locations of the identified variants. Tm, transmembrane. (C) Audiogram of family 1 (R, right ear; L, left ear; B, bilateral). (D) *MINAR2* exon 2 inserted into a vector consisting of 5' and 3' exons in the exon trap assay is shown. There are larger and smaller PCR products in the c.393G > T sample compared to wild type. Sanger sequencing confirms insertion of 85 bp at the donor site of exon 2 and skipping of exon 2.

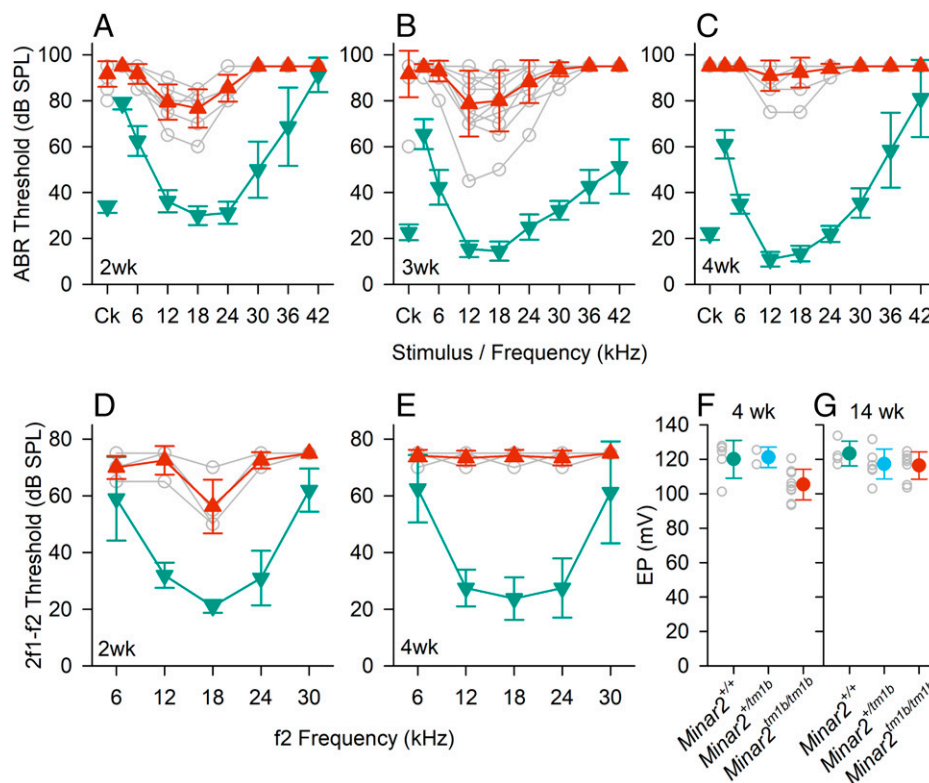


Fig. 2. Auditory studies in *Minar2* mutant mice. (A–C) ABR thresholds. Mean (\pm SD) ABR thresholds are plotted against stimulus for *Minar2*^{+/+} mice (teal, down triangles) and *Minar2*^{tm1b/tm1b} mice (red, up triangles). Open gray circles indicate thresholds for individual *Minar2*^{tm1b/tm1b} mice. Results are plotted for data obtained at P14 (A) ($n = 4$ *Minar2*^{+/+}, 9 *Minar2*^{tm1b/tm1b}); P21. (B) ($n = 11$ *Minar2*^{+/+}, 12 *Minar2*^{tm1b/tm1b}) and P27 to P28 (C) ($n = 10$ *Minar2*^{+/+}, 11 *Minar2*^{tm1b/tm1b}). Ck, click. (D and E) DPOAE thresholds are plotted against f2 stimulus frequency for *Minar2* control mice (teal, down triangles) and *Minar2*^{tm1b/tm1b} mice (red, up triangles). Open gray circles indicate thresholds for individual *Minar2*^{tm1b/tm1b} mice. Results are plotted for data obtained at P14 (D) ($n = 4$ controls, comprising 1 wild type and 3 heterozygotes, $n = 4$ mutants) and P27 to P28 (E) ($n = 4$ wild types, $n = 6$ mutants). (F and G) EP in *Minar2* mutant mice aged 4 wk (F) and 14 wk old (G). Colored circles indicate the mean (\pm SD) EP measurement in *Minar2*^{+/+} (teal), *Minar2*^{+/tm1b} (cyan), and *Minar2*^{tm1b/tm1b} (red) mice. Open gray circles indicate the EP values recorded in individual mice. At 4 wk old (P30 to P32) *Minar2*^{+/+} $n = 5$, range 101.2 to 127.8 mV; *Minar2*^{+/tm1b} $n = 2$ range 117.0 to 125.4 mV; and *Minar2*^{tm1b/tm1b} $n = 9$, range 93.4 to 120.5 mV. At 14 wk old *Minar2*^{+/+} $n = 4$, range 117 to 133.6 mV; *Minar2*^{+/tm1b} $n = 7$, range 113.8 to 131.6 mV; and *Minar2*^{tm1b/tm1b} $n = 8$, range 103.5 to 124.7 mV.

mutant mice showed severe elevations in threshold or no response at the highest sound levels used. Endocochlear potential was only slightly reduced from a mean of 120 mV to 105 mV in *Minar2*^{tm1b/tm1b} mice, with most mutant mice exhibiting an endocochlear potential (EP) in the normal physiological range for mice of over 100 mV (Fig. 2).

Minar2 Is Expressed in the Mouse Cochlea. To further understand the role of *Minar2* in hearing, we assessed the presence of *Minar2* transcript in different mouse tissues, including the inner ear, and specifically the cochlea. Total RNA was isolated from wild-type mice at embryonic day (E) 18.5, P0, and P30. RT-PCR with a forward primer located in exon 2 and a reverse primer in exon 3 of the *Minar2* gene (GenBank: NM_173759) produced a unique band of 171 bp corresponding to the wild-type mRNA in all analyzed tissues, with the exception of the liver. We find that *Minar2* is highly expressed in the inner ear, and specifically in the cochlea, at E18.5, P0, and P30 (Fig. 3A). To determine specific locations of *Minar2* expression within the cochlea, we proceeded to study *Minar2*^{tm1b} heterozygous mutant mice taking advantage of the reporter gene. β -Galactosidase staining of P1 cross-sections and whole mount organ of Corti preparations reveals that *Minar2* is mainly localized in the hair cells, the supporting cells, spiral ganglion (including the nerve fibers), the spiral limbus, and the stria vascularis (Fig. 3B and SI Appendix, Fig. S4 A and B). Of note, the gene expression analysis resource (gEAR; <https://umgear.org/>) portal shows *Minar2* expression both in hair cells and supporting cells

(SI Appendix, Fig. S4C) (19, 20). Double labeling for *Minar2* and Tuj1 in heterozygous mutant mice shows that the two are expressed in different cell types and *Minar2* is not present in the neurons of the spiral ganglion that were marked with Tuj1, suggesting that *Minar2* is located in spiral ganglion glial cells (Fig. 3 C, E, and F).

The Earliest Defect in *Minar2*^{tm1b} Mutant Mice Appears in Stereocilia Bundles. We used scanning electron microscopy (SEM) (Fig. 4) to examine the cochlea of mice aged 14 d old because at this age the ABR thresholds were raised but synapses appeared normal in numbers (Fig. 5). The organization of the organ of Corti appeared normal and there were very few missing stereocilia bundles in mutants, suggesting that hair cell degeneration cannot explain the raised ABR thresholds at this age (SI Appendix, Fig. S5). However, when we examined the stereocilia bundles of outer hair cells, we saw the shortest row was depleted, with reduced numbers and abnormally short stereocilia (Fig. 4). Outer hair cells along the entire length of the cochlear duct showed this feature. Inner hair cells appeared close to normal, although the middle row of stereocilia occasionally appeared more irregular than in the control littermates. Heterozygotes looked the same as wild-type littermates at this age.

Mechanoelectrical Transduction Channels Are Functional in *Minar2*^{tm1b/tm1b} Mice. To study the mechanoelectrical transduction (MET), we used the FM1-43 FX dye, a molecule commonly used to assay the MET channel function, since functional MET

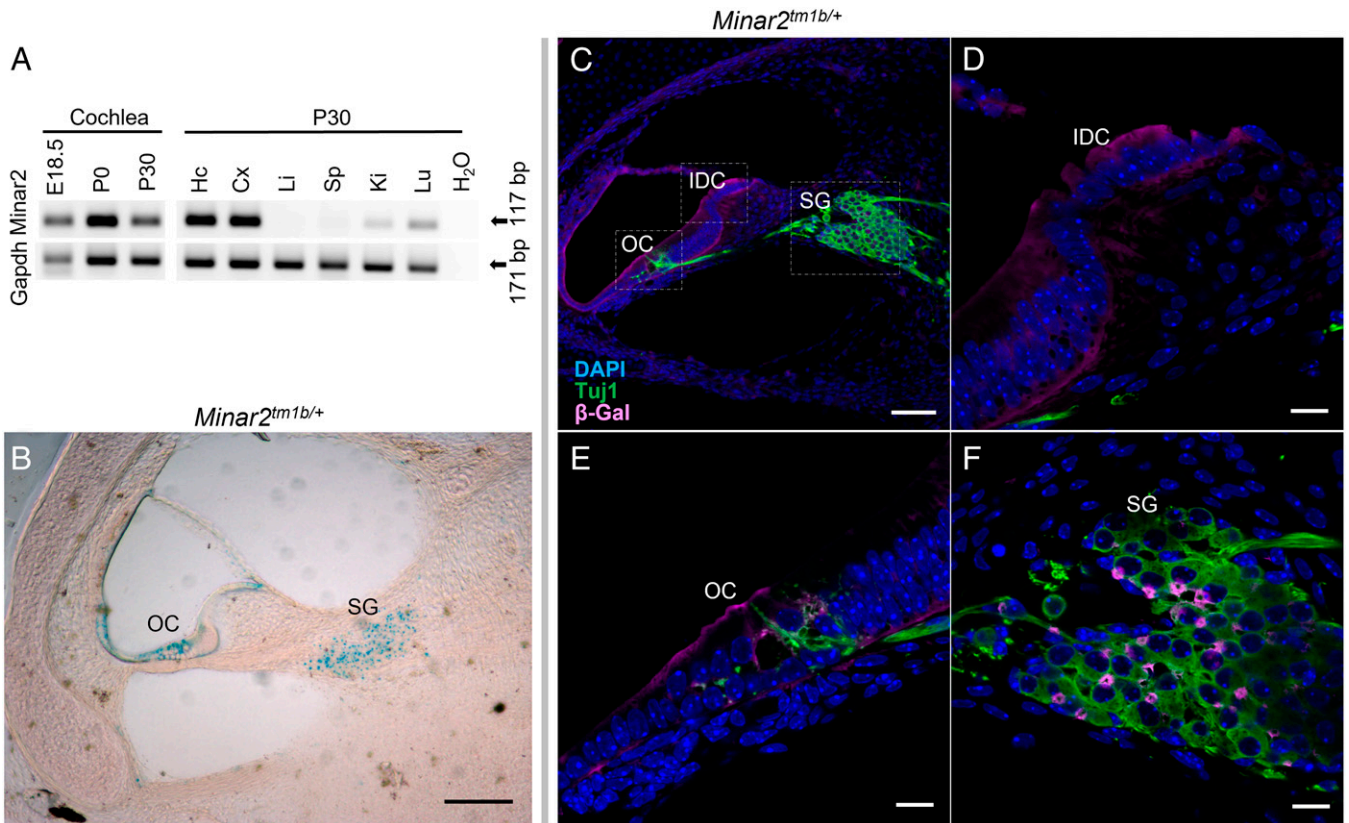


Fig. 3. Expression of *Minar2*, localization of the protein in the cochlea and innervation of cochlear hair cells in *Minar2* heterozygous mice, using the *LacZ* reporter gene component of the inserted cassette in the mutant allele, which expresses β -galactosidase (SI Appendix, Fig. S3). (A) RT-PCR of *Minar2* expression in the cochlea at E18.5, P0, and P30. Also, expression in different mouse tissues at P30 are Hc, hippocampus; Cx, cortex; Li, liver; Sp, spleen; Ki, kidney; Lu, lung. *Gapdh* was used as a control. (B) Localization of *Minar2* using the reporter gene *LacZ* of the mutant allele and in β -gal staining shown in blue. Note the localization of *Minar2* at the SG, spiral ganglion; OC, organ of Corti. (Scale bar: 70 μ m.) (C) Cross-section from 24-kHz region of P1 mutant inner ear was labeled with anti- β -gal (magenta) to detect *Minar2* localization and Tuj1 (green) to label neurons. (Scale bar: 70 μ m in C.) A zoom in is shown in D-F. (Scale bars: 10 μ m.) IDC, interdental cells.

channels are required for the uptake of this fluorescent dye into the hair cells (21). We perfused cochleae from P14 mice and observed FM1-43 FX dye uptake by both inner and outer hair

cells in *Minar2*^{+/+} and *Minar2*^{tm1b/tm1b} mice. Heterozygotes looked the same as wild-type littermates. While the intensity of the staining varied from mouse to mouse, all the samples showed

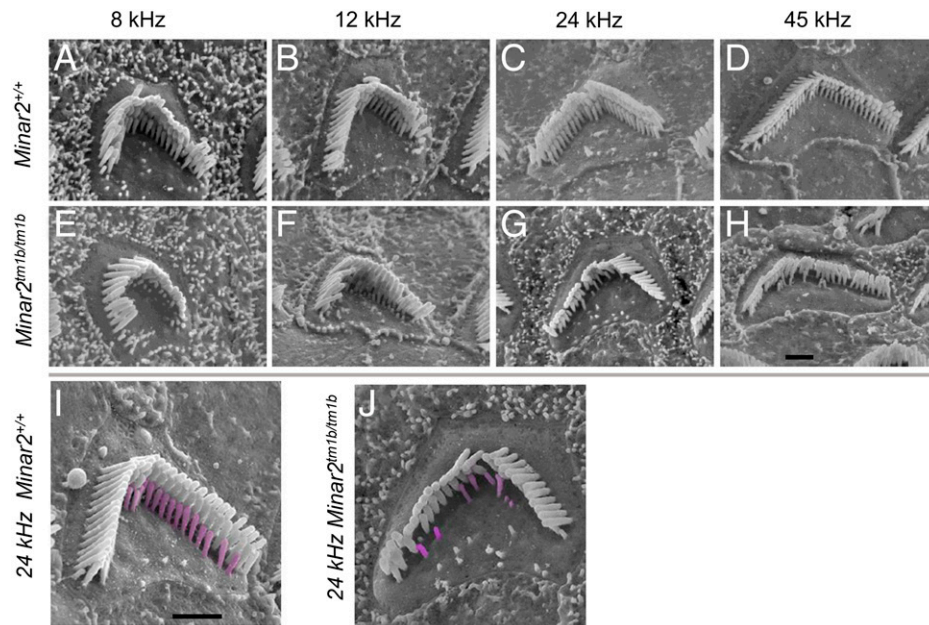


Fig. 4. Scanning electron microscopy reveals stereocilia defects. Outer hair cells at 8 kHz (85% of distance from base), 12 kHz (70%), 24 kHz (40%), and 45 kHz (20%) best frequency locations in wild-type mice (A-D) and *Minar2*^{tm1b/tm1b} homozygotes (E-H). Higher magnification images with the shortest row colored in magenta in a wild-type (I) and a mutant (J) outer hair cell, showing the reduction in numbers. (Scale bars in H and I: 1 μ m.)

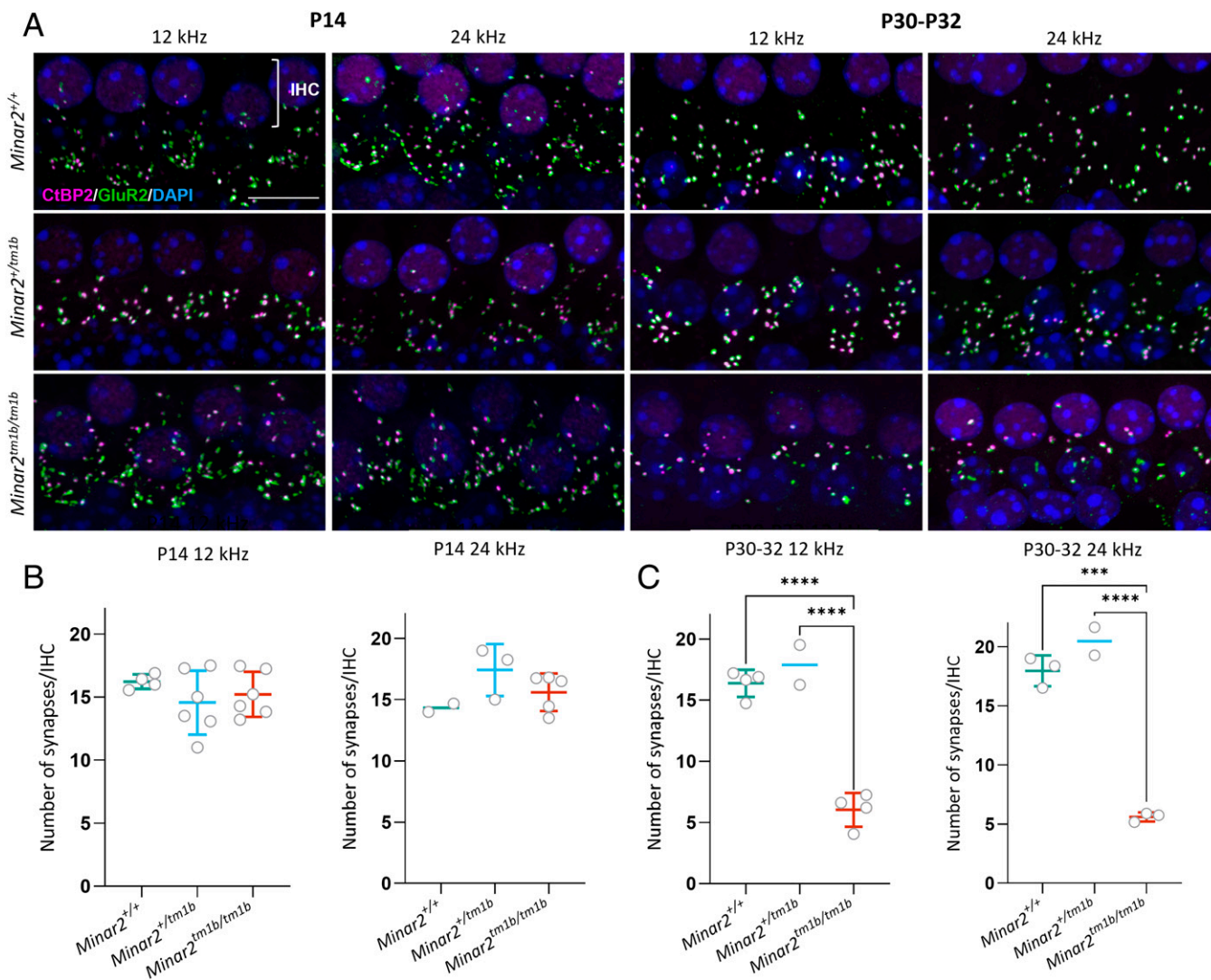


Fig. 5. Synaptic abnormalities of cochlear hair cells in *Minar2* mutant mice. (A) Synapses were examined using anti-CtBP2 antibody to mark presynaptic ribbons (magenta) and anti-GluR2 antibody to mark postsynaptic densities (green). Nuclei are shown in blue (DAPI). (Scale bar: 5 μ m.) The images correspond to the cochlear best-frequency regions of 12 kHz and 24 kHz. The row of nuclei at the *Top* of each image corresponds to the IHCs. (B and C) Quantification of ribbon synapses per IHC at P14 (B) and P30 to P32 (C). Colocalized pre- and postsynaptic components were defined as a synapse. The average for each mouse is plotted as a circle. All data are shown as mean \pm SD and statistically analyzed by one-way ANOVA with multiple comparisons. At P14, no significant difference was seen between homozygotes ($n = 6$ at 12 kHz and $n = 5$ at 24 kHz) and heterozygotes ($n = 6$ at 12 kHz and $n = 3$ at 24 kHz) or wild types ($n = 4$ at 12 kHz and $n = 2$ at 24 kHz). At P30 to P32, there are significantly fewer colocalized synapses in *Minar2*^{tm1b/tm1b} ($n = 4$ for 12 kHz and $n = 3$ for 24 kHz) compared to wild types ($n = 4$ at 12 kHz and $n = 3$ at 24 kHz) and compared to heterozygotes ($n = 2$). **** $P = 0.0001$ and ***** $P < 0.0001$.

uptake of the molecule specifically in hair cells, indicating that the MET channels are active in the *Minar2* mutants (SI Appendix, Fig. S6).

Hair Cell Degeneration Is a Secondary Feature in *Minar2*^{tm1b} Mutant Mice. Hair cell degeneration is a common feature in HL, and extensive loss of hair cells may preclude some approaches to treatments. Therefore, we examined older *Minar2*^{tm1b} mutant mice, aged 14 wk, to assess the loss of hair cells. We have previously reported that these mutants show no auditory brainstem responses at 14 wk old (11) and the EP is normal at this age (Fig. 2G). At earlier ages we see minimal evidence of any hair cell degeneration (SI Appendix, Fig. S5). However, by 14 wk of age, there is extensive loss of hair cells, with some discrete patches distributed along the length of the cochlear duct where the entire organ of Corti appears to have degenerated while other regions show scattered missing hair cells, both inner and outer, within the organ of Corti (Fig. 6). Heterozygotes had a similar appearance to the wild-type mice.

***Minar2*^{tm1b} Mutant Mice Show Reduction in the Number of Inner Hair Cell Ribbon Synapses at P30.** To understand underlying pathophysiology further, we evaluated the innervation pattern of hair cells by staining neurons with an anti-neurofilament antibody in the organ of Corti at P1 (SI Appendix, Fig. S7). Homozygous mutant mice show an altered innervation pattern of hair cells with a reduction in the nerve fibers around inner hair cells and a dispersed distribution of nerve fibers toward outer hair cells. *Minar2*^{tm1b} mutant mice show reduction in the number of crossings of type II nerves at P14 (Fig. 7). We subsequently examined synapses of inner hair cells using anti-CtBP2 antibody to label presynaptic ribbons and anti-GluR2 antibody to mark the AMPA receptor subunit R2, a part of the postsynaptic density. Ribbon synapses look qualitatively normal at both ages tested, P14 and P30, and the number of synapses per inner hair cell in homozygous mutants was not significantly different from numbers in heterozygotes or wild-type controls at P14, indicating that the raised **153** thresholds observed at that age in mutants are not due to the

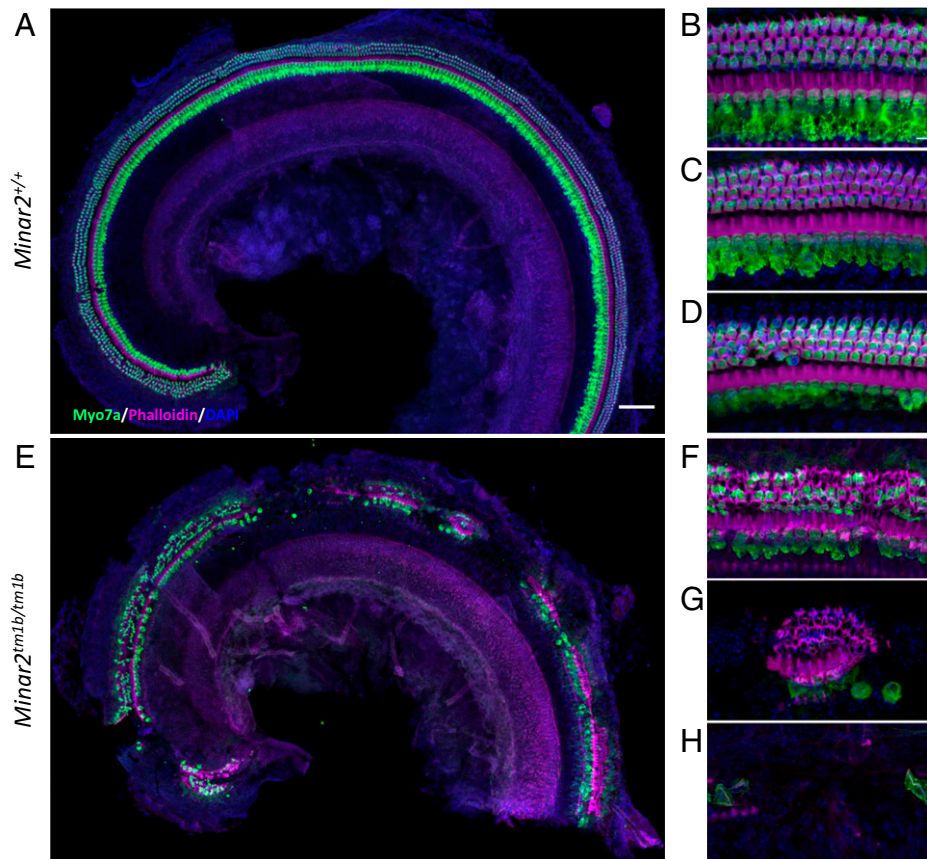


Fig. 6. Hair cell degeneration pattern in *Minar2^{tm1b}* mutant mice at 14 wk old. Confocal maximum intensity projection images of the whole-mount organ of Corti of 14-wk-old mice. Hair cells were examined using anti-Myo7a antibody (green) and phalloidin (magenta). Nuclei are shown in blue (DAPI). (Scale bars: 200 μ m in A and 10 μ m in B.) The images are representative examples of *Minar2^{+/+}* (A–D) and *Minar2^{tm1b/tm1b}* (E–H) mice. (A and E) Overview of the apical half of the cochlea. (B–D) High-magnification images corresponding to the 12 kHz, 24 kHz, and 36 kHz best-frequency regions, respectively. (F–H) High-magnification images of three different patterns of hair cell loss observed in *Minar2^{tm1b}* mutant mice. All five homozygotes that were studied at 14 wk old showed similar patches of loss of the organ of Corti at varying locations along the length of the cochlear duct interspersed with regions that showed only scattered hair cell loss. *Minar2^{+/+}* ($n = 4$), *Minar2^{+/tm1b}* ($n = 5$), and *Minar2^{tm1b/tm1b}* ($n = 5$).

loss of ribbon synapses (Fig. 5 A and B). However, by P30 to P32 *Minar2^{tm1b}* mutant mice did show a significant decrease in the number of synapses compared to wild-type mice (Fig. 5 A and C), and this may contribute to the progression of HL.

Overexpression of MINAR2 Suppresses Angiogenesis and MINAR2 Variants Abolish This Effect. As MINAR1 has been shown to inhibit angiogenesis (22), we investigated whether MINAR2 shows the same effect on angiogenesis in human umbilical vein endothelial cells (HUVEC). These studies reveal that transient overexpression of *MINAR2* suppresses angiogenesis (Fig. 8A). In addition, overexpressing each *MINAR2* variant detected in families 1 and 2 in HUVEC reduces suppression of angiogenesis, suggesting that they are loss-of-function variants (Fig. 8A).

Expression Levels of MINAR2 Are Inversely Correlated with Intracellular NOTCH2 Abundance. MINAR2 is named based on its structural similarity to MINAR1, which is shown to be involved in NOTCH2 signaling (22). While MINAR2 is a much smaller protein compared to MINAR1 (190 vs. 917 amino acids) (22), it has recently been shown to bind NOTCH2 in a coimmunoprecipitation assay (13). Thus, we set out to explore whether NOTCH2 abundance in cells is correlated with *MINAR2* expression (23, 24). Furthermore, as NOTCH and VEGF signaling pathways are known to interact during angiogenesis (25), we determined the effect of *MINAR2*

expression on VEGF. Our studies show that overexpression of wild-type *MINAR2* in HUVEC is associated with reduced abundance of NOTCH2 and VEGFA (a prominent VEGF protein in vascular endothelial cells) (Fig. 8B). Silencing of *MINAR2* in PC12 cells, which endogenously express *MINAR2*, leads to an increase in NOTCH2 and confirms the suppressor effect of *MINAR2* on NOTCH2 abundance (Fig. 8C and *SI Appendix*, Fig. S8).

MINAR2 Is Involved in MAP Kinase and mTOR Pathways.

MINAR1 has been shown to regulate neurite outgrowth in a neuroendocrine cell line PC12 (26), in which neurite outgrowth via nerve growth factor is achieved by MAPK and PI3K pathways (27). The mTOR complex is a downstream target of PI3K, which contains mTORC1 and mTORC2 complexes in its central catalytic domain (26). We tested the effects of *MINAR2* on the MAPK pathway by transiently overexpressing wild-type *MINAR2* in PC12 cells and detecting levels of ERK1/2 and pERK1/2, a crucial kinase of the MAPK signaling pathway. These studies show that overexpression of wild-type *MINAR2* reduces the abundance of pERK1/2, the active form of ERK1/2. On the other hand, overexpression of the two *MINAR2* deafness variants in families 1 and 2 does not show this effect, again supporting their loss of function (*SI Appendix*, Fig. S9A). When we silenced *MINAR2* in PC12 cells, we observed an increase in a functional protein in mTORC1 activity, P-S6, at 12 h (*SI Appendix*, Fig. S9B). However, there was

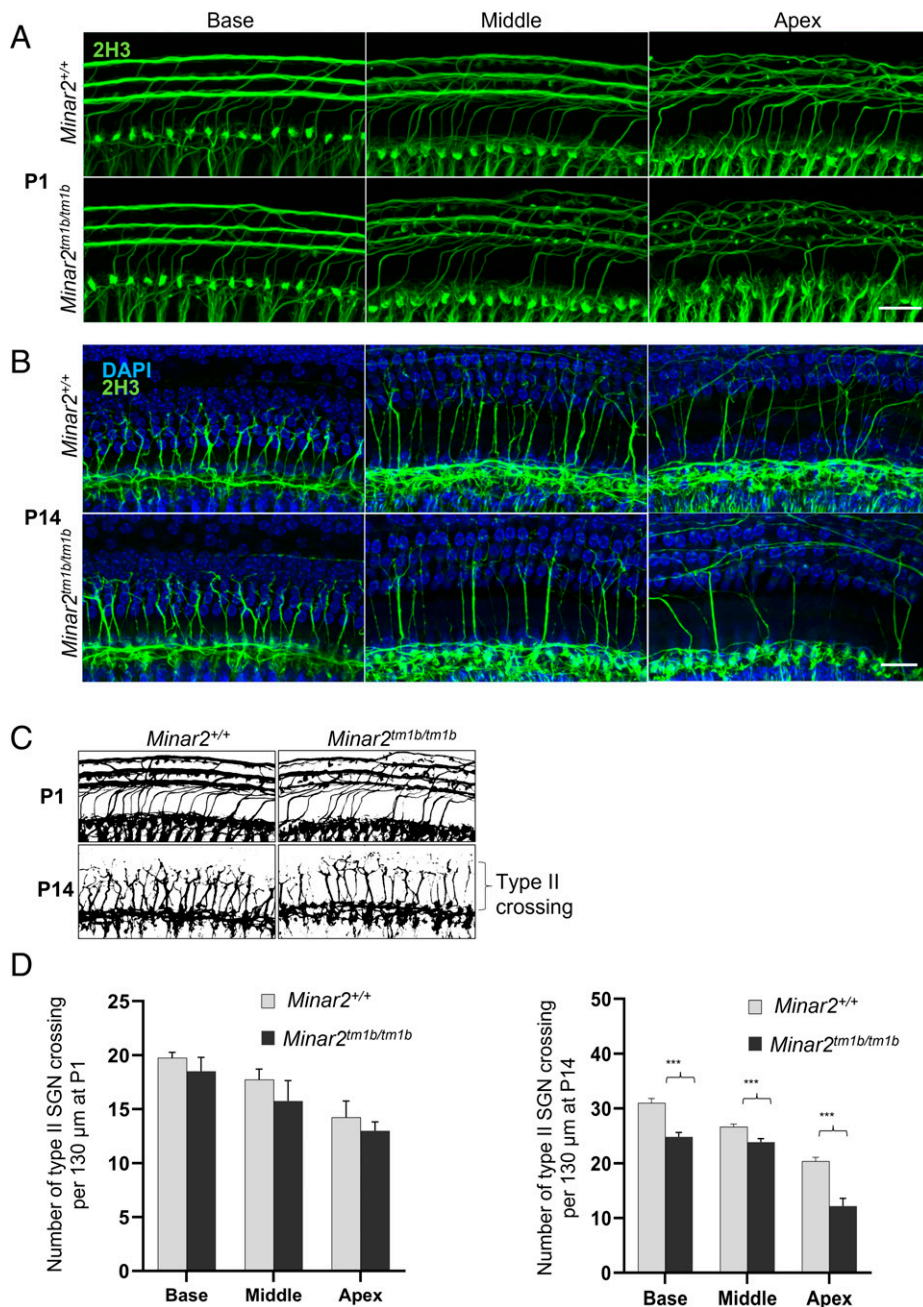


Fig. 7. Confocal maximum intensity projection images from a 24-kHz region of the whole-mount cochlea. (A and B) Total innervation with anti-2H3 neurofilament label (green) for P1 and P14 ($n = 3$ each group) wild-type and mutant mice. (Scale bars in A and B: 20 μm .) (C) Schematic diagram of whole-mount cochlea, demonstrating the innervation pattern of type II nerves at P1 and P14 wild-type and mutant mice. (D) The total number of crossings of type II nerves is shown as histogram ($n = 3$; $***P < 0.001$.)

no difference in pAKT, a component of mTORC2 activity (SI Appendix, Fig. S9B).

Discussion

In this study we present three loss-of-function variants in *MINAR2* in four families cosegregating with nonsyndromic sensorineural HL. Hearing loss started at birth or in early childhood in all 13 affected individuals. A progressive HL reaching a severe-to-profound degree during childhood was noted in four affected individuals. In addition to ABR thresholds showing sensorineural HL, otoacoustic emissions were absent in three children tested, suggesting dysfunction of both inner hair cell/acoustic nerve and outer hair cells. To support causality of the *MINAR2* mutations in deafness and to begin understanding

the mechanism of HL, we show that *Minar2*^{tm1b/tm1b} mice have a severe, progressive increase in ABR thresholds from 2 wk old onwards (around the time that mice start to hear), with very few responses by 4 wk old. Otoacoustic emissions can be detected in the mutant mice but at raised thresholds at 2 wk old, and these responses are mostly absent by 4 wk old, implicating outer hair cells in the pathology. In conclusion, audiological findings both in humans and mice show that loss of *MINAR2* function results in early-onset and sensorineural HL that rapidly progresses to severe to profound deafness.

The reduced number of stereocilia in the shortest row on outer hair cells would be expected to have a severe impact upon the number of transduction channel complexes available and suggests that the primary defect in these mutant mice is located at the top of the hair cell. However, we have demonstrated that

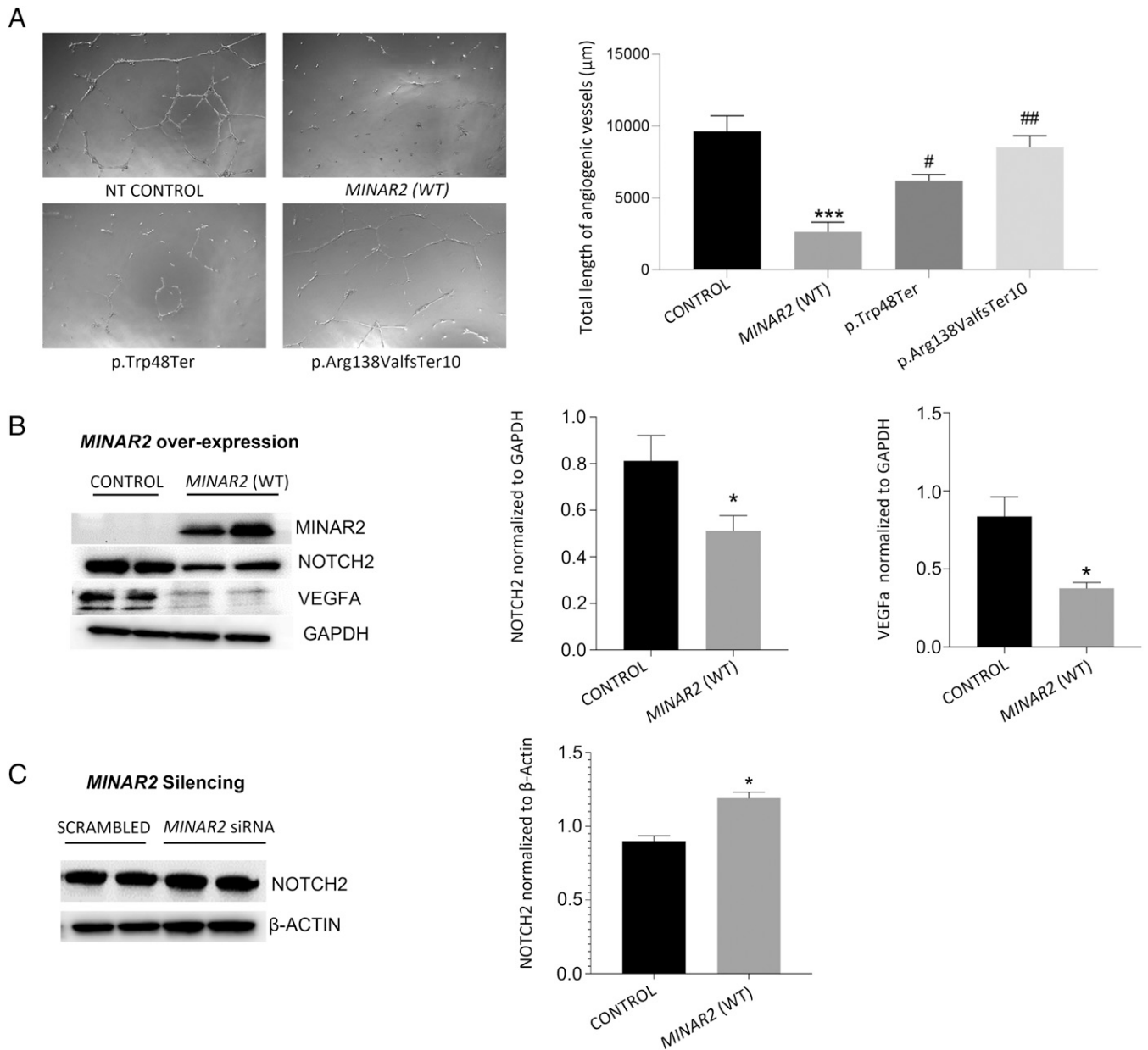


Fig. 8. Effects of *MINAR2* on angiogenesis, NOTCH2, and VEGFA. (A) Angiogenic potential of nontransfected (NT) HUVEC compared to cells transfected with *MINAR2* wild-type (WT), and *MINAR2* p.Trp48*, and p.Arg138Valfs*10 plasmid constructs. *Right* graph shows analysis of total length of angiogenic vessels formed after incubation of 12 h on Matrigel-coated wells; images were analyzed with ImageJ angioanalyzer and results are expressed as mean \pm SEM. Significant differences were shown as *** $P \leq 0.001$ when compared to control and as ## $P \leq 0.01$ when compared to *MINAR2*(WT). (B, *Left*) Immunoblot images showing the effect of *MINAR2*(WT) transient overexpression on NOTCH2 and VEGFA protein levels in HUVEC cells. (*Right*) Statistical analysis of GAPDH-normalized relative protein expressions of NOTCH2 and VEGFA. Results are expressed as mean \pm SEM and significant differences are shown as * $P \leq 0.05$ when compared to control. (C, *Left*) Immunoblot images of siRNA-induced *MINAR2* silencing on NOTCH2 protein levels in PC12 cells. (*Right*) β -Actin normalized relative protein expression of NOTCH2. Results are expressed as mean \pm SEM and significant differences are shown as * $P \leq 0.05$ when compared to control. Data were analyzed by one-way ANOVA with multiple comparisons.

the remaining MET channels are active in *Minar2^{tm1bl/tm1b}* mice, since the hair cells of these mice are able to uptake FM1-43 dye. Degeneration of hair cells (Fig. 6) and synaptic defects (Fig. 5) occur later in development and cannot explain the raised ABR and DPOAE thresholds at 14 d old in the *Minar2^{tm1b}* homozygotes. Mutations of other genes also lead to loss of the shorter stereocilia associated with hearing impairment, for example the *Baiap2l2* mutant (28) and the *Clrn2* mouse mutant (29).

The Notch pathway is a highly conserved intercellular signaling cascade that is activated by the interaction of transmembrane ligands (Delta and Jagged) with Notch receptors, which are usually expressed on the surface of neighboring cells.

Binding of the Notch ligand to receptor induces cleavage of the Notch receptors intracellular domain, which binds to multiple DNA-binding proteins in the nucleus (30–32). In the initial stages of angiogenesis, Notch activation is generally repressed to allow proliferation of endothelial cells in response to VEGF stimulation, and its expression is later up-regulated when endothelial cells stop proliferating and the vessels begin to stabilize (33–39). While it is possible that the effects of *MINAR2* on angiogenesis may play a role in hearing, we did not observe abnormal vascular structures in the cochlea of homozygous mutant mice. Moreover, the most sensitive part of the cochlea to vascular function is the generation of EP by the stria vascularis. In this study, EP was within the normal range in

homozygous mutant mice. Our results show that MINAR2 and NOTCH2 have a regulatory relationship. In the mammalian cochlea, there is no regeneration of sensory hair cells and the strictly controlled pattern of alternating hair cells and supporting cells in the organ of Corti is set up in early development. Notch signaling is believed to be a critical part of the process of cells deciding their fate as a hair cell or a supporting cell and many genes involved in Notch signaling underlie hearing impairment (40, 41). As our examination of the organ of Corti of young mice shows (SI Appendix, Fig. S5), the pattern is set up correctly, ruling out an early developmental defect of cell fate or differentiation. However, Notch signaling may also play a role in longer-term maintenance of the organ of Corti, and our findings of progressive deterioration of this organ resulting from mutation of a gene known to be involved in Notch signaling supports this suggestion.

MINAR family proteins (MINAR1 and MINAR2) have been proposed to be associated with the inhibition of cell proliferation (13, 22). In this study, we did not observe any proliferation effect in different ages of *Minar2^{tm1b/tm1b}* mice. Terminal mitoses of hair cells occur early at E12 to E14 before birth (42). The confocal images illustrated in Fig. 6 all indicate loss of cells from the normal regular array, with no sign of any proliferation.

Our findings of an abnormal innervation pattern of hair cells as early as P1, as well as a significant decrease in the numbers of intact synapses at 4 wk old, suggest that abnormal innervation of hair cells may contribute to the severe auditory dysfunction in *Minar2^{tm1b/tm1b}* mice. Based on these findings, Minar2 may be playing a role in the maintenance of hair cell synapses. MINAR2 is structurally similar to MINAR1, which has been reported to be involved in controlling neurite formation during neuronal differentiation through DEP domain containing MTOR interacting protein (DEPTOR). In this study, we show that similar to MINAR1, MINAR2 down-regulates mTOR signaling (SI Appendix, Fig. S9B), which may contribute to the abnormal innervation pattern observed in the organ of Corti of *Minar2* mutant mice.

It is notable that although the sensory hair cells are present up to 4 wk old and are able to take up FM1-43 dye through transduction channels, they do not appear to be functioning normally as shown by the raised ABR and DPOAE thresholds. Most genetic and environmental causes of sensorineural HL lead to permanent loss of hair cells, reducing the chance of gene therapy or gene editing approaches. Progressive HL associated with a relatively normal appearance of hair cells in young ages makes *MINAR2* a promising target for genetic therapies. Further elucidation of its role in the maintenance of hair cell synapses and stereocilia bundles may open new avenues to treat more common forms of HL resulting from similar mechanisms.

Materials and Methods

More details of materials and methods are in SI Appendix.

Study Approval. This study was approved by the University of Miami Institutional Review Board (20081138-USA), as well as by the Ethics Committees of Ankara University Medical School (012413-Turkey) and Rajarshi Shahu College of Pharmacy (180720-India). A signed informed consent was obtained from all participants or, in the case of a minor, from the parents.

DNA Sequencing and Bioinformatics Analysis. Genome sequencing was performed in family 1 individuals II:1, II:2, and II:3 and family 2 II:1 (Fig. 1A and SI Appendix, Table S3) (43, 44). Reads were mapped to human genome reference (National Center for Biotechnology Information [NCBI] build37/hg 19 version) with Burrows-Wheeler aligner (BWA). Genome Analysis Toolkit (GATK) was

used for variant calling (45–47). CNVs were called using CNVnator (48). Enlis Genome Research software (<https://www.enlis.com/>) was used to identify runs of homozygosity in family 1 and family 2 from genome sequencing data (SI Appendix, Tables S4–S6).

Illumina Infinium Global Screening Array (GSA) v2 (Illumina) kit was used for genotyping in 16 members of family 3 and three members of family 4 to map the shared homozygous regions in affected individuals. Additional exome sequencing was performed on a HiSeq 2000 platform (Illumina), as described previously (49), in individuals IV:3 and IV:5 in family 3 and IV:1 in family 4 (SI Appendix, Table S3).

Genome sequencing data were deposited in the NCBI's BioProject database: PRJNA623118, BioSample: SAMN27763770 (family 1, individual II:1) and BioSample: SAMN27763769 (family 2, individual II:1).

Ethics Statement for Animals. Mouse studies in the United Kingdom were carried out in accordance with UK Home Office regulations and the UK Animals (Scientific Procedures) Act of 1986 (ASPA) under UK Home Office licenses, and the study was approved by the King's College London Ethical Review Committee. Mice were culled using methods approved under these licenses to minimize any possibility of suffering. All procedures in Miami were approved by the University of Miami Institutional Animal Care and Use Committee and followed the NIH guidelines "Using Animals in Intramural Research."

Mouse Generation. *Minar2^{tm1a}* mutant mice were generated at the Wellcome Sanger Institute by blastocyst microinjection of targeted embryonic stem (ES) cells on a C57BL/6N genetic background (50, 51). *Minar2^{tm1b(KOMP)Wtsi}* mice (*Minar2^{tm1b}*) were generated from *Minar2^{tm1a(KOMP)Wtsi}* mice by exposure of preimplantation embryos to soluble Cre recombinase (52), which leads to recombination between LoxP sites, removing the selection cassette and exon 2 to produce mice carrying the *Minar2^{tm1b}* allele (SI Appendix, Fig. S3). Both *tm1a* and *tm1b* alleles are available via the European Mouse Mutant Archive (EMMA; <https://www.infrafrontier.eu>).

Statistics. A one-way ANOVA with multiple comparisons was used to compare groups for count of synapses in mouse inner ear and also for angiogenesis, MAPK, and mTOR assays.

Data Availability. Sequencing data have been deposited in publicly accessible database, Family 1, II:1 (14) and Family 2, II:1 (15).

ACKNOWLEDGMENTS. We are immensely grateful to all the patients and families participating in this study. This study was supported by R01DC009645 and R01DC012836 from the NIH/National Institute on Deafness (M.T.), the National Institute for Health and Care Research Biomedical Research Centre, King's College London (K.P.S.), and the Royal National Institute for Deaf People (K.P.S.). This research was funded in part by the Wellcome Trust. For the purpose of Open Access, the author has applied a CC BY public copyright license to any Author Accepted Manuscript version arising from this submission. We thank the Wellcome Sanger Institute Mouse Genetics Project for generating and providing the *Minar2* mouse mutant. M.D. and G.H. would also like to express sincere gratitude for all the support provided by Dr. S. P. Jain, Principal, Rajarshi Shahu College of Pharmacy, Malvahir, Buldana, India.

Author affiliations: ^aDr. John T. Macdonald Foundation Department of Human Genetics, University of Miami Miller School of Medicine, Miami, FL, 33136; ^bWolfson Centre for Age-Related Diseases, King's College London, London, SE1 1UL, United Kingdom; ^cServicio de Genética, Hospital Universitario Ramón y Cajal, IRYCIS, 28034 Madrid, Spain; ^dCentro de Investigación Biomédica en Red de Enfermedades Raras, 28034 Madrid, Spain; ^eDepartment of Pharmacology, Rajarshi Shahu College of Pharmacy, 443001 Malvahir, Buldana, India; ^fOriental College of Pharmacy and Research, Oriental University, 453555 Indore, Madhya Pradesh, India; ^gJohn P. Hussmann Institute for Human Genomics, University of Miami Miller School of Medicine, Miami, FL 33136; ^hDepartment of Otorhinolaryngology, Faculty of Medicine, Dicle University, Diyarbakir 21200, Turkey; ⁱCardiovascular Institute and Department of Cardiothoracic Surgery, Stanford University School of Medicine, Stanford, CA, 94305; ^jDepartment of Audiology, Faculty of Health Sciences, Ankara University, Ankara 06100, Turkey; ^kCollege of Medicine and Health, University of Exeter Medical School, RD&E NHS Foundation Trust, Exeter, EX2 5DW, United Kingdom; ^lMolecular Biosciences Research Group, Faculty of Health and Society, University of Northampton, Northampton, NN1 5PH, United Kingdom; and ^mDepartment of Otolaryngology, University of Miami Miller School of Medicine, Miami, FL, 33136

Author contributions: M.T. designed research; G.B., M.L.-R., M.D., M.F.Z., C.A., M.Y.B., N.J.I., J.C., C.J.S., N.V., I.K., S.G., D.D., N.S., G.H., S.P.J., B.A.C., K.W., K.P.S., J.N., and M.T. performed research; G.B., M.L.-R., N.J.I., K.P.S., and M.T. contributed new reagents/

analytic tools; G.B., M.L.-R., M.D., M.F.Z., C.A., M.Y.B., N.J.I., J.C., C.J.S., N.V., I.K., S.G., D.D., N.S., G.H., S.P.J., B.A.C., K.W., K.P.S., J.N., and M.T. analyzed data; and G.B., M.L.-R., M.D., M.F.Z., C.A., N.J.I., N.V., G.H., K.W., K.P.S., J.N., and M.T. wrote the paper.

1. A. L. Mehl, V. Thomson, The Colorado newborn hearing screening project, 1992-1999: On the threshold of effective population-based universal newborn hearing screening. *Pediatrics* **109**, E7 (2002).
2. C. C. Morton, W. E. Nance, Newborn hearing screening—A silent revolution. *N. Engl. J. Med.* **354**, 2151-2164 (2006).
3. G. Van Camp, R. J. H. Smith, Hereditary Hearing Loss Homepage. <https://hereditaryhearingloss.org>. Accessed 1 December 2021.
4. R. L. Alford *et al.*; ACMG Working Group on Update of Genetics Evaluation Guidelines for the Etiologic Diagnosis of Congenital Hearing Loss; Professional Practice and Guidelines Committee, American College of Medical Genetics and Genomics guideline for the clinical evaluation and etiologic diagnosis of hearing loss. *Genet. Med.* **16**, 347-355 (2014).
5. A. M. Korver *et al.*, Congenital hearing loss. *Nat. Rev. Dis. Primers* **3**, 16094 (2017).
6. G. Bademci *et al.*, Comprehensive analysis via exome sequencing uncovers genetic etiology in autosomal recessive nonsyndromic deafness in a large multiethnic cohort. *Genet. Med.* **18**, 364-371 (2016).
7. J. Doll *et al.*, Genetic spectrum of syndromic and non-syndromic hearing loss in Pakistani families. *Genes (Basel)* **11**, 1329 (2020).
8. C. M. Sloan-Heggen *et al.*, Characterising the spectrum of autosomal recessive hereditary hearing loss in Iran. *J. Med. Genet.* **52**, 823-829 (2015).
9. D. Yan *et al.*, Spectrum of DNA variants for non-syndromic deafness in a large cohort from multiple continents. *Hum. Genet.* **135**, 953-961 (2016).
10. T. Atik, G. Bademci, O. Diaz-Horta, S. H. Blanton, M. Tekin, Whole-exome sequencing and its impact in hereditary hearing loss. *Genet. Res.* **97**, e4 (2015).
11. N. J. Ingham *et al.*, Mouse screen reveals multiple new genes underlying mouse and human hearing loss. *PLoS Biol.* **17**, e3000194 (2019).
12. B. Vona, I. Nanda, M. A. Hofrichter, W. Shehata-Dieler, T. Haaf, Non-syndromic hearing loss gene identification: A brief history and glimpse into the future. *Mol. Cell. Probes* **29**, 260-270 (2015).
13. R. X.-Y. Ho *et al.*, Loss of MINAR2 impairs motor function and causes Parkinson's disease-like symptoms in mice. *Brain Commun.* **2**, faa047 (2020).
14. M. Tekin, SRX15001233 Family 1, II:1. NCBI Sequence Read Archive. <https://www.ncbi.nlm.nih.gov/sra/SRX15001233>. Deposited 26 April 2022.
15. M. Tekin, SRX15001232: Family 2, II:1. NCBI Sequence Read Archive. <https://www.ncbi.nlm.nih.gov/sra/SRX15001232>. Deposited 26 April 2022.
16. K. J. Karczewski *et al.*; Genome Aggregation Database Consortium, The mutational constraint spectrum quantified from variation in 141,456 humans. *Nature* **581**, 434-443 (2020).
17. A. M. Oza *et al.*; ClinGen Hearing Loss Clinical Domain Working Group, Expert specification of the ACMG/AMP variant interpretation guidelines for genetic hearing loss. *Hum. Mutat.* **39**, 1593-1613 (2018).
18. S. Richards *et al.*; ACMG Laboratory Quality Assurance Committee, Standards and guidelines for the interpretation of sequence variants: A joint consensus recommendation of the American College of Medical Genetics and Genomics and the Association for Molecular Pathology. *Genet. Med.* **17**, 405-424 (2015).
19. R. Elkon *et al.*, RFX transcription factors are essential for hearing in mice. *Nat. Commun.* **6**, 8549 (2015).
20. J. Orvis *et al.*, gEAR: Gene Expression Analysis Resource portal for community-driven, multi-omic data exploration. *Nat. Methods* **18**, 843-844 (2021).
21. J. E. Gale, W. Marcotti, H. J. Kennedy, C. J. Kros, G. P. Richardson, FM1-43 dye behaves as a permeant blocker of the hair-cell mechanotransducer channel. *J. Neurosci.* **21**, 7013-7025 (2001).
22. R. X. Ho *et al.*, MINAR1 is a Notch2-binding protein that inhibits angiogenesis and breast cancer growth. *J. Mol. Cell Biol.* **10**, 195-204 (2018).
23. P. J. Lanford *et al.*, Notch signalling pathway mediates hair cell development in mammalian cochlea. *Nat. Genet.* **21**, 289-292 (1999).
24. W. Pan, Y. Jin, B. Stanger, A. E. Kiernan, Notch signaling is required for the generation of hair cells and supporting cells in the mammalian inner ear. *Proc. Natl. Acad. Sci. U.S.A.* **107**, 15798-15803 (2010).
25. A. F. Siekmann, L. Covassin, N. D. Lawson, Modulation of VEGF signalling output by the Notch pathway. *BioEssays* **30**, 303-313 (2008).
26. H. Zhang *et al.*, UBTOR/KIAA1024 regulates neurite outgrowth and neoplasia through mTOR signaling. *PLoS Genet.* **14**, e1007583 (2018).
27. D. Vaudry, P. J. Stork, P. Lazarovici, L. E. Eiden, Signaling pathways for PC12 cell differentiation: Making the right connections. *Science* **296**, 1648-1649 (2002).
28. A. J. Carlton *et al.*, Loss of Baiap212 destabilizes the transducing stereocilia of cochlear hair cells and leads to deafness. *J. Physiol.* **599**, 1173-1198 (2021).
29. L. A. Dunbar *et al.*, Clarin-2 is essential for hearing by maintaining stereocilia integrity and function. *EMBO Mol. Med.* **11**, e10288 (2019).
30. E. R. Andersson, R. Sandberg, U. Lendahl, Notch signaling: Simplicity in design, versatility in function. *Development* **138**, 3593-3612 (2011).
31. C. R. Chillakuri *et al.*, Structural analysis uncovers lipid-binding properties of Notch ligands. *Cell Rep.* **5**, 861-867 (2013).
32. F. M. Lu, S. E. Lux, Constitutively active human Notch1 binds to the transcription factor CBF1 and stimulates transcription through a promoter containing a CBF1-responsive element. *Proc. Natl. Acad. Sci. U.S.A.* **93**, 5663-5667 (1996).
33. A. M. Henderson, S. J. Wang, A. C. Taylor, M. Aitkenhead, C. C. Hughes, The basic helix-loop-helix transcription factor HESR1 regulates endothelial cell tube formation. *J. Biol. Chem.* **276**, 6169-6176 (2001).
34. F. Itoh *et al.*, Synergy and antagonism between Notch and BMP receptor signaling pathways in endothelial cells. *EMBO J.* **23**, 541-551 (2004).
35. K. G. Leong *et al.*, Activated Notch4 inhibits angiogenesis: Role of beta 1-integrin activation. *Mol. Cell Biol.* **22**, 2830-2841 (2002).
36. Z. Liu *et al.*, Notch1 loss of heterozygosity causes vascular tumors and lethal hemorrhage in mice. *J. Clin. Invest.* **121**, 800-808 (2011).
37. M. Nosedá *et al.*, Notch activation induces endothelial cell cycle arrest and participates in contact inhibition: Role of p21Cip1 repression. *Mol. Cell Biol.* **24**, 8813-8822 (2004).
38. K. L. Taylor, A. M. Henderson, C. C. Hughes, Notch activation during endothelial cell network formation in vitro targets the basic HLH transcription factor HESR-1 and downregulates VEGFR-2/KDR expression. *Microvasc. Res.* **64**, 372-383 (2002).
39. S. E. Williams, S. Beronja, H. A. Pasolli, E. Fuchs, Asymmetric cell divisions promote Notch-dependent epidermal differentiation. *Nature* **470**, 353-358 (2011).
40. E. C. Driver, M. W. Kelley, Development of the cochlea. *Development* **147**, dev162263 (2020).
41. R. Brown, A. K. Groves, Hear, hear for notch: Control of cell fates in the inner ear by notch signaling. *Biomolecules* **10**, 370 (2020).
42. R. J. Ruben, Development of the inner ear of the mouse: A radioautographic study of terminal mitoses. *Acta Otolaryngol.* **220** (Suppl), 1-44 (1967).
43. G. Bademci *et al.*, FOXF2 is required for cochlear development in humans and mice. *Hum. Mol. Genet.* **28**, 1286-1297 (2019).
44. C. Li *et al.*, Dysfunction of GRAP, encoding the GRB2-related adaptor protein, is linked to sensorineural hearing loss. *Proc. Natl. Acad. Sci. U.S.A.* **116**, 1347-1352 (2019).
45. M. A. DePristo *et al.*, A framework for variation discovery and genotyping using next-generation DNA sequencing data. *Nat. Genet.* **43**, 491-498 (2011).
46. H. Li, R. Durbin, Fast and accurate long-read alignment with Burrows-Wheeler transform. *Bioinformatics* **26**, 589-595 (2010).
47. A. McKenna *et al.*, The Genome Analysis Toolkit: A MapReduce framework for analyzing next-generation DNA sequencing data. *Genome Res.* **20**, 1297-1303 (2010).
48. A. Abyzov, A. E. Urban, M. Snyder, M. Gerstein, CNVnator: An approach to discover, genotype, and characterize typical and atypical CNVs from family and population genome sequencing. *Genome Res.* **21**, 974-984 (2011).
49. M. Jelani *et al.*, A mutation in the major autophagy gene, WIPI2, associated with global developmental abnormalities. *Brain* **142**, 1242-1254 (2019).
50. W. C. Skarnes *et al.*, A conditional knockout resource for the genome-wide study of mouse gene function. *Nature* **474**, 337-342 (2011).
51. J. K. White *et al.*; Sanger Institute Mouse Genetics Project, Genome-wide generation and systematic phenotyping of knockout mice reveals new roles for many genes. *Cell* **154**, 452-464 (2013).
52. E. Ryder *et al.*; Sanger Mouse Genetics Project, Rapid conversion of EUCOMM/KOMP CSD alleles in mouse embryos using a cell-permeable Cre recombinase. *Transgenic Res.* **23**, 177-185 (2014).



Mutations in *MINAR2* encoding membrane integral NOTCH2-associated receptor 2 cause deafness in humans and mice

Guney Bademci^a, María Lachgar-Ruiz^{b,c,d}, Mangesh Deokar^{e,f}, Mohammad Faraz Zafeer^g, Clemer Abad^h, Muzeyyen Yildirim Baylan^h, Neil J. Ingham^b, Jing Chen^b, Claire J. Sineni^g, Nirmal Vadgamaⁱ, Ioannis Karakikesⁱ, Shengru Guo^g, Duygu Dumanⁱ, Nitu Singh^f, Gaurav Harlalka^e, Shirish P. Jain^e, Barry A. Chioza^k, Katherina Walz^{a,g}, Karen P. Steel^b, Jamal Nasir^l, and Mustafa Tekin^{a,g,m,1}

Edited by Mary-Claire King, University of Washington, Seattle, WA; received March 8, 2022; accepted May 11, 2022

Discovery of deafness genes and elucidating their functions have substantially contributed to our understanding of hearing physiology and its pathologies. Here we report on DNA variants in *MINAR2*, encoding membrane integral NOTCH2-associated receptor 2, in four families underlying autosomal recessive nonsyndromic deafness. Neurologic evaluation of affected individuals at ages ranging from 4 to 80 y old does not show additional abnormalities. *MINAR2* is a recently annotated gene with limited functional understanding. We detected three *MINAR2* variants, c.144G > A (p.Trp48*), c.412_419delCGGTTTGG (p.Arg138Valfs*10), and c.393G > T, in 13 individuals with congenital- or prelingual-onset severe-to-profound sensorineural hearing loss (HL). The c.393G > T variant is shown to disrupt a splice donor site. We show that *Minar2* is expressed in the mouse inner ear, with the protein localizing mainly in the hair cells, spiral ganglia, the spiral limbus, and the stria vascularis. Mice with loss of function of the *Minar2* protein (*Minar2^{tm1b/tm1b}*) present with rapidly progressive sensorineural HL associated with a reduction in outer hair cell stereocilia in the shortest row and degeneration of hair cells at a later age. We conclude that *MINAR2* is essential for hearing in humans and mice and its disruption leads to sensorineural HL. Progressive HL observed in mice and in some affected individuals and as well as relative preservation of hair cells provides an opportunity to interfere with HL using genetic therapies.

autosomal recessive | deafness | hearing loss | *MINAR2* | NOTCH2

Hearing loss (HL) is one of the most common sensory deficits, affecting ~1 in 500 newborns (1). Genetic factors are implicated in the majority of cases, with more than 80% of the inherited form exhibiting autosomal recessive transmission (2). No additional findings are present in over 70% of the cases, which are then classified as nonsyndromic HL (Hereditary Hearing Loss Homepage, <https://hereditaryhearingloss.org/>) (2, 3). Genetic testing for etiologic evaluation has become a standard of care in people with congenital or childhood-onset sensorineural HL, which is caused by pathologies of the inner ear and auditory nerve (4, 5). Recent studies have shown that screening all recognized HL genes for variants reveals underlying cause in about half of the affected individuals, leaving a significant portion of people with HL with an unknown etiology (6–9). In the era of emerging genetic therapies for HL, finding the etiology of HL in affected individuals has become a critical task. This is especially relevant for progressive HL, as genetic therapies may potentially stop progression while cochlear hair cells are still alive (10–12).

MINAR2 (previously known as uncharacterized protein KIAA1024L and mouse gene *A730017C20Rik*) has recently been identified, and based on its structural similarity to *MINAR1*, named as major intrinsically disordered NOTCH2-associated receptor 2 or membrane integral NOTCH2-associated receptor 2 (13). A mutant mouse model of *Minar2* showed motor deficits similar to those seen in Parkinson disease, with no information about hearing abnormalities (13). A *Minar2* mutant mouse line, *Minar2^{tm1b}*, has also recently been reported to show no auditory brainstem responses at 14 wk old as part of a large HL screen (Mouse Genome Informatics [MGI]: 2442934) (11). Functional aspects of *MINAR2* and consequences of its dysfunction in humans remain unknown.

In this study, to better map the landscape of hereditary HL, we sought DNA variants underlying deafness in 13 affected individuals from four families. We identified three different *MINAR2* variants in the families cosegregating with HL. We further showed that homozygous *Minar2^{tm1b}* mutant mice develop rapidly progressive HL associated with changes in outer hair cell stereocilia. Finally, via in vitro studies we demonstrated that *MINAR2* suppresses NOTCH2, suggesting that notch signaling might play a role in pathogenesis.

Significance

Molecular components of hearing in mammals are not completely delineated. Via a genetic approach conducted in families with sensorineural hearing loss, this study presents *MINAR2* as an indispensable element of hearing in humans. Similarly, disruption of *Minar2* in mice leads to progressive hearing loss associated with alterations in the stereocilia of hair cells, the receptors of hearing, while hair cells remain intact until later in life. We present *MINAR2* as a gene working in the inner ear that is essential for hearing in humans and mice. Degeneration of sensory epithelium is a common consequence of hereditary deafness precluding genetic therapies. The preservation of hair cells in mutant mice at young ages makes *MINAR2* a good candidate for intervention.

The authors declare no competing interest.

This article is a PNAS Direct Submission.

Copyright © 2022 the Author(s). Published by PNAS. This open access article is distributed under Creative Commons Attribution-NonCommercial-NoDerivatives License 4.0 (CC BY-NC-ND).

¹To whom correspondence may be addressed. Email: mtekin@miami.edu.

This article contains supporting information online at <http://www.pnas.org/lookup/suppl/doi:10.1073/pnas.2204084119/-/DCSupplemental>.

Published June 21, 2022.

Results

Nonsyndromic Sensorineural HL Is Diagnosed in 13 Individuals from Four Unrelated Families. A summary of the auditory phenotype is shown in *SI Appendix, Table S1*. Ages ranged from 4 to 80 y old at the last examination. Each affected individual was diagnosed with HL either at birth or during infancy. Families 1 and 2 were of Turkish ancestry (Fig. 1). Parents of family 1 stated that in individuals II:1 and II:2, HL was milder in younger ages and progressed to a severe or profound degree by around age 10. Otoacoustic emissions were absent in these individuals. These siblings received unilateral cochlear implants at ages 12 and 10, respectively, which improved their oral communication. Individual II:3 in family 1 was diagnosed with profound sensorineural HL after failing the newborn hearing screening test. Otoacoustic emissions were absent at diagnosis. He received a unilateral cochlear implant at age 1 and communicates orally. Pure tone audiograms in parents showed normal thresholds (*SI Appendix, Fig. S1*).

Families 3 and 4 were of Indian ancestry. While there is no known consanguinity in any of the marriages in these two pedigrees, they are all from the same small town belonging to the same ethnic background, i.e., Hindu (religion) and Mali (Caste). All affected individuals in family 3 were born deaf and used signs, simple words, or sounds to be able to communicate. Severity of HL appeared to have remained the same in all the affected individuals from the beginning of life. Individuals IV:1 and IV:2 in family 4 were diagnosed with severe to profound sensorineural HL at the age of 3 y via auditory brainstem response (ABR) studies. Parents indicated a progression in the severity of HL. Their mode of communication at that age was predominantly nonverbal.

A high-resolution temporal bone CT scan or MRI was normal in at least one affected member of each family (*SI Appendix, Fig. S1*). None of the affected individuals had additional clinical findings for a syndromic form of deafness. Their neurodevelopmental skills were on target except for speech delay. None of the affected individuals showed impaired balance on tandem walking and Romberg test. Neurological examination was normal except for hearing loss in six affected individuals with ages ranging from 4 to 80 y. No affected individual was noted to have bradykinesia, tremor, or rigidity similar to those seen in Parkinson disease (*SI Appendix, Table S2*).

MINAR2 Variants Cosegregate with Autosomal Recessive Deafness. We performed genome sequencing in four affected individuals in families 1 (14) and 2 (15) and exome sequencing in three affected individuals in families 3 and 4 (Fig. 1A, individuals marked with an asterisk and *SI Appendix, Table S3*). Sequencing data in affected individuals were first analyzed for variants [single nucleotide variants (SNVs); insertions and/or deletions (indels); and copy number variants (CNVs) in recognized HL genes retrieved from the Hereditary Hearing Loss Homepage (<https://hereditaryhearingloss.org/>) (3), Online Mendelian Inheritance in Man (OMIM: <https://omim.org/>), University of Miami Molecular Genetics Laboratory HL gene panel, and a virtual gene panel for HL (v2.176) from PanelApp (<https://www.genomicsengland.co.uk>)]. Minor allele frequency (MAF) thresholds of 0.005 for recessive and 0.001 for dominant variants were used. Population allele frequencies were obtained from the genome aggregation database (gnomAD: <https://gnomad.broadinstitute.org/>) (16) and the single nucleotide polymorphism database (dbSNP: <https://www.ncbi.nlm.nih.gov/projects/SNP/>), as well as from our internal exome/

genome database that includes >7,000 samples from different ethnicities. American College of Medical Genetics (ACMG) and ClinGen HL expert panel guidelines were followed for variant interpretation (17, 18). This analysis did not reveal a plausible variant under any inheritance model.

After excluding variants in previously recognized deafness genes, in family 1 we filtered shared homozygous coding and splice variants (SNVs, indels, and CNVs) in three affected siblings with a MAF of <0.005 in dbSNP, gnomAD highest subethnicity, and our internal control database. This filter reveals only a *MINAR2* (GeneBank: NM_001257308.2) c.412_419delCGGTTTTG (p.Arg138Valfs*10) variant in the family. The variant is located within a 9.4-MB shared homozygous run in three siblings, which is the only homozygous region >1 MB (*SI Appendix, Tables S4 and S5*). This frame-shift variant is predicted to introduce a premature stop codon and lead to early truncation of *MINAR2*.

In the proband of family 2, *MINAR2* is located within the second longest homozygous run at chromosome 5 (chr5):128,253,080 to 141,730,596 (hg19) (*SI Appendix, Table S6*). She is homozygous for the c.144G > A (p.Trp48*) variant in *MINAR2*. This nonsense variant is predicted to cause an early stop codon and result in truncation of *MINAR2*.

In the exome data of two affected individuals from family 3, filtering variants via the same criteria used in family 1 reveals only one variant for which both individuals are homozygous: *MINAR2* c.393G > T (p.Lys131Asn). SNP arrays show that this variant is located within the only shared homozygous run, >1 MB, in all seven affected individuals in family 3. This homozygous run is flanked by markers rs13174854 and rs37767449, which is 2.96 MB on chr5:128,738,407 to 131,705,915 (hg19). In family 4, two affected siblings share a 5.76-MB homozygous run on chr5:126,978,108 to 132,742,450 (hg19), flanked by markers rs11241936 and rs11242152. Exome sequencing showed that the proband in family 4 is homozygous for the same *MINAR2* variant detected in family 3.

None of the detected *MINAR2* variants is listed in dbSNP or gnomAD databases and all variants are predicted to be deleterious (*SI Appendix, Table S7*). Sanger sequencing confirmed all three *MINAR2* variants and showed that each variant cosegregates with autosomal recessive HL in all families (Fig. 1A).

MINAR2 c.393G > T (p.Lys131Asn) Leads to Aberrant Splicing. While it is a missense change, the c.393G > T (p.Lys131Asn) variant substitutes the last nucleotide of exon 2, and is predicted to abolish a splice donor site (*SI Appendix, Table S7 and Fig. S2*). Via exon trapping experiments, we show that this variant leads to an addition of 85 intronic nucleotides into exon 2, which alters the amino acid composition of the rest of the protein leading to a premature stop codon (Fig. 1D and *SI Appendix, Fig. S2*). The same variant also leads to skipping of exon 2 entirely (Fig. 1D).

Minar2^{tm1b} Homozygous Mutant Mice Show Sensorineural HL. To prove causality of disruption of *Minar2* in sensorineural HL, we evaluated hearing in *Minar2* mutant mice. Hearing sensitivity of *Minar2^{tm1b}* mutant mice (*SI Appendix, Fig. S3*) was assessed using two methods: ABR, a measure of neural activity in the auditory nerve and brainstem, and distortion product otoacoustic emission (DPOAE), a measure of outer hair cell electromotility and resulting nonlinearities in the cochlea. Thresholds for both ABRs and DPOAEs were raised in homozygous mutants compared with wild-type littermates from the earliest age studied, postnatal day (P) 14, only 2160 after the usual onset of hearing (Fig. 2). By 4 wk old, the

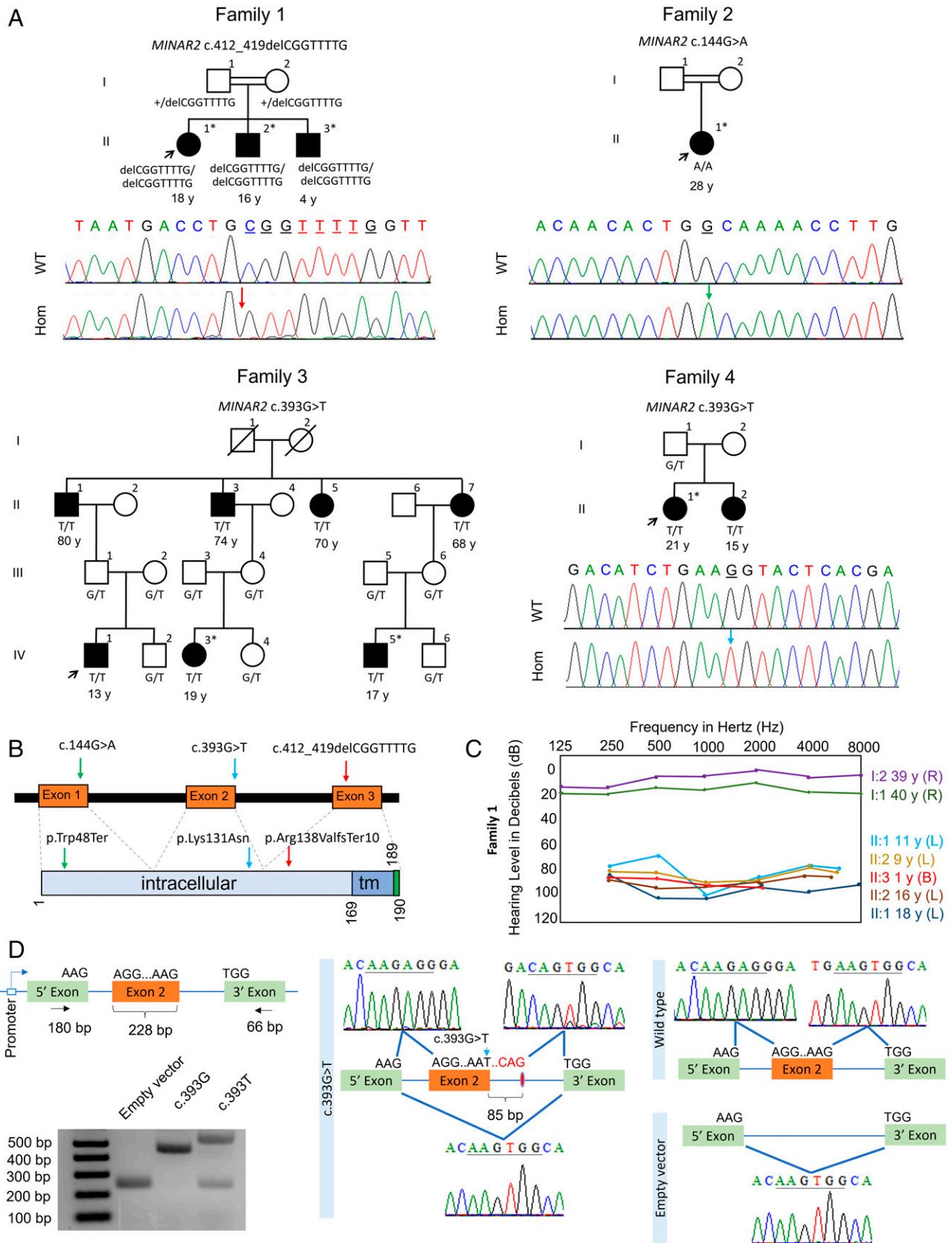


Fig. 1. Families, *MINAR2* variants, and the effects of the c.393G > T variant on splicing. (A) Pedigrees and segregation of the *MINAR2* variants in families. Filled symbols denote affected individuals and double lines indicate first cousin consanguinity. Electropherograms show the identified variant. The wild-type traces are from an unrelated individual. WT, wild type; Hom, homozygous mutant; exome/genome sequencing was performed in individuals marked with an (*) asterisk. (B) Locations of the identified variants. Tm, transmembrane. (C) Audiogram of family 1 (R, right ear; L, left ear; B, bilateral). (D) *MINAR2* exon 2 inserted into a vector consisting of 5' and 3' exons in the exon trap assay is shown. There are larger and smaller PCR products in the c.393G > T sample compared to wild type. Sanger sequencing confirms insertion of 85 bp at the donor site of exon 2 and skipping of exon 2. **161**

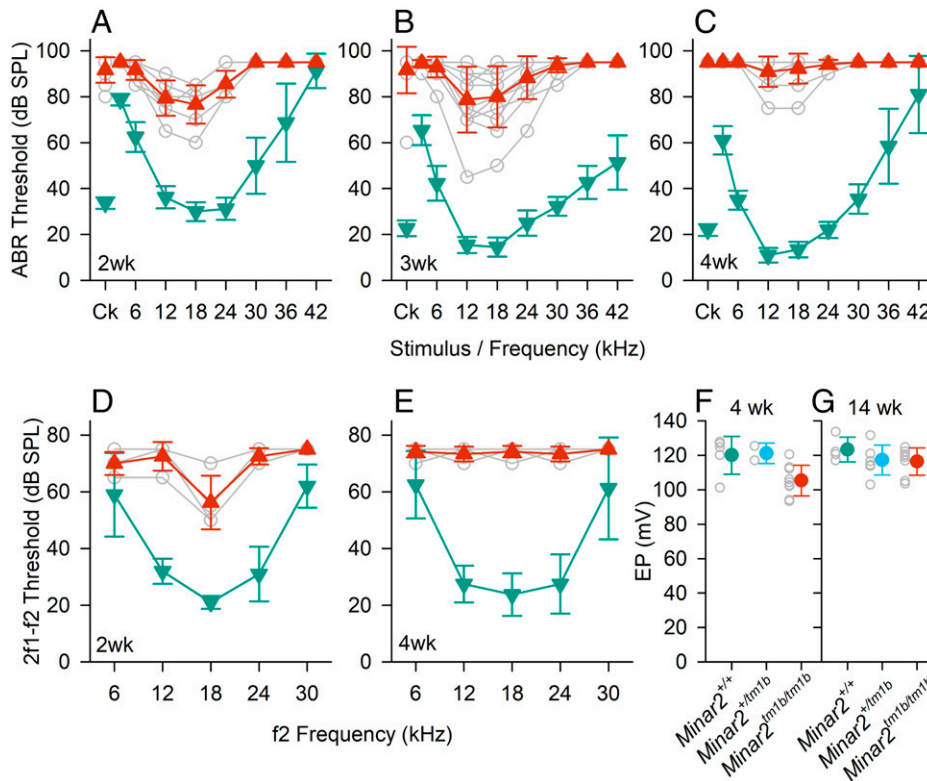


Fig. 2. Auditory studies in *Minar2* mutant mice. (A–C) ABR thresholds. Mean (\pm SD) ABR thresholds are plotted against stimulus for *Minar2*^{+/+} mice (teal, down triangles) and *Minar2*^{tm1b/tm1b} mice (red, up triangles). Open gray circles indicate thresholds for individual *Minar2*^{tm1b/tm1b} mice. Results are plotted for data obtained at P14 (A) ($n = 4$ *Minar2*^{+/+}, 9 *Minar2*^{tm1b/tm1b}); P21. (B) ($n = 11$ *Minar2*^{+/+}, 12 *Minar2*^{tm1b/tm1b}) and P27 to P28 (C) ($n = 10$ *Minar2*^{+/+}, 11 *Minar2*^{tm1b/tm1b}). Ck, click. (D and E) DPOAE thresholds. Mean (\pm SD) DPOAE thresholds are plotted against f2 stimulus frequency for *Minar2* control mice (teal, down triangles) and *Minar2*^{tm1b/tm1b} mice (red, up triangles). Open gray circles indicate thresholds for individual *Minar2*^{tm1b/tm1b} mice. Results are plotted for data obtained at P14 (D) ($n = 4$ controls, comprising 1 wild type and 3 heterozygotes, $n = 4$ mutants) and P27 to P28 (E) ($n = 4$ wild types, $n = 6$ mutants). (F and G) EP in *Minar2* mutant mice aged 4 wk (F) and 14 wk old (G). Colored circles indicate the mean (\pm SD) EP measurement in *Minar2*^{+/+} (teal), *Minar2*^{+/tm1b} (cyan), and *Minar2*^{tm1b/tm1b} (red) mice. Open gray circles indicate the EP values recorded in individual mice. At 4 wk old (P30 to P32) *Minar2*^{+/+} $n = 5$, range 101.2 to 127.8 mV; *Minar2*^{+/tm1b} $n = 2$ range 117.0 to 125.4 mV; and *Minar2*^{tm1b/tm1b} $n = 9$, range 93.4 to 120.5 mV. At 14 wk old *Minar2*^{+/+} $n = 4$, range 117 to 133.6 mV; *Minar2*^{+/tm1b} $n = 7$, range 113.8 to 131.6 mV; and *Minar2*^{tm1b/tm1b} $n = 8$, range 103.5 to 124.7 mV.

mutant mice showed severe elevations in threshold or no response at the highest sound levels used. Endocochlear potential was only slightly reduced from a mean of 120 mV to 105 mV in *Minar2*^{tm1b/tm1b} mice, with most mutant mice exhibiting an endocochlear potential (EP) in the normal physiological range for mice of over 100 mV (Fig. 2).

Minar2 Is Expressed in the Mouse Cochlea. To further understand the role of *Minar2* in hearing, we assessed the presence of *Minar2* transcript in different mouse tissues, including the inner ear, and specifically the cochlea. Total RNA was isolated from wild-type mice at embryonic day (E) 18.5, P0, and P30. RT-PCR with a forward primer located in exon 2 and a reverse primer in exon 3 of the *Minar2* gene (GenBank: NM_173759) produced a unique band of 171 bp corresponding to the wild-type mRNA in all analyzed tissues, with the exception of the liver. We find that *Minar2* is highly expressed in the inner ear, and specifically in the cochlea, at E18.5, P0, and P30 (Fig. 3A). To determine specific locations of *Minar2* expression within the cochlea, we proceeded to study *Minar2*^{tm1b} heterozygous mutant mice taking advantage of the reporter gene. β -Galactosidase staining of P1 cross-sections and whole mount organ of Corti preparations reveals that *Minar2* is mainly localized in the hair cells, the supporting cells, spiral ganglion (including the nerve fibers), the spiral limbus, and the stria vascularis (Fig. 3B and SI Appendix, Fig. S4 A and B). Of note, the gene expression analysis resource (gEAR; <https://umgear.org/>) portal shows *Minar2* expression both in hair cells and supporting cells

(SI Appendix, Fig. S4C) (19, 20). Double labeling for *Minar2* and Tuj1 in heterozygous mutant mice shows that the two are expressed in different cell types and *Minar2* is not present in the neurons of the spiral ganglion that were marked with Tuj1, suggesting that *Minar2* is located in spiral ganglion glial cells (Fig. 3 C, E, and F).

The Earliest Defect in *Minar2*^{tm1b} Mutant Mice Appears in Stereocilia Bundles. We used scanning electron microscopy (SEM) (Fig. 4) to examine the cochlea of mice aged 14 d old because at this age the ABR thresholds were raised but synapses appeared normal in numbers (Fig. 5). The organization of the organ of Corti appeared normal and there were very few missing stereocilia bundles in mutants, suggesting that hair cell degeneration cannot explain the raised ABR thresholds at this age (SI Appendix, Fig. S5). However, when we examined the stereocilia bundles of outer hair cells, we saw the shortest row was depleted, with reduced numbers and abnormally short stereocilia (Fig. 4). Outer hair cells along the entire length of the cochlear duct showed this feature. Inner hair cells appeared close to normal, although the middle row of stereocilia occasionally appeared more irregular than in the control littermates. Heterozygotes looked the same as wild-type littermates at this age.

Mechanoelectrical Transduction Channels Are Functional in *Minar2*^{tm1b/tm1b} Mice. To study the mechanoelectrical transduction (MET), we used the FM1-43 FX dye, a molecule commonly used to assay the MET channel function, since functional MET

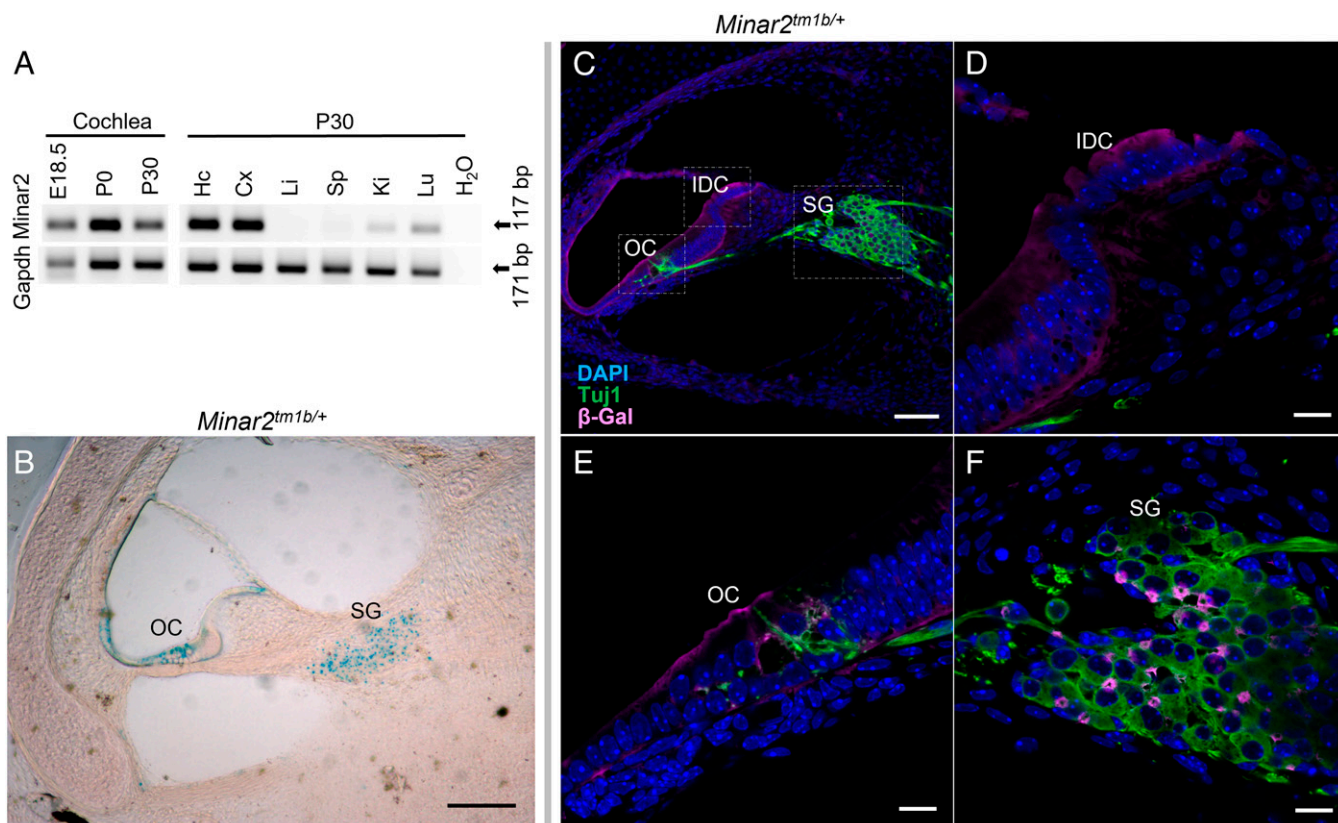


Fig. 3. Expression of *Minar2*, localization of the protein in the cochlea and innervation of cochlear hair cells in *Minar2* heterozygous mice, using the *LacZ* reporter gene component of the inserted cassette in the mutant allele, which expresses β -galactosidase (SI Appendix, Fig. S3). (A) RT-PCR of *Minar2* expression in the cochlea at E18.5, P0, and P30. Also, expression in different mouse tissues at P30 are Hc, hippocampus; Cx, cortex; Li, liver; Sp, spleen; Ki, kidney; Lu, lung. *Gapdh* was used as a control. (B) Localization of *Minar2* using the reporter gene *LacZ* of the mutant allele and in β -gal staining shown in blue. Note the localization of *Minar2* at the SG, spiral ganglion; OC, organ of Corti. (Scale bar: 70 μ m.) (C) Cross-section from 24-kHz region of P1 mutant inner ear was labeled with anti- β -gal (magenta) to detect *Minar2* localization and Tuj1 (green) to label neurons. (Scale bar: 70 μ m in C.) A zoom in is shown in D–F. (Scale bars: 10 μ m.) IDC, interdental cells.

channels are required for the uptake of this fluorescent dye into the hair cells (21). We perfused cochleae from P14 mice and observed FM1-43 FX dye uptake by both inner and outer hair

cells in *Minar2*^{+/+} and *Minar2*^{tm1b/tm1b} mice. Heterozygotes looked the same as wild-type littermates. While the intensity of the staining varied from mouse to mouse, all the samples showed

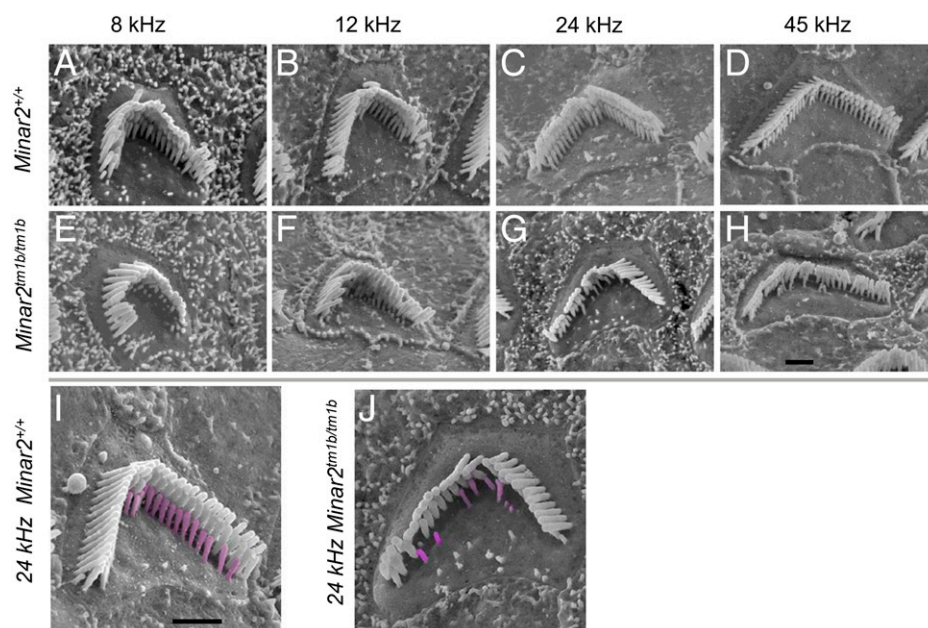


Fig. 4. Scanning electron microscopy reveals stereocilia defects. Outer hair cells at 8 kHz (85% of distance from base), 12 kHz (70%), 24 kHz (40%), and 45 kHz (20%) best frequency locations in wild-type mice (A–D) and *Minar2*^{tm1b} homozygotes (E–H). Higher magnification images with the shortest row colored in magenta in a wild-type (I) and a mutant (J) outer hair cell, showing the reduction in numbers. (Scale bars in H and I: 1 μ m.)

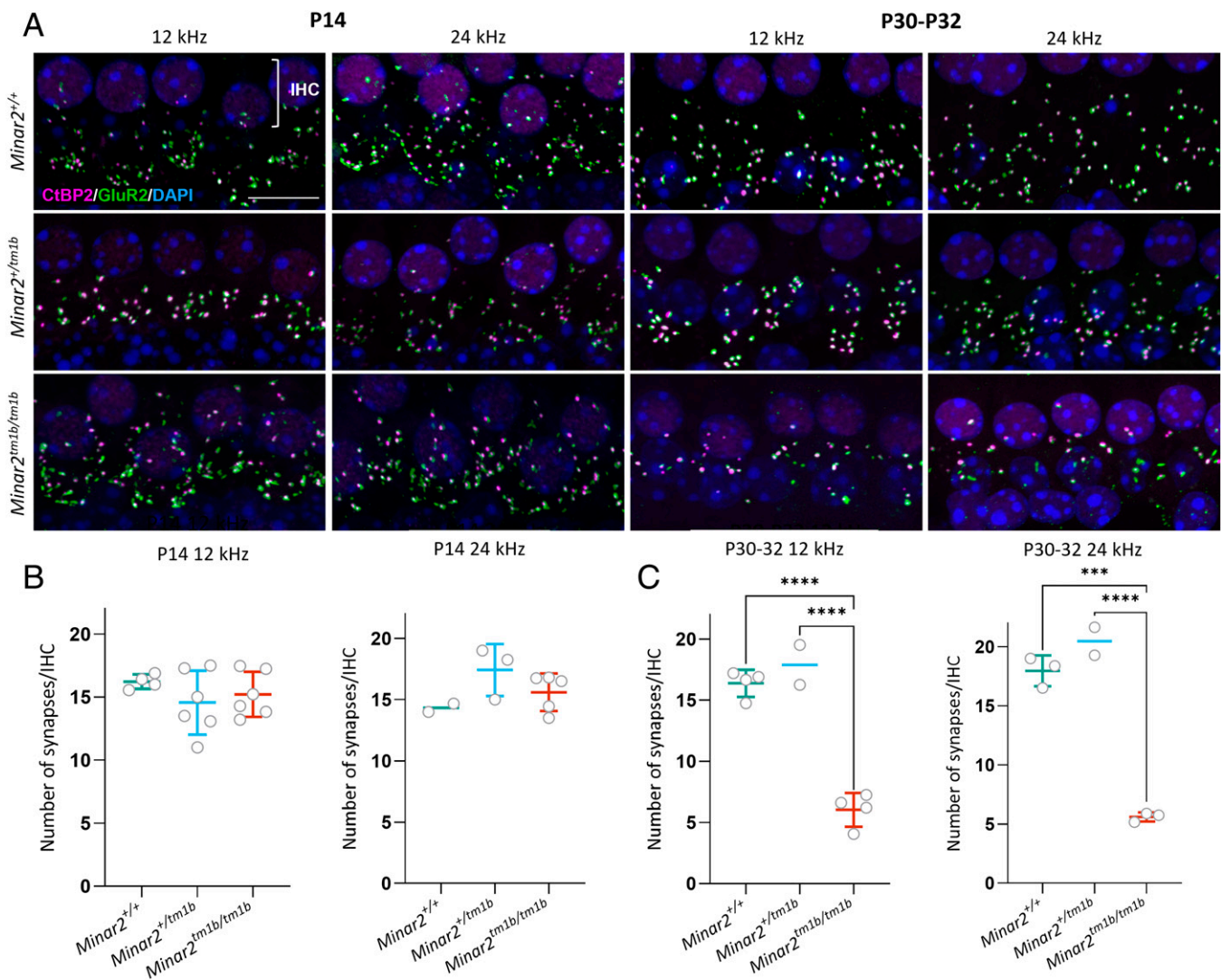


Fig. 5. Synaptic abnormalities of cochlear hair cells in *Minar2* mutant mice. (A) Synapses were examined using anti-CtBP2 antibody to mark presynaptic ribbons (magenta) and anti-GluR2 antibody to mark postsynaptic densities (green). Nuclei are shown in blue (DAPI). (Scale bar: 5 μ m.) The images correspond to the cochlear best-frequency regions of 12 kHz and 24 kHz. The row of nuclei at the *Top* of each image corresponds to the IHCs. (B and C) Quantification of ribbon synapses per IHC at P14 (B) and P30 to P32 (C). Colocalized pre- and postsynaptic components were defined as a synapse. The average for each mouse is plotted as a circle. All data are shown as mean \pm SD and statistically analyzed by one-way ANOVA with multiple comparisons. At P14, no significant difference was seen between homozygotes ($n = 6$ at 12 kHz and $n = 5$ at 24 kHz) and heterozygotes ($n = 6$ at 12 kHz and $n = 3$ at 24 kHz) or wild types ($n = 4$ at 12 kHz and $n = 2$ at 24 kHz). At P30 to P32, there are significantly fewer colocalized synapses in *Minar2*^{tm1b/tm1b} ($n = 4$ for 12 kHz and $n = 3$ for 24 kHz) compared to wild types ($n = 4$ at 12 kHz and $n = 3$ at 24 kHz) and compared to heterozygotes ($n = 2$). **** $P = 0.0001$ and **** $P < 0.0001$.

uptake of the molecule specifically in hair cells, indicating that the MET channels are active in the *Minar2* mutants (SI Appendix, Fig. S6).

Hair Cell Degeneration Is a Secondary Feature in *Minar2*^{tm1b} Mutant Mice. Hair cell degeneration is a common feature in HL, and extensive loss of hair cells may preclude some approaches to treatments. Therefore, we examined older *Minar2*^{tm1b} mutant mice, aged 14 wk, to assess the loss of hair cells. We have previously reported that these mutants show no auditory brainstem responses at 14 wk old (11) and the EP is normal at this age (Fig. 2G). At earlier ages we see minimal evidence of any hair cell degeneration (SI Appendix, Fig. S5). However, by 14 wk of age, there is extensive loss of hair cells, with some discrete patches distributed along the length of the cochlear duct where the entire organ of Corti appears to have degenerated while other regions show scattered missing hair cells, both inner and outer, within the organ of Corti (Fig. 6). Heterozygotes had a similar appearance to the wild-type mice.

Minar2^{tm1b} Mutant Mice Show Reduction in the Number of Inner Hair Cell Ribbon Synapses at P30.

To understand underlying pathophysiology further, we evaluated the innervation pattern of hair cells by staining neurons with an anti-neurofilament antibody in the organ of Corti at P1 (SI Appendix, Fig. S7). Homozygous mutant mice show an altered innervation pattern of hair cells with a reduction in the nerve fibers around inner hair cells and a dispersed distribution of nerve fibers toward outer hair cells. *Minar2*^{tm1b} mutant mice show reduction in the number of crossings of type II nerves at P14 (Fig. 7). We subsequently examined synapses of inner hair cells using anti-CtBP2 antibody to label presynaptic ribbons and anti-GluR2 antibody to mark the AMPA receptor subunit R2, a part of the postsynaptic density. Ribbon synapses look qualitatively normal at both ages tested, P14 and P30, and the number of synapses per inner hair cell in homozygous mutants was not significantly different from numbers in heterozygotes or wild-type controls at P14, indicating that the raised AI64 thresholds observed at that age in mutants are not due to the

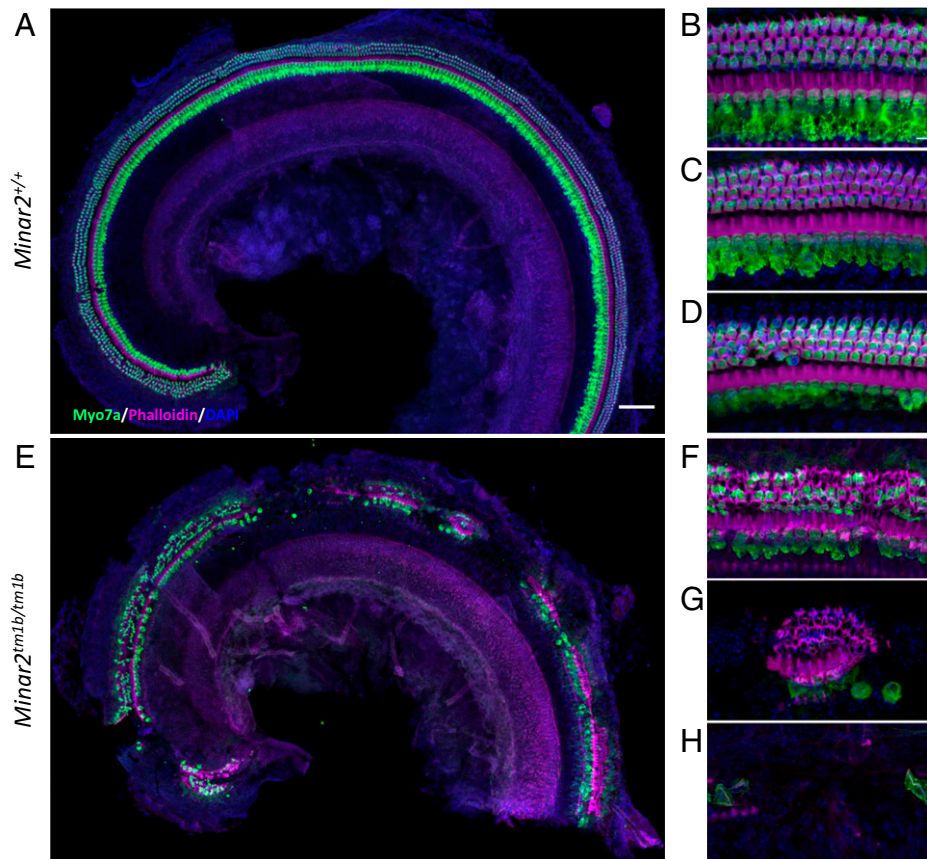


Fig. 6. Hair cell degeneration pattern in *Minar2^{tm1b}* mutant mice at 14 wk old. Confocal maximum intensity projection images of the whole-mount organ of Corti of 14-wk-old mice. Hair cells were examined using anti-Myo7a antibody (green) and phalloidin (magenta). Nuclei are shown in blue (DAPI). (Scale bars: 200 μ m in A and 10 μ m in B.) The images are representative examples of *Minar2^{+/+}* (A–D) and *Minar2^{tm1b/tm1b}* (E–H) mice. (A and E) Overview of the apical half of the cochlea. (B–D) High-magnification images corresponding to the 12 kHz, 24 kHz, and 36 kHz best-frequency regions, respectively. (F–H) High-magnification images of three different patterns of hair cell loss observed in *Minar2^{tm1b}* mutant mice. All five homozygotes that were studied at 14 wk old showed similar patches of loss of the organ of Corti at varying locations along the length of the cochlear duct interspersed with regions that showed only scattered hair cell loss. *Minar2^{+/+}* (n = 4), *Minar2^{+/tm1b}* (n = 5), and *Minar2^{tm1b/tm1b}* (n = 5).

loss of ribbon synapses (Fig. 5 A and B). However, by P30 to P32 *Minar2^{tm1b}* mutant mice did show a significant decrease in the number of synapses compared to wild-type mice (Fig. 5 A and C), and this may contribute to the progression of HL.

Overexpression of *MINAR2* Suppresses Angiogenesis and *MINAR2* Variants Abolish This Effect. As *MINAR1* has been shown to inhibit angiogenesis (22), we investigated whether *MINAR2* shows the same effect on angiogenesis in human umbilical vein endothelial cells (HUVEC). These studies reveal that transient overexpression of *MINAR2* suppresses angiogenesis (Fig. 8A). In addition, overexpressing each *MINAR2* variant detected in families 1 and 2 in HUVEC reduces suppression of angiogenesis, suggesting that they are loss-of-function variants (Fig. 8A).

Expression Levels of *MINAR2* Are Inversely Correlated with Intracellular *NOTCH2* Abundance. *MINAR2* is named based on its structural similarity to *MINAR1*, which is shown to be involved in *NOTCH2* signaling (22). While *MINAR2* is a much smaller protein compared to *MINAR1* (190 vs. 917 amino acids) (22), it has recently been shown to bind *NOTCH2* in a coimmunoprecipitation assay (13). Thus, we set out to explore whether *NOTCH2* abundance in cells is correlated with *MINAR2* expression (23, 24). Furthermore, as *NOTCH* and *VEGF* signaling pathways are known to interact during angiogenesis (25), we determined the effect of *MINAR2*

expression on *VEGF*. Our studies show that overexpression of wild-type *MINAR2* in HUVEC is associated with reduced abundance of *NOTCH2* and *VEGFA* (a prominent *VEGF* protein in vascular endothelial cells) (Fig. 8B). Silencing of *MINAR2* in PC12 cells, which endogenously express *MINAR2*, leads to an increase in *NOTCH2* and confirms the suppressor effect of *MINAR2* on *NOTCH2* abundance (Fig. 8C and *SI Appendix*, Fig. S8).

***MINAR2* Is Involved in MAP Kinase and mTOR Pathways.**

MINAR1 has been shown to regulate neurite outgrowth in a neuroendocrine cell line PC12 (26), in which neurite outgrowth via nerve growth factor is achieved by MAPK and PI3K pathways (27). The mTOR complex is a downstream target of PI3K, which contains mTORC1 and mTORC2 complexes in its central catalytic domain (26). We tested the effects of *MINAR2* on the MAPK pathway by transiently overexpressing wild-type *MINAR2* in PC12 cells and detecting levels of ERK1/2 and pERK1/2, a crucial kinase of the MAPK signaling pathway. These studies show that overexpression of wild-type *MINAR2* reduces the abundance of pERK1/2, the active form of ERK1/2. On the other hand, overexpression of the two *MINAR2* deafness variants in families 1 and 2 does not show this effect, again supporting their loss of function (*SI Appendix*, Fig. S9A). When we silenced *MINAR2* in PC12 cells, we observed an increase in a functional protein in mTORC1 activity, P-S6, at 12 h (*SI Appendix*, Fig. S9B). However, there was

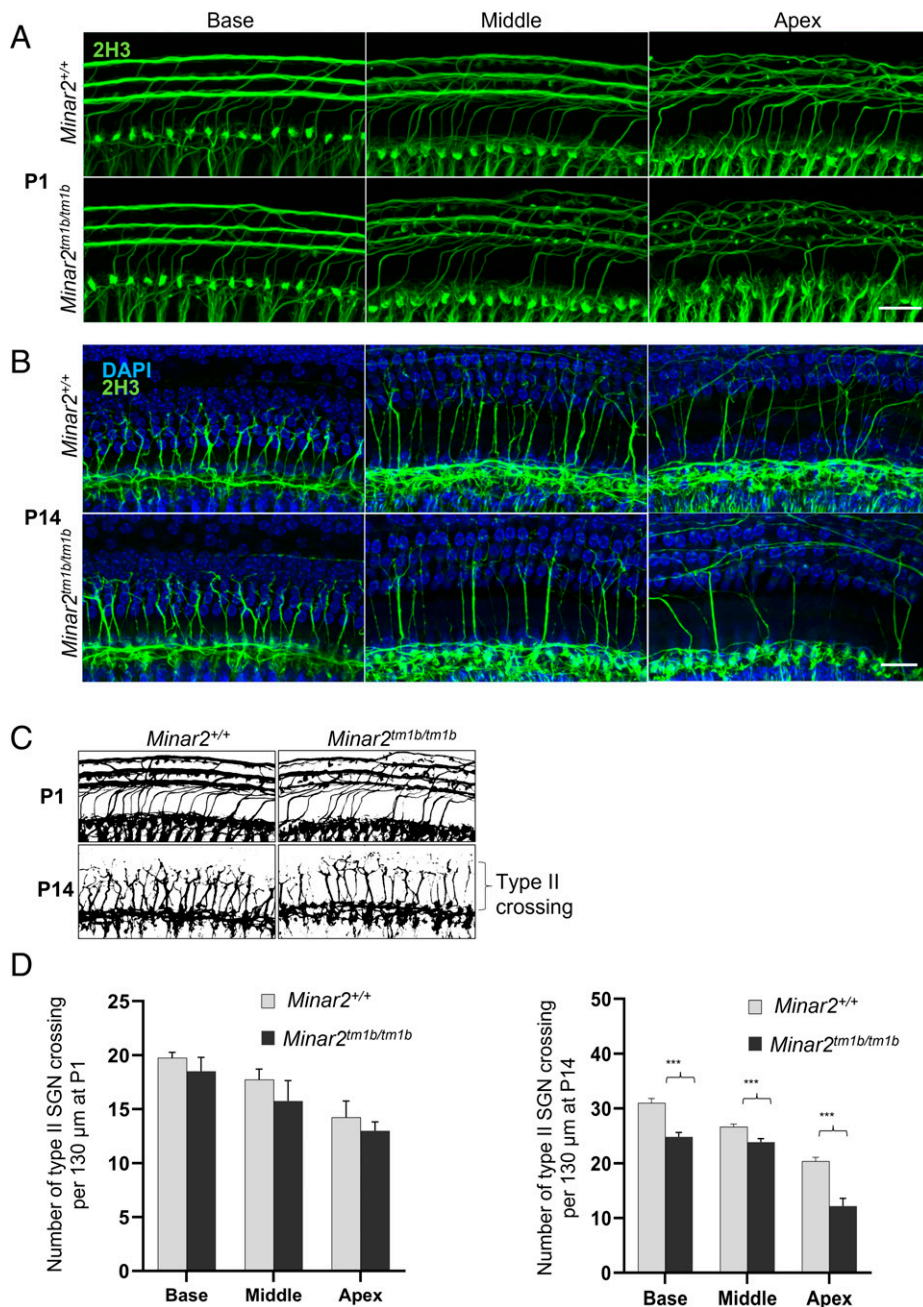


Fig. 7. Confocal maximum intensity projection images from a 24-kHz region of the whole-mount cochlea. (A and B) Total innervation with anti-2H3 neurofilament label (green) for P1 and P14 ($n = 3$ each group) wild-type and mutant mice. (Scale bars in A and B: 20 μm .) (C) Schematic diagram of whole-mount cochlea, demonstrating the innervation pattern of type II nerves at P1 and P14 wild-type and mutant mice. (D) The total number of crossings of type II nerves is shown as histogram ($n = 3$; $***P < 0.001$.)

no difference in pAKT, a component of mTORC2 activity (SI Appendix, Fig. S9B).

Discussion

In this study we present three loss-of-function variants in *MINAR2* in four families cosegregating with nonsyndromic sensorineural HL. Hearing loss started at birth or in early childhood in all 13 affected individuals. A progressive HL reaching a severe-to-profound degree during childhood was noted in four affected individuals. In addition to ABR thresholds showing sensorineural HL, otoacoustic emissions were absent in three children tested, suggesting dysfunction of both inner hair cell/acoustic nerve and outer hair cells. To support causality of the *MINAR2* mutations in deafness and to begin understanding

the mechanism of HL, we show that *Minar2^{tm1b/tm1b}* mice have a severe, progressive increase in ABR thresholds from 2 wk old onwards (around the time that mice start to hear), with very few responses by 4 wk old. Otoacoustic emissions can be detected in the mutant mice but at raised thresholds at 2 wk old, and these responses are mostly absent by 4 wk old, implicating outer hair cells in the pathology. In conclusion, audiological findings both in humans and mice show that loss of *MINAR2* function results in early-onset and sensorineural HL that rapidly progresses to severe to profound deafness.

The reduced number of stereocilia in the shortest row on outer hair cells would be expected to have a severe impact upon the number of transduction channel complexes available and suggests that the primary defect in these mutant mice is located at the top of the hair cell. However, we have demonstrated that

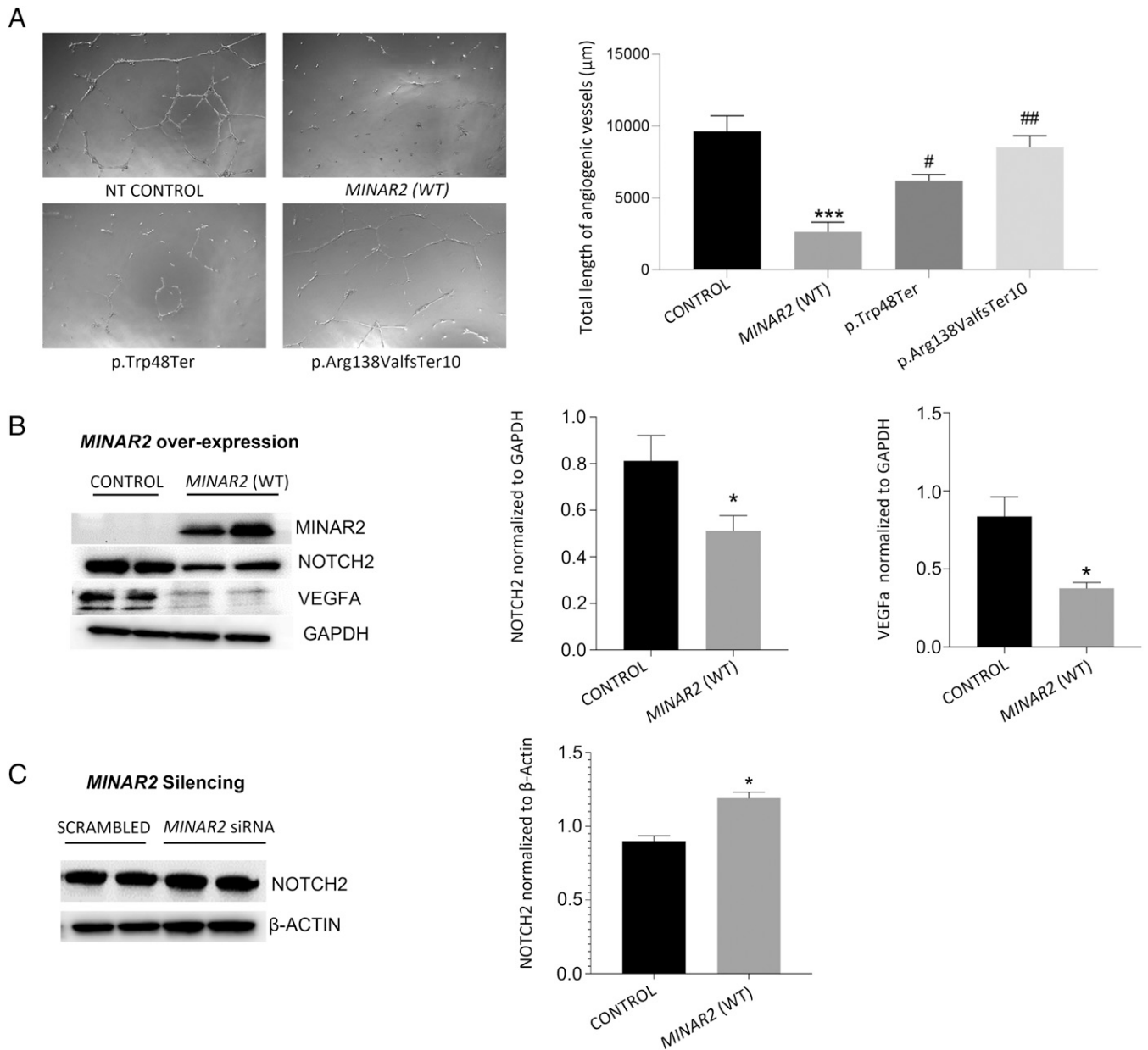


Fig. 8. Effects of *MINAR2* on angiogenesis, NOTCH2, and VEGFA. (A) Angiogenic potential of nontransfected (NT) HUVEC compared to cells transfected with *MINAR2* wild-type (WT), and *MINAR2* p.Trp48*, and p.Arg138Valfs*10 plasmid constructs. *Right* graph shows analysis of total length of angiogenic vessels formed after incubation of 12 h on Matrigel-coated wells; images were analyzed with ImageJ angioanalyzer and results are expressed as mean \pm SEM. Significant differences were shown as *** $P \leq 0.001$ when compared to control and as ## $P \leq 0.01$ when compared to *MINAR2*(WT). (B, Left) Immunoblot images showing the effect of *MINAR2*(WT) transient overexpression on NOTCH2 and VEGFA protein levels in HUVEC cells. (Right) Statistical analysis of GAPDH-normalized relative protein expressions of NOTCH2 and VEGFA. Results are expressed as mean \pm SEM and significant differences are shown as * $P \leq 0.05$ when compared to control. (C, Left) Immunoblot images of siRNA-induced *MINAR2* silencing on NOTCH2 protein levels in PC12 cells. (Right) β -Actin normalized relative protein expression of NOTCH2. Results are expressed as mean \pm SEM and significant differences are shown as * $P \leq 0.05$ when compared to control. Data were analyzed by one-way ANOVA with multiple comparisons.

the remaining MET channels are active in *Minar2^{tm1b/tm1b}* mice, since the hair cells of these mice are able to uptake FM1-43 dye. Degeneration of hair cells (Fig. 6) and synaptic defects (Fig. 5) occur later in development and cannot explain the raised ABR and DPOAE thresholds at 14 d old in the *Minar2^{tm1b}* homozygotes. Mutations of other genes also lead to loss of the shorter stereocilia associated with hearing impairment, for example the *Baiap2l2* mutant (28) and the *Clnr2* mouse mutant (29).

The Notch pathway is a highly conserved intercellular signaling cascade that is activated by the interaction of transmembrane ligands (Delta and Jagged) with Notch receptors, which are usually expressed on the surface of neighboring cells.

Binding of the Notch ligand to receptor induces cleavage of the Notch receptors intracellular domain, which binds to multiple DNA-binding proteins in the nucleus (30–32). In the initial stages of angiogenesis, Notch activation is generally repressed to allow proliferation of endothelial cells in response to VEGF stimulation, and its expression is later up-regulated when endothelial cells stop proliferating and the vessels begin to stabilize (33–39). While it is possible that the effects of *MINAR2* on angiogenesis may play a role in hearing, we did not observe abnormal vascular structures in the cochlea of homozygous mutant mice. Moreover, the most sensitive part of the cochlea to vascular function is the generation of EP by the stria vascularis. In this study, EP was within the normal range in

homozygous mutant mice. Our results show that MINAR2 and NOTCH2 have a regulatory relationship. In the mammalian cochlea, there is no regeneration of sensory hair cells and the strictly controlled pattern of alternating hair cells and supporting cells in the organ of Corti is set up in early development. Notch signaling is believed to be a critical part of the process of cells deciding their fate as a hair cell or a supporting cell and many genes involved in Notch signaling underlie hearing impairment (40, 41). As our examination of the organ of Corti of young mice shows (SI Appendix, Fig. S5), the pattern is set up correctly, ruling out an early developmental defect of cell fate or differentiation. However, Notch signaling may also play a role in longer-term maintenance of the organ of Corti, and our findings of progressive deterioration of this organ resulting from mutation of a gene known to be involved in Notch signaling supports this suggestion.

MINAR family proteins (MINAR1 and MINAR2) have been proposed to be associated with the inhibition of cell proliferation (13, 22). In this study, we did not observe any proliferation effect in different ages of *Minar2^{tm1b/tm1b}* mice. Terminal mitoses of hair cells occur early at E12 to E14 before birth (42). The confocal images illustrated in Fig. 6 all indicate loss of cells from the normal regular array, with no sign of any proliferation.

Our findings of an abnormal innervation pattern of hair cells as early as P1, as well as a significant decrease in the numbers of intact synapses at 4 wk old, suggest that abnormal innervation of hair cells may contribute to the severe auditory dysfunction in *Minar2^{tm1b/tm1b}* mice. Based on these findings, Minar2 may be playing a role in the maintenance of hair cell synapses. MINAR2 is structurally similar to MINAR1, which has been reported to be involved in controlling neurite formation during neuronal differentiation through DEP domain containing MTOR interacting protein (DEPTOR). In this study, we show that similar to MINAR1, MINAR2 down-regulates mTOR signaling (SI Appendix, Fig. S9B), which may contribute to the abnormal innervation pattern observed in the organ of Corti of *Minar2* mutant mice.

It is notable that although the sensory hair cells are present up to 4 wk old and are able to take up FM1-43 dye through transduction channels, they do not appear to be functioning normally as shown by the raised ABR and DPOAE thresholds. Most genetic and environmental causes of sensorineural HL lead to permanent loss of hair cells, reducing the chance of gene therapy or gene editing approaches. Progressive HL associated with a relatively normal appearance of hair cells in young ages makes *MINAR2* a promising target for genetic therapies. Further elucidation of its role in the maintenance of hair cell synapses and stereocilia bundles may open new avenues to treat more common forms of HL resulting from similar mechanisms.

Materials and Methods

More details of materials and methods are in SI Appendix.

Study Approval. This study was approved by the University of Miami Institutional Review Board (20081138-USA), as well as by the Ethics Committees of Ankara University Medical School (012413-Turkey) and Rajarshi Shahu College of Pharmacy (180720-India). A signed informed consent was obtained from all participants or, in the case of a minor, from the parents.

DNA Sequencing and Bioinformatics Analysis. Genome sequencing was performed in family 1 individuals II:1, II:2, and II:3 and family 2 II:1 (Fig. 1A and SI Appendix, Table S3) (43, 44). Reads were mapped to human genome reference (National Center for Biotechnology Information [NCBI] build37/hg 19 version) with Burrows-Wheeler aligner (BWA). Genome Analysis Toolkit (GATK) was

used for variant calling (45–47). CNVs were called using CNVnator (48). Enlis Genome Research software (<https://www.enlis.com/>) was used to identify runs of homozygosity in family 1 and family 2 from genome sequencing data (SI Appendix, Tables S4–S6).

Illumina Infinium Global Screening Array (GSA) v2 (Illumina) kit was used for genotyping in 16 members of family 3 and three members of family 4 to map the shared homozygous regions in affected individuals. Additional exome sequencing was performed on a HiSeq 2000 platform (Illumina), as described previously (49), in individuals IV:3 and IV:5 in family 3 and IV:1 in family 4 (SI Appendix, Table S3).

Genome sequencing data were deposited in the NCBI's BioProject database: PRJNA623118, BioSample: SAMN27763770 (family 1, individual II:1) and BioSample: SAMN27763769 (family 2, individual II:1).

Ethics Statement for Animals. Mouse studies in the United Kingdom were carried out in accordance with UK Home Office regulations and the UK Animals (Scientific Procedures) Act of 1986 (ASPA) under UK Home Office licenses, and the study was approved by the King's College London Ethical Review Committee. Mice were culled using methods approved under these licenses to minimize any possibility of suffering. All procedures in Miami were approved by the University of Miami Institutional Animal Care and Use Committee and followed the NIH guidelines "Using Animals in Intramural Research."

Mouse Generation. *Minar2^{tm1a}* mutant mice were generated at the Wellcome Sanger Institute by blastocyst microinjection of targeted embryonic stem (ES) cells on a C57BL/6N genetic background (50, 51). *Minar2^{tm1b(KOMP)Wtsi}* mice (*Minar2^{tm1b}*) were generated from *Minar2^{tm1a(KOMP)Wtsi}* mice by exposure of preimplantation embryos to soluble Cre recombinase (52), which leads to recombination between LoxP sites, removing the selection cassette and exon 2 to produce mice carrying the *Minar2^{tm1b}* allele (SI Appendix, Fig. S3). Both *tm1a* and *tm1b* alleles are available via the European Mouse Mutant Archive (EMMA; <https://www.infrafrontier.eu>).

Statistics. A one-way ANOVA with multiple comparisons was used to compare groups for count of synapses in mouse inner ear and also for angiogenesis, MAPK, and mTOR assays.

Data Availability. Sequencing data have been deposited in publicly accessible database, Family 1, II:1 (14) and Family 2, II:1 (15).

ACKNOWLEDGMENTS. We are immensely grateful to all the patients and families participating in this study. This study was supported by R01DC009645 and R01DC012836 from the NIH/National Institute on Deafness (M.T.), the National Institute for Health and Care Research Biomedical Research Centre, King's College London (K.P.S.), and the Royal National Institute for Deaf People (K.P.S.). This research was funded in part by the Wellcome Trust. For the purpose of Open Access, the author has applied a CC BY public copyright license to any Author Accepted Manuscript version arising from this submission. We thank the Wellcome Sanger Institute Mouse Genetics Project for generating and providing the *Minar2* mouse mutant. M.D. and G.H. would also like to express sincere gratitude for all the support provided by Dr. S. P. Jain, Principal, Rajarshi Shahu College of Pharmacy, Malvahir, Buldana, India.

Author affiliations: ^aDr. John T. Macdonald Foundation Department of Human Genetics, University of Miami Miller School of Medicine, Miami, FL, 33136; ^bWolfson Centre for Age-Related Diseases, King's College London, London, SE1 1UL, United Kingdom; ^cServicio de Genética, Hospital Universitario Ramón y Cajal, IRYCIS, 28034 Madrid, Spain; ^dCentro de Investigación Biomédica en Red de Enfermedades Raras, 28034 Madrid, Spain; ^eDepartment of Pharmacology, Rajarshi Shahu College of Pharmacy, 443001 Malvahir, Buldana, India; ^fOriental College of Pharmacy and Research, Oriental University, 453555 Indore, Madhya Pradesh, India; ^gJohn P. Hussmann Institute for Human Genomics, University of Miami Miller School of Medicine, Miami, FL 33136; ^hDepartment of Otorhinolaryngology, Faculty of Medicine, Dicle University, Diyarbakir 21200, Turkey; ⁱCardiovascular Institute and Department of Cardiothoracic Surgery, Stanford University School of Medicine, Stanford, CA, 94305; ^jDepartment of Audiology, Faculty of Health Sciences, Ankara University, Ankara 06100, Turkey; ^kCollege of Medicine and Health, University of Exeter Medical School, RD&E NHS Foundation Trust, Exeter, EX2 5DW, United Kingdom; ^lMolecular Biosciences Research Group, Faculty of Health and Society, University of Northampton, Northampton, NN1 5PH, United Kingdom; and ^mDepartment of Otolaryngology, University of Miami Miller School of Medicine, Miami, FL, 33136

Author contributions: M.T. designed research; G.B., M.L.-R., M.D., M.F.Z., C.A., M.Y.B., N.J.I., J.C., C.J.S., N.V., I.K., S.G., D.D., N.S., G.H., S.P.J., B.A.C., K.W., K.P.S., J.N., and M.T. performed research; G.B., M.L.-R., N.J.I., K.P.S., and M.T. contributed new reagents/

analytic tools; G.B., M.L.-R., M.D., M.F.Z., C.A., M.Y.B., N.J.I., J.C., C.J.S., N.V., I.K., S.G., D.D., N.S., G.H., S.P.J., B.A.C., K.W., K.P.S., J.N., and M.T. analyzed data; and G.B., M.L.-R., M.D., M.F.Z., C.A., N.J.I., N.V., G.H., K.W., K.P.S., J.N., and M.T. wrote the paper.

1. A. L. Mehl, V. Thomson, The Colorado newborn hearing screening project, 1992-1999: On the threshold of effective population-based universal newborn hearing screening. *Pediatrics* **109**, E7 (2002).
2. C. C. Morton, W. E. Nance, Newborn hearing screening—A silent revolution. *N. Engl. J. Med.* **354**, 2151-2164 (2006).
3. G. Van Camp, R. J. H. Smith, Hereditary Hearing Loss Homepage. <https://hereditaryhearingloss.org>. Accessed 1 December 2021.
4. R. L. Alford *et al.*; ACMG Working Group on Update of Genetics Evaluation Guidelines for the Etiologic Diagnosis of Congenital Hearing Loss; Professional Practice and Guidelines Committee, American College of Medical Genetics and Genomics guideline for the clinical evaluation and etiologic diagnosis of hearing loss. *Genet. Med.* **16**, 347-355 (2014).
5. A. M. Korver *et al.*, Congenital hearing loss. *Nat. Rev. Dis. Primers* **3**, 16094 (2017).
6. G. Bademci *et al.*, Comprehensive analysis via exome sequencing uncovers genetic etiology in autosomal recessive nonsyndromic deafness in a large multiethnic cohort. *Genet. Med.* **18**, 364-371 (2016).
7. J. Doll *et al.*, Genetic spectrum of syndromic and non-syndromic hearing loss in Pakistani families. *Genes (Basel)* **11**, 1329 (2020).
8. C. M. Sloan-Heggen *et al.*, Characterising the spectrum of autosomal recessive hereditary hearing loss in Iran. *J. Med. Genet.* **52**, 823-829 (2015).
9. D. Yan *et al.*, Spectrum of DNA variants for non-syndromic deafness in a large cohort from multiple continents. *Hum. Genet.* **135**, 953-961 (2016).
10. T. Atik, G. Bademci, O. Diaz-Horta, S. H. Blanton, M. Tekin, Whole-exome sequencing and its impact in hereditary hearing loss. *Genet. Res.* **97**, e4 (2015).
11. N. J. Ingham *et al.*, Mouse screen reveals multiple new genes underlying mouse and human hearing loss. *PLoS Biol.* **17**, e3000194 (2019).
12. B. Vona, I. Nanda, M. A. Hofrichter, W. Shehata-Dieler, T. Haaf, Non-syndromic hearing loss gene identification: A brief history and glimpse into the future. *Mol. Cell. Probes* **29**, 260-270 (2015).
13. R. X.-Y. Ho *et al.*, Loss of MINAR2 impairs motor function and causes Parkinson's disease-like symptoms in mice. *Brain Commun.* **2**, faa047 (2020).
14. M. Tekin, SRX15001233 Family 1, II:1. NCBI Sequence Read Archive. <https://www.ncbi.nlm.nih.gov/sra/SRX15001233>. Deposited 26 April 2022.
15. M. Tekin, SRX15001232: Family 2, II:1. NCBI Sequence Read Archive. <https://www.ncbi.nlm.nih.gov/sra/SRX15001232>. Deposited 26 April 2022.
16. K. J. Karczewski *et al.*; Genome Aggregation Database Consortium, The mutational constraint spectrum quantified from variation in 141,456 humans. *Nature* **581**, 434-443 (2020).
17. A. M. Oza *et al.*; ClinGen Hearing Loss Clinical Domain Working Group, Expert specification of the ACMG/AMP variant interpretation guidelines for genetic hearing loss. *Hum. Mutat.* **39**, 1593-1613 (2018).
18. S. Richards *et al.*; ACMG Laboratory Quality Assurance Committee, Standards and guidelines for the interpretation of sequence variants: A joint consensus recommendation of the American College of Medical Genetics and Genomics and the Association for Molecular Pathology. *Genet. Med.* **17**, 405-424 (2015).
19. R. Elkon *et al.*, RFX transcription factors are essential for hearing in mice. *Nat. Commun.* **6**, 8549 (2015).
20. J. Orvis *et al.*, gEAR: Gene Expression Analysis Resource portal for community-driven, multi-omic data exploration. *Nat. Methods* **18**, 843-844 (2021).
21. J. E. Gale, W. Marcotti, H. J. Kennedy, C. J. Kros, G. P. Richardson, FM1-43 dye behaves as a permeant blocker of the hair-cell mechanotransducer channel. *J. Neurosci.* **21**, 7013-7025 (2001).
22. R. X. Ho *et al.*, MINAR1 is a Notch2-binding protein that inhibits angiogenesis and breast cancer growth. *J. Mol. Cell Biol.* **10**, 195-204 (2018).
23. P. J. Lanford *et al.*, Notch signalling pathway mediates hair cell development in mammalian cochlea. *Nat. Genet.* **21**, 289-292 (1999).
24. W. Pan, Y. Jin, B. Stanger, A. E. Kiernan, Notch signaling is required for the generation of hair cells and supporting cells in the mammalian inner ear. *Proc. Natl. Acad. Sci. U.S.A.* **107**, 15798-15803 (2010).
25. A. F. Siekmann, L. Covassin, N. D. Lawson, Modulation of VEGF signalling output by the Notch pathway. *BioEssays* **30**, 303-313 (2008).
26. H. Zhang *et al.*, UBTOR/KIAA1024 regulates neurite outgrowth and neoplasia through mTOR signaling. *PLoS Genet.* **14**, e1007583 (2018).
27. D. Vaudry, P. J. Stork, P. Lazarovici, L. E. Eiden, Signaling pathways for PC12 cell differentiation: Making the right connections. *Science* **296**, 1648-1649 (2002).
28. A. J. Carlton *et al.*, Loss of Baiap212 destabilizes the transducing stereocilia of cochlear hair cells and leads to deafness. *J. Physiol.* **599**, 1173-1198 (2021).
29. L. A. Dunbar *et al.*, Clarin-2 is essential for hearing by maintaining stereocilia integrity and function. *EMBO Mol. Med.* **11**, e10288 (2019).
30. E. R. Andersson, R. Sandberg, U. Lendahl, Notch signaling: Simplicity in design, versatility in function. *Development* **138**, 3593-3612 (2011).
31. C. R. Chillakuri *et al.*, Structural analysis uncovers lipid-binding properties of Notch ligands. *Cell Rep.* **5**, 861-867 (2013).
32. F. M. Lu, S. E. Lux, Constitutively active human Notch1 binds to the transcription factor CBF1 and stimulates transcription through a promoter containing a CBF1-responsive element. *Proc. Natl. Acad. Sci. U.S.A.* **93**, 5663-5667 (1996).
33. A. M. Henderson, S. J. Wang, A. C. Taylor, M. Aitkenhead, C. C. Hughes, The basic helix-loop-helix transcription factor HESR1 regulates endothelial cell tube formation. *J. Biol. Chem.* **276**, 6169-6176 (2001).
34. F. Itoh *et al.*, Synergy and antagonism between Notch and BMP receptor signaling pathways in endothelial cells. *EMBO J.* **23**, 541-551 (2004).
35. K. G. Leong *et al.*, Activated Notch4 inhibits angiogenesis: Role of beta 1-integrin activation. *Mol. Cell Biol.* **22**, 2830-2841 (2002).
36. Z. Liu *et al.*, Notch1 loss of heterozygosity causes vascular tumors and lethal hemorrhage in mice. *J. Clin. Invest.* **121**, 800-808 (2011).
37. M. Nosedá *et al.*, Notch activation induces endothelial cell cycle arrest and participates in contact inhibition: Role of p21Cip1 repression. *Mol. Cell Biol.* **24**, 8813-8822 (2004).
38. K. L. Taylor, A. M. Henderson, C. C. Hughes, Notch activation during endothelial cell network formation in vitro targets the basic HLH transcription factor HESR-1 and downregulates VEGFR-2/KDR expression. *Microvasc. Res.* **64**, 372-383 (2002).
39. S. E. Williams, S. Beronja, H. A. Pasolli, E. Fuchs, Asymmetric cell divisions promote Notch-dependent epidermal differentiation. *Nature* **470**, 353-358 (2011).
40. E. C. Driver, M. W. Kelley, Development of the cochlea. *Development* **147**, dev162263 (2020).
41. R. Brown, A. K. Groves, Hear, hear for notch: Control of cell fates in the inner ear by notch signaling. *Biomolecules* **10**, 370 (2020).
42. R. J. Ruben, Development of the inner ear of the mouse: A radioautographic study of terminal mitoses. *Acta Otolaryngol.* **220** (Suppl), 1-44 (1967).
43. G. Bademci *et al.*, FOXF2 is required for cochlear development in humans and mice. *Hum. Mol. Genet.* **28**, 1286-1297 (2019).
44. C. Li *et al.*, Dysfunction of GRAP, encoding the GRB2-related adaptor protein, is linked to sensorineural hearing loss. *Proc. Natl. Acad. Sci. U.S.A.* **116**, 1347-1352 (2019).
45. M. A. DePristo *et al.*, A framework for variation discovery and genotyping using next-generation DNA sequencing data. *Nat. Genet.* **43**, 491-498 (2011).
46. H. Li, R. Durbin, Fast and accurate long-read alignment with Burrows-Wheeler transform. *Bioinformatics* **26**, 589-595 (2010).
47. A. McKenna *et al.*, The Genome Analysis Toolkit: A MapReduce framework for analyzing next-generation DNA sequencing data. *Genome Res.* **20**, 1297-1303 (2010).
48. A. Abyzov, A. E. Urban, M. Snyder, M. Gerstein, CNVnator: An approach to discover, genotype, and characterize typical and atypical CNVs from family and population genome sequencing. *Genome Res.* **21**, 974-984 (2011).
49. M. Jelani *et al.*, A mutation in the major autophagy gene, WIPI2, associated with global developmental abnormalities. *Brain* **142**, 1242-1254 (2019).
50. W. C. Skarnes *et al.*, A conditional knockout resource for the genome-wide study of mouse gene function. *Nature* **474**, 337-342 (2011).
51. J. K. White *et al.*; Sanger Institute Mouse Genetics Project, Genome-wide generation and systematic phenotyping of knockout mice reveals new roles for many genes. *Cell* **154**, 452-464 (2013).
52. E. Ryder *et al.*; Sanger Mouse Genetics Project, Rapid conversion of EUCOMM/KOMP-CSD alleles in mouse embryos using a cell-permeable Cre recombinase. *Transgenic Res.* **23**, 177-185 (2014).



Mutations in *MINAR2* encoding membrane integral NOTCH2-associated receptor 2 cause deafness in humans and mice

Guney Bademci^a, María Lachgar-Ruiz^{b,c,d}, Mangesh Deokar^{e,f}, Mohammad Faraz Zafeer^g, Clemer Abad^h, Muzeyyen Yildirim Baylan^h, Neil J. Ingham^b, Jing Chen^b, Claire J. Sineni^g, Nirmal Vadgamaⁱ, Ioannis Karakikesⁱ, Shengru Guo^g, Duygu Dumanⁱ, Nitu Singh^f, Gaurav Harlalka^e, Shirish P. Jain^e, Barry A. Chioza^k, Katherina Walz^{a,g}, Karen P. Steel^b, Jamal Nasir^l, and Mustafa Tekin^{a,g,m,1}

Edited by Mary-Claire King, University of Washington, Seattle, WA; received March 8, 2022; accepted May 11, 2022

Discovery of deafness genes and elucidating their functions have substantially contributed to our understanding of hearing physiology and its pathologies. Here we report on DNA variants in *MINAR2*, encoding membrane integral NOTCH2-associated receptor 2, in four families underlying autosomal recessive nonsyndromic deafness. Neurologic evaluation of affected individuals at ages ranging from 4 to 80 y old does not show additional abnormalities. *MINAR2* is a recently annotated gene with limited functional understanding. We detected three *MINAR2* variants, c.144G > A (p.Trp48*), c.412_419delCGGTTTGG (p.Arg138Valfs*10), and c.393G > T, in 13 individuals with congenital- or prelingual-onset severe-to-profound sensorineural hearing loss (HL). The c.393G > T variant is shown to disrupt a splice donor site. We show that *Minar2* is expressed in the mouse inner ear, with the protein localizing mainly in the hair cells, spiral ganglia, the spiral limbus, and the stria vascularis. Mice with loss of function of the *Minar2* protein (*Minar2^{tm1b/tm1b}*) present with rapidly progressive sensorineural HL associated with a reduction in outer hair cell stereocilia in the shortest row and degeneration of hair cells at a later age. We conclude that *MINAR2* is essential for hearing in humans and mice and its disruption leads to sensorineural HL. Progressive HL observed in mice and in some affected individuals and as well as relative preservation of hair cells provides an opportunity to interfere with HL using genetic therapies.

autosomal recessive | deafness | hearing loss | *MINAR2* | NOTCH2

Hearing loss (HL) is one of the most common sensory deficits, affecting ~1 in 500 newborns (1). Genetic factors are implicated in the majority of cases, with more than 80% of the inherited form exhibiting autosomal recessive transmission (2). No additional findings are present in over 70% of the cases, which are then classified as nonsyndromic HL (Hereditary Hearing Loss Homepage, <https://hereditaryhearingloss.org/>) (2, 3). Genetic testing for etiologic evaluation has become a standard of care in people with congenital or childhood-onset sensorineural HL, which is caused by pathologies of the inner ear and auditory nerve (4, 5). Recent studies have shown that screening all recognized HL genes for variants reveals underlying cause in about half of the affected individuals, leaving a significant portion of people with HL with an unknown etiology (6–9). In the era of emerging genetic therapies for HL, finding the etiology of HL in affected individuals has become a critical task. This is especially relevant for progressive HL, as genetic therapies may potentially stop progression while cochlear hair cells are still alive (10–12).

MINAR2 (previously known as uncharacterized protein KIAA1024L and mouse gene *A730017C20Rik*) has recently been identified, and based on its structural similarity to *MINAR1*, named as major intrinsically disordered NOTCH2-associated receptor 2 or membrane integral NOTCH2-associated receptor 2 (13). A mutant mouse model of *Minar2* showed motor deficits similar to those seen in Parkinson disease, with no information about hearing abnormalities (13). A *Minar2* mutant mouse line, *Minar2^{tm1b}*, has also recently been reported to show no auditory brainstem responses at 14 wk old as part of a large HL screen (Mouse Genome Informatics [MGI]: 2442934) (11). Functional aspects of *MINAR2* and consequences of its dysfunction in humans remain unknown.

In this study, to better map the landscape of hereditary HL, we sought DNA variants underlying deafness in 13 affected individuals from four families. We identified three different *MINAR2* variants in the families cosegregating with HL. We further showed that homozygous *Minar2^{tm1b}* mutant mice develop rapidly progressive HL associated with changes in outer hair cell stereocilia. Finally, via in vitro studies we demonstrated that *MINAR2* suppresses NOTCH2, suggesting that notch signaling might play a role in pathogenesis.

Significance

Molecular components of hearing in mammals are not completely delineated. Via a genetic approach conducted in families with sensorineural hearing loss, this study presents *MINAR2* as an indispensable element of hearing in humans. Similarly, disruption of *Minar2* in mice leads to progressive hearing loss associated with alterations in the stereocilia of hair cells, the receptors of hearing, while hair cells remain intact until later in life. We present *MINAR2* as a gene working in the inner ear that is essential for hearing in humans and mice. Degeneration of sensory epithelium is a common consequence of hereditary deafness precluding genetic therapies. The preservation of hair cells in mutant mice at young ages makes *MINAR2* a good candidate for intervention.

The authors declare no competing interest.

This article is a PNAS Direct Submission.

Copyright © 2022 the Author(s). Published by PNAS. This open access article is distributed under Creative Commons Attribution-NonCommercial-NoDerivatives License 4.0 (CC BY-NC-ND).

¹To whom correspondence may be addressed. Email: mtekin@miami.edu.

This article contains supporting information online at <http://www.pnas.org/lookup/suppl/doi:10.1073/pnas.2204084119/-DCSupplemental>.

Published June 21, 2022.

Results

Nonsyndromic Sensorineural HL Is Diagnosed in 13 Individuals from Four Unrelated Families. A summary of the auditory phenotype is shown in *SI Appendix, Table S1*. Ages ranged from 4 to 80 y old at the last examination. Each affected individual was diagnosed with HL either at birth or during infancy. Families 1 and 2 were of Turkish ancestry (Fig. 1). Parents of family 1 stated that in individuals II:1 and II:2, HL was milder in younger ages and progressed to a severe or profound degree by around age 10. Otoacoustic emissions were absent in these individuals. These siblings received unilateral cochlear implants at ages 12 and 10, respectively, which improved their oral communication. Individual II:3 in family 1 was diagnosed with profound sensorineural HL after failing the newborn hearing screening test. Otoacoustic emissions were absent at diagnosis. He received a unilateral cochlear implant at age 1 and communicates orally. Pure tone audiograms in parents showed normal thresholds (*SI Appendix, Fig. S1*).

Families 3 and 4 were of Indian ancestry. While there is no known consanguinity in any of the marriages in these two pedigrees, they are all from the same small town belonging to the same ethnic background, i.e., Hindu (religion) and Mali (Caste). All affected individuals in family 3 were born deaf and used signs, simple words, or sounds to be able to communicate. Severity of HL appeared to have remained the same in all the affected individuals from the beginning of life. Individuals IV:1 and IV:2 in family 4 were diagnosed with severe to profound sensorineural HL at the age of 3 y via auditory brainstem response (ABR) studies. Parents indicated a progression in the severity of HL. Their mode of communication at that age was predominantly nonverbal.

A high-resolution temporal bone CT scan or MRI was normal in at least one affected member of each family (*SI Appendix, Fig. S1*). None of the affected individuals had additional clinical findings for a syndromic form of deafness. Their neurodevelopmental skills were on target except for speech delay. None of the affected individuals showed impaired balance on tandem walking and Romberg test. Neurological examination was normal except for hearing loss in six affected individuals with ages ranging from 4 to 80 y. No affected individual was noted to have bradykinesia, tremor, or rigidity similar to those seen in Parkinson disease (*SI Appendix, Table S2*).

MINAR2 Variants Cosegregate with Autosomal Recessive Deafness. We performed genome sequencing in four affected individuals in families 1 (14) and 2 (15) and exome sequencing in three affected individuals in families 3 and 4 (Fig. 1A, individuals marked with an asterisk and *SI Appendix, Table S3*). Sequencing data in affected individuals were first analyzed for variants [single nucleotide variants (SNVs); insertions and/or deletions (indels); and copy number variants (CNVs) in recognized HL genes retrieved from the Hereditary Hearing Loss Homepage (<https://hereditaryhearingloss.org/>) (3), Online Mendelian Inheritance in Man (OMIM: <https://omim.org/>), University of Miami Molecular Genetics Laboratory HL gene panel, and a virtual gene panel for HL (v2.176) from PanelApp (<https://www.genomicsengland.co.uk>)]. Minor allele frequency (MAF) thresholds of 0.005 for recessive and 0.001 for dominant variants were used. Population allele frequencies were obtained from the genome aggregation database (gnomAD: <https://gnomad.broadinstitute.org/>) (16) and the single nucleotide polymorphism database (dbSNP: <https://www.ncbi.nlm.nih.gov/projects/SNP/>), as well as from our internal exome/

genome database that includes >7,000 samples from different ethnicities. American College of Medical Genetics (ACMG) and ClinGen HL expert panel guidelines were followed for variant interpretation (17, 18). This analysis did not reveal a plausible variant under any inheritance model.

After excluding variants in previously recognized deafness genes, in family 1 we filtered shared homozygous coding and splice variants (SNVs, indels, and CNVs) in three affected siblings with a MAF of <0.005 in dbSNP, gnomAD highest subethnicity, and our internal control database. This filter reveals only a *MINAR2* (GeneBank: NM_001257308.2) c.412_419delCGGTTTTG (p.Arg138Valfs*10) variant in the family. The variant is located within a 9.4-MB shared homozygous run in three siblings, which is the only homozygous region >1 MB (*SI Appendix, Tables S4 and S5*). This frame-shift variant is predicted to introduce a premature stop codon and lead to early truncation of *MINAR2*.

In the proband of family 2, *MINAR2* is located within the second longest homozygous run at chromosome 5 (chr5):128,253,080 to 141,730,596 (hg19) (*SI Appendix, Table S6*). She is homozygous for the c.144G > A (p.Trp48*) variant in *MINAR2*. This nonsense variant is predicted to cause an early stop codon and result in truncation of *MINAR2*.

In the exome data of two affected individuals from family 3, filtering variants via the same criteria used in family 1 reveals only one variant for which both individuals are homozygous: *MINAR2* c.393G > T (p.Lys131Asn). SNP arrays show that this variant is located within the only shared homozygous run, >1 MB, in all seven affected individuals in family 3. This homozygous run is flanked by markers rs13174854 and rs377767449, which is 2.96 MB on chr5:126,978,108 to 132,742,450 (hg19). In family 4, two affected siblings share a 5.76-MB homozygous run on chr5:126,978,108 to 132,742,450 (hg19), flanked by markers rs11241936 and rs11242152. Exome sequencing showed that the proband in family 4 is homozygous for the same *MINAR2* variant detected in family 3.

None of the detected *MINAR2* variants is listed in dbSNP or gnomAD databases and all variants are predicted to be deleterious (*SI Appendix, Table S7*). Sanger sequencing confirmed all three *MINAR2* variants and showed that each variant cosegregates with autosomal recessive HL in all families (Fig. 1A).

MINAR2 c.393G > T (p.Lys131Asn) Leads to Aberrant Splicing. While it is a missense change, the c.393G > T (p.Lys131Asn) variant substitutes the last nucleotide of exon 2, and is predicted to abolish a splice donor site (*SI Appendix, Table S7 and Fig. S2*). Via exon trapping experiments, we show that this variant leads to an addition of 85 intronic nucleotides into exon 2, which alters the amino acid composition of the rest of the protein leading to a premature stop codon (Fig. 1D and *SI Appendix, Fig. S2*). The same variant also leads to skipping of exon 2 entirely (Fig. 1D).

Minar2^{tm1b} Homozygous Mutant Mice Show Sensorineural HL. To prove causality of disruption of *Minar2* in sensorineural HL, we evaluated hearing in *Minar2* mutant mice. Hearing sensitivity of *Minar2^{tm1b}* mutant mice (*SI Appendix, Fig. S3*) was assessed using two methods: ABR, a measure of neural activity in the auditory nerve and brainstem, and distortion product otoacoustic emission (DPOAE), a measure of outer hair cell electromotility and resulting nonlinearities in the cochlea. Thresholds for both ABRs and DPOAEs were raised in homozygous mutants compared with wild-type littermates from the earliest age studied, postnatal day (P) 14, only 21 d after the usual onset of hearing (Fig. 2). By 4 wk old, the

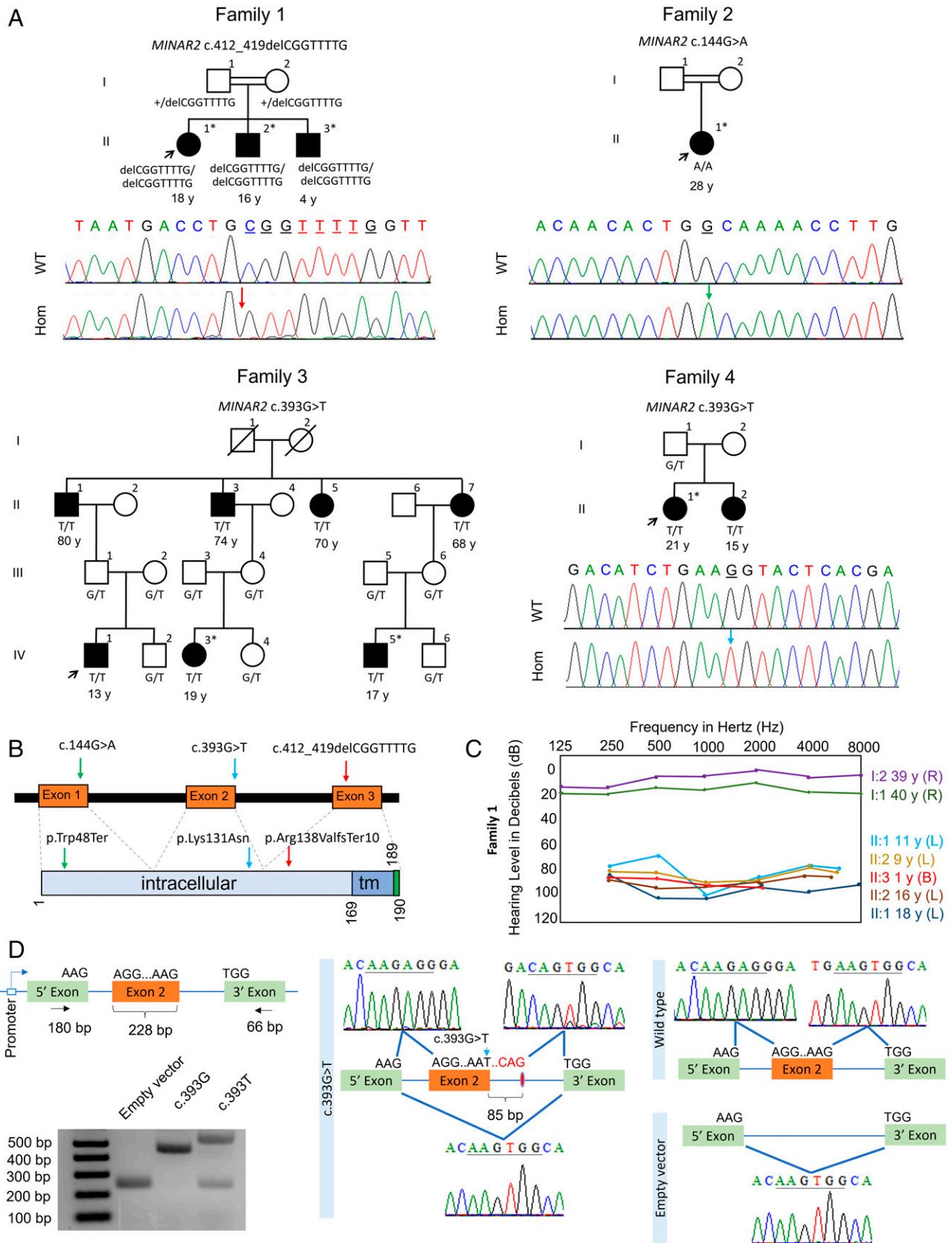


Fig. 1. Families, *MINAR2* variants, and the effects of the c.393G > T variant on splicing. (A) Pedigrees and segregation of the *MINAR2* variants in families. Filled symbols denote affected individuals and double lines indicate first cousin consanguinity. Electropherograms show the identified variant. The wild-type traces are from an unrelated individual. WT, wild type; Hom, homozygous mutant; exome/genome sequencing was performed in individuals marked with an (*) asterisk. (B) Locations of the identified variants. Tm, transmembrane. (C) Audiogram of family 1 (R, right ear; L, left ear; B, bilateral). (D) *MINAR2* exon 2 inserted into a vector consisting of 5' and 3' exons in the exon trap assay is shown. There are larger and smaller PCR products in the c.393G > T sample compared to wild type. Sanger sequencing confirms insertion of 85 bp at the donor site of exon 2 and skipping of exon 2.

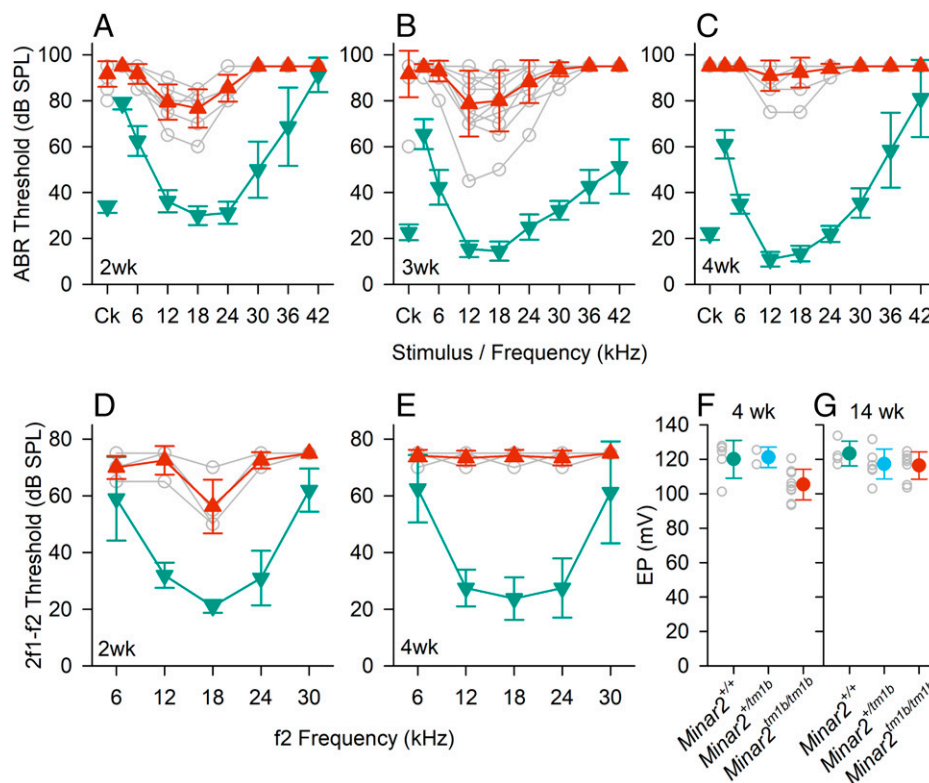


Fig. 2. Auditory studies in *Minar2* mutant mice. (A–C) ABR thresholds. Mean (\pm SD) ABR thresholds are plotted against stimulus for *Minar2*^{+/+} mice (teal, down triangles) and *Minar2*^{tm1b/tm1b} mice (red, up triangles). Open gray circles indicate thresholds for individual *Minar2*^{tm1b/tm1b} mice. Results are plotted for data obtained at P14 (A) ($n = 4$ *Minar2*^{+/+}, 9 *Minar2*^{tm1b/tm1b}); P21. (B) ($n = 11$ *Minar2*^{+/+}, 12 *Minar2*^{tm1b/tm1b}) and P27 to P28 (C) ($n = 10$ *Minar2*^{+/+}, 11 *Minar2*^{tm1b/tm1b}). Ck, click. (D and E) DPOAE thresholds. Mean (\pm SD) DPOAE thresholds are plotted against f2 stimulus frequency for *Minar2* control mice (teal, down triangles) and *Minar2*^{tm1b/tm1b} mice (red, up triangles). Open gray circles indicate thresholds for individual *Minar2*^{tm1b/tm1b} mice. Results are plotted for data obtained at P14 (D) ($n = 4$ controls, comprising 1 wild type and 3 heterozygotes, $n = 4$ mutants) and P27 to P28 (E) ($n = 4$ wild types, $n = 6$ mutants). (F and G) EP in *Minar2* mutant mice aged 4 wk (F) and 14 wk old (G). Colored circles indicate the mean (\pm SD) EP measurement in *Minar2*^{+/+} (teal), *Minar2*^{+/tm1b} (cyan), and *Minar2*^{tm1b/tm1b} (red) mice. Open gray circles indicate the EP values recorded in individual mice. At 4 wk old (P30 to P32) *Minar2*^{+/+} $n = 5$, range 101.2 to 127.8 mV; *Minar2*^{+/tm1b} $n = 2$ range 117.0 to 125.4 mV; and *Minar2*^{tm1b/tm1b} $n = 9$, range 93.4 to 120.5 mV. At 14 wk old *Minar2*^{+/+} $n = 4$, range 117 to 133.6 mV; *Minar2*^{+/tm1b} $n = 7$, range 113.8 to 131.6 mV; and *Minar2*^{tm1b/tm1b} $n = 8$, range 103.5 to 124.7 mV.

mutant mice showed severe elevations in threshold or no response at the highest sound levels used. Endocochlear potential was only slightly reduced from a mean of 120 mV to 105 mV in *Minar2*^{tm1b/tm1b} mice, with most mutant mice exhibiting an endocochlear potential (EP) in the normal physiological range for mice of over 100 mV (Fig. 2).

Minar2 Is Expressed in the Mouse Cochlea. To further understand the role of *Minar2* in hearing, we assessed the presence of *Minar2* transcript in different mouse tissues, including the inner ear, and specifically the cochlea. Total RNA was isolated from wild-type mice at embryonic day (E) 18.5, P0, and P30. RT-PCR with a forward primer located in exon 2 and a reverse primer in exon 3 of the *Minar2* gene (GenBank: NM_173759) produced a unique band of 171 bp corresponding to the wild-type mRNA in all analyzed tissues, with the exception of the liver. We find that *Minar2* is highly expressed in the inner ear, and specifically in the cochlea, at E18.5, P0, and P30 (Fig. 3A). To determine specific locations of *Minar2* expression within the cochlea, we proceeded to study *Minar2*^{tm1b} heterozygous mutant mice taking advantage of the reporter gene. β -Galactosidase staining of P1 cross-sections and whole mount organ of Corti preparations reveals that *Minar2* is mainly localized in the hair cells, the supporting cells, spiral ganglion (including the nerve fibers), the spiral limbus, and the stria vascularis (Fig. 3B and SI Appendix, Fig. S4 A and B). Of note, the gene expression analysis resource (gEAR; <https://umgear.org/>) portal shows *Minar2* expression both in hair cells and supporting cells

(SI Appendix, Fig. S4C) (19, 20). Double labeling for *Minar2* and Tuj1 in heterozygous mutant mice shows that the two are expressed in different cell types and *Minar2* is not present in the neurons of the spiral ganglion that were marked with Tuj1, suggesting that *Minar2* is located in spiral ganglion glial cells (Fig. 3 C, E, and F).

The Earliest Defect in *Minar2*^{tm1b} Mutant Mice Appears in Stereocilia Bundles. We used scanning electron microscopy (SEM) (Fig. 4) to examine the cochlea of mice aged 14 d old because at this age the ABR thresholds were raised but synapses appeared normal in numbers (Fig. 5). The organization of the organ of Corti appeared normal and there were very few missing stereocilia bundles in mutants, suggesting that hair cell degeneration cannot explain the raised ABR thresholds at this age (SI Appendix, Fig. S5). However, when we examined the stereocilia bundles of outer hair cells, we saw the shortest row was depleted, with reduced numbers and abnormally short stereocilia (Fig. 4). Outer hair cells along the entire length of the cochlear duct showed this feature. Inner hair cells appeared close to normal, although the middle row of stereocilia occasionally appeared more irregular than in the control littermates. Heterozygotes looked the same as wild-type littermates at this age.

Mechanoelectrical Transduction Channels Are Functional in *Minar2*^{tm1b/tm1b} Mice. To study the mechanoelectrical transduction (MET), we used the FM1-43 FX dye, a molecule commonly used to assay the MET channel function, since functional MET

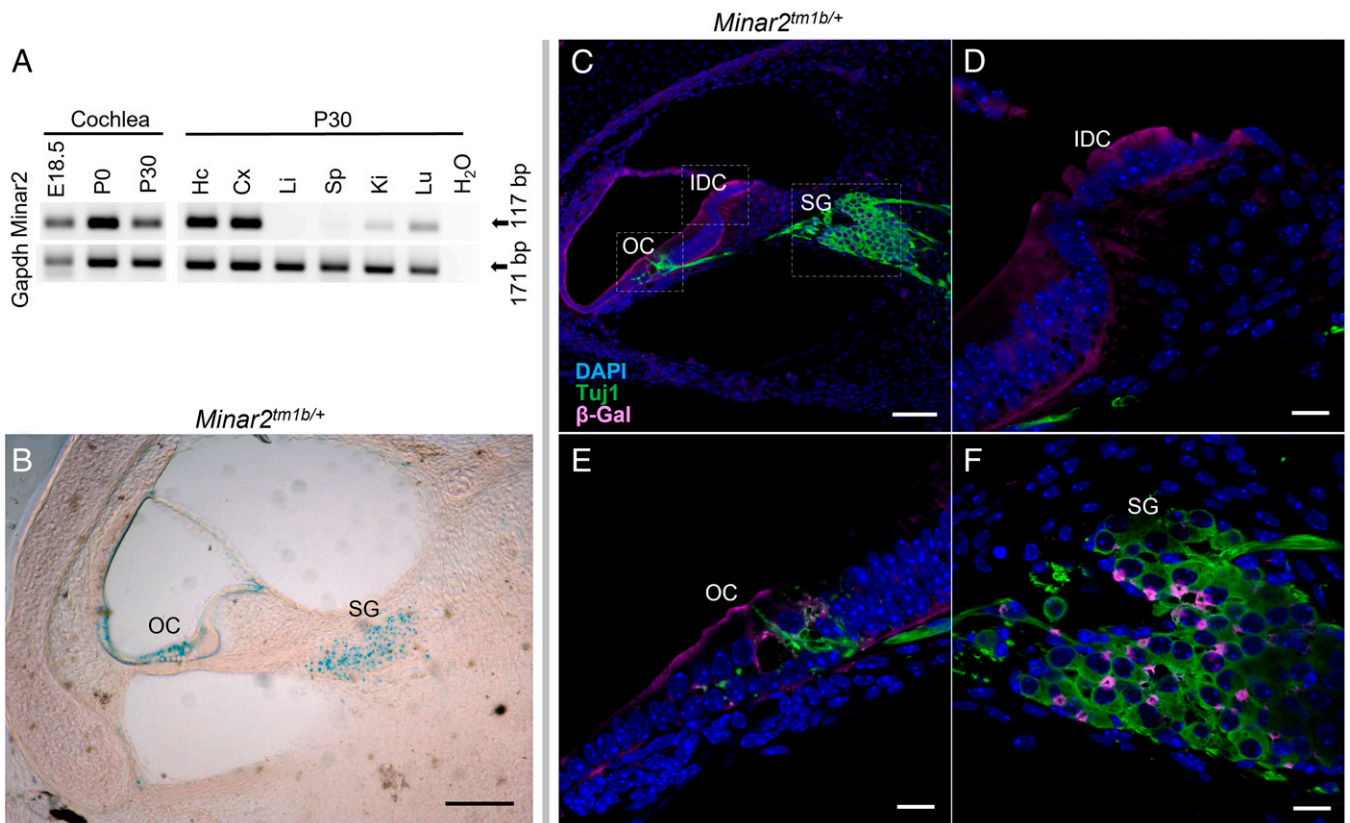


Fig. 3. Expression of *Minar2*, localization of the protein in the cochlea and innervation of cochlear hair cells in *Minar2* heterozygous mice, using the *LacZ* reporter gene component of the inserted cassette in the mutant allele, which expresses β -galactosidase (SI Appendix, Fig. S3). (A) RT-PCR of *Minar2* expression in the cochlea at E18.5, P0, and P30. Also, expression in different mouse tissues at P30 are Hc, hippocampus; Cx, cortex; Li, liver; Sp, spleen; Ki, kidney; Lu, lung. Gapdh was used as a control. (B) Localization of *Minar2* using the reporter gene *LacZ* of the mutant allele and in β -gal staining shown in blue. Note the localization of *Minar2* at the SG, spiral ganglion; OC, organ of Corti. (Scale bar: 70 μ m.) (C) Cross-section from 24-kHz region of P1 mutant inner ear was labeled with anti- β -gal (magenta) to detect *Minar2* localization and Tuj1 (green) to label neurons. (Scale bar: 70 μ m in C.) A zoom in is shown in D–F. (Scale bars: 10 μ m.) IDC, interdental cells.

channels are required for the uptake of this fluorescent dye into the hair cells (21). We perfused cochleae from P14 mice and observed FM1-43 FX dye uptake by both inner and outer hair

cells in *Minar2*^{+/+} and *Minar2*^{tm1b/tm1b} mice. Heterozygotes looked the same as wild-type littermates. While the intensity of the staining varied from mouse to mouse, all the samples showed

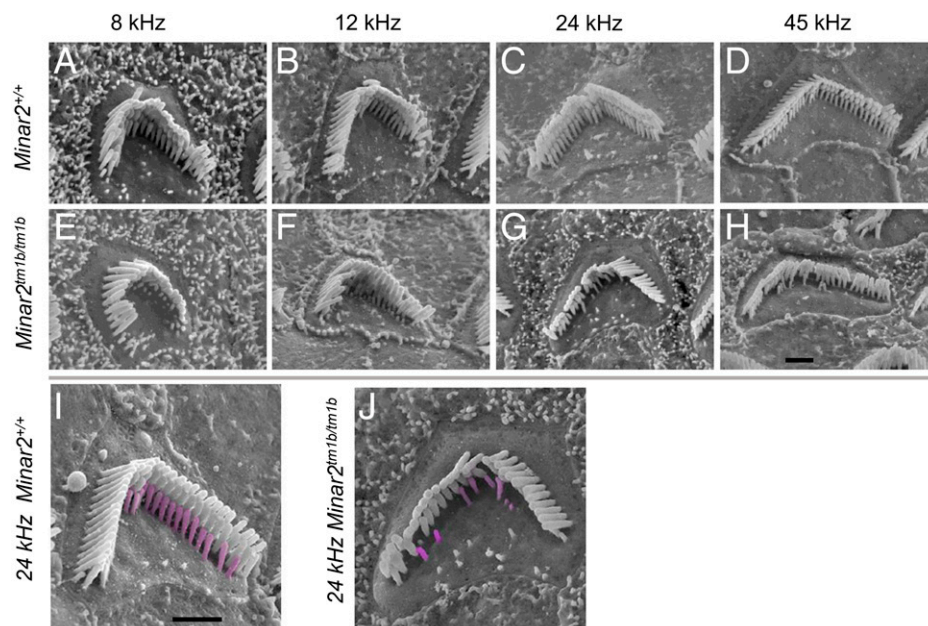


Fig. 4. Scanning electron microscopy reveals stereocilia defects. Outer hair cells at 8 kHz (85% of distance from base), 12 kHz (70%), 24 kHz (40%), and 45 kHz (20%) best frequency locations in wild-type mice (A–D) and *Minar2*^{tm1b/tm1b} homozygotes (E–H). Higher magnification images with the shortest row colored in magenta in a wild-type (I) and a mutant (J) outer hair cell, showing the reduction in numbers. (Scale bars in H and I: 1 μ m.)

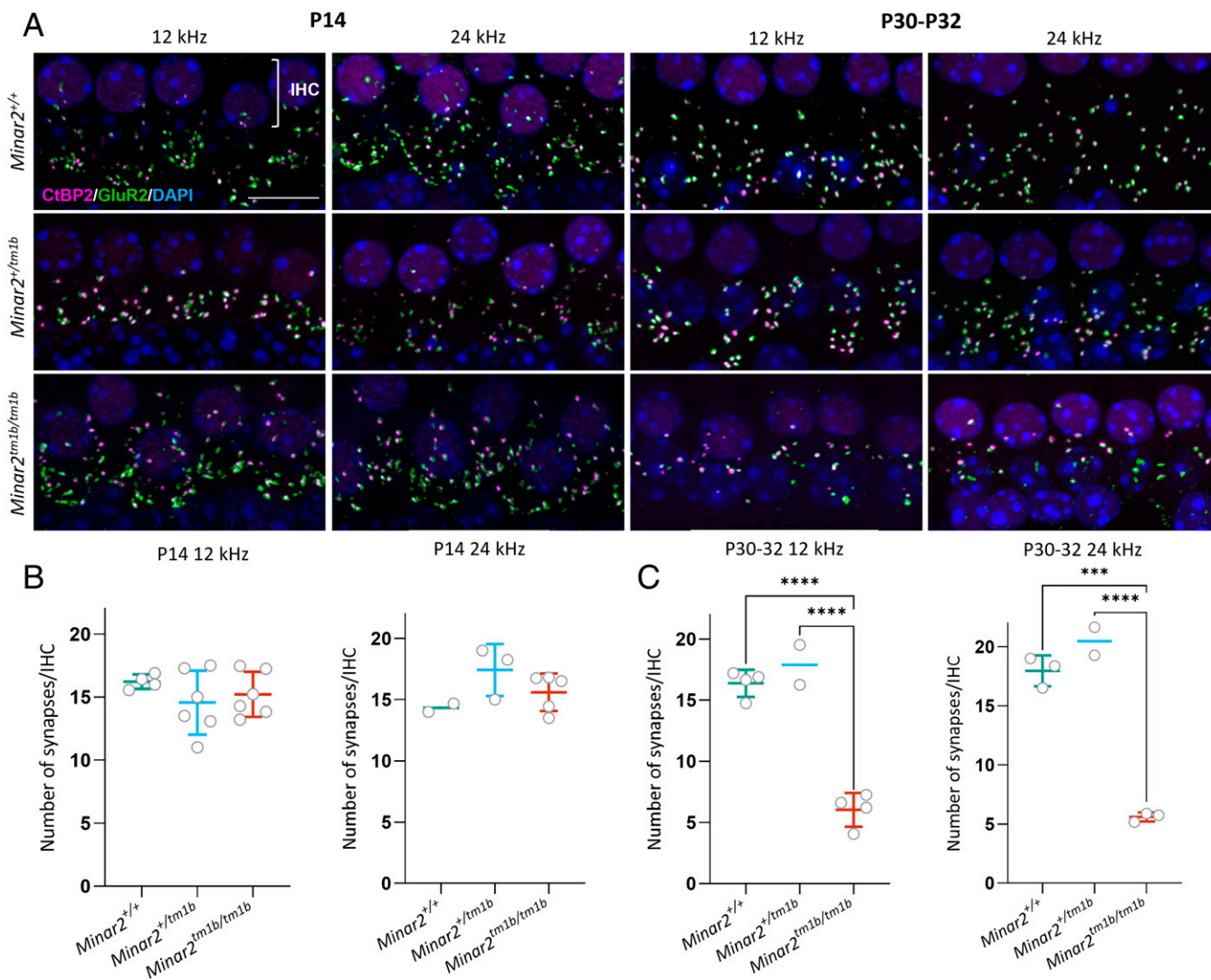


Fig. 5. Synaptic abnormalities of cochlear hair cells in *Minar2* mutant mice. (A) Synapses were examined using anti-CtBP2 antibody to mark presynaptic ribbons (magenta) and anti-GluR2 antibody to mark postsynaptic densities (green). Nuclei are shown in blue (DAPI). (Scale bar: 5 μ m.) The images correspond to the cochlear best-frequency regions of 12 kHz and 24 kHz. The row of nuclei at the *Top* of each image corresponds to the IHCs. (B and C) Quantification of ribbon synapses per IHC at P14 (B) and P30 to P32 (C). Colocalized pre- and postsynaptic components were defined as a synapse. The average for each mouse is plotted as a circle. All data are shown as mean \pm SD and statistically analyzed by one-way ANOVA with multiple comparisons. At P14, no significant difference was seen between homozygotes ($n = 6$ at 12 kHz and $n = 5$ at 24 kHz) and heterozygotes ($n = 6$ at 12 kHz and $n = 3$ at 24 kHz) or wild types ($n = 4$ at 12 kHz and $n = 2$ at 24 kHz). At P30 to P32, there are significantly fewer colocalized synapses in *Minar2*^{tm1b/tm1b} ($n = 4$ for 12 kHz and $n = 3$ for 24 kHz) compared to wild types ($n = 4$ at 12 kHz and $n = 3$ at 24 kHz) and compared to heterozygotes ($n = 2$). **** $P = 0.0001$ and **** $P < 0.0001$.

uptake of the molecule specifically in hair cells, indicating that the MET channels are active in the *Minar2* mutants (SI Appendix, Fig. S6).

Hair Cell Degeneration Is a Secondary Feature in *Minar2*^{tm1b} Mutant Mice. Hair cell degeneration is a common feature in HL, and extensive loss of hair cells may preclude some approaches to treatments. Therefore, we examined older *Minar2*^{tm1b} mutant mice, aged 14 wk, to assess the loss of hair cells. We have previously reported that these mutants show no auditory brainstem responses at 14 wk old (11) and the EP is normal at this age (Fig. 2G). At earlier ages we see minimal evidence of any hair cell degeneration (SI Appendix, Fig. S5). However, by 14 wk of age, there is extensive loss of hair cells, with some discrete patches distributed along the length of the cochlear duct where the entire organ of Corti appears to have degenerated while other regions show scattered missing hair cells, both inner and outer, within the organ of Corti (Fig. 6). Heterozygotes had a similar appearance to the wild-type mice.

***Minar2*^{tm1b} Mutant Mice Show Reduction in the Number of Inner Hair Cell Ribbon Synapses at P30.** To understand underlying pathophysiology further, we evaluated the innervation pattern of hair cells by staining neurons with an anti-neurofilament antibody in the organ of Corti at P1 (SI Appendix, Fig. S7). Homozygous mutant mice show an altered innervation pattern of hair cells with a reduction in the nerve fibers around inner hair cells and a dispersed distribution of nerve fibers toward outer hair cells. *Minar2*^{tm1b} mutant mice show reduction in the number of crossings of type II nerves at P14 (Fig. 7). We subsequently examined synapses of inner hair cells using anti-CtBP2 antibody to label presynaptic ribbons and anti-GluR2 antibody to mark the AMPA receptor subunit R2, a part of the postsynaptic density. Ribbon synapses look qualitatively normal at both ages tested, P14 and P30, and the number of synapses per inner hair cell in homozygous mutants was not significantly different from numbers in heterozygotes or wild-type controls at P14, indicating that the raised AI 175 thresholds observed at that age in mutants are not due to the

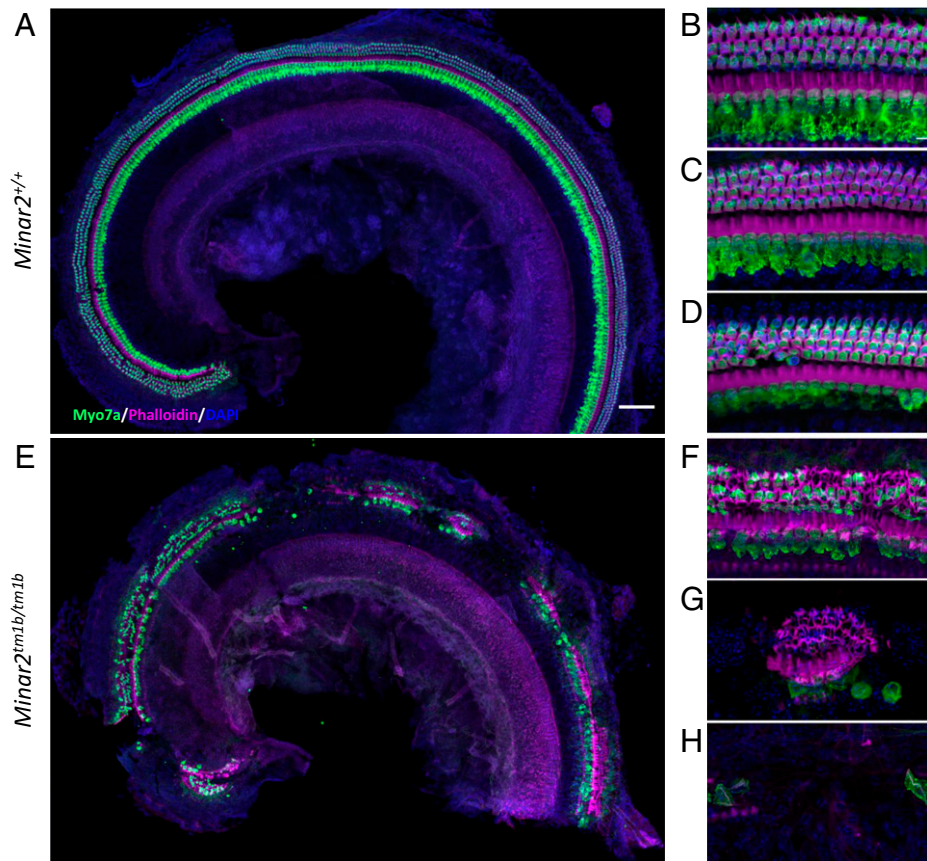


Fig. 6. Hair cell degeneration pattern in *Minar2^{tm1b}* mutant mice at 14 wk old. Confocal maximum intensity projection images of the whole-mount organ of Corti of 14-wk-old mice. Hair cells were examined using anti-Myo7a antibody (green) and phalloidin (magenta). Nuclei are shown in blue (DAPI). (Scale bars: 200 μ m in A and 10 μ m in B.) The images are representative examples of *Minar2^{+/+}* (A–D) and *Minar2^{tm1b/tm1b}* (E–H) mice. (A and E) Overview of the apical half of the cochlea. (B–D) High-magnification images corresponding to the 12 kHz, 24 kHz, and 36 kHz best-frequency regions, respectively. (F–H) High-magnification images of three different patterns of hair cell loss observed in *Minar2^{tm1b}* mutant mice. All five homozygotes that were studied at 14 wk old showed similar patches of loss of the organ of Corti at varying locations along the length of the cochlear duct interspersed with regions that showed only scattered hair cell loss. *Minar2^{+/+}* ($n = 4$), *Minar2^{+/tm1b}* ($n = 5$), and *Minar2^{tm1b/tm1b}* ($n = 5$).

loss of ribbon synapses (Fig. 5 A and B). However, by P30 to P32 *Minar2^{tm1b}* mutant mice did show a significant decrease in the number of synapses compared to wild-type mice (Fig. 5 A and C), and this may contribute to the progression of HL.

Overexpression of *MINAR2* Suppresses Angiogenesis and *MINAR2* Variants Abolish This Effect. As MINAR1 has been shown to inhibit angiogenesis (22), we investigated whether MINAR2 shows the same effect on angiogenesis in human umbilical vein endothelial cells (HUVEC). These studies reveal that transient overexpression of *MINAR2* suppresses angiogenesis (Fig. 8A). In addition, overexpressing each *MINAR2* variant detected in families 1 and 2 in HUVEC reduces suppression of angiogenesis, suggesting that they are loss-of-function variants (Fig. 8A).

Expression Levels of *MINAR2* Are Inversely Correlated with Intracellular NOTCH2 Abundance. MINAR2 is named based on its structural similarity to MINAR1, which is shown to be involved in NOTCH2 signaling (22). While MINAR2 is a much smaller protein compared to MINAR1 (190 vs. 917 amino acids) (22), it has recently been shown to bind NOTCH2 in a coimmunoprecipitation assay (13). Thus, we set out to explore whether NOTCH2 abundance in cells is correlated with *MINAR2* expression (23, 24). Furthermore, as NOTCH and VEGF signaling pathways are known to interact during angiogenesis (25), we determined the effect of *MINAR2*

expression on VEGF. Our studies show that overexpression of wild-type *MINAR2* in HUVEC is associated with reduced abundance of NOTCH2 and VEGFA (a prominent VEGF protein in vascular endothelial cells) (Fig. 8B). Silencing of *MINAR2* in PC12 cells, which endogenously express *MINAR2*, leads to an increase in NOTCH2 and confirms the suppressor effect of *MINAR2* on NOTCH2 abundance (Fig. 8C and *SI Appendix*, Fig. S8).

MINAR2 Is Involved in MAP Kinase and mTOR Pathways. MINAR1 has been shown to regulate neurite outgrowth in a neuroendocrine cell line PC12 (26), in which neurite outgrowth via nerve growth factor is achieved by MAPK and PI3K pathways (27). The mTOR complex is a downstream target of PI3K, which contains mTORC1 and mTORC2 complexes in its central catalytic domain (26). We tested the effects of *MINAR2* on the MAPK pathway by transiently overexpressing wild-type *MINAR2* in PC12 cells and detecting levels of ERK1/2 and pERK1/2, a crucial kinase of the MAPK signaling pathway. These studies show that overexpression of wild-type *MINAR2* reduces the abundance of pERK1/2, the active form of ERK1/2. On the other hand, overexpression of the two *MINAR2* deafness variants in families 1 and 2 does not show this effect, again supporting their loss of function (*SI Appendix*, Fig. S9A). When we silenced *MINAR2* in PC12 cells, we observed an increase in a functional protein in mTORC1 activity, P-S6, at 12 h (*SI Appendix*, Fig. S9B). However, there was

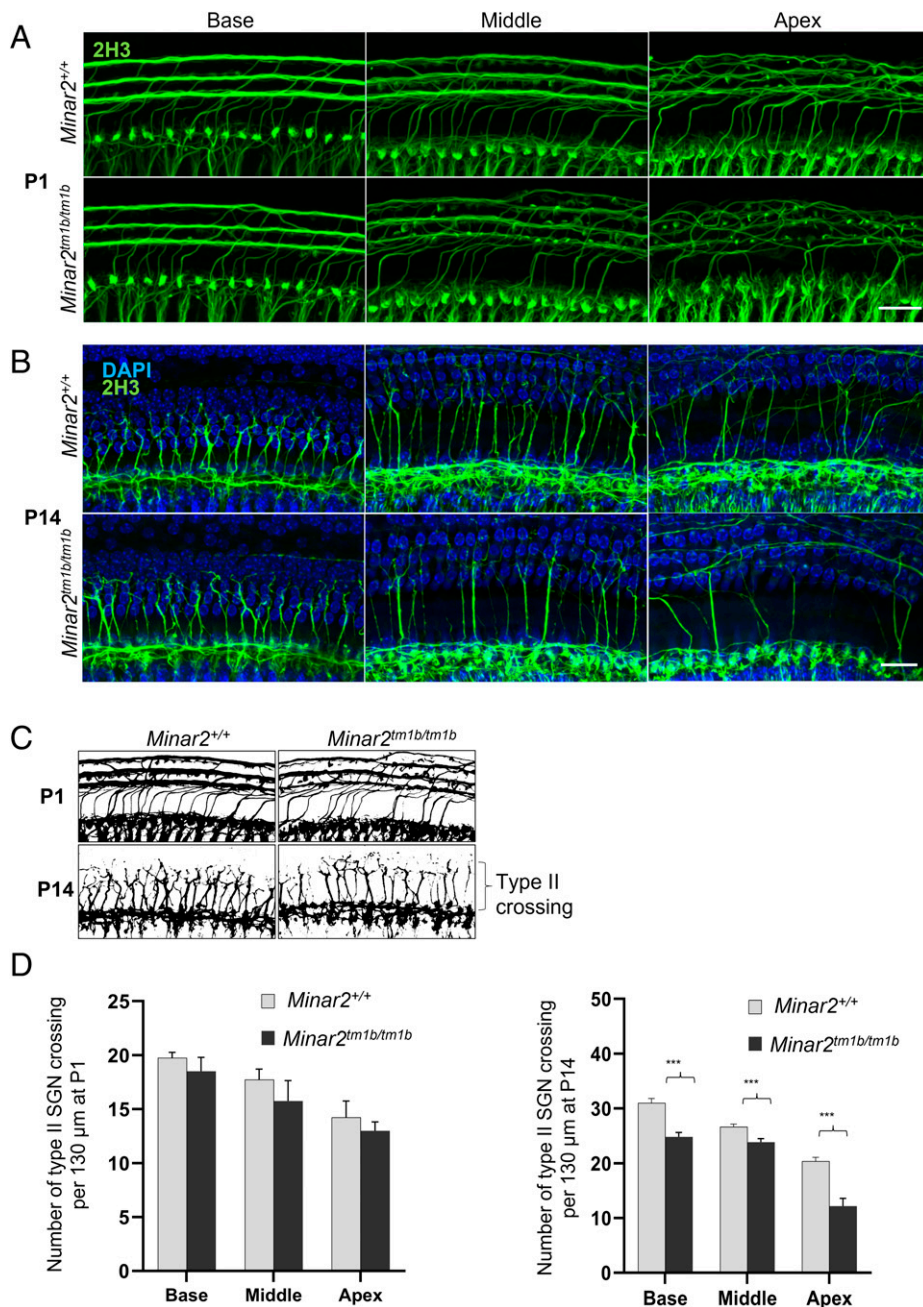


Fig. 7. Confocal maximum intensity projection images from a 24-kHz region of the whole-mount cochlea. (A and B) Total innervation with anti-2H3 neurofilament label (green) for P1 and P14 ($n = 3$ each group) wild-type and mutant mice. (Scale bars in A and B: 20 μm .) (C) Schematic diagram of whole-mount cochlea, demonstrating the innervation pattern of type II nerves at P1 and P14 wild-type and mutant mice. (D) The total number of crossings of type II nerves is shown as histogram ($n = 3$; $***P < 0.001$.)

no difference in pAKT, a component of mTORC2 activity (SI Appendix, Fig. S9B).

Discussion

In this study we present three loss-of-function variants in *MINAR2* in four families cosegregating with nonsyndromic sensorineural HL. Hearing loss started at birth or in early childhood in all 13 affected individuals. A progressive HL reaching a severe-to-profound degree during childhood was noted in four affected individuals. In addition to ABR thresholds showing sensorineural HL, otoacoustic emissions were absent in three children tested, suggesting dysfunction of both inner hair cell/acoustic nerve and outer hair cells. To support causality of the *MINAR2* mutations in deafness and to begin understanding

the mechanism of HL, we show that *Minar2*^{tm1b/tm1b} mice have a severe, progressive increase in ABR thresholds from 2 wk old onwards (around the time that mice start to hear), with very few responses by 4 wk old. Otoacoustic emissions can be detected in the mutant mice but at raised thresholds at 2 wk old, and these responses are mostly absent by 4 wk old, implicating outer hair cells in the pathology. In conclusion, audiological findings both in humans and mice show that loss of *MINAR2* function results in early-onset and sensorineural HL that rapidly progresses to severe to profound deafness.

The reduced number of stereocilia in the shortest row on outer hair cells would be expected to have a severe impact upon the number of transduction channel complexes available and suggests that the primary defect in these mutant mice is located at the top of the hair cell. However, we have demonstrated that

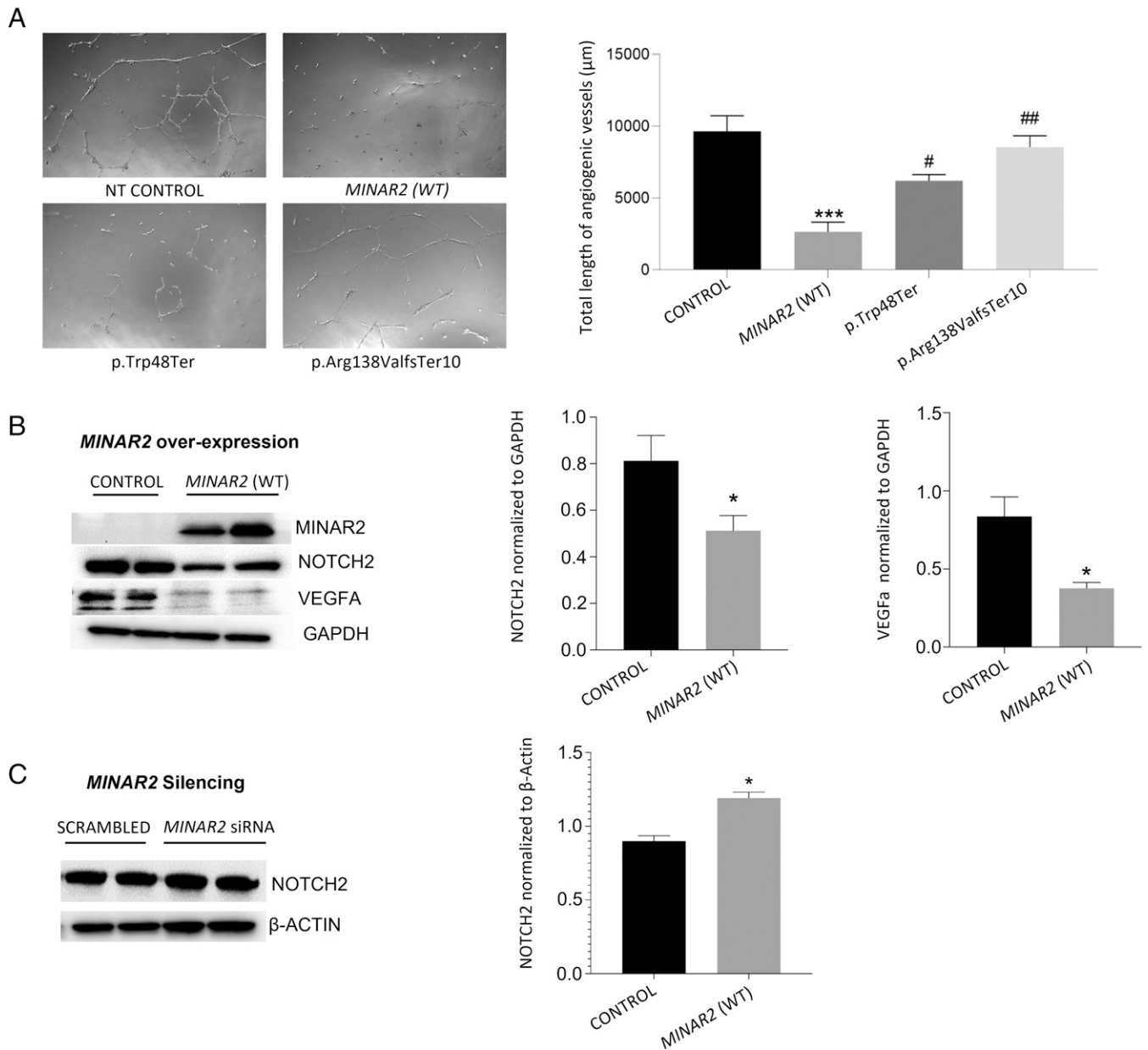


Fig. 8. Effects of *MINAR2* on angiogenesis, NOTCH2, and VEGFA. (A) Angiogenic potential of nontransfected (NT) HUVEC compared to cells transfected with *MINAR2* wild-type (WT), and *MINAR2* p.Trp48*, and p.Arg138Valfs*10 plasmid constructs. *Right* graph shows analysis of total length of angiogenic vessels formed after incubation of 12 h on Matrigel-coated wells; images were analyzed with ImageJ angioanalyzer and results are expressed as mean \pm SEM. Significant differences were shown as *** $P \leq 0.001$ when compared to control and as ## $P \leq 0.01$ when compared to *MINAR2*(WT). (B, *Left*) Immunoblot images showing the effect of *MINAR2*(WT) transient overexpression on NOTCH2 and VEGFA protein levels in HUVEC cells. (*Right*) Statistical analysis of GAPDH-normalized relative protein expressions of NOTCH2 and VEGFA. Results are expressed as mean \pm SEM and significant differences are shown as * $P \leq 0.05$ when compared to control. (C, *Left*) Immunoblot images of siRNA-induced *MINAR2* silencing on NOTCH2 protein levels in PC12 cells. (*Right*) β -Actin normalized relative protein expression of NOTCH2. Results are expressed as mean \pm SEM and significant differences are shown as * $P \leq 0.05$ when compared to control. Data were analyzed by one-way ANOVA with multiple comparisons.

the remaining MET channels are active in *Minar2^{tm1b/tm1b}* mice, since the hair cells of these mice are able to uptake FM1-43 dye. Degeneration of hair cells (Fig. 6) and synaptic defects (Fig. 5) occur later in development and cannot explain the raised ABR and DPOAE thresholds at 14 d old in the *Minar2^{tm1b}* homozygotes. Mutations of other genes also lead to loss of the shorter stereocilia associated with hearing impairment, for example the *Baiap2l2* mutant (28) and the *Clrn2* mouse mutant (29).

The Notch pathway is a highly conserved intercellular signaling cascade that is activated by the interaction of transmembrane ligands (Delta and Jagged) with Notch receptors, which are usually expressed on the surface of neighboring cells.

Binding of the Notch ligand to receptor induces cleavage of the Notch receptors intracellular domain, which binds to multiple DNA-binding proteins in the nucleus (30–32). In the initial stages of angiogenesis, Notch activation is generally repressed to allow proliferation of endothelial cells in response to VEGF stimulation, and its expression is later up-regulated when endothelial cells stop proliferating and the vessels begin to stabilize (33–39). While it is possible that the effects of *MINAR2* on angiogenesis may play a role in hearing, we did not observe abnormal vascular structures in the cochlea of homozygous mutant mice. Moreover, the most sensitive part of the cochlea to vascular function is the generation of EP by the stria vascularis. In this study, EP was within the normal range in

homozygous mutant mice. Our results show that MINAR2 and NOTCH2 have a regulatory relationship. In the mammalian cochlea, there is no regeneration of sensory hair cells and the strictly controlled pattern of alternating hair cells and supporting cells in the organ of Corti is set up in early development. Notch signaling is believed to be a critical part of the process of cells deciding their fate as a hair cell or a supporting cell and many genes involved in Notch signaling underlie hearing impairment (40, 41). As our examination of the organ of Corti of young mice shows (SI Appendix, Fig. S5), the pattern is set up correctly, ruling out an early developmental defect of cell fate or differentiation. However, Notch signaling may also play a role in longer-term maintenance of the organ of Corti, and our findings of progressive deterioration of this organ resulting from mutation of a gene known to be involved in Notch signaling supports this suggestion.

MINAR family proteins (MINAR1 and MINAR2) have been proposed to be associated with the inhibition of cell proliferation (13, 22). In this study, we did not observe any proliferation effect in different ages of *Minar2^{tm1b/tm1b}* mice. Terminal mitoses of hair cells occur early at E12 to E14 before birth (42). The confocal images illustrated in Fig. 6 all indicate loss of cells from the normal regular array, with no sign of any proliferation.

Our findings of an abnormal innervation pattern of hair cells as early as P1, as well as a significant decrease in the numbers of intact synapses at 4 wk old, suggest that abnormal innervation of hair cells may contribute to the severe auditory dysfunction in *Minar2^{tm1b/tm1b}* mice. Based on these findings, Minar2 may be playing a role in the maintenance of hair cell synapses. MINAR2 is structurally similar to MINAR1, which has been reported to be involved in controlling neurite formation during neuronal differentiation through DEP domain containing MTOR interacting protein (DEPTOR). In this study, we show that similar to MINAR1, MINAR2 down-regulates mTOR signaling (SI Appendix, Fig. S9B), which may contribute to the abnormal innervation pattern observed in the organ of Corti of *Minar2* mutant mice.

It is notable that although the sensory hair cells are present up to 4 wk old and are able to take up FM1-43 dye through transduction channels, they do not appear to be functioning normally as shown by the raised ABR and DPOAE thresholds. Most genetic and environmental causes of sensorineural HL lead to permanent loss of hair cells, reducing the chance of gene therapy or gene editing approaches. Progressive HL associated with a relatively normal appearance of hair cells in young ages makes *MINAR2* a promising target for genetic therapies. Further elucidation of its role in the maintenance of hair cell synapses and stereocilia bundles may open new avenues to treat more common forms of HL resulting from similar mechanisms.

Materials and Methods

More details of materials and methods are in SI Appendix.

Study Approval. This study was approved by the University of Miami Institutional Review Board (20081138-USA), as well as by the Ethics Committees of Ankara University Medical School (012413-Turkey) and Rajarshi Shahu College of Pharmacy (180720-India). A signed informed consent was obtained from all participants or, in the case of a minor, from the parents.

DNA Sequencing and Bioinformatics Analysis. Genome sequencing was performed in family 1 individuals II:1, II:2, and II:3 and family 2 II:1 (Fig. 1A and SI Appendix, Table S3) (43, 44). Reads were mapped to human genome reference (National Center for Biotechnology Information [NCBI] build37/hg 19 version) with Burrows-Wheeler aligner (BWA). Genome Analysis Toolkit (GATK) was

used for variant calling (45–47). CNVs were called using CNVnator (48). Enlis Genome Research software (<https://www.enlis.com/>) was used to identify runs of homozygosity in family 1 and family 2 from genome sequencing data (SI Appendix, Tables S4–S6).

Illumina Infinium Global Screening Array (GSA) v2 (Illumina) kit was used for genotyping in 16 members of family 3 and three members of family 4 to map the shared homozygous regions in affected individuals. Additional exome sequencing was performed on a HiSeq 2000 platform (Illumina), as described previously (49), in individuals IV:3 and IV:5 in family 3 and IV:1 in family 4 (SI Appendix, Table S3).

Genome sequencing data were deposited in the NCBI's BioProject database: PRJNA623118, BioSample: SAMN27763770 (family 1, individual II:1) and BioSample: SAMN27763769 (family 2, individual II:1).

Ethics Statement for Animals. Mouse studies in the United Kingdom were carried out in accordance with UK Home Office regulations and the UK Animals (Scientific Procedures) Act of 1986 (ASPA) under UK Home Office licenses, and the study was approved by the King's College London Ethical Review Committee. Mice were culled using methods approved under these licenses to minimize any possibility of suffering. All procedures in Miami were approved by the University of Miami Institutional Animal Care and Use Committee and followed the NIH guidelines "Using Animals in Intramural Research."

Mouse Generation. *Minar2^{tm1a}* mutant mice were generated at the Wellcome Sanger Institute by blastocyst microinjection of targeted embryonic stem (ES) cells on a C57BL/6N genetic background (50, 51). *Minar2^{tm1b(KOMP)Wtsi}* mice (*Minar2^{tm1b}*) were generated from *Minar2^{tm1a(KOMP)Wtsi}* mice by exposure of preimplantation embryos to soluble Cre recombinase (52), which leads to recombination between LoxP sites, removing the selection cassette and exon 2 to produce mice carrying the *Minar2^{tm1b}* allele (SI Appendix, Fig. S3). Both *tm1a* and *tm1b* alleles are available via the European Mouse Mutant Archive (EMMA; <https://www.infrafrontier.eu>).

Statistics. A one-way ANOVA with multiple comparisons was used to compare groups for count of synapses in mouse inner ear and also for angiogenesis, MAPK, and mTOR assays.

Data Availability. Sequencing data have been deposited in publicly accessible database, Family 1, II:1 (14) and Family 2, II:1 (15).

ACKNOWLEDGMENTS. We are immensely grateful to all the patients and families participating in this study. This study was supported by R01DC009645 and R01DC012836 from the NIH/National Institute on Deafness (M.T.), the National Institute for Health and Care Research Biomedical Research Centre, King's College London (K.P.S.), and the Royal National Institute for Deaf People (K.P.S.). This research was funded in part by the Wellcome Trust. For the purpose of Open Access, the author has applied a CC BY public copyright license to any Author Accepted Manuscript version arising from this submission. We thank the Wellcome Sanger Institute Mouse Genetics Project for generating and providing the *Minar2* mouse mutant. M.D. and G.H. would also like to express sincere gratitude for all the support provided by Dr. S. P. Jain, Principal, Rajarshi Shahu College of Pharmacy, Malvihar, Buldana, India.

Author affiliations: ^aDr. John T. Macdonald Foundation Department of Human Genetics, University of Miami Miller School of Medicine, Miami, FL, 33136; ^bWolfson Centre for Age-Related Diseases, King's College London, London, SE1 1UL, United Kingdom; ^cServicio de Genética, Hospital Universitario Ramón y Cajal, IRYCIS, 28034 Madrid, Spain; ^dCentro de Investigación Biomédica en Red de Enfermedades Raras, 28034 Madrid, Spain; ^eDepartment of Pharmacology, Rajarshi Shahu College of Pharmacy, 443001 Malvihar, Buldana, India; ^fOriental College of Pharmacy and Research, Oriental University, 453555 Indore, Madhya Pradesh, India; ^gJohn P. Hussmann Institute for Human Genomics, University of Miami Miller School of Medicine, Miami, FL 33136; ^hDepartment of Otorhinolaryngology, Faculty of Medicine, Dicle University, Diyarbakir 21200, Turkey; ⁱCardiovascular Institute and Department of Cardiothoracic Surgery, Stanford University School of Medicine, Stanford, CA, 94305; ^jDepartment of Audiology, Faculty of Health Sciences, Ankara University, Ankara 06100, Turkey; ^kCollege of Medicine and Health, University of Exeter Medical School, RD&E NHS Foundation Trust, Exeter, EX2 5DW, United Kingdom; ^lMolecular Biosciences Research Group, Faculty of Health and Society, University of Northampton, Northampton, NN1 5PH, United Kingdom; and ^mDepartment of Otolaryngology, University of Miami Miller School of Medicine, Miami, FL, 33136

Author contributions: M.T. designed research; G.B., M.L.-R., M.D., M.F.Z., C.A., M.Y.B., N.J.I., J.C., C.J.S., N.V., I.K., S.G., D.D., N.S., G.H., S.P.J., B.A.C., K.W., K.P.S., J.N., and M.T. performed research; G.B., M.L.-R., N.J.I., K.P.S., and M.T. contributed new reagents/

analytic tools; G.B., M.L.-R., M.D., M.F.Z., C.A., M.Y.B., N.J.I., J.C., C.J.S., N.V., I.K., S.G., D.D., N.S., G.H., S.P.J., B.A.C., K.W., K.P.S., J.N., and M.T. analyzed data; and G.B., M.L.-R., M.D., M.F.Z., C.A., N.J.I., N.V., G.H., K.W., K.P.S., J.N., and M.T. wrote the paper.

1. A. L. Mehl, V. Thomson, The Colorado newborn hearing screening project, 1992-1999: On the threshold of effective population-based universal newborn hearing screening. *Pediatrics* **109**, E7 (2002).
2. C. C. Morton, W. E. Nance, Newborn hearing screening—A silent revolution. *N. Engl. J. Med.* **354**, 2151-2164 (2006).
3. G. Van Camp, R. J. H. Smith, Hereditary Hearing Loss Homepage. <https://hereditaryhearingloss.org>. Accessed 1 December 2021.
4. R. L. Alford *et al.*; ACMG Working Group on Update of Genetics Evaluation Guidelines for the Etiologic Diagnosis of Congenital Hearing Loss; Professional Practice and Guidelines Committee, American College of Medical Genetics and Genomics guideline for the clinical evaluation and etiologic diagnosis of hearing loss. *Genet. Med.* **16**, 347-355 (2014).
5. A. M. Korver *et al.*, Congenital hearing loss. *Nat. Rev. Dis. Primers* **3**, 16094 (2017).
6. G. Bademci *et al.*, Comprehensive analysis via exome sequencing uncovers genetic etiology in autosomal recessive nonsyndromic deafness in a large multiethnic cohort. *Genet. Med.* **18**, 364-371 (2016).
7. J. Doll *et al.*, Genetic spectrum of syndromic and non-syndromic hearing loss in Pakistani families. *Genes (Basel)* **11**, 1329 (2020).
8. C. M. Sloan-Heggen *et al.*, Characterising the spectrum of autosomal recessive hereditary hearing loss in Iran. *J. Med. Genet.* **52**, 823-829 (2015).
9. D. Yan *et al.*, Spectrum of DNA variants for non-syndromic deafness in a large cohort from multiple continents. *Hum. Genet.* **135**, 953-961 (2016).
10. T. Atik, G. Bademci, O. Diaz-Horta, S. H. Blanton, M. Tekin, Whole-exome sequencing and its impact in hereditary hearing loss. *Genet. Res.* **97**, e4 (2015).
11. N. J. Ingham *et al.*, Mouse screen reveals multiple new genes underlying mouse and human hearing loss. *PLoS Biol.* **17**, e3000194 (2019).
12. B. Vona, I. Nanda, M. A. Hofrichter, W. Shehata-Dieler, T. Haaf, Non-syndromic hearing loss gene identification: A brief history and glimpse into the future. *Mol. Cell. Probes* **29**, 260-270 (2015).
13. R. X.-Y. Ho *et al.*, Loss of MINAR2 impairs motor function and causes Parkinson's disease-like symptoms in mice. *Brain Commun.* **2**, faa047 (2020).
14. M. Tekin, SRX15001233 Family 1, II:1. NCBI Sequence Read Archive. <https://www.ncbi.nlm.nih.gov/sra/SRX15001233>. Deposited 26 April 2022.
15. M. Tekin, SRX15001232: Family 2, II:1. NCBI Sequence Read Archive. <https://www.ncbi.nlm.nih.gov/sra/SRX15001232>. Deposited 26 April 2022.
16. K. J. Karczewski *et al.*; Genome Aggregation Database Consortium, The mutational constraint spectrum quantified from variation in 141,456 humans. *Nature* **581**, 434-443 (2020).
17. A. M. Oza *et al.*; ClinGen Hearing Loss Clinical Domain Working Group, Expert specification of the ACMG/AMP variant interpretation guidelines for genetic hearing loss. *Hum. Mutat.* **39**, 1593-1613 (2018).
18. S. Richards *et al.*; ACMG Laboratory Quality Assurance Committee, Standards and guidelines for the interpretation of sequence variants: A joint consensus recommendation of the American College of Medical Genetics and Genomics and the Association for Molecular Pathology. *Genet. Med.* **17**, 405-424 (2015).
19. R. Elkon *et al.*, RFX transcription factors are essential for hearing in mice. *Nat. Commun.* **6**, 8549 (2015).
20. J. Orvis *et al.*, gEAR: Gene Expression Analysis Resource portal for community-driven, multi-omic data exploration. *Nat. Methods* **18**, 843-844 (2021).
21. J. E. Gale, W. Marcotti, H. J. Kennedy, C. J. Kros, G. P. Richardson, FM1-43 dye behaves as a permeant blocker of the hair-cell mechanotransducer channel. *J. Neurosci.* **21**, 7013-7025 (2001).
22. R. X. Ho *et al.*, MINAR1 is a Notch2-binding protein that inhibits angiogenesis and breast cancer growth. *J. Mol. Cell Biol.* **10**, 195-204 (2018).
23. P. J. Lanford *et al.*, Notch signalling pathway mediates hair cell development in mammalian cochlea. *Nat. Genet.* **21**, 289-292 (1999).
24. W. Pan, Y. Jin, B. Stanger, A. E. Kiernan, Notch signaling is required for the generation of hair cells and supporting cells in the mammalian inner ear. *Proc. Natl. Acad. Sci. U.S.A.* **107**, 15798-15803 (2010).
25. A. F. Siekmann, L. Covassin, N. D. Lawson, Modulation of VEGF signalling output by the Notch pathway. *BioEssays* **30**, 303-313 (2008).
26. H. Zhang *et al.*, UBTOR/KIAA1024 regulates neurite outgrowth and neoplasia through mTOR signaling. *PLoS Genet.* **14**, e1007583 (2018).
27. D. Vaudry, P. J. Stork, P. Lazarovici, L. E. Eiden, Signaling pathways for PC12 cell differentiation: Making the right connections. *Science* **296**, 1648-1649 (2002).
28. A. J. Carlton *et al.*, Loss of Baiap212 destabilizes the transducing stereocilia of cochlear hair cells and leads to deafness. *J. Physiol.* **599**, 1173-1198 (2021).
29. L. A. Dunbar *et al.*, Clarin-2 is essential for hearing by maintaining stereocilia integrity and function. *EMBO Mol. Med.* **11**, e10288 (2019).
30. E. R. Andersson, R. Sandberg, U. Lendahl, Notch signaling: Simplicity in design, versatility in function. *Development* **138**, 3593-3612 (2011).
31. C. R. Chillakuri *et al.*, Structural analysis uncovers lipid-binding properties of Notch ligands. *Cell Rep.* **5**, 861-867 (2013).
32. F. M. Lu, S. E. Lux, Constitutively active human Notch1 binds to the transcription factor CBF1 and stimulates transcription through a promoter containing a CBF1-responsive element. *Proc. Natl. Acad. Sci. U.S.A.* **93**, 5663-5667 (1996).
33. A. M. Henderson, S. J. Wang, A. C. Taylor, M. Aitkenhead, C. C. Hughes, The basic helix-loop-helix transcription factor HESR1 regulates endothelial cell tube formation. *J. Biol. Chem.* **276**, 6169-6176 (2001).
34. F. Itoh *et al.*, Synergy and antagonism between Notch and BMP receptor signaling pathways in endothelial cells. *EMBO J.* **23**, 541-551 (2004).
35. K. G. Leong *et al.*, Activated Notch4 inhibits angiogenesis: Role of beta 1-integrin activation. *Mol. Cell Biol.* **22**, 2830-2841 (2002).
36. Z. Liu *et al.*, Notch1 loss of heterozygosity causes vascular tumors and lethal hemorrhage in mice. *J. Clin. Invest.* **121**, 800-808 (2011).
37. M. Nosedá *et al.*, Notch activation induces endothelial cell cycle arrest and participates in contact inhibition: Role of p21Cip1 repression. *Mol. Cell Biol.* **24**, 8813-8822 (2004).
38. K. L. Taylor, A. M. Henderson, C. C. Hughes, Notch activation during endothelial cell network formation in vitro targets the basic HLH transcription factor HESR-1 and downregulates VEGFR-2/KDR expression. *Microvasc. Res.* **64**, 372-383 (2002).
39. S. E. Williams, S. Beronja, H. A. Pasolli, E. Fuchs, Asymmetric cell divisions promote Notch-dependent epidermal differentiation. *Nature* **470**, 353-358 (2011).
40. E. C. Driver, M. W. Kelley, Development of the cochlea. *Development* **147**, dev162263 (2020).
41. R. Brown, A. K. Groves, Hear, hear for notch: Control of cell fates in the inner ear by notch signaling. *Biomolecules* **10**, 370 (2020).
42. R. J. Ruben, Development of the inner ear of the mouse: A radioautographic study of terminal mitoses. *Acta Otolaryngol.* **220** (Suppl), 1-44 (1967).
43. G. Bademci *et al.*, FOXF2 is required for cochlear development in humans and mice. *Hum. Mol. Genet.* **28**, 1286-1297 (2019).
44. C. Li *et al.*, Dysfunction of GRAP, encoding the GRB2-related adaptor protein, is linked to sensorineural hearing loss. *Proc. Natl. Acad. Sci. U.S.A.* **116**, 1347-1352 (2019).
45. M. A. DePristo *et al.*, A framework for variation discovery and genotyping using next-generation DNA sequencing data. *Nat. Genet.* **43**, 491-498 (2011).
46. H. Li, R. Durbin, Fast and accurate long-read alignment with Burrows-Wheeler transform. *Bioinformatics* **26**, 589-595 (2010).
47. A. McKenna *et al.*, The Genome Analysis Toolkit: A MapReduce framework for analyzing next-generation DNA sequencing data. *Genome Res.* **20**, 1297-1303 (2010).
48. A. Abyzov, A. E. Urban, M. Snyder, M. Gerstein, CNVnator: An approach to discover, genotype, and characterize typical and atypical CNVs from family and population genome sequencing. *Genome Res.* **21**, 974-984 (2011).
49. M. Jelani *et al.*, A mutation in the major autophagy gene, WIPI2, associated with global developmental abnormalities. *Brain* **142**, 1242-1254 (2019).
50. W. C. Skarnes *et al.*, A conditional knockout resource for the genome-wide study of mouse gene function. *Nature* **474**, 337-342 (2011).
51. J. K. White *et al.*; Sanger Institute Mouse Genetics Project, Genome-wide generation and systematic phenotyping of knockout mice reveals new roles for many genes. *Cell* **154**, 452-464 (2013).
52. E. Ryder *et al.*; Sanger Mouse Genetics Project, Rapid conversion of EUCOMM/KOMP CSD alleles in mouse embryos using a cell-permeable Cre recombinase. *Transgenic Res.* **23**, 177-185 (2014).

REVIEW ARTICLE

Polymeric Nanoparticles: Prospective on the Synthesis, Characterization and Applications in Nose-to-Brain Drug Delivery

Prakash N. Kendre^{1,*}, Dhiraj R. Kayande¹, Shirish P. Jain¹, Tejaswini G. Malge¹, Namrata N. Zadpe¹ and Bhupendra G. Prajapati²

¹Rajarshi Shahu College of Pharmacy, Buldana Maharashtra, 443001, India; ²S. K. Patel College of Pharmaceutical Education and Research Ganpat University, Ganpat Vidya Nagar, Mehsana, Gujarat 384012, India

Abstract: For the treatment of brain illnesses, there is growing interest in nose-to-brain drug administration. Other, more traditional methods of crossing the blood–brain barrier (BBB) are ineffective. As a result, the therapeutic concentration in the brain cannot be achieved, and the reaction is inadequate. Intranasal medication delivery is one intriguing technique for avoiding first-pass metabolism and bypassing the blood-brain barrier. It lowers medicine doses while reducing systemic side effects. Compared to conventional drug delivery platforms, a nanoparticulate drug delivery method allows for greater penetration via the nasal route. It is better to make the nanoparticles for nose-to-brain administration when a good carrier (polymers) is used. This review focuses on the many processes for creating polymeric nanoparticles, strategies and tactics for improving nose-to-brain drug delivery efficiency, and nanoparticle characterization. The use of the nose-to-brain drug delivery platform is being explored using a variety of nanoparticles created by researchers for the treatment of brain illnesses.

ARTICLE HISTORY

Received: May 18, 2022
Revised: July 17, 2022
Accepted: September 01, 2022

DOI:
10.2174/1573413718666220929102013

Keywords: Polymeric nanoparticles, synthesis, blood-brain-barrier, brain diseases, techniques

1. INTRODUCTION

Aside from being a leading cause of death and disability worldwide, brain problems are chronic and lifelong illnesses [1]. Because of the protective coverings of the brain, namely the blood–brain barrier, medical treatment of brain illnesses is a major issue for scientists and researchers (BBB). Because of their enormous molecular weights, most therapeutic and diagnostic agents are unable to diffuse through the BBB, and even tiny molecules (98%) are not transported through it [2, 3]. Drugs can be administered intranasally to prevent first-pass metabolism and gastrointestinal degradation, bypassing the BBB. Nasal administration of drug-loaded nanoparticles is another option for increasing efficiency. Drugs can be delivered directly to the brain by taking a nasal route. This might make it possible to treat mental illnesses [3, 4].

In 1959, Nobel Laureate Richard P. Feynman proposed the concept of nanotechnology. Nanotechnology is used to generate nanoparticles (NPs) from a variety of materials, including particulates. Solid particles with 1-100 nm dimensions are known as nanoparticles [4]. For delivering medications to target areas, several forms of drug-loaded nanoparticles have been created, including nanoemulsions, nanotubes,

liposomes, micelles, dendrimers, and quantum dots [5, 6]. Aside from their small size, nanoparticles exhibit special features. They are target-specific and have a high surface-to-volume ratio. Nanoparticles with polymer coatings can pass through the BBB [7]. As a result, nanoparticles are widely used in the treatment of a variety of brain disorders.

The medication for brain disease is difficult. After all, 98% of current pharmaceutical products are stopped by a protective barrier [7, 8]. The brain is the most complex organ and is separated from the other parts by strong barriers. The three barriers that protect the brain are

- The BBB, consists of a highly specialized endothelial barrier
- The blood-cerebrospinal fluid (CSF) barrier with the choroid plexus epithelium
- The arachnoid epithelium

These protective barriers prevent the entry of harmful and toxic agents as well as therapeutic and diagnostic agents into the brain [8]. Nanoparticles can enter the brain directly or indirectly after nasal administration. Transportation of molecules to the brain occurs by two pathways:

- The trigeminal neural pathway
- The olfactory neural pathway

*Address correspondence to this author at the Rajarshi Shahu College of Pharmacy, Buldana, Maharashtra, 443001, India; Tel: +919890506016; Fax: +912423222862; E-mail: prakashkendre@gmail.com

Some drugs can enter the blood circulation and are transported across the BBB into the brain [4]. Along the trigeminal neural pathway, molecules are transported by axonal transport or endocytosis. The trigeminal nerve is the fifth cranial nerve. It has three major branches [8, 9]:

- The ophthalmic nerve
- The maxillary nerve
- The mandibular nerve

In nose-to-brain delivery, the ophthalmic and maxillary nerves play a big part. The paracellular or transcellular method moves chemicals along the olfactory pathway. Olfactory receptor neurons are found in the mucosa of the olfactory epithelium and carry chemicals quickly to the brain. The process of transport from the nose to the brain is yet unknown. Fig. 1 [8, 9] shows a schematic illustration of nanoparticulate medication delivery.

The intranasal nose-to-brain delivery mechanism is the subject of this investigation. The various methods of nanoparticle preparation, strategies, and distinct approaches to drug delivery and nanoparticle characterization are explored within this broad topic. This review's main goal is to overview how nose-to-brain medication delivery systems can help people with brain illnesses get better.

2. SYNTHETIC TECHNIQUES FOR POLYMERIC NANOPARTICLES

Nanomaterials are synthesized or prepared using a variety of techniques. It's crucial to choose the right procedure, which is determined by the material's physicochemical prop-

erties. The top-down and bottom-up approaches to synthesis are the two main methodologies.

2.1. Top-down Approach

The top-down method entails using an external force to break down bigger chunks of heavy material into smaller chunks. This is a crucial technique in terms of business. Wet ball milling, high-pressure homogenisation, jet milling, laser sputtering, nanolithography, sputtering, thermal breakdown, and so on are all part of the top-down approach.

2.2. Bottom-up Approach

The required structure is constructed from atoms, molecules, or clusters under specific conditions in the bottom-up technique. The bottom-up strategy is used in methods like precipitation, chemical vapour deposition (CVD), pyrolysis, the sol-gel method, spinning, and biosynthesis [10]. Fig. 2 shows a classification of nanoparticles synthesis methods [11, 12]

2.3. Physical Method

The top-down strategy is used in physical approaches to nanoparticles production. Materials are abraded, melted, evaporated, or condensed using mechanical pressure, electric and thermal energy, and high-energy radiation. These technologies have the advantages of being solvent-free, toxic-chemical-free, and producing nanoparticles of consistent size and shape in a short amount of time. They use a lot of energy, need high temperatures and pressures, aren't very productive, are expensive, and don't make very stable nanoparticles.

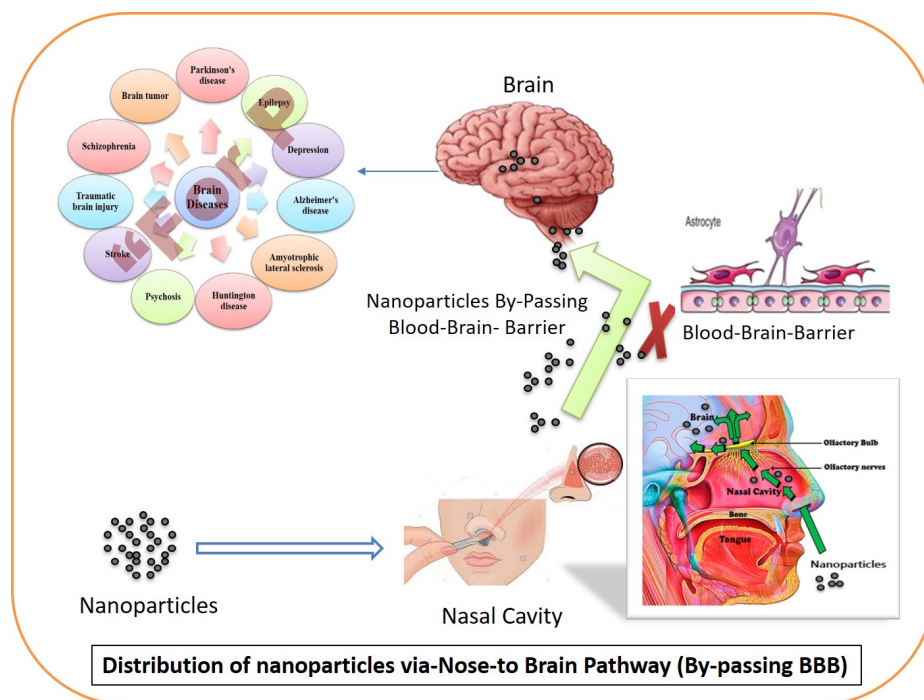


Fig. (1). Schematic presentation of nanoparticles distribution via nose-to-brain route; Selvaraj K, Gowthamarajan K, Karri VVSR (2017). (*A higher resolution / colour version of this figure is available in the electronic copy of the article*).

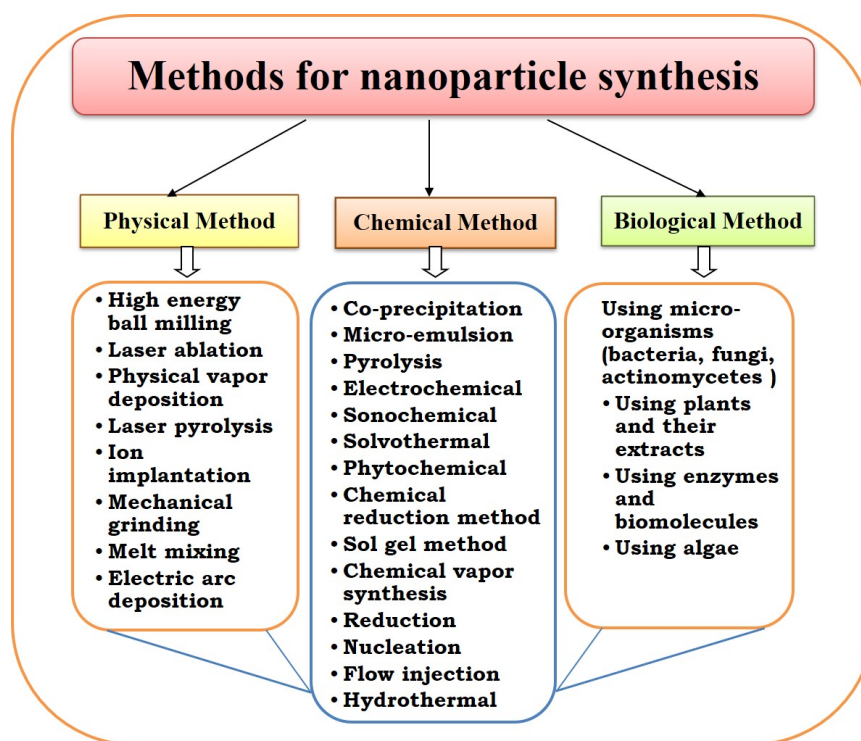


Fig. (2). Various methods used for the synthesis of nanoparticles; Patra JK, Baek K-H (2014). (A higher resolution / colour version of this figure is available in the electronic copy of the article).

2.4. Chemical Methods

The bottom-up approach to nanoparticles synthesis is chemical methods. Cost-effectiveness, ease of functionalization, thermal stability, high yield, and reduced dispersion are only a few of the advantages of this approach. The downsides include the use of harmful chemicals, a lower level of purity, and human health risks. Chemical reduction, sol-gel synthesis, sono-chemical synthesis, solvothermal synthesis, coprecipitation, the microemulsion method, and pyrolysis are some of the most extensively used chemical processes for nanoparticles synthesis [13].

2.5. Biological Methods

In contrast to physical and chemical processes, biological synthesis is environmentally beneficial. Microorganisms, enzymes, algae, viruses, plants, and biomolecules are used to synthesise nanoparticles. As a result, these techniques are referred to as "green synthesis techniques." The bottom-up strategy is used in these techniques. Reducing and stabilising substances found in microbes and plants are used in the synthesis [11]. They mostly make nanoparticles by breaking down chemicals found in microbes and plants, like amines, alkaloids, proteins, enzymes, phenolic compounds, and pigments, to make them smaller [14].

Nontoxicity, reproducibility in manufacturing, well-defined morphology, ease of scaling up, and lower energy requirements are all advantages of biological processes, which are environmentally beneficial. They're also free of potentially dangerous and costly chemicals [15].

2.6. Emulsion-solvent Evaporation Methods

The most prevalent ways of preparing nanoparticles are as follows. They're exclusively used for medications that aren't easily dissolved in water. The following steps are involved in emulsion-solvent evaporation: (1) to make an organic solution, the medication and polymer must first be dissolved in an organic solvent. (2) A surfactant or aqueous solution of a stabiliser is created in the second step. (3) The emulsification process is the third phase, in which the already prepared organic solution is dropped dropwise into the aqueous solution under the high shearing force of the homogeniser, resulting in an O/W (oil-in-water) type of emulsion. (4) The fourth step is solvent evaporation, which is done in a rotary evaporator with the organic solvent evaporated first and then the drug-loaded nanoparticles precipitated. (5) Ultracentrifugation is the fifth stage, which involves collecting the precipitated nanoparticles and washing them with distilled water to eliminate any residue. (6) Lyophilisation, a freeze-drying method, is the final step. In the final step, water is evaporated, and the dry nanoparticles are collected as a powder (Fig. 3). These procedures [16] have been modified by high-pressure emulsification and the solvent evaporation method. Because they only require mild conditions and continual stirring, emulsion-solvent evaporation methods are preferred over other methods. As a result, a stable emulsion can be made without interfering with the drug's activity [17].

Using the emulsion-solvent evaporation approach, the researchers created HupA-loaded lactoferrin coupled N-trimethylated chitosan nanoparticles (HupALf-TMC NPs).

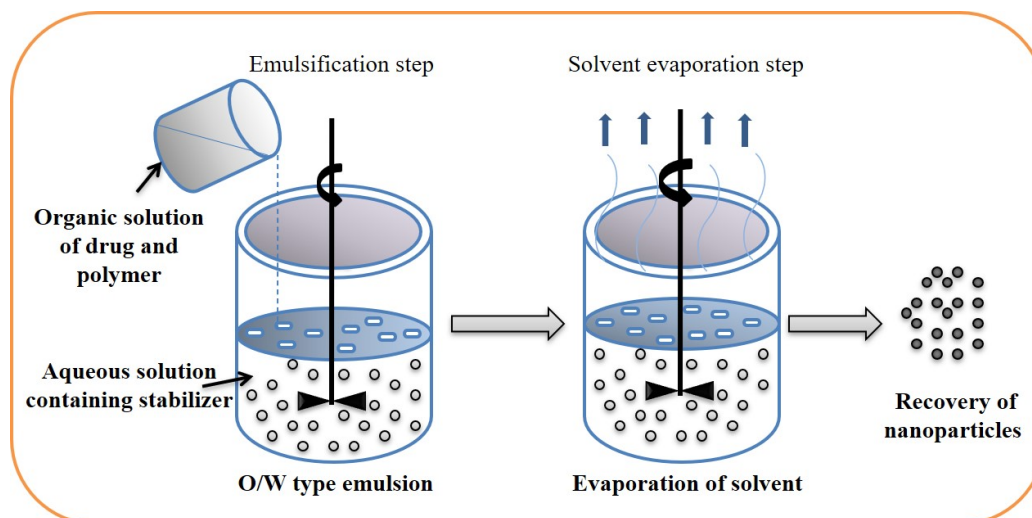


Fig. (3). Emulsion-solvent evaporation method for nanoparticles synthesis; Pal SL JUMP *et al.* (2011). (A higher resolution / colour version of this figure is available in the electronic copy of the article).

Their goal was to create an intranasal delivery system for HupA that could efficiently transfer the protein to the brain and cure Alzheimer's disease. Polylactide-co-glycoside was the polymer employed to make these nanoparticles (PLGA). The preparation included co-modification with lactoferrin (Lf) and N-trimethylated chitosan (TMC). TMC modification was thought to boost nasal adhesion and retention time. The conjugation of Lf was supposed to make drug administration from the nose to the brain easier. Using the Box-Behnken design, the nanoparticles were optimised. The nanoparticles' particle size, zeta potential, size distribution, entrapment efficiency, and polydispersity index (PDI) were all calculated. Biodistribution research and *in vitro* drug release tests were also conducted. The nanoparticles provided a good long-term release. The nasal adhesion and the capacity to target the brain were both excellent. The Lf-TMC NPs were found to be a promising nose-to-brain medication delivery method based on the drug's distribution profile in the brain [18].

2.7. Ionic Gelation Methods

In an ionic gelation technique, a positively or negatively charged hydrophilic molecule interacts with a cation or anion to generate a strongly cross-linked structure. As a result of this process, which produces very sticky gel particles, nanoparticles are formed. A drug-polymer solution is made by mixing the drug and polymer in distilled water. Drop by drop, stirring constantly, pure water is added. It is possible to obtain an opalescent suspension. The suspension is then centrifuged to obtain the nanoparticles. Fig. 4 shows lyophilization nanoparticles using an appropriate cryoprotectant [19]. The most common polymers used in ionic gelation procedures are chitosan and alginate. Other polymers include dextran, carboxymethyl cellulose, gelatine, collagen, hyaluronic acid, pectin, carbopol 934P, gum, and others [20].

Using an ionic gelation process, the researchers created bromocriptine (BRC)-loaded chitosan nanoparticles (CS NPs). Their goal was to look at the role of chitosan nanopar-

ticles in a nose-to-brain drug delivery system and see how they could improve bromocriptine's brain targeting efficiency. The nanoparticles were made from chitosan (a polymer) and sodium tripolyphosphate (cross-polymer). Pharmacodynamic, biodistribution, and pharmacokinetic experiments were conducted on Swiss albino mice. The nanoparticles were measured for particle size, polydispersity index, zeta potential, entrapment efficiency, and drug-loading capacity. Bromocriptine absorption in the brain was boosted by using nanoparticles. In addition, the antioxidant activity was improved. This technique for delivering drugs to the brain could be useful in the treatment of Parkinson's disease [21].

Using an ionic gelation technique, researchers synthesised and assessed RAS-loaded chitosan glutamate nanoparticles (CG-NPs). The researchers wanted to see if the nose-to-brain pathway was more effective than the intravenous approach for delivering medicines to the central nervous system (CNS). Chitosan glutamate (CG) was employed as the polymer, and sodium tripolyphosphate was used as the cross-polymer (STPP). The sodium anions of the sodium tripolyphosphate cause ionic gelation of CG, which results in CG-NPs. characterization of the produced nanoparticles *In vitro* drug release research was conducted after determining their particle size, size distribution, zeta potential, encapsulation efficiency, and polydispersity index. Following intranasal treatment, these nanoparticles greatly increased RAS bioavailability in mice's brains. Parkinson's disease may benefit from intranasal delivery [22].

2.8. Double Emulsion-solvent Evaporation Method

Methods of two-step emulsification include double emulsion-solvent evaporation. Both hydrophilic and hydrophobic medicines can be made with them. This approach is also known as "emulsions of emulsions" because the dispersed phase droplets are made up of smaller dispersed phase droplets, which are usually polydisperse in size. There are two types of common double emulsions:

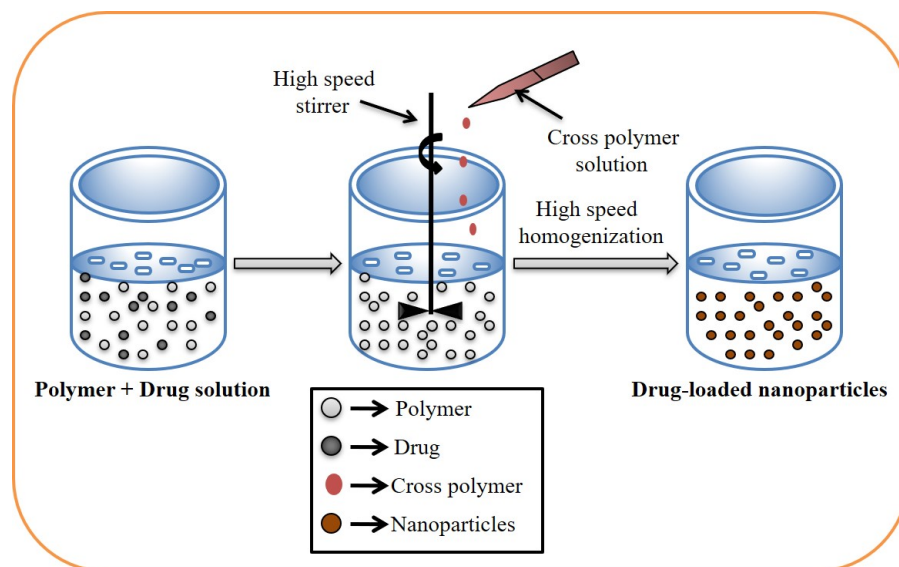


Fig. (4). Ionic-gelation method for nanoparticles synthesis; Patra JK, Das G, Fraceto LF, *et al.* (2018). (A higher resolution / colour version of this figure is available in the electronic copy of the article).

- Water–oil–water (W/O/W)
- Oil–water–oil (O/W/O)

A two-step emulsification technique is used to create nanoparticles in these procedures. The hydrophilic medications are added to the watery inner phase (W) first, followed by the infusion of polymer/hydrophobic pharmaceuticals into the organic phase, i.e., the oil phase (O). A primary emulsion (W/O) is created by homogenising the two phases. This primary emulsion is emulsified with the aqueous phase (W), which contains a stabiliser, in the second step to generate a double emulsion (W/O/W). The dispersed phase's solvent is next ejected and evaporated. As shown in Fig. 5, the polymer encasing the active ingredient hardens as a result.

Poly(lactic acid) (PLA), poly(lactic-co-glycolic acid) (PLGA), and polycaprolactone are the most prevalent polymers utilised in double emulsion–solvent evaporation processes (PCL). Poly(vinyl alcohol) (PVA), Tween 80, and Span 80 are some of the most regularly used stabilisers [23].

Alex *et al.* (2014) created carboplatin-loaded poly(caprolactone) (PCL) nanoparticles using a two-step emulsion–solvent evaporation method, W/O/W was the sort of emulsion that resulted. The polymer used for encapsulating carboplatin was polycaprolactone, which regulates drug release and boosts anticancer efficacy. The nanoparticles were measured in terms of size, zeta potential, entrapment efficiency, polydispersity index, scanning electron microscopy, and *in vitro* drug release profiles. The nanoparticles had a small particle size, a spherical shape, high entrapment efficiency, improved nasal absorption, and a long release profile. They could be employed in a carboplatin delivery system [24].

2.9. Nanoprecipitation Methods

Solvent displacement techniques are another name for nanoprecipitation. Polymeric nanoparticles are primarily

synthesised using these methods. Fig. 6 shows how the approach works: pre-formed polymer precipitation from an organic solution and organic solvent diffusion into the aqueous medium in the presence or absence of a surfactant. Nanoprecipitation is mostly employed for hydrophobic medicines since the solvents used are particularly miscible with the aqueous phase [25]. Nano-capsules can also be created by adding a small amount of harmless oil to the organic phase [19]. These techniques produce submicron (210 nm) nanoparticles. The size depends on the rate of addition of the organic phase to the aqueous phase and the low polydispersity index value [17].

2.10. Salting-out Methods

The separation of the water-soluble solvent from the aqueous phase is the basic concept behind these approaches. These techniques are variations of emulsification–solvent diffusion techniques [26].

An API and a polymer are dissolved in solvents to make a solution. After that, the solutions are emulsified into an aqueous gel that includes a colloidal stabiliser and a highly concentrated salting-out agent. The sort of emulsion that forms is O/W. It's diluted with enough water to lower the salting-out agent's concentration and increases the solvent's diffusion into the aqueous phase, resulting in nanosphere formation. Fig. 7 shows how cross-flow filtering removes the solvent and salting-out agent. The salting-out agent should be chosen carefully because it affects the drug's encapsulation efficiency [25].

3. POLYMERIC NANOPARTICLES FORMULATION APPROACHES

In the treatment of neurological illnesses, nanocarriers are utilised to carry medications across the BBB. Liposomes, solid-lipid nanoparticles, nanoemulsions, carbon nanotubes, dendrimers, micelles, and quantum dots are only a few **185**

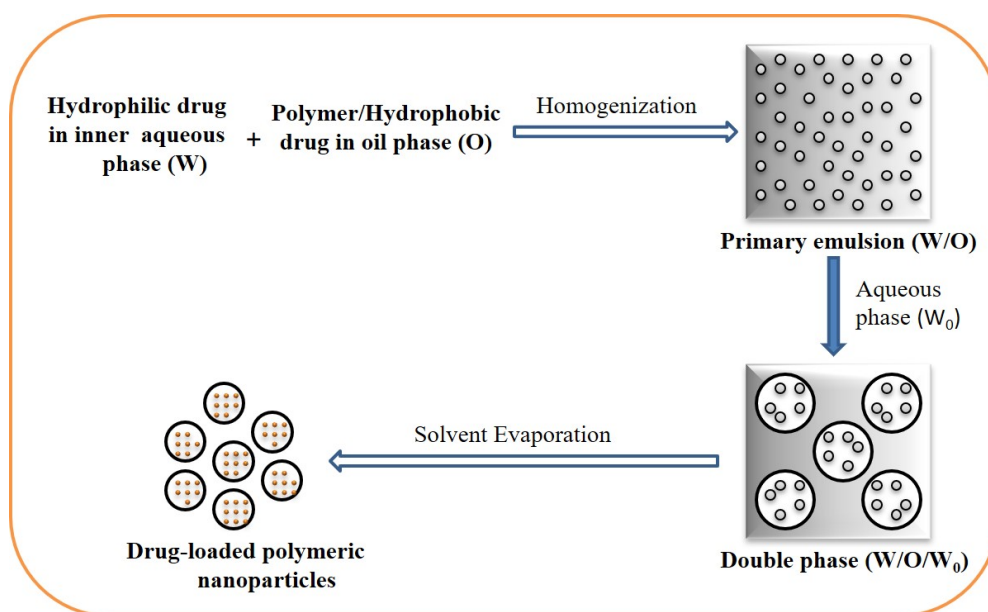


Fig. (5). Double emulsion-solvent evaporation method for nanoparticles synthesis; Iqbal M, Zafar N, Fessi H, Elaissari A (2015). (A higher resolution / colour version of this figure is available in the electronic copy of the article).

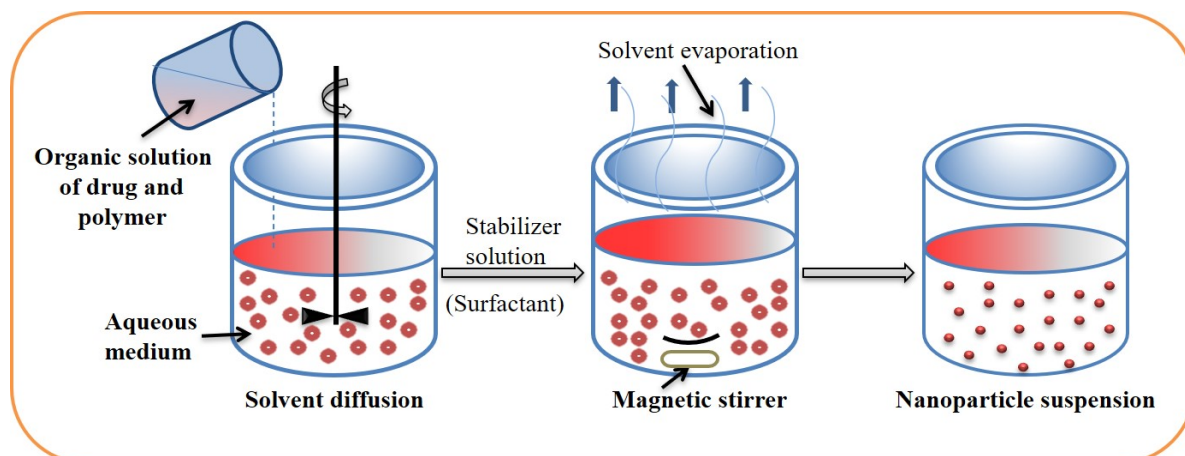


Fig. (6). Nanoprecipitation method of preparation for nanoparticles; Nagavarma BVN YHAA et al. (2012). (A higher resolution / colour version of this figure is available in the electronic copy of the article).

amples of biodegradable and biocompatible nanocarriers. These nanocarriers are utilised to increase the drug's stability and retention period while reducing adverse effects and toxicity. Conjugation or entrapment in the carrier system allows the medications to be absorbed. Because it improves nasal permeability, the nanocarrier technology has many uses in intranasal nose-to-brain transport.

3.1. Solid-lipid Nanoparticles

SLNs are spherical colloidal nanocarriers made of solid-lipid nanoparticles. They're about 50–100 nm in size. They're lipid-based nanoparticles that can be used instead of emulsions, liposomes, or nanoparticles [27]. An exterior surfactant layer stabilises the solid-lipid core matrix of these nanoparticles. A diglyceride, triglyceride, fatty acid, sterol, or wax can be used as a lipid [3]. Both lipophilic and hydro-

philic medicines can be included in SLNs. They are more effective at targeting, encapsulation, and stability. They are non-toxic, and they don't require the use of organic solvents to make them [28].

3.2. Polymeric Nanoparticles

Polymeric nanoparticles are colloidal particles with diameters ranging from 60 to 200 nanometers in diameter. Polymeric nanoparticles can be used to prolong medication release and intracellular absorption. Polymers utilised to make polymeric nanoparticles must be biodegradable, biocompatible, and non-toxic. Some of the most commonly used polymers are poly (lactide co-glycolides), polyglycolides, polylactides, polyanhydrides, polycaprolactone, and poly (cyanoacrylates) [28, 29].

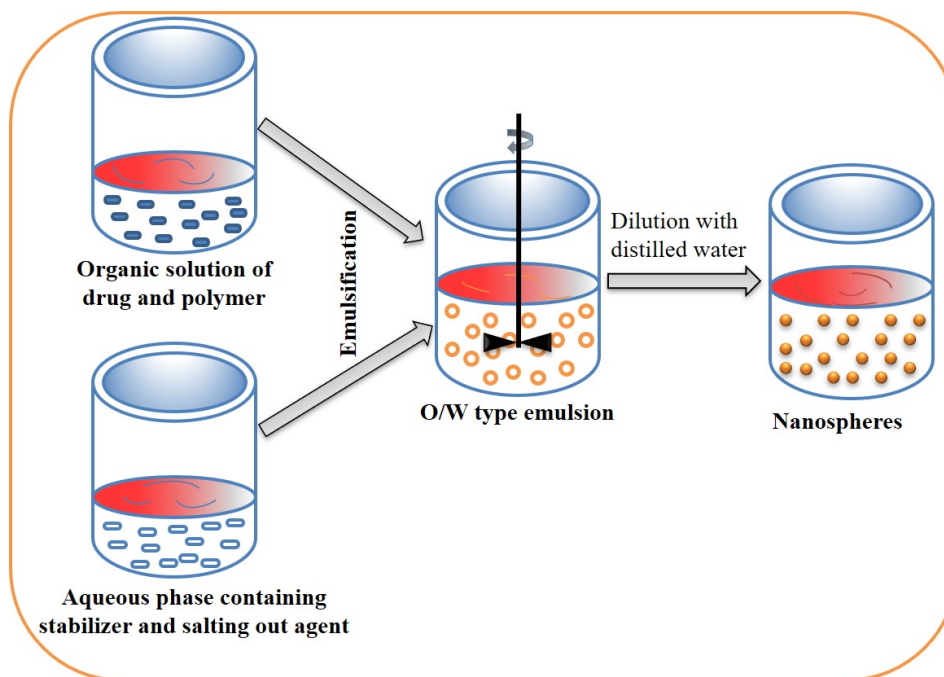


Fig. (7). Salting-out method for Schematic presentation of nanoparticles distribution via nose-to-brain route; Nagavarma BVN YHAA *et al.* (2012). (A higher resolution / colour version of this figure is available in the electronic copy of the article).

3.3. Nano-emulsions

Colloidal dispersions of two immiscible liquids stabilised by a surfactant are known as nano-emulsions. Nano-sized droplets (20–200 nm) are disseminated in a continuous phase. Nano-emulsions come in three varieties:

- a. oil-in-water (O/W)
- b. water-in-oil (W/O)
- c. bi-continuous nano-emulsion

Nano-emulsions have a number of advantages, including increased drug bioavailability, lipophilic drug solubility, and physical stability [30, 31]. A nano-emulsion is resistant to destabilising events such as coalescence, creaming, and sedimentation because of the size (nano-sized) of the droplets [5].

3.4. Liposomes

Liposomes are spherical vesicles with one or more lipid bilayers surrounding a central core. Phospholipids, sphingolipids, polymeric polymers, and synthetic phospholipids are biocompatible, biodegradable lipids that make up a lipid bilayer [32]. Liposomes can be used to encapsulate hydrophilic and lipophilic medicines. Lipophilic medications are entrapped in the liposomal lipid bilayer, while hydrophilic pharmaceuticals are enclosed in the central core [33]. Liposomes work well as diagnostic and therapeutic carriers. Polymers, polysaccharides, peptides, antibodies, and aptamers can be used to change the surface of a liposome, which can improve blood flow and the delivery of medications to the brain [34].

3.5. Dendrimers

Dendrimers are globular macromolecules with tree-like architectures that are synthesised at the nanoscale. Dendrimer comes from the Greek words dendron, which means "tree," and meros, which means "part." Three main components make up the three-dimensional dendrimer structure [35, 36]:

- An inner core
- Repeating branching units called 'generations'
- Outer functional groups

Dendrimers with a lot of branches can hold a lot of medicine. Divergent and convergent techniques are the most popular ways to create dendrimers. Poly (amidoamine) (PA-MAM) dendrimers, poly (propylene imine) (PPI) dendrimers, poly-L-lysine (PPL) dendrimers, and phosphorus (PPH) dendrimers are among the dendrimers used for drug delivery to the brain [37].

Nasal delivery of dendrimers has a number of benefits, like making the drug more water-soluble, making it easier for the drug to get to the brain, and making it easier for the drug to move across the blood-brain barrier [35].

3.6 Mesoporous silica Nanoparticles (MSNs)

Drug targeting platforms made of mesoporous silica nanoparticles are promising. These particles can hold a considerable amount of medication due to their porous nature (pore volume > 0.9cm³/g) and vast surface area (300–1000 m²/g). The medication can be entrapped in the pores of the micron-to nano-sized porous structure, which serves as a reservoir

for drug release to the appropriate administration site. Tissue engineering, diagnostics, and therapies are just a few of the biomedical applications of MSNs. MSNs have recently been discovered to be particularly effective for nose-to-brain targeting, allowing for regulated drug administration. Chemically and thermally, these nanoparticles are inert. They have high biocompatibility and low negative effects.

Inorganic compounds like silicon oxide are used to make MSNs. MSNs are made using a variety of techniques, including sol-gel, chemical etching, microwave-assisted processes, and so on. Depending on the raw materials utilised, MSNs have diverse geometric structures.

Particle size, shape, porosity, pore volume, surface area, drug loading, surface functionalization, and other factors all contribute to the overall characteristics of MSNs. In 2007, Mohanraj and Chen effectively synthesised mesoporous silica nanoparticles loaded with poorly soluble curcumin and chrysin for nose-to-brain transport. Spherical MSNs with a diameter of 220 nm were found to be effective in crossing the BBB and delivering medicines into the CNS [38].

4. CHARACTERIZATION OF NANOPARTICLES

The size, shape, surface charge, drug loading capacity, and encapsulation efficiency of nanoparticles are all factors that influence their effectiveness. Identifying nanoparticles can be done in a variety of ways. For example, electron microscopy is used to determine the particle size and shape.

4.1. Particle Size

The two primary factors investigated in nanoparticles characterization are particle size and particle size distribution. The size of nanoparticles affects their stability, encapsulation effectiveness, and drug loading capacity. The surface-to-volume ratios of smaller particles are higher. Due to the huge surface area available for absorption, nanoparticles can be absorbed quickly. Larger particles, on the other hand, encapsulate better and diffuse more slowly. During storage and transportation, smaller particles are more likely to aggregate than bigger particles [39]. The following are some of the methods for determining particle size [40]:

- Dynamic light scattering (DLS) or photon-correlation spectroscopy
- Scanning electron microscopy
- Transmission electron microscopy
- Atomic force microscopy
- Laser scattering techniques
- X-ray scattering techniques
- Centrifugation techniques

4.2. Percentage Yield

Preparation, collection, and weighting of nanoparticles are all done with precision. The following formula [41] is used to compute the percentage yield:

$$\% \text{ Yield} = \frac{\text{Weight of prepared nanoparticles}}{\text{Total weight of drug and polymer}} \times 100 \quad \dots \quad (1)$$

4.3. Surface Charge

The surface charge of nanoparticles affects their absorption on the cell membrane, which is a key element in delivery efficacy. To represent the surface charge of nanoparticles, the zeta potential is used [42]. If aggregation is to be avoided and nanoparticles are to remain stable, they must have high zeta potential values (either positive or negative). The zeta potential reveals the composition of the core material and coating [16]. Electroacoustic determination and electrophoretic light scattering are used to determine the zeta potential [43].

4.4. Drug Loading and Encapsulation Efficiency

Drug loading is defined as the amount of drug bound per mass of the polymer. Drug loading is achieved by:

- Incorporating the drug at the time of production (incorporation method)
- Adsorption or absorption

The amount of drug loaded into nanoparticles is determined by the following given equations:

$$\% \text{ Drug loading} = \frac{\text{Total weight of drug in particles}}{\text{Total weight of particles}} \times 100 \quad \dots (2)$$

The encapsulation efficiency (EE) is defined as the percentage of drug encapsulated within nanoparticles as a percentage of the polymer. The amount of free drug present in the supernatant is evaluated using the HPLC technique after nanoparticles have been dissolved in a suitable solvent. The following equation is used to compute the encapsulation efficiency:

$$\% \text{ EE} = \frac{\text{Initial amount of drug} - \text{Amount of free drug present in supernatant}}{\text{Initial amount of drug}} \times 100 \quad \dots (3)$$

Nanoparticles should have a high capacity for drug loading and encapsulation. The solid-state solubility of the drug in the polymer medium affects both how well the drug is encapsulated and how much of it is in the finished product [44].

4.5. Drug Release

The behaviour of nanoparticles is determined by the drug release. Under sink circumstances, drug release is achieved through diffusion or matrix degradation. The solubility, diffusion, and degradation of the nanoparticles' matrix are all factors that affect drug release [45]. The most popular method for studying drug release in vitro is dialysis. A dialysis membrane is used in this procedure to separate the nanoparticles. The following are examples of dialysis techniques:

- Dialysis bag diffusion method
- Reverse dialysis bag diffusion method
- Side-by-side diffusion method

In the dialysis bag diffusion method, nanoparticles are delivered into a dialysis bag (inner compartment) filled with media, which is then sealed. The inner compartment is housed in a huge media-filled exterior chamber. The inner

compartment has a smaller volume (1–10 mL) than the outer compartment (40–90 mL). A dialysis membrane is used to divide the two compartments. To decrease the effects of unstirred water layers, agitation is used. Through the dialysis membrane, the medication diffuses from the inner to outer compartments. For dialysis, the sample is taken out of the outer compartment. The nanoparticles are placed in the outer and inner compartments, and the drug release is sampled using the reverse dialysis procedure. A donor cell and a receiver cell with equal quantities of media and a magnetic stirrer comprise the side-by-side dialysis system. The sample is taken from the receiver cell, and a vertical Franz diffusion cell after a dialysis membrane separates the donor and receiver cells [46].

5. STABILITY STUDIES

Nanoparticles should be tested in terms of transport and storage. Long-term stability testing at 25°C/2°C, and 60% relative humidity are advised by the International Conference on Harmonization (ICH) on fast stability at 40°C/2°C and 5% relative humidity 5% RH [47]. Furthermore, the stability of the produced nanoparticles should be examined based on their physical and chemical characteristics. In vivo stability testing can be used to see how a nanoparticle formulation will work.

6. APPLICATIONS IN NOSE-TO-BRAIN DRUG DELIVERY

Many vital lifesaving treatments are delivered using nanoparticles, which is a difficult task. Many researchers have helped create and produce nanoparticles for the treatment of various ailments. It highlights the role of nanoparticles in medication delivery via nose-to-brain.

7. NANOPARTICLE CYTOTOXICITY AND MITIGATION TECHNIQUES

7.1. Limitations of Nanoparticles in Nose-to-brain Delivery

The intranasal approach is non-invasive and has numerous medical advantages. Intranasally given formulations have a faster onset of action and higher bioavailability, as well as avoid first-pass metabolism and have fewer adverse effects. Intranasal delivery, however, has a number of drawbacks, including limited permeability, enzymatic degradation, muco-ciliary clearance, and short retention periods [48]. Intranasal administration is a simple and easy alternative to conventional routes. Intranasally, however, only very minute amounts of a formulation can be given. As a result, only very effective medications can be given [49–51]. A variety of procedures are employed to improve a drug's absorption and permeability. Absorption enhancers help drugs go through the nasal mucosa more quickly [52]. Mucoadhesive systems, such as mucoadhesive polymers, viscous formulations, in situ gelation, and hydrogels, have improved retention time [53]. Some medications can irritate the nasal mucosa, putting the cilia of the nasal mucosa in jeopardy. The biological reaction to nanoparticles is altered, resulting in neurotoxicity.

7.2. Cytotoxicity of Nanoparticles

It is well established that certain nanoparticle exposure might have negative health impacts. Understanding their methods of action or toxicity and researching any potential health implications is crucial.

Smart medication delivery uses polymeric nanoparticles, which can be created from synthetic or natural polymers. In-depth research is being done on them as carriers for controlled/sustained release in drug delivery systems. These nanopharmaceuticals' action is constrained by safety concerns, toxicity concerns, poor biocompatibility, and physiological difficulties. These nanoparticles' drawbacks include the hazardous breakdown process, residual material attached to them, and toxic monomer aggregation [54].

Quantum size effects, which are connected to oxidative stress, cytotoxicity, and genotoxicity, have an impact on the toxicity of polymeric NPs [55]. Nadège et al. observed that the somewhat cytotoxic chitosan polymer gave considerable cytotoxicity to PLGA nanoparticles when employed as a nanoparticle stabilizer after investigating the toxicity of a range of poly(lactide-co-glycolic acid) (PLGA) nanoparticles on human-like THP-1 macrophages. Both polyvinyl alcohol and poloxamer 188 polymers significantly increased PLGA nano's cytotoxicity. These results showed that stabilizers used in PLGA nanoparticle formulation have a substantial toxicological function when utilized at high concentrations, which may have an impact on the local toxicity of PLGA-based nanomedicine [56].

Size, surface area, surface charge, and aggregation state affect NP toxicity [57]. These features impact NP dispersion, deposition, and molecular interactions with proteins and macromolecules. Size affects NP penetration, cellular absorption, and toxicity. Some investigations imply a link between NP size, distribution, and renal ROS production [58, 59]. Liver toxicity is size-dependent. 10 nm silver NPs had greater tissue dispersion and produced more liver toxicity than 40 and 100 nm NPs [60, 61].

Shape affects NP dispersion, deposition, and clearance together with size. Long fibrous particles, such as single-walled nanotubes, are hard for the body to remove and cause organ deposits [62]. Surface chemistry affects NP pharmacokinetics. Charged NPs tend to accumulate more in target organs. Ionic zinc oxide NPs accumulated more in organs after oral or intravenous treatment than uncharged NPs [63]. (Table 1) Polysaccharide conjugation increases NP accumulation in the brain, liver, and spleen, which correlates to their toxicity [64]. Altering NP surface qualities with coatings can lower their toxicity. PEG reduces NP toxicity by changing their protein interactions. PEGylation may affect NPs' cellular uptake and medication delivery effectiveness.

7.3. Strategies/mitigation Techniques to Overcome Cytotoxicity

The prior studies show increased concern regarding NP toxicity and emphasize the necessity to address toxicity during original design, whether for industrial or therapeutic usage. Structured nanoemulsions and solid lipid nanoparticles

Table 1. Various nanoparticulate systems for nose-to-brain drug delivery.

Therapeutic Payload	Nanocarrier system	Material	Formulation Technique	Therapeutic Outcome	Refs.
Huperzine A	LF-TMC NPs	Lactoferrin and N-trimethylated chitosan	Emulsion-solvent evaporation method	Good sustained release effect, adhesion and targeting ability and broad application as intranasal drug delivery carrier	[18]
Bromocriptine	CS NPs	Chitosan	Ionic-gelation-method	Nanocarrier has increased brain uptake of bromocriptine also enhanced its antioxidant activity and make effective system for treatment of Parkinson's disease	[21]
Rasagiline	CG NPs	Chitosan glutamate	Ionic-gelation method	These could be promising delivery system for the treatment of Parkinson's disease	[22]
Carboplatin	PCL NPs	Poly(ϵ -caprolactone)	Double emulsion-solvent evaporation method	Better nasal absorption and sustained release profile so can be used in intranasal administration of carboplatin for improved brain delivery	[24]
Teriflunomide	NLC	Compritol 888 ATO (Solid-Lipid) and Maisine 35-1 (Liquid-Lipid)	Melt emulsification ultra-sonification method	Enhanced the nasal residence time	[26]
Selegiline	NE	Grape seed oil	High energy emulsification method	Enhanced the uptake of selegiline to brain, improve brain bioavailability and restore normal dopamine level	[54]
Tarenfluril	PNPs SLNs	Poly (lactic-co-glycolic) acid	Emulsion-solvent-diffusion method Emulsion-solvent evaporation method	Desirable brain biodistribution profiles, effective in delivering Tarenfluril to brain for treatment of Alzheimer's disease	[55]
Lamotrigine	NLs	Phospholipid 90G and Cholesterol	Thin film hydration and rehydration method	High entrapment in lipid bilayer, high release rate and better penetration than suspension	[56]
Venlafaxine	PLGA NPs	Poly (lactic-co-glycolic acid)	Double emulsion-solvent evaporation method	Plain nanoparticles showed fast and highest ability to reach brain after intranasal administration via nose-to-brain delivery as compared to functionalized nanoparticles	[57]
Eugenol	CS PCL NPs	Chitosan and Poly(ϵ -caprolactone)	Modified double-emulsion (W/O/W ₀) method	Enhancement of drug bioavailability and can help in treating cerebral ischemia effectively	[58]
Pramipexole Dihydrochloride	CNs	Chitosan	Ionic-gelation-method	Showed significant brain targeting potential compared to other formulation so can be utilized for effective brain targeting via intranasal route for Parkinson's disease treatment	[59]
Pioglitazone	PLGA-PEG NPs	Poly (lactic-co-glycolic) acid-Poly ethylene glycol copolymer	Solvent displacement method	Nasal mucosa showed enhanced drug permeation in the tissues in the treatment of Alzheimer's disease and it could be a promising delivery route in treatment of Alzheimer's disease	[60]
Pioglitazone	NLC	Liquid lipid capmul MCM and Solid lipid tripalmitin	Microemulsion method	The formulation improves the permeability of Pioglitazone across nasal mucosa and also improved the concentration of drug reaching brain	[61]
Dopamine	LF-BNPs	Borneol and lactoferrin	Double emulsion-solvent evaporation method	NPs increased the Dopamine absorption into the brain demonstrating the co-modification significantly enhanced transport of drug towards brain	[62]
Kaempferol	MNE	Chitosan	High-pressure homogenization technique	MNE decreased viability of glioma cells by enhancing apoptosis and seems to be an important carrier for cancer treatment	[63]

NLC: Nanostructured lipid carriers; NE: Nano-emulsion; CGNPs: Chitosan glutamate nanoparticles; PNPs: Polymeric nanoparticles; SLNs: Solid-lipid nanoparticles; NLs: Nanoliposomes; PLGA NPs: Poly(lactic-co-glycolic acid) nanoparticles; CS PCL NPs: Chitosan coated poly(ϵ -caprolactone) nanoparticles; PCLNPs: Poly (ϵ -caprolactone) nanoparticles; CSNPs: Chitosan nanoparticles; CNs: Chitosan nanoparticles; PLGA-PEG NPs: Poly(lactic-co-glycolic) acid-Poly ethylene glycol copolymer nanoparticles; LF-TMCNPs: Lactoferrin conjugated N-trimethylated chitosan nanoparticles; LF-BNPs: Lactoferrin - borneol co-modified nanoparticles; MNE: Mucoadhesive nano-emulsion.

highlight one way to design safer NPs. These nanoparticles are made with FDA-approved, food-grade lipids, proteins, polysaccharides, and surfactants [65]. Solid or metal-containing NPs are similarly hazardous, according to studies. So, they're used less.

These problems have been the subject of many researches, such as the development of biocompatible and biodegradable pH-responsive hybrid nanoparticles by Palanikumar et al. To reduce interactions with serum proteins and macrophages, a cross-linked bovine serum albumin shell was added to these nanosystems built around a PLGA core filled with drugs. The drug-loaded NPs showed potent anticancer activity both in vitro and in vivo while having no negative effects on healthy tissue [66].

The following strategies may help to reduce the cytotoxicity of nanoparticles:

- Next generation lipids (smart lipids)
- Degradable nanoparticles
- Surface coating
- Doping
- Alteration of surface properties

"Next-generation lipids" that combine high potency and biodegradability may reduce the danger of certain NPs, notably lipid-based NPs. Martin et al. created biodegradable lipids by adding bio-cleavable ester functionalities to hydrophobic alkyl chains. This family of biodegradable lipids in preclinical trials demonstrated fast plasma clearance and enhanced tolerability [67]. Surface coating solutions are also offered to reduce NP risk and develop safer nanotechnology. Surface coating refers to modifying, functionalizing, or stabilizing NPs to change their characteristics. NPs can be coated with single- or multi-layer polymers that are full or partial [68]. If chosen appropriately, the coating material offers biocompatibility and impacts the behaviour (e.g., colloidal stability) and destiny (e.g., degradation, excretion, accumulation) of NPs after administration in biological fluids, cells, and organisms.

Inorganic NPs are often doped. This approach adds impurities to materials to improve their chemical and physical characteristics [69–71]. Aluminium, titanium, and iron are dopants. When equally integrated into nanoparticles, these dopants modify the density of reactive chemical entities on the surface and lower metal ion binding energy to oxygen. Doping NPs can reduce NP dissolution and hazardous ion release, altering reactive surfaces and reducing ROS formation [72, 73].

FSP is a well-established NP doping method. FSP employs a quick combustion process, liquid precursor, and self-sustaining flame with a high local temperature and huge temperature gradient [74].

Altering NPs' charge density and hydrophobicity may lower their risk and increase their efficacy in medicinal applications, such as targeted medication administration [75, 76].

CONCLUSION

The intranasal route offers a lot of promise for overcoming issues with drug delivery caused by protective barriers like the BBB. Many medications are delivered via various modes of administration, and these issues constitute a big issue. The trigeminal and olfactory nerve pathways are used to deliver medicine directly to the brain via the intranasal method. As a result, this method has a number of advantages, including increased bioavailability, avoidance of first-pass metabolism and enzymatic degradation, and a lower risk of side effects. Targeted drug delivery is significantly influenced by nanoparticles. They increase the amount of medication that can be given by enhancing retention duration and penetration in the nasal cavity. Intranasal administration of drug-loaded nanoparticles can thus be used to treat brain diseases effectively.

LIST OF ABBREVIATIONS

BBB	=	Blood–Brain Barrier
NPs	=	Nanoparticles
CSF	=	Blood Cerebrospinal Fluid
Lf	=	Lactoferrin
TMC	=	N-Trimethylated Chitosan
PDI	=	Polydispersity Index
BRC	=	Bromocriptine
CS NPs	=	Chitosan Nanoparticles
W/O/W	=	Water-Oil-Water
O/W/O	=	Oil–Water-Oil
PCL	=	Carboplatin-Loaded Poly
MSNs	=	Mesoporous Silica Nanoparticles

CONSENT FOR PUBLICATION

Not applicable.

FUNDING

None Declared.

CONFLICT OF INTEREST

Author(s) declares no conflict of interest

ACKNOWLEDGMENTS

The authors are very thankful to the Principal, Rajarshi Shahu College of Pharmacy, Buldana, for providing article writing and editing facilities. Finally, the authors extend thanks to all those whose cooperation helped complete this work successfully.

REFERENCES

- [1] Wang, Z.; Xiong, G.; Tsang, W.C.; Schätzlein, A.G.; Uchegbu, I.F. Nose-to-brain delivery. *J. Pharmacol. Exp. Ther.*, **2019**, *370*(3), 593-601.
<http://dx.doi.org/10.1124/jpet.119.258152> PMID: 31126978

- [2] Partridge, W.M. Drug transport across the blood-brain barrier. *J. Cereb. Blood Flow Metab.*, **2012**, 32(11), 1959-1972. <http://dx.doi.org/10.1038/jcbfm.2012.126> PMID: 22929442
- [3] Battaglia, L.; Panciani, P.P.; Muntoni, E.; Capucchio, M.T.; Bisibetti, E.; De Bonis, P.; Mioletti, S.; Fontanella, M.; Swaminathan, S. Lipid nanoparticles for intranasal administration: Application to nose-to-brain delivery. *Expert Opin. Drug Deliv.*, **2018**, 15(4), 369-378. <http://dx.doi.org/10.1080/17425247.2018.1429401> PMID: 29338427
- [4] Gao, H. Progress and perspectives on targeting nanoparticles for brain drug delivery. *Acta Pharm. Sin. B*, **2016**, 6(4), 268-286. <http://dx.doi.org/10.1016/j.apsb.2016.05.013> PMID: 27471668
- [5] Kumar, A.; Pandey, A.N.; Jain, S.K. Nasal-nanotechnology: Revolution for efficient therapeutics delivery. *Drug Deliv.*, **2016**, 23(3), 671-683. <http://dx.doi.org/10.3109/10717544.2014.920431> PMID: 24901207
- [6] Khan, I.; Saeed, K.; Khan, I. Nanoparticles: Properties, applications and toxicities. *Arab. J. Chem.*, **2019**, 12(7), 908-931. <http://dx.doi.org/10.1016/j.arabjc.2017.05.011>
- [7] Serlin, Y.; Shelef, I.; Knyazer, B.; Friedman, A. Anatomy and physiology of the blood-brain barrier. *Semin. Cell Dev. Biol.*, **2015**, 38, 2-6. <http://dx.doi.org/10.1016/j.semcdb.2015.01.002> PMID: 25681530
- [8] Selvaraj, K.; Gowthamarajan, K.; Karri, V.V.S.R. Nose to brain transport pathways an overview: Potential of nanostructured lipid carriers in nose to brain targeting. *Artif. Cells Nanomed. Biotechnol.*, **2018**, 46(8), 2088-2095. PMID: 29282995
- [9] Aderibigbe, B.A.; Naki, T. Chitosan-based nanocarriers for nose to brain delivery. *Appl. Sci.*, **2019**, 9(11), 2219. <http://dx.doi.org/10.3390/app9112219>
- [10] Anu, M.E.S.; Saravanakumar, M.P. A review on the classification, characterisation, synthesis of nanoparticles and their application. *IOP Conf. Ser. Mater. Sci. Eng.*, **2017**, 263, 032019. <http://dx.doi.org/10.1088/1757-899X/263/3/032019>
- [11] Patra, J.K.; Baek, K.H. Green nanobiotechnology: Factors affecting synthesis and characterization techniques. *J. Nanomater.*, **2014**, 2014, 417305. <http://dx.doi.org/10.1155/2014/417305>
- [12] Satyanarayana, T.; Reddy, S.S. A review on chemical and physical synthesis methods of nanomaterials. *Int. J. Res. Appl. Sci. Eng. Technol.*, **2018**, 6(1), 2885-2889. <http://dx.doi.org/10.22214/ijraset.2018.1396>
- [13] Jeyaraj, M.; Gurunathan, S.; Qasim, M.; Kang, M.H.; Kim, J.H. A comprehensive review on the synthesis, characterization, and biomedical application of platinum nanoparticles. *Nanomaterials*, **2019**, 9(12), 1719. <http://dx.doi.org/10.3390/nano9121719> PMID: 31810256
- [14] Hussain, I.; Singh, N.B.; Singh, A.; Singh, H.; Singh, S.C. Green synthesis of nanoparticles and its potential application. *Biotechnol. Lett.*, **2016**, 38(4), 545-560. <http://dx.doi.org/10.1007/s10529-015-2026-7> PMID: 26721237
- [15] Singh, P.; Kim, Y.J.; Zhang, D.; Yang, D.C. Biological synthesis of nanoparticles from plants and microorganisms. *Trends Biotechnol.*, **2016**, 34(7), 588-599. <http://dx.doi.org/10.1016/j.tibtech.2016.02.006> PMID: 26944794
- [16] Pal, S.L.; Jana, U.; Manna, P.K.; Mohanta, G.P.; Manavalan, R. Nanoparticle: An overview of preparation and characterisation. *J. Appl. Pharm. Sci.*, **2011**, 1(6), 228-234.
- [17] Hoa, L.T.M.; Chi, N.T.; Nguyen, L.H.; Chien, D.M. Preparation and characterisation of nanoparticles containing ketoprofen and acrylic polymers prepared by emulsion solvent evaporation method. *J. Exp. Nanosci.*, **2012**, 7(2), 189-197. <http://dx.doi.org/10.1080/17458080.2010.515247>
- [18] Meng, Q.; Wang, A.; Hua, H.; Jiang, Y.; Wang, Y.; Mu, H.; Wu, Z.; Sun, K. Intranasal delivery of huperzine A to the brain using lactoferrin-conjugated N-trimethylated chitosan surface-modified PLGA nanoparticles for treatment of Alzheimer's disease. *Int. J. Nanomed.*, **2018**, 13, 705-718. <http://dx.doi.org/10.2147/IJN.S151474> PMID: 29440896
- [19] Patra, J.K.; Das, G.; Fraceto, L.F.; Campos, E.V.R.; Rodriguez, T.M.P.; Acosta, T.L.S.; Diaz, T.L.A.; Grillo, R.; Swamy, M.K.; Sharma, S.; Habtemariam, S.; Shin, H.S. Nano based drug delivery systems: Recent developments and future prospects. *J. Nanobiotechnol.*, **2018**, 16(1), 71. <http://dx.doi.org/10.1186/s12951-018-0392-8> PMID: 30231877
- [20] Pedroso, S.S.; Fleitas, S.N. Ionotropic gelation method in the synthesis of nanoparticles/microparticles for biomedical purposes. *Polym. Int.*, **2020**, 69(5), 443-447. <http://dx.doi.org/10.1002/pi.5970>
- [21] Md, S.; Khan, R.A.; Mustafa, G.; Chuttani, K.; Baboota, S.; Sahni, J.K.; Ali, J. Bromocriptine loaded chitosan nanoparticles intended for direct nose to brain delivery: Pharmacodynamic, Pharmacokinetic and scintigraphy study in mice model. *Eur. J. Pharm. Sci.*, **2013**, 48(3), 393-405. <http://dx.doi.org/10.1016/j.ejps.2012.12.007> PMID: 23266466
- [22] Mittal, D.; Md, S.; Hasan, Q.; Fazil, M.; Ali, A.; Baboota, S.; Ali, J. Brain targeted nanoparticulate drug delivery system of rasagiline via intranasal route. *Drug Deliv.*, **2016**, 23(1), 130-139. <http://dx.doi.org/10.3109/10717544.2014.907372> PMID: 24786489
- [23] Iqbal, M.; Zafar, N.; Fessi, H.; Elaissari, A. Double emulsion solvent evaporation techniques used for drug encapsulation. *Int. J. Pharm.*, **2015**, 496(2), 173-190. <http://dx.doi.org/10.1016/j.ijpharm.2015.10.057> PMID: 26522982
- [24] Alex, A.T.; Joseph, A.; Shavi, G.; Rao, J.V.; Udupa, N. Development and evaluation of carboplatin-loaded PCL nanoparticles for intranasal delivery. *Drug Deliv.*, **2016**, 23(7), 2144-2153. <http://dx.doi.org/10.3109/10717544.2014.948643> PMID: 25544603
- [25] Nagavarma, B.V.N. Different techniques for preparation of polymeric nanoparticles – A review. *Asian J. Pharm. Clin. Res.*, **2012**, 5(3), 16-23.
- [26] Gadhave, D.G.; Kokare, C.R. Nanostructured lipid carriers engineered for intranasal delivery of triflunomide in multiple sclerosis: Optimization and *in vivo* studies. *Drug Dev. Ind. Pharm.*, **2019**, 45(5), 839-851. <http://dx.doi.org/10.1080/03639045.2019.1576724> PMID: 30702966
- [27] Hangargekar, S.R.; Mohanty, P.; Jain, A. Solid lipid nanoparticles for brain targeting. *J. Drug Deliv. Ther.*, **2019**, 9(6-s), 248-252. <http://dx.doi.org/10.22270/jddt.v9i6-s.3783>
- [28] Kuldeep, S. Nano formulation a novel approach for nose to brain drug delivery. *J. Chem. Pharm. Res.*, **2016**, 8(2), 208-215.
- [29] Bonferoni, M.; Rossi, S.; Sandri, G.; Ferrari, F.; Gavini, E.; Rassa, G.; Giunchedi, P. Nanoemulsions for "nose-to-brain" drug delivery. *Pharmaceutics*, **2019**, 11(2), 84. <http://dx.doi.org/10.3390/pharmaceutics11020084> PMID: 30781585
- [30] Jaiswal, M.; Dudhe, R.; Sharma, P. K. Nanoemulsion: An advanced mode of drug delivery system. *3 Biotech.*, **2015**, 5(2), 123-127.
- [31] Zarif, L. Cochleates as Nanoparticulate Drug Carriers. In: *Nanoparticulates as Drug Carriers*; PUBLISHED BY IMPERIAL COLLEGE PRESS AND DISTRIBUTED BY WORLD SCIENTIFIC PUBLISHING CO, Singapore, **2006**, pp. 349-366. http://dx.doi.org/10.1142/9781860949074_0016
- [32] Hong, S.S.; Oh, K.T.; Choi, H.G.; Lim, S.J. Liposomal formulations for nose-to-brain delivery: Recent advances and future perspectives. *Pharmaceutics*, **2019**, 11(10), 540. <http://dx.doi.org/10.3390/pharmaceutics11100540> PMID: 31627301
- [33] Vieira, D.; Gamarra, L. Getting into the brain: Liposome-based strategies for effective drug delivery across the blood-brain barrier. *Int. J. Nanomed.*, **2016**, 11, 5381-5414. <http://dx.doi.org/10.2147/IJN.S117210> PMID: 27799765
- [34] Parajapati, S.K.; Maurya, S.D.; Das, M.K.; Tilak, V.K.; Verma, K.K.; Dhakar, R.C. Potential application of dendrimers in drug delivery: A concise review and update. *J. Drug Deliv. Ther.*, **2016**, 6(2), 71-88. <http://dx.doi.org/10.22270/jddt.v6i2.1195>
- [35] Abbasi, E.; Aval, S.F.; Akbarzadeh, A.; Milani, M.; Nasrabadi, H.T.; Joo, S.W.; Hanifehpour, Y.; Nejati, K.K.; Pashaei, A.R. Dendrimers: Synthesis, applications, and properties. *Nanoscale Res. Lett.*, **2014**, 9(1), 247. <http://dx.doi.org/10.1186/1556-276X-9-247> PMID: 24994950
- [36] Zhu, Y.; Liu, C.; Pang, Z. Dendrimer-based drug delivery systems for brain targeting. *Biomolecules*, **2019**, 9(12), 790.

- <http://dx.doi.org/10.3390/biom9120790> PMID: 31783573
- [37] Lungare, S.; Hallam, K.; Badhan, R.K.S. Phytochemical-loaded mesoporous silica nanoparticles for nose-to-brain olfactory drug delivery. *Int. J. Pharm.*, **2016**, *513*(1-2), 280-293. <http://dx.doi.org/10.1016/j.ijpharm.2016.09.042> PMID: 27633279
- [38] Mohanraj, V.J.; Chen, Y. Nanoparticles - A review. *Trop. J. Pharm. Res.*, **2007**, *5*(1), 561-573. <http://dx.doi.org/10.4314/tjpr.v5i1.14634>
- [39] Caputo, F.; Clogston, J.; Calzolari, L.; Rösslein, M.; Prina-Mello, A. Measuring particle size distribution of nanoparticle enabled medicinal products, the joint view of EUNCL and NCI-NCL. A step by step approach combining orthogonal measurements with increasing complexity. *J. Control. Release*, **2019**, *299*, 31-43. <http://dx.doi.org/10.1016/j.jconrel.2019.02.030> PMID: 30797868
- [40] Pandey P., D.M. A brief review on inorganic nanoparticles. *Crit. Rev.*, **2016**, *3*(3), 18-26.
- [41] Rasmussen, M.K.; Pedersen, J.N.; Marie, R. Size and surface charge characterization of nanoparticles with a salt gradient. *Nat. Commun.*, **2020**, *11*(1), 2337. <http://dx.doi.org/10.1038/s41467-020-15889-3> PMID: 32393750
- [42] Honary, S.; Zahir, F. Effect of zeta potential on the properties of nano-drug delivery systems - A review (Part 1). *Trop. J. Pharm. Res.*, **2013**, *12*(2), 255-264.
- [43] Jain, A.K.; Thareja, S. *In vitro* and *in vivo* characterization of pharmaceutical nanocarriers used for drug delivery. *Artif. Cells Nanomed. Biotechnol.*, **2019**, *47*(1), 524-539. <http://dx.doi.org/10.1080/21691401.2018.1561457> PMID: 30784319
- [44] Ranjit, K.; Nanoparticle, B.A. An overview of preparation, characterization and application. *Int Res J Pharm.*, **2013**, *4*(4), 47-57.
- [45] D'Souza, S. A review of *in vitro* drug release test methods for nano-sized dosage forms. *Adv. Pharm.*, **2014**, *2014*, 304757. <http://dx.doi.org/10.1155/2014/304757> Muthu, M.S.; Feng, S.S. Pharmaceutical stability aspects of nano-medicines. *Nanomedicine*, **2009**, *4*(8), 857-860. <http://dx.doi.org/10.2217/nmm.09.75> PMID: 19958220
- [47] Mistry, A.; Stolnik, S.; Illum, L. Nanoparticles for direct nose-to-brain delivery of drugs. *Int. J. Pharm.*, **2009**, *379*(1), 146-157. <http://dx.doi.org/10.1016/j.ijpharm.2009.06.019> PMID: 19555750
- [48] Sonvico, F.; Clementino, A.; Buttini, F.; Colombo, G.; Pescina, S.; Stanisquaski, G.S.; Raffin, P.A.; Nicoli, S. Surface-modified nanocarriers for nose-to-brain delivery: From bioadhesion to targeting. *Pharmaceutics*, **2018**, *10*(1), 34. <http://dx.doi.org/10.3390/pharmaceutics10010034> PMID: 29543755
- [49] Erdő, F.; Bors, L.A.; Farkas, D.; Bajza, Á.; Gizurarson, S. Evaluation of intranasal delivery route of drug administration for brain targeting. *Brain Res. Bull.*, **2018**, *143*, 155-170. <http://dx.doi.org/10.1016/j.brainresbull.2018.10.009> PMID: 30449731
- [50] Md, S.; Mustafa, G.; Baboota, S.; Ali, J. Nanoneurotherapeutics approach intended for direct nose to brain delivery. *Drug Dev. Ind. Pharm.*, **2015**, *41*(12), 1922-1934. <http://dx.doi.org/10.3109/03639045.2015.1052081> PMID: 26057769
- [51] Ghadiri, M.; Young, P.; Traini, D. Strategies to enhance drug absorption *via* nasal and pulmonary routes. *Pharmaceutics*, **2019**, *11*(3), 113. <http://dx.doi.org/10.3390/pharmaceutics11030113> PMID: 30861990
- [52] Islam, S.U.; Shehzad, A.; Ahmed, M.B.; Lee, Y.S. Intranasal delivery of nanoformulations: A potential way of treatment for neurological disorders. *Molecules*, **2020**, *25*(8), 1929. <http://dx.doi.org/10.3390/molecules25081929> PMID: 32326318
- [53] Almasser, S. A review on nasal drug delivery system and its contribution in therapeutic management. *Asian J. Pharm. Clin. Res.*, **2019**, *12*(1), 40-45. <http://dx.doi.org/10.22159/ajpcr.2019.v12i1.29443>
- [54] Anagnostou, K.; Stylianakis, M.; Michaleas, S.; Skouras, A. Biodegradable nanomaterials. In: *Nanomaterials for Clinical Applications*; Elsevier: Amsterdam, Netherlands: **2020**; pp. 123-157.
- [55] Singh, N.; Joshi, A.; Toor, A.; Verma, G. Drug delivery: Advancements and challenges. In: *Nanostruct Drug Deliv*; Elsevier: Amsterdam, Netherlands: **2017**; pp. 865-886.
- [56] Suriya, P.A.; Dorothy, R.; Jancirani, S.; Rajendran, S.; Singh, G.; Senthil, K.S. Recent advances in the study of toxicity of polymer-based nanomaterials. In: *Nanotoxicity*; Elsevier: Amsterdam, Netherlands: **2020**; pp. 143-165. <http://dx.doi.org/10.1016/B978-0-12-819943-5.00007-5>
- [57] Wu, T.; Tang, M. Review of the effects of manufactured nanoparticles on mammalian target organs. *J. Appl. Toxicol.*, **2018**, *38*(1), 25-40. <http://dx.doi.org/10.1002/jat.3499> PMID: 28799656
- [58] Elsaesser, A.; Howard, C.V. Toxicology of nanoparticles. *Adv. Drug Deliv. Rev.*, **2012**, *64*(2), 129-137. <http://dx.doi.org/10.1016/j.addr.2011.09.001> PMID: 21925220
- [59] Sharifi, S.; Behzadi, S.; Laurent, S.; Forrest, M.L.; Stroeve, P.; Mahmoudi, M. *Toxicity of nanomaterials*. *Chem. Soc. Rev.*, **2012**, *41*, 2323-2343.
- [60] Wu, T.; Tang, M. Toxicity of quantum dots on respiratory system. *Inhal. Toxicol.*, **2014**, *26*(2), 128-139. <http://dx.doi.org/10.3109/08958378.2013.871762> PMID: 24495248
- [61] Recordati, C.; De Maglie, M.; Bianchessi, S.; Argenti, S.; Cella, C.; Mattiello, S.; Cubadda, F.; Aureli, F.; D'Amato, M.; Raggi, A.; Lenardi, C.; Milani, P.; Scanziani, E. Tissue distribution and acute toxicity of silver after single intravenous administration in mice: Nano-specific and size-dependent effects. *Part. Fibre Toxicol.*, **2015**, *13*(1), 12. <http://dx.doi.org/10.1186/s12989-016-0124-x> PMID: 26926244
- [62] Zoroddu, M.; Medici, S.; Ledda, A.; Nurchi, V.; Lachowicz, J.; Peana, M. Toxicity of nanoparticles. *Curr. Med. Chem.*, **2014**, *21*(33), 3837-3853. <http://dx.doi.org/10.2174/0929867321666140601162314> PMID: 25306903
- [63] Paek, H.J.; Lee, Y.J.; Chung, H.E.; Yoo, N.H.; Lee, J.A.; Kim, M.K.; Lee, J.K.; Jeong, J.; Choi, S.J. Modulation of the pharmacokinetics of zinc oxide nanoparticles and their fates *in vivo*. *Nanoscale*, **2013**, *5*(23), 11416-11427. <http://dx.doi.org/10.1039/c3nr02140h> PMID: 23912904
- [64] Shegokar, R.; Singh, K.K. Surface modified nevirapine nanosuspensions for viral reservoir targeting: *In vitro* and *in vivo* evaluation. *Int. J. Pharm.*, **2011**, *421*(2), 341-352. <http://dx.doi.org/10.1016/j.ijpharm.2011.09.041> PMID: 21986114
- [65] McClements, D.J. Emulsion design to improve the delivery of functional lipophilic components. *Annu. Rev. Food Sci. Technol.*, **2010**, *1*(1), 241-269. <http://dx.doi.org/10.1146/annurev.food.080708.100722> PMID: 22129337
- [66] Palanikumar, L.; Al-Hosani, S.; Kalmouni, M.; Nguyen, V.P.; Ali, L.; Pasricha, R.; Barrera, F.N.; Magzoub, M. pH-responsive high stability polymeric nanoparticles for targeted delivery of anticancer therapeutics. *Commun. Biol.*, **2020**, *3*(1), 95. <http://dx.doi.org/10.1038/s42003-020-0817-4> PMID: 32127636
- [67] Maier, M.A.; Jayaraman, M.; Matsuda, S.; Liu, J.; Barros, S.; Querbes, W.; Tam, Y.K.; Ansell, S.M.; Kumar, V.; Qin, J.; Zhang, X.; Wang, Q.; Panesar, S.; Hutabarat, R.; Carioto, M.; Hettinger, J.; Kandasamy, P.; Butler, D.; Rajeev, K.G.; Pang, B.; Charisse, K.; Fitzgerald, K.; Mui, B.L.; Du, X.; Cullis, P.; Madden, T.D.; Hope, M.J.; Manoharan, M.; Akinc, A. Biodegradable lipids enabling rapidly eliminated lipid nanoparticles for systemic delivery of RNAi therapeutics. *Mol. Ther.*, **2013**, *21*(8), 1570-1578. <http://dx.doi.org/10.1038/mt.2013.124> PMID: 23799535
- [68] Schubert, J.; Chanana, M. Coating matters: Review on colloidal stability of nanoparticles with biocompatible coatings in biological media, living cells and organisms. *Curr. Med. Chem.*, **2018**, *25*(35), 4553-4586. <http://dx.doi.org/10.2174/0929867325666180601101859> PMID: 29852857
- [69] Thirumala, R.G.; Babu, B.; Joyce, S.R.; Pushpa, M.V.; Ravikumar, R.V.S.S.N. Spectral investigations on undoped and Cu²⁺ doped ZnO-CdS composite nanopowders. *Spectrochim. Acta A Mol. Biomol. Spectrosc.*, **2015**, *139*, 86-93. <http://dx.doi.org/10.1016/j.saa.2014.12.021> PMID: 25554956

- [70] Adeleye, A.S.; Pokhrel, S.; Mädler, L.; Keller, A.A. Influence of nanoparticle doping on the colloidal stability and toxicity of copper oxide nanoparticles in synthetic and natural waters. *Water Res.*, **2018**, *132*, 12-22.
<http://dx.doi.org/10.1016/j.watres.2017.12.069> PMID: 29304444
- [71] Ahmad, J.; Siddiqui, M.A.; Akhtar, M.J.; Alhadlaq, H.A.; Alshamsan, A.; Khan, S.T.; Wahab, R.; Al-Khedhairi, A.A.; Al-Salim, A.; Musarrat, J.; Saquib, Q.; Fareed, M.; Ahamed, M. Copper doping enhanced the oxidative stress-mediated cytotoxicity of TiO₂ nanoparticles in A549 cells. *Hum. Exp. Toxicol.*, **2018**, *37*(5), 496-507.
<http://dx.doi.org/10.1177/0960327117714040> PMID: 28621211
- [72] Sun, B.; Pokhrel, S.; Dunphy, D.R.; Zhang, H.; Ji, Z.; Wang, X.; Wang, M.; Liao, Y.P.; Chang, C.H.; Dong, J.; Li, R.; Mädler, L.; Brinker, C.J.; Nel, A.E.; Xia, T. Reduction of acute inflammatory effects of fumed silica nanoparticles in the lung by adjusting silanol display through calcination and metal doping. *ACS Nano*, **2015**, *9*(9), 9357-9372.
<http://dx.doi.org/10.1021/acsnano.5b03443> PMID: 26200133
- [73] Naatz, H.; Lin, S.; Li, R.; Jiang, W.; Ji, Z.; Chang, C.H.; Köser, J.; Thöming, J.; Xia, T.; Nel, A.E.; Mädler, L.; Pokhrel, S. Safe-by-Design CuO nanoparticles via Fe-doping. Cu–O bond length variation, and biological assessment in cells and zebrafish embryos. *ACS Nano*, **2017**, *11*(1), 501-515.
<http://dx.doi.org/10.1021/acsnano.6b06495> PMID: 28026936
- [74] Teoh, W.Y.; Amal, R.; Mädler, L. Flame spray pyrolysis: An enabling technology for nanoparticles design and fabrication. *Nanoscale*, **2010**, *2*(8), 1324-1347.
<http://dx.doi.org/10.1039/c0nr00017e> PMID: 20820719
- [75] Hola, K.; Markova, Z.; Zoppellaro, G.; Tucek, J.; Zboril, R. Tailored functionalization of iron oxide nanoparticles for MRI, drug delivery, magnetic separation and immobilization of biosubstances. *Biotechnol. Adv.*, **2015**, *33*(6), 1162-1176.
<http://dx.doi.org/10.1016/j.biotechadv.2015.02.003> PMID: 25689073
- [76] Mout, R.; Moyano, D.F.; Rana, S.; Rotello, V.M. Surface functionalization of nanoparticles for nanomedicine. *Chem. Soc. Rev.*, **2012**, *41*(7), 2539-2544.
<http://dx.doi.org/10.1039/c2cs15294k> PMID: 22310807

REVIEW ARTICLE

Polymeric Nanoparticles: Prospective on the Synthesis, Characterization and Applications in Nose-to-Brain Drug Delivery

Prakash N. Kendre^{1,*}, Dhiraj R. Kayande¹, Shirish P. Jain¹, Tejaswini G. Malge¹, Namrata N. Zadpe¹ and Bhupendra G. Prajapati²

¹Rajarshi Shahu College of Pharmacy, Buldana Maharashtra, 443001, India; ²S. K. Patel College of Pharmaceutical Education and Research Ganpat University, Ganpat Vidya Nagar, Mehsana, Gujarat 384012, India

Abstract: For the treatment of brain illnesses, there is growing interest in nose-to-brain drug administration. Other, more traditional methods of crossing the blood–brain barrier (BBB) are ineffective. As a result, the therapeutic concentration in the brain cannot be achieved, and the reaction is inadequate. Intranasal medication delivery is one intriguing technique for avoiding first-pass metabolism and bypassing the blood-brain barrier. It lowers medicine doses while reducing systemic side effects. Compared to conventional drug delivery platforms, a nanoparticulate drug delivery method allows for greater penetration via the nasal route. It is better to make the nanoparticles for nose-to-brain administration when a good carrier (polymers) is used. This review focuses on the many processes for creating polymeric nanoparticles, strategies and tactics for improving nose-to-brain drug delivery efficiency, and nanoparticle characterization. The use of the nose-to-brain drug delivery platform is being explored using a variety of nanoparticles created by researchers for the treatment of brain illnesses.

ARTICLE HISTORY

Received: May 18, 2022
Revised: July 17, 2022
Accepted: September 01, 2022

DOI:
[10.2174/1573413718666220929102013](https://doi.org/10.2174/1573413718666220929102013)

Keywords: Polymeric nanoparticles, synthesis, blood-brain-barrier, brain diseases, techniques

1. INTRODUCTION

Aside from being a leading cause of death and disability worldwide, brain problems are chronic and lifelong illnesses [1]. Because of the protective coverings of the brain, namely the blood–brain barrier, medical treatment of brain illnesses is a major issue for scientists and researchers (BBB). Because of their enormous molecular weights, most therapeutic and diagnostic agents are unable to diffuse through the BBB, and even tiny molecules (98%) are not transported through it [2, 3]. Drugs can be administered intranasally to prevent first-pass metabolism and gastrointestinal degradation, bypassing the BBB. Nasal administration of drug-loaded nanoparticles is another option for increasing efficiency. Drugs can be delivered directly to the brain by taking a nasal route. This might make it possible to treat mental illnesses [3, 4].

In 1959, Nobel Laureate Richard P. Feynman proposed the concept of nanotechnology. Nanotechnology is used to generate nanoparticles (NPs) from a variety of materials, including particulates. Solid particles with 1-100 nm dimensions are known as nanoparticles [4]. For delivering medications to target areas, several forms of drug-loaded nanoparticles have been created, including nanoemulsions, nanotubes,

liposomes, micelles, dendrimers, and quantum dots [5, 6]. Aside from their small size, nanoparticles exhibit special features. They are target-specific and have a high surface-to-volume ratio. Nanoparticles with polymer coatings can pass through the BBB [7]. As a result, nanoparticles are widely used in the treatment of a variety of brain disorders.

The medication for brain disease is difficult. After all, 98% of current pharmaceutical products are stopped by a protective barrier [7, 8]. The brain is the most complex organ and is separated from the other parts by strong barriers. The three barriers that protect the brain are

- The BBB, consists of a highly specialized endothelial barrier
- The blood-cerebrospinal fluid (CSF) barrier with the choroid plexus epithelium
- The arachnoid epithelium

These protective barriers prevent the entry of harmful and toxic agents as well as therapeutic and diagnostic agents into the brain [8]. Nanoparticles can enter the brain directly or indirectly after nasal administration. Transportation of molecules to the brain occurs by two pathways:

- The trigeminal neural pathway
- The olfactory neural pathway

*Address correspondence to this author at the Rajarshi Shahu College of Pharmacy, Buldana, Maharashtra, 443001, India; Tel: +919890506016; Fax: +912423222862; E-mail: prakashkendre@gmail.com

Some drugs can enter the blood circulation and are transported across the BBB into the brain [4]. Along the trigeminal neural pathway, molecules are transported by axonal transport or endocytosis. The trigeminal nerve is the fifth cranial nerve. It has three major branches [8, 9]:

- The ophthalmic nerve
- The maxillary nerve
- The mandibular nerve

In nose-to-brain delivery, the ophthalmic and maxillary nerves play a big part. The paracellular or transcellular method moves chemicals along the olfactory pathway. Olfactory receptor neurons are found in the mucosa of the olfactory epithelium and carry chemicals quickly to the brain. The process of transport from the nose to the brain is yet unknown. Fig. 1 [8, 9] shows a schematic illustration of nanoparticulate medication delivery.

The intranasal nose-to-brain delivery mechanism is the subject of this investigation. The various methods of nanoparticle preparation, strategies, and distinct approaches to drug delivery and nanoparticle characterization are explored within this broad topic. This review's main goal is to overview how nose-to-brain medication delivery systems can help people with brain illnesses get better.

2. SYNTHETIC TECHNIQUES FOR POLYMERIC NANOPARTICLES

Nanomaterials are synthesized or prepared using a variety of techniques. It's crucial to choose the right procedure, which is determined by the material's physicochemical prop-

erties. The top-down and bottom-up approaches to synthesis are the two main methodologies.

2.1. Top-down Approach

The top-down method entails using an external force to break down bigger chunks of heavy material into smaller chunks. This is a crucial technique in terms of business. Wet ball milling, high-pressure homogenisation, jet milling, laser sputtering, nanolithography, sputtering, thermal breakdown, and so on are all part of the top-down approach.

2.2. Bottom-up Approach

The required structure is constructed from atoms, molecules, or clusters under specific conditions in the bottom-up technique. The bottom-up strategy is used in methods like precipitation, chemical vapour deposition (CVD), pyrolysis, the sol-gel method, spinning, and biosynthesis [10]. Fig. 2 shows a classification of nanoparticles synthesis methods [11, 12]

2.3. Physical Method

The top-down strategy is used in physical approaches to nanoparticles production. Materials are abraded, melted, evaporated, or condensed using mechanical pressure, electric and thermal energy, and high-energy radiation. These technologies have the advantages of being solvent-free, toxic-chemical-free, and producing nanoparticles of consistent size and shape in a short amount of time. They use a lot of energy, need high temperatures and pressures, aren't very productive, are expensive, and don't make very stable nanoparticles.

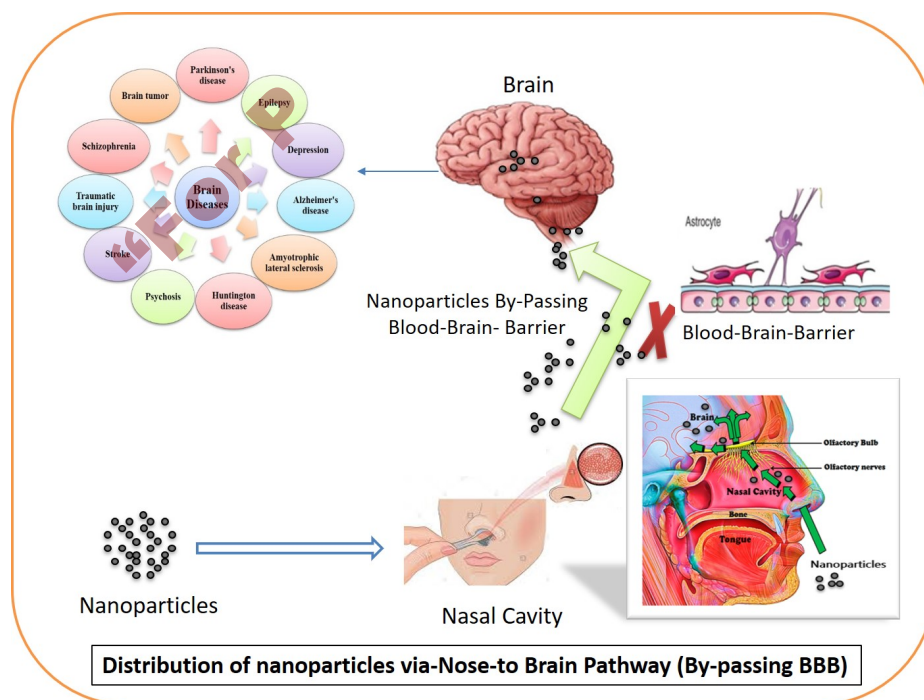


Fig. (1). Schematic presentation of nanoparticles distribution via nose-to-brain route; Selvaraj K, Gowthamarajan K, Karri VVSR (2017). (*A higher resolution / colour version of this figure is available in the electronic copy of the article*).

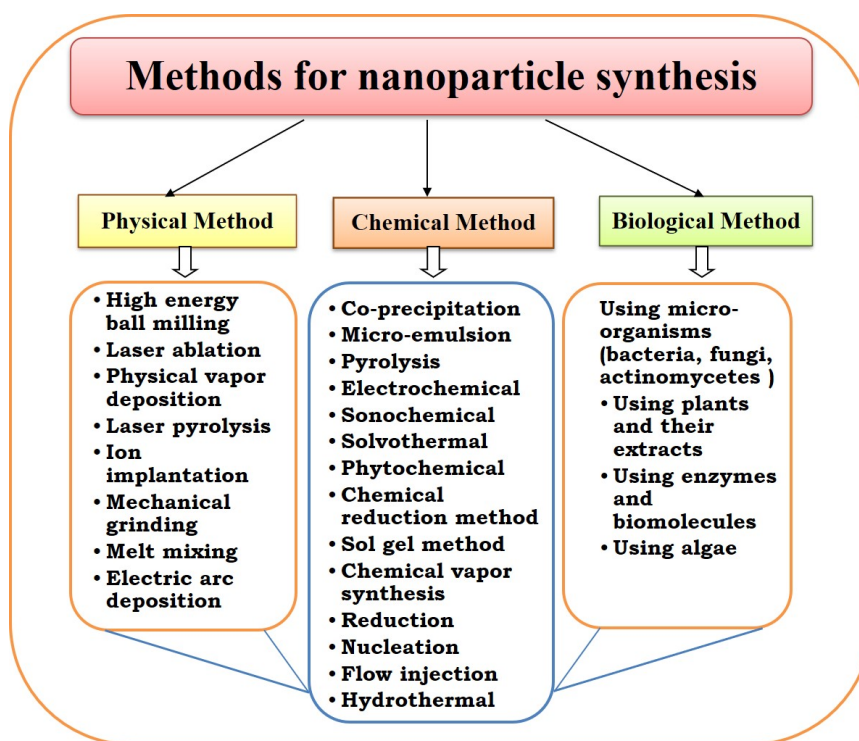


Fig. (2). Various methods used for the synthesis of nanoparticles; Patra JK, Baek K-H (2014). (A higher resolution / colour version of this figure is available in the electronic copy of the article).

2.4. Chemical Methods

The bottom-up approach to nanoparticles synthesis is chemical methods. Cost-effectiveness, ease of functionalization, thermal stability, high yield, and reduced dispersion are only a few of the advantages of this approach. The downsides include the use of harmful chemicals, a lower level of purity, and human health risks. Chemical reduction, sol-gel synthesis, sono-chemical synthesis, solvothermal synthesis, coprecipitation, the microemulsion method, and pyrolysis are some of the most extensively used chemical processes for nanoparticles synthesis [13].

2.5. Biological Methods

In contrast to physical and chemical processes, biological synthesis is environmentally beneficial. Microorganisms, enzymes, algae, viruses, plants, and biomolecules are used to synthesise nanoparticles. As a result, these techniques are referred to as "green synthesis techniques." The bottom-up strategy is used in these techniques. Reducing and stabilising substances found in microbes and plants are used in the synthesis [11]. They mostly make nanoparticles by breaking down chemicals found in microbes and plants, like amines, alkaloids, proteins, enzymes, phenolic compounds, and pigments, to make them smaller [14].

Nontoxicity, reproducibility in manufacturing, well-defined morphology, ease of scaling up, and lower energy requirements are all advantages of biological processes, which are environmentally beneficial. They're also free of potentially dangerous and costly chemicals [15].

2.6. Emulsion-solvent Evaporation Methods

The most prevalent ways of preparing nanoparticles are as follows. They're exclusively used for medications that aren't easily dissolved in water. The following steps are involved in emulsion-solvent evaporation: (1) to make an organic solution, the medication and polymer must first be dissolved in an organic solvent. (2) A surfactant or aqueous solution of a stabiliser is created in the second step. (3) The emulsification process is the third phase, in which the already prepared organic solution is dropped dropwise into the aqueous solution under the high shearing force of the homogeniser, resulting in an O/W (oil-in-water) type of emulsion. (4) The fourth step is solvent evaporation, which is done in a rotary evaporator with the organic solvent evaporated first and then the drug-loaded nanoparticles precipitated. (5) Ultracentrifugation is the fifth stage, which involves collecting the precipitated nanoparticles and washing them with distilled water to eliminate any residue. (6) Lyophilisation, a freeze-drying method, is the final step. In the final step, water is evaporated, and the dry nanoparticles are collected as a powder (Fig. 3). These procedures [16] have been modified by high-pressure emulsification and the solvent evaporation method. Because they only require mild conditions and continual stirring, emulsion-solvent evaporation methods are preferred over other methods. As a result, a stable emulsion can be made without interfering with the drug's activity [17].

Using the emulsion-solvent evaporation approach, the researchers created HupA-loaded lactoferrin coupled N-trimethylated chitosan nanoparticles (HupALf-TMC NPs).

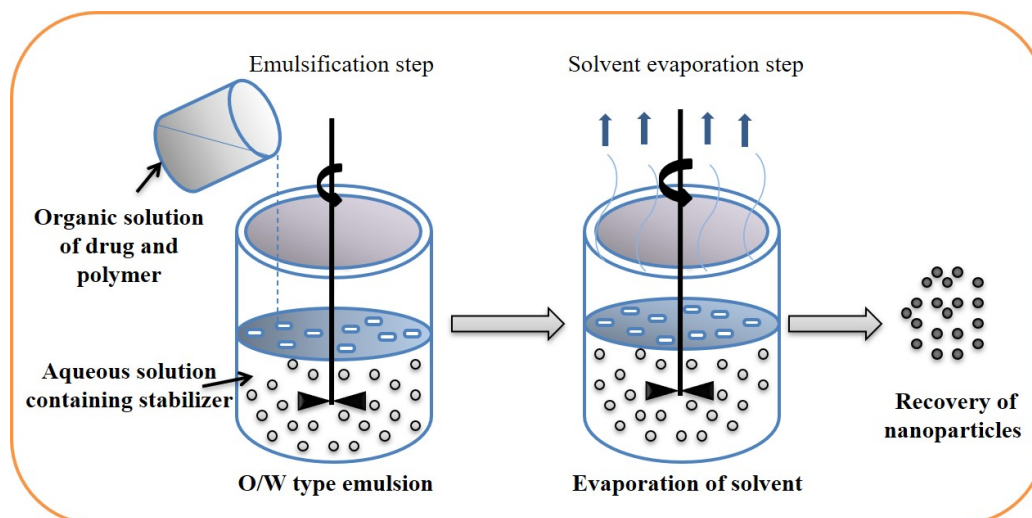


Fig. (3). Emulsion-solvent evaporation method for nanoparticles synthesis; Pal SL JUMP *et al.* (2011). (A higher resolution / colour version of this figure is available in the electronic copy of the article).

Their goal was to create an intranasal delivery system for HupA that could efficiently transfer the protein to the brain and cure Alzheimer's disease. Polylactide-co-glycoside was the polymer employed to make these nanoparticles (PLGA). The preparation included co-modification with lactoferrin (Lf) and N-trimethylated chitosan (TMC). TMC modification was thought to boost nasal adhesion and retention time. The conjugation of Lf was supposed to make drug administration from the nose to the brain easier. Using the Box-Behnken design, the nanoparticles were optimised. The nanoparticles' particle size, zeta potential, size distribution, entrapment efficiency, and polydispersity index (PDI) were all calculated. Biodistribution research and *in vitro* drug release tests were also conducted. The nanoparticles provided a good long-term release. The nasal adhesion and the capacity to target the brain were both excellent. The Lf-TMC NPs were found to be a promising nose-to-brain medication delivery method based on the drug's distribution profile in the brain [18].

2.7. Ionic Gelation Methods

In an ionic gelation technique, a positively or negatively charged hydrophilic molecule interacts with a cation or anion to generate a strongly cross-linked structure. As a result of this process, which produces very sticky gel particles, nanoparticles are formed. A drug-polymer solution is made by mixing the drug and polymer in distilled water. Drop by drop, stirring constantly, pure water is added. It is possible to obtain an opalescent suspension. The suspension is then centrifuged to obtain the nanoparticles. Fig. 4 shows lyophilization nanoparticles using an appropriate cryoprotectant [19]. The most common polymers used in ionic gelation procedures are chitosan and alginate. Other polymers include dextran, carboxymethyl cellulose, gelatine, collagen, hyaluronic acid, pectin, carbopol 934P, gum, and others [20].

Using an ionic gelation process, the researchers created bromocriptine (BRC)-loaded chitosan nanoparticles (CS NPs). Their goal was to look at the role of chitosan nanopar-

ticles in a nose-to-brain drug delivery system and see how they could improve bromocriptine's brain targeting efficiency. The nanoparticles were made from chitosan (a polymer) and sodium tripolyphosphate (cross-polymer). Pharmacodynamic, biodistribution, and pharmacokinetic experiments were conducted on Swiss albino mice. The nanoparticles were measured for particle size, polydispersity index, zeta potential, entrapment efficiency, and drug-loading capacity. Bromocriptine absorption in the brain was boosted by using nanoparticles. In addition, the antioxidant activity was improved. This technique for delivering drugs to the brain could be useful in the treatment of Parkinson's disease [21].

Using an ionic gelation technique, researchers synthesised and assessed RAS-loaded chitosan glutamate nanoparticles (CG-NPs). The researchers wanted to see if the nose-to-brain pathway was more effective than the intravenous approach for delivering medicines to the central nervous system (CNS). Chitosan glutamate (CG) was employed as the polymer, and sodium tripolyphosphate was used as the cross-polymer (STPP). The sodium anions of the sodium tripolyphosphate cause ionic gelation of CG, which results in CG-NPs. characterization of the produced nanoparticles *In vitro* drug release research was conducted after determining their particle size, size distribution, zeta potential, encapsulation efficiency, and polydispersity index. Following intranasal treatment, these nanoparticles greatly increased RAS bioavailability in mice's brains. Parkinson's disease may benefit from intranasal delivery [22].

2.8. Double Emulsion-solvent Evaporation Method

Methods of two-step emulsification include double emulsion-solvent evaporation. Both hydrophilic and hydrophobic medicines can be made with them. This approach is also known as "emulsions of emulsions" because the dispersed phase droplets are made up of smaller dispersed phase droplets, which are usually polydisperse in size. There are two types of common double emulsions:

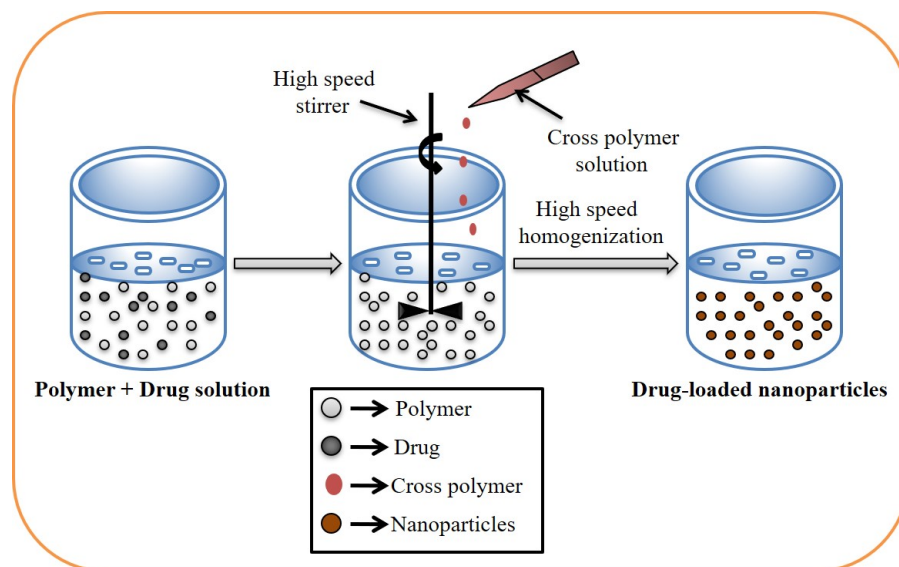


Fig. (4). Ionic-gelation method for nanoparticles synthesis; Patra JK, Das G, Fraceto LF, *et al.* (2018). (A higher resolution / colour version of this figure is available in the electronic copy of the article).

- Water–oil–water (W/O/W)
- Oil–water–oil (O/W/O)

A two-step emulsification technique is used to create nanoparticles in these procedures. The hydrophilic medications are added to the watery inner phase (W) first, followed by the infusion of polymer/hydrophobic pharmaceuticals into the organic phase, i.e., the oil phase (O). A primary emulsion (W/O) is created by homogenising the two phases. This primary emulsion is emulsified with the aqueous phase (W), which contains a stabiliser, in the second step to generate a double emulsion (W/O/W). The dispersed phase's solvent is next ejected and evaporated. As shown in Fig. 5, the polymer encasing the active ingredient hardens as a result.

Poly(lactic acid) (PLA), poly(lactic-co-glycolic acid) (PLGA), and polycaprolactone are the most prevalent polymers utilised in double emulsion–solvent evaporation processes (PCL). Poly(vinyl alcohol) (PVA), Tween 80, and Span 80 are some of the most regularly used stabilisers [23].

Alex *et al.* (2014) created carboplatin-loaded poly(caprolactone) (PCL) nanoparticles using a two-step emulsion–solvent evaporation method, W/O/W was the sort of emulsion that resulted. The polymer used for encapsulating carboplatin was polycaprolactone, which regulates drug release and boosts anticancer efficacy. The nanoparticles were measured in terms of size, zeta potential, entrapment efficiency, polydispersity index, scanning electron microscopy, and *in vitro* drug release profiles. The nanoparticles had a small particle size, a spherical shape, high entrapment efficiency, improved nasal absorption, and a long release profile. They could be employed in a carboplatin delivery system [24].

2.9. Nanoprecipitation Methods

Solvent displacement techniques are another name for nanoprecipitation. Polymeric nanoparticles are primarily

synthesised using these methods. Fig. 6 shows how the approach works: pre-formed polymer precipitation from an organic solution and organic solvent diffusion into the aqueous medium in the presence or absence of a surfactant. Nanoprecipitation is mostly employed for hydrophobic medicines since the solvents used are particularly miscible with the aqueous phase [25]. Nano-capsules can also be created by adding a small amount of harmless oil to the organic phase [19]. These techniques produce submicron (210 nm) nanoparticles. The size depends on the rate of addition of the organic phase to the aqueous phase and the low polydispersity index value [17].

2.10. Salting-out Methods

The separation of the water-soluble solvent from the aqueous phase is the basic concept behind these approaches. These techniques are variations of emulsification–solvent diffusion techniques [26].

An API and a polymer are dissolved in solvents to make a solution. After that, the solutions are emulsified into an aqueous gel that includes a colloidal stabiliser and a highly concentrated salting-out agent. The sort of emulsion that forms is O/W. It's diluted with enough water to lower the salting-out agent's concentration and increases the solvent's diffusion into the aqueous phase, resulting in nanosphere formation. Fig. 7 shows how cross-flow filtering removes the solvent and salting-out agent. The salting-out agent should be chosen carefully because it affects the drug's encapsulation efficiency [25].

3. POLYMERIC NANOPARTICLES FORMULATION APPROACHES

In the treatment of neurological illnesses, nanocarriers are utilised to carry medications across the BBB. Liposomes, solid-lipid nanoparticles, nanoemulsions, carbon nanotubes, dendrimers, micelles, and quantum dots are only a few **199**

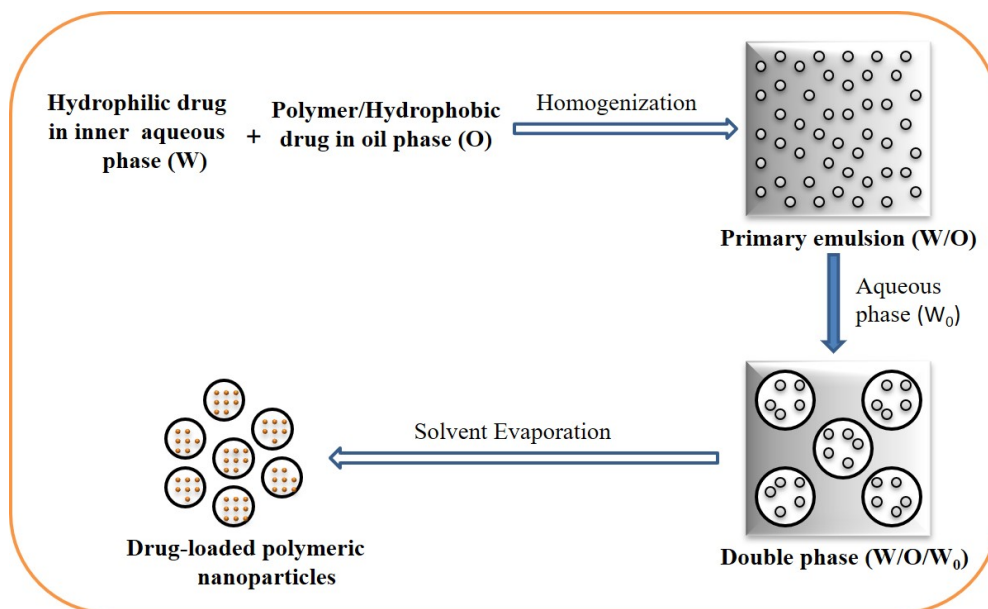


Fig. (5). Double emulsion-solvent evaporation method for nanoparticles synthesis; Iqbal M, Zafar N, Fessi H, Elaissari A (2015). (A higher resolution / colour version of this figure is available in the electronic copy of the article).

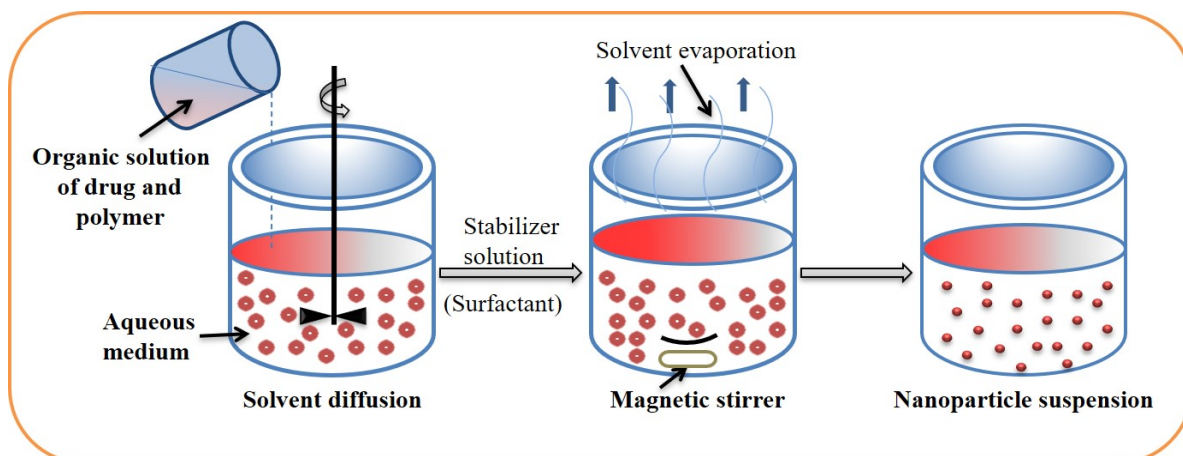


Fig. (6). Nanoprecipitation method of preparation for nanoparticles; Nagavarma BVN YHAA et al. (2012). (A higher resolution / colour version of this figure is available in the electronic copy of the article).

amples of biodegradable and biocompatible nanocarriers. These nanocarriers are utilised to increase the drug's stability and retention period while reducing adverse effects and toxicity. Conjugation or entrapment in the carrier system allows the medications to be absorbed. Because it improves nasal permeability, the nanocarrier technology has many uses in intranasal nose-to-brain transport.

3.1. Solid-lipid Nanoparticles

SLNs are spherical colloidal nanocarriers made of solid-lipid nanoparticles. They're about 50–100 nm in size. They're lipid-based nanoparticles that can be used instead of emulsions, liposomes, or nanoparticles [27]. An exterior surfactant layer stabilises the solid-lipid core matrix of these nanoparticles. A diglyceride, triglyceride, fatty acid, sterol, or wax can be used as a lipid [3]. Both lipophilic and hydro-

philic medicines can be included in SLNs. They are more effective at targeting, encapsulation, and stability. They are non-toxic, and they don't require the use of organic solvents to make them [28].

3.2. Polymeric Nanoparticles

Polymeric nanoparticles are colloidal particles with diameters ranging from 60 to 200 nanometers in diameter. Polymeric nanoparticles can be used to prolong medication release and intracellular absorption. Polymers utilised to make polymeric nanoparticles must be biodegradable, biocompatible, and non-toxic. Some of the most commonly used polymers are poly (lactide co-glycolides), polyglycolides, polylactides, polyanhydrides, polycaprolactone, and poly (cyanoacrylates) [28, 29].

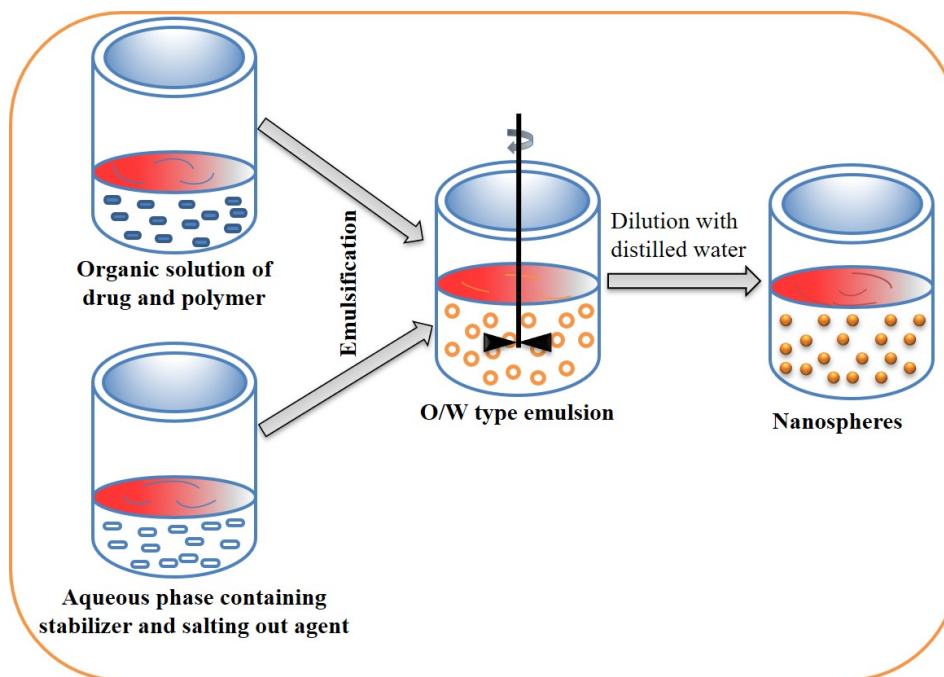


Fig. (7). Salting-out method for Schematic presentation of nanoparticles distribution via nose-to-brain route; Nagavarma BVN YHAA *et al.* (2012). (A higher resolution / colour version of this figure is available in the electronic copy of the article).

3.3. Nano-emulsions

Colloidal dispersions of two immiscible liquids stabilised by a surfactant are known as nano-emulsions. Nano-sized droplets (20–200 nm) are disseminated in a continuous phase. Nano-emulsions come in three varieties:

- oil-in-water (O/W)
- water-in-oil (W/O)
- bi-continuous nano-emulsion

Nano-emulsions have a number of advantages, including increased drug bioavailability, lipophilic drug solubility, and physical stability [30, 31]. A nano-emulsion is resistant to destabilising events such as coalescence, creaming, and sedimentation because of the size (nano-sized) of the droplets [5].

3.4. Liposomes

Liposomes are spherical vesicles with one or more lipid bilayers surrounding a central core. Phospholipids, sphingolipids, polymeric polymers, and synthetic phospholipids are biocompatible, biodegradable lipids that make up a lipid bilayer [32]. Liposomes can be used to encapsulate hydrophilic and lipophilic medicines. Lipophilic medications are entrapped in the liposomal lipid bilayer, while hydrophilic pharmaceuticals are enclosed in the central core [33]. Liposomes work well as diagnostic and therapeutic carriers. Polymers, polysaccharides, peptides, antibodies, and aptamers can be used to change the surface of a liposome, which can improve blood flow and the delivery of medications to the brain [34].

3.5. Dendrimers

Dendrimers are globular macromolecules with tree-like architectures that are synthesised at the nanoscale. Dendrimer comes from the Greek words dendron, which means "tree," and meros, which means "part." Three main components make up the three-dimensional dendrimer structure [35, 36]:

- An inner core
- Repeating branching units called 'generations'
- Outer functional groups

Dendrimers with a lot of branches can hold a lot of medicine. Divergent and convergent techniques are the most popular ways to create dendrimers. Poly (amidoamine) (PA-MAM) dendrimers, poly (propylene imine) (PPI) dendrimers, poly-L-lysine (PPL) dendrimers, and phosphorus (PPH) dendrimers are among the dendrimers used for drug delivery to the brain [37].

Nasal delivery of dendrimers has a number of benefits, like making the drug more water-soluble, making it easier for the drug to get to the brain, and making it easier for the drug to move across the blood-brain barrier [35].

3.6 Mesoporous silica Nanoparticles (MSNs)

Drug targeting platforms made of mesoporous silica nanoparticles are promising. These particles can hold a considerable amount of medication due to their porous nature (pore volume > 0.9cm³/g) and vast surface area (300–1000 m²/g). The medication can be entrapped in the pores of the micron-to nano-sized porous structure, which serves as a reservoir

for drug release to the appropriate administration site. Tissue engineering, diagnostics, and therapies are just a few of the biomedical applications of MSNs. MSNs have recently been discovered to be particularly effective for nose-to-brain targeting, allowing for regulated drug administration. Chemically and thermally, these nanoparticles are inert. They have high biocompatibility and low negative effects.

Inorganic compounds like silicon oxide are used to make MSNs. MSNs are made using a variety of techniques, including sol-gel, chemical etching, microwave-assisted processes, and so on. Depending on the raw materials utilised, MSNs have diverse geometric structures.

Particle size, shape, porosity, pore volume, surface area, drug loading, surface functionalization, and other factors all contribute to the overall characteristics of MSNs. In 2007, Mohanraj and Chen effectively synthesised mesoporous silica nanoparticles loaded with poorly soluble curcumin and chrysin for nose-to-brain transport. Spherical MSNs with a diameter of 220 nm were found to be effective in crossing the BBB and delivering medicines into the CNS [38].

4. CHARACTERIZATION OF NANOPARTICLES

The size, shape, surface charge, drug loading capacity, and encapsulation efficiency of nanoparticles are all factors that influence their effectiveness. Identifying nanoparticles can be done in a variety of ways. For example, electron microscopy is used to determine the particle size and shape.

4.1. Particle Size

The two primary factors investigated in nanoparticles characterization are particle size and particle size distribution. The size of nanoparticles affects their stability, encapsulation effectiveness, and drug loading capacity. The surface-to-volume ratios of smaller particles are higher. Due to the huge surface area available for absorption, nanoparticles can be absorbed quickly. Larger particles, on the other hand, encapsulate better and diffuse more slowly. During storage and transportation, smaller particles are more likely to aggregate than bigger particles [39]. The following are some of the methods for determining particle size [40]:

- Dynamic light scattering (DLS) or photon-correlation spectroscopy
- Scanning electron microscopy
- Transmission electron microscopy
- Atomic force microscopy
- Laser scattering techniques
- X-ray scattering techniques
- Centrifugation techniques

4.2. Percentage Yield

Preparation, collection, and weighting of nanoparticles are all done with precision. The following formula [41] is used to compute the percentage yield:

$$\% \text{ Yield} = \frac{\text{Weight of prepared nanoparticles}}{\text{Total weight of drug and polymer}} \times 100 \quad \dots \quad (1)$$

4.3. Surface Charge

The surface charge of nanoparticles affects their absorption on the cell membrane, which is a key element in delivery efficacy. To represent the surface charge of nanoparticles, the zeta potential is used [42]. If aggregation is to be avoided and nanoparticles are to remain stable, they must have high zeta potential values (either positive or negative). The zeta potential reveals the composition of the core material and coating [16]. Electroacoustic determination and electrophoretic light scattering are used to determine the zeta potential [43].

4.4. Drug Loading and Encapsulation Efficiency

Drug loading is defined as the amount of drug bound per mass of the polymer. Drug loading is achieved by:

- Incorporating the drug at the time of production (incorporation method)
- Adsorption or absorption

The amount of drug loaded into nanoparticles is determined by the following given equations:

$$\% \text{ Drug loading} = \frac{\text{Total weight of drug in particles}}{\text{Total weight of particles}} \times 100 \quad \dots (2)$$

The encapsulation efficiency (EE) is defined as the percentage of drug encapsulated within nanoparticles as a percentage of the polymer. The amount of free drug present in the supernatant is evaluated using the HPLC technique after nanoparticles have been dissolved in a suitable solvent. The following equation is used to compute the encapsulation efficiency:

$$\% \text{ EE} = \frac{\text{Initial amount of drug} - \text{Amount of free drug present in supernatant}}{\text{Initial amount of drug}} \times 100 \quad \dots (3)$$

Nanoparticles should have a high capacity for drug loading and encapsulation. The solid-state solubility of the drug in the polymer medium affects both how well the drug is encapsulated and how much of it is in the finished product [44].

4.5. Drug Release

The behaviour of nanoparticles is determined by the drug release. Under sink circumstances, drug release is achieved through diffusion or matrix degradation. The solubility, diffusion, and degradation of the nanoparticles' matrix are all factors that affect drug release [45]. The most popular method for studying drug release in vitro is dialysis. A dialysis membrane is used in this procedure to separate the nanoparticles. The following are examples of dialysis techniques:

- Dialysis bag diffusion method
- Reverse dialysis bag diffusion method
- Side-by-side diffusion method

In the dialysis bag diffusion method, nanoparticles are delivered into a dialysis bag (inner compartment) filled with media, which is then sealed. The inner compartment is housed in a huge media-filled exterior chamber. The inner

compartment has a smaller volume (1–10 mL) than the outer compartment (40–90 mL). A dialysis membrane is used to divide the two compartments. To decrease the effects of unstirred water layers, agitation is used. Through the dialysis membrane, the medication diffuses from the inner to outer compartments. For dialysis, the sample is taken out of the outer compartment. The nanoparticles are placed in the outer and inner compartments, and the drug release is sampled using the reverse dialysis procedure. A donor cell and a receiver cell with equal quantities of media and a magnetic stirrer comprise the side-by-side dialysis system. The sample is taken from the receiver cell, and a vertical Franz diffusion cell after a dialysis membrane separates the donor and receiver cells [46].

5. STABILITY STUDIES

Nanoparticles should be tested in terms of transport and storage. Long-term stability testing at 25°C/2°C, and 60% relative humidity are advised by the International Conference on Harmonization (ICH) on fast stability at 40°C/2°C and 5% relative humidity 5% RH [47]. Furthermore, the stability of the produced nanoparticles should be examined based on their physical and chemical characteristics. In vivo stability testing can be used to see how a nanoparticle formulation will work.

6. APPLICATIONS IN NOSE-TO-BRAIN DRUG DELIVERY

Many vital lifesaving treatments are delivered using nanoparticles, which is a difficult task. Many researchers have helped create and produce nanoparticles for the treatment of various ailments. It highlights the role of nanoparticles in medication delivery via nose-to-brain.

7. NANOPARTICLE CYTOTOXICITY AND MITIGATION TECHNIQUES

7.1. Limitations of Nanoparticles in Nose-to-brain Delivery

The intranasal approach is non-invasive and has numerous medical advantages. Intranasally given formulations have a faster onset of action and higher bioavailability, as well as avoid first-pass metabolism and have fewer adverse effects. Intranasal delivery, however, has a number of drawbacks, including limited permeability, enzymatic degradation, muco-ciliary clearance, and short retention periods [48]. Intranasal administration is a simple and easy alternative to conventional routes. Intranasally, however, only very minute amounts of a formulation can be given. As a result, only very effective medications can be given [49–51]. A variety of procedures are employed to improve a drug's absorption and permeability. Absorption enhancers help drugs go through the nasal mucosa more quickly [52]. Mucoadhesive systems, such as mucoadhesive polymers, viscous formulations, in situ gelation, and hydrogels, have improved retention time [53]. Some medications can irritate the nasal mucosa, putting the cilia of the nasal mucosa in jeopardy. The biological reaction to nanoparticles is altered, resulting in neurotoxicity.

7.2. Cytotoxicity of Nanoparticles

It is well established that certain nanoparticle exposure might have negative health impacts. Understanding their methods of action or toxicity and researching any potential health implications is crucial.

Smart medication delivery uses polymeric nanoparticles, which can be created from synthetic or natural polymers. In-depth research is being done on them as carriers for controlled/sustained release in drug delivery systems. These nanopharmaceuticals' action is constrained by safety concerns, toxicity concerns, poor biocompatibility, and physiological difficulties. These nanoparticles' drawbacks include the hazardous breakdown process, residual material attached to them, and toxic monomer aggregation [54].

Quantum size effects, which are connected to oxidative stress, cytotoxicity, and genotoxicity, have an impact on the toxicity of polymeric NPs [55]. Nadège et al. observed that the somewhat cytotoxic chitosan polymer gave considerable cytotoxicity to PLGA nanoparticles when employed as a nanoparticle stabilizer after investigating the toxicity of a range of poly(lactide-co-glycolic acid) (PLGA) nanoparticles on human-like THP-1 macrophages. Both polyvinyl alcohol and poloxamer 188 polymers significantly increased PLGA nano's cytotoxicity. These results showed that stabilizers used in PLGA nanoparticle formulation have a substantial toxicological function when utilized at high concentrations, which may have an impact on the local toxicity of PLGA-based nanomedicine [56].

Size, surface area, surface charge, and aggregation state affect NP toxicity [57]. These features impact NP dispersion, deposition, and molecular interactions with proteins and macromolecules. Size affects NP penetration, cellular absorption, and toxicity. Some investigations imply a link between NP size, distribution, and renal ROS production [58, 59]. Liver toxicity is size-dependent. 10 nm silver NPs had greater tissue dispersion and produced more liver toxicity than 40 and 100 nm NPs [60, 61].

Shape affects NP dispersion, deposition, and clearance together with size. Long fibrous particles, such as single-walled nanotubes, are hard for the body to remove and cause organ deposits [62]. Surface chemistry affects NP pharmacokinetics. Charged NPs tend to accumulate more in target organs. Ionic zinc oxide NPs accumulated more in organs after oral or intravenous treatment than uncharged NPs [63]. (Table 1) Polysaccharide conjugation increases NP accumulation in the brain, liver, and spleen, which correlates to their toxicity [64]. Altering NP surface qualities with coatings can lower their toxicity. PEG reduces NP toxicity by changing their protein interactions. PEGylation may affect NPs' cellular uptake and medication delivery effectiveness.

7.3. Strategies/mitigation Techniques to Overcome Cytotoxicity

The prior studies show increased concern regarding NP toxicity and emphasize the necessity to address toxicity during original design, whether for industrial or therapeutic usage. Structured nanoemulsions and solid lipid nanoparticles

Table 1. Various nanoparticulate systems for nose-to-brain drug delivery.

Therapeutic Payload	Nanocarrier system	Material	Formulation Technique	Therapeutic Outcome	Refs.
Huperzine A	LF-TMC NPs	Lactoferrin and N-trimethylated chitosan	Emulsion-solvent evaporation method	Good sustained release effect, adhesion and targeting ability and broad application as intranasal drug delivery carrier	[18]
Bromocriptine	CS NPs	Chitosan	Ionic-gelation-method	Nanocarrier has increased brain uptake of bromocriptine also enhanced its antioxidant activity and make effective system for treatment of Parkinson's disease	[21]
Rasagiline	CG NPs	Chitosan glutamate	Ionic-gelation method	These could be promising delivery system for the treatment of Parkinson's disease	[22]
Carboplatin	PCL NPs	Poly(ϵ -caprolactone)	Double emulsion-solvent evaporation method	Better nasal absorption and sustained release profile so can be used in intranasal administration of carboplatin for improved brain delivery	[24]
Teriflunomide	NLC	Compritol 888 ATO (Solid-Lipid) and Maisine 35-1 (Liquid-Lipid)	Melt emulsification ultra-sonification method	Enhanced the nasal residence time	[26]
Selegiline	NE	Grape seed oil	High energy emulsification method	Enhanced the uptake of selegiline to brain, improve brain bioavailability and restore normal dopamine level	[54]
Tarenfluril	PNPs SLNs	Poly (lactic-co-glycolic) acid	Emulsion-solvent-diffusion method Emulsion-solvent evaporation method	Desirable brain biodistribution profiles, effective in delivering Tarenfluril to brain for treatment of Alzheimer's disease	[55]
Lamotrigine	NLs	Phospholipid 90G and Cholesterol	Thin film hydration and rehydration method	High entrapment in lipid bilayer, high release rate and better penetration than suspension	[56]
Venlafaxine	PLGA NPs	Poly (lactic-co-glycolic acid)	Double emulsion-solvent evaporation method	Plain nanoparticles showed fast and highest ability to reach brain after intranasal administration via nose-to-brain delivery as compared to functionalized nanoparticles	[57]
Eugenol	CS PCL NPs	Chitosan and Poly(ϵ -caprolactone)	Modified double-emulsion (W/O/W ₀) method	Enhancement of drug bioavailability and can help in treating cerebral ischemia effectively	[58]
Pramipexole Dihydrochloride	CNs	Chitosan	Ionic-gelation-method	Showed significant brain targeting potential compared to other formulation so can be utilized for effective brain targeting via intranasal route for Parkinson's disease treatment	[59]
Pioglitazone	PLGA-PEG NPs	Poly (lactic-co-glycolic) acid-Poly ethylene glycol copolymer	Solvent displacement method	Nasal mucosa showed enhanced drug permeation in the tissues in the treatment of Alzheimer's disease and it could be a promising delivery route in treatment of Alzheimer's disease	[60]
Pioglitazone	NLC	Liquid lipid capmul MCM and Solid lipid tripalmitin	Microemulsion method	The formulation improves the permeability of Pioglitazone across nasal mucosa and also improved the concentration of drug reaching brain	[61]
Dopamine	LF-BNPs	Borneol and lactoferrin	Double emulsion-solvent evaporation method	NPs increased the Dopamine absorption into the brain demonstrating the co-modification significantly enhanced transport of drug towards brain	[62]
Kaempferol	MNE	Chitosan	High-pressure homogenization technique	MNE decreased viability of glioma cells by enhancing apoptosis and seems to be an important carrier for cancer treatment	[63]

NLC: Nanostructured lipid carriers; NE: Nano-emulsion; CGNPs: Chitosan glutamate nanoparticles; PNPs: Polymeric nanoparticles; SLNs: Solid-lipid nanoparticles; NLs: Nanoliposomes; PLGA NPs: Poly(lactic-co-glycolic acid) nanoparticles; CS PCL NPs: Chitosan coated poly(ϵ -caprolactone) nanoparticles; PCLNPs: Poly (ϵ -caprolactone) nanoparticles; CSNPs: Chitosan nanoparticles; CNs: Chitosan nanoparticles; PLGA-PEG NPs: Poly(lactic-co-glycolic) acid-Poly ethylene glycol copolymer nanoparticles; LF-TMCNPs: Lactoferrin conjugated N-trimethylated chitosan nanoparticles; LF-BNPs: Lactoferrin - borneol co-modified nanoparticles; MNE: Mucoadhesive nano-emulsion.

highlight one way to design safer NPs. These nanoparticles are made with FDA-approved, food-grade lipids, proteins, polysaccharides, and surfactants [65]. Solid or metal-containing NPs are similarly hazardous, according to studies. So, they're used less.

These problems have been the subject of many researches, such as the development of biocompatible and biodegradable pH-responsive hybrid nanoparticles by Palanikumar et al. To reduce interactions with serum proteins and macrophages, a cross-linked bovine serum albumin shell was added to these nanosystems built around a PLGA core filled with drugs. The drug-loaded NPs showed potent anticancer activity both in vitro and in vivo while having no negative effects on healthy tissue [66].

The following strategies may help to reduce the cytotoxicity of nanoparticles:

- Next generation lipids (smart lipids)
- Degradable nanoparticles
- Surface coating
- Doping
- Alteration of surface properties

"Next-generation lipids" that combine high potency and biodegradability may reduce the danger of certain NPs, notably lipid-based NPs. Martin et al. created biodegradable lipids by adding bio-cleavable ester functionalities to hydrophobic alkyl chains. This family of biodegradable lipids in preclinical trials demonstrated fast plasma clearance and enhanced tolerability [67]. Surface coating solutions are also offered to reduce NP risk and develop safer nanotechnology. Surface coating refers to modifying, functionalizing, or stabilizing NPs to change their characteristics. NPs can be coated with single- or multi-layer polymers that are full or partial [68]. If chosen appropriately, the coating material offers biocompatibility and impacts the behaviour (e.g., colloidal stability) and destiny (e.g., degradation, excretion, accumulation) of NPs after administration in biological fluids, cells, and organisms.

Inorganic NPs are often doped. This approach adds impurities to materials to improve their chemical and physical characteristics [69–71]. Aluminium, titanium, and iron are dopants. When equally integrated into nanoparticles, these dopants modify the density of reactive chemical entities on the surface and lower metal ion binding energy to oxygen. Doping NPs can reduce NP dissolution and hazardous ion release, altering reactive surfaces and reducing ROS formation [72, 73].

FSP is a well-established NP doping method. FSP employs a quick combustion process, liquid precursor, and self-sustaining flame with a high local temperature and huge temperature gradient [74].

Altering NPs' charge density and hydrophobicity may lower their risk and increase their efficacy in medicinal applications, such as targeted medication administration [75, 76].

CONCLUSION

The intranasal route offers a lot of promise for overcoming issues with drug delivery caused by protective barriers like the BBB. Many medications are delivered via various modes of administration, and these issues constitute a big issue. The trigeminal and olfactory nerve pathways are used to deliver medicine directly to the brain via the intranasal method. As a result, this method has a number of advantages, including increased bioavailability, avoidance of first-pass metabolism and enzymatic degradation, and a lower risk of side effects. Targeted drug delivery is significantly influenced by nanoparticles. They increase the amount of medication that can be given by enhancing retention duration and penetration in the nasal cavity. Intranasal administration of drug-loaded nanoparticles can thus be used to treat brain diseases effectively.

LIST OF ABBREVIATIONS

BBB	=	Blood–Brain Barrier
NPs	=	Nanoparticles
CSF	=	Blood Cerebrospinal Fluid
Lf	=	Lactoferrin
TMC	=	N-Trimethylated Chitosan
PDI	=	Polydispersity Index
BRC	=	Bromocriptine
CS NPs	=	Chitosan Nanoparticles
W/O/W	=	Water-Oil-Water
O/W/O	=	Oil–Water-Oil
PCL	=	Carboplatin-Loaded Poly
MSNs	=	Mesoporous Silica Nanoparticles

CONSENT FOR PUBLICATION

Not applicable.

FUNDING

None Declared.

CONFLICT OF INTEREST

Author(s) declares no conflict of interest

ACKNOWLEDGMENTS

The authors are very thankful to the Principal, Rajarshi Shahu College of Pharmacy, Buldana, for providing article writing and editing facilities. Finally, the authors extend thanks to all those whose cooperation helped complete this work successfully.

REFERENCES

- [1] Wang, Z.; Xiong, G.; Tsang, W.C.; Schätzlein, A.G.; Uchegbu, I.F. Nose-to-brain delivery. *J. Pharmacol. Exp. Ther.*, **2019**, *370*(3), 593-601.
<http://dx.doi.org/10.1124/jpet.119.258152> PMID: 31126978

- [2] Pardridge, W.M. Drug transport across the blood-brain barrier. *J. Cereb. Blood Flow Metab.*, **2012**, 32(11), 1959-1972. <http://dx.doi.org/10.1038/jcbfm.2012.126> PMID: 22929442
- [3] Battaglia, L.; Panciani, P.P.; Muntoni, E.; Capucchio, M.T.; Bisibetti, E.; De Bonis, P.; Mioletti, S.; Fontanella, M.; Swaminathan, S. Lipid nanoparticles for intranasal administration: Application to nose-to-brain delivery. *Expert Opin. Drug Deliv.*, **2018**, 15(4), 369-378. <http://dx.doi.org/10.1080/17425247.2018.1429401> PMID: 29338427
- [4] Gao, H. Progress and perspectives on targeting nanoparticles for brain drug delivery. *Acta Pharm. Sin. B*, **2016**, 6(4), 268-286. <http://dx.doi.org/10.1016/j.apsb.2016.05.013> PMID: 27471668
- [5] Kumar, A.; Pandey, A.N.; Jain, S.K. Nasal-nanotechnology: Revolution for efficient therapeutics delivery. *Drug Deliv.*, **2016**, 23(3), 671-683. <http://dx.doi.org/10.3109/10717544.2014.920431> PMID: 24901207
- [6] Khan, I.; Saeed, K.; Khan, I. Nanoparticles: Properties, applications and toxicities. *Arab. J. Chem.*, **2019**, 12(7), 908-931. <http://dx.doi.org/10.1016/j.arabjc.2017.05.011>
- [7] Serlin, Y.; Shelef, I.; Knyazer, B.; Friedman, A. Anatomy and physiology of the blood-brain barrier. *Semin. Cell Dev. Biol.*, **2015**, 38, 2-6. <http://dx.doi.org/10.1016/j.semcdb.2015.01.002> PMID: 25681530
- [8] Selvaraj, K.; Gowthamarajan, K.; Karri, V.V.S.R. Nose to brain transport pathways an overview: Potential of nanostructured lipid carriers in nose to brain targeting. *Artif. Cells Nanomed. Biotechnol.*, **2018**, 46(8), 2088-2095. PMID: 29282995
- [9] Aderibigbe, B.A.; Naki, T. Chitosan-based nanocarriers for nose to brain delivery. *Appl. Sci.*, **2019**, 9(11), 2219. <http://dx.doi.org/10.3390/app9112219>
- [10] Anu, M.E.S.; Saravanakumar, M.P. A review on the classification, characterisation, synthesis of nanoparticles and their application. *IOP Conf. Ser. Mater. Sci. Eng.*, **2017**, 263, 032019. <http://dx.doi.org/10.1088/1757-899X/263/3/032019>
- [11] Patra, J.K.; Baek, K.H. Green nanobiotechnology: Factors affecting synthesis and characterization techniques. *J. Nanomater.*, **2014**, 2014, 417305. <http://dx.doi.org/10.1155/2014/417305>
- [12] Satyanarayana, T.; Reddy, S.S. A review on chemical and physical synthesis methods of nanomaterials. *Int. J. Res. Appl. Sci. Eng. Technol.*, **2018**, 6(1), 2885-2889. <http://dx.doi.org/10.22214/ijraset.2018.1396>
- [13] Jeyaraj, M.; Gurunathan, S.; Qasim, M.; Kang, M.H.; Kim, J.H. A comprehensive review on the synthesis, characterization, and biomedical application of platinum nanoparticles. *Nanomaterials*, **2019**, 9(12), 1719. <http://dx.doi.org/10.3390/nano9121719> PMID: 31810256
- [14] Hussain, I.; Singh, N.B.; Singh, A.; Singh, H.; Singh, S.C. Green synthesis of nanoparticles and its potential application. *Biotechnol. Lett.*, **2016**, 38(4), 545-560. <http://dx.doi.org/10.1007/s10529-015-2026-7> PMID: 26721237
- [15] Singh, P.; Kim, Y.J.; Zhang, D.; Yang, D.C. Biological synthesis of nanoparticles from plants and microorganisms. *Trends Biotechnol.*, **2016**, 34(7), 588-599. <http://dx.doi.org/10.1016/j.tibtech.2016.02.006> PMID: 26944794
- [16] Pal, S.L.; Jana, U.; Manna, P.K.; Mohanta, G.P.; Manavalan, R. Nanoparticle: An overview of preparation and characterisation. *J. Appl. Pharm. Sci.*, **2011**, 1(6), 228-234.
- [17] Hoa, L.T.M.; Chi, N.T.; Nguyen, L.H.; Chien, D.M. Preparation and characterisation of nanoparticles containing ketoprofen and acrylic polymers prepared by emulsion solvent evaporation method. *J. Exp. Nanosci.*, **2012**, 7(2), 189-197. <http://dx.doi.org/10.1080/17458080.2010.515247>
- [18] Meng, Q.; Wang, A.; Hua, H.; Jiang, Y.; Wang, Y.; Mu, H.; Wu, Z.; Sun, K. Intranasal delivery of huperzine A to the brain using lactoferrin-conjugated N-trimethylated chitosan surface-modified PLGA nanoparticles for treatment of Alzheimer's disease. *Int. J. Nanomed.*, **2018**, 13, 705-718. <http://dx.doi.org/10.2147/IJN.S151474> PMID: 29440896
- [19] Patra, J.K.; Das, G.; Fraceto, L.F.; Campos, E.V.R.; Rodriguez, T.M.P.; Acosta, T.L.S.; Diaz, T.L.A.; Grillo, R.; Swamy, M.K.; Sharma, S.; Habtemariam, S.; Shin, H.S. Nano based drug delivery systems: Recent developments and future prospects. *J. Nanobiotechnol.*, **2018**, 16(1), 71. <http://dx.doi.org/10.1186/s12951-018-0392-8> PMID: 30231877
- [20] Pedroso, S.S.; Fleitas, S.N. Iontropic gelation method in the synthesis of nanoparticles/microparticles for biomedical purposes. *Polym. Int.*, **2020**, 69(5), 443-447. <http://dx.doi.org/10.1002/pi.5970>
- [21] Md, S.; Khan, R.A.; Mustafa, G.; Chuttani, K.; Baboota, S.; Sahni, J.K.; Ali, J. Bromocriptine loaded chitosan nanoparticles intended for direct nose to brain delivery: Pharmacodynamic, Pharmacokinetic and scintigraphy study in mice model. *Eur. J. Pharm. Sci.*, **2013**, 48(3), 393-405. <http://dx.doi.org/10.1016/j.ejps.2012.12.007> PMID: 23266466
- [22] Mittal, D.; Md, S.; Hasan, Q.; Fazil, M.; Ali, A.; Baboota, S.; Ali, J. Brain targeted nanoparticulate drug delivery system of rasagiline via intranasal route. *Drug Deliv.*, **2016**, 23(1), 130-139. <http://dx.doi.org/10.3109/10717544.2014.907372> PMID: 24786489
- [23] Iqbal, M.; Zafar, N.; Fessi, H.; Elaissari, A. Double emulsion solvent evaporation techniques used for drug encapsulation. *Int. J. Pharm.*, **2015**, 496(2), 173-190. <http://dx.doi.org/10.1016/j.ijpharm.2015.10.057> PMID: 26522982
- [24] Alex, A.T.; Joseph, A.; Shavi, G.; Rao, J.V.; Udupa, N. Development and evaluation of carboplatin-loaded PCL nanoparticles for intranasal delivery. *Drug Deliv.*, **2016**, 23(7), 2144-2153. <http://dx.doi.org/10.3109/10717544.2014.948643> PMID: 25544603
- [25] Nagavarma, B.V.N. Different techniques for preparation of polymeric nanoparticles – A review. *Asian J. Pharm. Clin. Res.*, **2012**, 5(3), 16-23.
- [26] Gadhave, D.G.; Kokare, C.R. Nanostructured lipid carriers engineered for intranasal delivery of triflunomide in multiple sclerosis: Optimization and *in vivo* studies. *Drug Dev. Ind. Pharm.*, **2019**, 45(5), 839-851. <http://dx.doi.org/10.1080/03639045.2019.1576724> PMID: 30702966
- [27] Hangargekar, S.R.; Mohanty, P.; Jain, A. Solid lipid nanoparticles for brain targeting. *J. Drug Deliv. Ther.*, **2019**, 9(6-s), 248-252. <http://dx.doi.org/10.22270/jddt.v9i6-s.3783>
- [28] Kuldeep, S. Nano formulation a novel approach for nose to brain drug delivery. *J. Chem. Pharm. Res.*, **2016**, 8(2), 208-215.
- [29] Bonferoni, M.; Rossi, S.; Sandri, G.; Ferrari, F.; Gavini, E.; Rassa, G.; Giunchedi, P. Nanoemulsions for "nose-to-brain" drug delivery. *Pharmaceutics*, **2019**, 11(2), 84. <http://dx.doi.org/10.3390/pharmaceutics11020084> PMID: 30781585
- [30] Jaiswal, M.; Dudhe, R.; Sharma, P. K. Nanoemulsion: An advanced mode of drug delivery system. *3 Biotech.*, **2015**, 5(2), 123-127.
- [31] Zarif, L. Cochleates as Nanoparticulate Drug Carriers. In: *Nanoparticulates as Drug Carriers*; PUBLISHED BY IMPERIAL COLLEGE PRESS AND DISTRIBUTED BY WORLD SCIENTIFIC PUBLISHING CO, Singapore, **2006**, pp. 349-366. http://dx.doi.org/10.1142/9781860949074_0016
- [32] Hong, S.S.; Oh, K.T.; Choi, H.G.; Lim, S.J. Liposomal formulations for nose-to-brain delivery: Recent advances and future perspectives. *Pharmaceutics*, **2019**, 11(10), 540. <http://dx.doi.org/10.3390/pharmaceutics11100540> PMID: 31627301
- [33] Vieira, D.; Gamarra, L. Getting into the brain: Liposome-based strategies for effective drug delivery across the blood-brain barrier. *Int. J. Nanomed.*, **2016**, 11, 5381-5414. <http://dx.doi.org/10.2147/IJN.S117210> PMID: 27799765
- [34] Parajapati, S.K.; Maurya, S.D.; Das, M.K.; Tilak, V.K.; Verma, K.K.; Dhakar, R.C. Potential application of dendrimers in drug delivery: A concise review and update. *J. Drug Deliv. Ther.*, **2016**, 6(2), 71-88. <http://dx.doi.org/10.22270/jddt.v6i2.1195>
- [35] Abbasi, E.; Aval, S.F.; Akbarzadeh, A.; Milani, M.; Nasrabadi, H.T.; Joo, S.W.; Hanifehpour, Y.; Nejati, K.K.; Pashaei, A.R. Dendrimers: Synthesis, applications, and properties. *Nanoscale Res. Lett.*, **2014**, 9(1), 247. <http://dx.doi.org/10.1186/1556-276X-9-247> PMID: 24994950
- [36] Zhu, Y.; Liu, C.; Pang, Z. Dendrimer-based drug delivery systems for brain targeting. *Biomolecules*, **2019**, 9(12), 790.

- <http://dx.doi.org/10.3390/biom9120790> PMID: 31783573
- [37] Lungare, S.; Hallam, K.; Badhan, R.K.S. Phytochemical-loaded mesoporous silica nanoparticles for nose-to-brain olfactory drug delivery. *Int. J. Pharm.*, **2016**, *513*(1-2), 280-293. <http://dx.doi.org/10.1016/j.ijpharm.2016.09.042> PMID: 27633279
- [38] Mohanraj, V.J.; Chen, Y. Nanoparticles - A review. *Trop. J. Pharm. Res.*, **2007**, *5*(1), 561-573. <http://dx.doi.org/10.4314/tjpr.v5i1.14634>
- [39] Caputo, F.; Clogston, J.; Calzolari, L.; Rösslein, M.; Prina-Mello, A. Measuring particle size distribution of nanoparticle enabled medicinal products, the joint view of EUNCL and NCI-NCL. A step by step approach combining orthogonal measurements with increasing complexity. *J. Control. Release*, **2019**, *299*, 31-43. <http://dx.doi.org/10.1016/j.jconrel.2019.02.030> PMID: 30797868
- [40] Pandey P., D.M. A brief review on inorganic nanoparticles. *Crit. Rev.*, **2016**, *3*(3), 18-26.
- [41] Rasmussen, M.K.; Pedersen, J.N.; Marie, R. Size and surface charge characterization of nanoparticles with a salt gradient. *Nat. Commun.*, **2020**, *11*(1), 2337. <http://dx.doi.org/10.1038/s41467-020-15889-3> PMID: 32393750
- [42] Honary, S.; Zahir, F. Effect of zeta potential on the properties of nano-drug delivery systems - A review (Part 1). *Trop. J. Pharm. Res.*, **2013**, *12*(2), 255-264.
- [43] Jain, A.K.; Thareja, S. *In vitro* and *in vivo* characterization of pharmaceutical nanocarriers used for drug delivery. *Artif. Cells Nanomed. Biotechnol.*, **2019**, *47*(1), 524-539. <http://dx.doi.org/10.1080/21691401.2018.1561457> PMID: 30784319
- [44] Ranjit, K.; Nanoparticle, B.A. An overview of preparation, characterization and application. *Int Res J Pharm.*, **2013**, *4*(4), 47-57.
- [45] D'Souza, S. A review of *in vitro* drug release test methods for nano-sized dosage forms. *Adv. Pharm.*, **2014**, *2014*, 304757. <http://dx.doi.org/10.1155/2014/304757> Muthu, M.S.; Feng, S.S. Pharmaceutical stability aspects of nano-medicines. *Nanomedicine*, **2009**, *4*(8), 857-860. <http://dx.doi.org/10.2217/nmm.09.75> PMID: 19958220
- [47] Mistry, A.; Stolnik, S.; Illum, L. Nanoparticles for direct nose-to-brain delivery of drugs. *Int. J. Pharm.*, **2009**, *379*(1), 146-157. <http://dx.doi.org/10.1016/j.ijpharm.2009.06.019> PMID: 19555750
- [48] Sonvico, F.; Clementino, A.; Buttini, F.; Colombo, G.; Pescina, S.; Stanisquaski, G.S.; Raffin, P.A.; Nicoli, S. Surface-modified nanocarriers for nose-to-brain delivery: From bioadhesion to targeting. *Pharmaceutics*, **2018**, *10*(1), 34. <http://dx.doi.org/10.3390/pharmaceutics10010034> PMID: 29543755
- [49] Erdő, F.; Bors, L.A.; Farkas, D.; Bajza, Á.; Gizurarson, S. Evaluation of intranasal delivery route of drug administration for brain targeting. *Brain Res. Bull.*, **2018**, *143*, 155-170. <http://dx.doi.org/10.1016/j.brainresbull.2018.10.009> PMID: 30449731
- [50] Md, S.; Mustafa, G.; Baboota, S.; Ali, J. Nanoneurotherapeutics approach intended for direct nose to brain delivery. *Drug Dev. Ind. Pharm.*, **2015**, *41*(12), 1922-1934. <http://dx.doi.org/10.3109/03639045.2015.1052081> PMID: 26057769
- [51] Ghadiri, M.; Young, P.; Traini, D. Strategies to enhance drug absorption *via* nasal and pulmonary routes. *Pharmaceutics*, **2019**, *11*(3), 113. <http://dx.doi.org/10.3390/pharmaceutics11030113> PMID: 30861990
- [52] Islam, S.U.; Shehzad, A.; Ahmed, M.B.; Lee, Y.S. Intranasal delivery of nanoformulations: A potential way of treatment for neurological disorders. *Molecules*, **2020**, *25*(8), 1929. <http://dx.doi.org/10.3390/molecules25081929> PMID: 32326318
- [53] Almasser, S. A review on nasal drug delivery system and its contribution in therapeutic management. *Asian J. Pharm. Clin. Res.*, **2019**, *12*(1), 40-45. <http://dx.doi.org/10.22159/ajpcr.2019.v12i1.29443>
- [54] Anagnostou, K.; Stylianakis, M.; Michaleas, S.; Skouras, A. Biodegradable nanomaterials. In: *Nanomaterials for Clinical Applications*; Elsevier: Amsterdam, Netherlands: **2020**; pp. 123-157.
- [55] Singh, N.; Joshi, A.; Toor, A.; Verma, G. Drug delivery: Advancements and challenges. In: *Nanostruct Drug Deliv*; Elsevier: Amsterdam, Netherlands: **2017**; pp. 865-886.
- [56] Suriya, P.A.; Dorothy, R.; Jancirani, S.; Rajendran, S.; Singh, G.; Senthil, K.S. Recent advances in the study of toxicity of polymer-based nanomaterials. In: *Nanotoxicity*; Elsevier: Amsterdam, Netherlands: **2020**; pp. 143-165. <http://dx.doi.org/10.1016/B978-0-12-819943-5.00007-5>
- [57] Wu, T.; Tang, M. Review of the effects of manufactured nanoparticles on mammalian target organs. *J. Appl. Toxicol.*, **2018**, *38*(1), 25-40. <http://dx.doi.org/10.1002/jat.3499> PMID: 28799656
- [58] Elsaesser, A.; Howard, C.V. Toxicology of nanoparticles. *Adv. Drug Deliv. Rev.*, **2012**, *64*(2), 129-137. <http://dx.doi.org/10.1016/j.addr.2011.09.001> PMID: 21925220
- [59] Sharifi, S.; Behzadi, S.; Laurent, S.; Forrest, M.L.; Stroeve, P.; Mahmoudi, M. *Toxicity of nanomaterials*. *Chem. Soc. Rev.*, **2012**, *41*, 2323-2343.
- [60] Wu, T.; Tang, M. Toxicity of quantum dots on respiratory system. *Inhal. Toxicol.*, **2014**, *26*(2), 128-139. <http://dx.doi.org/10.3109/08958378.2013.871762> PMID: 24495248
- [61] Recordati, C.; De Maglie, M.; Bianchessi, S.; Argenti, S.; Cella, C.; Mattiello, S.; Cubadda, F.; Aureli, F.; D'Amato, M.; Raggi, A.; Lenardi, C.; Milani, P.; Scanziani, E. Tissue distribution and acute toxicity of silver after single intravenous administration in mice: Nano-specific and size-dependent effects. *Part. Fibre Toxicol.*, **2015**, *13*(1), 12. <http://dx.doi.org/10.1186/s12989-016-0124-x> PMID: 26926244
- [62] Zoroddu, M.; Medici, S.; Ledda, A.; Nurchi, V.; Lachowicz, J.; Peana, M. Toxicity of nanoparticles. *Curr. Med. Chem.*, **2014**, *21*(33), 3837-3853. <http://dx.doi.org/10.2174/0929867321666140601162314> PMID: 25306903
- [63] Paek, H.J.; Lee, Y.J.; Chung, H.E.; Yoo, N.H.; Lee, J.A.; Kim, M.K.; Lee, J.K.; Jeong, J.; Choi, S.J. Modulation of the pharmacokinetics of zinc oxide nanoparticles and their fates *in vivo*. *Nanoscale*, **2013**, *5*(23), 11416-11427. <http://dx.doi.org/10.1039/c3nr02140h> PMID: 23912904
- [64] Shegokar, R.; Singh, K.K. Surface modified nevirapine nanosuspensions for viral reservoir targeting: *In vitro* and *in vivo* evaluation. *Int. J. Pharm.*, **2011**, *421*(2), 341-352. <http://dx.doi.org/10.1016/j.ijpharm.2011.09.041> PMID: 21986114
- [65] McClements, D.J. Emulsion design to improve the delivery of functional lipophilic components. *Annu. Rev. Food Sci. Technol.*, **2010**, *1*(1), 241-269. <http://dx.doi.org/10.1146/annurev.food.080708.100722> PMID: 22129337
- [66] Palanikumar, L.; Al-Hosani, S.; Kalmouni, M.; Nguyen, V.P.; Ali, L.; Pasricha, R.; Barrera, F.N.; Magzoub, M. pH-responsive high stability polymeric nanoparticles for targeted delivery of anticancer therapeutics. *Commun. Biol.*, **2020**, *3*(1), 95. <http://dx.doi.org/10.1038/s42003-020-0817-4> PMID: 32127636
- [67] Maier, M.A.; Jayaraman, M.; Matsuda, S.; Liu, J.; Barros, S.; Querbes, W.; Tam, Y.K.; Ansell, S.M.; Kumar, V.; Qin, J.; Zhang, X.; Wang, Q.; Panesar, S.; Hutabarat, R.; Carioto, M.; Hettinger, J.; Kandasamy, P.; Butler, D.; Rajeev, K.G.; Pang, B.; Charisse, K.; Fitzgerald, K.; Mui, B.L.; Du, X.; Cullis, P.; Madden, T.D.; Hope, M.J.; Manoharan, M.; Akinc, A. Biodegradable lipids enabling rapidly eliminated lipid nanoparticles for systemic delivery of RNAi therapeutics. *Mol. Ther.*, **2013**, *21*(8), 1570-1578. <http://dx.doi.org/10.1038/mt.2013.124> PMID: 23799535
- [68] Schubert, J.; Chanana, M. Coating matters: Review on colloidal stability of nanoparticles with biocompatible coatings in biological media, living cells and organisms. *Curr. Med. Chem.*, **2018**, *25*(35), 4553-4586. <http://dx.doi.org/10.2174/0929867325666180601101859> PMID: 29852857
- [69] Thirumala, R.G.; Babu, B.; Joyce, S.R.; Pushpa, M.V.; Ravikumar, R.V.S.S.N. Spectral investigations on undoped and Cu²⁺ doped ZnO-CdS composite nanopowders. *Spectrochim. Acta A Mol. Biomol. Spectrosc.*, **2015**, *139*, 86-93. <http://dx.doi.org/10.1016/j.saa.2014.12.021> PMID: 25554956

- [70] Adeleye, A.S.; Pokhrel, S.; Mädler, L.; Keller, A.A. Influence of nanoparticle doping on the colloidal stability and toxicity of copper oxide nanoparticles in synthetic and natural waters. *Water Res.*, **2018**, *132*, 12-22.
<http://dx.doi.org/10.1016/j.watres.2017.12.069> PMID: 29304444
- [71] Ahmad, J.; Siddiqui, M.A.; Akhtar, M.J.; Alhadlaq, H.A.; Alshamsan, A.; Khan, S.T.; Wahab, R.; Al-Khedhairi, A.A.; Al-Salim, A.; Musarrat, J.; Saquib, Q.; Fareed, M.; Ahamed, M. Copper doping enhanced the oxidative stress-mediated cytotoxicity of TiO₂ nanoparticles in A549 cells. *Hum. Exp. Toxicol.*, **2018**, *37*(5), 496-507.
<http://dx.doi.org/10.1177/0960327117714040> PMID: 28621211
- [72] Sun, B.; Pokhrel, S.; Dunphy, D.R.; Zhang, H.; Ji, Z.; Wang, X.; Wang, M.; Liao, Y.P.; Chang, C.H.; Dong, J.; Li, R.; Mädler, L.; Brinker, C.J.; Nel, A.E.; Xia, T. Reduction of acute inflammatory effects of fumed silica nanoparticles in the lung by adjusting silanol display through calcination and metal doping. *ACS Nano*, **2015**, *9*(9), 9357-9372.
<http://dx.doi.org/10.1021/acsnano.5b03443> PMID: 26200133
- [73] Naatz, H.; Lin, S.; Li, R.; Jiang, W.; Ji, Z.; Chang, C.H.; Köser, J.; Thöming, J.; Xia, T.; Nel, A.E.; Mädler, L.; Pokhrel, S. Safe-by-Design CuO nanoparticles via Fe-doping. Cu–O bond length variation, and biological assessment in cells and zebrafish embryos. *ACS Nano*, **2017**, *11*(1), 501-515.
<http://dx.doi.org/10.1021/acsnano.6b06495> PMID: 28026936
- [74] Teoh, W.Y.; Amal, R.; Mädler, L. Flame spray pyrolysis: An enabling technology for nanoparticles design and fabrication. *Nanoscale*, **2010**, *2*(8), 1324-1347.
<http://dx.doi.org/10.1039/c0nr00017e> PMID: 20820719
- [75] Hola, K.; Markova, Z.; Zoppellaro, G.; Tucek, J.; Zboril, R. Tailored functionalization of iron oxide nanoparticles for MRI, drug delivery, magnetic separation and immobilization of biosubstances. *Biotechnol. Adv.*, **2015**, *33*(6), 1162-1176.
<http://dx.doi.org/10.1016/j.biotechadv.2015.02.003> PMID: 25689073
- [76] Mout, R.; Moyano, D.F.; Rana, S.; Rotello, V.M. Surface functionalization of nanoparticles for nanomedicine. *Chem. Soc. Rev.*, **2012**, *41*(7), 2539-2544.
<http://dx.doi.org/10.1039/c2cs15294k> PMID: 22310807

REVIEW ARTICLE

Polymeric Nanoparticles: Prospective on the Synthesis, Characterization and Applications in Nose-to-Brain Drug Delivery

Prakash N. Kendre^{1,*}, Dhiraj R. Kayande¹, Shirish P. Jain¹, Tejaswini G. Malge¹, Namrata N. Zadpe¹ and Bhupendra G. Prajapati²

¹Rajarshi Shahu College of Pharmacy, Buldana Maharashtra, 443001, India; ²S. K. Patel College of Pharmaceutical Education and Research Ganpat University, Ganpat Vidya Nagar, Mehsana, Gujarat 384012, India

Abstract: For the treatment of brain illnesses, there is growing interest in nose-to-brain drug administration. Other, more traditional methods of crossing the blood–brain barrier (BBB) are ineffective. As a result, the therapeutic concentration in the brain cannot be achieved, and the reaction is inadequate. Intranasal medication delivery is one intriguing technique for avoiding first-pass metabolism and bypassing the blood-brain barrier. It lowers medicine doses while reducing systemic side effects. Compared to conventional drug delivery platforms, a nanoparticulate drug delivery method allows for greater penetration via the nasal route. It is better to make the nanoparticles for nose-to-brain administration when a good carrier (polymers) is used. This review focuses on the many processes for creating polymeric nanoparticles, strategies and tactics for improving nose-to-brain drug delivery efficiency, and nanoparticle characterization. The use of the nose-to-brain drug delivery platform is being explored using a variety of nanoparticles created by researchers for the treatment of brain illnesses.

ARTICLE HISTORY

Received: May 18, 2022
Revised: July 17, 2022
Accepted: September 01, 2022

DOI:
[10.2174/1573413718666220929102013](https://doi.org/10.2174/1573413718666220929102013)

Keywords: Polymeric nanoparticles, synthesis, blood-brain-barrier, brain diseases, techniques

1. INTRODUCTION

Aside from being a leading cause of death and disability worldwide, brain problems are chronic and lifelong illnesses [1]. Because of the protective coverings of the brain, namely the blood–brain barrier, medical treatment of brain illnesses is a major issue for scientists and researchers (BBB). Because of their enormous molecular weights, most therapeutic and diagnostic agents are unable to diffuse through the BBB, and even tiny molecules (98%) are not transported through it [2, 3]. Drugs can be administered intranasally to prevent first-pass metabolism and gastrointestinal degradation, bypassing the BBB. Nasal administration of drug-loaded nanoparticles is another option for increasing efficiency. Drugs can be delivered directly to the brain by taking a nasal route. This might make it possible to treat mental illnesses [3, 4].

In 1959, Nobel Laureate Richard P. Feynman proposed the concept of nanotechnology. Nanotechnology is used to generate nanoparticles (NPs) from a variety of materials, including particulates. Solid particles with 1-100 nm dimensions are known as nanoparticles [4]. For delivering medications to target areas, several forms of drug-loaded nanoparticles have been created, including nanoemulsions, nanotubes,

liposomes, micelles, dendrimers, and quantum dots [5, 6]. Aside from their small size, nanoparticles exhibit special features. They are target-specific and have a high surface-to-volume ratio. Nanoparticles with polymer coatings can pass through the BBB [7]. As a result, nanoparticles are widely used in the treatment of a variety of brain disorders.

The medication for brain disease is difficult. After all, 98% of current pharmaceutical products are stopped by a protective barrier [7, 8]. The brain is the most complex organ and is separated from the other parts by strong barriers. The three barriers that protect the brain are

- The BBB, consists of a highly specialized endothelial barrier
- The blood-cerebrospinal fluid (CSF) barrier with the choroid plexus epithelium
- The arachnoid epithelium

These protective barriers prevent the entry of harmful and toxic agents as well as therapeutic and diagnostic agents into the brain [8]. Nanoparticles can enter the brain directly or indirectly after nasal administration. Transportation of molecules to the brain occurs by two pathways:

- The trigeminal neural pathway
- The olfactory neural pathway

*Address correspondence to this author at the Rajarshi Shahu College of Pharmacy, Buldana, Maharashtra, 443001, India; Tel: +919890506016; Fax: +912423222862; E-mail: prakashkendre@gmail.com

Some drugs can enter the blood circulation and are transported across the BBB into the brain [4]. Along the trigeminal neural pathway, molecules are transported by axonal transport or endocytosis. The trigeminal nerve is the fifth cranial nerve. It has three major branches [8, 9]:

- The ophthalmic nerve
- The maxillary nerve
- The mandibular nerve

In nose-to-brain delivery, the ophthalmic and maxillary nerves play a big part. The paracellular or transcellular method moves chemicals along the olfactory pathway. Olfactory receptor neurons are found in the mucosa of the olfactory epithelium and carry chemicals quickly to the brain. The process of transport from the nose to the brain is yet unknown. Fig. 1 [8, 9] shows a schematic illustration of nanoparticulate medication delivery.

The intranasal nose-to-brain delivery mechanism is the subject of this investigation. The various methods of nanoparticle preparation, strategies, and distinct approaches to drug delivery and nanoparticle characterization are explored within this broad topic. This review's main goal is to overview how nose-to-brain medication delivery systems can help people with brain illnesses get better.

2. SYNTHETIC TECHNIQUES FOR POLYMERIC NANOPARTICLES

Nanomaterials are synthesized or prepared using a variety of techniques. It's crucial to choose the right procedure, which is determined by the material's physicochemical prop-

erties. The top-down and bottom-up approaches to synthesis are the two main methodologies.

2.1. Top-down Approach

The top-down method entails using an external force to break down bigger chunks of heavy material into smaller chunks. This is a crucial technique in terms of business. Wet ball milling, high-pressure homogenisation, jet milling, laser sputtering, nanolithography, sputtering, thermal breakdown, and so on are all part of the top-down approach.

2.2. Bottom-up Approach

The required structure is constructed from atoms, molecules, or clusters under specific conditions in the bottom-up technique. The bottom-up strategy is used in methods like precipitation, chemical vapour deposition (CVD), pyrolysis, the sol-gel method, spinning, and biosynthesis [10]. Fig. 2 shows a classification of nanoparticles synthesis methods [11, 12]

2.3. Physical Method

The top-down strategy is used in physical approaches to nanoparticles production. Materials are abraded, melted, evaporated, or condensed using mechanical pressure, electric and thermal energy, and high-energy radiation. These technologies have the advantages of being solvent-free, toxic-chemical-free, and producing nanoparticles of consistent size and shape in a short amount of time. They use a lot of energy, need high temperatures and pressures, aren't very productive, are expensive, and don't make very stable nanoparticles.

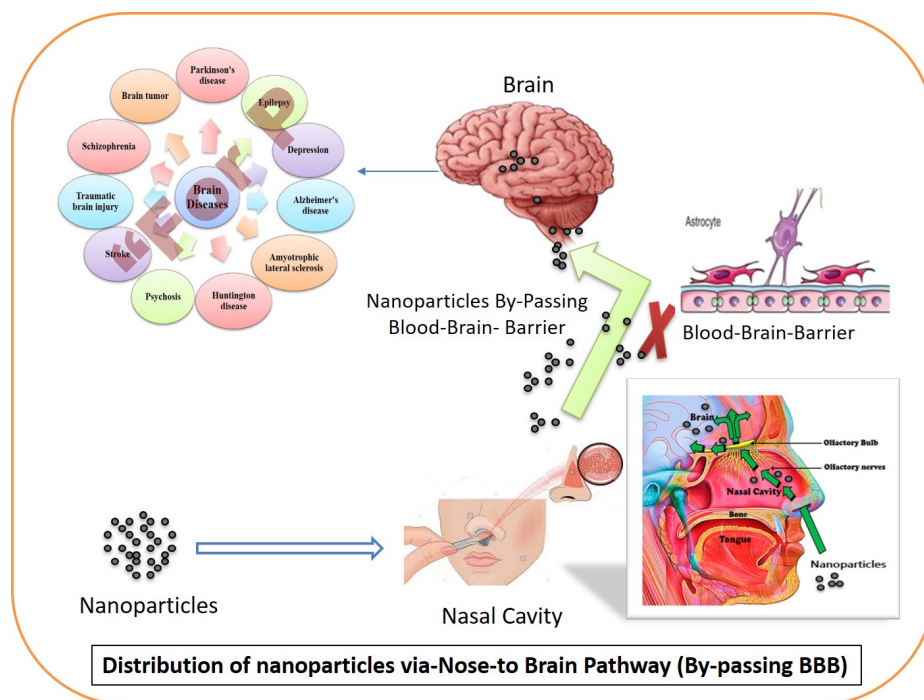


Fig. (1). Schematic presentation of nanoparticles distribution via nose-to-brain route; Selvaraj K, Gowthamarajan K, Karri VVSR (2017). (*A higher resolution / colour version of this figure is available in the electronic copy of the article*).

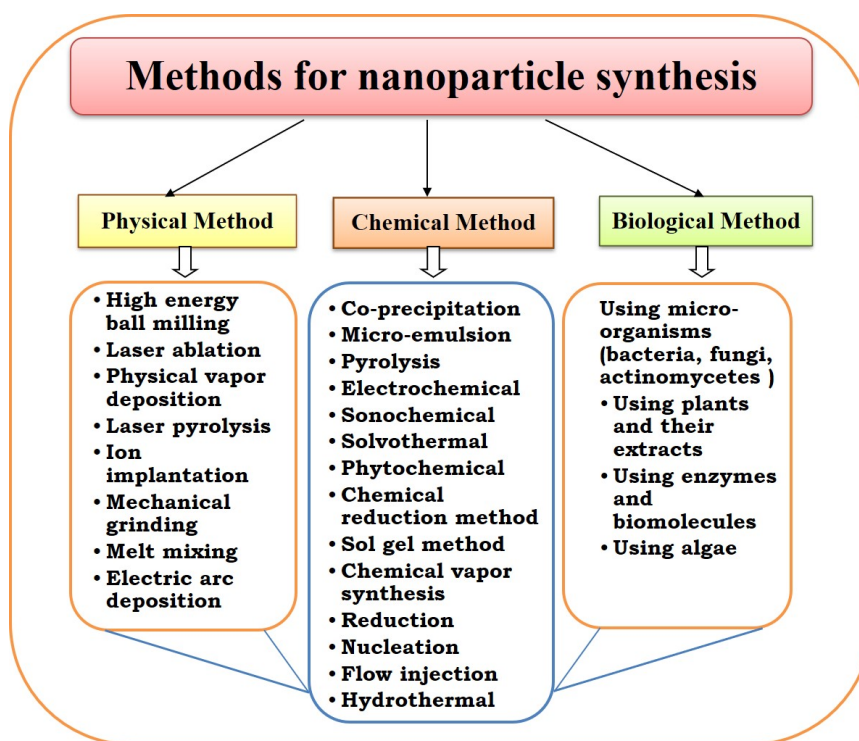


Fig. (2). Various methods used for the synthesis of nanoparticles; Patra JK, Baek K-H (2014). (A higher resolution / colour version of this figure is available in the electronic copy of the article).

2.4. Chemical Methods

The bottom-up approach to nanoparticles synthesis is chemical methods. Cost-effectiveness, ease of functionalization, thermal stability, high yield, and reduced dispersion are only a few of the advantages of this approach. The downsides include the use of harmful chemicals, a lower level of purity, and human health risks. Chemical reduction, sol-gel synthesis, sono-chemical synthesis, solvothermal synthesis, coprecipitation, the microemulsion method, and pyrolysis are some of the most extensively used chemical processes for nanoparticles synthesis [13].

2.5. Biological Methods

In contrast to physical and chemical processes, biological synthesis is environmentally beneficial. Microorganisms, enzymes, algae, viruses, plants, and biomolecules are used to synthesise nanoparticles. As a result, these techniques are referred to as "green synthesis techniques." The bottom-up strategy is used in these techniques. Reducing and stabilising substances found in microbes and plants are used in the synthesis [11]. They mostly make nanoparticles by breaking down chemicals found in microbes and plants, like amines, alkaloids, proteins, enzymes, phenolic compounds, and pigments, to make them smaller [14].

Nontoxicity, reproducibility in manufacturing, well-defined morphology, ease of scaling up, and lower energy requirements are all advantages of biological processes, which are environmentally beneficial. They're also free of potentially dangerous and costly chemicals [15].

2.6. Emulsion-solvent Evaporation Methods

The most prevalent ways of preparing nanoparticles are as follows. They're exclusively used for medications that aren't easily dissolved in water. The following steps are involved in emulsion-solvent evaporation: (1) to make an organic solution, the medication and polymer must first be dissolved in an organic solvent. (2) A surfactant or aqueous solution of a stabiliser is created in the second step. (3) The emulsification process is the third phase, in which the already prepared organic solution is dropped dropwise into the aqueous solution under the high shearing force of the homogeniser, resulting in an O/W (oil-in-water) type of emulsion. (4) The fourth step is solvent evaporation, which is done in a rotary evaporator with the organic solvent evaporated first and then the drug-loaded nanoparticles precipitated. (5) Ultracentrifugation is the fifth stage, which involves collecting the precipitated nanoparticles and washing them with distilled water to eliminate any residue. (6) Lyophilisation, a freeze-drying method, is the final step. In the final step, water is evaporated, and the dry nanoparticles are collected as a powder (Fig. 3). These procedures [16] have been modified by high-pressure emulsification and the solvent evaporation method. Because they only require mild conditions and continual stirring, emulsion-solvent evaporation methods are preferred over other methods. As a result, a stable emulsion can be made without interfering with the drug's activity [17].

Using the emulsion-solvent evaporation approach, the researchers created HupA-loaded lactoferrin coupled N-trimethylated chitosan nanoparticles (HupALf-TMC NPs).

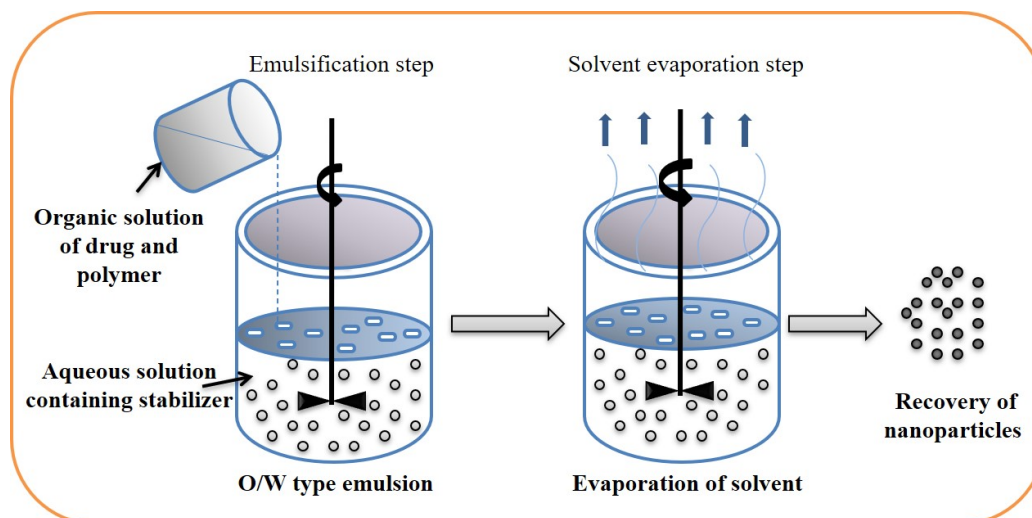


Fig. (3). Emulsion-solvent evaporation method for nanoparticles synthesis; Pal SL JUMP *et al.* (2011). (A higher resolution / colour version of this figure is available in the electronic copy of the article).

Their goal was to create an intranasal delivery system for HupA that could efficiently transfer the protein to the brain and cure Alzheimer's disease. Polylactide-co-glycoside was the polymer employed to make these nanoparticles (PLGA). The preparation included co-modification with lactoferrin (Lf) and N-trimethylated chitosan (TMC). TMC modification was thought to boost nasal adhesion and retention time. The conjugation of Lf was supposed to make drug administration from the nose to the brain easier. Using the Box-Behnken design, the nanoparticles were optimised. The nanoparticles' particle size, zeta potential, size distribution, entrapment efficiency, and polydispersity index (PDI) were all calculated. Biodistribution research and *in vitro* drug release tests were also conducted. The nanoparticles provided a good long-term release. The nasal adhesion and the capacity to target the brain were both excellent. The Lf-TMC NPs were found to be a promising nose-to-brain medication delivery method based on the drug's distribution profile in the brain [18].

2.7. Ionic Gelation Methods

In an ionic gelation technique, a positively or negatively charged hydrophilic molecule interacts with a cation or anion to generate a strongly cross-linked structure. As a result of this process, which produces very sticky gel particles, nanoparticles are formed. A drug-polymer solution is made by mixing the drug and polymer in distilled water. Drop by drop, stirring constantly, pure water is added. It is possible to obtain an opalescent suspension. The suspension is then centrifuged to obtain the nanoparticles. Fig. 4 shows lyophilization nanoparticles using an appropriate cryoprotectant [19]. The most common polymers used in ionic gelation procedures are chitosan and alginate. Other polymers include dextran, carboxymethyl cellulose, gelatine, collagen, hyaluronic acid, pectin, carbopol 934P, gum, and others [20].

Using an ionic gelation process, the researchers created bromocriptine (BRC)-loaded chitosan nanoparticles (CS NPs). Their goal was to look at the role of chitosan nanopar-

ticles in a nose-to-brain drug delivery system and see how they could improve bromocriptine's brain targeting efficiency. The nanoparticles were made from chitosan (a polymer) and sodium tripolyphosphate (cross-polymer). Pharmacodynamic, biodistribution, and pharmacokinetic experiments were conducted on Swiss albino mice. The nanoparticles were measured for particle size, polydispersity index, zeta potential, entrapment efficiency, and drug-loading capacity. Bromocriptine absorption in the brain was boosted by using nanoparticles. In addition, the antioxidant activity was improved. This technique for delivering drugs to the brain could be useful in the treatment of Parkinson's disease [21].

Using an ionic gelation technique, researchers synthesised and assessed RAS-loaded chitosan glutamate nanoparticles (CG-NPs). The researchers wanted to see if the nose-to-brain pathway was more effective than the intravenous approach for delivering medicines to the central nervous system (CNS). Chitosan glutamate (CG) was employed as the polymer, and sodium tripolyphosphate was used as the cross-polymer (STPP). The sodium anions of the sodium tripolyphosphate cause ionic gelation of CG, which results in CG-NPs. characterization of the produced nanoparticles *In vitro* drug release research was conducted after determining their particle size, size distribution, zeta potential, encapsulation efficiency, and polydispersity index. Following intranasal treatment, these nanoparticles greatly increased RAS bioavailability in mice's brains. Parkinson's disease may benefit from intranasal delivery [22].

2.8. Double Emulsion-solvent Evaporation Method

Methods of two-step emulsification include double emulsion-solvent evaporation. Both hydrophilic and hydrophobic medicines can be made with them. This approach is also known as "emulsions of emulsions" because the dispersed phase droplets are made up of smaller dispersed phase droplets, which are usually polydisperse in size. There are two types of common double emulsions:

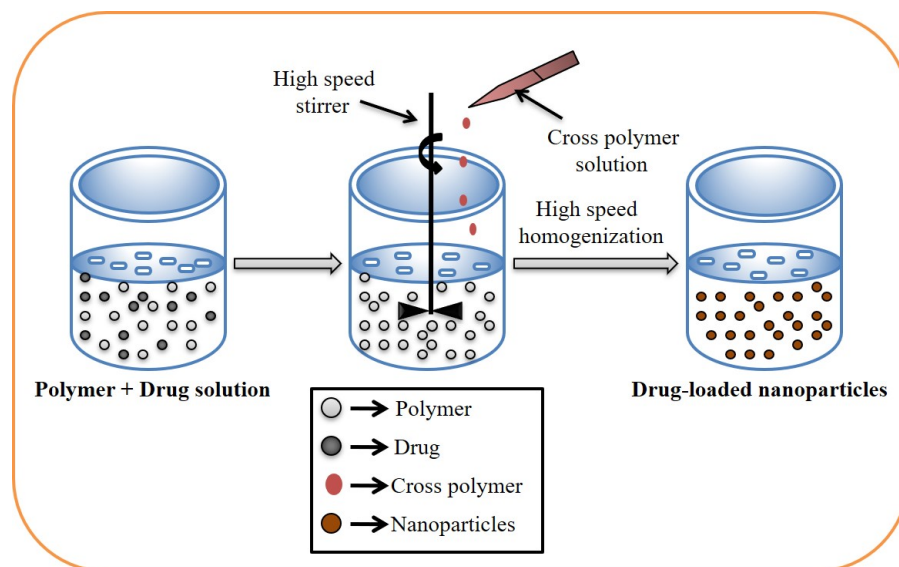


Fig. (4). Ionic-gelation method for nanoparticles synthesis; Patra JK, Das G, Fraceto LF, *et al.* (2018). (A higher resolution / colour version of this figure is available in the electronic copy of the article).

- Water–oil–water (W/O/W)
- Oil–water–oil (O/W/O)

A two-step emulsification technique is used to create nanoparticles in these procedures. The hydrophilic medications are added to the watery inner phase (W) first, followed by the infusion of polymer/hydrophobic pharmaceuticals into the organic phase, i.e., the oil phase (O). A primary emulsion (W/O) is created by homogenising the two phases. This primary emulsion is emulsified with the aqueous phase (W), which contains a stabiliser, in the second step to generate a double emulsion (W/O/W). The dispersed phase's solvent is next ejected and evaporated. As shown in Fig. 5, the polymer encasing the active ingredient hardens as a result.

Poly(lactic acid) (PLA), poly(lactic-co-glycolic acid) (PLGA), and polycaprolactone are the most prevalent polymers utilised in double emulsion–solvent evaporation processes (PCL). Poly(vinyl alcohol) (PVA), Tween 80, and Span 80 are some of the most regularly used stabilisers [23].

Alex *et al.* (2014) created carboplatin-loaded poly(caprolactone) (PCL) nanoparticles using a two-step emulsion–solvent evaporation method, W/O/W was the sort of emulsion that resulted. The polymer used for encapsulating carboplatin was polycaprolactone, which regulates drug release and boosts anticancer efficacy. The nanoparticles were measured in terms of size, zeta potential, entrapment efficiency, polydispersity index, scanning electron microscopy, and *in vitro* drug release profiles. The nanoparticles had a small particle size, a spherical shape, high entrapment efficiency, improved nasal absorption, and a long release profile. They could be employed in a carboplatin delivery system [24].

2.9. Nanoprecipitation Methods

Solvent displacement techniques are another name for nanoprecipitation. Polymeric nanoparticles are primarily

synthesised using these methods. Fig. 6 shows how the approach works: pre-formed polymer precipitation from an organic solution and organic solvent diffusion into the aqueous medium in the presence or absence of a surfactant. Nanoprecipitation is mostly employed for hydrophobic medicines since the solvents used are particularly miscible with the aqueous phase [25]. Nano-capsules can also be created by adding a small amount of harmless oil to the organic phase [19]. These techniques produce submicron (210 nm) nanoparticles. The size depends on the rate of addition of the organic phase to the aqueous phase and the low polydispersity index value [17].

2.10. Salting-out Methods

The separation of the water-soluble solvent from the aqueous phase is the basic concept behind these approaches. These techniques are variations of emulsification–solvent diffusion techniques [26].

An API and a polymer are dissolved in solvents to make a solution. After that, the solutions are emulsified into an aqueous gel that includes a colloidal stabiliser and a highly concentrated salting-out agent. The sort of emulsion that forms is O/W. It's diluted with enough water to lower the salting-out agent's concentration and increases the solvent's diffusion into the aqueous phase, resulting in nanosphere formation. Fig. 7 shows how cross-flow filtering removes the solvent and salting-out agent. The salting-out agent should be chosen carefully because it affects the drug's encapsulation efficiency [25].

3. POLYMERIC NANOPARTICLES FORMULATION APPROACHES

In the treatment of neurological illnesses, nanocarriers are utilised to carry medications across the BBB. Liposomes, solid-lipid nanoparticles, nanoemulsions, carbon nanotubes, dendrimers, micelles, and quantum dots are only a few

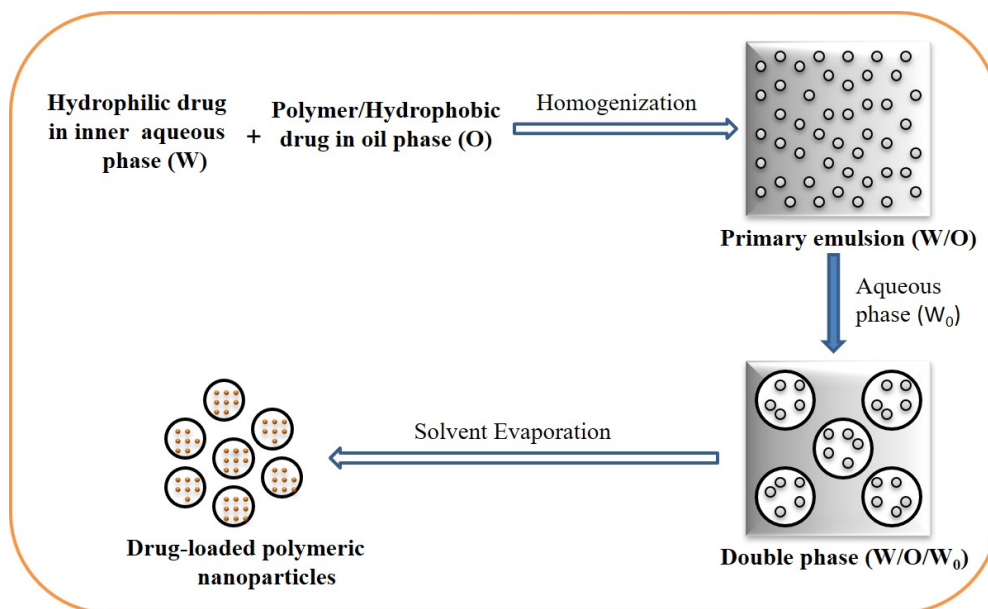


Fig. (5). Double emulsion-solvent evaporation method for nanoparticles synthesis; Iqbal M, Zafar N, Fessi H, Elaissari A (2015). (A higher resolution / colour version of this figure is available in the electronic copy of the article).

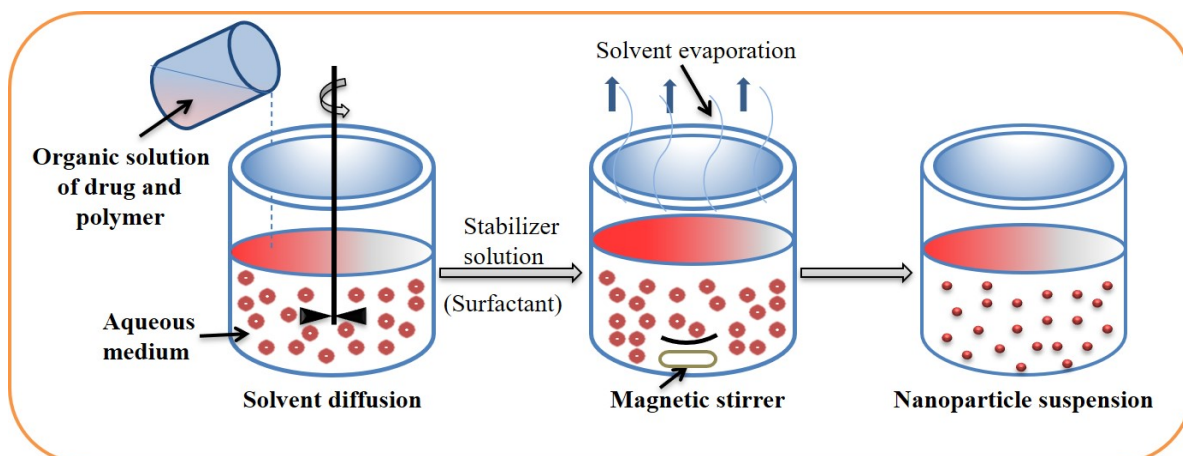


Fig. (6). Nanoprecipitation method of preparation for nanoparticles; Nagavarma BVN YHAA et al. (2012). (A higher resolution / colour version of this figure is available in the electronic copy of the article).

amples of biodegradable and biocompatible nanocarriers. These nanocarriers are utilised to increase the drug's stability and retention period while reducing adverse effects and toxicity. Conjugation or entrapment in the carrier system allows the medications to be absorbed. Because it improves nasal permeability, the nanocarrier technology has many uses in intranasal nose-to-brain transport.

3.1. Solid-lipid Nanoparticles

SLNs are spherical colloidal nanocarriers made of solid-lipid nanoparticles. They're about 50–100 nm in size. They're lipid-based nanoparticles that can be used instead of emulsions, liposomes, or nanoparticles [27]. An exterior surfactant layer stabilises the solid-lipid core matrix of these nanoparticles. A diglyceride, triglyceride, fatty acid, sterol, or wax can be used as a lipid [3]. Both lipophilic and hydro-

philic medicines can be included in SLNs. They are more effective at targeting, encapsulation, and stability. They are non-toxic, and they don't require the use of organic solvents to make them [28].

3.2. Polymeric Nanoparticles

Polymeric nanoparticles are colloidal particles with diameters ranging from 60 to 200 nanometers in diameter. Polymeric nanoparticles can be used to prolong medication release and intracellular absorption. Polymers utilised to make polymeric nanoparticles must be biodegradable, biocompatible, and non-toxic. Some of the most commonly used polymers are poly (lactide co-glycolides), polyglycolides, polylactides, polyanhydrides, polycaprolactone, and poly (cyanoacrylates) [28, 29].

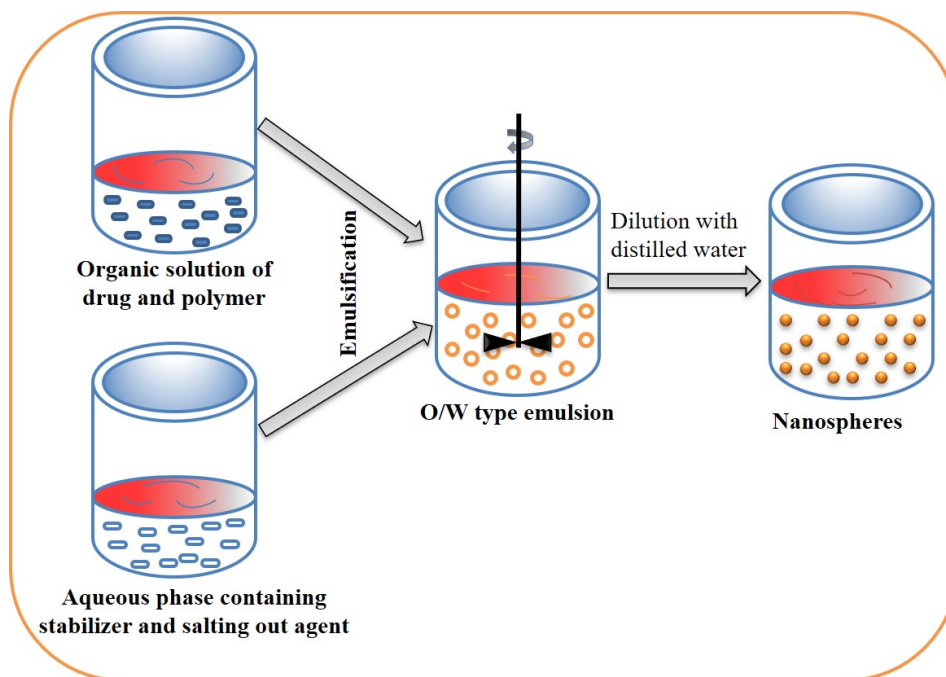


Fig. (7). Salting-out method for Schematic presentation of nanoparticles distribution via nose-to-brain route; Nagavarma BVN YHAA *et al.* (2012). (A higher resolution / colour version of this figure is available in the electronic copy of the article).

3.3. Nano-emulsions

Colloidal dispersions of two immiscible liquids stabilised by a surfactant are known as nano-emulsions. Nano-sized droplets (20–200 nm) are disseminated in a continuous phase. Nano-emulsions come in three varieties:

- oil-in-water (O/W)
- water-in-oil (W/O)
- bi-continuous nano-emulsion

Nano-emulsions have a number of advantages, including increased drug bioavailability, lipophilic drug solubility, and physical stability [30, 31]. A nano-emulsion is resistant to destabilising events such as coalescence, creaming, and sedimentation because of the size (nano-sized) of the droplets [5].

3.4. Liposomes

Liposomes are spherical vesicles with one or more lipid bilayers surrounding a central core. Phospholipids, sphingolipids, polymeric polymers, and synthetic phospholipids are biocompatible, biodegradable lipids that make up a lipid bilayer [32]. Liposomes can be used to encapsulate hydrophilic and lipophilic medicines. Lipophilic medications are entrapped in the liposomal lipid bilayer, while hydrophilic pharmaceuticals are enclosed in the central core [33]. Liposomes work well as diagnostic and therapeutic carriers. Polymers, polysaccharides, peptides, antibodies, and aptamers can be used to change the surface of a liposome, which can improve blood flow and the delivery of medications to the brain [34].

3.5. Dendrimers

Dendrimers are globular macromolecules with tree-like architectures that are synthesised at the nanoscale. Dendrimer comes from the Greek words dendron, which means "tree," and meros, which means "part." Three main components make up the three-dimensional dendrimer structure [35, 36]:

- An inner core
- Repeating branching units called 'generations'
- Outer functional groups

Dendrimers with a lot of branches can hold a lot of medicine. Divergent and convergent techniques are the most popular ways to create dendrimers. Poly (amidoamine) (PA-MAM) dendrimers, poly (propylene imine) (PPI) dendrimers, poly-L-lysine (PPL) dendrimers, and phosphorus (PPH) dendrimers are among the dendrimers used for drug delivery to the brain [37].

Nasal delivery of dendrimers has a number of benefits, like making the drug more water-soluble, making it easier for the drug to get to the brain, and making it easier for the drug to move across the blood-brain barrier [35].

3.6 Mesoporous silica Nanoparticles (MSNs)

Drug targeting platforms made of mesoporous silica nanoparticles are promising. These particles can hold a considerable amount of medication due to their porous nature (pore volume > 0.9cm³/g) and vast surface area (300–1000 m²/g). The medication can be entrapped in the pores of the micron-to nano-sized porous structure, which serves as a reservoir

for drug release to the appropriate administration site. Tissue engineering, diagnostics, and therapies are just a few of the biomedical applications of MSNs. MSNs have recently been discovered to be particularly effective for nose-to-brain targeting, allowing for regulated drug administration. Chemically and thermally, these nanoparticles are inert. They have high biocompatibility and low negative effects.

Inorganic compounds like silicon oxide are used to make MSNs. MSNs are made using a variety of techniques, including sol-gel, chemical etching, microwave-assisted processes, and so on. Depending on the raw materials utilised, MSNs have diverse geometric structures.

Particle size, shape, porosity, pore volume, surface area, drug loading, surface functionalization, and other factors all contribute to the overall characteristics of MSNs. In 2007, Mohanraj and Chen effectively synthesised mesoporous silica nanoparticles loaded with poorly soluble curcumin and chrysin for nose-to-brain transport. Spherical MSNs with a diameter of 220 nm were found to be effective in crossing the BBB and delivering medicines into the CNS [38].

4. CHARACTERIZATION OF NANOPARTICLES

The size, shape, surface charge, drug loading capacity, and encapsulation efficiency of nanoparticles are all factors that influence their effectiveness. Identifying nanoparticles can be done in a variety of ways. For example, electron microscopy is used to determine the particle size and shape.

4.1. Particle Size

The two primary factors investigated in nanoparticles characterization are particle size and particle size distribution. The size of nanoparticles affects their stability, encapsulation effectiveness, and drug loading capacity. The surface-to-volume ratios of smaller particles are higher. Due to the huge surface area available for absorption, nanoparticles can be absorbed quickly. Larger particles, on the other hand, encapsulate better and diffuse more slowly. During storage and transportation, smaller particles are more likely to aggregate than bigger particles [39]. The following are some of the methods for determining particle size [40]:

- Dynamic light scattering (DLS) or photon-correlation spectroscopy
- Scanning electron microscopy
- Transmission electron microscopy
- Atomic force microscopy
- Laser scattering techniques
- X-ray scattering techniques
- Centrifugation techniques

4.2. Percentage Yield

Preparation, collection, and weighting of nanoparticles are all done with precision. The following formula [41] is used to compute the percentage yield:

$$\% \text{ Yield} = \frac{\text{Weight of prepared nanoparticles}}{\text{Total weight of drug and polymer}} \times 100 \quad \dots \quad (1)$$

4.3. Surface Charge

The surface charge of nanoparticles affects their absorption on the cell membrane, which is a key element in delivery efficacy. To represent the surface charge of nanoparticles, the zeta potential is used [42]. If aggregation is to be avoided and nanoparticles are to remain stable, they must have high zeta potential values (either positive or negative). The zeta potential reveals the composition of the core material and coating [16]. Electroacoustic determination and electrophoretic light scattering are used to determine the zeta potential [43].

4.4. Drug Loading and Encapsulation Efficiency

Drug loading is defined as the amount of drug bound per mass of the polymer. Drug loading is achieved by:

- Incorporating the drug at the time of production (incorporation method)
- Adsorption or absorption

The amount of drug loaded into nanoparticles is determined by the following given equations:

$$\% \text{ Drug loading} = \frac{\text{Total weight of drug in particles}}{\text{Total weight of particles}} \times 100 \quad \dots (2)$$

The encapsulation efficiency (EE) is defined as the percentage of drug encapsulated within nanoparticles as a percentage of the polymer. The amount of free drug present in the supernatant is evaluated using the HPLC technique after nanoparticles have been dissolved in a suitable solvent. The following equation is used to compute the encapsulation efficiency:

$$\% \text{ EE} = \frac{\text{Initial amount of drug} - \text{Amount of free drug present in supernatant}}{\text{Initial amount of drug}} \times 100 \quad \dots (3)$$

Nanoparticles should have a high capacity for drug loading and encapsulation. The solid-state solubility of the drug in the polymer medium affects both how well the drug is encapsulated and how much of it is in the finished product [44].

4.5. Drug Release

The behaviour of nanoparticles is determined by the drug release. Under sink circumstances, drug release is achieved through diffusion or matrix degradation. The solubility, diffusion, and degradation of the nanoparticles' matrix are all factors that affect drug release [45]. The most popular method for studying drug release in vitro is dialysis. A dialysis membrane is used in this procedure to separate the nanoparticles. The following are examples of dialysis techniques:

- Dialysis bag diffusion method
- Reverse dialysis bag diffusion method
- Side-by-side diffusion method

In the dialysis bag diffusion method, nanoparticles are delivered into a dialysis bag (inner compartment) filled with media, which is then sealed. The inner compartment is housed in a huge media-filled exterior chamber. The inner

compartment has a smaller volume (1–10 mL) than the outer compartment (40–90 mL). A dialysis membrane is used to divide the two compartments. To decrease the effects of unstirred water layers, agitation is used. Through the dialysis membrane, the medication diffuses from the inner to outer compartments. For dialysis, the sample is taken out of the outer compartment. The nanoparticles are placed in the outer and inner compartments, and the drug release is sampled using the reverse dialysis procedure. A donor cell and a receiver cell with equal quantities of media and a magnetic stirrer comprise the side-by-side dialysis system. The sample is taken from the receiver cell, and a vertical Franz diffusion cell after a dialysis membrane separates the donor and receiver cells [46].

5. STABILITY STUDIES

Nanoparticles should be tested in terms of transport and storage. Long-term stability testing at 25°C/2°C, and 60% relative humidity are advised by the International Conference on Harmonization (ICH) on fast stability at 40°C/2°C and 5% relative humidity 5% RH [47]. Furthermore, the stability of the produced nanoparticles should be examined based on their physical and chemical characteristics. In vivo stability testing can be used to see how a nanoparticle formulation will work.

6. APPLICATIONS IN NOSE-TO-BRAIN DRUG DELIVERY

Many vital lifesaving treatments are delivered using nanoparticles, which is a difficult task. Many researchers have helped create and produce nanoparticles for the treatment of various ailments. It highlights the role of nanoparticles in medication delivery via nose-to-brain.

7. NANOPARTICLE CYTOTOXICITY AND MITIGATION TECHNIQUES

7.1. Limitations of Nanoparticles in Nose-to-brain Delivery

The intranasal approach is non-invasive and has numerous medical advantages. Intranasally given formulations have a faster onset of action and higher bioavailability, as well as avoid first-pass metabolism and have fewer adverse effects. Intranasal delivery, however, has a number of drawbacks, including limited permeability, enzymatic degradation, muco-ciliary clearance, and short retention periods [48]. Intranasal administration is a simple and easy alternative to conventional routes. Intranasally, however, only very minute amounts of a formulation can be given. As a result, only very effective medications can be given [49–51]. A variety of procedures are employed to improve a drug's absorption and permeability. Absorption enhancers help drugs go through the nasal mucosa more quickly [52]. Mucoadhesive systems, such as mucoadhesive polymers, viscous formulations, in situ gelation, and hydrogels, have improved retention time [53]. Some medications can irritate the nasal mucosa, putting the cilia of the nasal mucosa in jeopardy. The biological reaction to nanoparticles is altered, resulting in neurotoxicity.

7.2. Cytotoxicity of Nanoparticles

It is well established that certain nanoparticle exposure might have negative health impacts. Understanding their methods of action or toxicity and researching any potential health implications is crucial.

Smart medication delivery uses polymeric nanoparticles, which can be created from synthetic or natural polymers. In-depth research is being done on them as carriers for controlled/sustained release in drug delivery systems. These nanopharmaceuticals' action is constrained by safety concerns, toxicity concerns, poor biocompatibility, and physiological difficulties. These nanoparticles' drawbacks include the hazardous breakdown process, residual material attached to them, and toxic monomer aggregation [54].

Quantum size effects, which are connected to oxidative stress, cytotoxicity, and genotoxicity, have an impact on the toxicity of polymeric NPs [55]. Nadège et al. observed that the somewhat cytotoxic chitosan polymer gave considerable cytotoxicity to PLGA nanoparticles when employed as a nanoparticle stabilizer after investigating the toxicity of a range of poly(lactide-co-glycolic acid) (PLGA) nanoparticles on human-like THP-1 macrophages. Both polyvinyl alcohol and poloxamer 188 polymers significantly increased PLGA nano's cytotoxicity. These results showed that stabilizers used in PLGA nanoparticle formulation have a substantial toxicological function when utilized at high concentrations, which may have an impact on the local toxicity of PLGA-based nanomedicine [56].

Size, surface area, surface charge, and aggregation state affect NP toxicity [57]. These features impact NP dispersion, deposition, and molecular interactions with proteins and macromolecules. Size affects NP penetration, cellular absorption, and toxicity. Some investigations imply a link between NP size, distribution, and renal ROS production [58, 59]. Liver toxicity is size-dependent. 10 nm silver NPs had greater tissue dispersion and produced more liver toxicity than 40 and 100 nm NPs [60, 61].

Shape affects NP dispersion, deposition, and clearance together with size. Long fibrous particles, such as single-walled nanotubes, are hard for the body to remove and cause organ deposits [62]. Surface chemistry affects NP pharmacokinetics. Charged NPs tend to accumulate more in target organs. Ionic zinc oxide NPs accumulated more in organs after oral or intravenous treatment than uncharged NPs [63]. (Table 1) Polysaccharide conjugation increases NP accumulation in the brain, liver, and spleen, which correlates to their toxicity [64]. Altering NP surface qualities with coatings can lower their toxicity. PEG reduces NP toxicity by changing their protein interactions. PEGylation may affect NPs' cellular uptake and medication delivery effectiveness.

7.3. Strategies/mitigation Techniques to Overcome Cytotoxicity

The prior studies show increased concern regarding NP toxicity and emphasize the necessity to address toxicity during original design, whether for industrial or therapeutic usage. Structured nanoemulsions and solid lipid nanoparticles

Table 1. Various nanoparticulate systems for nose-to-brain drug delivery.

Therapeutic Payload	Nanocarrier system	Material	Formulation Technique	Therapeutic Outcome	Refs.
Huperzine A	LF-TMC NPs	Lactoferrin and N-trimethylated chitosan	Emulsion-solvent evaporation method	Good sustained release effect, adhesion and targeting ability and broad application as intranasal drug delivery carrier	[18]
Bromocriptine	CS NPs	Chitosan	Ionic-gelation-method	Nanocarrier has increased brain uptake of bromocriptine also enhanced its antioxidant activity and make effective system for treatment of Parkinson's disease	[21]
Rasagiline	CG NPs	Chitosan glutamate	Ionic-gelation method	These could be promising delivery system for the treatment of Parkinson's disease	[22]
Carboplatin	PCL NPs	Poly(ϵ -caprolactone)	Double emulsion-solvent evaporation method	Better nasal absorption and sustained release profile so can be used in intranasal administration of carboplatin for improved brain delivery	[24]
Teriflunomide	NLC	Compritol 888 ATO (Solid-Lipid) and Maisine 35-1 (Liquid-Lipid)	Melt emulsification ultra-sonification method	Enhanced the nasal residence time	[26]
Selegiline	NE	Grape seed oil	High energy emulsification method	Enhanced the uptake of selegiline to brain, improve brain bioavailability and restore normal dopamine level	[54]
Tarenfluril	PNPs SLNs	Poly (lactic-co-glycolic) acid	Emulsion-solvent-diffusion method Emulsion-solvent evaporation method	Desirable brain biodistribution profiles, effective in delivering Tarenfluril to brain for treatment of Alzheimer's disease	[55]
Lamotrigine	NLs	Phospholipid 90G and Cholesterol	Thin film hydration and rehydration method	High entrapment in lipid bilayer, high release rate and better penetration than suspension	[56]
Venlafaxine	PLGA NPs	Poly (lactic-co-glycolic acid)	Double emulsion-solvent evaporation method	Plain nanoparticles showed fast and highest ability to reach brain after intranasal administration via nose-to-brain delivery as compared to functionalized nanoparticles	[57]
Eugenol	CS PCL NPs	Chitosan and Poly(ϵ -caprolactone)	Modified double-emulsion (W/O/W ₀) method	Enhancement of drug bioavailability and can help in treating cerebral ischemia effectively	[58]
Pramipexole Dihydrochloride	CNs	Chitosan	Ionic-gelation-method	Showed significant brain targeting potential compared to other formulation so can be utilized for effective brain targeting via intranasal route for Parkinson's disease treatment	[59]
Pioglitazone	PLGA-PEG NPs	Poly (lactic-co-glycolic) acid-Poly ethylene glycol copolymer	Solvent displacement method	Nasal mucosa showed enhanced drug permeation in the tissues in the treatment of Alzheimer's disease and it could be a promising delivery route in treatment of Alzheimer's disease	[60]
Pioglitazone	NLC	Liquid lipid capmul MCM and Solid lipid tripalmitin	Microemulsion method	The formulation improves the permeability of Pioglitazone across nasal mucosa and also improved the concentration of drug reaching brain	[61]
Dopamine	LF-BNPs	Borneol and lactoferrin	Double emulsion-solvent evaporation method	NPs increased the Dopamine absorption into the brain demonstrating the co-modification significantly enhanced transport of drug towards brain	[62]
Kaempferol	MNE	Chitosan	High-pressure homogenization technique	MNE decreased viability of glioma cells by enhancing apoptosis and seems to be an important carrier for cancer treatment	[63]

NLC: Nanostructured lipid carriers; NE: Nano-emulsion; CGNPs: Chitosan glutamate nanoparticles; PNPs: Polymeric nanoparticles; SLNs: Solid-lipid nanoparticles; NLs: Nanoliposomes; PLGA NPs: Poly(lactic-co-glycolic acid) nanoparticles; CS PCL NPs: Chitosan coated poly(ϵ -caprolactone) nanoparticles; PCLNPs: Poly (ϵ -caprolactone) nanoparticles; CSNPs: Chitosan nanoparticles; CNs: Chitosan nanoparticles; PLGA-PEG NPs: Poly(lactic-co-glycolic) acid-Poly ethylene glycol copolymer nanoparticles; LF-TMCNPs: Lactoferrin conjugated N-trimethylated chitosan nanoparticles; LF-BNPs: Lactoferrin - borneol co-modified nanoparticles; MNE: Mucoadhesive nano-emulsion.

highlight one way to design safer NPs. These nanoparticles are made with FDA-approved, food-grade lipids, proteins, polysaccharides, and surfactants [65]. Solid or metal-containing NPs are similarly hazardous, according to studies. So, they're used less.

These problems have been the subject of many researches, such as the development of biocompatible and biodegradable pH-responsive hybrid nanoparticles by Palanikumar et al. To reduce interactions with serum proteins and macrophages, a cross-linked bovine serum albumin shell was added to these nanosystems built around a PLGA core filled with drugs. The drug-loaded NPs showed potent anticancer activity both in vitro and in vivo while having no negative effects on healthy tissue [66].

The following strategies may help to reduce the cytotoxicity of nanoparticles:

- Next generation lipids (smart lipids)
- Degradable nanoparticles
- Surface coating
- Doping
- Alteration of surface properties

"Next-generation lipids" that combine high potency and biodegradability may reduce the danger of certain NPs, notably lipid-based NPs. Martin et al. created biodegradable lipids by adding bio-cleavable ester functionalities to hydrophobic alkyl chains. This family of biodegradable lipids in preclinical trials demonstrated fast plasma clearance and enhanced tolerability [67]. Surface coating solutions are also offered to reduce NP risk and develop safer nanotechnology. Surface coating refers to modifying, functionalizing, or stabilizing NPs to change their characteristics. NPs can be coated with single- or multi-layer polymers that are full or partial [68]. If chosen appropriately, the coating material offers biocompatibility and impacts the behaviour (e.g., colloidal stability) and destiny (e.g., degradation, excretion, accumulation) of NPs after administration in biological fluids, cells, and organisms.

Inorganic NPs are often doped. This approach adds impurities to materials to improve their chemical and physical characteristics [69–71]. Aluminium, titanium, and iron are dopants. When equally integrated into nanoparticles, these dopants modify the density of reactive chemical entities on the surface and lower metal ion binding energy to oxygen. Doping NPs can reduce NP dissolution and hazardous ion release, altering reactive surfaces and reducing ROS formation [72, 73].

FSP is a well-established NP doping method. FSP employs a quick combustion process, liquid precursor, and self-sustaining flame with a high local temperature and huge temperature gradient [74].

Altering NPs' charge density and hydrophobicity may lower their risk and increase their efficacy in medicinal applications, such as targeted medication administration [75, 76].

CONCLUSION

The intranasal route offers a lot of promise for overcoming issues with drug delivery caused by protective barriers like the BBB. Many medications are delivered via various modes of administration, and these issues constitute a big issue. The trigeminal and olfactory nerve pathways are used to deliver medicine directly to the brain via the intranasal method. As a result, this method has a number of advantages, including increased bioavailability, avoidance of first-pass metabolism and enzymatic degradation, and a lower risk of side effects. Targeted drug delivery is significantly influenced by nanoparticles. They increase the amount of medication that can be given by enhancing retention duration and penetration in the nasal cavity. Intranasal administration of drug-loaded nanoparticles can thus be used to treat brain diseases effectively.

LIST OF ABBREVIATIONS

BBB	=	Blood–Brain Barrier
NPs	=	Nanoparticles
CSF	=	Blood Cerebrospinal Fluid
Lf	=	Lactoferrin
TMC	=	N-Trimethylated Chitosan
PDI	=	Polydispersity Index
BRC	=	Bromocriptine
CS NPs	=	Chitosan Nanoparticles
W/O/W	=	Water-Oil-Water
O/W/O	=	Oil–Water-Oil
PCL	=	Carboplatin-Loaded Poly
MSNs	=	Mesoporous Silica Nanoparticles

CONSENT FOR PUBLICATION

Not applicable.

FUNDING

None Declared.

CONFLICT OF INTEREST

Author(s) declares no conflict of interest

ACKNOWLEDGMENTS

The authors are very thankful to the Principal, Rajarshi Shahu College of Pharmacy, Buldana, for providing article writing and editing facilities. Finally, the authors extend thanks to all those whose cooperation helped complete this work successfully.

REFERENCES

- [1] Wang, Z.; Xiong, G.; Tsang, W.C.; Schätzlein, A.G.; Uchegbu, I.F. Nose-to-brain delivery. *J. Pharmacol. Exp. Ther.*, **2019**, *370*(3), 593-601.
<http://dx.doi.org/10.1124/jpet.119.258152> PMID: 31126978

- [2] Pardridge, W.M. Drug transport across the blood-brain barrier. *J. Cereb. Blood Flow Metab.*, **2012**, 32(11), 1959-1972. <http://dx.doi.org/10.1038/jcbfm.2012.126> PMID: 22929442
- [3] Battaglia, L.; Panciani, P.P.; Muntoni, E.; Capucchio, M.T.; Bisibetti, E.; De Bonis, P.; Mioletti, S.; Fontanella, M.; Swaminathan, S. Lipid nanoparticles for intranasal administration: Application to nose-to-brain delivery. *Expert Opin. Drug Deliv.*, **2018**, 15(4), 369-378. <http://dx.doi.org/10.1080/17425247.2018.1429401> PMID: 29338427
- [4] Gao, H. Progress and perspectives on targeting nanoparticles for brain drug delivery. *Acta Pharm. Sin. B*, **2016**, 6(4), 268-286. <http://dx.doi.org/10.1016/j.apsb.2016.05.013> PMID: 27471668
- [5] Kumar, A.; Pandey, A.N.; Jain, S.K. Nasal-nanotechnology: Revolution for efficient therapeutics delivery. *Drug Deliv.*, **2016**, 23(3), 671-683. <http://dx.doi.org/10.3109/10717544.2014.920431> PMID: 24901207
- [6] Khan, I.; Saeed, K.; Khan, I. Nanoparticles: Properties, applications and toxicities. *Arab. J. Chem.*, **2019**, 12(7), 908-931. <http://dx.doi.org/10.1016/j.arabjc.2017.05.011>
- [7] Serlin, Y.; Shelef, I.; Knyazer, B.; Friedman, A. Anatomy and physiology of the blood-brain barrier. *Semin. Cell Dev. Biol.*, **2015**, 38, 2-6. <http://dx.doi.org/10.1016/j.semcdb.2015.01.002> PMID: 25681530
- [8] Selvaraj, K.; Gowthamarajan, K.; Karri, V.V.S.R. Nose to brain transport pathways an overview: Potential of nanostructured lipid carriers in nose to brain targeting. *Artif. Cells Nanomed. Biotechnol.*, **2018**, 46(8), 2088-2095. PMID: 29282995
- [9] Aderibigbe, B.A.; Naki, T. Chitosan-based nanocarriers for nose to brain delivery. *Appl. Sci.*, **2019**, 9(11), 2219. <http://dx.doi.org/10.3390/app9112219>
- [10] Anu, M.E.S.; Saravanakumar, M.P. A review on the classification, characterisation, synthesis of nanoparticles and their application. *IOP Conf. Ser. Mater. Sci. Eng.*, **2017**, 263, 032019. <http://dx.doi.org/10.1088/1757-899X/263/3/032019>
- [11] Patra, J.K.; Baek, K.H. Green nanobiotechnology: Factors affecting synthesis and characterization techniques. *J. Nanomater.*, **2014**, 2014, 417305. <http://dx.doi.org/10.1155/2014/417305>
- [12] Satyanarayana, T.; Reddy, S.S. A review on chemical and physical synthesis methods of nanomaterials. *Int. J. Res. Appl. Sci. Eng. Technol.*, **2018**, 6(1), 2885-2889. <http://dx.doi.org/10.22214/ijraset.2018.1396>
- [13] Jeyaraj, M.; Gurunathan, S.; Qasim, M.; Kang, M.H.; Kim, J.H. A comprehensive review on the synthesis, characterization, and biomedical application of platinum nanoparticles. *Nanomaterials*, **2019**, 9(12), 1719. <http://dx.doi.org/10.3390/nano9121719> PMID: 31810256
- [14] Hussain, I.; Singh, N.B.; Singh, A.; Singh, H.; Singh, S.C. Green synthesis of nanoparticles and its potential application. *Biotechnol. Lett.*, **2016**, 38(4), 545-560. <http://dx.doi.org/10.1007/s10529-015-2026-7> PMID: 26721237
- [15] Singh, P.; Kim, Y.J.; Zhang, D.; Yang, D.C. Biological synthesis of nanoparticles from plants and microorganisms. *Trends Biotechnol.*, **2016**, 34(7), 588-599. <http://dx.doi.org/10.1016/j.tibtech.2016.02.006> PMID: 26944794
- [16] Pal, S.L.; Jana, U.; Manna, P.K.; Mohanta, G.P.; Manavalan, R. Nanoparticle: An overview of preparation and characterisation. *J. Appl. Pharm. Sci.*, **2011**, 1(6), 228-234.
- [17] Hoa, L.T.M.; Chi, N.T.; Nguyen, L.H.; Chien, D.M. Preparation and characterisation of nanoparticles containing ketoprofen and acrylic polymers prepared by emulsion solvent evaporation method. *J. Exp. Nanosci.*, **2012**, 7(2), 189-197. <http://dx.doi.org/10.1080/17458080.2010.515247>
- [18] Meng, Q.; Wang, A.; Hua, H.; Jiang, Y.; Wang, Y.; Mu, H.; Wu, Z.; Sun, K. Intranasal delivery of huperzine A to the brain using lactoferrin-conjugated N-trimethylated chitosan surface-modified PLGA nanoparticles for treatment of Alzheimer's disease. *Int. J. Nanomed.*, **2018**, 13, 705-718. <http://dx.doi.org/10.2147/IJN.S151474> PMID: 29440896
- [19] Patra, J.K.; Das, G.; Fraceto, L.F.; Campos, E.V.R.; Rodriguez, T.M.P.; Acosta, T.L.S.; Diaz, T.L.A.; Grillo, R.; Swamy, M.K.; Sharma, S.; Habtemariam, S.; Shin, H.S. Nano based drug delivery systems: Recent developments and future prospects. *J. Nanobiotechnol.*, **2018**, 16(1), 71. <http://dx.doi.org/10.1186/s12951-018-0392-8> PMID: 30231877
- [20] Pedroso, S.S.; Fleitas, S.N. Ionotropic gelation method in the synthesis of nanoparticles/microparticles for biomedical purposes. *Polym. Int.*, **2020**, 69(5), 443-447. <http://dx.doi.org/10.1002/pi.5970>
- [21] Md, S.; Khan, R.A.; Mustafa, G.; Chuttani, K.; Baboota, S.; Sahni, J.K.; Ali, J. Bromocriptine loaded chitosan nanoparticles intended for direct nose to brain delivery: Pharmacodynamic, Pharmacokinetic and scintigraphy study in mice model. *Eur. J. Pharm. Sci.*, **2013**, 48(3), 393-405. <http://dx.doi.org/10.1016/j.ejps.2012.12.007> PMID: 23266466
- [22] Mittal, D.; Md, S.; Hasan, Q.; Fazil, M.; Ali, A.; Baboota, S.; Ali, J. Brain targeted nanoparticulate drug delivery system of rasagiline via intranasal route. *Drug Deliv.*, **2016**, 23(1), 130-139. <http://dx.doi.org/10.3109/10717544.2014.907372> PMID: 24786489
- [23] Iqbal, M.; Zafar, N.; Fessi, H.; Elaissari, A. Double emulsion solvent evaporation techniques used for drug encapsulation. *Int. J. Pharm.*, **2015**, 496(2), 173-190. <http://dx.doi.org/10.1016/j.ijpharm.2015.10.057> PMID: 26522982
- [24] Alex, A.T.; Joseph, A.; Shavi, G.; Rao, J.V.; Udupa, N. Development and evaluation of carboplatin-loaded PCL nanoparticles for intranasal delivery. *Drug Deliv.*, **2016**, 23(7), 2144-2153. <http://dx.doi.org/10.3109/10717544.2014.948643> PMID: 25544603
- [25] Nagavarma, B.V.N. Different techniques for preparation of polymeric nanoparticles – A review. *Asian J. Pharm. Clin. Res.*, **2012**, 5(3), 16-23.
- [26] Gadhave, D.G.; Kokare, C.R. Nanostructured lipid carriers engineered for intranasal delivery of triflunomide in multiple sclerosis: Optimization and *in vivo* studies. *Drug Dev. Ind. Pharm.*, **2019**, 45(5), 839-851. <http://dx.doi.org/10.1080/03639045.2019.1576724> PMID: 30702966
- [27] Hangargekar, S.R.; Mohanty, P.; Jain, A. Solid lipid nanoparticles for brain targeting. *J. Drug Deliv. Ther.*, **2019**, 9(6-s), 248-252. <http://dx.doi.org/10.22270/jddt.v9i6-s.3783>
- [28] Kuldeep, S. Nano formulation a novel approach for nose to brain drug delivery. *J. Chem. Pharm. Res.*, **2016**, 8(2), 208-215.
- [29] Bonferoni, M.; Rossi, S.; Sandri, G.; Ferrari, F.; Gavini, E.; Rassa, G.; Giunchedi, P. Nanoemulsions for "nose-to-brain" drug delivery. *Pharmaceutics*, **2019**, 11(2), 84. <http://dx.doi.org/10.3390/pharmaceutics11020084> PMID: 30781585
- [30] Jaiswal, M.; Dudhe, R.; Sharma, P. K. Nanoemulsion: An advanced mode of drug delivery system. *3 Biotech.*, **2015**, 5(2), 123-127.
- [31] Zarif, L. Cochleates as Nanoparticulate Drug Carriers. In: *Nanoparticulates as Drug Carriers*; PUBLISHED BY IMPERIAL COLLEGE PRESS AND DISTRIBUTED BY WORLD SCIENTIFIC PUBLISHING CO, Singapore, **2006**, pp. 349-366. http://dx.doi.org/10.1142/9781860949074_0016
- [32] Hong, S.S.; Oh, K.T.; Choi, H.G.; Lim, S.J. Liposomal formulations for nose-to-brain delivery: Recent advances and future perspectives. *Pharmaceutics*, **2019**, 11(10), 540. <http://dx.doi.org/10.3390/pharmaceutics11100540> PMID: 31627301
- [33] Vieira, D.; Gamarra, L. Getting into the brain: Liposome-based strategies for effective drug delivery across the blood-brain barrier. *Int. J. Nanomed.*, **2016**, 11, 5381-5414. <http://dx.doi.org/10.2147/IJN.S117210> PMID: 27799765
- [34] Parajapati, S.K.; Maurya, S.D.; Das, M.K.; Tilak, V.K.; Verma, K.K.; Dhakar, R.C. Potential application of dendrimers in drug delivery: A concise review and update. *J. Drug Deliv. Ther.*, **2016**, 6(2), 71-88. <http://dx.doi.org/10.22270/jddt.v6i2.1195>
- [35] Abbasi, E.; Aval, S.F.; Akbarzadeh, A.; Milani, M.; Nasrabadi, H.T.; Joo, S.W.; Hanifehpour, Y.; Nejati, K.K.; Pashaei, A.R. Dendrimers: Synthesis, applications, and properties. *Nanoscale Res. Lett.*, **2014**, 9(1), 247. <http://dx.doi.org/10.1186/1556-276X-9-247> PMID: 24994950
- [36] Zhu, Y.; Liu, C.; Pang, Z. Dendrimer-based drug delivery systems for brain targeting. *Biomolecules*, **2019**, 9(12), 790.

- <http://dx.doi.org/10.3390/biom9120790> PMID: 31783573
- [37] Lungare, S.; Hallam, K.; Badhan, R.K.S. Phytochemical-loaded mesoporous silica nanoparticles for nose-to-brain olfactory drug delivery. *Int. J. Pharm.*, **2016**, *513*(1-2), 280-293. <http://dx.doi.org/10.1016/j.ijpharm.2016.09.042> PMID: 27633279
- [38] Mohanraj, V.J.; Chen, Y. Nanoparticles - A review. *Trop. J. Pharm. Res.*, **2007**, *5*(1), 561-573. <http://dx.doi.org/10.4314/tjpr.v5i1.14634>
- [39] Caputo, F.; Clogston, J.; Calzolari, L.; Rösslein, M.; Prina-Mello, A. Measuring particle size distribution of nanoparticle enabled medicinal products, the joint view of EUNCL and NCI-NCL. A step by step approach combining orthogonal measurements with increasing complexity. *J. Control. Release*, **2019**, *299*, 31-43. <http://dx.doi.org/10.1016/j.jconrel.2019.02.030> PMID: 30797868
- [40] Pandey P., D.M. A brief review on inorganic nanoparticles. *Crit. Rev.*, **2016**, *3*(3), 18-26.
- [41] Rasmussen, M.K.; Pedersen, J.N.; Marie, R. Size and surface charge characterization of nanoparticles with a salt gradient. *Nat. Commun.*, **2020**, *11*(1), 2337. <http://dx.doi.org/10.1038/s41467-020-15889-3> PMID: 32393750
- [42] Honary, S.; Zahir, F. Effect of zeta potential on the properties of nano-drug delivery systems - A review (Part 1). *Trop. J. Pharm. Res.*, **2013**, *12*(2), 255-264.
- [43] Jain, A.K.; Thareja, S. *In vitro* and *in vivo* characterization of pharmaceutical nanocarriers used for drug delivery. *Artif. Cells Nanomed. Biotechnol.*, **2019**, *47*(1), 524-539. <http://dx.doi.org/10.1080/21691401.2018.1561457> PMID: 30784319
- [44] Ranjit, K.; Nanoparticle, B.A. An overview of preparation, characterization and application. *Int Res J Pharm.*, **2013**, *4*(4), 47-57.
- [45] D'Souza, S. A review of *in vitro* drug release test methods for nano-sized dosage forms. *Adv. Pharm.*, **2014**, *2014*, 304757. <http://dx.doi.org/10.1155/2014/304757> Muthu, M.S.; Feng, S.S. Pharmaceutical stability aspects of nano-medicines. *Nanomedicine*, **2009**, *4*(8), 857-860. <http://dx.doi.org/10.2217/nmm.09.75> PMID: 19958220
- [47] Mistry, A.; Stolnik, S.; Illum, L. Nanoparticles for direct nose-to-brain delivery of drugs. *Int. J. Pharm.*, **2009**, *379*(1), 146-157. <http://dx.doi.org/10.1016/j.ijpharm.2009.06.019> PMID: 19555750
- [48] Sonvico, F.; Clementino, A.; Buttini, F.; Colombo, G.; Pescina, S.; Stanisquaski, G.S.; Raffin, P.A.; Nicoli, S. Surface-modified nanocarriers for nose-to-brain delivery: From bioadhesion to targeting. *Pharmaceutics*, **2018**, *10*(1), 34. <http://dx.doi.org/10.3390/pharmaceutics10010034> PMID: 29543755
- [49] Erdő, F.; Bors, L.A.; Farkas, D.; Bajza, Á.; Gizurarson, S. Evaluation of intranasal delivery route of drug administration for brain targeting. *Brain Res. Bull.*, **2018**, *143*, 155-170. <http://dx.doi.org/10.1016/j.brainresbull.2018.10.009> PMID: 30449731
- [50] Md, S.; Mustafa, G.; Baboota, S.; Ali, J. Nanoneurotherapeutics approach intended for direct nose to brain delivery. *Drug Dev. Ind. Pharm.*, **2015**, *41*(12), 1922-1934. <http://dx.doi.org/10.3109/03639045.2015.1052081> PMID: 26057769
- [51] Ghadiri, M.; Young, P.; Traini, D. Strategies to enhance drug absorption *via* nasal and pulmonary routes. *Pharmaceutics*, **2019**, *11*(3), 113. <http://dx.doi.org/10.3390/pharmaceutics11030113> PMID: 30861990
- [52] Islam, S.U.; Shehzad, A.; Ahmed, M.B.; Lee, Y.S. Intranasal delivery of nanoformulations: A potential way of treatment for neurological disorders. *Molecules*, **2020**, *25*(8), 1929. <http://dx.doi.org/10.3390/molecules25081929> PMID: 32326318
- [53] Almasser, S. A review on nasal drug delivery system and its contribution in therapeutic management. *Asian J. Pharm. Clin. Res.*, **2019**, *12*(1), 40-45. <http://dx.doi.org/10.22159/ajpcr.2019.v12i1.29443>
- [54] Anagnostou, K.; Stylianakis, M.; Michaleas, S.; Skouras, A. Biodegradable nanomaterials. In: *Nanomaterials for Clinical Applications*; Elsevier: Amsterdam, Netherlands: **2020**; pp. 123-157.
- [55] Singh, N.; Joshi, A.; Toor, A.; Verma, G. Drug delivery: Advancements and challenges. In: *Nanostruct Drug Deliv*; Elsevier: Amsterdam, Netherlands: **2017**; pp. 865-886.
- [56] Suriya, P.A.; Dorothy, R.; Jancirani, S.; Rajendran, S.; Singh, G.; Senthil, K.S. Recent advances in the study of toxicity of polymer-based nanomaterials. In: *Nanotoxicity*; Elsevier: Amsterdam, Netherlands: **2020**; pp. 143-165. <http://dx.doi.org/10.1016/B978-0-12-819943-5.00007-5>
- [57] Wu, T.; Tang, M. Review of the effects of manufactured nanoparticles on mammalian target organs. *J. Appl. Toxicol.*, **2018**, *38*(1), 25-40. <http://dx.doi.org/10.1002/jat.3499> PMID: 28799656
- [58] Elsaesser, A.; Howard, C.V. Toxicology of nanoparticles. *Adv. Drug Deliv. Rev.*, **2012**, *64*(2), 129-137. <http://dx.doi.org/10.1016/j.addr.2011.09.001> PMID: 21925220
- [59] Sharifi, S.; Behzadi, S.; Laurent, S.; Forrest, M.L.; Stroeve, P.; Mahmoudi, M. *Toxicity of nanomaterials*. *Chem. Soc. Rev.*, **2012**, *41*, 2323-2343.
- [60] Wu, T.; Tang, M. Toxicity of quantum dots on respiratory system. *Inhal. Toxicol.*, **2014**, *26*(2), 128-139. <http://dx.doi.org/10.3109/08958378.2013.871762> PMID: 24495248
- [61] Recordati, C.; De Maglie, M.; Bianchessi, S.; Argenti, S.; Cella, C.; Mattiello, S.; Cubadda, F.; Aureli, F.; D'Amato, M.; Raggi, A.; Lenardi, C.; Milani, P.; Scanziani, E. Tissue distribution and acute toxicity of silver after single intravenous administration in mice: Nano-specific and size-dependent effects. *Part. Fibre Toxicol.*, **2015**, *13*(1), 12. <http://dx.doi.org/10.1186/s12989-016-0124-x> PMID: 26926244
- [62] Zoroddu, M.; Medici, S.; Ledda, A.; Nurchi, V.; Lachowicz, J.; Peana, M. Toxicity of nanoparticles. *Curr. Med. Chem.*, **2014**, *21*(33), 3837-3853. <http://dx.doi.org/10.2174/0929867321666140601162314> PMID: 25306903
- [63] Paek, H.J.; Lee, Y.J.; Chung, H.E.; Yoo, N.H.; Lee, J.A.; Kim, M.K.; Lee, J.K.; Jeong, J.; Choi, S.J. Modulation of the pharmacokinetics of zinc oxide nanoparticles and their fates *in vivo*. *Nanoscale*, **2013**, *5*(23), 11416-11427. <http://dx.doi.org/10.1039/c3nr02140h> PMID: 23912904
- [64] Shegokar, R.; Singh, K.K. Surface modified nevirapine nanosuspensions for viral reservoir targeting: *In vitro* and *in vivo* evaluation. *Int. J. Pharm.*, **2011**, *421*(2), 341-352. <http://dx.doi.org/10.1016/j.ijpharm.2011.09.041> PMID: 21986114
- [65] McClements, D.J. Emulsion design to improve the delivery of functional lipophilic components. *Annu. Rev. Food Sci. Technol.*, **2010**, *1*(1), 241-269. <http://dx.doi.org/10.1146/annurev.food.080708.100722> PMID: 22129337
- [66] Palanikumar, L.; Al-Hosani, S.; Kalmouni, M.; Nguyen, V.P.; Ali, L.; Pasricha, R.; Barrera, F.N.; Magzoub, M. pH-responsive high stability polymeric nanoparticles for targeted delivery of anticancer therapeutics. *Commun. Biol.*, **2020**, *3*(1), 95. <http://dx.doi.org/10.1038/s42003-020-0817-4> PMID: 32127636
- [67] Maier, M.A.; Jayaraman, M.; Matsuda, S.; Liu, J.; Barros, S.; Querbes, W.; Tam, Y.K.; Ansell, S.M.; Kumar, V.; Qin, J.; Zhang, X.; Wang, Q.; Panesar, S.; Hutabarat, R.; Carioto, M.; Hettinger, J.; Kandasamy, P.; Butler, D.; Rajeev, K.G.; Pang, B.; Charisse, K.; Fitzgerald, K.; Mui, B.L.; Du, X.; Cullis, P.; Madden, T.D.; Hope, M.J.; Manoharan, M.; Akinc, A. Biodegradable lipids enabling rapidly eliminated lipid nanoparticles for systemic delivery of RNAi therapeutics. *Mol. Ther.*, **2013**, *21*(8), 1570-1578. <http://dx.doi.org/10.1038/mt.2013.124> PMID: 23799535
- [68] Schubert, J.; Chanana, M. Coating matters: Review on colloidal stability of nanoparticles with biocompatible coatings in biological media, living cells and organisms. *Curr. Med. Chem.*, **2018**, *25*(35), 4553-4586. <http://dx.doi.org/10.2174/0929867325666180601101859> PMID: 29852857
- [69] Thirumala, R.G.; Babu, B.; Joyce, S.R.; Pushpa, M.V.; Ravikumar, R.V.S.S.N. Spectral investigations on undoped and Cu²⁺ doped ZnO-CdS composite nanopowders. *Spectrochim. Acta A Mol. Biomol. Spectrosc.*, **2015**, *139*, 86-93. <http://dx.doi.org/10.1016/j.saa.2014.12.021> PMID: 25554956

- [70] Adeleye, A.S.; Pokhrel, S.; Mädler, L.; Keller, A.A. Influence of nanoparticle doping on the colloidal stability and toxicity of copper oxide nanoparticles in synthetic and natural waters. *Water Res.*, **2018**, *132*, 12-22.
<http://dx.doi.org/10.1016/j.watres.2017.12.069> PMID: 29304444
- [71] Ahmad, J.; Siddiqui, M.A.; Akhtar, M.J.; Alhadlaq, H.A.; Alshamsan, A.; Khan, S.T.; Wahab, R.; Al-Khedhairi, A.A.; Al-Salim, A.; Musarrat, J.; Saquib, Q.; Fareed, M.; Ahamed, M. Copper doping enhanced the oxidative stress-mediated cytotoxicity of TiO₂ nanoparticles in A549 cells. *Hum. Exp. Toxicol.*, **2018**, *37*(5), 496-507.
<http://dx.doi.org/10.1177/0960327117714040> PMID: 28621211
- [72] Sun, B.; Pokhrel, S.; Dunphy, D.R.; Zhang, H.; Ji, Z.; Wang, X.; Wang, M.; Liao, Y.P.; Chang, C.H.; Dong, J.; Li, R.; Mädler, L.; Brinker, C.J.; Nel, A.E.; Xia, T. Reduction of acute inflammatory effects of fumed silica nanoparticles in the lung by adjusting silanol display through calcination and metal doping. *ACS Nano*, **2015**, *9*(9), 9357-9372.
<http://dx.doi.org/10.1021/acsnano.5b03443> PMID: 26200133
- [73] Naatz, H.; Lin, S.; Li, R.; Jiang, W.; Ji, Z.; Chang, C.H.; Köser, J.; Thöming, J.; Xia, T.; Nel, A.E.; Mädler, L.; Pokhrel, S. Safe-by-Design CuO nanoparticles via Fe-doping. Cu–O bond length variation, and biological assessment in cells and zebrafish embryos. *ACS Nano*, **2017**, *11*(1), 501-515.
<http://dx.doi.org/10.1021/acsnano.6b06495> PMID: 28026936
- [74] Teoh, W.Y.; Amal, R.; Mädler, L. Flame spray pyrolysis: An enabling technology for nanoparticles design and fabrication. *Nanoscale*, **2010**, *2*(8), 1324-1347.
<http://dx.doi.org/10.1039/c0nr00017e> PMID: 20820719
- [75] Hola, K.; Markova, Z.; Zoppellaro, G.; Tucek, J.; Zboril, R. Tailored functionalization of iron oxide nanoparticles for MRI, drug delivery, magnetic separation and immobilization of biosubstances. *Biotechnol. Adv.*, **2015**, *33*(6), 1162-1176.
<http://dx.doi.org/10.1016/j.biotechadv.2015.02.003> PMID: 25689073
- [76] Mout, R.; Moyano, D.F.; Rana, S.; Rotello, V.M. Surface functionalization of nanoparticles for nanomedicine. *Chem. Soc. Rev.*, **2012**, *41*(7), 2539-2544.
<http://dx.doi.org/10.1039/c2cs15294k> PMID: 22310807



Design, synthesis, and pharmacological evaluation of [1,3]dioxolo-chromeno[2,3-*b*]pyridines as anti-seizure agents

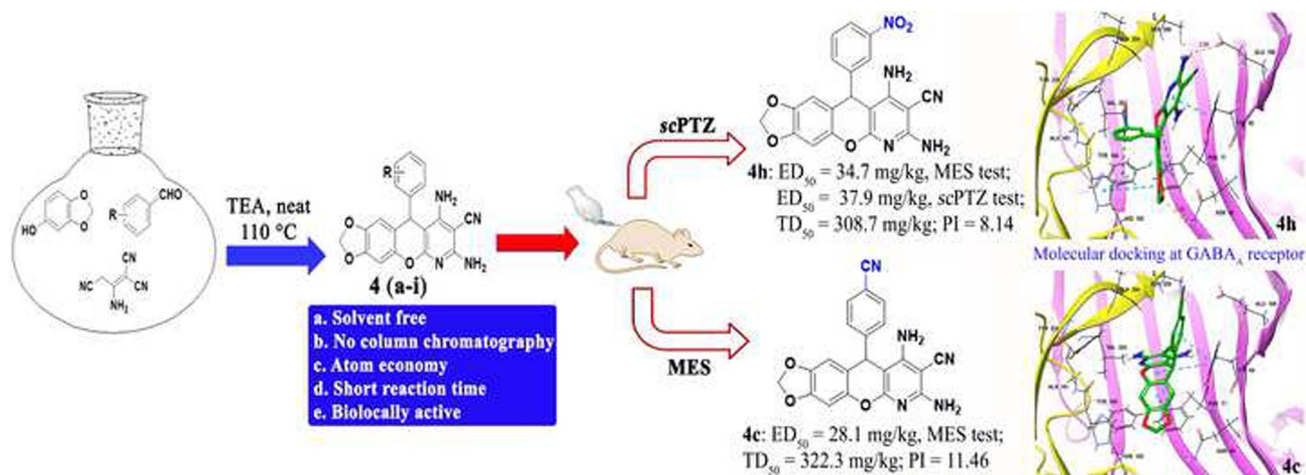
Visarapu Malathi¹ · Nissi Sharon¹ · Pannala Padmaja² · Deepak Lokwani³ · Saurabh Khadse⁴ · Prashant Chaudhari⁴ · Atul A. Shirkhedkar⁴ · Pedavenkatagari Narayana Reddy¹ · Vinod G. Ugale^{4,5}

Received: 18 July 2022 / Accepted: 29 September 2022
© The Author(s), under exclusive licence to Springer Nature Switzerland AG 2022

Abstract

An efficient one-pot three-component reaction for the synthesis of [1,3]dioxolo[4',5':6,7]chromeno[2,3-*b*]pyridines **4(a-i)** has been developed. Synthesis was achieved by reacting sesamol (**1**), aromatic aldehydes **2(a-i)**, and 2-aminopropene-1,1,3-tricarbonitrile (**3**) in the presence of triethylamine at 100 °C under neat reaction condition. Simple operational procedure, broad substrate scope, column chromatography free separations, and high yield of products make it an efficient and largely acceptable synthetic strategy. Synthesized compounds **4(a-i)** were further screened for preliminary anticonvulsant activity using MES and *sc*PTZ tests. These analogs were also checked for neurotoxicity and hepatotoxicity. Selected active compounds have been then screened quantitatively to determine ED₅₀ and TD₅₀ values. Analog **4h** was found effective in both preclinical seizure models with significant therapeutic/toxicity profile (**4h**: ED₅₀ = 34.7 mg/kg, MES test; ED₅₀ = 37.9 mg/kg, *sc*PTZ test; TD₅₀ = 308.7 mg/kg). Molecular dynamic simulation for 100 ns of compound **4h**-complexed with GABA_A receptor revealed good thermodynamic behavior and fairly stable interactions (**4h**, Docking score = -10.94). In conclusion, effective synthetic strategy, significant anticonvulsant activity with good toxicity profile and detailed molecular modeling studies led us to anticipate the emergence of these analogs as valid leads for the development of future effective neurotherapeutic agents.

Graphical abstract



Keywords Design · Synthesis · [1,3]Dioxolochromeno[2,3-*b*]pyridines · Anticonvulsants · Molecular docking

✉ Pedavenkatagari Narayana Reddy
npedaven@gitam.edu

✉ Vinod G. Ugale
vinod.ugale@rediffmail.com

Extended author information available on the last page of the article

Introduction

Epilepsy is a complex neurological disorder characterized by impulsive and recurring seizures [1]. Alteration of brain function due to an abnormal and excessive electrical discharge from neuronal cells results into seizures [2]. Epilepsy is a serious neurological disorder affecting approximately 1% of human population worldwide [1, 2]. According to the recent data, 20% of epilepsy patients using first generation of antiepileptic drugs (AEDs) were unable to acquire satisfactory control against seizures [3]. Relatively recently, several third-generation AEDs are introduced but number of epilepsy patients are still refractory to currently available AEDs [4, 5]. Most of the marketed drugs are undermined by extreme adverse reactions such as sluggishness, gastrointestinal unsettling influences, gingival hyperplasia, ataxia, and megaloblastic anemia; besides, around 30% of patients have uncontrolled seizures [6–8]. Thus, there is a substantial need to create more efficacious and safer neurotherapeutic strategies in order to offer these patients a significant reduction of seizures and/or a state of freedom from resistant seizures. Hence, nowadays, medicinal chemists focused at design and discovery of novel anticonvulsants possessing wider

therapeutic spectrum with minimal or no side effects. Much endeavors dedicated as of late dependent on pharmacophoric hybridization for the improvement of novel therapeutics.

Chromeno[2,3-*b*]pyridine is a fused heterocyclic scaffold with multiple bioactivities such as antibacterial, anti-convulsant, antiproliferative, anticancer, antirheumatic, antihistaminic, and antimycotic [9–13]. Chromenotacrine CT6 is used as non-toxic antioxidant and neuroprotective agent [13]. Amlexanox is known as antiallergic drug for the treatment of rhinitis and asthma [14, 15]. Pranoprofen is used as a non-steroidal anti-inflammatory drug with analgesic and antipyretic properties [16]. 5-Carbon substituted 2,4-diaminochromeno[2,3-*b*]pyridine (**I**) acts as anti-rheumatoid and anti-psoriatic agent. The scaffold inhibited mitogen-activated protein kinase-2 and suppressed the expression of TNF α in U937 cells [17]. More prominently, efficient procedures were also reported for the synthesis of chromeno[2,3-*b*]pyridines [18–26]. Alternatively, 1,3-dioxolochroman is a heterocyclic framework constituting the core structure of important natural products and bioactive compounds (Fig. 1). 1,3-Dioxolochroman has important biological properties such as antioxidants, anti-inflammatory, antimalarials, anticonvulsants, and anticancer activities [26–31]. However, as per our knowledge, till

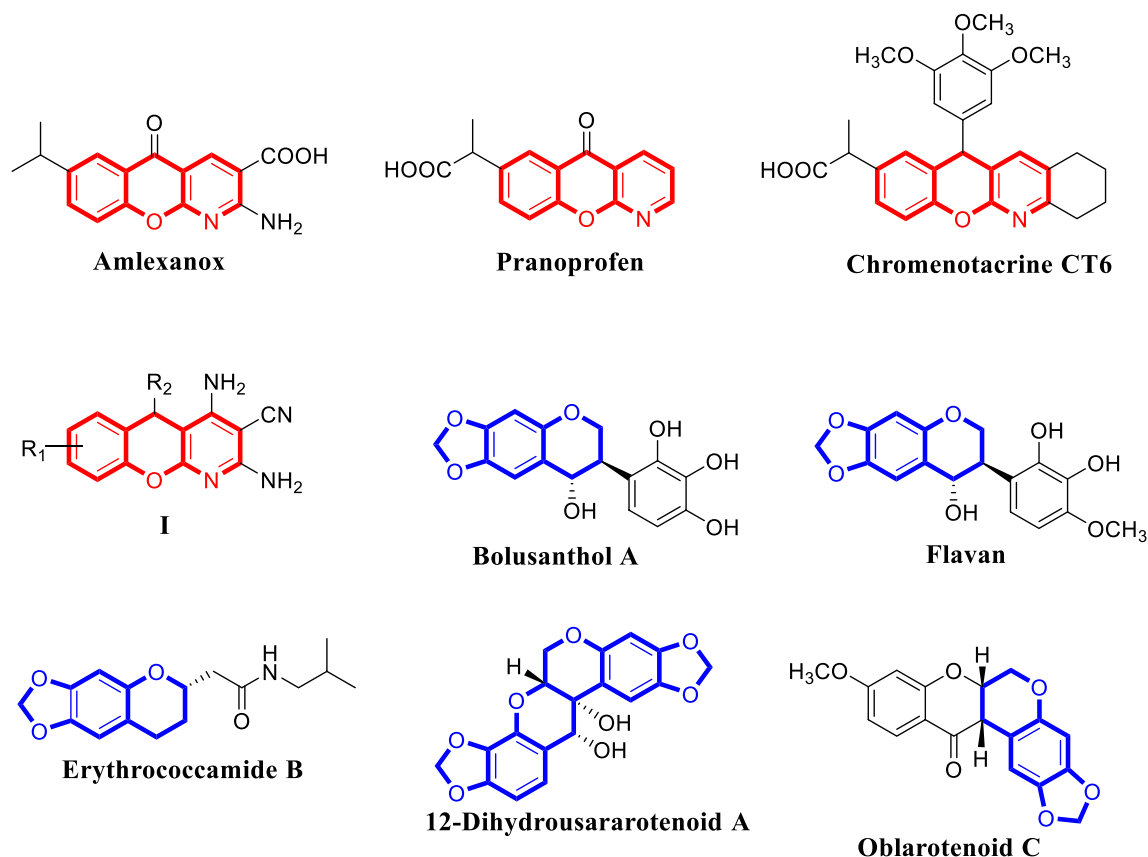
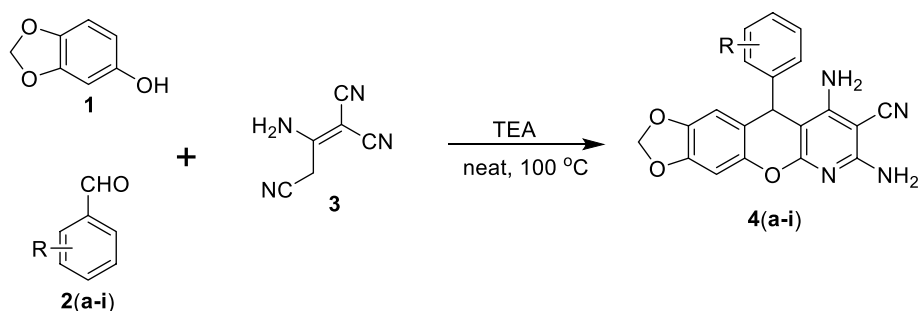


Fig. 1 Biologically active compounds with chromenopyridine and 1,3-dioxolochroman scaffolds

Scheme 1 Synthesis of [1, 3]dioxolo[4',5':6,7]chromeno[2,3-*b*]pyridine derivatives **4(a-i)****Table 1** Optimization reaction conditions for [1, 3]dioxolo[4',5':6,7]chromeno[2,3-*b*]pyridine (**4a**)

Entry	Solvent	Catalyst ^a	Temperature (°C)	Time (h)	Yield ^b (%)
1	Ethanol	–	80	24	n.r. ^c
2	Ethanol	Et ₃ N	80	24	36
3	Ethanol	Pyridine	80	24	22
4	Ethanol	Piperidine	80	24	18
5	Acetonitrile	Et ₃ N	82	24	26
6	1-Propanol	Et ₃ N	97	24	32
7	–	Et ₃ N	80	4	81
8	–	Et ₃ N	100	4	93
9	–	Et ₃ N	110	4	85

n.r. No reaction

^a10 mol% catalyst

^bIsolated yield

date, there are no reports available on the synthesis of dioxolochromenopyridine analogs. Owing to the biological significance of these heterocyclic frameworks, combination of chromeno[2,3-*b*]pyridine and 1,3-dioxolochroman scaffolds in one hybrid structure would serve as a useful approach to exploit their biomedical properties against seizures. Thus, as a part of our continuous effort in heterocyclic synthesis and search for potential safer anticonvulsants [32–37], herein, we have reported the union of scaffolds as novel structures with different substitution patterns and evaluated them for anticonvulsant activity and plausible toxicities. Molecular docking and dynamic simulation were also executed for synthesized compounds in order to rationalize anticonvulsant activity in a qualitative way.

Results and discussion

Chemistry

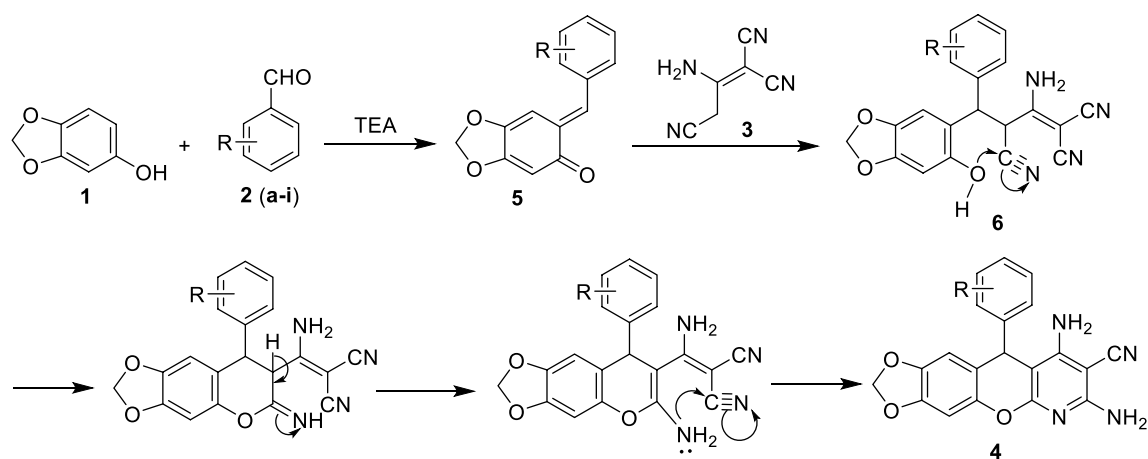
We began our initial investigation by the reaction between sesamol (**1**), 4-methoxybenzaldehyde (**2a**) and 2-amino-propene-1,1,3-tricarbonitrile (**3**) as a model reaction under

Table 2 Synthesis of [1, 3]dioxolo[4',5':6,7]chromeno[2,3-*b*]pyridine derivatives **4(a-i)**

Entry	Aromatic aldehydes 2(a-i)	Product 4(a-i)	Yield ^a (%)
1	4-Methoxybenzaldehyde	4a	93
2	4-Bromobenzaldehyde	4b	91
3	4-Cyanobenzaldehyde	4c	92
4	4-Isopropylbenzaldehyde	4d	86
5	3-Ethoxy-4-hydroxybenzaldehyde	4e	88
6	3-Hydroxy-4-methoxybenzaldehyde	4f	90
7	1-Naphthaldehyde	4g	89
8	3-Nitrobenzaldehyde	4h	84
9	3,4-Dimethoxybenzaldehyde	4i	86

^aIsolated yield

various conditions (Scheme 1). The reaction was first carried out in ethanol under reflux for 24 h (Table 1, entry 1). As shown in Table 1, no reaction occurred in ethanol. After addition of 10 mol% triethylamine to a reaction mixture in an ethanol gave the desired product **4a** in 36% yield (Table 1, entry 2). Use of pyridine and piperidine as a base did not improve the product yield (Table 1, entries 3–4). Model reaction in acetonitrile and propanol under reflux condition with 10 mol% triethylamine, resulted into the product **4a** with 26% and 32% yields, respectively (Table 1, entries 5–6). However, when the reaction was carried out at 80 °C under neat reaction conditions, the product was isolated as 81% yield within 4 h (Table 1, entry 7). After further optimization of reaction conditions, we found that increasing the reaction temperature up to 100 °C led to the improvement in yield up to 93% (Table 1, entry 8). Moreover, we examined the reaction at 110 °C and it resulted into the desired product **4a** with 85% yield (Table 1, entry 9). The product **4a** was isolated without using column chromatography purification process as a racemic mixture. After completion of the reaction, precipitated solid was filtered and then washed with ethanol to give pure 7,9-diamino-10-(4-methoxyphenyl)-10*H*-[1,3]dioxolo[4',5':6,7]chromeno[2,3-*b*]pyridine-8-carbonitrile (**4a**).



Scheme 2 Proposed mechanism for the synthesis of [1,3]dioxolo[4',5':6,7]chromeno[2,3-*b*]pyridine derivatives

Through optimization of reaction conditions, here, we have explored the scope of our three-component reaction using variety of aromatic aldehydes for the synthesis of a library of new [1,3]dioxolo[4',5':6,7]chromeno[2,3-*b*]pyridine derivatives (Table 2). Aromatic aldehydes with isopropyl, bromo, nitro, and cyano groups reacted smoothly and afforded the appropriate products in good yields (Table 2). Naphthaldehyde was also used in three-component reaction to afford corresponding product **4g** in 89% yield. However, when acetaldehyde and propionaldehyde were used under outlined optimized conditions, unfortunately, the expected products were not obtained. Targeted compounds were synthesized as a racemic mixture.

All reactions were clean without any side products. Structures of synthesized compounds were confirmed through ^1H NMR, ^{13}C NMR, IR, and mass spectroscopy. For example, the ^1H NMR spectrum of compound **4a** showed a sharp singlet for the benzylic methine proton at 5.10 ppm and methoxy protons at 3.66 ppm. NH_2 protons were appeared at 6.29 and 6.40 ppm. ^1H decoupled ^{13}C NMR spectrum of **4a** showed 19 resonance peaks in agreement with the suggested structure. A proposed mechanism for the formation of **4a** is shown as Scheme 2. Nucleophilic attack of sesamol to the appropriate aldehyde, followed by the elimination of water provides intermediate **5**. Michael addition of 2-aminoprop-1-ene-1,1,3-tricarbonitrile (activated by TEA) to intermediate **5** provided intermediate **6** which on tautomerization and subsequent intramolecular cyclization afforded corresponding [1,3]dioxolo[4',5':6,7]chromeno[2,3-*b*]pyridine.

Pharmacological screening

Preliminary in vivo anticonvulsant screening in mice involves classical animal models such as maximal electroshock seizure (MES) and subcutaneous pentylenetetrazole (*sc*PTZ)

tests. The targeted [1,3]dioxolo[4',5':6,7]chromeno[2,3-*b*]pyridines were synthesized as racemic mixtures and then biological activity was evaluated with racemic mixtures.

Anticonvulsant activity evaluation using MES test

MES test was used to identify the ability of synthesized compounds to prevent spread of seizures. More specifically, MES test detects analogs with anticonvulsant activity against human generalized tonic-clonic seizures induced by an electrical stimulus. All synthesized compounds **4(a-i)** were screened using MES test at two different time intervals, 30 min and 4 h. In MES screen, at short duration of time (30 min), most of the tested compounds have shown ability to prevent tonic-clonic seizures indicated by delayed onset of extensor component and reduction in mean duration of hind leg extension (Table 3). At a small dose of 30 mg/kg, test compounds **4a**, **4c**, and **4d** exhibited moderate anticonvulsant response as compared to control at $P < 0.01$. Compounds **4a**, **4c**, **4f**, and **4h** were also found effective in MES test at 100 mg/kg dose. These compounds significantly decreased overall extent of tonic convulsions, when compared to standard drug. In MES test, compounds **4a**, **4c**, and **4f** have shown moderate to excellent anticonvulsant effect with increased dose of compounds as compared to control and standard. Results indicated that these compounds were showing fast absorption and onset of action against tonic-clonic seizures. However, compound **4b** (4-Br) and **4g** (naphthalene ring) showed no response with unexpected death of animals. Both compounds have not shown any significant response at a dose of 30 mg/kg and thus, further not tested at lower doses. At high dose of **4b** and **4g** (300 mg/kg), 50% of animals were dead with no response against convulsions induced by electroshock method. Test compounds **4d**, **4e**, and **4i**

Table 3 Pharmacological screening of synthesized compounds for anticonvulsant activity by MES test after 30 min, **4(a–i)**

Code	Dose mg/kg (i.p.)	Onset time of convulsion (s) [mean \pm SEM] ^a	Duration of tonic hind leg extension (s) [mean \pm SEM] ^a	R/D
C	Vehicle	4.57 \pm 0.28	15.25 \pm 0.28	3/3
S	30	15.60 \pm 0.63**	9.80 \pm 0.15**	5/1
	100	18.90 \pm 0.38**	6.94 \pm 0.45**	6/0
	300	21.40 \pm 0.35**	4.35 \pm 0.29***	6/0
4a	30	13.88 \pm 0.78**	10.10 \pm 0.49**	5/1
	100	14.10 \pm 0.83**	9.41 \pm 0.73**	6/0
	300	15.89 \pm 0.75**	8.10 \pm 0.44**	6/0
4b	30	7.79 \pm 0.66ns	12.94 \pm 1.23ns	4/2
	100	7.10 \pm 0.34ns	13.49 \pm 0.89ns	4/2
	300	9.22 \pm 0.57*	13.56 \pm 1.00ns	3/3
4c	30	13.82 \pm 0.59**	9.45 \pm 0.89**	5/1
	100	15.45 \pm 0.46**	8.80 \pm 0.21**	5/1
	300	17.99 \pm 0.66**	6.85 \pm 0.52**	6/0
4d	30	10.25 \pm 0.46*	11.85 \pm 0.80*	4/2
	100	11.80 \pm 0.69**	10.36 \pm 0.64**	5/1
	300	12.56 \pm 0.77**	10.14 \pm 0.68**	6/0
4e	30	9.00 \pm 0.29*	12.40 \pm 0.23ns	4/2
	100	11.29 \pm 0.60**	10.66 \pm 0.50**	5/1
	300	13.90 \pm 0.45**	9.20 \pm 0.34**	5/1
4f	30	13.63 \pm 0.56**	9.25 \pm 0.22**	5/1
	100	15.27 \pm 0.65**	8.00 \pm 0.15**	6/0
	300	16.49 \pm 0.78**	7.15 \pm 0.43**	6/0
4g	30	6.14 \pm 0.56ns	13.00 \pm 0.31ns	4/2
	100	7.00 \pm 1.56ns	13.40 \pm 0.24ns	4/2
	300	8.14 \pm 0.45*	13.21 \pm 0.44ns	3/3
4h	30	12.77 \pm 0.35**	11.05 \pm 0.16*	6/0
	100	13.63 \pm 0.66**	10.00 \pm 0.78**	5/1
	300	14.94 \pm 0.71**	9.31 \pm 0.69**	5/1
4i	30	9.45 \pm 1.23*	11.60 \pm 0.45*	5/1
	100	11.30 \pm 0.90**	10.75 \pm 0.39**	5/1
	300	13.10 \pm 0.35**	9.57 \pm 0.35**	4/2

C Control (vehicle), **S** Standard drug (Phenytoin), **R** Recovery, **D** Death

Significantly different from the control at * $P < 0.05$ (significant); ** $P < 0.01$ (very significant); *** $P < 0.001$ (extremely significant), *ns* not significant

^aEach value represents mean \pm SEM

have displayed less activity when compared to other compounds of series in MES test. Compounds **4e** and **4i** were showing significant activity at a high dose (300 mg/kg) but with 75% recovery of animals used in the MES test.

Synthesized compounds were then screened at 4 h to assess anticonvulsant activity at longer duration of time. Results are displayed in Table 4. Compounds **4b** and **4g** were not considered for MES test at 4 h; due to lack of recovery and higher deaths of animals in initial screening. Test compounds **4c**, **4f**, and **4h** have displayed better to excellent protection against maximal seizures after 4 h with increased doses of compounds (30, 100, and 300 mg/kg). Test compounds **4c** and **4f** have shown excellent

anticonvulsant response with decreased duration of tonic hind leg extension (**4c** = 6.20 s and **4f** = 6.89 s) at a dose of 300 mg/kg. Compounds **4d**, **4e**, and **4i** were found to be less effective with respect to onset of convulsions and duration of extensor phase at $P < 0.01$ at all doses used. In conclusion, synthesized derivatives **4a**, **4c**, **4f**, and **4h** have exhibited significant anticonvulsant activity after 30 min and 4 h of time intervals in the MES test.

Anticonvulsant activity evaluation using scPTZ test

In scPTZ test, myoclonic seizures were induced through subcutaneous injection of PTZ to mice at a convulsive

Table 4 Pharmacological screening of selected synthesized compounds for anticonvulsant activity by MES test after 4h, **4(a–i)**

Code	Dose mg/kg (i.p.)	Onset time of convulsion (s) [mean ± SEM] ^a	Duration of tonic hind leg extension (s) [mean ± SEM] ^a	R/D
C	Vehicle	4.33 ± 0.30	15.40 ± 0.25	2/4
S	30	16.00 ± 0.54**	8.10 ± 0.42**	6/0
	100	19.33 ± 0.33**	5.50 ± 0.34**	6/0
	300	21.75 ± 0.10**	4.21 ± 0.16**	6/0
4a	30	13.00 ± 0.26**	10.79 ± 0.28**	4/2
	100	15.09 ± 0.48**	9.67 ± 0.35**	5/1
	300	16.87 ± 0.44**	8.00 ± 0.17**	5/1
4c	30	15.55 ± 0.78**	9.25 ± 0.21**	5/1
	100	16.41 ± 0.53**	8.69 ± 0.24**	6/0
	300	17.22 ± 0.33**	6.20 ± 0.41**	6/0
4d	30	14.00 ± 0.40**	11.40 ± 0.24**	5/1
	100	14.88 ± 0.13**	10.60 ± 0.31**	5/1
	300	15.46 ± 0.66**	9.55 ± 0.28**	6/0
4e	30	8.35 ± 0.14*	13.20 ± 0.20ns	4/2
	100	9.00 ± 0.27*	12.64 ± 0.58*	5/1
	300	10.65 ± 0.89**	11.35 ± 0.27**	5/1
4f	30	14.23 ± 0.45**	9.31 ± 0.23**	5/1
	100	15.00 ± 1.14**	8.59 ± 0.41**	5/1
	300	16.56 ± 0.47**	7.45 ± 0.20**	6/0
4h	30	14.63 ± 0.56**	8.25 ± 0.22**	6/0
	100	16.27 ± 0.65**	7.12 ± 0.15**	5/1
	300	17.20 ± 0.78**	6.89 ± 0.43**	5/1
4i	30	9.89 ± 0.61*	13.93 ± 0.25ns	5/1
	100	13.17 ± 1.08*	11.92 ± 0.21*	5/1
	300	10.79 ± 0.55**	10.43 ± 0.23**	6/0

C Control (vehicle), **S** Standard drug (Phenytoin), **R** Recovery, **D** Death

Significantly different from the control at * $P < 0.05$ (significant); ** $P < 0.01$ (very significant); *** $P < 0.001$ (extremely significant); *ns* not significant

^aEach value represents mean ± SEM

Table 5 Anticonvulsant screening of selected synthesized compounds using *sc*PTZ test at 30 min

Code	Onset of clonic convulsions (s) [mean ± SEM] ^a		
	30 mg/kg	100 mg/kg	300 mg/kg
4a	80.00 ± 1.50**	87.14 ± 1.60**	94.30 ± 1.25**
4c	93.35 ± 1.37**	98.37 ± 1.44**	102.12 ± 1.41***
4d	75.33 ± 1.24**	84.25 ± 1.70**	88.35 ± 1.32**
4f	91.26 ± 0.79**	95.42 ± 1.13**	100.24 ± 0.95***
4h	83.67 ± 1.78**	89.39 ± 1.44**	93.12 ± 0.35**
4i	60.42 ± 0.85*	52.50 ± 3.59ns	Not tested
S	110.2 ± 1.35		
C	52.87 ± 1.41		

C Control (Vehicle), **S** Standard drug (Carbamazepine = 30 mg/kg)

Significantly different from the control at * $P < 0.05$ (significant); ** $P < 0.01$ (very significant); *** $P < 0.001$ (extremely significant); *ns* not significant

^aEach value represents mean ± SEM

dose (80 mg/kg). *sc*PTZ model was proposed to identify compounds that could provide protection by elevating the onset time of generalized absence seizures threshold [38]. Only compounds showing significant anticonvulsant activity against maximal seizures were selected for *sc*PTZ test. To assess anticonvulsant effect against chemically induced seizures, onset time of clonic convulsion after doses of compounds was noted and results are expressed as Table 5 (Fig. 2). Test compounds **4c** and **4f** have shown significant anticonvulsant effect against chemically induced seizures at a small dose of 30 mg/kg, when compared to control at $P < 0.01$, after 30 min. These compounds were showing significantly extended onset of clonic convulsion time indicating proconvulsant effect. Tested compounds **4a**, **4c**, **4d**, and **4h** have shown significant elevation of seizure threshold at a dose of 100 mg/kg. At a high dose of 300 mg/kg, compounds **4c** and **4f** have revealed substantial protection comparable to standard drug. Active analogs were devoid of toxicity as indicated by 100% recovery of

Fig. 2 Effect of selected synthesized compounds, standard drug, and for control group in *sc*PTZ test, after 30 min

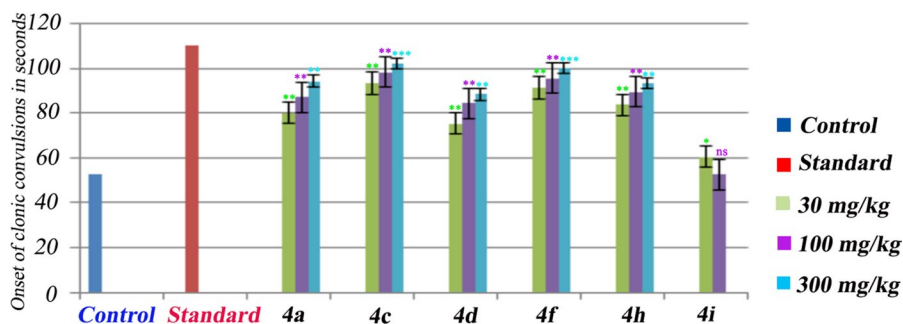


Table 6 Preliminary anticonvulsant screening of selected synthesized compounds using *sc*PTZ-induced seizure model at 4h

Code	Onset of clonic convulsions (s) [mean ± SEM] ^a		
	30 mg/kg	100 mg/kg	300 mg/kg
4a	86.45 ± 0.98*	90.14 ± 0.27**	99.27 ± 1.14**
4c	95.61 ± 1.55**	101.15 ± 1.29***	105.49 ± 0.30**
4d	72.00 ± 1.70*	80.14 ± 1.22**	89.20 ± 1.50**
4f	91.44 ± 0.57**	97.00 ± 1.58**	101.25 ± 2.32**
4h	97.44 ± 1.81**	103.44 ± 2.10**	106.69 ± 1.87***
S	116.45 ± 0.98		
C	55.61 ± 1.55		

C Control (Vehicle), S Standard drug (Carbamazepine = 30 mg/kg)

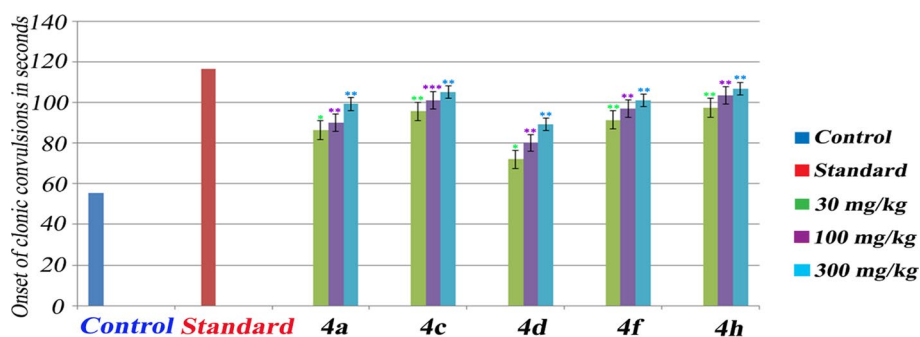
Significantly different from the control at * $P < 0.05$ (significant); ** $P < 0.01$ (very significant); *** $P < 0.001$ (extremely significant); *ns* not significant

^aEach value represents mean ± SEM

animals in *sc*PTZ test. Test compound **4i** was unable to exhibit favorable anticonvulsant response at both doses of 30 and 100 mg/kg. Compound **4i** caused neurotoxicity followed by death of animals; thus, it was not further tested at a higher dose of 300 mg/kg.

Results of *sc*PTZ test after 30 min were used to filter out actives for further screening after delayed absorption at 4 h. Only compounds exhibiting significant protection were subjected further for *sc*PTZ test at longer duration of time (Table 6; Fig. 3). We have also considered PTZ-induced mortality within 24 h as one of the parameters to select

Fig. 3 Effect of selected synthesized compounds, standard drug, and for control group in *sc*PTZ test, after 4 h



compounds for additional *sc*PTZ screening. Compound **4i** was found to be toxic with high mortality ratio at 30 min with no significant anticonvulsant activity, thus, excluded from *sc*PTZ test after 4 h. From tested compounds, **4c** and **4h** have shown significant abolition of clonic convulsions at a lowest dose of 30 mg/kg and also resulted in 100% recovery in *sc*PTZ test. At 100 mg/kg dose, compounds **4c** and **4h** were showing more significant proconvulsant effect when compared to earlier protocol at 30 min, as indicated by the extended onset of myoclonic convulsions in mice (**4c** = 101.15 s and **4h** = 103.44 s). These results specified that compounds were absorbed slowly and thus, able to exert better anticonvulsant response only at longer duration of time. Compounds **4a**, **4c**, **4f**, and **4h** exhibited prolonged anticonvulsant effect after a dose of 300 mg/kg comparable to standard drug used.

Exclusively, compounds **4c**, **4f**, and **4h** provided very significant protection against myoclonic seizures at different doses without symptoms of toxicity when compared to standard. Again, these compounds (**4c**, **4f**, and **4h**) have not shown any mortality after 24 h of study. Compounds **4c**, and **4h** exhibited significant anti-seizure response when compared to control and standard drugs in both in vivo screening tests, indicating importance of electron withdrawing substituents around synthesized analogs.

Neurotoxicity screening

Neurotoxic effect of synthesized compounds was evaluated at intraperitoneal doses of 30, 100, and 300 mg/kg.

Table 7 Effects of selected active compounds on serum levels of liver enzymes in mice

Code ^a	Alkaline phosphatase ^b	SGOT ^b (units/ml)	SGPT ^b (units/ml)	Total protein ^b (g/100 ml)
C ^c	14.14 ± 0.07	144.2 ± 1.07	27.33 ± 0.66	1.96 ± 0.012
4c	14.73 ± 0.41	147.5 ± 1.09	28.91 ± 0.26	1.90 ± 0.044
4f	14.05 ± 0.38	146.8 ± 0.60	29.67 ± 1.45	1.89 ± 0.018
4h	14.50 ± 0.34	148.2 ± 0.87	30.50 ± 1.06	1.86 ± 0.026
PHY ^d	18.65 ± 0.28*	153.7 ± 0.80*	35.33 ± 1.05*	1.61 ± 0.015*
CBZ ^e	20.21 ± 0.43*	158.4 ± 0.35*	38.49 ± 0.87*	1.48 ± 0.045*

*Significantly compared with control ($P < 0.05$)

^aCompounds were administered at a dose of 100 mg/kg for 14 days

^bEach value represents the mean ± SEM of six mice, were calculated using one-way ANOVA followed by Dunnett's comparison test

^cControl animals were treated with 0.5% polyethylene glycol for 14 days

^dTested at 25 mg/kg for 14 days

^eTested at 100 mg/kg for 14 days

Carbamazepine was used as a standard drug in neurotoxicity test. According to test protocol, if animals were unable to maintain an equilibrium on a rotarod for minimum 1 min in each of three consecutive trials; it was considered as a neurological deficit.

Dose at which an animal fell off the rod was noted and neurotoxicity was then determined. Most of the tested compounds were devoid of any symptoms of neurological deficits. Only compounds **4b** and **4g** displayed signs of neurotoxicity namely sedation, tremors, and ataxia after 30 min and 4 h. These compounds have shown neurotoxic symptoms only at higher doses (100 and 300 mg/kg) as compared to standard drug (Table S1).

Biochemical assessment of liver function parameters for synthesized compounds

AEDs such as carbamazepine, phenobarbital, and phenytoin are potent enzyme inducers and have demonstrated hepatotoxicity after their chronic use. Hepatotoxic adverse effects have contributed to the clinical failure of many AEDs [39]. Hepatotoxicity of AEDs can be assessed by observing serum levels of liver enzymes such as *alkaline phosphatase* (ALP), *alanine aminotransferase* (ALT) [*serum glutamate oxaloacetate transaminase* (SGOT), *serum glutamate pyruvate transaminase* (SGPT)], and total protein. Increased levels of liver enzymes can act as markers of hepatocellular injury or an obstruction in the bile flow cholestasis (ALP and ALT). A decrease in total protein values along with elevated level of liver enzymes is a more specific marker of liver dysfunction. Thus, most effective synthesized compounds and standard drug used were evaluated for biochemical parameters of liver functions. Collected values for biochemical parameters are given in Table 7. All the values of concern liver metabolism enzymes and total protein for selected active compounds are in agreement with control group values that clearly assured

Table 8 Results of quantification studies for selected active compounds in MES test

Code	TPE	ED ₅₀ (mg/kg)	TD ₅₀ (mg/kg)	PI (TD ₅₀ /ED ₅₀)
4c	30	28.1 (25.0–36.1)	322.3 (305.2–339.0)	11.46
4f	30	47.9 (40.1–58.4)	399.7 (381.5–409.7)	8.34
4h	4	34.7 (27.5–43.4)	308.7 (295.9–325.7)	8.89
PHY ^a	1	25.7 (21.1–31.3)	79.1 (68.2–93.1)	3.07

TPE time to peak effect, ED₅₀ median effective dose, TD₅₀ median toxic dose, PI TD₅₀/ED₅₀

^aTPE for standard drug phenytoin (PHY) was taken from literature [43]. Data in parentheses are the 95% confidence limits

Table 9 Results of quantification studies for selected active compounds in scPTZ test

Code	TPE	ED ₅₀ (mg/kg)	TD ₅₀ (mg/kg)	PI (TD ₅₀ /ED ₅₀)
4c	30	62.3 (49.6–71.1)	322.3 (305.2–339.0)	5.17
4f	30	75.4 (68.1–82.3)	399.7 (381.5–409.7)	5.30
4h	4	37.9 (31.1–48.3)	308.7 (295.9–325.7)	8.14
CBZ ^a	30	115.4 (93.5–131.4)	75.3 (52.7–126.5)	0.65
ETX ^a	0.25	147.8 (130.7–167.3)	722.1 (647.0–805.8)	4.89

TPE time to peak effect, ED₅₀ median effective dose, TD₅₀ median toxic dose, PI TD₅₀/ED₅₀

^aTPE and activity data for standard drugs carbamazepine (CBZ) and ethosuximide (ETX) were taken from literature [43]. Data in parentheses are the 95% confidence limits

liver safety of these analogs. On the other hand, phenytoin (PHY) and carbamazepine (CBZ) significantly elevated the level of liver enzymes with decrease in the amount of total protein as indicator of liver dysfunction or hepatic injury.

Quantification studies

Quantitative evaluation was performed to determine the median effective dose (ED_{50}) and median toxic dose (TD_{50}) for selected compounds with prominent anticonvulsant activities in initial preclinical screening models. Quantitative evaluation of selected analogs was performed at their time of peak pharmacodynamic effect obtained from qualitative screening tests. In parallel, quantitative evaluation was also executed for standard drugs as **PHY**, **CBZ**, and ethosuximide (**ETX**) for comparison of effects of the tested compounds. Quantitative estimation data were further used to calculate protective indices (PIs), considered as a measure of benefit-to-risk ratio of clinical probes. Results of quantification studies in MES and *scPTZ* tests are displayed in Tables 8 and 9, respectively. Herein, we have compared and discussed the results of quantification studies for active compounds and standard drugs. On the basis of preliminary screening, we have selected active compounds **4c**, **4f**, and **4h** for detailed quantification studies using MES and *scPTZ* test to determine ED_{50} and TD_{50} values. Compound **4c** have displayed significant anticonvulsant activity in MES test indicated by good ED_{50} (ED_{50} = 28.1 mg/kg, MES test, mice, i.p.); however, same compound showed \sim 2-fold lesser effect against *scPTZ* seizures when compared to MES test (ED_{50} = 62.3 mg/kg, *scPTZ* test, mice, i.p.). Analog **4c** has lower neurotoxicity and resulted in acceptable PI value indicating safety and efficacy against tonic-clonic seizures (TD_{50} = 322.3 mg/kg, mice, i.p.; PI = 11.46, MES test). On the other hand, compound **4h** with a nitro group has shown characteristic anti-seizure effect in both in vivo screening tests (ED_{50} = 34.7 mg/kg, MES test, mice, i.p.; ED_{50} = 37.9 mg/kg, *scPTZ* test, mice, i.p.). More specifically, the analog **4h** has shown \sim 3-fold higher anticonvulsant activity than *scPTZ*-active standard drugs (**4h**, ED_{50} = 37.9 mg/kg, mice, i.p.; **CBZ**, ED_{50} = 115.4 mg/kg, mice, i.p.; **ETX**,

ED_{50} = 147.8 mg/kg, mice, i.p.). A compound has excellent anticonvulsant activity with admirable toxicity profile compared to standard drugs (**4h**, TD_{50} = 308.7 mg/kg, mice, i.p.; **PHY**, TD_{50} = 79.1 mg/kg, mice, i.p.; **CBZ**, TD_{50} = 75.3 mg/kg, mice, i.p.), and thus, resulted in excellent PI values [PI = 8.89 (**4h**), MES test; PI = 8.14 (**4h**), *scPTZ* test; PI = 3.07 (**PHY**), MES test; PI = 0.65 (**CBZ**), 4.89 (**ETX**), *scPTZ* test]. In MES screening, compound **4f** exhibited good anticonvulsant activity with maximum neuroprotection at high dose, and resulted in good PI values when compared to MES-active phenytoin (**4f**, ED_{50} = 47.9 mg/kg, mice, i.p.; TD_{50} = 399.7 mg/kg, mice, i.p.; PI = 8.34). Compound **4f** also exhibited good response against *scPTZ*-induced seizures without any symptoms of toxicities when compared to reference drugs (**4f**, ED_{50} = 75.4 mg/kg; TD_{50} = 399.7 mg/kg, mice, i.p.).

Molecular modeling

Docking study

Modulators of type-A γ -aminobutyric ($GABA_A$) receptors such as classical benzodiazepines (carbamazepine and diazepam) are critically known for their anticonvulsant activity [40]. $GABA_A$ is an ionotropic ligand-gated ion channel receptor with GABA as an endogenous inhibitory neurotransmitter of central nervous system. Upon activation, the receptor primarily flows Cl^- ions via its pore to cause hyperpolarization and thereby inhibits neurotransmission [41]. Thus, molecular docking was performed at $GABA_A$ receptor in order to predict possible mechanism of synthesized analogs.

Initially, a co-crystallized ligand was re-docked into the binding pocket of $GABA_A$ and then replaced with synthesized compounds **4(a-i)** to compare binding interactions with the co-crystallized ligand (Supplementary Fig. S1,

Table 10 Molecular docking results of representative active compound (**4h**), co-crystallized ligand, and standard drug showing maximum dock scores with $GABA_A$ receptor

Sr. No	Dock score	Glide energy	H-bond interaction with amino acid			Hydrophobic interactions
			Atom of ligand	Amino acids	Bond distance (Å)	
4h	12.05	-76.84	NH ₂	GLU 189	2.66	(a) C ₆ H ₅ -NO ₂ and phenyl ring of TYR 160 (π -cation interaction) (b) Chromeno[2,3- <i>b</i>]pyridine with HIS 102 and TYR 58, PHE 77 (π - π stacking)
			CH ₂ -O-CH ₂	ASN 60	2.66	
CBZ	10.32	-69.52	CONH ₂	ASN 60	2.61	Phenyl rings showed π - π stacking with TYR 58 and PHE 100
Co-crystallized ligand	11.20	-73.44	NH	SER 205	2.37	C-F interaction with CONH ₂ ; Heterocyclic ring shown π - π stacking with TYR 58

docking score = -11.20). To explore possible binding mechanism, herein, we have docked all synthesized compounds **4(a-i)** and standard drugs (**CBZ**, docking score = -10.32 ; Fig. S2A and **ETH**, docking score = -9.69 ; Fig. S2B) in the agonist binding domain of GABA_A receptors. Molecular docking results are evaluated as glide-dock scores by the assessment of docked poses of co-crystallized structure, standard drugs, and synthesized compounds **4(a-i)**. Through comparison of docking results of synthesized compounds, standard drugs, and co-crystallized ligand, we could be able to predict how compounds bind at the active site of GABA_A receptors (Table 10). Herein, we have discussed the docking results of potent anticonvulsant active compounds with their interactions at critical amino acid residues of GABA_A receptors. Compounds **4c**, **4f**, and **4h** have exhibited good anticonvulsant activity in the initial pharmacological screening without the symptoms of toxicity.

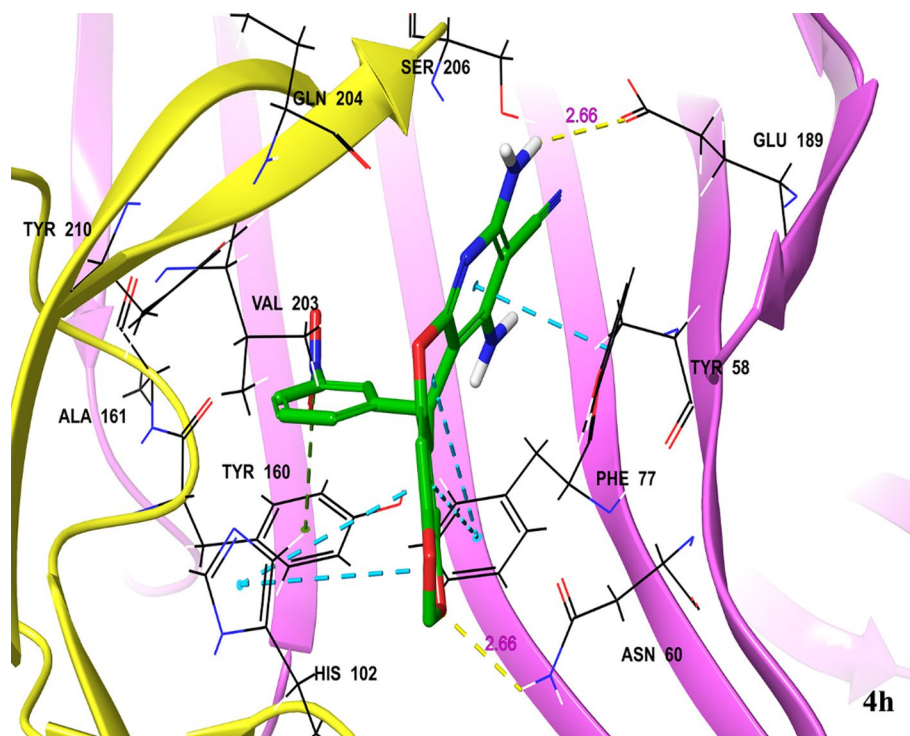
From docking studies, it is clearly observed that the active compound **4h** has shown H-bonding interaction with crucial amino acids such as GLU 189 and ASN 60 (Docking score = -10.94 ; Fig. 4). More specifically, NH₂ group of **4h** has shown H-bonding interaction with carboxyl terminal of GLU 189 (**H-bond distance**: 2.66 Å). Electron-rich oxygen of benzo[1,3]dioxole binds with amino terminal of ASN 66 (**H-bond distance**: 2.66 Å), indicating the importance of given structural feature in the designed compounds. Additionally, NO₂ group has displayed π -cation interaction with a phenyl ring of TYR 160. These interactions may be responsible for good

anticonvulsant activity of compound **4h** in both preclinical seizure models (**4h**: ED₅₀ = 34.7 mg/kg, MES test; ED₅₀ = 37.9 mg/kg, scPTZ test; TD₅₀ = 308.7 mg/kg). Central chromeno[2,3-*b*]pyridine structure has also shown π - π stacking with HIS 102 (imidazole ring) and aromatic ring of TYR 58 along with PHE 77 that prone to additional affinity towards GABA_A receptor. Compounds **4c** and **4f** were also well surrounded by critical amino acid residues and fit adequately at the cavity GABA_A receptors (Docking scores, **4c** = -9.95 ; Fig. S3A and **4f** = -10.32 ; Fig. S3B). Pharmacophoric region (chromeno[2,3-*b*]pyridine) of these compounds also showed π - π stacking with hydrophobic amino acids such as TYR 58 and PHE 77; it may be the reason for good anticonvulsant response against seizures.

Molecular dynamic (MD) simulation of compound **4h**-GABA_A receptor complex

MD simulation is a characteristic protocol for prediction of the thermodynamic stability and behavior of a ligand at specific receptor. Here, we have used MD simulation protocol of Desmond program to investigate the molecular stability a most active ligand **4h**-complexed with GABA_A receptor. MD simulation at 100 ns was performed and discussed using crucial pharmacoinformatic parameters such as root mean square deviation (RMSD), root mean square fluctuation (RMSF), and receptor-ligand contact mapping to determine the stability of compound **4h** in GABA_A receptor. MD

Fig. 4 3D docking image of compound **4h** in the binding pocket of GABA_A receptor (PDB ID: 6HUO). H-bonds are depicted as yellow dotted sticks with bond distance as numerical in red color, π -cation interaction is denoted by green dotted sticks and π - π stacking as blue dotted lines



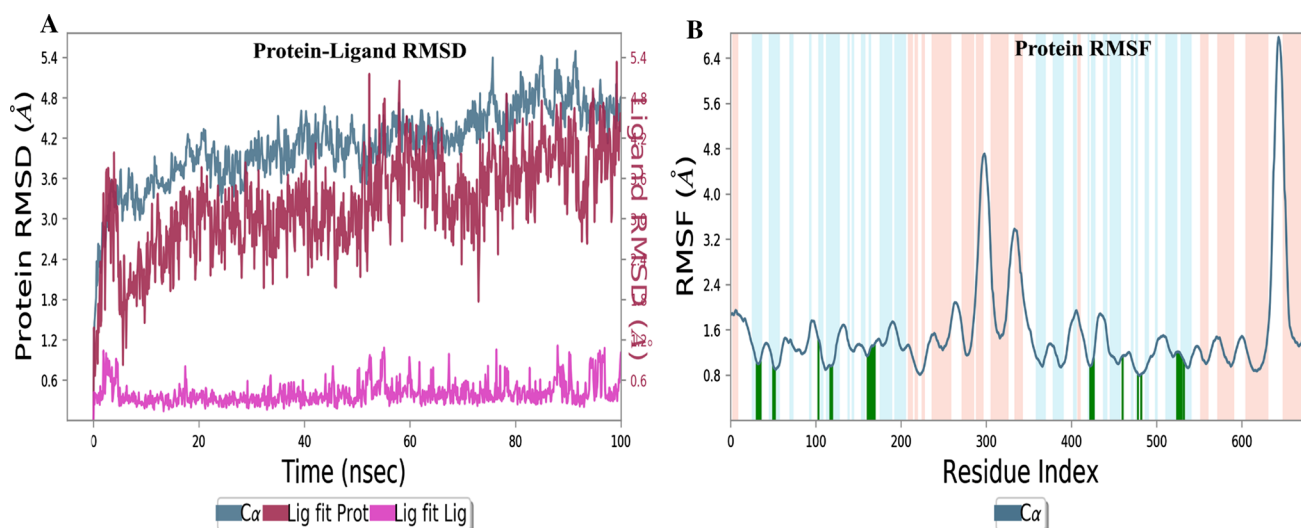


Fig. 5 MD simulation studies of compound **4h**-complexed with GABA_A receptor; **A** RMSD (gray shed denotes protein RMSD; red shed represents RMSD of compound **4h**), and **B** RMSF for complexed **4h**-GABA_A receptor

trajectory data for RMSD and RMSF are given in Fig. 5A and B, respectively.

RMSD was calculated based on the atom selection after ligand (**4h**) frames were aligned on the reference frame backbone of receptor. RMSD plot showed that the simulated system was very well equilibrated as fluctuations in C- α atoms of protein were constantly around 4 Å during 100 ns run time for the ligand (Fig. 5A). These values clearly supported the good in vivo anticonvulsant response of ligand (**4h**), as it is fairly stabilized in the agonist binding pocket of GABA_A receptor.

RMSF has given detailed information about local conformational variations (overall fluctuations of the residues) in GABA_A receptor chain and interactions of residues with

active ligand (**4h**) during entire path of simulation (100 ns). In Fig. 5B, loop regions are represented by white sheds; other α -helices and β -strands are denoted as blue and pink sheds, respectively. Protein α -helical and β -strands regions are firms compared to unstructured loop regions, and thus show less fluctuation than loop regions of receptor. Protein RMSF plot also indicated higher stability of ligand in receptor as overall fluctuations of residues were seen in the range of 0.8–1.8 Å. Again, it was clearly observed that compound **4h** has shown interactions with critical amino acid residues of GABA_A receptor such as, ASP 56, MET 57, TYR 58, ASN 60, PHE 77, ASN 128, THR 142, ARG 144, GLU 189, ASP 192, PHE 100, HIS 102, GLU 138, LYS 156, TYR 160, VAL 203, GLN 204, SER 205, SER

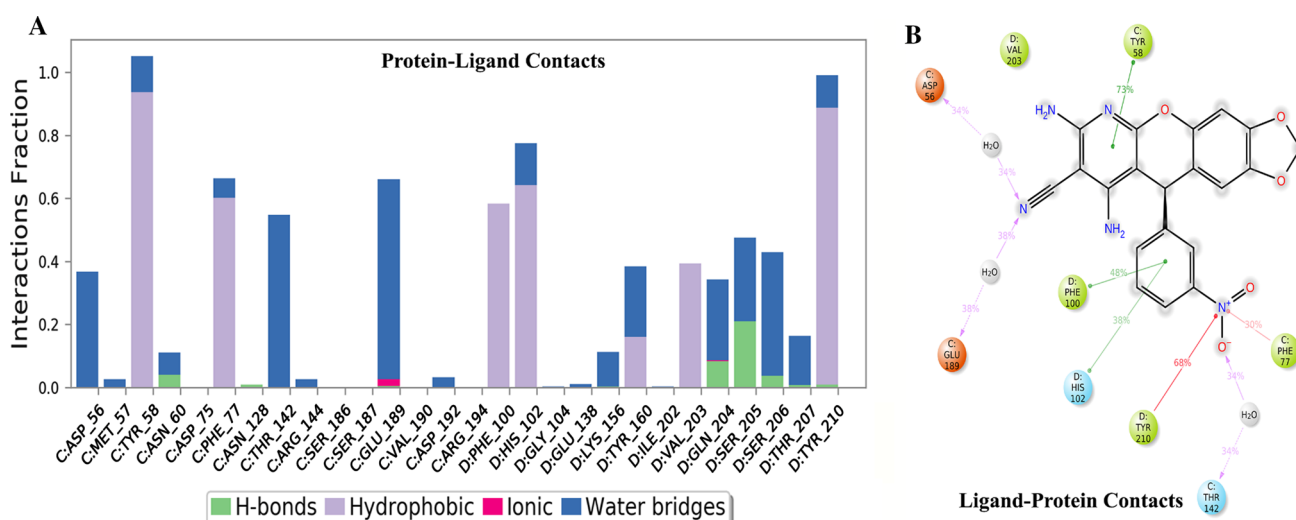


Fig. 6 A Protein–ligand contact mapping from MD trajectory, and B 2D ligand-interaction diagram for compound **4h**

206, THR 207, and TYR 210 (Fig. 6A). All interacted residues are marked as green-colored vertical bars with RMSF value ≤ 1.6 Å. Active ligand **4h** was able to show good binding interactions that includes H-bond with cyanide nitrogen atom via water bridge (GLU 189, 38% and ASP 68, 34%); π - π stacking with TYR 58 (73%), PHE 100 (48%), and HIS 102 (38%); π -cation interaction with TYR 210 (68%) and

eventually contributes in higher stability of ligand at active site of receptor (Fig. 6B).

Metabolites and sites of metabolism (SoM) predictions

Drug metabolism has a vital role in the process of drug discovery and development. Thus, the consideration of

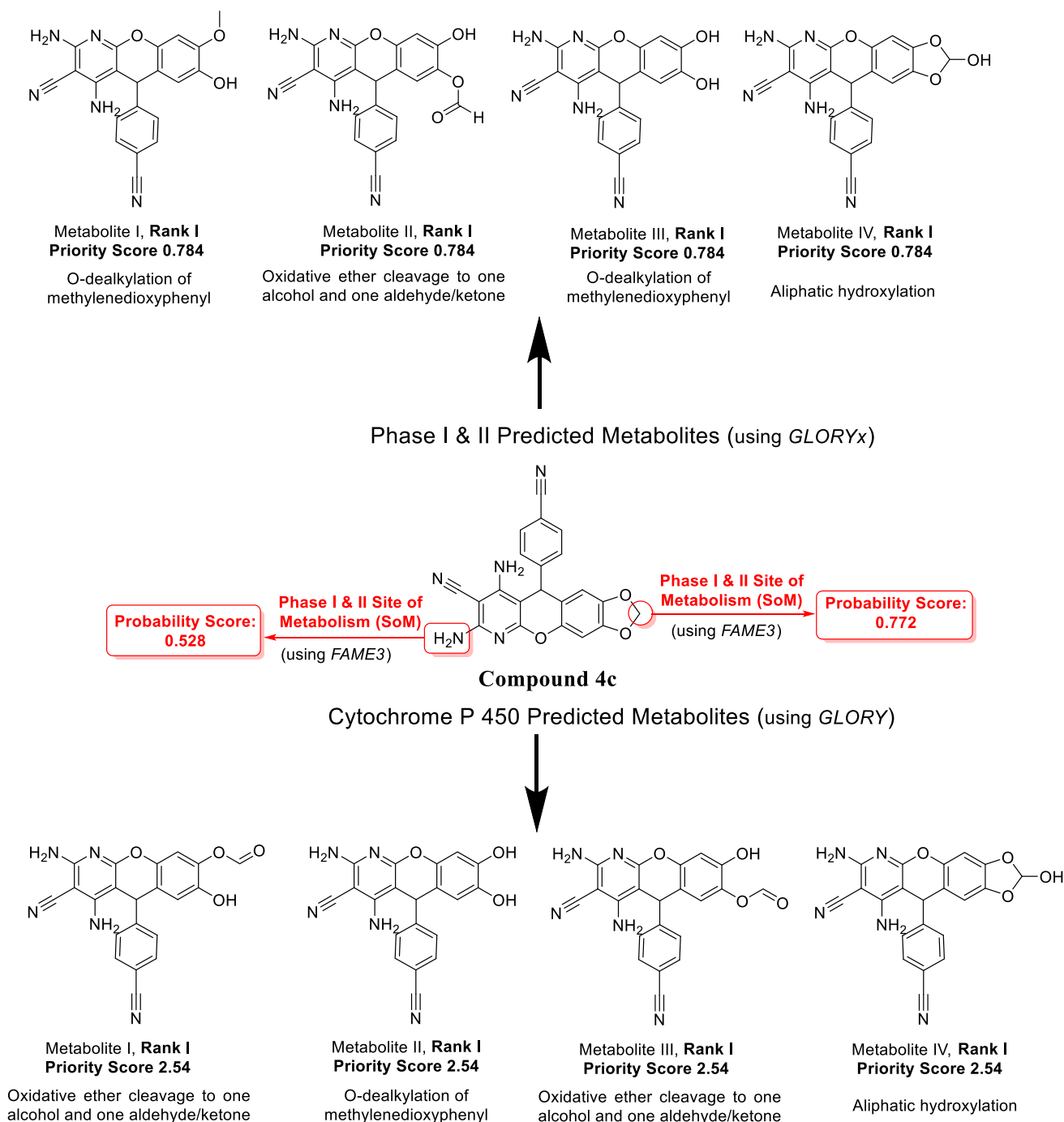


Fig. 7 Potential metabolites and site of metabolism (SoM) for representative compound **4c**

co-relation between drug metabolism and pharmacodynamics/safety should be required. Here, we have predicted probable metabolites and SoM (effect of CYP 450 enzyme, phase I and II pathways) for representative compound **4c** using the *GLORY*, *GLORYx*, and *FAME3* tools. These metabolites are shown in Fig. 7 in the order of their priority scores. *FAME3* tool predicted that 1,3-dioxolane ring of compound **4c** provides the site of metabolism (SoM) for various metabolic reactions including oxidative ether cleavage to generate alcohol and carbonyls. Aliphatic hydroxylation and *O*-dealkylation of methylenedioxyphenyl are also observed as SoM for the same compound. The highest probability score of **0.772** suggested that the 1,3-dioxolane ring (C₁₆ position) of compound **4c** is the top priority site for phase I and II metabolism than free amino group (N29 position) with probability score of **0.528**.

Structure–activity relationship details

Most of the synthesized compounds have shown moderate to better anticonvulsant efficacy. Our anticonvulsant evaluation results lead to a better understanding of tested compounds through development of preliminary structural–activity relationship (SAR). SAR investigations revealed that substituted aromatic ring has variable effects on the anticonvulsant efficiency of synthesized compounds. Compounds with electron withdrawing substitutions such as **4h** with nitro group (3-NO₂) and **4c** with cyanide group (4-CN) over phenyl ring showed the highest protection in both MES and *sc*PTZ tests, whereas compounds **4d** and **4g** with 4-bromo and 4-naphthyl groups at *para* position of phenyl ring lead to neurotoxicity. On the other hand, replacement of electron releasing group in compound **4d**, with 4-methoxy and 3-hydroxy moiety **4f** showed increased anticonvulsant effects. Obtained data confirmed that the substitution of a tiny lipophilic group (cyanide or nitro) at *para* position of phenyl ring resulted in higher anticonvulsant activity. According to the developed SAR, the substitution of small electron donating or withdrawing groups over phenyl ring connected to chromeno[2,3-*b*]pyridine plays a crucial role in governing the anticonvulsant efficacy.

Conclusion

In conclusion, we have reported efficient one-pot three-component synthesis of 1,3-dioxolochromeno[2,3-*b*]pyridine derivatives **4(a–i)** as effective anticonvulsant agents. Outlined synthetic method has multiple advantages such as neat reaction conditions, short reaction time, and atom-economy with good yields. Again, these synthesized compounds did not require any further column

chromatographic purification. Synthesized derivatives were then evaluated for anticonvulsant activity using preclinical seizure models (MES and *sc*PTZ tests). Synthesized compounds were also evaluated for neurotoxicity and concern hepatotoxicity parameters. Compounds **4c**, **4f**, and **4h** hold a broad spectrum of anticonvulsant activity with less neurotoxicity and no hepatotoxicity compared to standard drugs. Molecular docking details also supported the anticonvulsant activity of these synthesized compounds. Additionally, MD simulation data showed that the compound **4h**-GABA_A receptor complex is stable throughout the run time 100 ns and provided concrete support to develop lead molecules effective against seizures.

Overall, results indicated that compounds **4c**, **4f**, and **4h** could be promising probes for further development in this field for the treatment of seizure disorders. In conclusion, effective synthetic strategy, significant anticonvulsant activity with good toxicity profile and detailed molecular modeling studies led us to anticipate the emergence of these analogs as valid leads for the development of future effective neurotherapeutic agents.

Experimental

All reactions were monitored by TLC, performed on silica gel glass plates containing 60 F-254 and visualized by UV light or iodine indicator. IR spectra were recorded on a PerkinElmer 1000 FT-IR spectrometer in KBr pellet. ¹H NMR and ¹³C NMR spectra were recorded on Bruker NMR spectrometers (400 MHz for ¹H NMR and 100 MHz for ¹³C NMR) in DMSO-*d*₆. Melting points were determined in open capillary tubes in H₂SO₄ bath equipped with a digital thermometer and are uncorrected.

General procedure for the synthesis of [1, 3] dioxolo[4',5':6,7]chromeno[2,3-*b*]pyridine derivatives **4(a–i)**

An equivalent mixture of sesamol (**1**, 1 mmol), aromatic aldehydes (1 mmol), 2-aminopropene-1,1,3-tricarbonitrile (**3**, 1 mmol), and triethylamine (10 mol%) were taken in a 10 mL round bottom flask and heated at 100 °C for 4 h. After cooling, the reaction mixture was diluted with ethanol (10 mL). The precipitated solid was then filtered, washed with ethanol (5 mL), and dried to afford pure products **4(a–i)**. The products were further purified by recrystallization with hot ethanol.

9-Diamino-10-(4-methoxyphenyl)-10H-[1,3]dioxolo[4',5':6,7]chromeno[2,3-b]pyridine-8-carbonitrile (4a)

Pale brown solid; yield: 93%; m.p. 276–278 °C; IR: 3474, 3226, 2914, 2206, 1649, 1491, 1277, 991, 810 cm⁻¹; ¹H NMR (DMSO, 400 MHz) δ : 7.15 (d, J =8.3 Hz, 2H, ArH), 6.79 (d, J =8.3 Hz, 2H, ArH), 6.78 (s, 1H, ArH), 6.74 (s, 1H, ArH), 6.40 (s, 2H, NH₂), 6.29 (s, 2H, NH₂), 5.98 (s, 1H, OCHO), 5.92 (1H, s, OCHO), 5.10 (s, 1H, CH), 3.66 (s, 3H, OCH₃); ¹³C NMR (DMSO, 100 MHz) δ : 159.5, 159.2, 157.8, 156.6, 146.4, 144.0, 143.6, 137.6, 127.9, 117.4, 116.4, 113.9, 107.0, 101.4, 98.2, 90.1, 70.7, 55.0, 37.3; Elemental Analysis: Calc. C, 64.94; H, 4.15; N, 14.43. C₂₁H₁₆N₄O₄ Found. C, 64.75; H, 4.14; N, 14.39.

9-Diamino-10-(4-bromophenyl)-10H-[1,3]dioxolo[4',5':6,7]chromeno[2,3-b]pyridine-8-carbonitrile (4b)

Dark brown solid; yield: 91%; m.p. 242–244 °C; IR: 3489, 3401, 2923, 2206, 1649, 1482, 1041, 935, 810 cm⁻¹; ¹H NMR (DMSO, 400 MHz) δ : 7.43 (d, J =6.3 Hz, 2H, ArH), 7.20 (d, J =6.3 Hz, 2H, ArH), 6.71 (s, 1H, ArH), 6.67 (s, 1H, ArH), 6.48 (s, 2H, NH₂), 6.41 (s, 2H, NH₂), 6.00 (s, 1H, OCHO), 5.94 (s, 1H, OCHO), 5.19 (s, 1H, CH); ¹³C NMR (DMSO, 100 MHz) δ : 159.6, 159.2, 156.6, 146.7, 144.8, 144.1, 143.7, 131.3, 129.1, 119.6, 116.4, 106.9, 101.4, 98.3, 89.4, 70.7, 57.0, 37.5; Elemental Analysis: Calc. C, 54.94; H, 3.00; Br, 18.27; N, 12.81. C₂₀H₁₃BrN₄O₃ Found. C, 54.99; H, 3.06; Br, 18.19; N, 12.75.

9-Diamino-10-(4-cyanophenyl)-10H-[1,3]dioxolo[4',5':6,7]chromeno[2,3-b]pyridine-8-carbonitrile (4c)

Brown solid; yield: 92%; m.p. 260–261 °C; IR: 3401, 3184, 2917, 2201, 1630, 1481, 1037, 932, 806 cm⁻¹; ¹H NMR (DMSO, 400 MHz) δ : 7.72 (d, J =6.3 Hz, 2H, ArH), 7.43 (d, J =6.3 Hz, 2H, ArH), 6.78 (s, 1H, ArH), 6.71 (s, 1H, ArH), 6.51 (s, 2H, NH₂), 6.46 (s, 2H, NH₂), 6.00 (s, 1H, OCHO), 5.94 (1H, s, OCHO), 5.31 (s, 1H, CH); ¹³C NMR (DMSO, 100 MHz) δ : 159.8, 159.3, 156.7, 150.7, 147.0, 144.3, 143.8, 132.5, 127.9, 116.3, 115.8, 109.4, 106.9, 101.5, 98.4, 88.9, 70.8, 57.1, 38.1; Elemental Analysis: Calc. C, 65.79; H, 3.42; N, 18.27. C₂₁H₁₃N₅O₃ Found. C, 65.68; H, 3.49; N, 18.21.

9-Diamino-10-(4-isopropylphenyl)-10H-[1,3]dioxolo[4',5':6,7]chromeno[2,3-b]pyridine-8-carbonitrile (4d)

Dark brown solid; yield: 86%; m.p. 271–272 °C; IR: 3468, 3189, 2942, 2223, 1660, 1459, 1017, 989, 822 cm⁻¹; ¹H NMR (DMSO, 400 MHz) δ : 7.28–7.25 (m, 1H, ArH),

7.15–7.14 (m, 1H, ArH), 7.10–7.04 (m, 2H, ArH), 6.76–6.74 (m, 1H, ArH), 6.66–6.64 (m, 1H, ArH), 6.44–6.41 (m, 2H), 6.37–6.31 (m, 2H), 5.99–5.92 (m, 2H), 5.21 (s, 1H, CH); 3.41–3.40 (m, 1H, CH), 1.12 (d, J =6.5 Hz, 6H, (CH₃)₂); ¹³C NMR (DMSO, 100 MHz) δ : 159.6, 156.5, 146.5, 144.1, 128.7, 126.7, 126.4, 115.2, 115.1, 107.0, 106.9, 101.46, 101.41, 98.3, 98.2, 89.7, 37.7, 37.3, 32.9, 23.8; Elemental Analysis: Calc. C, 68.99; H, 5.03; N, 13.99. C₂₃H₂₀N₄O₃ Found. C, 68.87; H, 5.07; N, 13.92.

7,9-Diamino-10-(3-ethoxy-4-hydroxyphenyl)-10H-[1,3]dioxolo[4',5':6,7]chromeno[2,3-b]pyridine-8-carbonitrile (4e)

Dark brown solid; yield: 88%; m.p. 233–235 °C; IR: 3477, 3389, 2979, 2198, 1620, 1478, 1037, 935, 834 cm⁻¹; ¹H NMR (DMSO, 400 MHz) δ : 8.76 (s, 1H, OH), 6.91 (s, 1H, ArH), 6.74 (s, 1H, ArH), 6.65–6.60 (m, 2H, ArH), 6.52–6.49 (m, 1H, ArH), 6.41 (s, 2H, NH₂), 6.28 (s, 2H, NH₂), 5.98 (s, 1H, OCHO), 5.92 (1H, s, OCHO), 4.98 (s, 1H, CH), 3.95 (q, J =7.5 Hz, 2H, CH₂), 1.29 (t, J =6.6 Hz, 3H, CH₃); ¹³C NMR (DMSO, 100 MHz) δ : 159.9, 159.6, 146.8, 145.9, 144.4, 144.0, 137.0, 119.6, 118.0, 117.0, 116.1, 113.4, 107.6, 101.8, 98.6, 90.6, 71.1, 64.4, 38.3; 15.2; Elemental Analysis: Calc. C, 63.15; H, 4.34; N, 13.39. C₂₂H₁₈N₄O₅ Found. C, 63.04; H, 4.40; N, 13.34.

7,9-Diamino-10-(3-hydroxy-4-methoxyphenyl)-10H-[1,3]dioxolo[4',5':6,7]chromeno[2,3-b]pyridine-8-carbonitrile (4f)

Pale yellow solid; yield: 90%; m.p. 204–206 °C; IR: 3472, 3226, 2914, 2214, 1650, 1464, 1181, 992, 824 cm⁻¹; ¹H NMR (DMSO, 400 MHz) δ : 8.88 (s, 1H, OH), 6.79–6.72 (m, 2H, ArH), 6.60 (s, 1H, ArH), 6.56 (s, 1H, ArH), 6.43 (s, 2H, NH₂), 6.28 (s, 2H, NH₂), 5.99 (s, 1H, OCHO), 5.92 (1H, s, OCHO), 5.00 (s, 1H, CH), 3.68 (s, 3H, OCH₃); ¹³C NMR (DMSO, 100 MHz) δ : 159.4, 159.1, 156.6, 146.6, 146.4, 144.0, 143.5, 138.2, 117.5, 117.4, 116.4, 114.1, 112.1, 107.0, 101.3, 98.1, 90.0, 70.7, 59.2, 57.1, 55.6, 37.5; Elemental Analysis: Calc. C, 62.37; H, 3.99; N, 13.86. C₂₁H₁₆N₄O₅ Found. C, 62.31; H, 3.91; N, 13.67.

9-Diamino-10-(naphthalene-1-yl)-10H-[1,3]dioxolo[4',5':6,7]chromeno[2,3-b]pyridine-8-carbonitrile (4g)

Dark brown solid; yield: 89%; m.p. 262–264 °C; IR: 3474, 3445, 2926, 2203, 1658, 1485, 1247, 986, 814 cm⁻¹; ¹H NMR (DMSO, 400 MHz) δ : 8.60 (s, 1H, ArH), 7.96–7.93 (m, 1H, ArH), 7.81–7.79 (m, 1H, ArH), 7.60–7.54 (m, 2H, ArH), 7.42–7.40 (m, 2H, ArH), 6.79 (s, 1H, ArH), 6.56–6.53

(m, 2H, ArH + OCHO), 5.95 (s, 2H, NH₂), 5.83 (m, 3H, NH₂ + OCHO), 4.36 (s, 1H, CH); ¹³C NMR (DMSO, 100 MHz) δ : 160.5, 159.5, 159.1, 156.8, 146.7, 143.4, 133.8, 130.0, 129.0, 127.6, 126.7, 126.5, 126.2, 126.0, 125.9, 125.8, 123.2, 116.3, 106.2, 101.4, 98.3, 90.0, 87.0, 59.0, 57.0; Elemental Analysis: Calc. C, 70.58; H, 3.95; N, 13.72. C₂₄H₁₆N₄O₃ Found. C, 70.45; H, 3.99; N, 13.62.

9-Diamino-10-(3-nitrophenyl)-10H-[1,3]dioxolo[4',5':6,7]chromeno[2,3-b]pyridine-8-carbonitrile (4h)

Brown solid; yield: 84%; m.p. 238–239 °C; IR: 3423, 2922, 2197, 1627, 1474, 1034, 931, 851 cm⁻¹; ¹H NMR (DMSO, 400 MHz) δ : 8.20 (s, 1H, ArH), 8.04–8.02 (m, 1H, ArH), 7.66–7.63 (m, 1H, ArH), 7.58–7.52 (m, 1H, ArH), 6.82 (s, 1H, ArH), 6.73 (s, 1H, ArH), 6.55 (s, 4H, 2NH₂), 6.0 (s, 1H, OCHO), 5.94 (1H, s, OCHO), 5.39 (s, 1H, CH); ¹³C NMR (DMSO, 100 MHz) δ : 160.3, 159.8, 157.2, 148.2, 148.0, 147.5, 144.8, 144.4, 134.2, 130.7, 122.2, 121.9, 116.8, 116.4, 107.4, 102.1, 99.0, 89.5, 71.2, 38.2; Elemental Analysis: Calc. C, 59.56; H, 3.25; N, 17.36. C₂₀H₁₃N₅O₅ Found. C, 59.45; H, 3.30; N, 17.28.

7,9-Diamino-10-(3,4-dimethoxyphenyl)-10H-[1,3]dioxolo[4',5':6,7]chromeno[2,3-b]pyridine-8-carbonitrile (4i)

Dark brown solid; yield: 86%; m.p. 248–250 °C; IR: 3471, 3226, 2914, 2214, 1644, 1464, 1184, 992, 836 cm⁻¹; ¹H NMR (DMSO, 400 MHz) δ : 6.99 (s, 1H, ArH), 6.82–6.69 (m, 2H, ArH), 6.69–6.62 (m, 2H, ArH), 6.42 (s, 2H, NH₂), 6.28 (s, 2H, NH₂), 5.99 (s, 1H, OCHO), 5.93 (1H, s, OCHO), 5.05 (s, 1H, CH), 3.71 (s, 3H, OCH₃), 3.66 (s, 3H, OCH₃); ¹³C NMR (DMSO, 100 MHz) δ : 159.5, 159.1, 156.6, 148.5, 147.4, 146.5, 144.0, 143.6, 138.2, 118.7, 117.2, 116.4, 112.2, 111.3, 107.1, 101.3, 98.1, 90.0, 70.7, 55.5, 37.8; Elemental Analysis: Calc. C, 63.15; H, 4.34; N, 13.39. C₂₂H₁₈N₄O₅ Found. C, 63.11; H, 4.40; N, 13.28.

Pharmacology

All experiments were performed on Swiss Albino mice (25–30 g). Mice were kept in polyethylene cages with free access to food and water ad libitum, under standard housing conditions with relative humidity (30–60%). The animals were divided into three groups as control, standard, and test (*N* = 18 for each compound for single dose) and assigned to experimental groups (*n* = 6). Anticonvulsant activity was predicted using MES and *scPTZ* test [40–43]. Rotarod test was used to determine neurotoxicity. Synthesized compounds **4(a–i)** and standards were injected intraperitoneally to mice as a suspension of 0.5% polyethylene glycol in normal saline

at different doses. Pharmacological evaluation was done at two different time intervals (30 min and 4 h). Data were analyzed using one-way ANOVA followed by Dunnett's test. GraphPad Prism 5 was used for statistical calculations (**P* < 0.05 = statistically significant and ***P* < 0.01 = very significant). Results were expressed as mean \pm SEM.

Pharmacological tests were performed according to guidelines framed by Institutional Animal Ethics Committee (IAEC). Animal activity protocol was approved by R. C. Patel Institute of Pharmaceutical Education and Research, Shirpur, Dist: Dhule (IAEC/RCPIPR/2021-22/14).

MES test

MES test is a recognized protocol for generalized tonic and clonic convulsions. Animals were divided into three groups (control, standard, and test) with six mice in each group. First group acts as a control (*n* = 6) and second as a standard (*n* = 6) to predict the anticonvulsant effect of Phenytoin (Eptoin, Abbott). For each test group (*n* = 6 for individual compound and separately for different doses), animals received synthesized compounds in different doses (30, 100, and 300 mg/kg) according to body weight [42]. MES test describes the use of electroshock-induced convulsions to determine anticonvulsant activity of test compounds. MES test was carried out 30 min after intraperitoneal injection of standard, control, and test compounds. Mice were subjected to electrical shock for 0.2 s (50 mA) delivered via corneal electrode. Under experimental condition, all control group mice (*n* = 6) had exhibited the distinctive extensor tonus. Animals were then observed closely for 2 min. Abolition of hind leg and tonic maximal extension was considered as a protection against electrical seizures. Duration of tonic seizures and number of deaths were noted. Results of test compounds were compared with control and standard drug.

scPTZ test

Seizures produced by subcutaneous injection of pentylenetetrazole (PTZ, 80 mg/kg) are considered equivalent to the petit mal type of convulsions in human. Thus, *scPTZ* test is used to identify the anticonvulsant potential of synthesized compounds against clonic convulsions [43]. Clonic convulsions were characterized by episodes of chronic muscle spasms that persist for at least 5 s. PTZ was administered in the posterior midline of mice and onset of convulsion was noted for control group (*n* = 6). Standard drug and synthesized compounds were injected intraperitoneally to mice (*n* = 6, separately for standard drug and different doses of tested compounds), prior to the subcutaneous injection of PTZ.

Blockade of episodes of clonic convulsions was considered as an anticonvulsant effect, whereas increase in seizure

latency was considered as proconvulsant effect of tested compounds. PTZ-induced seizure model proposed to identify compounds that could provide protection by elevating the seizure threshold. Results of test compounds were compared with standard and control.

Neurotoxicity screening

Rotarod test was used to assess the effect of compounds on muscle strength and motor abilities. Test was performed according to protocol described by Ugale and Bari [33].

Evaluation of liver function parameters

Most of the marketed anticonvulsants suffered from drawback of hepatotoxicity. Prolonged treatment of existing anticonvulsants such as carbamazepine, phenytoin, diazepam, and valproic acid demonstrates liver toxicity due to hampered hepatic biotransformation. Hence, active compounds from series were evaluated for biochemical parameters concerns with liver disease. Biochemical indicators of hepatotoxicity were estimated by our reported procedure [32].

Quantification studies

For determination of ED_{50} and TD_{50} , groups of animals ($n=6$) were injected with various doses of tested compounds until three points were found in the range of 10–90% seizure protection or minimal neurotoxicity. Both of these values were investigated for selected active compounds from preliminary in vivo pharmacological screening. ED_{50} and TD_{50} was calculated using previously described method [44–46]. PIs for tested compounds were calculated by following formula: TD_{50}/ED_{50} . TPE and activity data for standard drugs as **PHY**, **CBZ**, and **ETX** were taken from literature. All efforts were made to minimize both the suffering of the animals and the number of animals used in the experiments at the basis of obtaining reliable data.

Molecular docking

Molecular docking was performed using Schrödinger's *Glide 5.5* as incorporated in Maestro 8.0 installed on a PC Pentium IV 3.06 GHz, Core 2 Quad PC with Windows 7 operating systems [35]. *Ligprep 2.3 module* was effectively utilized for the preparation of ligands with low energy conformers [47]. *Glide 5.5* was docking module used for molecular docking at GABA_A receptor binding pocket [48]. *Glide XP* docking mode was used for docking studies using protein crystal structure of the human GABA_A receptor (**PDB ID: 6HUO**) [49]. Protein Preparation Wizard in Maestro 8.0 was used to prepare protein structure with

OPLS3 force field. After ensuring chemical correctness, water molecules were deleted and hydrogens were added [33, 35]. The structures were further refined to augment the H-bond network and minimization were done using a standard procedure [50]. Grid was identified by focusing on the centroid of co-crystallized ligand to restrict the centroid of the ligand to be docked. For all remaining parameters, the default setting in Maestro 8.0 was used. The docking glide score, hydrogen bonding, and π – π interactions with the surrounding amino acids were analyzed and best-suited conformations of ligands with maximum dock score were explored precisely and discussed.

MD simulation

The MD simulation was performed using Desmond (Schrodinger LLC) for the highest conformation of active compound **4h**-complexed with the human GABA_A receptor (**PDB: 6HUO**), which allows to understand the binding of a ligand–protein complex with thermodynamic behavior and stability in a simulated physiological solvent-based environment.

MD simulation was carried out through reported procedure of Khadse and colleagues [50]. Ligand–receptor complex system was solvated by simple point charge (SPC) water model with an orthorhombic box of dimension 10 Å on each side and then naturalized with the addition of counter ions (Na^+ and Cl^-). The water layer thickening was set at 10 Å. Systems were minimized with a maximum iteration of 2000 steps and each system after equilibration of 1 ns were submitted for the development of MD runs for 100 ns MD simulations. Default parameters of OPLS 2005 force field were used for simulation with temperature and pressure set 300 K and 1.01325 bar, respectively, in an isothermal–isobaric ensemble. Simulation time was set as 100 ns and trajectories were recorded every 100 ps intervals to obtain approximately 1000 frames for analysis. Desmond's simulation interaction diagram (SID) was used to explore thermodynamic stability and behavior of active ligand through biophysical information such as RMSD, RMSF, and ligand–interaction profile using MD trajectories. The stability of MD simulations was monitored by viewing the RMSD of the ligand and protein atom positions in time.

Prediction of metabolites and sites for metabolism

Cytochrome P 450, Phase I and II metabolites, as well as regioselectivity of metabolism for the representative compounds **4c** were predicted using algorithms utilized by machine learning (ML) tools *GLORY*, *GLORYx*, and *FAME3*, respectively, which are publicly available on a non-profit basis (<https://nerdd.univie.ac.at/>). The cytochrome

P450 (CYP) enzyme family in humans can generate metabolites, which are predicted using the *GLORY* tool [51, 52]. *GLORYx* was used to predict the phase I and phase II-facilitated metabolites [53]. Based on the provided chemical structures, the *FAME3* algorithm is used to compute the regioselectivity of phase I and II metabolism [54].

Supplementary Information The online version contains supplementary material available at <https://doi.org/10.1007/s11030-022-10538-x>.

Acknowledgements Dr. P. Narayana Reddy acknowledges the financial support of GITAM University through the GITAM: Research Seed Grants (RSG) (Ref. F. No. 2021/0016). Dr. Pannala Padmaja acknowledges the financial support of Department of Science and Technology (DST) through the Grant WOS-A (No.SR/WOS-A/CS-2/2019). Dr. Vinod G. Ugale acknowledges the financial support from Science and Engineering Research Board (SERB), New Delhi, India (Ref. No. TAR/2021/000140). Dr. Vinod G. Ugale is also thankful to the Principal Dr. S. J. Surana, R. C. Patel Institute of Pharmaceutical Education and Research, Shirpur, Maharashtra (India) for providing necessary facilities.

References

- Raveesha R, Kumar KY, Raghu MS, Prasad SB, Alsalmeh A, Krishnaiah P, Prashanth MK (2022) Synthesis, *in silico* ADME, toxicity prediction and molecular docking studies of *N*-substituted [1,2,4] triazolo [4,3-*a*] pyrazine derivatives as potential anticonvulsant agents. *J Mol Struct* 1257:132587
- Ugale VG, Bari SB (2014) Quinazolines: new horizons in anticonvulsant therapy. *Eur J Med Chem* 80:447–501
- Pal R, Akhtar MJ, Raj K, Singh S, Sharma P, Kalra S, Chawla PA, Kumar B (2022) Design, synthesis and evaluation of piperazine clubbed 1,2,4-triazine derivatives as potent anticonvulsant agents. *J Mol Struct* 1257:132587
- Grover G, Nath R, Bhatia R, Akhtar MJ (2020) Synthetic and therapeutic perspectives of nitrogen containing heterocycles as anticonvulsants. *Bioorg Med Chem* 28:115585
- Pal R, Singh K, Khan SA, Chawla P, Kumar B, Akhtar MJ (2021) Reactive metabolites of the anticonvulsant drugs and approaches to minimize the adverse drug reaction. *Eur J Med Chem* 226:113890
- Kennedy GM, Lhatoo SD (2008) CNS adverse events associated with antiepileptic drugs. *CNS Drugs* 22:739–760
- Cramer JA, Mintzer S, Wheless J, Mattson RH (2010) Adverse effects of antiepileptic drugs: a brief overview of important issues. *Expert Rev Neurother* 10:885–891
- Sarco DP, Bourgeois BF (2010) The safety and tolerability of newer antiepileptic drugs in children and adolescents. *CNS Drugs* 24:399–430
- Srivastava SK, Tripathi RP, Ramachandran R (2005) NAD⁺ dependent DNA ligase (Rv3014c) from *Mycobacterium tuberculosis*: crystal structure of the adenylation domain and identification of novel inhibitors. *J Biol Chem* 280:30273–30281
- Brotz-Oesterhelt H, Knezevic I, Bartel S, Lampe T, Warnecke-Eberz U, Ziegelbauer K, Habich D, Labischinski H (2003) Specific and potent inhibition of NAD⁺ dependent DNA ligase by pyridochromanones. *J Biol Chem* 278:39435–39442
- Kolokythas G, Pouli N, Marakos P, Pratsinis H, Kletsas D (2006) Design, synthesis and antiproliferative activity of some new azapyranoxanthone amino derivatives. *Eur J Med Chem* 41:71–79
- Azuine MA, Tokuda H, Takayasu J, Enjo F, Mukainaka T, Konoshima T, Nishino H, Kapadia GJ (2004) Cancer chemopreventive effect of phenothiazines and related tri-heterocyclic analogues in the 12-*O*-tetradecanoylphorbol-13-acetate promoted Epstein-Barr virus early antigen activation and the mouse skin two-stage carcinogenesis models. *Pharmacol Res* 49:161–169
- Oset-Gasque MG, Gonz ales MP, P eres-Pe na JP, Garcia-Font N, Romero A, del Pino J, Ramos E, Hadjipavlou-Litina D, Soriano E, Chioua M, Samadi A, Raghuvanshi DS, Singh KM, Marco-Contelles J (2014) Toxicological and pharmacological evaluation, antioxidant, ADMET and molecular modeling of selected racemic chromenotacrine 11-amino-12-aryl-8,9,10,12-tetrahydro-7H-chromeno[2,3-*b*]quinolin-3-ols for the potential prevention and treatment of Alzheimer's disease. *Eur J Med Chem* 74:491–501
- Ukawa K, Ishiguro T, Kuriki H, Nohara A (1985) Synthesis of the metabolites and degradation products of 2-amino-7-isopropyl-5-oxo-5H-[1]benzopyrano[2,3-*b*] pyridine-3-carboxylic Acid (Amoxanox). *Chem Pharm Bull* 33:4432–4437
- Makino H, Saijo T, Ashida Y, Kuriki H, Maki Y (1987) Mechanism of action of an antiallergic agent, Amlexanox (AA-673), in inhibiting histamine release from mast cells. *Int Arch Allergy Appl Immunol* 82:66–71
- Maeda A, Tsuruoka S, Kanai Y, Endou H, Saito K, Miyamoto A, Fujimura A (2008) Evaluation of the interaction between nonsteroidal anti-inflammatory drugs and methotrexate using human organic anion transporter 3-transfected cells. *Eur J Pharmacol* 596:166–172
- Anderson DR, Hegde S, Reinhard E, Gomez L, Vernier WF, Sambandam A, Snider PA (2005) Aminocyanopyridine inhibitors of mitogen activated protein kinase-activated protein kinase 2 (MK-2). *Bioorg Med Chem Lett* 15:1587–1590
- Elinson MN, Vereshchagin AN, Anisina YE, Egorov MP (2020) Efficient multicomponent approach to the medicinally relevant 5-aryl-chromeno[2,3-*b*]pyridine scaffold. *Polycycl Aromat Compd* 40:108–115
- Elinson MN, Vereshchagin AN, Anisina YE, Krymov SK, Fakhrutdinov AN, Egorov MP (2019) Selective multicomponent 'one-pot' approach to the new 5-(4-hydroxy-6-methyl-2-oxo-2H-pyran-3-yl)chromeno[2,3-*b*]pyridine scaffold in pyridine-ethanol catalyst/solvent system. *Mon Chem* 150:1073–1078
- Elinson M, Vereshchagin A, Anisina Y, Krymov S, Fakhrutdinov A, Egorov M (2019) Potassium fluoride catalysed multicomponent approach to medicinally privileged 5-[3-hydroxy-6-(hydroxymethyl)-4H-pyran-2-yl] substituted chromeno[2,3-*b*]pyridine scaffold. *ARKIVOC* II:38–49
- Vereshchagin AN, Elinson MN, Anisina YE, Ryzhkov FV, Goloveshkin AS, Novikov RA, Egorov MP (2017) Synthesis, structural, spectroscopic and docking studies of new 5C-substituted 2,4-diamino-5H-chromeno[2,3-*b*]pyridine-3-carbonitriles. *J Mol Struct* 1146:766–772
- Elinson MN, Ryzhkov FV, Korolev VA, Egorov MP (2016) Pot, atom and step-economic (PASE) synthesis of medicinally relevant spiro[oxindole-3,4'-pyrano[4,3-*b*]pyran] scaffold. *Heterocycl Commun* 22:11–15
- Elinson MN, Nasybullin RF, Ryzhkov FV, Zaimovskaya TA, Nikishin GI (2015) Solvent-free and 'on-water' multicomponent assembling of aldehydes, 3-methyl-2-pyrazoline-5-one, and malononitrile: fast and efficient approach to medicinally relevant pyrano[2,3-*c*]pyrazole scaffold. *Mon Chem* 146:631–635
- Mishra S, Ghosh R (2012) K₂CO₃-mediated, one-pot, multicomponent synthesis of medicinally potent pyridine and chromeno[2,3-*b*]pyridine scaffolds. *Synth Commun* 42:2229–2244
- Evdokimov NM, Kireev AS, Yakovenko AA, Antipin MY, Magdov IV, Kornienko A (2006) Convenient one-step synthesis of a

- medicinally relevant benzopyranopyridine system. *Tetrahedron Lett* 47:9309–9312
26. Bojase G, Wanjala CCW, Majinda RRT (2001) Flavonoids from the stem bark of *Bolusanthus speciosus*. *Phytochemistry* 56:837–841
 27. de Rezende LC, Juck DBF, David JM, David JP, Lima MVB, Lima LS, Alves CQ (2015) New flavans isolated from the leaves and stems of *Cratylia mollis* (Leguminosae). *Phytochem Lett* 14:165–169
 28. Latif Z, Hartley TG, Rice MJ, Waigh RD, Waterman PG (1998) Novel and insecticidal isobutylamides from *Dinosperma erythrococca*. *J Nat Prod* 61:614–619
 29. Awouafack MD, Tchuenguem RT, Ito T, Dzoyem JP, Tane P, Morita H (2016) A new isoflavanol from the fruits of *Kotschyia strigosa* (Fabaceae). *Helv Chim Acta* 99:321–324
 30. Huang D, Zhu H, Chen Y, Chen W, Xue D, Sun L (2015) Prenylated phenylpropanoid compounds from the stem bark of *Illium burmanicum*. *Fitoterapia* 107:22–28
 31. Katritzky AR, Kulshyn OV, Stoyanova-Slavova I, Dobchev DA, Kuanar M, Fara DC, Karelson M (2006) Antimalarial activity: a QSAR modeling using CODESSA PRO software. *Bioorg Med Chem* 14:2333–2357
 32. Ugale VG, Bari SB, Khadse SC, Reddy PN, Bonde CG, Chaudhari PJ (2020) Exploring quinazolinones as anticonvulsants by molecular fragmentation approach: structural optimization, synthesis and pharmacological evaluation studies. *ChemistrySelect* 5:2902–2912
 33. Ugale VG, Bari SB (2016) Structural exploration of quinazolin-4(3*H*)-ones as anticonvulsants: rational design, synthesis, pharmacological evaluation, and molecular docking studies. *Arch Pharm Chem Life Sci* 349:864–880
 34. Nikalje AP, Ansari A, Bari SB, Ugale VG (2015) Synthesis, biological activity, and docking study of novel isatin coupled thiazolidin-4-one derivatives as anticonvulsants. *Arch Pharm Chem Life Sci* 348:433–445
 35. Ugale VG, Bari SB (2016) Identification of potential Gly/NMDA receptor antagonists by cheminformatics approach: a combination of pharmacophore modeling, virtual screening and molecular docking studies. *SAR QSAR Environ Res* 27:125–145
 36. Ugale VG, Patel HM, Wadodkar SG, Bari SB, Shirkhedkar AA, Surana SJ (2012) Quinazolino-benzothiazoles: fused pharmacophores as anticonvulsant agents. *Eur J Med Chem* 53:107–113
 37. Ugale VG, Wani R, Khadse SC, Bari SB (2020) *N*-methyl-D-aspartate receptor antagonists: emerging drugs to treat neurodegenerative diseases. In: *Biochemistry, biophysics and molecular chemistry: applied research interaction*. Routledge, London, p 14
 38. Stables JP, Kupferberg HJ (1997) The NIH anticonvulsant drug development (ADD) program: preclinical anticonvulsant screening project. In: Avanzini G, Tanganelli P, Avoli M (eds) *Molecular and cellular targets for antiepileptic drugs*. John Libbey & Co., Ltd., London, pp 191–198
 39. Yogeewari P, Sriram D, Thirumurugan R, Raghavendran JV, Sudhan K, Pavana RK, Stables J (2005) Discovery of *N*-(2,6-dimethylphenyl)-substituted semicarbazones as anticonvulsants: hybrid pharmacophore-based design. *J Med Chem* 48:6202–6211
 40. Hammer H, Bader BM, Ehnert C, Bundgaard C, Bunch L, Hoestgaard-Jensen K, Schroeder OH, Bastlund JF, Gramowski-Voß A, Jensen AA (2015) A multifaceted GABAA receptor modulator: functional properties and mechanism of action of the sedative-hypnotic and recreational drug methaqualone (Quaalude). *Mol Pharmacol* 88(2):401–420
 41. Zayed MF, Ihmaid SK, Ahmed HE, El-Adl K, Asiri AM, Omar AM (2017) Synthesis, modelling, and anticonvulsant studies of new quinazolines showing three highly active compounds with low toxicity and high affinity to the GABA-A receptor. *Molecules* 22(2):188
 42. Swinyard EA (1989) *General Principles: experimental selection, quantification, and evaluation of antiepileptic drugs*, 4th edn. Raven Press, New York
 43. White HS, Johnson M, Wolf H, Kupferberg H (1995) The early identification of anticonvulsant activity: role of the maximal electroshock and subcutaneous pentylenetetrazol seizure models. *Ital J Neurol Sci* 16:73–77
 44. White HS, Woodhead JH, Wilcox KS, Stables JP, Kupferberg HJ, Wolf HH (2002) *Discovery and preclinical development of antiepileptic drugs*, 5th edn. Lippincott Williams & Wilkins, Philadelphia
 45. Firke SD, Cheke RS, Ugale VG, Khadse SC, Gagarani MB, Bari SB, Surana SJ (2021) Rationale design, synthesis, and pharmacological evaluation of isatin analogues as antiseizure agents. *Lett Drug Des Discov* 18:1146–1164
 46. Giardina WJ, Gasior M (2009) Acute seizure tests in epilepsy research: electroshock and chemical induced convulsions in the mouse. *Curr Protoc Pharmacol S* 45:5–22
 47. Schrödinger, LLC (2009) LigPrep, version 2.3. Schrödinger, LLC, New York
 48. Schrödinger, LLC (2009) Glide, version 5.5. Schrödinger, LLC, New York
 49. Masiulis S, Desai R, Uchański T, Serna I, Laverty D, Karia D, Malinauskas T, Zivanov J, Pardon E, Kotecha A, Steyaert J (2019) GABAA receptor signalling mechanisms revealed by structural pharmacology. *Nature* 565:454–459
 50. Dhote AM, Patil VR, Lokwani DK, Amnerkar ND, Ugale VG, Charbe NB, Bhongade BA, Khadse SC (2021) Strategic analyses to identify key structural features of antiviral/antimalarial compounds for their binding interactions with 3CLpro, PLpro and RdRp of SARS-CoV-2: in silico molecular docking and dynamic simulation studies. *J Biomol Struct Dyn*. <https://doi.org/10.1080/07391102.2021.1965912>
 51. de Bruyn Kops C, Stork C, Šícho M, Kochev N, Svozil D, Jeliázková N, Kirchmair J (2019) GLORY: generator of the structures of likely cytochrome P450 metabolites based on predicted sites of metabolism. *Front Chem* 7:402
 52. Stork C, Embruch G, Šícho M, de Bruyn Kops C, Chen Y, Svozil D, Kirchmair J (2020) NERDD: a web portal providing access to *in silico* tools for drug discovery. *Bioinformatics* 36:1291–1292
 53. de Bruyn Kops C, Šícho M, Mazzolari A, Kirchmair J (2021) GLORYx: prediction of the metabolites resulting from phase 1 and phase 2 biotransformations of xenobiotics. *Chem Res Toxicol* 34:286–299
 54. Chaudhari PJ, Bari SB, Surana SJ, Shirkhedkar AA, Bonde CG, Khadse SC, Ugale VG, Nagar AA, Cheke RS (2022) Discovery and anticancer activity of novel 1,3,4-thiadiazole- and aziridine-based indolin-2-ones *via in silico* design followed by supramolecular green synthesis. *ACS Omega* 7:17270–17294

Publisher's Note Springer Nature remains neutral with regard to jurisdictional claims in published maps and institutional affiliations.

Springer Nature or its licensor holds exclusive rights to this article under a publishing agreement with the author(s) or other rightsholder(s); author self-archiving of the accepted manuscript version of this article is solely governed by the terms of such publishing agreement and applicable law.

Authors and Affiliations

Visarapu Malathi¹ · Nissi Sharon¹ · Pannala Padmaja² · Deepak Lokwani³ · Saurabh Khadse⁴ · Prashant Chaudhari⁴ · Atul A. Shirkhedkar⁴ · Pedavenkatagari Narayana Reddy¹ · Vinod G. Ugale^{4,5} 

¹ Department of Chemistry, School of Science, Gitam Deemed to be University, Hyderabad, TS, India

² Centre for Semio Chemicals, CSIR-Indian Institute of Chemical Technology, Hyderabad, India

³ Rajarshi Shahu College of Pharmacy, Buldana, Maharashtra, India

⁴ Department of Pharmaceutical Chemistry, R. C. Patel Institute of Pharmaceutical Education and Research, Shirpur, Maharashtra 425405, India

⁵ Bioprospecting Group, Agharkar Research Institute, Savitribai Phule Pune University, G. G. Agarkar Road, Pune, Maharashtra 411004, India

Potential Herbal Anti-Cancer Drug Formulations Using Modern Drug Delivery Methods

Chirag Goda^{1*}, Ashish Kandalkar², Manish Bhise³, Vinod Kumar Tiwari⁴, Sanjay Vasu⁵, Sunny Pahuja⁶, Sandip Hurpade⁷, Balaji Thakare⁸ and Satish Shelke⁹

¹IBN Sina National College for Medical Studies, Jeddah, Saudi Arabia

²Late Shri Ramraoji Gawande Institute of Pharmacy, Akola, India

^{3,5,6}SGSPS, Institute of Pharmacy, Akola, India

⁴Narayan Singh University, Jamuhar, Rohatas, Bihar, India

⁷Rajashri Shahu College of Pharmacy, Buldana, India

⁸MUP College of Pharmacy, Degaon, Taluka-Risod, Washim (MS), India

⁹Rajashri Shahu College of Pharmacy, Buldana, India

ABSTRACT

Objectives: The goal of the current effort is to create and assess chewing gum containing a potassium salt of curcumin extract for its ability to carry medication into the buccal cavity and fight cancer. It helps with the treatment of metabolic syndrome, arthritis, anxiety, and hyperlipidemia as well as oxidative and inflammatory diseases. Chewing gums containing curcumin were created to examine its anticancer properties.

Method: To increase the solubility of potassium Curcumin, a solid dispersion of the compound was created utilising cyclodextrin. For the purpose of improving solubility, the obtained solid dispersion of potassium curcumin was examined. Curcumin Sucrose, castor oil, chewing gum base, potassium curcumin, and other ingredients were then combined to create chewing gums. The prepared chewing gum was assessed for colour, flavour, hardness, and drug-excipient compatibility.

Results: The compatibility study's findings demonstrated that there was no interaction between the chosen medicine and excipients. When compared to curcumin and other common anticancer medications like 5-Fu, Mito-C, and Paclitaxel, potassium curcumin has greater anticancer activity: 85% against prostate cancer cells, 80% against liver cancer cells, and 92% on average against colon cancer cells. In-vivo studies of the chewing gums were optimised based on in-vitro drug release.

Conclusion: According to the results of this study, chewing gum containing the potassium salt of the cancer-fighting compound curcumin can be deemed a good delivery mechanism.

Keywords: Chewing gums, Cancer, Anticancer, Tumor, Normal cells, Curcumin.

INTRODUCTION

The oral route is arguably the one that both patients and doctors favour among the other administration methods. Drugs administered orally, however, have drawbacks such hepatic first pass metabolism and gastrointestinal enzymatic degradation that make oral administration of some medication types inappropriate.¹ The outermost layer of the oral mucosa is made up of stratum distendum, stratum filamentosum, stratum suprabasale, and stratum basale, all of which are stratified squamous epithelium and are mucous-covered. Lamina propria and submucosa cover the area beneath the basal lamina. The lamina propria serves as a mechanical support and also carries the blood vessels and nerves, whilst the epithelium acts as a mechanical barrier to protect underlying tissues. The oral mucosa contains keratinized areas.² In general, the oral mucosa is an intermediate layer of leaky epithelia between the epidermis and the intestinal mucosa. The buccal mucosa's permeability is thought to be 4–4000 times greater than that of skin. Because of the various forms and functions of various oral mucosae, there are significant variances in permeability between different parts of the oral cavity, as seen by the wide range in this reported value.³ In general, the oral mucosa is an intermediate layer of leaky epithelia between the epidermis and the intestinal mucosa. The buccal mucosa's permeability is thought to be 4–4000 times greater than that of skin. Because of the various forms and functions of various oral mucosae, there are significant variances in permeability between different parts of the oral cavity, as seen by the wide range in this reported value.⁴ In general, buccal mucosae are more permeable than sublingual, and buccal mucosae are more permeable than palatal.⁵ The sublingual mucosa is relatively thin and non-keratinized, the buccal mucosa is thicker and non-keratinized, and the palatal mucosa is intermediate in thickness but keratinized. These tissues are ranked according to their relative thickness and degree of keratinization.⁶ The paracellular and transcellular routes are the two penetration routes for passive drug transport over the oral mucosa. These two routes can be used simultaneously by permeants, although depending on the physiochemical characteristics of the diffusant, one is typically chosen over the other. Since the cytoplasm and intercellular gaps

have a hydrophilic nature, lipophilic substances would have poor solubilities in this setting.⁷ The pace and amount of drug absorption through the buccal mucosa are slowed down by barriers such as saliva, mucus, membrane coating granules, basement membrane, etc. Within the outermost quarter to a third of the epithelium, there lies the major penetration barrier.⁸ The buildup of lipids and cytokeratins in the keratinocytes is less obvious and the change in morphology is much less pronounced in non-keratinized epithelia than in keratinized epithelia. The cytokeratins do not consolidate to form bundles of filaments as seen in keratinizing epithelia, and the mature cells in the outer region of non-keratinized epithelia grow big and flat and retain their nuclei and other organelles.⁹ Although the basement membrane is also a factor in controlling connective tissue, the oral epithelium's superficial layers still serve as the main barrier to the entry of substances from the outside. The opposing direction appears to be controlled by a comparable process. Lipophilic substances that can reasonably easily cross the superficial epithelial barrier may have their rate of penetration slowed down by the charge on the basal lamina's constituents.¹⁰ The buccal mucosa's epithelial cells are encircled by mucus, an intercellular ground substance that can range in thickness from 40 m to 300 m. Even though the small salivary glands and sublingual glands together only provide around 10% of all saliva, they create the majority of mucus and are essential for preserving the mucin layer over the oral mucosa.¹¹ A salivary layer that is unstirred and is thought to be 70 m thick covers the mucosal surface. High molecular weight mucin, found in saliva, can bind to the surface of the oral mucosa to prevent drying out, lubricate, concentrate protective chemicals like secretory immunoglobulins, and prevent microbial adhesion.¹² Buccal delivery is the process of administering a medicine to the systemic circulation through the buccal mucosa. The buccal mucosa is substantially more permeable than skin and has additional benefits over other delivery methods, although being significantly less permeable than the sublingual mucosa and typically not able to enable quick drug absorption or adequate bioavailability.¹³ A different option is for the medicine released from chewing gum to be eaten and delivered into the stomach in a dissolved or dispersed form in saliva if it is not absorbed through the oral cavity membrane. As a result, the medicine would be available for absorption by the gastro intestinal tract.¹⁴ As an alternative, medication released from medical chewing gum and lozenges can be ingested and received into the stomach in a dissolved or dispersed form by saliva if it is not absorbed through the oral cavity barrier. As a result, the medicine would be available for absorption by the gastro intestinal tract.¹⁵ The gender factor may affect how frequently a certain cancer occurs. For both sexes, skin cancer is the most prevalent kind of malignancy, followed by breast cancer in women and prostate cancer in men. Its frequency is not a direct indicator of cancer mortality. Skin malignancies can frequently be cured. The main cause of death for both men and women is lung cancer.¹⁶

MATERIALS AND METHOD

Materials

Potassium di Hydrogen Orthophosphate was obtained from Qualigens Fine Chemicals, Sodium Hydroxide was gotten from Qualigens Fine Chemicals, Liquid Glucose from Laxmi Confectionaries Ltd, Akola, and Curcumin from CHR-Hansen Pvt Ltd, Mumbai

Drug Profile

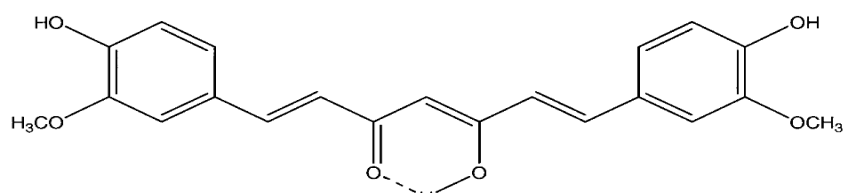


Figure-1 Curcumin chemical structure

Synonym: Diferuloyl Methane

Molecular Weight: 368.37

Description:

Curcumin occurs as orange yellowish powder. It is practically insoluble in Water¹⁷

METHOD

Preparation of Potassium Curcumin Salt:¹⁸

Curcumin diferuloyl methane is insoluble in water. It is considered worthwhile to prepare water soluble alkali phenates of curcumin which might possess enhanced activity compared to curcumin.

The procedure followed to prepare alkali salt of the curcumin is as follows:

Curcumin was added to alcoholic potassium hydroxide (1:2 moles respectively) and stirred to homogeneous thin paste which soon liquefied to a deep red solution. After adding an excess of about 5% curcumin and thorough stirring, the liquid was dried in a current of air at 400 C. The dried mass was then dissolved in minimum quantity of cold water and filtered under reduced pressure. The filtrate containing the potassium phenates were evaporated to dryness as above and finally in vacuum desiccators to constant weights.

Solid dispersion of potassium curcumin ate was prepared using β -cyclodextrin to enhance the solubility of potassium Curcumin ate.

Cell Lines and Cell Culture Preparation¹⁹

PC-3, HEP-2, A-549, 502713, HCT-15 and SW-620 cell lines were obtained from Indian Institute of Integrated Medicine, Jammu. cells were cultured in 2-3 ml of 0.05% trypsin-EDTA. And addition of 10 ml of 5% serum containing RPMI 1640 medium.

In Vitro Dissolution Studies for Potassium Curcumin ate²⁰

The vessel was filled with 200 ml phosphate buffer (6.4) and the gum was placed in the inner perforated vessel. The metal bob was attached to the rod, the height of rod and bob was previously adjusted so that the bob completely touches the bottom of the perforated vessel.

The apparatus was switched on and the bob was allowed to impact on the chewing gum.

This process was continued for 2 hours. 5 ml sample of the buffer solution was withdrawn at a regular interval of 10 min and every time it was replaced with equal amount of phosphate buffer, thus the samples were collected at 10, 20, 30 up-to 120 minutes

Formulation of Chewing Gum²¹

The chewing gums with chewing gum base and drug and glucose were prepared by the method described below.

Numbers of trials were extensively carried out to arrive at the correct concentration of each ingredient in order to have a desirable consistency as well as non-adhering properties.

In case of the chewing gums various plasticizers such as soyabean oil cottonseed oil, castor oil, diethyl phthalate, dibutyl phthalate were tried. The optimum concentration was decided for each plasticizer and two of them which showed good result, were selected. The two selected plasticizer castor oil and dibutyl phthalate were used subsequently bees wax was often incorporated in the gum bases in order to improve the chewability that is to give desired consistency to product prepared from the gum bases.

The chewing gum formulation is always sweetened. This is obvious as the product is used for the chewing and hence the taste of the product must be considered. In this study the model drug selected has bitter taste and hence large quantities of sucrose is added to mask the taste.

Talc was employed in the gum base as an anti-sticking agent. The purpose is to avoid adhering of the gum to dental surfaces. The concentration of talc was fixed to 5 to 10 % of total gum base composition.

Table-1 Formulation of Chewing Gum

Potassium curcumin ate	100 mg
Chewing Gum Base	800 mg
Sucrose	150 mg
Castor oil	0.5 ml

Evaluation of Chewing Gums:²²

Stability Testing:

The purpose of this testing is to determine the physical and chemical stabilities of medicament, flavour, candy base and colour both under accelerated temperature and humidity conditions and at ambient storage conditions. This testing will enable the formulator to predict the acceptable shelf life of the product in a relatively short period of time and make changes as required to eliminate any incompatibilities that may influence product stability.

Elevated Temperature and Elevated Humidity Testing

Elevated temperature and elevated humidity testing is initiated as soon as product is manufactured. Product should be tested at elevated temperatures and elevated humidity conditions. Testing conditions generally utilized by the product development laboratory include 25°C at 80% relative humidity for 6-12 months, 37°C at 80% humidity for 3 months, and 25°C at 70% relative humidity for 6-12 months. The elevated humidity studies are carried out both at constant humidity and in humidity cabinets with day and night cycling. Elevated humidity tests are vital for ascertaining medicament stability and candy stickiness including surface graining characteristics

Physical Stability

Concurrent with the chemical stability evaluation, a physical stability study is carried out on the product in order to determine what factors will detract from organoleptic appeal of the product and how long these changes will take place to occur. A routine physical stability evaluation includes:

Colour:

Chewing gums are checked for the colour stability by keeping them in direct sunlight and at elevated temperatures to determine if the colours are light fast, also changes occurring due to presence of medicaments are to be evaluated. Table no. 2

Odour:

Changes in the odour of flavours at elevated temperature are evaluated by sealing the Chewing gums in glass bottles and determining if any odour is there.

Taste:

The product is tasted and compared to production controls in order to determine if any flavour change has occurred. Many small flavour changes that cannot be detected via gas-liquid chromatography can be ascertained when lozenge is tasted. Any change in the surface texture is also evaluated during the taste evaluation. Result mentioned in table no.2

Table-2 Study for stability of potassium curcuminatate Chewing gums

Parameters	Appearance		Colour		Dissolution	
First day 4°C	--	--	--	--	--	--
Room Temp	--	--	--	--	--	--
37° C	--	--	--	--	--	--
50° C	--	--	--	--	--	--
1 st Month 4° C	--	--	--	--	--	--
Room Temp	--	--	--	--	--	--
37° C	--	--	--	--	--	--
50° C	--	--	--	--	+	--
2 nd Month 4° C	--	--	--	--	--	--
Room Temp	--	--	--	--	--	--
37° C	--	--	--	--	--	--
50° C	--	--	--	--	+	--
3 rd Month 4° C	--	--	--	--	--	--
Room Temp	--	--	--	--	--	--
37° C	--	--	--	--	--	--
50° C	--	--	--	--	+	--

-- No Change + Slight change

Weight Variation Test:

Twenty Chewing gum were taken and their weight was decided exclusively and all things considered on a computerized weighing balance. The typical load of one not set in stone from the system weight. The weight variety test would be a agreeable strategy for deciding the medication content consistency. The percent deviation was determined utilizing the accompanying equation. The outcomes are introduced in

% Deviation =

(Individual weight – Average weight /

Average weight) × 100

Hardness:

Compressed tablet Chewing gum are tested for proper hardness using Pfizer hardness tester. The force required to penetrate the lozenge is used as measure of chewiness, surface harness and stability. Results are mentioned in table no. 3

Chewing Gum Thickness:

Chewing gum thickness is a significant trademark in repeating appearance. Twenty chewing gum were taken and their thickness was recorded utilizing Digital Micrometer. The typical thickness for Chewing gum was determined and given standard deviation. The outcomes are introduced in Table no-3

Friability:

It is a proportion of mechanical strength of Chewing gum. Roche friabilator was utilized to decide the friability by following method. Pre weighed Chewing gum (20) were put in the friabilator. The Chewing gums were turned at 25 rpm for 4 minutes (100 revolutions). Toward the finish of test, the Chewing gums were re-gauged, misfortune in the heaviness of capsules is the proportion of friability and is communicated in Table no.3

$$\% \text{ Friability} = [(W1 - W2) / W1] \times 100$$

Where,

W1 = Initial weight of 20 chewing gums

W2 = Weight of the 20 chewing gum after testing

Table- 3 Evaluation of Chewing gum

Parameters	Potassium Curcuminat
Weight variation (mg)	2804±2.16
Thickness (mm)	3.23±0.08
Hardness (kg/cm ²)	1.40±0.45
Friability (%)	0.11
Content uniformity	95.21

*All information is offered in Mean ± SD, n=3, SD = standard deviation

Preparation of Standard Solution:

Estimation of Potassium Curcuminat in 6.4 pH phosphate buffer.

100 mg of potassium curcuminat was dissolved in 100 ml of 6.4 pH phosphate buffer; the resulting solution was subsequently diluted with 6.4 pH phosphate buffer to obtain series of diluted concentrations i.e. 50, to 500 mcg/ml the absorbance of above diluted concentrations was measured at 464 nm using 6.4 pH buffer as blank.

Estimation of Potassium Curcuminat in 6.4 Ph Phosphate Buffer.

100 mg of potassium curcuminat was dissolved in 100 ml of 6.4 pH phosphate buffer; the resulting solution was subsequently diluted with 6.4 pH phosphate buffer to obtain series of diluted concentrations i.e. 50, to 350 mcg/ml the absorbance of above diluted concentrations was measured at 272 nm using 6.4 pH buffer as blank. Standard curve data reading are shown in table no.4

Table-4 Standard curve data for potassium curcuminat by UV-Visible spectrophotometer

Serial No	Concentration in µg/ml	Average Absorbance (n=3)
1	50	0.079±0.004
2	100	0.156±0.007
3	150	0.235±0.008
4	200	0.316±0.011
5	250	0.393±0.007
6	300	0.465±0.008
7	350	0.549±0.007
8	400	0.625±0.008

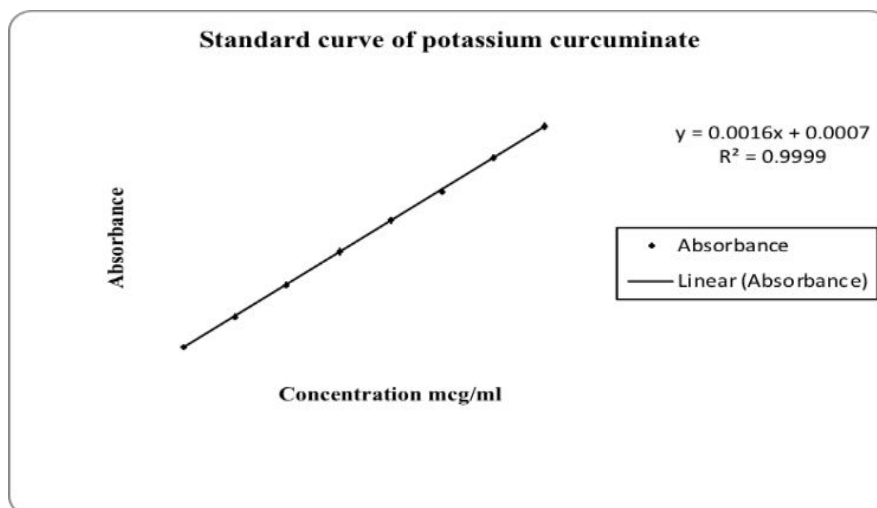


Figure-2 Standard Curve of Potassium Curcuminat

Dissolution Studies:¹⁴

In Vitro Dissolution Studies for Potassium Curcuminat

The vessel was filled with 200 ml phosphate buffer (6.4) and the Chewing gums was placed in the inner perforated vessel. The metal bob was attached to the rod, the height of rod and bob was previously adjusted so that the bob completely touches the bottom of the perforated vessel.

The apparatus was switched on and the bob was allowed to impact on the Chewing gums.

This process was continued for 2 hours. 5 ml sample of the buffer solution was withdrawn at a regular interval of 10 min and every time it was replaced with equal amount of phosphate buffer, thus the samples were collected at 10, 20, 30 upto 60 minutes. Results are shown in table-5

Table-5: In vitro dissolution profile of potassium curcuminat

Time in Minutes	Average Percent Drug Release
5	4.733±0.681
10	12.400±0.529
15	14.833±0.289
20	24.500±0.500
25	36.000±1.000
30	39.667±0.577
35	49.667±1.528
40	64.000±1.732
45	71.000±2.646
50	82.000±3.000
55	92.833±1.041
60	92.833±0.764

*All information is offered in Mean ± SD, n=3, SD = standard deviation

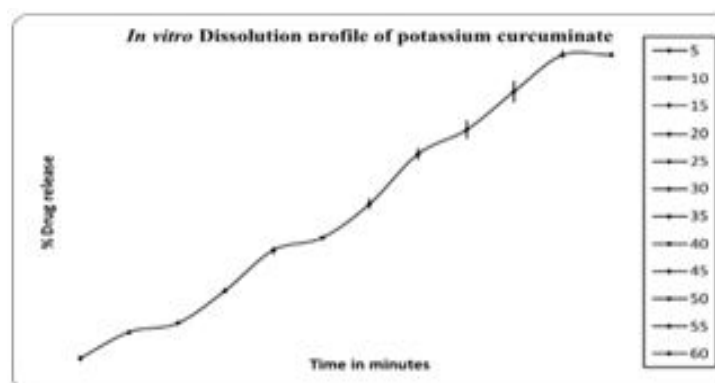


Figure-3 Drug release from potassium curcuminat

Drug Release Kinetics

The mechanism of drug release from Chewing gums was determined by fitting the in vitro release profiles of optimized batches with zero order, first order, Hixson, Higuchi and Korsmeyer models. The obtained correlation coefficient values are given in the Table-6 & figure4-8

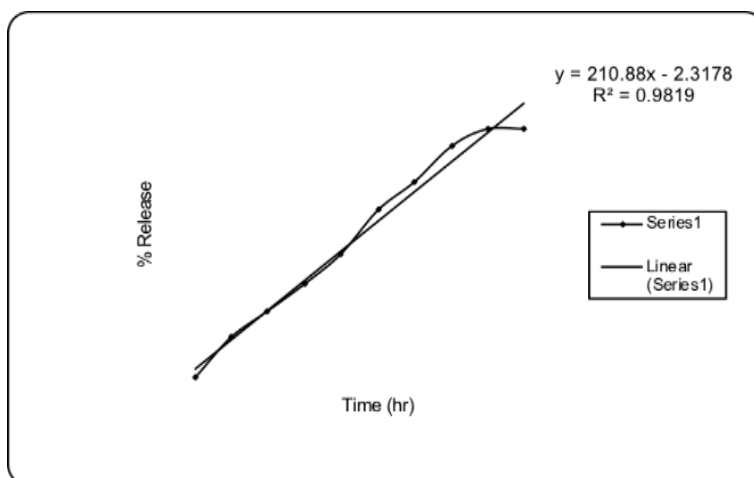


Figure -4 Zero order model for drug release from potassium curcumin Chewing gums

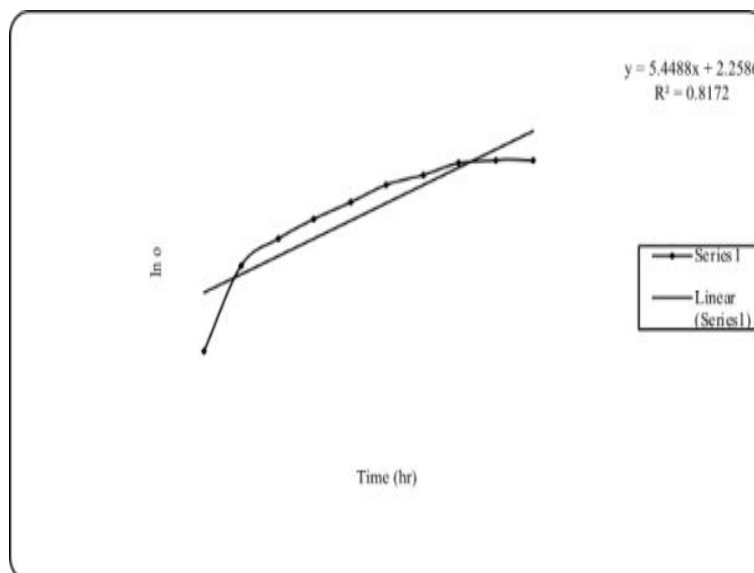


Figure-5 First order model for drug release from potassium curcumin Chewing gums

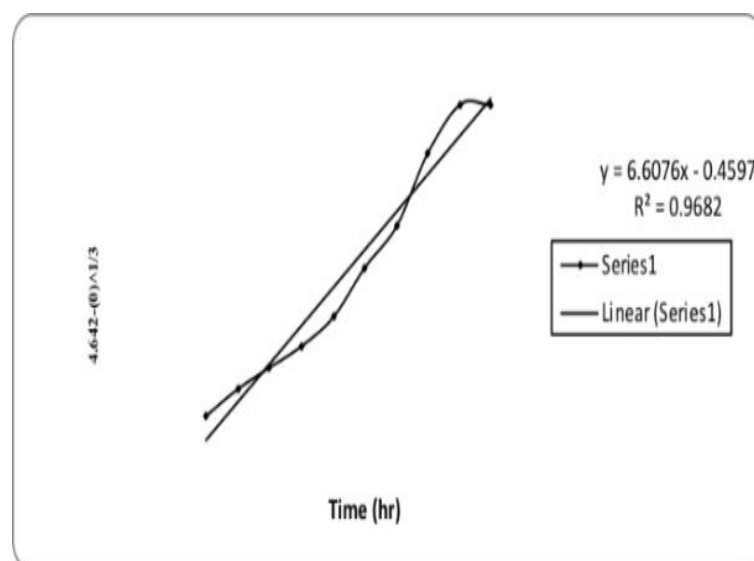


Figure-6 Hixson Cromwell model for drug release from potassium curcumin Chewing gum

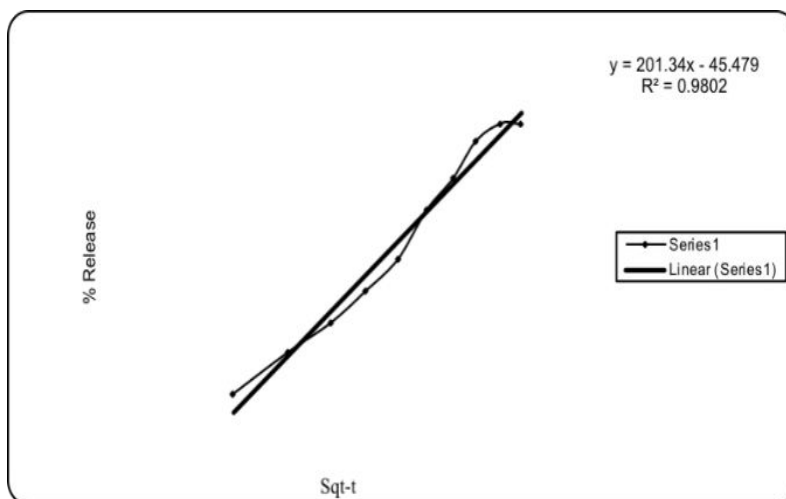


Figure-7 Higuchi square root model for drug release from potassium curcumin chewing gum

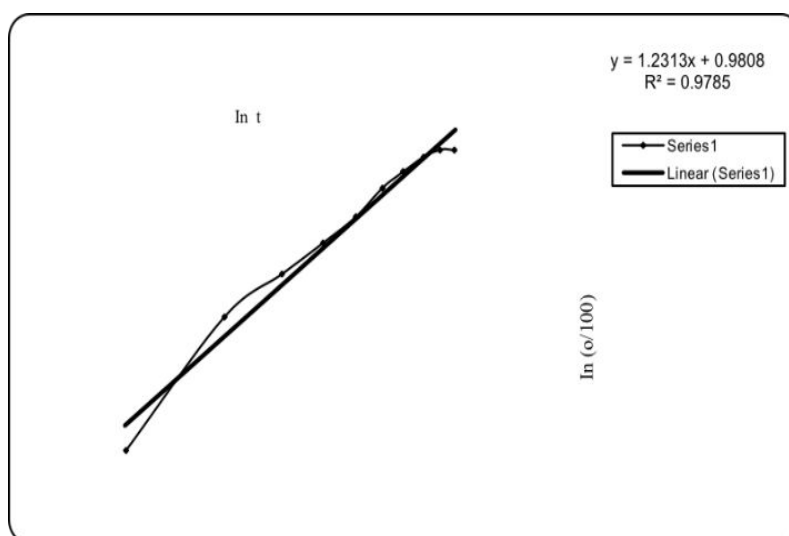


Figure-8 Korsmeyer model for drug release from potassium curcumin chewing gum

Table-6 Comparative study of drug release from different models for potassium curcumin chewing gum

Time	Observed % rel.	ZERO		FIRST		HIGUCHI		HIXSON		KORSMEYER	
		Calculated % rel. (Q)	RS	Calculated % rel. (Q)	RS	Calculated % rel. (Q)	RS	Calculated % rel. (Q)	RS	Calculated % rel. (Q)	RS
0.050	5.233	8.226	8.957	12.567	53.776	-0.458	32.391	-8.621	191.955	6.668	2.058
0.100	19.167	18.770	0.157	16.502	7.101	18.190	0.953	12.416	45.571	15.655	12.331
0.150	28.667	29.314	0.419	21.670	48.956	32.500	14.692	30.545	3.528	25.792	8.266
0.200	38.667	39.858	1.420	28.456	104.257	44.563	34.767	45.982	53.516	36.755	3.655
0.250	49.333	50.402	1.142	37.367	143.182	55.191	34.312	58.944	92.356	48.377	0.914
0.300	65.000	60.946	16.433	49.070	253.777	64.799	0.040	69.646	21.582	60.553	19.776
0.350	75.333	71.490	14.770	64.436	118.741	73.635	2.883	78.305	8.829	73.209	4.511
0.400	88.000	82.034	35.591	84.616	11.453	81.860	37.705	85.137	8.195	86.292	2.916
0.450	93.667	92.578	1.185	111.114	304.422	89.584	16.668	90.360	10.935	99.760	37.129
0.500	93.667	103.122	89.407	145.911	2729.518	96.890	10.389	94.188	0.272	113.579	396.498
SSR			169.482		3775.185		184.801		436.740		488.056
SSR/R²			172.606		4619.659		188.534		451.085		498.780

ZERO $Q = 210.88t - 2.3178$ $R^2 = 0.9819$

FIRST $\ln Q = 5.4488T + 2.2586$ $R^2 = 0.8172$

HIXSON $4.642 - (Q)/3 = 0.3106t - 0.3225$ $R^2 = 0.9493$

HIGUCHI $Q = 201.34 t^{1/2} - 45.479$ $R^2 = 0.9802$

KORSMEYER $\ln(Q/100) = 1.2313 \ln t + 0.9808$ $R^2 = 0.9785$

Procedure for in Vitro Analysis of Anti-Cancer Activity²³

The criteria for selection of a cell line for use in the interim panel were as follows.

- a) Adaptability to growth on a single medium (RPMI-1640 plus 5% fetal bovine serum and 2mM glutamine):
- b) A negative test for mycoplasma and mouse antibody production.
- c) Isoenzyme and karyotype profiles verifying the human origin of cells.
- d) Mass doubling that allows for harnessing of approximately 3×10^7 cells twice a week: and
- e) Suitability for use with microculture assays.

Once a line had been established as suitable, the number of cells was massively expanded in minimal number of passages and the cells were cryopreserved in a large repository of ampoules each containing 1×10^6 cells to provide a consistent frozen stock for future use. Once the growth in the in the new stock is established at the second or third passage, the older passage line is replaced with the new stock established at the second or third passage, the older passage line is replaced with the new stock for use in the screening laboratory.

Cell Line Maintenance

Cells are maintained in multiple of T150 tissue culture flasks. Cells for each inoculation day are maintained separately (no common reagents) and passaged on separate days to prevent catastrophic loss of growing cell line stocks to microbial contamination. Additional backup flasks of cells are also maintained. For each cell line, the seeding density per flask is determined for production of healthy culture of 70% to 90% after 7 days for continued routine maintenance. These seeding densities than utilized twice a week to maintain sufficient cells for anti-cancer drug screening.

Preparation and Inoculation of Cells

All of the adherent cell lines are detached from the culture flasks by addition of 2-3 ml of 0.05% trypsin-EDTA. Thereafter trypsin is inactivated by addition of 10 ml of 5% serum containing RPMI 1640 medium. Cells are separated into single cell suspension by gentle pipetting action then counted using trypan blue exclusion on a hemacytometer or by Coulter counter which is used when viability as determined by trypan- blue exclusion routinely greater than 97%. After counting dilutions were made to give the appropriate cell densities for inoculation onto the micrometer plate. Cells were inoculated in a volume of 100 μ l per well at densities between 5000 and 40000 cells per well. Cells were counted diluted and inoculated onto microculture plates within 4 hours period on 2 days each week. The micrometer plates containing the cells are preincubated for approximately 24 hours at 37 $^{\circ}$ C to allow stabilization prior to addition of drug.

Solubilization and Dilution of Samples

For the initial screening of pure compounds each agent is routinely tested at five 10 fold dilutions starting from a maximum concentration of 10 4 M. Alternatively a maximum of 10 M can be selected if solubility permits. All samples are initially solubilized in dimethyl sulfoxide (DMSO) or water at 400 times the desired final maximum test concentration. Drug stocks are not filtered or sterilized, but microbial contamination is controlled by addition of gentamicin to the drug diluent. Multiple aliquots are stored at frozen at -70 $^{\circ}$ C to provide uniform samples for initial for tests as well as retests, if required just prior to preparation of the drug dilutions in cell-culture medium. These frozen concentrates are thawed at room temperature for 5 minutes. The concentrates are then diluted with complete medium containing 50 μ g/ml gentamicin to twice the desire final concentrations.

Drug Incubation

Immediately after preparation of these intermediate dilutions 100 μ L aliquots of each dilution were added to the appropriate microtiter plate wells according to the format. As the microtiter wells already contain the cells in 100 μ L of medium, the final drug concentration tested is 50% of that in the intermediate dilutions. Agents are than added immediately to the cultures in the microtiter plates. During development of these procedures, drug incubation time was 1, 2, 3, 4 or 6 days at 37 $^{\circ}$ C in an atmosphere of 5% CO₂ and 100% relative humidity. The plates were been assayed for the cellular growth and viability by microculture assay by tetrazolium assay or by SRB assay. In the current screening procedure, the cultures were incubated with test agents for 2 days and the end point is measured by the SRB assay.

Microculture Tetrazolium Assay

The MTT assay is based on metabolic reduction of 3-(4, 5- dimethyl thiazol-2-yl)-2,5-diphenyltetrazolium bromide (MTT). A 50 μ l aliquot of MTT solution (1mg/ml) in RPMI-1640 medium, with no serum or glutamine, is added directly to all the appropriate microtiter plate wells containing cells complete growth medium and test agents. The culture is then incubated for 4 hrs to allow for MTT metabolism to formazan. After this time the supernatant is aspired and 150 μ l of Dimithyl sulfoxide is added to dissolve the formazan. Plates are agitated on

plate shaker to ensure a homogenous solution, and the optical densities are read on an automated spectrophotometric plate reader.

Sulforhodamine Bio Assay

Adherent cell cultures were fixed in situ by adding 50 µl of cold 50 % (wt/vol) trichloroacetic acid (TCA) and incubating for 60 minutes at 40C. The supernatant is then discarded and the plates were washed five times with deionized water and dried. One hundred microliters of SRB solution (0.4% wt/vol in acetic acid) is added to each microtiter well and the culture is incubated for 10 minutes at room temperature. Unbound SRB is removed by washing five times with 1 % acetic acid. Then the plates are air dried. Bound stain is solubilized with Tris buffer and the optical densities are read.

Data Calculations

Unprocessed optical density data from each microtiter plate are automatically transferred from the plate reader to a microcomputer, where the background optical density (OD) measurements (i.e. complete medium plus stain minus cells) are subtracted from the appropriate control well values and where the appropriate drug- blank measurements (i.e. complete medium plus test compound dilution plus stain, minus cells) are subtracted from appropriate test well values. The values for mean + SD of data from replicate wells were calculated. Data are expressed in terms of % T/C [(OD of treated cells/ OD of control cells) x 100] as measure of cells viability and survival in the presence of test materials. Calculations are also made for the concentration of test agents giving a T/C value of 50% or 50% growth inhibition (IC50) and a T/C value of 10% or 90% growth inhibition (IC90).

With the SRB assay, a measure is also made of the cells population density at time (the time at which drugs are added) from two extra reference plates of inoculated cells fixed with TCA just prior to drug addition to the test plates. Thus we have three measurements controls optical density (C), test optical density (T) and optical density at tie zero (T0).

Using these measurements, cellular responses can be calculated for growth stimulations for no drug effect and for growth inhibition. If T is greater than or equal to T0, the calculation is $100 \times [(T-T_0)/(C-T_0)]$. If T is less than T0, cell killing has occurred and can be calculated from $100 \times [(T-T_0)/T_0]$. Growth inhibition of 50% (GI50) was calculated from $100 \times [(T-T_0)/(C-T_0)] = 50$, which is the drug concentration causing a 50% reduction in the net protein increase in control cells during the drug incubation. The drug concentration resulting in total growth inhibition (TGI) was calculated from $T = T_0$. Where the amount of protein at the end of drug incubation is equal to the amount of protein at the end of drug incubation is equal to the amount at the beginning. The final calculation, LC50, is the concentration of drug causing a 50% reduction in the measured protein at the end of the drug incubation, compared with that at the beginning. Indicating a net loss of cells following drug treatment. LC50 is calculated from $100 \times [(T-T_0)/T_0] = -50$. Results are shown in table no. 7

Table-7 Comparative in vitro cytotoxicity evaluation against human cancer cell lines with fixed concentration

Name of Drug	Conc. (µg/ml)	PC-3	HEP-2	A-549	502713	HCT-15	SW-620
		Prostate	Liver	Lung	Colon		
Green tea extract	100	46%	4%	28%	94%	83%	9%
Potassium curcumin	100	85%	80%	52%	92%	89%	95%
Curcumin	100	58%	32%	36%	74%	82%	51%
5-Fu	1x10-4M	51%	24%	32%	65%	44%	40%
Mito-C	1x10-5M	60%	69%	24%	85%	66%	62%
Paclitaxel	1x10-6M	26%	-	37%	71%	73%	-

RESULTS

potassium curcumin exhibits targeted anticancer effect against Prostate, Liver, Lungs and colon cancer cell line Anticancer effect of potassium curcumin was estimated by MTT assay and morphological studies. The results of the MTT assay, Sulforhodamine bio assay revealed wide anticancer activity of the potassium curcumin towards Prostate, Liver, Lungs and Colon cancer cells. Potassium curcumin greatest anticancer activity 85% towards prostate cancer cell, 80% towards liver cancer cell, and average of 92% towards colon cancer cell compared to curcumin and standard anticancer drugs like 5-Fu, Mito-C and Paclitaxel.

CONCLUSION

Chewing gum show many benefits over the other dose type of these are; direct simple to geriatric and pediatric populace, has great taste, it draws out the time of medication in the oral cavity to deliver a particular impact, arranged effectively and no need water consumption for organization, this study planned to form potassium

curcumin as Chewing gum to further develop conveyance to treat oral thrush. The pre-arranged definitions were exposed to different physical and Chemical tests like assay, weight variation in-vitro drug release. Finally, it was concluded that the potassium salt of Curcumin Chewing gum can be considered as a suitable delivery system for the treatment variety of Cancer.

REFERENCES

1. Rathbone M, Drummond B, and tucker I. 1994. Oral Cavity as a site for systemic drug delivery. *Adv. Drug. Del. Rev.* 13; 1-22 pp.
2. Shojaei H.A. 1998. Buccal mucosa as route for systemic drug delivery: A review. *Journal of Pharmaceutical Sciences.* 1; 1: 15-30 pp.
3. Devrajan V.P, Adani H.M, Oral Transmucosal drug delivery, New delhi, 1997. 65 pp.
4. Squier C.A. 1991. The permeability of oral mucosa. *Crit Rev Oral Biol. Med.* 2; 13-32 pp.
5. de Vries M. E, Bodde H. E, Verhoef J. C, Junginger H. E, 1991. Developments in buccal drug delivery. *Crit. Rev. Ther Drug Carr. Sys.* 8; 271- 303 pp.
6. Kurosaki Y., Hisaichi S., Hamada C., Nakayama T. and Kimura T. 1988. Effects of surfactants on the absorption of salicylic acid from hamster cheek pouch as a model of keratinized oral mucosa. *Int. J. Pharm.* 47; 13-19 pp.
7. Gennaro R.A, Remington: The Sciences and Practice of Pharmacy, 1995, Mack Publishing Company, 710 pp.
8. YajamanSudhakar, KetousetuoKuotsu, A.K.Bandyopadhyay. 2006. Buccal bioadhesive drug delivery. A promising option for orally less efficient drugs. *Journal of Controlled Release* 114 15-40
9. R.B.Gandhi, J.R. Robinson. 1988. Bioadhesion in drug delivery. *Ind. J.PharmSci* 50 (3) 145-152.
10. C.A. Squier, J. *Ultrastruct.*1977. Res 60 212-220.
11. K.Wolf, H.J.Honigsmann, J.*Ultrastruct* 1971. Res36 176-190.
12. F.S.Rosen, B.J.Bailey, Anatomy and physiology of salivary glands, Grand Rounds presentation, UTMB, Department of Otolaryngology.
13. Rathbone M. J and Hadgraft J. 1991. Absorption of drugs from the human oral cavity. *Int J Pharm* 79; 9-24 pp
14. Morjaria Y, Irwin WJ, Barnett PX, Chan RS and Conway BR: 2004 In vitro Release of Nicotine From Chewing Gum Formulations. *Dissolution Technologies*, 12-15.
15. Cohen Lee M, Britt Dana M, Collins Fank L. 2001. Multimodal assessment of the effect of chewing gum on nicotine withdrawal. *Addictive Behaviors.* 26; 289-295 pp.
16. Yamanaka N, Oda O, Nagao S. 1997. Pro-oxidant activity of caffeic acid, dietary non-flavonoid phenolic acid, on Cu²⁺-induced low density lipoprotein oxidation. *FEBS Lett.* 405:186-90
17. Gupta S, Saha B, Giri A.K. 2002. Comparative antimutagenic and anticlastogenic effects of green tea and black tea: a review. *Reviews in Mutation Research.* 512; 37-65 pp.
18. Tonnesen H.H., Masson M., Loftsson, T. 2002. Studies of curcumin and curcuminoids. XXVII. Cyclodextrin complexation: solubility, chemical and photochemical stability. *Int. J. Pharm.* 244; 127-135 pp.
19. Monks Anne, et.al.1991. Feasibility of high flux anticancer drug screen using a diverse panel of cultured human tumor cell lines. *J Natl Cancer Inst.* 11; 5. 757-766 pp.
20. Morjaria Y, Irwin WJ, Barnett PX, Chan RS and Conway BR: 2004 In vitro Release of Nicotine from Chewing Gum Formulations. *Dissolution Technologies*, 12-15.
21. Buschang P.H, Hayasaki H, Throckmorton G.S. 2000. Quantification of human chewing cycle kinematics. *Arch of Oral Biology.* 45; 461-474 pp.
22. Tonnesen H.H., Krlsen J. 1985. Studies on curcumin and curcuminoids. VI. Kinetics of curcumin degradation in aqueous solution. *Z. Lebensm. Unters. Forsch.* 180; 402-404 pp.
23. Monks Anne, et.al.1991. Feasibility of high flux anticancer drug screen using a diverse panel of cultured human tumor cell lines. *J Natl Cancer Inst.* 11; 5. 757-766 pp..

A Study on Medicinal Plants and Its Hepatoprotective Activity

Dr. Ajay Sharma¹, Dr. Shailesh M. Kewatkar^{2*}, Mr. Dipak Vikram Bhusari³, Dr. Manmeet Singh⁴, Dr. Gaurav Jain⁵, Mr. Salaj Khare⁶, Miss. Vidhi Jain⁷

1. Department of Pharmacology, MIPS, Ujjain, Madhya Pradesh
2. Department of Pharmacognosy, Rajarshi Shahu College of Pharmacy, Buldana, Maharashtra
3. Department of Pharmaceutics, Shri. Sant. Gajanan Maharaj College of Pharmacy, Buldhana, Maharashtra
4. Department of Pharmacology, TIT Pharmacy, Bhopal, Madhya Pradesh
5. Department of Pharmacognosy, IES Institute of Pharmacy, IES University, Bhopal, Madhya Pradesh
6. Department of Pharmacology, ITM (SLS) Baroda University, Vadodara, Gujarat
7. Department of Pharmaceutics, Kota college of pharmacy, Kota, Rajasthan
8. **Received** 2022 August 10; **Revised** 2022 September 22; **Accepted** 2022 October 05
- 9.

Abstract

We, the human being possess a huge wealth of medicinal plants which have been explored and validated for their therapeutic properties. Still there are so many plants whose medicinal properties are not yet published and lots of research works are needed to be carried out on such medicinal plants. Herbal drugs play a vital role in the management of various liver disorder, most of them speed up the natural healing process of liver. Numerous medicinal plants and their formulations are used in liver disorders in ethno medicinal practices as well as traditional system of medicine in India. Various types of treatment modalities are available to treat liver diseases. In allopathic medical practices, herbs play role in the management of various liver disorders. Since however, we do not have satisfactory remedy for disorders of liver, the search for finding out effective hepatoprotective drugs continues.

Keyword:-Herbal, Medicinal plant, Hepatoprotective, liver, modern drugs, herbal medicine.

Introduction

In recent times natural products are becoming an integral part of human health care system, because there is a now popular concern over toxicity and side effects of modern drugs. There is also a

realization that natural medicines are safer and allopathic drugs are often ineffective in several ailments. Medicinal plants existed even before human being made their appearance on the earth. Man's existence on this earth has been made possible only because of the vital role played by plant kingdom in sustaining his life.

India has about 45000 plant species; medicinal properties have been assigned to several thousands. Currently, with over 4,00,000 registered ayurvedic practitioners, the government of India has formal structure to regulate quality, safety, efficacy and practice of herbal medicine. The turnover of herbal medicine in India as over the counter products, ethical and classical formulation and have remedies of ayurveda, unani and siddha systems is of about \$ 1 billion with a merge export of \$ 80 million. Even though India is the gold mine of herbal medicine, 80% of its export to the developed countries are crude and not finished formulation leading to low revenue of the country.[1]

Herbal medicine

Today, the U.S. Pharmacopoeia, with its reliance on herbal compounds, has been all but forgotten. Most modern physicians rely on the Physician's Desk Reference, an extensive listing of chemically manufactured drugs. It is important to note that each entry in this enormous volume, in addition to specifying the chemical compound and actions of a particular drug, also includes an extensive list of contraindications and possible side effects. [2]

Rather than using a whole plant, pharmacologists identify, isolate, extract, and synthesize individual components, thus capturing the active principles. This can create problems. However, in addition to active ingredients, plants contain minerals, vitamins, volatile oils, glycosides, alkaloids, bioflavonoid, and other substances that are important in supporting a particular herb's medicinal properties. (Boots et al., 2008) These elements also provide an important natural safeguard isolated or synthesized active compounds can become toxic in relatively small doses. It usually takes a much greater amount of a whole herb, with all of its components, to reach a toxic level. Herbs are medicines, however, and they can have powerful effects. They should not be taken lightly.[3]

Herbal hepatotoxicity

Substantial progress has been made in understanding the interaction between herbal drugs and the liver. However, our knowledge of the potentials and risks of botanical drugs is still limited. Therapies developed along the principles of conventional (western) medicine are often limited in efficacy and unaffordable for many individuals throughout the developing world. Therefore, treating diseases with plant derived compounds which do not require extensive preclinical testing and laborious pharmaceutical synthesis is attractive.

The liver is the central drug metabolizing organ and is, therefore, a prime target of drug related pathologies. Foreign compounds are predominantly bio transformed in the liver by the action of drug metabolizing enzymes including microsomal cytochrome P450 enzymes, mixed function mono oxygenases, glutathione S transferases, sulfotransferases and UDP glucuronosyltransferases. Some of these can be induced through variable mechanisms which may lead to large interindividual variability in susceptibility for drug related liver damage. Hepatic damage from conventional drugs is widely acknowledged and most physicians are well aware of them. Herbals as a cause of adverse hepatic reactions, however, have only recently been recognized as their use has become more widespread.[4]

Various parameters to evaluate hepatoprotective activity on liver

As liver is a multifunctional organ, a battery of liver function tests is employed to evaluate the effect of drug on liver, which are non invasive functional methods:

- Pentobarbitone induced sleeping time
Toxic liver prolongs duration of sleeping time for pentobarbitone, hexobarbitone, zoxazolamine etc in mice and rats.
- Morphological test of weight of liver/100 gm body weight:
Morphological parameters like weight of the animals, weight and volume of the liver have also been used to evaluate the protective effect of the drug. Hepatotoxicity causes loss in liver weight/100 gm body weight of rats.[5]

Review of Literature

For pharmaceutical purposes, the quality of medicinal plant material must be as high as that of their medicinal preparations. However, it is impossible to assay for a specific chemical entity when the bioactive ingredient is not known. In practice, assay procedures are not carried out even for those medicinal plant materials where there are known active ingredients. (Kuruvilla, 1999)[6]

There are many approaches to the search for new biologically active principles in higher plants. One can simply look for new chemical constitution and hope to find a biologist who is willing to test each substance with whatever pharmacological tests available. (Boots et al., 2008)[7]

A second approach is simply to collect every readily available plant, prepare extract and test each extract for one (or) more types of pharmacological activity. This random collection, broad screening method is a reasonable approach that eventually should produce useful drugs, but it is contingent as

the availability of adequate findings and appropriate predictable bioassay systems. (Faransworth et al., 1983)[8]

The liver has an enormous task of maintaining the body's metabolic homeostasis. This includes, the processing of dietary amino acids, carbohydrates, lipids, and vitamins; synthesis of serum proteins; and detoxification and excretion into bile of endogenous waste products and pollutant xenobiotics. (Robbins, 1998)[9]

Liver is the largest organ of the body enclosed within the right lower rib cage beneath the diaphragm. It is almost completely covered by visceral peritoneum and a dense irregular connective tissue layer that lies deep to the peritoneum. Liver is divided in two principle lobes, a large right lobe and a smaller left lobe separated by falciform ligament. The right lobe is considered by many anatomists to include an inferior quadrate lobe and a posterior quadrate lobe. (Tortora and Grabowski, 2002)[10]

The inflammation and damage of parenchyma of liver is known as cirrhosis of liver. This may results in degeneration of hepatic cells and dysfunction of liver. Cirrhosis is a diffuse, chronic, necrotic (degenerative) liver disorder characterized by progressive hepatocyte injury followed by regeneration and fibrosis leading to disorganization of lobular architecture, pseudo lobule formation and acquired vascular malformation. (Ghadi, 2000)[11]

Objectives

The aim of the research is to find out new hepatoprotective drugs from indigenous plants which are potent and nontoxic agents. These plants are traditional medicinal plants. Their chemical characterization, mode of action and toxicity studies are yet to be established. Present study deals with the phytochemical screening and pharmacological evaluation of some medicinal plants (leaves of *Adina cordifolia*, *Sida veronicaefolia* and stem bark of *Nyctanthes arbortristis*) with special reference to hepatoprotective activity in different animal models.

Research Methodology

Research Methodology refers the discussion regarding the specific methods chosen and used in a research paper. This discussion also encompasses the theoretical concepts that further provide information about the methods selection and application. In order to apply the analytical and descriptive methods to the research a close reading and detailed analysis of secondary sources available. It is significant to get other perceptions to elaborate the textual analysis and this would need close reading analysis of few secondary materials.

Result and Discussion

Alcohol toxicity may be associated with increased oxidative stress and free radical associated injury. Generation of oxygen metabolites such as super oxide (O_2^-) hydrogen peroxide (H_2O_2) and hydroxyl radicals (OH^-) is believed to be important in the pathogenesis of alcoholic liver injury. [12-14]

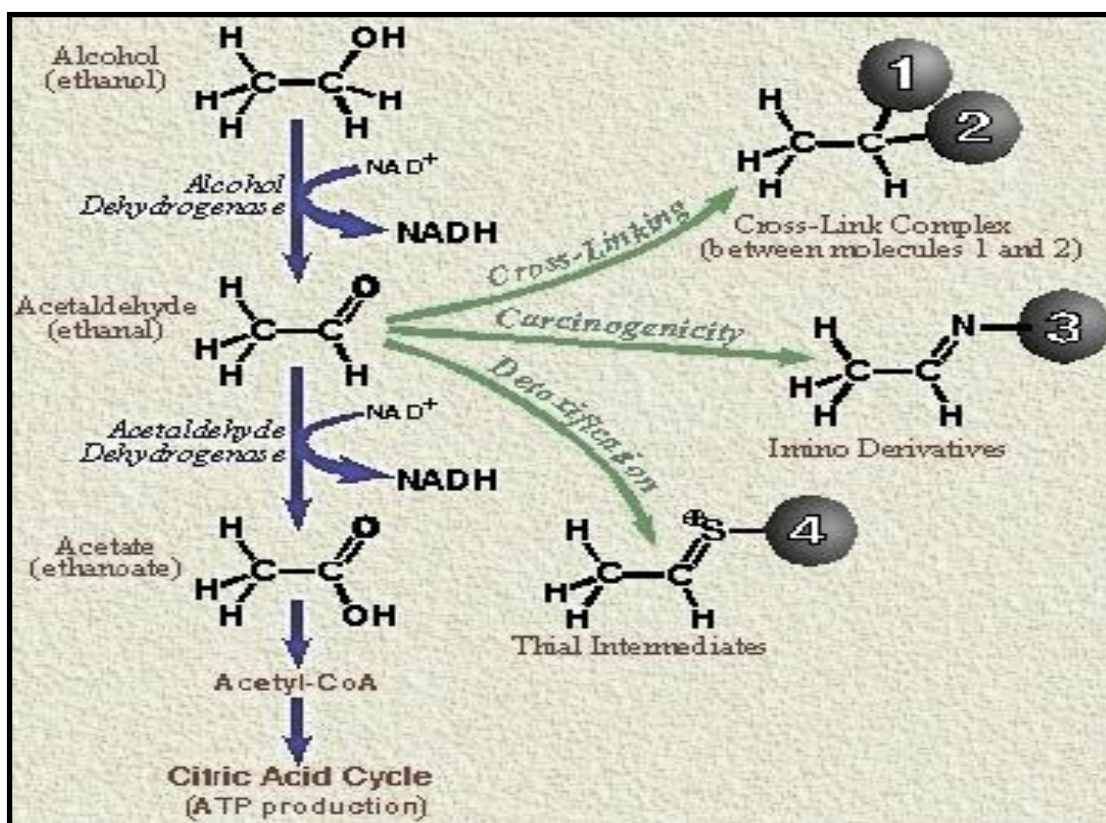


Fig. 1 Ethanol induced hepatic necrosis

Table 1 : Effect of selected plant extracts on functional parameters in CCl_4 induced hepatotoxic rats.

S.No.	Treatment/ Dose	Onset of sleep(Sec.)	Duration of sleep (Min.)
1	Normal	170.0 ± 2.06	110.2 ± 2.80
2	Induced (CCl_4)	80.2 ± 5.28*	235.8 ± 6.80*
3	Standard (Silymarin)	156.2 ± 3.48***	149.7 ± 2.49***

4	AEAC (500mg/kg)	110.2 ± 4.48**	210.8 ± 5.88**
5	AQEAC (500mg/kg)	130.8 ± 4.76***	192.2 ± 5.76***
6	EESV(500mg/kg)	118.8 ± 5.86**	199.3 ± 5.87**
7	AQESV (500mg/kg)	150.2 ± 5.42***	170.7 ± 3.98***
8	AENA (500mg/kg)	125.6 ± 5.26**	202.9 ± 4.89**
9	AQENA (500mg/kg)	141.8 ± 4.81***	180.3 ± 4.75***

Values are mean ± SEM, n = 6. (One way ANOVA Followed by Dunnette multiple comparisons test). Statistically significance of ** P<0.01, *** P<0.001, when compared with CCl4 induced group and * P<0.05, when compared with normal group. [14-17]

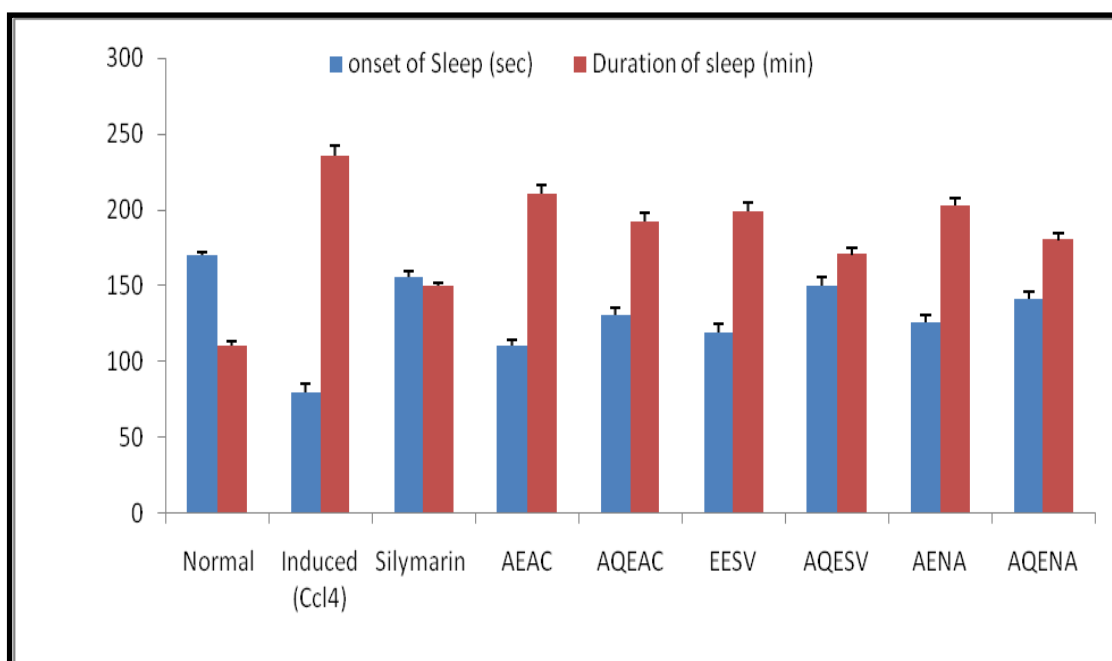


Figure 1: Effect of selected plant extracts on functional parameters in CCl4 induced hepatotoxic rats

Table 2: Effect of selected plant extracts on functional parameters in paracetamol induced hepatotoxic rats.

S.No.	Treatment/ Dose	Onset of sleep (Sec)	Duration of sleep (Min)
1	Normal	170.0 ± 2.06	110.2 ± 2.80
2	Induced (Paracetamol)	98.4 ± 6.28*	255.8 ± 5.90*
3	Standard (Silymarin)	176.6 ± 4.48***	140.2 ± 4.49***
4	AEAC (500mg/kg)	121.5 ± 4.80**	228.2 ± 5.02**
5	AQEAC (500mg/kg)	140.8 ± 5.76***	199.2 ± 5.96***
6	EESV(500mg/kg)	138.8 ± 5.86**	211.3 ± 4.87**
7	AQESV (500mg/kg)	162.6 ± 4.42***	184.7 ± 4.52***
8	AENA (500mg/kg)	135.1 ± 6.20**	202.9 ± 5.99**
9	AQENA (500mg/kg)	149.8 ± 5.81***	192.3 ± 4.55***

Thiopentone sodium (40 mg/kg, i.p) induced sleep in experimental animals in all groups. It was found that rats treated with paracetamol showed a marked decrease in onset of sleep (sec) and increase the duration of sleeping time (min) when compared against normal control group. Onset of sleep had significantly increased in the rats pretreated with AEAC, AQEAC, EESV, AQESV, AENA, AQENA (500 mg/kg, po) extracts and silymarin treated rats while the duration of sleeping time had significantly decreased for the same, when compared to paracetamol treated group. [18-19]

Values are mean ± SEM, n = 6. (One way ANOVA Followed by Dunnett multiple comparisons test). Statistically significance of ** P<0.01, *** P<0.001, when compared with Paracetamol induced group and * P<0.05, when compared with normal group. [20]

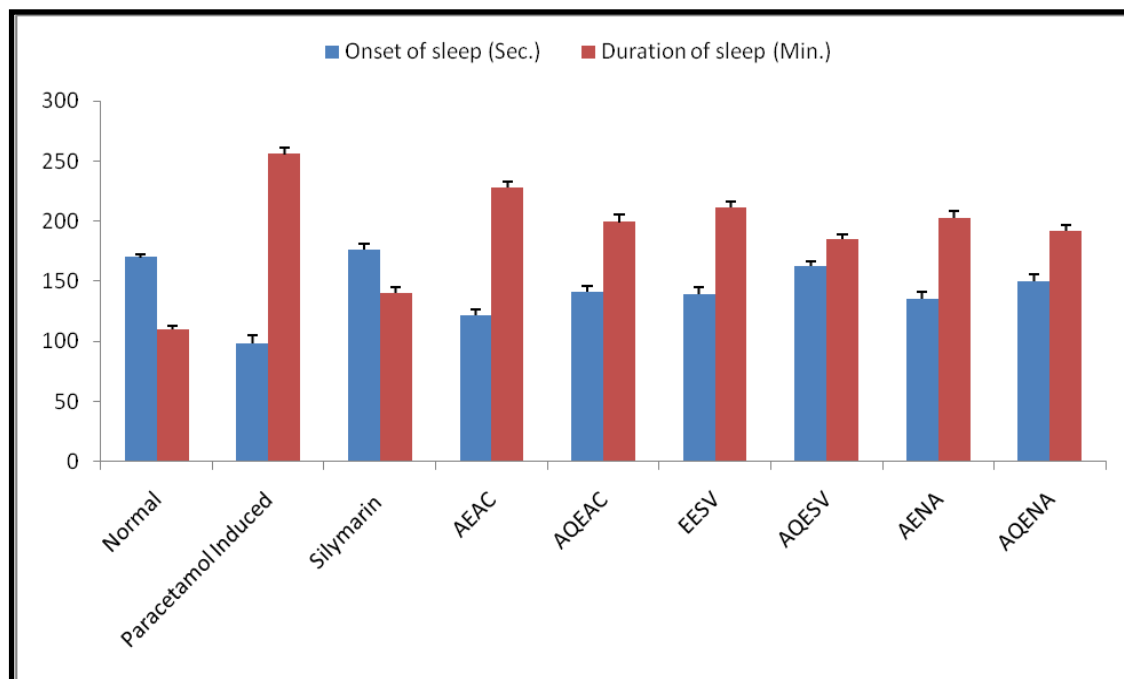


Fig. 2 Effect of selected plant extracts on functional parameters in paracetamol induced hepatotoxic rats

Conclusion

Liver participates in a variety of metabolic activities perhaps by virtue of presence of number of enzymes and thus may self expose too many hepatotoxicants, chemicals and drugs which could injure it. Every year 18,000 people are reported to die due to liver cirrhosis caused by hepatitis. Traditional systems of medicine, especially Ayurveda contains number of preparations for treating liver and GIT disorders. Modern medicine provides only symptomatic relief with side effects in the treatment of liver disease. Herbal drugs, used in Indian system of medicine are however claimed to be effective and safe in such ailments. Polyherbal preparations are considered safe and effective products consisting of multiple extracts active principles from medicinal plants with additive or synergistic benefit. In hepatotoxicant groups, hepatotoxin gets converted into radicals in liver by action of enzymes and these attacks the unsaturated fatty acids of membranes in presence of oxygen to give lipid peroxides consequently. The functional integrity of hepatic mitochondria is altered, leading to liver damage.

References

1. Tang X, Gao J, Wang Y, Fan Y, Xu LZ, Zhao XN, Xu Q and Qian ZM. (2006). Effective protection of Terminalia catappa L. Leaves from damage induced by carbon tetrachloride in liver mitochondria. *J Nutr Biochem*, 17(3): 177-182.

2. Tasduq SA, Kaisar P, Gupta DK, Kapahi BK, Maheshwari HS, Jyotsna S and Johri RK. (2005). Protective effect of a 50% hydroalcoholic fruit extract of *Emblica officinalis* against anti tuberculosis drugs induced liver toxicity. *Phytother Res*, 19(3): 193 197.
3. Tuntiwachwuttikul P, Rayanil K and Taylor WC. (2003). Chemical Constituents from the Flowers of *Nyctanthes arbor tristis*. *ScienceAsia*, 29, 21 30.
4. Vadivu R, Krithika A, Biplab C, Dedeepya P, Shoeb N and Lakshmi KS. (2008). Evaluation of hepatoprotective activity of the fruits of *Coccinia grandis* Linn. *I J Health Res*, 1(3): 163 168.
5. Sembulingam K and Sembulingam P. (2004). *Liver and Gallbladder: Essentials of Medical Physiology*. 3rd ed. New Delhi: Jaypee brother's medical publishers, 200 1.
6. Kuruvilla A. (1999). Herbal formulations as pharmacotherapeutic agents. *J Ethnopharmacol.*, 66(3):355 61.
7. Boots AW, Haenen GR and Bast A. (2008). Health effects of quercetin: from antioxidant to nutraceutical. *Eur J Pharmacol*, 585: 325-337.
8. Ghadi PS. (2000). *Disorders of Liver: Pathophysiology for pharmacy*. 2nd ed. Nashik: Career publications, 106 8 and 125 30.
9. Shapiro Haim, Ashkenazi Michal, Weizman Nir, Shahmurov Mark Hussein Aeed and Bruck Rafael. (2006). Curcumin ameliorates acute ethanol induced hepatotoxicity. *J of Gastroenterol and Hepato*, 21, 358 366.
10. Rosa MP, Gutiérrez and Rosario VS. (2009). Hepatoprotective and inhibition of oxidative stress of *Prostechea michuacana*. *Rec Nat Prod*, 3(1): 46 51.
11. Roy CK, Kamath JV, Asad M. (2006). Hepatoprotective activity of *Psidium guajava* Linn. leaf extract. *Indian. J Exp Bio*, 44(4): 305 311.
12. Porchezian E, Ansari SH. (2000). Effect of liquid extract from fresh *Abutilon indicum* leaves and *Alliumcepa* bulbs on Paracetamol and Carbontetrachloride induced hepatotoxicity. *Pharmazie*. 55(9) : 702 3.
13. Pramyothin P, Chirdchupunsare H, Rungsipipat A and Chaichantipyuth C. (2005). Hepatoprotective activity of *Thunbergia laurifolia* Linn extract in rats treated with ethanol: In vitro and In vivo studies. *J Ethnopharmacol.*, 102(3): 408 411.
14. Padma W, Suja V, Shyamala DCS and Prema. (1998). Hepatoprotective effect of Liv 52 on antitubercular drug induced hepatotoxicity in rats. *Fitoterapia*, 69(6): 520 22.
15. Pandey M. (2009). *Sida Veronicaefolia* as a Source of Natural Antioxidant. *International Journal of Pharmaceutical Sciences and Drug Research*, 1(3): 180 182.

16. Kokate CK and Gokhale SB. (2008). Practical Pharmacognosy (12th ed). In: Physical and Chemical testes for evaluation of crude drugs, Nirali Prakashan, Pune, India, 14 19, 107 111 and 121.
17. Kokate CK, Purohit AP and Gokhale SB. (2005). Pharmacognosy (31st ed). In: Traditional and Alternative System of Medicin, Nirali Prakshan, Pune, India, 4 5.
18. Harshmohan. (2002). The liver, biliary tract and exocrine pancreas. In: Text book of pathology, 4th Ed, Jaypee Brothers Medical Publishers (P) Ltd. New Delhi. 22 4, 569 630.
19. Hemieda FA, Abdel Hady el SK and Elnga MA. (2005). Biochemical and histological studies on H2 receptor antagonist ranitidine induced hepatotoxicity in rats. Ind J Exp Biol., 43(9): 782 5.
20. Festa F, Aglitti T, Duranti G, Ricordy R, Perticone P and Cozzi R. (2001). Strong antioxidant activity of ellagic acid in mammalian cells in vitro revealed by the comet assay. Anticancer Res,1,21:3903-3908.



Research paper

Design, synthesis, and biological evaluation of novel quinoline derivatives as small molecule mutant EGFR inhibitors targeting resistance in NSCLC: *In vitro* screening and ADME predictions

Ramakant A. Kardile^a, Aniket P. Sarkate^b, Deepak K. Lokwani^c, Shailee V. Tiwari^d,
Rajaram Azad^e, Shankar R. Thopate^{a,*}

^a Department of Chemistry, Radhabai Kale Mahila Mahavidyalaya, Ahmednagar, 414001, Maharashtra, India

^b Department of Chemical Technology, Dr. Babasaheb Ambedkar Marathwada University, Aurangabad, 431004, Maharashtra, India

^c Rajarshi Shahu College of Pharmacy, Buldhana, 443001, Maharashtra, India

^d Shri Ramkrishna Paramhans College of Pharmacy, Hasnapur, Parbhani, 431401, Maharashtra, India

^e Department of Animal Biology, University of Hyderabad, Hyderabad, 500046, India



ARTICLE INFO

Keywords:

Allosteric site
NSCLC
Fourth generation EGFR inhibitors
Molecular docking
ADME study
Molecular dynamics simulations

ABSTRACT

Here in, we report the design, synthesis and *in vitro* anticancer activity of a novel series of 24 quinoline analogues of substituted amide and sulphonamide derivatives. The anticancer activity of the synthesised compounds was evaluated against the HCC827, H1975 (L858R/T790 M), A549 (WT EGFR), A-549 and BEAS-2B cell lines. The majority of quinoline compounds demonstrated a significant cytotoxic effect. Compound **21** was found to be the most potent, with IC₅₀ values of 0.010 μM, 0.21 μM, 0.99 μM and 2.99 μM as compared to Osimertinib with IC₅₀ values with of 0.0042 μM, 0.04 μM, 0.92 μM and 2.67 μM. Compound **21** exhibited promising inhibitory enzymatic activity against the EGFR L858R/T790 M with IC₅₀ value of 138 nM, comparable to Osimertinib's 110 nM. Employing a Western blot assay on the phosphorylation of EGFR and the signalling pathways transmission in HCC827 cells, the anticancer activity of the synthesised compounds **18** and **21** was evaluated in terms of its mechanism of action. All the compounds were subjected to a comparative molecular docking study against various EGFR enzyme types, including the wild-type (PDB: 4I23) and T790 M mutant (PDB: 2JIV) enzymes. Furthermore, compounds were examined at the allosteric binding site of the EGFR enzyme with the L858R/T790 M/C797S mutation (PDB ID: 5D41). The MD simulation study was also performed for EGFR-compound **21** complex which indicates the stability compound **21** in both ATP and allosteric site of enzyme. Further, *in silico* ADME prediction studies of all derivatives were found promising, signifying the drug like properties.

1. Introduction

Non-small-cell lung cancer, often known as NSCLC, is the most lethal form of the disease and the main cause of cancer-related mortality on a global scale. It is estimated that 12.9% of all newly diagnosed cases of cancer are lung cancer, making it the most prevalent form of the disease and the leading cause of cancer-related deaths. Approximately 85% of lung cancers are NSCLC [1,2] and life-threatening malignancy worldwide, accounting for around one-third of all cancer-related deaths each year. It has been stated that the median age at which lung cancer is diagnosed is between 63 and 70 years, and that NSCLC accounts for 85% of lung cancer cases in individuals over the age of 65. Although the

progression of NSCLC is slower than that of small cell lung cancer, the disease has frequently metastasized by the time it is detected in other parts of the body. Therefore, identification and therapy at an early stage are crucial [3]. Consequently, people with early-stage disease have surgery or radiation, and patients with more advanced disease are frequently treated initially with systemic chemotherapy, immunotherapy, or targeted therapy. The standard treatment consists of cytotoxic chemotherapy, which is nonspecific and nonselective, and it only produces a moderate improvement in the patient's chances of survival while causing severe harm to the patient. At first, targeted medications are only successful in treating a specific, limited subset of patients. However, over time, most patients develop resistance to additional

* Corresponding author.

E-mail address: srthopate@gmail.com (S.R. Thopate).

<https://doi.org/10.1016/j.ejmech.2022.114889>

Received 22 August 2022; Received in revised form 21 October 2022; Accepted 24 October 2022

Available online 29 October 2022

0223-5234/© 2022 Elsevier Masson SAS. All rights reserved.

therapy. The existing treatments for NSCLC have limitations in their efficacy as well as safety, which highlights the necessity of developing new medicines that have enhanced efficacy as well as safety profiles. The first-line therapy regimen and the most effective treatment for NSCLC with Epidermal Growth Factor Receptor (EGFR) -activating mutations is EGFR-tyrosine kinase inhibitors (EGFR-TKIs) [4–6].

1.1. Mechanism of EGFR-TKIs resistance in NSCLC

In NSCLC, the development of primary and secondary resistance to EGFR-TKIs is attributable to many causes [7,8]. An Exon 20 insertion is a unique EGFR mutation that occurs in 4–10% of patients with NSCLC. In NSCLC, this can lead to resistance both to reversible and irreversible

EGFR-TKIs. Several new mutations in EGFR associated with secondary resistance to EGFR-TKIs have also been found. However, 50–60% of NSCLC patients who develop acquired resistance to first- and second-generation EGFR-TKIs due to a gatekeeper T790 M mutation in the ATP-binding gap of EGFR. Although the T790 M mutation induces steric hindrance in the binding of TKIs to EGFR, it decreases the affinity of TKIs while increasing the affinity of ATP for EGFR. This prevents EGFR suppression by first- and second-generation EGFR-TKIs, extending the survival of mutant NSCLC cells. In addition, Src, YAP1, STAT3, K-RAS activating mutations, C-Met amplification, HGF overexpression, HER2 amplification, loss of PTEN, and PIK3CA mutations are identified as processes that contribute to primary and acquired EGFR-TKI resistance in NSCLC patients. In order to circumvent the T790 M

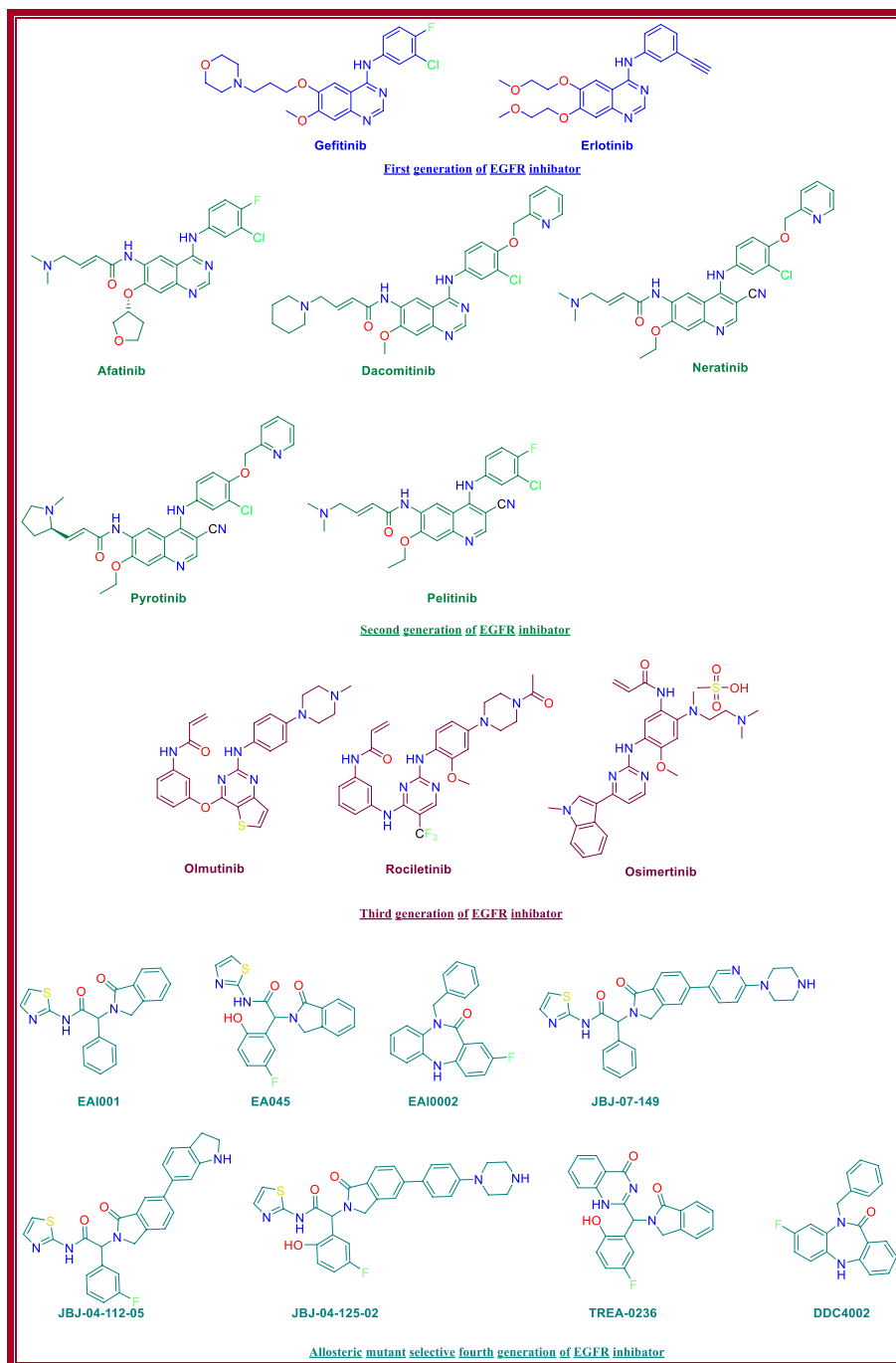


Fig. 1. Previously reported first, second, third and fourth generation EGFR inhibitors.

mutation-mediated resistance to first- and second-generation EGFR-TKIs in NSCLC, third-generation EGFR-TKIs have been created. Third-generation EGFR-TKIs can covalently bind to a cysteine residue at position 797 of the ATP-binding pocket of the EGFR-tyrosine kinase domain. Patients treated with EGFR-TKIs of the third generation acquire heterogeneous resistance to these medications over time. Resistance to third-generation EGFR-TKIs is mostly due to the appearance of a tertiary point mutation at the C797 site (C797S) in the ATP binding cleft. Loss of the secondary T790 M mutation is another acknowledged reason for Osimertinib's ineffectiveness [9–11].

1.2. Current treatment/therapies for NSCLC and its limitations

EGFR were discovered by Stanley Cohen of Vanderbilt University in the United States, who was awarded the Nobel Prize. The protein kinase (PK) family, of which EGFR is a member, is widely represented in human tissues. Despite the initial efficacy of first- to third-generation EGFR-TKIs, EGFR mutation-mediated resistance renders these drugs ineffective very quickly. To overcome resistance, allosteric mutant-selective fourth-generation EGFR inhibitors appear to be a viable treatment approach. These EGFR inhibitors are less effective as a single agent but when combined with standard chemo- or immunotherapeutic agents, they have a synergistic effect. EGFR is a cell surface receptor tyrosine kinase (RTK) that is a member of the ErbB or HER/ErbB family. It includes an extracellular cysteine-rich ligand-binding domain, a tyrosine kinase (TK) site with a cytoplasmic domain, and autophosphorylation sites with a C-terminal tail. EGFR is involved in various cellular signaling pathways that regulate cell survival and proliferation, migration, angiogenesis, and cell death. But mutations in its catalytic domain increase kinase activity and make it less dependent on ligands. This makes malignancies like NSCLC appear and get worse.

1.3. First generation EGFR-TKI inhibitors

In 2003 and 2004, the US-FDA authorised Gefitinib and Erlotinib (Fig. 1) were the first-generation EGFR tyrosine kinase inhibitors (TKIs). In NSCLC patients, they show significant and effective therapeutic advantages against activating mutations L858R (exon 21) and exon 19 deletion. Both activated mutations are competitive inhibitors of the ATP site of the tyrosine kinase domain of EGFR, with higher binding to mutant EGFR than to the wild-type (WT) receptor. In certain cases, however, treatment resistance can rapidly develop due to a subsequent mutation of T790 M near the ATP-binding region and proximal to the adenosine moiety of ATP in EGFR-mutant NSCLC. This mutation (T790 M) increases the mutant receptor's affinity for ATP. The clinical efficacy of EGFR inhibitors after long-term usage is the most difficult constraint, and this is a new problem in cancer therapy. Although the EGFR T790 M mutation is present in approximately 60% of patients with EGFR-mutant NSCLC, first-generation EGFR TKIs become less effective in all of these patients [12–30].

1.4. Second generation EGFR-TKI inhibitors

The aniline quinazoline derivatives, especially afatinib, dacomitinib, and neratinib (Fig. 1) were developed to address the shortcomings of first-generation medications. Later, in 2010 or 2011, the US FDA authorised these medications. According to reports, these medicines are multitarget TK inhibitors for anti-NSCLC therapy. The principal mechanism of action of second-generation medications is irreversibly binding to the kinase domain, which inhibits the mutant EGFR-T790 M enzymatically. The second-generation medications target the inactive region of the kinase domain because they recognise inactive T790 M, wild-type, and numerous other human EGFRs. However, the kinase dimer complex is the only form that the inactive site can recognise. Only when the TK domain has been autophosphorylated does the dimer state occur. One of the limitations of second-generation medications was that EGFR-TKIs

were restricted because they failed to target the monomeric state of the kinase domain and had unacceptable low to maximum tolerable dose and daily dosage side effects, such as skin rash and gastrointestinal disorders. As a result, these therapeutic classes are not entirely appropriate for NSCLC inhibition [12–30].

1.5. Third generation EGFR-TKI inhibitors

In response to these challenges, researchers have developed a new class of third-generation EGFR-TKIs that are more effective, target-selective, and potent than previous generations. These drugs include Rociletinib (CO-1686, AVL-301), Olmutinib, and Osimertinib (Fig. 1) all of which have recently been given the go-ahead for use (Fig. 1) showed that the treatment had a high level of selectivity for carcinogenic mutant EGFR with both the T790 M mutation and had no effect on WT EGFR. They achieve this by forming a covalent link with a cysteine residue that is located at position 797 in the ATP binding pocket of the EGFR-tyrosine kinase domain. Osimertinib is currently the first-line therapy for hitherto untreated advanced EGFR T790 M mutant patients. It was approved by the FDA in 2015 with excellent treatment outcomes and negligible on-target toxicity, and that was one of the reasons why it was approved. In addition, resistance has developed because of novel mutations, in particular the point mutation C797S and the significant loss of the T790 M mutation in the ATP binding loop, which is the most important factor in the development of resistance [12–30].

1.6. Fourth-generation EGFR-TKIs/allosteric EGFR inhibitors

In order to overcome T790 M and C797S mutation-mediated resistance to EGFR-TKIs, it is necessary to identify drugs with binding abilities other than the ATP binding of the EGFR-TK-domain. Current fourth-generation mutant specific allosteric inhibitors could bind to locations other than the ATP-binding pocket of EGFR; therefore, they may be a viable treatment option for EGFR mutant NSCLC. Allosterism is the phenomenon in which the binding of an effector/ligand/molecule to one side of a molecule produces a conformational change in another region of the protein. This finally causes the protein complex to undergo dynamic or shape modifications. When a ligand binds to the allosteric site, it doesn't change the shape of the active site in any way [12–30].

EAI001 and EAI045 (Fig. 1) are two recently developed allosteric EGFR mutant-selective drugs. These allosteric drugs can counteract the T790 M mutation-induced increase in ATP affinity and potential decrease in autophosphorylation of T790 M mutant EGFR. EGFR allosteric inhibitor-EAI001 using a pure L858R/T790 M EGFR kinase as a target. The X-ray crystallographic findings confirmed the formation of a selective complex between EAI001 and an allosteric region next to the ATP-binding site of T790M-mutant EGFR.

To enhance the stability, pharmacokinetic, and pharmacodynamic characteristics, scientists have developed and discovered a few additional EGFR allosteric inhibitors based on these compounds. For example, TREA-0236 (Fig. 1) was synthesised by substituting non-hydrolyzable quinazoline-4-one for aminothiazole in the synthesis of EAI045; however, despite having a strong metabolic pathway, TREA-0236 (IC₅₀ = 5.3 mM) was less effective than the parent EAI045 [31–37].

1.7. Combination therapeutic allosteric EGFR inhibitors

The use of allosteric EGFR inhibitors as a mono-therapeutic agent for the treatment of NSCLC may not be as effective in light of current *in vitro* and *in vivo* investigations. Emphasis on allosteric EGFR inhibitors as a combined treatment provides an effective treatment option for NSCLC in this scenario. Cetuximab (10 mg/mL) and EAI045 (10 mg/mL) combinations exhibited synergistic inhibition of EGFR dimerization and an antiproliferative impact (IC₅₀ = 10 nM) in the L858R/T790 M mutant Ba/F3 cells, despite being ineffective when used alone. Furthermore, in

mouse xenograft models with L858R/T790 M or L858R/T790 M/C797S mutant EGFR, oral administration of EAI045 (60 mg/kg/day) in combination with cetuximab (intraperitoneal; 1 mg every other day) results in a significant regression in tumour growth.

1.8. Importance of quinoline as anticancer therapeutics

Quinoline has been one of the most important scaffolds in drug development during the past several decades, particularly in anticancer research. Quinoline is an N-based heterocyclic molecule with biological activity. The presence of nitrogen atoms increases the basicity of quinoline-containing compounds considerably. Several anticancer compounds incorporating the quinoline framework are undergoing clinical testing. Quinoline derivatives exhibit excellent anticancer activities via a variety of mechanisms of action, such as the inhibition of tyrosine kinase, pi3k-pkb inhibitors, inhibitors of epidermal growth factor receptors, mitogen activated protein kinase inhibitors, ALK5 inhibitors, inhibitors of platelet-d, inhibitors of kinase insert domain receptors, nonreceptor tyrosine kinase inhibitors. Anticancer medicines derived from quinolines include the protein kinase inhibitors bosutinib, lenvatinib, and cabozantinib.

Quinoline derivatives have demonstrated potential in a variety of cancer cell lines, including those from the breast, colon, lung, colorectal, renal, etc. [38–51].

Allosteric strategy for overcoming C797S EGFR resistance. The crystalline structures (PDB codes 3IKA and 4ZAU) of the EGFR T790 M coding region in association with WZ4002 (Fig. 2) and AZD9291 revealed that a "U-shaped" configuration comprising a pyrimidine core, along with an aniline ring harbouring a hydrophilic group and an acrylamide moiety, is favourable for EGFR binding. Similarly, we investigated the binding relationship between allosteric inhibitors and EAI045 using the PDB ID 5D41.105. EAI045 was an allosteric, non-ATP selective inhibitor of the mutant T790 M EGFR with a Y-shaped structure, as depicted in Fig. 1. Focusing on these compounds and analysing their design techniques (U to Y shaped configuration) as well as their usual anticancer activity can provide valuable hints for the development of more effective EGFR T790 M inhibitors. Compound 21 was created with a U-shaped structure, resulting in enhanced anticancer action (Fig. 2).

We present efficient synthetic procedures for the preparation of novel amide and sulphonamide quinoline derivatives that act as potent allosteric site EGFR inhibitors and, if used in combination therapy with existing clinical drugs, may be better therapeutics in the future. These procedures were developed through this study as well as others.

2. Results and discussion

2.1. Rational design of EGFR inhibitor

The previous work was employed as influence for the development of

the novel quinoline-based EGFR inhibitor that was designed in this research. The multiple small molecule inhibitors of the EGFR kinase are currently several scaffolds, such as quinazolines, pyridopyrimidines, benzamides, indolinones, and pyrrolotriazines, as we have previously reported. The screening of these scaffolds indicates that the 4-anilinoquinazoline derivatives (gefitinib, erlotinib, and lapatinib) are demonstrating a more potent range in enzymatic assays. These derivatives are now employed in the treatment of medical conditions. The crystal structure and the biological evidence indicate that the nitrogen atom in the third position is an important component of quinazoline inhibitors and plays an important role in activity. This is scenario since that the nitrogen atom may interact with water molecules, which in turn encourages the drug and the enzyme to interact with one another. The capacity to inhibit the enzyme is significantly diminished if nitrogen atoms are exchanged out for carbon atoms [52].

Wissner et al., did this just to create 4-anilinoquinoline-3-carbonitrile I (Fig. 3), which was one of the first quinoline inventions as an effective EGFR kinase inhibitor (IC₅₀ value of 7.5 nM) with activity comparable to approved 4-anilinoquinazoline series lead molecules. They were doing this by substituting the nitrogen atom with a carbon atom and trying to attach a withdrawing cyano group. Using molecular modelling studies of lead compounds from the market-approved EGFR 4-anilinoquinazoline series, they designed the strategy. They had used hypothesis that the space created by the removal of the water molecule that was attached to Thr830 could accommodate a small group. The same research group reported a second class of EGFR inhibitors, which were derivatives of 4-anilinoquinoline 3-carbonitrile containing various Michael acceptor groups at the C-6 position. These compounds have revealed to be effective anticancer drugs with irreversible EGFR inhibitory activity. This is the molecule identified as pelitinib (Fig. 1) (EKB-569; EGFR IC₅₀ = 0.083 M), and it is responsible for initiating a covalent binding between the HER-2 and the ATP pocket of EGFR (Cys773 or Cys797) and HER-2 (Cys805) and demonstrated encouraging oral and *in vivo* activity, which is now being tested in a clinical phase reviewed to understand [53].

In furthermore, Tsou et al. introduced Neratinib (Fig. 1), an EGFR inhibitor that is more active than pelitinib. Neratinib was approved in 2017 to be used as adjuvant therapy against early-stage HER2/ErbB2-amplified/overexpressed breast cancer patients a novel irreversible EGFR/HER2 tyrosine kinase inhibitor called pyrotinib was developed. This is the fact so long as pyrotinib and neratinib are totally superimposed on one another, the exception of the substituents on the Michael acceptor group. According to *in vitro* study, the high potency of this compound is on par with that of neratinib in its effectiveness in killing HER2 dependent BT474 (breast cancer) and SK-OV-3 (ovarian cancer) cell lines. In moreover, investigations conducted *in vivo* showed that pyrotinib exhibits a high level of selectivity when examined against a variety of kinases. Pyrotinib has recently become the subject of studies for potential treatment in non-small cell lung cancer and HER2-positive gastric cancer.



Fig. 2. Evolution of Fourth generation allosteric binding EGFR kinase inhibitors and activations of new mutations in enzyme like Del19, L858R and C797S were observed along with T790 M.

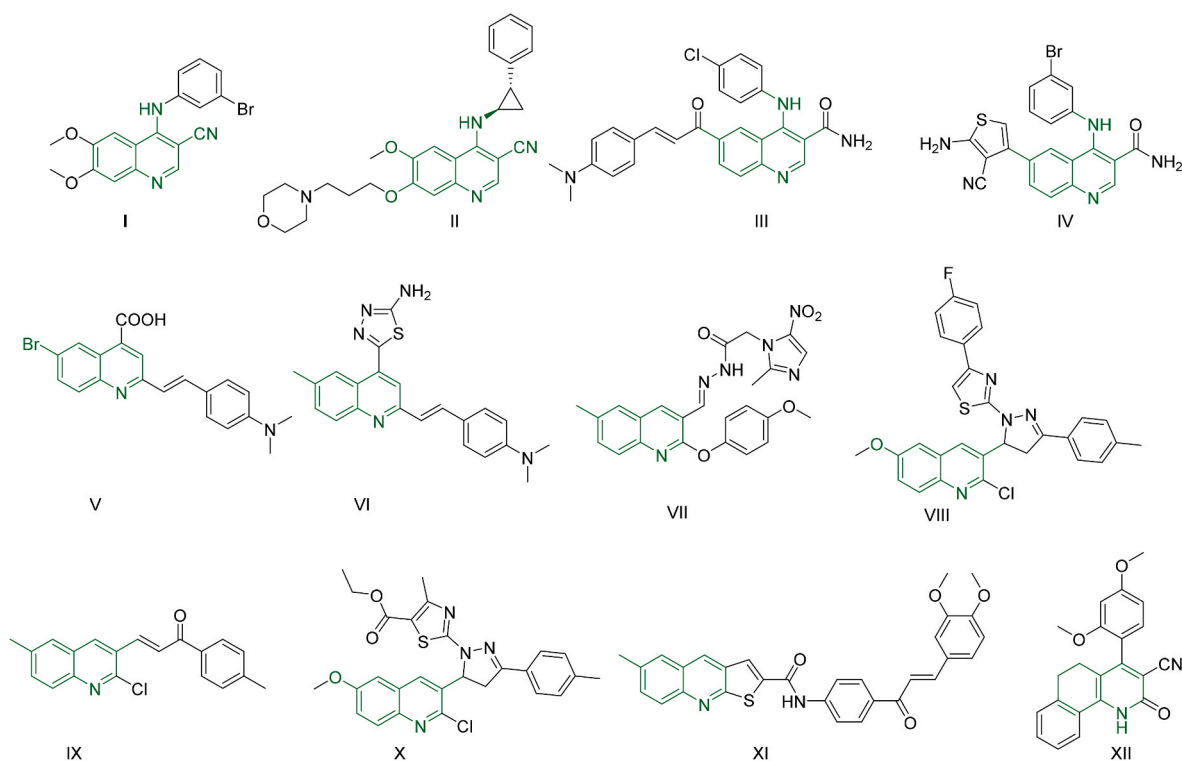


Fig. 3. Reported Quinoline based EGFR inhibitors.

In addition, Pannala et al., successfully synthesised a novel EGFR inhibitory compound II, which (Fig. 3) has a robust inhibition action on EGFR and has an IC_{50} value of 5 nM as a result. Aly et al., developed and synthesised 3-carboxamide derivatives such as III and IV (Fig. 3) that shown promising EGFR inhibitory action (EGFR IC_{50} = 5.283 M and 0.49 M respectively). In addition, El-Sayed et al., investigated new 2-styryl quinolines V and VI (Fig. 3) and discovered that these compounds inhibited EGFR in a way that was beneficial. In 2019, Makawana et al., have synthesised hybrid derivatives of the quinoline scaffold VII (Fig. 3), linking to the heterocyclic ring systems that have the potential to block EGFR function. George et al., describe a new hybrid quinoline moiety that has potent anticancer activity, particularly against the DLD1 cancer cell line and EGFR. This moiety is attached to pyrazoline or pirazolinythiazole heterocycles VIII, IX, and X (Fig. 3) and has a pyrazoline or pirazolinythiazole heterocycle attached to it. Abdelbaset et al., developed quinoline-2-carboxamide-chalcone derivatives XI (Fig. 3) that demonstrated potential for use against cancer cell lines that were put to the test (IC_{50} values in the range of 0.9–1.2 M and EGFR IC_{50} = 0.5 M). After that, Abdelsalam and her colleagues published a report on the development of novel benzo[h]quinoline derivatives XII (Fig. 3) that exhibited promising anticancer activity against the MCF-7 cancer cell line [54–58].

It was demonstrated in the study that was referenced earlier that all of these quinoline scaffolds interact with one another by vying with ATP for binding at the catalytic domain of EGFR-TK while also taking into account the essential pharmacophoric features required for evaluating EGFR-TK inhibition. The adenine-binding site is occupied by quinoline or one of several different modified quinoline hybrid analogues with a central heteroaromatic ring, and the 3-position carbon atom attached group such as cyano, carboxamide, or ester substitution for H-bond formation with the ATP-binding site, the hydrophobic head (region I), and the hydrophobic tail (region II).

We planned, developed, and synthesised new modified quinoline scaffolds by basing them on the findings that were found in the relevant literature. As a result, we have developed new anticancer EGFR-TKI compounds with a central hetero-core quinoline ring scaffold, which is

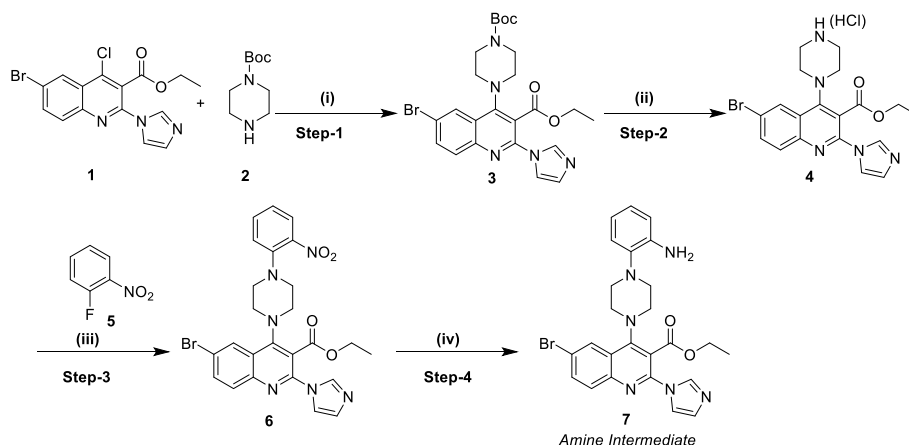
comparable to the already potent EGFR-TKI 4-anilinoquinoline series target. This ring occupies the adenine binding area (Figs. 1 and 3). The carbon atom in the 3-position that was attached to a cyano or amide (carboxylic) group was replaced with an ethyl ester so that an H-bond could be formed with the ATP-binding site. Additionally, the carbon atom in the 4-position, which acted as a hydrophobic head, was replaced with a hydrophobic piperazine linker that featured aromatic amine coupling with various aliphatic and heterocyclic aromatic moieties (occupying the hydrophobic binding region I). To further improve the hydrophilic area, in addition to the 2-position, the more polar and versatile biologically active imidazole moiety was inserted. This was done in order to achieve the desired effect. Because bromine was inserted into the 6-position as a halogen group, it functions as a hydrophobic tail (occupies the hydrophobic binding region II).

2.2. Chemistry

The synthesis of compounds with quinoline substitution amine intermediate ethyl 4-(4-(2-aminophenyl) piperazin-1-yl)-6-bromo-2-(1H-imidazole-1-yl) quinoline-3-carboxylate (3–7) were depicted in Scheme 1.

Preparation of ethyl 6-bromo-4-(4-(tert-butoxycarbonyl) piperazin-1-yl)-2-(1H-imidazole-1-yl) quinoline-3-carboxylate 3 from Refs. [59,60]. Ethyl 6-bromo-4-chloro-2-(1H-imidazole-1-yl) quinoline-3-carboxylate 1 intermediate and commercially available Boc protected piperazine 2 in simple displacement reaction by using DIPEA. Deprotection of selectively Boc group using acidic condition like 4 M HCl in 1,4 dioxane at 0 °C to r.t for 4 h to gave requisite HCl salt of ethyl 6-bromo-2-(1H-imidazole-1-yl)-4-(piperazin-1-yl)quinoline-3-carboxylate 4 which was used for next step without purification [61]. N-alkylation carried out by fluoro nitro benzene and fluoro group displaced by using K_2CO_3 as a base in DMF at 80 °C for 8 h to obtained nitro compound 6 with moderate yield 84.7% [62]. Finally, the reduction of nitro to amine by using Fe metal in NH_4Cl in $EtOH:H_2O$ at 80 °C for 2 h to obtained prime scaffold of amine intermediate 7 with good yield 85.1% as brown solid.

The synthesis of compounds with quinoline substitution sulphonamide derivative of ethyl 4-(4-(2-aminophenyl) piperazin-1-yl)-6-bromo-



Scheme-1. Synthesis of compounds with quinoline substitution amine intermediates (3–7).

^a**Reaction conditions:** (i) 1 (1 eq), 2 (1.2 eq), DIPEA (2 eq), DMSO, 80 °C, 8 h, 86.9%; (ii) 3 (1 eq), 4 M HCl in 1,4 dioxane, r.t., 4 h, 96.1%; (iii) 4 (1 eq), 5 (1.01 eq), K₂CO₃ (2 eq), DMF, 80 °C, 8 h, 84.7%; (iv) 6 (1 eq), Fe powder (2 eq), NH₄Cl (2 eq), EtOH: H₂O (4:1), 80 °C, 2 h, 85.1%.

2-(1H-imidazole-1-yl) quinoline-3-carboxylate (**9–21**) were depicted in [Scheme 2](#).

Compounds **9–21** with moderate yields (60–90%) were prepared by reaction between amine intermediate **7** and different sulphonyl chlorides **8** by using pyridine as a base in acetonitrile at room temperature for 6 h to give the requisite desired sulphonamide derivatives [63].

The synthesis of compounds with quinoline substitution amide derivative of ethyl 4-(4-(2-aminophenyl) piperazin-1-yl)-6-bromo-2-(1H-imidazole-1-yl) quinoline-3-carboxylate (**23–29**) was depicted in [Scheme 3](#).

Compounds **23–29** with moderate yields ~70–90% was prepared by coupling reaction between amine intermediate **7** and different acids **22** by using coupling agent HATU and DIPEA as base in dry DMF at room temperature to requisite desired amide derivatives [62,64].

2.3. Biological activity

2.3.1. In vitro anticancer activity

To assess the efficiency of EGFR inhibitory activity, selected 24 compounds were examined *in vitro* against the HCC827 cell line, harbouring an EGFR-activating mutation (EGFR Del E746-A750), the gefitinib-resistant non-small cell lung cancer NSCLC cell H1975 possessing L858R/T790 M mutant EGFR, the A549 over-expressing wild-

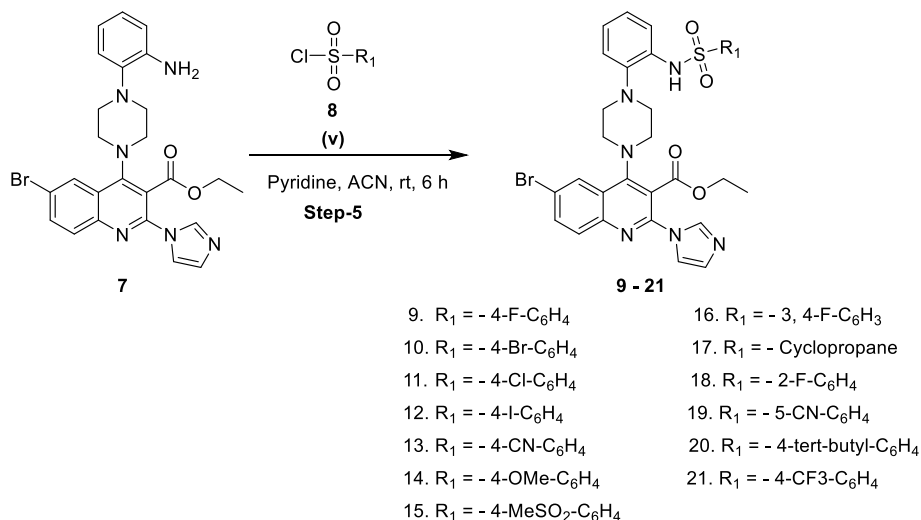
type EGFR (WT-EGFR) and A549 (normal lung cancer cell lines). BEAS-2B normal lung cell lines were also used to check the selectivity of the synthesised compounds on normal cell lines.

The MTT assay was used to screen the anticancer activity against the selected cancer cell lines. Osimertinib was used as a standard drug. The values of the results are presented in the form of IC₅₀ values as shown in [Table 1](#).

A total of twenty-four compounds were synthesised. The structural modification was made as such to study in detail the effect of substituents on the anticancer activity. Basically, two main types of series were synthesised. From compound **9** to **21**, the synthesised derivatives can be considered as sulfonamide and quinoline derivatives. Compounds from **23** to **29** can be considered as amide and quinoline derivatives.

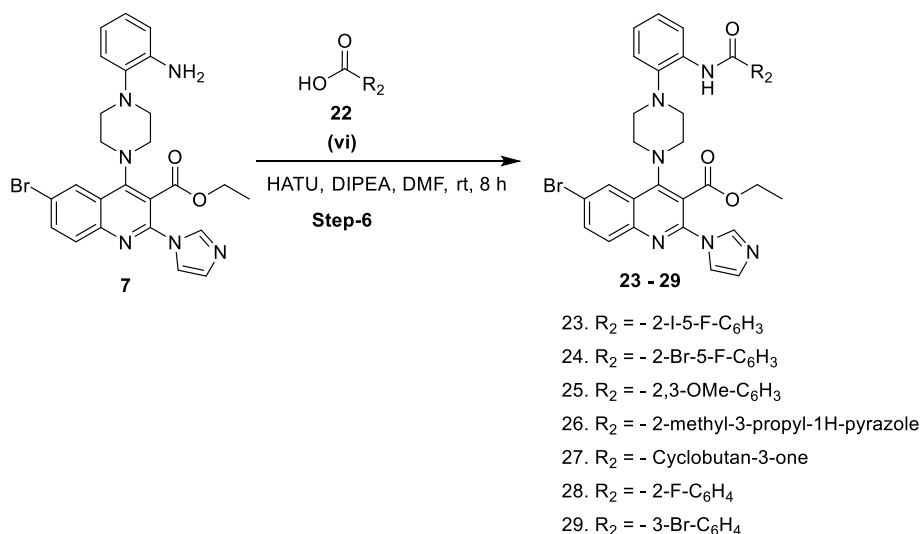
The synthesised derivative **21** was found to be potent with IC₅₀ values of 0.010 μM, 0.21 μM, 0.99 μM and 2.99 μM against HCC827 (EGFR Del E746-A750), NCI-H1975 (EGFR L858R/T790 M), A549/ATCC (WT EGFR) and A549 respectively. The synthesised derivative **27** was found to be potent against NCI-H1975 (EGFR L858R/T790 M) with an IC₅₀ value of 0.11 μM.

The most active synthesised compounds **9**, **16** and **21** were also evaluated against BEAS-2B normal lung cell lines. The results of the evaluation as reported in [Table 1](#). [Table 1](#) reports that the most active synthesised compounds **9**, **16** and **21** had shown the selectivity towards



Scheme-2. Synthesis of compounds with quinoline substitution sulphonamide derivatives of amine (**9–21**).

^a**Reaction conditions:** (vi) 7 (1 eq), 8 (1.2 eq), pyridine (2 eq), CH₃CN, r.t., 2 h, ~60–90%.



Scheme-3. Synthesis of compounds with quinoline substitution amide derivatives of amine (**23–29**).

Reaction conditions: (vi) **7** (1 eq), **22** (1.5 eq), HATU (1.5 eq), DIPEA (2 eq), CH_3CN , r.t., 8 h, ~70–90%

the cancer cell lines when compared with the normal cell lines.

The result of *in vitro* anticancer activity data helped us in proposing the structure activity data of the synthesised twenty-four compounds. Overall, when compared, the compounds of the sulfonamide series were found to be more active than those of the amide series against the selected cancer cell lines, except for compound **27**, which was found to be more active against NCI-H1975 (EGFR L858R/T790 M).

In the sulfonamide series, the derivatives in which the phenyl ring was substituted by the "F" group (**9**, **16** and **18**) were found to be more active than those of other derivatives. Similarly, in the amide series, the derivatives in which the phenyl ring was substituted by "halogen" (**23**, **24**, **28** and **29**) were found to be more active than those of other derivatives.

In the sulfonamide series, the derivatives in which the phenyl ring was substituted by the "CN" group (**13** and **19**) were also found to have good anticancer activity. From activity data, we predict the substitution of the phenyl ring by the electron withdrawing group (**9**, **10**, **11**, **12**, **13**, **14**, **16**, **18**, **19**, **21**, **23**, **24**, **28** and **29**) favours the activity. Substitution of the phenyl ring by the electron donating group leads to less active compounds (**6**, **7** and **20**).

2.3.2. *In vitro* enzymatic activity assay

The synthesised compounds **9**, **16**, **18** and **21** were screened to check their inhibitory enzymatic activity against EGFR L858R/T790 M *in vitro*. The standard drug used was Osimertinib in this process. The results are as represented in Table 2. According to the results obtained, it can be observed that the synthesised derivative **21** has shown good inhibition against the EGFR with an IC_{50} value of 138 nM.

2.3.3. Western blot assay

To study the mechanism of the action of the anticancer activity of the synthesised compounds, **18** and **21** were tested using a Western blot assay on the phosphorylation of EGFR and the downstream signalling transduction in HCC827 cells. HCC827 cells were treated with the synthesised compounds **18** and **21** using various concentrations such as 1.00, 0.10 and 0.01 μM for each compound. The results of the activity are as shown in Fig. 4.

The abnormal over expression or activation of AKT has been observed in many cancers and is associated with increased cancer cell proliferation and survival. Therefore, targeting AKT could provide an important approach for cancer prevention and therapy. We, in this test, evaluated phosphorylation of Akt by our synthesised compounds **18** and **21** using various concentrations such as 1.00, 0.10 and 0.01 μM for each

compound. The results show that the synthesised compounds **18** and **21** have an ability to phosphorylate AKT.

2.3.4. Apoptosis

Apoptosis, autophagy, and necrosis are the major types of cell death. The EGFR protein is involved in cell signaling pathways that control cell division and survival. Sometimes, mutations (changes) in the EGFR gene cause EGFR proteins to be made in higher-than-normal amounts on some types of cancer cells. This causes cancer cells to divide more rapidly [65]. Therefore, it's very much necessary to induce apoptosis in cancer cell to control their growth. The ability of the synthesised compound **21** to induce apoptosis was determined using an Annexin V (conjugated to FITC) apoptosis detection kit. From Fig. 5, it is clear that the compound **21** has induced early apoptosis and late apoptosis of 26.8% and 4.2% respectively, in comparison with control, with early apoptosis of 2.1% and late apoptosis of 1.1%.

2.3.5. Docking and MD simulation studies

To study the binding affinity and poses of synthesised compounds, molecular docking studies of all compounds were performed against wild-type EGFR (WT-EGFR) (PDB id 4I23), T790 M mutant EGFR (EGFR^{T790M}) (PDB id 2JIU), and at the allosteric site of L858R/T790 M/C797S mutant EGFR (EGFR^{L858R/T790M/C797S}) (PDB id 5D41) using Smina Software (fork of Autodock Vina). The docking methodology was validated by performing redocking of the bound ligand and determining the RMSD value by superimposing the docked ligand over the bound ligand. The RMSD values were found to be 0.55 Å, 1.27 Å, and 0.70 Å for ligands taken from PDB 4I23, 2JIU and 5D41 respectively.

The molecular docking studies showed that compound **21** (binding affinity = -9.94, -8.62, -7.7 for WT-EGFR, EGFR^{T790M} and EGFR^{L858R/T790M/C797S} respectively) could fit into the ATP binding site as well as the allosteric site of the EGFR kinase, which indicates that compound **21** could effectively compete with ATP and thus may overcome resistance.

The MD simulation study was also performed to study the influence of compound **21** on the ATP site of the WT-EGFR, EGFR^{T790M} and allosteric site of EGFR^{L858R/T790M/C797S} enzyme, thus to quantify the stability of the docked conformation. The RMSD of the EGFR-compound **21** complex was determined from MD trajectory frames. The evolution of the RMSD of all three systems during 100 ns MD simulations was shown in Fig. 6. The RMSD value for compound 21-WT-EGFR complex and compound 21-EGFR^{L858R/T790M/C797S} complex indicated that the systems were stable during the entire MD simulation. Whereas, the RMSD value for compound 21-EGFR^{T790M} complex increased to about 2.6

Table 1

In vitro anticancer activity of the synthesised compounds against cells harbouring a different status of the EGFR.

Compound	IC ₅₀ μM				
	HCC827 (EGFR Del E746-A750)	NCI-H1975 (EGFR L858R/ T790 M)	A549 (WT EGFR)	A549	BEAS- 2B
3	2.11 ± 0.07	15.98 ± 0.15	12.16 ± 0.35	14.22 ± 0.30	–
4	2.45 ± 0.05	15.22 ± 0.05	11.40 ± 0.66	16.21 ± 0.22	–
6	0.28 ± 0.11	4.43 ± 0.06	6.09 ± 0.09	10.11 ± 0.15	–
7	0.97 ± 0.23	13.11 ± 0.75	11.52 ± 0.07	16.77 ± 0.35	–
9	0.062 ± 0.09	0.82 ± 0.28	1.88 ± 0.04	4.22 ± 0.12	86.48 ± 0.24
10	0.22 ± 0.15	2.86 ± 0.11	5.02 ± 0.1	8.22 ± 0.32	–
11	0.22 ± 0.33	2.86 ± 0.62	5.64 ± 0.95	8.36 ± 0.15	–
12	0.29 ± 0.12	2.88 ± 0.45	5.60 ± 0.66	9.18 ± 0.24	–
13	0.33 ± 0.06	4.12 ± 0.76	5.82 ± 0.05	9.11 ± 0.09	–
14	0.38 ± 0.09	4.80 ± 0.09	6.11 ± 0.42	10.16 ± 0.02	–
15	0.89 ± 0.05	11.06 ± 0.05	10.32 ± 0.05	14.55 ± 0.16	–
16	0.099 ± 0.01	0.77 ± 0.24	1.09 ± 0.11	3.09 ± 0.22	45.78 ± 0.04
17	0.67 ± 0.11	7.16 ± 0.15	7.84 ± 0.26	11.07 ± 0.11	–
18	0.050 ± 0.04	0.86 ± 0.42	2.41 ± 0.28	4.87 ± 0.63	–
19	0.38 ± 0.17	4.30 ± 0.05	5.99 ± 0.33	9.22 ± 0.35	–
20	0.96 ± 0.22	11.76 ± 0.65	10.84 ± 0.32	15.06 ± 0.33	–
21	0.010 ± 0.02	0.21 ± 0.99	0.99 ± 0.11	2.99 ± 0.21	85.14 ± 0.12
23	0.11 ± 0.06	2.18 ± 0.34	4.30 ± 0.09	6.98 ± 0.42	–
24	0.18 ± 0.14	2.69 ± 0.28	4.82 ± 0.09	7.01 ± 0.56	–
25	0.52 ± 0.9	6.14 ± 0.09	8.73 ± 0.06	11.21 ± 0.47	–
26	0.88 ± 0.06	9.36 ± 0.22	8.22 ± 0.1	11.45 ± 0.36	–
27	0.10 ± 0.05	0.11 ± 0.64	7.94 ± 0.35	11.02 ± 0.55	–
28	0.17 ± 0.10	2.81 ± 0.34	4.88 ± 0.44	8.32 ± 0.18	–
29	0.16 ± 0.99	2.82 ± 0.02	4.92 ± 0.26	8.58 ± 0.24	–
Osimertinib	0.0042 ± 0.09	0.04 ± 0.05	0.92 ± 0.28	2.67 ± 0.07	–

Table 2

Synthesised compounds' *in vitro* enzymatic inhibitory activity against EGFR L858R/T790 M.

Compound	EGFR inhibition IC ₅₀ (nM) ^a
9	152 ± 0.31
16	159 ± 0.12
18	144 ± 0.48
21	138 ± 0.37
Osimertinib	110 ± 0.22

^aThe data reported are the mean values from three independent experiments.

0.75 nm at the first 5–6 ns, then increased to 0.83 nm at around 20 ns, then tended to be converging with fluctuations between 0.7 nm and 0.75 nm at the end of the simulation, indicating that systems were stable

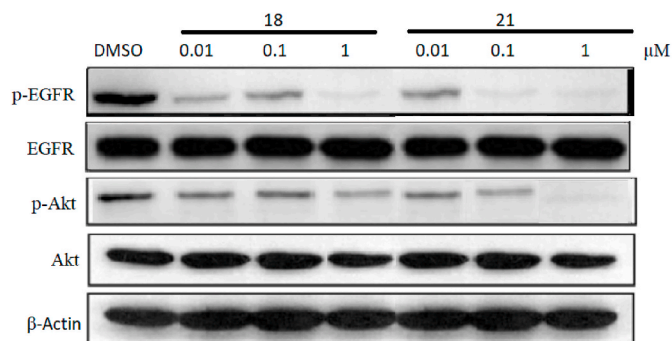


Fig. 4. Effects of compounds **18** and **21** on EGFR signalling in HCC827 cells.

during entire MD simulations after a small rearrangement from the initial conformational changes.

In addition, the RMSF of Cα atoms of amino acid residues and the radius of gyration (Rg) of protein were also calculated for three complexes (Fig. 7). The lower atomic fluctuations in Cα atoms of the active site of the enzyme suggested small conformational changes. Further, the RMSF and Rg graphs revealed the stability of each amino acid in three EGFR-compound **21** complexes. The above analysis therefore showed that compound **21** formed a stable complex with the EGFR enzyme without much structural rearrangement.

We further investigated the formation and stability of H-bonds under dynamic conditions. Individual occupancies of detected H-bonds for compound **21**-EGFR complexes are detailed in Fig. 8. The cluster analyses of all three complexes were also performed to find the conformation with the highest frequency and to visualise the H-bond interaction between compound **21** and the EGFR enzyme during the entire MD run.

As predicted in the docking study, the review of clusters in WT-EGFR also showed the presence of the hydrogen bond between imidazole ring of compound **21** with the side chain of amino acid residues Lys 728 and Lys 716, which remained stable for 96% and 93% of the MD simulation time, respectively. It was also found that the sulphonamide group of compound **21** forms H-bond interactions with the backbone of Cys 797 and the side chain of Ser 720 with occupancies of 16.2% and less than 10%, respectively (Fig. 9). Similarly, the review of clusters of EGFR^{T790M} showed the presence of hydrogen bonds between the sulphonamide group of compound **21** and Met 793 with occupancy of 93.8% (Fig. 10). The analysis of EGFR^{L858R/T790 M/C797S} complex clusters reveals the presence of hydrogen bonds between the imidazole ring and the side chain of amino acid residue Arg 889 that remained stable for 93.9% and 97.4% of the MD simulation time, respectively. The sulphonamide group also forms hydrogen bonds with Phe 723 and Gly 721, which stabilises the ligand inside the allosteric site of EGFR^{L858R/T790M/C797S} (Fig. 11).

The overall review of the results of the MD simulations revealed that the compound **21**-EGFR enzyme docking complexes maintained conformational stability and consistent structural flexibility throughout the period of the MD run.

2.3.6. ADME Prediction

Properties such as absorption, distribution, metabolism, and excretion (ADME) are important in order to determine the success of a compound for human therapeutic use. In the present study, we have calculated molecular weight (MW), number of hydrogen bond donors (HBD), number of hydrogen bond acceptors (HBA), logarithm of partition coefficient (log Po/w), predicted aqueous solubility (log S), predicted log of apparent Caco-2 cell permeability in cm/s (QPPCaco), steady state volume of distribution (VD_{ss}) in log L/kg, primary metabolites (metab), intestinal absorption, P-glycoprotein substrate, CYP2D6/CYP3A4 substrate, renal OCT2 substrate and Lipinski's rule of five (RO5) by using the SwissADME and pkCSM servers. The results of ADME prediction are shown in supporting information.

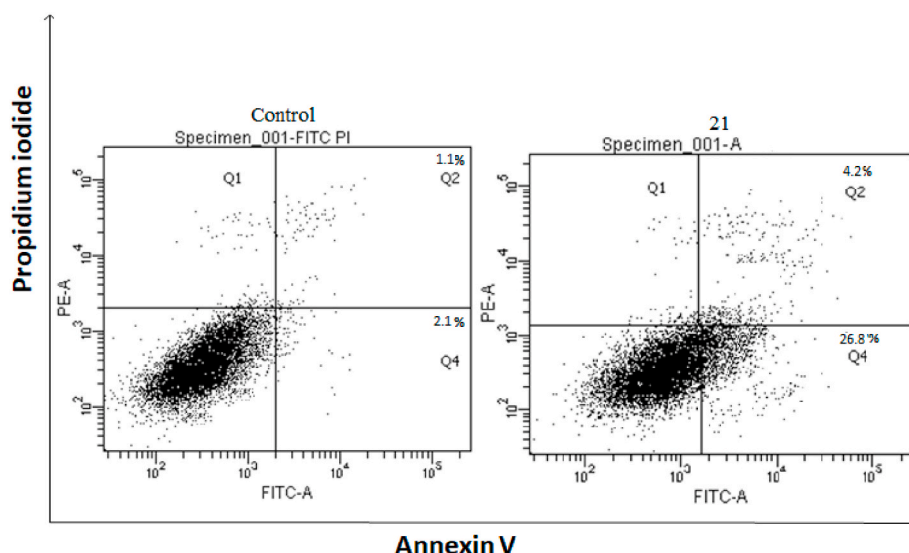


Fig. 5. Apoptosis study by Annexin V/FITC assay of compound 21.

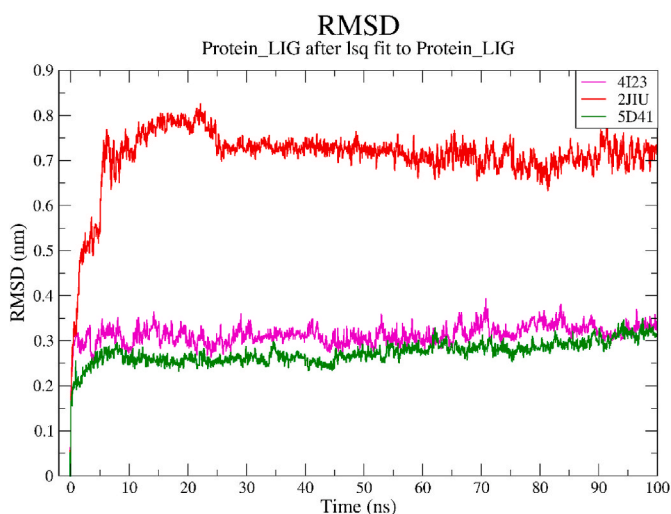


Fig. 6. RMSD of compound 21-EGFR enzyme complex with respect to time over the course of the 100 ns MD simulations run.

The drug-likeness assessment of all compounds was performed by predicting the Lipinski rule of five, which includes molecular weights ($MW < 500$), lipophilicity ($\log Po/w < 5$), number of hydrogen bond acceptors ($HBA \leq 10$) and number of hydrogen bond donors ($HBD \leq 5$) to determine the "drug-likeness" of all synthetic compounds. It was noted that compounds 3–29 show violations of Lipinski's only in terms of MW. As per the Swiss ADME server, very few compounds were found to be the substrate of P-glycoprotein and the pkCSM server showed that most of the compounds showed 70%–85% for predicted human oral absorption, indicating that the synthesised compounds have medium to high oral absorption.

The steady state volume of distribution (VD_{ss}) represents the degree to which a drug is distributed in body tissue rather than in plasma. The predicted VD_{ss} values showed that most compounds were observed in the range of -0.15 to 0.45 , which indicates the compounds have a steady distribution in blood plasma and tissue. Most compounds are found to be substrates of CYP3A4 substrates, which indicates the ease of metabolism of compounds. Renal OCT2 translocate endogenous and exogenous substances of cationic nature and, therefore, plays an important role in the detoxification of exogenous compounds. Most

compounds are found to be substrates of renal OCT2 and therefore indicate ease of excretion of compounds. The findings of ADME showed that most of drugs have drug-like properties.

3. Conclusion

In this study, we have highlighted the discovery of a novel series of quinoline substituted sulphonamide (9–21) and amide (23–29) analogues that were synthesised and biologically evaluated against the anticancer activity. Most of the compounds are covalent, mutant-selective EGFR inhibitors with virtually equal potency against oncogenic L858R and T790M-resistant mutations and strong selectivity against small molecule mutant EGFR inhibitors. These compounds also exhibited strong antiproliferative activity against HCC827 cells bearing EGFR del E746-A750, H1975 cells harbouring EGFR L858R/T790 M and A549/ATCC cells bearing WT-EGFR. The synthesised compound 21 was found to be potent with IC_{50} values of $0.010 \mu M$, $0.21 \mu M$, $0.99 \mu M$ and $2.99 \mu M$ against HCC827 (EGFR Del E746-A750), NCI-H1975 (EGFR L858R/T790 M), A549/ATCC (WT EGFR) and A549 respectively. They also showed promising inhibitory enzymatic activity against the EGFR with an IC_{50} value of 138 nM , comparable with Osimertinib. The synthesised derivative 27 was found to be potent against NCI-H1975 (EGFR L858R/T790 M) with an IC_{50} value of $0.11 \mu M$. Compound 21 showed lower to moderate inhibition of normal cells with A549 and BEAS-2B cells. The MD simulation study was also performed for the EGFR-compound 21 complex, which indicates the stability of the enzyme in both the ATP and allosteric sites. Furthermore, docking studies revealed the binding of synthesised compounds is identical to binding patterns and interactions at the binding site of the allosteric site of EGFR-TK inhibitor's protein. To further illustrate, additional research is needed. However, the described compounds and analogues synthesised here are promising in the pursuit of leads for the treatment of NSCLC.

4. Experimental section

4.1. Chemistry

All chemicals and reagents used were of reagent grade. Purification and drying of reagents and solvents was carried out according to literature procedure. Thin layer chromatographic analyses were performed on E-Merck 60 F₂₅₄ precoated silica thin layer chromatographic plates with detection by UV light. Purification by normal phase silica gel (silica

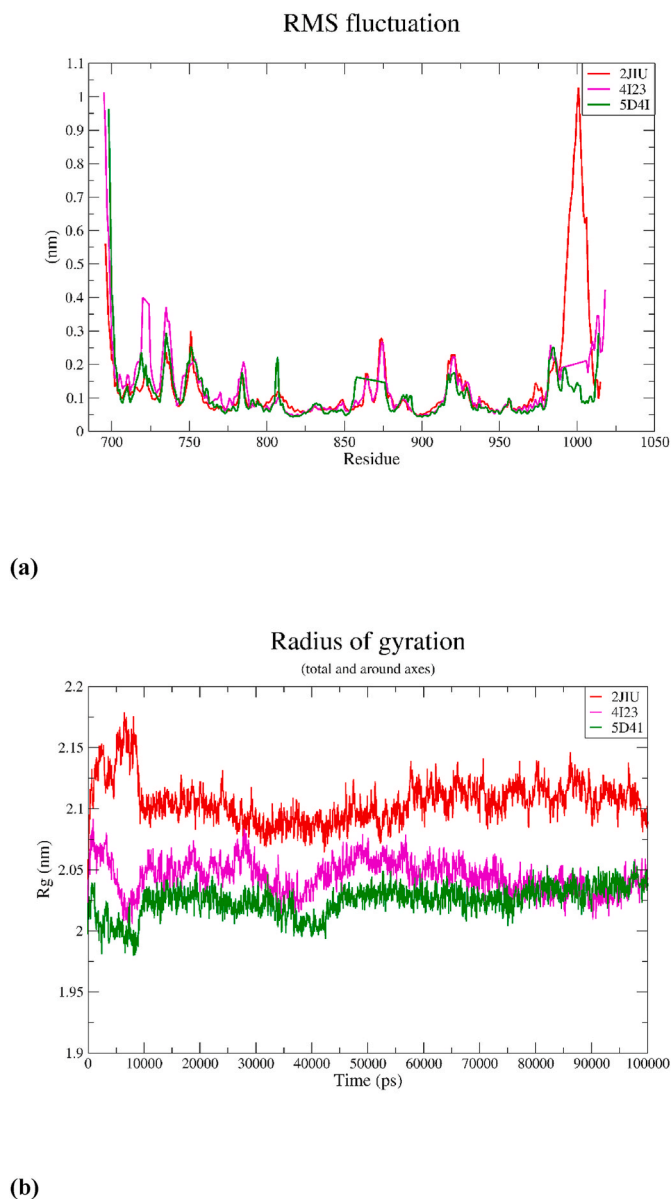


Fig. 7. (a) RMSF of protein α atoms of EGFR enzyme and (b) Radius of gyration of protein with respect to time over the course of the 100 ns MD simulations run.

gel 100–200) was used for chromatography. All air-sensitive reactions were carried out under nitrogen atmosphere. Melting points were determined on a Büchi melting point B540 instrument and are uncorrected. ^1H NMR and ^{13}C NMR spectra were recorded on a Bruker Biospin 400 MHz spectrometer in the indicated solvents (TMS as an internal standard). The values of chemical shifts are expressed in ppm and the coupling constants (J) in hertz (Hz). Mass spectra were recorded in API 2000 LC/MS/MS system spectrometer and the IR spectra were recorded on PerkinElmer FT-IR spectrometer. HPLC purity analysis performed by AGILENT HPLC Instrument (A-1100), all the compounds HPLC purity is more than 95%.

4.1.1. Representative procedure for synthesis of compound 3 to 7

Ethyl 6-bromo-4-(4-(tert-butoxy carbonyl) piperazin-1-yl)-2-(1H-imidazole-1-yl) quinoline-3-carboxylate (3): A mixture of ethyl 6-bromo-4-chloro-2-(1H-imidazole-1-yl) quinoline-3-carboxylate (1) (5 g, 1.0 eq, 13.15 mmol) and *tert*-butyl piperazine-1-carboxylate (2) (2.9 g, 1.2 eq, 15.59 mmol) in DMSO (100 mL) were added DIPEA (4.60 mL,

2 eq, 26.41 mmol) was heated to 80 °C for 8 h. After completion of the reaction, the mixture was poured into water (200 mL) and extracted with ethyl acetate (3 × 200 mL). The combined organic layer was washed with brine and dried over anhydrous sodium sulfate. The organic layer was filtered and concentrated under reduced pressure to obtain the crude product. The crude product was purified by column chromatography (silica gel 100–200 mesh, eluent: 5% ethyl acetate in *n*-hexane) to afford compound 3 (6.0 g, 86.9%) as a pale yellow solid; mp: 141–142 °C; IR (ν max, cm^{-1}): 1720.50 ($-\text{C}=\text{O}$, ester), 1681.92 ($-\text{C}=\text{O}$, Boc), 1589.34 ($-\text{C}=\text{N}$), 1226.72 ($-\text{C}-\text{N}$), 1002.98 ($-\text{C}-\text{O}$), 655.79 ($-\text{C}-\text{Br}$); ^1H NMR (400 MHz, $\text{DMSO}-d_6$): δ 1.03 (t, $J = 14.0$ Hz, 3H, $-\text{CH}_3\text{CH}_2$), 1.42 (s, 9H, $-\text{Boc}$), 3.45 (s, 8H, 2 × CH_2CH_2 , piperazine ring), 4.08 (q, $J = 14.0$ Hz, 2H, $-\text{CH}_2\text{CH}_3$), 7.08 (s, 1H, Ar-H), 7.21 (s, 1H, Ar-H), 7.49 (s, 1H, Ar-H), 7.73–7.75 (m, 1H, Ar-H), 7.87–7.90 (m, 2H, Ar-H). ^{13}C NMR (100.6 MHz, $\text{DMSO}-d_6$): δ 13.35 ($-\text{CH}_3\text{CH}_2$), 28.01 ($-\text{CH}_3$, Boc), 47.76 ($-\text{CH}_2$, Piperazine), 62.23 ($-\text{CH}_3\text{CH}_2$), 79.11 ($-\text{C}(\text{CH}_3)_3$, Boc), 117.57 (Ar-C), 118.61 (Ar-C), 121.72 (Ar-C), 122.02 (Ar-C), 124.54 (Ar-C), 129.10 (Ar-C), 129.15 (Ar-C), 134.79 (Ar-C), 138.61 (Ar-C), 141.01 (Ar-C), 145.76 (Ar-C), 153.88 (Ar-C), 155.18 (Ar-C), 164.74 ($-\text{C}=\text{O}$, ethyl ester); HPLC: 99.7%. ESI-MS m/z of $\text{C}_{24}\text{H}_{28}\text{BrN}_5\text{O}_4$ $[\text{M}+\text{H}]^+$ 530.00 was obtained for a calculated mass of 529.13.

Ethyl 6-bromo-2-(1H-imidazole-1-yl)-4-(piperazin-1-yl) quinoline-3-carboxylate (4): To the cooled solution of compound 3 (6 g, 1.0 eq, 11.36 mmol) was added dropwise 4M HCl in 1,4 Dioxane (20 mL) and reaction, mixture stirred at R.T. for 4 h. After completion of reaction, mixture was concentrated on rotatory evaporator and the crude material was used for next step as HCl salt. 4 (5.0 g, 96.1%, crude) as a brown solid; mp: 122.5–123.8 °C; ^1H NMR (400 MHz, $\text{DMSO}-d_6$): δ 1.09 (t, $J = 14.4$ Hz, 3H, $-\text{CH}_3\text{CH}_2$), 3.18 (s, 4H, $-\text{CH}_2\text{CH}_2$, piperazine ring), 3.71 (s, 4H, $-\text{CH}_2\text{CH}_2$, piperazine ring), 4.16 (q, $J = 14.0$ Hz, 2H, $-\text{CH}_2\text{CH}_3$), 7.54–7.55 (m, 1H, Ar-H), 7.81–7.83 (m, 1H, Ar-H), 7.97–8.02 (m, 2H, Ar-H), 8.07 (s, 1H, Ar-H), 9.56 (s, 1H, Ar-H), 9.75 (bs, 2H, $-\text{NH}$, D_2O exchangeable). ^{13}C NMR (100.6 MHz, $\text{DMSO}-d_6$): δ 14.06 ($-\text{CH}_3\text{CH}_2$), 42.75 ($-\text{CH}_2$, Piperazine), 45.90 ($-\text{CH}_2$, Piperazine), 60.65 ($-\text{CH}_2$, Piperazine), 62.78 ($-\text{CH}_3\text{CH}_2$), 103.46 (Ar-C), 115.54 (Ar-C), 119.14 (Ar-C), 120.66 (Ar-C), 122.52 (Ar-C), 124.40 (Ar-C), 126.78 (Ar-C), 134.08 (Ar-C), 134.47 (Ar-C), 137.78 (Ar-C), 153.61 (Ar-C), 166.43 ($-\text{C}=\text{O}$, ethyl ester); HPLC: 99.7%. ESI-MS m/z of $\text{C}_{19}\text{H}_{20}\text{BrN}_5\text{O}_2$ $[\text{M}+\text{H}]^+$ 430.10 was obtained for a calculated mass of 429.08.

Ethyl 6-bromo-2-(1H-imidazole-1-yl)-4-(4-(2-nitrophenyl) piperazin-1-yl) quinoline-3-carboxylate (6): To this solution of compound 4 (5 g, 1.0 eq, 10.77 mmol) in dry DMF (70 mL) were added compound 5 (1.53 g, 1.01 eq, 10.88 mmol) and K_2CO_3 (2.97 g, 2.0 eq, 21.55 mmol) heated to 80 °C for 8 h. After completion of reaction, mixture was poured in ice:water (200 mL) mixture and extracted with ethyl acetate (3 × 100 mL). Combined organic layer was washed with brine and dried over anhydrous sodium sulfate. Organic layer was filtered and concentrated under reduced pressure to obtain crude product. Crude product was purified by column chromatography (silica gel 100–200 mesh, eluent: 5–7% ethyl acetate in *n*-hexane) to afford compound 6 (5 g, 84.7%) as a yellow solid; mp: 147.6–148.6 °C; IR (ν max, cm^{-1}): 1728.21 ($-\text{C}=\text{O}$, ester), 1489.04, 1589.34 ($-\text{NO}_2$), 1226.72 ($-\text{C}-\text{N}$), 1095.56 ($-\text{C}-\text{O}$), 663.51 ($-\text{C}-\text{Br}$); ^1H NMR (400 MHz, $\text{DMSO}-d_6$): δ 1.05 (t, $J = 14.4$ Hz, 3H, $-\text{CH}_3\text{CH}_2$), 3.17 (s, 4H, $-\text{CH}_2\text{CH}_2$, piperazine ring), 3.60 (s, 4H, $-\text{CH}_2\text{CH}_2$, piperazine ring), 4.09 (q, $J = 14.4$ Hz, 2H, $-\text{CH}_2\text{CH}_3$), 7.09–7.10 (m, 1H, Ar-H), 7.13–7.17 (m, 1H, Ar-H), 7.21 (s, 1H, Ar-H), 7.37–7.39 (m, 1H, Ar-H), 7.50 (s, 1H, Ar-H), 7.59–7.63 (m, 1H, Ar-H), 7.74–7.77 (m, 1H, Ar-H), 7.84–7.91 (m, 3H, Ar-H). ^{13}C NMR (100.6 MHz, $\text{DMSO}-d_6$): δ 13.41 ($-\text{CH}_3\text{CH}_2$), 47.96 ($-\text{CH}_2$, Piperazine), 50.65 ($-\text{CH}_2$, Piperazine), 62.28 ($-\text{CH}_3\text{CH}_2$), 117.57 (Ar-C), 118.54 (Ar-C), 121.47 (Ar-C), 121.74 (Ar-C), 122.04 (Ar-C), 122.08 (Ar-C), 124.58 (Ar-C), 125.55 (Ar-C), 129.14 (Ar-C), 129.19 (Ar-C), 133.87 (Ar-C), 134.84 (Ar-C), 138.67 (Ar-C), 141.07 (Ar-C), 142.61 (Ar-C), 144.90 (Ar-C), 145.83 (Ar-C), 155.14 (Ar-C), 164.81 ($-\text{C}=\text{O}$, ethyl ester); HPLC: 99.3%. ESI-MS m/z of $\text{C}_{25}\text{H}_{23}\text{BrN}_6\text{O}_4$ $[\text{M}+\text{H}]^+$ 551 was obtained

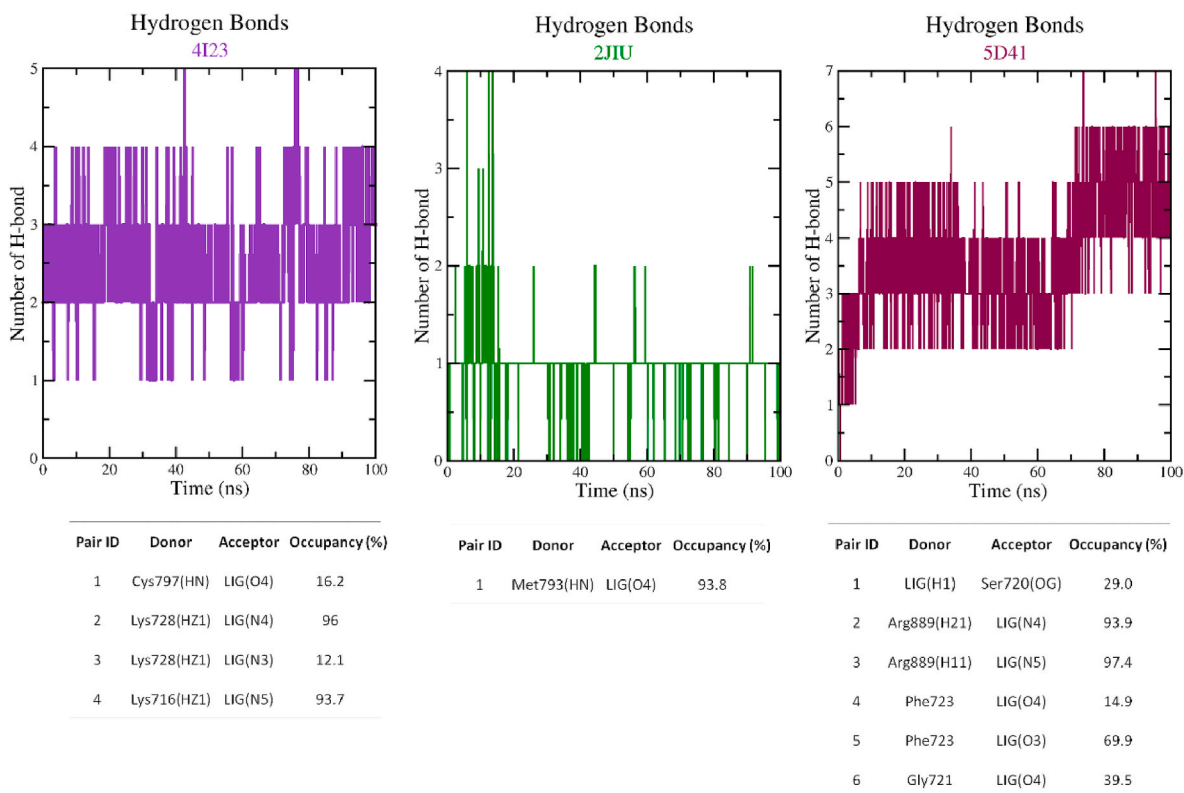


Fig. 8. A timeline representation of the H-bond interactions between compound 21 and EGFR enzyme. The top panel shows the number of H-bonds the enzyme EGFR makes with the compound 21 over the course of the trajectory. The bottom panel shows name of amino acid residues interact with the compound 21 along with occupancy of more than 10% in each trajectory frame.

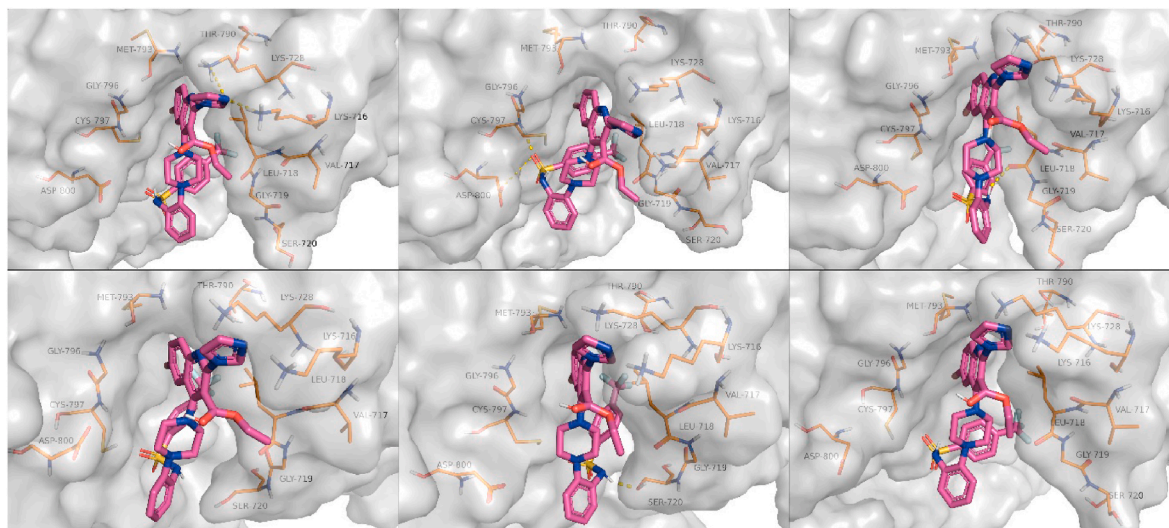


Fig. 9. Representative structures of compound 21-WT-EGFR enzyme complex extracted from the cluster analysis of the MD trajectory. Representatives of the first 6 most populated clusters are shown. The yellow colour dotted line indicates H-bond between ligand and enzyme.

for a calculated mass of 550.1.

Ethyl 4-(4-(2-aminophenyl)piperazin-1-yl)-6-bromo-2-(1H-imidazole-1-yl)quinoline-3-carboxylate (7): A mixture of compound 6 (5 g, 1.0 eq, 9.07 mmol) in EtOH: H₂O (4:1, 100 mL) was added Fe powder (1.0 g, 2.0 eq, 18.14 mmol) and NH₄Cl (0.96 g, 2.0 eq, 18.14 mmol). Reaction was heated at 80 °C for 2 h. After completion of reaction mixture was filtrated through Celite and filtrate was concentrated under reduced pressure, crude mixture was poured in water and then extracted with ethyl acetate (3 × 100 mL). Combined organic layer was

washed with brine and dried over anhydrous sodium sulfate. Organic layer was filtered and concentrated under reduced pressure to obtain crude product. Crude product was purified by column chromatography (silica gel 100–200 mesh, eluent: 10–12% ethyl acetate in n-hexane) to afford compound 7 (4 g, 85.1%) as a yellow solid; mp: 220.4–221.4 °C; IR (ν max, cm⁻¹): 1728.22 (–C=O, ester), 1581.63 (–C=N), 1211.30 (–C–N), 1041.56 (–C–O), 663.51 (–C–Br); ¹H NMR (400 MHz, DMSO-*d*₆): δ 1.06 (t, *J* = 14.4 Hz, 3H, –CH₂CH₂), 2.91 (s, 4H, –CH₂CH₂, piperazine ring), 3.65 (s, 4H, –CH₂CH₂, piperazine ring), 4.09 (q, *J* = 14.0 Hz, 2H,

Piperazine), 62.17 (-CH₃CH₂), 116.27 (Ar-C), 116.49 (Ar-C), 117.42 (Ar-C), 118.57 (Ar-C), 121.62 (Ar-C), 122.02 (Ar-C), 122.61 (Ar-C), 124.56 (Ar-C), 125.08 (Ar-C), 125.81 (Ar-C), 129.07 (Ar-C), 129.66 (Ar-C), 129.76 (Ar-C), 131.90 (Ar-C), 134.80 (Ar-C), 136.71 (Ar-C), 141.02 (Ar-C), 144.53 (Ar-C), 145.90 (Ar-C), 155.16 (Ar-C), 163.08 (Ar-C), 164.86 (-C=O, ethyl ester), 165.59 (Ar-CF); HPLC: 99.6%. ESI-MS *m/z* of C₃₁H₂₈BrFN₆O₄S [M + H+2]⁺ 681.1 was obtained for a calculated mass of 678.1.

Ethyl 6-bromo-4-(4-(2-((4-bromophenyl)sulfonamido)phenyl)piperazin-1-yl)-2-(1H-imidazole-1-yl) quinoline-3-carboxylate (10): Procedure A, (R₁: 4-bromobenzenesulfonyl chloride) Yield: 73.9%, off white solid; mp: 240.7–241.7 °C; IR (ν max, cm⁻¹): 1728.21 (-C=O, ester), 1442.75 (-S=O), 1226.72 (-C-N), 1095.56 (-C-O), 655.79 (-C-Br); ¹H NMR (400 MHz, DMSO-*d*₆): δ 1.05 (t, *J* = 14.4 Hz, 3H, -CH₃CH₂), 2.62 (s, 4H, -CH₂CH₂, piperazine ring), 3.54 (s, 4H, -CH₂CH₂, piperazine ring), 4.08 (q, *J* = 14.0 Hz, 2H, -CH₂CH₃), 7.08–7.21 (m, 5H, Ar-H), 7.30–7.32 (m, 1H, Ar-H), 7.50 (s, 1H, Ar-H), 7.68–7.79 (m, 5H, Ar-H), 7.81–7.91 (m, 2H, Ar-H), 9.24 (s, 1H, -NH, D₂O exchangeable). ¹³C NMR (100.6 MHz, DMSO-*d*₆): δ 13.46 (-CH₃CH₂), 47.92 (-CH₂, Piperazine), 51.62 (-CH₂, Piperazine), 62.21 (-CH₃CH₂), 117.42 (Ar-C), 118.56 (Ar-C), 121.63 (Ar-C), 122.04 (Ar-C), 123.06 (Ar-C), 124.56 (Ar-C), 125.06 (Ar-C), 126.02 (Ar-C), 126.73 (Ar-C), 128.65 (Ar-C), 129.08 (Ar-C), 131.73 (Ar-C), 132.29 (Ar-C), 134.81 (Ar-C), 139.60 (Ar-C), 141.02 (Ar-C), 144.81 (Ar-C), 145.89 (Ar-C), 155.14 (Ar-C), 164.86 (-C=O, ethyl ester); HPLC: 96.3%. ESI-MS *m/z* of C₃₁H₂₈Br₂N₆O₄S [M + H+2]⁺ 741.1 was obtained for a calculated mass of 738.03.

Ethyl 6-bromo-4-(4-(2-((4-chlorophenyl)sulfonamido)phenyl)piperazin-1-yl)-2-(1H-imidazole-1-yl) quinoline-3-carboxylate (11): Procedure A, (R₁: 4-chlorobenzenesulfonyl chloride) Yield: 67.6%, pale yellow solid; mp: 233–234.0 °C; IR (ν max, cm⁻¹): 1728.21 (-C=O, ester), 1581.62 (-C=N), 1350.17 (-S=O), 1226.72 (-C-N), 1080.13 (-C-O), 756.09 (-C-Cl), 617.22 (-C-Br); ¹H NMR (400 MHz, DMSO-*d*₆): δ 1.08 (t, *J* = 14.4 Hz, 3H, -CH₃CH₂), 2.63 (m, 4H, -CH₂CH₂, piperazine ring), 3.56 (m, 4H, -CH₂CH₂, piperazine ring), 4.09–4.11 (m, 2H, -CH₂CH₃), 7.10–7.15 (m, 3H, Ar-H), 7.24–7.37 (m, 2H, Ar-H), 7.54–7.59 (m, 2H, Ar-H), 7.63–7.65 (m, 1H, Ar-H), 7.74–7.79 (m, 4H, Ar-H), 7.89–7.91 (m, 1H, Ar-H), 8.59 (s, 1H, Ar-H), 9.29 (s, 1H, -NH, D₂O exchangeable). ¹³C NMR (100.6 MHz, DMSO-*d*₆): δ 13.42 (-CH₃CH₂), 47.90 (-CH₂, Piperazine), 51.58 (-CH₂, Piperazine), 62.31 (-CH₃CH₂), 117.53 (Ar-C), 118.34 (Ar-C), 121.27 (Ar-C), 121.98 (Ar-C), 122.53 (Ar-C), 122.95 (Ar-C), 124.57 (Ar-C), 125.03 (Ar-C), 125.97 (Ar-C), 127.31 (Ar-C), 127.42 (Ar-C), 127.60 (Ar-C), 128.56 (Ar-C), 129.02 (Ar-C), 129.32 (Ar-C), 131.69 (Ar-C), 135.00 (Ar-C), 137.74 (Ar-C), 138.50 (Ar-C), 139.19 (Ar-C), 140.50 (Ar-C), 144.73 (Ar-C), 145.94 (Ar-C), 155.03 (Ar-C), 164.64 (-C=O, ethyl ester); HPLC: 99.6%. ESI-MS *m/z* of C₃₁H₂₈BrClN₆O₄S [M + H+2]⁺ 696.95 was obtained for a calculated mass of 694.08.

Ethyl 6-bromo-2-(1H-imidazole-1-yl)-4-(4-(2-((4-iodophenyl)sulfonamido)phenyl)piperazin-1-yl) quinoline-3-carboxylate (12): Procedure A, (R₁: 4-iodobenzenesulfonyl chloride) Yield: 82.7%, pale yellow solid; mp: 221.5–222.5 °C; IR (ν max, cm⁻¹): 1728.22 (-C=O, ester), 1581.63 (-C=N), 1489.05 (-S=O), 1219.01 (-C-N), 1080.14 (-C-O), 740.67 (-C-I), 655.80 (-C-Br); ¹H NMR (400 MHz, DMSO-*d*₆): δ 1.06 (t, *J* = 14.4 Hz, 3H, -CH₃CH₂), 2.61 (m, 4H, -CH₂CH₂, piperazine ring), 3.53 (m, 4H, -CH₂CH₂, piperazine ring), 4.08–4.10 (m, 2H, -CH₂CH₃), 7.09–7.16 (m, 4H, Ar-H), 7.24–7.25 (m, 1H, Ar-H), 7.30–7.32 (m, 1H, Ar-H), 7.49–7.58 (m, 3H, Ar-H), 7.74–7.77 (m, 1H, Ar-H), 7.87–7.89 (m, 1H, Ar-H), 7.94–7.96 (m, 3H, Ar-H), 9.26 (s, 1H, -NH, D₂O exchangeable). ¹³C NMR (100.6 MHz, DMSO-*d*₆): δ 13.48 (-CH₃CH₂), 47.92 (-CH₂, Piperazine), 51.61 (-CH₂, Piperazine), 62.25 (-CH₃CH₂), 100.99 (Ar-C), 117.43 (Ar-C), 118.52 (Ar-C), 121.57 (Ar-C), 122.04 (Ar-C), 122.20 (Ar-C), 123.06 (Ar-C), 124.56 (Ar-C), 125.06 (Ar-C), 125.99 (Ar-C), 128.27 (Ar-C), 128.89 (Ar-C), 129.08 (Ar-C), 131.74 (Ar-C), 134.83 (Ar-C), 138.09 (Ar-C), 138.64 (Ar-C), 139.90 (Ar-C), 140.94 (Ar-C), 144.79 (Ar-C), 145.90 (Ar-C), 155.12

(Ar-C), 164.82 (-C=O, ethyl ester); HPLC: 94.0%. ESI-MS *m/z* of C₃₁H₂₈BrIN₆O₄S [M + H+2]⁺ 788.8 was obtained for a calculated mass of 786.01.

Ethyl 6-bromo-4-(4-(2-((4-cyanophenyl)sulfonamido)phenyl)piperazin-1-yl)-2-(1H-imidazole-1-yl) quinoline-3-carboxylate (13): Procedure A, (R₁: 4-cyanobenzenesulfonyl chloride) Yield: 76.4%, pale yellow solid; mp: 227.9–228.9 °C; IR (ν max, cm⁻¹): 2237.42 (-CN), 1728.21 (-C=O, ester), 1581.62 (-C=N), 1496.76, 1350.17 (-S=O), 1226.72 (-C-N), 1087.85 (-C-O), 655.79 (-C-Br); ¹H NMR (400 MHz, DMSO-*d*₆): δ 1.06 (t, *J* = 14.4 Hz, 3H, -CH₃CH₂), 2.65 (s, 4H, -CH₂CH₂, piperazine ring), 3.51 (s, 4H, -CH₂CH₂, piperazine ring), 4.08 (q, *J* = 14.4 Hz, 2H, -CH₂CH₃), 7.08–7.09 (m, 2H, Ar-H), 7.15–7.16 (m, 2H, Ar-H), 7.21 (s, 1H, Ar-H), 7.28 (d, *J* = 8.0 Hz, 1H, Ar-H), 7.50 (s, 1H, Ar-H), 7.76 (d, *J* = 9.6 Hz, 1H, Ar-H), 7.87–7.95 (m, 4H, Ar-H), 8.07 (d, *J* = 8.4 Hz, 2H, Ar-H), 9.53 (s, 1H, -NH, D₂O exchangeable). ¹³C NMR (100.6 MHz, DMSO-*d*₆): δ 13.41 (-CH₃CH₂), 47.90 (-CH₂, Piperazine), 51.58 (-CH₂, Piperazine), 62.16 (-CH₃CH₂), 115.16 (Ar-C), 117.43 (Ar-C), 117.54 (Ar-C), 118.59 (Ar-C), 121.63 (Ar-C), 121.93 (Ar-C), 122.05 (Ar-C), 123.82 (Ar-C), 124.54 (Ar-C), 124.92 (Ar-C), 126.43 (Ar-C), 127.37 (Ar-C), 129.07 (Ar-C), 129.14 (Ar-C), 131.19 (Ar-C), 133.37 (Ar-C), 134.78 (Ar-C), 138.64 (Ar-C), 140.98 (Ar-C), 144.52 (Ar-C), 145.31 (Ar-C), 145.88 (Ar-C), 155.17 (Ar-C), 164.82 (-C=O, ethyl ester); HPLC: 96.3%. ESI-MS *m/z* of C₃₂H₂₈BrN₇O₄S [M + H+2]⁺ 688.11 was obtained for a calculated mass of 685.11.

Ethyl 6-bromo-2-(1H-imidazole-1-yl)-4-(4-(2-((4-methoxyphenyl)sulfonamido)phenyl)piperazin-1-yl)quinoline-3-carboxylate (14): Procedure A, (R₁: 4-methoxybenzenesulfonyl chloride) Yield: 78.4%, off white solid; mp: 228.9–229.9 °C; IR (ν max, cm⁻¹): 1720.50 (-C=O, ester), 1581.63 (-C=N), 1489.05, 1442.75 (-S=O), 1219.01 (-C-N), 1087.85 (-C-O), 663.51 (-C-Br); ¹H NMR (400 MHz, DMSO-*d*₆): δ 1.05 (t, *J* = 13.2 Hz, 3H, -CH₃CH₂), 2.60 (s, 4H, -CH₂CH₂, piperazine ring), 3.58 (s, 4H, -CH₂CH₂, piperazine ring), 3.80 (s, 3H, -OCH₃), 4.06–4.08 (m, 2H, -CH₂CH₃), 7.06–7.08 (m, 5H, Ar-H), 7.15–7.21 (m, 2H, Ar-H), 7.34–7.41 (m, 1H, Ar-H), 7.50 (s, 1H, Ar-H), 7.71–7.76 (m, 3H, Ar-H), 7.87–7.91 (m, 2H, Ar-H), 8.94 (s, 1H, -NH, D₂O exchangeable). ¹³C NMR (100.6 MHz, DMSO-*d*₆): δ 13.37 (-CH₃CH₂), 47.98 (-CH₂, Piperazine), 51.59 (-CH₂, Piperazine), 55.64 (-OCH₃), 62.15 (-CH₃CH₂), 114.30 (Ar-C), 117.38 (Ar-C), 118.54 (Ar-C), 118.56 (Ar-C), 121.63 (Ar-C), 121.99 (Ar-C), 122.04 (Ar-C), 124.54 (Ar-C), 125.14 (Ar-C), 125.24 (Ar-C), 128.81 (Ar-C), 129.04 (Ar-C), 129.14 (Ar-C), 131.75 (Ar-C), 131.77 (Ar-C), 132.42 (Ar-C), 134.78 (Ar-C), 138.64 (Ar-C), 140.99 (Ar-C), 143.87 (Ar-C), 145.87 (Ar-C), 155.14 (Ar-C), 162.52 (Ar-C), 164.85 (-C=O, ethyl ester); HPLC: 99.1%. ESI-MS *m/z* of C₃₂H₃₁BrN₆O₅S [M + H+2]⁺ 693.5 was obtained for a calculated mass of 690.13.

Ethyl 6-bromo-2-(1H-imidazole-1-yl)-4-(4-(2-((4-methylsulfonyl)phenyl)sulfonamido)phenyl)piperazin-1-yl)quinoline-3-carboxylate (15): Procedure A, (R₁: 4-(methylsulfonyl)benzenesulfonyl chloride) Yield: 67.0%, brown solid; mp: 235.0–236.0 °C; IR (ν max, cm⁻¹): 1720.50 (-C=O, ester), 1589.34 (-C=N), 1489.04 (-S=O), 1226.72 (-C-N), 1095.56 (-C-O), 633.51 (-C-Br); ¹H NMR (400 MHz, DMSO-*d*₆): δ 1.04 (t, *J* = 13.2 Hz, 3H, -CH₃CH₂), 2.63 (s, 4H, -CH₂CH₂, piperazine ring), 3.29–3.32 (m, 3H, -SCH₃), 3.48 (s, 4H, -CH₂CH₂, piperazine ring), 4.06–4.08 (m, 2H, -CH₂CH₃), 7.08–7.21 (m, 5H, Ar-H), 7.29–7.31 (m, 1H, Ar-H), 7.49 (s, 1H, Ar-H), 7.73–7.75 (m, 1H, Ar-H), 7.87–7.91 (m, 2H, Ar-H), 8.00–8.02 (m, 2H, Ar-H), 8.11–8.13 (m, 2H, Ar-H), 9.52 (s, 1H, -NH, D₂O exchangeable). ¹³C NMR (100.6 MHz, DMSO-*d*₆): δ 13.37 (-CH₃CH₂), 47.98 (-CH₂, Piperazine), 51.59 (-CH₂, Piperazine), 55.64 (-OCH₃), 62.15 (-CH₃CH₂), 114.30 (Ar-C), 117.38 (Ar-C), 118.54 (Ar-C), 118.56 (Ar-C), 121.63 (Ar-C), 121.99 (Ar-C), 122.04 (Ar-C), 124.54 (Ar-C), 125.14 (Ar-C), 125.24 (Ar-C), 128.81 (Ar-C), 129.04 (Ar-C), 129.14 (Ar-C), 131.75 (Ar-C), 131.77 (Ar-C), 132.42 (Ar-C), 134.78 (Ar-C), 138.64 (Ar-C), 140.99 (Ar-C), 143.87 (Ar-C), 145.87 (Ar-C), 155.14 (Ar-C), 162.52 (Ar-C), 164.85 (-C=O, ethyl ester); HPLC: 99.0%. ESI-MS *m/z* of C₃₂H₃₁BrN₆O₅S [M + H+2]⁺ 693.5 was obtained for a calculated mass of 690.13.

Ethyl 6-bromo-4-(4-(2-((3,4-difluorophenyl)sulfonamido)phenyl)piperazin-1-yl)-2-(1H-imidazole-1-yl)quinoline-3-carboxylate (16): Procedure A, (R_1 : 3,4-difluorobenzenesulfonyl chloride) Yield: 73.7%, brown solid; mp: 245.0–248.0 °C; IR (ν max, cm^{-1}): 1728.21 (-C=O , ester), 1512.19 (-C=N), 1411.89 (-S=O), 1273.01 (-C-N), 1064.70 (-C-O), 694.37 (-C-Br), 470.03 (-C-F); ^1H NMR (400 MHz, $\text{DMSO-}d_6$): δ 1.05 (t, $J = 14.0$ Hz, 3H, $\text{-CH}_3\text{CH}_2$), 2.69 (s, 4H, $\text{-CH}_2\text{CH}_2$, piperazine ring), 3.58 (s, 4H, $\text{-CH}_2\text{CH}_2$, piperazine ring), 4.08 (q, $J = 14.0$ Hz, 2H, $\text{-CH}_3\text{CH}_2$), 7.09–7.22 (m, 5H, Ar-H), 7.29–7.30 (m, 1H, Ar-H), 7.51 (s, 1H, Ar-H), 7.66–7.67 (m, 2H, Ar-H), 7.74–7.76 (m, 1H, Ar-H), 7.87–7.95 (m, 3H, Ar-H), 9.38 (s, 1H, -NH , D_2O exchangeable). ^{13}C NMR (100.6 MHz, $\text{DMSO-}d_6$): δ 13.36 ($\text{-CH}_3\text{CH}_2$), 47.91 (-CH_2 , Piperazine), 51.62 (-CH_2 , Piperazine), 62.14 ($\text{-CH}_3\text{CH}_2$), 116.43 (Ar-C), 116.63 (Ar-C), 117.43 (Ar-C), 118.55 (Ar-C), 118.60 (Ar-C), 118.74 (Ar-C), 121.64 (Ar-C), 121.91 (Ar-C), 122.14 (Ar-C), 123.00 (Ar-C), 124.54 (Ar-C), 124.98 (Ar-C), 126.08 (Ar-C), 129.05 (Ar-C), 131.41 (Ar-C), 134.78 (Ar-C), 137.57 (Ar-C), 141.03 (Ar-C), 144.81 (Ar-C), 145.87 (Ar-C), 147.83 (Ar-C), 147.96 (Ar-C), 150.33 (Ar-C), 150.47 (Ar-C), 150.72 (Ar-C), 150.85 (Ar-C), 153.26 (Ar-C), 153.37 (Ar-C), 155.19 (Ar-C), 164.82 (-C=O , ethyl ester); HPLC: 99.5%. ESI-MS m/z of $\text{C}_{32}\text{H}_{27}\text{BrF}_2\text{N}_6\text{O}_4\text{S}$ [$\text{M} + \text{H} + 2$] $^+$ 699.00 was obtained for a calculated mass of 696.10.

Ethyl 6-bromo-4-(4-(2-(cyclopropanesulfonamido)phenyl)piperazin-1-yl)-2-(1H-imidazole-1-yl)quinoline-3-carboxylate (17): Procedure A, (R_1 : cyclopropane sulfonyl chloride) Yield: 67.3%, light brown solid; mp: 186.8–187.8 °C; IR (ν max, cm^{-1}): 1720.50 (-C=O , ester), 1589.34 (-C=N), 1489.05 (-S=O), 1226.73 (-C-N), 1072.42 (-C-O), 756.10 (-C-Br); ^1H NMR (400 MHz, $\text{DMSO-}d_6$): δ 0.93–0.98 (m, 4H, -CH_2 , cyclopropane), 1.06 (t, $J = 14.0$ Hz, 3H, $\text{-CH}_3\text{CH}_2$), 2.77–2.80 (m, 1H, -CH , cyclopropane), 2.95–2.96 (m, 4H, $\text{-CH}_2\text{CH}_2$, piperazine ring), 3.69–3.71 (m, 4H, $\text{-CH}_2\text{CH}_2$, piperazine ring), 4.10 (q, $J = 14.4$ Hz, 2H, $\text{-CH}_3\text{CH}_2$), 7.09–7.14 (m, 3H, Ar-H), 7.22 (s, 1H, Ar-H), 7.25–7.28 (m, 1H, Ar-H), 7.43–7.46 (m, 1H, Ar-H), 7.51 (s, 1H, Ar-H), 7.75 (d, $J = 8.8$ Hz, 1H, Ar-H), 7.88 (dd, $J = 8.8$ Hz and 8.8 Hz, 1H, Ar-H), 7.93 (s, 1H, Ar-H), 8.57 (s, 1H, -NH , D_2O exchangeable). ^{13}C NMR (100.6 MHz, $\text{DMSO-}d_6$): δ 5.20 (-CH_2 , cyclopropane), 13.41 ($\text{-CH}_3\text{CH}_2$), 30.34 (-CH , cyclopropane), 48.27 (-CH_2 , Piperazine), 51.62 (-CH_2 , Piperazine), 62.19 ($\text{-CH}_3\text{CH}_2$), 117.43 (Ar-C), 118.67 (Ar-C), 121.68 (Ar-C), 122.06 (Ar-C), 124.55 (Ar-C), 125.03 (Ar-C), 129.06 (Ar-C), 132.65 (Ar-C), 134.78 (Ar-C), 138.66 (Ar-C), 141.01 (Ar-C), 143.90 (Ar-C), 145.88 (Ar-C), 155.30 (Ar-C), 164.86 (-C=O , ethyl ester); HPLC: 99.4%. ESI-MS m/z of $\text{C}_{28}\text{H}_{29}\text{BrN}_6\text{O}_4\text{S}$ [$\text{M} + \text{H} + 2$] $^+$ 627.15 was obtained for a calculated mass of 624.12.

Ethyl 6-bromo-4-(4-(2-((2-fluorophenyl)sulfonamido)phenyl)piperazin-1-yl)-2-(1H-imidazole-1-yl)quinoline-3-carboxylate (18): Procedure A, (R_1 : 2-fluorobenzenesulfonyl chloride) Yield: 76.9%, light brown solid; mp: 185.9–186.9 °C; IR (ν max, cm^{-1}): 1720.50 (-C=O , ester), 1589.34 (-C=N), 1496.76 (-S=O), 1226.73 (-C-N), 1080.14 (-C-O), 756.10 (-C-Br); ^1H NMR (400 MHz, $\text{DMSO-}d_6$): δ 1.06 (t, $J = 14.4$ Hz, 3H, $\text{-CH}_3\text{CH}_2$), 2.73 (s, 4H, $\text{-CH}_2\text{CH}_2$, piperazine ring), 3.56 (s, 4H, $\text{-CH}_2\text{CH}_2$, piperazine ring), 4.08 (q, $J = 14.0$ Hz, 2H, $\text{-CH}_3\text{CH}_2$), 7.06–7.13 (m, 3H, Ar-H), 7.19–7.21 (m, 2H, Ar-H), 7.29–7.37 (m, 2H, Ar-H), 7.42–7.51 (m, 2H, Ar-H), 7.68–7.72 (m, 1H, Ar-H), 7.75–7.77 (m, 2H, Ar-H), 7.87–7.92 (m, 2H, Ar-H), 9.33 (s, 1H, -NH , D_2O exchangeable). ^{13}C NMR (100.6 MHz, $\text{DMSO-}d_6$): δ 13.41 ($\text{-CH}_3\text{CH}_2$), 48.07 (-CH_2 , Piperazine), 51.71 (-CH_2 , Piperazine), 62.18 ($\text{-CH}_3\text{CH}_2$), 117.17 (Ar-C), 117.38 (Ar-C), 117.46 (Ar-C), 118.62 (Ar-C), 121.66 (Ar-C), 122.05 (Ar-C), 122.24 (Ar-C), 122.41 (Ar-C), 124.54 (Ar-C), 124.90 (Ar-C), 125.10 (Ar-C), 125.95 (Ar-C), 127.54 (Ar-C), 127.67 (Ar-C), 129.09 (Ar-C), 130.09 (Ar-C), 131.42 (Ar-C), 134.78 (Ar-C), 135.79 (Ar-C), 135.87 (Ar-C), 141.04 (Ar-C), 144.45 (Ar-C), 144.58 (Ar-C), 145.86 (Ar-C), 155.18 (Ar-C), 156.87 (Ar-C), 159.39 (Ar-C), 164.82 (-C=O , ethyl ester); HPLC: 99.6%. ESI-MS m/z of $\text{C}_{31}\text{H}_{28}\text{BrFN}_6\text{O}_4\text{S}$ [$\text{M} + \text{H} + 2$] $^+$ 681.20 was obtained for a calculated mass of 678.11.

Ethyl 6-bromo-4-(4-(2-((3-cyanophenyl)sulfonamido)phenyl)

piperazin-1-yl)-2-(1H-imidazole-1-yl)quinoline-3-carboxylate (19): Procedure A, (R_1 : 3-cyanobenzenesulfonyl chloride) Yield: 66.5%, off white solid; mp: 219.5–220.5 °C; IR (ν max, cm^{-1}): 2237.42 (-CN), 1720.50 (-C=O , ester), 1581.62 (-C=N), 1211.29 (-C-N), 1033.84 (-C-O), 586.36 (-C-Br); ^1H NMR (400 MHz, $\text{DMSO-}d_6$): δ 1.05 (t, $J = 12.8$ Hz, 3H, $\text{-CH}_3\text{CH}_2$), 2.66 (s, 4H, $\text{-CH}_2\text{CH}_2$, piperazine ring), 3.54 (s, 4H, $\text{-CH}_2\text{CH}_2$, piperazine ring), 4.08–4.09 (m, 2H, $\text{-CH}_3\text{CH}_2$), 7.09–7.22 (m, 5H, Ar-H), 7.29–7.31 (m, 1H, Ar-H), 7.49–7.51 (m, 1H, Ar-H), 7.74–7.80 (m, 2H, Ar-H), 7.87–7.94 (m, 2H, Ar-H), 8.06–8.14 (m, 2H, Ar-H), 8.24–8.26 (m, 1H, Ar-H), 9.42 (s, 1H, -NH , D_2O exchangeable). ^{13}C NMR (100.6 MHz, $\text{DMSO-}d_6$): δ 13.40 ($\text{-CH}_3\text{CH}_2$), 47.94 (-CH_2 , Piperazine), 51.60 (-CH_2 , Piperazine), 62.19 ($\text{-CH}_3\text{CH}_2$), 112.41 (Ar-C), 117.31 (Ar-C), 117.46 (Ar-C), 118.58 (Ar-C), 121.58 (Ar-C), 121.91 (Ar-C), 122.16 (Ar-C), 123.50 (Ar-C), 124.54 (Ar-C), 124.99 (Ar-C), 126.31 (Ar-C), 128.80 (Ar-C), 129.06 (Ar-C), 130.13 (Ar-C), 130.72 (Ar-C), 131.06 (Ar-C), 131.22 (Ar-C), 134.81 (Ar-C), 136.38 (Ar-C), 138.63 (Ar-C), 140.89 (Ar-C), 141.67 (Ar-C), 145.03 (Ar-C), 145.88 (Ar-C), 155.15 (Ar-C), 164.78 (-C=O , ethyl ester); HPLC: 99.6%. ESI-MS m/z of $\text{C}_{32}\text{H}_{28}\text{BrN}_7\text{O}_4\text{S}$ [$\text{M} + \text{H}$] $^+$ 686.00 was obtained for a calculated mass of 685.11.

Ethyl 6-bromo-4-(4-(2-((4-(tert-butyl)phenyl)sulfonamido)phenyl)piperazin-1-yl)-2-(1H-imidazole-1-yl)quinoline-3-carboxylate (20): Procedure A, (R_1 : 4-tert-butylbenzenesulfonyl chloride) Yield: 81.8%, pale yellow solid; mp: 205.5–206.5 °C; IR (ν max, cm^{-1}): 1720.50 (-C=O , ester), 1589.34 (-C=N), 1496.70 (-S=O), 1226.73 (-C-N), 1087.85 (-C-O), 748.38 (-C-Br); ^1H NMR (400 MHz, CDCl_3): δ 1.13 (t, $J = 14.0$ Hz, 3H, $\text{-CH}_3\text{CH}_2$), 1.31 (s, 9H, $(\text{CH}_3)_3$, tert-butyl), 2.63 (s, 4H, $\text{-CH}_2\text{CH}_2$, piperazine ring), 3.58 (s, 4H, $\text{-CH}_2\text{CH}_2$, piperazine ring), 4.12 (q, $J = 14.0$ Hz, 2H, $\text{-CH}_3\text{CH}_2$), 7.06–7.09 (m, 1H, Ar-H), 7.13–7.19 (m, 3H, Ar-H), 7.32–7.34 (m, 2H, Ar-H), 7.45–7.47 (m, 2H, Ar-H), 7.63–7.67 (m, 2H, Ar-H), 7.74–7.77 (m, 4H, Ar-H), 7.92 (s, 1H, -NH , D_2O exchangeable). ^{13}C NMR (100.6 MHz, $\text{DMSO-}d_6$): δ 13.40 ($\text{-CH}_3\text{CH}_2$), 30.68 ($\text{-(CH}_3)_3$, tert-butyl), 34.82 ($\text{-C-CH}_3)_3$, tert-butyl), 48.03 (-CH_2 , Piperazine), 51.60 (-CH_2 , Piperazine), 62.14 ($\text{-CH}_3\text{CH}_2$), 117.40 (Ar-C), 118.55 (Ar-C), 121.61 (Ar-C), 122.05 (Ar-C), 122.15 (Ar-C), 123.10 (Ar-C), 124.55 (Ar-C), 125.22 (Ar-C), 125.75 (Ar-C), 125.98 (Ar-C), 126.43 (Ar-C), 128.99 (Ar-C), 129.14 (Ar-C), 132.31 (Ar-C), 134.81 (Ar-C), 137.41 (Ar-C), 138.63 (Ar-C), 141.01 (Ar-C), 144.58 (Ar-C), 145.85 (Ar-C), 155.15 (Ar-C), 155.95 (Ar-C), 164.84 (-C=O , ethyl ester); HPLC: 99.4%. ESI-MS m/z of $\text{C}_{35}\text{H}_{37}\text{BrN}_6\text{O}_4\text{S}$ [$\text{M} + \text{H} + 2$] $^+$ 719.1 was obtained for a calculated mass of 716.18.

Ethyl 6-bromo-2-(1H-imidazole-1-yl)-4-(4-(2-((4-(trifluoromethyl)phenyl)sulfonamido)phenyl)piperazin-1-yl)quinoline-3-carboxylate (21): Procedure A, (R_1 : 4-trifluoro methylbenzene sulfonyl chloride) Yield: 60.9%, pale yellow solid; mp: 215.5–216.5 °C; IR (ν max, cm^{-1}): 1720.50 (-C=O , ester), 1589.34 (-C=N), 1489.05 (-S=O), 1226.73 (-C-N), 1087.85 (-C-O), 709.80 (-C-Br); ^1H NMR (400 MHz, CDCl_3): δ 1.13 (t, $J = 14.0$ Hz, 3H, $\text{-CH}_3\text{CH}_2$), 2.69 (s, 4H, $\text{-CH}_2\text{CH}_2$, piperazine ring), 3.60 (s, 4H, $\text{-CH}_2\text{CH}_2$, piperazine ring), 4.12 (q, $J = 14.0$ Hz, 2H, $\text{-CH}_3\text{CH}_2$), 7.08–7.20 (m, 4H, Ar-H), 7.33–7.35 (m, 2H, Ar-H), 7.59–7.61 (m, 1H, Ar-H), 7.67–7.69 (m, 1H, Ar-H), 7.73–7.78 (m, 4H, Ar-H), 7.97–7.99 (m, 2H, Ar-H), 8.02–8.06 (m, 1H, -NH , D_2O exchangeable). ^{13}C NMR (100.6 MHz, $\text{DMSO-}d_6$): δ 13.36 ($\text{-CH}_3\text{CH}_2$), 47.91 (-CH_2 , Piperazine), 51.60 (-CH_2 , Piperazine), 62.12 ($\text{-CH}_3\text{CH}_2$), 117.44 (Ar-C), 118.57 (Ar-C), 121.63 (Ar-C), 122.04 (Ar-C), 124.08 (Ar-C), 124.56 (Ar-C), 124.74 (Ar-C), 125.02 (Ar-C), 126.47 (Ar-C), 127.61 (Ar-C), 129.05 (Ar-C), 131.33 (Ar-C), 131.97 (Ar-C), 132.28 (Ar-C), 132.61 (Ar-C), 132.91 (Ar-C), 134.81 (Ar-C), 141.04 (Ar-C), 144.30 (Ar-C), 145.37 (Ar-C), 145.87 (Ar-C), 155.14 (Ar-C), 164.83 (-C=O , ethyl ester); HPLC: 99.3%. ESI-MS m/z of $\text{C}_{32}\text{H}_{28}\text{BrF}_3\text{N}_6\text{O}_4\text{S}$ [$\text{M} + \text{H} + 2$] $^+$ 731.14 was obtained for a calculated mass of 728.10.

4.1.3. Representative procedure for synthesis of compound 23 to 29: (Procedure B)

To a mixture of compound 7 (1.0 eq) was dissolved in dry DMF (10 mL) were added different acid 22, (R_2 , 1.5 eq), HATU (1.5 eq) and

DIPEA (2 eq), reaction was stirred for 8 h at R.T., after completion of reaction, mixture was concentrated under reduced pressure and poured in water, extracted with ethyl acetate (3 × 50 mL). Combined organic layer was washed with brine and dried over anhydrous sodium sulfate. Organic layer was filtered and concentrated under reduced pressure to obtain crude product. Crude product was purified by column chromatography (silica gel 100–200 mesh, eluent: 10–20% ethyl acetate in n-hexane) to afford compounds **23** to **29**.

Ethyl 6-bromo-4-(4-(2-(5-fluoro-2-iodobenzamido)phenyl)piperazin-1-yl)-2-(1H-imidazole-1-yl)quinoline-3-carboxylate (23): Procedure B, (**R**₂: 5-fluoro-2-iodobenzoic acid) Yield: 64.4%, pale yellow solid; mp: 187.6–188.6 °C; IR (ν max, cm⁻¹): 1720.50 (C=O, ester), 1674.21 (C=O, amide), 1589.34 (C=N), 1226.72 (C-N), 1080.13 (C-O), 756.03 (C-Br), 633.79 (C-I), 563.21 (C-F); ¹H NMR (400 MHz, DMSO-*d*₆): δ 1.06 (t, *J* = 14.0 Hz, 3H, -CH₃CH₂), 3.02 (s, 4H, -CH₂CH₂, piperazine ring), 3.56 (s, 4H, -CH₂CH₂, piperazine ring), 4.09 (q, *J* = 14.0 Hz, 2H, -CH₃CH₂), 7.07 (d, *J* = 2.0, Hz, 1H, Ar-H), 7.12–7.23 (m, 5H, Ar-H), 7.46 (dd, *J* = 8.8 Hz and 8.8 Hz, 1H, Ar-H), 7.50 (s, 1H, Ar-H), 7.72 (d, *J* = 2.0, Hz, 1H, Ar-H), 7.87 (dd, *J* = 8.8 Hz and 9.2 Hz, 1H, Ar-H), 7.91–8.01 (m, 3H, Ar-H), 9.61 (s, 1H, -NH, D₂O exchangeable). ¹³C NMR (100.6 MHz, DMSO-*d*₆): δ 13.41 (-CH₃CH₂), 48.07 (-CH₂, Piperazine), 51.15 (-CH₂, Piperazine), 62.19 (-CH₃CH₂), 115.43 (Ar-C), 115.67 (Ar-C), 117.37 (Ar-C), 118.15 (Ar-C), 118.37 (Ar-C), 118.58 (Ar-C), 120.31 (Ar-C), 121.66 (Ar-C), 122.04 (Ar-C), 122.99 (Ar-C), 123.05 (Ar-C), 123.88 (Ar-C), 124.53 (Ar-C), 125.39 (Ar-C), 129.00 (Ar-C), 129.12 (Ar-C), 131.87 (Ar-C), 134.76 (Ar-C), 138.64 (Ar-C), 140.86 (Ar-C), 140.94 (Ar-C), 141.04 (Ar-C), 143.82 (Ar-C), 144.63 (Ar-C), 144.71 (Ar-C), 145.83 (Ar-C), 155.27 (Ar-C), 160.67 (Ar-C), 163.13 (Ar-C), 164.80 (C=O, amide), 166.31 (C=O, ethyl ester); HPLC: 98.9%. ESI-MS *m/z* of C₃₂H₂₇BrFIN₆O₃ [M+H]⁺ 769.20 was obtained for a calculated mass of 768.04.

Ethyl 6-bromo-4-(4-(2-(2-bromo-5-fluorobenzamido)phenyl)piperazin-1-yl)-2-(1H-imidazole-1-yl)quinoline-3-carboxylate (24): Procedure B, (**R**₂: 5-fluoro-2-bromobenzoic acid) Yield: 75.0%, pale yellow solid; mp: 201.6–202.6 °C; IR (ν max, cm⁻¹): 1720.50 (C=O, ester), 1674.21 (C=O, amide), 1581.63 (C=N), 1226.73 (C-N), 1080.14 (C-O), 748.38 (C-Br); ¹H NMR (400 MHz, DMSO-*d*₆): δ 1.06 (t, *J* = 14.0 Hz, 3H, -CH₃CH₂), 3.01 (s, 4H, -CH₂CH₂, piperazine ring), 3.65 (s, 4H, -CH₂CH₂, piperazine ring), 4.09 (q, *J* = 14.4 Hz, 2H, -CH₃CH₂), 7.07–7.08 (m, 1H, Ar-H), 7.13–7.23 (m, 4H, Ar-H), 7.29–7.33 (m, 1H, Ar-H), 7.50–7.58 (m, 2H, Ar-H), 7.71–7.78 (m, 2H, Ar-H), 7.85–7.91 (m, 2H, Ar-H), 7.99–8.01 (m, 1H, Ar-H), 9.65 (s, 1H, -NH, D₂O exchangeable). ¹³C NMR (100.6 MHz, DMSO-*d*₆): δ 13.42 (-CH₃CH₂), 48.07 (-CH₂, Piperazine), 51.17 (-CH₂, Piperazine), 62.19 (-CH₃CH₂), 113.43 (Ar-C), 113.46 (Ar-C), 116.04 (Ar-C), 116.29 (Ar-C), 117.24 (Ar-C), 117.40 (Ar-C), 117.49 (Ar-C), 118.13 (Ar-C), 118.36 (Ar-C), 118.59 (Ar-C), 119.60 (Ar-C), 119.73 (Ar-C), 120.33 (Ar-C), 121.68 (Ar-C), 122.07 (Ar-C), 123.04 (Ar-C), 123.92 (Ar-C), 124.56 (Ar-C), 125.40 (Ar-C), 129.02 (Ar-C), 131.82 (Ar-C), 134.60 (Ar-C), 134.68 (Ar-C), 134.78 (Ar-C), 135.56 (Ar-C), 135.63 (Ar-C), 138.67 (Ar-C), 140.60 (Ar-C), 140.67 (Ar-C), 141.00 (Ar-C), 143.84 (Ar-C), 145.85 (Ar-C), 155.28 (Ar-C), 159.63 (Ar-C), 159.88 (Ar-C), 162.12 (Ar-C), 162.33 (Ar-C), 164.59 (Ar-C), 164.83 (C=O, amide), 166.20 (C=O, ethyl ester); HPLC: 93.5%. ESI-MS *m/z* of C₃₂H₂₇Br₂FN₆O₃ [M+H]⁺ 723.20 was obtained for a calculated mass of 720.05.

Ethyl 6-bromo-4-(4-(2-(2,3-dimethoxybenzamido)phenyl)piperazin-1-yl)-2-(1H-imidazole-1-yl)quinoline-3-carboxylate (25): Procedure B, (**R**₂: 2,3-dimethoxybenzoic acid) Yield: 80.1%, pale yellow solid; mp: 240.1–241.1 °C; IR (ν max, cm⁻¹): 1720.50 (C=O, ester), 1589.34 (C=N), 1226.72 (C-N), 1049.27 (C-O), 748.38 (C-Br); ¹H NMR (400 MHz, DMSO-*d*₆): δ 1.05 (t, *J* = 14.0 Hz, 3H, -CH₃CH₂), 2.99 (s, 4H, -CH₂CH₂, piperazine ring), 3.69 (s, 4H, -CH₂CH₂, piperazine ring), 3.86 (s, 3H, -OCH₃), 3.92 (s, 3H, -OCH₃), 4.08–4.09 (m, 2H, *J* = 14.4 Hz, 2H, -CH₃CH₂), 7.09–7.33 (m, 7H, Ar-H), 7.51 (s, 1H, Ar-H), 7.61–7.63 (m, 1H, Ar-H), 7.75–7.77 (m, 1H, Ar-H), 7.88–7.92 (m, 2H, Ar-H), 8.54–8.56 (m, 1H, Ar-H), 11.00 (s, 1H, -NH, D₂O exchangeable).

¹³C NMR (100.6 MHz, DMSO-*d*₆): δ 13.36 (-CH₃CH₂), 48.36 (-CH₂, Piperazine), 51.60 (-CH₂, Piperazine), 56.07 (-OCH₃), 61.38 (-OCH₃), 62.22 (-CH₃CH₂), 116.36 (Ar-C), 117.51 (Ar-C), 118.56 (Ar-C), 119.64 (Ar-C), 120.77 (Ar-C), 121.77 (Ar-C), 121.96 (Ar-C), 122.07 (Ar-C), 123.87 (Ar-C), 124.51 (Ar-C), 124.56 (Ar-C), 125.03 (Ar-C), 126.72 (Ar-C), 129.09 (Ar-C), 133.86 (Ar-C), 134.81 (Ar-C), 138.67 (Ar-C), 141.12 (Ar-C), 141.47 (Ar-C), 145.81 (Ar-C), 147.07 (Ar-C), 152.60 (Ar-C), 155.19 (Ar-C), 162.22 (C=O, amide), 164.81 (C=O, ethyl ester); HPLC: 98.0%. ESI-MS *m/z* of C₃₄H₃₃BrN₆O₅ [M+H+2]⁺ 687.10 was obtained for a calculated mass of 684.17.

Ethyl 6-bromo-2-(1H-imidazole-1-yl)-4-(4-(2-(1-methyl-3-propyl-1H-pyrazole-5-carboxamido)phenyl)piperazin-1-yl)quinoline-3-carboxylate (26): Procedure B, (**R**₂: 1-methyl-3-propyl-1H-pyrazole-5-carboxylic acid) Yield: 77.0%, pale yellow solid; mp: 163.5–164.5 °C; IR (ν max, cm⁻¹): 1720.50 (C=O, ester), 1634.21 (C=O, amide), 1589.34 (C=N), 1226.72 (C-N), 1041.56 (C-O), 748.38 (C-Br); ¹H NMR (400 MHz, DMSO-*d*₆): δ 0.91 (t, *J* = 14.4 Hz, 3H, -CH₃CH₂CH₂, pyrazole), 1.05 (t, *J* = 14.4 Hz, 3H, -CH₃CH₂), 1.61 (q, *J* = 14.8 Hz, 2H, -CH₃CH₂CH₂, pyrazole), 2.53–2.55 (m, 2H, -CH₃CH₂CH₂, pyrazole), 2.99 (s, 4H, -CH₂CH₂, piperazine ring), 3.65 (s, 4H, -CH₂CH₂, piperazine ring), 4.10–4.11 (m, 5H, -CH₃CH₂ and -N-CH₃), 6.82 (s, 1H, Ar-H), 7.10 (s, 1H, Ar-H), 7.16–7.21 (m, 3H, Ar-H), 7.27–7.28 (m, 1H, Ar-H), 7.50 (s, 1H, Ar-H), 7.73–7.75 (m, 1H, Ar-H), 7.88–7.91 (m, 2H, Ar-H), 8.00–8.02 (m, 1H, Ar-H), 9.40 (s, 1H, -NH, D₂O exchangeable). ¹³C NMR (100.6 MHz, DMSO-*d*₆): δ 13.37 (-CH₃CH₂), 13.63 (-CH₃CH₂CH₂, pyrazole), 22.17 (-CH₃CH₂CH₂, pyrazole), 29.34 (-CH₃CH₂CH₂, pyrazole), 48.69 (-CH₂, Piperazine), 51.19 (-CH₂, Piperazine), 62.18 (-CH₃CH₂), 105.51 (-N-CH₃), 117.59 (Ar-C), 118.72 (Ar-C), 120.77 (Ar-C), 121.75 (Ar-C), 121.81 (Ar-C), 122.05 (Ar-C), 124.50 (Ar-C), 124.56 (Ar-C), 125.00 (Ar-C), 129.07 (Ar-C), 129.16 (Ar-C), 132.12 (Ar-C), 132.15 (Ar-C), 134.80 (Ar-C), 135.59 (Ar-C), 135.61 (Ar-C), 138.65 (Ar-C), 141.03 (Ar-C), 143.09 (Ar-C), 145.82 (Ar-C), 150.35 (Ar-C), 155.30 (Ar-C), 157.55 (Ar-C), 162.18 (C=O, amide), 164.79 (C=O, ethyl ester); HPLC: 96.3%. ESI-MS *m/z* of C₃₃H₃₅BrN₈O₃ [M+H+2]⁺ 673.20 was obtained for a calculated mass of 670.20.

Ethyl 6-bromo-2-(1H-imidazole-1-yl)-4-(4-(2-(3-oxocyclobutane-1-carboxamido)phenyl)piperazin-1-yl)quinoline-3-carboxylate (27): Procedure B, (**R**₂: 3-oxocyclobutane-1-carboxylic acid) Yield: 78.3%, light brown solid; mp: 207.9–208.9 °C; IR (ν max, cm⁻¹): 1728.21 (C=O, ester), 1634.21 (C=O, amide), 1589.34 (C=N), 1226.72 (C-N), 1103.28 (C-O), 748.38 (C-Br); ¹H NMR (400 MHz, CDCl₃): δ 1.14 (t, *J* = 14.0 Hz, 3H, -CH₃CH₂), 3.01 (s, 4H, -CH₂CH₂, piperazine ring), 3.21–3.36 (m, 4H, -CHCH₂COCH₂, cyclobutane), 3.58–3.64 (m, 1H, -CHCH₂COCH₂, cyclobutane), 3.69 (s, 4H, -CH₂CH₂, piperazine ring), 4.15 (q, *J* = 14.4 Hz, 2H, -CH₃CH₂), 7.09–7.15 (m, 2H, Ar-H), 7.19–7.23 (m, 2H, Ar-H), 7.32–7.35 (m, 2H, Ar-H), 7.68–7.79 (m, 3H, Ar-H), 8.40–8.42 (m, 1H, Ar-H), 8.75 (s, 1H, -NH, D₂O exchangeable). ¹³C NMR (100.6 MHz, DMSO-*d*₆): δ 13.41 (-CH₃CH₂), 28.26 (-CHCH₂COCH₂, cyclobutane), 48.22 (-CH₂, Piperazine), 50.87 (-CHCH₂COCH₂, cyclobutane), 51.05 (-CH₂, Piperazine), 62.21 (-CH₃CH₂), 117.52 (Ar-C), 118.76 (Ar-C), 120.02 (Ar-C), 121.73 (Ar-C), 122.07 (Ar-C), 122.39 (Ar-C), 123.93 (Ar-C), 124.58 (Ar-C), 124.64 (Ar-C), 129.09 (Ar-C), 129.15 (Ar-C), 132.21 (Ar-C), 134.81 (Ar-C), 138.66 (Ar-C), 141.03 (Ar-C), 143.00 (Ar-C), 145.85 (Ar-C), 155.38 (Ar-C), 164.84 (C=O, amide), 171.97 (C=O, ethyl ester), 205.16 (C=O, cyclobutane); HPLC: 96.0%. ESI-MS *m/z* of C₃₀H₂₉BrN₆O₄ [M+H]⁺ 617.25 was obtained for a calculated mass of 616.14.

Ethyl 6-bromo-4-(4-(2-(2-fluorobenzamido)phenyl)piperazin-1-yl)-2-(1H-imidazole-1-yl)quinoline-3-carboxylate (28): Procedure B, (**R**₂: 2-fluoro benzoic acid) Yield: 86.5%, pale yellow solid; mp: 178.5–179.5 °C; IR (ν max, cm⁻¹): 1728.21 (C=O, ester), 1658.78 (C=O, amide), 1589.34 (C=N), 1226.72 (C-N), 1041.56 (C-O), 748.38 (C-Br), 655.79 (C-F); ¹H NMR (400 MHz, DMSO-*d*₆): δ 1.06 (t, *J* = 14.0 Hz, 3H, -CH₃CH₂), 3.00 (s, 4H, -CH₂CH₂, piperazine ring), 3.68

(s, 4H, $-\text{CH}_2\text{CH}_2$, piperazine ring), 4.09 (q, $J = 14.0$ Hz, 2H, $-\text{CH}_2\text{CH}_3$), 7.18–7.22 (m, 4H, Ar-H), 7.35–7.52 (m, 4H, Ar-H), 7.65–7.66 (m, 1H, Ar-H), 7.76–7.78 (m, 1H, Ar-H), 7.88–8.03 (m, 3H, Ar-H), 8.40–8.42 (m, 1H, Ar-H), 9.98–10.01 (m, 1H, $-\text{NH}$, D_2O exchangeable). ^{13}C NMR (100.6 MHz, $\text{DMSO}-d_6$): δ 13.43 ($-\text{CH}_3\text{CH}_2$), 48.58 ($-\text{CH}_2$, Piperazine), 51.62 ($-\text{CH}_2$, Piperazine), 62.26 ($-\text{CH}_3\text{CH}_2$), 116.41 (Ar-C), 116.65 (Ar-C), 117.62 (Ar-C), 118.70 (Ar-C), 120.15 (Ar-C), 121.33 (Ar-C), 121.79 (Ar-C), 121.88 (Ar-C), 122.10 (Ar-C), 124.52 (Ar-C), 124.61 (Ar-C), 125.27 (Ar-C), 129.16 (Ar-C), 131.35 (Ar-C), 133.41 (Ar-C), 133.97 (Ar-C), 134.07 (Ar-C), 134.86 (Ar-C), 138.70 (Ar-C), 141.12 (Ar-C), 141.87 (Ar-C), 145.84 (Ar-C), 155.28 (Ar-C), 158.51 (Ar-C), 160.73 (Ar-C), 160.97 (Ar-C), 164.85 ($-\text{C}=\text{O}$, amide), 171.99 ($-\text{C}=\text{O}$, ethyl ester); HPLC: 97.8%. ESI-MS m/z of $\text{C}_{32}\text{H}_{28}\text{BrFN}_6\text{O}_3$ [$\text{M} + \text{H} + 2$] $^+$ 645.20 was obtained for a calculated mass of 642.14.

Ethyl 6-bromo-4-(4-(2-(3-bromobenzamido)phenyl)piperazin-1-yl)-2-(1H-imidazole-1-yl) quinoline-3-carboxylate (29): Procedure B, (R_2 : 3-bromo benzoic acid) Yield: 78.1%, off white solid; mp: 191.9–192.9 °C; IR (ν max, cm^{-1}): 1728.21 ($-\text{C}=\text{O}$, ester), 1666.49 ($-\text{C}=\text{O}$, amide), 1519.90 ($-\text{C}=\text{N}$), 1211.29 ($-\text{C}-\text{N}$), 995.26 ($-\text{C}-\text{O}$), 717.51 ($-\text{C}-\text{Br}$); ^1H NMR (400 MHz, $\text{DMSO}-d_6$): δ 1.04 (t, $J = 13.6$ Hz, 3H, $-\text{CH}_3\text{CH}_2$), 3.01 (s, 4H, $-\text{CH}_2\text{CH}_2$, piperazine ring), 3.65 (s, 4H, $-\text{CH}_2\text{CH}_2$, piperazine ring), 4.07–4.09 (m, 2H, $-\text{CH}_2\text{CH}_3$), 7.09–7.28 (m, 5H, Ar-H), 7.50–7.54 (m, 2H, Ar-H), 7.74–7.76 (m, 1H, Ar-H), 7.81–7.83 (m, 1H, Ar-H), 7.87–7.91 (m, 2H, Ar-H), 7.97–8.13 (m, 3H, Ar-H), 9.75 (s, 1H, $-\text{NH}$, D_2O exchangeable). ^{13}C NMR (100.6 MHz, $\text{DMSO}-d_6$): δ 13.41 ($-\text{CH}_3\text{CH}_2$), 48.67 ($-\text{CH}_2$, Piperazine), 51.20 ($-\text{CH}_2$, Piperazine), 62.21 ($-\text{CH}_3\text{CH}_2$), 117.58 (Ar-C), 118.71 (Ar-C), 120.72 (Ar-C), 121.75 (Ar-C), 121.96 (Ar-C), 122.05 (Ar-C), 122.54 (Ar-C), 124.43 (Ar-C), 124.56 (Ar-C), 125.24 (Ar-C), 126.10 (Ar-C), 129.17 (Ar-C), 130.15 (Ar-C), 130.97 (Ar-C), 132.39 (Ar-C), 134.40 (Ar-C), 134.81 (Ar-C), 136.82 (Ar-C), 138.66 (Ar-C), 141.05 (Ar-C), 143.72 (Ar-C), 145.82 (Ar-C), 155.27 (Ar-C), 163.16 ($-\text{C}=\text{O}$, amide), 164.81 ($-\text{C}=\text{O}$, ethyl ester); HPLC: 98.4%. ESI-MS m/z of $\text{C}_{32}\text{H}_{28}\text{Br}_2\text{N}_6\text{O}_3$ [$\text{M} + \text{H} + 2$] $^+$ 705.00 was obtained for a calculated mass of 702.06.

4.2. MTT assay

Virtually screened compounds had been screened against HCC827, H1975 and A549 cells by standard MTT assay. These cell lines were cultured in 10% fetal bovine serum (FBS). Inexact 4×10^3 cells have been suspended in MEM medium and plated into the 96-well plate in 5% CO_2 for 24 h. The virtually screened compounds were added to the culture medium and cell cultured maintained for 72 h. Freshly prepared MTT was added to each well and incubated with cells at 37 °C for 4 h. Absorbency at 492 nm were recorded utilizing the formazon crystals to determine the IC_{50} value [66–69].

4.3. In vitro enzymatic activity assay

The assay was performed as reported by Kashem et al. Three mechanistically distinct kinase assays compared: measurement of intrinsic ATPase activity identified the most comprehensive set of ITK inhibitors. All the enzymatic reactions were conducted at 30 °C for 40 min. The 50 μL reaction mixture contains 40 mM Tris, pH 7.4, 10 mM MgCl_2 , 0.1 mg/mL BSA, 1 mM DTT, 10 μM ATP, 25 ng kinase and the 0.2 mg/mL enzyme substrate (Poly (Glu, Tyr)). The compounds were diluted in 10% DMSO and 5 μL of the dilution was added to a 50 μL reaction so that the final concentration of DMSO is 1% in all of reactions. The assay was performed by using Kinase-Glo Plus luminescence kinase assay kit. It measures kinase activity by quantitating the amount of ATP remaining in solution following a kinase reaction. The luminescent signal from the assay is correlated with the amount of ATP present and is inversely correlated with the amount of kinase activity. The IC_{50} values were calculated using nonlinear regression with normalized dose-response fit using GraphPad Prism 5.0 Software [70,71].

4.4. Apoptosis study

Apoptosis was determined by staining the cells with Annexin V-Fluorescein isothiocyanate (FITC) and counterstaining with PI using the Annexin V-FITC/PI apoptosis detection kit (BD Biosciences, San Diego, CA) according to the manufacturer's instructions. Briefly, 4×10^6 cell/T 75 flasks were exposed to compound at its IC_{50} concentration for 24 and 48 h. The cells then were collected by trypsinization and 0.5×10^6 cells were washed twice with phosphate-buffered saline (PBS) and stained with 5 μL Annexin V-FITC and 5 μL PI in 1x binding buffer for 15 min at room temperature in the dark. Analyses were performed using BD LSR Fortessa with FACS Diva version 6.2 software [29,65].

4.5. Computational studies

The docking calculations of all synthesised molecules were carried out against EGFR tyrosine kinase using Smina molecular docking software. Smina is the fork of AutoDock Vina and is customized to better support scoring function development and high-performance energy minimization. The 2D structure of all ligands were drawn in Marvin-Sketch software, converted to 3D structure and were subjected to energy minimization using steepest descent algorithm by Open Babel chemical toolbox. The X-ray crystal structure of enzymes was obtained from the Protein Data Bank and prepared for docking using Dock Prep, a built-in tool in UCSF Chimera Software. The generated lower energy conformers of all ligands were docked into defined active site of enzyme by using default scoring function of Smina. The images of docking results were saved using academic version of Maestro software.

The GROningen MAchine for Chemical Simulations (GROMACS) version 2021.2 was used to run the MD simulations for EGFR-Compound 6 complex. The CHARMM36 force field was used to do the energy minimization. The 'pdb2gmx' software was used to create the protein topology. The system was solvated in a cubic box using TIP3P as a water model, then neutralised by introducing counter ions. During the MD simulation, periodic boundary conditions were applied. The system's energy was minimised using the steepest descent technique with a limitation of $1000 \text{ kJ mol}^{-1} \text{ nm}^{-1}$. The system was then equilibrated for 100 ps utilizing NVT and NPT ensembles. During the equilibration process, the Berendsen algorithm was employed for the thermostat and barostat. Finally, the system was subjected to a 100 ns production MD.

The ADMET properties of compounds were predicted using PKcsm server and Swiss ADME [72–74].

Abbreviation used

EGFR, epidermal growth factor receptor; NSCLC, non-small cell lung cancer; ADME, absorption, distribution, metabolism and excretion; MD, Molecular dynamics; RMSD, root-mean-square deviation; DIPEA, N,N-Diisopropylethylamine, RMSF, Rocky Mountain spotted fever.

Declaration of competing interest

The authors declare that they have no known competing financial interests or personal relationships that could have appeared to influence the work reported in this paper.

Data availability

The data that has been used is confidential.

Acknowledgement

We acknowledge financial support from Council of Scientific and Industrial Research (CSIR), New Delhi India (File No. 02(0288)/17/EMR-II) and we are also thankful to The Head, Department of Chemistry, Radhabai Kale Mahila Mahavidyalaya, Ahmednagar, India, for support.

Appendix A. Supplementary data

Supplementary data to this article can be found online at <https://doi.org/10.1016/j.ejmech.2022.114889>.

References

- [1] B.R. Voldborg, L. Damstrup, M.S. Thomsen, H.S. Poulsen, Epidermal growth factor receptor (EGFR) and EGFR mutations, function and possible role in clinical trial, *Ann. Oncol.* 8 (1997) 1197–1206, <https://doi.org/10.1023/a:1008209720526>.
- [2] <https://my.clevelandclinic.org/health/articles/6203-non-small-cell-lung-cancer-rMeng>.
- [3] Y. Meng, B. Yu, H. Huang, Y. Peng, E. Li, Y. Yao, C. Song, W. Yu, K. Zhu, K. Wang, D. Yi, J. Du, J. Chang, Discovery of Osimertinib, a highly potent, selective and orally efficacious deuterated EGFR targeting clinical candidate for the treatment of non-small-cell lung cancer, *J. Med. Chem.* 2 (2021) 925–937, <https://doi.org/10.1021/acs.jmedchem.0c02005>.
- [4] F. Bray, J. Ferlay, I. Soerjomataram, R.L. Siegel, L.A. Torre, A. Jemal, Global cancer statistics 2018: GLOBOCAN estimates of incidence and mortality worldwide for 36 cancers in 185 countries, *CA A Cancer J. Clin.* 68 (2018) 394–424, <https://doi.org/10.3322/caac.21492>.
- [5] Y. Mao, D. Yang, J. He, M. Krasna, J. Epidemiology of lung cancer, *Surgical oncology clinics of North 25* (2016) 439–445, <https://doi.org/10.1016/j.soc.2016.02.001>. America. 25.
- [6] World Health Organization. <https://www.who.int/news-room/fact-sheets/detail/cancer>. 2021.
- [7] S.K. Tripathi, B.K. Biswal, Allosteric mutant-selective fourth generation EGFR inhibitors as an efficient combination therapeutic in the treatment of non-small cell lung carcinoma, *Drug Discov. Today* 26 (2021) 1466–1472, <https://doi.org/10.1016/j.drudis.2021.02.005>.
- [8] M. Scaltriti, J. Baselga, The epidermal growth factor receptor pathway: a model for targeted therapy, *Clin. Cancer Res.* 12 (2006) 5268–5272, <https://doi.org/10.1158/1078-0432.CCR-05-1554>.
- [9] P. He, S. Niu, S. Wang, X. Shi, S. Feng, L. Du, X. Zhang, Z. Ma, B. Yu, H. Liu, Discovery of WS-157 as a highly potent, selective and orally active EGFR inhibitor, *Acta Pharm. Sin. B* 9 (2019) 1193–1203, <https://doi.org/10.1016/j.apsb.2019.06.010>.
- [10] Z. Song, Y. Ge, C. Wang, S. Huang, X. Shu, K. Liu, Y. Zhou, X. Ma, Challenges, and perspectives on the development of small molecule EGFR inhibitors against T790M-mediated resistance in non-small-cell lung cancer, *J. Med. Chem.* 59 (2016) 6580–6594, <https://doi.org/10.1021/acs.jmedchem.5b00840>.
- [11] Y. Yarden, The EGFR family and its ligands in human cancer: signalling mechanisms and therapeutic opportunities, *Eur. J. Cancer* 37 (2001) 3–8, [https://doi.org/10.1016/s0959-8049\(01\)00230-1](https://doi.org/10.1016/s0959-8049(01)00230-1).
- [12] H. Patel, R. Pawara, A. Ansari, S. Surana, Recent updates on third generation EGFR inhibitors and emergence of fourth generation EGFR inhibitors to combat C797S resistance, *Eur. J. Med. Chem.* 142 (2017) 32–47, <https://doi.org/10.1016/j.ejmech.2017.05.027>.
- [13] V.D. Cataldo, D.L. Gibbons, S.R. Pérez, Treatment of non-small-cell lung cancer with erlotinib or gefitinib, *N. Engl. J. Med.* 364 (2011) 947–955, <https://doi.org/10.1056/NEJMc0807960>.
- [14] C.H. Yun, K.E. Mengwasser, A.V. Toms, M.S. Woo, H. Greulich, K.K. Wong, M. Meyerson, M.J. Eck, The T790M mutation in EGFR kinase causes drug resistance by increasing the affinity for ATP, *Proc. Natl. Acad. Sci. U.S.A.* 105 (2008) 2070–2075, <https://doi.org/10.1073/pnas.0709662105>.
- [15] D. Westover, J. Zugazagoitia, B.C. Cho, C.M. Lovly, L. PazAres, Mechanisms of acquired resistance to first- and second-generation EGFR tyrosine kinase inhibitors, *Ann. Oncol.* 29 (2018) 10–19, <https://doi.org/10.1093/annonc/mdx703>.
- [16] L.V. Sequist, Second-generation epidermal growth factor receptor tyrosine kinase inhibitors in non-small cell lung cancer, *Oncol.* 12 (2007) 325–330, <https://doi.org/10.1634/theoncologist.12-3-325>.
- [17] P.A. Jänne, Challenges of detecting EGFR T790M in gefitinib/erlotinib-resistant tumours, *Lung Cancer* 60 (2008) 3–9, [https://doi.org/10.1016/S0169-5002\(08\)70099-0](https://doi.org/10.1016/S0169-5002(08)70099-0).
- [18] L.V. Sequist, J.C. Soria, J.W. Goldman, H.A. Wakelee, S.M. Gadgeel, A. Varga, V. Papadimitrakopoulou, B.J. Solomon, G.R. Oxnard, R. Dziadziuszko, D.L. Aisner, R.C. Doebele, C. Galasso, E.B. Garon, R.S. Heist, J. Logan, J.W. Neal, M. A. Mendenhall, S. Nichols, Z. Piotrowska, A.J. Wozniak, M. Raponi, C.A. Karlovich, S. Jaw-Tsai, J. Isaacson, D. Despain, S.L. Matheny, L. Rolfe, A.R. Allen, D. R. Camidge, Rociletinib in EGFR-mutated non-small-cell lung cancer, *N. Engl. J. Med.* 372 (2015) 1700–1709, <https://doi.org/10.1056/NEJMoa1413654>.
- [19] S. Maity, S.K. Ranganath, P.Y. Nayak, Advances in targeting EGFR allosteric site as anti-NSCLC therapy to overcome the drug resistance, *Pharmacol. Rep.* 72 (2020) 799–813, <https://doi.org/10.1007/s43440-020-00131-0>.
- [20] X.E. Yan, P. Ayaz, S.J. Zhu, P. Zhao, L. Liang, C.H. Zhang, Y.C. Wu, J.L. Li, H. G. Choi, X. Huang, Y. Shan, D.E. Shaw, C.H. Yun, Structural basis of AZD9291 selectivity for EGFR T790M, *J. Med. Chem.* 63 (2020) 8502–8511, <https://doi.org/10.1021/acs.jmedchem.0c00891>.
- [21] A. Yver, Osimertinib (AZD9291) a science-driven, collaborative approach to rapid drug design and development, *Ann. Oncol.* 27 (2016) 1165–1170, <https://doi.org/10.1093/annonc/mdw129>.
- [22] H. Engelhardt, D. Böse, M. Petronczki, D. Scharn, G. Bader, A. Baum, A. Bergner, E. Chong, S. Döbel, G. Egger, C. Engelhardt, P. Ettmayer, J.E. Fuchs, T. Gerstberger, N. Gonnella, A. Grimm, E. Grondal, N. Haddad, B. Hopfgartner, R. Kousek, M. Krawiec, M. Kriz, L. Lamarre, J. Leung, M. Mayer, N.D. Patel, B.P. Simov, J. T. Reeves, R. Schnitzer, A. Schrenk, B. Sharps, F. Solca, H. Stadtmüller, Z. Tan, T. Wunberg, A. Zoephel, D.B. McConnell, Start selective and rigidify: the discovery path toward a next generation of EGFR tyrosine kinase inhibitors, *J. Med. Chem.* 62 (2019) 10272–10293, <https://doi.org/10.1021/acs.jmedchem.9b01169>.
- [23] J. Shen, T. Zhang, S.J. Zhu, M. Sun, L. Tong, M. Lai, R. Zhang, W. Xu, R. Wu, J. Ding, C.H. Yun, H. Xie, X. Lu, K. Ding, Structure-based design of 5-methylpyrimidopyridone derivatives as new wild-type sparing inhibitors of the epidermal growth factor receptor triple mutant (EGFR L858R/T790M/C797S), *J. Med. Chem.* 62 (2019) 7302–7308, <https://doi.org/10.1021/acs.jmedchem.9b00576>.
- [24] J. Engel, S. Smith, J. Lategahn, H.L. Tumbink, L. Goebel, C. Becker, E. Hennes, M. Keul, A. Unger, H. Müller, M. Baumann, C. Schultz-Fademrecht, G. Günther, J. G. Hengstler, D. Rauh, Structure-guided development of covalent and mutant-selective pyrazolopyrimidines to target T790M drug resistance in epidermal growth factor receptor, *J. Med. Chem.* 60 (2017) 7725–7744, <https://doi.org/10.1021/acs.jmedchem.7b00515>.
- [25] M. Günther, J. Lategahn, M. Juchum, E. Döring, M. Keul, J. Engel, H.L. Tumbink, D. Rauh, S. Laufer, Trisubstituted pyridinylimidazoles as potent inhibitors of the clinically resistant L858R/T790M/C797S EGFR mutant: targeting of both hydrophobic regions and the phosphate binding site, *J. Med. Chem.* 60 (2017) 5613–5637, <https://doi.org/10.1021/acs.jmedchem.7b00316>.
- [26] D.E. Heppner, M. Günther, F. Wittlinger, S.A. Laufer, M. J. Eck, Structural basis for EGFR mutant inhibition by trisubstituted imidazole inhibitors, *J. Med. Chem.* 63 (2020) 4293–4305, <https://doi.org/10.1021/acs.jmedchem.0c00200>.
- [27] H. Cheng, S.K. Nair, B.W. Murray, C. Almadden, S. Bailey, S. Baxi, D. Behenna, S. C. Schultz, D. Dalvie, D.M. Dinh, M.P. Edwards, J.L. Feng, R.A. Ferre, K. S. Gajiwala, M.D. Hemkens, A.J. Fisher, M. Jalaie, T.O. Johnson, R.S. Kania, S. Kephart, J. Lafontaine, B. Lunney, K.K.C. Liu, Z. Liu, J. Matthews, A. Nagata, S. Niessen, M.A. Ornelas, S.T.M. Orr, M. Pairish, S. Planken, S. Ren, D. Richter, K. Ryan, N. Sach, H. Shen, T. Smeal, J. Solowiej, S. Sutton, K. Tran, E. Tseng, W. Vernier, M. Walls, S. Wang, S.L. Weinrich, S. Xin, H. Xu, M.J. Yin, M. Zientek, R. Zhou, J.C. Kath, Discovery of 1-((3R,4R)-3-[(5-Chloro-2-[(1-methyl-1H-pyrazol-4-yl)amino]-7H-pyrrolo[2,3-d]-pyrimidin-4-yl)oxy)methyl]-4-methoxyppyridin-1-yl)prop-2-en-1-one (PF-06459888), a potent, WT sparing, irreversible inhibitor of T790M-containing EGFR mutants, *J. Med. Chem.* 59 (2016) 2005–2024, <https://doi.org/10.1021/acs.jmedchem.5b01633>.
- [28] K.S. Thress, C.P. Pawelczek, E. Felip, B.C. Cho, D. Stetson, B. Dougherty, Z. Lai, A. Markovets, A. Vivancos, Y. Kuang, D. Ercan, S.F. Matthews, M. Cantarini, J. C. Barrett, P.A. Janne, G.R. Oxnard, Acquired EGFR C797S mutation mediates resistance to AZD9291 in non-small cell lung cancer harboring EGFR T790M, *Nat. Med.* 21 (2015) 560–562, <https://doi.org/10.1038/nm.3854>.
- [29] K.S. Karnik, A.P. Sarkate, S.V. Tiwari, R. Azad, P.V.L.S. Burra, P.S. Wakte, Computational and synthetic approach with biological evaluation of substituted quinoline derivatives as small molecule L858R/T790M/C797S triple mutant EGFR inhibitors targeting resistance in non-small cell lung cancer (NSCLC), *Bioorg. Chem.* 107 (2021), 104612, <https://doi.org/10.1016/j.bioorg.2020.104612>.
- [30] H.A. Yu, S.K. Tian, A.E. Drilon, L. Borsu, G.J. Rieley, M.E. Arcila, M. Ladanyi, Acquired resistance of EGFR-mutant lung cancer to a T790M-specific EGFR inhibitor: emergence of a third mutation (C797S) in the EGFR tyrosine kinase domain, *JAMA Oncol.* 1 (2015) 982–984, <https://doi.org/10.1001/jamaoncol.2015.1066>.
- [31] P.A. Dickinson, M.V. Cantarini, J. Collier, P. Frewer, S. Martin, K. Pickup, P. Ballard, Metabolic disposition of Osimertinib in rats, dogs, and humans: insights into a drug designed to bind covalently to a cysteine residue of epidermal growth factor receptor, *Drug Metab. Dispos.* 44 (2016) 1201–1212, <https://doi.org/10.1124/dmd.115.069203>.
- [32] R. Minari, P. Bordi, M. Tiseo, Third-generation epidermal growth factor receptor tyrosine kinase inhibitors in T790M-positive non-small cell lung cancer: review on emerged mechanisms of resistance, *Transl. Lung Cancer Res.* 5 (2016) 695–708, <https://doi.org/10.21037/tlcr.2016.12.02>.
- [33] H. Patel, R. Pawara, A. Ansari, S. Surana, Recent updates on third generation EGFR inhibitors and emergence of fourth generation EGFR inhibitors to combat C797S resistance, *Eur. J. Med. Chem.* 142 (2017) 32–47, <https://doi.org/10.1016/j.ejmech.2017.05.027>.
- [34] Y. Jia, C.H. Yun, E. Park, D. Ercan, M. Manuia, J. Juarez, C. Xu, K. Rhee, T. Chen, H. Zhang, S. Palakurthi, J. Jang, G. Lelais, M. DiDonato, B. Bursulaya, P. Y. Michellys, R. Epple, T.H. Marsilje, M. McNeill, W. Lu, J. Harris, S. Bender, K. K. Wong, P.A. Jänne, M.J. Eck, Overcoming EGFR(T790M) and EGFR(C797S) resistance with mutant-selective allosteric inhibitors, *Nature* 534 (2016) 129–132, <https://doi.org/10.1038/nature17960>.
- [35] S. Wang, Y. Song, D. Liu, EAI045: the fourth-generation EGFR inhibitor overcoming T790M and C797S resistance, *Cancer Lett.* 385 (2017) 51–54, <https://doi.org/10.1016/j.canlet.2016.11.008>.
- [36] J. Zhao, A. Guerrero, K. Kelnar, H.P. Peltire, A.G. Bader, Synergy between next generation EGFR tyrosine kinase inhibitors and miR-34a in the inhibition of non-small-cell lung cancer, *Lung Cancer* 108 (2017) 96–102, <https://doi.org/10.1016/j.lungcan.2017.02.020>.
- [37] Y. Zheng, W. Zhang, L. Meng, X. Wu, L. Zhang, L. An, C. Lia, C. Gao, L. Xu, Y. Liu, C. Li, Design, synthesis and biological evaluation of 4-aniline quinazoline derivatives conjugated with hydrogen sulfide (H₂S) donors as potent EGFR inhibitors against L858R resistance mutation, *Eur. J. Med. Chem.* 202 (2020), 112555, <https://doi.org/10.1016/j.ejmech.2020.112522>.
- [38] L.M. Antypenko, S.I. Kovalenko, O.V. Karpenko, A.M. Katsev, V.P. Novikov, N. S. Fedynyuna, 1-R-2-(1,2,4 triazol-1,5-c quinazolin-2-ylthio) etanon (ol) s: synthesis, bioluminescence inhibition, molecular docking studies, antibacterial and antifungal activities, *Curr. Comput. Aided Drug Des.* 12 (2016) 29–41.

- [39] M. Yulya, A. Oleksii, N. Inna, B. Galina, K. Sergii, Directed search of anti-inflammatory agents among (3H-Quinazoline-4-ylidene) hydrazides of N-protected amino acids and their heterocyclization products, *Antiinflamm. Antiallergy Agents. Med. Chem.* 19 (2020) 61–73, <https://doi.org/10.2174/1871523018666190115092215>.
- [40] R. Musiol, M. Serda, S.H. Bielowska, J. Polanski, Quinoline-based antifungals, *Curr. Med. Lett.* 17 (2010) 1960–1973, <https://doi.org/10.2174/092986710791163966>.
- [41] R. Neelarapu, J.R. Maignan, C.L. Lichorowic, A. Monastyrskiy, T.S. Mutka, A.N. L. Crue, L.D. Blake, D. Casandra, S. Mashkouri, J.N. Burrows, P.A. Willis, D.E. Kyle, R. Manetsch, Design and synthesis of orally bioavailable piperazine substituted 4 (1H)-Quinolones with potent antimalarial activity: structure-activity and structure-property relationship studies, *J. Med. Chem.* 61 (2018) 1450–1473, <https://doi.org/10.1021/acs.jmedchem.7b00738>.
- [42] H.S.A.A. Salem, G.H. Hegazy, K.E.H. El-Taher, S.M. El-Messery, A.M. Al-Obaid, H. I. El-Subbagh, Synthesis, anticonvulsant activity and molecular modelling study of some new hydrazinecarbothioamide, benzenesulfonohydrazide, and phenacylacetylhydrazide analogues of 4(3H)-quinazolinone, *Bioorg. Med. Chem. Lett.* 25 (2015) 1490–1499, <https://doi.org/10.1016/j.bmcl.2015.02.025>.
- [43] R.P. Modh, E.D. Clercq, C. Pannecouque, K.H. Chikhalia, Design, synthesis, antimicrobial activity and anti-HIV activity evaluation of novel hybrid quinazolinotriazine derivatives, *J. Enzym. Inhib. Med. Chem.* 29 (2014) 100–108, <https://doi.org/10.3109/14756366.2012.755622>.
- [44] M.U. Rahman, A. Rathore, A.A. Siddiqui, G. Parveen, M.S. Yar, Synthesis and characterization of quinazoline derivatives: search for hybrid molecule as diuretic and antihypertensive agents, *J. Enzym. Inhib. Med. Chem.* 29 (2014) 733–743, <https://doi.org/10.3109/14756366.2013.845820>.
- [45] G.I. Solyanik, Quinazoline compounds for antitumor treatment, *Exp. Oncol.* 41 (2019) 3–6.
- [46] M.A. Pradeep, R.K. Nagiri, S. Krishana, N.S. Reddy, S. Kanugala, C.G. Kumar, N. J. Babu, T. Ganapathi, N. Banda, Design and synthesis of novel pyrimidine/hexahydroquinazoline-fused pyrazolo 3,4-b pyridine derivatives. Their biological evaluation and docking studies, *Chem. Select.* 4 (2019) 138–144, <https://doi.org/10.1002/slct.201803078>.
- [47] A. Martorana, G.L. Monica, A. Lauria, Quinoline-based molecules targeting c-met, EGF, and VEGF receptors and the proteins involved in related carcinogenic pathways, *Molecules* 25 (2020) 4279, <https://doi.org/10.3390/molecules25184279>.
- [48] M.A. Shaheen, A.A. El-Emam, N.S. El-Gohary, Design, synthesis and biological evaluation of new series of hexahydroquinoline and fused quinoline derivatives as potent inhibitors of wild-type EGFR and mutant EGFR (L858R and T790M), *Bioorg. Chem.* 105 (2020), 104274, <https://doi.org/10.1016/j.bioorg.2020.104274>.
- [49] V.R. Solomon, H. Lee, Quinoline as a privileged scaffold in cancer drug discovery, *Curr. Med. Chem.* 18 (2011) 1488–1508, <https://doi.org/10.2174/092986711795328382>.
- [50] M.F.A. Mohamed, G.D.A. Abuo-Rahma, Molecular targets and anticancer activity of quinoline–chalcone hybrids: literature review, *RSC Adv.* 10 (2020), 31139, <https://doi.org/10.1039/D0RA05594H>.
- [51] A. Erguc, M.D. Altintop, O. Atli, B. Sever, G. Iscan, G. Gormus, A. Ozdemir, Synthesis and biological evaluation of new quinoline-based thiazolyl hydrazone derivatives as potent antifungal and anticancer agents, *Lett. Drug Des. Discov.* 15 (2018) 193–202, <https://doi.org/10.2174/1570180814666171003145227>.
- [52] H.H. Li, H. Huang, X.H. Zhang, X.M. Luo, L.P. Lin, H.L. Jiang, J. Ding, K.X. Chen, H. Liu, Discovering novel 3-nitroquinolines as a new class of anticancer agents, *Acta Pharmacol. Sin.* 29 (2008) 1529–1538, <https://doi.org/10.1111/j.1745-7254.2008.00907.x>.
- [53] A. Martorana, G.L. Monica, A. Lauria, Quinoline-based molecules targeting c-met, EGF, and VEGF receptors and the proteins involved in related carcinogenic pathways, *Molecules* 25 (2020) 4279, <https://doi.org/10.3390/molecules25184279>.
- [54] M.A. El-Sayed, W.M. El-Husseiny, N.I. Abdel-Aziz, A.S. El-Azab, H.A. Abuelizz, A. A. Abdel-Aziz, Synthesis and biological evaluation of 2-styrylquinolines as antitumor agents and EGFR kinase inhibitors: molecular docking study, *J. Enzym. Inhib. Med. Chem.* 33 (2018) 199–209, <https://doi.org/10.1080/14756366.2017.1407926>.
- [55] J.A. Makawana, C.B. Sangani, L. Lin, H.L. Zhu, Schiff's base derivatives bearing nitroimidazole and quinoline nuclei: new class of anticancer agents and potential EGFR tyrosine kinase inhibitors, *Bioorg. Med. Chem. Lett.* 24 (2014) 1734–1736, <https://doi.org/10.1016/j.bmcl.2014.02.041>.
- [56] R.F. George, E.M. Samir, M.N. Abdelhamed, H.A. Abdel-Aziz, S.E. Abbas, Synthesis and anti-proliferative activity of some new quinoline based 4,5-dihydropyrazoles and their thiazole hybrids as EGFR inhibitors, *Bioorg. Chem.* 83 (2019) 186–197, <https://doi.org/10.1016/j.bioorg.2018.10.038>.
- [57] M.S. Abdelbaset, M. Abdel-Aziz, M. Ramadan, M.H. Abdelrahman, S.N. Abbas Bukhari, T.F.S. Ali, G.E.A. Abuo-Rahma, Discovery of novel thienoquinoline-2-carboxamide chalcone derivatives as antiproliferative EGFR tyrosine kinase inhibitors, *Bioorg. Med. Chem.* 27 (2019) 1076–1086, <https://doi.org/10.1016/j.bmc.2019.02.012>.
- [58] E.A. Abdelsalam, W.A. Zaghary, K.M. Amin, N.A.A. Taleb, A.A.I. Mekawey, W. M. Eldehna, H.A. Abdel-Aziz, S.F. Hammad, Synthesis and in vitro anticancer evaluation of some fused indazoles, quinazolines and quinolines as potential EGFR inhibitors, *Bioorg. Chem.* 89 (2019), 102985, <https://doi.org/10.1016/j.bioorg.2019.102985>.
- [59] R.A. Kardile, A.P. Sarkate, A.S. Borude, R.S. Mane, D.K. Lokwani, S.V. Tiwari, R. Azad, P.V.L.S. Burra, S.R. Thopate, Design and synthesis of novel conformationally constrained 7,12-dihydrodibenzo[b,h][1,6] naphthyridine and 7H-Chromeno[3,2-c] quinoline derivatives as topoisomerase I inhibitors: *In vitro* screening, molecular docking and ADME predictions, *Bioorg. Chem.* 115 (2021), 105174, <https://doi.org/10.1016/j.bioorg.2021.105174>.
- [60] G. Johansson, A.J. Jensen, K.Beierlein, New compounds useful for the treatment of obesity, type ii diabetes and cns disorders. *PCT Int. Appl.* 2004000828A1.
- [61] M. Berger, C. Kern, M. Eck, J. Schröder, N-heteroaryl compounds with cyclic bridging unit for the treatment of parasitic diseases. *PCT Int. Appl.* 2012041872A1.
- [62] H. Yu, J. Li, T.E. Richardson, P. Bharathi, B.H. Heasley, A. Goutopoulos, Preparation of benzamide derivatives for use in the treatment of fertility disorders, *PCT Int. Appl.* 2013012848A1 (2013).
- [63] C. Liang, Preparation of piperazine derivatives as TRPML modulators for the treatment of diseases, *PCT Int. Appl.* (2018), 2018005713.
- [64] R.M. Angell, N.M. Aston, P. Bamborough, M.J. Bamford, G.S. Cockerill, S. Joy, M.L. A. Walker, Preparation 5'-carbamoyl-1,1'-biphenyl-4-carboxamides as p38 kinase inhibitors, *PCT Int. Appl.* 2003032980 (2003).
- [65] K.S. Karnik, A.P. Sarkate, S.V. Tiwari, R. Azad, P.S. Wakte, Free energy perturbation guided Synthesis with Biological Evaluation of Substituted Quinoline derivatives as small molecule L858R/T790M/C797S mutant EGFR inhibitors targeting resistance in Non-Small Cell Lung Cancer (NSCLC), *Bioorg. Chem.* 115 (2021), 105226, <https://doi.org/10.1016/j.bioorg.2021.105226>.
- [66] T.R. Deshmukh, A.P. Sarkate, D.K. Lokwani, S.V. Tiwari, R. Azad, B.B. Shingate, New amide linked dimeric 1,2,3-triazoles bearing aryloxy scaffolds as a potent antiproliferative agents and EGFR tyrosine kinase phosphorylation inhibitors, *Bioorg. Med. Chem. Lett.* 29 (2019), 126618, <https://doi.org/10.1016/j.bmcl.2019.08.022>.
- [67] S.V. Tiwari, S. Siddiqui, J.A. Seijas, M.P. Vazquez-Tato, A.P. Sarkate, D.K. Lokwani, A.P.G. Nikalje, Microwave-assisted facile synthesis, anticancer evaluation and docking study of N-((5-(substituted methylene amino)-1,3,4, thiadiazol-2-yl) methyl) benzamide derivatives, *Molecules* 22 (2017) 995, <https://doi.org/10.3390/molecules22060995>.
- [68] A.V. Chate, S.P. Kamdi, A.N. Bhagat, C.K. Jadhav, A. Nipte, A.P. Sarkate, S. V. Tiwari, C.H. Gill, Design, synthesis and SAR study of novel spiro[pyrimido[5,4-b]quinoline-10,5'-pyrrolo[2,3-d]pyrimidine] derivatives as promising anticancer agents, *J. Het. Chem.* 55 (2018) 2297–2302, <https://doi.org/10.1002/jhet.3286>.
- [69] M.R. Bhosle, L.D. Khillare, J.R. Mali, A.P. Sarkate, D.K. Lokwani, S.V. Tiwari, DIPEAc promoted one-pot synthesis of dihydropyrido[2,3-d:6,5-d'] dipyrimidinetetraone and pyrimido[4,5-d]pyrimidine derivatives as potent tyrosinase inhibitors and anticancer agents: in vitro screening, Molecular docking and ADMET predictions, *New J. Chem.* 42 (2018) 18621–18632, <https://doi.org/10.1039/C8NJ04622K>.
- [70] M.A. Kashema, R.M. Nelson, J.D. Yingling, S.S. Pullen, A.S. Prokopowicz, J. W. Jones, J.P. Wolak, G.R. Rogers, M.M. Morelock, R.J. Snow, C.A. Homon, S. Jakes, Three mechanistically distinct kinase assays compared: measurement of intrinsic ATPase activity identified the most comprehensive set of ITK inhibitors, *J. Biomol. Screen* 12 (2007) 70–83, <https://doi.org/10.1177/1087057106296047>.
- [71] H. Lei, S. Fan, H. Zhang, Y.J. Liu, Y.Y. Hei, J.J. Zhang, A.Q. Zheng, M. Xin, M. Zhang, Discovery of novel 9-heterocyclized substituted 9H-purines as L858R/T790M/C797S mutant EGFR tyrosine kinase inhibitors, *Eur. J. Med. Chem.* 186 (2020), 111888, <https://doi.org/10.1016/j.ejmech.2019.111888>.
- [72] W. Doherty, N. Adler, A. Knox, D. Nolan, J. McGouran, A.P. Nikalje, D. Lokwani, A. Sarkate, P. Evans, Synthesis and evaluation of 1,2,3-triazole-containing vinyl and allyl sulfones as anti-trypanosomal agents, *Eur. J. Org. Chem.* 1 (2017) 175–185, <https://doi.org/10.1002/ejoc.201601221>.
- [73] D. Lokwani, R. Azad, A. Sarkate, P. Reddanna, D. Shinde, Structure based library design (SBLD) for new 1, 4-dihydropyrimidine scaffold as simultaneous COX-1/COX-2 and 5-LOX inhibitors, *bio, Med. Chem.* 23 (2015) 4533–4543, <https://doi.org/10.1016/j.bmc.2015.06.008>.
- [74] K.S. Karnik, A.P. Sarkate, D.K. Lokwani, S.V. Tiwari, R. Azad, P.S. Wakte, Molecular Dynamic Simulations based Discovery and Development of Thiazolidin-4-one derivatives as EGFR inhibitors targeting resistance in Non-Small Cell Lung Cancer (NSCLC). *J. Biomol. Struct. Dyn.*, <https://doi.org/10.1080/07391102.2022.2071339>.

Formulation Development and Evaluation of Herbal Nanoparticles containing Ointment of Leaves extract of *Rhynchosia rothii*

Sharad D. Tayade^{1,2*}, Narendra Silawat¹, Neetesh Jain¹

¹Faculty of Pharmacy, Oriental University, Indore, Madhya Pradesh, India-453555;

²Department of Pharmaceutics, Rajarshi Shahu College of Pharmacy, Buldhana, Maharashtra, India-443001.

*Corresponding Author: - Sharad D. Tayade

Email: sharad_tayade1@rediffmail.com

Doi: 10.47750/pnr.2022.13. S05.113

Abstract

In our previous work we have reported wound healing activity of leaves extract of *Rhynchosia rothii* in which we got excellent activity. Therefore in present study, the development of *Rhynchosia rothii* loaded Lycoat RS 720-BSA conjugated polymeric nanoparticles and subsequent ointment formulation has been aimed. Maillard Reaction was used to develop the Lycoat RS 720-BSA conjugate. The solvent evaporation approach was used to produce nanoparticles with *Rhynchosia rothii* loaded on them. The nanoparticles had a 257nm particle size and exhibited a spherical shape. The zeta potential in the formulation was -22.4 mV. Entrapment efficiency was 88.32% in the enhanced batch. The extracted content of the optimized batch was found to be 78.10%. A continuous release pattern was found by the *in-vitro* diffusion investigation, with 94.24% diffusion after 24 hours. The *Rhynchosia rothii* extract was created as an absorbent ointment formulation with a pH of 6.80–6.92 and a spread ability of 80.00–110.16 g.cm/s. It also has a distinctive aroma. Ointment containing herbal nanoparticles from the F4 batch has produced positive results. A new method of promoting nanoparticles in herbal medication delivery systems is by employing them in nanoparticles and an ointment. From present investigations we concluded that prepared ointment can be used clinically for the treatment of wounds if optimized further using more *in vitro* and *in vivo* models along with toxicity predictions.

Keywords: Herbal Nanoparticles, Lycoat RS-720, Solvent evaporation, Ointment, BSA

INTRODUCTION

For the treatment of skin conditions, a variety of topical dermatologic treatments, spanning from solids to liquids, are offered [1, 2]. The majority of ointments are made up of a base that primarily serves as a vehicle or carrier for the medications. The type of base also affects how well it works; therefore choosing an ointment base is a crucial step in formulation [3]. In contrast to fatty alcohols, traditional ointment bases have been oleaginous in nature, consisting of hydrocarbons like petrolatum, beeswax, and vegetable oils that do not permit the addition of any water. Topically applied ointments can serve a variety of functions, including protective, antimicrobial, emollient, antipruritic, keratolytic, and astringent. If the end product is to fulfill any of the aforementioned functions, the base of the ointment is crucial. The ointment base composition regulates the transfer of medications from the base to the human tissues as well as the depth of penetration [3, 4].

Particulate dispersions or solid particles with a size between 10 and 1000 nm are referred to as nanoparticles [5]. Their small size, variable composition, surface functionalization, and stability, which provide unique opportunities to interact with and target the tumor microenvironment, make them particularly alluring for the therapy of cancer [6, 7]. Polymeric nanoparticles are nanoparticles made of biocompatible and biodegradable polymers, either natural or manmade. Due to their small particle size and prolonged blood circulation, they have received specific attention during inspections for medication delivery and drug targeting [8].

The protein that is most abundant in plasma is BSA. It demonstrates significant buildup in the body's inflammatory and malignant regions [9]. It has a lengthy 19-day blood circulation half-life and several binding sites [10]. A serum albumin protein generated from cows is called bovine serum albumin. It is widely used as a benchmark for protein concentration. Lycoat RS 720 is a pea starch-based synthetic polymer. It exhibits strong film-forming and solution stability. It is the polymer with a regulated and sustained release [11, 12].

There are many species of *Rhynchosia* (Fabaceae) that are found in tropical and subtropical regions of the world. As an antibacterial, antidiabetic, abortive, healing, hepatoprotective, healer of boils, rheumatoid arthritis pain, and skin infection treatment, some plants from this genus have been utilized in traditional medicine [13]. So far, the genus *Rhynchosia* has yielded a total of 77 identified compounds, including as flavonoids, isoflavonoids, flavan-3-ols, xanthenes, biphenyls, simple polyphenols, and sterols. Interestingly, prenylated C-glycosylflavonoids and isoflavonoids are abundant in the genus *Rhynchosia rothii* [13, 14].

In addition, nanoparticles have been used as a pharmaceutical medium for a number of years as part of the technology used in the manufacturing of herbal medicines. The microscopic shape of nanoparticles that will increase the compound solution and reduce the dosage of medication is one of the benefits of the nanoparticle technology. Additionally, nanoparticles maintain skin moisture, penetrate the skin, and improve skin stability [15]. Ointments are oil-based, semi-solid medications for external use that are simple to apply. Ointments shouldn't smell rancid; hence they should be made of oil or a fat emulsion or wax with high water content [16]. The objective of this research was to use the ionic glass process to create an ointment with a nanoparticle formulation that contained paraffin wax and *Rhynchosia rothii* extract. Various amounts of *Rhynchosia rothii* extract nanoparticles were combined with the ointment base.

MATERIALS AND METHODS

Rhynchosia rothii herb leaves were collected from near region of Buldhana in Maharashtra. We received a gift sample of bovine serum albumin (Fraction V) from HiMedia Pvt. Ltd. in Mumbai, India. The supplier of Lycoat RS 720 was Roquette Pharma Pvt. Ltd. in Mumbai, India. The sunflower wax was received from M/s Mahesh Ltd. in Mumbai, India as a gift sample. Analytical-grade compounds were utilized for all other substances.

Preparation of methanolic extract from leaves of *Rhynchosia rothii*

Researchers used the procedures listed below to produce the extract. 1.5 kg of dry plant leaf material were subjected to continuous methanol extraction in a Soxhlet thimble until the material was consumed. When the solvent has evaporated, the result is an amorphous dark green powder. Whatman No. 1 filter paper was used to filter this solution. A Rotary evaporator was used to evaporate the solvent under reduced pressure and 90°C, and the gummy extract was then stored at 4°C for later research [17].

Pharmacognostic and Qualitative phytochemical evaluation of plant extract

Using established techniques, the extracts of *Rhynchosia rothii* produced during the extraction process were subjected to pharmacognostic and preliminary phytochemical testing for the presence of several phytoconstituents. [17]

Compatibility study

On the DSC Lab: Mettler Instrument, the differential scanning calorimetry (DSC) thermograms of the pure extract and the improved formulation were captured. All samples (2-4 mg) were precisely weighed into standard aluminum pans for analysis, and then the pans were sealed with aluminum lids. Analysis was done between 0-350°C at a heating rate of 10 degrees per minute 10°C/min in a nitrogen gas atmosphere (30 mL/min) [18].

FORMULATION AND DEVELOPMENT

Formulation of BSA-LYCOAT RS-720 conjugates

These Conjugates were prepared by Maillard reaction.

BSA and Lycoat RS 720 were dissolved together in water with a (1:1) molar ratio. The pH of the solution was adjusted to 7.1 with NaOH solution, then, the mixture solution was lyophilized. The lyophilized powder reacted at 60°C and 79% relative humidity in a desiccator containing saturated KBr solution for 24 h. The resultant products were kept at -20°C before use [19].

Nano preparation of extract

Polymeric nanoparticles were prepared by the solvent evaporation method. The polymeric nanoparticles were prepared by using plant extract to polymer conjugates ratio (1:2). The mixture was then subjected to Rotary evaporator for removal of the methanol. The dispersion is formed. It was subjected to high speed homogenizer (10,000 RPM for 15 min) and then passed through high pressure homogenizer at pressure of 700 bars and 7 cycles. Nanoparticles solution subjected to lyophilization and dry lyophilized powder of herbal polymeric nanoparticles was formed [20].

Formulation of ointment

Oily Base Preparation: Paraffin wax is melted on a hot plate and liquid paraffin is added to it followed by preservative benzoic acid. The mixture was transferred to pestle and mortar and polymeric nanoparticle containing the plant extract was added and grinded at room temperature to obtain a fine paste like substance. The ratio of chemicals to be taken is optimized by hit and trial method. Flavoring agents were also added later.

FORMULATION DESIGN AND OPTIMIZATION OF BATCH:

Formulation Design

Different batches of herbal polymeric nanoparticles were prepared based on the 3² factorial designs. The independent variables were Polymeric conjugates concentration in terms of mg (X₁) and HPH pressure in terms of bar (X₂) for all formulation batches.

Optimization data analysis and model-validation

ANOVA was used to establish the statistical validation of the polynomial equations generated by Design Expert® Software. Fitting a multiple linear regression model to a 3² Factorial design give a predictor equation incorporating interactive and polynomial term to evaluate the responses:

$$Y = b_0 + b_1X_1 + b_2X_2 + b_{12}X_1X_2 + b_{11}X_1^2 + b_{22}X_2^2 \text{ ----- (1)}$$

Where Y is the measured response associated with each factor level combination; b_0 is an intercept representing the arithmetic average of all quantitative outcomes of nine runs; b_i (b_1 , b_2 , b_{11} , b_{12} and b_{22}) are regression coefficients computed from the observed experimental values of Y and X_1 and X_2 are the coded levels of independent variables. The terms $X_1 X_2$ represent the interaction terms.

Three dimensional response surface plots resulting from equations were obtained by the Design Expert® software [21].

CHARACTERIZATION OF BSA-LYCOAT RS-720 CONJUGATES AND HERBAL POLYMERIC NANOPARTICLES

Differential Scanning Calorimetry (DSC)

DSC was used to compare the DSC thermograms of BSA, Lycoat RS 720, and BSA-LYCOAT RS 720 at a heating rate of 10°C/min. The measurements were carried out in nitrogen atmospheres with a heating range of 30 to 250°C [22].

X-Ray Diffractometry (XRD)

Using an X-ray diffractometer with Cu as a target and a voltage of 40 kV, the powder X-ray diffraction (PXRD) patterns of BSA, Lycoat RS 720, and BSA-LYCOAT RS 720 were examined. Samples were examined at a scanning rate of 30/2U/min in the 2θ angle range of 10-50°C.

Particle size, Zeta potential and PDI analysis

Through the use of dynamic light scattering, the particle size and PDI were determined. By measuring Brownian motion and correlating it to particle size, dynamic light scattering (also known as PCS—Photon Correlation Spectroscopy) analyzes the movement of the particles. It accomplishes this by laser-illuminating the particles and examining the variations in light intensity in the scattered light. To create an acceptable scattering intensity, double distilled water was used to dilute all samples. Using disposable polystyrene cells with a 10 mm diameter and 25°C, the zeta potential and PDI values were measured at a 90° angle. By calculating the electrophoretic mobility, the zeta potential was calculated. For the optimized batch, the zeta potential and average particle size of the nanoparticles were calculated. (n = 3) [23].

Entrapment efficiency and Drug Loading

Nanoparticles dispersion was centrifuge at 12,000 rpm for 2 hrs, 1.0 mL of the supernatant collected after centrifugation was diluted with phosphate buffer pH7.4 and then makes up volume up to 10 ml in 10ml volumetric flask and measured. The pellets were re-dissolved in distilled water, and the supernatant was scanned with a UV-visible spectrophotometer in this parameter. The entrapment efficiency of the nanoparticles was calculated for each batch. The entrapment efficiency (EE %) in herbal polymeric nanoparticles was calculated from the following equation [24]:

$$\% EE = \frac{\text{amount of drug added} - \text{amount of drug in supernatant}}{\text{amount of drug added}} \times 100 \text{ ----- (1)}$$

Production Yield

The production yield of nanoparticles of various formulation were calculated using the weight of final product after drying with respect to the initial total weight of the extract and polymer conjugates used for preparation of polymeric nanoparticles [25].

$$\text{Production yield} = \frac{\text{Amount of freezed dried powder}}{\text{Amount of extract and Polymer in feed}} \times 100 \text{ ----- (3)}$$

Surface Morphological Study

Surface morphology of the herbal polymer nanoparticles was performed by using transmission electron microscopy. A formulation (1mg/ml) was placed on Formvars coated copper grids and allowed to equilibrate. Excess liquid was removed with a filter paper and dried at room temperature for about half an hour. The dried grid containing the herbal nanoparticles was visualized using TEM [26].

In-vitro diffusion study

For the drug release studies, Franz diffusion cells were employed. Onto the cellulose membrane's surface, ointment was equally distributed. Between the donor and the receptor chambers of the diffusion cell, the cellulose membrane was clamped. Phosphate buffer with a pH of 7.4 was placed in the receptor compartment, and the assembly was kept at 37°C with intermittent magnetic stirring. The donor compartment membrane received 300 mg of ointment, which was subsequently wrapped in aluminum foil to prevent drying out. Over the course of one hour, aliquots were taken out at regular intervals for analysis using a UV spectrophotometer [27, 35].

Stability of Nanoparticle

The stability of the produced nanoparticles was evaluated by keeping the optimum formulation in a stability chamber (at 4°C) for three months. The particle size, zeta potential, entrapment efficiency and physical appearance were determined at different time intervals of one, two and three months (According to ICH Q1A) [28-30].

EVALUATION OF OINTMENT

Organoleptic characteristics

Physical appearance, color, texture, phase separation, and homogeneity tests were performed on all blank formulations (i.e., formulations devoid of an active component) and extract-loaded formulations. Visual observation was used to assess these qualities. By pressing a tiny amount of the prepared ointment between the thumb and index finger, homogeneity and texture were evaluated. The texture and homogeneity of the formulations were assessed using the formulations' consistency and the presence of coarse particles. Also assessed was the immediate skin feel (including stiffness, grit, and greasiness) [31].

Water number

The greatest amount of water that can be added to 100 g of base at a specific temperature is known as the water number. It was discovered by adding distilled water while mixing the base continually. The amount of water still in the container was considered the end point when no more water could be absorbed into the base as shown by water droplets.

pH

In a dry beaker, 2.5 g of each formulation was added together with 50 ml of water. Ointments were cooked in a beaker on a water bath at 60 to 70°C. Using a pH meter, determine the ointment's pH (pH Tutor, Eutech Instruments). The calculations were done three times, and the averages of the three measurements were recorded [32].

Spreadability

An instrument suggested by Multimer was modified to measure the spreadability of the formulation. It is made up of a wooden block with a pulley attached to one end and a fixed glass slide on the other. A 3g overabundance of cream applied on a ground plate. Between this plate and a second glass plate with the dimensions of a fixed ground plate and a hook, the ointment was sandwiched. To remove air and create a consistent film of ointment between the plates, a 1 kg weight was set on top of the two plates for five minutes. The borders were scraped clean of extra ointment. Next, a 240 g pull was applied to the top plate. The top plate's time to travel a distance of 10 cm was measured with the aid of a spring attached to the hook. Better Spreadability is indicated by a shorter interval [33]. In order to determine spreadability, the following formula was used:

$$S = M \times L / T$$

Where, S = Spreadability

M = Weight in the pan (tied to the upper slide)

L = Length moved by the glass slide and

T = Time (in seconds) taken to separate the slide completely each other.

Viscosity

Rheological tests were conducted using a Brookfield Synchro-Lectric Viscometer (Model RVT) with a Helipath Stand. Before measuring the dial reading with a T-D spindle at 10, 20, 30, 50, 60, and 100 rpm, the sample (50 g) was put in a beaker and allowed to equilibrate for 5 min. The dial reading on the viscometer was recorded for each speed. The dial reading that corresponded to each decrease in spindle speed was recorded. At room temperature, the measurements were made in triplicate. The viscosity in centipoises (CPS) was obtained by directly multiplying the dial readings by the coefficients listed in the Brookfield Viscometer catalog [34].

Stability testing

According to the International Conference on Harmonization (ICH) criteria, a stability analysis of the developed ointment formulations was conducted. The prepared ointment was placed in collapsible tubes, stored for three months at three different temperatures and humidity levels 25°C±2°C/60%±5% RH, 30°C±2°C/65%±5% RH, and 40°C±2°C/75%±5% RH respectively and then its appearance, pH, viscosity, and spreadability were examined [36, 37].

RESULT AND DISCUSSION

Method of extraction

The methanol is used as organic solvent for the extraction process. The extract (100g) was refluxed with the methanol. The solvent from the extract were removed under a vacuum. The extractive value was calculated by weighing. The sample was stored at 4°C. The extraction value for the plant in methanol is given in Table 1.

Table 1. Pharmacognostic parameter of extract

Solvent	Value (g)
Methanol soluble extractive values (% w/w)	15.2
Total ash value (% w/w)	7.5%
Acid insoluble ash value (% w/w)	0.7%
Water soluble ash value (% w/w)	3.2%
Foreign organic matter (% w/w)	0.5%
Moisture content (% w/w)	0.220%
Loss on drying (% w/w)	3.9%

Qualitative phytochemical screening of plant extract

The curative properties of medicinal plants are perhaps due to the presence of various secondary metabolites such as alkaloids, flavonoids, glycosides, saponins, tannins, triterpenes, sterols *etc.* Thus the preliminary screening tests may be useful in the detection of the bioactive principles and subsequently may lead to the drug discovery and development. Further, these tests facilitate their quantitative estimation and qualitative separation of pharmacologically active chemical compounds.

Preliminary phytochemical screening with various qualitative chemical tests revealed the presence of alkaloids, tannins, flavonoids, proteins, and mucilages present in the *Rhynchosia rothii* leaf extracts and Glycosides, saponins, and amino acid were absent in the *Rhynchosia rothii* leaf extracts as per given in Table 2.

Table 2. Qualitative phytochemical screening of plant extract

Test performed	Observation
Tests for Carbohydrates (Molish Test)	-
Test for Monosaccharide (Barfoed's Test)	-
Test for Non-reducing polysaccharides (Iodine Test)	-
Test for Proteins (Biuret test, Millions test)	+
Tests for Steroids (Liebermann Burchard reaction)	-
Tests for Terpenoids	-
Test for Saponin (Foam test)	-
Tests for Flavonoids (Shinoda test)	+
Tests for Flavonoids (Ferric chloride test, Lead ethanoate test, Sod-hydroxide Test)	-
Test for Tannins & Phenolic compounds (FeCl ₃ Lead acetate)	+
Test for alkaloids (Mayer's reagent)	+

+ Indicates presence of phytoconstituents, - Indicates absence of phytoconstituent

Compatibility study

The improved formulation F6 and pure extract underwent DSC analysis. Pure extract and the improved formulation both had separate melting endotherms at 313.41°C and 162.65°C, respectively, with enthalpy values of -51.93 J/g and -168.44 J/g. Thermograms of the pure extract and optimal formulation chosen for the investigation are shown in Figs. 1-2. No peak was seen in the region of 313.41°C in the formulation (F6) Fig. 2 example, confirming the drug's molecular dispersion in the polymer matrix and trapping inside the polymeric nanoparticles. Most of the time, the medicines' melting endotherm was well preserved. In all instances of optimal formulation, the drug's melting endotherm was well conserved with little to no change in enthalpy value, showing the drug's compatibility with the study's selected excipients.

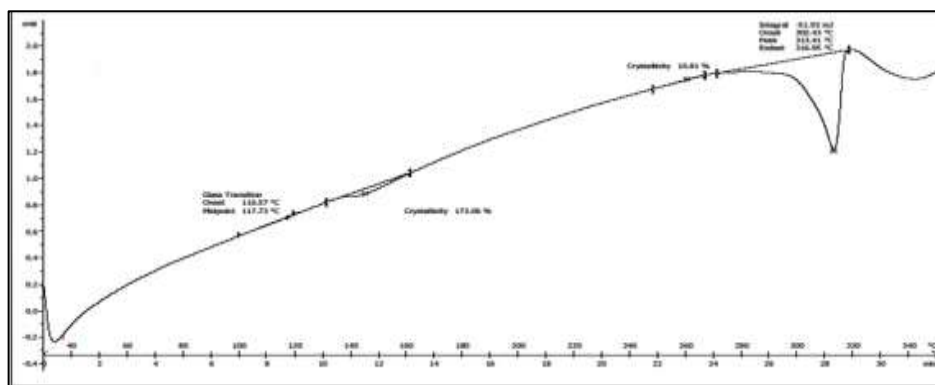


Fig. 1. DSC of Pure Extract

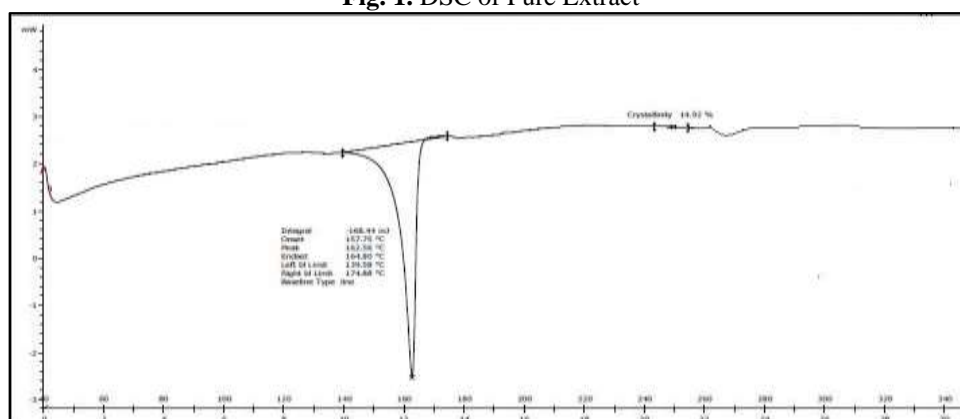


Fig. 2. DSC of Optimized Formulation (F6)

FORMULATION AND DEVELOPMENT

Formulation Design and Optimization of Batch

Formulation Design

Various Formulation batches of Herbal Polymeric nanoparticles were prepared based on 3² factorial designs. The independent variables were Polymer conjugates concentration in terms of mg (X₁) and HPH pressure in terms of bar (X₂) and their levels are shown in table 1 MPS i.e. Mean Particle Size (d.nm) (Y1) and Entrapment Efficiency (%) (Y2), were taken as response parameters as the dependent variables.

Table 3. Design Batches of Herbal Nanoparticles contain Extract

Formulation Code	X1 (mg)	X2 (Bar)	Y1 (d.nm)	Y2 (%)
F1	10	800	430	80.5
F2	10	800	450	80.9
F3	40	500	329	86.6
F4	40	300	377	87
F5	20	500	343	85.32
F6	20	500	257	88.32
F7	10	300	390	87.32
F8	20	800	456	80
F9	40	500	325	87

OPTIMIZATION DATA ANALYSIS AND MODEL-VALIDATION

A) Fitting of data to model

The two factors with lower, middle and upper design points in coded and un-coded values are shown in Table 3. The ranges of responses Y1 and Y2 were 255-715 d.nm and 80-89% respectively. All the responses observed for nine formulations prepared were fitted to main effect model, which was found as the best fitted model for Y1 and Y2, using Design Expert® software. The values of R², adjusted R², predicted R², SD and % CV are given in (Table 4), along with the regression equation generated for each response. The results of ANNOVA in (Table 5), for the dependent variables demonstrate that the model was significant for all the response variables. It was observed that independent variables X1 (mg) and X2 (bar) had a positive effect on the entrapment efficiency and a desired particle size of nano-formulation i.e. nanoparticles was achieved.

Table 4. Summary of results of regression analysis for responses Y1 and Y2

Models	R ²	Adjusted R ²	Predicted R ²	SD	%CV
Response (Y1) Main Effect	0.8834	0.7668	0.6595	31.92	8.56
Response (Y2) Main Effect	0.9438	0.8875	0.8723	1.12	1.32

Regression Equations

$$Y1 = +374.11 + 17.67 * A[1] - 22.33 * A[2] - 1.78 * B[1] - 51.78 * B[2] \text{ ----- (8)}$$

$$Y2 = +84.76 + 0.21 * A[1] - 0.093 * A[2] + 2.35 * B[1] + 2.15 * B[2] \text{ ----- (9)}$$

B) Model Assessment for Dependent Variables:

After putting the data in Design Expert® software for, Fit summary applied to data in that Main Effect Model had been suggested by the software for all the responses. The statistical evaluation was performed by using ANNOVA. Results are shown in (Table 5). The coefficients with more than one factor term in the regression equation represent interaction terms. It also shows that the relationship between factors and responses is not always linear. When more than one factor are changes simultaneously and used at different levels in a formulation, a factor can produce different degrees of responses.

Table 5. Results of Analysis of Variance for Measured Response

Source of Variation	Sum of Square	DF	Mean of Square	F Value	p-value Prob> F	Summary Significant
Model (MPS)	30891.33	4	7722.83	7.58	0.0376	Significant
X1-Polymer Conc. (mg)	813.50	2	406.75	0.40	0.6950	
X2-HPH Press. (bar)	3963.00	2	1981.50	1.94	0.02571	
Model (EE)	83.68	4	20.92	16.78	0.0091	Significant
X1-Polymer Conc. (mg)	0.052	2	0.026	0.021	0.9796	
X2-HPH Press. (bar)	35.25	2	17.63	14.14	0.0154	

C) Response Surface Plot Analysis

Three dimensional response surface plots were generated by the Design Expert® software are presented in (Fig.3 and Fig.4) for the studied responses, i.e. Mean Particle Size (Y1) and Entrapment Efficiency (Y2). Fig.17 depicts response surface plot of Polymer Conjugate Concentration (X1) and HPH Pressure (X2) on Mean Particle Size. Nanoparticles being nanoparticulated structures, formulation batch amongst all the design batches giving least particle size will be preferred more and selected as an optimized batch. Where F6 Design Batch, with a polymer concentration of about 20 mg and HPH pressure 500 bar, shows the least particle size i.e. 257 nm.

Fig. 4 depicts response surface plot of Polymer Conjugate Concentration (X1) and HPH Pressure (X2) on entrapment efficiency. The 3-D surface image shows a linear response, which indicates with the increase in the polymer concentration the entrapment efficiency increases, as more the polymer available more will be the entrapment efficiency.

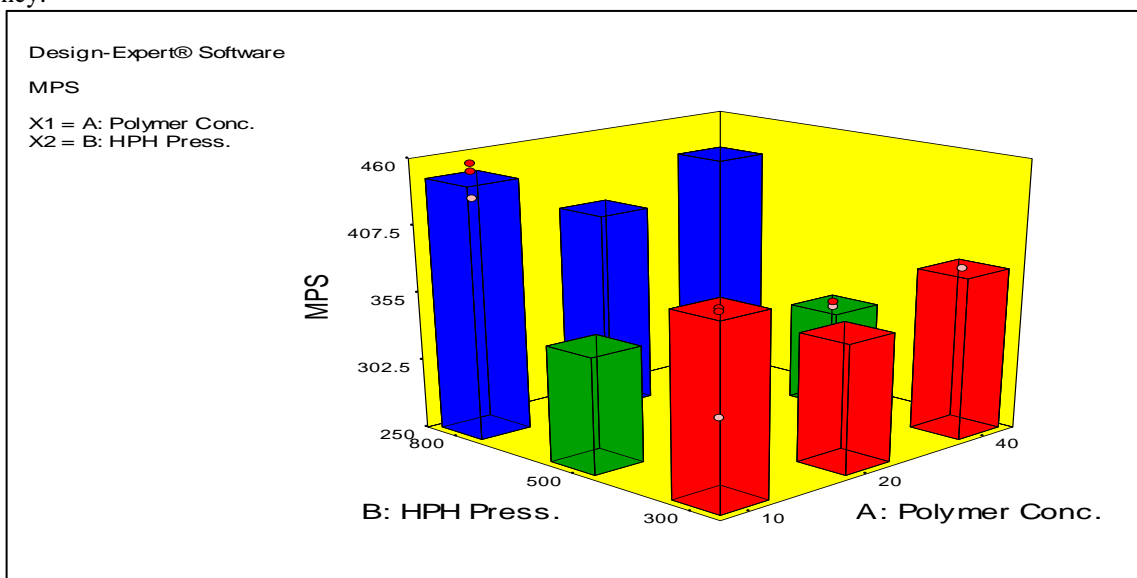


Fig. 3. Response surface plots for X1 and X2 on Mean Particle Size (Y1), where X1= Polymer Conjugates Concentration and X2= HPH Pressure

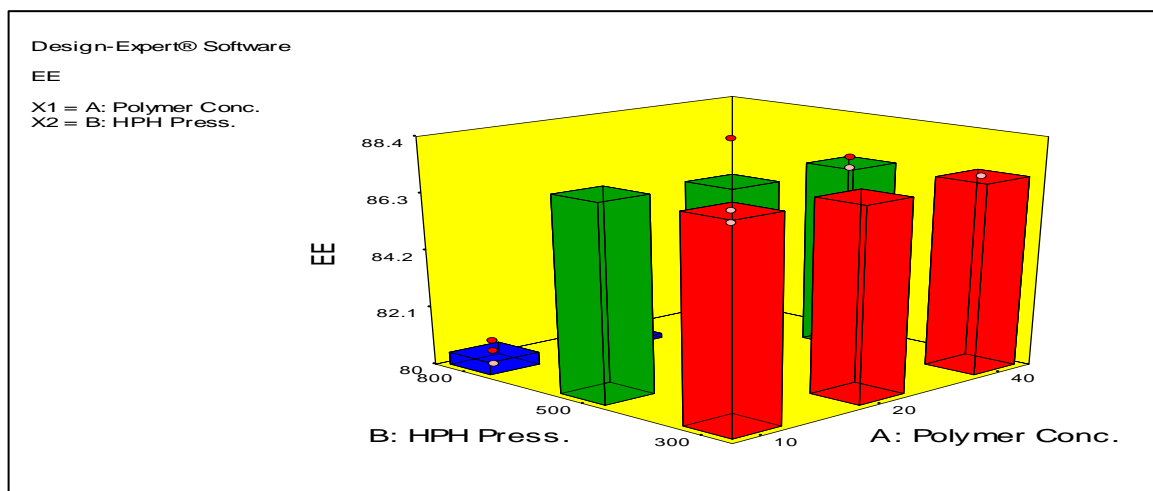


Fig. 4. Response surface plots for X1 and X2 on Entrapment Efficiency (Y1), where X1= Polymer Conjugates Concentration and X2= HPH Pressure

D) Optimisation of Result

The Optimization was performed on the basis of response surface modelling by using the numerical and graphical optimization model. Desirability is an objective function that ranges from zero outside of the limits to one at the goal. The numerical optimization finds a point that maximizes the desirability function. The Characteristics of a goal may be altered by adjusting the weight or importance. For several responses and factors, all goals get combined into one desirability function. The goal of optimization is to find a good set of conditions that will meet all the goals.

In case of Response Surface Graph for X1 and X2 on Mean Particle Size it is observed that considering the Polymer Concentration (X1) as the Polymer Concentration increases, more amount of drug is being incorporated into the nanoparticles and so the particle size reduces. In case of HPH pressure (X2) particle size found least at intermediate value i.e. 500 bars that indicate particle size 257 nm. But as there are two response factors so we cannot conclude the selection of Optimized batch based on just one response surface.

So, now considering the second Response surface graph for X1 and X2 on entrapment efficiency it was observed that as the polymer concentration increases the entrapment efficiency increases accordingly. Here two design batches i.e. F6 and F7 show maximum entrapment efficiency i.e. 88.32% and 87.32% respectively as shown in Table 6. But as seen in first response Surface graph being a nanoparticle formulation considering the least particle size is also a crucial factor. So, the Design Batch with least particle size and maximum entrapment efficiency is selected. Therefore, F6 is considered as an optimised Batch.

Table 6. Optimization Result

Parameters	Lower Limit	Upper Limit	Goal	Solution
X1	10	40	In Range	20
X2	500	800	In Range	500
Y1	250	500	In Range	257
Y2	80	89	In Range	88.32

Formulation Of Ointment

Different formulations were made to optimize the composition of the ointment base and it was found that 1:3 ratio of paraffin wax: liquid paraffin showed the best consistency over the other ratios (1:1, 1:2, 2:1) as shown in Table 7.

Table 7. Formulation of ointment batches

Formulations	Hard Paraffin (g)	Liquid Paraffin (ml)	Preservative Benzoic acid (µl)	(Optimized F6) Plant Extract (ml)
F1	10	5	100	1
F2	5	5	100	1
F3	5	10	200	1
F4	10	30	300	2

CHARACTERIZATION OF BSA-LYCOAT RS 720 CONJUGATES AND NANOPARTICLES

Differential Scanning Calorimetry (DSC)

In Fig. 5, 6, and 7, DSC Thermogram of BSA and LYCOAT RS 720 showed sharp endothermic peak at 31.54°C and 77.18°C respectively, indicating crystalline nature. However, the both BSA and LYCOAT RS 720 peaks were disappeared in the conjugate with appearance of new peaks at 156.36°C indicating compound BSA-LYCOAT RS 720 conjugate.

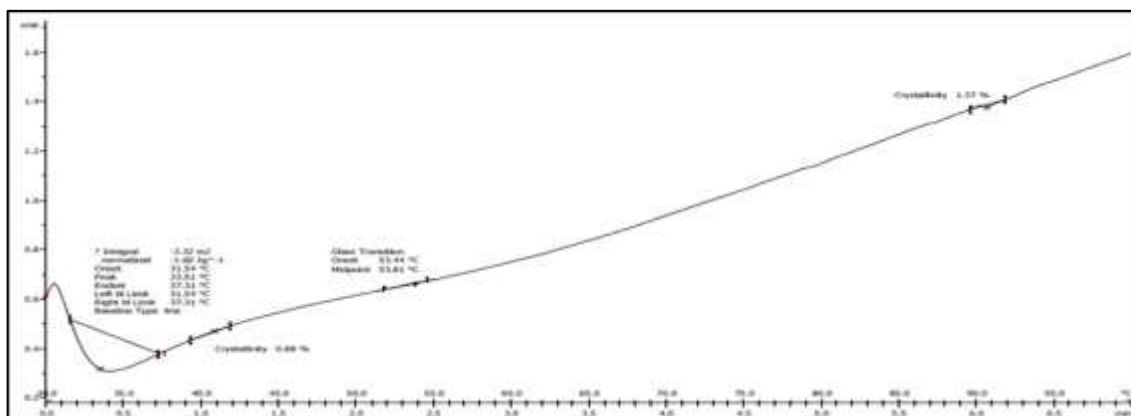


Fig. 5. DSC Thermogram of BSA

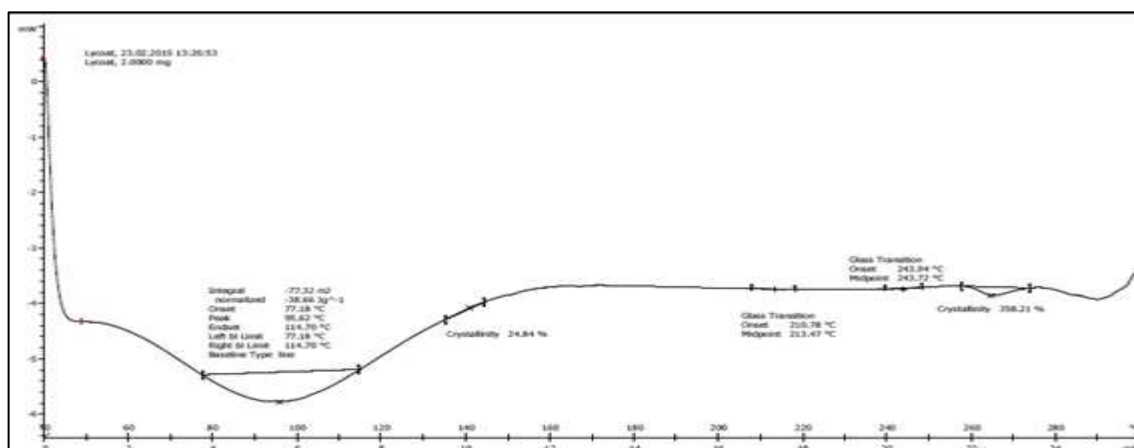


Fig. 6. DSC Thermogram of LYCOAT RS 720

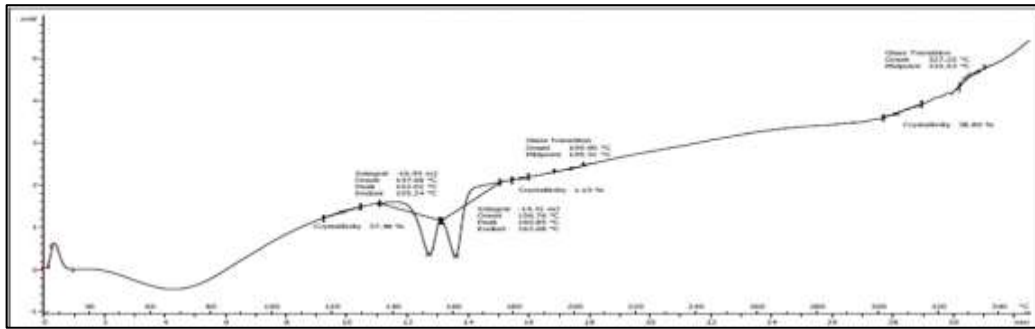


Fig. 7. DSC Thermogram of BSA-LYCOAT RS 720

X-Ray Diffractometry (XRD)

In Fig. 8, 9, and 10, BSA-LYCOAT RS 720 conjugates showed partly amorphous structure as observed from powder X-ray diffraction pattern. The diffractogram of BSA showed characteristics diffraction peaks at 2θ values of 7.368° , 12.280° , and 19.342° indicating crystalline nature. LYCOAT RS 720 showed blunt diffraction peaks at 9.671° and 20.339° indicating amorphous nature. BSA-LYCOAT RS 720 conjugates showed different diffraction peaks of Lycoat RS 720 at 2θ values of 9.62° and 20.418° with less intensity and intensity of BSA peaks decreased instantly showed amorphous nature.

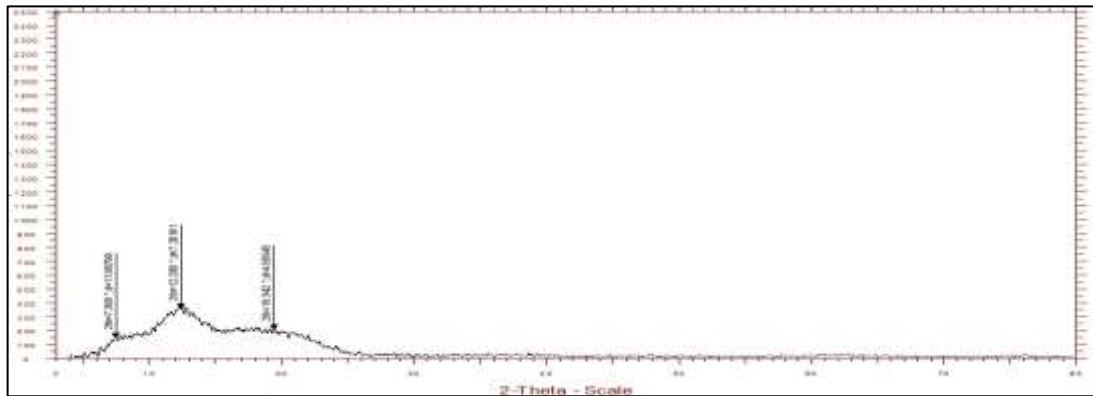


Fig. 8. XRD Pattern of BSA

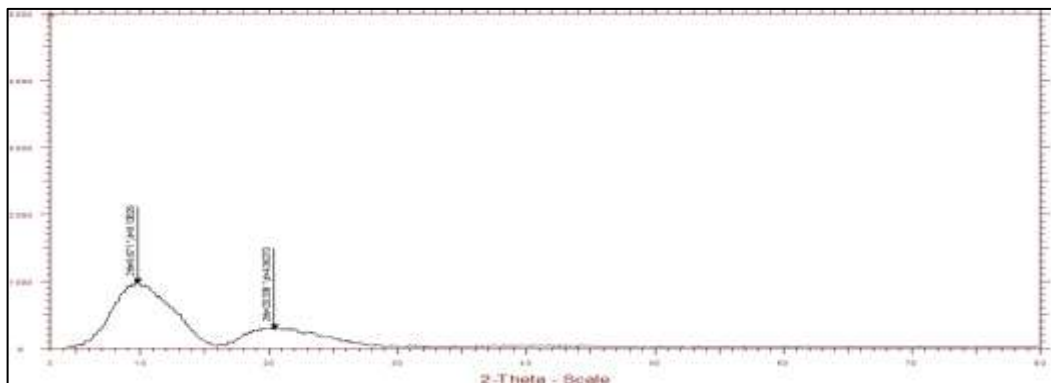


Fig. 9. XRD Pattern of Lycoat RS 720

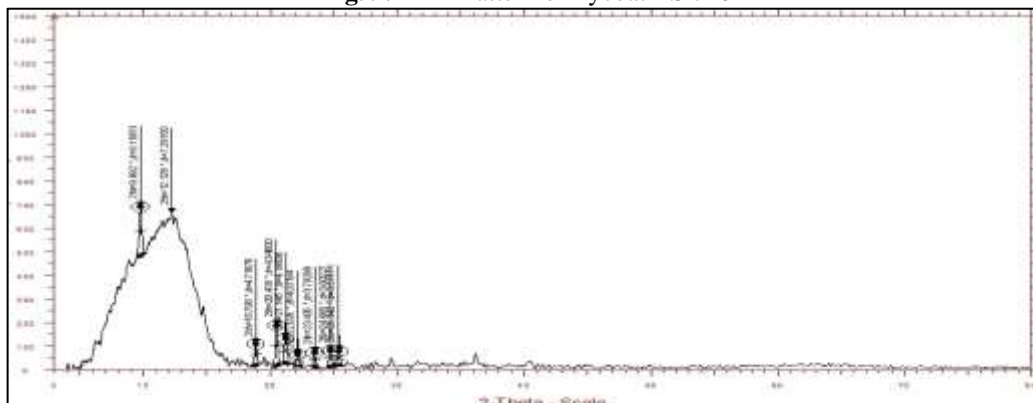


Fig. 10. XRD Pattern of Conjugates

Particle Size and Particle size distribution study

The particle size of the PNs is a fundamental factor because it decides the rate and extent of drug release as well as drug absorption. The smaller particle size offers a larger interfacial surface area for drug absorption and improves the bioavailability. The calculation of polydispersity index takes into account the particle mean size, the refractive index of the solvent, the measurement angle and the variance of the distribution. Low polydispersity index value might be associated with a high homogeneity in the particle population, whereas high polydispersity index values suggest a broad size distribution or even several populations. The optimized formulation batch (F6) showed mean particle size 310 nm before lyophilization while 257 nm after lyophilization with PDI 0.589 and 0.533 respectively as shown in figs.11-12. The MPS and PDI were decreased in freeze-dried powder. This might be due to adherence of cryoprotectant throughout freeze-drying. The optimization of cryoprotectant was based on appearance of cake and ease of reconstitution.

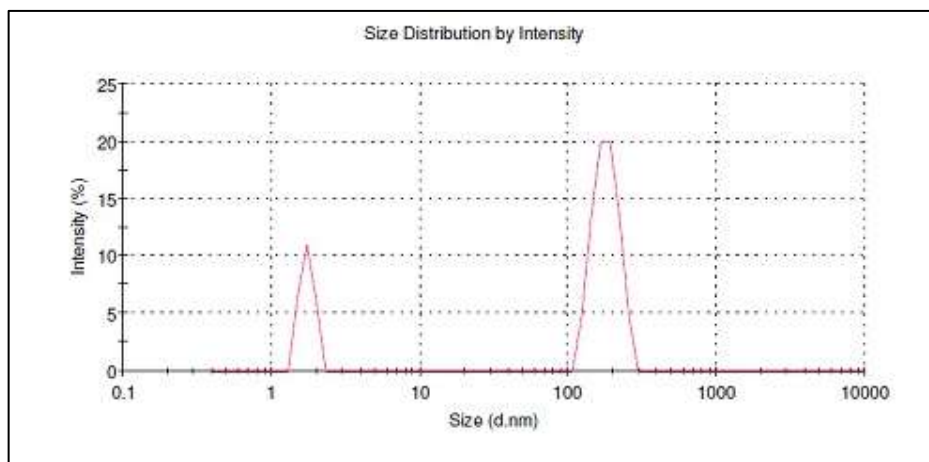


Fig. 11. Particle size of Formulation Batch before Lyophilization (F6)

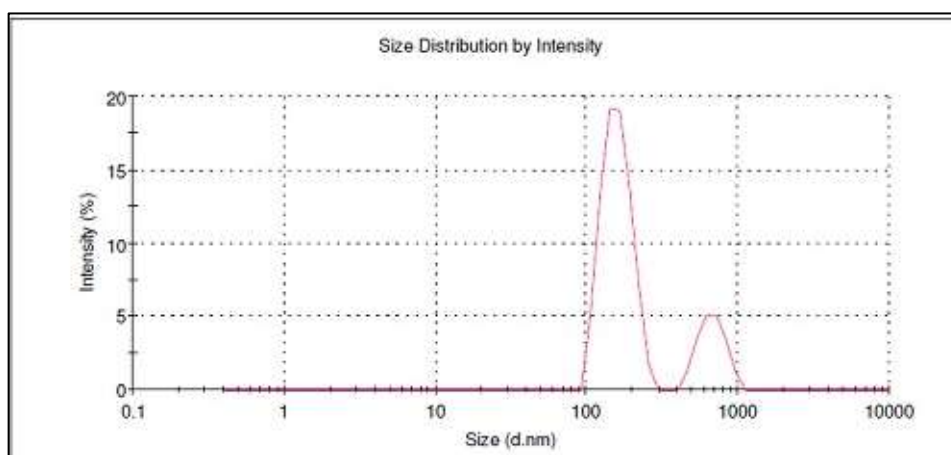


Fig. 12. Particle size of Formulation Batch after Lyophilization (F6)

Zeta Potential Measurement:

The zeta potential values of plain drug, blank nanoparticles and drug loaded nanoparticles that was found to be -10.2 mV, -30.9 mV and -22.4 mV respectively as shown in figs. 13-15.

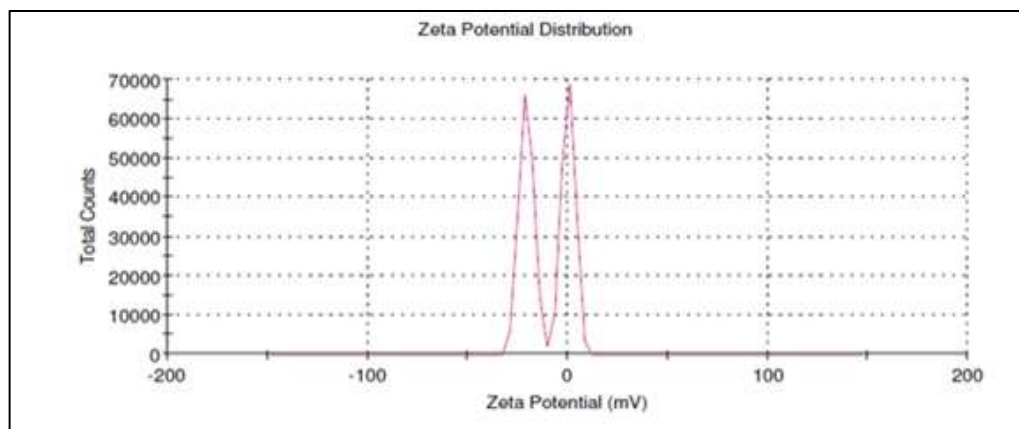


Fig. 13. Zeta Potential of Pure extracts

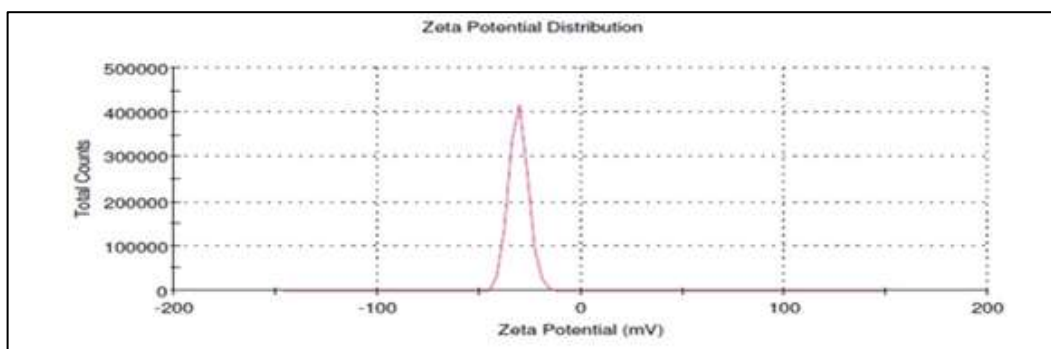


Fig. 14. Zeta Potential of Blank Nanoparticles

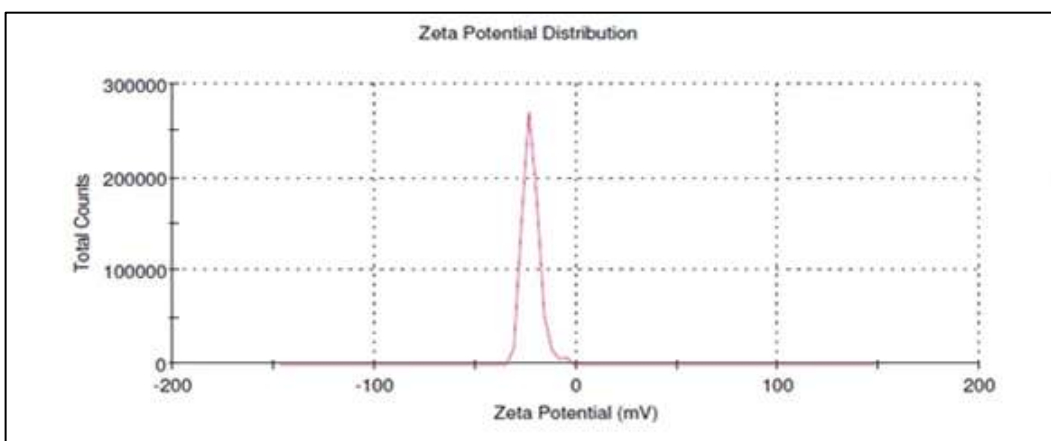


Fig. 15. Zeta Potential of Formulation Batch (F6)

Entrapment efficiency

The % EE depends on the properties of drug and polymer used. Amongst of all batches % EE was good due to solvent evaporation method. The % EE of optimized batch was found to be 88.32 as shown in table 8. From result we concluded, with the increase in the polymer conjugates concentration the entrapment efficiency increases, as more the polymer available more will be the entrapment efficiency.

Table 8. Entrapment Efficiency of Different Formulation Batches

Formulation Batches	Entrapment Efficiency (%)
F1	80.5
F2	80.9
F3	86.6
F4	87
F5	85.32
F6	88.32
F7	87.32
F8	80
F9	87

Production Yield

All the batches showed production yield in between 86-96% as shown in table 9. The resultant yield is an indication that the method can be appropriate for technology transfer that is production on large scale.

Table 9. Production Yield of Different batches

Batch Code	Production Yield (%)
F1	86.50±0.18
F2	92.12±0.22
F3	94.50±0.16
F4	93.50±0.14
F5	94.33±0.23
F6	95.66±0.24
F7	95.60±0.22
F8	94.10±0.15
F9	96.80±0.18

Surface Morphological Study (TEM)

Surface morphology of the Polymeric Nanoparticles was evaluated using transmission electron microscope (TEM) from which it can be seen that the nanoparticles have smooth surfaces. Nanoparticles show spherical shape with size 200 nm as shown in fig.16.

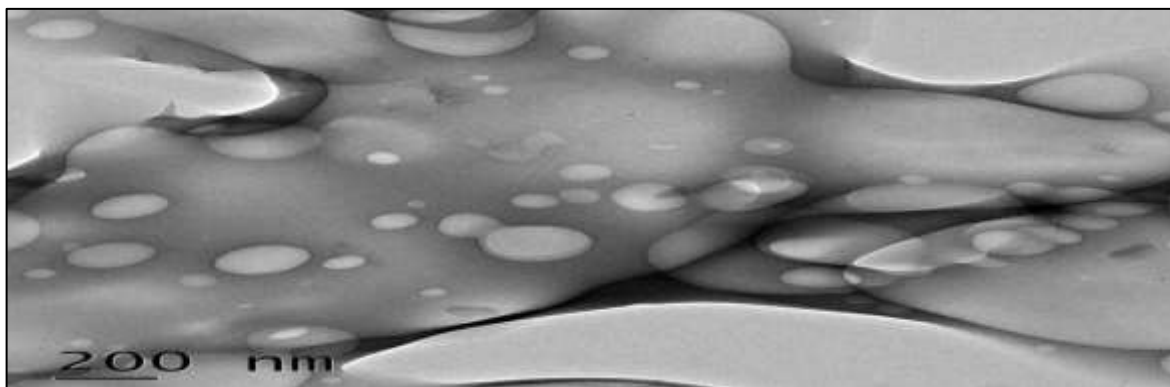


Fig. 16. TEM Image of Formulation Batch (F6)

8) In-Vitro Drug Release:

Rhynchosia rothii loaded polymeric nanoparticles of all batches were studied *in-vitro* for drug release. For batches F6, the maximal drug release was found to be about 91-94% as shown in Table 10 and fig.17. The *in-vitro* release of produced polymeric nanoparticles in phosphate buffer saline (PBS) (PH 7.4) at 37°C was studied. Polymeric nanoparticles were dialyzed for 60 min. The quantity of medication released was measured by using a UV-visible spectrophotometer to measure absorbance

Table 10. *In-vitro* release profile of *Rhynchosia rothii* loaded Nanoparticles

Sr. No.	Time (Min.)	Herbal Nanoparticles (%) (F4)
1	0	0
2	10	27.42
3	20	41.04
4	30	46.62
5	40	61.52
6	50	91.02
7	60	94.24

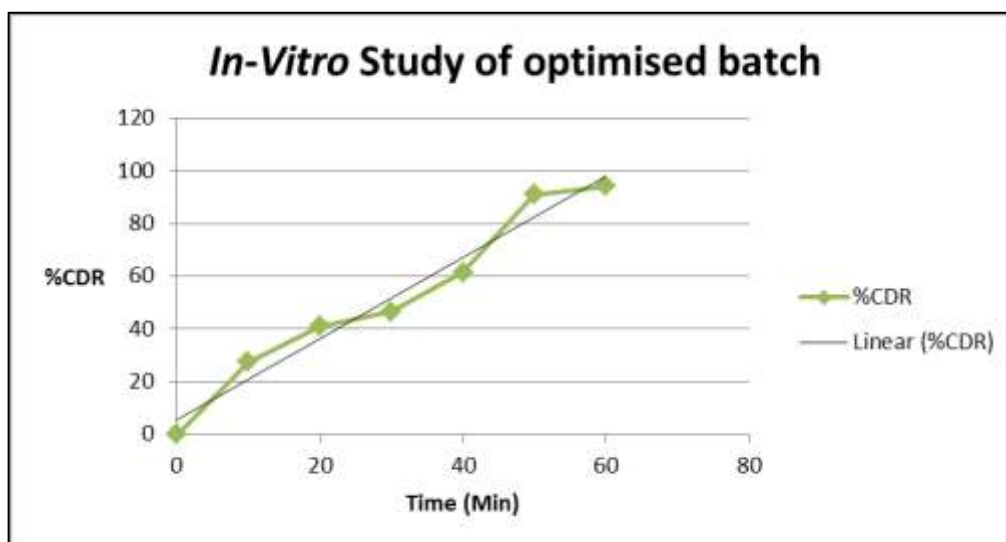


Fig. 17. *In-vitro* drug release of optimized Polymeric Nanoparticle

Stability Study of polymeric nanoparticles:

Accelerated stability studies of formulation were conducted by measurement of particle size, PDI, zeta potential and drug content. Before stability studies, *Rhynchosia rothii* loaded PNPs showed mean particle size 257 nm with PDI 0.533. After stability studies mean particle size and PDI was found to be 261 nm and 0.539 respectively. There were no significant changes in particle size and PDI after three month storage. Zeta potential of optimized formulation before and after stability study was found to be -22.4 and -22.2 mV, respectively. Based on these results it is revealed that,

Rhynchosia rothii loaded PNPs (Formulation batch F6) were found to be stable formulation at the given temperature and humidity condition.

EVALUATION OF OINTMENT

Organoleptic characteristics

Table 11 displays the ointment compositions' organoleptic characteristics, such as their physical appearance, color, texture, phase separation, homogeneity, and initial skin sensation. The ointments had good aesthetic appeal, a smooth texture, and were all homogeneous with no evidence of phase separation, according to the results. Each mixture had an aromatic scent and was white in color.

Table 11. Physicochemical evaluation of ointment formulations

Formulations	Physical appearance	Texture	Phase separation	Homogeneity	Immediate skin feel
F1	Opaque	Rough & Hard	No	Homogenous	No grittiness
F2	Opaque	Smooth	No	Homogenous	Yes grittiness
F3	Opaque	Smooth	Yes	Homogenous	No grittiness
F4	Opaque	Smooth	No	Homogenous	No grittiness

pH

The pH of all formulations was discovered to be within the acceptable range of 6.80 ± 0.152 and 7.02 ± 0.174 , which is shown in Table 12. All formulas' pH values fall within the skin's typical pH range.

Viscosity

All of the formulations' viscosities were recorded and discovered to range between 2314 ± 6.13 and 2851 ± 9.93 CPS at 10 rpm, as indicated in Table 12. Each and every composition displayed pseudo-plastic flow. Three readings were averaged, and the standard deviation was calculated ($n=3$).

Spreadability

Three categories of ointment spreadability exist: low, moderate, and high. Following screening, it was discovered to be directly inversely related to the volume of liquid paraffin. The ointment grew thinner and more spreadable when the amount of liquid paraffin was increased. All formulations' spreadabilities were assessed, and it was found that formulation F4 spreads more readily than the other formulations in Table 12.

Table 12. Evaluation parameters of ointment formulations

Formulations	pH (mean±SD)	Viscosity at 10 rpm (CPS) (mean±SD)	Spreadability g.cm/s (mean±SD)	Water number (mean±SD)
F1	6.80 ± 0.152	2851 ± 9.93	80.00 ± 3.83	1.2 ± 0.25
F2	7.01 ± 0.185	2612 ± 8.13	109.09 ± 5.13	1.3 ± 0.08
F3	6.90 ± 0.189	2472 ± 7.23	112.57 ± 4.23	1.3 ± 0.12
F4	6.92 ± 0.244	2412 ± 8.03	110.16 ± 3.53	1.4 ± 0.10

Stability study

According to ICH requirements, a stability study was conducted on each ointment formulation, and the findings are displayed in Table 13. For the duration of the stability studies, the formulations' appearance was clear and there was no appreciable change in the pH, spreadability, or viscosity of the optimized formulation.

Table 13. Evaluation parameters of ointment formulations

Formulations	pH (mean±SD)	Viscosity at 10 rpm (CPS) (mean±SD)	Spreadability g.cm/s (mean±SD)
F4			
Before Stability Study	6.59 ± 0.96	2470 ± 6.96	102.91 ± 4.12
After Stability Study	6.79 ± 0.12	2470 ± 06.23	102.25 ± 3.20

The prepared ointment formulations were evaluated using a variety of criteria, and the results were within the set limits, which are shown in Tables 11 to 13. All of the formulations were discovered to have an alkaline pH. In comparison to previous formulations and prototype formulations, formulation F4 has a higher spreadability. It can be seen that lowering the concentration of was improved spreadability overall. Based on the spreadability, viscosity, and water number results, the formulation F4 made with paraffin wax was chosen as the best formulation. According to a stability analysis, the improved formulation is stable for a month.

CONCLUSION

Following the ointment formulation, *Rhynchosia rothii* loaded Lycoat RS 720-BSA conjugated polymeric nanoparticles were added. Maillard Reaction was used to develop the Lycoat RS 720-BSA conjugate. The solvent evaporation approach was used to create nanoparticles with *Rhynchosia rothii* loaded on them. The nanoparticles had a 257nm particle size and exhibited a spherical shape. The zeta potential in the formulation was -22.4 mV. The *Rhynchosia rothii* extract was created as an absorbent ointment formulation with a pH of 6.80–6.92 and a spreadability of 80.00–110.16 g.cm/s. It also has a distinctive aroma. Ointment containing herbal nanoparticles from the F4 batch has produced positive results. It was observed that the ointment containing the active ingredient of paraffin wax had good strength, viscosity, and spread ability. It is hoped that this work would spur additional investigation into and belief in the use of natural active components in medications. A new method of promoting nanoparticles in herbal medication delivery systems is by employing them in nanoparticles and an ointment.

Conflict of Interest

Authors declared that there are no conflicts of interest exists.

Acknowledgement

None

Competing Interests

Authors have declared that no competing interests exist

REFERENCES

1. Rawlings AV, Harding CR. Moisturization and skin barrier function. *Dermatol Ther* 2004;17(1):43-8.
2. Marty JP. NMF and cosmetology of cutaneous hydration. *Ann Dermatol Venereol* 2002;129(1):131-6.
3. Cravello B, Ferri A. Relationships between skin properties and environmental parameters. *Skin Res Technol* 2008;14(2):180-6.
4. Cancalon P. Chemical composition of sunflower seed hulls. *J Am Oil Chem Soc* 1971;48(12):29-32.
5. Nikam, A.P., Mukesh, P.R. and Haudhary, S.P. Nanoparticles—an overview. *J. Drug Deliv. Ther*, 2014;3(1):1121-1127.
6. Jawahar, N. and Memyathan, S.N. Polymeric nanoparticles for drug delivery and targeting: A comprehensive review. *Int. j. health allied sci.* 2012;1(4):217-223.
7. Abhilash, M. Potential applications of Nanoparticles. *Int J Pharm Bio Sci.* 2010;1(1):7-9.
8. Nagavarma, B.V.N., Yadav, H.K., Ayaz, A., Vasudha, L.S. and Shivakumar, H.G. Different techniques for preparation of polymeric nanoparticles-a review. *Asian J. Pharm. Clin. Res.* 2012;5(3):16-23.
9. Smith, A.A., Zuwala, K., Pilgram, O., Johansen, K.S., Tolstrup, M., Dagnæs-Hansen, F. and Zelikin, A.N. Albumin-polymer-drug conjugates: long circulating, high payload drug delivery vehicles. *ACS Macro Letters*, 2016;5(10):1089-1094.
10. Edelman, R., Assaraf, Y.G., Levitzky, I., Shahrar, T. and Livnev, Y.D. Hyaluronic acid-serum albumin conjugate-based nanoparticles for targeted cancer therapy. *Oncotarget*, 2017;8(15):24337-24353.
11. Ratnayake, W.S., Hoover, R. and Warkentin, T. Pea starch: composition, structure and properties-a review. *Starch-Stärke*, 2002;54(6):217-234.
12. Suryawanshi MV, Mahajan HS. Formulation and Characterization of Betulinic Acid Loaded Polymeric Nanoparticles for the Treatment of Breast Cancer. *IJARW.* 2019;1(10):15-27.
13. Rammohan A, Reddy GM, Bhaskar BV, Gunasekar D, Zyryanov GV. Phytochemistry and pharmacological activities of the genus *Rhynchosia*: a comprehensive review. *Planta.* 2020;251(1):1-5.
14. Mary JL, Raghavendra NM, Subrahmanyam CV. Antidiabetic and Antioxidant activity of *Rhynchosia beddomei* baker. *Int J Med Res Rev.* 2014;2(1):1323-32.
15. Rawat M, Singh D, Saraf S. Nanocarriers: Promising Vehicle For Bioactive Drugs. *Biol. Pharm. Bull.* 2006;29(1):1790-8.
16. Ansel. *Pengantar Bentuk Sediaan Farmasi Edisi IV.* Jakarta: UI Press; 2005.
17. Tayade, S. D., & Silawat, N. (2021). Phytochemical Screening and Wound Healing Activity of Different Leaf Extracts of *Rhynchosia rothii* in Rats. *J. Pharm. Res. Int.* 33(46B), 386-393.
18. Sharma PP. *Cosmetics-formulation, Manufacturing and Quality Control*, Delhi, India: Vandana Publications; 2014;7(5)181-91.
19. Pawar A, Singh S, Rajalakshmi S, Shaikh K, Bothiraja C. Development of fisetin-loaded folate functionalized pluronic micelles for breast cancer targeting. *Artif Cells Nanomed Biotechnol.* 2018;46(sup1):347-61.
20. Cavazzuti, M., 2013. Design of experiments. In *Optimization Methods* (pp. 13-42). Springer Berlin Heidelberg.
21. Qi J, Yao P, He F, Yu C, Huang C. Nanoparticles with dextran/chitosan shell and BSA/chitosan core—doxorubicin loading and delivery. *Int. J. Pharm.* 2010;393(1-2):177-85.
22. Zhao L, Du J, Duan Y, Zhang H, Yang C, Cao F, Zhai G. Curcumin loaded mixed micelles composed of Pluronic P123 and F68: preparation, optimization and in vitro characterization. *Colloids and Surfaces B: Biointerfaces.* 2012;97(1):101-8.
23. Mahajan HS, Mahajan PR. Development of grafted xyloglucan micelles for pulmonary delivery of curcumin: in vitro and in vivo studies. *Int. J. Biol. Macromol.* 2016;82(1):621-7.
24. Bothiraja C, Rajput N, Poudel I, Rajalakshmi S, Panda B, Pawar A. Development of novel biofunctionalized chitosan decorated nanocochleates as a cancer targeted drug delivery platform. *Artif Cells Nanomed Biotechnol.* 2018;46(sup1):447-61.
25. Bronze-Uhle ES, Costa BC, Ximenes VF, Lisboa-Filho PN. Synthetic nanoparticles of bovine serum albumin with entrapped salicylic acid. *Nanotechnol. Sci. Appl.* 2017;10(1):11.
26. Taralkar SV, Chattopadhyay S. A HPLC Method for determination of ursolic acid and betulinic acids from their methanolic extracts of *Vitex Negundo* Linn. *J. Anal. Bioanal. Tech.* 2012;3(3):1-6.
27. Madane RG, Mahajan HS. Curcumin-loaded nanostructured lipid carriers (NLCs) for nasal administration: design, characterization, and in vivo study. *Drug deliv.* 2016;23(4):1326-34.
28. Sahib MN, Abdulameer SA, Darwis Y, Peh KK, Tan YT. Solubilization of beclomethasone dipropionate in sterically stabilized phospholipid nanomicelles (SSMs): physicochemical and in vitro evaluations. *Drug Des. Devel.* 2012;6(1):29-42.
29. Costa P, Lobo JM. Modeling and comparison of dissolution profiles. *Eur J Pharm Sci.* 2001;13(2):123-33.
30. Jain S, Mittal A, K Jain A, R Mahajan R, Singh D. Cyclosporin A loaded PLGA nanoparticle: preparation, optimization, in-vitro characterization and stability studies. *Curr. Nanosci.* 2010;6(4):422-31.
31. Lachman L, Herbert AL, Joseph LK. *The Theory and Practice of Industrial Pharmacy*, Chp 3. India: Varghese Publication House; 1999;569.
32. Kilor V, Sapkal N, Vaidya G. Design and development of novel microemulsion based topical formulation of hesperidin. *Int J Pharm Pharm Sci.* 2015;7:142-8.
33. Multimer M. Spreadability determination by an apparatus. *J Am Pharm Assoc.* 1956;45:212-4.

34. Dua D, Srivastava NS. Study on antioxidant and anti-aging properties of few medicinal plants. *Int J Pharm Pharm Sci.* 2016;8:344-7.
35. Ayobami OO, Okikiolu OJ, Hannah OO, Samuel OO. Ocular tolerance and in-vitro release of chloramphenicol in prospective eye ointment bases. *Int J Pharm Pharm Sci.* 2015;7:306-11.
36. Daniels R, Knie U. Galenics of dermal products vehicles, properties and drug release. *J Dtsch Dermatol Ges.* 2007;5:367-83.
37. Suchiwa PO, Soravoot R, Ounaron A, Kongkaew C, Tiyaboonchaia W. Development, characterization and skin irritation of mangosteen peel extract solid dispersion containing clay facial mask. *Int J Appl Pharm.* 2018;10:202-8.

RP-HPLC METHOD DEVELOPMENT AND VALIDATION OF PHARMACEUTICAL TABLET DOSAGE FORM CONTAINING AMBRISENTAN

ABSTRACT

The objective of the current study was to develop a simple, precise and accurate RP-HPLC assay method and its validation for determination of ambrisentan in pharmaceutical tablet dosage form. Gradient RP-HPLC separation was achieved on an analytical Primisil C18 R column (250 mm × 4.6 mm; 5 µm particle size) using mobile phase containing mixture of acetonitrile: water (65:35 V/V). The developed method was validated for specificity, linearity, precision, accuracy and robustness study. The method was linear in the drug concentration range of 10-50 µg mL⁻¹ with a correlation coefficient 0.998. The percent RSD values were found to be less than 2 %, indicating the developed method was also robust. The method was completely validated and shows satisfactory result for the all method parameter. Hence it is concluded that the proposed method is precise, simple, sensitive, accurate, rugged and rapid and can be applied successfully for the estimation of ambrisentan in pharmaceutical dosage form.

Keywords: Ambrisentan, chromatographic analysis, RP-HPLC, method validation, system suitability

INTRODUCTION

Ambrisentan, chemically (2S)-2-[(4,6-dimethylpyrimidin-2-yl)oxy]-3-methoxy-3,3-diphenylpropanoic acid, is a pulmonary antihypertensive agent. Ambrisentan is one of several newly developed vasodilator drugs that selectively target the endothelin type A (ETA) receptor, inhibiting its action and preventing vasoconstriction¹⁻³. High performance liquid chromatography (HPLC) is the most versatile and widely used analytical technique. It utilizes a liquid mobile phase to separate the components of a mixture⁴. These components (or analytes) are first dissolved in a solvent, and then forced to flow through a chromatographic column under high pressure. In the column, the mixture is resolved into its components. The interaction of solute with mobile and stationary phases can be manipulated through different choices of both solvent and stationary phases⁵. As a result, HPLC acquires a high degree of versatility not found in other chromatographic systems and it has the ability to separate a wide variety of chemical mixtures⁶. Validation parameters to be studied before finalization of the method include specificity, linearity, range, accuracy, precision, limit of detection, limit of quantitation, ruggedness and robustness⁷. To the best of our knowledge, the assay of ambrisentan (AMB) is not official in pharmacopoeias of IP, USP and BP. The detailed survey of literature revealed that very few methods have been reported for the estimation of AMB alone. Hence the aim of present study was to develop, validate and stabilize RP-HPLC method for ambrisentan in pharmaceutical dosage form¹.

MATERIALS AND METHODS

Chemicals and reagent

The standard ambrisentan, marketed preparation and other required chemicals used for the present investigation were procured from Cipla Pharmaceuticals Ltd., Mumbai (India). The entire chemicals used were of HPLC grade.

Instruments

RP-HPLC method development and validation was done on Younglin (S.K.) Gradient system UV Detector HPLC instrument UV- detector and column Primisil C18, 250×4.6 mm, 5 µm particle size. The instruments used were UV- spectrophotometer (Waters), ultra sonic cleaning bath (Spectralab model USB), pH analyser (Labindia), weighing balance (Shimadzu), Fuming chamber (Labexel), hot air oven (Thermo Lab 905) and magnetic stirrer (Whilmatic).

Trials for selection of chromatographic conditions

Seven trials for selection of chromatographic condition were carried out using C18 (250×4.6 mm, 5µm) column with different mobile phases, methanol-water and acetonitrile-water with different ratios. The pH of the mobile phase was adjusted to 3.2 ± 0.05 with ortho phosphoric acid and solution was filtered through nylon filter (0.45 µm), and flow rate was adjust at 0.7 mL min⁻¹, and injection volume was 20 µm⁸⁻¹¹.

Table I: Chromatographic data for sample and standard with accuracy

Conc. in $\mu\text{g mL}^{-1}$	RT [min]	Area [mV*s]	Amount found	% Label claim	Level of accuracy	Recovery			
						Area	% Recovery	Mean \pm SD	% RSD
20	6.6500	493.8365	15.05	75.25	Recovery	911.2929	1) 101.18	101.87 \pm 0.98	0.96
20	6.6833	503.3324	15.26	76.30	- 80%	916.8100	2) 102.56		
		Mean	24.85	75.78	Recovery - 100%	989.3316	1) 98.26	98.34 \pm 0.11	0.12
		\pm SD	0.15	0.35		998.2233	2) 98.42		
		% RSD	0.60	0.37	Recovery - 120%	1104.7869	1) 83.19	83.05 \pm 0.21	0.25
						1103.0601	2) 82.90		

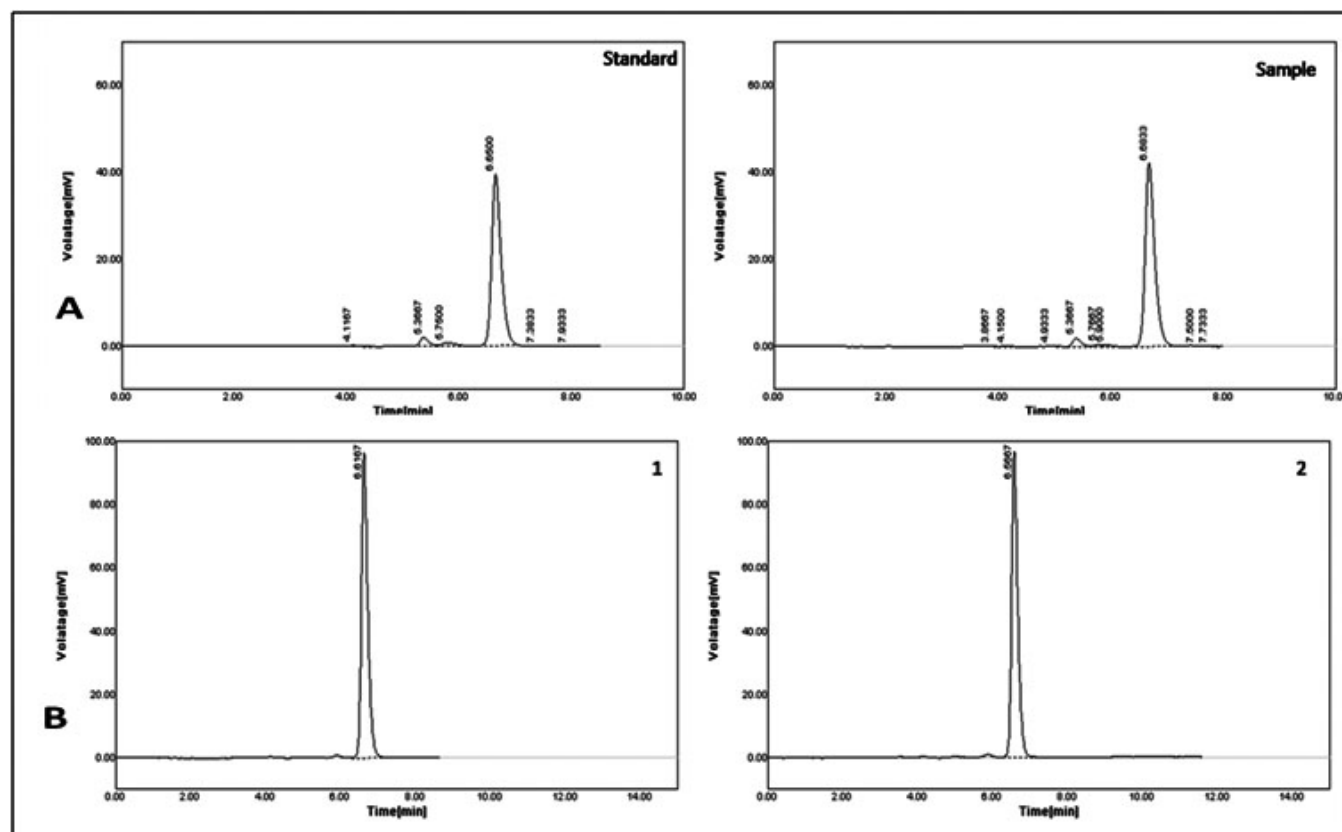


Fig. 1: Chromatogram of A) standard and sample solution B) 120% accuracy

Preparation of mobile phase

Mobile phase was prepared by mixing 650:350 ratio of acetonitrile and water. This mixture was degassed in ultrasonic water bath for 10 minutes and was filtered through nylon filter 0.45 μ under vacuum. This mobile phase was also used as diluents.

RP-HPLC method development

Preparation of standard solution

Standard solution was prepared by dissolving 10 mg of ambrisentan in about 10 mL of mobile phase in clean dry volumetric flask, and sonicated to dissolve it completely and volume was made up to the mark with diluent.

Preparation of sample solution

Accurately 20 tablets were weighed, finely powdered and an accurately weighed sample of powdered tablets equivalent to 10 mg of ambrisentan was treated with diluent in 10 mL volumetric flask using ultra sonicator. This solution was filtered through 0.45 μm filter paper. Suitable aliquot of the filtered solution was added to a volumetric flask and made up to volume with mobile phase to yield a starting concentration of 10 $\mu\text{g mL}^{-1}$ ¹².

Validation of RP-HPLC method

The various parameters were validated according to International Conference on Harmonization guidelines for validation of analytical procedures. Intra and inter-day precision were determined by analyzing the drug at three different concentrations of 20 $\mu\text{g mL}^{-1}$, 30 $\mu\text{g mL}^{-1}$, 40 $\mu\text{g mL}^{-1}$ of ambrisentan twice, on same day. Linearity was determined at 5 levels over the range of 10 % to 50 % with respect to the test concentration. A standard stock solution was prepared and further diluted to attain concentration of about 10 %, 20 %, 30 %, 40 % and 50 % of sample concentration. The specificity of the method was performed by injecting blank solution and then a drug solution of 20 μL was injected into the column, under optimized chromatographic conditions, to demonstrate the separation of ambrisentan from any of the impurities, if present. The accuracy of the method was carried out at three levels 80 %, 100 % and 120 % of the working concentration of sample. The ruggedness was found to be well within specific limits % RSD NMT 2.0 %. Suitability values were calculated from the first injection of six replicates of standard and % RSD was calculated from six replicate injections of standard ^{7,13}.

RESULTS AND DISCUSSION

Spectral study showed that the λ_{max} of the AMB was at 260 nm. To achieve resolution of the drug and its degradation product by RP-HPLC, stationary phase C-18 was used. A mobile phase consisting of acetonitrile:water ratio was selected in proportion of 650: 350. This shows good resolution chromatogram with symmetrical peak. The final RP-HPLC method was successfully developed for estimation of AMB. The method was developed in consideration of optimized chromatographic parameters. The chromatogram of developed method for standard and sample are mentioned in Fig. 1. The percent assay by developed method is mentioned in Table I. The chromatograms of standard and sample of AMB indicate the retention time for 6.65 and 6.68 min for standard and sample, respectively. In intra-day and inter-day precision for 20 $\mu\text{g mL}^{-1}$, 30 $\mu\text{g mL}^{-1}$ and 40 $\mu\text{g mL}^{-1}$; the % RSD of

AMB was found to within acceptable limit of ≤ 2 . Hence, the method is reproducible. The accuracy of developed method was determined and the data is shown in Table I and Fig. 1B. The specificity of the method was determined by checking the interference of the components against placebo. No interference was observed for any of the excipients of drug. The % mean recoveries of ambrisentan was found in range of 83.19-101.18 % and % RSD of ambrisentan was within limit of ≤ 2 . Hence the proposed method is accurate. The method employed by different analysts, at different time intervals did not significantly affect the recoveries, peak area and retention time of the above drug- indicating that the proposed method is rugged. The total run time required for the method is only 15 minutes for eluting AMB. In stability study, the % RSD limits are ≤ 2 . The solution stability in terms of percent assay was found in the range of 41 % to 115.05 % for the drug, indicating good solution stability.

CONCLUSION

Statistical analysis result showed that the proposed procedure has good precision and accuracy. The method was completely validated and shows satisfactory results for all the method parameter. Hence, it is concluded that the proposed method is precise, simple, sensitive, accurate, rugged and rapid and can be applied successfully for the estimation of ambrisentan in pharmaceutical dosage form.

REFERENCES

1. Barst R. J.: A review of pulmonary arterial hypertension: Role of ambrisentan. **Vasc. Health Risk Manag.**, 2007, 3(1), 11-22.
2. Patel J. K. and Patel N. K.: Stability-Indicating RP-HPLC Method for the Determination of ambrisentan and tadalafil in Pharmaceutical Dosage Form. **Scientific Pharmaceutica**, 2014, 82, 749-763.
3. European medicine agency; Evaluation of medicines for human use, Assessment report for volibris Doc. Ref.: EMEA/123999/2008. P.N.1-44.
4. Anjeneyula Y., Chandrasekhar K. and Manickam V.: 'A Textbook of Analytical Chemistry'; ISBN no: 9788188449194, Pharma Med Press, Hyderabad, 2005, 3-10.
5. Kasture A. V., Mahadik K. R., Wadodkar S. G. and More H. N.: 'A Text Book of Pharmaceutical Analysis'; 17th Edⁿ. ISBN10 no: 8185790086, Nirali prakashan, Pune, 2001. volume II, 27.
6. Skoog D., Holler F., Timothy A. and Nieman N.: 'A Text book of Principles of Instrumental Analysis'; 4th Edⁿ. ISBN-10 no: 0495012017, Philadelphia: Saunders College Pub; 1999. 1-2, 338-340.

7. Robbert A. N. and Alfrd H. W.: 'Pharmaceutical Process Validation', ISBN 10 no: 1138367621 An International Third Edition, Drugs and Pharmaceutical Sciences, Published by T&F INDIA, 2018, 129 xiii.
8. Ramadoss K., Oruganti S. K. and Babu P. S.: Simple Validated RP-HPLC Method For Estimation Of Ambrisentan In Pharmaceutical Dosage Forms, **Int. Bull. Drug Res.**, 2015, 5(9), 1-18.
9. Balakrishna M., Unnisa A., Reddy P. and Suma CH.: RP-HPLC-PDA method for the analysis of ambrisentan in bulk drug and pharmaceutical dosage forms. **Int. J. Chem. Pharm. Sci.**, 2013, 4(4), 45-50.
10. Nagpure S. V., Deshmane S. V. and Biyani K. R.: Validation of proposed RP-HPLC method for simultaneous estimation of fempiverinium bromide and pitofenone HCL. **Indian Drugs**, 2014, 51(07), 39-45.
11. Desai R., Bhamre P. R. and Rajput S. J.: Bioanalytical method development and validation for estimation of Ambrisentan in rat plasma by solid phase extraction technique: application to pharmacokinetic study, Scholars Research Library, **Der Pharm. Lett.**, 2015, 7(9), 320-327.
12. Yunoos M., N.S.L. Lavanya, G. Sravani, Rao P. M. and Ch. Krishna: Development of a Validated UV Spectrophotometric Method for the Estimation of Ambrisentan in Pure and Marketed Formulations. **Sch. Acad. J. Pharm.**, 2014, 3(6), 427-431.
13. Bharati A. R., Deshmane S.V. and Biyani K. R.: Stability indicating RP-HPLC method development and validation for simultaneous estimation of amlodipine and hydrochlorothiazide in pharmaceutical dosage form. **Int. J. Curr. Pharm. Res.**, 2014, 6(4), 16-19.

^a Department of Quality Assurance, KJ's Institute, Trinity College of Pharmacy, Pune - 411 048, Maharashtra, India

Rupali M. Petkar^a, Subhash V. Deshmane^{b*}, Snehal S. Deshmane^b and Shirish P. Jain^c

^b Department of Pharmaceutics, Rajarshi Shahu College of Pharmacy, Buldana - 443 001, Maharashtra, India

^c Department of Pharmacology, Rajarshi Shahu College of Pharmacy, Buldana - 443 001, Maharashtra, India

*For Correspondence: E-mail: subdeshmane@yahoo.co.in

(Received 15 April 2021) (Accepted 19 October 2021)

<https://doi.org/10.53879/id.59.09.12966>

RP-HPLC METHOD DEVELOPMENT AND VALIDATION OF PHARMACEUTICAL TABLET DOSAGE FORM CONTAINING AMBRISENTAN

ABSTRACT

The objective of the current study was to develop a simple, precise and accurate RP-HPLC assay method and its validation for determination of ambrisentan in pharmaceutical tablet dosage form. Gradient RP-HPLC separation was achieved on an analytical Primisil C18 R column (250 mm × 4.6 mm; 5 µm particle size) using mobile phase containing mixture of acetonitrile: water (65:35 V/V). The developed method was validated for specificity, linearity, precision, accuracy and robustness study. The method was linear in the drug concentration range of 10-50 µg mL⁻¹ with a correlation coefficient 0.998. The percent RSD values were found to be less than 2 %, indicating the developed method was also robust. The method was completely validated and shows satisfactory result for the all method parameter. Hence it is concluded that the proposed method is precise, simple, sensitive, accurate, rugged and rapid and can be applied successfully for the estimation of ambrisentan in pharmaceutical dosage form.

Keywords: Ambrisentan, chromatographic analysis, RP-HPLC, method validation, system suitability

INTRODUCTION

Ambrisentan, chemically (2S)-2-[(4,6-dimethylpyrimidin-2-yl)oxy]-3-methoxy-3,3-diphenylpropanoic acid, is a pulmonary antihypertensive agent. Ambrisentan is one of several newly developed vasodilator drugs that selectively target the endothelin type A (ETA) receptor, inhibiting its action and preventing vasoconstriction¹⁻³. High performance liquid chromatography (HPLC) is the most versatile and widely used analytical technique. It utilizes a liquid mobile phase to separate the components of a mixture⁴. These components (or analytes) are first dissolved in a solvent, and then forced to flow through a chromatographic column under high pressure. In the column, the mixture is resolved into its components. The interaction of solute with mobile and stationary phases can be manipulated through different choices of both solvent and stationary phases⁵. As a result, HPLC acquires a high degree of versatility not found in other chromatographic systems and it has the ability to separate a wide variety of chemical mixtures⁶. Validation parameters to be studied before finalization of the method include specificity, linearity, range, accuracy, precision, limit of detection, limit of quantitation, ruggedness and robustness⁷. To the best of our knowledge, the assay of ambrisentan (AMB) is not official in pharmacopoeias of IP, USP and BP. The detailed survey of literature revealed that very few methods have been reported for the estimation of AMB alone. Hence the aim of present study was to develop, validate and stabilize RP-HPLC method for ambrisentan in pharmaceutical dosage form¹.

MATERIALS AND METHODS

Chemicals and reagent

The standard ambrisentan, marketed preparation and other required chemicals used for the present investigation were procured from Cipla Pharmaceuticals Ltd., Mumbai (India). The entire chemicals used were of HPLC grade.

Instruments

RP-HPLC method development and validation was done on Younglin (S.K.) Gradient system UV Detector HPLC instrument UV- detector and column Primisil C18, 250×4.6 mm, 5 µm particle size. The instruments used were UV- spectrophotometer (Waters), ultra sonic cleaning bath (Spectralab model USB), pH analyser (Labindia), weighing balance (Shimadzu), Fuming chamber (Labexel), hot air oven (Thermo Lab 905) and magnetic stirrer (Whilmatic).

Trials for selection of chromatographic conditions

Seven trials for selection of chromatographic condition were carried out using C18 (250×4.6 mm, 5µm) column with different mobile phases, methanol-water and acetonitrile-water with different ratios. The pH of the mobile phase was adjusted to 3.2 ± 0.05 with ortho phosphoric acid and solution was filtered through nylon filter (0.45 µm), and flow rate was adjust at 0.7 mL min⁻¹, and injection volume was 20 µm⁸⁻¹¹.

Table I: Chromatographic data for sample and standard with accuracy

Conc. in $\mu\text{g mL}^{-1}$	RT [min]	Area [mV*s]	Amount found	% Label claim	Level of accuracy	Recovery			
						Area	% Recovery	Mean \pm SD	% RSD
20	6.6500	493.8365	15.05	75.25	Recovery	911.2929	1) 101.18	101.87 \pm 0.98	0.96
20	6.6833	503.3324	15.26	76.30	- 80%	916.8100	2) 102.56		
		Mean	24.85	75.78	Recovery - 100%	989.3316	1) 98.26	98.34 \pm 0.11	0.12
		\pm SD	0.15	0.35		998.2233	2) 98.42		
		% RSD	0.60	0.37	Recovery - 120%	1104.7869	1) 83.19	83.05 \pm 0.21	0.25
						1103.0601	2) 82.90		

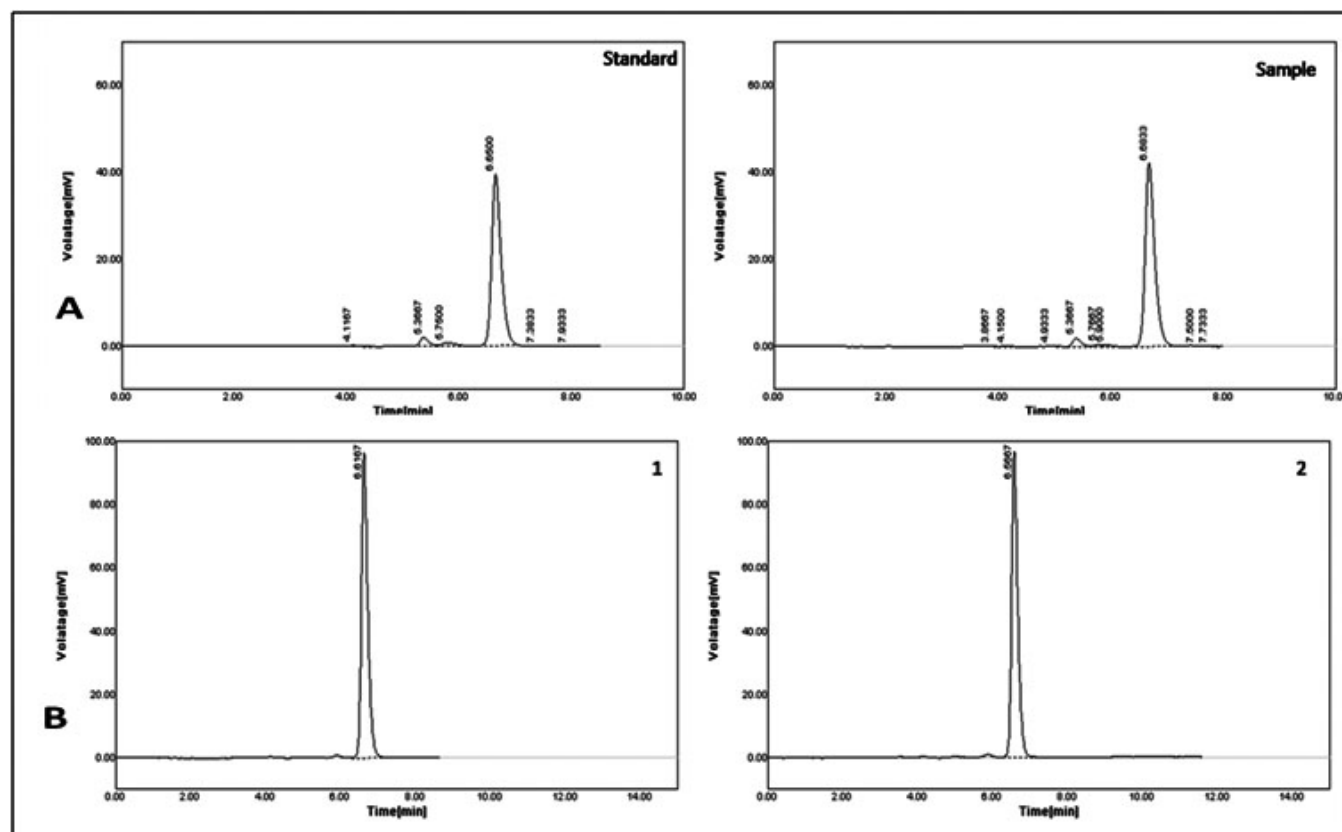


Fig. 1: Chromatogram of A) standard and sample solution B) 120% accuracy

Preparation of mobile phase

Mobile phase was prepared by mixing 650:350 ratio of acetonitrile and water. This mixture was degassed in ultrasonic water bath for 10 minutes and was filtered through nylon filter 0.45 μ under vacuum. This mobile phase was also used as diluents.

RP-HPLC method development

Preparation of standard solution

Standard solution was prepared by dissolving 10 mg of ambrisentan in about 10 mL of mobile phase in clean dry volumetric flask, and sonicated to dissolve it completely and volume was made up to the mark with diluent.

Preparation of sample solution

Accurately 20 tablets were weighed, finely powdered and an accurately weighed sample of powdered tablets equivalent to 10 mg of ambrisentan was treated with diluent in 10 mL volumetric flask using ultra sonicator. This solution was filtered through 0.45 μm filter paper. Suitable aliquot of the filtered solution was added to a volumetric flask and made up to volume with mobile phase to yield a starting concentration of 10 $\mu\text{g mL}^{-1}$ ¹².

Validation of RP-HPLC method

The various parameters were validated according to International Conference on Harmonization guidelines for validation of analytical procedures. Intra and inter-day precision were determined by analyzing the drug at three different concentrations of 20 $\mu\text{g mL}^{-1}$, 30 $\mu\text{g mL}^{-1}$, 40 $\mu\text{g mL}^{-1}$ of ambrisentan twice, on same day. Linearity was determined at 5 levels over the range of 10 % to 50 % with respect to the test concentration. A standard stock solution was prepared and further diluted to attain concentration of about 10 %, 20 %, 30 %, 40 % and 50 % of sample concentration. The specificity of the method was performed by injecting blank solution and then a drug solution of 20 μL was injected into the column, under optimized chromatographic conditions, to demonstrate the separation of ambrisentan from any of the impurities, if present. The accuracy of the method was carried out at three levels 80 %, 100 % and 120 % of the working concentration of sample. The ruggedness was found to be well within specific limits % RSD NMT 2.0 %. Suitability values were calculated from the first injection of six replicates of standard and % RSD was calculated from six replicate injections of standard ^{7,13}.

RESULTS AND DISCUSSION

Spectral study showed that the λ_{max} of the AMB was at 260 nm. To achieve resolution of the drug and its degradation product by RP-HPLC, stationary phase C-18 was used. A mobile phase consisting of acetonitrile:water ratio was selected in proportion of 650: 350. This shows good resolution chromatogram with symmetrical peak. The final RP-HPLC method was successfully developed for estimation of AMB. The method was developed in consideration of optimized chromatographic parameters. The chromatogram of developed method for standard and sample are mentioned in Fig. 1. The percent assay by developed method is mentioned in Table I. The chromatograms of standard and sample of AMB indicate the retention time for 6.65 and 6.68 min for standard and sample, respectively. In intra-day and inter-day precision for 20 $\mu\text{g mL}^{-1}$, 30 $\mu\text{g mL}^{-1}$ and 40 $\mu\text{g mL}^{-1}$; the % RSD of

AMB was found to within acceptable limit of ≤ 2 . Hence, the method is reproducible. The accuracy of developed method was determined and the data is shown in Table I and Fig. 1B. The specificity of the method was determined by checking the interference of the components against placebo. No interference was observed for any of the excipients of drug. The % mean recoveries of ambrisentan was found in range of 83.19-101.18 % and % RSD of ambrisentan was within limit of ≤ 2 . Hence the proposed method is accurate. The method employed by different analysts, at different time intervals did not significantly affect the recoveries, peak area and retention time of the above drug- indicating that the proposed method is rugged. The total run time required for the method is only 15 minutes for eluting AMB. In stability study, the % RSD limits are ≤ 2 . The solution stability in terms of percent assay was found in the range of 41 % to 115.05 % for the drug, indicating good solution stability.

CONCLUSION

Statistical analysis result showed that the proposed procedure has good precision and accuracy. The method was completely validated and shows satisfactory results for all the method parameter. Hence, it is concluded that the proposed method is precise, simple, sensitive, accurate, rugged and rapid and can be applied successfully for the estimation of ambrisentan in pharmaceutical dosage form.

REFERENCES

1. Barst R. J.: A review of pulmonary arterial hypertension: Role of ambrisentan. **Vasc. Health Risk Manag.**, 2007, 3(1), 11-22.
2. Patel J. K. and Patel N. K.: Stability-Indicating RP-HPLC Method for the Determination of ambrisentan and tadalafil in Pharmaceutical Dosage Form. **Scientific Pharmaceutica**, 2014, 82, 749-763.
3. European medicine agency; Evaluation of medicines for human use, Assessment report for volibris Doc. Ref.: EMEA/123999/2008. P.N.1-44.
4. Anjeneyula Y., Chandrasekhar K. and Manickam V.: 'A Textbook of Analytical Chemistry'; ISBN no: 9788188449194, Pharma Med Press, Hyderabad, 2005, 3-10.
5. Kasture A. V., Mahadik K. R., Wadodkar S. G. and More H. N.: 'A Text Book of Pharmaceutical Analysis'; 17th Edⁿ. ISBN10 no: 8185790086, Nirali prakashan, Pune, 2001. volume II, 27.
6. Skoog D., Holler F., Timothy A. and Nieman N.: 'A Text book of Principles of Instrumental Analysis'; 4th Edⁿ. ISBN-10 no: 0495012017, Philadelphia: Saunders College Pub; 1999. 1-2, 338-340.

7. Robbert A. N. and Alfrd H. W.: 'Pharmaceutical Process Validation', ISBN 10 no: 1138367621 An International Third Edition, Drugs and Pharmaceutical Sciences, Published by T&F INDIA, 2018, 129 xiii.
8. Ramadoss K., Oruganti S. K. and Babu P. S.: Simple Validated RP-HPLC Method For Estimation Of Ambrisentan In Pharmaceutical Dosage Forms, **Int. Bull. Drug Res.**, 2015, 5(9), 1-18.
9. Balakrishna M., Unnisa A., Reddy P. and Suma CH.: RP-HPLC-PDA method for the analysis of ambrisentan in bulk drug and pharmaceutical dosage forms. **Int. J. Chem. Pharm. Sci.**, 2013, 4(4), 45-50.
10. Nagpure S. V., Deshmane S. V. and Biyani K. R.: Validation of proposed RP-HPLC method for simultaneous estimation of fempiverinium bromide and pitofenone HCL. **Indian Drugs**, 2014, 51(07), 39-45.
11. Desai R., Bhamre P. R. and Rajput S. J.: Bioanalytical method development and validation for estimation of Ambrisentan in rat plasma by solid phase extraction technique: application to pharmacokinetic study, Scholars Research Library, **Der Pharm. Lett.**, 2015, 7(9), 320-327.
12. Yunoos M., N.S.L. Lavanya, G. Sravani, Rao P. M. and Ch. Krishna: Development of a Validated UV Spectrophotometric Method for the Estimation of Ambrisentan in Pure and Marketed Formulations. **Sch. Acad. J. Pharm.**, 2014, 3(6), 427-431.
13. Bharati A. R., Deshmane S.V. and Biyani K. R.: Stability indicating RP-HPLC method development and validation for simultaneous estimation of amlodipine and hydrochlorothiazide in pharmaceutical dosage form. **Int. J. Curr. Pharm. Res.**, 2014, 6(4), 16-19.

^a Department of Quality Assurance, KJ's Institute, Trinity College of Pharmacy, Pune - 411 048, Maharashtra, India

Rupali M. Petkar^a, Subhash V. Deshmane^{b*}, Snehal S. Deshmane^b and Shirish P. Jain^c

^b Department of Pharmaceutics, Rajarshi Shahu College of Pharmacy, Buldana - 443 001, Maharashtra, India

^c Department of Pharmacology, Rajarshi Shahu College of Pharmacy, Buldana - 443 001, Maharashtra, India

*For Correspondence: E-mail: subdeshmane@yahoo.co.in

(Received 15 April 2021) (Accepted 19 October 2021)

<https://doi.org/10.53879/id.59.09.12966>

RP-HPLC METHOD DEVELOPMENT AND VALIDATION OF PHARMACEUTICAL TABLET DOSAGE FORM CONTAINING AMBRISENTAN

ABSTRACT

The objective of the current study was to develop a simple, precise and accurate RP-HPLC assay method and its validation for determination of ambrisentan in pharmaceutical tablet dosage form. Gradient RP-HPLC separation was achieved on an analytical Primisil C18 R column (250 mm × 4.6 mm; 5 µm particle size) using mobile phase containing mixture of acetonitrile: water (65:35 V/V). The developed method was validated for specificity, linearity, precision, accuracy and robustness study. The method was linear in the drug concentration range of 10-50 µg mL⁻¹ with a correlation coefficient 0.998. The percent RSD values were found to be less than 2 %, indicating the developed method was also robust. The method was completely validated and shows satisfactory result for the all method parameter. Hence it is concluded that the proposed method is precise, simple, sensitive, accurate, rugged and rapid and can be applied successfully for the estimation of ambrisentan in pharmaceutical dosage form.

Keywords: Ambrisentan, chromatographic analysis, RP-HPLC, method validation, system suitability

INTRODUCTION

Ambrisentan, chemically (2S)-2-[(4,6-dimethylpyrimidin-2-yl)oxy]-3-methoxy-3,3-diphenylpropanoic acid, is a pulmonary antihypertensive agent. Ambrisentan is one of several newly developed vasodilator drugs that selectively target the endothelin type A (ETA) receptor, inhibiting its action and preventing vasoconstriction¹⁻³. High performance liquid chromatography (HPLC) is the most versatile and widely used analytical technique. It utilizes a liquid mobile phase to separate the components of a mixture⁴. These components (or analytes) are first dissolved in a solvent, and then forced to flow through a chromatographic column under high pressure. In the column, the mixture is resolved into its components. The interaction of solute with mobile and stationary phases can be manipulated through different choices of both solvent and stationary phases⁵. As a result, HPLC acquires a high degree of versatility not found in other chromatographic systems and it has the ability to separate a wide variety of chemical mixtures⁶. Validation parameters to be studied before finalization of the method include specificity, linearity, range, accuracy, precision, limit of detection, limit of quantitation, ruggedness and robustness⁷. To the best of our knowledge, the assay of ambrisentan (AMB) is not official in pharmacopoeias of IP, USP and BP. The detailed survey of literature revealed that very few methods have been reported for the estimation of AMB alone. Hence the aim of present study was to develop, validate and stabilize RP-HPLC method for ambrisentan in pharmaceutical dosage form¹.

MATERIALS AND METHODS

Chemicals and reagent

The standard ambrisentan, marketed preparation and other required chemicals used for the present investigation were procured from Cipla Pharmaceuticals Ltd., Mumbai (India). The entire chemicals used were of HPLC grade.

Instruments

RP-HPLC method development and validation was done on Younglin (S.K.) Gradient system UV Detector HPLC instrument UV- detector and column Primisil C18, 250×4.6 mm, 5 µm particle size. The instruments used were UV- spectrophotometer (Waters), ultra sonic cleaning bath (Spectralab model USB), pH analyser (Labindia), weighing balance (Shimadzu), Fuming chamber (Labexel), hot air oven (Thermo Lab 905) and magnetic stirrer (Whilmatic).

Trials for selection of chromatographic conditions

Seven trials for selection of chromatographic condition were carried out using C18 (250×4.6 mm, 5µm) column with different mobile phases, methanol-water and acetonitrile-water with different ratios. The pH of the mobile phase was adjusted to 3.2 ± 0.05 with ortho phosphoric acid and solution was filtered through nylon filter (0.45 µm), and flow rate was adjust at 0.7 mL min⁻¹, and injection volume was 20 µm⁸⁻¹¹.

Table I: Chromatographic data for sample and standard with accuracy

Conc. in $\mu\text{g mL}^{-1}$	RT [min]	Area [mV*s]	Amount found	% Label claim	Level of accuracy	Recovery			
						Area	% Recovery	Mean \pm SD	% RSD
20	6.6500	493.8365	15.05	75.25	Recovery	911.2929	1) 101.18	101.87 \pm 0.98	0.96
20	6.6833	503.3324	15.26	76.30	- 80%	916.8100	2) 102.56		
		Mean	24.85	75.78	Recovery - 100%	989.3316	1) 98.26	98.34 \pm 0.11	0.12
		\pm SD	0.15	0.35		998.2233	2) 98.42		
		% RSD	0.60	0.37	Recovery - 120%	1104.7869	1) 83.19	83.05 \pm 0.21	0.25
						1103.0601	2) 82.90		

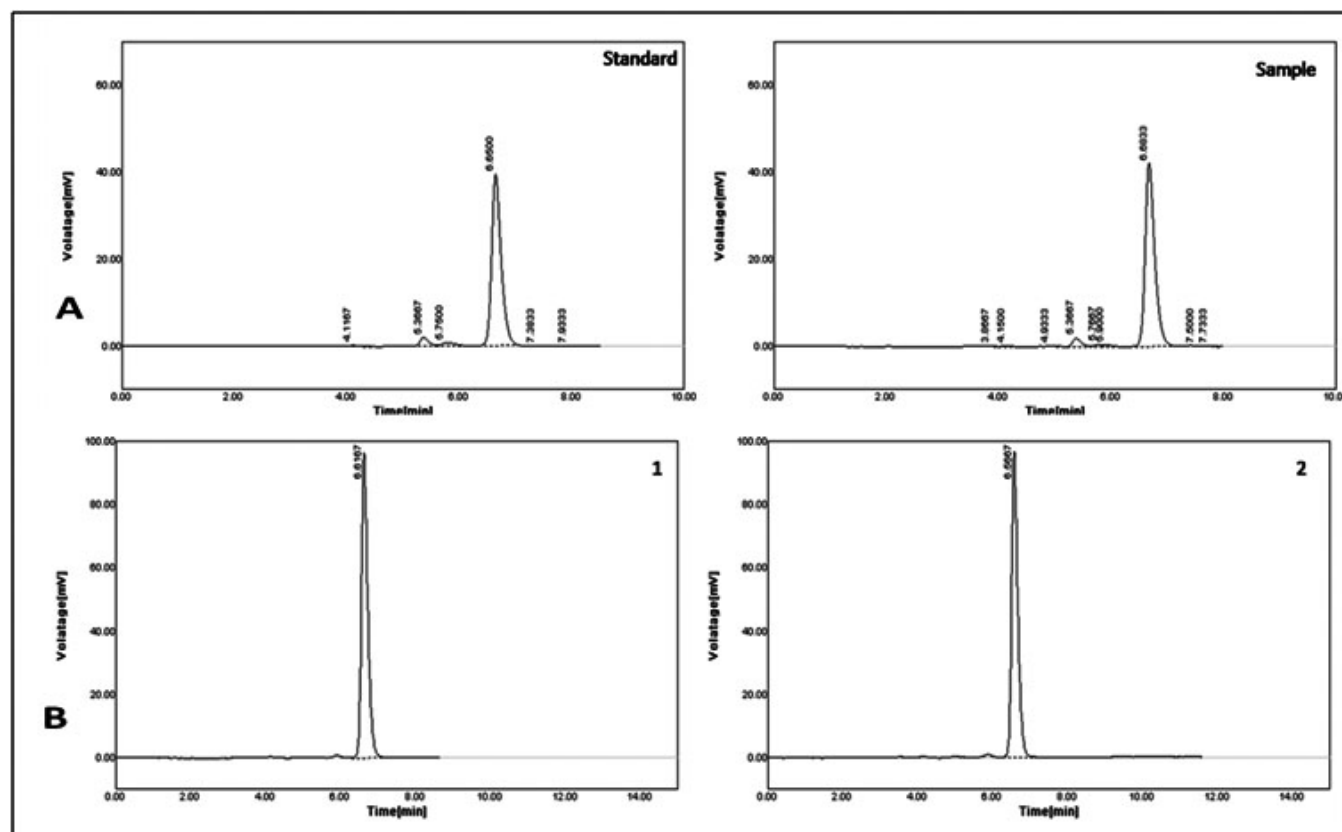


Fig. 1: Chromatogram of A) standard and sample solution B) 120% accuracy

Preparation of mobile phase

Mobile phase was prepared by mixing 650:350 ratio of acetonitrile and water. This mixture was degassed in ultrasonic water bath for 10 minutes and was filtered through nylon filter 0.45 μ under vacuum. This mobile phase was also used as diluents.

RP-HPLC method development

Preparation of standard solution

Standard solution was prepared by dissolving 10 mg of ambrisentan in about 10 mL of mobile phase in clean dry volumetric flask, and sonicated to dissolve it completely and volume was made up to the mark with diluent.

Preparation of sample solution

Accurately 20 tablets were weighed, finely powdered and an accurately weighed sample of powdered tablets equivalent to 10 mg of ambrisentan was treated with diluent in 10 mL volumetric flask using ultra sonicator. This solution was filtered through 0.45 μm filter paper. Suitable aliquot of the filtered solution was added to a volumetric flask and made up to volume with mobile phase to yield a starting concentration of 10 $\mu\text{g mL}^{-1}$ ¹².

Validation of RP-HPLC method

The various parameters were validated according to International Conference on Harmonization guidelines for validation of analytical procedures. Intra and inter-day precision were determined by analyzing the drug at three different concentrations of 20 $\mu\text{g mL}^{-1}$, 30 $\mu\text{g mL}^{-1}$, 40 $\mu\text{g mL}^{-1}$ of ambrisentan twice, on same day. Linearity was determined at 5 levels over the range of 10 % to 50 % with respect to the test concentration. A standard stock solution was prepared and further diluted to attain concentration of about 10 %, 20 %, 30 %, 40 % and 50 % of sample concentration. The specificity of the method was performed by injecting blank solution and then a drug solution of 20 μL was injected into the column, under optimized chromatographic conditions, to demonstrate the separation of ambrisentan from any of the impurities, if present. The accuracy of the method was carried out at three levels 80 %, 100 % and 120 % of the working concentration of sample. The ruggedness was found to be well within specific limits % RSD NMT 2.0 %. Suitability values were calculated from the first injection of six replicates of standard and % RSD was calculated from six replicate injections of standard ^{7,13}.

RESULTS AND DISCUSSION

Spectral study showed that the λ_{max} of the AMB was at 260 nm. To achieve resolution of the drug and its degradation product by RP-HPLC, stationary phase C-18 was used. A mobile phase consisting of acetonitrile:water ratio was selected in proportion of 650: 350. This shows good resolution chromatogram with symmetrical peak. The final RP-HPLC method was successfully developed for estimation of AMB. The method was developed in consideration of optimized chromatographic parameters. The chromatogram of developed method for standard and sample are mentioned in Fig. 1. The percent assay by developed method is mentioned in Table I. The chromatograms of standard and sample of AMB indicate the retention time for 6.65 and 6.68 min for standard and sample, respectively. In intra-day and inter-day precision for 20 $\mu\text{g mL}^{-1}$, 30 $\mu\text{g mL}^{-1}$ and 40 $\mu\text{g mL}^{-1}$; the % RSD of

AMB was found to within acceptable limit of ≤ 2 . Hence, the method is reproducible. The accuracy of developed method was determined and the data is shown in Table I and Fig. 1B. The specificity of the method was determined by checking the interference of the components against placebo. No interference was observed for any of the excipients of drug. The % mean recoveries of ambrisentan was found in range of 83.19-101.18 % and % RSD of ambrisentan was within limit of ≤ 2 . Hence the proposed method is accurate. The method employed by different analysts, at different time intervals did not significantly affect the recoveries, peak area and retention time of the above drug- indicating that the proposed method is rugged. The total run time required for the method is only 15 minutes for eluting AMB. In stability study, the % RSD limits are ≤ 2 . The solution stability in terms of percent assay was found in the range of 41 % to 115.05 % for the drug, indicating good solution stability.

CONCLUSION

Statistical analysis result showed that the proposed procedure has good precision and accuracy. The method was completely validated and shows satisfactory results for all the method parameter. Hence, it is concluded that the proposed method is precise, simple, sensitive, accurate, rugged and rapid and can be applied successfully for the estimation of ambrisentan in pharmaceutical dosage form.

REFERENCES

1. Barst R. J.: A review of pulmonary arterial hypertension: Role of ambrisentan. **Vasc. Health Risk Manag.**, 2007, 3(1), 11-22.
2. Patel J. K. and Patel N. K.: Stability-Indicating RP-HPLC Method for the Determination of ambrisentan and tadalafil in Pharmaceutical Dosage Form. **Scientific Pharmaceutica**, 2014, 82, 749-763.
3. European medicine agency; Evaluation of medicines for human use, Assessment report for volibris Doc. Ref.: EMEA/123999/2008. P.N.1-44.
4. Anjeneyula Y., Chandrasekhar K. and Manickam V.: 'A Textbook of Analytical Chemistry'; ISBN no: 9788188449194, Pharma Med Press, Hyderabad, 2005, 3-10.
5. Kasture A. V., Mahadik K. R., Wadodkar S. G. and More H. N.: 'A Text Book of Pharmaceutical Analysis'; 17th Edⁿ. ISBN10 no: 8185790086, Nirali prakashan, Pune, 2001. volume II, 27.
6. Skoog D., Holler F., Timothy A. and Nieman N.: 'A Text book of Principles of Instrumental Analysis'; 4th Edⁿ. ISBN-10 no: 0495012017, Philadelphia: Saunders College Pub; 1999. 1-2, 338-340.

7. Robbert A. N. and Alfrd H. W.: 'Pharmaceutical Process Validation', ISBN 10 no: 1138367621 An International Third Edition, Drugs and Pharmaceutical Sciences, Published by T&F INDIA, 2018, 129 xiii.
8. Ramadoss K., Oruganti S. K. and Babu P. S.: Simple Validated RP-HPLC Method For Estimation Of Ambrisentan In Pharmaceutical Dosage Forms, **Int. Bull. Drug Res.**, 2015, 5(9), 1-18.
9. Balakrishna M., Unnisa A., Reddy P. and Suma CH.: RP-HPLC-PDA method for the analysis of ambrisentan in bulk drug and pharmaceutical dosage forms. **Int. J. Chem. Pharm. Sci.**, 2013, 4(4), 45-50.
10. Nagpure S. V., Deshmane S. V. and Biyani K. R.: Validation of proposed RP-HPLC method for simultaneous estimation of fempiverinium bromide and pitofenone HCL. **Indian Drugs**, 2014, 51(07), 39-45.
11. Desai R., Bhamre P. R. and Rajput S. J.: Bioanalytical method development and validation for estimation of Ambrisentan in rat plasma by solid phase extraction technique: application to pharmacokinetic study, Scholars Research Library, **Der Pharm. Lett.**, 2015, 7(9), 320-327.
12. Yunoos M., N.S.L. Lavanya, G. Sravani, Rao P. M. and Ch. Krishna: Development of a Validated UV Spectrophotometric Method for the Estimation of Ambrisentan in Pure and Marketed Formulations. **Sch. Acad. J. Pharm.**, 2014, 3(6), 427-431.
13. Bharati A. R., Deshmane S.V. and Biyani K. R.: Stability indicating RP-HPLC method development and validation for simultaneous estimation of amlodipine and hydrochlorothiazide in pharmaceutical dosage form. **Int. J. Curr. Pharm. Res.**, 2014, 6(4), 16-19.

^a Department of Quality Assurance, KJ's Institute, Trinity College of Pharmacy, Pune - 411 048, Maharashtra, India

Rupali M. Petkar^a, Subhash V. Deshmane^{b*}, Snehal S. Deshmane^b and Shirish P. Jain^c

^b Department of Pharmaceutics, Rajarshi Shahu College of Pharmacy, Buldana - 443 001, Maharashtra, India

^c Department of Pharmacology, Rajarshi Shahu College of Pharmacy, Buldana - 443 001, Maharashtra, India

*For Correspondence: E-mail: subdeshmane@yahoo.co.in

(Received 15 April 2021) (Accepted 19 October 2021)

<https://doi.org/10.53879/id.59.09.12966>

TO ENHANCE THE SOLUBILITY OF IVERMECTIN WITH PHYSICAL MIXING METHOD FOR THE PREPARATION OF ORODISPERSIBLE TABLETS

Vaishali Adsare^{*1}, Lokhande Rahul Prakash², Pallavi Gholap³, Sangameshwar Baburao Kanthale⁴, Shubham Choudante⁵

¹ Department of Pharmaceutics, SGMSPM'S Sharadchandra Pawar College of Pharmacy, Dumberwadi, Tal: Junnar, Dist: Pune, Maharashtra 410504, India.

² Samarth Institute of Pharmacy, Belhe, Tal: Junner, Dist: Pune, Maharashtra 412410, India.

³ Dr. D.Y. Patil college of Pharmacy, Akurdi, Pune, Maharashtra 411044, India.

⁴ Rajarshi Shahu College of Pharmacy, At post: Malvihir, Botha Road, Buldhana, Maharashtra 443001, India.

⁵ Department of Pharmaceutics, Modern College of Pharmacy, Nigdi, Pune, Maharashtra 411044, India.

Email: vaibhavikk@yahoo.co.in¹

DOI: 10.47750/pnr.2022.13.S01.115

Abstract

This study was aimed to enhance solubility of ivermectin and developed the orodispersible tablet (ODT) in solid unit dosage forms which administer orally it is dissolve and disintegrate instantly within few seconds. Fast disintegrating tablet is useful for paediatric, geriatric, it improve the patient compliance. In this article the ivermectin fast disintegrating tablet were prepared by using superdisintegrant ingredient like cross carmellose sodium. The solubility of ivermectin was enhanced by using solid dispersion techniques in these technique PEG 600 are used it increased the solubility of FDT. Total 06 formulation prepared and evaluated. And the formulation F2 was shown best result as per ICH guideline. Optimized formulation F2 contained cross carmallose sodium and show better result in disintegration time 16 sec and maximum in vitro drug release of FDT is 98 %.

Keywords: Ivermectin, Crosscarmellose sodium, Sodium starch glycolate. ODT.

INTRODUCTION

Drug delivery system is tool for in market external product life. The oral route is mostly preferred route of administration of therapeutic drug because it has low cost have accurate dosing self-medication and easy to administer and high patient compliance. The most popular dose is conventional tablet.

The oral route of administration is used for mostly conventional drugs like tablets, capsules & solution. Mostof the things of oral route of administration consist of the desire characteristics like easy to administration flexibility of dosage form, fast disintegration and also convenience. FDT have most advantages like easy manufacturing, accurate dosing, good stability, and also ideal alternative for both geriatric and paediatric patients. Fast disintegrating tablet absorbed fastly orally disintegrating tablet is developed by combined hardness, dosage uniformity, stability, and other parameters.

Ivermectin (IVM) is new wide spectrum, efficient, less toxic antibiotics antiparasitic agent, to internal ectoparasite Be respectively provided with it is good kill effect, it is preferable especially for the repelling and killing efficacy of nematode and arthropod.

The mostly found drawback of these dosage form is difficulty in swelling for many patient above 50% peoples are affect by this difficulty but in recent trademark the fast disintegration drug delivery started to gain popularity and it is also acceptable a new drug delivery system because of easy administration and it is also show better patient compliance according to the centre of drug evaluation and research USFDA define FDT it is a solid dosage form which contains medicinal substance which

308

disintegrated rapidly with in few second when place upon the tongue. The fast disintegrating tablet are formulating by using super disintegrates like crosscarmellose sodium crosspovidone and sodium starch glycolate.

The varies technology use for the manufacturing FDT and these are prepared by direct compression method. Ivermectin is oral anthelmintic agent use for to treat strongyloidosis. ^[1]

MATERIALS AND METHOD

Materials

The drug Ivermectin was purchased as a gift sample from tosc International Pvt. Ltd. New Delhi. The solvent polyethylene glycol (PEG) was purchased from Research lab fine chem. Crosscarmellose sodium was purchased from Vishal chem. Magnesium stearate, cross povidone, fructose, was purchased from Pallav chemicals & solvents Pvt. Ltd. sodium, starch, glycolate was purchased from Yarrow chem products. MCC (microcrystalline cellulose) was purchased from Loba chemie Pvt. Ltd. Talc was purchased from Chemdyes corporation, mannitol was purchased from Merck Specialities Pvt. Ltd. fructose,

Method:

For preparation of solid dispersion the physical mixing method are used.

Physical Mixing:

In the physical mixing method of drug is prepared by geometric mixing of drug and carrier respectively without allying pressure. An excess quantity of drug and carrier is taken in a glass mortar and mix for 20 minutes. ^[2]

Formulation of Tablet:

Tablets were formulated using solid dispersion containing equivalent quantity of 12mg of ivermectin by the physical mixing techniques. In the formulation were prepared using direct compression technique and different concentration of superdisintegrants as shown in Table 1.

Powder mixture was compressed into tablets by using 6mm diameter punch in rotary tablet machine. Ivermectin, super disintegrating, microcrystalline cellulose, mannitol, magnesium stearate and talc, fructose were accurately weighed. All the materials were passed through 60#screen prior to mixed uniformly. The mixture evaluated for pre-compression parameters. After the powder mixing compress the tablet by using 6mm diameter punch in a rotary tablet machine. ^[3]

Table 1: Formulation of Ivermectin Orodisperible Tablet

Ingredients	F1	F2	F3	F4	F5	F6
Ivermectin	12	12	12	12	12	12
Cross carmellose Na	6	7.5	-	-	-	-
Cross povidone	-	-	6	7.5	-	-
Sodium starch glycoate	-	-	-	-	9	12
Mannitol	58	55.5	58	55.5	55	52
MCC	63	64	63	64	63	63
Magnesium stearate	3	3	3	3	3	3

Talc	3	3	3	3	3	3
Fructose	5	5	5	5	5	5
Total (mg)	150	150	150	150	150	150

RESULTS

Preformulation Studies

UV Spectroscopy of Drug:

Absorption maxima (λ_{max}):-

100mg drug dissolved in HCL (0.1 N) solution and dilute to 100ml with same solvent Solution. Then dilute 1 ml of solution to 100ml with HCL (0.1 N). This test solution take in cubets and spectra was run from 200- 400 nm and absorption maxima peak were discovered and result shown in Table number 2.

Fourier-transform infrared spectroscopy:

The FT-IR spectrum was recorded for pure drug Ivermectin and Orodispersible tablet of ivermectin. The FT-IR spectrum was recorded in the region of 4000-600cm⁻¹.

Bulk Density:

Apparent bulk density was determined by pouring a weigh quantity of tablet blend into graduated cylinder and measuring the height. Bulk density is the ratio of mass of tablet blend to bulk volume. Result shown in Table number 3.

Tapped Density:

Tapped density is the ratio of mass of tablet blend to tapped volume of tablet blend. Accurately to weighed amount of tablet blend poured in graduate cylinder and height is measured. Cylinder was allowed to 100 tapped under its own weight on to hard surface. The tapping was continue until no further changes in height was noted. Result shown in Table number 3.

Angle of Repose:

Angle of repose was determined using fixed funnel method. Result shown in Table number 3. The blend was poured through a funnel that can be raised vertically until maximum cone height was obtained. Radius of the heap was measured and angle of repose was calculated by using following formula:

$$\Theta = \tan^{-1} (h/r)$$

Where, Θ is angle of repose, h is height of pile, r is the radius of base piles

Hausner Ratio:

Hausner ratio is an indirect index of ease of powder flow. Result shown in Table number 3. It is calculated by using this formula.
Hausner ratio = pt/pb

Where, pt is tapped density and pb is bulk density.

Carr's Compressibility Index:

Compressibility is the ability of powder to decrease in a volume under pressure using bulk density and tapped density. Result shown in Table number 3. The percentage compressibility of powder were determined which is given as a carr's compressibility index which is calculated by using following formula. $1 = \{ (pb - pt) / pt \} \times 100$, [4-6]

Table 2: Calibration curve of Ivermectin in 0.1 N HCL

Sr. No.	Parameters	Observations
	λ max	248 nm
	Regression equation	$y = 0.0002x + 0.0359$
	Correlation Coefficient (r2)	0.9993

Figure 1: Calibration curve of Ivermectin

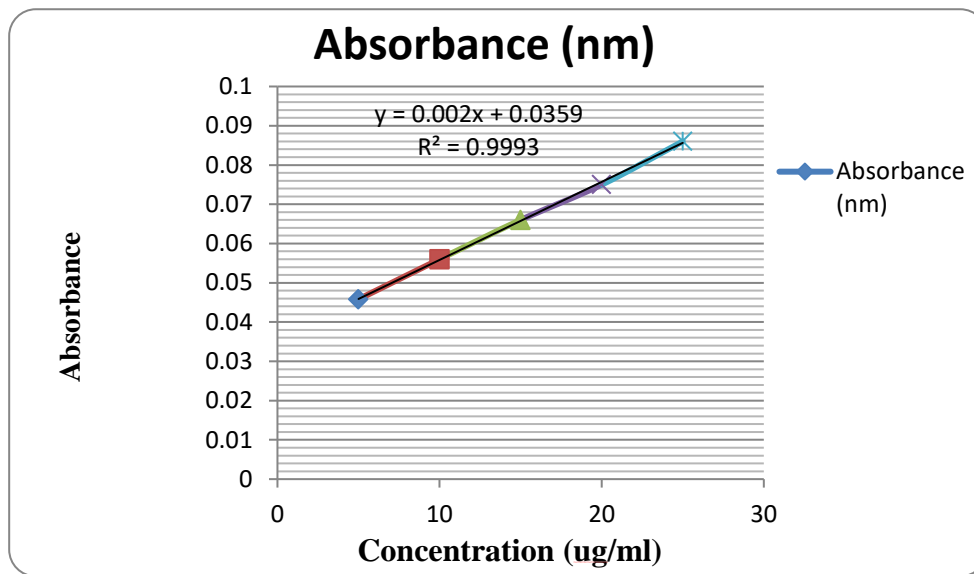


Table 3: Evaluation of mixed blend of drug and excipients

Formulation code	Angle of repose (Θ)	Bulk density (g/cm ³)	Tapped density (g/cm ³)	Hausner's ratio	Carr's compressibility index (%)
F1	30.11	0.38	0.5	1.66	24%
F2	22.02	0.37	0.47	1.27	21%
F3	25.61	0.40	0.55	1.37	27%
F4	29.37	0.4	0.52	1.32	23%
F5	35.37	0.39	0.51	1.30	23%
F6	35.23	0.38	0.51	1.30	25%

Figure 2: FTIR of Pure drug Ivermectin Drug

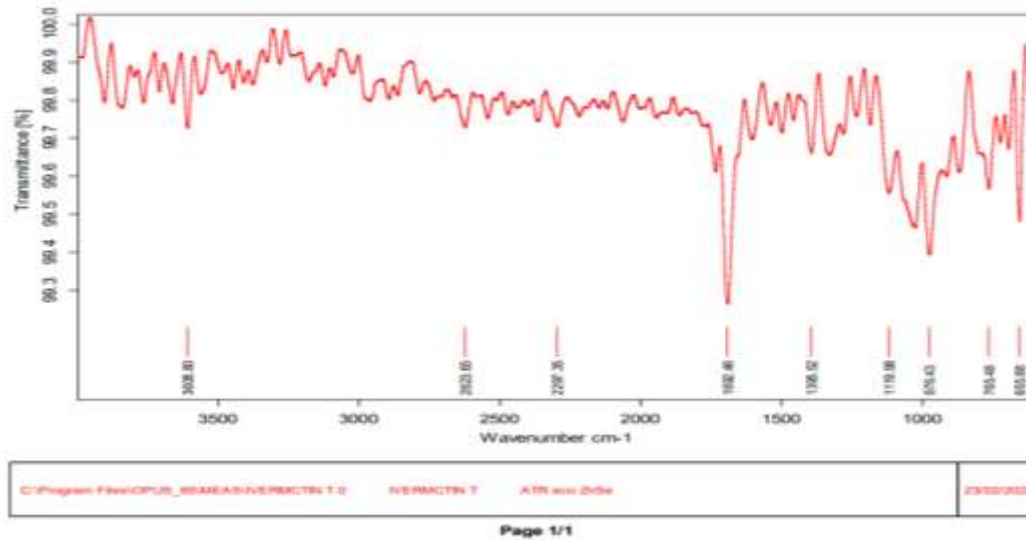
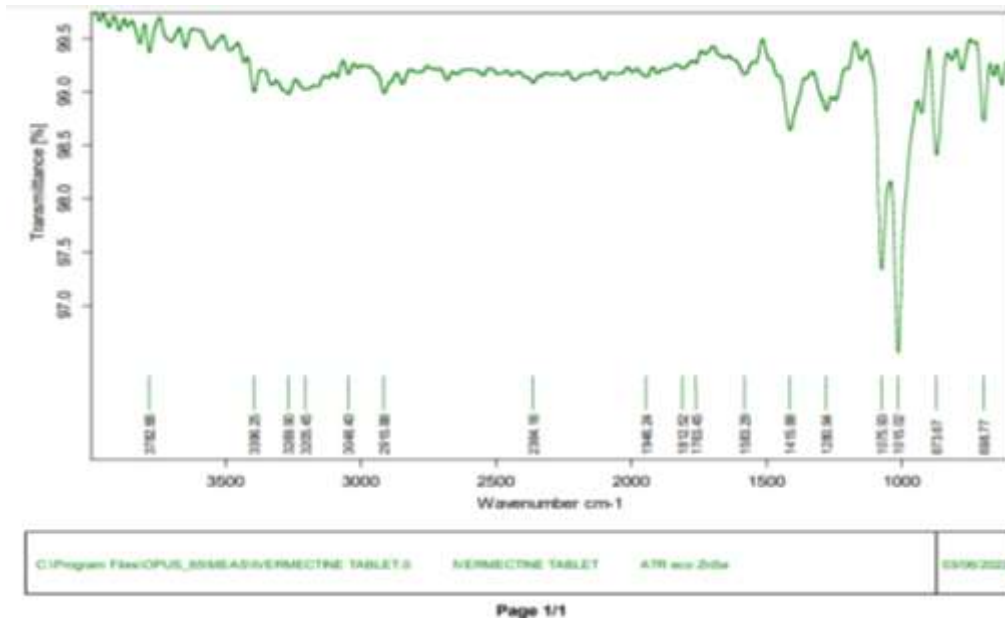


Figure 3: FTIR of Ivermectin Orodispersible Tablet



Post – Compression Tablet

Tablet Hardness:

The hardness of tablet is the force applied across the diameter of the tablet in the in order to break the tablet. A hardness of tablet of each formulation was determined by using Monsanto hardness tester. Result shown in Table number 4.

Tablet Thickness:

The thickness of tablet can be determined by using simple procedure. A thickness was measured by using tablet between two arms of the vernier calipers. Result shown in Table number 4.

Friability:

The measured of a mechanical strength of tablet. Roche friabilitor was used to measure the tablet. As per the weight of tablet was placed in friabilitor. Result shown in Table number 4. It consists of a plastic chamber that revolves at 25 rpm dropping those tablets at a distance of 6 inches with each revolution. The tablets are rotated in the friabilitor for at least 4 minutes. At the end of tablet were dusted and reweighed. The loss in the weight is measured of friability and is expressed in a percentage as:

$$\% \text{ friability} = \text{loss in a weight} / \text{initial weight} \times 100.$$

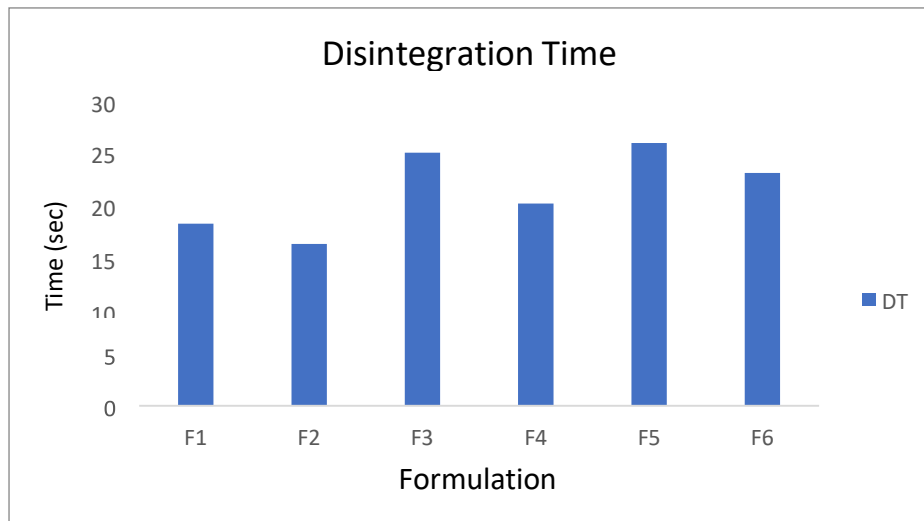
Table 4: Evaluation of Fast Disintegrating Tablet of Ivermectin

Formulation code	Hardness (kg/cm ²)	Thickness (mm)	Disintegration time (sec)	Friability (%)	Average weight
F1	3±0.098	3±0.577	18±0.577	0.60±0.0057	149±1.00
F2	2.8±0.251	2.93±0.598	16±1.00	0.32±0.01	150±1.154
F3	2.83±0.098	3.3±0.173	25±0.577	0.31±0.015	149±1.00
F4	3±0.144	3±0.577	20±1.527	0.35±0.025	151±1.154
F5	2.70±0.15	3.3±0.173	26±1.00	0.30±0.026	149±1.00
F6	3±0.188	3±0.173	23±0.577	0.31±0.015	150±1.153

Disintegration Time:

In the test was carried out with 6 tablet using distilled water at 37°C±2 °C was used as a disintegration media and the time in a second taken for a complete disintegration of the tablet with no palatable mass remaining in the apparatus measuring in the seconds. Result shown in Table number 4 and figure number 4. [7-9]

Figure 4: Disintegration Time



Uniformity of Weight:

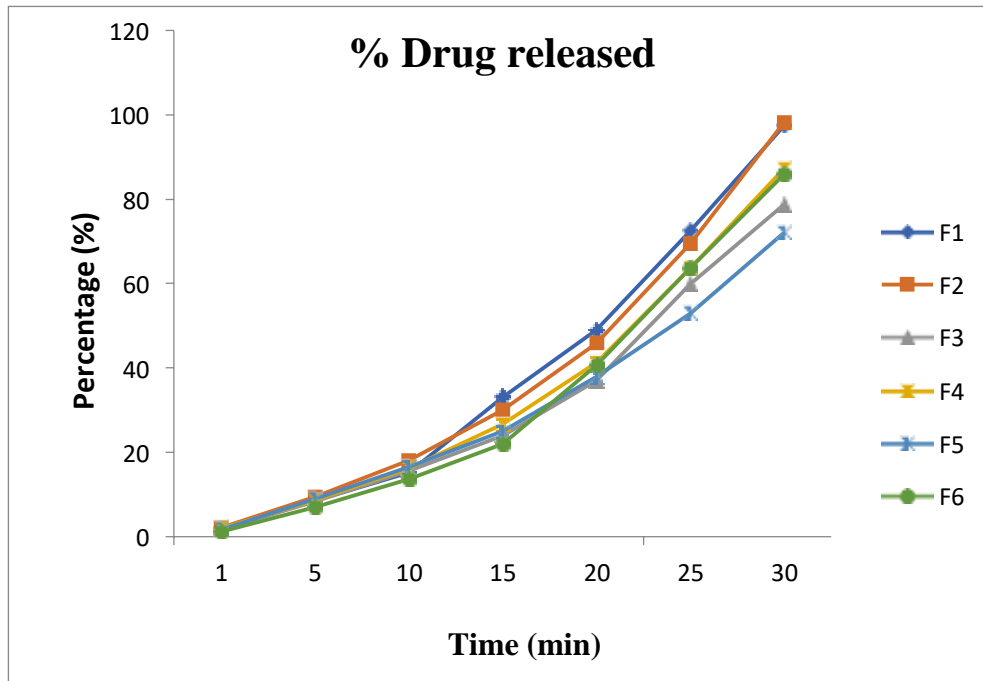
As per IP procedure for uniformity of weight was followed by using 20 tablets and there weight was determined individually and correctly on a digital weighing balance the average weight was the tablet was determined from the collective weight.

In Vitro Drug Released Studies:

The immediate released tablets are subjected to *in vitro* drug release studies in pH 0.1 N HCL for 25 minutes to access the ability of the formulation for providing immediate drug delivery.

Drug release studies were carried out in dissolution test apparatus using specified volume 900ml of dissolution media maintained $37 \pm 2^\circ \text{C}$. The tablet are kept in a cylindrical basket or directly placed in a medium with paddle then rotate at a 100 rpm. 5 ml of the sample for the dissolution medium are withdrawn at each time interval (1, 5, 10, 15, 20, 25, 30, minutes) and 5ml fresh medium was replaced each time. The sample are filtered 1ml was taken in diluted in 10ml. This sample were analysed spectrophotometrically and the further calculation are carried out of drug release. The *in vitro* dissolution kinetics parameter, dissolution rate constant, correlation coefficient and dissolution efficiency were calculated.^[10-11]

Figure 5: *In vitro* Drug released of all formulations



DISCUSSION

The fast disintegrating tablet of Ivermectin were prepared by using super disintegrating agents are crosscarmellose sodium, cross povidone, sodium starch glycolate at different concentration by direct compression methods. The powder blends are evaluated by using different Preformulation parameters and results in table no.2. The angle of repose was in the range of 22.02° - 35.37° indicates the good and passable flow properties. Then bulk density found in the range of $0.4-0.40 \text{ g/cm}^3$. Hausner's ratio was in the range of 1.27-1.66 it's indicate good flow ability. The Carr's compressibility index was found to between 21-27%. The powder blend containing drug was compressed by using direct compression methods and Ivermectin fast disintegrating tablet were prepared. The compressed tablets were evaluated for physical properties and the results arrange in table no 3. The hardness was in the range of $2.8 \pm 0.251 - 3 \pm 0.188 \text{ kg/cm}^2$. The thickness varies between $2.93 \pm 0.598 - 3.3 \pm 0.173 \text{ mm}$. The uniformity of average weight was found to be in the range of $149 \pm 1.00 - 151 \pm 1.154 \text{ mg}$. The friability of all formulation was found to be less than 1.0% & was in the range of $0.30 \pm 0.026 - 0.60 \pm 0.0057\%$ indicates good mechanical resistance of tablet. The disintegration time of all the formulated tablets was found to be in the range of $16 \pm 1.00 - 26 \pm 1.00 \text{ sec}$. The formulation F2 shows lowest disintegration time i.e. 16 sec. The result of *in vitro* drug released was 98 %.

CONCLUSION:

The fast disintegrating tablet of Ivermectin can be successfully prepared by direct compression techniques used in different concentration of super disintegrant crosscarmellose sodium, cross povidone, sodium starch glycolate, alone and its combination. The prepared FDT were evaluated for varies parameters like disintegration time, wetting time, drug content, *in vitro* drug released study etc. and shows, the satisfactory results. Among two super disintegrants used, cross carmellose sodium showed better results in disintegrationtime and *in vitro* drug released when compared to sodium starch glycolate. The formulation of F2 containingcross carmellose sodium (5%) showed better results in disintegration time 16 sec. and maximum *in vitro* drug released.

ACKNOWLEDGEMENT:

The authors sincerely thanks to tosc International Pvt. Ltd for providing Pure drug for completion of this project.

REFERENCES

1. Vishakha S. Hastak*, Kiran C. Mahajan, Formulation and Evaluation of Glicazide Mouth Dissolving Tablet, International Journal of Pharmaceutical Science Review and Research 21(2), 2013, 325-329.
2. Somya Verma, Urmi Patel, Formulation and Evaluation of Ivermectin Solid Dispersion, Journal of Drug Delivery and Therapeutics 7(7) 2017, 15-17
3. Raymond C Rowe. Paul J sheskey and paul J Weller Handbook of pharmaceutical excipient 4th edition page no. 181 to 185.
4. Joseph L. kanic, Leon Lachman 3rd edition published by K. M . Varghese company page no. 182 to 184
5. K.D Tripathi essentials of Medical pharmacology by 7 th edition page no. 849 – 854.
6. Indian pharmacopeia 2018 Volume I page no 236 Government of India ministry of Health & family welfare published by the Indian pharmacopeia commission Ghaziabad
7. IP 2018 volume II page no. 2340 to 2342 government of India ministry of Health and Family welfare published by the Indian pharmacopeia commission Ghaziabad
8. Joseph L. kanic, Leon Lachman 3rd edition published by K. M . Varghese company page no. 182 to 184
9. E. A. RAWLINS Bentley's textbook of pharmaceutics 8th edition page no 278 to 280
10. Michael E. Auton kevin M. G. Taylor 5th edition. Aulton's pharmaceutics published by Elsevier page no. 27
11. Patric J. Sinko, Martin's Physical Pharmacy and Pharmaceutics 7th edition published by Wolters Kluwer Page no.300

Molecular Docking Studies and Application of 6-(1-Arylmethanamino)-2-Phenyl-4*H*-Chromen-4-Ones as Potent Antibacterial Agents

Nitin M. Thorat, Vinnayak S. Khodade, Ajit P. Ingale, Deepak K. Lokwani, Aniket P. Sarkate & Shankar R. Thopate

To cite this article: Nitin M. Thorat, Vinnayak S. Khodade, Ajit P. Ingale, Deepak K. Lokwani, Aniket P. Sarkate & Shankar R. Thopate (2022): Molecular Docking Studies and Application of 6-(1-Arylmethanamino)-2-Phenyl-4*H*-Chromen-4-Ones as Potent Antibacterial Agents, Polycyclic Aromatic Compounds, DOI: [10.1080/10406638.2022.2150238](https://doi.org/10.1080/10406638.2022.2150238)

To link to this article: <https://doi.org/10.1080/10406638.2022.2150238>



Published online: 09 Dec 2022.



Submit your article to this journal [↗](#)







View related articles [↗](#)



View Crossmark data [↗](#)



Molecular Docking Studies and Application of 6-(1-Arylmethanamino)-2-Phenyl-4*H*-Chromen-4-Ones as Potent Antibacterial Agents

Nitin M. Thorat^a , Vinnayak S. Khodade^b, Ajit P. Ingale^c , Deepak K. Lokwani^d , Aniket P. Sarkate^e, and Shankar R. Thopate^f 

^aDepartment of Chemistry, Maharaja Jivajirao Shinde Arts, Science, Commerce College, Shrigonda, India;

^bDepartment of Chemistry, Johns Hopkins University Baltimore, Baltimore, MD, USA; ^cDepartment of Chemistry, Dada Patil College, Karjat, India; ^dDepartment of Pharmaceutical Chemistry, Rajarshi Shahu College of Pharmacy, Buldana, India; ^eDepartment of Chemical Technology, Dr. Babasaheb Ambedkar Marathwada University, Aurangabad, India; ^fDepartment of Chemistry, Radhabai Kale Mahila Mahavidyalaya Ahmednagar, Ahmednagar, India

ABSTRACT

The present article depicts the synthesis of the series of 6-(1-arylmethanamino)-2-phenyl-4*H*-chromen-4-ones and their antibacterial activity against the *S. aureus*. 6-(1-arylmethanamino)-2-phenyl-4*H*-chromen-4-ones (**1a–1n**) were obtained via reductive amination reaction of 6-aminoflavone with various commercially available aldehydes. Synthesized compounds and 6-aminoflavone (**1**) were assessed for their antimicrobial activities against the *S. aureus*. 6-aminoflavone (**1**) was found to have an MIC of 2 µg/mL. The compounds with side chains 4-fluorobenzyl (**1a**), 4-chlorobenzyl (**1b**), 4-nitrobenzyl (**1e**), 4-methoxybenzyl (**1g**) and (quinolin-2-yl)methyl (**1n**) were found to have an MIC of 2 µg/mL. We have demonstrated that 6-(1-arylmethanamino)-2-phenyl-4*H*-chromen-4-ones are easily accessible via reductive amination reaction. These compounds are found to have antibacterial effect against *S. aureus*.

ARTICLE HISTORY

Received 1 August 2022

Accepted 16 November 2022

KEYWORDS

Molecular docking; 6-aminoflavone; reductive amination; antibacterial agent

Introduction

Flavonoids are well known for having significant biological activities. Recently, medicinal plant extracts rich in secondary plant metabolites are reported to have antibacterial activities against multidrug-resistant *Staphylococcus aureus*. Today the entire world is up against bacterial infections that are leading to significant morbidity and mortality worldwide because of developed and/or developing resistance against the existing antibiotics.¹ Given that the versatile evolutionary method in microbes that enables them to develop quick resistance, at the same time curtailed joint efforts, investments and innovation from the private and government sector was indeed a major bottleneck to combat drug-resistant infections. Eventually, it is estimated that undermining efforts in this context would lead to 10 million deaths per year by 2050.² In 2017, the World Health Organization (WHO) disclosed the list of priority pathogens in concern with the emerging resistance, which is poised for the next outbreak.³ Inclusion of *Staphylococcus aureus*, in priority list by 'WHO,' was attributed to increased human health burden because of emerging resistance against the first-line medicines used for its treatment.^{3,4} Flavonoids, a class of secondary plant

metabolites with the unique architecture of C₆-C₃-C₆ carbon frame called a 'chroman', has gained importance over the years due to multifarious biological activity against both metabolic and infective diseases.^{5,6} This class of compounds exhibits a number of biological activities, including anti-cancer,⁷ anti-inflammatory,⁸ anti-oestrogenic,⁵ antifungal⁹ and anti-allergic¹⁰ among others. In addition, a flavonoid also exhibits antibacterial activity, which was anticipated by different mechanisms like inhibition of nucleic acid synthesis, inhibition of cell membrane porin and inhibition of energy metabolism.⁶ Moreover, other mechanisms like moderation in cell attachment and biofilm formation,^{11,12} varying the membrane permeability¹³ and damaging the cytoplasmic membrane^{14,15} have been proposed for their antibacterial activity. Furthermore, some flavonoids are also suitable antibacterial agents showing good activity against methicillin-resistant *Staphylococcus aureus* strains.¹⁶ Recently, plant-derived polymethoxyflavones was found to have an anti-mycobacterial activity through the inhibition of the efflux pump.¹⁷ Amino-functionalized benzopyranes, especially those in which there is no direct linkage between nitrogen and aromatic or heteroaromatic ring, are an important class of photochemicals and are well evaluated for their biological potential.¹⁸ A couple of biologically active and amino-functionalized flavones are shown in Figure 1.

Interestingly, another subclass represented by aminoflavones in which the nitrogen atom is attached with aromatic or hetero-aromatic ring by direct linkage, also possesses good biological activities *viz.* kinase inhibitory, anti-proliferative, antibacterial, and tyrosine-kinase inhibitory activity.¹⁸ Antibacterial effects against *M. tuberculosis* was reported for 7-Aminoflavone.¹⁹

Designing of 6-(1-Arylmethanamino)-2-phenyl-4H-chromen-4-ones

In the literature, there are number of review articles available that illuminate the importance of flavonoid drugs in *viz.* antibacterial, anticancer, antimicrobial and anti-inflammatory activity. This inspired us to combine two molecules by C-N bond to get hybrid molecules in hunt of improved biological activity. This strategy of molecular hybridization in designing drug molecules has been used successfully in the literature. Molecular hybridization is one of the well-established strategies used by medicinal chemists to design and synthesize new molecules with improved potency and efficacy. As mentioned earlier, meticulously combining structural characteristics of two different biologically significant pharmacophores to enhance potency and to combat problems like poor physical and pharmacodynamic properties of drug leads is a one of the strategies used by medicinal chemists. Our endeavor is to combine structural features of biologically important molecule flavones to build various 6-(1-Arylmethanamino)-2-phenyl-4H-chromen-4-ones, the intent is to improve potency of structural hybrid than individual pharmacophores. Over the last many years efforts have been focused to discover novel flavones derivatives with desirable biological activity which will be beneficial for the treatment of patient. Our goal was to discover novel and potent biologically activity 6-(1-Arylmethanamino)-2-phenyl-4H-chromen-4-ones.

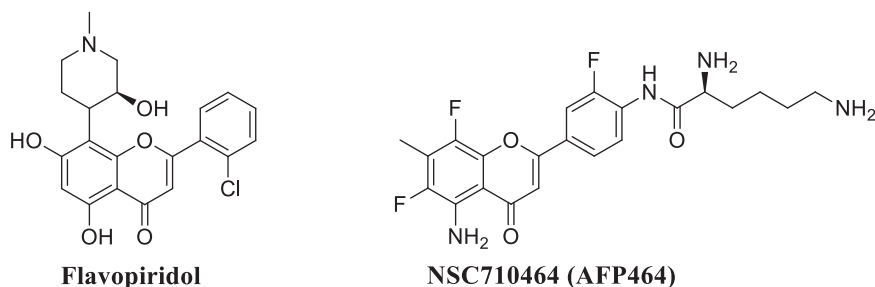


Figure 1. Biologically active flavonoids.

Despite diverse biological activities, aminoflavones are limitedly explored to build the structure activity relationship data, which can be anticipated by allied synthetic limitations.^{18,19}

Experimental

All reactions were performed in oven-dried glassware. All reagents and solvents were obtained from commercial suppliers and used as received. Analytical thin-layer chromatography (TLC) was performed on precoated Merck silica gel plates (60 F-254), visualized with a UV254 lamp and stained with KMnO₄. Melting points are uncorrected and were determined in open capillary tubes using paraffin oil bath. ¹H and ¹³C NMR spectra were obtained as solutions in deuterated solvents. Standard ¹H NMR (400 MHz) and ¹³C NMR (100 MHz) were recorded on a Varian Mercury spectrometer in DMSO-d₆ and CDCl₃ solution and with tetramethylsilane as an internal standard. IR spectra were recorded on Perkin Elmer Model 1600 series FTIR instrument. Mass spectra were recorded on Agilent 1200SL-6100 LC/MS (ES-API) instrument. High-resolution mass spectra (HRMS) were performed with a QTOF Micromass Mass Spectrometer in electro-spray ionization mode.

General procedure for the synthesis of 6-amino-2-phenyl-4*H*-chromen-4-ones (9a–9n)^{20,21}

To a solution of 6-amino-2-phenyl-4*H*-chromen-4-one (**1**, 1.0 g, 4.21 mmol) and substituted aromatic aldehydes (4.21 mmol) in 1, 2-dichloroethane (10 mL), sodium triacetoxyborohydride (1.33 g, 6.30 mmol) was added at 0 °C. Trifluoroacetic acid (0.99 g, 8.41 mmol) was added to the above solution and the reaction mixture was stirred at 0 °C to RT for 45 min. After completion of the reaction (TLC check), the mixture was diluted by adding DCM, the organic layer was first washed with aq. NH₄Cl and then with a saturated solution of brine. The organic layer was dried over anhydrous Na₂SO₄ and concentrated in *vacuo*. The crude product was purified through column chromatography on silica gel using hexane-ethylacetate (85:15) solvent system to give the corresponding flavones derivatives in high yields (Table 1).

The plausible mechanism for the synthesis of 6-(1-Arylmethanamino)-2-phenyl-4*H*-chromen-4-ones is shown in Figure 2.

Spectral data for the synthesized compounds 4(a–i)

6-(4-Fluorobenzylamino)-2-phenyl-4*H*-chromen-4-one (1a)

Yellow Solid, mp 132–135 °C; IR (KBr)/cm⁻¹: 3288, 3066, 1613, 1537, 1431, 842 cm⁻¹; ¹H NMR (DMSO-d₆, 400 MHz, ppm) δ: 7.91 (s, 2H), 7.63–7.26 (m, 8H), 7.08–7.02 (m, 3H), 6.78 (s, 1H), 4.38

Table 1. Synthesis of compounds 1a–1n.

Entry	Aldehydes	^a Aldehydes in g	Compounds	Yield ^b
1	4-Fluorobenzaldehyde	0.52	1a	86
2	4-chlorobenzaldehyde	0.56	1b	85
3	4-Bromobenzaldehyde	0.78	1c	88
4	2,3-Dichlorobenzaldehyde	0.73	1d	83
5	4-Nitrobenzaldehyde	0.63	1e	82
6	4-Cyanoobenzaldehyde	0.55	1f	85
7	4-Methoxybenzaldehyde	0.50	1g	86
8	4-Ethoxybenzaldehyde	0.56	1h	84
9	2,4-Dimethoxybenzaldehyde	0.70	1i	82
10	3,4-Dimethoxybenzaldehyde	0.70	1j	86
11	2-Hydroxy-5-bromobenzaldehyde	0.85	1k	82
12	2-Methoxy-5-bromobenzaldehyde	0.90	1l	82
13	2-Ethoxy-5-bromobenzaldehyde	0.96	1m	81
14	(Quinolin-2-yl)methylaldehyde	0.96	1n	80

^aVarious Aldehydes in g.

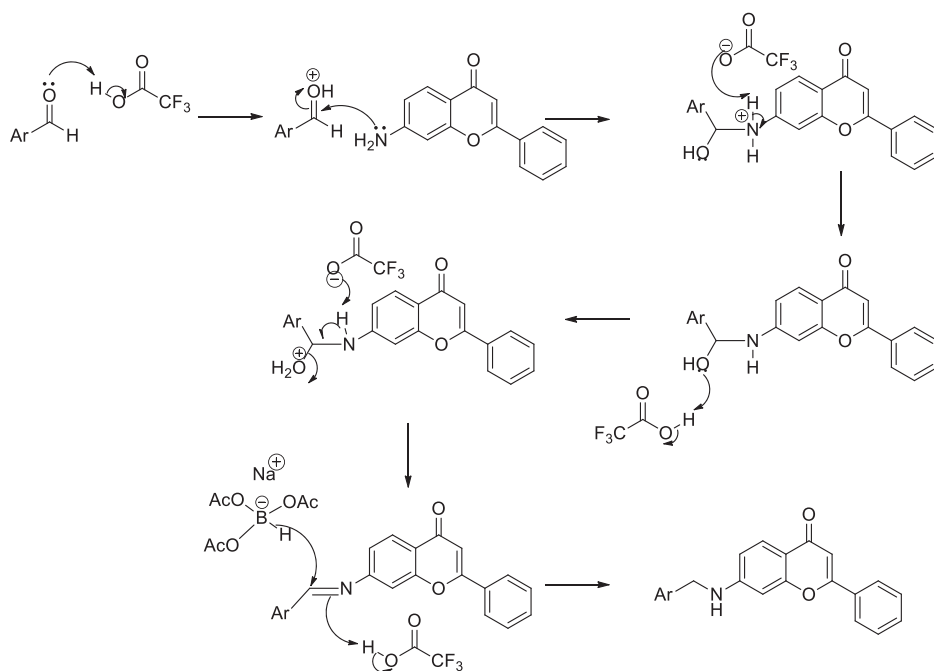


Figure 2. Plausible mechanism for synthesis of 6-(1-Arylmethanamino)-2-phenyl-4*H*-chromen-4-ones.

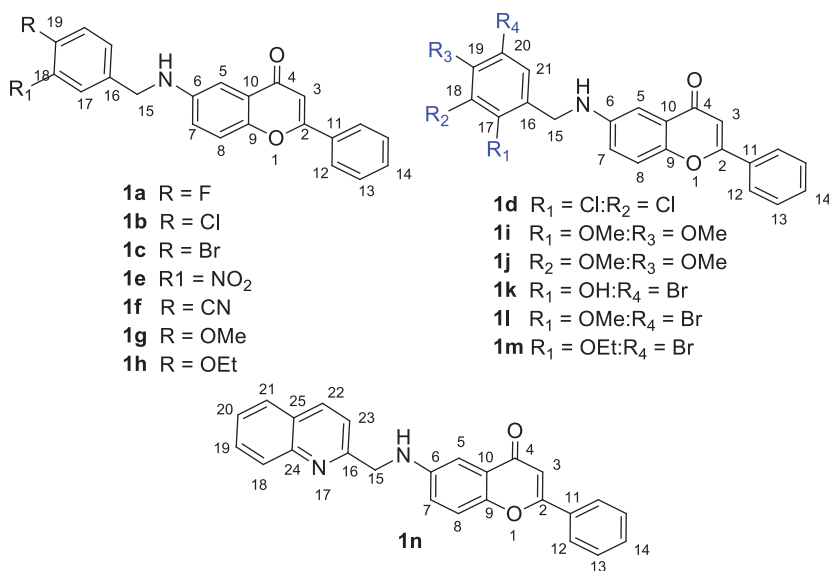


Figure 3. Structure of various derivatives of 6-(1-Arylmethanamino)-2-phenyl-4*H*-chromen-4-ones.

(s, 2H); ¹³C NMR (DMSO-*d*₆, 100 MHz, ppm) δ: 178.6(C4), 162.9(C2), 149.8(C19), 145.4(C9), 137.7(C6), 132.2(C16), 131.9(C11), 131.4(C13), 129.3(C17), 129.1(C14), 126.3(C12), 124.9(C10), 121.4(C7), 121.2(C8), 119.2(C18), 106.8(C5), 104.6(C3), 47.9(C15); LCMS (ES-API) *m/z*: 346.2 (M + H)⁺; HRMS (ESI) *m/z* [M + H]⁺: calcd for C₂₂H₁₇FNO₂: 345.1165, found: 345.1172 (Figure 3).

6-(4-Chlorobenzylamino)-2-phenyl-4H-chromen-4-one (1b)

Yellow Solid, mp 164–166 °C; IR (KBr)/cm⁻¹: 3285, 3061, 1791, 1611, 1047, 999, 578 cm⁻¹; ¹H NMR (DMSO-d₆, 400 MHz, ppm) δ: 7.94–7.92 (m, 2H), 7.55–7.54 (m, 4H), 7.53–7.43 (m, 1H), 7.34–7.29 (m, 5H), 7.04 (t, *J* = 8 Hz, 1H), 6.81 (s, 1H), 4.41 (s, 2H); ¹³C NMR (DMSO-d₆, 100 MHz, ppm) δ: 178.5(C4), 162.9(C2), 149.7(C9), 145.4(C6), 137.1(C16), 132.1(C19), 131.3(C11), 129.0(C18), 128.9(C13), 128.8(C17), 126.2(C14), 124.8(C12), 121.1(C7), 119.1(C10), 106.9(C8), 104.4(C3), 100.0(C5), 47.7(C15); LCMS (ES-API) *m/z*: 362.8(M + H)⁺; HRMS (ESI) *m/z* [M + H]⁺: calcd for C₂₂H₁₇ClNO₂: 362.0869, found: 362.0873.

6-(4-Bromobenzylamino)-2-phenyl-4H-chromen-4-one (1c)

White Solid, mp 174–176 °C; IR (KBr)/cm⁻¹: 3287, 3037, 1745, 1611, 1135, 793 cm⁻¹; ¹H NMR (DMSO-d₆, 400 MHz, ppm) δ: 8.05–8.03 (m, 2H), 7.61–7.51 (m, 6H), 7.38 (s, 1H), 7.34 (s, 1H), 7.18 (dd, *J* = 8.8 and 2.8 Hz, 1H), 6.94 (d, *J* = 2.8 Hz, 1H), 6.89 (s, 1H), 6.80–6.77 (m, 1H), 4.35–4.33 (m, 2H); ¹³C NMR (DMSO-d₆, 100 MHz, ppm) δ: 178.6(C4), 162.9(C2), 149.8(C9), 145.4(C6), 137.7(C19), 132.2(C18), 131.9(C11), 131.4(C17), 129.3(C13), 129.1(C12), 126.3(C14), 124.9(C10), 121.4(C19), 121.2(C7), 119.2(C8), 106.8(C5), 104.6(C3), 47.9(C15); LCMS (ES-API) *m/z*: 408.0 (M + H)⁺; HRMS (ESI) *m/z* [M + H]⁺: calcd for C₂₂H₁₇BrNO₂: 406.0442, found: 406.0446.

6-(2, 3-Dichlorobenzylamino)-2-phenyl-4H-chromen-4-one (1d)

Yellow Solid, mp 168–171 °C; IR (KBr)/cm⁻¹: 3299, 3068, 1685, 1288, 1096, 811, 770 cm⁻¹; ¹H NMR (DMSO-d₆, 400 MHz, ppm) δ: 8.06–8.04 (m, 2H), 7.60–7.55 (m, 5H), 7.36–7.33 (m, 2H), 7.21–7.18 (m, 1H), 6.86–6.90 (m, 3H), 4.47–4.47 (m, 2H); ¹³C NMR (DMSO-d₆, 100 MHz, ppm) δ: 178.3(C4), 162.6(C2), 149.3(C9), 145.5(C6), 138.6(C16), 134.3(C18), 132.9(C11), 131.9(C13), 131.3(C19), 129.0(C20), 128.9(C14), 127.3(C17), 126.7(C21), 126.0(C12), 124.5(C10), 121.1(C7), 119.0(C8), 106.3(C5), 103.5(C3), 46.1(C15); LCMS (ES-API) *m/z*: 396, 397.9, 400 (M + H)⁺; HRMS (ESI) *m/z* [M + H]⁺: calcd for C₂₂H₁₆Cl₂NO₂: 396.0558, found: 396.0552.

6-(3-Nitrobenzylamino)-2-phenyl-4H-chromen-4-one (1e)

Yellow Solid, mp 157–160 °C; IR (KBr)/cm⁻¹: 3280, 3062, 1762, 1222, 1188, 830, 504 cm⁻¹; ¹H NMR (DMSO-d₆, 400 MHz, ppm) δ: 8.25 (s, 1H), 8.12–8.10 (m, 1H), 8.05–8.03 (m, 2H), 7.87–7.85 (m, 1H), 7.67–7.63 (m, 1H), 7.59–7.57 (m, 4H), 7.23–7.20 (m, 1H), 6.98–6.96 (m, 1H), 6.91–6.90 (m, 1H), 6.88 (s, 1H), 4.54–4.52 (m, 2H); ¹³C NMR (DMSO-d₆, 100 MHz, ppm) δ: 177.3(C4), 172.7(C2), 159.2(C19), 144.3(C9), 134.0(C16), 132.0(C6), 130.0(C11), 129.0(C13), 128.4(C14), 127.6(C17), 126.2(C12), 124.9(C10), 121.2(C18), 119.9(C7), 118.0(C8), 105.4(C5), 103.1(C3), 46.4(C15); LCMS (ES-API) *m/z*: 372.0 (M + H)⁺; HRMS (ESI) *m/z* [M + H]⁺: calcd for C₂₂H₁₇N₂O₄: 373.1188, found: 373.1195.

6-(4-Cyanobenzylamino)-2-phenyl-4H-chromen-4-one (1f)

Yellow Solid, mp 167–168 °C; IR (KBr)/cm⁻¹: 3287, 3043, 2222, 1613, 1497, 671, 543 cm⁻¹; ¹H NMR (DMSO-d₆, 400 MHz, ppm) δ: 8.05–8.03 (m, 2H), 7.81 (d, *J* = 8.4 Hz, 2H), 7.62–7.56 (m, 6H), 7.18 (dd, *J* = 9.6 and 3.2 Hz, 1H), 6.92 (d, *J* = 2.8 Hz, 1H), 6.88–6.86 (m, 2H), 4.48–4.47 (m, 2H); ¹³C NMR (DMSO-d₆, 100 MHz, ppm) δ: 178.5(C4), 163.1(C2), 149.9(C15), 144.9(C9), 144.4(C6), 132.7(C16), 132.1(C11), 131.5(C13), 129.1(C14), 127.9(C17), 126.3(C12), 124.9(C10), 121.2(C7), 119.4(C8), 118.9(CN), 111.3(C5), 106.8(C19), 104.8(C3), 48.0(C15); LCMS (ES-API) *m/z*: 353.0 (M + H)⁺; HRMS (ESI) *m/z* [M + H]⁺: calcd for C₂₃H₁₇N₂O₂: 353.1290, found: 353.1286.

6-(4-Methoxybenzylamino)-2-phenyl-4H-chromen-4-one (1g)

Yellow Solid, mp 134–136 °C; IR (KBr)/cm⁻¹: 3296, 3107, 1613, 1484, 1177, 769 cm⁻¹; ¹H NMR (DMSO-d₆, 400 MHz, ppm) δ: 8.06–8.03 (m, 2H), 7.60–7.52 (m, 4H), 7.30 (d, *J* = 8 Hz, 2H), 7.18 (dd, *J* = 8.8 and 2.8 Hz, 1H), 6.96 (d, *J* = 2.8 Hz, 1H), 6.92–6.89 (m, 3H), 6.66–6.64 (m, 1H), 4.28–4.26 (m, 2H), 3.66 (s, 3H); ¹³C NMR (DMSO-d₆, 100 MHz, ppm) δ: 178.1(C4), 162.2(C2), 150.1(C19), 146.1(C9), 132.1(C6), 131.8(C16), 131.1(C11), 130.7(C13), 128.8(C14), 128.6(C17), 125.9(C12), 124.4(C10), 121.4(C7), 118.7(C8), 113.7(C18), 106.1(C3), 102.8(C9), 55.1(OCH₃), 47.2(C15); LCMS (ES-API) *m/z*: 358.0 (M + H)⁺; HRMS (ESI) *m/z* [M + H]⁺: calcd for C₂₃H₂₀NO₃: 358.1443, found: 358.1441.

6-(4-Ethoxybenzylamino)-2-phenyl-4H-chromen-4-one (9h)

Yellow Solid, mp 159–162 °C; IR (KBr)/cm⁻¹: 3306, 3107, 1683, 1452, 1292, 767, 686 cm⁻¹; ¹H NMR (DMSO-d₆, 400 MHz, ppm) δ: 8.08–8.01 (m, 2H), 7.60–7.51 (m, 4H), 7.28 (d, *J* = 8.4 Hz, 2H), 7.17 (dd, *J* = 6.4 and 2.4 Hz, 1H), 6.96 (d, *J* = 6.8 Hz, 1H), 6.91–6.88 (m, 3H), 6.64 (d, *J* = 3.6 Hz, 1H), 4.27–4.25 (d, *J* = 8 Hz, 2H), 3.98 (q, *J* = 14 and 6.8 Hz, 2H), 1.30 (t, *J* = 6.8 Hz, 3H); ¹³C NMR (DMSO-d₆, 100 MHz, ppm) δ: 178.6(C4), 162.7(C2), 158.4(C19), 149.5(C9), 145.7(C6), 132.2(C16), 131.2(C11), 130.4(C13), 128.9(C17), 128.1(C14), 126.2(C12), 124.8(C10), 121.2(C7), 118.9(C8), 114.7(C18), 106.6(C5), 104.1(C3), 63.4(OCH₂), 48.0(C15), 14.8(CH₃); LCMS (ES-API) *m/z*: 372.9 (M + H)⁺; HRMS (ESI) *m/z* [M + H]⁺: calcd for C₂₄H₂₁NO₃: 372.1599, found: 372.1599.

6-(2, 4-Dimethoxybenzylamino)-2-phenyl-4H-chromen-4-one (1i)

Yellow Solid, mp 126–129 °C; IR (KBr)/cm⁻¹: 3359, 3038, 1613, 1523, 1274, 1120, 719 cm⁻¹; ¹H NMR (DMSO-d₆, 400 MHz, ppm) δ: 8.09–8.01 (m, 2H), 7.57–7.53 (m, 4H), 7.18–7.13 (m, 2H), 6.93 (d, *J* = 2.8 Hz, 1H), 6.88 (s, 1H), 6.59 (d, *J* = 2.4 Hz, 1H), 6.47–6.45 (m, 2H), 4.21–4.20 (m, 2H), 3.84 (s, 3H), 3.73 (s, 3H); ¹³C NMR (DMSO-d₆, 100 MHz, ppm) δ: 178.3(C4), 162.4(C2), 160.1(C19), 158.3(C17), 149.4(C9), 146.2(C6), 131.9(C11), 131.1(C21), 129.5(C13), 126.9(C14), 126.0(C12), 124.5(C10), 121.5(C7), 118.9(C16), 118.7(C8), 106.2(C5), 103.9(C3), 103.5(C18), 98.3(C20), 55.3(OCH₃), 55.2(OCH₃), 42.8(C15); LCMS (ES-API) *m/z*: 388.2 (M + H)⁺; HRMS (ESI) *m/z* [M + H]⁺: calcd for C₂₄H₂₂NO₄: 388.1549, found: 388.1544.

6-(3,4-Dimethoxybenzylamino)-2-phenyl-4H-chromen-4-one (1j)

Yellow Solid, mp 138–141 °C; IR (KBr)/cm⁻¹: 3288, 3106, 1613, 1484, 1152, 936, 541 cm⁻¹; ¹H NMR (DMSO-d₆, 400 MHz, ppm) δ: 8.08–8.01 (m, 2H), 7.57–7.53 (m, 4H), 7.18 (dd, *J* = 8.8 and 2.8 Hz, 1H), 7.01–6.99 (d, *J* = 2.8 Hz, 2H), 6.92–6.89 (m, 3H), 6.68–6.61 (m, 1H), 4.27–4.25 (m, 2H), 3.74 (s, 3H), 3.71 (s, 3H); ¹³C NMR (DMSO-d₆, 100 MHz, ppm) δ: 178.6(C4), 162.6(C2), 160.4(C18), 158.5(C19), 149.4(C9), 146.0(C6), 132.2(C16), 131.2(C11), 129.9(C13), 128.9(C14), 126.1(C12), 124.7(C10), 121.4(C21), 119.0(C7), 118.8(C8), 106.6(C20), 104.5(C3), 103.9(C17), 98.7(C5), 65.8(OCH₃), 55.4(OCH₃), 43.5(C15); LCMS (ES-API) *m/z*: 388.2 (M + H)⁺; HRMS (ESI) *m/z* [M + H]⁺: calcd for C₂₄H₂₂NO₄: 388.1548, found: 388.1551.

6-(5-Bromo-2-hydroxybenzylamino)-2-phenyl-4H-chromen-4-one (1k)

Yellow Solid, mp 188–191 °C; IR (KBr)/cm⁻¹: 3287, 3105, 1719, 1643, 1413, 808, 548 cm⁻¹; ¹H NMR (DMSO-d₆, 400 MHz, ppm) δ: 9.99 (s, 1H), 8.10–7.90 (m, 2H), 7.57–7.54 (m, 4H), 7.31–7.10 (m, 3H), 6.99–6.93 (m, 2H), 6.92 (s, 1H), 6.61 (d, *J* = 6.4 Hz, 1H), 4.27–4.27 (m, 2H); ¹³C NMR (DMSO-d₆, 100 MHz, ppm) δ: 178.4(C4), 162.6(C2), 154.6(C17), 149.4(C9), 146.0(C6), 131.9(C21), 131.2(C16), 131.1(C19), 130.7(C11), 128.9(C13), 127.3(C14), 126.0(C12), 124.5(C10), 121.7(C7), 118.9(C18), 117.2(C20), 111.0(C8), 106.3(C5), 104.0(C3), 43.51(C15); LCMS (ES-API) *m/z*: 423.7 (M + H)⁺; HRMS (ESI) *m/z* [M + H]⁺: calcd for C₂₂H₁₇BrNO₃: 422.0392, found: 422.0398.

6-(5-Bromo-2-methoxybenzylamino)-2-phenyl-4H-chromen-4-one (1l)

Yellow Solid, mp 173–176 °C; IR (KBr)/cm⁻¹: 3366, 3067, 1684, 1450, 1029, 708, 549 cm⁻¹; ¹H NMR (DMSO-d₆, 400 MHz, ppm) δ: 8.05–8.03 (m, 2H), 7.58–7.56 (m, 4H), 7.42–7.32 (m, 2H), 7.18 (dd, *J* = 5.6 and 3.2 Hz, 1H), 7.01 (d, *J* = 8 Hz, 1H), 6.92–6.89 (m, 2H), 6.67–6.65 (m, 1H), 4.30–4.29 (m, 2H), 3.89 (s, 3H); ¹³C NMR (DMSO-d₆, 100 MHz, ppm) δ: 178.6(C4), 162.8(C2), 156.5(C17), 149.6(C9), 145.6(C6), 132.1(C21), 131.2(C19), 131.2(C11), 131.0(C16), 129.0(C13), 128.9(C14), 128.8(C12), 126.2(C10), 124.8(C7), 121.2(C8), 119.0(C18), 110.9(C20), 106.6(C5), 104.6(C3), 55.6(OCH₃), 43.2(C15); LCMS (ES-API) *m/z*: 437.9 (M + H)⁺; HRMS (ESI) *m/z* [M + H]⁺: calcd for C₂₃H₁₉BrNO₃: 436.0558, found: 436.0548.

6-(5-Bromo-2-ethoxybenzylamino)-2-phenyl-4H-chromen-4-one (9m)

Yellow Solid, Mp 180–184 °C; IR (KBr)/cm⁻¹: 3374, 3038, 1618, 1506, 910, 753 cm⁻¹; ¹H NMR (DMSO-d₆, 400 MHz, ppm) δ: 7.90 (s, 2H), 7.51–7.27 (m, 8H), 7.07–7.03 (m, 1H), 6.77 (s, 2H), 4.39 (s, 2H), 4.07 (d, *J* = 5.4 Hz, 2H), 1.45 (m, 3H); ¹³C NMR (DMSO-d₆, 100 MHz, ppm) δ: 178.6(C4), 162.8(C2), 155.9(C17), 149.7(C9), 145.7(C6), 132.2(C21), 131.3(C19), 131.0(C11), 129.2(C16), 128.4(C13), 128.9(C14), 126.2(C12), 124.9(C10), 122.2(C7), 121.2(C8), 119.0(C18), 112.9(C20), 106.7(C5), 104.7(C3), 63.9(OCH₂), 43.3(C15), 14.8(CH₃); LCMS (ES-API) *m/z*: 450.1 (M + H)⁺; HRMS (ESI) *m/z* [M + H]⁺: calcd for C₂₄H₂₁BrNO₃: 450.0705, found: 450.0707.

6-((Quinolin-2-yl)methylamino)-2-phenyl-4H-chromen-4-one (1n)

Brown Solid, mp 146–149 °C; IR ((KBr)/cm⁻¹: 3347, 3037, 1696, 1198, 773 cm⁻¹; ¹H NMR (DMSO-d₆, 400 MHz, ppm) δ: 8.42 (d, *J* = 8.6 Hz, 1H), 8.10–7.89 (m, 4H), 7.82–7.69 (m, 1H), 7.70–7.50 (m, 7H), 7.26–7.21 (m, 1H), 7.03–7.01 (m, 1H), 6.84 (s, 1H), 4.68–4.70 (m, 2H); ¹³C NMR (DMSO-d₆, 100 MHz, ppm) δ: 178.4(C4), 162.0(C2), 159.6 (C16), 153.3(C24), 149.8(C9), 145.3(C6), 138.3(C22), 132.2(C11), 132.08(C19), 130.6(C13), 129.1(C18), 126.3(C25), 126.2(C14), 124.9(C21), 122.2(C25), 119.3(C12), 124.9(C20), 122.2(C10), 119.3(C7), 118.7(C8), 106.7(C3), 103.7(C5), 48.8(C15); LCMS (ES-API) *m/z*: 379.0 (M + H)⁺; HRMS (ESI) *m/z* [M + H]⁺: calcd for C₂₅H₁₉N₂O₂: 379.1450, found: 379.1446.

Minimum Inhibitory Concentration Determination Antibiotic susceptibility testing was measured by calculating the Minimum Inhibitory Concentration (MIC) according to standard CLSI guidelines. MIC is defined as the minimum concentration of compound at which bacterial growth is inhibited and it can be detected visibly. Bacterial cultures were grown in Mueller Hinton II Broth (MHB). Optical density (OD600) of the cultures was measured, followed by dilution for ~10⁵–6 CFU/mL. These inoculums is added into a series of test wells in a microtitre plate that contains various concentrations of compound under test. Plates were incubated at 37 °C for 16–18 h. Minimum inhibitory concentration (MIC) was determined as the concentration at which no visible growth was seen. For each compound, MIC determinations were carried out independently 3 times.^{22–32}

Docking methodology

The docking calculations were carried out against *Staphylococcus aureus* DNA gyrase (Type II topoisomerases) (PDB Id: 5CDQ) and tyrosyl-tRNA synthetases (TyrRS) (PDB Id: 1JIL), using Smina molecular docking software.³³ Smina is an extension of AutoDock Vina that has been modified to facilitate scoring function development and high-performance energy minimization. The 2D structure of all ligands was built in Marvin Sketch software and converted to 3D structure and their energy was minimized using steepest descent algorithm by the Open Babel chemical toolbox. The X-ray crystal structure of enzymes was obtained from the Protein Data Bank and prepared for docking using Dock Prep, a built-in tool in UCSF Chimera Software. The

preparation involved the addition of hydrogens, removal of the water molecule, removal of non-complexed ions, and filling of the missing side chain. It also involves energy minimization and geometry optimization of crystal structure using AMBER ff99SB force field. The binding site was defined by the coordinates of the co-crystal ligand from PDB extended by 4 Å in each dimension. The generated lower energy conformers of all ligands were docked into the defined active site of enzyme by using the default scoring function of Smina.^{34,35} By default, Smina returns up to nine predicted poses with their associated predicted binding affinity. The images of docking results were saved using the academic version of Maestro software (Schrodinger).

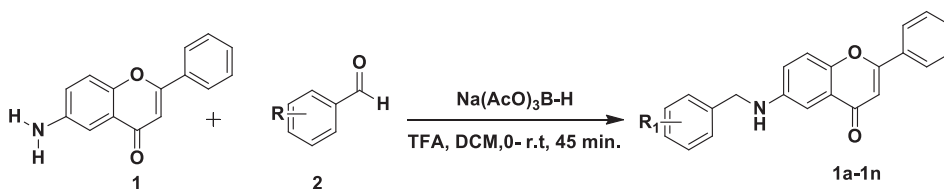
Result and discussion

Recently we have reported the synthesis of a series of 6-(1-arylmethanamino)-2-phenyl-4*H*-chromen-4-ones derivatives of 6-aminoflavones (**1**).²⁰ These compounds were accessed by reductive amination reaction of commercially available aldehydes with synthesized 6-aminoflavones (Table 1; Scheme 1). Thus, to widen the scope further and to investigate the biological potential of these compounds we have tested these compounds for their antibacterial activity against the *Staphylococcus aureus*. The minimum inhibitory concentrations (MICs) of the synthesized compounds and that of antibiotic 'vancomycin' as the reference against the studied strains are as summarized in Table 1. 6-aminoflavone (**1**), was found to be potent, with a MIC of 2 µg/L. Almost all *N*-benzyl derivatives of 6-aminoflavone showed good inhibitory activity against *S. aureus* with a MIC value ranging from 2 to >32 µg/mL.

Structure-activity relationship (SAR)

Compounds having halogens at the para position in the *N*-benzyl group exhibited strong antibacterial activities with MIC values ranging from 2 to >32 µg/mL. Compounds **1a** and **1b** having 4-fluorobenzyl and 4-chlorobenzyl side-chain, respectively, showed good inhibitory activity with a MIC of 2 µg/mL. Comparatively, compound **1c** having quite a big halogen atom in size, i.e. 4-bromobenzyl side chain, leads to also in activity by 16 folds with a MIC value of >32 µg/mL.

A compound having pseudo-halogen *viz.* **1f** with 4-cyanobenzyl (MIC of >32 µg/mL) side chain leads to a loss in activity, however, on the contrary, compound **1e** with 4-nitrobenzyl (MIC of 2 µg/mL) has retained the inhibitory activity. Compound 4-methoxybenzyl (**1g**) was found to be superior in inhibitory activity with a MIC of 2 µg/mL when compared to its disubstituted analogues *viz.* 2,4-dimethoxybenzyl (**1i**) and 3,4-dimethoxybenzyl (**1j**). Besides, any di-substitution in *N*-benzyl side always leads to loss in activity compared to mono-substitution (Table 2). Compound **1n** with heterocyclic side chain (quinolin-2-yl)methyl- was also found to be very potent with a MIC value of 2 µg/mL. This study also reveals that electron donating or electron withdrawing groups at the para position in *N*-benzyl side chain did not have much impact on inhibitory activity (**1g** and **1e**, Table 2).



Scheme 1. Synthesis of 6-amino-2-phenyl-4*H*-chromen-4-ones

Table 2. Antimicrobial activity of compounds.

Entry	R	Compounds	Yield ^a	MIC in $\mu\text{g/mL}^b$
1	6-Aminoflavone	1	81	2
2	4-Fluorobenzyl	1a	86	2
3	4-Chlorobenzyl	1b	85	2
4	4-Bromobenzyl	1c	88	>32
5	2,3-Dichlorobenzyl	1d	83	>32
6	3-Nitrobenzyl	1e	82	4
7	4-Cyanoabenzyl	1f	85	>32
8	4-Methoxybenzyl	1g	86	2
9	4-Ethoxybenzyl	1h	84	>32
10	2,4-Dimethoxybenzyl	1i	82	>32
11	3,4-Dimethoxybenzyl	1j	86	>32
12	2-Hydroxy-5-bromobenzyl	1k	82	>32
13	2-Methoxy-5-bromobenzyl	1l	82	>32
14	2-Ethoxy-5-bromobenzyl	1m	81	>32
15	(Quinolin-2-yl)methyl	1n	80	2
16	Vancomycin			1

^aIsolated yields in %; ^bMIC in $\mu\text{g/mL}$.

Table 3. Docking score of synthesized compounds (**1–1n**) against DNA gyrase and TyrRS enzymes.

Compound code	Docking score	
	DNA gyrase (PDB Id: 5CDQ)	TyrRS (PDB Id: 1JIL)
1.sdf	−8.85	−8.72
1a.sdf	−10.13	−9.40
1b.sdf	−9.57	−9.52
1c.sdf	−9.60	−9.52
1d.sdf	−9.79	−9.52
1e.sdf	−9.83	−9.79
1f.sdf	−10.19	−9.19
1g.sdf	−10.13	−9.39
1h.sdf	−9.87	−9.62
1i.sdf	−10.02	−9.32
1j.sdf	−10.31	−9.54
1k.sdf	−9.97	−9.63
1l.sdf	−9.63	−9.27
1m.sdf	−9.55	−9.16
1n.sdf	−10.60	−10.98
Moxifloxacin	−11.81	−
SB-219383	−	−11.07

Docking studies

In order to study the binding affinity of synthesized compounds against *Staphylococcus aureus* DNA gyrase (Type II topoisomerases) and tyrosyl-tRNA synthetases (TyrRS), the molecular docking studies were performed. In the present investigation the proposed docking algorithm was initially validated by the self-docking of the co-crystallized ligands to each of the aforementioned targets. Whereby, the ligands were removed from the complex and then docked back into the binding site. RMSD values between the top-ranked pose and the experimental crystal structure for DNA gyrase and TyrRS enzymes were found to be 0.265Å and 0.122Å respectively. Subsequently, the docking procedures have been accomplished for the tested compounds (**1–1n**). Based on their docking scores (Table 3), it can be suggested that all compounds showed the comparable binding affinity against both enzymes. However, the compound **1n** showed higher binding affinity against both enzymes.

Analysis of the co-crystallized *S. aureus* DNA-gyrase cleavage complex with moxifloxacin revealed binding between Ser 84 and Arg 122 of DNA gyrase and COO[−] groups of quinolone nucleus and Mg²⁺ metal bond with C=O and COO[−]. In addition there are hydrophobic

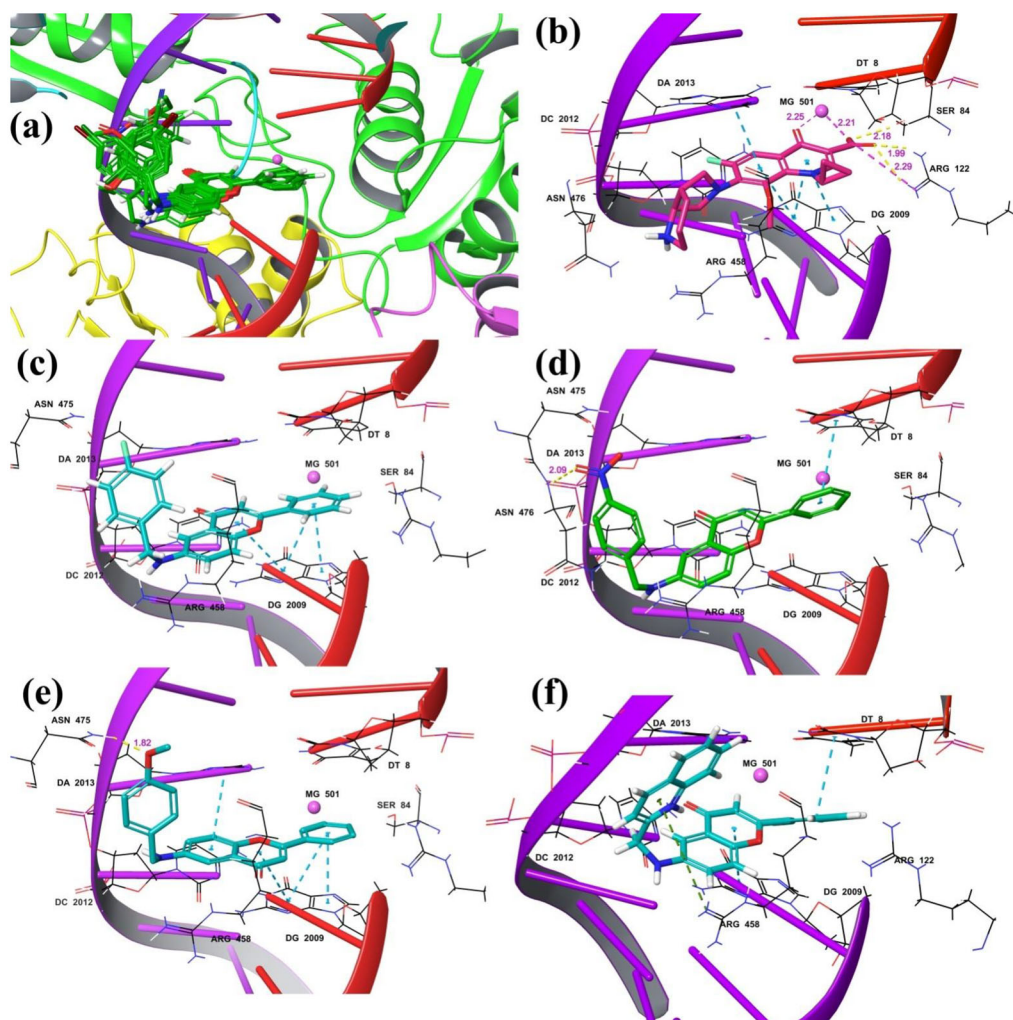


Figure 4. Docking Pose of compounds in the active site of DNA-gyrase enzyme (a) Overlapping of all synthesized compounds, (b) Co-crystallized ligand **moxifloxacin**, (c) Compound **1a**, (d) Compound **1e**, (e) Compound **1g** and (f) Compound **1n**. Yellow colored dotted line indicates H-bonds, cyan colored dotted line indicates pi-pi stacking, magenta colored dotted line indicates salt bridge and metal interaction, and green colored dotted line indicates pi-cation interactions.

interactions with adenine and guanine DNA bases with quinolone nucleus. It was found that all compounds acquire similar binding poses in the active site of DNA gyrase enzyme (Figure 4). Similarly, all compounds showed the hydrophobic interaction with the DT8, DG2009, and/or DA2013. In addition, some of the compounds also interacted with ASN475, and ASN476 by H-bond. Furthermore, we found pi-cation interactions involving residue Arg-1122 only for compound **1n** and some more compounds.

The docking results also revealed that all synthesized compounds were fitted into the active pocket TyrRS enzymes. Analysis of the co-crystallized *S. aureus* TyrRS enzyme with SB-219383 revealed the interaction of the small molecule with number of amino acid residues, Tyr36, Asp40, His50, Asp80, Tyr170, Gln174, Gly193, and Asp195 via H-bonds (Figure 5). Likewise, all docked compounds find the similar docking poses in the active site of TyrRS enzyme. It was seen that the compound **1n** formed H-bond and pi-cation interaction with amino acid residue Asp40 and weak aromatic H-bond interaction with amino acid residues His50, Gly49, Gly72, Asp195, and Pro222. Whereas the some other compounds like **1e** and **1g** showed the H-bond interaction

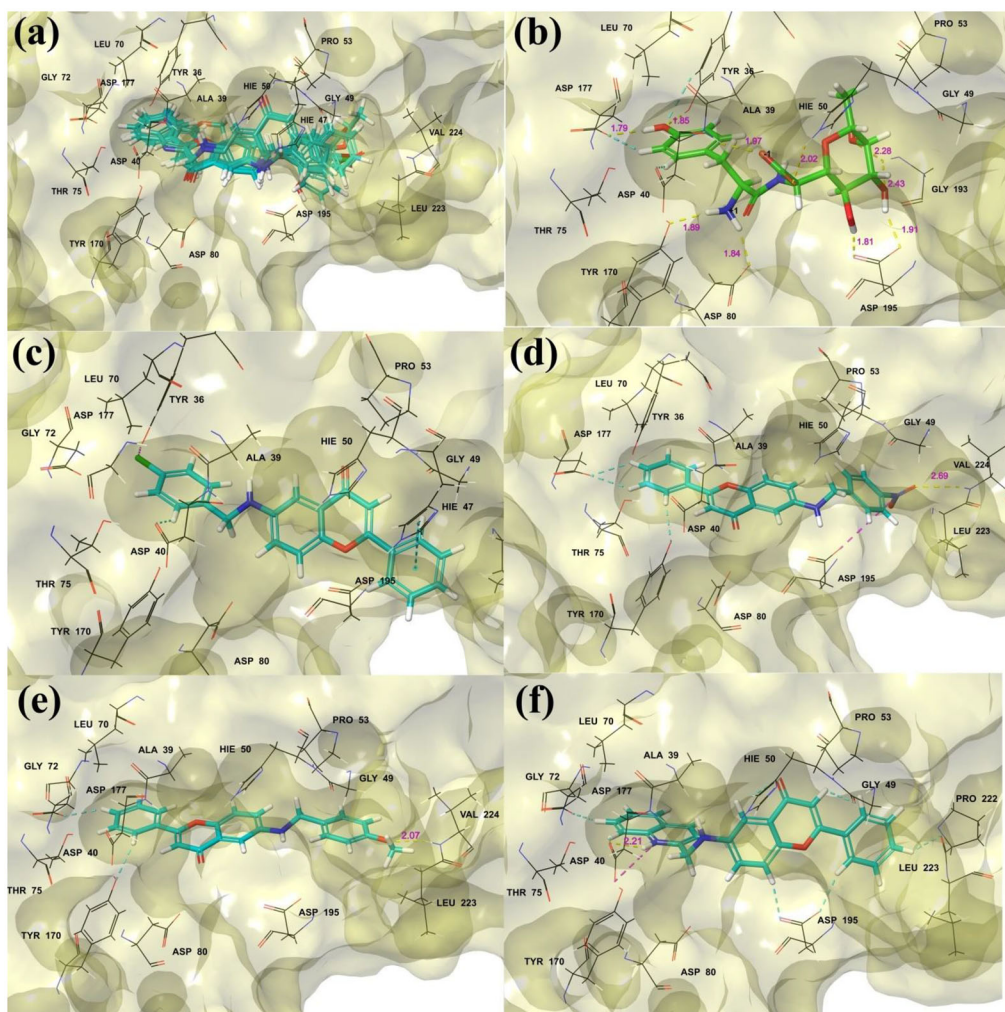


Figure 5. Docking Pose of compounds in the active site of TyrRS enzyme (a) Overlapping of all synthesized compounds, (b) Co-crystallized ligand **SB-219383**, (c) Compound **1b**, (d) Compound **1e**, (e) Compound **1g** and (f) Compound **1n**. Yellow colored dotted line indicates H-bonds, cyan colored dotted line indicates pi-pi stacking and weak aromatic H-bond interaction and Magenta colored dotted line indicates salt bridge.

with amino acid residue Val224 and weak aromatic interaction with amino acid residues Asp40 and Tyr170, Asp177. Overall it was found that all compounds have equal binding affinity for both DNA gyrase and TyrRS enzymes. According to obtained docking results, it is conceded that the docked ligands form a stable complex with the receptors.

Conclusion

We have demonstrated that 6-(1-arylmethanamino)-2-phenyl-4H-chromen-4-ones as antimicrobial agents against the *Staphylococcus aureus*. Compounds *viz.* 4-fluorobenzyl (**9a**), 4-chlorobenzyl (**9b**), 4-nitrobenzyl (**9e**) and 4-methoxybenzyl (**9g**) were found to be the most potent with MIC of 2 µg/mL which is comparable with vancomycin having MIC of 1 µg/mL. Compound **9n** with heterocyclic side chain (quinolin-2-yl)methyl was also found to have MIC of 2 µg/mL

Acknowledgements

We thank Dr. S.R. Thopate (S. S. G. M. College Kopargaon) and Dr. D. K. Mhaske (M. J. S. College Shrigonda) for helpful discussion and suggestions. I acknowledge to Department of Science and Technology (DST-FIST) for their support.

Disclosure statement

No potential conflict of interest was reported by the author(s).

ORCID

Nitin M. Thorat  <http://orcid.org/0000-0003-2880-1523>

Ajit P. Ingale  <http://orcid.org/0000-0001-9940-052X>

Deepak K. Lokwani  <http://orcid.org/0000-0003-2858-678X>

Shankar R. Thopate  <http://orcid.org/0000-0001-5092-0196>

References

1. (a) R. Laxminarayan, and D. Heymann, "Challenges of Drug Resistance in the Developing World," *BMJ (Clinical Research ed.)* 344 (2012): e1567. doi:10.1136/bmj.e1567 (b) K. Gowoon, G. Ren-You, Z. Dan, K. F. Arakkaveetil, H. Olivier, M. Vuyo, L. Hua-Bin, W. Xiao-Hong, and C. Harold, "Large-Scale Screening of 239 Traditional Chinese Medicinal Plant Extracts for Their Antibacterial Activities against Multidrug-Resistant *Staphylococcus aureus* and Cytotoxic Activities," *Pathogens* 9 (2020): 185. doi:10.3390/pathogens9030185 (c) C. Stella, P. Barbara, C. Daniela, S. Domenico, G. Elisa, C. Girolamo, and D. Patrizia, "Thiazoles, Their Benzofused Systems, and Thiazolidinone Derivatives: Versatile and Promising Tools to Combat Antibiotic Resistance," *Journal of Medicinal Chemistry*. 63 (2020): 7923–56. doi:10.1021/acs.jmedchem.9b01245
2. M. S. Jonathan, Y. Kevin, S. Kyle, J. Wengong, C. R. Andres, M. D. Nina, R. M. Craig, F. Shawn, A. C. Lindsey, B. A. Zohar, et al., "A Deep Learning Approach to Antibiotic Discovery," *Cell* 180 (2020): 688–702. doi:10.1016/j.cell.2020.01.021
3. World Health Organization. "WHO/EMP/IAU/2017.12, Prioritization of Pathogens to Guide Discovery Research and Development of New Antibiotics for Drug-Resistant Bacterial Infections, Including Tuberculosis," <https://apps.who.int/iris/handle/10665/311820>.
4. M. S. Lisa, M. P. Brian, P. K. Bastiaan, A. F. Jeffrey, M. H. Gertrud, G. F. Scott, Jabra-Rizk Mary, and Ann E. S. Mark, "Systemic *Staphylococcus aureus* Infection Mediated by *Candida albicans* Hyphal Invasion of Mucosal Tissue," *Microbiology* 161, no. Pt 1 (2015): 168–81. doi:10.1099/mic.0.083485-0
5. K. V. Alok, and P. Ram, "The Biological Potential of Flavones," *Natural Product Reports*. 27 (2010): 1571–93. doi:10.1039/C004698C
6. F. Faegheh, K. Bahman, I. Mehrdad, and I. Milad, "Antibacterial Activity of Flavonoids and Their Structure–Activity Relationship: An Update Review," *Phytotherapy Research* 33 (2019): 13–40. doi:10.1002/ptr.6208
7. A. Mariam, M. S. Samson, V. Elizabeth, V. Sharon, K. Peter, L. Alena, and B. Dietrich, "Flavonoids in Cancer and Apoptosis," *Cancers* 11 (2019): 28. doi:10.3390/cancers11010028
8. J. M. Soheila, F. C. Jesus, and C. Beatriz, "Anti-Inflammatory Effects of Flavonoids," *Food Chemistry* 299 (2019): 125124. doi:10.1016/j.foodchem.2019.125124
9. Yong-Sheng Jin, "Recent Advances in Natural Antifungal Flavonoids and Their Derivatives," *Bioorganic & Medicinal Chemistry Letters* 29, no. 19 (2019): 126589. doi:10.1016/j.bmcl.2019.07.048
10. T. Toshio, "Flavonoids for Allergic Diseases: present Evidence and Future Perspective," *Current Pharmaceutical Design* 20 (2014): 879–85. doi:10.2174/13816128113199990060
11. L. A. Lopes, J. B. dos Santos Rodrigues, M. Magnani, E. L. de Souza, and J. P. de Siqueira-Júnior, "Inhibitory Effects of Flavonoids on Biofilm Formation by *Staphylococcus aureus* That over Expresses Efflux Protein Genes," *Microbial Pathogenesis* 107 (2017): 193–7. doi:10.1016/j.micpath.2017.03.033
12. Shuai Wang, Chang Wang, Lingfei Gao, Hua Cai, Yonghui Zhou, Yanbei Yang, Changgeng Xu, Wenya Ding, Jianqing Chen, Ishfaq Muhammad, et al., "Rutin Inhibits *Streptococcus suis* Biofilm Formation by Affecting CPS Biosynthesis," *Frontiers in Pharmacology* 8 (2017): 379. doi:10.3389/fphar.2017.00379

13. Y. Xie, W. Yang, F. Tang, X. Chen, and L. Ren, "Antibacterial Activities of Flavonoids: Structure-Activity Relationship and Mechanism," *Current Medicinal Chemistry* 22, no. 1 (2015): 132–49. doi:10.2174/0929867321666140916113443
14. T. T. Cushnie, and A. Lamb, "Antimicrobial Activity of Flavonoids," *International Journal of Antimicrobial Agents* 26, no. 5 (2005a): 343–56. doi:10.1016/j.ijantimicag.2005.09.002
15. T. T. Cushnie, and A. J. Lamb, "Detection of Galangin-Induced Cytoplasmic Membrane Damage in *Staphylococcus aureus* by Measuring Potassium Loss," *Journal of Ethnopharmacology* 101, no. 1-3 (2005b): 243–8. doi:10.1016/j.jep.2005.04.014
16. L. E. Alcaraz, S. E. Blanco, O. N. Puig, F. Tomas, and F. H. Ferretti, "Antibacterial Activity of Flavonoids against Methicillin-Resistant *Staphylococcus aureus* Strain," *Journal of Theoretical Biology* 205, no. 2 (2000): 231–40. doi:10.1006/jtbi.2000.2062
17. J. Solnier, L. Martin, S. Bhakta, and B. Franz, "Flavonoids as Novel Efflux Pump Inhibitors and Antimicrobials against Both Environmental and Pathogenic Intracellular Mycobacterial Species," *Molecules* 25, no. 3 (2020): 734. doi:10.3390/molecules25030734
18. Dávid Pajtás, Krisztina Kónya, Attila Kiss-Szikszai, Petr Džubák, Zoltán Pethő, Zoltán Varga, György Panyi, and Tamás Patonay, "Optimization of the Synthesis of Flavone–Amino Acid and Flavone–Dipeptide Hybrids via Buchwald–Hartwig Reaction," *The Journal of Organic Chemistry* 82, no. 9 (2017): 4578–87. doi:10.1021/acs.joc.7b00124
19. K. Konya, D. Pajtás, A. Kiss-Szikszai, and T. Patonay, "Buchwald–Hartwig Reactions of Monohalo-flavones," *European Journal of Organic Chemistry* 2015, no. 4 (2015): 828–39. doi:10.1002/ejoc.201403108
20. Nitin M. Thorat, Aniket P. Sarkate, Deepak K. Lokwani, Shailee V. Tiwari, Rajaram Azad, and Shankar R. Thopate, "N-Benylation of 6-Amino-flavone by Reductive Amination and Efficient Access to Some Novel Anticancer Agents via Topoisomerase II Inhibition," *Molecular Diversity* 25, no. 2 (2021): 937–48. doi:10.1007/s11030-020-10079-1
21. N. M. Thorat, S. R. Kote, and S. R. Thopate, "An Efficient and Green Synthesis of Flavones Using Natural Organic Acids as Promoter under Solvent-Free Condition," *Letters in Organic Chemistry* 11, no. 8 (2014): 601–5. doi:10.2174/157017861108140613163214
22. S. A. Melha, Z. A. Muhammad, A. S. Abouzid, M. M. Edrees, A. S. Abo Dena, S. Nabil, and S. M. Gomha, "Multicomponent Synthesis, DFT Calculations and Molecular Docking Studies of Novel Thiazolyl-Pyridazinones as Potential Antimicrobial Agents against Antibiotic-Resistant Bacteria," *Journal of Molecular Structure* 1234 (2021): 130180. doi:10.1016/j.molstruc.2021.130180
23. W. A. M. A. El-Enany, S. M. Gomha, W. Hussein, H. A. Sallam, R. S. Ali, and A. K. El-Ziati, "Synthesis and Biological Evaluation of Some Novel Bis-Thiadiazoles as Antimicrobial and Antitumor Agents," *Polycyclic Aromatic Compounds* 41, no. 10 (2021): 2071–82. doi:10.1080/10406638.2019.1709874
24. Refaie M. Kassab, Sobhi M. Gomha, Sami A. Al-Hussain, Ahmed S. Abo Dena, Marwa M. Abdel-Aziz, Magdi E. A. Zaki, and Zeinab A. Muhammad, "Synthesis and in-Silico Simulation of Some New Bis-Thiazole Derivatives and Their Preliminary Antimicrobial Profile: Investigation of Hydrazonoyl Chloride Addition to Hydroxy-Functionalized Bis-Carbazones," *Arabian Journal of Chemistry* 14, no. 11 (2021): 103396. doi:10.1016/j.arabjc.2021.103396
25. M. Gomha, Z. A. Muhammad, S. A. Al-Hussain, M. E. A. Zaki, and H. M. Abdel-Aziz, "Characterization, and Antimicrobial Evaluation of Some New 1,4-Dihydropyridine Hybrid with 1,3,4-Thiadiazole," *Polycyclic Aromatic Compounds* 42, no. 4 (2022): 1697–709. doi:10.1080/10406638.2020.1804410
26. S. M. Gomha, M. M. Edrees, Z. A. Muhammad, N. A. Kheder, S. Abu-Melha, and A. M. Saad, "Synthesis, Characterization, and Antimicrobial Evaluation of Some New 1, 4-Dihydropyridines-1, 2, 4-Triazole Hybrid Compounds," *Polycyclic Aromatic Compounds* 42, no. 1 (2022): 173–85. doi:10.1080/10406638.2020.1720751
27. F. B. Essa, A. Bazbouz, S. Alhilal, S. A. Ouf, and S. M. Gomha, "Synthesis and Biological Evaluation of an Indole Core-Based Derivative with Potent Antimicrobial Activity," *Research on Chemical Intermediates* 44, no. 9 (2018): 5345–56. doi:10.1007/s11164-018-3426-9
28. M. A. Abdallah, S. M. Riyadh, I. M. Abbas, and S. M. Gomha, "Synthesis and Biological Activities of 7-Arylazo-7H-Pyrazolo [5, 1-c][1, 2, 4] Triazol-6 (5H)-Ones and 7-Arylhydrazono-7H-[1, 2, 4] Triazolo [3, 4-b][1, 3, 4] Thiadiazines," *Journal of the Chinese Chemical Society* 52, no. 5 (2005): 987–94. doi:10.1002/jccs.200500137
29. I. Abbas, S. Gomha, M. Elaasser, and M. Bauomi, "Synthesis and Biological Evaluation of New Pyridines Containing Imidazole Moiety as Antimicrobial and Anticancer Agents," *Turkish Journal of CHEMISTRY* 39 (2015): 334–46. doi:10.3906/kim-1410-25
30. S. M. Gomha, and K. M. Dawood, "Synthesis of Novel Indolizine, Pyrrolo[1,2-a] Quinoline, and 4,5-Dihydrothiophene Derivatives via Nitrogen Ylides and Their Antimicrobial Evaluation," *Journal of Chemical Research* 38, no. 9 (2014): 515–9. doi:10.3184/174751914X1406733830712

31. Y. H. Zaki, S. M. Gomha, and A. M. G. Mohamed, "Utility of 2-Thioxo-Pyrido[2,3-d]Pyrimidinone in Synthesis of Pyridopyrimido[2,1-b][1,3,5]-Thiadiazinones and Pyridopyrimido[2,1-b][1,3]Thiazinones as Antimicrobial Agents," *Chemistry Central Journal*. 11 (2017): 57. doi:[10.1186/s13065-017-0286-0](https://doi.org/10.1186/s13065-017-0286-0)
32. F. M. Abdelrazek, S. M. Gomha, M. E. B. Shaaban, K. A. Rabee, H. N. El-Shemy, M. Abdallah, and P. Metz, "One-Pot Three-Component Synthesis and Molecular Docking of Some Novel 2-Thiazolyl Pyridines as Potent Antimicrobial Agents," *Mini Reviews in Medicinal Chemistry* 19, no. 6 (2019): 527–38. doi:[10.2174/1389557518666181019124104](https://doi.org/10.2174/1389557518666181019124104)
33. D. R. Koes, M. P. Baumgartner, and C. J. Camacho, "Lessons Learned in Empirical Scoring with Smina from the Csar 2011 Benchmarking Exercise," *Journal of Chemical Information and Modeling* 53, no. 8 (2013): 1893–904. doi:[10.1021/ci300604z](https://doi.org/10.1021/ci300604z)
34. S. V. Tiwari, A. P. Sarkate, D. K. Lokwani, D. N. Pansare, S. G. Gattani, S. S. Sheaikh, S. P. Jain, and S. V. Bhandari, "Explorations of Novel Pyridine-Pyrimidine Hybrid Phosphonate Derivatives as Aurora Kinase Inhibitors," *Bioorganic & Medicinal Chemistry Letters* 67, no. 2022 (2022): 128747. doi:[10.1016/j.bmcl.2022.128747](https://doi.org/10.1016/j.bmcl.2022.128747)
35. I. M. Abbas, S. M. Riyadh, M. A. Abdallah, and S. M. Gomha, "A Novel Route to Tetracyclic Fused Tetrazines and Thiadiazines," *Journal of Heterocyclic Chemistry* 43, no. 4 (2006): 935–42. doi:[10.1002/jhet.5570430419](https://doi.org/10.1002/jhet.5570430419)

Drug-Repurposing Of Some COX-2 Inhibitors As Potential Glucokinase Activators For The Treatment Of T2DM

Badrud Duza Mohammad¹, Ramsha Aslam², Shyamlila B. Bavage³, Vijay Kumar Putta⁴, Nandkishor Dinkarrao Gawhale⁵, Shailejkumar D Bonde⁶, Rihana Begum Patnool⁷, Vikram Nirmal Sancheti^{8*}

¹Department of Pharmaceutical Chemistry, G R T Institute of Pharmaceutical Education and Research, GRT Mahalakshmi Nagar, Tiruttani-631209, Tamil Nadu, India;

²Devsthali Vidyapeeth College of Pharmacy, Lalpur, Rudrapur-263148, Uttarakhand, India;

³Latur College of pharmacy, Hasegaon, Maharashtra-413512, India;

⁴Department of Pharmacology, J S S College of Pharmacy, Ooty-643001, India;

⁵Department of Chemistry, G. S. Tompe Arts, Commerce and Science College, Chandur Bazar, Amravati-444704, Maharashtra, India;

⁶Department of Pharmacognosy, Govindrao Nikam College of Pharmacy, Sawarde, Maharashtra- 415606, India;

⁷Research Scholar, Department of Pharmacy Practice, J.S.S. College of Pharmacy, Ooty-643001, India;

⁸Department of Pharmaceutics, Rajarshi Shahu College of Pharmacy, Buldana, Maharashtra-443001, India.

*Corresponding Author Email: vikram.sancheti@gmail.com

DOI: 10.47750/pnr.2022.13.S09.563

Abstract

NSAIDs are still used frequently to treat and prevent a variety of inflammatory disorders nowadays. Obesity and type 2 diabetes mellitus (T2DM) are metabolic chronic diseases that are connected to mild to moderate proinflammatory states, which may play a role in the aetiology of certain of these diseases' outcomes. So far, preclinical and clinical models have examined how NSAIDs affect a variety of illnesses. In the current work, we used computational analysis to examine the GK activation potential of a few COX-2 inhibitors. The native ligand, Celecoxib, Rofecoxib, and Valdecoxib showed corresponding binding free energies of -10.3, -7.8, -8.6, and -8.6 kcal/mol. Celecoxib and Valdecoxib formed four typical hydrogen bonds with the glucokinase enzyme, although none of the COX-2 inhibitors revealed less binding free energy than the native ligand. It suggests that they may be able to control the glucokinase enzyme's activity. As a result of the current work, we came to the conclusion that celecoxib and valdecoxib might be used as lead compounds for the future development of new glucokinase activators.

Keywords: NSAIDs; glucokinase; molecular docking; COX-2 inhibitors

Introduction

COX-1 and COX-2 are the two primary isoforms that may be found in the cyclooxygenase (COX) enzyme. While COX-1 is produced constitutively in the majority of cells, COX-2 may be detected in endothelial cells, macrophages, and smooth muscle and is responsible for mediating the majority of the consequences of inflammation and cancer. The term "nonsteroidal anti-inflammatory medications," or NSAIDs for short, refers to a category of heterogeneous substances that are most often recommended for the anti-inflammatory, antipyretic, and pain-relieving effects they provide. These objectives may be accomplished by the suppression of COX. Aspirin is the only substance known to acetylate COX-1 and COX-2, which results in an irreversible reduction of the production of prostaglandins when

taken. The other members of this group's agents interact with these enzymes via a process known as competitive antagonism. Additionally, a number of COX-2 specific antagonists such as celecoxib and valdecoxib have been developed[1–5]. As of now, NSAIDs are still the go-to for treating and preventing numerous inflammatory diseases. Mild to moderate proinflammatory state is linked to metabolic chronic illnesses including obesity and type 2 diabetes mellitus (T2DM), and may have a role in the pathogenesis of some of the consequences of these diseases. Preclinical and clinical models have so investigated the impact of NSAIDs on various conditions[1]. Hypoglycemia, which is often observed in diabetic patients using sulphonylureas, may be induced by certain NSAIDs inadvertently. The ion channel properties of insulin secreting beta cells may be altered by NSAIDs, leading to hypoglycemia[6].

Glucokinase activators, often known as GKAs, are an innovative family of drugs that work to reduce glucose levels. The findings collected in preclinical studies provide credence to the hypothesis that these medicines reduce blood glucose levels by exerting their effects not only in the liver but also in the pancreas. It is anticipated that diabetic patients would have significant improvements in their glucose control as a result of the dual compartment mode of action shown by GKAs[7–10]. In present study, we have investigated the GK activation potential of some COX-2 inhibitors through computational analysis. The structures of COX-2 inhibitors selected for the study are illustrated in Figure 1 along with structure of native ligand present in the pdb structure.

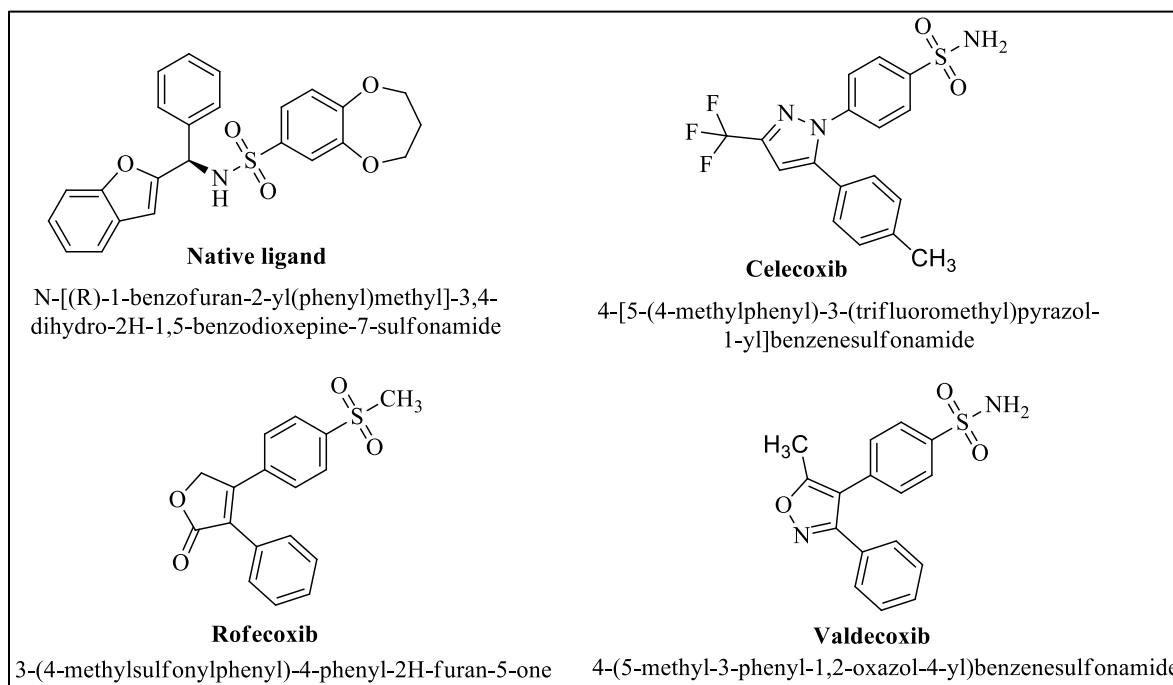


Figure 1. The structures of selected COX-2 inhibitors and native ligand present in crystal structure of enzyme

Method

Molecular docking studies

The molecular docking was conducted on Lenovo ThinkPad T440p using PyRx-Virtual Screening Tool[11]. The structures of all the COX-2 inhibitors and native ligand (.sdf File format) were downloaded from official website of National Center for Biotechnology Information PubChem (<https://pubchem.ncbi.nlm.nih.gov/>). The energy minimization (optimization) was performed by Universal Force Field (UFF)[12].

A crystalline structures of glucokinase enzyme with native ligand (PDB ID: 4PX2, <https://www.rcsb.org/structure/4PX2>) were obtained from RCSB's Protein Data Bank (PDB). The inhibitor present in 4PX2 is already depicted in Figure 1. The native ligand of PDB structure was used as reference molecule for the validation of results obtained from molecular docking. Autodock vina 1.1.2 in PyRx 0.8 was used to perform the

molecular docking studies of all the COX-2 inhibitors and native ligand against the crystal structure of glucokinase enzyme[11]. The enzyme structure, with the aid of Discovery Studio Visualizer 2019, were optimized, purified and prepared for MD[13]. Molecules (PDBQT Files), both ligands as well as target (glucokinase enzyme) were selected for molecular docking[14]. For the purpose of molecular docking simulation, the three-dimensional grid box (size_x = 49.23A⁰; size_y = 64.87A⁰; size_z = 44.93A⁰) was built using Autodock tool 1.5.6 with exhaustiveness value of 8[11]. The active amino acids in the protein were analyzed and illuminated using Visualizer in BIOVIA Discovery Studio (version-19.1.0.18287)[13]. The full molecular docking process, the identification of cavity and active amino acid residues were performed as per the procedure described by S. L. Khan et al.[15–23]. The allosteric site of the enzyme is portrayed in the Figure 2 with the native ligand.

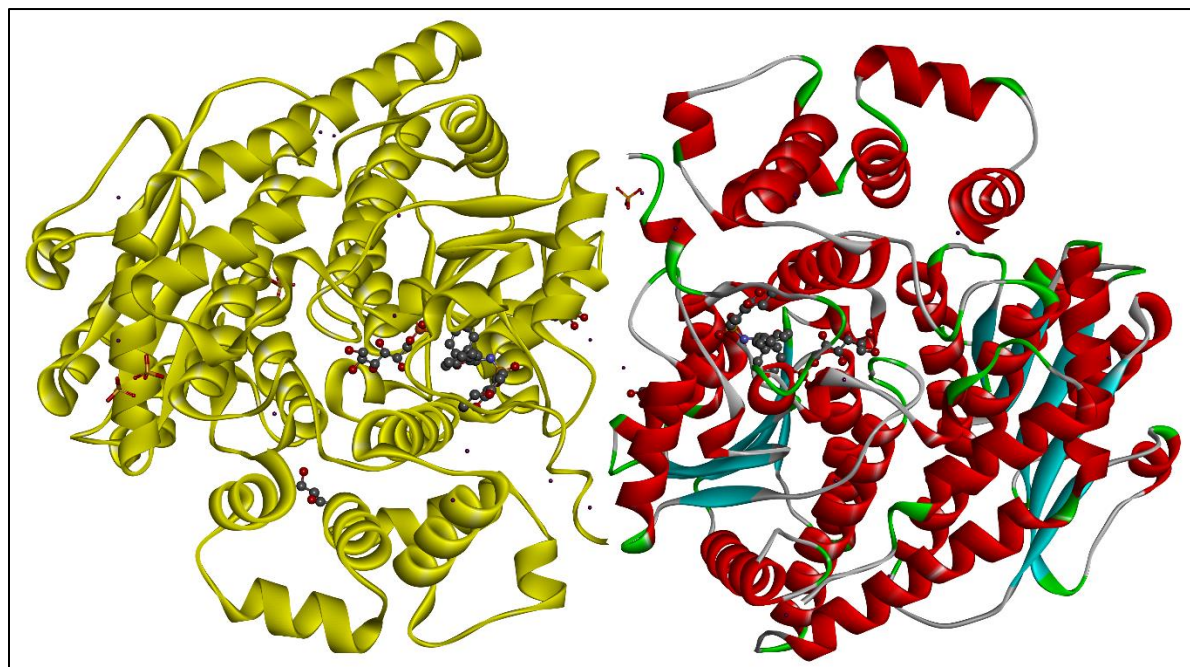


Figure 2. The 3D-ribbon view of glucokinase enzyme (PDB ID: 4PX2); Chain A is displayed in red and blue color combination and Chain B is displayed in yellow color with native ligand in allosteric cavity

Results and Discussion

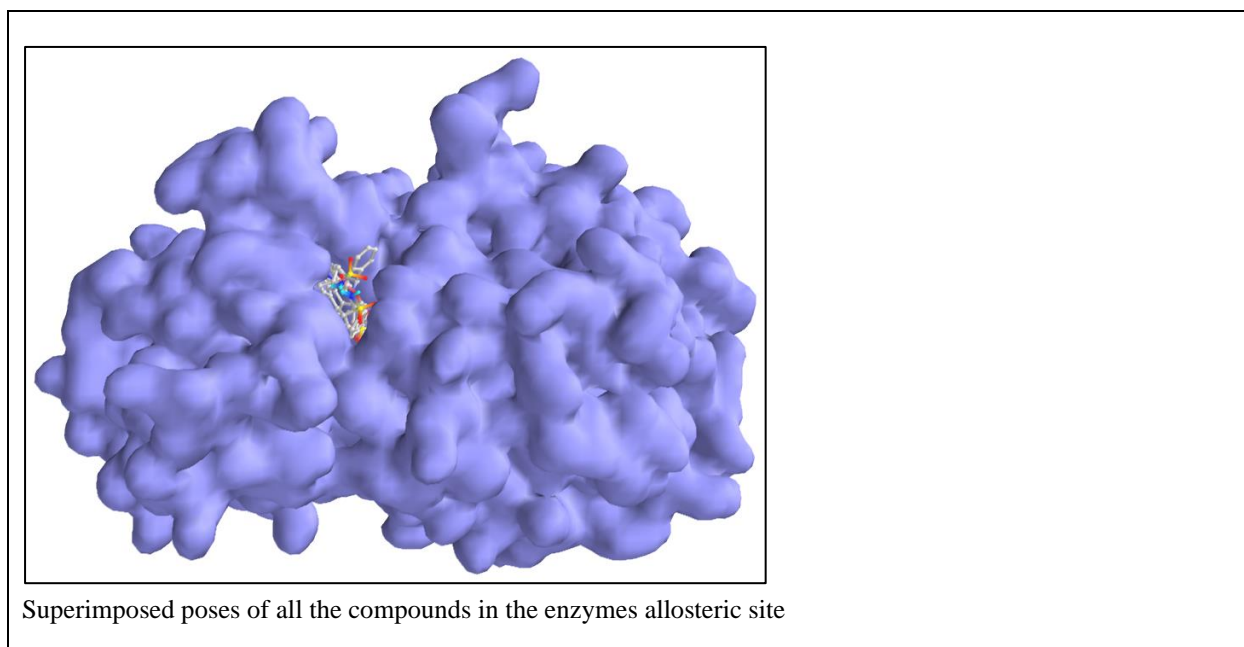
The ligand-enzyme interactions are tabulated in Table 1 along with docking scores and ligand energies. The 2D-docking poses along with superimposed poses of all the compounds in the enzymes allosteric site are depicted in Figure 3.

Table 1. The ligand-enzyme interactions along with docking scores and ligand energies

Reacting amino acids	Bond length (A ⁰)	Bond type	Bond category	Docking score (Kcal/mol)	Ligand energy (Kcal/mol)
Native ligand					
ASN216	2.30549	Hydrogen Bond	Conventional Hydrogen Bond	-10.3	790.76
ARG227	2.63318		Carbon Hydrogen Bond		
TRP517	3.27767				
ARG227	3.83291	Hydrophobic	Pi-Cation;Pi-Donor Hydrogen Bond		

ARG215	3.82511		Pi-Sigma		
TYR24	5.06078		Pi-Pi T-shaped		
PRO29	5.43931		Alkyl		
LYS514	4.17877				
ARG215	4.76895		Pi-Alkyl		
ALA27	4.14409				
ALA27	4.4457				
PRO29	5.10368				
ALA27	5.19545				
VAL28	4.42978				
PRO29	5.39434				
ALA521	5.44718				
Celecoxib					
HIS9	2.47838	Hydrogen Bond	Conventional Hydrogen Bond	-7.8	901.61
HIS9	2.19683				
ARG227	2.24327				
ARG525	2.76972	Hydrogen Bond;Halogen	Conventional Hydrogen Bond;Halogen (Fluorine)		
GLU32	4.10498	Electrostatic	Pi-Anion		
VAL28	3.89628	Hydrophobic	Pi-Sigma		
ALA27, VAL28	4.13907		Amide-Pi Stacked		
ARG215	4.72668		Alkyl		
LYS514	3.45813				
VAL28	3.72457		Pi-Alkyl		
ALA521	3.39583				
PRO29	5.16516				
ALA521	3.90747				
ALA27	4.69582				
PRO29	4.91421				
PRO29	5.10172				
TRP517	5.16007				
Rofecoxib					
TRP517	3.50829	Hydrogen Bond	Carbon Hydrogen Bond	-8.6	635.41
TYR24	5.22283	Hydrophobic	Pi-Pi T-shaped		
PRO29	5.19836		Pi-Alkyl		
ARG215	4.69141				
ILE11	4.32548				
ALA27	4.7248				
Valdecoxib					
GLU32	2.45596	Hydrogen Bond	Conventional Hydrogen Bond	-9.2	789.55

HIS9	2.66552				
ASN216	2.31555				
ARG227	2.6207				
GLU32	4.00031	Electrostatic	Pi-Anion		
ALA521	3.38078	Hydrophobic	Pi-Sigma		
TRP517, ARG518	5.57088		Amide-Pi Stacked		
ARG215	4.98429		Alkyl		
LYS514	4.00349				
ARG518	5.16068				
PRO29	5.34099				
ARG215	5.21887			Pi-Alkyl	
VAL28	4.42837				
TRP517	4.68932				



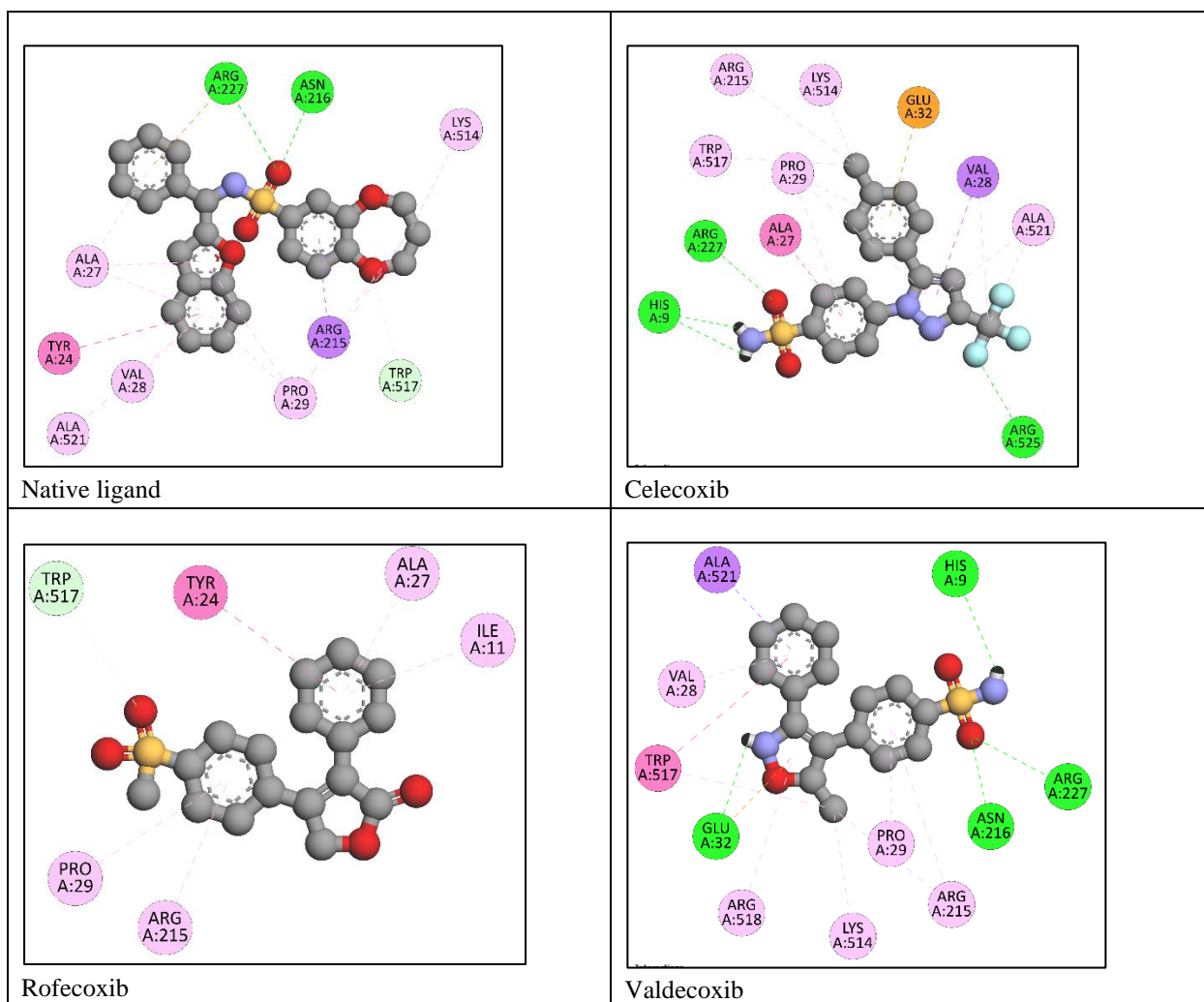


Figure 3. The 2D-docking poses along with superimposed poses of all the compounds in the enzymes allosteric site

The native ligand displayed -10.3 kcal/mol of binding affinity and formed four hydrogen bonds (conventional hydrogen bond, carbon-hydrogen bond, Pi-cation;Pi-donor hydrogen bond) with Asn216, Arg227 and Trp517. It also showed hydrophobic interactions (Pi-Sigma, Pi-Pi T-shaped, alkyl, Pi-alkyl) with Arg215, Tyr24, Pro29, Lys514, Ala27 and Ala521. Celecoxib showed -7.8 kcal/mol of binding affinity and formed four conventional hydrogen bonds with His9, Arg227 and Arg527. It also showed hydrophobic interactions (Pi-sigma, amide-pi stacked, alkyl, Pi-alkyl) with Ala27, Val28, Arg215, Lys514, Val28, Ala521, Pro29, and Trp517. It also showed one electrostatic interactions (Pi-anion) with Val28. Rofecoxib exhibited docking score of -8.6 kcal/mol with the formation of one carbon hydrogen bond with Trp517 and hydrophobic interactions (Pi-Pi T-shaped, Pi-alkyl) with Tyr24, Pro29, Arg215, Ile11 and Ala27. Valdecoxib displayed docking score of -8.6 kcal/mol and formed four hydrogen bonds with Glu32, His9, Asn216, Arg227 and hydrophobic interactions (Pi-sigma, amide-pi stacked, alkyl, Pi-alkyl) with Ala521, Trp517, Arg215, Lys514, Arg518, Pro29 and Val28. It also showed one electrostatic interactions (Pi-anion) with Glu32. Although none of the COX-2 inhibitors displayed less binding free energy than the native ligand but Celecoxib and Valdecoxib exhibited four conventional hydrogen bonds with the glucokinase enzyme. It indicates their potential to modulate the activity of glucokinase enzyme.

Conclusion

As of now, NSAIDs are still the go-to for treating and preventing numerous inflammatory diseases. Mild to moderate proinflammatory state is linked to metabolic chronic illnesses including obesity and type 2 diabetes mellitus (T2DM), and may have a role in the pathogenesis of some of the consequences of these diseases. Preclinical and clinical models have so investigated the impact of NSAIDs on various conditions. In present study, we have investigated the GK activation potential of some COX-2 inhibitors through computational analysis. The native ligand, Celecoxib, Rofecoxib, and Valdecoxib displayed -10.3, -7.8, -8.6, and -8.6 kcal/mol binding free energy respectively. Although none of the COX-2 inhibitors displayed less binding free energy than the native ligand but Celecoxib and Valdecoxib exhibited four conventional hydrogen bonds with the glucokinase enzyme. It indicates their potential to modulate the activity of glucokinase enzyme. Therefore from present study we concluded that, Celecoxib and Valdecoxib can be treated as potential lead molecules for further development of novel glucokinase activators.

References

- Bellucci, P.N.; González Bagnes, M.F.; Di Girolamo, G.; González, C.D. Potential Effects of Nonsteroidal Anti-Inflammatory Drugs in the Prevention and Treatment of Type 2 Diabetes Mellitus. *J. Pharm. Pract.* **2017**, *30*, 549–556, doi:10.1177/0897190016649551.
- Chandrasekharan, N. V.; Dai, H.; Roos, K.L.T.; Evanson, N.K.; Tomsik, J.; Elton, T.S.; Simmons, D.L. COX-3, a Cyclooxygenase-1 Variant Inhibited by Acetaminophen and Other Analgesic/Antipyretic Drugs: Cloning, Structure, and Expression. *Proc. Natl. Acad. Sci. U. S. A.* **2002**, *99*, 13926–13931, doi:10.1073/pnas.162468699.
- Praveen Rao, P.N.; Knaus, E.E. Evolution of Nonsteroidal Anti-Inflammatory Drugs (NSAIDs): Cyclooxygenase (COX) Inhibition and Beyond. *J. Pharm. Pharm. Sci.* **2008**, *11*, doi:10.18433/j3t886.
- Bastard, J.P.; Maachi, M.; Lagathu, C.; Kim, M.J.; Caron, M.; Vidal, H.; Capeau, J.; Feve, B. Recent Advances in the Relationship between Obesity, Inflammation, and Insulin Resistance. *Eur. Cytokine Netw.* **2006**, *17*, 4–12.
- King, G.L. The Role of Inflammatory Cytokines in Diabetes and Its Complications. *J. Periodontol.* **2008**, *79*, 1527–1534, doi:10.1902/jop.2008.080246.
- Li, J.; Zhang, N.; Ye, B.; Ju, W.; Orser, B.; Fox, J.E.M.; Wheeler, M.B.; Wang, Q.; Lu, W.Y. Non-Steroidal Anti-Inflammatory Drugs Increase Insulin Release from Beta Cells by Inhibiting ATP-Sensitive Potassium Channels. *Br. J. Pharmacol.* **2007**, *151*, 483–493, doi:10.1038/sj.bjp.0707259.
- Coghlan, M.; Leighton, B. Glucokinase Activators in Diabetes Management. *Expert Opin. Investig. Drugs* **2008**, *17*, 145–167, doi:10.1517/13543784.17.2.145.
- Olokoba, A.B.; Obateru, O.A.; Olokoba, L.B. Type 2 Diabetes Mellitus: A Review of Current Trends. *Oman Med. J.* **2012**, *27*, 269–273, doi:10.5001/omj.2012.68.
- Grewal, A.S.; Kharb, R.; Prasad, D.N.; Dua, J.S.; Lather, V. N-Pyridin-2-Yl Benzamide Analogues as Allosteric Activators of Glucokinase: Design, Synthesis, in Vitro, in Silico and in Vivo Evaluation. *Chem. Biol. Drug Des.* **2019**, *93*, 364–372, doi:10.1111/cbdd.13423.
- Ajmer Singh Grewal; Kapil Sharma; Sukhbir Singh; Vikramjeet Singh; Deepti Pandita; Viney Lather Design, Synthesis and Antidiabetic Activity of Novel Sulfamoyl Benzamide Derivatives as Glucokinase Activators. *J. Pharm. Technol. Res. Manag.* **2018**, *6*, 115–124, doi:10.15415/jptrm.2018.62008.
- Dallakyan, S.; Olson, A.J. Small-Molecule Library Screening by Docking with PyRx. *Methods Mol. Biol.* **2015**, *1263*, 243–250, doi:10.1007/978-1-4939-2269-7_19.
- Rappé, A.K.; Casewit, C.J.; Colwell, K.S.; Goddard, W.A.; Skiff, W.M. UFF, a Full Periodic Table Force Field for Molecular Mechanics and Molecular Dynamics Simulations. *J. Am. Chem. Soc.* **1992**, *114*, 10024–10035, doi:10.1021/ja00051a040.
- San Diego: Accelrys Software Inc. Discovery Studio Modeling Environment, Release 3.5. Accelrys Softw. Inc. **2012**.
- Chaudhari, R.N.; Khan, S.L.; Chaudhary, R.S.; Jain, S.P.; Siddiqui, F.A. B-Sitosterol: Isolation from Muntingia Calabura Linn Bark Extract, Structural Elucidation And Molecular Docking Studies As Potential Inhibitor of SARS-CoV-2 Mpro (COVID-19). *Asian J. Pharm. Clin. Res.* **2020**, *13*, 204–209, doi:10.22159/ajpcr.2020.v13i5.37909.
- Khan, S.L.; Siddiqui, F.A.; Jain, S.P.; Sonwane, G.M. Discovery of Potential Inhibitors of SARS-CoV-2 (COVID-19) Main Protease (Mpro) from Nigella Sativa (Black Seed) by Molecular Docking Study. *Coronaviruses* **2020**, *2*, 384–402, doi:10.2174/2666796701999200921094103.
- Khan, S.L.; Sonwane, G.M.; Siddiqui, F.A.; Jain, S.P.; Kale, M.A.; Borkar, V.S. Discovery of Naturally Occurring Flavonoids as Human Cytochrome P450 (CYP3A4) Inhibitors with the Aid of Computational Chemistry. *Indo Glob. J. Pharm. Sci.* **2020**, *10*, 58–69, doi:10.35652/igjps.2020.10409.
- Unnisa, A.; Khan, S.L.; Sheikh, F.A.H.; Mahefooz, S.; Kazi, A.A.; Siddiqui, F.A.; Gawai, N.; Saboo, S.G. In-Silico Inhibitory Potential of Triphala Constituents Against Cytochrome P450 2E1 for the Prevention of Thioacetamide-Induced Hepatotoxicity. *J. Pharm. Res. Int.* **2021**, 367–375, doi:10.9734/jpri/2021/v33i43a32499.
- Shntaif, A.H.; Khan, S.; Tapadiya, G.; Chettupalli, A.; Saboo, S.; Shaikh, M.S.; Siddiqui, F.; Amara, R.R. Rational Drug Design, Synthesis, and Biological Evaluation of Novel N-(2-Arylamino-phenyl)-2,3-Diphenylquinoxaline-6-Sulfonamides as Potential Antimalarial, Antifungal, and Antibacterial Agents. *Digit. Chinese Med.* **2021**, *4*, 290–304, doi:10.1016/j.dcm.2021.12.004.
- Khan, Sharuk L.; Siddiqui, F.A. Beta-Sitosterol: As Immunostimulant, Antioxidant and Inhibitor of SARS-CoV-2 Spike Glycoprotein.

- Arch. Pharmacol. Ther. **2020**, 2, doi:10.33696/pharmacol.2.014.
20. Khan, A.; Unnisa, A.; Sohel, M.; Date, M.; Panpaliya, N.; Saboo, S.G.; Siddiqui, F.; Khan, S. Investigation of Phytoconstituents of *Enicostemma Littorale* as Potential Glucokinase Activators through Molecular Docking for the Treatment of Type 2 Diabetes Mellitus. *Silico Pharmacol.* **2022**, 10, doi:10.1007/s40203-021-00116-8.
 21. Khan, S.; Kale, M.; Siddiqui, F.; Nema, N. Novel Pyrimidine-Benzimidazole Hybrids with Antibacterial and Antifungal Properties and Potential Inhibition of SARS-CoV-2 Main Protease and Spike Glycoprotein. *Digit. Chinese Med.* **2021**, 4, 102–119, doi:10.1016/j.dcm.2021.06.004.
 22. Khan, S.L.; Siddiqui, F.A.; Shaikh, M.S.; Nema, N. V.; Shaikh, A.A. Discovery of Potential Inhibitors of the Receptor-Binding Domain (RBD) of Pandemic Disease-Causing SARS-CoV-2 Spike Glycoprotein from *Triphala* through Molecular Docking. *Curr. Chinese Chem.* **2021**, 01, doi:10.2174/2666001601666210322121802.
 23. Siddiqui, F.A.; Khan, S.L.; Marathe, R.P.; Nema, N. V. Design, Synthesis, and In Silico Studies of Novel N-(2-Aminophenyl)-2,3-Diphenylquinoxaline-6-Sulfonamide Derivatives Targeting Receptor- Binding Domain (RBD) of SARS-CoV-2 Spike Glycoprotein and Their Evaluation as Antimicrobial and Antimalarial Agents. *Lett. Drug Des. Discov.* **2021**, 18, 915–931, doi:10.2174/1570180818666210427095203.



PREPARATION AND RELEASE CHARACTERISTIC FOR EUDRAGIT COATED CHITOSAN MICROSPHERE FOR 5-FLUOROURACIL

Mr. Dipak V. Bhusari^{1*}, Dr. Shailesh M. Kewatkar², Amol Nanduji Jaybhaye³, Dr. Koshish B. Gabhane⁴,

Girijesh Kumar Pandey⁵, Dr Manmeet S.Saluja⁶, Dr. Shirish P.Jain², Mrs Neelam M Patel⁷

¹Department of Pharmacy Sunrise University Alwar, Rajasthan, India – 301028

²RajarshiShahu College of Pharmacy, Buldana, Maharashtra, India – 443001

³Western Kentucky University, Bowling Green, KY, USA

⁴P.R.Patil Institute of Pharmacy, Talegaon S.P Ashti, Wardha, Maharashtra, India - 442201

⁵VNS Group of Institutions - Faculty of Pharmacy, Neelbud, Bhopal, Madhya Pradesh, India - 462044.

⁶Head, Dept. of Pharmacology, TIT Pharmacy, AnandNagar, Bhopal, Madhya Pradesh, India - 462021

⁷Assistant Professor, Gurukul Pharmacy College, Kota, Rajasthan, India - 324001

Corresponding author: Mr. Dipak V. Bhusari

Research scholar

Department Of Pharmacy

Sunrise University

Alwar, Rajasthan, India

Email ID: dipakbhusari90@gmail.com

Mobile No: +91 9309736988

3157

ABSTRACT:

Patients diagnosed with tumours typically participate in a multimodal treatment programme that includes radiation therapy, surgical excision of the tumour, and continuous chemotherapy. The purpose of this study was to come up with an original approach of loading 5-fluorouracil (5-FU) onto microspheres as the active ingredient. If this were to be done, chemotherapy would have a higher rate of success, patients would have an improved quality of life, and the intensity of the detrimental effects that chemotherapy has on the body as a whole would be decreased. Chitosan was used as a mucoadhesive and sustained release polymer, while glutaraldehyde was used as a cross-linker in order to make microspheres. This was done since 5-FU requires frequent doses, has significant side effects, and is not very effective at targeting cancer cells. The coating on the microspheres is made of Eudragit S100. The stomach is unable to absorb drugs when this chemical is present. P-XRD analysis was out on microspheres with a coating of 5-FU indicated that the substance did not have a crystalline structure. During the TGA inquiry, there was no evidence of a decrease in bulk, and in-vitro testing revealed that there was a 90% increase in mucoadhesion. Scanning electron microscopy provided evidence that demonstrated that microspheres had a spherical shape. After being soaked for a whole day in a phosphate buffer solution with a pH of 7.4, the medicine was able to be dissolved in 0.1 N hydrochloric acid. In order to treat colon cancer successfully, the use of chitosan microspheres that have an enteric coating is therefore likely to be useful.

Keywords: Colon cancer, 5-Fluorouracil, Eudragit, Chitosan, Microspheres



INTRODUCTION:

Because it is the third most frequent form of cancer worldwide and the second most lethal, colorectal cancer, also known as colorectal cancer (CRC), is a major cause for worry when it comes to the state of public health. CRC can affect either the colon or the rectum. By the year 2020, colorectal cancer has already been attributed to 9.4% of all fatalities caused by cancer. However, it is anticipated that the number of cases of colorectal cancer will more than quadruple across the globe by the year 2035 [1-3], with the least developed countries experiencing the greatest increase in the number of cases diagnosed in their ageing populations as a direct result of the substantial increase. The progression of colorectal cancer can be somewhat unpredictable, despite the fact that it has a complex genetic make-up. For instance, a significant number of somaclonal mutations were discovered in a large sample of CRC cells as a result of variations in the levels of gene expression [1-4].

The anticancer drug known as 5-fluorouracil (5-FU) is often utilised in clinical practice today. Since 1957, it has been applied in the treatment of a variety of cancers, including those of the head and neck, colon, and breasts. The treatment of colon cancer is yet another significant area in which it plays a role. 5-fluorouracil is a kind of anticancer medication known as an antimetabolite. Its mechanism of action involves preventing cancer cells from producing their own nucleic acids and DNA. Since it is effective against a wide variety of solid tumours, it is one of the anticancer medications that is prescribed the most frequently nowadays. Although though 5-FU has poor gastrointestinal (GI) absorption and extremely variable oral bioavailability [5-8], it was frequently administered intravenously in hospitals and clinics.

An inventive method for the administration of drugs is provided by carrier technology. This method involves attaching the medication to a particle (such as microspheres, nanoparticles, or liposomes) that modifies the release and absorption properties of the drug. Because of their diminutive size and their advantageous carrier qualities, microspheres are a prevalent form of the particulate DDS. These innovative DDS have a lot of potential, but their utility is limited because they only stay at the absorption site for a short amount of time. The perfect design would be one that would provide direct

physical contact with DDS as well as absorbent membranes. It's possible that the answer lies in the creation of something called "mucoadhesive microspheres," which contain features related to mucoadhesion. Microparticles or microcapsules having a drug core and measuring between 1 and 1000 m in diameter can be referred to as mucoadhesive microspheres. These microspheres are produced from a mucoadhesive polymer in whole or in part and range in size from 1 to 1000 m. Despite the fact that mucoadhesive properties may be connected to microspheres, the use of microspheres for the targeted and controlled release of pharmaceuticals is favorable. This is the case even though these qualities can be attached to microspheres. It is possible to develop a mucoadhesive drug delivery system for buccal, oral, vaginal, nasal, rectal, and ocular routes of administration due to the fact that the mucosal layer provides potential places for bioadhesive system attachment [9-13]. Mucosal layer provides potential places for bioadhesive system attachment [9-13].

The polymer known as Eudragit S-100 is made up of methylmethacrylic acid and methyl methacrylate in proportions that are identical to one another. Because of this polymer's resistance to both pH and water, it has been utilised in the development of a variety of distinct sustained-release formulations. The typical weight of a molecule is around 150,000 grammes. According to the book USP NF 23, the results of the anionic copolymerization of methyl methacrylate and Methacrylic acid are referred to as eudragit L and S. Eudragit L (Type A) contains about one-one thousandth as many free carboxyl groups as Eudragit S (Type B), and vice versa. (Type B). Both types of polymers degrade quickly in settings that range from slightly basic to moderately alkaline (pH 6-7),

3158



resulting in the formation of salts that react with the gastric medium to generate film coatings that are insoluble. They are supplied in a plasticizer-free solution at a concentration of 12.5% in propan-2-ol. Although while polymers that are used for colon targeting need to be stable in the acidic stomach and first portion of the small intestine, they also need to be able to breakdown in the neutral or slightly alkaline terminal ileum, especially in the vicinity of the ileocecal junction. By dispersing the medication across the whole of the large intestine, these approaches increase the effectiveness of colon-focused delivery systems [14-16].

MATERIAL AND METHODS:

Materials:

Khandelwal labs Pvt. Ltd. provided complimentary five-fluorouracil distribution (Thane, India). SD Fine Chemicals was the supplier of the chitosan that went into the Span-80 (Mumbai, India). We make use of Eudragit S-100, which is a product that was created by Ranbaxy Laboratories Ltd. and then given to us for free (Haryana, India). Both the glutaraldehyde and the paraffin oil came from Sigma-Aldrich Chemie. These were the company's original suppliers. Notwithstanding this, SD Fine Chemicals was the company that provided the acetic acid. E. Merck was the one who offered the scientists cyclohexane, methanol, and dichloromethane to use in their experiments (Darmstadt, Germany). The remaining reagents were of a quality that either met or surpassed the requirements for their usage in analytical procedures.

Methods:

Method of preparation of Chitosan Microspheres:

Either the complicated approach of chemical denaturation or the more straightforward procedures of emulsification and phase separation can be used to produce microspheres. The former method is more difficult to comprehend. The polypropylene beaker initially had 250 millilitres of liquid, and then an additional 100 millilitres of normal paraffin oil was poured to it. In a solution of 3.5% weight-per-volume chitosan, 50 mg of 5-fluorouracil was injected into 3 mL using a hypodermic syringe with a 22-gauge needle.

Chitosan was dissolved in 1% acetic acid in oil, and the resulting mixture was stirred with 1 mL of span-80 before being used to make this solution. In addition to this, the paraffin oil was mixed using a high-speed stirrer that had propellers attached to it at a rate of 2,000 revolutions per minute. Before adding 0.25 mL of glutaraldehyde, the oil was mixed with the full chitosan solution for fifteen minutes at the same speed before adding the glutaraldehyde. Preserving the same rate of one thousand revolutions per minute for the stirring action. After waiting for thirty minutes, 0.50 millilitres of glutaraldehyde was added to the mixture while it was continuously stirred. Once an hour had passed, the identical activity was repeated once again. In this particular instance, the procedure was terminated when we added the remaining glutaraldehyde and stirred for a total of one hour. Following a period of 24 hours, the chitosan microspheres that were produced sank to the bottom of the paraffin oil due to the weight of the microspheres. Microspheres were discovered when the clear supernatant was removed and the residue was washed four or five times with diethyl ether. This process was repeated until the residue was clean. Following the completion of the last washing step, the microspheres were allowed to air dry. After that, the powder was gathered up and stored in a dark, dry, and cold location [17–19].

Preparation of Eudragit Coated Microspheres

Using a method that involved the evaporation of the solvent, Eudragit was used to coat the chitosan microspheres. Developing microspheres that are packed with chitosan (B2) and then dispersing them in Eudragit S-100 (500 mg of Eudragit in ethanol: acetone 2:1). In order to create this emulsion, 70 millilitres of liquid paraffin oil containing 1% volume/volume of span 80 were combined with Eudragit S-100 and core microspheres, and then the mixture was spun at a high speed. After around three to four hours of steady stirring, the solvent in question was completely soaked up. Using a method that involved filtration, microspheres were then encapsulated after being screened. After having the liquid paraffin removed from them by washing them three to four times in n-hexane, they were left out in the air to dry for a period of

3159



twenty-four hours. In preparation for future studies, we put aside some microspheres coated with Eudragit [20-23].

EVALUATION PARAMETERS

Morphological Study of Eudragit Coated Microspheres

Using Digital Technology into Optical Microscopes to ensure that Eudragit-coated chitosan spheres were spherical and non-sticky, micrographs of the spheres were examined. Microspheres might be produced by combining eudragit with a 3.5% chitosan solution and spinning the resulting mixture at 2000-2500 rpm [24, 25].

Scanning Electron Microscopy

By using scanning electron microscopy, both pectin microspheres and pectin microspheres that had been coated with eudragit were compared regarding their dimensions and contours (SEM). In order to conduct a SEM examination, a sample of the slurry was dusted onto a piece of double-sided tape, and then the tape was glued to a piece of aluminium. After that, a gold sputter module was used inside of a high-vacuum evaporator with an argon atmosphere so that 300 microns of gold could be sputtered onto the tips. After scanning random samples with a Jeol JSM-6400 scanning electron microscope (Tokyo, Japan), photomicrographs were created and made. [26]

Determination of Percentage Drug Entrapment

Calculations were done for each batch based on the amount of substance that was seized (PDE). During the theoretical drug loading calculation, it was assumed that all of the drug that was present in the Eudragit chitosan solution had been integrated into the microspheres and that none of it had been lost. After putting 25 mg of Eudragit microspheres in a 25 mL volumetric flask and weighing the mixture, we were able to calculate the appropriate drug loading for the formulation. Methanol, in total volume of 25 millilitres, was poured into the container until it was entirely full. While we let the suspension to stay out at room temperature for twenty-four hours, we did give it a shake every so often. After centrifuging the sample between 2000 and 3000 revolutions per minute (rpm), the concentration of the drug in the supernatant was measured using UV Spectrophotometry at 266 nm [21, 22].

Determination of Particle size and particle size distribution

The behaviour of eudragit-coated microspheres during release is substantially impacted by the particle size of the microspheres. Using a particle size Analyser, we were able to measure the particle size distribution of Eudragit-coated microspheres in distilled water over the course of 10 mg and 2 mL. (Malvern Master Sizer, model E, UK). [25–26] A measure known as the Z-average was frequently utilised in the process of describing the particles (in nanometers).

Determination of Zeta potential

The zeta potential may be used to examine the surface charges that are present on microspheres. It is envisaged that mucoadhesive delivery methods would have a high zeta potential. [Citation needed] The surface charge of microparticles in deionized water was measured with a Zeta master (made in Malvern, United Kingdom) and laser Doppler anemometry [27, 28].

IR Spectra of Eudragit coated microspheres

The infrared spectroscopy was performed with the use of the FT/IR Spectrometer, which was located at the MPCST Quality Assurance Laboratory. The validity of the study was determined by examining the congruence between the expected values and the correlation that existed between the transmittance percentage and the frequency (cm⁻¹). [24, 25] Bruker conducted an investigation on a sample of eudragit-coated microspheres.

DSC Studies

The DSC analysis was conducted to determine whether or not 5 fluorouracil was compatible with the excipients (chitosan and Eudragit S100) that were utilised in the production of the microspheres. The Pyris 6 DSC makes use of indium as the standard DSC reference material in its analysis. We studied what would happen to Eudragit S100 using a 5FU thermometer and subjected it to temperatures ranging from -20 to +350 degrees Fahrenheit. [29, 30] A comparison was done between the peaks of thermogram generated with 5 FU and different fillers and those made with the pure substance.

In vitro Release Profile of 5-

FU from Eudragit Coated Microspheres

3160



Microspheres that had been coated with eudragit were put through tests to determine whether or not they could release medications when placed in an environment that mimicked the acidity of the stomach (SGF). In accordance with USP XXIII, the paddle method was utilised to conduct an analysis of the dissolution of a microsphere-based medicine (model Sentwin, India). In order to simulate the viscosity of blood, dialysis membranes were immersed in a solution that included one hundred milligramme of microspheres (SGF). The temperature range for spinning the material was 370 degrees Celsius (plus or minus 0.50 degrees Celsius), and the revolutions per minute (rpm) was 100. Research on the ease with which medications may be dissolved was carried out in the most perfect conditions in the kitchen sink. Adjustments were made to the pH of the dissolving solution at regular intervals so that we could imitate the acidic and alkaline environments of the stomach and small intestine, respectively. With 0.1 N HCL, the pH of the solution was kept at 1.2 for the entirety of the allotted time. Once the pH of the dissolving solution was brought down to 4.5 with 1.0M sodium hydroxide, an additional 1.7 grammes of potassium hydroxide (KH₂PO₄) and 2.2 grammes of sodium hydrogen phosphate (Na₂HPO₄.2H₂O) were added. It was decided to continue monitoring the discharge rate for an additional two hours. After adjusting the solution with 0.1 N NaOH for four hours, the pH was brought up to 7.4, where it remained stable over the following 24 hours. After being taken from the solvent at various intervals, the samples were then diluted using a pipette. When the same quantity of SGF was administered instead, there was no discernible change in the size of the receptor. Using UV spectrophotometry, we were able to calculate the rate at which FU is released by plotting the cumulative drug release against the passage of time.

***In-vivo*Release Profile of 5-FU from Eudragit Coated Microspheres**

In the actual experiments that were carried out, albino rats were used. Food and water were never in limited supply for the rats at any point in time. The experiment was carried out using rats of a healthy weight, and no medications were given to the animals in any way. Following careful consideration, the ethics committee gave its blessing to proceed with this treatment.

In order to investigate the effects of time-dependent dosing with pure treatment (5-FU) and Eudragit-coated chitosan microspheres, Albino rats were employed in the study. The analysis of the release kinetics *In-vivo* required the construction of a calibration curve that linked the concentration of the drug in the plasma to the height of the peak. This curve was then employed. In order for the drug to be dissolved, 10 millilitres of the phosphate buffer with a 7.4 pH was necessary. Hence, a stock solution with a concentration of 1 g/mL was created. After adding 10 mL of water to a volumetric flask that was initially filled with 10 mL, 1 mL of the stock solution was pipetted in.

The chromatography was carried out with the assistance of a highperformance liquid chromatography (HPLC) system that was outfitted with a Shimadzu R 1100 series RP C-18 column that was made in Japan (HPLC column). 7.4 was the pH of the phosphate buffer that was utilised in the investigation of 5-fluorouracil. At a rate of one milliliter per minute, mobile phase was injected into the column from the solvent reservoir. Essential components of the apparatus, each injection loop has the capacity to hold 20 g/mL. The length of time it takes to have a thought is 3.51 minutes on average, with the median time being 2.33 minutes. A standard curve was constructed with a concentration range of 10-50 g/mL as the variable of interest.

3161

Table 1: Standard curve of 5FU by HPLC

Sr.No.	Concentration(µg/mL)	Area
1.	0	0
2.	10	1847788
3.	20	3594180



4.	30	5741272
5.	40	7897365
6.	50	9835458

There were so many of the albino rats that we split them up into two groups of three. Eudragit was extracted from the materials and utilised to coat microspheres for future experiments. It was the other rats that served as the "control" group. Microscopic spheres coated with eudragit floated in a bath of carboxymethyl cellulose (CMC). The microsphere suspension was orally delivered to the third group. Every two, four, six, eight, ten, and twenty-four hours, a prick to the tail vein was made to draw half a milliliter of blood. The blood pool technique was used to collect the blood samples in 0.9% normal saline. To prevent blood from clotting during collection, 0.1 ml of heparin was administered into Eppendorf tubes. After centrifuging the samples at 5000 rpm for 15 minutes to separate the medication, the concentration was determined

using high performance liquid chromatography (HPLC) [31-32].

RESULT AND DISCUSSION:

EudragitCoatedChitosanMicrospheres

Chitosan microspheres were then coated with Eudragit S-100 as the solvent was allowed to evaporate (B2). We were able to do this by first emulsifying the core microsphere dispersions in liquid paraffin using span-80, and then dispersing chitosan microspheres in a solution containing Eudragit S-100. The microspheres were put aside for later use after first having their capsules opened, then being cleaned in n-hexane, and then being dried at 600 degrees Celsius for one hour. After this step, the generated Eudragit-coated microspheres were tested to see whether or not they could function well as enteric coated delivery vehicles.

Evaluation Parameters of Eudragit Coated Microspheres

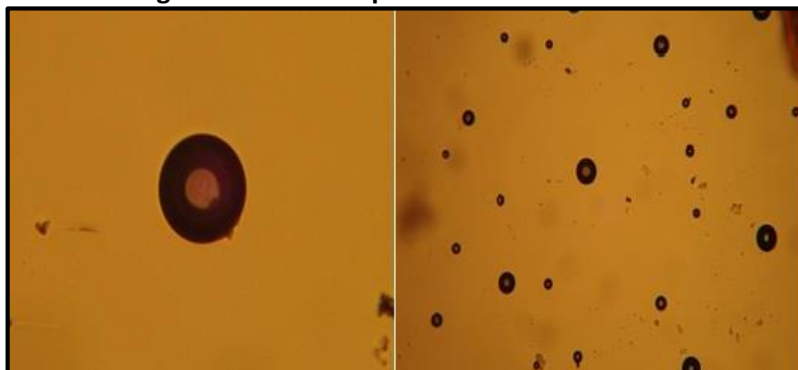


Figure 1: Morphological study of Eudragit coated microspheres

Scanning Electron Microscopy

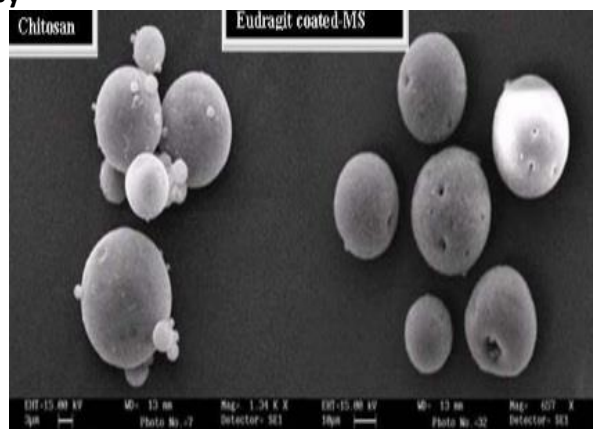


Figure 2: Phase contrast photographs of Eudragit coated microspheres

3162



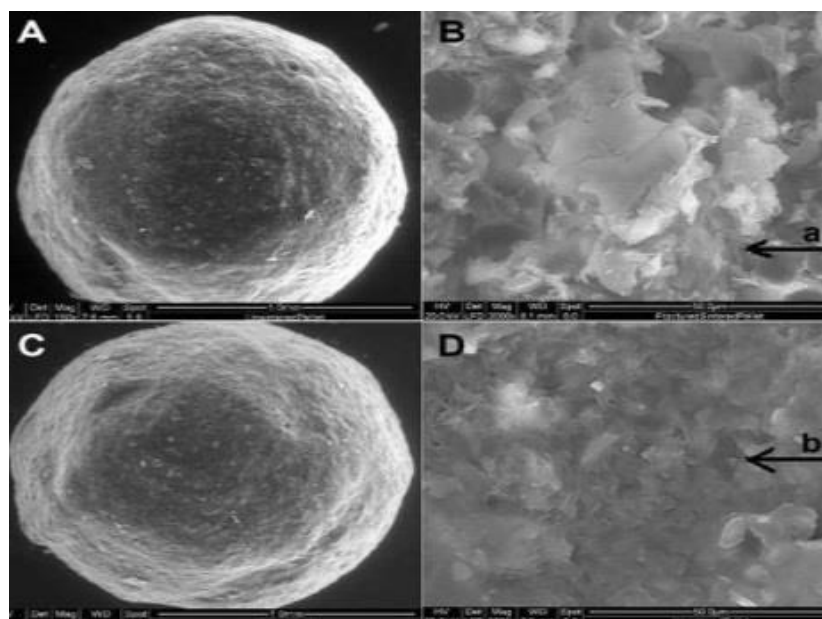


Figure 3: SEM photographs of Eudragit coated microspheres

In phase contrast pictures, it was possible to make clearly the microspheres' spherical form, the absence of any clumping, as well as their inner structure and outside coating. Scanning electron microscopy was utilised in order to do an analysis on the topography as well as the solid dispersion of the physical combination (SEM). The JSM6400 scanning electron microscope with a 10,000X magnification was used to take the photos, and room temperature was maintained throughout the process. The conductivity of the solid dispersions was enhanced by sputtering gold onto the surface of the particles. As a result,

this made scanning much easier. Figures 2 and 3 contain photomicrographs that are exemplary examples of the phenomenon being studied. Electron microscopy was used to investigate microspheres coated with Eudragit. The results showed that the crystals were intact throughout the investigation. Scanning electron microscopy showed that chitosan microspheres are clear, spherical, and have a rough outer surface due to crystals on the surface of the medication [23-28]. Chitosan microspheres also have a smooth interior.

3163

Other Evaluation Parameters of Eudragit Coated Chitosan Microspheres

Table 2: Evaluation parameters of eudragit coated microspheres

Sr.No.	Evaluation parameters	Eudragit coated Microspheres
1.	Percentage drug entrapment	30.69
2.	Particle size and size distribution	11365nm
3.	Zeta potential	+39.7mV
4.	Swelling properties	No significant

Entrapment was achieved at a rate of 30.69 percent using microspheres coated with eudragit. The quantity of the cross-linking agent that is used, the amount of time that it is permitted to set, as well as the speed at which it is stirred, are all elements that contribute to the quality of the microspheres' coating and entrapping. The particle size of chitosan

microspheres grew to 11365 nm when Eudragit was added to them. According to the findings, the particle size distribution of the Eudragit-coated microspheres was quite narrow. Because of the positive charge that is present on the surface of the microspheres, the zeta potential of microspheres that have been coated with eudragit is +39.7 mV.



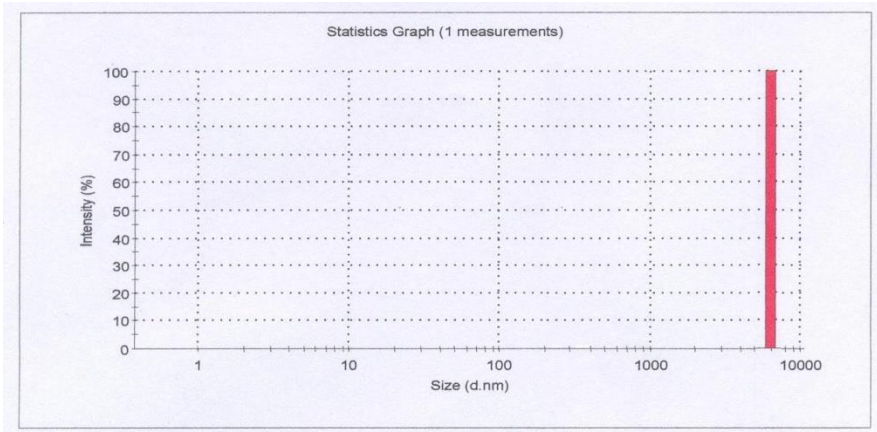


Figure 4: Particle size distribution of eudragit coated microspheres

IR Spectra of Eudragit Coated Microspheres

Figure 5: IR Spectra of Eudragit coated microspheres

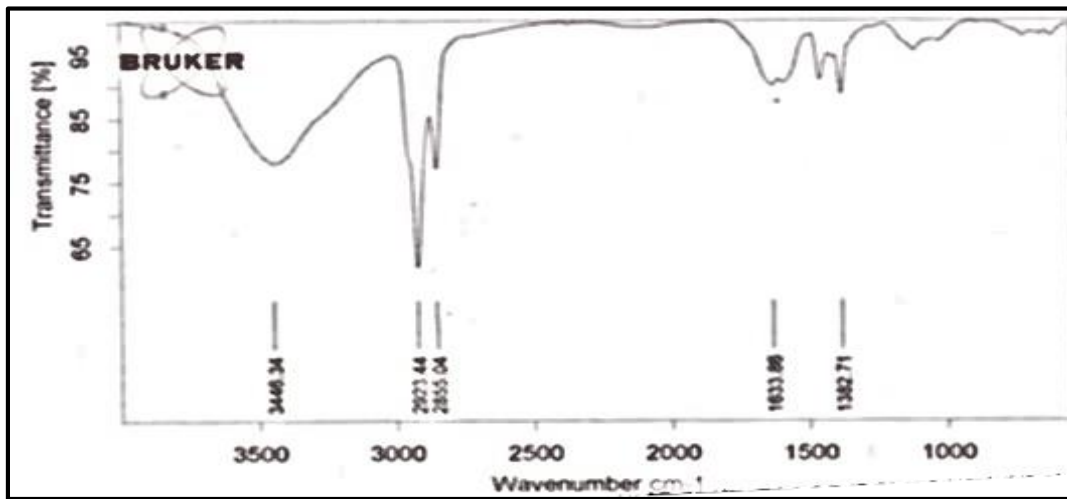


Table 3: IR Spectral characteristics of Eudragit coated microspheres of 5-FU

Sr.No.	WaveNumber (cm ⁻¹)	Interpretation
1.	2923.44	NH Stretching
2.	1633.86	C=O Stretching
3.	1382.71	CH in plane deformation

When the data was analyzed for its clinical relevance, it was found that the 5-FU-loaded Eudragit-coated microspheres had peaks that were equivalent to those of the pure medicine. The medicine was successfully loaded into Eudragit-coated chitosan microspheres, and results showed that there was no interaction between the polymer and pure medication.

Differential Scanning Calorimetry Studies

DSC can determine how the sample is interacting by monitoring the disappearance or presence of thermal events, such as endothermic or

exothermic peaks. When conditions are favorable, peaks can expand and temperatures can change. This may or may not suggest a substantial level of interaction between them. Compatibility is possible so long as there is not a great deal of complex alteration and the thermal properties do not vary significantly. It was easy to determine how well a medicine interacted with its diluents using this method. Figure 6 depicts the thermogram of 5 FU, Eudragit S100, and their mixtures from 20 to 3500 degrees Celsius. The endothermic peak of pure 5FU was



between 180 and 850 degrees Celsius. You can get 5FU and Eudragit S 100 thermogram at 242.590C simultaneously. When the endothermic peaks are generated at roughly the same temperature for both pure pharmaceuticals and mixtures, this indicates that there is no incompatibility between the drug and the excipient. The DSC values suggested that the medication would be stable and mix well with

the other components of the formulation; hence, this conclusion remained valid. Figure 6 depicts the differential scanning Calorimetry (DSC) pattern of the final formulation. This endothermic peak occurs between 180 and 850 degrees Fahrenheit, the melting temperature of both uncoated chitosan microspheres and free 5-fluorouracil.

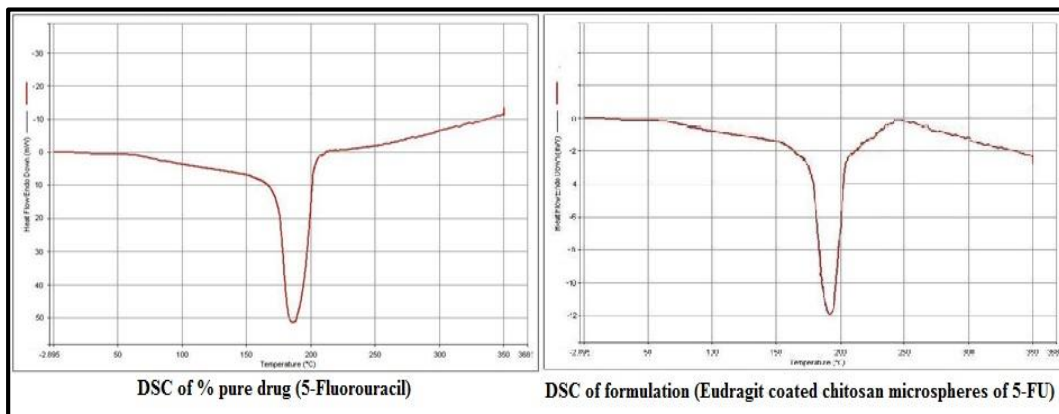


Figure 6: DSC for Pure drug and formulation

***In-vitro*ReleaseProfileof5-FUfromEudragitCoatedMicrospheres**

Little capsules containing chitosan core microspheres were the primary target of this formulation method. Only in the colon, where the pH is more than 7.0, does the coated polymer, Eudragit S-100, melt, allowing the drug

to be absorbed. There is hope that chitosan placed at the location of drug release will work once the enteric coating has degraded. When the stomach pH was barely 2.0, no medicine was absorbed for two hours. None of the drugs were administered at a pH higher than the polymer could handle (Figure 7) [28-30].

3165

Table 4: *In vitro* release profile of 5-Fluorouracil

Time(hrs.)	Sq.rootoftime	Logtime	Cumulative % drugrelease	Cumulative % drugremain	Logcumulative % drugrelease	Logcumulative % drugremain
1.	1	0	1.32	98.68	0.1205	1.994
2.	1.414	0.3010	4.18	95.82	0.6211	1.981
3.	1.732	0.4771	5.78	94.22	0.7619	1.974
4.	2.000	0.6020	7.46	92.54	0.8727	1.966
5.	2.236	0.6989	10.25	89.75	1.010	1.953
6.	2.449	0.7781	18.37	81.63	1.264	1.911
7.	2.645	0.8450	35.69	64.31	1.5525	1.8082
8.	2.828	0.9030	58.23	41.77	1.7651	1.620



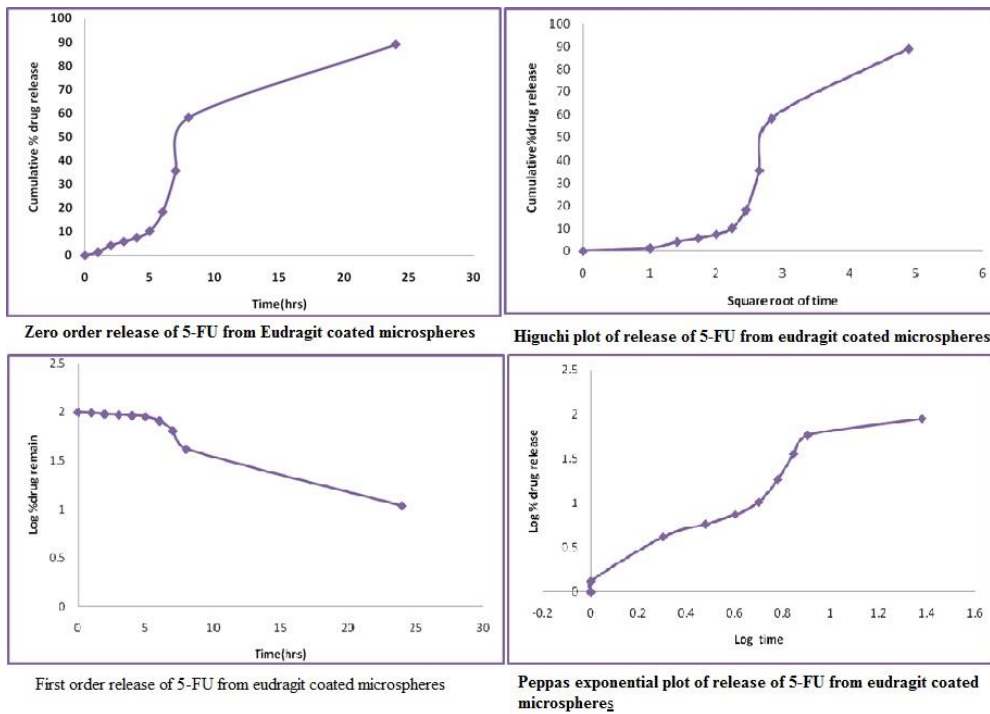


Figure 7: In-vitro release kinetic parameters of Eudragit coated microspheres

Table 5: In vitro release kinetic parameters of Eudragit coated microspheres

Sr.No.	Name of Model	Eq. for St. line	Value R ²
1.	Zero Order	Y = 4.025x - 1.109	R ² = 0.8566
2.	Higuchi release	Y = 20.46x - 20.33	R ² = 0.799
3.	First Order	Y = 0.042x + 2.081	R ² = 0.947
4.	Peppas release	Y = 1.491x + 0.099	R ² = 0.939

Analysis of the drug released data

Zero-order rates are used to talk about systems where the rate of drug release doesn't change based on how much drug is present. Figure 7 shows the relationship between the total amount of drug released and the amount of time. Figure 7 is a graph that shows how the concentration of the system's release affects the first order rate. This rate is used to explain how systems release things. Higuchi's model says that the rate of drug release from an insoluble matrix is proportional to the square root of time. Figure 7 shows the Higuchi square root kinetics. The regression coefficients for the zero-order, first-order, and Higuchi models, in order, were found to be 0.8566, 0.947, and 0.799, respectively. The best way to describe the *In-vitro* drug release of 5-FU microspheres was with first order equations, which had the most linear plot, and then Peppas' model. So, Peppas' model and the

way things started out seem to work with the release. So, the main way the drug got out of the microspheres was for it to diffuse out of them. Several release equations were used to describe the rate of drug release from these microspheres based on the results of *In-vitro* release studies. Models of kinetics were used, such as first order, zero-order, Higuchi release, and Korsneyer and Peppas. Table 5 shows the results of linear regression analyses. By looking at the R2 coefficient of determination, we were able to figure out that both the core microspheres and the coated microspheres used the diffusion control mechanism, which led to a controlled release of the drug. As shown by the R2 value of 0.947, the 5-FU release from the Eudragit-coated microspheres follows the First-order release.

In-vivo Release Profile of 5-FU from Eudragit Coated Microspheres



It was necessary to create a calibration curve between the drug concentration in the blood and the peak area in order to investigate the release kinetics *In-vivo*. A phosphate buffer solution of pH 7.4 was added to the drug, totaling 10 millilitres. As a result, a 10 g/mL stock solution was prepared. Then, using the transfer pipette, 1 ml of the stock solution was pipetted into the final 10 ml of solution in the volumetric flask [21-25]. The chromatography was performed using a high performance liquid chromatography (HPLC) system equipped with a ShimadzuR 1100 series RP C-18 column manufactured in Japan (HPLC column). The pH of the equation of line was found to as : $Y=198495x-143021$ Where x =Concentration Value of $R^2=0.9987$ Intercept=143021

the phosphate buffer used in this study of 5-fluorouracil was 7.4. The solvent reservoir pumped mobile phase into the column at a rate of 1 ml/min. important pieces of kit, each injection loop could store 20 g/mL. The average duration of a thought process is 3.51 minutes, with a median of 2.33 minutes. Table 6 displays the standard curve we generated by applying Beer's and Lambert's laws to a concentration range of 10-50 g/mL; this curve demonstrates that the corresponding equation is linear. In future research, this concentration range should be employed.

Table 6: Standardcurveof5FUby HPLC

Sr.No.	Concentration($\mu\text{g/mL}$)	Area
1.	0	0
2.	10	1947090
3.	20	3894180
4.	30	5841270
5.	40	7788360
6.	50	9735450

3167

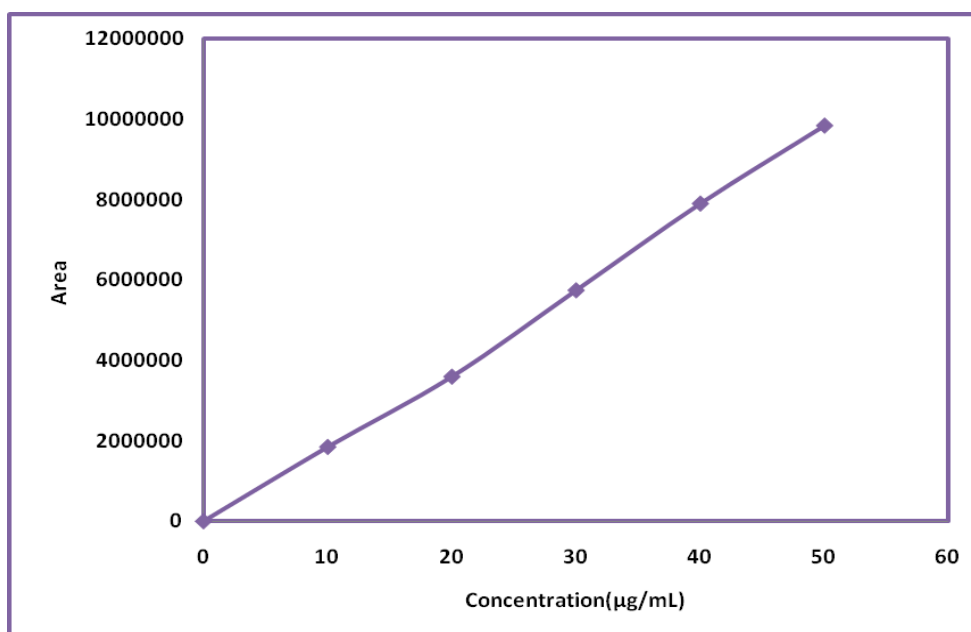


Figure 8: Standardcurveof5FUbyHPLC

Table 7: *In-vivo* release profile of 5-FU from Eudragit coated microspheres

Sr.No.	Time(hrs.)	Concentration($\mu\text{g/mL}$)
1.	0	0



2.	2	2.596
3.	4	3.432
4.	6	6.047
5.	8	20.272
6.	10	22.362
7.	24	38.48

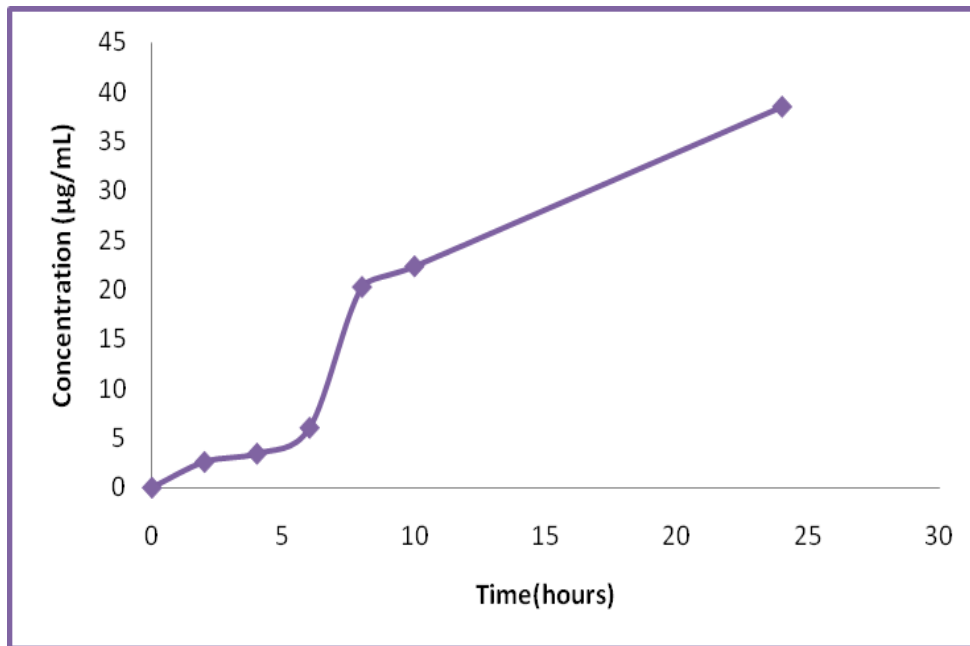


Figure 9: *In-vivo* release of 5-FU from Eudragit-coated microspheres

Time-course analysis of 5-FU blood levels following oral administration of eudragit-coated microspheres is depicted in Figure 9. Researchers utilised blood samples to observe the release of the extended-release medication. The half-life of this medication is significantly longer than average. Up to 24 hours of blood levels can be tested. Comparing *In-vivo* and *In-vitro* data, it was revealed that the rate of release increased. The enzymes probably dissolved the polymer and stripped it of its coating, which explains the result. In laboratory tests, Eudragit S-100 demonstrated poor solubility in acid. As a result, the coated microspheres gradually released the medicine over a period of four to five hours. The medication was rapidly soluble, and the stomach's acidity removed its protective coating, resulting in a dramatic increase in the drug's blood concentration within just 4-5 hours (above 7). As the blood medication concentration rose and remained stable for up to 24 hours, this indicates that the delivery mechanism may keep

releasing pharmaceuticals indefinitely. Based on preliminary experimental studies [24-30], it appears that these Eudragit-coated chitosan microspheres will be able to target the colon since Eudragit S-100 dissolves best in the pH of the colon.

CONCLUSION

Our results contribute to the growing body of evidence suggesting that eudragit-S-100-coated dextran microspheres may be useful for the targeted delivery of 5-FU. This method of delivery would allow for a gradual and manageable release of 5-FU from the microspheres. Studies of the drug's pharmacokinetics and organ distribution demonstrated that it was predominantly localized in colon tissue and had few systemic effects. Because of how rapidly it is absorbed in the upper gastrointestinal tract, 5-FU at conventional dosages, such as pills, might induce undesirable side effects. There may be less of an impact if the medication exits the body in a



variety of places. The results confirmed that Eudragit-coated 5-fluorouracil (FU) chitosan microspheres may be used to target drug delivery to the colon.

Acknowledgments

The authors thank RajarshiShahu College of pharmacy, Buldana for providing facilities to conduct the research.

Authors Funding

None

Conflicts of interest

There are no conflicts of interest among all the authors with publication of manuscript.

REFERENCE

1. Center MM, Jemal A, Smith RA, Ward E. Worldwide variations in colorectal cancer. CA: a cancer journal for clinicians. 2009 Nov; 59(6):366-78.
2. Ten Hoorn S, de Back TR, Sommeijer DW, Vermeulen L. Clinical value of consensus molecular subtypes in colorectal cancer: a systematic review and meta-analysis. JNCI: Journal of the National Cancer Institute. 2022 Apr; 114(4):503-16.
3. Wu Y, Yang S, Ma J, Chen Z, Song G, Rao D, Cheng Y, Huang S, Liu Y, Jiang S, Liu J. Spatiotemporal Immune Landscape of Colorectal Cancer Liver Metastasis at Single-Cell Level Spatial and Cellular Landscape of CRLM. Cancer discovery. 2022 Jan 1; 12(1):134-53.
4. Sinicrope FA. Increasing incidence of early-onset colorectal cancer. New England Journal of Medicine. 2022 Apr 21; 386(16):1547-58.
5. Qin L, Liang F, Li Y, Wu J, Guan S, Wu M, Xie S, Luo M, Ma D. A 2D porous zinc-organic framework platform for loading of 5-fluorouracil. Inorganics. 2022 Nov 9; 10(11):202.
6. Esrafili MD, Khan AA. Alkali metal decorated C 60 fullerenes as promising materials for delivery of the 5-fluorouracil anticancer drug: a DFT approach. RSC advances. 2022; 12(7):3948-56.
7. Nguyen CH, Banh KS, Dang CH, Nguyen CH, Nguyen TD. β -cyclodextrin/alginate nanoparticles encapsulated 5-fluorouracil as an effective and safe anticancer drug delivery system. Arabian Journal of Chemistry. 2022 Jun 1; 15(6):103814.
8. Barary M, Hosseinzadeh R, Kazemi S, Liang JJ, Mansoori R, Sio TT, Hosseini M, Moghadamnia AA. The effect of propolis on 5-fluorouracil-induced cardiac toxicity in rats. Scientific Reports. 2022 May 23; 12(1):8661.
9. Surya R, Mullassery MD, Fernandez NB, Thomas D, Jayaram PS. Synthesis and characterization of a pH responsive and mucoadhesive drug delivery system for the controlled release application of anti-cancerous drug. Arabian Journal of Chemistry. 2020 May 1; 13(5):5262-76.
10. Kumar A, Naik PK, Pradhan D, Ghosh G, Rath G. Mucoadhesive formulations: Innovations, merits, drawbacks, and future outlook. Pharmaceutical Development and Technology. 2020 Aug 8; 25(7):797-814.
11. Li X, Chen K, Ji X, Yuan X, Lei Z, Ullah MW, Xiao J, Yang G. Microencapsulation of poorly water-soluble finasteride in polyvinyl alcohol/chitosan microspheres as a long-term sustained release system for potential embolization applications. Engineered Science. 2020 Dec 14; 13(2):106-20.
12. Zeng D, Yu C, Fan Q, Zeng J, Wei L, Li Z, Yang K, Ji H. Theoretical and experimental research of novel fluorine doped hierarchical Sn3O4 microspheres with excellent photocatalytic performance for removal of Cr (VI) and organic pollutants. Chemical Engineering Journal. 2020 Jul 1; 391:123607.
13. Bui TH, Lee W, Jeon SB, Kim KW, Lee Y. Enhanced Gold (III) adsorption using glutaraldehyde-cross-linked chitosan beads: Effect of crosslinking degree on adsorption selectivity, capacity, and mechanism. Separation and Purification Technology. 2020 Oct 1; 248:116989.
14. Thakral NK, Ray AR, Majumdar DK. Eudragit S-100 entrapped chitosan microspheres of valdecoxib for colon cancer. Journal of Materials Science: Materials in Medicine. 2010 Sep; 21:2691-9.
15. Mehta R, Chawla A, Sharma P, Pawar P. Formulation and *In-vitro* evaluation of Eudragit S-100 coated naproxen matrix tablets for colon-targeted drug delivery system. Journal of advanced pharmaceutical



- technology & research. 2013 Jan; 4(1):31.
16. Garala KC, Shinde AJ, Shah PH. Formulation and in-vitro characterization of monolithic matrix transdermal systems using HPMC/Eudragit S 100 polymer blends. *Int J Pharm Sci.* 2009; 1(1):108-20.
 17. Xia H, Li A, Man J, Li J, Li J. Fabrication of multi-layered microspheres based on phase separation for drug delivery. *Micro machines.* 2021 Jun 19; 12(6):723.
 18. Jiang H, Hu X, Li Y, Ngai T. A green and facile strategy for the fabrication of all-natural porous proteinaceous microspheres. *Materials Chemistry Frontiers.* 2021; 5(10):3897-902.
 19. Li G, Yu Y, Han W, Zhu L, Si T, Wang H, Li K, Sun Y, He Y. Solvent evaporation self-motivated continual synthesis of versatile porous polymer microspheres via foaming-transfer. *Colloids and Surfaces A: Physicochemical and Engineering Aspects.* 2021 Apr 20; 615:126239.
 20. Paharia A, Yadav AK, Rai G, Jain SK, Pancholi SS, Agrawal GP. Eudragit-coated pectin microspheres of 5-fluorouracil for colon targeting. *AapsPharmscitech.* 2007 Mar; 8:E87-93.
 21. Chawla A, Sharma P, Pawar P. Eudragit S-100 coated sodium alginate microspheres of naproxen sodium: formulation, optimization and *In-vitro* evaluation. *Acta pharmaceutica.* 2012 Dec 31; 62(4):529-45.
 22. Ramasamy T, Ruttala HB, Shanmugam S, Umadevi SK. Eudragit-coated aceclofenac-loaded pectin microspheres in chronopharmacological treatment of rheumatoid arthritis. *Drug delivery.* 2013 Feb 1; 20(2):65-77.
 23. Zhang L, Cao F, Ding B, Li Q, Xi Y, Zhai G. Eudragit® S100 coated calcium pectinate microspheres of curcumin for colon targeting. *Journal of microencapsulation.*
 24. Ibrahim M, Sarhan HA, Naguib YW, Abdelkader H. Design, characterization and *In-vivo* evaluation of modified release baclofen floating coated beads. *International Journal of Pharmaceutics.* 2020 May 30; 582:119344.
 25. Souto EB, Ana RD, Souto SB, Zielińska A, Marques C, Andrade LN, HorbańczukOK, Atanasov AG, Lucarini M, Durazzo A, Silva AM. *In-vitro* characterization, modelling, and antioxidant properties of polyphenon-60 from green tea in Eudragit S100-2 chitosan microspheres. *Nutrients.* 2020 Mar 31; 12(4):967.
 26. Ibrahim M, Sarhan HA, Naguib YW, Abdelkader H. Design, characterization and *In-vivo* evaluation of modified release baclofen floating coated beads. *International Journal of Pharmaceutics.* 2020 May 30; 582:119344.
 27. Deshmukh R, Harwansh RK, Paul SD, Shukla R. Controlled release of sulfasalazine loaded amidated pectin microparticles through Eudragit S 100 coated capsule for management of inflammatory bowel disease. *Journal of Drug Delivery Science and Technology.* 2020 Feb 1; 55:101495.
 28. De Leo V, Di Gioia S, Milano F, Fini P, Comparelli R, Mancini E, Agostiano A, Conese M, Catucci L. Eudragit S100 entrapped liposome for curcumin delivery: Anti-oxidative effect in Caco-2 cells. *Coatings.* 2020 Jan 30; 10(2):114.
 29. Almurisi SH, Akkawi ME, Chatterjee B, Sarker MZ. Taste masking of paracetamol encapsulated in chitosan-coated alginate beads. *Journal of Drug Delivery Science and Technology.* 2020 Apr 1; 56:101520.
 30. Maestrelli F, Cirri M, Corti G, Mennini N, Mura P. Development of enteric-coated calcium pectinate microspheres intended for colonic drug delivery. *European journal of pharmaceutics and bio pharmaceutics.* 2008 Jun 1; 69(2):508-18.
 31. Contado C, Caselotto L, Mello P, Maietti A, Marvelli L, Marchetti N, Dalpiaz A. Design and formulation of Eudragit-coated zein/pectin nanoparticles for the colon delivery of resveratrol. *European Food Research and Technology.* 2020 Dec; 246:2427.
 32. Bogataj M, Mrhar A, Kristl A, Kozjek F. Preparation and evaluation of Eudragit E microspheres containing bacampicillin. *Drug Development and Industrial Pharmacy.* 1989 Jan 1; 15(14-16):2295-313.



PREPARATION AND RELEASE CHARACTERISTIC FOR EUDRAGIT COATED CHITOSAN MICROSPHERE FOR 5-FLUOROURACIL

Mr. Dipak V. Bhusari^{1*}, Dr. Shailesh M. Kewatkar², Amol Nanduji Jaybhaye³, Dr. Koshish B. Gabhane⁴,

Girijesh Kumar Pandey⁵, Dr Manmeet S.Saluja⁶, Dr. Shirish P.Jain², Mrs Neelam M Patel⁷

¹Department of Pharmacy Sunrise University Alwar, Rajasthan, India– 301028

²RajarshiShahu College of Pharmacy, Buldana, Maharashtra, India – 443001

³Western Kentucky University, Bowling Green, KY, USA

⁴P.R.Patil Institute of Pharmacy, Talegaon S.P Ashti, Wardha, Maharashtra, India - 442201

⁵VNS Group of Institutions - Faculty of Pharmacy, Neelbud, Bhopal, Madhya Pradesh, India - 462044.

⁶Head, Dept. of Pharmacology, TIT Pharmacy, AnandNagar, Bhopal, Madhya Pradesh, India - 462021

⁷Assistant Professor, Gurukul Pharmacy College, Kota, Rajasthan, India - 324001

Corresponding author: Mr. Dipak V. Bhusari

Research scholar

Department Of Pharmacy

Sunrise University

Alwar, Rajasthan, India

Email ID: dipakbhusari90@gmail.com

Mobile No: +91 9309736988

3157

ABSTRACT:

Patients diagnosed with tumours typically participate in a multimodal treatment programme that includes radiation therapy, surgical excision of the tumour, and continuous chemotherapy. The purpose of this study was to come up with an original approach of loading 5-fluorouracil (5-FU) onto microspheres as the active ingredient. If this were to be done, chemotherapy would have a higher rate of success, patients would have an improved quality of life, and the intensity of the detrimental effects that chemotherapy has on the body as a whole would be decreased. Chitosan was used as a mucoadhesive and sustained release polymer, while glutaraldehyde was used as a cross-linker in order to make microspheres. This was done since 5-FU requires frequent doses, has significant side effects, and is not very effective at targeting cancer cells. The coating on the microspheres is made of Eudragit S100. The stomach is unable to absorb drugs when this chemical is present. P-XRD analysis was out on microspheres with a coating of 5-FU indicated that the substance did not have a crystalline structure. During the TGA inquiry, there was no evidence of a decrease in bulk, and in-vitro testing revealed that there was a 90% increase in mucoadhesion. Scanning electron microscopy provided evidence that demonstrated that microspheres had a spherical shape. After being soaked for a whole day in a phosphate buffer solution with a pH of 7.4, the medicine was able to be dissolved in 0.1 N hydrochloric acid. In order to treat colon cancer successfully, the use of chitosan microspheres that have an enteric coating is therefore likely to be useful.

Keywords: Colon cancer, 5-Fluorouracil, Eudragit, Chitosan, Microspheres



INTRODUCTION:

Because it is the third most frequent form of cancer worldwide and the second most lethal, colorectal cancer, also known as colorectal cancer (CRC), is a major cause for worry when it comes to the state of public health. CRC can affect either the colon or the rectum. By the year 2020, colorectal cancer has already been attributed to 9.4% of all fatalities caused by cancer. However, it is anticipated that the number of cases of colorectal cancer will more than quadruple across the globe by the year 2035 [1-3], with the least developed countries experiencing the greatest increase in the number of cases diagnosed in their ageing populations as a direct result of the substantial increase. The progression of colorectal cancer can be somewhat unpredictable, despite the fact that it has a complex genetic make-up. For instance, a significant number of somaclonal mutations were discovered in a large sample of CRC cells as a result of variations in the levels of gene expression [1-4].

The anticancer drug known as 5-fluorouracil (5-FU) is often utilised in clinical practice today. Since 1957, it has been applied in the treatment of a variety of cancers, including those of the head and neck, colon, and breasts. The treatment of colon cancer is yet another significant area in which it plays a role. 5-fluorouracil is a kind of anticancer medication known as an antimetabolite. Its mechanism of action involves preventing cancer cells from producing their own nucleic acids and DNA. Since it is effective against a wide variety of solid tumours, it is one of the anticancer medications that is prescribed the most frequently nowadays. Although though 5-FU has poor gastrointestinal (GI) absorption and extremely variable oral bioavailability [5-8], it was frequently administered intravenously in hospitals and clinics.

An inventive method for the administration of drugs is provided by carrier technology. This method involves attaching the medication to a particle (such as microspheres, nanoparticles, or liposomes) that modifies the release and absorption properties of the drug. Because of their diminutive size and their advantageous carrier qualities, microspheres are a prevalent form of the particulate DDS. These innovative DDS have a lot of potential, but their utility is limited because they only stay at the absorption site for a short amount of time. The perfect design would be one that would provide direct

physical contact with DDS as well as absorbent membranes. It's possible that the answer lies in the creation of something called "mucoadhesive microspheres," which contain features related to mucoadhesion. Microparticles or microcapsules having a drug core and measuring between 1 and 1000 m in diameter can be referred to as mucoadhesive microspheres. These microspheres are produced from a mucoadhesive polymer in whole or in part and range in size from 1 to 1000 m. Despite the fact that mucoadhesive properties may be connected to microspheres, the use of microspheres for the targeted and controlled release of pharmaceuticals is favorable. This is the case even though these qualities can be attached to microspheres. It is possible to develop a mucoadhesive drug delivery system for buccal, oral, vaginal, nasal, rectal, and ocular routes of administration due to the fact that the mucosal layer provides potential places for bioadhesive system attachment [9-13]. Mucosal layer provides potential places for bioadhesive system attachment [9-13].

The polymer known as Eudragit S-100 is made up of methylmethacrylic acid and methyl methacrylate in proportions that are identical to one another. Because of this polymer's resistance to both pH and water, it has been utilised in the development of a variety of distinct sustained-release formulations. The typical weight of a molecule is around 150,000 grammes. According to the book USP NF 23, the results of the anionic copolymerization of methyl methacrylate and Methacrylic acid are referred to as eudragit L and S. Eudragit L (Type A) contains about one-one thousandth as many free carboxyl groups as Eudragit S (Type B), and vice versa. (Type B). Both types of polymers degrade quickly in settings that range from slightly basic to moderately alkaline (pH 6-7),

3158



resulting in the formation of salts that react with the gastric medium to generate film coatings that are insoluble. They are supplied in a plasticizer-free solution at a concentration of 12.5% in propan-2-ol. Although while polymers that are used for colon targeting need to be stable in the acidic stomach and first portion of the small intestine, they also need to be able to breakdown in the neutral or slightly alkaline terminal ileum, especially in the vicinity of the ileocecal junction. By dispersing the medication across the whole of the large intestine, these approaches increase the effectiveness of colon-focused delivery systems [14-16].

MATERIAL AND METHODS:

Materials:

Khandelwal labs Pvt. Ltd. provided complimentary five-fluorouracil distribution (Thane, India). SD Fine Chemicals was the supplier of the chitosan that went into the Span-80 (Mumbai, India). We make use of Eudragit S-100, which is a product that was created by Ranbaxy Laboratories Ltd. and then given to us for free (Haryana, India). Both the glutaraldehyde and the paraffin oil came from Sigma-Aldrich Chemie. These were the company's original suppliers. Notwithstanding this, SD Fine Chemicals was the company that provided the acetic acid. E. Merck was the one who offered the scientists cyclohexane, methanol, and dichloromethane to use in their experiments (Darmstadt, Germany). The remaining reagents were of a quality that either met or surpassed the requirements for their usage in analytical procedures.

Methods:

Method of preparation of Chitosan Microspheres:

Either the complicated approach of chemical denaturation or the more straightforward procedures of emulsification and phase separation can be used to produce microspheres. The former method is more difficult to comprehend. The polypropylene beaker initially had 250 millilitres of liquid, and then an additional 100 millilitres of normal paraffin oil was poured to it. In a solution of 3.5% weight-per-volume chitosan, 50 mg of 5-fluorouracil was injected into 3 mL using a hypodermic syringe with a 22-gauge needle.

Chitosan was dissolved in 1% acetic acid in oil, and the resulting mixture was stirred with 1 mL of span-80 before being used to make this solution. In addition to this, the paraffin oil was mixed using a high-speed stirrer that had propellers attached to it at a rate of 2,000 revolutions per minute. Before adding 0.25 mL of glutaraldehyde, the oil was mixed with the full chitosan solution for fifteen minutes at the same speed before adding the glutaraldehyde. Preserving the same rate of one thousand revolutions per minute for the stirring action. After waiting for thirty minutes, 0.50 millilitres of glutaraldehyde was added to the mixture while it was continuously stirred. Once an hour had passed, the identical activity was repeated once again. In this particular instance, the procedure was terminated when we added the remaining glutaraldehyde and stirred for a total of one hour. Following a period of 24 hours, the chitosan microspheres that were produced sank to the bottom of the paraffin oil due to the weight of the microspheres. Microspheres were discovered when the clear supernatant was removed and the residue was washed four or five times with diethyl ether. This process was repeated until the residue was clean. Following the completion of the last washing step, the microspheres were allowed to air dry. After that, the powder was gathered up and stored in a dark, dry, and cold location [17–19].

Preparation of Eudragit Coated Microspheres

Using a method that involved the evaporation of the solvent, Eudragit was used to coat the chitosan microspheres. Developing microspheres that are packed with chitosan (B2) and then dispersing them in Eudragit S-100 (500 mg of Eudragit in ethanol: acetone 2:1). In order to create this emulsion, 70 millilitres of liquid paraffin oil containing 1% volume/volume of span 80 were combined with Eudragit S-100 and core microspheres, and then the mixture was spun at a high speed. After around three to four hours of steady stirring, the solvent in question was completely soaked up. Using a method that involved filtration, microspheres were then encapsulated after being screened. After having the liquid paraffin removed from them by washing them three to four times in n-hexane, they were left out in the air to dry for a period of

3159



twenty-four hours. In preparation for future studies, we put aside some microspheres coated with Eudragit [20-23].

EVALUATION PARAMETERS

Morphological Study of Eudragit Coated Microspheres

Using Digital Technology into Optical Microscopes to ensure that Eudragit-coated chitosan spheres were spherical and non-sticky, micrographs of the spheres were examined. Microspheres might be produced by combining eudragit with a 3.5% chitosan solution and spinning the resulting mixture at 2000-2500 rpm [24, 25].

Scanning Electron Microscopy

By using scanning electron microscopy, both pectin microspheres and pectin microspheres that had been coated with eudragit were compared regarding their dimensions and contours (SEM). In order to conduct a SEM examination, a sample of the slurry was dusted onto a piece of double-sided tape, and then the tape was glued to a piece of aluminium. After that, a gold sputter module was used inside of a high-vacuum evaporator with an argon atmosphere so that 300 microns of gold could be sputtered onto the tips. After scanning random samples with a Jeol JSM-6400 scanning electron microscope (Tokyo, Japan), photomicrographs were created and made. [26]

Determination of Percentage Drug Entrapment

Calculations were done for each batch based on the amount of substance that was seized (PDE). During the theoretical drug loading calculation, it was assumed that all of the drug that was present in the Eudragit chitosan solution had been integrated into the microspheres and that none of it had been lost. After putting 25 mg of Eudragit microspheres in a 25 mL volumetric flask and weighing the mixture, we were able to calculate the appropriate drug loading for the formulation. Methanol, in total volume of 25 millilitres, was poured into the container until it was entirely full. While we let the suspension to stay out at room temperature for twenty-four hours, we did give it a shake every so often. After centrifuging the sample between 2000 and 3000 revolutions per minute (rpm), the concentration of the drug in the supernatant was measured using UV Spectrophotometry at 266 nm [21, 22].

Determination of Particle size and particle size distribution

The behaviour of eudragit-coated microspheres during release is substantially impacted by the particle size of the microspheres. Using a particle size Analyser, we were able to measure the particle size distribution of Eudragit-coated microspheres in distilled water over the course of 10 mg and 2 mL. (Malvern Master Sizer, model E, UK). [25–26] A measure known as the Z-average was frequently utilised in the process of describing the particles (in nanometers).

Determination of Zeta potential

The zeta potential may be used to examine the surface charges that are present on microspheres. It is envisaged that mucoadhesive delivery methods would have a high zeta potential. [Citation needed] The surface charge of microparticles in deionized water was measured with a Zeta master (made in Malvern, United Kingdom) and laser Doppler anemometry [27, 28].

IR Spectra of Eudragit coated microspheres

The infrared spectroscopy was performed with the use of the FT/IR Spectrometer, which was located at the MPCST Quality Assurance Laboratory. The validity of the study was determined by examining the congruence between the expected values and the correlation that existed between the transmittance percentage and the frequency (cm⁻¹). [24, 25] Bruker conducted an investigation on a sample of eudragit-coated microspheres.

DSC Studies

The DSC analysis was conducted to determine whether or not 5 fluorouracil was compatible with the excipients (chitosan and Eudragit S100) that were utilised in the production of the microspheres. The Pyris 6 DSC makes use of indium as the standard DSC reference material in its analysis. We studied what would happen to Eudragit S100 using a 5FU thermometer and subjected it to temperatures ranging from -20 to +350 degrees Fahrenheit. [29, 30] A comparison was done between the peaks of thermogram generated with 5 FU and different fillers and those made with the pure substance.

In vitro Release Profile of 5-

FU from Eudragit Coated Microspheres

3160



Microspheres that had been coated with eudragit were put through tests to determine whether or not they could release medications when placed in an environment that mimicked the acidity of the stomach (SGF). In accordance with USP XXIII, the paddle method was utilised to conduct an analysis of the dissolution of a microsphere-based medicine (model Sentwin, India). In order to simulate the viscosity of blood, dialysis membranes were immersed in a solution that included one hundred milligramme of microspheres (SGF). The temperature range for spinning the material was 370 degrees Celsius (plus or minus 0.50 degrees Celsius), and the revolutions per minute (rpm) was 100. Research on the ease with which medications may be dissolved was carried out in the most perfect conditions in the kitchen sink. Adjustments were made to the pH of the dissolving solution at regular intervals so that we could imitate the acidic and alkaline environments of the stomach and small intestine, respectively. With 0.1 N HCL, the pH of the solution was kept at 1.2 for the entirety of the allotted time. Once the pH of the dissolving solution was brought down to 4.5 with 1.0M sodium hydroxide, an additional 1.7 grammes of potassium hydroxide (KH₂PO₄) and 2.2 grammes of sodium hydrogen phosphate (Na₂HPO₄.2H₂O) were added. It was decided to continue monitoring the discharge rate for an additional two hours. After adjusting the solution with 0.1 N NaOH for four hours, the pH was brought up to 7.4, where it remained stable over the following 24 hours. After being taken from the solvent at various intervals, the samples were then diluted using a pipette. When the same quantity of SGF was administered instead, there was no discernible change in the size of the receptor. Using UV spectrophotometry, we were able to calculate the rate at which FU is released by plotting the cumulative drug release against the passage of time.

***In-vivo*ReleaseProfileof5-FUfromEudragitCoatedMicrospheres**

In the actual experiments that were carried out, albino rats were used. Food and water were never in limited supply for the rats at any point in time. The experiment was carried out using rats of a healthy weight, and no medications were given to the animals in any way. Following careful consideration, the ethics committee gave its blessing to proceed with this treatment.

In order to investigate the effects of time-dependent dosing with pure treatment (5-FU) and Eudragit-coated chitosan microspheres, Albino rats were employed in the study. The analysis of the release kinetics *In-vivo* required the construction of a calibration curve that linked the concentration of the drug in the plasma to the height of the peak. This curve was then employed. In order for the drug to be dissolved, 10 millilitres of the phosphate buffer with a 7.4 pH was necessary. Hence, a stock solution with a concentration of 1 g/mL was created. After adding 10 mL of water to a volumetric flask that was initially filled with 10 mL, 1 mL of the stock solution was pipetted in.

The chromatography was carried out with the assistance of a highperformance liquid chromatography (HPLC) system that was outfitted with a ShimadzuR 1100 series RP C-18 column that was made in Japan (HPLC column). 7.4 was the pH of the phosphate buffer that was utilised in the investigation of 5-fluorouracil. At a rate of one milliliter per minute, mobile phase was injected into the column from the solvent reservoir. Essential components of the apparatus, each injection loop has the capacity to hold 20 g/mL. The length of time it takes to have a thought is 3.51 minutes on average, with the median time being 2.33 minutes. A standard curve was constructed with a concentration range of 10-50 g/mL as the variable of interest.

3161

Table 1: Standard curve of 5FU by HPLC

Sr.No.	Concentration(μ g/mL)	Area
1.	0	0
2.	10	1847788
3.	20	3594180



4.	30	5741272
5.	40	7897365
6.	50	9835458

There were so many of the albino rats that we split them up into two groups of three. Eudragit was extracted from the materials and utilised to coat microspheres for future experiments. It was the other rats that served as the "control" group. Microscopic spheres coated with eudragit floated in a bath of carboxymethyl cellulose (CMC). The microsphere suspension was orally delivered to the third group. Every two, four, six, eight, ten, and twenty-four hours, a prick to the tail vein was made to draw half a milliliter of blood. The blood pool technique was used to collect the blood samples in 0.9% normal saline. To prevent blood from clotting during collection, 0.1 ml of heparin was administered into Eppendorf tubes. After centrifuging the samples at 5000 rpm for 15 minutes to separate the medication, the concentration was determined

using high performance liquid chromatography (HPLC) [31-32].

RESULT AND DISCUSSION:

EudragitCoatedChitosanMicrospheres

Chitosan microspheres were then coated with Eudragit S-100 as the solvent was allowed to evaporate (B2). We were able to do this by first emulsifying the core microsphere dispersions in liquid paraffin using span-80, and then dispersing chitosan microspheres in a solution containing Eudragit S-100. The microspheres were put aside for later use after first having their capsules opened, then being cleaned in n-hexane, and then being dried at 600 degrees Celsius for one hour. After this step, the generated Eudragit-coated microspheres were tested to see whether or not they could function well as enteric coated delivery vehicles.

Evaluation Parameters of Eudragit Coated Microspheres

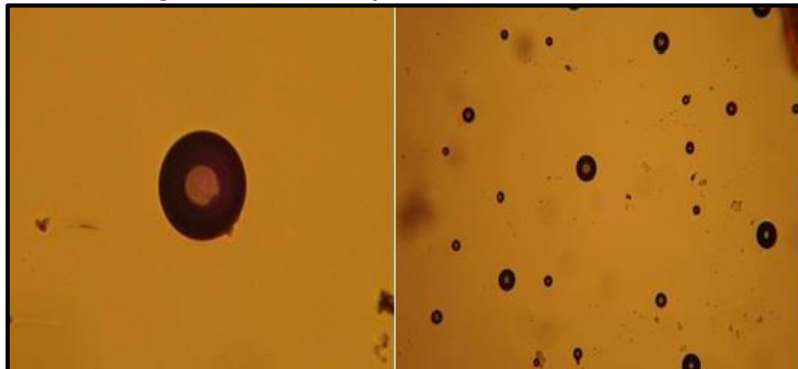


Figure 1: Morphological study of Eudragit coated microspheres

Scanning Electron Microscopy

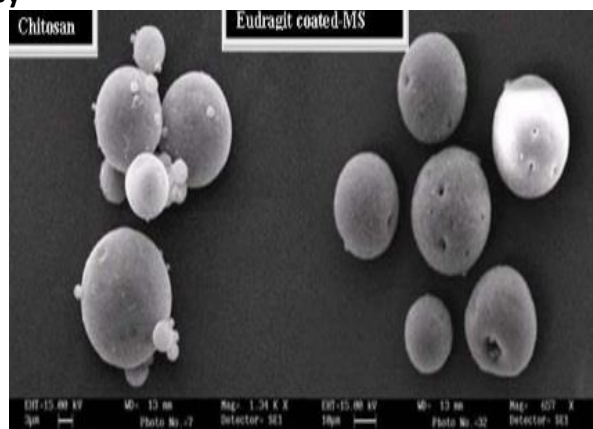


Figure 2: Phase contrast photographs of Eudragit coated microspheres

3162



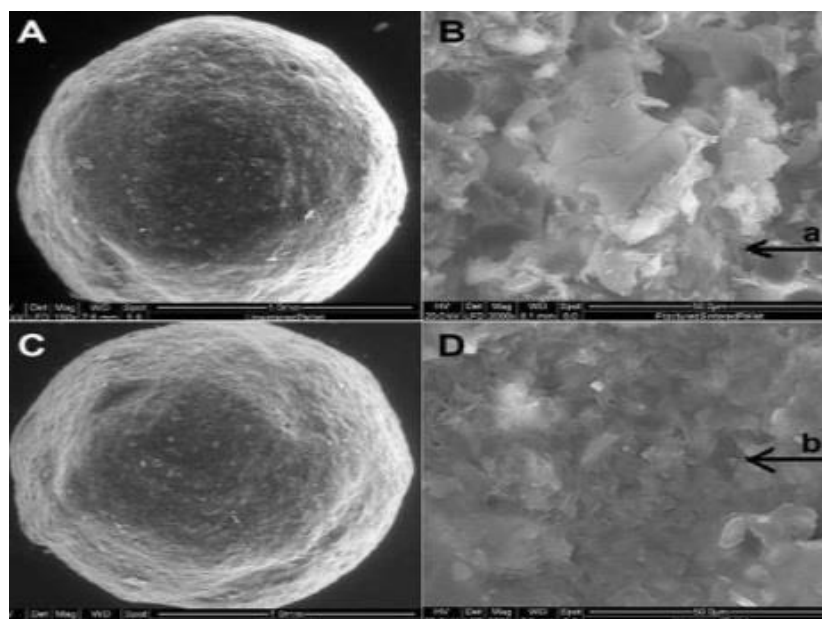


Figure 3: SEM photographs of Eudragit coated microspheres

In phase contrast pictures, it was possible to make clearly the microspheres' spherical form, the absence of any clumping, as well as their inner structure and outside coating. Scanning electron microscopy was utilised in order to do an analysis on the topography as well as the solid dispersion of the physical combination (SEM). The JSM6400 scanning electron microscope with a 10,000X magnification was used to take the photos, and room temperature was maintained throughout the process. The conductivity of the solid dispersions was enhanced by sputtering gold onto the surface of the particles. As a result,

this made scanning much easier. Figures 2 and 3 contain photomicrographs that are exemplary examples of the phenomenon being studied. Electron microscopy was used to investigate microspheres coated with Eudragit. The results showed that the crystals were intact throughout the investigation. Scanning electron microscopy showed that chitosan microspheres are clear, spherical, and have a rough outer surface due to crystals on the surface of the medication [23-28]. Chitosan microspheres also have a smooth interior.

3163

Other Evaluation Parameters of Eudragit Coated Chitosan Microspheres

Table 2: Evaluation parameters of eudragit coated microspheres

Sr.No.	Evaluation parameters	Eudragit coated Microspheres
1.	Percentage drug entrapment	30.69
2.	Particle size and size distribution	11365nm
3.	Zeta potential	+39.7mV
4.	Swelling properties	No significant

Entrapment was achieved at a rate of 30.69 percent using microspheres coated with eudragit. The quantity of the cross-linking agent that is used, the amount of time that it is permitted to set, as well as the speed at which it is stirred, are all elements that contribute to the quality of the microspheres' coating and entrapping. The particle size of chitosan

microspheres grew to 11365 nm when Eudragit was added to them. According to the findings, the particle size distribution of the Eudragit-coated microspheres was quite narrow. Because of the positive charge that is present on the surface of the microspheres, the zeta potential of microspheres that have been coated with eudragit is +39.7 mV.



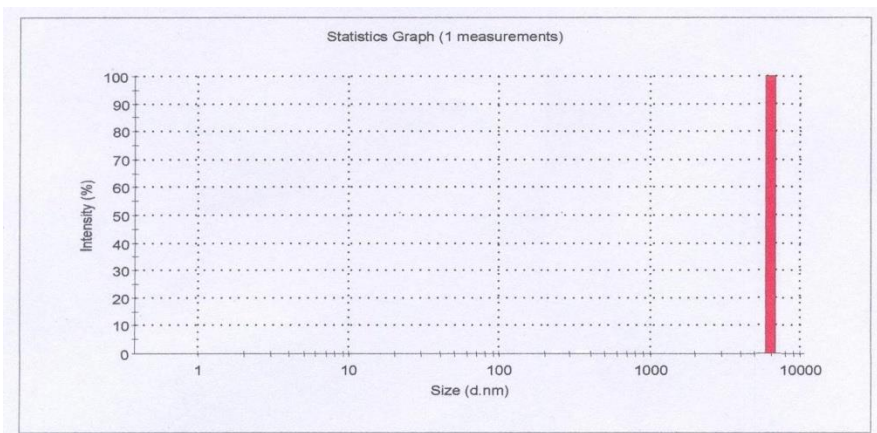


Figure 4: Particle size distribution of eudragit coated microspheres

IR Spectra of Eudragit Coated Microspheres

Figure 5: IR Spectra of Eudragit coated microspheres

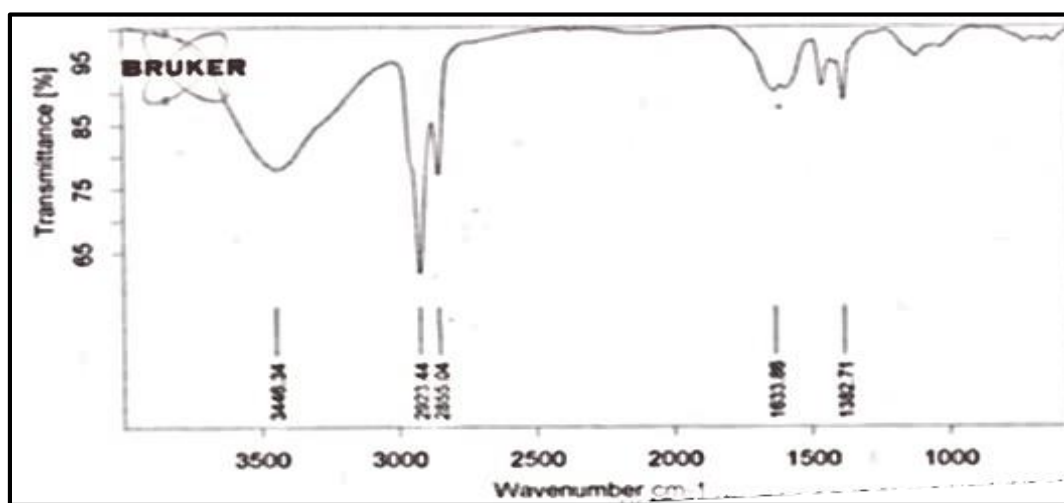


Table 3: IR Spectral characteristics of Eudragit coated microspheres of 5-FU

Sr.No.	WaveNumber (cm ⁻¹)	Interpretation
1.	2923.44	NH Stretching
2.	1633.86	C=O Stretching
3.	1382.71	CH in plane deformation

When the data was analyzed for its clinical relevance, it was found that the 5-FU-loaded Eudragit-coated microspheres had peaks that were equivalent to those of the pure medicine. The medicine was successfully loaded into Eudragit-coated chitosan microspheres, and results showed that there was no interaction between the polymer and pure medication.

Differential Scanning Calorimetry Studies

DSC can determine how the sample is interacting by monitoring the disappearance or presence of thermal events, such as endothermic or

exothermic peaks. When conditions are favorable, peaks can expand and temperatures can change. This may or may not suggest a substantial level of interaction between them. Compatibility is possible so long as there is not a great deal of complex alteration and the thermal properties do not vary significantly. It was easy to determine how well a medicine interacted with its diluents using this method. Figure 6 depicts the thermogram of 5 FU, Eudragit S100, and their mixtures from 20 to 3500 degrees Celsius. The endothermic peak of pure 5FU was



between 180 and 850 degrees Celsius. You can get 5FU and Eudragit S 100 thermogram at 242.590C simultaneously. When the endothermic peaks are generated at roughly the same temperature for both pure pharmaceuticals and mixtures, this indicates that there is no incompatibility between the drug and the excipient. The DSC values suggested that the medication would be stable and mix well with

the other components of the formulation; hence, this conclusion remained valid. Figure 6 depicts the differential scanning Calorimetry (DSC) pattern of the final formulation. This endothermic peak occurs between 180 and 850 degrees Fahrenheit, the melting temperature of both uncoated chitosan microspheres and free 5-fluorouracil.

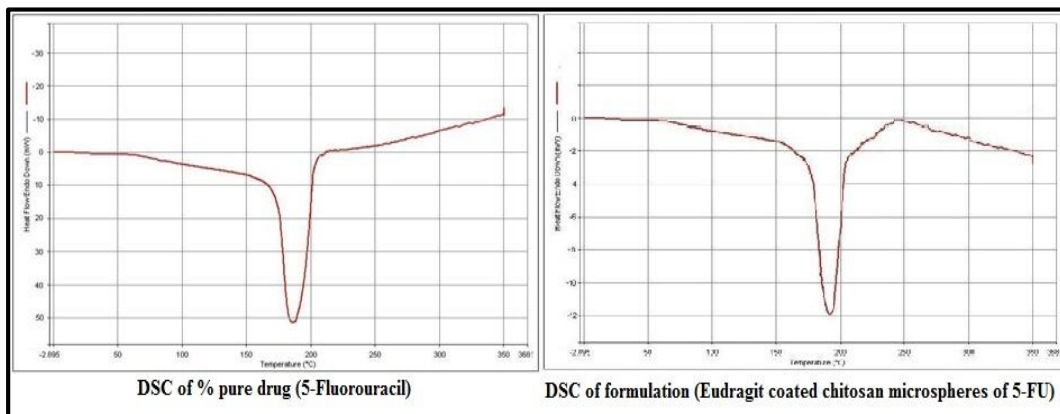


Figure 6: DSC for Pure drug and formulation

***In-vitro*ReleaseProfileof5-FUfromEudragitCoatedMicrospheres**

Little capsules containing chitosan core microspheres were the primary target of this formulation method. Only in the colon, where the pH is more than 7.0, does the coated polymer, Eudragit S-100, melt, allowing the drug

to be absorbed. There is hope that chitosan placed at the location of drug release will work once the enteric coating has degraded. When the stomach pH was barely 2.0, no medicine was absorbed for two hours. None of the drugs were administered at a pH higher than the polymer could handle (Figure 7) [28-30].

3165

Table 4: *In vitro* release profile of 5-Fluorouracil

Time(hrs.)	Sq.rootoftime	Logtime	Cumulative % drugrelease	Cumulative % drugremain	Logcumulative % drugrelease	Logcumulative % drugremain
1.	1	0	1.32	98.68	0.1205	1.994
2.	1.414	0.3010	4.18	95.82	0.6211	1.981
3.	1.732	0.4771	5.78	94.22	0.7619	1.974
4.	2.000	0.6020	7.46	92.54	0.8727	1.966
5.	2.236	0.6989	10.25	89.75	1.010	1.953
6.	2.449	0.7781	18.37	81.63	1.264	1.911
7.	2.645	0.8450	35.69	64.31	1.5525	1.8082
8.	2.828	0.9030	58.23	41.77	1.7651	1.620



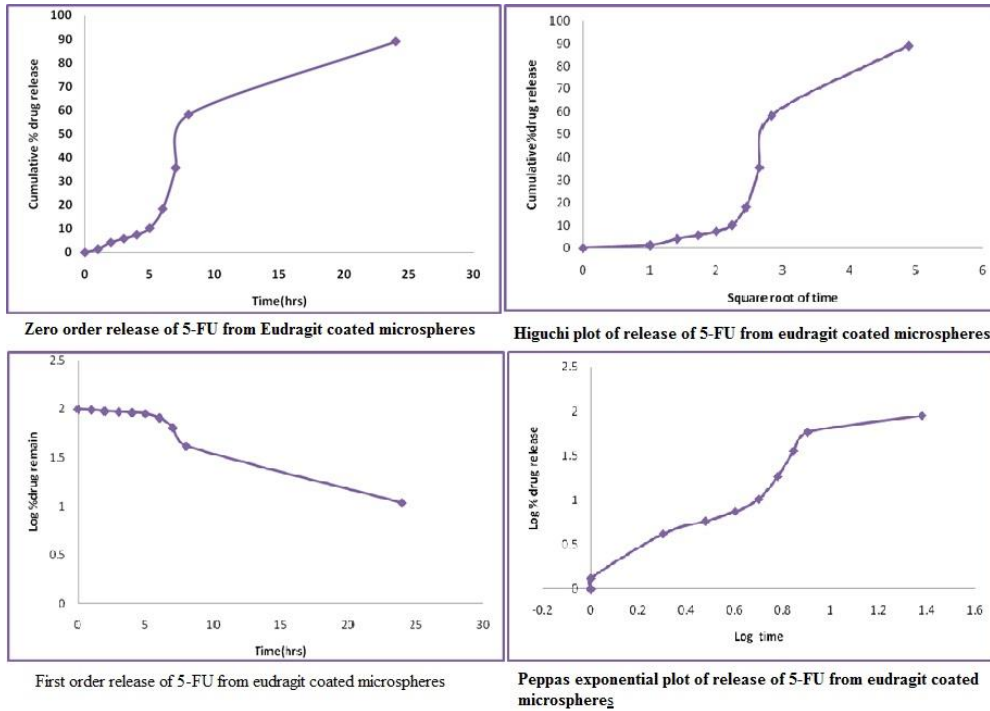


Figure 7: In-vitro release kinetic parameters of Eudragit coated microspheres

Table 5: In vitro release kinetic parameters of Eudragit coated microspheres

Sr.No.	Name of Model	Eq. for St. line	Value R ²
1.	Zero Order	Y = 4.025x - 1.109	R ² = 0.8566
2.	Higuchi release	Y = 20.46x - 20.33	R ² = 0.799
3.	First Order	Y = 0.042x + 2.081	R ² = 0.947
4.	Peppas release	Y = 1.491x + 0.099	R ² = 0.939

Analysis of the drug released data

Zero-order rates are used to talk about systems where the rate of drug release doesn't change based on how much drug is present. Figure 7 shows the relationship between the total amount of drug released and the amount of time. Figure 7 is a graph that shows how the concentration of the system's release affects the first order rate. This rate is used to explain how systems release things. Higuchi's model says that the rate of drug release from an insoluble matrix is proportional to the square root of time. Figure 7 shows the Higuchi square root kinetics. The regression coefficients for the zero-order, first-order, and Higuchi models, in order, were found to be 0.8566, 0.947, and 0.799, respectively. The best way to describe the *In-vitro* drug release of 5-FU microspheres was with first order equations, which had the most linear plot, and then Peppas' model. So, Peppas' model and the

way things started out seem to work with the release. So, the main way the drug got out of the microspheres was for it to diffuse out of them. Several release equations were used to describe the rate of drug release from these microspheres based on the results of *In-vitro* release studies. Models of kinetics were used, such as first order, zero-order, Higuchi release, and Korsneyer and Peppas. Table 5 shows the results of linear regression analyses. By looking at the R2 coefficient of determination, we were able to figure out that both the core microspheres and the coated microspheres used the diffusion control mechanism, which led to a controlled release of the drug. As shown by the R2 value of 0.947, the 5-FU release from the Eudragit-coated microspheres follows the First-order release.

In-vivo Release Profile of 5-FU from Eudragit Coated Microspheres



It was necessary to create a calibration curve between the drug concentration in the blood and the peak area in order to investigate the release kinetics *In-vivo*. A phosphate buffer solution of pH 7.4 was added to the drug, totaling 10 millilitres. As a result, a 10 g/mL stock solution was prepared. Then, using the transfer pipette, 1 ml of the stock solution was pipetted into the final 10 ml of solution in the volumetric flask [21-25]. The chromatography was performed using a high performance liquid chromatography (HPLC) system equipped with a ShimadzuR 1100 series RP C-18 column manufactured in Japan (HPLC column). The pH of the equation of line was found to as : $Y=198495x-143021$ Where x =Concentration Value of $R^2=0.9987$ Intercept=143021

the phosphate buffer used in this study of 5-fluorouracil was 7.4. The solvent reservoir pumped mobile phase into the column at a rate of 1 ml/min. important pieces of kit, each injection loop could store 20 g/mL. The average duration of a thought process is 3.51 minutes, with a median of 2.33 minutes. Table 6 displays the standard curve we generated by applying Beer's and Lambert's laws to a concentration range of 10-50 g/mL; this curve demonstrates that the corresponding equation is linear. In future research, this concentration range should be employed.

Table 6: Standardcurveof5FUby HPLC

Sr.No.	Concentration($\mu\text{g/mL}$)	Area
1.	0	0
2.	10	1947090
3.	20	3894180
4.	30	5841270
5.	40	7788360
6.	50	9735450

3167

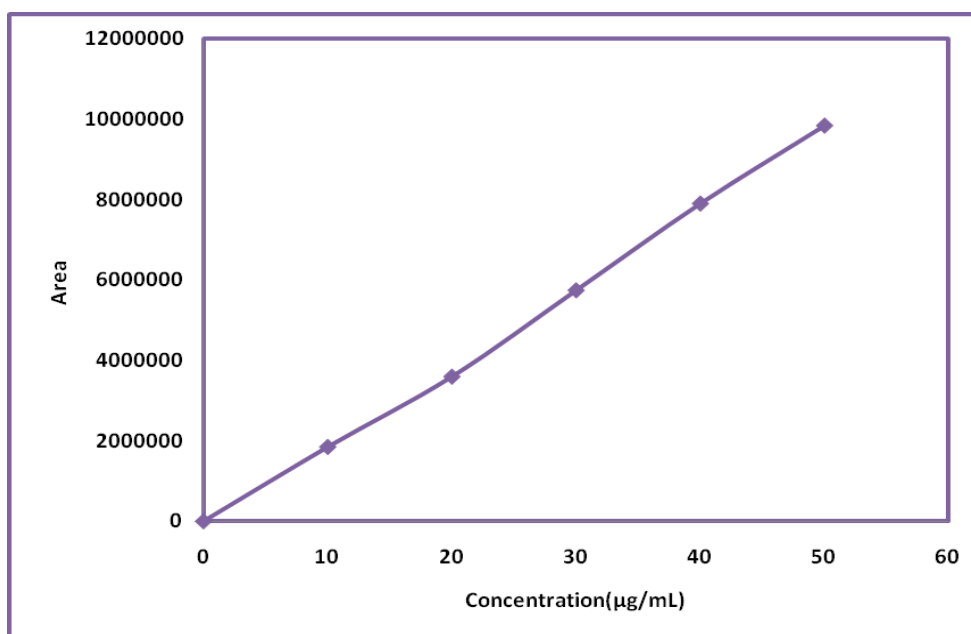


Figure 8: Standardcurveof5FUbyHPLC

Table 7: *In-vivo* release profile of 5-FU from Eudragit coated microspheres

Sr.No.	Time(hrs.)	Concentration($\mu\text{g/mL}$)
1.	0	0



2.	2	2.596
3.	4	3.432
4.	6	6.047
5.	8	20.272
6.	10	22.362
7.	24	38.48

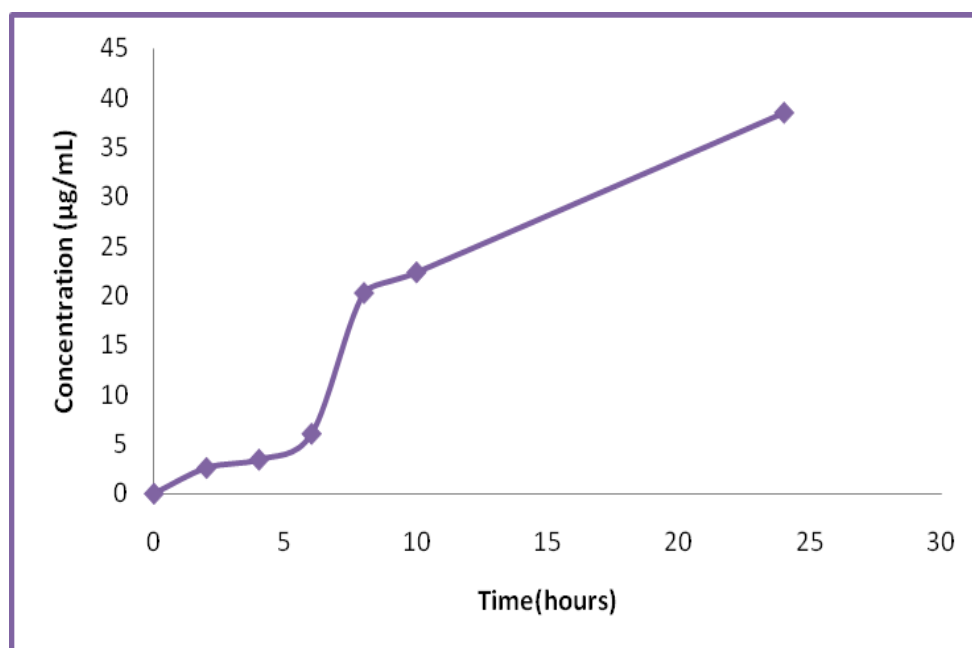


Figure 9: *In-vivo* release of 5-FU from Eudragit-coated microspheres

Time-course analysis of 5-FU blood levels following oral administration of eudragit-coated microspheres is depicted in Figure 9. Researchers utilised blood samples to observe the release of the extended-release medication. The half-life of this medication is significantly longer than average. Up to 24 hours of blood levels can be tested. Comparing *In-vivo* and *In-vitro* data, it was revealed that the rate of release increased. The enzymes probably dissolved the polymer and stripped it of its coating, which explains the result. In laboratory tests, Eudragit S-100 demonstrated poor solubility in acid. As a result, the coated microspheres gradually released the medicine over a period of four to five hours. The medication was rapidly soluble, and the stomach's acidity removed its protective coating, resulting in a dramatic increase in the drug's blood concentration within just 4-5 hours (above 7). As the blood medication concentration rose and remained stable for up to 24 hours, this indicates that the delivery mechanism may keep

releasing pharmaceuticals indefinitely. Based on preliminary experimental studies [24-30], it appears that these Eudragit-coated chitosan microspheres will be able to target the colon since Eudragit S-100 dissolves best in the pH of the colon.

CONCLUSION

Our results contribute to the growing body of evidence suggesting that eudragit-S-100-coated dextran microspheres may be useful for the targeted delivery of 5-FU. This method of delivery would allow for a gradual and manageable release of 5-FU from the microspheres. Studies of the drug's pharmacokinetics and organ distribution demonstrated that it was predominantly localized in colon tissue and had few systemic effects. Because of how rapidly it is absorbed in the upper gastrointestinal tract, 5-FU at conventional dosages, such as pills, might induce undesirable side effects. There may be less of an impact if the medication exits the body in a



variety of places. The results confirmed that Eudragit-coated 5-fluorouracil (FU) chitosan microspheres may be used to target drug delivery to the colon.

Acknowledgments

The authors thank RajarshiShahu College of pharmacy, Buldana for providing facilities to conduct the research.

Authors Funding

None

Conflicts of interest

There are no conflicts of interest among all the authors with publication of manuscript.

REFERENCE

1. Center MM, Jemal A, Smith RA, Ward E. Worldwide variations in colorectal cancer. CA: a cancer journal for clinicians. 2009 Nov; 59(6):366-78.
2. Ten Hoorn S, de Back TR, Sommeijer DW, Vermeulen L. Clinical value of consensus molecular subtypes in colorectal cancer: a systematic review and meta-analysis. JNCI: Journal of the National Cancer Institute. 2022 Apr; 114(4):503-16.
3. Wu Y, Yang S, Ma J, Chen Z, Song G, Rao D, Cheng Y, Huang S, Liu Y, Jiang S, Liu J. Spatiotemporal Immune Landscape of Colorectal Cancer Liver Metastasis at Single-Cell Level Spatial and Cellular Landscape of CRLM. Cancer discovery. 2022 Jan 1; 12(1):134-53.
4. Sinicrope FA. Increasing incidence of early-onset colorectal cancer. New England Journal of Medicine. 2022 Apr 21; 386(16):1547-58.
5. Qin L, Liang F, Li Y, Wu J, Guan S, Wu M, Xie S, Luo M, Ma D. A 2D porous zinc-organic framework platform for loading of 5-fluorouracil. Inorganics. 2022 Nov 9; 10(11):202.
6. Esrafil MD, Khan AA. Alkali metal decorated C 60 fullerenes as promising materials for delivery of the 5-fluorouracil anticancer drug: a DFT approach. RSC advances. 2022; 12(7):3948-56.
7. Nguyen CH, Banh KS, Dang CH, Nguyen CH, Nguyen TD. β -cyclodextrin/alginate nanoparticles encapsulated 5-fluorouracil as an effective and safe anticancer drug delivery system. Arabian Journal of Chemistry. 2022 Jun 1; 15(6):103814.
8. Barary M, Hosseinzadeh R, Kazemi S, Liang JJ, Mansoori R, Sio TT, Hosseini M, Moghadamnia AA. The effect of propolis on 5-fluorouracil-induced cardiac toxicity in rats. Scientific Reports. 2022 May 23; 12(1):8661.
9. Surya R, Mullassery MD, Fernandez NB, Thomas D, Jayaram PS. Synthesis and characterization of a pH responsive and mucoadhesive drug delivery system for the controlled release application of anti-cancerous drug. Arabian Journal of Chemistry. 2020 May 1; 13(5):5262-76.
10. Kumar A, Naik PK, Pradhan D, Ghosh G, Rath G. Mucoadhesive formulations: Innovations, merits, drawbacks, and future outlook. Pharmaceutical Development and Technology. 2020 Aug 8; 25(7):797-814.
11. Li X, Chen K, Ji X, Yuan X, Lei Z, Ullah MW, Xiao J, Yang G. Microencapsulation of poorly water-soluble finasteride in polyvinyl alcohol/chitosan microspheres as a long-term sustained release system for potential embolization applications. Engineered Science. 2020 Dec 14; 13(2):106-20.
12. Zeng D, Yu C, Fan Q, Zeng J, Wei L, Li Z, Yang K, Ji H. Theoretical and experimental research of novel fluorine doped hierarchical Sn3O4 microspheres with excellent photocatalytic performance for removal of Cr (VI) and organic pollutants. Chemical Engineering Journal. 2020 Jul 1; 391:123607.
13. Bui TH, Lee W, Jeon SB, Kim KW, Lee Y. Enhanced Gold (III) adsorption using glutaraldehyde-cross-linked chitosan beads: Effect of crosslinking degree on adsorption selectivity, capacity, and mechanism. Separation and Purification Technology. 2020 Oct 1; 248:116989.
14. Thakral NK, Ray AR, Majumdar DK. Eudragit S-100 entrapped chitosan microspheres of valdecoxib for colon cancer. Journal of Materials Science: Materials in Medicine. 2010 Sep; 21:2691-9.
15. Mehta R, Chawla A, Sharma P, Pawar P. Formulation and *In-vitro* evaluation of Eudragit S-100 coated naproxen matrix tablets for colon-targeted drug delivery system. Journal of advanced pharmaceutical



- technology & research. 2013 Jan; 4(1):31.
16. Garala KC, Shinde AJ, Shah PH. Formulation and in-vitro characterization of monolithic matrix transdermal systems using HPMC/Eudragit S 100 polymer blends. *Int J Pharm Sci.* 2009; 1(1):108-20.
 17. Xia H, Li A, Man J, Li J, Li J. Fabrication of multi-layered microspheres based on phase separation for drug delivery. *Micro machines.* 2021 Jun 19; 12(6):723.
 18. Jiang H, Hu X, Li Y, Ngai T. A green and facile strategy for the fabrication of all-natural porous proteinaceous microspheres. *Materials Chemistry Frontiers.* 2021; 5(10):3897-902.
 19. Li G, Yu Y, Han W, Zhu L, Si T, Wang H, Li K, Sun Y, He Y. Solvent evaporation self-motivated continual synthesis of versatile porous polymer microspheres via foaming-transfer. *Colloids and Surfaces A: Physicochemical and Engineering Aspects.* 2021 Apr 20; 615:126239.
 20. Paharia A, Yadav AK, Rai G, Jain SK, Pancholi SS, Agrawal GP. Eudragit-coated pectin microspheres of 5-fluorouracil for colon targeting. *AapsPharmscitech.* 2007 Mar; 8:E87-93.
 21. Chawla A, Sharma P, Pawar P. Eudragit S-100 coated sodium alginate microspheres of naproxen sodium: formulation, optimization and *In-vitro* evaluation. *Acta pharmaceutica.* 2012 Dec 31; 62(4):529-45.
 22. Ramasamy T, Ruttala HB, Shanmugam S, Umadevi SK. Eudragit-coated aceclofenac-loaded pectin microspheres in chronopharmacological treatment of rheumatoid arthritis. *Drug delivery.* 2013 Feb 1; 20(2):65-77.
 23. Zhang L, Cao F, Ding B, Li Q, Xi Y, Zhai G. Eudragit® S100 coated calcium pectinate microspheres of curcumin for colon targeting. *Journal of microencapsulation.*
 24. Ibrahim M, Sarhan HA, Naguib YW, Abdelkader H. Design, characterization and *In-vivo* evaluation of modified release baclofen floating coated beads. *International Journal of Pharmaceutics.* 2020 May 30; 582:119344.
 25. Souto EB, Ana RD, Souto SB, Zielińska A, Marques C, Andrade LN, HorbańczukOK, Atanasov AG, Lucarini M, Durazzo A, Silva AM. *In-vitro* characterization, modelling, and antioxidant properties of polyphenon-60 from green tea in Eudragit S100-2 chitosan microspheres. *Nutrients.* 2020 Mar 31; 12(4):967.
 26. Ibrahim M, Sarhan HA, Naguib YW, Abdelkader H. Design, characterization and *In-vivo* evaluation of modified release baclofen floating coated beads. *International Journal of Pharmaceutics.* 2020 May 30; 582:119344.
 27. Deshmukh R, Harwansh RK, Paul SD, Shukla R. Controlled release of sulfasalazine loaded amidated pectin microparticles through Eudragit S 100 coated capsule for management of inflammatory bowel disease. *Journal of Drug Delivery Science and Technology.* 2020 Feb 1; 55:101495.
 28. De Leo V, Di Gioia S, Milano F, Fini P, Comparelli R, Mancini E, Agostiano A, Conese M, Catucci L. Eudragit S100 entrapped liposome for curcumin delivery: Anti-oxidative effect in Caco-2 cells. *Coatings.* 2020 Jan 30; 10(2):114.
 29. Almurisi SH, Akkawi ME, Chatterjee B, Sarker MZ. Taste masking of paracetamol encapsulated in chitosan-coated alginate beads. *Journal of Drug Delivery Science and Technology.* 2020 Apr 1; 56:101520.
 30. Maestrelli F, Cirri M, Corti G, Mennini N, Mura P. Development of enteric-coated calcium pectinate microspheres intended for colonic drug delivery. *European journal of pharmaceutics and bio pharmaceutics.* 2008 Jun 1; 69(2):508-18.
 31. Contado C, Caselotto L, Mello P, Maietti A, Marvelli L, Marchetti N, Dalpiaz A. Design and formulation of Eudragit-coated zein/pectin nanoparticles for the colon delivery of resveratrol. *European Food Research and Technology.* 2020 Dec; 246:2427.
 32. Bogataj M, Mrhar A, Kristl A, Kozjek F. Preparation and evaluation of Eudragit E microspheres containing bacampicillin. *Drug Development and Industrial Pharmacy.* 1989 Jan 1; 15(14-16):2295-313.



FORMULATION AND COMPARISON BETWEEN TWO METHODS FOR 5-FLUOROURACIL-LOADED CHITOSAN MICROSPHERES

Mr. Dipak V. Bhusari^{1*}, Dr. Shailesh M. Kewatkar², Amol Nanduji Jaybhaye³, Puja G. Vyawahare⁴, Yogita Mahesh Vispute³, Dr. Manmeet S. Saluja⁵, Dr. Shirish P. Jain², Mrs. Neelam M Patel⁶

¹ Department of Pharmacy Sunrise University Alwar, Rajasthan, India – 301028

² Rajarshi Shahu College of Pharmacy, Buldana, Maharashtra, India – 443001

³ Western Kentucky University, Bowling Green, KY, USA

⁴ Yadavrao Tasgaonkar Institute of Pharmacy, Karjat, Maharashtra, India – 410201

⁵ Head, Dept of Pharmacology, TIT Pharmacy, Anand nagar, Bhopal, Madhya Pradesh, India, 462021.

⁶ Assistant Professor, Gurukul Pharmacy College, Kota, Rajasthan, India, 324001

3171

Corresponding author:

Mr. Dipak V. Bhusari
Research scholar
Department Of Pharmacy
Sunrise University
Alwar (Raj.) India

Email ID: dipakbhusari90@gmail.com

Mobile No: +91 9309736988

ABSTRACT:

In order to achieve complete remission from most tumours, patients often need to undergo radiation therapy, have the tumour removed surgically, and undergo lengthy chemotherapy. The objective of this study was to find an alternate method of encapsulating 5-fluorouracil (5-FU) in microspheres that would improve the effectiveness of chemotherapy without having a detrimental effect on the patients' quality of life or causing as many severe adverse effects on the system as the current method does. In the present experiment, chitosan microspheres were cross-linked in two distinct ways utilizing 5-fluorouracil (5-FU). It was hypothesized that altering factors such as the concentration of chitosan, the type of the oily phase, the nature of the cross-linker, and the amount of time spent cross-linking would provide a diverse set of features for the microspheres. The concentration of chitosan, the viscosity of the oil phase, and the glutaraldehyde content all had an influence on the pace at which 5-FU was released from the microspheres. Chitosan microspheres containing 5-fluorouracil (5-FU) that have been cross-linked release their contents very quickly. The goal of this study was to identify the most effective technique for manufacturing porous microspheres, which have the potential to postpone the breakdown of medications by stomach acid for up to six hours.

Keywords: 5-Fluorouracil, Chitosan, Microspheres, Colon cancer

DOI Number: 10.48047/nq.2022.20.19.NQ99277

NeuroQuantology2022;20(19): 3171-3181



INTRODUCTION:

Colorectal cancer, often known as colorectal cancer (CRC), is the third most frequent form of cancer overall and the second most lethal variety. It can affect either the colon or the rectum. It poses a significant danger to one's health. In the year 2020, colorectal cancer will be the underlying cause of 9.4% of all cancer fatalities. In spite of this, it is anticipated that the number of individuals living with colorectal cancer will more than double throughout the world by the year 2035, with the greatest increase occurring in less developed nations, where the number of cases discovered in older people is on the rise [1-3]. The genes that cause CRC are diverse, and the disease can originate in a variety of different ways. For instance, various degrees of gene expression in a large number of CRC cells were responsible for the development of hundreds of somaclonal mutations [1-4].

The chemotherapy medicine known as 5-fluorouracil (5-FU) is frequently used to treat patients who have cancer. Since 1957, it has been utilised in the treatment of malignancies of several locations, including the breast, the colon, the head and the neck. In addition to this, it is an essential component of the treatment for colon cancer. The anticancer medicine known as 5-fluorouracil belongs to a family of medications known as "antimetabolites." It does this by inhibiting the creation of nucleic acids and DNA, which ultimately results in the death of cancer cells. It is one of the cancer medications that is prescribed to patients the most frequently. As a treatment for solid tumours such colon, breast, liver, brain, and pancreatic cancer, it can be administered on its own or in combination with other medications. Since it was difficult for the body to absorb via the digestive tract and was not always successful when taken by mouth [5-8], 5-FU was frequently administered in clinics through the use of intravenous (IV) therapy.

The use of carrier technology is a clever method for the delivery of pharmaceuticals. The drug is fastened to a carrier particle such as microspheres, nanoparticles, or liposomes, for example, and this attachment modifies the manner in which the medication is absorbed

and released into the body. Because to their diminutive size and capacity to perform admirably in the role as carriers, microspheres constitute a significant portion of these particulate DDS. Nevertheless, due to the fact that they only remain at the site of absorption for a brief period of time, these novel DDS have a restricted scope of use. It would be beneficial if the design allowed the DDS membranes and the absorbing membranes to be placed in close proximity to one another. It's feasible that this can be accomplished by developing brand-new delivery methods known as "mucoadhesive microspheres" and incorporating mucoadhesion into those systems. Microparticles and microcapsules with a drug core are known as mucoadhesive microspheres. These microparticles and microcapsules range in diameter from 1-1000 m and are constructed of a mucoadhesive polymer in either its entirety or in part. In spite of the fact that microspheres may be engineered to adhere to mucous membranes, there are still valid reasons to utilise them for the targeted and controlled release of drugs. It is feasible for the bioadhesive system to adhere to the mucosal layer [9–13]. Hence, the mucoadhesive drug delivery system might be designed for buccal, oral, vaginal, nasal, rectal, and ocular routes of administration.

Chitosan is a biodegradable, hydrophilic, biocompatible, natural linear biopoly-aminosaccharide that has a lot of potential for use in the medical field. It has a high charge density, is non-toxic, and has the ability to adhere to mucous membranes. Chitosan is a natural linear biopoly-aminosaccharide. Chitosan was also investigated as a potential means of encapsulating pharmaceuticals within microspheres. Chitosan molecules form bonds with one another after being subjected to reactions with trace levels of multivalent anions. The production of chitosan microspheres has seen extensive application of this crosslinking technique. These are the medication delivery techniques that have received the most investigation [14–16]. Controlling the release of medications such as antibiotics, antihypertensive pharmaceuticals, anticancer treatments, proteins, peptide

3172



therapies, and vaccines are some of the applications for these devices.

MATERIAL AND METHODS:

Materials:

As a sign of good will, Khandelwal labs Pvt. Ltd. gave away a free sample of the drug (5-fluorouracil) (Thane, India). SD Fine Chemicals took our order for Span-80 chitosan (Mumbai, India). Sigma-Aldrich Chemie made the glutaraldehyde and the paraffin oil, while SD Fine Chemicals made the acetic acid. E. Merck provided calcium chloride, potassium dihydrogen phosphate, cyclohexane, Tween 80, methanol, and dichloromethane (Darmstadt, Germany). All of the other reagents were at least of analytical grade.

Method:

Method of preparation of Chitosan Microspheres I (CMS-I):

Microspheres can be made through chemical denaturation or, if that's too hard, through emulsification, which involves less phase separation. A 250 mL polypropylene beaker was filled with 100 mL of regular paraffin oil. In a beaker, oil was mixed with 1 mL of span-80. A 22-gauge hypodermic syringe was used to inject small amounts of a chitosan solution that was 3.5% w/v and had 50 mg of 5-fluorouracil in it. To make the delivery vehicle, 1% acetic acid was mixed with chitosan. During this method, a high-speed stirrer with propellers was used to stir paraffin oil at a rate of 2,000 revolutions per minute (rpm). After 15 minutes, 0.25 mL of glutaraldehyde was added to the oil, and then the chitosan solution was added. Even though everything else stayed the same, the speed of the stirring was cut in half, from 2,000 turns per minute to 1,000. At 30 minutes and 1 hour, 0.50 mL of glutaraldehyde was added while constantly stirring. After another hour of mixing, the last amount of glutaraldehyde was added, and the process was stopped. Before sinking to the bottom, the chitosan microspheres floated in paraffin oil for twenty-four hours. After the clear supernatant was taken away, microspheres were taken from the residue and washed four or five times in diethyl ether. After the microspheres were washed for the last time, they were left at room temperature to dry by air. The powder was then

collected and kept at room temperature [17–19].

Method of preparation of Chitosan Microspheres II (CMS-II):

Emulsification and chemical cross-linking are two additional processes that may be used when producing microspheres for the purpose of phase separation. A polypropylene beaker with a capacity of 250 millilitres was given 35 millilitres of light paraffin oil and 25 millilitres of petroleum ether. Spinning the contents of the beaker allowed us to mix one milliliter of span-80 with one milliliter of oil. We did this using the beaker. Using a hypodermic syringe with a 22-gauge needle, a solution of chitosan that was 4% water by volume was introduced very slowly. In order to make this solution, chitosan was first diluted to a concentration of one percent using acetic acid. This combination had a 5-fluorouracil dosage of fifty milligramme total. This was then added to the oil, which was being stirred at a rate of 2,000 revolutions per minute by a high-speed stirrer that was fitted with a propeller. The oil was stirred for a further five minutes so that the chitosan solution would be well mixed. This was done to guarantee that the solution would be thoroughly blended. At the same time, 1.6 millilitres of glutaraldehyde-saturated toluene (GST) was added to the mixture, and it was thoroughly combined after each addition. After waiting for half an hour, add 1.6 more mL of GST to the mixture. After an hour, include 1.8 mL of aqueous aldehyde in the mixture. When the last SGST was added, the mixture was allowed to sit without being stirred for the next 1 hour and 30 minutes. After being retrieved, the chitosan microspheres were shown to be floating in the oil. It took them twenty-four hours to finally settle to the bottom. After discarding the clear supernatant, the microspheres were washed many times with petroleum ether, methanol, a 5% solution of sodium bisulfide, and acetone. After receiving one more washing, the microspheres were allowed to dry in the air. The remaining quantity of dry powder was kept in airtight containers and kept at room temperature [20, 22].

Evaluation Parameter

Determination of Percentage Drug Entrapment



How effectively each batch fared in capturing drugs was measured by the PDE (percentage of drug entrapment).

$PDE = \frac{\text{Practical drug loading}}{\text{Theoretical drug loading}} \times 100$

We made the assumption that the end product would absorb all of the medicine that was present in the chitosan solution that was used to make the microspheres so that we could accurately calculate the potential drug loading. It was concluded that the best way to load a drug would be to use 25 mg of chitosan microspheres, and a 25 mL volumetric flask was used to do this. The bottle was then filled with methanol (around 25 mL). After continuously agitating the suspension at room temperature for twenty-four hours, we made the decision to let it alone. After centrifugation at 2000-3000 rpm, the concentration of the supernatant was measured utilizing UV Spectrophotometry at 266 nm [23, 24].

Determination of Particle Size and Particle Size Distribution

The releasing properties of microspheres coated with eudragit are shown to be greatly impacted by the particle size of the microspheres. To evaluate the distribution of particles in a suspension of chitosan microspheres (10 mg) in sterile water, a particle size analyzer (Malvern Master Sizer, model E, UK) and laser light diffraction were employed. The particle size analyzer was manufactured in the United Kingdom (2 mL). [25, 26] It was said that the Z-average particle size was the typical value (d.nm).

Determination of Zeta Potential

The zeta potential is a representation of the surface charge that may be seen on microspheres. It takes a significant amount of zeta potential for mucoadhesive substances to disperse. Using laser Doppler anemometry on a Zeta master (Malvern, UK), the researchers were able to estimate the surface charge of microparticles that were suspended in deionized water [27].

IN-VITRO Wash-Off Test for Microspheres

The IN-VITRO wash-off procedure was utilised in order to assess the mucoadhesiveness of the microspheres. That was done by threading the mucosa that lined the rat's stomach onto a glass

slide, and it covered an area that was one centimeter squared. Within the USP pill dissolving test apparatus, the sample was placed on a slide, which was then suspended from a groove. They were able to determine the pace at which microspheres dissolved in a tissue sample by using this procedure. Using disintegration testing equipment, tissue samples were often shaken while being held in a beaker containing phosphate buffer pH [28, 29].

Morphological Study of Microspheres

Digital microscopes are a type of optical microscope. With the use of photomicrographs, we were able to characterise the shape and cohesion of loaded chitosan microspheres. Microspheres made from chitosan solutions with concentrations of 3.5 and 4% remained mainly distinct after being spun at a speed of 2000-2500 rpm [30, 31].

IN-VITRO Release Study of CMS-1 and CMS-2

In a fluid model of the gastrointestinal system, drug release investigations from chitosan microspheres were conducted in the laboratory (SGF). The paddle technique (model Sentwin, India) was utilised to conduct dissolving experiments on microsphere-encapsulated drugs. These examinations were conducted in line with USP XXIII. Microspheres weighing a total of 100 milligramme were mixed with the dialysis membrane and the solubilizing solvent (SGF). The material was spun at a rate of 100 revolutions per minute at a temperature of 370 ° C +/- 0.50 ° C. The best circumstances for observing the dissolution of tablets were provided by the sink. We were able to reproduce the circumstances of gastrointestinal transit by adjusting the pH of the dissolving solution in minute increments at regular intervals. With the aid of 0.1 N HCL, the pH of the dissolving liquid was maintained at 1.2 during the course of two hours. To facilitate the dissolution of the substance, the pH of the medium was decreased to 4.5 using 1.0M sodium hydroxide. The mixture was then supplemented with 1.7 grammes of KH₂PO₄ and 2.2 grammes of Na₂HPO₄.2H₂O. The study of the discharge's flow rate consumed an additional two hours. After 4 hours of incubation, the pH of the solubilizing media was

3174



adjusted to 7.4 using 0.1 N sodium hydroxide. As soon as it reached that location, it remained there for the remainder of the next day. Using a pipette, samples were obtained at various stages of the procedure from the solutions used for dissolving and diluting the chemical in concern. Researchers substituted saline solution for soluble growth factor (SGF) because they understood the importance of maintaining a constant receptor size. Using UV soctrophometry, the researchers were able to determine the rate of FU release; they then created a release curve to illustrate how the rate of release altered over time [25-28].

RESULT AND DISCUSSION:

A number of processes, including as solvent evaporation, single emulsification (of the w/o type), and multiple emulsification (of the w/o/w type), were utilised throughout the manufacturing process of microspheres. The results are summarized in the table that can be seen below. The evaporation of liquid paraffin and acetone resulted in the formation of minuscule spheres. For the purpose of creating an emulsion, the drug solution that was dissolved in acetone was mixed with the chitosan solution and the liquid paraffin. To begin, we filtered the emulsion that included the microspheres. This was done in order to dry the object, which was followed by sterilizing it. Unfortunately, it does not appear that acetone

is an efficient solvent for the dissolution of 5-FU. It was assumed that re-emulsifying would be ineffective and would result in the waste of solvent.

Because 5-FU and chitosan are soluble in a solution containing 5% acetic acid, there is no need to emulsify the mixture before attempting to form microspheres out of the two substances. As solvents, acetic acid and diethyl ether are typically utilised. In order to improve the stability of the emulsion, glutaraldehyde, which is a cross-linking agent, was added to it. The microsphere emulsion was prepared for use after being washed, filtered, and then baked in an oven at a temperature of 600 degrees for one hour. The microspheres that you make should be consistent throughout in terms of their size and shape, and they should be able to effectively capture individual particles. After that, we generated microspheres using two different methods, none of which involved emulsification. We were able to tailor the concentration of chitosan, the length of the oily phase, the concentration of the cross-linking agent, the amount of time spent cross-linking, and the washing solvent to our specifications by utilizing these methods. Table 1 contains an inventory of the components required for the production of chitosan microspheres using either Method I or Method II.

3175

Table 1: Chitosan microspherespreparedby MethodI&MethodII

PROCESSVARIABLES	METHOD I	METHODII
Concentrationofchitosan	3.5%	4.0%
Typeofoilyphase	Lightliquidparaffin	Liquidparaffin&petroleumether
Typesofcross-linker	Glutaraldehyde	Glutaraldehydesaturateddtoluene
Cross-linkingtime	15, 30, 60min	60&120min
Washingsolvent	Diethylether	Petroleumether,methanol,acetone

For the purpose of this inquiry, we decided to use a method that combines traditional emulsification with chemical cross-linking. Our decision was based on the concerns outlined above. Because this method is versatile, it may

be used to a wide variety of various types of polymers and solvents. It has the capability of capturing molecules that have a predisposition for either water or oil as their natural environment. Oil-in-water, or o/w, emulsions



are a delivery method that can be used for medicines that do not dissolve in water. Because of this, the manufacturing of hydrophilic pharmaceuticals must make use of emulsion or double emulsion technology. So, in the not-too-distant future, there will be an increased emphasis placed on research aimed at perfecting the straightforward chemical denaturation process of emulsification. In this method, a layer of chitosan that has been treated with acetic acid is shielded by a layer of

liquid paraffin. Throughout processing, there were a number of elements that had an effect on the particle size. It was important to take into account the drug polymer ratio, as well as the stirring speed, cross-linker concentration, and cross-linking agent time. In Table 2, comparisons are made between microspheres made in two different ways with regard to their IN-VITRO wash-off efficiency, swelling profile, zeta potential, particle size distribution, and drug entrapment.

Table 2: Evaluation parameters of CMS-1&CMS-2

Sr.No.	Evaluation parameters	CMS-1	CMS-2
1.	Percentage drug entrapment	25.89	14.57
2.	Particle size and size distribution	4352.53nm	2761.80nm
3.	Zeta potential	+41.0mV	+51.2mV
4.	Swelling properties	Less	More
5.	IN-VITRO wash-off test	>24hrs	<24hrs

It was discovered that Method 1 had a higher value for the amount of medication that was entrapped (25.89) than Method 2. (14.57). although if the total amount of chitosan used in all three methods is the same, the entrapment efficiency may be improved by increasing the polymer concentration. Nevertheless, the efficiency of the trapping reduces with rising drug concentration if there is not enough chitosan available to bind the drug. This is the case if there is not enough chitosan present.

The decreased entrapment efficiency in Process 2 needed longer cross-linking times to make up for it. This was necessary since there was a possibility that the emulsion did not form properly. In order to make these microspheres as effective as possible, method 1 was used because of their consistent size, high entrapment efficiency, and predictable release profile.

Even though the total volume of the polymer stayed the same, the microspheres produced by increasing the polymer concentration were

much bigger. It was discovered that the concentration of the cross-linking agent had an effect on the size of the particles, with larger cross-linking concentrations producing smaller microspheres. A denser packing of the microspheres is produced as a result of the higher glutaraldehyde concentration in Step 2. The fact that both formulations had positive zeta potentials suggests that the negatively charged sialic acid and fucose residues in stomach mucus interact electrostatically with the positively charged chitosan, which in turn extends the amount of time the medicine is present in the stomach. It is possible that the level of cross-linking can govern the quantity of free amino groups that are found on the surface of a positively charged chitosan microsphere. In fewer than 15 minutes, the cross-linking caused by glutaraldehyde caused the zeta potential of the microspheres to drop from around +55 mV to approximately +47 mV. Now the surface charge has reached a state of equilibrium [22-27].



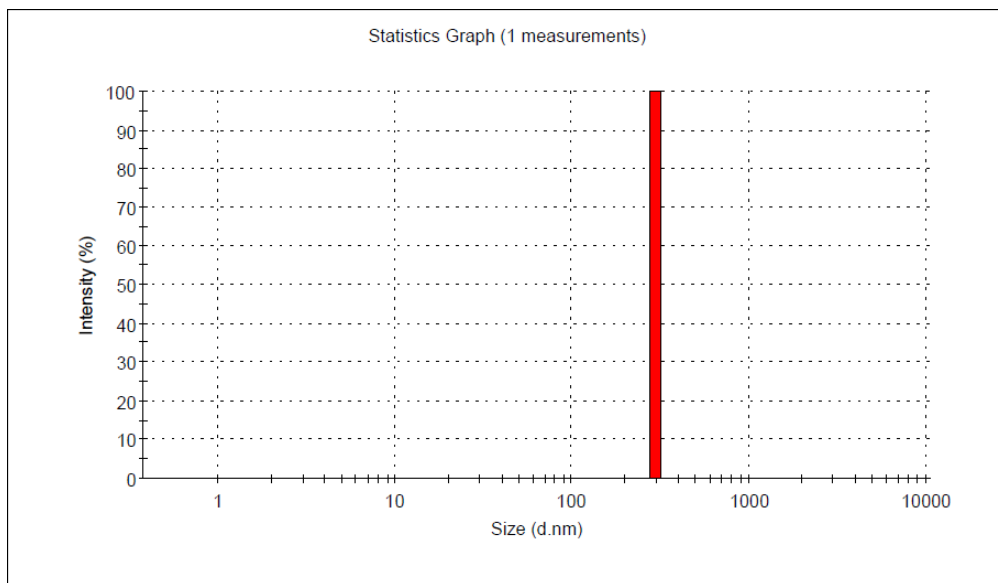


Figure 1: Particlesizedistributionofchitosanmicrospherespreparedby method-1

3177

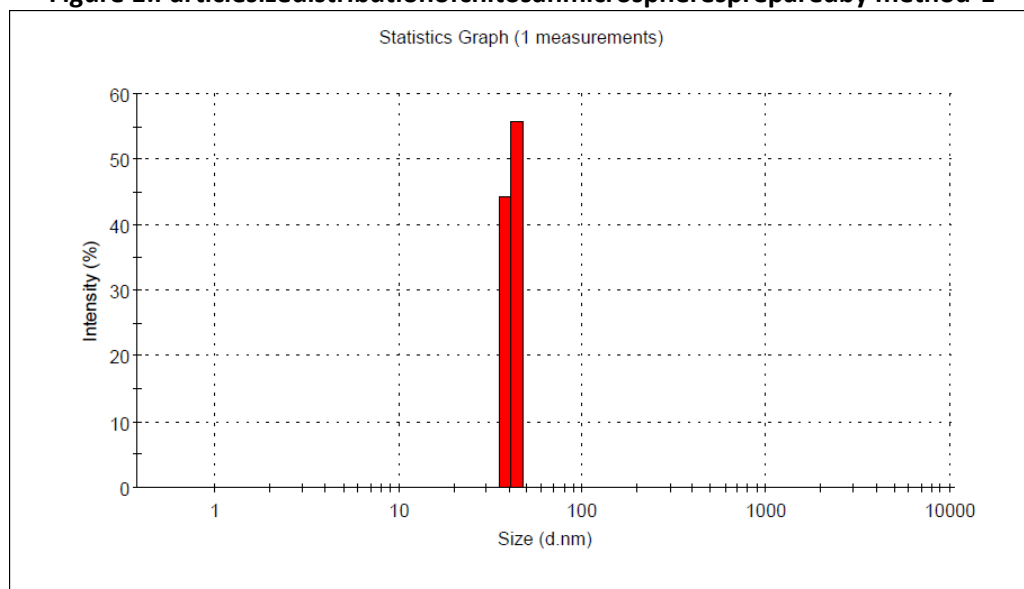


Figure 2: Particle size distribution of chitosan microspheres prepared by method-2

Morphological Study of Microspheres

Digital microscopes are a type of optical microscope. The shape and size of the unloaded chitosan microspheres were characterized by the use of photomicrographs, which revealed

that the microspheres were spherical and grouped together. Microspheres made from a solution containing 1% chitosan and spun at 2000-2500 rpm were perfectly spherical.

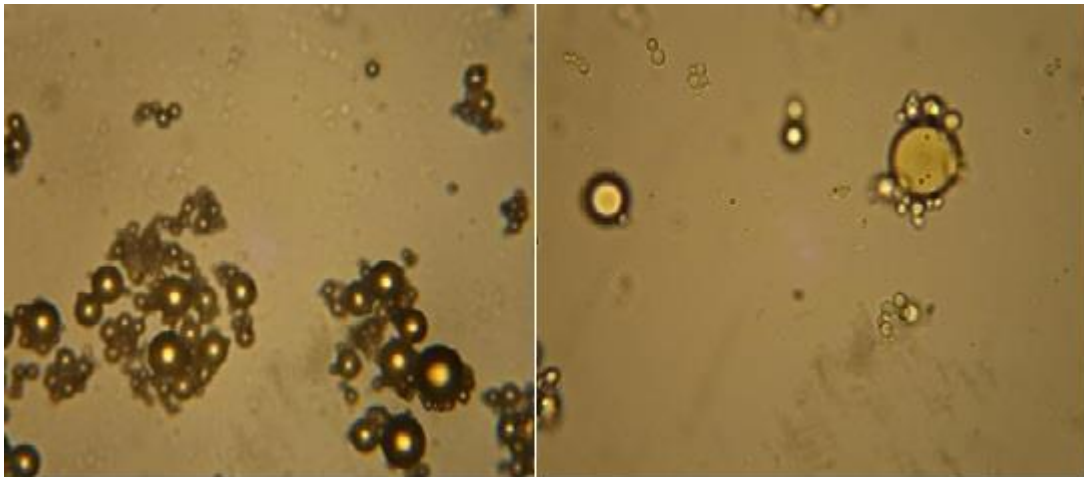


Figure 3: Photographs of unloaded chitosan microspheres

IN-VITRO Release Profile of CMS-1 and CMS-2

Table 3: IN-VITRO release profile of 5-FU from CMS-1 & CMS-2

Sr.No.	Time(hrs)	% Drug Release of CMS-1	% Drug Release of CMS-2
1.	1	8.96	7.56
2.	2	17.25	17.78
3.	3	22.64	21.34
4.	4	28.46	26.49
5.	5	33.49	31.56
6.	6	38.43	33.56
7.	7	44.37	40.78
8.	8	50.46	45.18
9.	9	57.64	48.64
10.	10	63.49	50.87
11.	11	67.18	55.67
12.	12	72.34	57.64
13.	24	80.64	60.49

3178



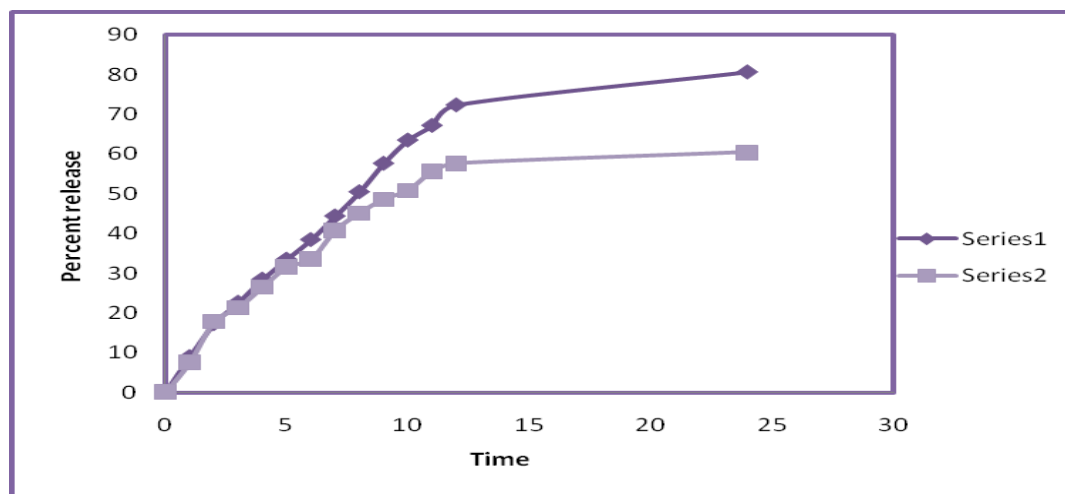


Figure 4: Percent release of 5-Fluorouracil from CMS-1 & CMS-2

Because the appropriate amount of cross-linking agent was used, and the cross-linking process was quick, the microspheres that were created using Method 1 had a superb, linear release pattern. This was possible due to two factors. When the amount of time spent cross-linking increases, drug release decreases [26-31].

CONCLUSION:

The application of the emulsion method resulted in the successful manufacture of microspheres that contained 5-fluorouracil. In order to pack the chitosan microspheres with the maximum number of 5 FU feasible, the variables in the recipe were optimized. If you want to improve the efficacy of the cytotoxic drug at a lower dose, the evidence shows that Method B chitosan microspheres loaded with 5-fluorouracil (5-FU) may be superior to CMS-1 microspheres. It might be beneficial for injecting 5 FU into the lungs, which is where it is most likely to have a significant impact on the state of the patient. In order to keep the anticancer medicine 5 FU active for a longer length of time, a biodegradable carrier system was devised. According to the results of our research, CMS-1 has the potential to be a successful long-term treatment for cancer that is safer, less costly, and offers a lower danger to patients than the conventional approach of administering medications through parenteral route.

Acknowledgments

eISSN1303-5150

The authors thank Rajarshi Shahu College of pharmacy, Buldana for providing facilities to conduct the research.

Authors Funding

None

Conflicts of interest

There are no conflicts of interest among all the authors with publication of manuscript.

REFERENCES:

- Center MM, Jemal A, Smith RA, Ward E. Worldwide variations in colorectal cancer. CA: a cancer journal for clinicians. 2009 Nov; 59(6):366-78.
- Ten Hoorn S, de Back TR, Sommeijer D-W, Vermeulen L. Clinical value of consensus molecular subtypes in colorectal cancer: a systematic review and meta-analysis. JNCI: Journal of the National Cancer Institute. 2022 Apr; 114(4):503-16.
- Wu Y, Yang S, Ma J, Chen Z, Song G, Rao D, Cheng Y, Huang S, Liu Y, Jiang S, Liu J. Spatiotemporal Immune Landscape of Colorectal Cancer Liver Metastasis at Single-Cell Level Spatial and Cellular Landscape of CRLM. Cancer discovery. 2022 Jan 1; 12(1):134-53.
- Sinicrope FA. Increasing incidence of early-onset colorectal cancer. New England Journal of Medicine. 2022 Apr 21; 386(16):1547-58.
- Qin L, Liang F, Li Y, Wu J, Guan S, Wu M, Xie S, Luo M, Ma D. A 2D porous zinc-organic framework platform for loading of 5-fluorouracil. Inorganics. 2022 Nov 9; www.neuroquantology.com



- 10(11):202.
6. Esrafil MD, Khan AA. Alkali metal decorated C 60 fullerenes as promising materials for delivery of the 5-fluorouracil anticancer drug: a DFT approach. *RSC advances*. 2022; 12(7):3948-56.
 7. Nguyen CH, Banh KS, Dang CH, Nguyen CH, Nguyen TD. β -cyclodextrin/alginate nanoparticles encapsulated 5-fluorouracil as an effective and safe anticancer drug delivery system. *Arabian Journal of Chemistry*. 2022 Jun 1; 15(6):103814.
 8. Barary M, Hosseinzadeh R, Kazemi S, Liang JJ, Mansoori R, Sio TT, Hosseini M, Moghadamnia AA. The effect of propolis on 5-fluorouracil-induced cardiac toxicity in rats. *Scientific Reports*. 2022 May 23; 12(1):8661.
 9. Surya R, Mullassery MD, Fernandez NB, Thomas D, Jayaram PS. Synthesis and characterization of a pH responsive and mucoadhesive drug delivery system for the controlled release application of anti-cancerous drug. *Arabian Journal of Chemistry*. 2020 May 1; 13(5):5262-76.
 10. Kumar A, Naik PK, Pradhan D, Ghosh G, Rath G. Mucoadhesive formulations: Innovations, merits, drawbacks, and future outlook. *Pharmaceutical Development and Technology*. 2020 Aug 8; 25(7):797-814.
 11. Li X, Chen K, Ji X, Yuan X, Lei Z, Ullah MW, Xiao J, Yang G. Microencapsulation of poorly water-soluble finasteride in polyvinyl alcohol/chitosan microspheres as a long-term sustained release system for potential embolization applications. *Engineered Science*. 2020 Dec 14; 13(2):106-20.
 12. Zeng D, Yu C, Fan Q, Zeng J, Wei L, Li Z, Yang K, Ji H. Theoretical and experimental research of novel fluorine doped hierarchical Sn3O4 microspheres with excellent photocatalytic performance for removal of Cr (VI) and organic pollutants. *Chemical Engineering Journal*. 2020 Jul 1; 391:123607.
 13. Bui TH, Lee W, Jeon SB, Kim KW, Lee Y. Enhanced Gold (III) adsorption using glutaraldehyde-cross-linked chitosan beads: Effect of crosslinking degree on adsorption selectivity, capacity, and mechanism. *Separation and Purification Technology*. 2020 Oct 1; 248:116989.
 14. Pooresmaeil M, Namazi H. Facile preparation of pH-sensitive chitosan microspheres for delivery of curcumin; characterization, drug release kinetics and evaluation of anticancer activity. *International journal of biological macromolecules*. 2020 Nov 1; 162:501-11.
 15. Li G, Row KH. Deep eutectic solvents skeleton typed molecularly imprinted chitosan microsphere coated magnetic graphene oxide for solid-phase microextraction of Chlorophenols from environmental water. *Journal of separation science*. 2020 Mar; 43(6):1063-70.
 16. Zhang Q, Zhuang S, Wang J. Biosorptive removal of cobalt (II) from aqueous solutions using magnetic cyanoethyl chitosan beads. *Journal of Environmental Chemical Engineering*. 2020 Dec 1; 8(6):104531.
 17. Xia H, Li A, Man J, Li J, Li J. Fabrication of multi-layered microspheres based on phase separation for drug delivery. *Micromachines*. 2021 Jun 19; 12(6):723.
 18. Jiang H, Hu X, Li Y, Ngai T. A green and facile strategy for the fabrication of all-natural porous proteinaceous microspheres. *Materials Chemistry Frontiers*. 2021; 5(10):3897-902.
 19. Li G, Yu Y, Han W, Zhu L, Si T, Wang H, Li K, Sun Y, He Y. Solvent evaporation self-motivated continual synthesis of versatile porous polymer microspheres via foaming-transfer. *Colloids and Surfaces A: Physicochemical and Engineering Aspects*. 2021 Apr 20; 615:126239.
 20. Qiao L, Wang S, Wang T, Yu S, Guo S, Du K. High-strength and low-swelling chitosan/cellulose microspheres as a high-efficiency adsorbent for dye removal. *Cellulose*. 2021 Sep; 28:9323-33.
 21. Xu JH, Li SW, Tostado C, Lan WJ, Luo GS. Preparation of Monodispersed chitosan microspheres and in situ encapsulation of BSA in a co-axial microfluidic device. *Biomedical micro devices*. 2009 Feb; 11:243-9.
 22. Wong SK, Lawrencia D, Supramaniam J, Goh



- BH, Manickam S, Wong TW, Pang CH, Tang SY. In vitro digestion and swelling kinetics of thymoquinone-loaded Pickering emulsions incorporated in alginate-chitosan hydrogel beads. *Frontiers in Nutrition*. 2021 Oct 4; 8:752207.
23. Rehman S, Ranjha NM, Raza MR, Hanif M, Majed A, Ameer N. Enteric-coated Calcium alginate hydrogel beads: a promising tool for colon targeted drug delivery system. *Polymer Bulletin*. 2021 Sep; 78:5103-17.
 24. Moin A, Wani SU, Osmani RA, Abu Lila AS, Khafagy ES, Arab HH, Gangadharappa HV, Allam AN. Formulation, characterization, and cellular toxicity assessment of tamoxifen-loaded silk fibroin nanoparticles in breast cancer. *Drug Delivery*. 2021 Jan 1; 28(1):1626-36.
 25. Afrazi M, Yazdani M. Determination of the effect of soil particle size distribution on the shear behavior of sand. *Journal of Advanced Engineering and Computation*. 2021 Jun 30; 5(2):125-34.
 26. Caputo F, Vogel R, Savage J, Vella G, Law A, Della Camera G, Hannon G, Peacock B, Mehn D, Ponti J, Geiss O. Measuring particle size distribution and mass concentration of Nano plastics and micro plastics: addressing some analytical challenges in the sub-micron size range. *Journal of Colloid and Interface Science*. 2021 Apr 15; 588:401-17.
 27. Sharifi F, Jahangiri M, Nazir I, Asim MH, Ebrahimnejad P, Hupfauf A, Gust R, Bernkop-Schnürch A. Zeta potential changing nanoemulsions based on a simple zwitterion. *Journal of Colloid and Interface Science*. 2021 Mar 1; 585:126-37.
 28. Dewangan HK, Sharma A, Mishra A, Singour P. Mucoadhesive microspheres of atorvastatin calcium: rational design, evaluation and enhancement of bioavailability. *Microscopy*. 2021 Jul 1; 19:20.
 29. Mahor S, Chandra P, Prasad N. Design and IN-VITRO Evaluation of Float-adhesive Famotidine Microspheres by using Natural Polymers for Gastro retentive Properties. *Indian J. Pharm. Educ. Res*. 2021 Apr 1; 55:407-17.
 30. Li X, Ji X, Chen K, Ullah MW, Yuan X, Lei Z, Cao J, Xiao J, Yang G. Development of finasteride/PHBV@ polyvinyl alcohol/chitosan reservoir-type microspheres as a potential embolic agent: from in vitro evaluation to animal study. *Biomaterials Science*. 2020; 8(10):2797-813.
 31. Li X, Chen K, Ji X, Yuan X, Lei Z, Ullah MW, Xiao J, Yang G. Microencapsulation of poorly water-soluble finasteride in polyvinyl alcohol/chitosan microspheres as a long-term sustained release system for potential embolization applications. *Engineered Science*. 2020 Dec 14; 13(2):106-20.



FORMULATION AND COMPARISON BETWEEN TWO METHODS FOR 5-FLUOROURACIL-LOADED CHITOSAN MICROSPHERES

Mr. Dipak V. Bhusari^{1*}, Dr. Shailesh M. Kewatkar², Amol Nanduji Jaybhaye³, Puja G. Vyawhare⁴, Yogita Mahesh Vispute³, Dr. Manmeet S. Saluja⁵, Dr. Shirish P. Jain², Mrs. Neelam M Patel⁶

¹ Department of Pharmacy Sunrise University Alwar, Rajasthan, India – 301028

² Rajarshi Shahu College of Pharmacy, Buldana, Maharashtra, India – 443001

³ Western Kentucky University, Bowling Green, KY, USA

⁴ Yadavrao Tasgaonkar Institute of Pharmacy, Karjat, Maharashtra, India – 410201

⁵ Head, Dept of Pharmacology, TIT Pharmacy, Anand nagar, Bhopal, Madhya Pradesh, India, 462021.

⁶ Assistant Professor, Gurukul Pharmacy College, Kota, Rajasthan, India, 324001

3171

Corresponding author:

Mr. Dipak V. Bhusari
Research scholar
Department Of Pharmacy
Sunrise University
Alwar (Raj.) India

Email ID: dipakbhusari90@gmail.com

Mobile No: +91 9309736988

ABSTRACT:

In order to achieve complete remission from most tumours, patients often need to undergo radiation therapy, have the tumour removed surgically, and undergo lengthy chemotherapy. The objective of this study was to find an alternate method of encapsulating 5-fluorouracil (5-FU) in microspheres that would improve the effectiveness of chemotherapy without having a detrimental effect on the patients' quality of life or causing as many severe adverse effects on the system as the current method does. In the present experiment, chitosan microspheres were cross-linked in two distinct ways utilizing 5-fluorouracil (5-FU). It was hypothesized that altering factors such as the concentration of chitosan, the type of the oily phase, the nature of the cross-linker, and the amount of time spent cross-linking would provide a diverse set of features for the microspheres. The concentration of chitosan, the viscosity of the oil phase, and the glutaraldehyde content all had an influence on the pace at which 5-FU was released from the microspheres. Chitosan microspheres containing 5-fluorouracil (5-FU) that have been cross-linked release their contents very quickly. The goal of this study was to identify the most effective technique for manufacturing porous microspheres, which have the potential to postpone the breakdown of medications by stomach acid for up to six hours.

Keywords: 5-Fluorouracil, Chitosan, Microspheres, Colon cancer

DOI Number: 10.48047/nq.2022.20.19.NQ99277

NeuroQuantology2022;20(19): 3171-3181



INTRODUCTION:

Colorectal cancer, often known as colorectal cancer (CRC), is the third most frequent form of cancer overall and the second most lethal variety. It can affect either the colon or the rectum. It poses a significant danger to one's health. In the year 2020, colorectal cancer will be the underlying cause of 9.4% of all cancer fatalities. In spite of this, it is anticipated that the number of individuals living with colorectal cancer will more than double throughout the world by the year 2035, with the greatest increase occurring in less developed nations, where the number of cases discovered in older people is on the rise [1-3]. The genes that cause CRC are diverse, and the disease can originate in a variety of different ways. For instance, various degrees of gene expression in a large number of CRC cells were responsible for the development of hundreds of somaclonal mutations [1-4].

The chemotherapy medicine known as 5-fluorouracil (5-FU) is frequently used to treat patients who have cancer. Since 1957, it has been utilised in the treatment of malignancies of several locations, including the breast, the colon, the head and the neck. In addition to this, it is an essential component of the treatment for colon cancer. The anticancer medicine known as 5-fluorouracil belongs to a family of medications known as "antimetabolites." It does this by inhibiting the creation of nucleic acids and DNA, which ultimately results in the death of cancer cells. It is one of the cancer medications that is prescribed to patients the most frequently. As a treatment for solid tumours such colon, breast, liver, brain, and pancreatic cancer, it can be administered on its own or in combination with other medications. Since it was difficult for the body to absorb via the digestive tract and was not always successful when taken by mouth [5-8], 5-FU was frequently administered in clinics through the use of intravenous (IV) therapy.

The use of carrier technology is a clever method for the delivery of pharmaceuticals. The drug is fastened to a carrier particle such as microspheres, nanoparticles, or liposomes, for example, and this attachment modifies the manner in which the medication is absorbed

and released into the body. Because to their diminutive size and capacity to perform admirably in the role as carriers, microspheres constitute a significant portion of these particulate DDS. Nevertheless, due to the fact that they only remain at the site of absorption for a brief period of time, these novel DDS have a restricted scope of use. It would be beneficial if the design allowed the DDS membranes and the absorbing membranes to be placed in close proximity to one another. It's feasible that this can be accomplished by developing brand-new delivery methods known as "mucoadhesive microspheres" and incorporating mucoadhesion into those systems. Microparticles and microcapsules with a drug core are known as mucoadhesive microspheres. These microparticles and microcapsules range in diameter from 1-1000 m and are constructed of a mucoadhesive polymer in either its entirety or in part. In spite of the fact that microspheres may be engineered to adhere to mucous membranes, there are still valid reasons to utilise them for the targeted and controlled release of drugs. It is feasible for the bioadhesive system to adhere to the mucosal layer [9–13]. Hence, the mucoadhesive drug delivery system might be designed for buccal, oral, vaginal, nasal, rectal, and ocular routes of administration.

Chitosan is a biodegradable, hydrophilic, biocompatible, natural linear biopoly-aminosaccharide that has a lot of potential for use in the medical field. It has a high charge density, is non-toxic, and has the ability to adhere to mucous membranes. Chitosan is a natural linear biopoly-aminosaccharide. Chitosan was also investigated as a potential means of encapsulating pharmaceuticals within microspheres. Chitosan molecules form bonds with one another after being subjected to reactions with trace levels of multivalent anions. The production of chitosan microspheres has seen extensive application of this crosslinking technique. These are the medication delivery techniques that have received the most investigation [14–16]. Controlling the release of medications such as antibiotics, antihypertensive pharmaceuticals, anticancer treatments, proteins, peptide

3172



therapies, and vaccines are some of the applications for these devices.

MATERIAL AND METHODS:

Materials:

As a sign of good will, Khandelwal labs Pvt. Ltd. gave away a free sample of the drug (5-fluorouracil) (Thane, India). SD Fine Chemicals took our order for Span-80 chitosan (Mumbai, India). Sigma-Aldrich Chemie made the glutaraldehyde and the paraffin oil, while SD Fine Chemicals made the acetic acid. E. Merck provided calcium chloride, potassium dihydrogen phosphate, cyclohexane, Tween 80, methanol, and dichloromethane (Darmstadt, Germany). All of the other reagents were at least of analytical grade.

Method:

Method of preparation of Chitosan Microspheres I (CMS-I):

Microspheres can be made through chemical denaturation or, if that's too hard, through emulsification, which involves less phase separation. A 250 mL polypropylene beaker was filled with 100 mL of regular paraffin oil. In a beaker, oil was mixed with 1 mL of span-80. A 22-gauge hypodermic syringe was used to inject small amounts of a chitosan solution that was 3.5% w/v and had 50 mg of 5-fluorouracil in it. To make the delivery vehicle, 1% acetic acid was mixed with chitosan. During this method, a high-speed stirrer with propellers was used to stir paraffin oil at a rate of 2,000 revolutions per minute (rpm). After 15 minutes, 0.25 mL of glutaraldehyde was added to the oil, and then the chitosan solution was added. Even though everything else stayed the same, the speed of the stirring was cut in half, from 2,000 turns per minute to 1,000. At 30 minutes and 1 hour, 0.50 mL of glutaraldehyde was added while constantly stirring. After another hour of mixing, the last amount of glutaraldehyde was added, and the process was stopped. Before sinking to the bottom, the chitosan microspheres floated in paraffin oil for twenty-four hours. After the clear supernatant was taken away, microspheres were taken from the residue and washed four or five times in diethyl ether. After the microspheres were washed for the last time, they were left at room temperature to dry by air. The powder was then

collected and kept at room temperature [17–19].

Method of preparation of Chitosan Microspheres II (CMS-II):

Emulsification and chemical cross-linking are two additional processes that may be used when producing microspheres for the purpose of phase separation. A polypropylene beaker with a capacity of 250 millilitres was given 35 millilitres of light paraffin oil and 25 millilitres of petroleum ether. Spinning the contents of the beaker allowed us to mix one milliliter of span-80 with one milliliter of oil. We did this using the beaker. Using a hypodermic syringe with a 22-gauge needle, a solution of chitosan that was 4% water by volume was introduced very slowly. In order to make this solution, chitosan was first diluted to a concentration of one percent using acetic acid. This combination had a 5-fluorouracil dosage of fifty milligramme total. This was then added to the oil, which was being stirred at a rate of 2,000 revolutions per minute by a high-speed stirrer that was fitted with a propeller. The oil was stirred for a further five minutes so that the chitosan solution would be well mixed. This was done to guarantee that the solution would be thoroughly blended. At the same time, 1.6 millilitres of glutaraldehyde-saturated toluene (GST) was added to the mixture, and it was thoroughly combined after each addition. After waiting for half an hour, add 1.6 more mL of GST to the mixture. After an hour, include 1.8 mL of aqueous aldehyde in the mixture. When the last SGST was added, the mixture was allowed to sit without being stirred for the next 1 hour and 30 minutes. After being retrieved, the chitosan microspheres were shown to be floating in the oil. It took them twenty-four hours to finally settle to the bottom. After discarding the clear supernatant, the microspheres were washed many times with petroleum ether, methanol, a 5% solution of sodium bisulfide, and acetone. After receiving one more washing, the microspheres were allowed to dry in the air. The remaining quantity of dry powder was kept in airtight containers and kept at room temperature [20, 22].

Evaluation Parameter

Determination of Percentage Drug Entrapment



How effectively each batch fared in capturing drugs was measured by the PDE (percentage of drug entrapment).

$PDE = \frac{\text{Practical drug loading}}{\text{Theoretical drug loading}} \times 100$

We made the assumption that the end product would absorb all of the medicine that was present in the chitosan solution that was used to make the microspheres so that we could accurately calculate the potential drug loading. It was concluded that the best way to load a drug would be to use 25 mg of chitosan microspheres, and a 25 mL volumetric flask was used to do this. The bottle was then filled with methanol (around 25 mL). After continuously agitating the suspension at room temperature for twenty-four hours, we made the decision to let it alone. After centrifugation at 2000-3000 rpm, the concentration of the supernatant was measured utilizing UV Spectrophotometry at 266 nm [23, 24].

Determination of Particle Size and Particle Size Distribution

The releasing properties of microspheres coated with eudragit are shown to be greatly impacted by the particle size of the microspheres. To evaluate the distribution of particles in a suspension of chitosan microspheres (10 mg) in sterile water, a particle size analyzer (Malvern Master Sizer, model E, UK) and laser light diffraction were employed. The particle size analyzer was manufactured in the United Kingdom (2 mL). [25, 26] It was said that the Z-average particle size was the typical value (d.nm).

Determination of Zeta Potential

The zeta potential is a representation of the surface charge that may be seen on microspheres. It takes a significant amount of zeta potential for mucoadhesive substances to disperse. Using laser Doppler anemometry on a Zeta master (Malvern, UK), the researchers were able to estimate the surface charge of microparticles that were suspended in deionized water [27].

IN-VITRO Wash-Off Test for Microspheres

The IN-VITRO wash-off procedure was utilised in order to assess the mucoadhesiveness of the microspheres. That was done by threading the mucosa that lined the rat's stomach onto a glass

slide, and it covered an area that was one centimeter squared. Within the USP pill dissolving test apparatus, the sample was placed on a slide, which was then suspended from a groove. They were able to determine the pace at which microspheres dissolved in a tissue sample by using this procedure. Using disintegration testing equipment, tissue samples were often shaken while being held in a beaker containing phosphate buffer pH [28, 29].

Morphological Study of Microspheres

Digital microscopes are a type of optical microscope. With the use of photomicrographs, we were able to characterise the shape and cohesion of loaded chitosan microspheres. Microspheres made from chitosan solutions with concentrations of 3.5 and 4% remained mainly distinct after being spun at a speed of 2000-2500 rpm [30, 31].

IN-VITRO Release Study of CMS-1 and CMS-2

In a fluid model of the gastrointestinal system, drug release investigations from chitosan microspheres were conducted in the laboratory (SGF). The paddle technique (model Sentwin, India) was utilised to conduct dissolving experiments on microsphere-encapsulated drugs. These examinations were conducted in line with USP XXIII. Microspheres weighing a total of 100 milligramme were mixed with the dialysis membrane and the solubilizing solvent (SGF). The material was spun at a rate of 100 revolutions per minute at a temperature of 370 ° C +/- 0.50 ° C. The best circumstances for observing the dissolution of tablets were provided by the sink. We were able to reproduce the circumstances of gastrointestinal transit by adjusting the pH of the dissolving solution in minute increments at regular intervals. With the aid of 0.1 N HCL, the pH of the dissolving liquid was maintained at 1.2 during the course of two hours. To facilitate the dissolution of the substance, the pH of the medium was decreased to 4.5 using 1.0M sodium hydroxide. The mixture was then supplemented with 1.7 grammes of KH₂PO₄ and 2.2 grammes of Na₂HPO₄.2H₂O. The study of the discharge's flow rate consumed an additional two hours. After 4 hours of incubation, the pH of the solubilizing media was

3174



adjusted to 7.4 using 0.1 N sodium hydroxide. As soon as it reached that location, it remained there for the remainder of the next day. Using a pipette, samples were obtained at various stages of the procedure from the solutions used for dissolving and diluting the chemical in concern. Researchers substituted saline solution for soluble growth factor (SGF) because they understood the importance of maintaining a constant receptor size. Using UV soctrophometry, the researchers were able to determine the rate of FU release; they then created a release curve to illustrate how the rate of release altered over time [25-28].

RESULT AND DISCUSSION:

A number of processes, including as solvent evaporation, single emulsification (of the w/o type), and multiple emulsification (of the w/o/w type), were utilised throughout the manufacturing process of microspheres. The results are summarized in the table that can be seen below. The evaporation of liquid paraffin and acetone resulted in the formation of minuscule spheres. For the purpose of creating an emulsion, the drug solution that was dissolved in acetone was mixed with the chitosan solution and the liquid paraffin. To begin, we filtered the emulsion that included the microspheres. This was done in order to dry the object, which was followed by sterilizing it. Unfortunately, it does not appear that acetone

is an efficient solvent for the dissolution of 5-FU. It was assumed that re-emulsifying would be ineffective and would result in the waste of solvent.

Because 5-FU and chitosan are soluble in a solution containing 5% acetic acid, there is no need to emulsify the mixture before attempting to form microspheres out of the two substances. As solvents, acetic acid and diethyl ether are typically utilised. In order to improve the stability of the emulsion, glutaraldehyde, which is a cross-linking agent, was added to it. The microsphere emulsion was prepared for use after being washed, filtered, and then baked in an oven at a temperature of 600 degrees for one hour. The microspheres that you make should be consistent throughout in terms of their size and shape, and they should be able to effectively capture individual particles. After that, we generated microspheres using two different methods, none of which involved emulsification. We were able to tailor the concentration of chitosan, the length of the oily phase, the concentration of the cross-linking agent, the amount of time spent cross-linking, and the washing solvent to our specifications by utilizing these methods. Table 1 contains an inventory of the components required for the production of chitosan microspheres using either Method I or Method II.

3175

Table 1: Chitosan microspherespreparedby MethodI&MethodII

PROCESSVARIABLES	METHOD I	METHODII
Concentrationofchitosan	3.5%	4.0%
Typeofoilyphase	Lightliquidparaffin	Liquidparaffin&petroleumether
Typesofcross-linker	Glutaraldehyde	Glutaraldehydesaturateddtoluene
Cross-linkingtime	15, 30, 60min	60&120min
Washingsolvent	Diethylether	Petroleumether,methanol,acetone

For the purpose of this inquiry, we decided to use a method that combines traditional emulsification with chemical cross-linking. Our decision was based on the concerns outlined above. Because this method is versatile, it may

be used to a wide variety of various types of polymers and solvents. It has the capability of capturing molecules that have a predisposition for either water or oil as their natural environment. Oil-in-water, or o/w, emulsions



are a delivery method that can be used for medicines that do not dissolve in water. Because of this, the manufacturing of hydrophilic pharmaceuticals must make use of emulsion or double emulsion technology. So, in the not-too-distant future, there will be an increased emphasis placed on research aimed at perfecting the straightforward chemical denaturation process of emulsification. In this method, a layer of chitosan that has been treated with acetic acid is shielded by a layer of

liquid paraffin. Throughout processing, there were a number of elements that had an effect on the particle size. It was important to take into account the drug polymer ratio, as well as the stirring speed, cross-linker concentration, and cross-linking agent time. In Table 2, comparisons are made between microspheres made in two different ways with regard to their IN-VITRO wash-off efficiency, swelling profile, zeta potential, particle size distribution, and drug entrapment.

Table 2: Evaluation parameters of CMS-1 & CMS-2

Sr.No.	Evaluation parameters	CMS-1	CMS-2
1.	Percentage drug entrapment	25.89	14.57
2.	Particle size and size distribution	4352.53nm	2761.80nm
3.	Zeta potential	+41.0mV	+51.2mV
4.	Swelling properties	Less	More
5.	IN-VITRO wash-off test	>24hrs	<24hrs

It was discovered that Method 1 had a higher value for the amount of medication that was entrapped (25.89) than Method 2. (14.57). although if the total amount of chitosan used in all three methods is the same, the entrapment efficiency may be improved by increasing the polymer concentration. Nevertheless, the efficiency of the trapping reduces with rising drug concentration if there is not enough chitosan available to bind the drug. This is the case if there is not enough chitosan present.

The decreased entrapment efficiency in Process 2 needed longer cross-linking times to make up for it. This was necessary since there was a possibility that the emulsion did not form properly. In order to make these microspheres as effective as possible, method 1 was used because of their consistent size, high entrapment efficiency, and predictable release profile.

Even though the total volume of the polymer stayed the same, the microspheres produced by increasing the polymer concentration were

much bigger. It was discovered that the concentration of the cross-linking agent had an effect on the size of the particles, with larger cross-linking concentrations producing smaller microspheres. A denser packing of the microspheres is produced as a result of the higher glutaraldehyde concentration in Step 2. The fact that both formulations had positive zeta potentials suggests that the negatively charged sialic acid and fucose residues in stomach mucus interact electrostatically with the positively charged chitosan, which in turn extends the amount of time the medicine is present in the stomach. It is possible that the level of cross-linking can govern the quantity of free amino groups that are found on the surface of a positively charged chitosan microsphere. In fewer than 15 minutes, the cross-linking caused by glutaraldehyde caused the zeta potential of the microspheres to drop from around +55 mV to approximately +47 mV. Now the surface charge has reached a state of equilibrium [22-27].



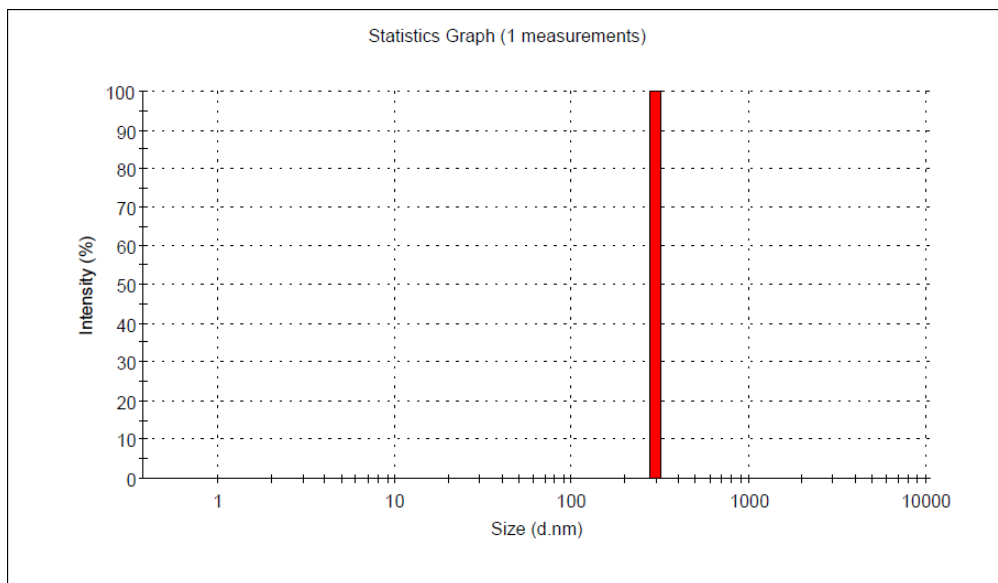


Figure 1: Particlesizedistributionofchitosanmicrospherespreparedby method-1

3177

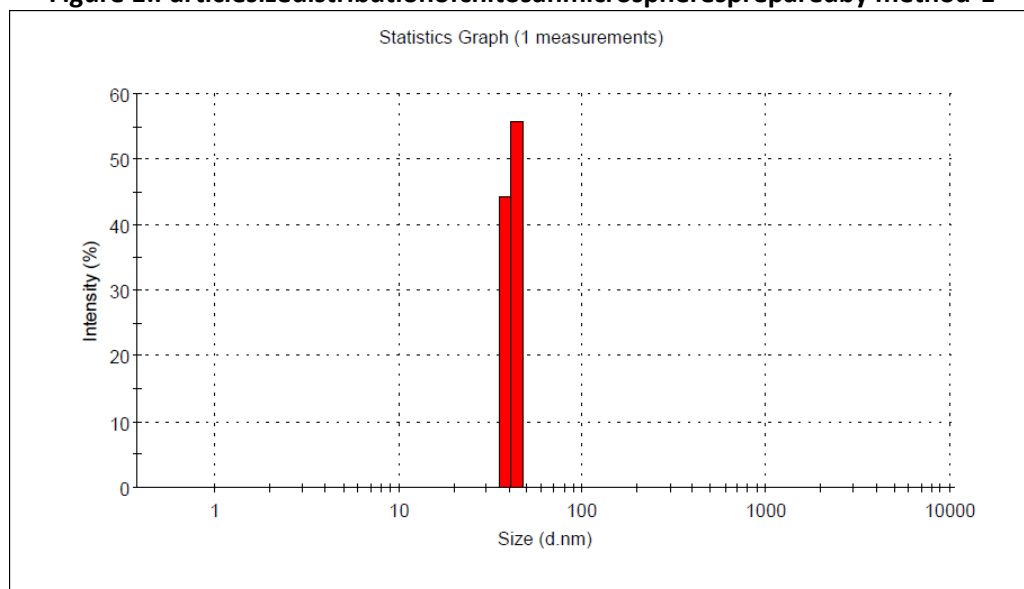


Figure 2: Particle size distribution of chitosan microspheres prepared by method-2

Morphological Study of Microspheres

Digital microscopes are a type of optical microscope. The shape and size of the unloaded chitosan microspheres were characterized by the use of photomicrographs, which revealed

that the microspheres were spherical and grouped together. Microspheres made from a solution containing 1% chitosan and spun at 2000-2500 rpm were perfectly spherical.



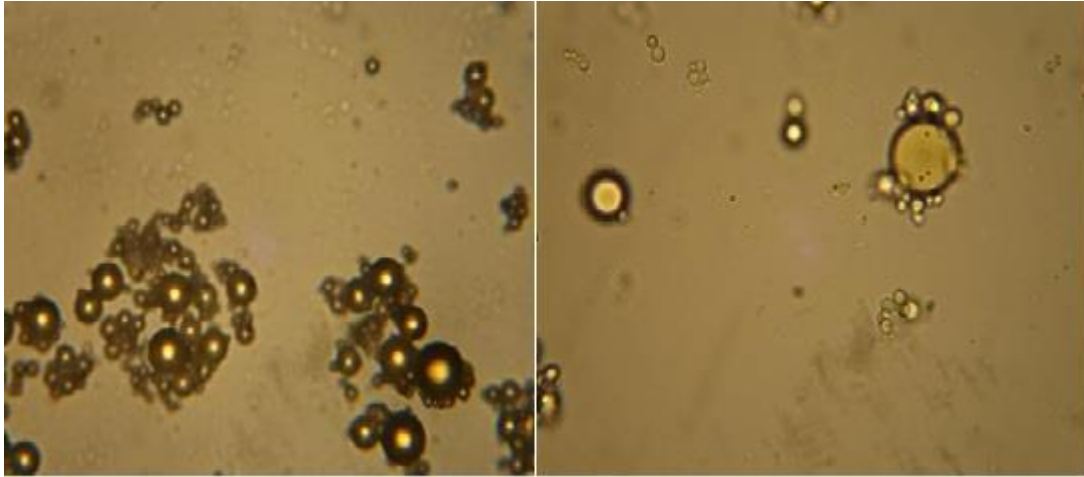


Figure 3: Photographs of unloaded chitosan microspheres

IN-VITRO Release Profile of CMS-1 and CMS-2

Table 3: IN-VITRO release profile of 5-FU from CMS-1 & CMS-2

Sr.No.	Time(hrs)	% Drug Release of CMS-1	% Drug Release of CMS-2
1.	1	8.96	7.56
2.	2	17.25	17.78
3.	3	22.64	21.34
4.	4	28.46	26.49
5.	5	33.49	31.56
6.	6	38.43	33.56
7.	7	44.37	40.78
8.	8	50.46	45.18
9.	9	57.64	48.64
10.	10	63.49	50.87
11.	11	67.18	55.67
12.	12	72.34	57.64
13.	24	80.64	60.49

3178



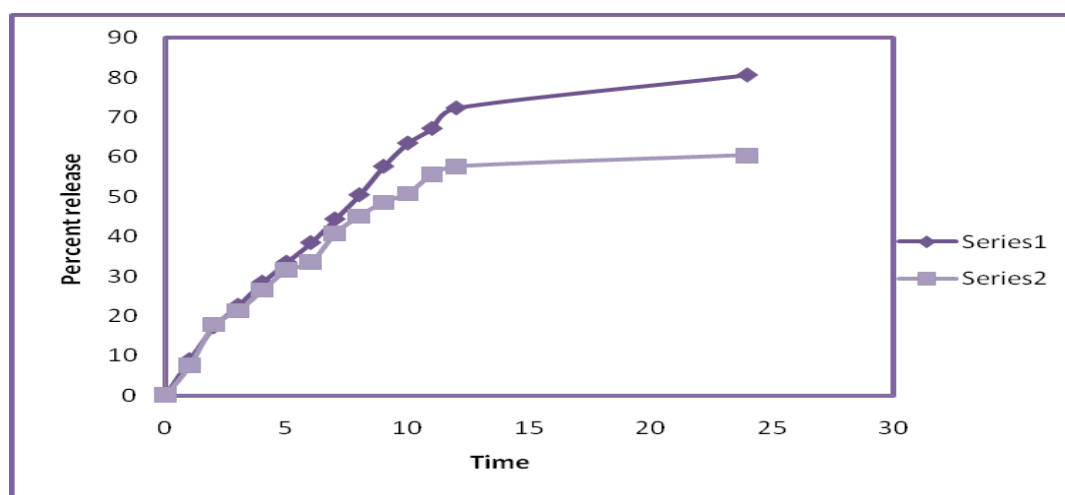


Figure 4: Percent release of 5-Fluorouracil from CMS-1 & CMS-2

Because the appropriate amount of cross-linking agent was used, and the cross-linking process was quick, the microspheres that were created using Method 1 had a superb, linear release pattern. This was possible due to two factors. When the amount of time spent cross-linking increases, drug release decreases [26-31].

CONCLUSION:

The application of the emulsion method resulted in the successful manufacture of microspheres that contained 5-fluorouracil. In order to pack the chitosan microspheres with the maximum number of 5 FU feasible, the variables in the recipe were optimized. If you want to improve the efficacy of the cytotoxic drug at a lower dose, the evidence shows that Method B chitosan microspheres loaded with 5-fluorouracil (5-FU) may be superior to CMS-1 microspheres. It might be beneficial for injecting 5 FU into the lungs, which is where it is most likely to have a significant impact on the state of the patient. In order to keep the anticancer medicine 5 FU active for a longer length of time, a biodegradable carrier system was devised. According to the results of our research, CMS-1 has the potential to be a successful long-term treatment for cancer that is safer, less costly, and offers a lower danger to patients than the conventional approach of administering medications through parenteral route.

Acknowledgments

eISSN1303-5150

The authors thank Rajarshi Shahu College of pharmacy, Buldana for providing facilities to conduct the research.

Authors Funding

None

Conflicts of interest

There are no conflicts of interest among all the authors with publication of manuscript.

REFERENCES:

1. Center MM, Jemal A, Smith RA, Ward E. Worldwide variations in colorectal cancer. *CA: a cancer journal for clinicians*. 2009 Nov; 59(6):366-78.
2. Ten Hoorn S, de Back TR, Sommeijer D-W, Vermeulen L. Clinical value of consensus molecular subtypes in colorectal cancer: a systematic review and meta-analysis. *JNCI: Journal of the National Cancer Institute*. 2022 Apr; 114(4):503-16.
3. Wu Y, Yang S, Ma J, Chen Z, Song G, Rao D, Cheng Y, Huang S, Liu Y, Jiang S, Liu J. Spatiotemporal Immune Landscape of Colorectal Cancer Liver Metastasis at Single-Cell Level Spatial and Cellular Landscape of CRLM. *Cancer discovery*. 2022 Jan 1; 12(1):134-53.
4. Sinicrope FA. Increasing incidence of early-onset colorectal cancer. *New England Journal of Medicine*. 2022 Apr 21; 386(16):1547-58.
5. Qin L, Liang F, Li Y, Wu J, Guan S, Wu M, Xie S, Luo M, Ma D. A 2D porous zinc-organic framework platform for loading of 5-fluorouracil. *Inorganics*. 2022 Nov 9; www.neuroquantology.com



- 10(11):202.
6. Esrafil MD, Khan AA. Alkali metal decorated C 60 fullerenes as promising materials for delivery of the 5-fluorouracil anticancer drug: a DFT approach. *RSC advances*. 2022; 12(7):3948-56.
 7. Nguyen CH, Banh KS, Dang CH, Nguyen CH, Nguyen TD. β -cyclodextrin/alginate nanoparticles encapsulated 5-fluorouracil as an effective and safe anticancer drug delivery system. *Arabian Journal of Chemistry*. 2022 Jun 1; 15(6):103814.
 8. Barary M, Hosseinzadeh R, Kazemi S, Liang JJ, Mansoori R, Sio TT, Hosseini M, Moghadamnia AA. The effect of propolis on 5-fluorouracil-induced cardiac toxicity in rats. *Scientific Reports*. 2022 May 23; 12(1):8661.
 9. Surya R, Mullassery MD, Fernandez NB, Thomas D, Jayaram PS. Synthesis and characterization of a pH responsive and mucoadhesive drug delivery system for the controlled release application of anti-cancerous drug. *Arabian Journal of Chemistry*. 2020 May 1; 13(5):5262-76.
 10. Kumar A, Naik PK, Pradhan D, Ghosh G, Rath G. Mucoadhesive formulations: Innovations, merits, drawbacks, and future outlook. *Pharmaceutical Development and Technology*. 2020 Aug 8; 25(7):797-814.
 11. Li X, Chen K, Ji X, Yuan X, Lei Z, Ullah MW, Xiao J, Yang G. Microencapsulation of poorly water-soluble finasteride in polyvinyl alcohol/chitosan microspheres as a long-term sustained release system for potential embolization applications. *Engineered Science*. 2020 Dec 14; 13(2):106-20.
 12. Zeng D, Yu C, Fan Q, Zeng J, Wei L, Li Z, Yang K, Ji H. Theoretical and experimental research of novel fluorine doped hierarchical Sn3O4 microspheres with excellent photocatalytic performance for removal of Cr (VI) and organic pollutants. *Chemical Engineering Journal*. 2020 Jul 1; 391:123607.
 13. Bui TH, Lee W, Jeon SB, Kim KW, Lee Y. Enhanced Gold (III) adsorption using glutaraldehyde-cross-linked chitosan beads: Effect of crosslinking degree on adsorption selectivity, capacity, and mechanism. *Separation and Purification Technology*. 2020 Oct 1; 248:116989.
 14. Pooresmaeil M, Namazi H. Facile preparation of pH-sensitive chitosan microspheres for delivery of curcumin; characterization, drug release kinetics and evaluation of anticancer activity. *International journal of biological macromolecules*. 2020 Nov 1; 162:501-11.
 15. Li G, Row KH. Deep eutectic solvents skeleton typed molecularly imprinted chitosan microsphere coated magnetic graphene oxide for solid-phase microextraction of Chlorophenols from environmental water. *Journal of separation science*. 2020 Mar; 43(6):1063-70.
 16. Zhang Q, Zhuang S, Wang J. Biosorptive removal of cobalt (II) from aqueous solutions using magnetic cyanoethyl chitosan beads. *Journal of Environmental Chemical Engineering*. 2020 Dec 1; 8(6):104531.
 17. Xia H, Li A, Man J, Li J, Li J. Fabrication of multi-layered microspheres based on phase separation for drug delivery. *Micromachines*. 2021 Jun 19; 12(6):723.
 18. Jiang H, Hu X, Li Y, Ngai T. A green and facile strategy for the fabrication of all-natural porous proteinaceous microspheres. *Materials Chemistry Frontiers*. 2021; 5(10):3897-902.
 19. Li G, Yu Y, Han W, Zhu L, Si T, Wang H, Li K, Sun Y, He Y. Solvent evaporation self-motivated continual synthesis of versatile porous polymer microspheres via foaming-transfer. *Colloids and Surfaces A: Physicochemical and Engineering Aspects*. 2021 Apr 20; 615:126239.
 20. Qiao L, Wang S, Wang T, Yu S, Guo S, Du K. High-strength and low-swelling chitosan/cellulose microspheres as a high-efficiency adsorbent for dye removal. *Cellulose*. 2021 Sep; 28:9323-33.
 21. Xu JH, Li SW, Tostado C, Lan WJ, Luo GS. Preparation of Monodispersed chitosan microspheres and in situ encapsulation of BSA in a co-axial microfluidic device. *Biomedical micro devices*. 2009 Feb; 11:243-9.
 22. Wong SK, Lawrencia D, Supramaniam J, Goh



- BH, Manickam S, Wong TW, Pang CH, Tang SY. In vitro digestion and swelling kinetics of thymoquinone-loaded Pickering emulsions incorporated in alginate-chitosan hydrogel beads. *Frontiers in Nutrition*. 2021 Oct 4; 8:752207.
23. Rehman S, Ranjha NM, Raza MR, Hanif M, Majed A, Ameer N. Enteric-coated Calcium alginate hydrogel beads: a promising tool for colon targeted drug delivery system. *Polymer Bulletin*. 2021 Sep; 78:5103-17.
 24. Moin A, Wani SU, Osmani RA, Abu Lila AS, Khafagy ES, Arab HH, Gangadharappa HV, Allam AN. Formulation, characterization, and cellular toxicity assessment of tamoxifen-loaded silk fibroin nanoparticles in breast cancer. *Drug Delivery*. 2021 Jan 1; 28(1):1626-36.
 25. Afrazi M, Yazdani M. Determination of the effect of soil particle size distribution on the shear behavior of sand. *Journal of Advanced Engineering and Computation*. 2021 Jun 30; 5(2):125-34.
 26. Caputo F, Vogel R, Savage J, Vella G, Law A, Della Camera G, Hannon G, Peacock B, Mehn D, Ponti J, Geiss O. Measuring particle size distribution and mass concentration of Nano plastics and micro plastics: addressing some analytical challenges in the sub-micron size range. *Journal of Colloid and Interface Science*. 2021 Apr 15; 588:401-17.
 27. Sharifi F, Jahangiri M, Nazir I, Asim MH, Ebrahimnejad P, Hupfauf A, Gust R, Bernkop-Schnürch A. Zeta potential changing nanoemulsions based on a simple zwitterion. *Journal of Colloid and Interface Science*. 2021 Mar 1; 585:126-37.
 28. Dewangan HK, Sharma A, Mishra A, Singour P. Mucoadhesive microspheres of atorvastatin calcium: rational design, evaluation and enhancement of bioavailability. *Microscopy*. 2021 Jul 1; 19:20.
 29. Mahor S, Chandra P, Prasad N. Design and IN-VITRO Evaluation of Float-adhesive Famotidine Microspheres by using Natural Polymers for Gastro retentive Properties. *Indian J. Pharm. Educ. Res*. 2021 Apr 1; 55:407-17.
 30. Li X, Ji X, Chen K, Ullah MW, Yuan X, Lei Z, Cao J, Xiao J, Yang G. Development of finasteride/PHBV@ polyvinyl alcohol/chitosan reservoir-type microspheres as a potential embolic agent: from in vitro evaluation to animal study. *Biomaterials Science*. 2020; 8(10):2797-813.
 31. Li X, Chen K, Ji X, Yuan X, Lei Z, Ullah MW, Xiao J, Yang G. Microencapsulation of poorly water-soluble finasteride in polyvinyl alcohol/chitosan microspheres as a long-term sustained release system for potential embolization applications. *Engineered Science*. 2020 Dec 14; 13(2):106-20.